Frontiers in Earth Sciences

2

Victor A. Melezhik *Editor-in-Chief*
Anthony R. Prave · Anthony E. Fallick
Eero J. Hanski · Aivo Lepland
Lee R. Kump · Harald Strauss *Editors*

Reading the Archive of Earth's Oxygenation

Volume 2: The Core Archive of the Fennoscandian Arctic Russia – Drilling Early Earth Project

EXTRA MATERIALS
extras.springer.com

Springer

Frontiers in Earth Sciences

Series Editors: J.P. Brun, O. Oncken, H. Weissert, W.-C. Dullo

Victor A. Melezhik *Editor-in-Chief*
Anthony R. Prave
Anthony E. Fallick
Eero J. Hanski
Aivo Lepland
Lee R. Kump
Harald Strauss *Editors*

Reading the Archive of Earth's Oxygenation

Volume 2: The Core Archive of the Fennoscandian Arctic Russia - Drilling Early Earth Project

Springer

Editor-in-Chief
Victor A. Melezhik
Geological Survey of Norway,
Trondheim

Centre of Excellence in Geobiology
University of Bergen
Norway

Editors
Anthony R. Prave
Department of Earth Science
University of St Andrews
United Kingdom

Anthony E. Fallick
Environmental Research Centre
Scottish Universities
East Kilbride
United Kingdom

Eero J. Hanski
Department of Geosciences
University of Oulu
Oulu
Finland

Aivo Lepland
Geological Survey of Norway
Trondheim
Norway

Lee R. Kump
Department of Geosciences
Pennsylvania State University
Pennsylvania
USA

Harald Strauss
Institut für Geologie
Westfälische Wilhelms-Univ. Münster
Münster
Germany

Additional material to this book can be downloaded from http://extras.springer.com.

ISSN 1863-4621
ISBN 978-3-642-29658-1 ISBN 978-3-642-29659-8 (eBook)
DOI:10.1007/978-3-642-29659-8
Springer Heidelberg New York Dordrecht London

Library of Congress Control Number: 2012944339

Printed on acid-free paper

Springer is part of Springer Science+Business Media (www.springer.com)

Dedication

The editors respectfully dedicate this three-volume treatise to Dr. Alexander Predovsky of the Geological Institute of the Russian Academy of Sciences in Apatity. He is one of the earliest explorers of the Precambrian geology in Russian Fennoscandia, and his half century of active work on the geochemistry of sedimentary and igneous rocks provided important foundations for the current understanding of Palaeoproterozoic stratigraphy, geochemistry of sedimentary and volcanic processes and ore formation in the region.

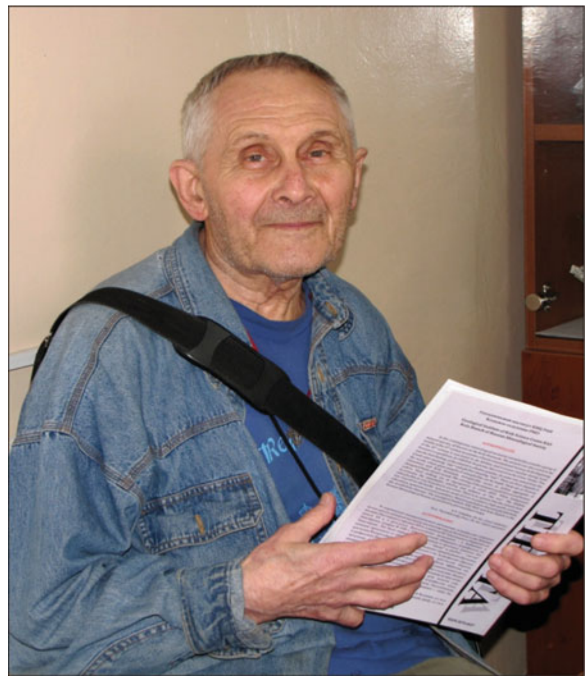

Contributors to Three-Volume Treatise "Reading the Archive of Earth's Oxygenation", Volume 2: "The Core Archive of the Fennoscandian Arctic Russia: Drilling Early Earth Project"

Maria M. Bogina Institute of Geology of Ore Deposits, Petrography, Mineralogy and Geochemistry, Russian Academy of Sciences (IGEM RAS), Moscow, Russia

Alex T. Brasier Scottish Universities Environmental Research Centre, East Kilbride, Glasgow, Scotland, UK

Ronald Conze Scientific Drilling, GFZ German Research Centre for Geosciences, Potsdam, Germany

Alenka E. Črne Geological Survey of Norway, Trondheim, Norway

Karl Fabian Geological Survey of Norway, Trondheim, Norway

Anthony E. Fallick Scottish Universities Environmental Research Centre, East Kilbride, Glasgow, Scotland, UK

Eero J. Hanski Department of Geosciences, University of Oulu, Oulu, Finland

Aivo Lepland Geological Survey of Norway, Trondheim, Norway

Zhen-Yu Luo Department of Geosciences, University of Oulu, Oulu, Finland / Key Laboratory of Isotope Geochronology and Geochemistry, Guangzhou Institute of Geochemistry, Chinese Academy of Sciences, Guangzhou, China

Pavel V. Medvedev Institute of Geology, Karelian Research Centre, Russian Academy of Sciences, Petrozavodsk, Russia

Victor A. Melezhik Geological Survey of Norway, Trondheim, Norway / Centre for Geobiology, University of Bergen, Bergen, Norway

Melanie Mesli Geological Survey of Norway, Trondheim, Norway

Anthony R. Prave Department of Earth Science, University of St. Andrews, St Andrews, Scotland, UK

Alexander E. Romashkin Institute of Geology, Karelian Research Centre, Russian Academy of Sciences, Petrozavodsk, Russia

Dmitry V. Rychanchik Institute of Geology, Karelian Research Centre, Russian Academy of Sciences, Petrozavodsk, Russia

Paula E. Salminen Department of Geosciences and Geography, University of Helsinki, Helsinki, Finland

Evgenii V. Sharkov Institute of Geology of Ore Deposits, Petrography, Mineralogy and Geochemistry, Russian Academy of Sciences (IGEM RAS), Moscow, Russia

Reviewers for Three-Volume Treatise: Reading the Archive of Earth's Oxygenation

Prof. Ariel Anbar
Arizona State University, Tempe, AZ, USA
Dr. Victor Balagansky
Geological Institute, Apatity, Russia
Prof. Mark Barley
University of Western Australia, Crawley, Australia
Prof. Jochen Brocks
The Australian National University, Canberra, Australia
Prof. Louis Derry
Cornell University, Ithaca, NY, USA
Prof. Anton Eisenhauer
GEOMAR, Kiel, Germany
Prof. Anthony E. Fallick
Scottish Universities Environmental Research Centre, East Kilbride, Scotland, UK
Prof. David Fike
Washington University, St. Louis, USA
Prof. Karl Föllmi
University of Lausanne, Lausanne, Switzerland
Prof. Robert Frei
University of Copenhagen, Copenhagen, Denmark
Dr. Dieter Garbe-Schönberg
Christian-Albrechts-Universität, Kiel, Germany
Prof. Eero Hanski
University of Oulu, Oulu, Finland
Prof. Raimo Lahtinen
Geological Survey of Finland, Espoo, Finland
Prof. Michail Mints
Geological Institute, Moscow, Russia
Prof. David Mossman
Mount Allison University, Sackville, NB, Canada
Prof. Richard Ojakangas
University of Minnesota, Duluth, USA
Prof. John Parnell
University of Aberdeen, Aberdeen, Scotland, UK
Prof. Adina Paytan
University of California, Santa Cruz, USA
Dr. Bernhard Peucker-Ehrenbrink
Woods Hole Oceanographic Institution, Woods Hole, MA, USA

Prof. Igor Puchtel
University of Maryland, College Park, MD, USA
Prof. Robert Raiswell
University of Leeds, Leeds, UK
Prof. Robert Riding
University of Tennessee, USA/
Cardiff University, Wales, UK
Dr. Nathaniel Sheldon
University of Michigan, Ann Arbor, MI, USA
Dr. Graham Shields-Zhou
University College, London, UK
Dr. Craig Storey
University of Portsmouth, Portsmouth, UK
Prof. Kari Strand
Thule Institute, University of Oulu, Oulu, Finland
Prof. Frances Westall
Centre de Biophysique Moléculaire, CNRS, Orléans, France

Acknowledgements

The idea of making an atlas with comprehensive descriptions and illustrations of the Palaeoproterozoic rocks from the Fennoscandian Shield was initiated in 2009 during a workshop held in Trondheim, Norway, under the auspices of the International Continental Scientific Drilling Program (ICDP). Starting from this workshop, a plan was developed and finalised. Chris Bendall, Senior Editor for Springer, is acknowledged for encouragement and editorial supervision of the project.

The three-volume set has three major underpinnings. The first is many years of research in Precambrian geology of the Fennoscandian Shield by many workers, and we acknowledge particularly the support of the Geological Survey of Norway; the University of Oulu, Finland; and the Institute of Geology, Petrozavodsk, Russia.

The second is the unique core material obtained during the drilling operations by the Fennoscandian Arctic Russia – Drilling Early Earth Project (FAR-DEEP). The drilling operations were largely supported by the ICDP and by additional funding from several other agencies and institutions. We are grateful for the financial support to the Norwegian Research Council (NFR), the German Research Council (DFG), the National Science Foundation (NSF), the NASA Astrobiology Institutes, the Geological Survey of Norway (NGU) and the Centre of Excellence in Geobiology, the University of Bergen, Norway. The core archive and associated analytical work were supported by NGU, the Scottish Universities Environmental Research Centre (SUERC) and by the Pennsylvanian State University.

The third is a multidisciplinary approach to investigate complicated geological processes. This was provided by the international scientific community and we acknowledge the support of many universities in Scandinavia, Europe and the USA.

Many individuals helped in the preparation of the drilling operations and offered logistical support. We are sincerely grateful to Anatoly Borisov (Kola Geological Information and Laboratory Centre) for providing geological assistance for precise positioning of drillholes in unexposed, boggy and forested terrains in the Imandra/Varzuga Greenstone Belt. Stanislav Sokolov (Kola Mining Metallurgical Company) is acknowledged for logistic support and geological guidance in the Pechenga Greenstone Belt. Logistical organisation of the drilling operations and core transport across national borders by the State Company Mineral, St. Petersburg, Russia, is appreciated. The Finnish company, SMOY, performed the drilling.

Many organisations and people have provided rock samples, photographs, SEM images and permission to use figures. Thanks are due to the Geological Museum of the Department of Geosciences, University of Oulu; Geological Museum of the Geological Institute, Kola Science Centre, Apatity; Geological Survey of Finland; and to the following people: Wlady Altermann, Lawrence Aspler, Alex Brasier, Ronald Conze, Alenka Črne, Kathleen Grey, Jens Gutzmer, Eero Hanski, Emmanuelle Javaux, Yrjö Kähkönen, Vadim Kamenetsky, Reino Kesola, Andrew Knoll, Kauko Laajoki, Reijo Lampela, Aivo Lepland, Kevin Lepot, Zhen-Yu Luo, Vladimir Makarikhin, Tuomo Manninen, Jukka Marmo, Nicola McLoughlin, Pavel Medvedev, Victor Melezhik, Satu Mertanen, Tapani Mutanen, Lutz Nasdala, Richard W. Ojakangas, Domenic Papineau, Petri Peltonen, Vesa Perttunen, Vladimir Pozhilenko, Anthony Prave, Igor Puchtel, Jorma Räsänen, Pentti Rastas, Raimo Ristimäki, Alexander Romashkin, Dmitry Rychanchik, Ronny Schoenberg, Evgeny Sharkov, Igor Sokolov, Hubert Staudigel, Kari Strand, Sergey Svetov, Vladimir Voloshin, Frances Westall, Grant Young, Valery Zlobin and Bouke Zwaan.

Unpublished geochemical data were kindly provided by the Geological Survey of Finland, Zhorzh Fedotov, Valery Smol'kin and Peter Skuf'in. Permission to use published material was kindly given by the Royal Society of Edinburgh, Elsevier, John Wiley and Sons and Blackwell Publishing Ltd.

The book preparation was supported by the NFR (grant 191530/V30 to Victor Melezhik), Natural Environment Research Council (grant NE/G00398X/1 to Anthony Fallick, Anthony Prave and Daniel Condon), DFG (grants Str281/29, 32, 35 to Harald Strauss), NASA (grant NNA09DA76A to Lee Kump), NSF (grant EAR 0704984 to Lee Kump) and the Academy of Finland (grant 116845 to Eero Hanski).

To be embedded in the family of science always requires sacrifices such as time lost in family contact. We wish to extend our gratitude to our families for patience, understanding and constant encouragement.

Finally and most importantly, the editors wish to thank those colleagues and students who will use and read these books or some parts of them. We hope that this will encourage them to reach a more complete understanding of those processes that played an important role in the irreversible modification of Earth's surface environments and in shaping the face of our emerging aerobic planet. We would also like to thank those scientists who will use the offered advantage of rich illustrative material linked to the core collection to undertake new research projects.

Preface to Volume 2

Earth's present-day environments are the outcome of a 4.5-billion-year period of evolution reflecting the interaction of global-scale geological and biological processes. Punctuating that evolution were several extraordinary events and episodes that perturbed the entire Earth system and led to the creation of new environmental conditions, sometimes even to fundamental changes in how planet Earth operated. One of the earliest and arguably the greatest of these events was a substantial increase (orders of magnitude) in the atmospheric oxygen abundance, sometimes referred to as the Great Oxidation Event. Given our present knowledge, this oxygenation of the terrestrial atmosphere and the surface ocean, during the Palaeoproterozoic Era between 2.4 and 2.0 billion years ago, irreversibly changed the course of Earth's evolution. Understanding why and how it happened and what its consequences were are among the most challenging problems in Earth sciences.

The three-volume treatise entitled "Reading the Archive of Earth's Oxygenation" (1) provides a comprehensive review of the Palaeoproterozoic Eon with an emphasis on the Fennoscandian Shield geology; (2) serves as an initial report of the preliminary analysis of one of the finest lithological and geochemical archives of early Palaeoproterozoic Earth history, created under the auspices of the International Continental Scientific Drilling Programme (ICDP); (3) synthesises the current state of our understanding of aspects of early Palaeoproterozoic events coincident with and likely related to Earth's progressive oxygenation with an emphasis on still-unresolved problems that are ripe for and to be addressed by future research. Combining this information in three coherent volumes offers an unprecedented cohesive and comprehensive elucidation of the Great Oxidation Event and related global upheavals that eventually led to the emergence of the modern aerobic Earth System.

The format of these books centres on high-quality photo-documentation of Fennoscandian Arctic Russia – Drilling Early Earth Project (FAR-DEEP) cores and natural exposures of the Palaeoproterozoic rocks of the Fennoscandian Shield. The photos are linked to geochemical data sets, summary figures and maps, time-slice reconstructions of basinal and palaeoenvironmental settings that document the response of the Earth system to the Great Oxidation Event. The emphasis on a thorough, well-illustrated characterisation of rocks reflects the importance of sedimentary and volcanic structures that form a basis for interpreting ancient depositional environments, and chemical, physical and biological processes operating on Earth's surface. Most of the structural features are sufficiently complex as to challenge the description by other than a visual representation, and high-quality photographs are themselves a primary resource for presenting essential information. Although nothing can replace the wealth of information that a geologist can obtain from examining an outcrop first hand, the utility of photographs offers the next best source of data for assessing and evaluating palaeoenvironmental reconstructions. This three-volume treatise will, thus, act as an information source and guide to other researchers and help them identify and interpret such features elsewhere, and will serve as an illustrated guidebook to the Precambrian for geology students.

Finally, the three-volume treatise provides a link to the FAR-DEEP core collection archived at the Geological Survey of Norway. These drillcores are a unique resource that can be used to solve the outstanding problems in understanding the causes and consequences of the multiple processes associated with the progressive oxygenation of terrestrial environments. It is anticipated that the well-archived core will provide the geological foundation for future research aimed at testing and generating new ideas about the Palaeoproterozoic Earth. The three-volume treatise will be of interest to researchers involved directly in studying this hallmark period in Earth history, as well as professionals and students interested in Earth System evolution in general.

Volume 2: “The Core Archive of the Fennoscandian Arctic Russia – Drilling Early Earth Project” provides a description of the newly generated archive hosting ICDP’s FAR-DEEP drill cores through key geological formations in Russian Fennoscandia. The book contains several hundred high-quality, representative photographs illustrating 3,650 m of fresh, uncontaminated core documenting a series of global palaeoenvironmental upheavals linked to the Great Oxidation Event. The core exhibits sedimentary and volcanic formations that record a transition from anoxic to oxic Earth surface environments, the first global glaciation (the Huronian glaciation), an unprecedented perturbation of the global carbon cycle (the Lomagundi-Jatulian Event), a radical increase in the size of the seawater sulphate reservoir, an apparent upper mantle oxidising event, the Earth’s earliest documented sedimentary phosphates, one of the greatest accumulations of organic matter (the Shunga Event) and generation of the Earth’s earliest supergiant petroleum deposit. The volume highlights the potential of the FAR-DEEP core archive for future research of the Great Oxidation Event and the biogeochemical cycles operating during that time.

Welcome to the illustrative journey through one of the most exciting periods of planet Earth!

Contents to Volume 1

Contents to Volume 2

Contents to Volume 3

Part V

FAR-DEEP Core Archive and Database

5.1 FAR-DEEP Core Archive and Database

Aivo Lepland, Melanie Mesli, Ronald Conze, Karl Fabian, Anthony E. Fallick, and L.R. Kump

The collection of FAR-DEEP (Fennoscandian Arctic Russia Drilling Early Earth Project) cores includes material from 15 drill holes through 2,500–2,000 Ma sedimentary and volcanic successions in Russian Fennoscandia amounting to a total core length of 3,650 m, the recovered material provides one of the best available rock records for studying the major environmental upheavals during the early Palaeoproterozoic, and for assessing timing, causes and effects of the rise of atmospheric oxygen (Melezhik et al. 2010). The great scientific promise that the FAR-DEEP material holds for current and future studies of the Palaeoproterozoic Earth calls for a dedicated cataloguing system that facilitates an easy capture of generated technical, geological and geochemical data on the cores, and provides means for effective sharing of information among researchers. In order to make the unique material available for future studies, all cores and related documentation have been thoroughly archived in the core repository and the database, respectively. This archive is linked tightly to the user-friendly and Web-accessible database system serving as an essential gateway for exploring the full potential of the material.

5.1.1 Drilling Information System and Core Archive

The technical and geological data gathered during the FAR-DEEP drilling operations and throughout the subsequent archiving and research phases have been catalogued using the Drilling Information System (DIS; Fig. 5.1) developed by the Operational Support Group at the International Continental Scientific Drilling Program (ICDP). This system has been employed in many ICDP and IODP (Integrated Ocean Drilling Program) projects since 1998 to catalogue the drilling and core information. The DIS contains a toolkit that allows the user to build customised data management systems and environments and infrastructures for drilling projects (Conze et al. 2007, 2010). It has tools to define, generate and administrate data structures, a graphical user interface, a Web interface and other elements necessary for a drilling information management system. A central component of the DIS is a set of generic data structures (templates) and dictionaries for scientific drilling purposes. These templates and dictionaries can be adapted and modified to meet project needs, for example to capture cuttings data, hard-rock core data, long-term monitoring data and engineering data. The graphical user interface is utilized to generate input forms for entering data (Fig. 5.2), report templates and data views. Other tools allow the user to build specific data import modules (data pumps) and to generate customised internet Web pages documenting progress during the project. To visualise data, the DIS generates Scalable Vector Graphics, which are used in tools such as the Downhole-Measurement-Profile-Builder and the Lithological-Profile-Builder.

The deployment of the DIS is highly scalable, ranging from a standalone installation on a laptop with runtime versions of Microsoft Access® and Microsoft SQL Server®[1], to a client–server installation with one or more DIS database servers and several client computers (Fig. 5.3). All client computers can either be connected directly to the DIS server on the network, or through the XDIS Web interface. During the course of FAR-DEEP, the database structure and the set-up of input forms have been continuously updated to meet the specific needs of the project. Data entry during the drilling campaign in the field (May–October 2007) primarily included technical information about drilling progress and

A. Lepland (✉)
Geological Survey of Norway, Postboks 6315 Sluppen, Trondheim NO-7491, Norway
e-mail: Aivo.Lepland@NGU.NO

[1] Microsoft Access and Microsoft SQL Server are either registered trademarks or trademarks of Microsoft Corporation in the United States and/or other countries.

V.A. Melezhik et al. (eds.), *Reading the Archive of Earth's Oxygenation*, Volume 2: The Core Archive of the Fennoscandian Arctic Russia – Drilling Early Earth Project, DOI 10.1007/978-3-642-29659-8_1, © Springer-Verlag Berlin Heidelberg 2013

sectioning and placement of core into core boxes. Daily transfer of notes by drillers and on-site geologists into the database in the field facilitated the correction of occasional inconsistencies and secured correct recording of depths and other parameters. Core box images and preliminary lithostratigraphic descriptions provided an immediate overview of the obtained rock record. To secure all these recordings and to update the central database and the Web portal, a cell phone was used to connect the field laptop to the internet (Fig. 5.3) and the entire database, including numerical data, text data and images, was uploaded to the ICDP server in Potsdam on a daily basis.

The core archive process at the repository of the Geological Survey of Norway (NGU) started in March 2008, and was completed in December 2008. The archiving included (1) high-resolution photographing of core boxes in dry and wet conditions (Fig. 5.4), (2) magnetic susceptibility measurements of whole round core at c. 0.2 m intervals using a Bartington ring sensor, (3) core splitting by sawing, (4) image scanning of split (slabbed) core (Fig. 5.5), (5) detailed lithological description (Fig. 5.4), and (6) routine sampling at intervals of about 7 m for general geochemical and petrographic characterisation of the core. All core boxes have been documented throughout the whole core processing and sampling period. The individual core sections are stored in certain slots of core boxes as shown in Fig. 5.3. The boxes are aligned in portrait orientation with top at the upper left corner of the box. The flat faces of the split core sections have been scanned digitally using the DMT CoreScan® Colour I[2] before sampling (Fig. 5.5). The original images are generated as bitmap (bmp) files using a resolution of 5 pixel/mm and full RGB colour values. For the Web presentation these images have been reduced to smaller JPG image files.

5.1.2 FAR-DEEP Samples

Access to samples from the FAR-DEEP cores requires the submission of a sample request that details the information about the planned project, applied methods, funding situation and timeline of the study, and specifies the core intervals to be sampled. The exact positions of requested samples can be defined either by using the descriptions, images and analytical data available on the Web without a visit to the repository, or by working directly with cores in the core repository. Upon approval of the request by the project's principle investigator (PI), the details about the requested samples are entered into the DIS creating a unique number for each new sample. This ID allows to identify any sample, and to search for the sample related information about expedition, site and hole, core and section, box and slot number, interval in section, core depth, requesting researcher and the purpose of the sample request. The same array of information is printed on the sample label (Fig. 5.6). Two sets of these labels are printed; one is placed on a sample bag and the other is affixed to the slot divider in the core box, next to the sample. To facilitate the visual tracking of distributed samples, and to show the core sections that are still available for sampling, the core boxes are photographed during each sampling session (Fig. 5.4). This photographing is done after pencil marking the samples on cores and affixing the labels on slot dividers, but before the extraction. Only after the completion of these steps the samples can be extracted from the cores. A record is also made in DIS if a sample with unique ID is further divided into different parts (subsamples and aliquots) for various analyses on splits of the same sample. A strict sampling procedure secures a full track record of sample distribution, essential for planning new research initiatives on the FAR-DEEP material, and for avoiding overlapping projects and conflicts of interest.

The ICDP and the Integrated Ocean Drilling Program (IODP) are using the same naming conventions for addressing any recovered material related to a certain drillhole as a common standard. In case of FAR-DEEP, a label starts with the expedition number 5,018 followed by the site number, and drillhole ID, e.g. 5018_1_A represents the first drillhole at site 1. The cores and sections are numbered accordingly: e.g. 5018_1_A_3_2 representing the second section of the third core run. In addition, all cores and all samples taken will have unique identifiers assigned, an International Geo Sample Number (IGSN). The IGSN system is operated by an international consortium of science operators, research institutions and geological survey organizations. Any IGSN can be resolved through the internet to display information about the identified sample. IGSNs allow unambiguous identification and referencing and can be used to link samples to associated metadata about the original project, core repository, laboratory, and analytical data (Lehnert and Klump 2008).

5.1.3 FAR-DEEP Archive Samples, Dataset and Analytical Methods

The archive sample set consisting of 554 specimens was analysed for whole-rock major and trace elements, carbonate composition, C and S abundances, and was used for making thin sections. Selected specimens were analysed for isotopic composition of S in sulphides, C in organic matter, and C, O and Sr in carbonates. All documentation obtained during the

[2] DMT CoreScan is either a registered trademark or trademark of Deutsche Montan Technologie GmbH & Co.KG in Germany and/or other countries.

archiving process including stratigraphic logs, general geochemical and isotopic datasets and magnetic susceptibility profiles was catalogued using the DIS. Tables of geochemical data (Fig. 5.7) and stratigraphic logs were available for the FAR-DEEP partners on the password protected Web site (Fig. 5.8) prior to the main research phase that started with the sampling party at the NGU's core repository in March 2009. Although the archiving documentation resulted in a dataset with great scientific value in itself, its main purpose was to provide a general overview of cores to be used for planning specific projects and detailed sampling schemes. A significant part of this documentation on the FAR-DEEP cores obtained during archiving including lithostratigraphic descriptions, major and trace element data and magnetic susceptibility profiles is presented in core description chapters of this book.

5.1.3.1 Magnetic Susceptibility Measurements

K. Fabian

Magnetic susceptibility on whole cores was measured using a Bartington MS2 with ring sensors MS2C/D = 68 mm or MS2C/D = 133 mm. Measurements were taken at ~20 cm intervals with 10 s integration time. Measurement positions were chosen such that within a range of ± D the cylindrical core was completely intact without cracks or other volume defects. This ensures that >95% of the sensor volume-response curve is covered by the sample and each susceptibility measurement represents an average over the same volume.

The instrument reading K′ is then corrected for the ratio between core diameter (d = 51 mm) and the sensor diameter (D) using the relations given in the MS2 instrument manual. The corresponding correction factors f are f = 1.4 for D = 68 mm and f = 0.33 for D = 133 mm. The diameter corrected K* values are calculated using

$$K^* = K'/f$$

These K* values represent precise relative volume susceptibilities, which are consistent between different sensors and different cores. To obtain absolute magnetic susceptibility (K) in SI, these K* values must be calibrated using homogenous cores of known susceptibility. Using density corrected sand samples, cross-calibrated to MnO_2 using a MS2B sensor, we determined a calibration factor of $\beta = 11.7 \pm 0.7$, such that estimates of absolute volume susceptibility K can be obtained from

$$K = \beta K^*$$

To avoid calibration errors, all data plots use the internally consistent relative susceptibility K*. Note that volume susceptibility K is a pure number without unit, but depends on the unit system used. Here we use SI units and numerical values are typically given in mSI, e.g. K = 100 μSI = $100*10^{-6}$ SI.

5.1.3.2 Acid-Soluble Major and Trace Element Analysis of Carbonates by ICP-AES

Acid-soluble (10% HCl) Fe, Ca, Mg, Mn and Sr concentrations were determined by inductively coupled plasma-atomic emission spectrometry (ICP-AES) at NGU using a Thermo Jarrell Ash ICP 61 instrument, with detection limits for Fe, Mg, Ca, Mn and Sr being 5, 100, 200, 0.2 and 2 $\mu g \cdot g^{-1}$, respectively. The precision (1σ), including element extraction, was ± 10%.

5.1.3.3 Major and Trace Element Analysis by XRF

Major and trace elements were determined by X-ray fluorescence spectrometry (XRF) at the NGU, using a Philips PW 1480 X-ray spectrometer equipped with a Rh X-ray tube. For major elements 0.6 g of pre-ignited (1,000°C) fine-ground sample material was mixed with 4.2 g $Li_2B_4O_7$ and fused to a bead in a CLAISSE FLUXER-BIS. For trace element analysis 1.2 g (±0.005 g) of Hoechst wax and 5.4 g (±0.005 g) of sample were mixed in a Spex Mixer/Mill for at least 1 min. The mixture was then pressed to a pellet in a Herzog pelletizing press (approx. 20kN, time = 20 s). Detection limits for major element oxides were 0.01 % except for SiO_2 (0.5%), Al_2O_3 (0.02%), MgO (0.04%) and Na_2O (0.1%). Detection limits for trace elements were ≤ 10 $\mu g \cdot g^{-1}$ except for Ce (20 $\mu g \cdot g^{-1}$), Sb (15 $\mu g \cdot g^{-1}$), Hg (20 $\mu g \cdot g^{-1}$), Tl (20 $\mu g \cdot g^{-1}$), I (10 $\mu g \cdot g^{-1}$), Cl (0.05%), F (0.1%) and S (0.02%). The precision (1σ) was typically around 2 % for the major oxides present.

5.1.3.4 Carbon and Sulphur Analysis by CS Elemental Analyser

The Leco SC-444 analyser at the NGU was employed for measuring the concentration of total carbon (TC), total organic carbon (TOC) and total sulphur (TS) using 100–350 mg of powdered samples. The TOC content was determined on acid-treated (10% HCl) material. Detection limits for TS, TC and TOC were 0.01 wt.%, 0.07 wt.% and

0.1 wt.%, respectively, and the precision was $< 2.5\%$ (1σ) for TC, and $< 10\%$ (1σ) for TS and TOC.

5.1.3.5 Carbon and Oxygen Isotope Analyses of Carbonates

A.E. Fallick

Carbon isotope analyses of whole-rock carbonate samples were performed at the Scottish Universities Environmental Research Centre (SUERC) in Glasgow, using the phosphoric acid method of McCrea (1950), modified by Rosenbaum and Sheppard (1986) for operation at high temperature. C isotope ratios in carbonate of the bulk rock sample were measured on purified CO_2 released from a sample weight equivalent to 1–2 mg carbonate. The mass spectrometer was either a triple collector, dual inlet VG SIRA 10 or a triple collector continuous-flow AP 2003. Analyses were calibrated against NBS 19 and reproducibility (1σ) was generally better than $\pm$ 0.2 ‰. Carbon isotope data are reported in per mil (‰) relative to the V-PDB standard.

5.1.3.6 Carbon Isotope Analysis of Organic Carbon

L. Kump

Prior to extraction, the samples were gently washed with deionised distilled water to remove any surface contamination. 5–10 g samples were then milled with a Retsch PM100 Ball Mill resulting in a homogeneous powdered sample (size ~75 µm). The powdered samples were decarbonated in centrifuge tubes using HCl (10 %) for 24 h and rinsed repeatedly to remove acidity (checked with pH paper). The samples were then freeze-dried for analysis. For carbon isotope ratio determination a continuous flow Elemental Analyzer (COSTECH ECS4010)-Isotope Ratio Mass Spectrometer (EA-IRMS: Thermo Delta Plus) system via an open split interface (CONFLO III) was employed. Sample sizes varied from 1 to 30 mg depending on organic carbon content. Approximately 10 mg of V_2O_5 was added to aid combustion. Carbon isotope data are reported in per mil (‰) relative to the V-PDB standard.

5.1.4 FAR-DEEP Information on the Web

The FAR-DEEP project is represented by a project Web site (http://far-deep.icdp-online.org) on the ICDP Web portal (http://www.icdp-online.org). This platform has been used to provide basic information about the project (e.g. the proposal, who are the principal investigators (PIs), and who are the members of the central science team). It was utilized to distribute news and daily updates for the interested general public including representatives of printed and electronic media. Parallel to the public platform an internal area (Fig. 5.8) has been created to provide more detailed information about the visited sites, drilled holes, recovered core, lithological descriptions, and distributed samples along with common reference data sets authorized by the FAR-DEEP Central Science Team. The science team members were permitted to download these data sets and add the results of their own analyses enabling all members to share the available information. During the operational drilling phase, the core handling and sampling, and the following moratorium period only the registered members of the FAR-DEEP science team had access to core data (‘Internal Data FARDEEP’).

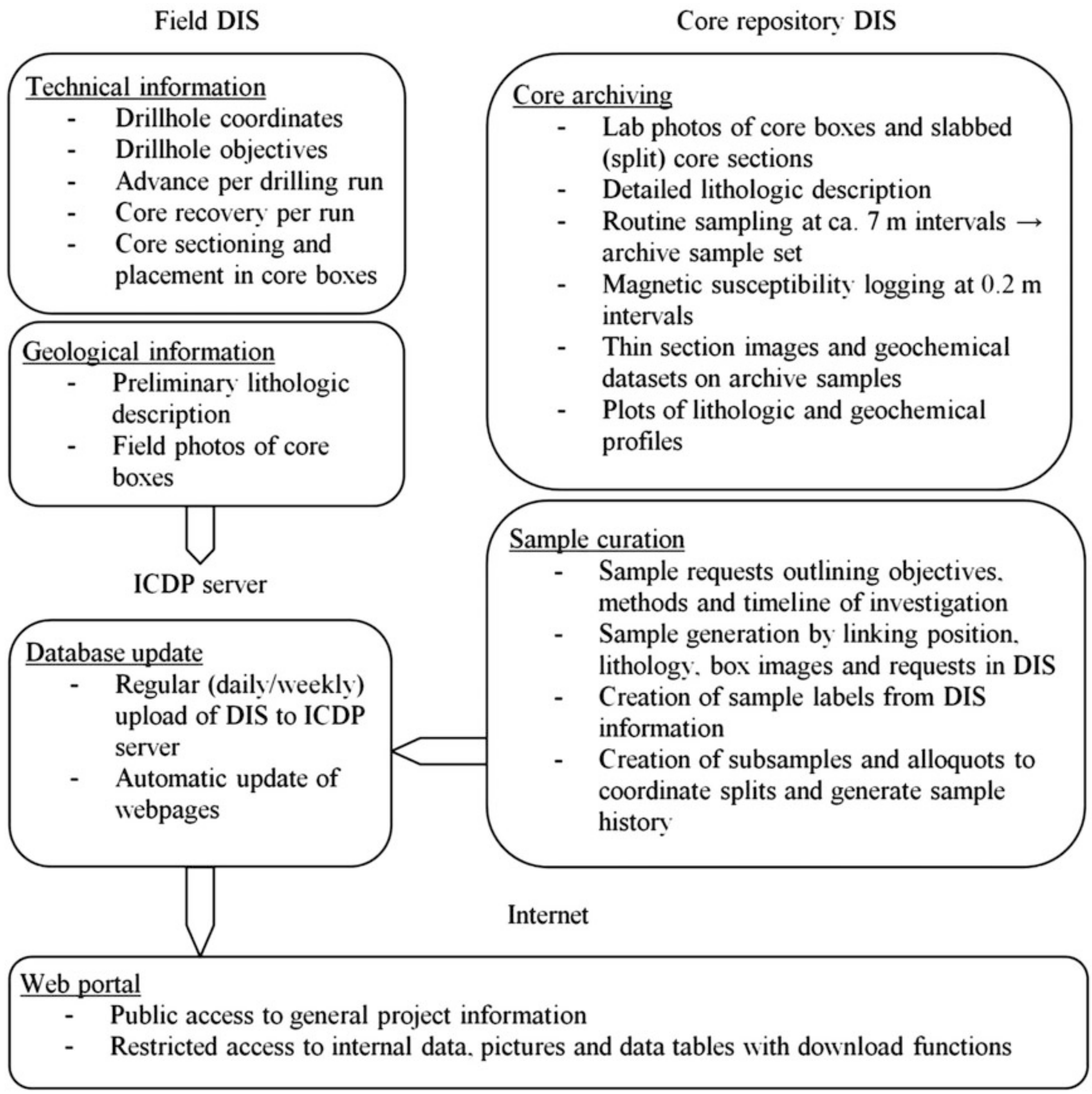

Fig. 5.1 A scheme showing the conceptual design and functions of the drilling information system (DIS), and various data types entered during the course of drilling-based research projects both in the field and in the core repository

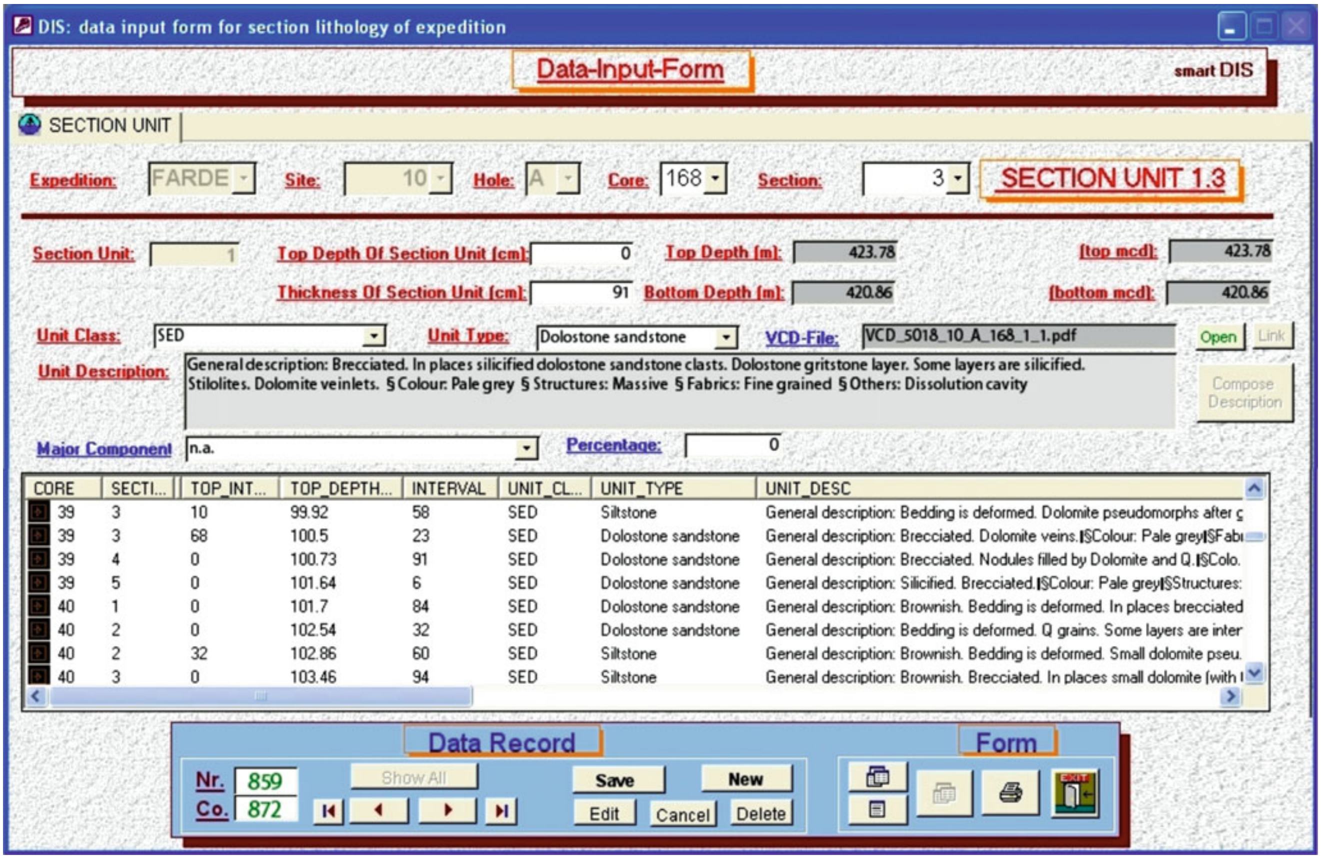

Fig. 5.2 Screenshot of the DIS data-input-form for entering lithologic descriptions of defined core intervals

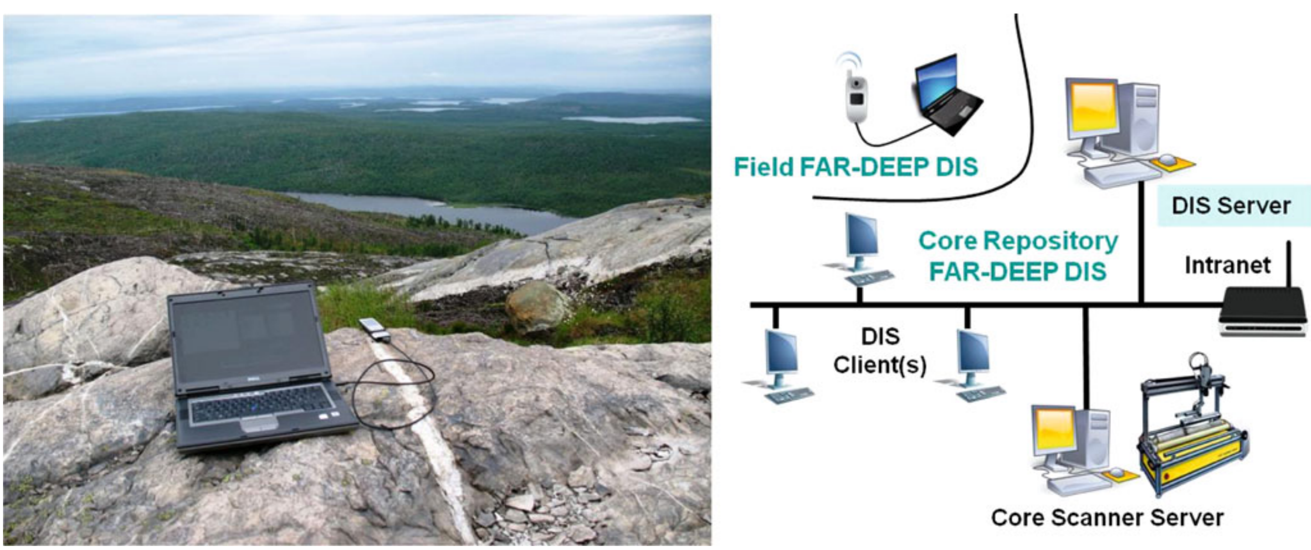

Fig. 5.3 To the *left*: The cell phone was used during the field expedition for the transfer of data from the FAR-DEEP DIS server installed on a standalone laptop to the central ICDP server in Potsdam (Photo from the hill top (best cell phone signal) in the Pechenga Greenstone Belt near the Russian-Norwegian border). To the *right*: Diagram showing the configuration of the local area network at the NGU core repository during core processing and sampling

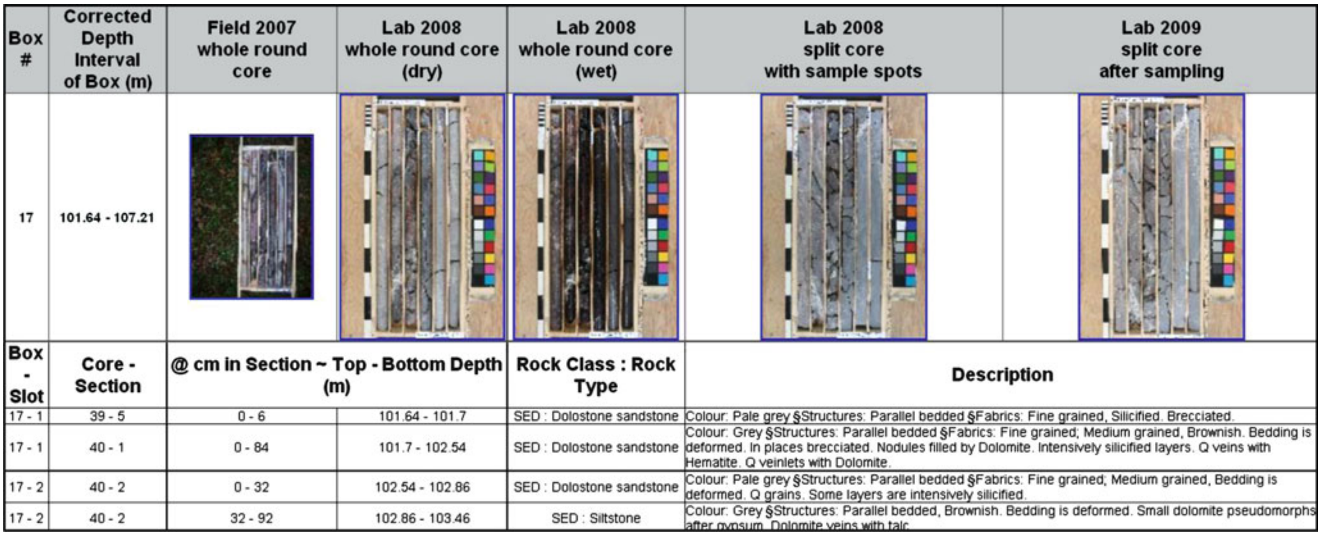

Box #	Corrected Depth Interval of Box (m)	Field 2007 whole round core	Lab 2008 whole round core (dry)	Lab 2008 whole round core (wet)	Lab 2008 split core with sample spots	Lab 2009 split core after sampling
17	101.64 - 107.21					

Box - Slot	Core - Section	@ cm in Section ~ Top - Bottom Depth (m)		Rock Class : Rock Type	Description
17 - 1	39 - 5	0 - 6	101.64 - 101.7	SED : Dolostone sandstone	Colour: Pale grey §Structures: Parallel bedded §Fabrics: Fine grained, Silicified. Brecciated.
17 - 1	40 - 1	0 - 84	101.7 - 102.54	SED : Dolostone sandstone	Colour: Grey §Structures: Parallel bedded §Fabrics: Fine grained; Medium grained, Brownish. Bedding is deformed. In places brecciated. Nodules filled by Dolomite. Intensively silicified layers. Q veins with Hematite. Q veinlets with Dolomite.
17 - 2	40 - 2	0 - 32	102.54 - 102.86	SED : Dolostone sandstone	Colour: Pale grey §Structures: Parallel bedded §Fabrics: Fine grained; Medium grained, Bedding is deformed. Q grains. Some layers are intensively silicified.
17 - 2	40 - 2	32 - 92	102.86 - 103.46	SED : Siltstone	Colour: Grey §Structures: Parallel bedded, Brownish. Bedding is deformed. Small dolomite pseudomorphs after gypsum. Dolomite veins with talc.

Fig. 5.4 Screenshot from the FAR-DEEP internal data webpage showing an example set of images of core box 17 from hole 10A including the initial lithological description of the core

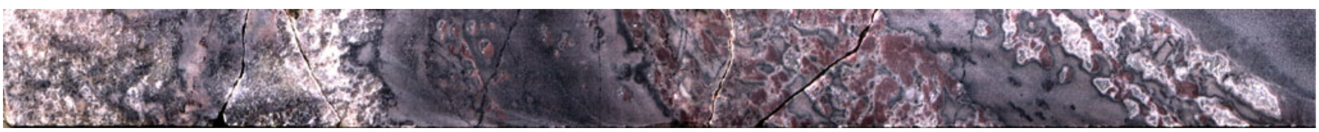

Fig. 5.5 Example of a 53 cm long scanned core section from drillhole 10A

SBM003106964

ICDP FAR-DEEP Expedition 2007

Exp. /Site/ H /Core/ T/Sec/Half /Interval

5018 10 A 40 Z 2 W 0.0 - 13.0

MSP0001 A Depth:**102.54**

Box: **17 -2**

Victor Melezhik

11/14/2008 1:29:31 PM

Fig. 5.6 Example of a printed sample label. From *top*: Unique sample identifier, same as bar code, expedition title, sample label, sample request number (bar code *below*), drilling depth (m), core box and slot number, name of sample request proponent, date and time of sampling

XRF - Major Elements Data

Select hole 5018_10_A Go Current selection: **5018_10_A**

View Header-File
download data in ASCII-Format (Info) or Excel-Format

Hole	Core	Section	Sample ID	Top Depth m	SiO2 %	Al2O3 %	Fe2O3 %	TiO2 %	MgO %	CaO %	Na2O %	K2O %	MnO %	P2O5 %	LOI %	SUI Maj %
Clear																
5018_10_A	1	1	3106772	19.57	36.7	0.931	1.08	0.045	13.9	18.2	<0.1	0.476	0.103	0.190	27.0	98.7
5018_10_A	6	1	3106784	27.1	9.78	0.307	0.224	0.028	19.3	27.4	<0.1	0.153	0.214	0.051	41.1	98.6
5018_10_A	9	3	3106802	34.71	1.54	0.176	0.161	<0.01	20.8	30.2	<0.1	0.082	0.064	0.041	45.3	98.3
5018_10_A	13	2	3106816	41.22	13.6	0.026	0.051	<0.01	18.3	26.7	<0.1	<0.01	0.066	0.063	39.6	98.3
5018_10_A	18	2	3106830	49.17	25.0	0.087	0.043	<0.01	16.3	23.0	<0.1	0.053	0.061	0.032	34.1	98.8
5018_10_A	21	2	3106852	56.91	48.1	12.4	6.13	0.408	17.0	1.72	0.17	4.04	0.055	0.191	8.12	98.4
5018_10_A	23	2	3106866	62.46	7.48	0.642	0.346	0.030	19.6	28.3	<0.1	0.354	0.019	0.023	41.8	98.6
5018_10_A	25	2	3106880	69.48	37.7	0.682	0.320	0.025	13.7	18.2	<0.1	0.324	0.018	0.033	28.2	99.2
5018_10_A	30	2	3106904	76.19	27.2	5.44	2.57	0.224	14.9	17.5	<0.1	3.89	0.026	0.183	27.8	99.8
5018_10_A	31	4	3106914	80.55	34.1	9.28	5.30	0.439	12.8	12.5	0.12	4.66	0.188	0.094	20.2	99.6
5018_10_A	34	1	3106934	87.39	7.35	0.175	0.082	0.012	19.7	28.6	<0.1	0.129	0.050	0.014	42.0	98.1
5018_10_A	37	2	3106950	95.02	53.4	10.2	5.03	0.418	9.63	5.30	0.18	4.60	0.051	0.158	10.6	99.5
5018_10_A	40	1	3106962	101.7	11.9	1.90	0.918	0.083	18.6	24.9	<0.1	1.59	0.018	0.036	38.4	98.3
5018_10_A	42	2	3106968	107.47	50.3	6.17	2.93	0.236	9.60	9.55	<0.1	3.77	0.033	0.121	16.0	98.8
5018_10_A	48	1	3106980	114.6	54.8	2.95	1.27	0.113	9.29	11.2	<0.1	1.88	0.016	0.076	17.7	99.3
5018_10_A	50	4	3106992	122.08	22.2	0.125	0.091	<0.01	16.4	24.1	<0.1	0.037	0.016	0.178	35.4	98.6
5018_10_A	53	2	3107010	128.44	57.9	2.14	1.05	0.087	9.11	10.7	<0.1	1.02	0.011	0.060	17.0	99.1
5018_10_A	54	4	3107020	133.14	2.95	0.452	0.202	0.018	20.8	30.1	<0.1	0.176	<0.01	0.024	44.1	98.8
5018_10_A	57	2	3107030	140.44	18.9	0.045	0.020	<0.01	17.3	25.2	<0.1	0.028	0.012	0.066	37.0	98.5
5018_10_A	61	2	3107052	149.48	17.3	0.309	0.095	0.015	18.0	25.2	<0.1	0.251	0.039	0.094	37.8	99.1
5018_10_A	64	2	3107066	156.3	9.06	0.049	<0.01	<0.01	19.5	28.3	<0.1	0.029	0.046	0.030	41.3	98.3
5018_10_A	67	1	3107082	164.45	23.0	0.040	<0.01	<0.01	16.4	23.8	<0.1	0.025	0.039	0.012	35.9	99.3
5018_10_A	71	1	3107098	173.42	46.5	7.91	3.53	0.295	11.7	8.87	0.25	5.76	0.028	0.145	14.8	99.8
5018_10_A	73	3	3107116	181.57	40.1	7.14	2.96	0.304	14.6	11.0	0.86	3.48	0.043	0.114	19.2	99.8

Fig. 5.7 Screenshot from the FAR-DEEP internal data webpage showing an example set of available geochemical data on cores

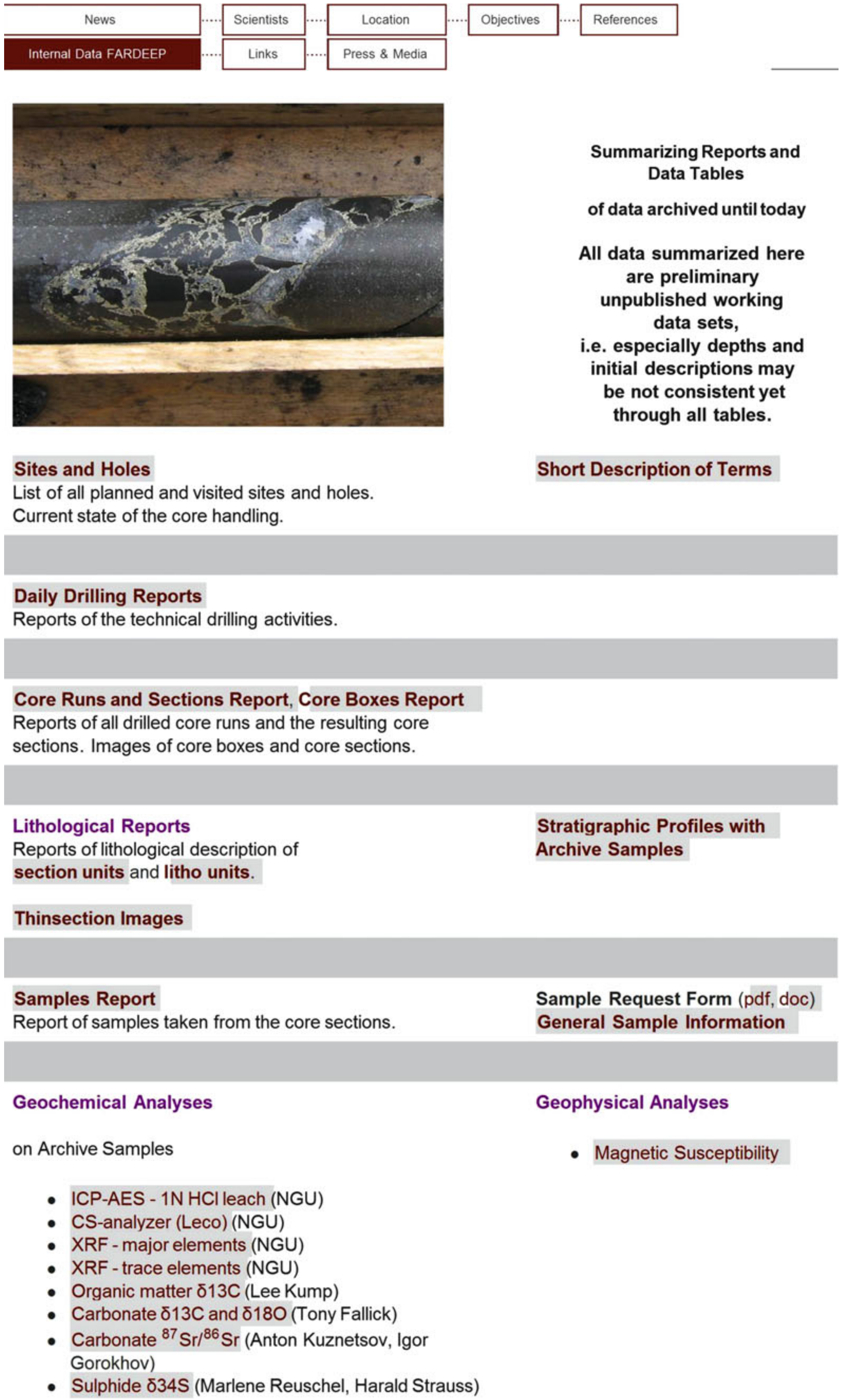

News · Scientists · Location · Objectives · References
Internal Data FARDEEP · Links · Press & Media

Summarizing Reports and Data Tables

of data archived until today

All data summarized here are preliminary unpublished working data sets, i.e. especially depths and initial descriptions may be not consistent yet through all tables.

Sites and Holes
List of all planned and visited sites and holes.
Current state of the core handling.

Short Description of Terms

Daily Drilling Reports
Reports of the technical drilling activities.

Core Runs and Sections Report, **Core Boxes Report**
Reports of all drilled core runs and the resulting core sections. Images of core boxes and core sections.

Lithological Reports
Reports of lithological description of **section units** and **litho units**.

Stratigraphic Profiles with Archive Samples

Thinsection Images

Samples Report
Report of samples taken from the core sections.

Sample Request Form (pdf, doc)
General Sample Information

Geochemical Analyses

on Archive Samples

- ICP-AES - 1N HCl leach (NGU)
- CS-analyzer (Leco) (NGU)
- XRF - major elements (NGU)
- XRF - trace elements (NGU)
- Organic matter δ13C (Lee Kump)
- Carbonate δ13C and δ18O (Tony Fallick)
- Carbonate $^{87}Sr/^{86}Sr$ (Anton Kuznetsov, Igor Gorokhov)
- Sulphide δ34S (Marlene Reuschel, Harald Strauss)

Geophysical Analyses

- Magnetic Susceptibility

Fig. 5.8 Screenshot from the FAR-DEEP internal data webpage showing the types of technical information and geological data available on cores

References

Conze R, Wallrabe-Adams HJ, Graham C, Krysiak F (2007) Joint data management on ICDP projects and IODP mission specific platform expeditions. Sci Drill 4:32–34

Conze R, Krysiak F, Reed J, Chen J-C, Wallrabe-Adams H-J, Graham C, and the New Jersey Shallow Shelf Science Team, Wennrich V, and the Lake El'gygytgyn Science Team (2010) New integrated data analyses software components. Sci Drill 9:30–31

Lehnert K, Klump J, (2008) Facilitating research in mantle petrology with geoinformatics, S. 9IKCA00250, Copernicus Society, Frankurt. [online] Available from: http://www.cosis.net/abstracts/9IKC/00250/9IKC-A-00250-1.pdf

McCrea JM (1950) On the isotopic chemistry of carbonates and a paleotemperature scale. J Chem Phys 18:849–857

Melezhik VA, Lepland A, Romashkin A, Rychanchik DV, Mesli M, Finne TE, Conze R, and the FAR-DEEP Scientists (2010) FAR-DEEP (Fennoscandian Arctic Russia – Drilling Early Earth Project) a remarkable opportunity for studying the great oxidation event. Sci Drill 9:23–29

Rosenbaum JM, Sheppard SMF (1986) An isotopic study of siderites, dolomites and ankerites at high temperatures. Geochim Cosmochim Acta 50:1147–1159

Part VI

FAR-DEEP Core Descriptions and Rock Atlas

6.1 The Imandra/Varzuga Greenstone Belt

Victor A. Melezhik, Anthony R. Prave, Aivo Lepland, Eero J. Hanski, Alexander E. Romashkin, Dmitry V. Rychanchik, Zhen-Yu Luo, Evgenii V. Sharkov, Maria M. Bogina, Alex T. Brasier, and Anthony E. Fallick

6.1. The Imandra/Varzuga Greenstone Belt

Victor A. Melezhik

The Late Archaean-Early Palaeoproterozoic transition (2500–2000 Ma) represents a hallmark period when the Earth System experienced a series of fundamental upheavals. Among them, the most important was the establishment of an oxygen-rich atmosphere (sometimes referred to as the Great Oxidation Event) and the emergence of an aerobic biosphere. Associated with this, either incidentally or causally, was a cascade of other prominent, global-scale events that considerably modified Earth's surface environments, either temporarily or permanently; these are reviewed in Parts 1 and 8 in full, and detailed in Part 7. Briefly mentioned here, these include: the severe and global climatic event known as the Huronian glaciation; an unprecedented perturbation of the global carbon cycle, the large-magnitude Lomagundi-Jatuli positive excursion of $\delta^{13}C_{carb}$, lasted over 160 Ma; radical changes in the phosphorus and sulphur cycles resulting in accumulation of the first-known massive sulphates and sedimentary phosphates; a radical modification in recycling of organic matter leading to the emergence of a new ^{13}C-depleted carbon reservoir in the form of carbonate concretions; and an unprecedented accumulation of organic-rich sediments and formation of the earliest supergiant petroleum deposits.

However, the combined processes that led to the irreversible alteration of Earth's surface environments during the late Archaean-Palaeoproterozoic transition are not well understood. Deciphering the causative relationships of those global palaeoenvironmental events as a whole represents one of the most challenging fundamental problems in the geosciences. Essential for advancing knowledge in this area of research is a continuous rock record that would provide information on the various processes operating through the 2500–2000 Ma interval. Because of limited exposures through key stratigraphic intervals, potential anthropogenic contamination and modification by recent oxidation and weathering, drilling provides the solution: to obtain the appropriate and informative rock record and enhance the likelihood of success in furthering understanding of the hallmark geological events of this time interval.

The ICDP FAR-DEEP implemented in the eastern part of the Fennoscandian Shield made available for the international scientific community 3650 m of core that was obtained by drilling numerous holes in the Onega Basin, Pechenga and Imandra/Varzuga Greenstone belts. Stretching over a distance of c. 800 km, from the Barents Sea in the north to Lake Onega in the south (Fig. 6.1), these three regions collectively provided complementary geological information that, when combined, produces a composite, representative and comprehensive geological record of the most important global events known from Fennoscandia through the 2440–1970 Ma interval. Well-characterised, well-archived and well-illustrated cores from these three regions are presented below.

Geology and stratigraphy of the Imandra/Varzuga Greenstone Belt is comprehensively described in Chap. 4.1. The brief geological outline presented here aims to provide a scientific context and background information for the FAR-DEEP implemented in this area.

The Imandra/Varzuga Greenstone Belt represents a southeastern part of the c. 800-km-long, discontinuously developed system of supracrustal belts extending from northern Norway through northern Finland, and then into NW Russia where it crosses the Kola Peninsula (Fig. 6.1).

The stratigraphic subdivision of the Imandra/Varzuga Greenstone Belt was established in the 1960s, refined in the 1970s, and has remained essentially unchanged since

V.A. Melezhik (✉)
Geological Survey of Norway, Postboks 6315 Sluppen, NO-7491 Trondheim, Norway

Centre for Geobiology, University of Bergen, Allegaten 41, Bergen N-5007, Norway
e-mail: victor.melezhik@ngu.no

V.A. Melezhik et al. (eds.), *Reading the Archive of Earth's Oxygenation*, Volume 2: The Core Archive of the Fennoscandian Arctic Russia – Drilling Early Earth Project, DOI 10.1007/978-3-642-29659-8_2, © Springer-Verlag Berlin Heidelberg 2013

Zagorodny et al. (1982) published a summary monograph on the regional geology. The belt comprises the Imandra/Varzuga Supergroup (e.g., Melezhik and Sturt 1994), which was originally subdivided into the Strel'na, Varzuga and Tominga series (Zagorodny et al. 1982), later renamed as groups (Melezhik and Sturt 1994). The groups were further subdivided into several formations, as shown in the generalised lithostratigraphic column (Fig. 6.2).

The lower age limit of the Strel'na Group is constrained by the presence of 2504.4 ± 1.5 Ma gabbro-norite pebbles in the basal conglomerates of the Kuksha Sedimentary Formation (Fig. 6.2). The upper age limit of the Tominga Group is older than 1907 ± 18 Ma as based on the timing of emplacement of subvolcanic trachydacite (U-Pb-zircon, Skuf'in et al. 2006). Consequently, the deposition of the Imandra/Varzuga Supergroup spans the important transition from largely anoxic to oxic conditions (Fig. 6.2). Three holes drilled by FAR-DEEP in the western part of the belt (Fig. 6.3) targeted: (1) the temporal record of mass-independently fractionated sulphur as a proxy for atmospheric oxygen (the Seidorechka Sedimentary Formation); (2) the onset of the Huronian-age glaciations (the Polisarka Sedimentary Formation); and (3) the Palaeoproterozoic perturbation of the global carbon cycle as recorded in marine carbonates.

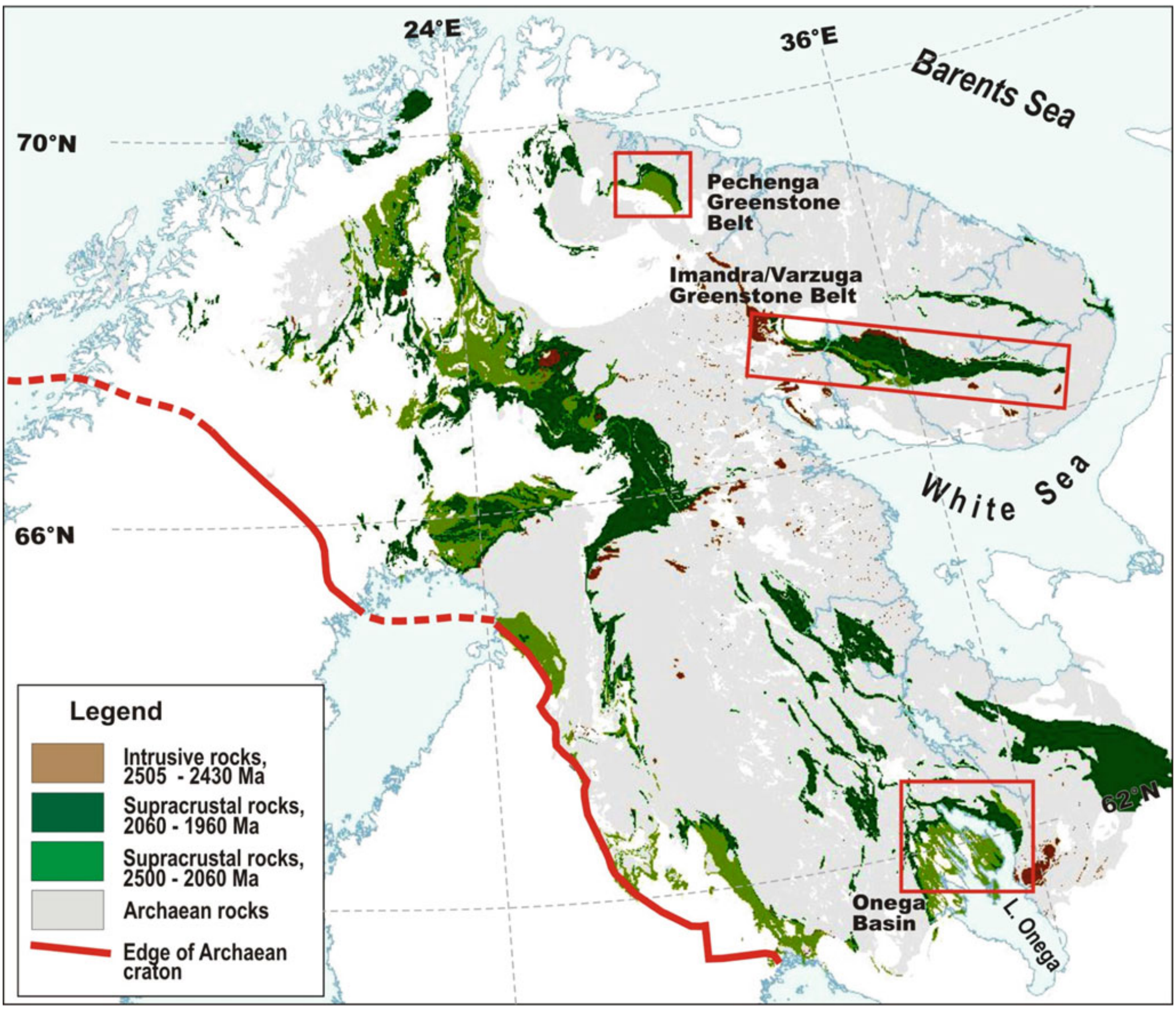

Fig. 6.1 Geological map showing the occurrence of early Palaeoproterozoic supracrustal complexes and 2505–2430 Ma layered gabbro-norite intrusions in the eastern part of the Fennoscandian Shield. Framed are the three regions where the FAR-DEEP drilling operations were carried out (Geological map modified after Koistinen et al. (2001))

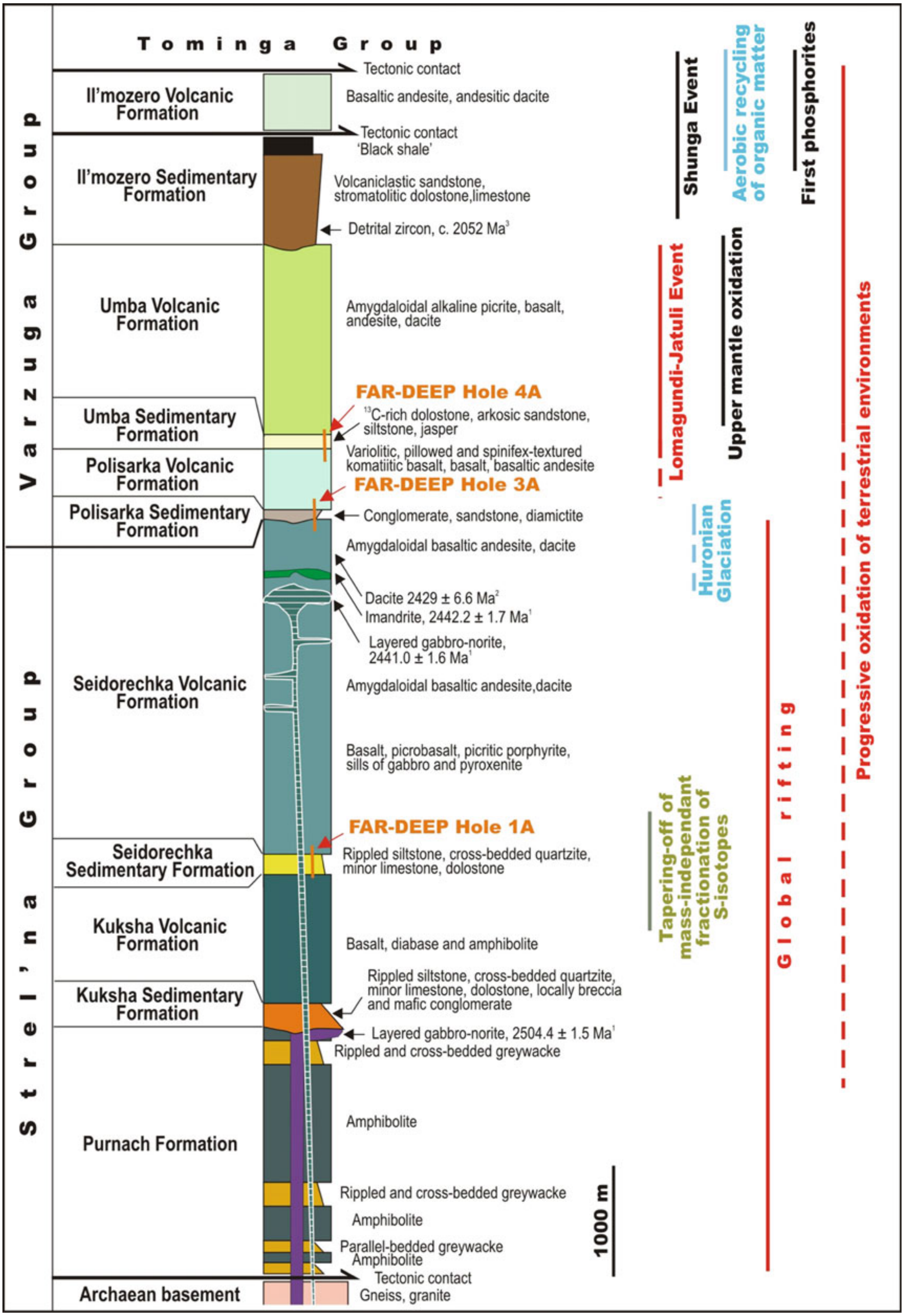

Fig. 6.2 Simplified lithological column through the Stre'lna and Varzuga groups of the Imandra/Varzuga Greenstone Belt. Also shown is how the evolution of the Imandra/Varzuga Greenstone Belt is related to global palaeoenvironmental events. *Superscripts* denote radiometric ages from (1) Amelin et al. (1995), (2) Vrevsky et al. (2010), and (3) Martin et al. (2010)

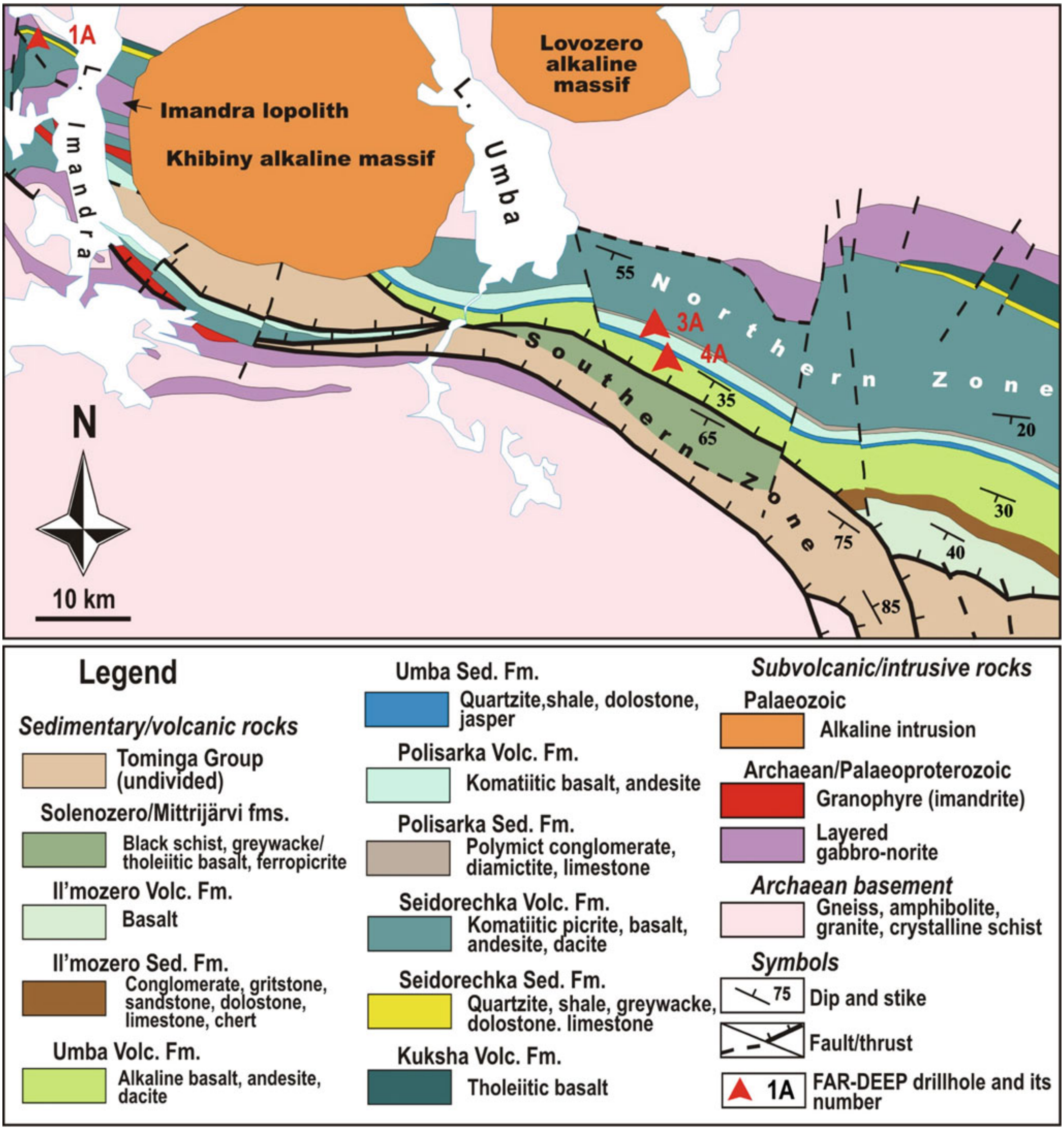

Fig. 6.3 Simplified geological map of the western part of the Imandra/Varzuga Greenstone Belt showing the locations of FAR-DEEP Holes 1A, 3A, 4A (Geological map modified after Zagorodny et al. (1982))

References

Amelin YuV, Heaman LM, Semenov VS (1995) U-Pb geochronology of layered mafic intrusions in the eastern Baltic Shield: implications for the timing and duration of Palaeoproterozoic continental rifting. Precambrian Res 75:31–46

Koistinen T, Stephens MB, Bogatchev V, Nordgulen Ø, Wennesträm M, Korhonen J (Comps) (2001) Geological map of the Fennoscandian Shield, scale 1:2 000 000, Espoo, Trondheim, Uppsala, Moscow

Martin AP, Condon DJ, Prave AR, Melezhik VA, Fallick A (2010) Constraining the termination of the Lomagundi-Jatuli positive isotope excursion in the Imandra-Varzuga segment (Kola Peninsula, Russia) of the North Transfennoscandian Greenstone Belt by high-precision ID-TIMS, AGU, Dec 2010, pp 13–17

Melezhik VA, Sturt BA (1994) General geology and evolutionary history of the early Proterozoic Polmak-Pasvik-Pechenga-Imandra/Varzuga-Ust'Ponoy Greenstone Belt in the north-eastern Baltic Shield. Earth Sci Rev 36:205–241

Skuf'in PK, Bayanova TB, Mitrofanov FP (2006) Isotope age of subvolcanic graditoid rocks of the early Proterozoic Panarechka volcanotectonic structure, Kola Peninsula. Proc Russ Acad Sci Earth Sci 409:774–778

Vrevsky AB, Bogomolov ES, Zinger TF, Sergeev SA (2010) Polychronic sources and isotopic age of the volcanogenic complex (Arvarench unit) of the Imandra-Varzuga structure, Kola Peninsula. Dokl Trans Russ Acad Sci 431(1):386–389

Zagorodny VG, Predovsky AA, Basalaev AA, Batieva ID, Borisov AE, Vetrin VR, Voloshina ZM, Dokuchaeva VS, Zhangurov AA, Kozlova NE, Kravtsov NA, Latyshev LN, Melezhik VA, Petrov VP, Radchenko MK, Radchenko AT, Smolkin VF, Fedotov ZhA (1982) Imandra/Varzuga Zone of the Karelides, Geology, geochemistry, history of development). Nauka (Science), Leningrad, 280p, in Russian

6.1.1 Seidorechka Sedimentary Formation: FAR-DEEP Hole 1A and Neighbouring Quarries

Victor A. Melezhik, Anthony R. Prave, Aivo Lepland, Eero J. Hanski, Alexander E. Romashkin, Dmitry V. Rychanchik, Zhen-Yu Luo, Evgenii V. Sharkov, and Maria M. Bogina

Scientific Targets

– Tectonic and depositional settings
– Geochemical rock record at the dawn of the Great Oxidation Event and Huronian glaciation(s)
– Mass-dependent and mass-independent sulphur isotope fractionation
– Carbon-isotopic composition of seawater
– Provenance composition
– Microfossil record
– Radiometric age constraint of the deposition

Hole 1A samples the Seidorechka Sedimentary Formation in the western Imandra-Varzuga Greenstone Belt (Figs. 6.1, 6.2, 6.3, and 6.4). The Seidorechka Sedimentary Formation has a depositional age of c. 2442 Ma (Amelin et al. 1995) and provides a rock record from a transitional period in atmosphere evolution from largely anoxic to a state of its incipient oxidation, as indicated by sulphur isotope data elsewhere (e.g. Bekker et al. 2004; Hannah et al. 2004). In addition, the Seidorechka Sedimentary Formation represents one of the rare pre-Huronian marine carbonate-bearing successions (Figs. 6.5, 6.6, and 6.7). Thus the drillhole has a great potential to address the global sulphur and carbon cycles at the dawn of the Great Oxidation Event, and prior to the first global Huronian-time glaciation(s) (Figs. 6.8 and 6.9). Ongoing research has shown the presence of sulphides containing mass-independently fractionated sulphur isotopes, characteristic for sediments pre-dating the Great Oxidation Event (see Chap. 7.1).

The 200.3-m-long Hole 1A intersects the entire thickness of the Seidorechka Sedimentary Formation (120 m), and also includes 60 m of overlying, chemically monotonous basalts of the Seidorechka Volcanic Formation and c. 13 m of underlying basalts of the Kuksha Volcanic Formation (Fig. 6.5). Magnetic susceptibility tests reveal that the basalts in both volcanic formations are characterised by low values whereas the Seidorechka Sedimentary Formation rocks show variable values ranging between 60 and 5600 μSI (K* = 5 to 500 × 10^{-6} SI) (Fig. 6.7). Chemical composition of analysed samples is presented in Appendices 1–3. Figure 6.7 shows stratigraphic profiles of selected major and trace elements as well as magnetic susceptibility.

V.A. Melezhik (✉)
Geological Survey of Norway, Postboks 6315 Sluppen, NO-7491 Trondheim, Norway

Centre for Geobiology, University of Bergen, Allegaten 41, Bergen N-5007, Norway

The Kuksha Volcanic Formation

The Kuksha Volcanic Formation has been intersected in the lower part of the core between 187 and 200 m. It displays a massive, coarse-grained igneous texture and no obvious volcanic structures are observed, thus we do not know whether the unit is intrusive or extrusive. Phenocrysts (2 mm) of albitised plagioclase and amphibolised clinopyroxene occur in a fine-grained groundmass of albitised plagioclase, amphibolised clinopyroxene and magnetite. At 40.67 m, crystals of blue-green amphibole are observed. The groundmass is cross-cut by veins of quartz + mica + apatite. These veins, and general alteration elsewhere in the formation, are recording metasomatism by a fluid whose composition would be felsic, probably close to a granitoid composition. This may affect the entire bulk rock chemistry and should be considered in future geochemical reconstructions. Chemically the Kuksha basalts are tholeiitic with c. 7–8 wt.% MgO (Fig. 6.10a) and 0.8–0.9 wt.% TiO_2 (Appendix 1). Chromium and nickel levels are c. 240–250 and 110–130 ppm, respectively. Incompatible elements have low abundances, as exemplified by TiO_2 (0.8–0.9 wt.%), P_2O_5 (<0.1 wt.%), Zr (40–50 ppm) and Nb (2–3 ppm). One sample analysed for rare earth elements shows a slightly LREE-enriched chondrite-normalised REE pattern with the level of REEs being 10–20 times chondritic (Fig. 6.11a). Our major element data are similar to earlier chemical analyses of rocks from the Kuksha Volcanic Formation, given by Fedotov et al. (1982) and Fedotov (1983a) (Fig. 6.10b).

The Seidorechka Sedimentary Formation

The Seidorechka Sedimentary Formation has a depositional base on the Kuksha basalt and the contact is marked by intensive calcitisation and sericitisation (Appendix 1) extending from the contact down to a depth of 7 m (Figs. 6.5 and 6.12am, an). This alteration has been interpreted as a palaeoweathering crust (e.g. Fedotov et al. 1982). The formation comprises a succession of interbedded greywacke, siltstone, shale with minor quartz sandstone, dolostone and limestone, and it has been informally subdivided into five lithostratigraphic units, from base to top: Sandstone-Siltstone,

V.A. Melezhik et al. (eds.), *Reading the Archive of Earth's Oxygenation*, Volume 2: The Core Archive of the Fennoscandian Arctic Russia – Drilling Early Earth Project, DOI 10.1007/978-3-642-29659-8_2, © Springer-Verlag Berlin Heidelberg 2013

Dolostone, Quartzite, Limestone-Shale and Shale members (Fig. 6.5). Photos of core and rocks exposed in nearby quarries (Fig. 6.12) provide a detailed documentation of major lithological features throughout the stratigraphy.

The Sandstone-Siltstone Member

In outcrop, the thickness of the Sandstone-Siltstone member varies from c. 10 m in the easternmost exposures to more than 50 m in the western quarries. The thickness variation occurs over a horizontal distance of 5 km and results from progressive west-to-east truncation of the section beneath an angular unconformity at the base of the overlying Dolostone member, or at the base of the Quartzite member when the Dolostone member is completely eroded (Figs. 6.5 and 6.12p). The basal bed of the Sandstone-Siltstone member has a transitional contact with underlying mafic volcanic rocks through a calcite-quartz-sericite schist zone (weathered basalts? Fig. 6.12am). Above the contact, the member changes progressively from siltstone-shale (Fig. 6.12am) into sandstone-siltstone-shale (Fig. 6.12ak, al, ao–aq), and then sandstone-shale (Fig. 6.12ar–at). The Sandstone-Siltstone member has a moderate Al_2O content (16–17 wt. %), a variable K_2O/Na_2O ratio, and is low in sulphur (0.3–0.6 wt.%).

The Dolostone Member

The Dolostone member (Figs. 6.5 and 6.12ab–aj) is a 1–2-m-thick, laterally discontinuous unit. It consists of a lower part containing lenticular beds and irregularly shaped lenses of pale grey dolograinstone intercalated with green-grey shale (Fig. 6.12o, ab, ae, af), and an upper part of pale grey, variably calcitised dolomicrosparite (Fig. 6.12ab, aj) with minor dolarenites (Fig. 6.12r) and dolorudites (Fig. 6.12q, ac, af, ag). In numerous places, the shale appears to have been injected as thin filaments and flame-like structures into the dolostone beds (Fig. 6.12ag, ah). Some beds show dissolution cavities filled with sparry calcite and shale (Fig. 6.12ad, ai). The member has a depositional base on a surface that defines a cryptic shale-on-shale angular unconformity. The upper contact with the overlying Quartzite Member is erosional and, in places, the Dolostone member is entirely cut out (Fig. 6.12p).

The Quartzite Member

The Quartzite member lies with an erosive, discordant contact on rocks of either the Sandstone-Siltstone or Dolostone members (Fig. 6.12n–r). It is c. 15 m thick and is composed of cross-bedded, silica- or dolomite-cemented quartz and arkosic sandstone with ripple and wrinkle marks, and desiccated mudstone layers (Fig. 6.12e, k–m, q, s–y). The basal bed contains abundant, angular blocks and clasts derived from the underlying Dolostone member (Fig. 6.12z, aa) and; the middle part is a 2-m-thick bed of sandstone-shale couplets. Quartzites have a variable SiO_2 content (76–94 wt. %) depending on clast and cement composition. The latter ranges from silica-rich to calcitic and dolomitic.

The Limestone-Shale Member

The Limestone-Shale member is c. 30 m thick and has a gradational contact with the underlying Quartzite member. The member consists of dolostone-limestone and siltstone-shale couplets (Fig. 6.12b–d, f–j) with a c. 7-m-thick bed of variably dolomitised, sparitic limestone in the middle (Fig. 6.5). Thinner layers of sparitic limestone also occur irregularly through the member. Minor beds of massive greywacke and quartz arenite are also present. Limestones are impure with 45–60 wt.% of non-carbonate components, and variable Mg/Ca ratios, depending on the degree of dedolomitisation (Fig. 6.12f–h). Shales have moderate Al_2O_3 abundances (9–13 wt.%), due to a variable content of dolomitic and calcitic components, and K_2O/Na_2O ratios are <1. The TOC content in the *Limestone-Shale member* is around 0.15 wt.%.

The Shale Member

The Shale member is a c. 50-m-thick, lithologically homogeneous unit. It is composed mainly of shale (Fig. 6.12a) with rare beds of limestone, greywacke and siltstone. There is a pronounced upward increase in Al_2O_3, TiO_2, P_2O_5, Na_2O, Cr, Ni, and V concentrations (Fig. 6.7). This may be due to a gradual increase of influx of reworked/weathered mafic volcanic material. The top of the Seidorechka Sedimentary Formation is placed at the appearance of the first volcanic unit of the overlying Seidorechka Volcanic Formation. The basalts of the Seidorechka Volcanic Formation rest sharply on the Shale member.

The Seidorechka Volcanic Formation

The Seidorechka Volcanic Formation occurs in the upper part of Hole 1A (interval 1–64 m). The section is composed of homogeneous basaltic rock having a finer texture than the Kuksha Formation rocks. Macroscopically the volcanic unit is massive without any recognisable contact zones between individual lava flows and probably represents a single lava flow; the flow top was not intersected by the drillhole. Samples of the unit are evolved tholeiitic andesites or basaltic andesites and, relative to the Kuksha Formation at the base of Core 1A, have lower MgO (4.4–6.1 wt.%) (Fig. 6.10) and higher TiO_2 (1.2–1.3 wt.%). This also applies to other incompatible elements, which are significantly higher in the Seidorechka Volcanic Formation (for example, Zr 150–170 ppm vs. 40–50 ppm). There is a slight fractionation trend within the unit: MgO, Ni, and Cr decrease and

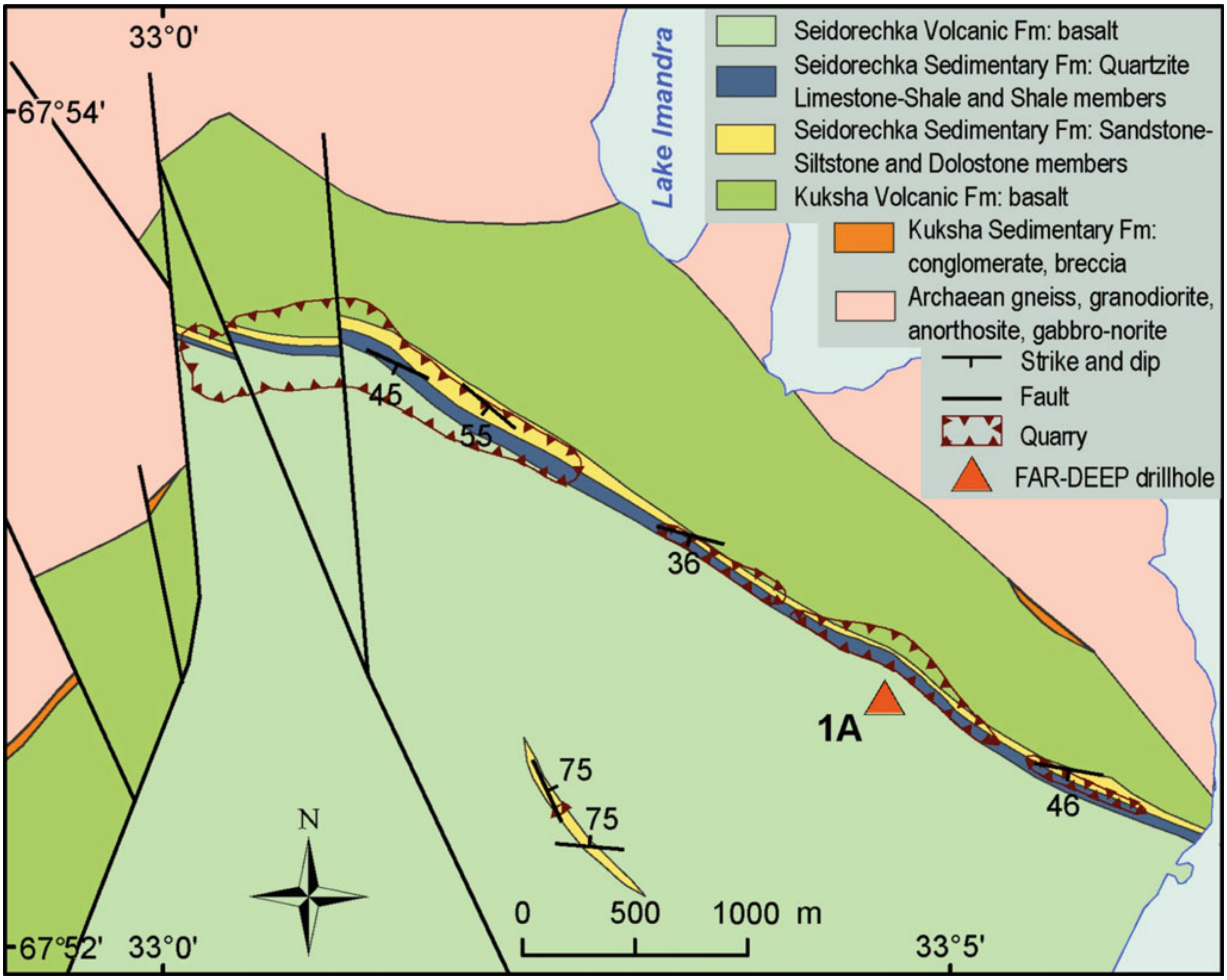

Fig. 6.4 Geological map of the drilling site emphasising thickness variation of the Seidorechka Sedimentary Formation based on mapping by Anthony Prave and Aivo Lepland

incompatible elements increase with decreasing depth in the core. Otherwise the unit is homogeneous with constant incompatible trace element ratios such as Ti/Zr (45 ± 1). The rocks are enriched in LREEs compared to HREEs (Fig. 6.11) and have high primitive mantle-normalised (PM) $(Ce/Nb)_{PM}$ ratios of c. 2.9, indicating effects of crustal contamination. This is also reflected in pronounced negative Nb-Ta and P anomalies in the spidergram of Fig. 6.11. Compared to FAR-DEEP Core 1A, the previous literature descriptions from the Seidorechka Formation (Fedotov et al. 1982; Fedotov 1983a, b) report more variable rock types ranging from picritic basalts to dacites. Furthermore, basaltic andesites reported by Fedotov et al. (1982) and Fedotov (1983a) do not match well with basaltic andesites from Core 1A, as the former are lower in TiO_2 and especially P_2O_5 (Fig. 6.10) and in this respect are more akin to the Kuksha Volcanic Formation basalts.

The Depositional Framework

The depositional framework of the Seidorechka Sedimentary Formation is considered based on core logging, geological mapping and sedimentological research in the vicinity of the drilling site. The formation is divided into two depositional packages separated by the intra-formational angular unconformity at the base of the Dolostone member. The pre-unconformity, lower depositional package is represented by the Sandstone-Siltstone member. This member consists of facies associations (Fig. 6.12ak–am, ao–at) that define an overall thickening and coarsening-upward progradational depositional cycle (Fig. 6.4). The overall vertical facies trend records deposition under progressively shallowing conditions, from outer through inner shelf, occasionally experiencing storms, to shallower-marine, tide-dominated palaeoenvironments. Repetitive mm- and cm-scale bedding

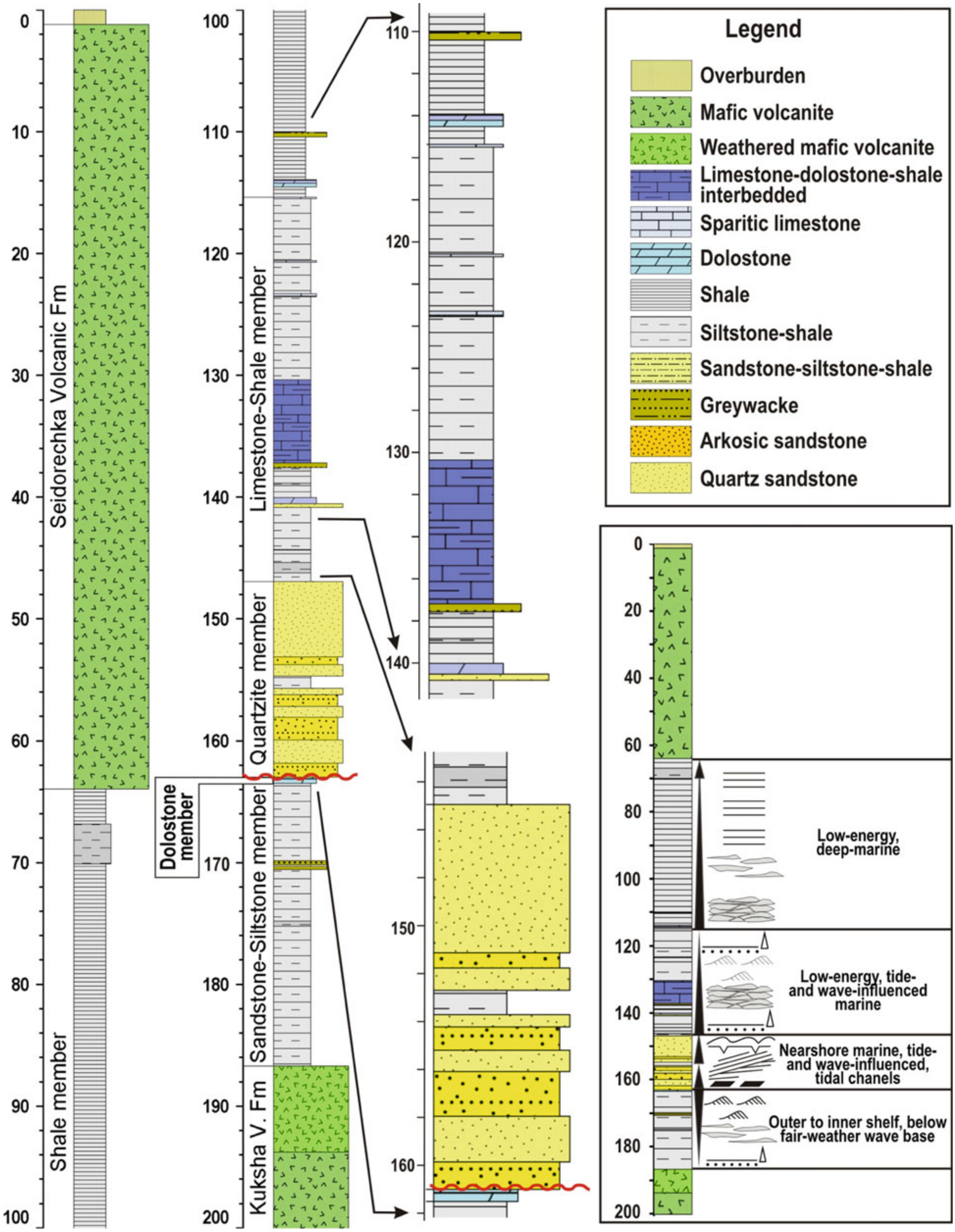

Fig. 6.5 Lithological section of the Seidorechka Sedimentary Formation based on core log of Hole 1A. Reconstructed depositional environments based on core logging, geological mapping and sedimentological research in the vicinity of the drilling site. Lithological symbols are explained in Fig. 6.6

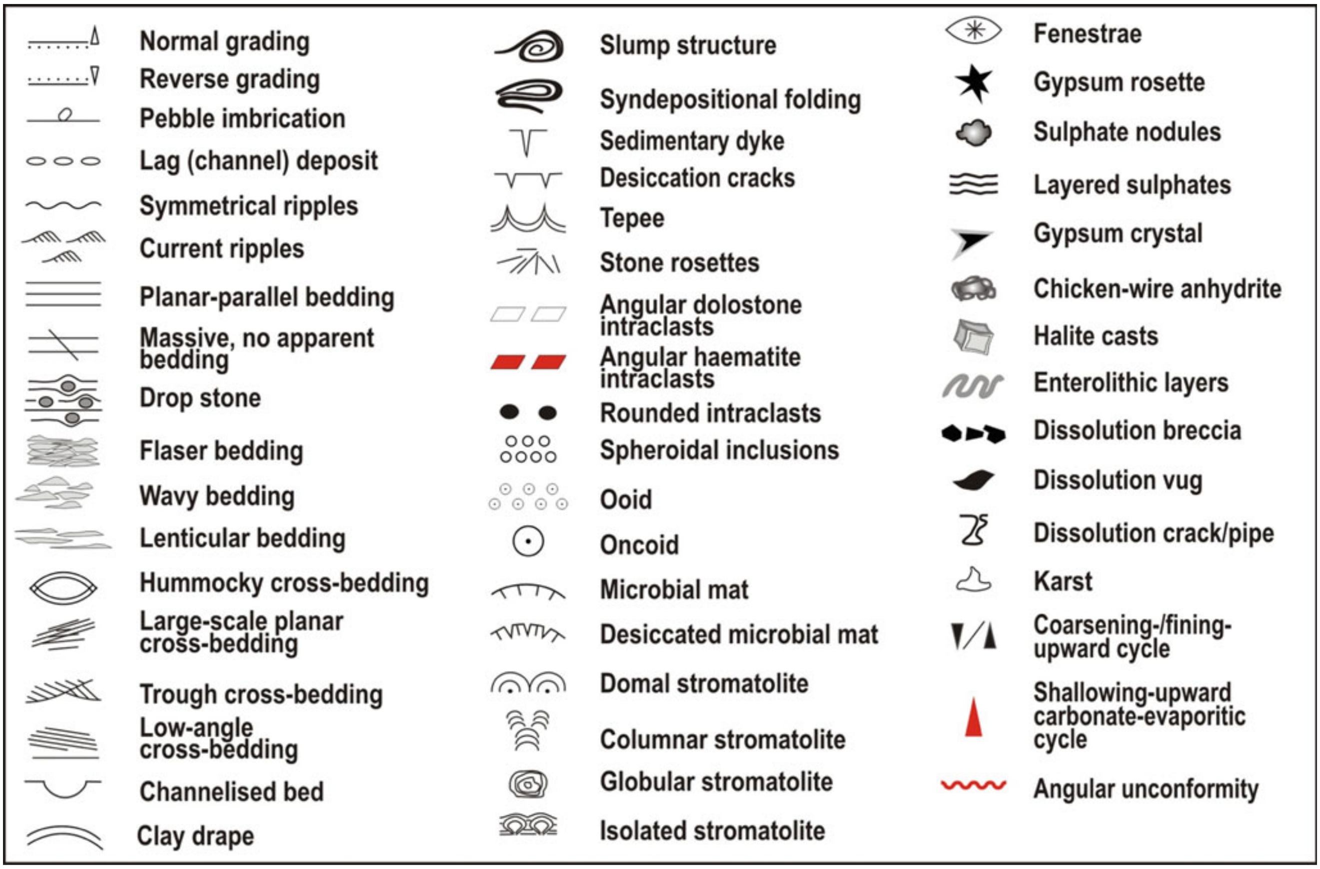

Fig. 6.6 Lithological symbols used in FAR-DEEP drillhole logs

of sandstone and shale (Fig. 6.12ao–at) in the uppermost part of the Sandstone-Siltstone member may represent daily tidal cycles.

The lower lithofacies of the Dolostone member (Fig. 6.12ac–ai) record an incipient carbonate shelf or platform established during episodic transgression across the unconformity surface. The tepee-like structures, broken beds, shale-injection features, and dissolution cavities were apparently produced by deposition and reworking of carbonate material during periods of exposure. The lithofacies of the upper part of the member (Fig. 6.12ab) – uniform dolomicrosparite with the local development of cross bedded intervals – suggest a marine flooding episode with periods of higher-energy reworking.

The post-unconformity, upper depositional package starts at a sharp, erosive contact at the base of the Quartzite member. The presence of abundant, angular dolostone fragments in the lower beds is evidence for an erosion episode, the duration of which is not known. The chemical maturity and sedimentary features of the Quartzite member lithofacies indicate that quartz sand was deposited under tides and waves (Fig. 6.12w, x) and indicate deposition in energetic, shallow marine and shoreline settings that at times experienced subaerial exposure (Fig. 6.12v). The substrate on such emerged surfaces could have been bound and stabilised by microbial mats (Fig. 6.12y). Metre-scale fining-upward cycles can be attributed to the progressive infill, abandonment and subsequent lateral migration of broad, shallow tidal channels. The compositional maturity of sand material implies a period of prolonged and/or intense weathering in source areas. The overall upward trend in depositional cycles from coarser to finer-grained sandstones, and higher to lower sandstone/shale ratios is evidence for a backstepping depositional system and basinal deepening event.

The rather abrupt loss of coarse-grained mature sandstone and the presence of a dolomarl bed at the base of the Limestone-Shale member indicate a likely rapid marine flooding event. Above this, the depositional pattern is defined by intervals alternating between graded, low-angle cross-laminated siltstone-shale, sparitic limestone and siliceous limestone-dolostone laminite (Fig. 6.12a–d, f, i, j), which reflects either periods of variable siliciclastic influx and/or the switching on and turning off of the carbonate production factory. The overall fining-upward vertical trend, as initiated by a progressive thinning and loss of the

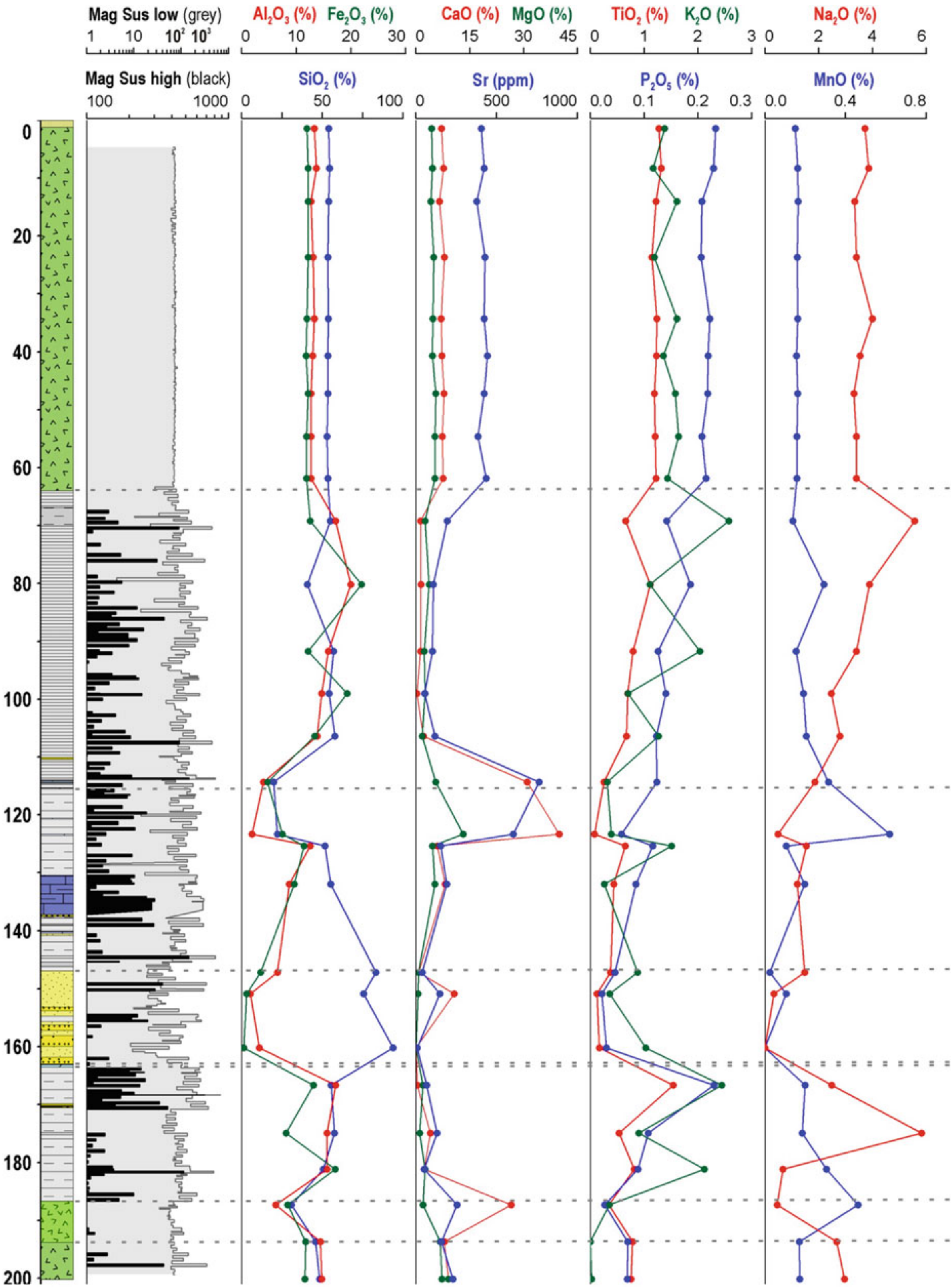

Fig. 6.7 Relative magnetic susceptibility (K*), and geochemical profiles of selected elements based on the archive samples collected with c. 8 m-spacing. For analytical techniques and data quality see Part 5

Fig. 6.8 Seidorechka Sedimentary Formation lenticular and wavy-bedded sandstone-shale couplets suggest a tidal marine setting – an ideal rock and depositional setting to address global sulphur cycle during the course of the Great Oxidation Event. Width of the photograph is 30 cm (Photograph of Victor Melezhik)

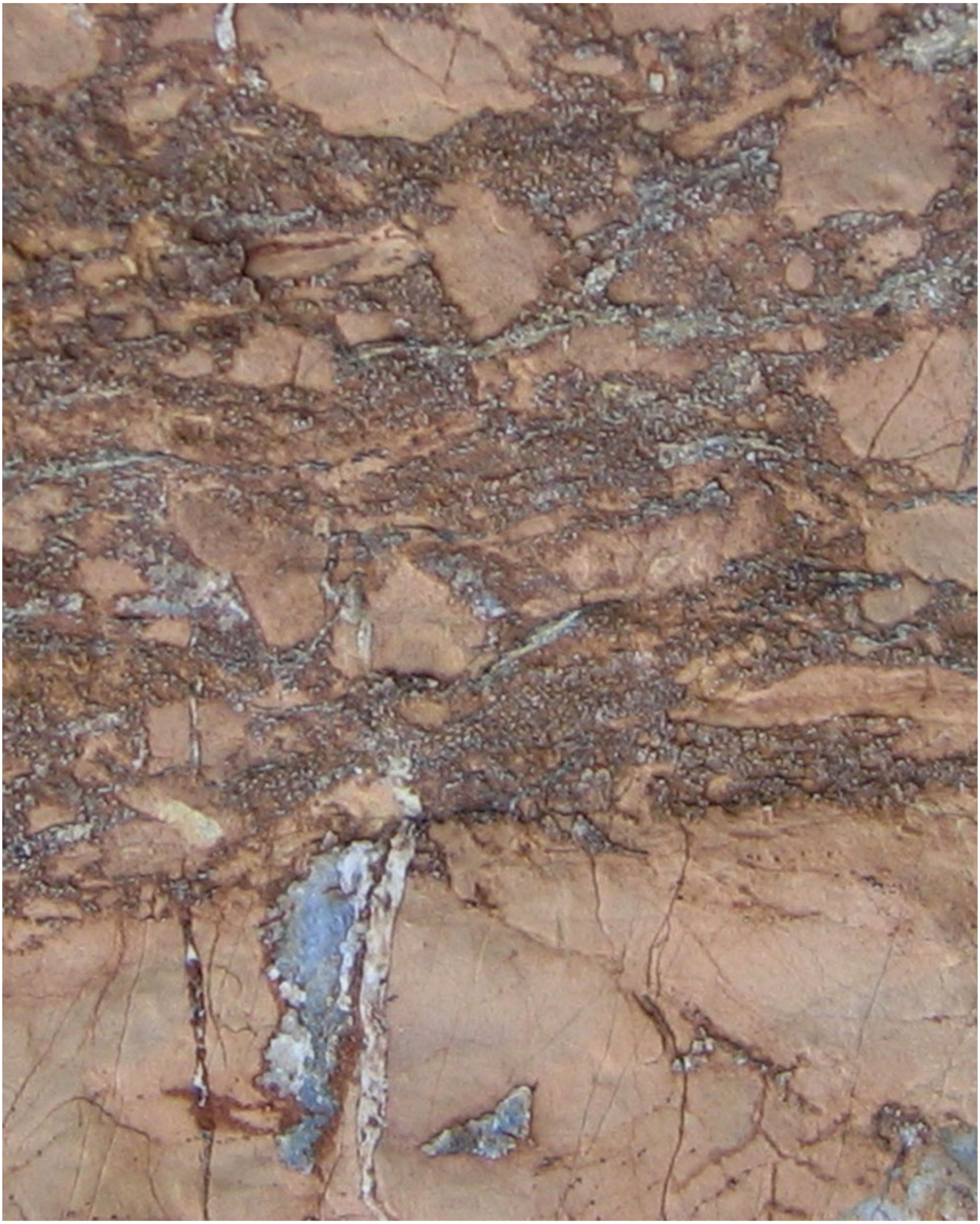

Fig. 6.9 Seidorechka Sedimentary Formation massive dolostone overlain by matrix-supported dolostone breccia representing an incipient carbonate platform that underwent a subsequent phase of emergence and partial erosion. Both lithologies are valuable material for depicting carbon cycle at the dawn of the Great Oxidation Event. Width of the photograph is 20 cm (Photograph of Victor Melezhik)

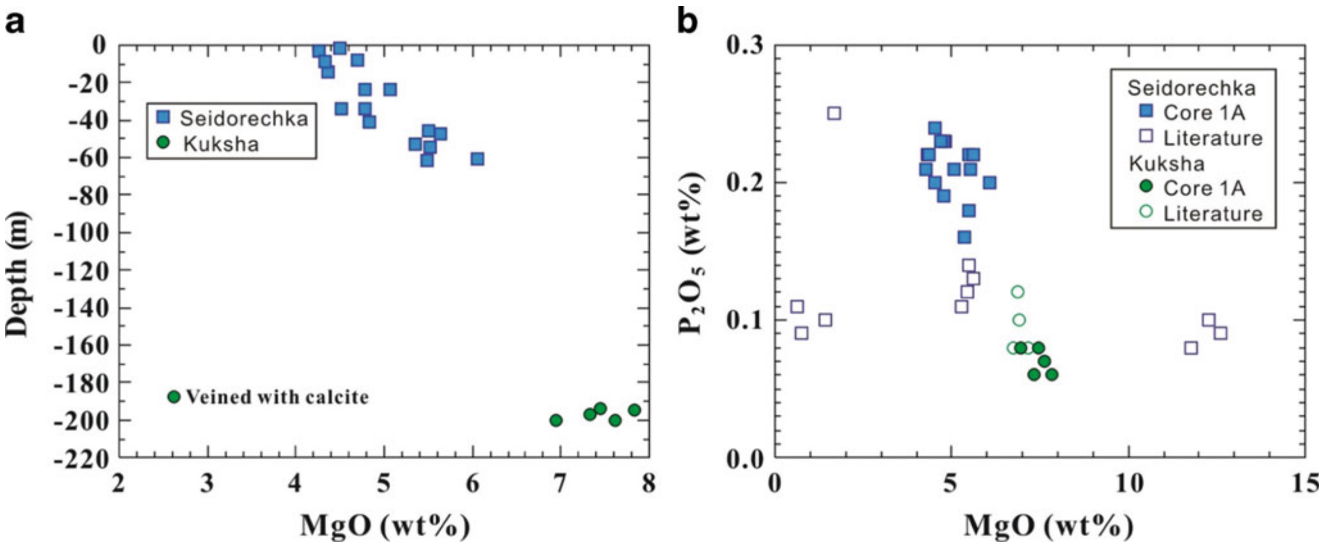

Fig. 6.10 MgO versus depth (**a**) and MgO versus P_2O_5 (**b**) diagrams for igneous rocks in Core 1A. Literature data for the Kuksha and Seidorechka Volcanic formations are from Fedotov et al. (1982) and Fedotov (1983a, b)

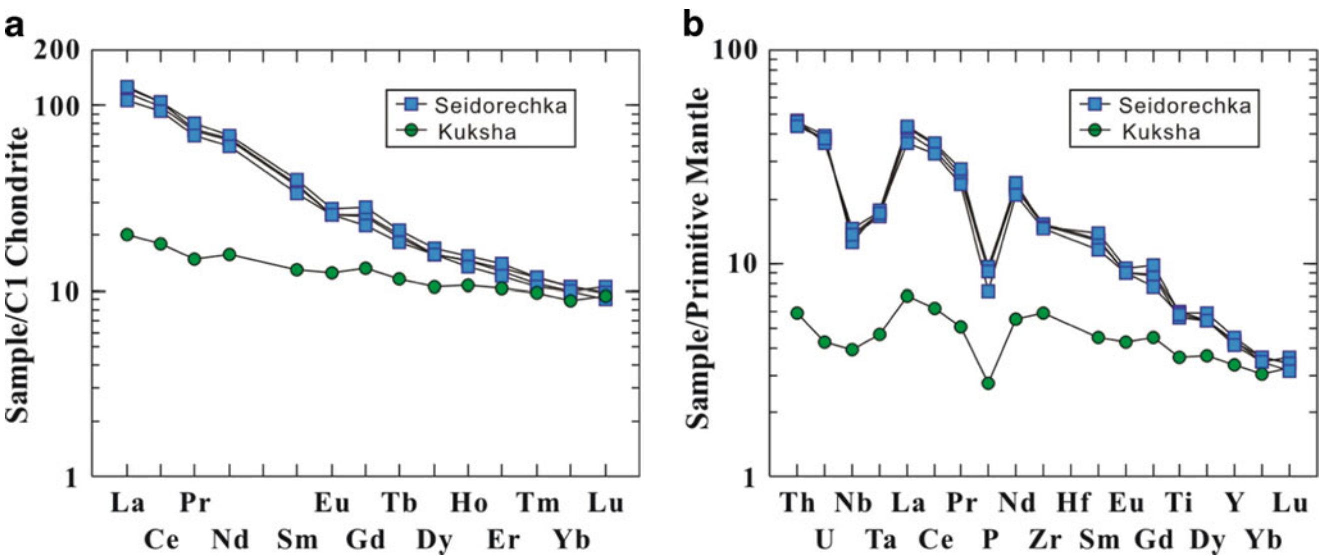

Fig. 6.11 Chondrite-normalised REE patterns (**a**) and primitive mantle-normalised trace element patterns (**b**) for igneous rocks in Core 1A. Normalising values taken from Sun and McDonough (1989)

carbonate-dominated intervals and an increase in the fine-grained siliciclastic materials, records a continued basinal deepening event and deposition in low-energy, relatively deep-marine settings. The sedimentological features of the upper parallel-laminated shale lithofacies of the Shale member is indicative of progressive deepening of the basin and accumulation below fair and storm-weather wave base.

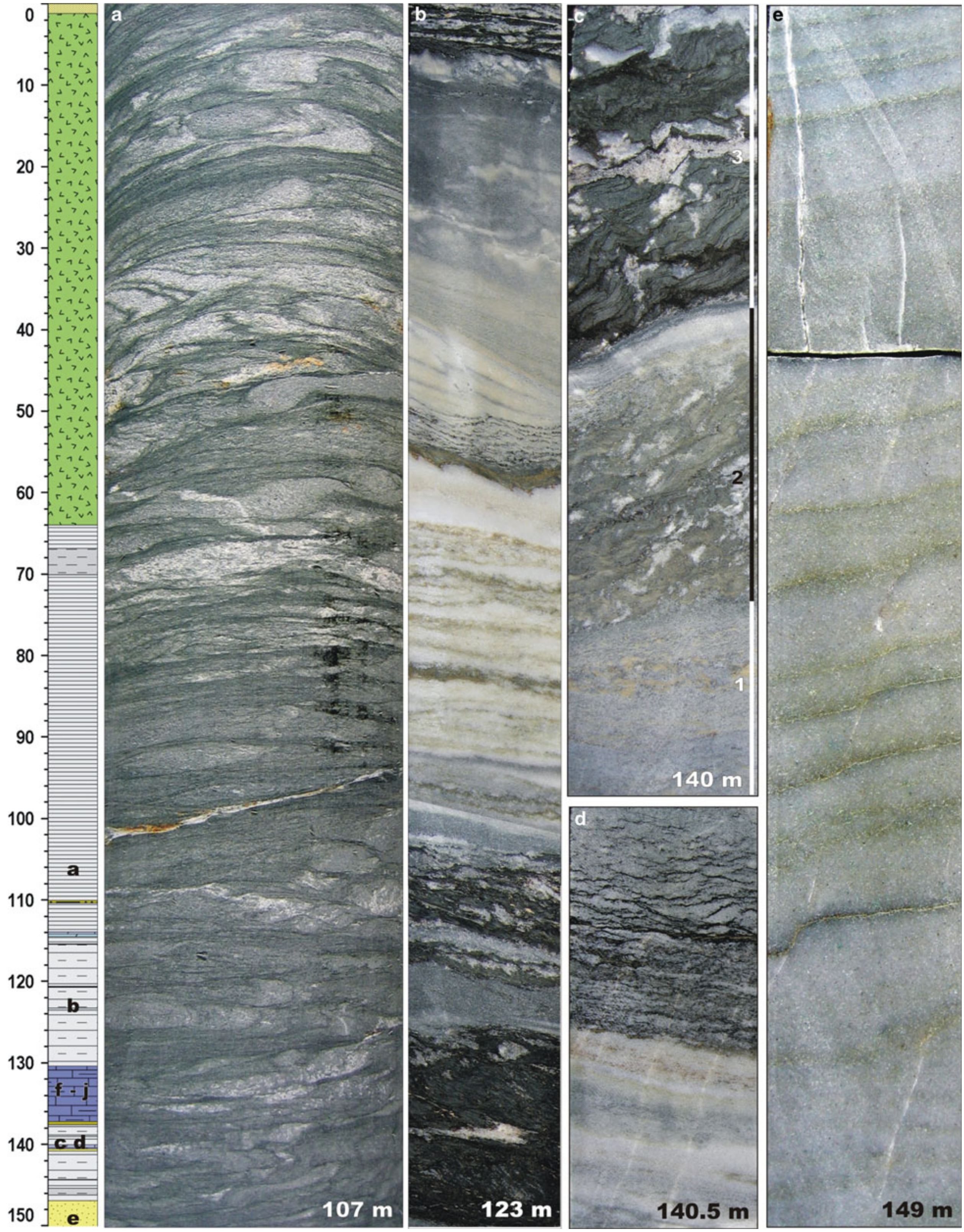

Fig. 6.12 Sedimentological features of main rock types of the Seidorechka Sedimentary Formation based on Hole 1A cores and quarries in the vicinity of the drilling site. Core diameter in all plates is 50 mm unless specified otherwise

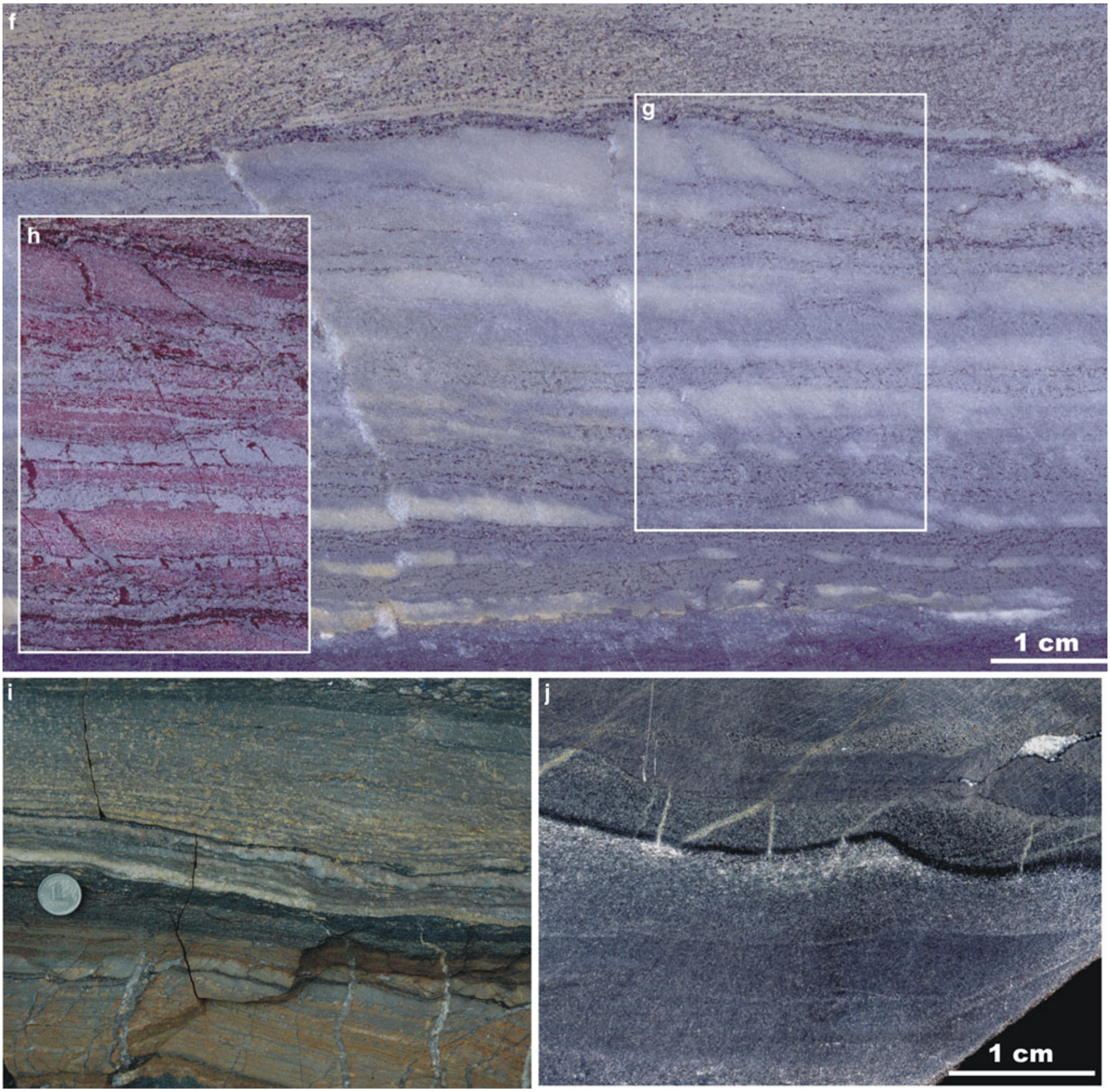

Fig. 6.12 (continued) (**a**) Tectonically-modified flaser, lenticular and wavy bedding in siltstone-shale of the Shale member. (**b**) Tectonically-modified parallel and rhythmically bedded limestone (*bluish-grey*)-dolostone (*white*)-shale (*dark-grey*, *brown-grey*) couplets of the Limestone-Shale member. (**c**) Limestone (1) passing *upward* to marl (2) and then to shale (3); Limestone-Shale member. (**d**) Intensively calcitised dolostone overlain by limestone-shale with tectonically modified flaser and wavy bedding in the Limestone-Shale member. (**e**) Quartz-cemented quartz sandstone beds with shale partings from the upper Quartzite member. (**f**) Polished slab of dolostone (*white*)-clayey limestone (*bluish-grey*) couplets overlain by calcareous shale. (**g**, **h**) '**h**' is Alizarin-red-stained polished surface of the '**g**' area and illustrates replacement of dolomite by calcite (*red*). (**i**) Hand-specimen of dolostone (*pale-brown*)-limestone (*bluish-grey*)-shale rhythmite; coin diameter is 1.5 cm. (**j**) Polished slab of parallel-bedded limestone overlain by sandstone-siltstone with lenticular and wavy bedding. Samples "**f**, **i** and **j**" represent the Limestone-Shale member and were collected in a quarry located west of the drilling site

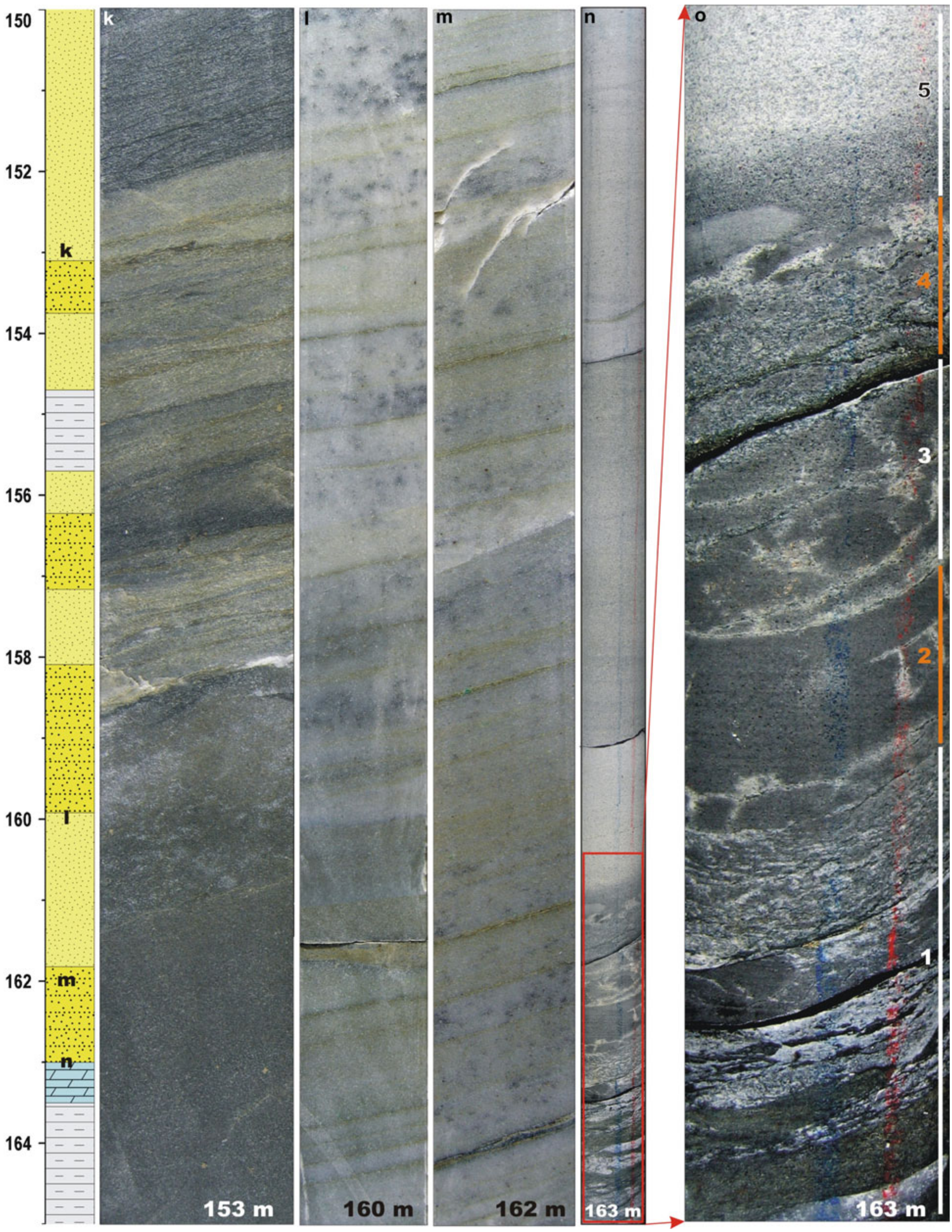

Fig. 6.12 Sedimentological features of main rock types of the Seidorechka Sedimentary Formation based on Hole 1A cores and quarries in the vicinity of the drilling site (continued)

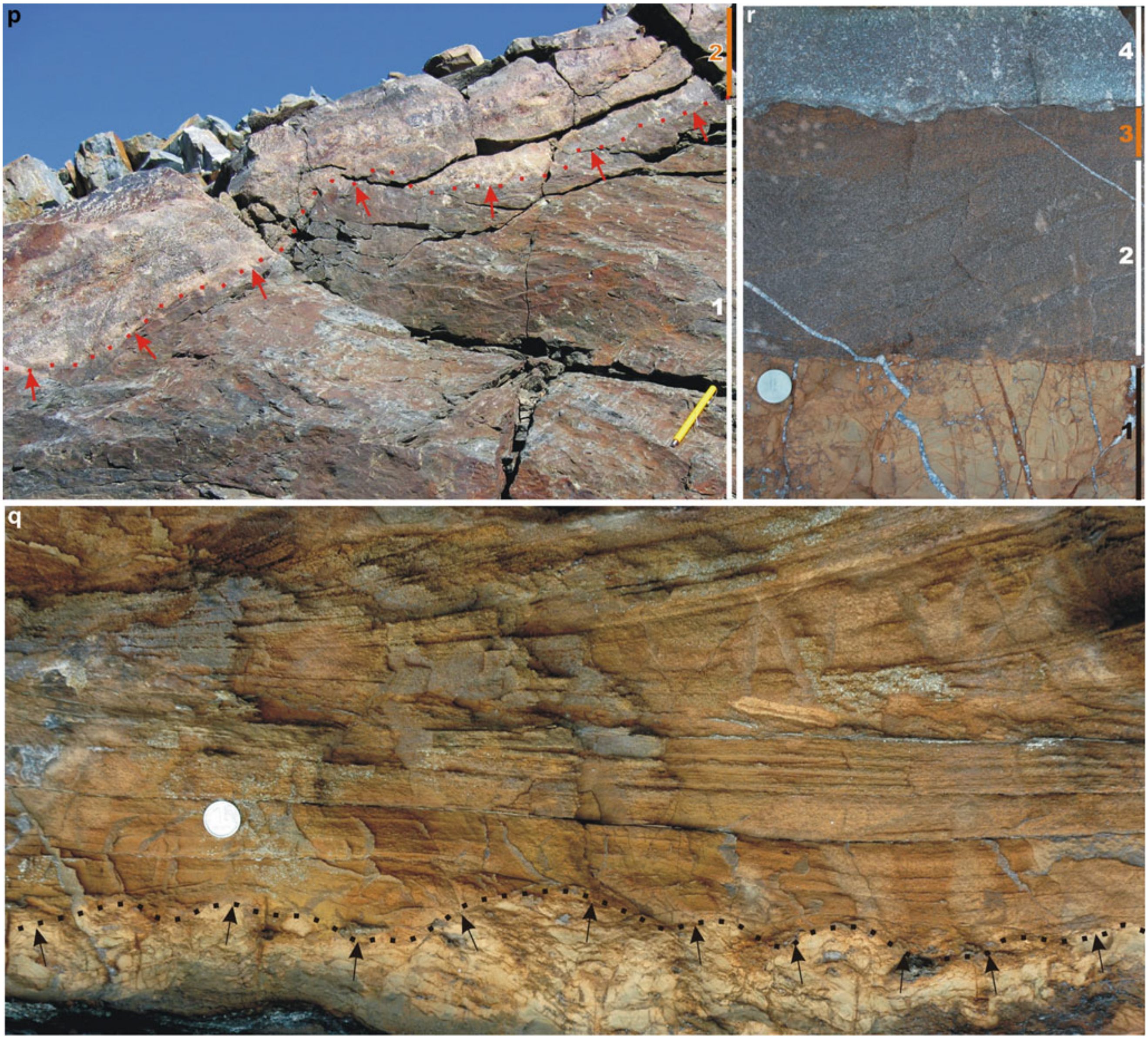

Fig. 6.12 (continued) **(k)** Massive arkosic sandstone passing upward into low-angle cross-bedded clayey arkosic sandstone capped by pale-grey shale; shale interval in middle of the Quartzite member. (**l**, **m**) Low-angle cross-bedded, quartz sandstone beds with shale partings from lower Quartzite member. (**n**) Three low-angle cross-bedded cosets of quartz sandstone of the Quartzite member on top of the Dolostone member. (**o**) Close-up of erosional contact between the Quartzite (5, 4) and Dolostone (3–1) members; (1) calcareous shale containing lenticular beds of dolograinstone (1) passes *upward* into calcitised dolomicrosparite (2) with clay-calcite-filled dissolution cracks (3), in turn overlain by dolostone-clast, sandstone-matrix conglomerate (4) capped by quartz sandstone (5). (**p**) Erosional contact beneath the Quartzite member (indicated by red dashed line and red arrows); yellow pen (15 cm long) shows bedding orientation which defines an angular unconformity between the Sandstone-Siltstone (1) and Quartzite (2) members; note that the Dolostone member is completely eroded. (**q**) Cross-bedded dolarenite at the base of the Quartzite member (*dotted* and *arrowed*) exposed in a quarry; cross-bedding shows 180° reversal; coin diameter is 1.5 cm. (**r**) The Quartzite member (4) on silicieous dolarenite (3) passes *downward* into cross-bedded, dolomite-cemented, quartz sandstone (2) that in turn rests on the basal erosional surface of the Dolostone member microsparitic dolostone (1); coin diameter is 1.5 cm (Photographs '**p–r**' were taken from a quarry located west of the drilling site)

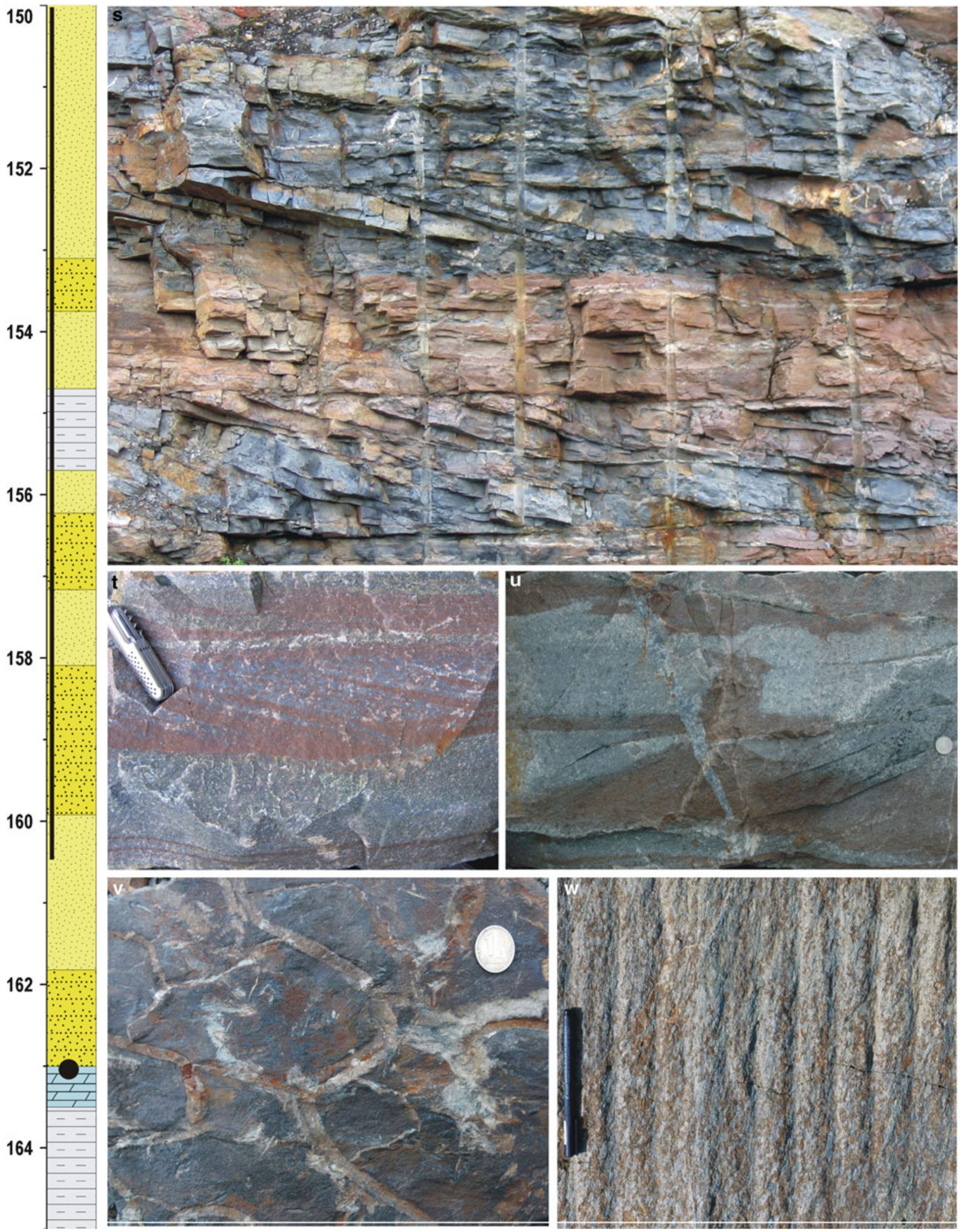

Fig. 6.12 Sedimentological features of main rock types of the Seidorechka Sedimentary Formation based on Hole 1A cores and quarries in the vicinity of the drilling site. (continued)

Fig. 6.12 (continued) (**s**) Alternation of 2-m-scale cross-bedded and ripple-bedded quartzite beds with lenticular geometries in quarry wall; height of the photo is c. 10 m; black line on the lithological column indicates stratigraphic position of the photo. (**t**) Planar cross-bedded, dolomite-cemented (*brown* stain) quartz sandstone sandwiched between quartz sandstones with wavy bedding. (**u**) Irregular cementation of cross-bedded quartzite by dolomite (*brown*). (**v**) Sand-filled desiccation cracks developed in shale drapes. (**w**) Symmetric ripples in quartz sandstone from the Quartzite member; pen length 12 cm. (**x**) Bedding surface on quartz sandstone marked by bifurcating oscillation ripple marks occurring in a trough that is superimposed on a hummocky surface; note groove casts next to the coin. (**y**) Bedding surface on quartz sandstone marked by rhomb-shaped interference ripple marks. (**z**) Dolofloatstone with rounded and angular, imbricated dolostone fragments emplaced in a dolomite-cemented quartz sandstone matrix; base of the Quartzite member. (**aa**) Unsorted, angular, dolostone-clast quartz-sand-cemented breccia at the base of the Quartzite member. Positions of (**z**, **aa**) marked by dots on the stratigraphic column. All photos were taken from quarries located west of the drilling site. White-coloured coin diameter is 1.5 cm; bronze-coloured coin diameter is 1.2 cm; knife length is 10 cm, pen length is 13 cm

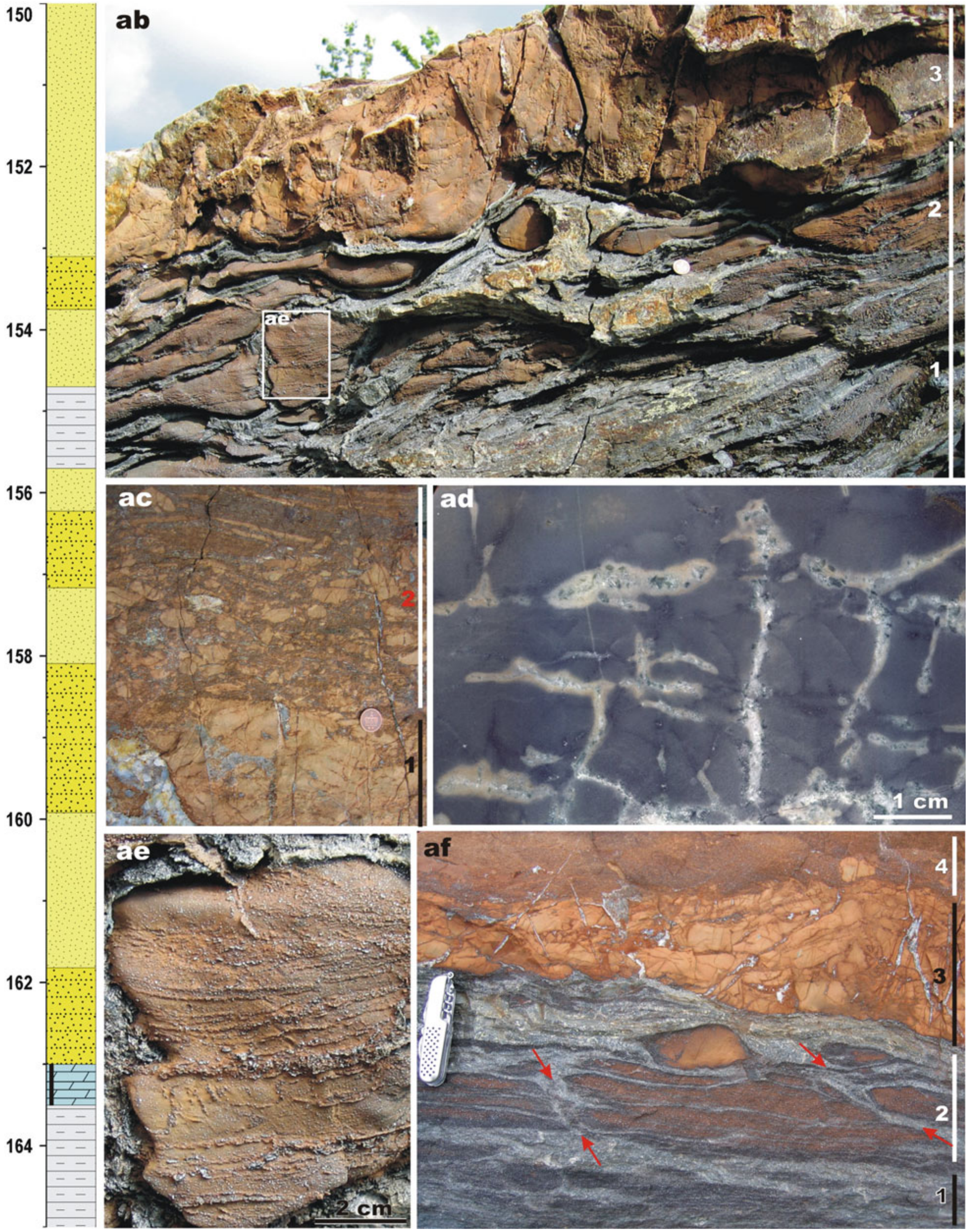

Fig. 6.12 Sedimentological features of main rock types of the Seidorechka Sedimentary Formation based on Hole 1A cores and quarries in the vicinity of the drilling site (continued)

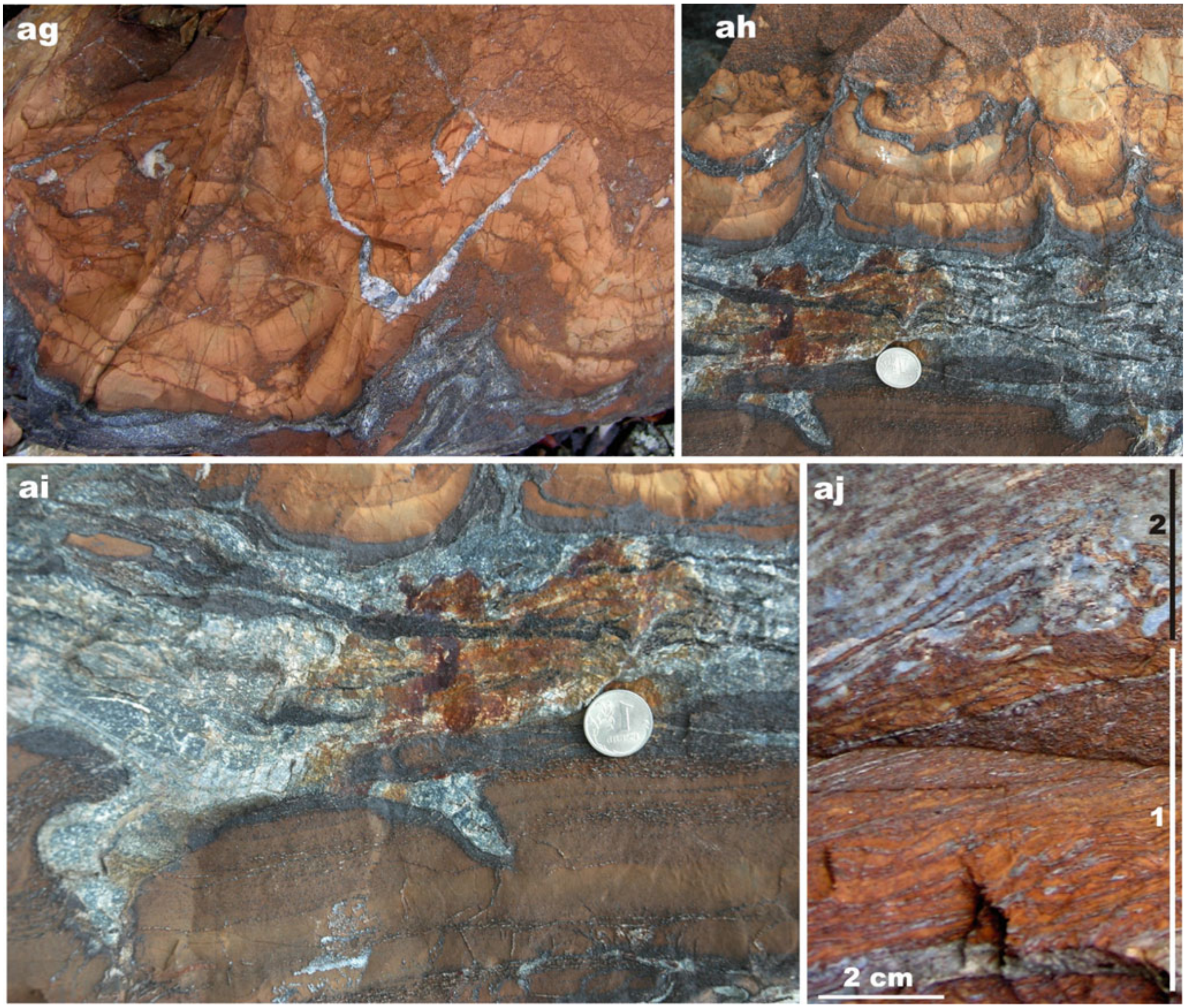

Fig. 6.12 (continued) (**ab**) Quarry wall illustrating Dolostone member calcitised dolomicrosparite (3) underlain by green-grey shale containing lenticular beds and irregularly shaped lenses of brownish-grey dolograinstone (2) passing downward into green-grey shale free of carbonate inclusions (1); black line on the lithological column indicates stratigraphic position of the photo. (**ac**) Massive microsparitic dolostone (1) overlain by poorly sorted matrix-supported dolorudites (2); coin diameter is 1.2 cm. (**ad**) Probable dissolution cavities on top of the microsparitic dolostone bed. (**ae**) Enlarged fragment of '**ab**' illustrating low-angle cross-bedding in dolograinstone. (**af**) *Green-grey* shale (1) overlain by shale intercalated with lenses of pale grey dolograinstone (2) followed by thickly bedded dolorudite (3), then massive dolarenite (4); note separation of dolarenite lenses by shale (*arrowed*); the Dolostone member; knife length is 10 cm. (**ag**) Dolarenite, dolorudite, and thickly-bedded, microsparitic dolostone; note anticlinal feature along the dolostone-shale contact; width of the photograph 25 cm. (**ah**) Calcareous shale overlain by thickly-bedded, microsparitic dolostone and dolarenite with well-pronounced anticlinal feature along the dolostone-shale contact. (**ai**) Sparitic calcite-filled dissolution cavities on top of parallel-bedded dolarenite bed overlain by calcareous schist, which is, in turn, "injected" into an anticlinal structure developed in the overlying bedded dolostone shown in '**ah**'. (**aj**) Bedding-parallel (1) and bedding-cross-cutting (2) calcitisation (*bluish-white*) of sparitic dolostone (*brown*) (Photos '**ab–ag**' were taken in quarries located west of the drilling site. Photos '**ac**' and '**af–ag**' were taken from blocks in quarries. Coin diameter in (**ab**, **ah**, and **ai**) is 1.5 cm)

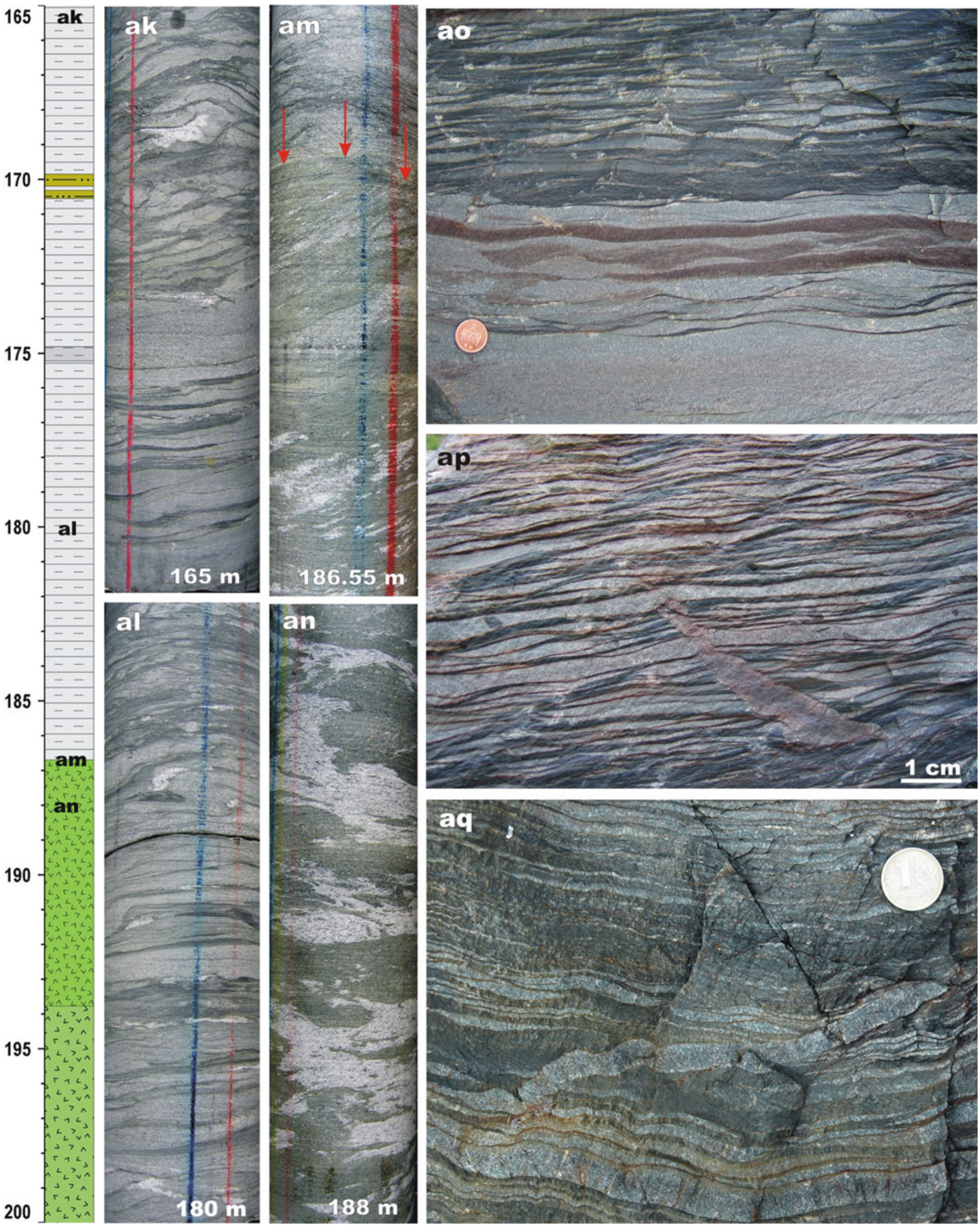

Fig. 6.12 Sedimentological features of main rock types of the Seidorechka Sedimentary Formation based on Hole 1A cores and quarries in the vicinity of the drilling site (continued)

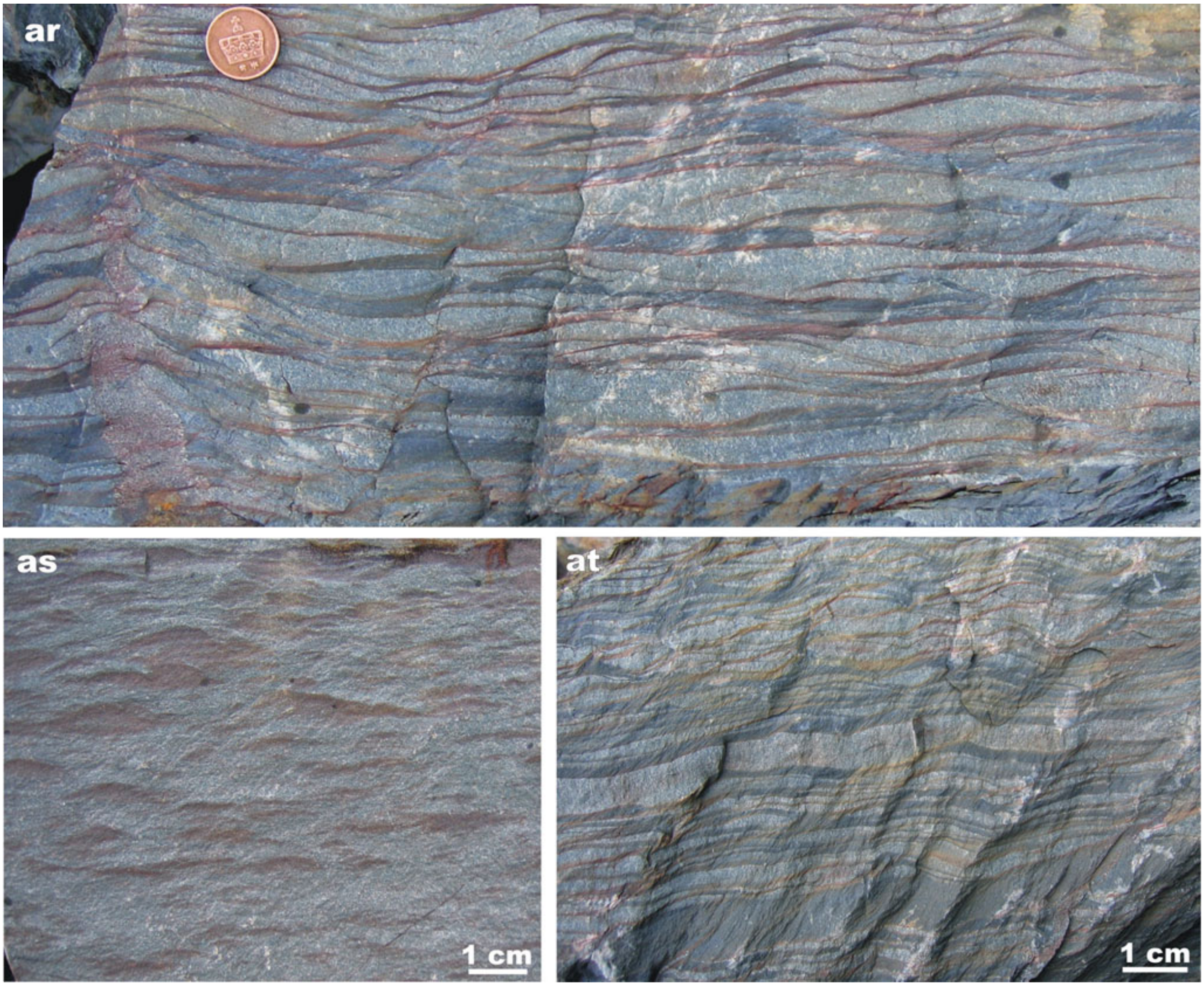

Fig. 6.12 (continued) (**ak**) Flaser bedding (*lower half*) passing into wavy bedding in the siltstone-shale of the Sandstone-Siltstone member. (**al**) Flaser bedding (*lower half*) passing into lenticular bedding in the siltstone-shale of the Sandstone-Siltstone member. (**am**) Contact between the Seidorechka Sedimentary Formation and the Kuksha Volcanic Formation (*red-arrowed*); note that the Kuksha basalt appears as sericite-chlorite-plagioclase schist and apparently represents a weathering crust formed prior to deposition of the Seidorechka sediments. (**an**) Intensively calcitised (*white*) and sericitised (palaeoweathered) basalt. (**ao**) Vertical change from flaser through wavy to lenticular bedding in the upper part of the Sandstone-Siltstone member; coin diameter is 1.2 cm. (**ap**) Well-preserved lenticular and wavy bedding and a sandstone dyke in the upper part of the Sandstone-Siltstone member. (**aq**) Lenticular-bedded sandstone-shale of the Sandstone-Siltstone member injected by a sandstone dyke; coin for scale is 1.5 cm. (**ar**) Well-preserved lenticular and wavy bedding in the upper part of the Sandstone-Siltstone member; coin diameter is 1.2 cm. (**as**, **at**) Lenticular bedding in the *upper* part of the Sandstone-Siltstone member (Photos (**ao–at**) were taken in quarries located west of the drilling site. Photographs (**a–g**, **k–p**, **s**, **t**, **z–ag**) by Victor Melezhik; (**i**, **j**, **q**, **r**, **u–y**, **ah–aj**) by Anthony Prave)

References

Amelin YuV, Heaman LM, Semenov VS (1995) U-Pb geochronology of layered mafic intrusions in the eastern Baltic Shield: implications for the timing and duration of Palaeoproterozoic continental rifting. Precambrian Res 75:31–46

Bekker A, Holland HD, Wang PL, Rumble D III, Stein HJ, Hannah JL, Coetzee LL, Beukes NJ (2004) Dating the rise of atmospheric oxygen. Nature 427:117–120

Fedotov ZhA, Basalaev AA, Melezhik VA, Latyshev LN (1982) The Srel'na group. In: Gorbunov GI (ed) The Imandra/Varzuga Zone of Karelids. Nauka (Science), Leningrad, pp 33–56, in Russian

Fedotov ZhA (1983a) Volcanic rocks of the komatiite series in the in the Proterozoic Imandra-Varzuga sedimentary-volcanic complex. In: Predovsky AA (ed) Sedimentary basins and volcanic zones in the Precambrian of the Kola Peninsula. Nauka (Science), Apatity, pp 81–99, in Russian

Fedotov ZhA (1983b) On the acidic volcanism ending the first Strel'na stage of the evolution of the Imandra-Varzuga synclinorium zone (in Russian). In: Predovsky AA (ed) Sedimentary basins and volcanic zones in the Precambrian of the Kola Peninsula. Nauka (Science), Apatity, pp 99–107, in Russian

Hannah JL, Bekker A, Stein HJ, Markey RJ, Holland HD (2004) Primitive Os and 2316 Ma age for marine shale: implications for Palaeoproterozoic glacial events and the rise of atmospheric oxygen. Earth Planet Sci Lett 225:43–52

Sun S-S, McDonough WF (1989) Chemical and isotopic systematics of oceanic basalts; implications for mantle composition and processes. In: Saunders AD, Norry MJ (eds) Magmatism in the Ocean Basins, vol 42, Geological society special publication. Published for the Geological Society by Blackwell Scientific Publications, Oxford/Boston, pp 313–345

6.1.2 Polisarka Sedimentary Formation: FAR-DEEP Hole 3A

Victor A. Melezhik, Eero J. Hanski, Anthony R. Prave, Aivo Lepland, Alexander E. Romashkin, Dmitry V. Rychanchik, Alex T. Brasier, Anthony E. Fallick, Zhen-Yu Luo, Evgenii V. Sharkov, and Maria M. Bogina

Scientific Targets

- Tectonic and depositional settings associated with Huronian-age glaciation
- Geochemical rock record during Huronian glaciation
- Mass-dependent and mass-independent sulphur isotope fractionation
- Carbon, sulphur and strontium isotopic composition of seawater
- Provenance composition
- Microfossil record
- Radiometric age constraint on timing of deposition

Hole 3A intersected the Polisarka Sedimentary Formation (Figs. 6.13 and 6.14) in the western part of the Imandra-Varzuga Greenstone Belt (Figs. 6.1, 6.2, and 6.3). The depositional age of the Polisarka Sedimentary formation is younger than c. 2442 Ma, which is the age of the underlying volcanic rocks of the Seidorechka Volcanic Formation (Amelin et al. 1995). However, these two formations are separated by a hiatus of unknown duration, thus the actual depositional age of the Polisarka Sedimentary Formation remains uncertain. This formation records the Huronian-age glaciations and the cored rock succession contains sedimentary sulphide, diamictite units with associated dropstone intervals and abundant carbonate beds (Figs. 6.15 and 6.16), which can be used for environmental reconstructions using Sr-, S- and C-isotopic records during the glaciation and the beginning of the Great Oxidation Event.

The 255.00 m long Hole 3A intersected the entire thickness of the Polisarka Sedimentary Formation (129 m), 99 m of overlying lavas of the Polisarka Volcanic Formation and c. 22 m of underlying volcanic rocks of the Seidorechka Volcanic Formation (Fig. 6.13). Six volcanic units have been distinguished in Core 3A and, from bottom to top, are assigned to Units A, B, C, D, E and F (Figs. 6.17 and 6.18). Unit A represents an upper part of the Seidorechka Volcanic Formation, Units E and F form a lower part of the Polisarka Volcanic Formation, whereas Units B, C and D occur within the Polisarka Sedimentary Formation; each is described below.

In Core 3A, the Polisarka Sedimentary Formation contains greywacke, tuff, diamictite and various carbonate rocks and is informally subdivided into two lithostratigraphic members, a lower Limestone member and an upper Greywacke-Diamictite member (Fig. 6.13). The igneous bodies of Units B, C and D occur within the Limestone member. Core photos provide a detailed documentation of major lithological and structural features of the sedimentary and igneous rocks throughout the stratigraphy (Fig. 6.19a–as). Chemical composition of analysed samples is presented in Appendices 4–6. Figure 6.14 shows stratigraphic profiles of selected major and trace elements as well as magnetic susceptibility.

All sedimentary rocks have a low magnetic susceptibility (100–880 µSI, K* = 9–80 $\times$ 10^{-6} SI) with one exception in the lower part of the formation (Fig. 6.14), a carbonate-sandstone-siltstone bed with up to 23,500 µSI (K* = 2,140 $\times$ 10^{-6} SI). Most of the igneous rocks intersected by Hole 3A, irrespective of chemical composition, are characterised by a low magnetic susceptibility of 120–940 µSI (relative susceptibility K* = 10–80 $\times$ 10^{-6} SI in Fig. 6.14). Unit D has low values in its lower part (around 300 µSI, K* = 30 $\times$ 10^{-6} SI in Fig. 6.14) and elevated magnetic susceptibility in its upper part (up to 47,000 µSI, K* = 4,000 $\times$ 10^{-6} SI in Fig. 6.14). Unit B is marked by a magnetic susceptibility at around 41,000 µSI (K* = 3,500 $\times$ 10^{-6} SI).

The Seidorechka Volcanic Formation

The Seidorechka Volcanic Formation (Unit A, interval 228–255 m) is represented in Core 3A by two felsic lava flows, with thicknesses of ~18 and 3.5 m; both are overlain by thinner layers of tuffaceous rocks. The lavas contain plagioclase and quartz phenocrysts and rare amygdales. Based on bulk-rock major element compositions, the rocks can be classified as tholeiitic rhyodacites to rhyolites with SiO_2 ranging between 70 and 80 wt.% (Appendix 4). The high SiO_2 contents may reflect alteration. The trace element signature is very similar in all analysed samples. The rocks have high concentrations of REE and large-ion lithophile elements (LILE) and high LREE/HREE ratios (Fig. 6.18a). They are depleted in high field strength elements (HFSE) resulting in very high $(Th/Nb)_{PM}$ and $(Ce/Nb)_{PM}$ ratios of 5.5–6.2 and 2.7–3.4, respectively, and pronounced negative anomalies at Nb-Ta and P in primitive mantle-normalised trace element diagrams (Fig. 6.18b). Ti/Zr ratios show a limited range between 7.3 and 8.8.

V.A. Melezhik (✉)
Geological Survey of Norway, Postboks 6315 Sluppen, NO-7491 Trondheim, Norway

Centre for Geobiology, University of Bergen, Allegaten 41, Bergen N-5007, Norway

V.A. Melezhik et al. (eds.), *Reading the Archive of Earth's Oxygenation*, Volume 2: The Core Archive of the Fennoscandian Arctic Russia – Drilling Early Earth Project, DOI 10.1007/978-3-642-29659-8_2,

The Polisarka Sedimentary Formation

Limestone Member

In Core 3A, the initial deposits of the Polisarka Sedimentary Formation are represented by the Limestone member. Lithologically, the member is a heterogeneous unit consisting of crystalline limestone and dolostone, fine to coarse-grained clastic carbonates and rudites, marls and carbonate-shale rhythmites with subordinate calcareous shale (Fig. 6.19u–z, ac–ar). Primary bedding is commonly overprinted by ductile deformation, however rhythmical alternation of carbonate and calcareous shale components and layering occurring on different scales is well pronounced and locally preserves original textural relationships (Fig. 6.19ac, af, an, v–z). Some of the thicker carbonate units comprise pure limestone beds (Fig. 6.19ao, aq, ar). Ripples and small-scale cross-lamination have been preserved in places (Fig. 6.19ad, ae). Several intervals show affinities of varve sediments (Fig. 6.19ag) with lonestones and dropstones (Fig. 6.15).

The basal beds of this member consist of c. 2 m of carbonate wackestone that sit sharply on (at c. 228.2 m) the calcitised-sericitised rhyodacites of the underlying Seidorechka Volcanic Formation. The overlying several metres comprise dcm-scale pure limestone layers exhibiting sharp-bases and relatively gradational tops into inter-laminated shale-marl and thin limestone couplets (Fig. 6.19ao–ar). This lithology gives way upward to cm-thick beds of fine-grained wackestone and limestone grainstone containing numerous shale partings and layers (Fig. 6.19an), and probable ribbon-rock limestone (Fig. 6.19af, am). At c. 217.5 m in the core, a sharp-based medium-grained wackestone and overlying carbonate-clast rudite (Fig. 6.19al) mark a change in facies style; above this the member is dominated by limestone laminites and rhythmites and thin rhythmite breccia beds (Fig. 6.19ag–ak). These lithologies continue to c. 197 m where dcm-thick intervals start appearing in which limestone layers tend to be somewhat thicker than their associated shale layers and also exhibit an overall increase in the thicknesses of the limestone-shale couplets, from several millimetres to several centimetres. At c. 193 m, a dcm-thick, fine-grained greywacke sits sharply on what appears to be a ribbon-rock-textured limestone (upper part of Fig. 6.19af), albeit subsequently tectonically deformed and overprinted. Note that it is within the interval between the sharp-based wackestone and the few metres above the fine-grained greywacke that the probable lava flows of Unit C are present. Above the greywacke, limestone rhythmite and laminite reoccur and, at 183.2 m, an outsized, lone carbonate clast can be seen to have pierced underlying laminae (Fig. 6.15). The thinly bedded lithologies pass progressively upward into thicker layered (cm-scale) limestone-shale couplets, rhythmite breccias and fine-grained wackestones and packstones interbedded with shales (Fig. 6.19w–y). In the uppermost c. 10 m, shales become subordinate to and thinner than the limestones, which occur as interbedded fine-grained grainstones and packstones (Fig. 6.19u), including one rudite bed (Fig. 6.19v). The komatiitic body defined as Unit D occurs within this package of rocks. The upper beds of the Limestone member, above Unit D and below the contact with the overlying Greywacke-Diamictite member, consist of alternating layers, typically 2–5 cm thick, of fine-grained limestone and light–dark laminated limestone. The topmost beds of the member consist of a 1.6-m-thick, fine dolarenite capped by a 0.4 m thick pure limestone.

All analysed intervals of carbonate rocks are highly siliceous ($SiO_2 = 13$–26 wt.%), with moderate to low concentration of Al_2O_3 (1–3 wt.%), and a low to moderate Mn content (940–2,900 $\mu g\ g^{-1}$) (Fig. 6.13, Appendices 4 and 6). The limestones are variably dolomitised (MgO = 1.5–15 wt.%). High Sr abundances (600–1,030 $\mu g\ g^{-1}$) suggest aragonite as a precursor. K_2O/Na_2O ratios are variable, the sulphur content is low (0–0.6 wt.%) and the rocks are devoid of organic carbon (Appendix 5).

Whole-rock analyses of carbonate rocks based on 8-cm-long bulk samples yielded $\delta^{13}C$ fluctuating within a narrow range (−2.2 to +0.8 ‰ V-PDB) around “normal seawater” values. $\delta^{18}O$ shows a strong depletion in ^{18}O with $\delta^{18}O$ ranging between 8.0 and 12.2 ‰ V-SMOW (FAR-DEEP Database). A positive $\delta^{18}O$-$\delta^{13}C$ correlation ($r = +0.61$, $n = 15$, >95 %) would suggest a post-depositional alteration. We do not discount unequivocally that the Polisarka limestones may have been post-depositionally reset at high temperatures. The strong ductile deformation hints at this possibility via a high temperature fluid; however, high Sr abundances (600–1,030 $\mu g\ g^{-1}$) and moderate to low Mn concentrations (900–2,700 $\mu g\ g^{-1}$) do not favour such an interpretation.

The Greywacke-Diamictite Member

The Greywacke-Diamictite member sits sharply on the Limestone member. The contact (at c. 123.8 m) is marked by a 0.8-m-thick, sharp-based, medium- to coarse-grained feldspathic sandstone/greywacke. This, in turn, is sharply overlain by c. 2 m of finely interlayered mudstone and fine-grained clayey (15 wt.% Al_2O_3) and sodium-rich (3 wt.% Na_2O) greywacke; two thin calcsilicate layers are present. Above this, for the next 7 m, the succession progressively coarsens upward and consists of fine- to medium-grained greywacke with thin shale partings and layers; mudstone-chip intraclasts are present in places. Internal laminations display parallel to low-angle geometries, and small-scale cross-bedding (Fig. 6.19r, s). At c. 114 m, the first of a succession of diamictite beds occurs, typically internally massive, with clay-silt matrix (15 wt.% Al_2O_3, 3 wt.% Na_2O) and containing an assortment of dispersed clasts ranging in size from granules to pebbles (Fig. 6.19i–q). Detailed measurements and descriptions of the diamictitc part of Core 3A reveal that there are three main, massive, diamictite beds separated by thinner intervals of compositionally layered diamictite having sharp bases and tops (layering is defined by alternations between fine-sand/silt-rich to fine-sand/silt-poor bedding) and greywacke; from base to top: 0.41 m of compositionally layered mixed-clast diamictite, 3.26 m of massive diamictite containing mostly carbonate clasts, 0.24 m of compositionally layered diamictite, 0.66 m of massive diamictite with sparse clasts, 0.2 m of medium-grained greywacke, 9.54 m of massive diamictite containing a heterolithic clast assemblage and 0.52 m of compositionally layered diamictite with carbonate and fine-grained siliciclastic clasts that appear to pierce layering. Sitting sharply on the topmost diamictite is a 0.2-m-thick shale containing abundant pyrite. This unit, in turn, is capped by the basal komatiite of the overlying Polisarka Volcanic Formation (Units E and F).

Igneous Bodies Within the Sedimentary Succession

The igneous rocks comprising Units B, C and D occur within the *Limestone member*. Unit B interval 225.16–225.97 m is 0.8 m thick with abundant olivine phenocrysts. Its lower and upper margins are fine-grained and phenocryst-free. XRF analysis (calculated volatile-free) shows high contents of MgO (25.2 wt.%) and FeO_T (15.8 wt.%) and elevated concentrations of compatible trace elements Cr and Ni (1,220 and 850 ppm) coupled with high contents of TiO_2 (3.7 wt.%, see Fig. 6.17) and other incompatible trace elements (Ba 435, Rb 22, Sr 658, Zr 212 and Nb 35 ppm). These compositional features are similar to those of alkaline ultramafic magmas such as meimechites (e.g. Arndt et al. 1995). Such magmatism is unknown in the Palaeoproterozoic of the Fennoscandian Shield and we interpret this body as a dyke belonging to the Palaeozoic Alkaline Province of the Kola Peninsula (cf. Downes et al. 2005).

Unit C (interval 212–189 m) is composed of eight mafic layers each separated by sedimentary interlayers ranging from 0.2 to 4 m in thickness (Fig. 6.13). The two uppermost layers are thin (0.4 and 0.6 m) and have relatively high MgO content (12.2, 13.9 wt.%) (Fig. 6.17a), but Cr (c. 40 ppm) and Ni (c. 20 ppm) are low and indicate that the rocks have gained MgO during post-magmatic processes. A high degree of alteration is also manifested by high LOI values in the samples (11 and 15 wt.%). The other igneous layers have thicknesses between 0.5 and 4 m and are less altered. One, a c. 2-m-thick unit at a depth of 205 m (Fig. 6.13) displays flattened amygdaloidal structures close to its upper and lower contacts confirming that it is a lava flow. Exact classification of the rocks is hampered by secondary alteration, but the abundances of major elements correspond to basic to intermediate compositions and the concentrations of the most immobile elements are relatively high (TiO_2 1.7, 2.1 wt.%, Zr 185, 205 ppm), suggesting a transitional or mildly alkaline character for the magma.

Unit D (interval 132–176 m, Fig. 6.13) is a 45-m-thick, massive ultramafic body. The rock is strongly altered to talc-carbonate-chlorite schist and contains quartz-carbonate veins and carbonate porphyroblasts (Fig. 6.19aa, ab). No structure has been seen in the core that could be used to discriminate between an extrusive or intrusive origin and it remains to be resolved if it is a volcanic or an intrusive rock. Loss of ignition varies between 10 and 15 wt.%. The MgO contents (calculated volatile-free) range between 28 and 34 wt.% (Fig. 6.17a) and Ni and Cr contents are high, varying between 1200–1400 and 3300–4100 ppm: thus we interpret this rock as an ultramafic komatiite. The upper half of the body is more elevated in MgO, Cr and Ni, and depleted in Al_2O_3 and TiO_2 relative to the lower part. The upper part also shows higher magnetic susceptibilities (Fig. 6.14). This is opposite to what would be expected from internal magmatic differentiation of the body and it is possible that the unit was formed by two magma pulses. An ICP-MS analysis of a sample from 161 m yielded low contents of incompatible elements (Nb 0.23 ppm, Y 1.8 ppm, La 0.58 ppm) as expected for a komatiitic rock. The sample shows a flat chondrite-normalised REE pattern with a slight enrichment in LREE and a negative Eu anomaly (Fig. 6.18a).

The Polisarka Volcanic Formation

The Polisarka Volcanic Formation is represented in the drilled interval by mafic and ultramafic, globular- and spinifex-textured komatiitic lavas (Fig. 6.19a–c, h) with rare beds of shale and dacitic tuff-breccias (Fig. 6.19d–f). These are combined into Units E and F. Unit E (interval 42–99 m) contains a 54-m-thick komatiitic body and a 3-m-thick mafic tuff separated by a 0.4 m shale bed. The komatiite consists of a lower, 20-m-thick, ultramafic talc-chlorite or talc-chlorite-carbonate schist with abundant carbonate-quartz veins and an upper mafic section c. 34 m in thickness. The exact boundary cannot be recognised in the core due to alteration but is located near a depth of 77 m. The MgO content of the ultramafic section is high and roughly constant at c. 26 wt.%, although alteration may have disturbed the original values, and seems to be internally differentiated with Ni 820–1140 ppm and TiO_2 0.36 wt.% in its lower part and Ni 340–450 ppm and TiO_2 0.56 wt.% in its upper part. The mafic section is composed of magnesian basalt displaying pyroxene-spinifex textures (Fig. 6.19h) and

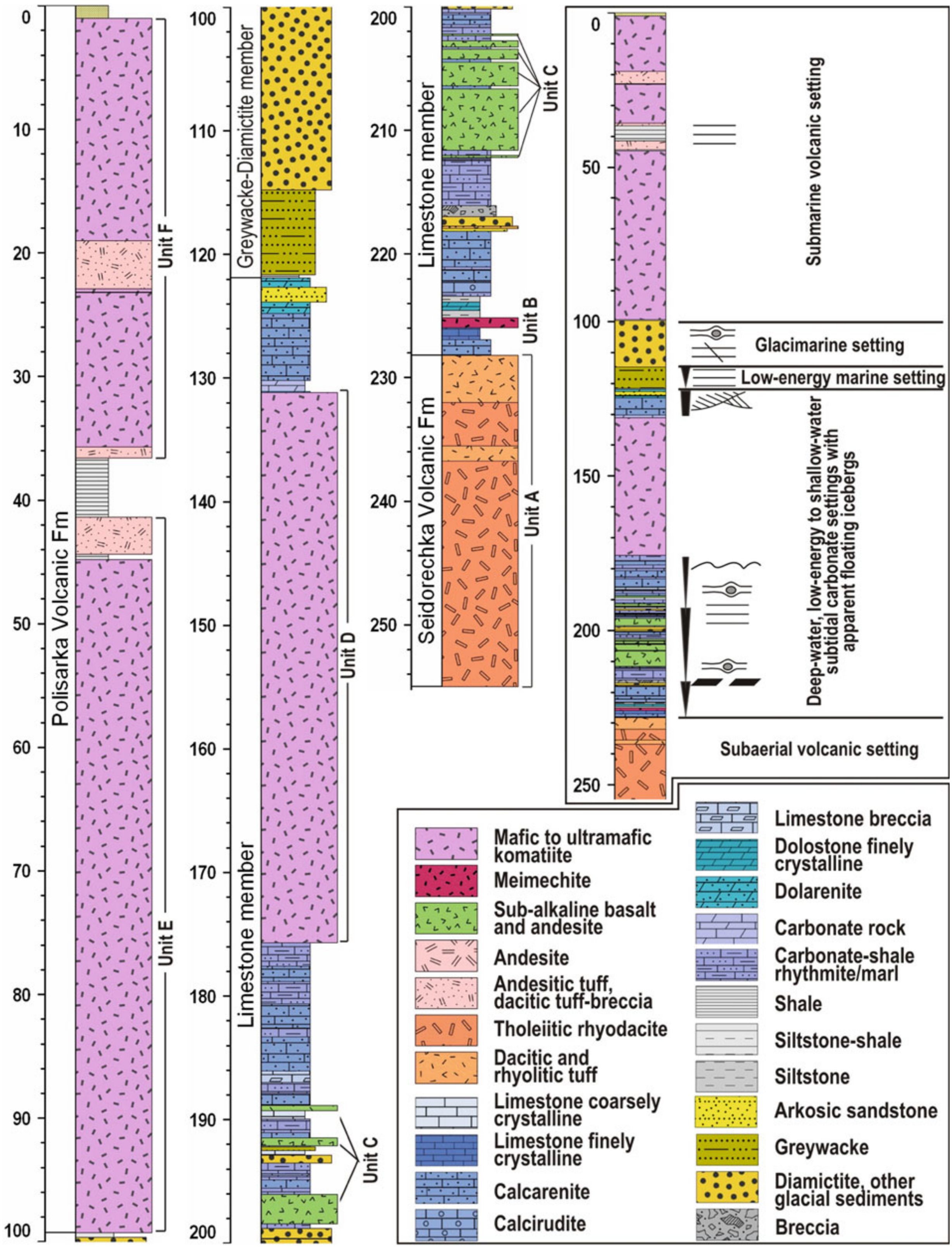

Fig. 6.13 Lithological section of the Polisarka Sedimentary Formation based on core log of Hole 3A, and a tentative reconstruction of depositional environments based on core logging, geological mapping and sedimentological research in the vicinity of the drilling site. Lithological symbols are explained in Fig. 6.6

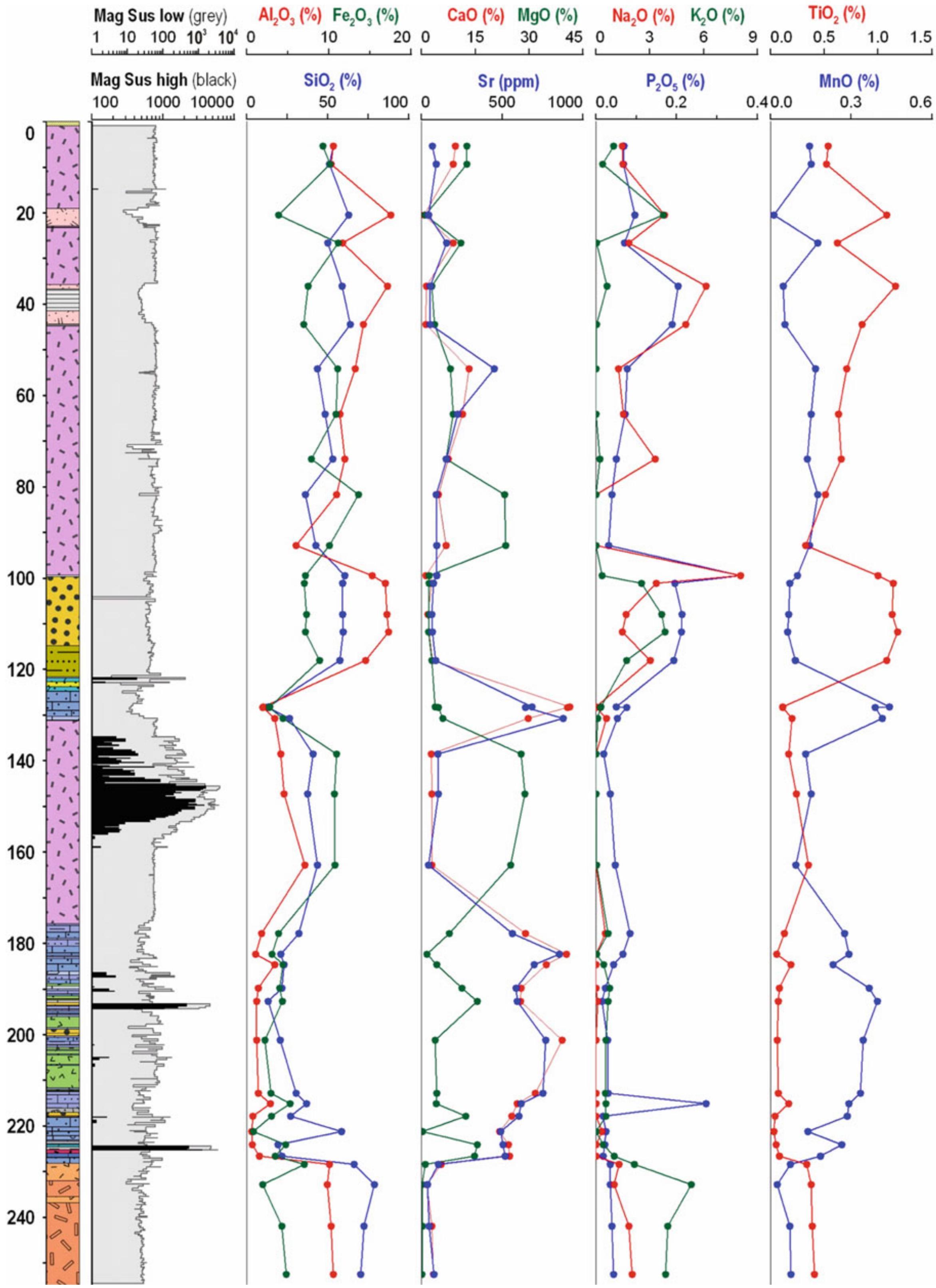

Fig. 6.14 Relative magnetic susceptibility (K*), and geochemical profiles of selected elements based on the archive samples collected with c. 8 m-spacing. For analytical techniques and data quality see Part 5

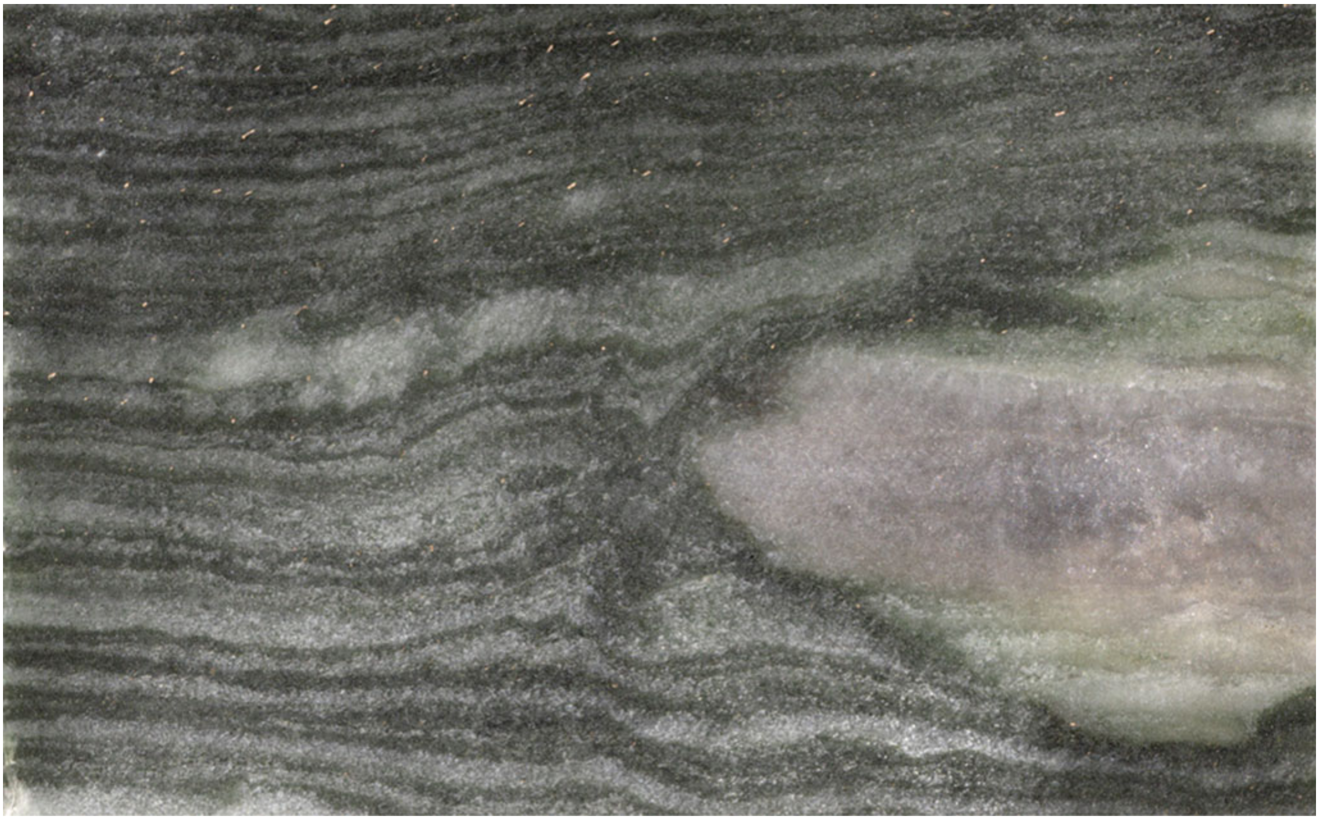

Fig. 6.15 Thinly laminated, limestone-shale couplets with dropstone having pierced lamination beneath it, whereas laminae above the clast are gently arched. This is interpreted as evidence for a glaciomarine environment and perhaps floating icebergs. FAR-DEEP Hole 3A, depth 183.2 m. Width of the image is 5 cm

MgO contents between 7.5 and 9.5 wt.%. There is no systematic upward decrease in the concentration of compatible elements or increase in incompatible elements suggesting that the mafic section may contain more than one lava flow. The ultramafic and mafic sections have slightly different chondrite-normalised REE patterns as shown by Fig. 6.18a. Consequently, they are not related to each other by simple fractional crystallisation, even though the general incompatible element characteristics are similar with pronounced negative anomalies at Nb-Ta and P and a smaller one at Ti in primitive mantle-normalised element diagrams (Fig. 6.18b). It is noteworthy that the komatiitic rocks in Unit E have a strong LREE-enrichment, while the ultramafic rock in the underlying Unit D has essentially an unfractionated REE pattern (Fig. 6.18a).

Unit F (interval 1–37 m) in the top part of Core 3A is separated from the underlying volcanic Unit E by 5 m of shale (Fig. 6.19g). Unit F can be divided into two lava flows, each underlain by tuff layers a few metres thick. The lower lava flow (22.9–35.7 m) is c. 13 m thick, has a pyroxene spinifex texture and is variolitic in its upper part. Although no definite pillow structure has been identified in the core, the variolitic textures are similar to those in the overlying pillowed lavas; thus it is probable that the lower lava also represents a pillowed unit. Three samples from the lower lava flow show MgO contents between 11.5 and 13.2 wt.% (volatile-free). The upper (1–19 m) variolitic pillow lava flow (Fig. 6.19a–c) is sparsely olivine-phyric with complete alteration of the phenocrysts to talc, serpentine, chlorite and carbonate. Three analyses yielded komatiitic basalt compositions with MgO contents between 12.9 and 14.1 wt.%. Both lava flows are enriched in LREEs compared to HREEs with a slight difference in the slope of the chondrite-normalised spectrum (Fig. 6.18a). The tuff layers underlying the komatiitic flows are dacitic to andesitic in composition (Fig. 6.17a).

As shown in Fig. 6.17b, the mafic to ultramafic lava flows from Units E and F form an extensive differentiation series. The rocks seem to have been generated from a similar komatiitic parental magma, though there are minor differences in incompatible trace element ratios. The mafic parts of the series have variable but typically high SiO_2 contents (52–54 wt.%), which may warrant classifying the rocks as siliceous high-magnesian basalts (SHMB; Sun and McDonough 1989; Sun et al. 1989). The Al_2O_3/TiO_2 ratio in lavas of Units E and F ranges between 16 and 20 indicating

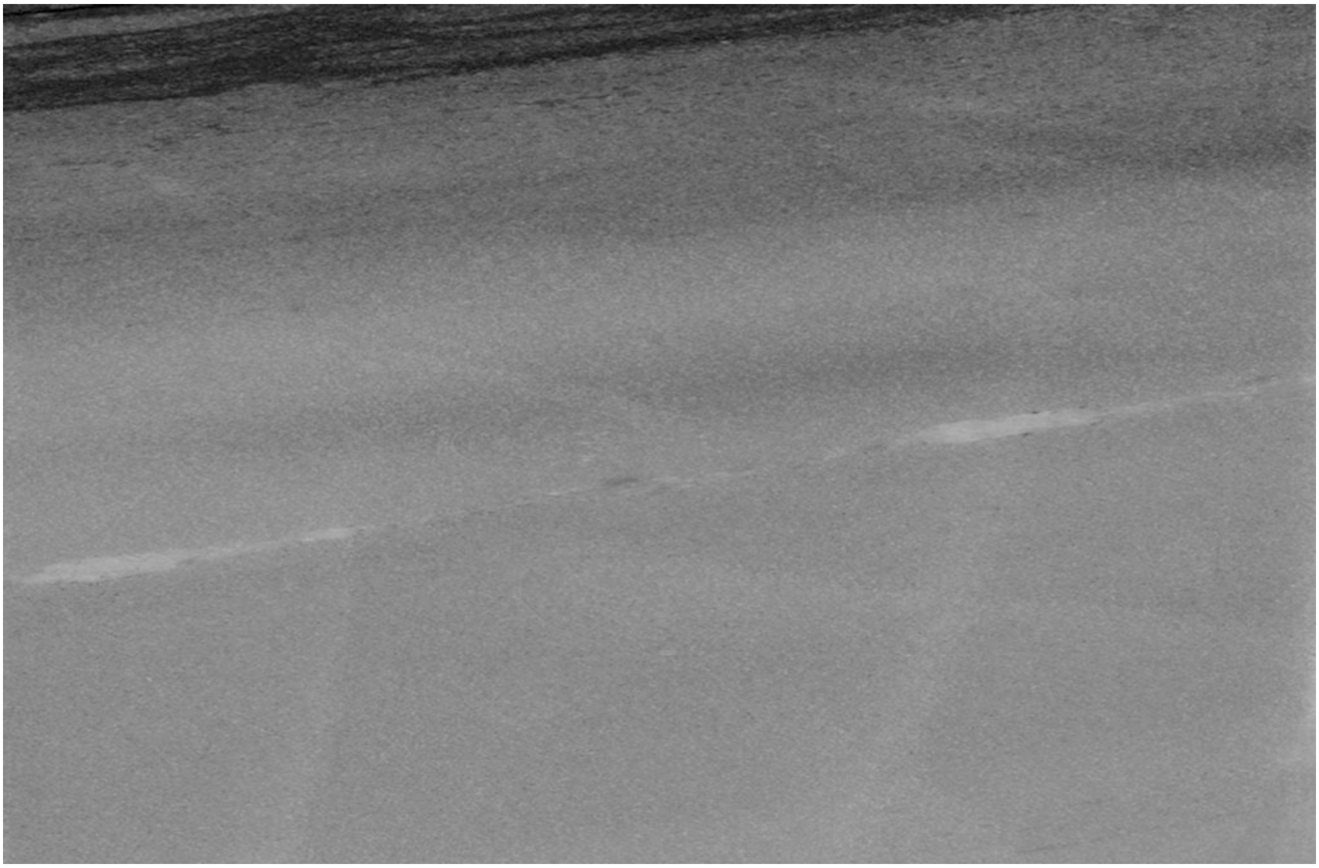

Fig. 6.16 Pure, finely crystalline, Sr-rich limestone associated with glaciomarine sediments has a great potential to contribute to our knowledge on seawater composition during the Huronian glaciation. FAR-DEEP Hole 3A, depth of 220.8 m. Width of the image is 5 cm

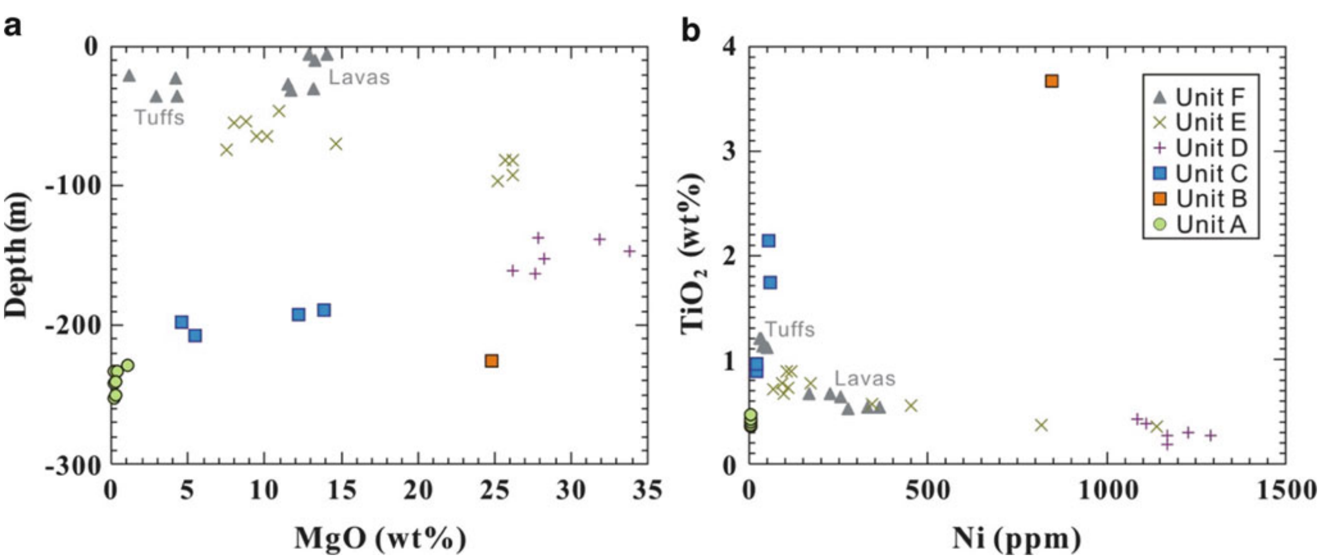

Fig. 6.17 (**a**) MgO versus depth and (**b**) Ni versus TiO_2 diagrams for igneous rocks in core 3A

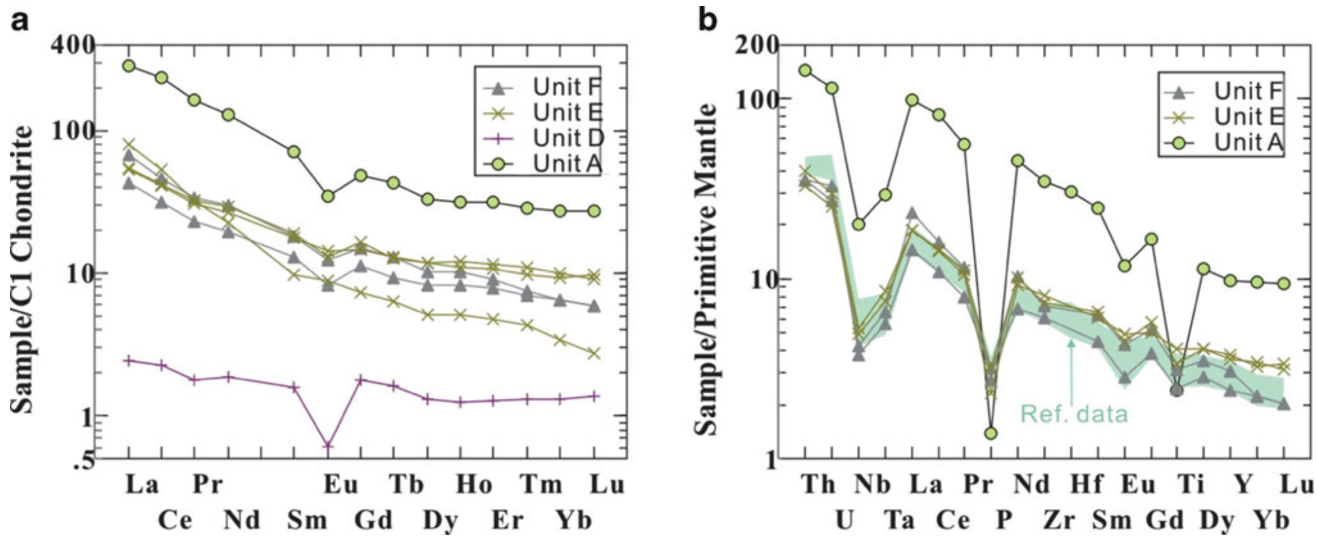

Fig. 6.18 (**a**) Chondrite-normalised REE patterns for igneous rocks from Units A, D, E and F. (**b**) Primitive mantle-normalised trace element patterns for igneous rocks from Units A, E and F. Reference data are based on analyses from outcrop sections in the central part of the Imandra/Varzuga Greenstone Belt (Smolkin and Hanski unpublished data). Normalising values are taken from Sun and McDonough (1989)

an Al-undepleted komatiitic parental magma (cf. Nesbitt et al. 1979). However, typical Al-undepleted komatiites from Archean greenstone belts have subchondritic LREE/HREE whereas the komatiitic rocks from Units E and F are strongly enriched in LREE, probably due to extensive interaction between the magma and sialic crust. A crustal signature is also evident in very low P_2O_5 and Nb contents and high LILE/HREE ratios. These features are typical of the Polisarka Volcanic Formation. Figure 6.18b exhibits a primitive mantle-normalized spidergram, in which our chemical data from Units E and F are compared with previously obtained trace element analyses of magnesian basalts of the Polisarka Volcanic Formation, representing outcrops from the central part of the Imandra/Varzuga Greenstone Belt (Hanski and Smolkin unpublished data).

The chemical data from different units of Core 3A are compatible with earlier data from the Polisarka Volcanic Formation containing low-Ti basalts and magnesian basalts with MgO in the range of 5–18 wt.% (e.g. Melezhik et al. 1982; Predovsky et al. 1987). The only exceptions are the ultramafic rocks in Core 3A, which widen the MgO range to higher than 30 wt.%, and thin Units B and C, which contain high-Ti rocks with a strongly and mildly alkaline affinity, respectively.

Depositional Framework

The depositional framework of the Polisarka Sedimentary Formation presented below is based on interpretation of sedimentary features in the logged drillcore (Fig. 6.19). The initial stage of the sedimentation, recorded in the thinly interlayered limestone-shale laminites and rhythmites of the Limestone member, is assigned to a relatively deep water, low-energy setting. The less common and thin intraclastic rhythmite breccia beds are resedimented carbonate rocks, which are apparently derived from nearby areas of oversteepened slopes. The progressive upward transition occurring over many metres to a few tens of metres from thinner to somewhat thicker layering concomitant with an increase in the limestone-to-shale ratio and a change from rhythmite to wackestone to grainstone is inferred to indicate a progressive shallowing; the presence of ribbon-rock textures in the upper part of those trends likewise suggests a change from deeper-water, low-energy settings into shallower, subtidal environments. Such a depositional pattern is repeated at least three times within the member. Such ‘cyclicity’ is a common feature of marine carbonate settings and defines shallowing cycles driven by relative changes in sea level.

The contact between the Limestone and the Greywacke-Diamictite members is sharp, and implies an abrupt change from carbonate- to siliciclastic-dominated sedimentation. The presence of mostly flat to low-angle lamination and rare small-scale cross-lamination suggests that depositing flows were of relatively low energy. That combined with the overall fineness of the greywacke and the lack of large-scale trough cross-bedding and superposed erosion/scour surfaces, casts doubt on a fluvial origin for the greywacke and, although not unequivocal evidence, is suggestive of a probable low-energy marine depositional setting devoid of carbonate production. The overall development of a

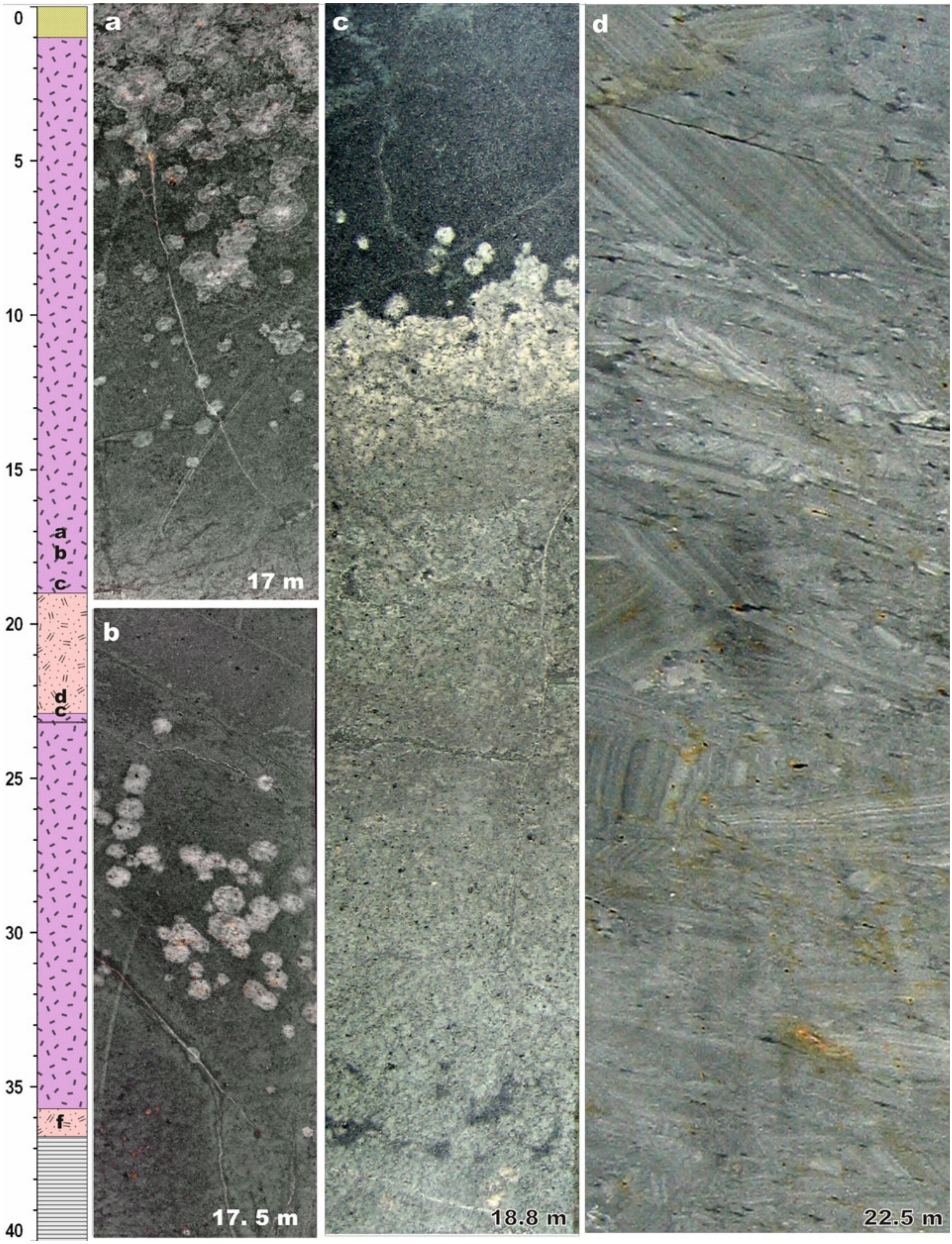

Fig. 6.19 Sedimentological and petrological features of the main rock types intersected by Hole 3A. Polisarka Volcanic Formation: (**a–c**) Komatiitic basalts with a globular texture typify Unit F. Core diameter is 50 mm unless specified otherwise

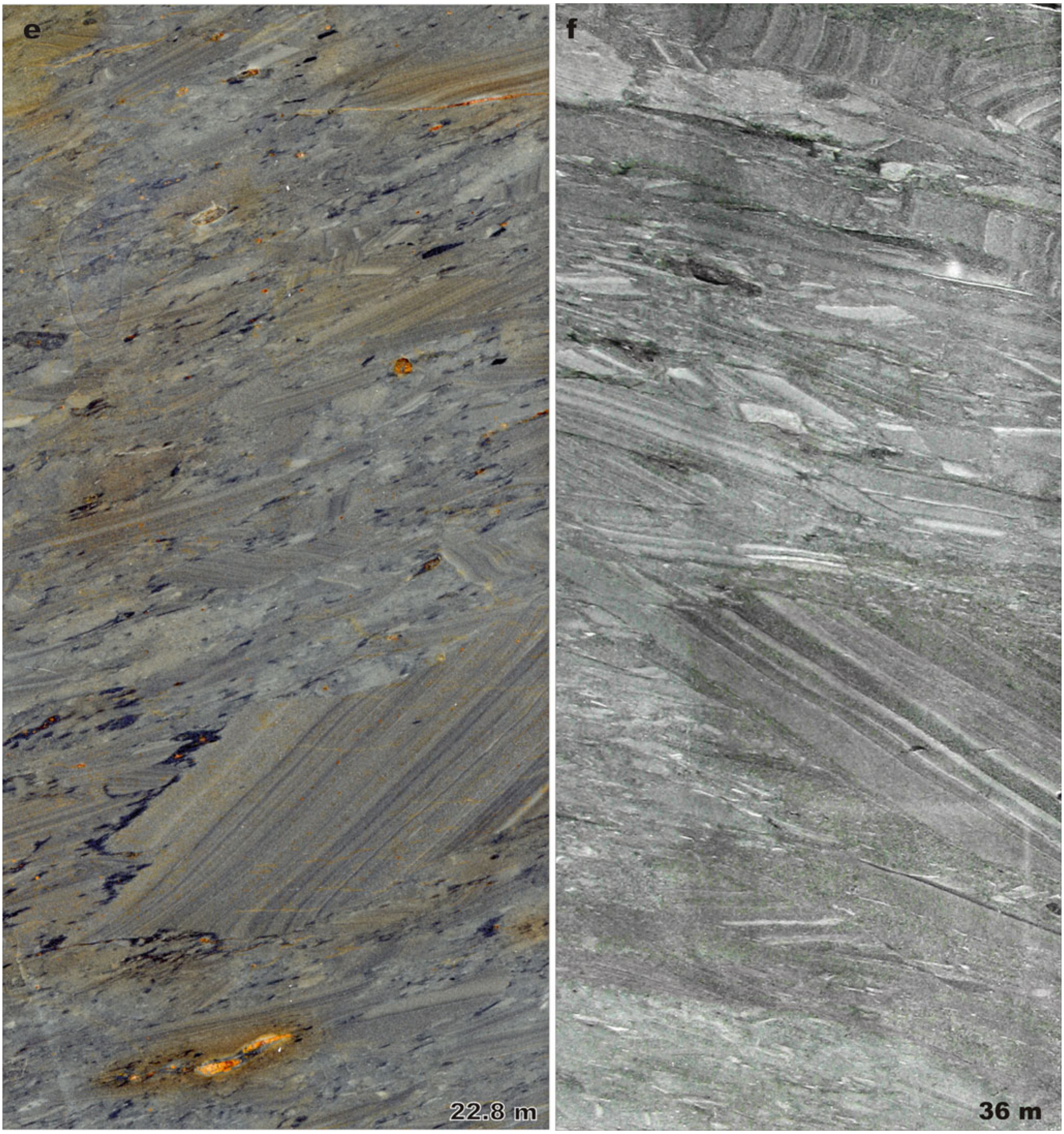

Fig. 6.19 (continued) (**d–f**) Redeposited dacitic tuff occurring as clast-supported breccia, which is composed of angular and platy fragments of finely-laminated tuff

systematic coarsening-upward trend over many metres also implies a marine, rather than a lacustrine, environment. This facies is sharply terminated by the development of the diamictites. The diamictic interval records deposition of several mass-flow deposits (debrites). The inference that these are of glacigenic origin, rather than 'normal' debris-flow deposits, is based on three observations: (1) numerous clasts are 'exotic' (e.g. granites, schists) in that they do not occur in the associated underlying or laterally adjacent lithologies; (2) several clasts exhibit faceted margins; and (3) the thinner compositionally layered diamictite beds in which some clasts pierce layering can be reasonably

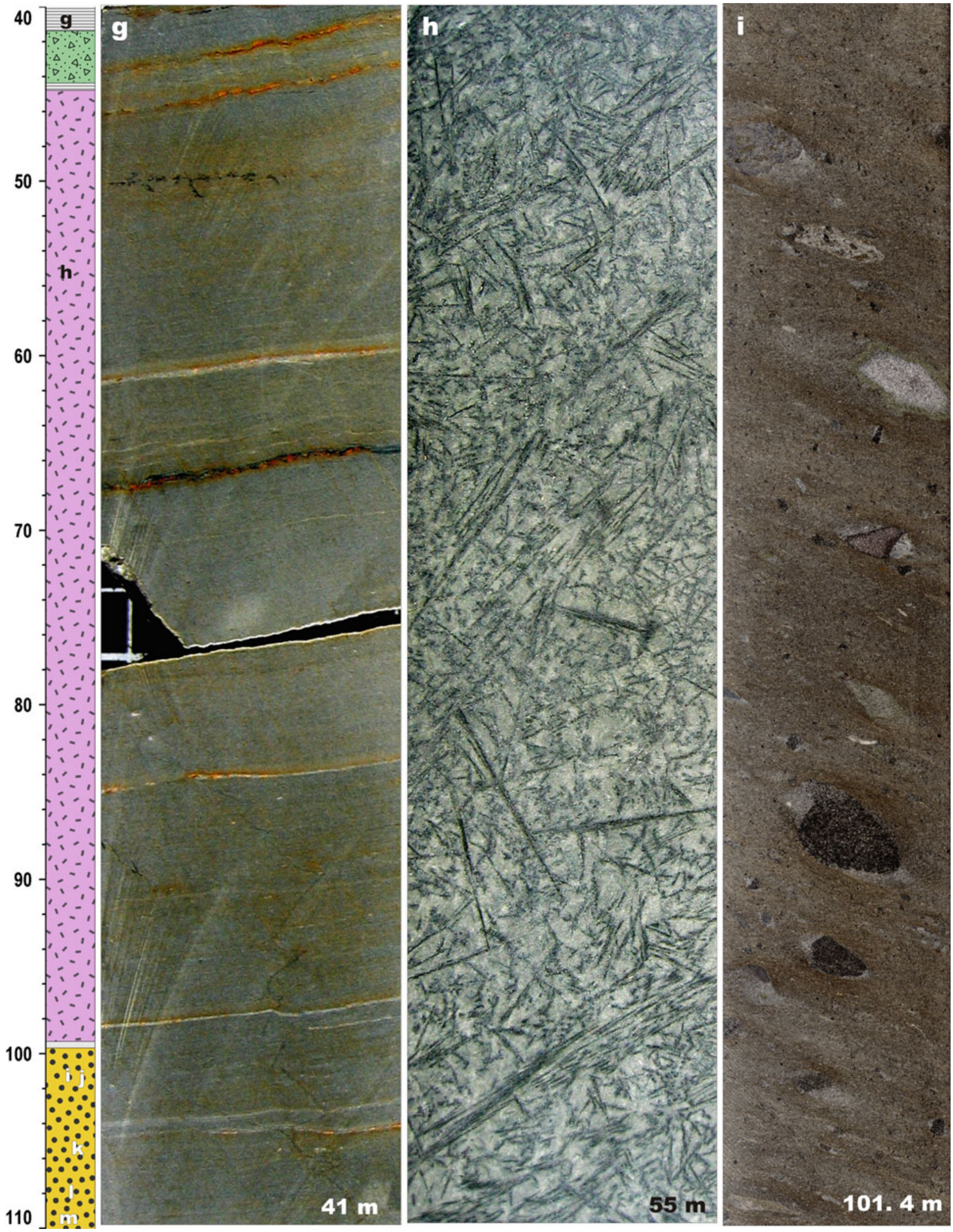

Fig. 6.19 (continued) (**g**) Parallel-laminated shale, which separates two units of komatiitic volcanic rocks. (**h**) High-magnesium komatiitic basalt with a pyroxene-spinifex texture. Polisarka Sedimentary Formation: (**i**) Diamictite composed of scattered andesite and dacite clasts set in a massive clayey siltstone matrix (rock flower); the clasts are tectonically flattened and oriented; quartz and chlorite are concentrated in triangular regions (pressure shadow) next to the margins of rigid clasts

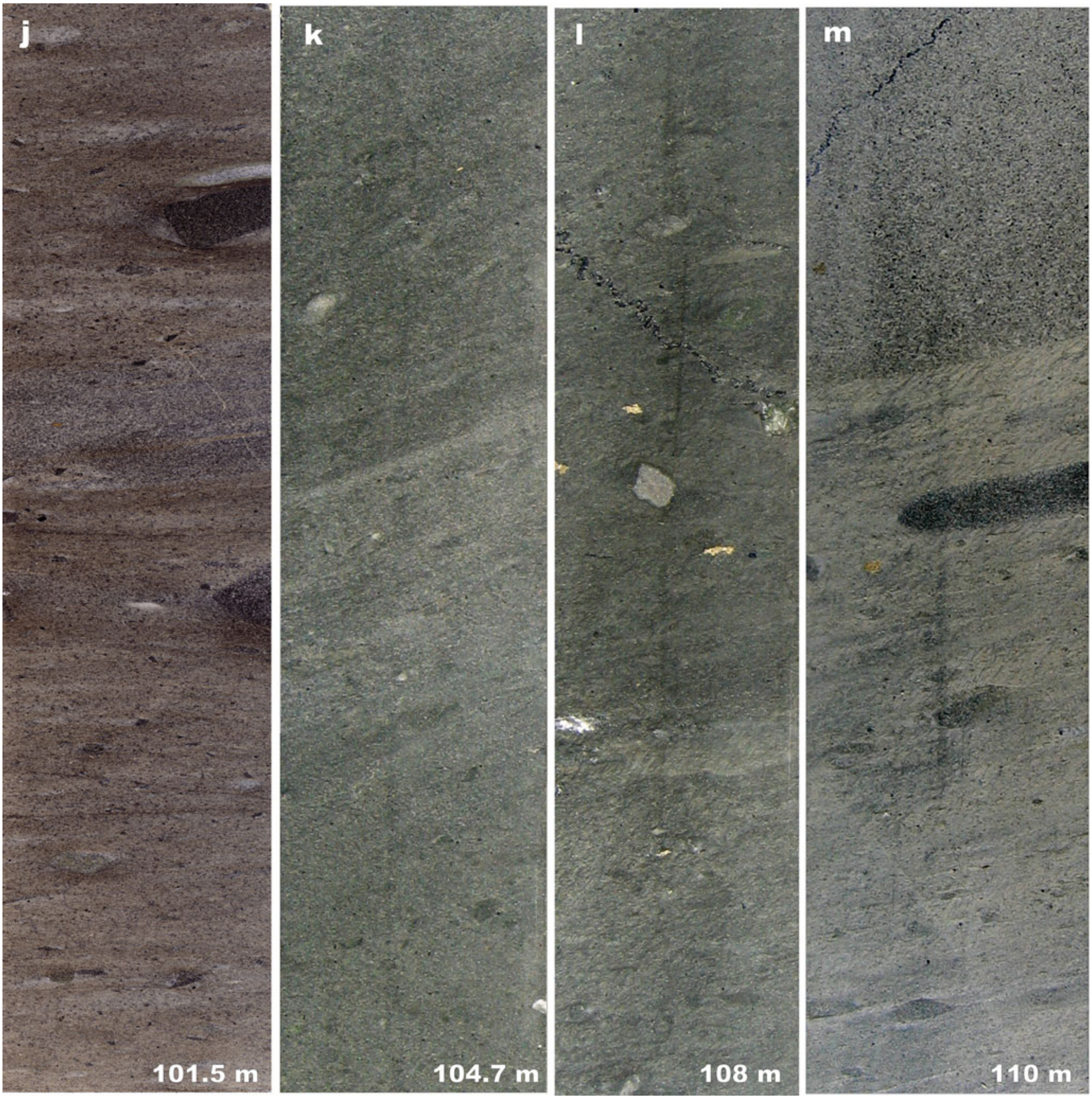

Fig. 6.19 (continued) (**j**) Clayey siltstone with indistinct parallel bedding and scattered oversized clasts of andesites. (**k**) Two beds of clayey and sandy siltstone with the lower one (*pale grey*) showing reverse grading whereas the upper bed is rather massive; both beds contain scattered unsorted clasts. (**l**) Indistinctly bedded clayey and sandy siltstone with scattered oversized clasts. (**m**) Clayey siltstone (*pale grey*) with tectonically flattened oversized clasts overlain by massive fine-grained sandstone (*dark grey*)

interpreted as dropstone diamictites. Further, the occurrence of one such dropstone nearly 70 m below the base of the first diamictite bed and in the laminites of the Limestone member is perhaps evidence for floating icebergs. This suggests that the entirety of the Polisarka Sedimentary Formation was deposited during a time when apparent icebergs were present. It also lends additional support to the inference that the formation is entirely of marine (Limestone member) and glacimarine (Greywacke(?)-Diamictite member) origin.

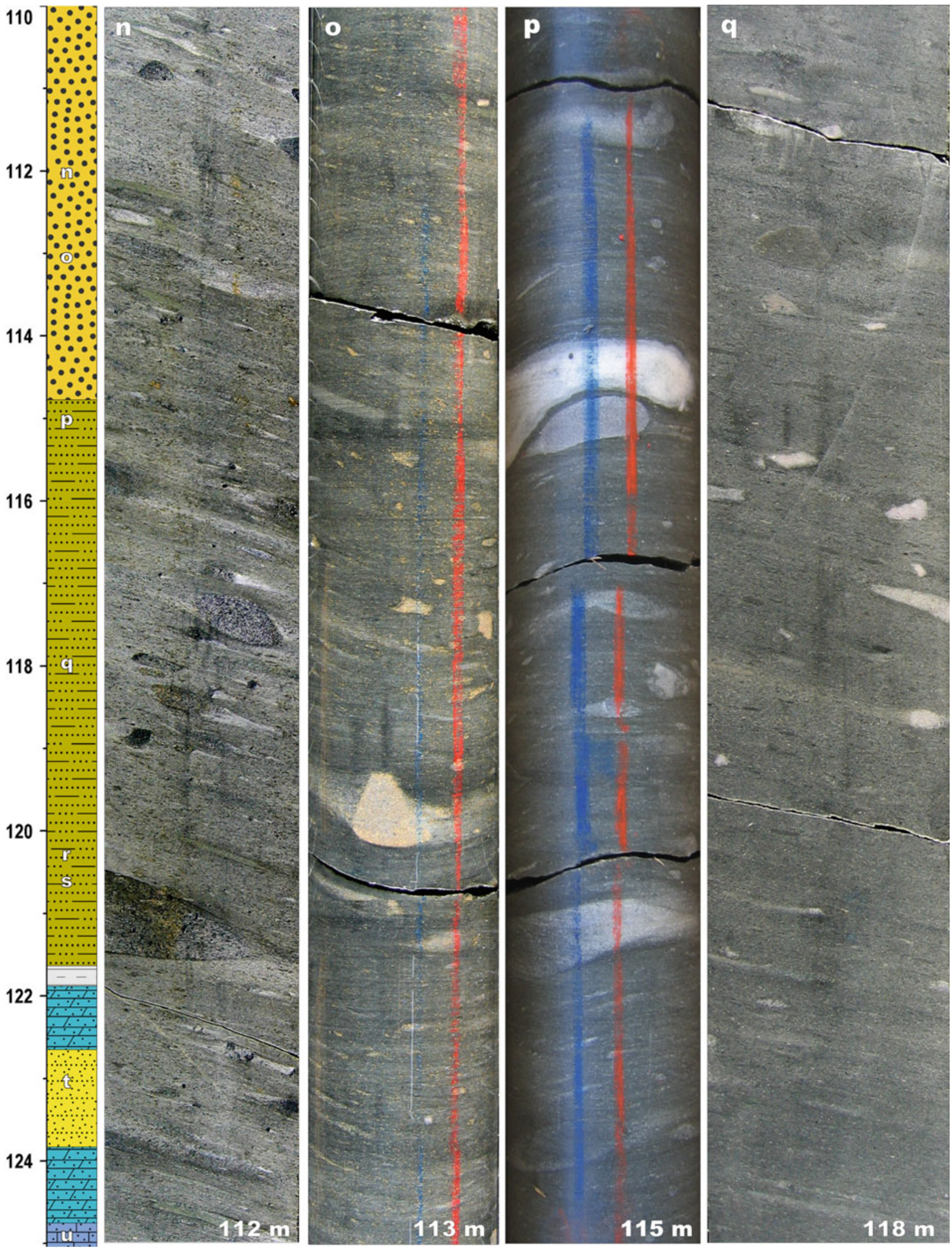

Fig. 6.19 (continued) (**n**, **o**) Tectonically modified massive diamictite containing scattered, oversized, polymict, angular and rounded clasts set in a clayey siltstone matrix; apparent layering is due to foliation and considerably flattened shale clasts. (**p**) Massive diamictite with tectonically flattened polymict clasts set in a clayey siltstone matrix. (**q**) Massive diamictite containing scattered angular and rounded clasts set in a clayey siltstone matrix; extremely flattened shale clasts produce apparent pseudo-bedding

Fig. 6.19 (continued) (**r**) Indistinctly cross-bedded, fine-grained sandstone overlain by a layer of clayey siltstone (*dark grey*) followed by a sandstone bed. (**s**) Cross-bedded layer (*red arrow*) in crudely bedded greywacke. (**t**) Interbedded thin clayey siltstone (*dark grey*) and thicker massive sandstone (*grey*) beds. (**u**) Clayey limestone with bedding denoted by a change in colour caused by the clay component content

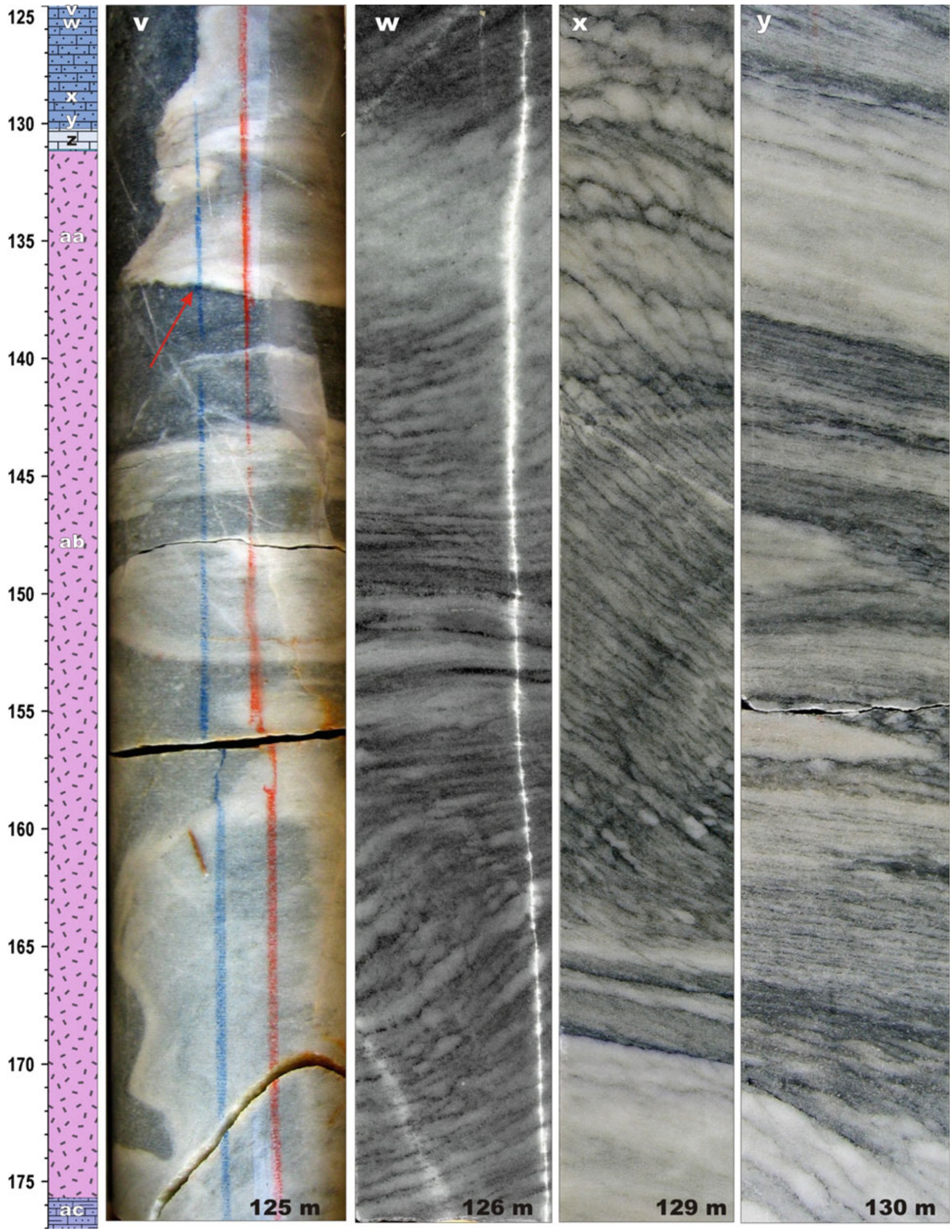

Fig. 6.19 (continued) (**v**) Marl-matrix-supported limestone rudite; although the clast shape was tectonically modified, their angular nature is still well-preserved (*arrowed*). (**w**) Clayey limestone showing thin composite layering; bright vertical line is a crack filled with re-crystallised calcite. (**x**) Interbedded pure limestone (*white*) and clayey limestone beds; the clayey beds show well-pronounced cleavage. (**y**) Tectonically modified interbedded clayey (*dark grey*) and pure (*white*) limestones

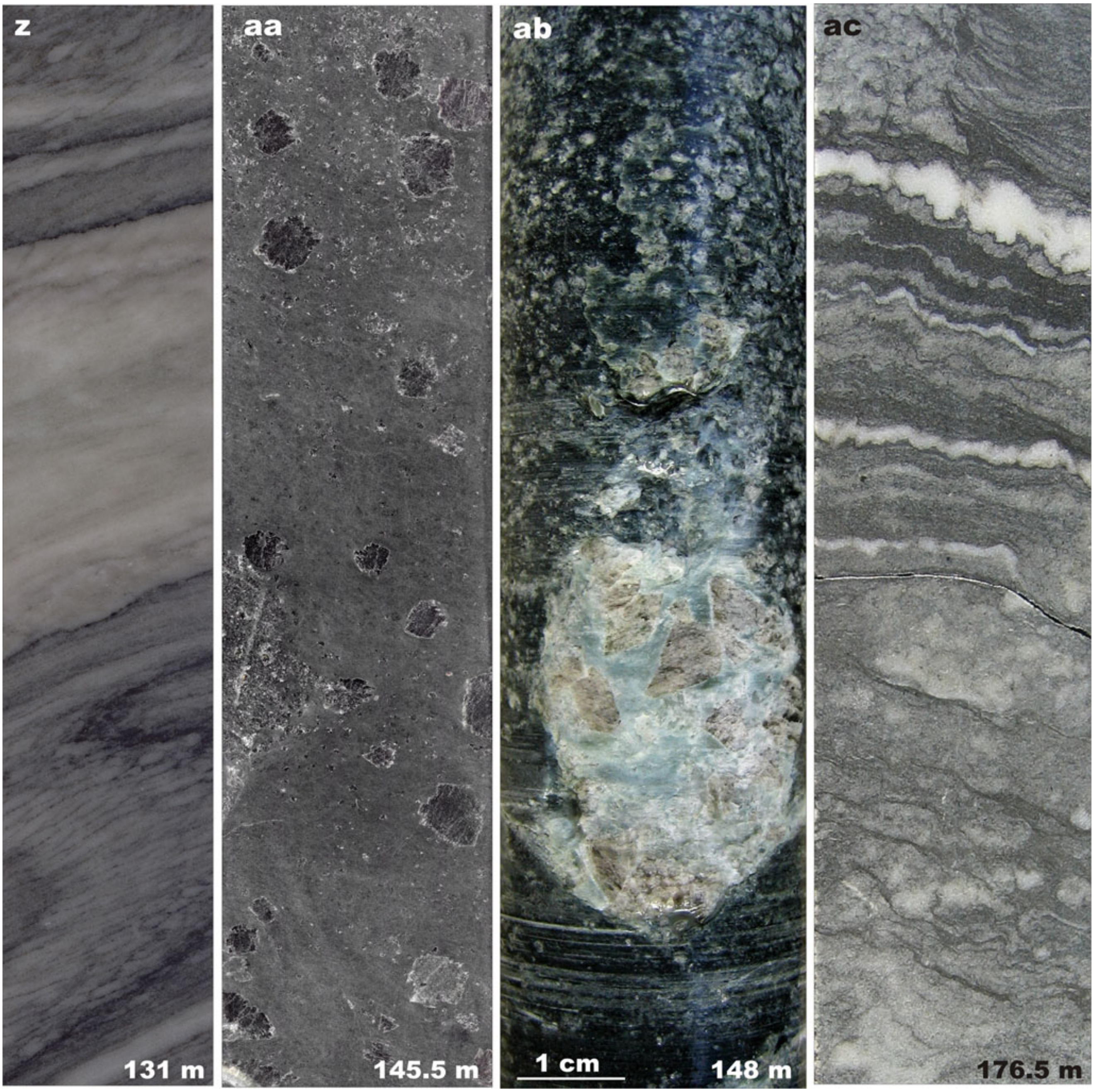

Fig. 6.19 (continued) (**z**) Interbedded pure limestone and clayey limestone showing isoclinal fold. (**aa**) Ultramafic komatiite with carbonate porphyroblasts. (**ab**) Ultramafic komatiite with large talc (*pale blue*)-carbonate porphyroblast. (**ac**) Pale grey clayey limestone with granular structure (former limestone gritstone-conglomerate) overlain by laminated limestone, clayey limestone and mudstone units

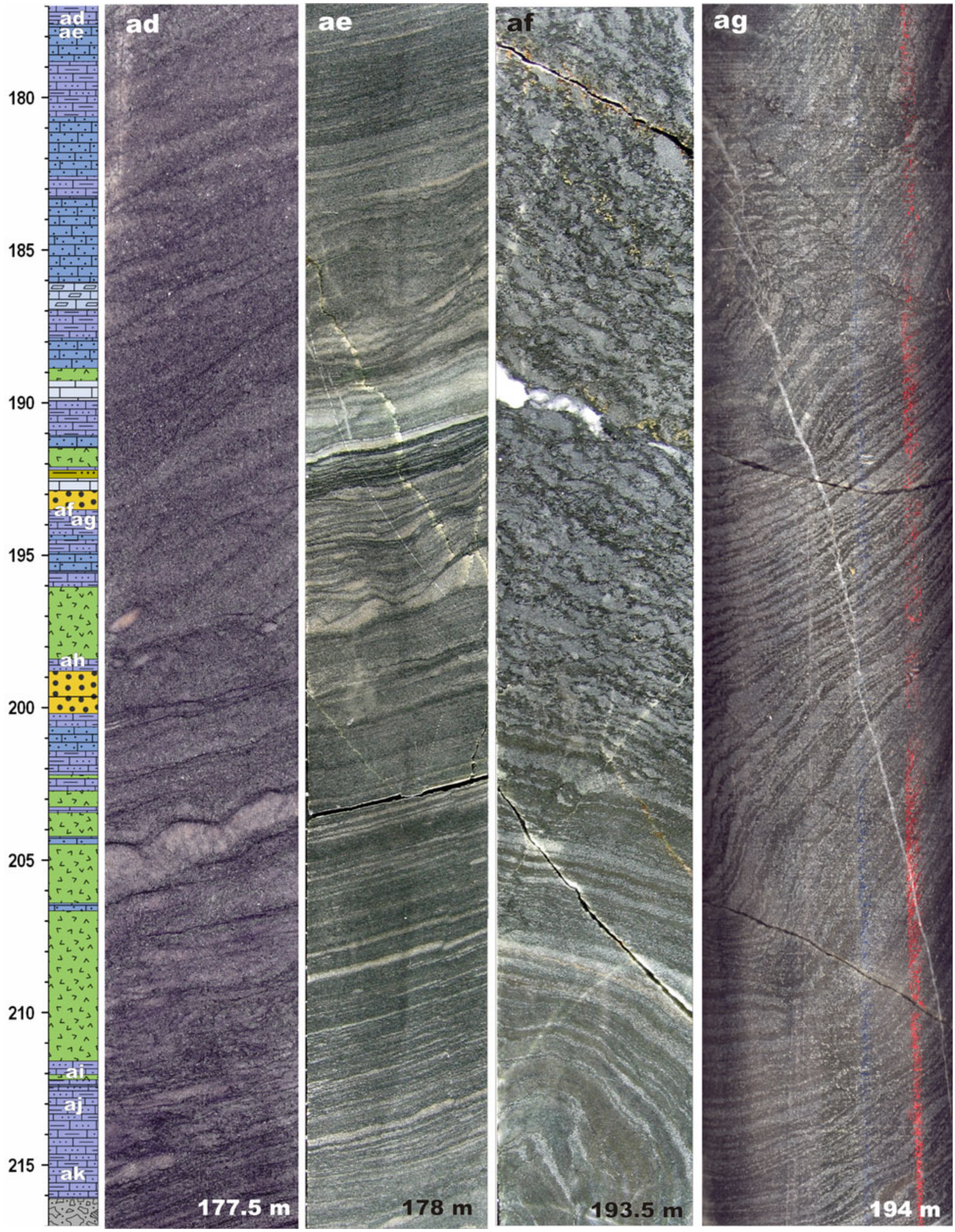

Fig. 6.19 (continued) (**ad**) Tectonically modified rippled and cross-bedded calcareous shale. (**ae**) Parallel-laminated calcareous shale with bed in the *middle* displaying deformed wavy and flaser bedding. (**af**) Parallel-laminated marl overlain by shale-matrix-supported limestone gritstone to fine-clast limestone conglomerate. (**ag**) Finely-laminated limestone (*pale grey*) and siltstone (*dark grey*) couplets resembling varved sediments

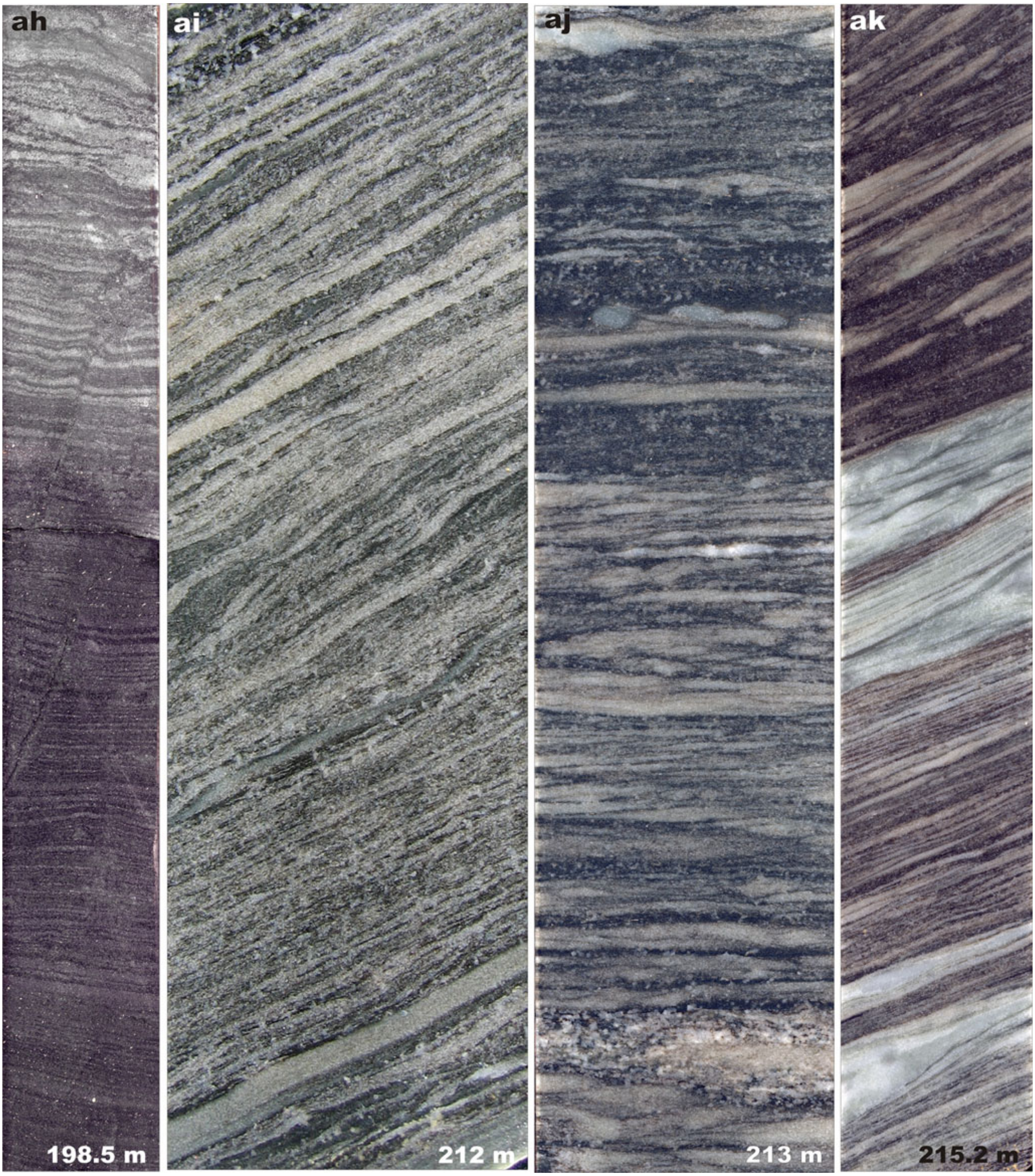

Fig. 6.19 (continued) (**ah**) Finely-laminated limestone and siltstone couplets (varved sediments?) in *dark grey* and *grey* beds overlain by a *pale grey* bed showing wavey lamination. (**ai**) Parallel- and flaser-bedded limestone-shale couplets. (**aj**) Shale-limestone with tectonically modified lenticular bedding. (**ak**) Tectonically-modified interbedded pure limestone, marl and shale units

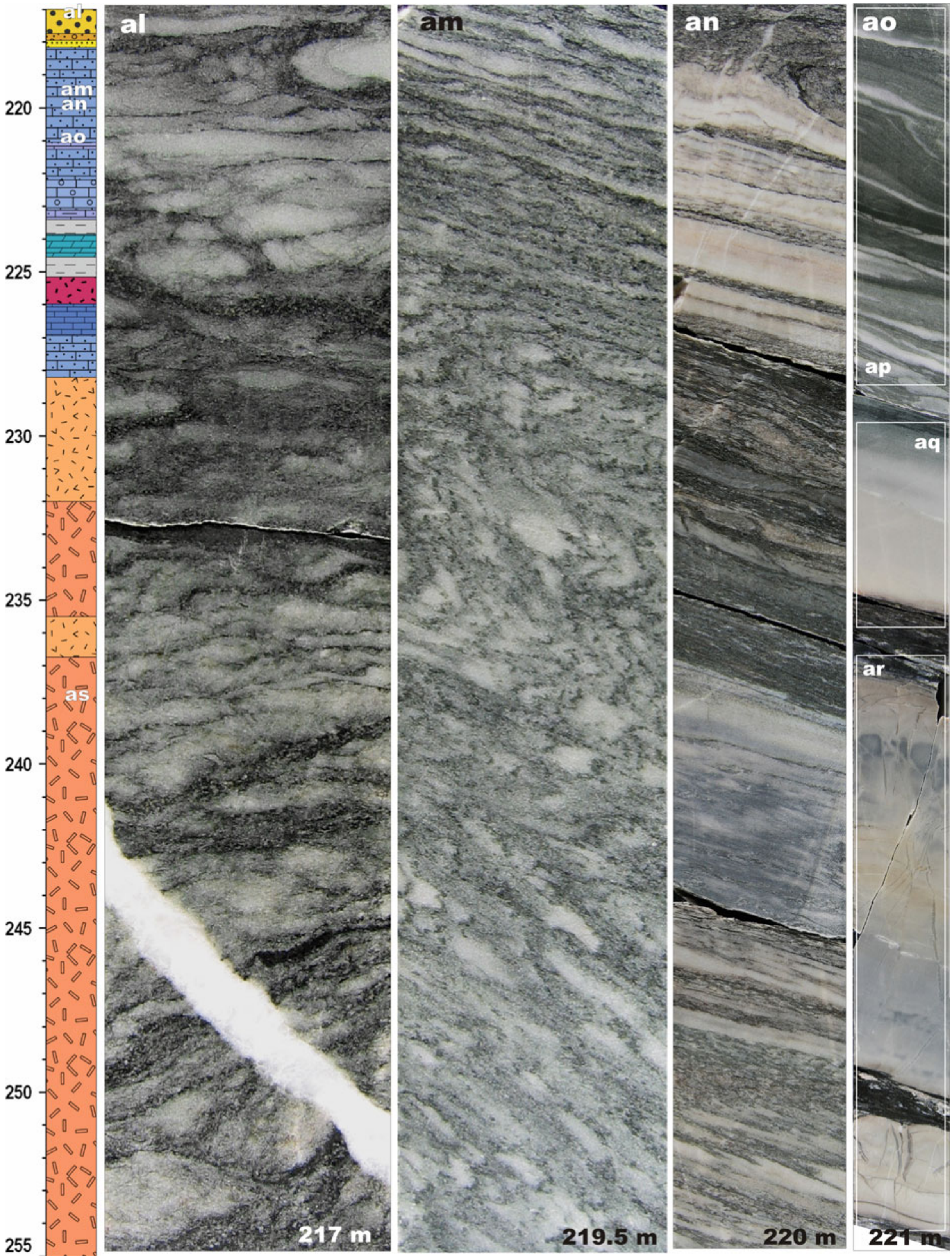

Fig. 6.19 (continued) (**al**) Tectonically modified shale-matrix calcirudite; white band in the lower part of the core is an extensional crack filled with quartz. (**am**) Tectonically modified ribbon-rock limestone. (**an**) Tectonically modified interbedded limestone, marl and shale units. (**ao**) Interbedded finely-laminated and thickly bedded limestone-shale couplets

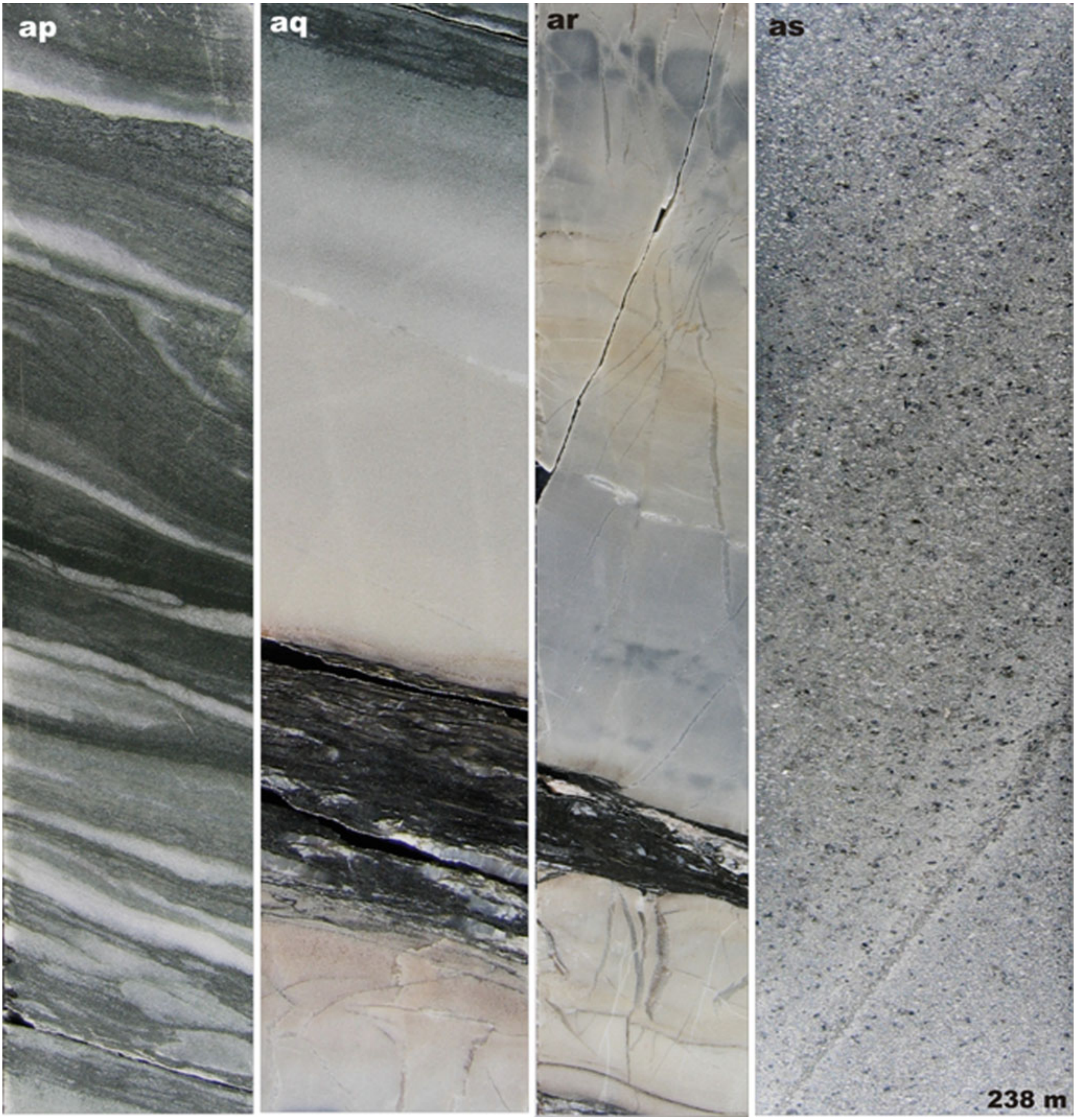

Fig. 6.19 (continued) (**ap–ar**) Detailed images of "**ao**" showing internal structure of finely-laminated (**ap**) and thickly-bedded (**aq–ar**) shale-limestone couplets. Seidorechka Volcanic Formation: (**as**) Finely crystalline tholeiitic rhyodacite (All photos by Victor Melezhik)

References

Arndt N, Lehnert K, Vasil'ev Y (1995) Meimechites: highly magnesian lithosphere-contaminated alkaline magmas from deep subcontinental mantle. Lithos 34:41–59

Amelin YuV, Heaman LM, Semenov VS (1995) U-Pb geochronology of layered mafic intrusions in the eastern Baltic Shield: implications for the timing and duration of Palaeoproterozoic continental rifting. Precambrian Res 75:31–46

Downes H, Balaganskaya E, Beard A, Liferovich R, Demaiffe D (2005) Petrogenetic processes in the ultramafic, alkaline and carbonatitic magmatism in the Kola Alkaline Province: a review. Lithos 85:48–75

Melezhik VA, Borisov AA, Fedotov ZhA, Predovsky AA (1982) Varzuga Series. In: Gorbunov GI (ed) The Imandra/Varzuga zone of Karelids. Nauka (Science), Leningrad, pp 57–85, in Russian

Nesbitt RW, Sun S-S, Purvis AC (1979) Komatiites: geochemistry and genesis. Can Mineral 17:165–186

Predovsky AA, Melezhik VA, Bolotov VI, Fedotov ZhA, Basalaev AA, Kozlov NE, Ivanov AA, Zhangurov AA, Skufin PK, Lyubtsov VV (1987) Precambrian Volcanism and Sedimentology in the North-Eastern Part of the Baltic Shield. Nauka (Science), Leningrad, 185p, in Russian

Sun S-S, McDonough WF (1989) Chemical and isotopic systematics of oceanic basalts; implications for mantle composition and processes. In: Saunders AD, Norry MJ (eds) Magmatism in the ocean basins, vol 42, Geological society special publication. Published for the Geological Society by Blackwell Scientific Publications, Oxford/Boston, pp 313–345

Sun S-S, Nesbitt RW, McCulloch MT (1989) Geochemistry and petrogenesis of Archean and early Proterozoic siliceous high-magnesian basalts. In: Crawford AJ (ed) Boninites. Unwin Hyman, London, pp 149–173

6.1.3 Umba Sedimentary Formation: FAR-DEEP Hole 4A

Victor A. Melezhik, Eero J. Hanski, Anthony R. Prave, Aivo Lepland, Alexander E. Romashkin, Dmitry V. Rychanchik, Zhen-Yu Luo, Evgenii V. Sharkov, and Maria M. Bogina

Scientific Targets

- Tectonic and depositional settings associated with the Lomagundi-Jatuli isotopic event
- Geochemical rock record during the global perturbation of the carbon cycle
- Influence of depositional setting on carbon and strontium isotopic composition of basinal water
- Provenance composition
- Microfossil record
- Radiometric age constraint on timing of deposition

Hole 4A intersects the Umba Sedimentary Formation (Figs. 6.20 and 6.21) in the western Imandra-Varzuga Greenstone Belt (Figs. 6.1, 6.2, and 6.3). The depositional age of the formation remains unconstrained. It sits stratigraphically above the Huronian-age glacial deposits of the Polisarka Formation and contains isotopically heavy, ^{13}C-rich carbonate rocks that have been considered to be coeval with the time period corresponding to the Lomagundi-Jatuli carbon isotope excursion (see Chap. 1.2 and 7.3). Core 4A includes one of the five successions in the FAR-DEEP drillcore collection that contain the Lomagundi-Jatuli ^{13}C-rich sedimentary carbonates. Many of these, and other Lomagundi-Jatuli carbonate successions in Fennoscandia are inferred to have been deposited in restricted basins. However, the core material of Hole 4A provides a sedimentary record from what is presently considered to be a more open marine environment and has a great potential to address the carbon cycle on both regional and global scales in the aftermath of the Huronian glaciation and during the course of the Lomagundi-Jatuli Isotopic Event (Figs. 6.22 and 6.23).

The 233.9-m-long Hole 4A intersects 203.4 m of the Umba Sedimentary Formation and 5.7 m of the overlying basalts of the Umba Volcanic Formation (Fig. 6.20). Several bodies of mafic igneous rocks have been intersected at various depths, and Figs. 6.24, 6.25, and 6.26 illustrate their main geochemical features. Chemical compositions of all analysed archive samples are presented in Appendices 7–9, and Fig. 6.21 shows stratigraphic profiles of selected major and trace elements as well as magnetic susceptibility. Core photos and thin section scans provide detailed documentation of the major lithological features (Fig. 6.27).

Eleven mafic magmatic bodies occur at various stratigraphic levels and have thicknesses between 0.2 and 16 m; these have been grouped into four units (from A to D) based on their geochemistry and stratigraphic position (Fig. 6.20). Units A-C within the sedimentary succession are comprised of mafic rocks with rather homogeneous and low magnetic susceptibility ranging between 360 and 870 μSI ($K^* = 33–79 \times 10^{-6}$ SI in Fig. 6.21), with one exception of one body at 152–157.5 m, which has a magnetic susceptibility of 74,600 μSI ($K^* = 6{,}780 \times 10^{-6}$ SI). Unit D is the basal alkaline basalt of the Umba Volcanic Formation and is characterised by a high though variable magnetic susceptibility of 810–24,200 μSI ($K^* = 74–2{,}200 \times 10^{-6}$ SI).

The Umba Sedimentary Formation

In the drillcore, and based on observations of outcrops from around the drilling site, the Umba Sedimentary Formation occurs as a succession of interbedded greywacke, arkosic and quartzitic sandstone, siltstone, shale, dolostone and limestone. The first volcanic unit (Unit D) of the overlying Umba Volcanic Formation defines the formational top at a depth of 20.3 m (Fig. 6.20). The Umba Sedimentary Formation is informally subdivided into four lithostratigraphic units, from base to top: Sandstone-Siltstone, Dolostone, Shale and Quartzite members (Fig. 6.20).

The Sandstone-Siltstone Member

This member is c. 43 m thick; it may be thicker given that the bottom of the core is cut by a mafic igneous body that is interpreted as a sill. The upper contact at a depth of 179 m (Fig. 6.20) is defined by a thin unit of Na_2O-rich (3.9 wt.%) tuffite ($SiO_2 = 68$ wt.%, Appendix 7) showing reverse grading (Fig. 6.27p–q). Although thinly alternating sandstone-siltstone-shale (Fig. 6.27r–ab) is a dominant lithology of the member, its base is comprised of two intervals of impure dolostone-limestone rhythmites (Fig. 6.27ac) separated by a siltstone-shale unit (Fig. 6.20). The remainder of the member is characterised by thin, rhythmic bedding between sandstone-siltstone-shale displaying normal grading (Fig. 6.27r, v, wz–ab) and the presence of reworked beds (Fig. 6.27u) and abundant soft-sediment deformation features (Fig. 6.27s, t, x, y). Probable fine, lenticular bedding structures are noticeable in the uppermost part of the member.

V.A. Melezhik (✉)
Geological Survey of Norway, Postboks 6315 Sluppen, NO-7491 Trondheim, Norway

Centre for Geobiology, University of Bergen, Allegaten 41, Bergen N-5007, Norway

V.A. Melezhik et al. (eds.), *Reading the Archive of Earth's Oxygenation*, Volume 2: The Core Archive of the Fennoscandian Arctic Russia – Drilling Early Earth Project, DOI 10.1007/978-3-642-29659-8_2,

The lower part of the member is relatively enriched in Al_2O_3 (16.4 wt.%), K_2O (4.4 wt.%) and Ba (2210 ppm). The impure carbonate rocks are siliceous (SiO_2 = 23–48 wt.%), have highly variable contents of Al_2O_3, K_2O and Na_2O, and a Mg/Ca ratio of 0.03–0.49. Concentrations of sulphur and organic carbon in all lithologies are below the detection limit. The overlying sandstone-siltstone-shale is also rich in K_2O (K_2O/Na_2O = 1.7–2.6), and has moderate and uniform Al_2O_3 abundances (14.3–15.3 wt.%). Some intervals are enriched in P_2O_5 (0.25 wt.%) and Ba (2210 ppm). These rocks contain low though measurable concentrations of sulphur (0.08–0.24 wt.%) and organic carbon (0.11–0.21 wt.%). A pronounced stratigraphic enrichment in Na_2O, from 1.6 to 2.2 wt.% over a thickness of 20 m (Fig. 6.21), is suggestive of possible incorporation of some Na_2O-rich volcanic input (Fig. 6.27pq). Both the ash bed and the sandstone-siltstone-shale show an elevated Zr content, 143, and 203–264 ppm, respectively.

The Dolostone Member

This member (Fig. 6.27ab–ac) is 61 m thick and comprises mainly carbonate rocks, marl and siltstone-shale layers with rare arkosic sandstone, and two mafic lava units in its lower part (Fig. 6.20). Many of the layers (beds) are thin and define mm- to cm-scale rhythmic alternations between carbonate-rich and siliciclastic lithologies. Some carbonate units exhibit faint bedding expressed by variation of colour from white through beige to pale grey (Fig. 6.27k–m), whereas others show tectonic brecciation (Fig. 6.27f, h). The lowermost dolostone unit contains several 1- to 5-cm-thick intervals of weathered sand- and grit-size ultramafic grains (Fig. 6.27n, o). The siltstone-shale and marl commonly show parallel lamination of alternating carbonate-and shale-rich layers (Fig. 6.27j).

All carbonate rocks are impure, and SiO_2 is the main non-carbonate component (3–23 wt.%). The analysed carbonate rocks are devoid of organic carbon and only three samples contain sulphur above the detection limit (0.29–0.70 wt.%). Barium contents are highly variable (61–3310 ppm). Limestones (Mg/Ca = 0.03) are enriched in Mn (777 $\mu g\ g^{-1}$), and have 850 $\mu g\ g^{-1}$ Sr (Appendix 9) The dolostones have variable Mg/Ca ratios (0.39–0.55), are rich in Sr (293–638 $\mu g\ g^{-1}$) and have widely fluctuating Mn concentrations (88–2,050 $\mu g\ g^{-1}$) (Appendix 9). The carbonate rocks are characterised by elevated $\delta^{13}C_{carb}$ values, thus representing the Lomagundi-Jatuli positive isotopic excursion of $\delta^{13}C$ in sedimentary carbonates (for details see Chap. 7.3).

The Shale Member

This member is a c. 54-m-thick package marked by a basal arkosic gritstone-sandstone bed having a sharp contact on the underlying dolostone unit. The member consists mainly of thin siltstone-shale couplets displaying mostly parallel lamination, albeit tectonically modified (Fig. 6.27c). A few shale, marl, greywacke and arkosic sandstone intervals are present in the middle part of the section (Fig. 6.20). The sandstone forms massive beds with poorly sorted, rounded and angular clasts (Fig. 6.27e). Other lithologies exhibit either fine, parallel or low-angle cross-lamination (Fig. 6.27d), and in places, lenticular bedding.

The siltstone-shale has a moderate Al_2O_3 content (13–14 wt.%), the Fe_2O_{3tot} content decreases up section from 5.6 to 3.1 wt.% (Fig. 6.20), and the K_2O/Na_2O ratio is commonly >1. In contrast, the marl and a calcareous variety of the siltstone-shale facies are rich in sodium (Na_2O = 3.6–4.1 wt.%) and P_2O_5, (0.38–0.44 wt.%). The marl contains 2090 ppm Ba. The arkosic sandstone is notably enriched in P_2O_5 (1.2 wt.%), which is a common feature of some Lomagundi-Jatuli-age sedimentary rocks of the Fennoscandian Shield (Melezhik and Predovsky 1982; Melezhik and Fallick 2005). All the rocks of the *Shale member* have a low sulphur content, and two samples yielded 0.14–0.17 wt.% organic carbon.

The Quartzite Member

The member is a 24-m-thick unit of massive, parallel-bedded and low-angle cross-bedded quartz arenite (Fig. 6.27b) deposited with a sharp contact on underlying shales. It displays a texture of well-sorted and rounded quartz grains (Fig. 6.27a). The arenites have a variable SiO_2 content (86–95 wt.%) and a low Al_2O_3 content (13–14 wt.%), and are devoid of Na_2O and enriched in Fe_2O_{3tot} (3.0–11.6 wt.%). The latter is bound in haematite and magnetite, which is reflected in the high magnetic susceptibility (Fig. 6.21). Some intervals contain up to 0.84 wt.% P_2O_5.

Volcanic Units Within the Sedimentary Succession

Volcanic Unit A (209.4–233.9 m) is located at the bottom of the core and includes two igneous bodies separated by a 13-m-thick sedimentary unit. The lowermost body comprises a homogeneous, medium-grained, subalkaline mafic rock lacking obvious volcanic structures or amygdales. It contains a few sedimentary xenoliths ≤12 cm in size. Three of the four analysed samples show the following wt.% oxide contents: MgO 7.6–8.0 (Fig. 6.24), TiO_2 2.0–2.2, and total iron ($FeOto_{tot}$) 11.9–13.9. Loss of ignition values of c. 10 wt.% demonstrate a strongly hydrated nature of the rock, but it seems that major element mobility has been limited, apart from potassium (0.02–2.5 wt.%) due to biotitisation. Given the MgO content to be equal to or less than 8 wt.%, the rock is relatively rich in Cr (460–650 ppm). One exceptional sample from depth of 229.8 m has only 4.8 wt.% MgO and 40 ppm Cr. The body shows downward increase in Ba and Rb contents (970–1170 and 80–110 ppm, respectively), thus suggesting alteration caused by a fluid containing mobile elements. A 1.7-m-thick body at depth of c. 210 m included in Unit A is chemically similar to the underlying igneous rock though having a relatively high TiO_2 content (2.7 wt.%) and a transitional affinity between subalkaline and alkaline rocks. As neither body displays obvious volcanic structures, they can be sills or lava flows. We tentatively interpret them as sills.

Unit B (176.3–179.05 m) contains three thin (0.2–1.1 m), amygdaloidal lava flows showing a relatively high TiO_2 concentration (2.1 wt.%, volatile free), which is compatible with Nb/Y of 0.82 classifying the rock as alkaline basalt (Fig. 6.24). The rock displays a strong enrichment in LREE (Fig. 6.25) and has negative Nb-Ta and P anomalies (Fig. 6.25). In addition, Unit B has a distinct positive Ti anomaly (Fig. 6.25). Based on one analysis, the rock is strongly carbonatised (CaO 13.1 wt.%, LOI 12.3 wt.%).

Unit C combines a group of five, 2–8-m-thick magmatic bodies recognized at a depth interval of 99.7–174.6 m. Individual bodies are separated by up to 10–15 m of interfingering sedimentary strata. The basis for combining them into one group is their similarities in chemical composition and textures: each has a coarser grain size in the centre compared to their marginal parts. Although no unambiguous volcanic structures are present, we tentatively interpret all five bodies as lava flows. All analysed samples show an alkaline basaltic composition, with MgO ranging between 6.4 and 8.8 wt.%, and TiO_2 between 1.7 and 2.2 wt.% (Appendix 7). There has been some fractionation during crystallisation, as shown by decreasing Ni content (from 165 to 72 ppm) accompanied by decreasing MgO concentration. The Cr content is clearly lower (22–87 ppm) than in the underlying Unit A (460–650 ppm), or in the overlying Unit D (600–670 ppm). Unit C has the most fractionated REE patterns (Fig. 6.25) and high contents of incompatible trace elements such as Nb (32–50 mm), which together with low Y, results in a high Nb/Y ratio (2.8–4.9). This causes the rocks to plot in the basanite field in the Zr/TiO_2 versus Nb/Y diagram (Fig. 6.24). La/Nb is close to a primitive mantle value ($La_{PM}/Nb_{PM} = 0.95–1.26$) suggesting that the magma of Unit C essentially avoided crustal assimilation. In addition, Unit C rocks have a distinct positive Ti anomaly (Fig. 6.25) and a negative P anomaly (Fig. 6.25). The latter may suggest that the rock geochemistry has been influenced by the mantle beneath the depositional site rather than by crustal contamination. The two lowermost lava flows in Unit C are more altered than the others in terms of enrichment in mobile trace elements (Ba 800–870 ppm, Rb 26–56 ppm). A trachybasalt analysis from the Umba Volcanic Formation reported by Borisov (1990) is similar to our analyses obtained from Unit C rocks (Appendix 7).

The Umba Volcanic Formation

The formation is represented by Unit D at the top of the core (4.6–20.3 m) comprising a massive and amygdaloidal lava flow with olivine phenocrysts replaced by epidote, and large amygdales filled with calcite, epidote and chlorite. The flow top was not intersected by the drillhole. The rocks are medium-grained with the grain size becoming slightly coarser downwards in the core. Chemically the lava flow is a subalkaline magnesian basalt and has the following compositional features: MgO 10–11 wt.%, TiO_2 1.0 wt.%, Cr 590–670 ppm, and Ni 270–320 ppm (Appendices 7 and 8). A broad negative trend is seen in the P_2O_5 versus MgO plot for all Core 4A igneous samples (Fig. 6.26) where Unit D appears to be the most primitive though having the highest P_2O_5 content (0.39–0.46 wt.%). This together with a relatively low TiO_2 content results in a high P_2O_5/TiO_2 ratio of around 0.4 (Fig. 6.26). In this respect, Unit D is unique, as all other mafic to ultramafic rock samples from the FAR-DEEP drillcores have $P_2O_5/TiO_2 \leq 0.23$. A sample from Unit D analysed for trace elements displays a straight, slightly LREE-enriched chondrite-normalised pattern (Fig. 6.25) and in the spidergram it exhibits a distinct positive phosphorus anomaly (Fig. 6.25), which is explained by its exceptionally high P_2O_5 content.

Even though Unit D is rather primitive, earlier literature data on picrites from the Umba Volcanic Formation show higher contents of MgO (c. 15–16 wt.%), Cr (980–1370 ppm) and Ni (540–640 ppm) (e.g. Borisov 1990; Fedotov et al. 1982; Suslova et al. 1981; Zhangurov and Smolkin 1982). In addition, Al_2O_3/TiO_2 in Unit D is 12–14, while in the reference data it is 8–9, implying that two slightly different parental magmas were involved. Correlation of all the above-mentioned primitive volcanic rocks to the same stratigraphic level cannot be substantiated.

The Depositional Framework

The thinness of bedding, normal grading above sharp basal contacts, fine parallel lamination and overall fineness of the lower part of the Sandstone-Siltstone member imply that sedimentation occurred in a deep-water, low-energy setting; deposition was likely to have been by weak, dilute turbidity currents. The abundance of soft-sediment deformation features combined with the above observations suggests that a mechanism other than fluidal shear stress generated the slumping and disruption of layering, and this could reflect either a seismic genesis or deposition along relatively steep palaeoslopes. The uppermost part of the member exhibits intervals that contain reasonably well-developed examples of mud-draping across low-angle bedforms, and probable very fine-grained linsen bedding, suggesting the likelihood that weak tidal currents, or at least repetitively

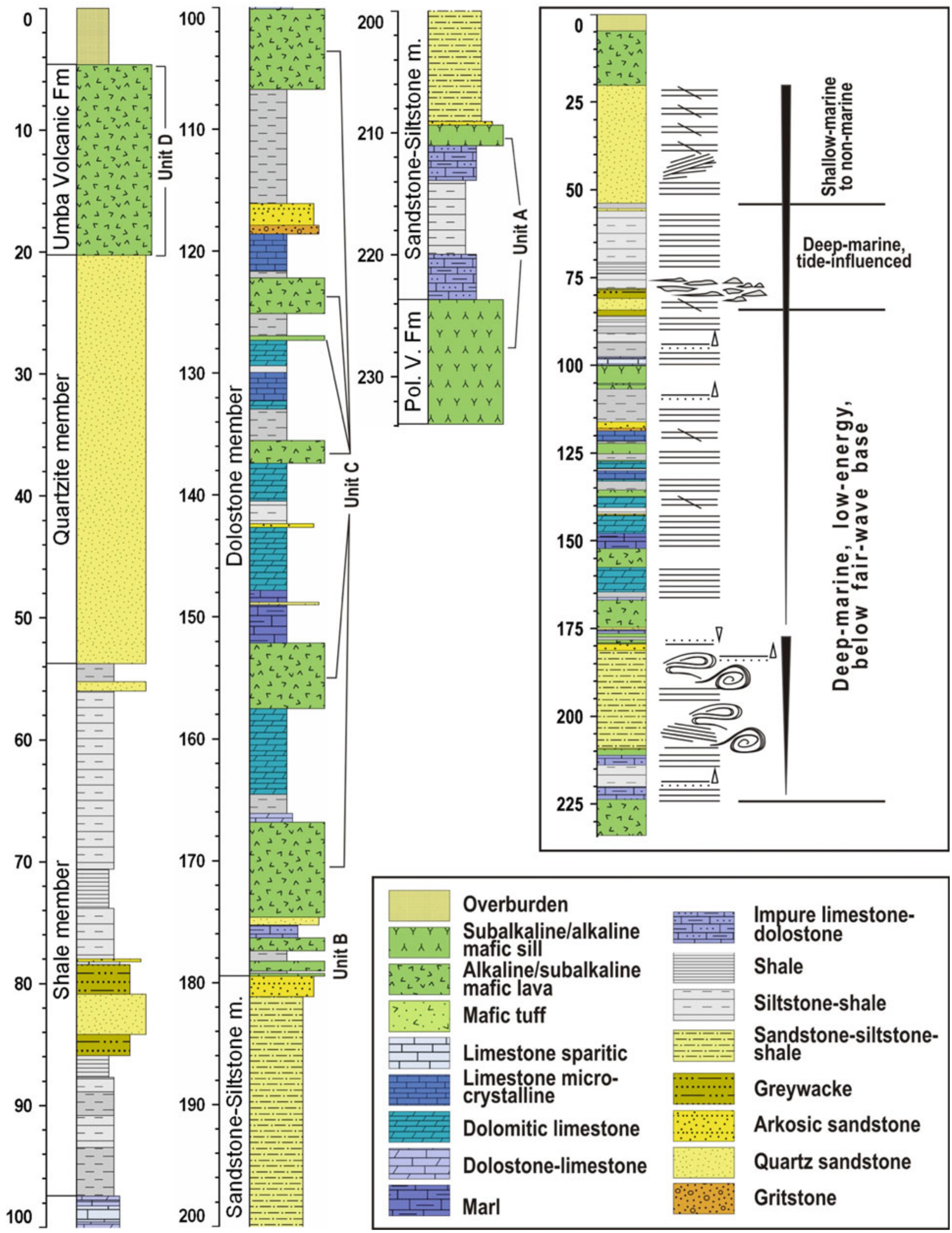

Fig. 6.20 Lithological section of the Umba Sedimentary Formation based on core log of Hole 4A, and a tentative reconstruction of depositional environments based on core logging, geological mapping and sedimentological research in the vicinity of the drilling site. Lithological symbols are explained in Fig. 6.6

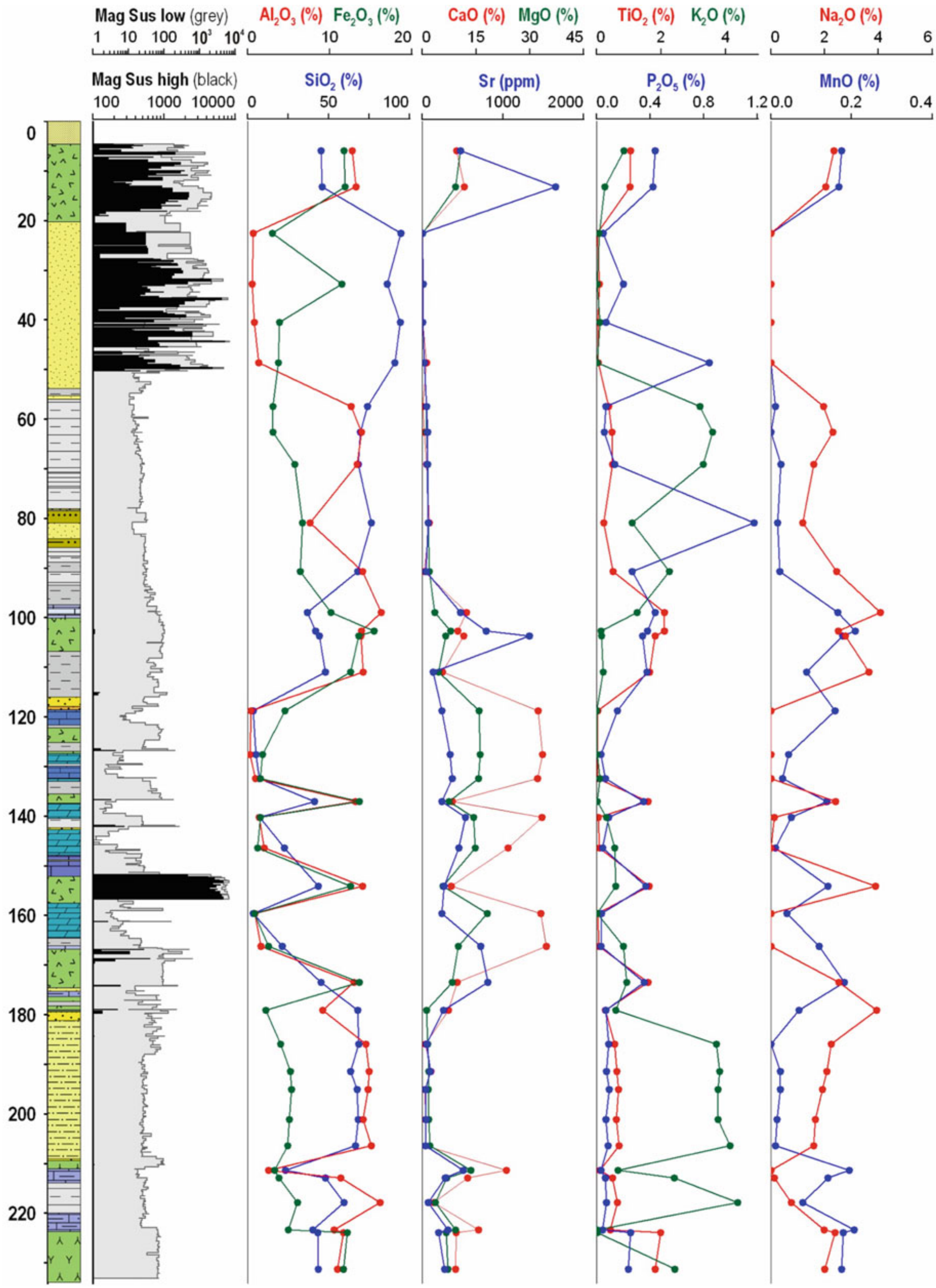

Fig. 6.21 Relative magnetic susceptibility (K*), and geochemical profiles of selected elements based on the archive samples collected with c. 8 m-spacing. For analytical techniques and data quality see Part 5

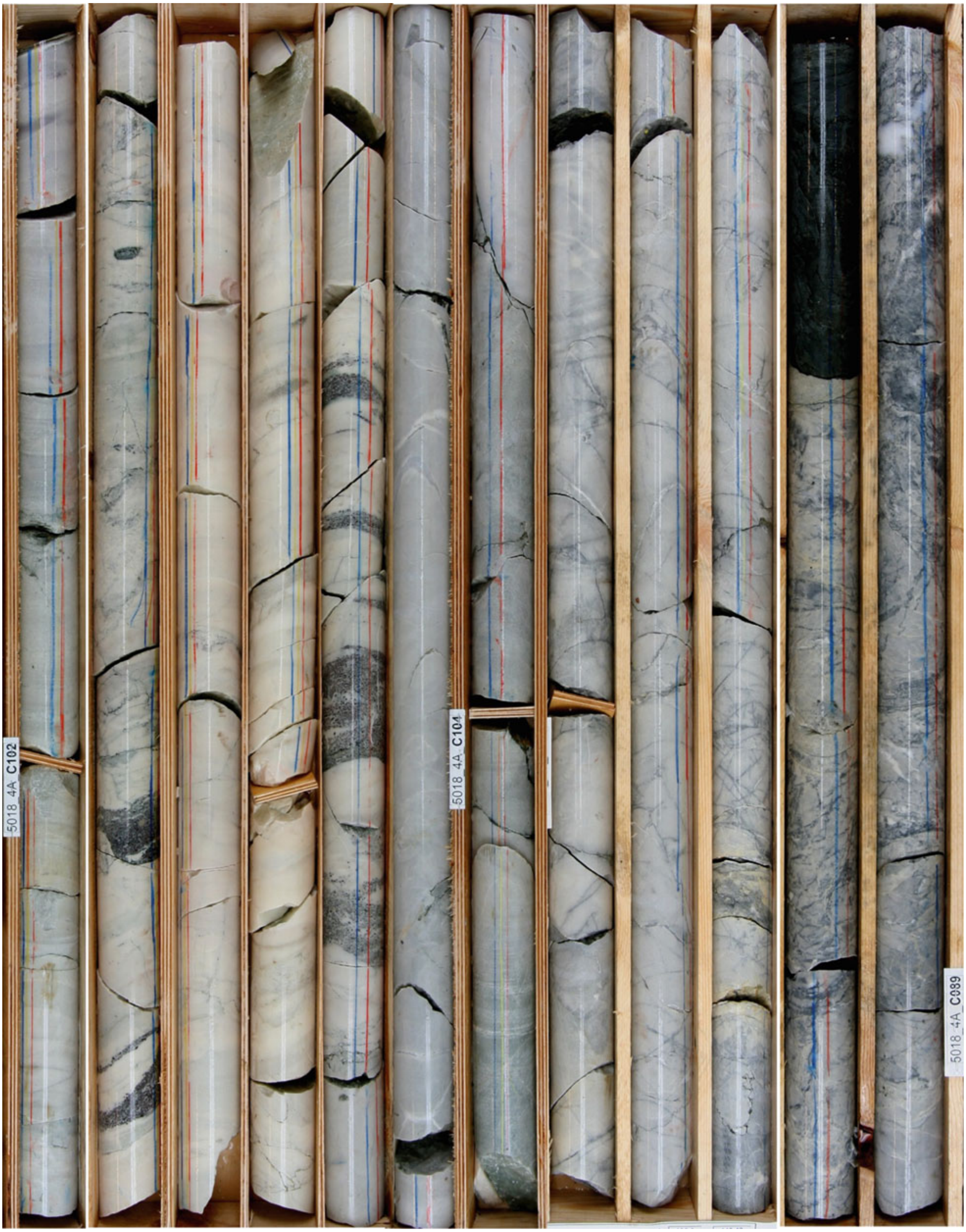

Fig. 6.22 FAR-DEEP Hole 4A intersects several intervals of ^{13}C-rich dolostones recording the Lomagundi-Jatuli positive isotopic excursion of carbonate carbon. The dolostone-bearing sedimentary succession was accumulated in an open marine setting thus with minimal influence by local factors on the carbon isotopic composition of precipitated carbonates. Their isotopic comparison with other drilled time-equivalent successions, though from more restricted settings, will permit investigating the effect of local factors on the C-isotopic composition of ^{13} C-rich carbonates. Core diameter is 5 cm (Photograph by Victor Melezhik)

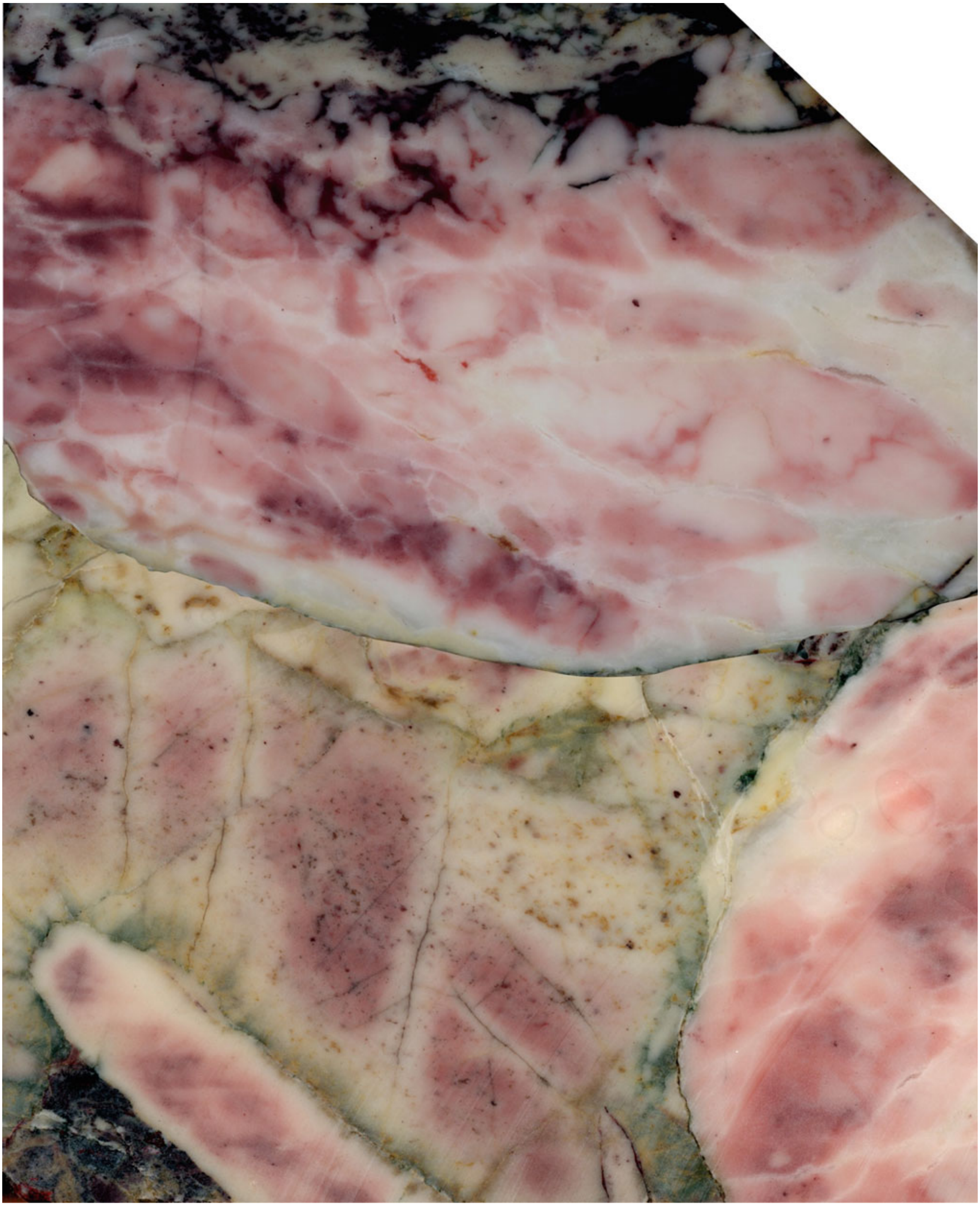

Fig. 6.23 FAR-DEEP drillcore material is supplemented by samples from outcrops exposed in the vicinity of the drilling site such as this polished slab (20 cm in width) of dolostone breccia that records a complex sedimentation history: (1) chemical(?) precipitation of carbonates; (2) lithification; and (3) erosion and redeposition. The uppermost clast is itself a rudite and exhibits partial dissolution and calichification of its upper surface, which suggests a phase of emergence. Such material offers a possibility to address the sequence of environments in terms of evolution of isotopic composition of seawater coeval with deposition and redeposition of carbonate material during the Lomagudi-Jatuli isotopic event (Photograph by Victor Melezhik)

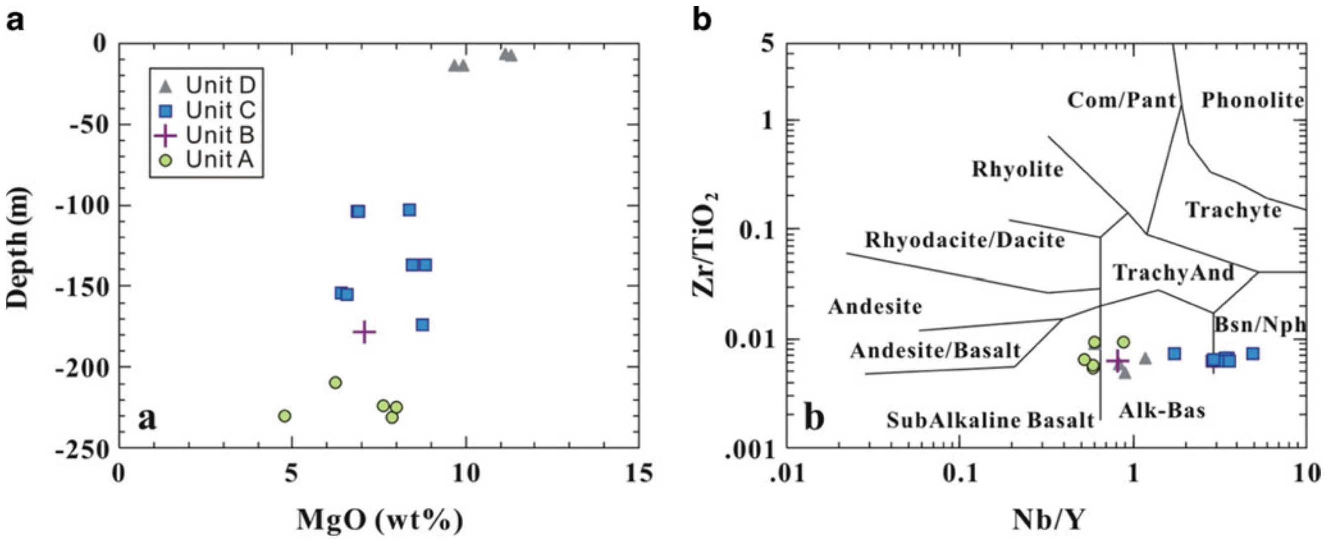

Fig. 6.24 (**a**) MgO versus depth and (**b**) Nb/Y versus Zr/TiO_2 diagrams for igneous rocks intersected by Hole 4A. Boundaries of the fields in B after Winchester and Floyd (1977)

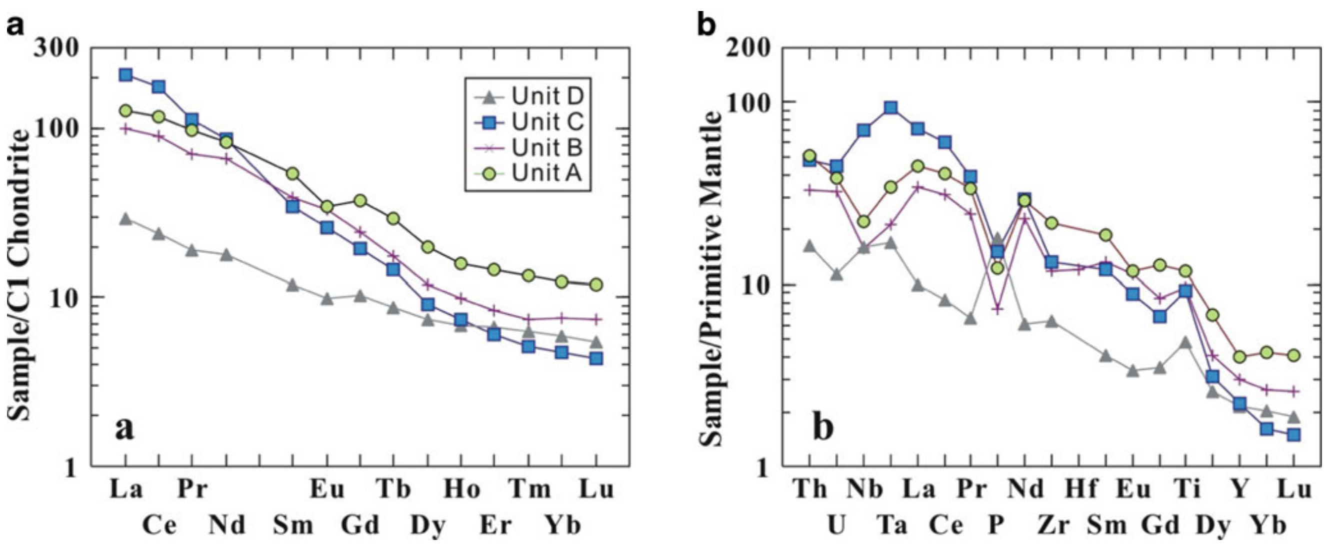

Fig. 6.25 (**a**) Chondrite-normalised REE patterns and (**b**) primitive mantle-normalised trace element patterns (B) for igneous rocks intersected by Hole 4A. Normalising values are taken from Sun and McDonough (1989)

fluctuating current strengths, influenced sedimentation. Three thickening- and coarsening-upward depositional cycles can be recognised, as based on an overall increase in bed thicknesses and sandstone:shale ratio: the top of the first cycle is at c. 220 m, the top of the second is at c. 210.5 m, and the top of the third is taken to be at c. 166 m (this latter sedimentation cycle encompasses the lowermost c. 10 m of the lithostratigraphically defined Dolostone member). Three cycles do not provide a statistically significant number to infer overall basinal trends, but taken at face value the upward increase in cycle thickness combined with a net greater proportion of each cycle being comprised of finer-grained (i.e. deeper water) facies implies an overall deepening-upward pattern for this member.

The Dolostone member is defined by the presence of two main facies of carbonate rocks: thicker bedded (dcm- to m-scale) finely textured carbonate units and subordinate thin beds (mm- to cm-thick) of alternating fine carbonate and fine siliciclastic rocks. The latter facies (thin bedded carbonates) are reasonably interpreted as carbonate-shale rhythmites deposited in a deep-marine setting. The thicker and purer carbonate beds display sharp bases and tops with

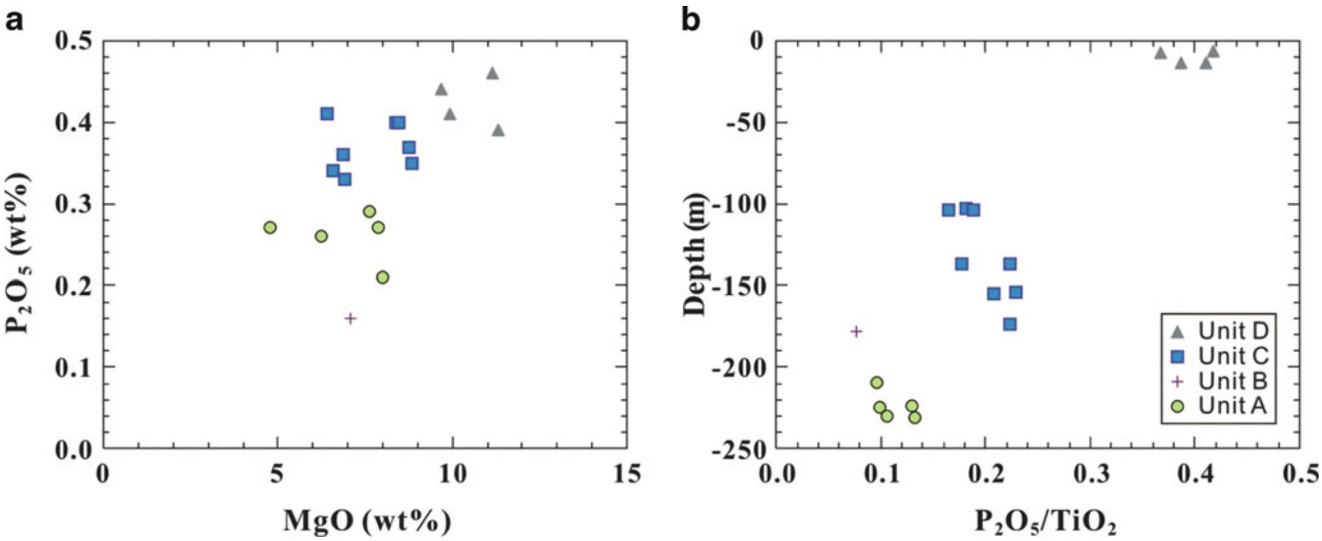

Fig. 6.26 (**a**) P_2O_5 versus MgO and (**b**) P_2O_5/TiO_2 versus depth for igneous rocks intersected by Hole 4A

their encompassing siliciclastic layers. This characteristic is interpreted as reflecting their emplacement as 'event' beds, an interpretation supported by the presence of thin lenses of reworked jasper and mafic/ultramafic grains within some of the thicker carbonate units (e.g. Fig. 6.27n, o). The absence of sedimentary features diagnostic of shallow-water settings, combined with the observation that the enclosing siliciclastic rocks are dark-coloured and fine-grained, implies that deposition was in relatively deep-marine environments; in fact, given the sharp bed contacts exhibited by many of the carbonate beds, and even though fine-grained, the beds likely owe their origin to resedimentation processes. Also, no clear depositional cyclicity appears to have been developed in the Dolostone member, which further supports an inference that the carbonate beds are resedimented into a deep-marine setting. Although speculative, the lack of vesicles/amygdales in the Unit C igneous bodies interpreted to be lava flows could be attributed to emplacement under high hydrostatic pressure in the deep-water environment.

The overlying Shale member is, unfortunately, strongly tectonised, but nevertheless depositional patterns can be gleaned from the less deformed portions of the core. Depositional cycles can again be recognised, ranging in thickness from several metres to a few tens of metres, and consist of an upward trend from mudstone/shale-dominated in lower parts of the cycles to interbedded shale-thin sandstone in upper parts, in other words, a coarsening-upward trend. The beds in the lower parts of the cycles are cm-thick and sharp-based with normal grading, and these are reasonably interpreted as turbidites. No wave or other traction-bedded structures were observed, thus the inferred turbidites were likely emplaced at depths well below wave base (both storm and fair-weather wave base). The upper parts of the thicker cycles are typified by fine-grained linsen- and flaser-bedded intervals, and rarer tidal couplets, indicating that the topmost parts of the cycles record water depths shallow enough for sediment to be moulded by tidal currents.

Thus, the overall basinal trend recorded by the first three members of the Umba Sedimentary Formation recovered in Core 4A is an initial deepening in the deep-marine setting (deep enough to be uninfluenced by tide, storm and/or marine shelf currents) of the Sandstone-Siltstone member into the Dolostone member, then a shallowing through the Shale member into bathymetries influenced by tidal currents.

The Quartzite member sits with sharp contact on the underlying fine-grained and feldspathic rocks of the topmost part of the underlying Shale member; this contact is a good candidate for a possible sequence boundary. Above this contact the member consists of ill-defined variations between fine- to medium-grained textures accompanied by flat laminations and low-angle cross-bedding. It is difficult to interpret this particular unit, but the dearth of abundant and diverse sedimentary structures, the absence of fine-grained (mudstone/shale) interbeds and the lack of well-defined depositional cycles, tend to rule out sedimentation by shallow-marine processes, and it is possible that this member represents a non-marine setting. Further work is required before a more definitive interpretation can be advanced.

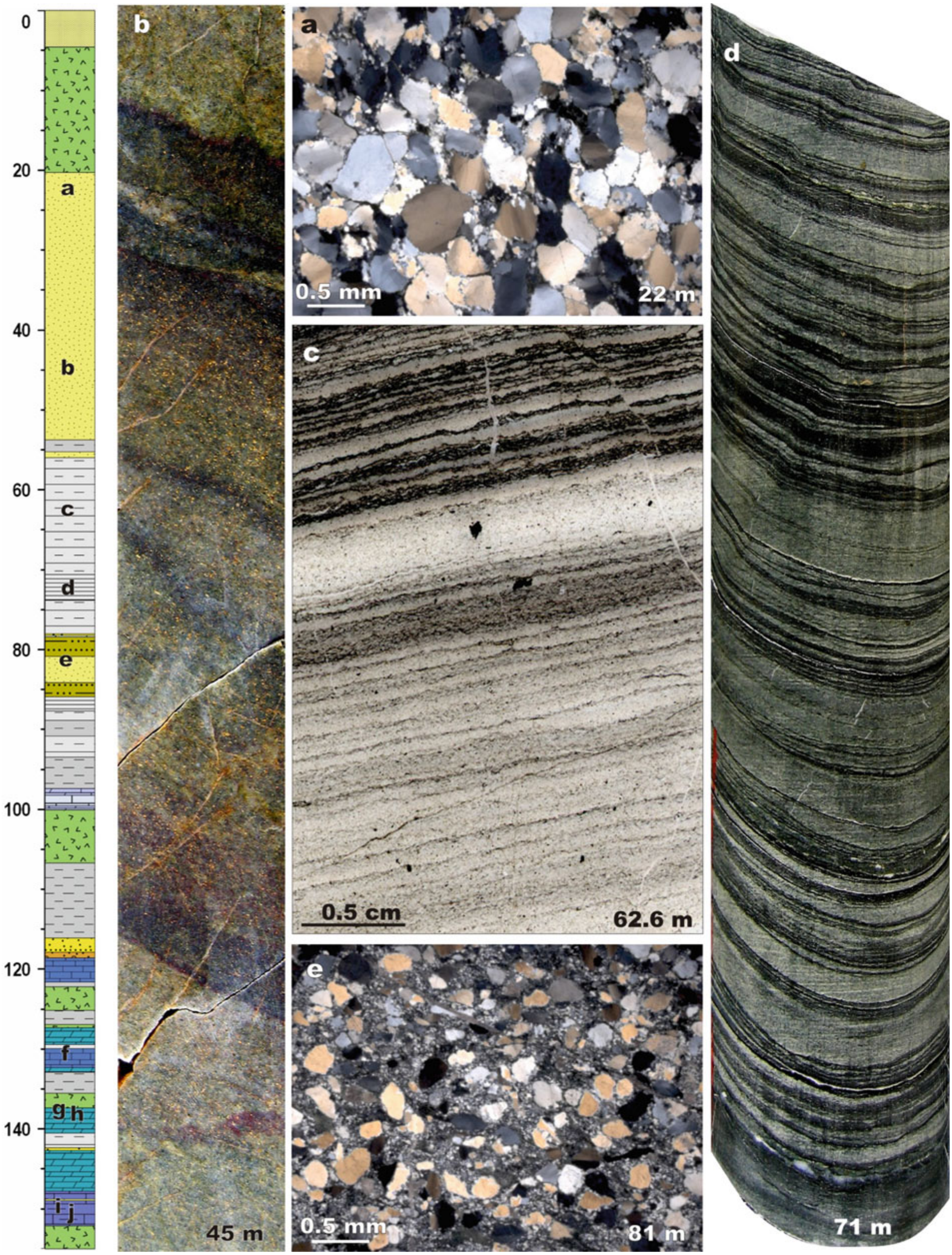

Fig. 6.27 Sedimentological and petrological features of main rock types intersected by Hole 4A. Core diameter in all plates is 5 cm unless specified otherwise. (**a**) Photomicrograph in polarised light showing arenite composed of moderately-sorted and tightly-packed quartz grains

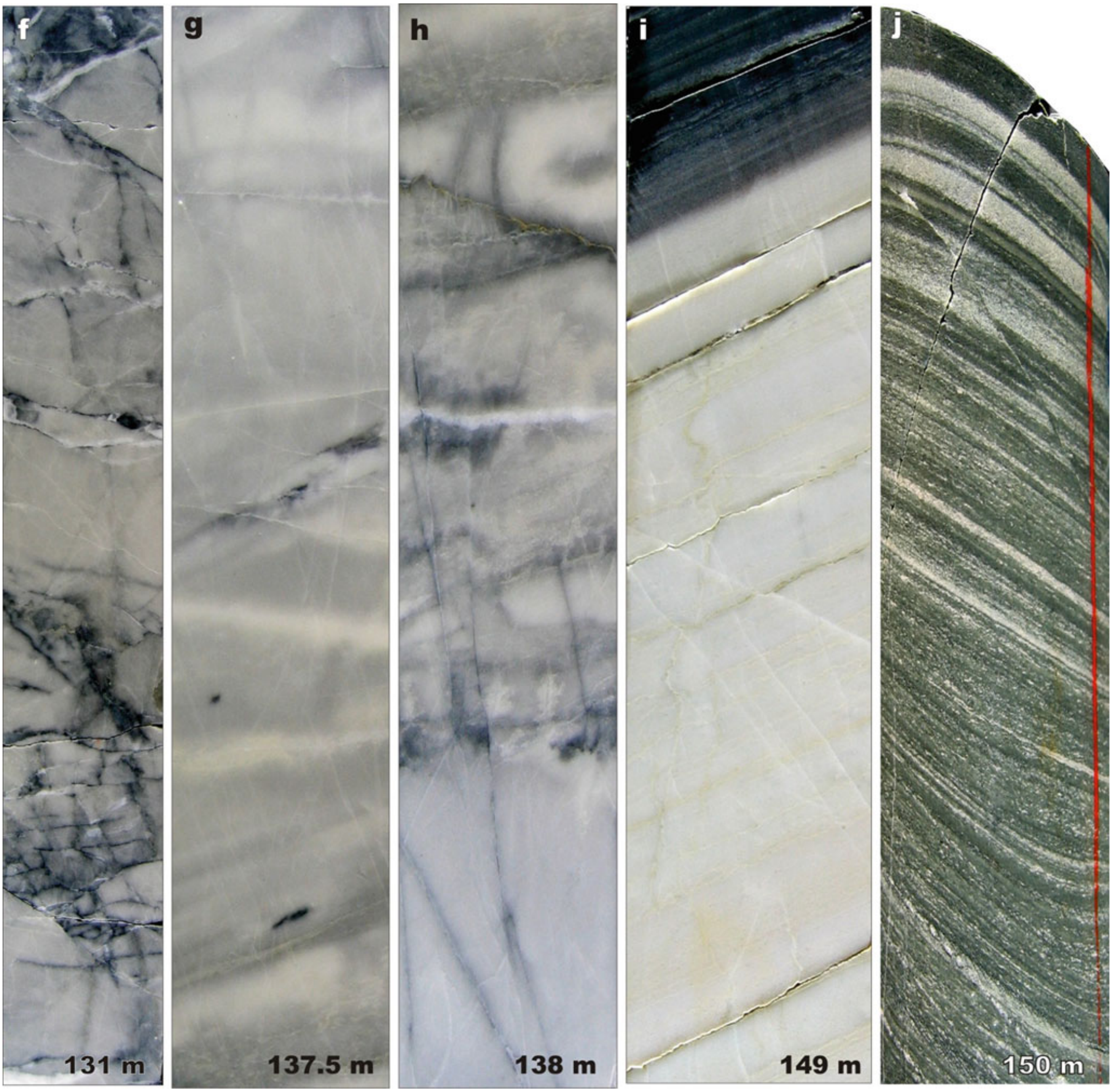

Fig. 6.27 (continued) (**b**) Haematite- and magnetite-bearing quartzite with a hint of cross-bedding; iron oxides (*black*) show a tendency to be accumulated at the base of beds. (**c**) Photomicrograph in non-polarised light of parallel-laminated siltstone-shale comprising alternating quartz-rich siltstone (*white*) and shale (*black*) layers. (**d**) Alternating siltstone (*pale grey*) and shale (*black*) layers comprising parallel-bedded siltstone-shale; although the parallel bedding is the overall sedimentary characteristic, many siltstone layers have erosive bases with some showing low-angle cross-laminations and microslumping. (**e**) Photomicrograph in polarised light of arenitic wacke composed of moderately sorted, subangular quartz grains set in a fine-grained quartz matrix. (**f**) *Pale grey*, finely-crystalline dolostone with relicts of parallel-bedding; tectonically brecciated parts are enriched in haematite and magnetite (*black*). (**g**) *Pale grey*, finely-crystalline dolostone with relicts of parallel-bedding in the lower part. (**h**) *Pale grey*, finely-crystalline, massive, dolostone bed (lower part) overlain by tectonically brecciated, and partially recrystallised dolostone enriched in haematite (*black*). (**i**) *White*, finely-crystalline, parallel-bedded dolostone overlain by black shale; note that some dolostone beds have thin, black shale partings. (**j**) Marl comprised of alternating dolostone (*white*) and shale (*dark grey*) layers; lower part of the core exhibits low-angle cross-bedding, whereas the upper part is parallel-bedded

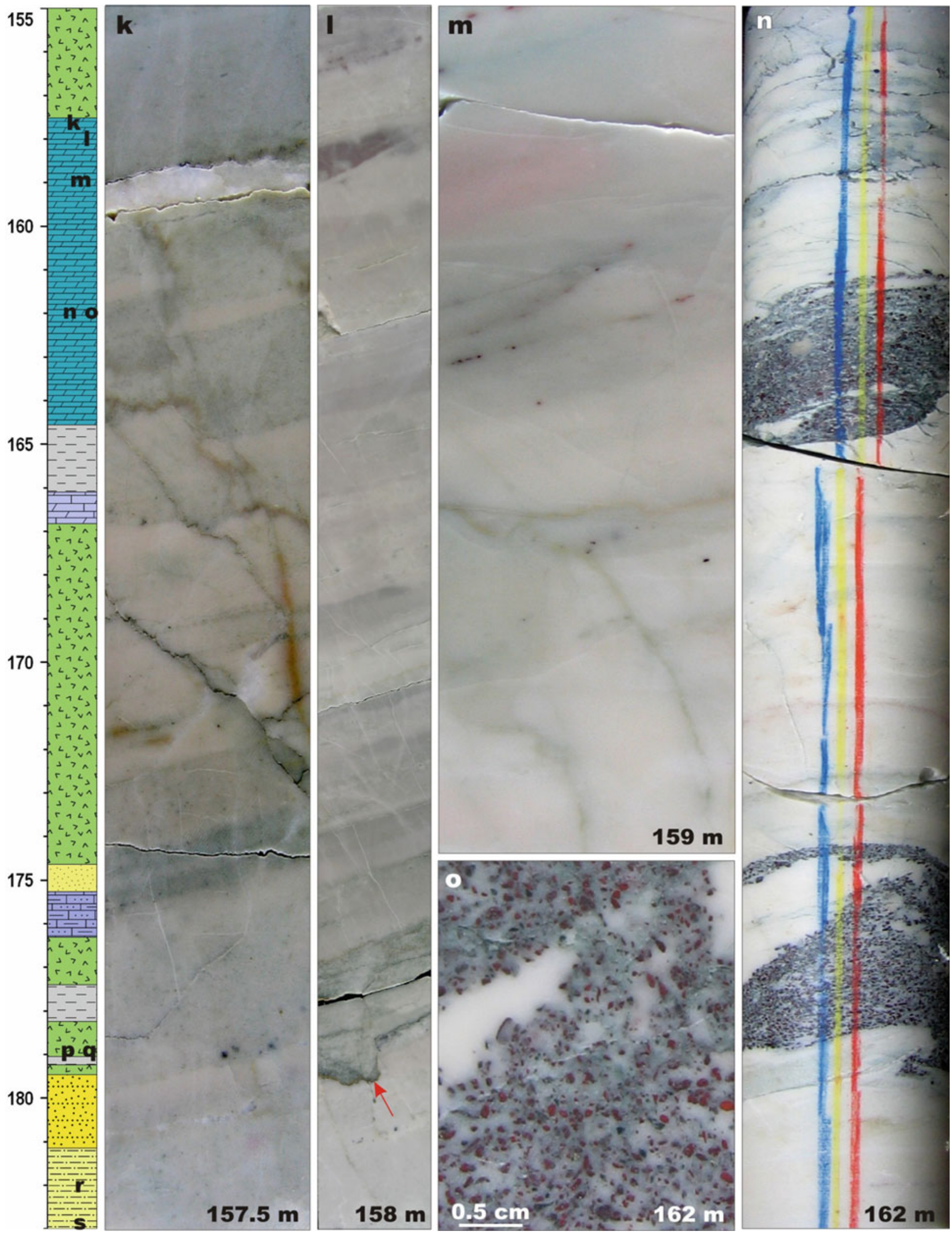

Fig. 6.27 (continued) (**k**) *Pale-grey*, parallel-bedded dolostone. (**l**) *Pale grey*, parallel-bedded dolostone overlying white, massive dolostone bed; stylolitic dissolution is arrowed. (**m**) Variegated, massive dolostone. (**n**) *White*, indistinctly bedded dolostones with lenses containing fine particles of altered mafic-ultramafic material (*dark grey*). (**o**) Enlarged image of the lens with particles of altered ultramafic material (*dark grey*) and rounded clasts of jasper (*red*)

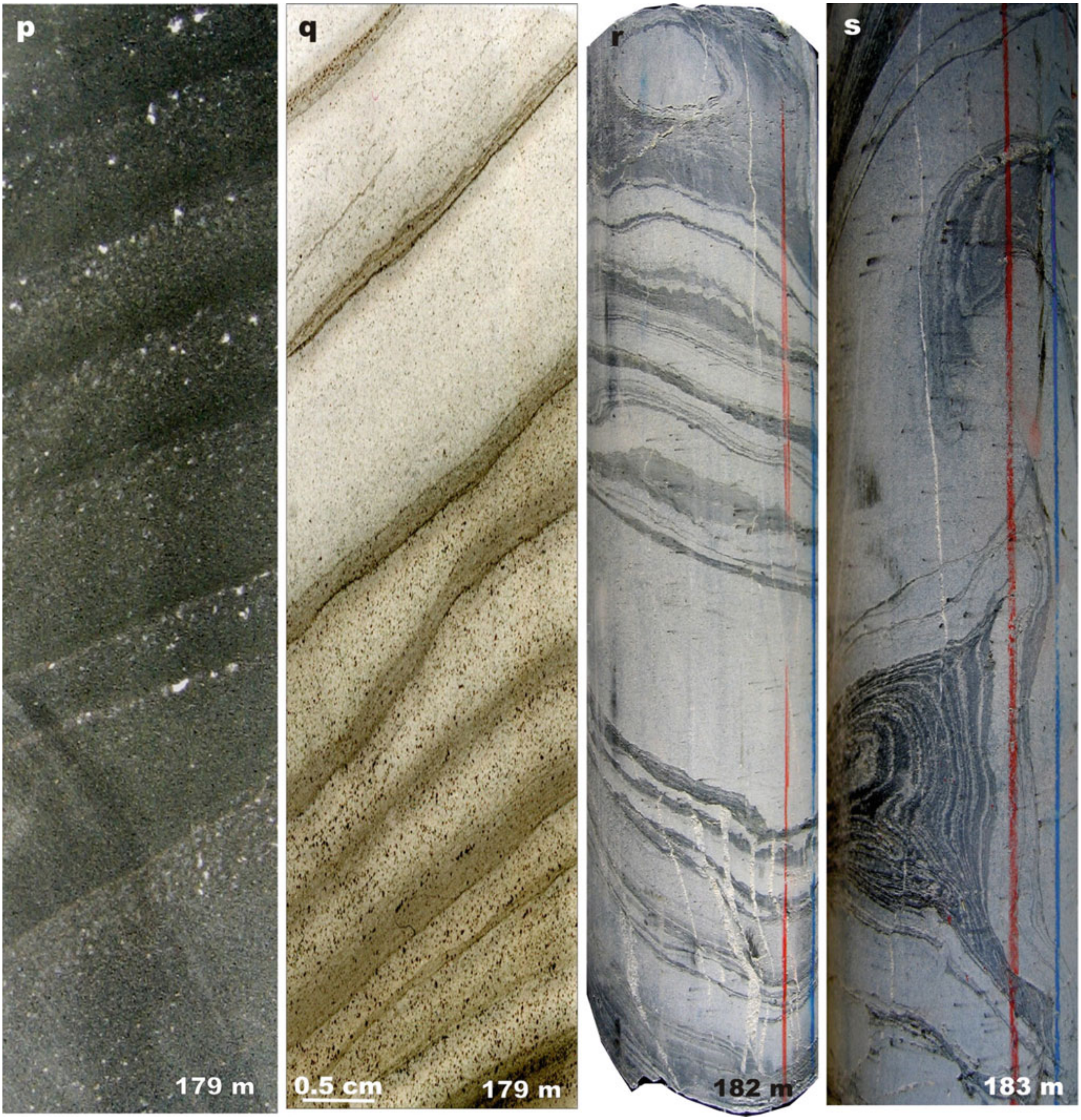

Fig. 6.27 (continued) (**p**) Lower-angle cross-bedded (*lower part*) and parallel-bedded (*upper part*) tuff with reverse grading. (**q**) Scanned thin section showing parallel-bedded tuff with reverse grading; some layers exhibit wavy surface. (**r**) Alternating thick siltstone-sandstone (*pale grey*) and thin shale (*grey*) layers showing wavy and low-angle cross-lamination; note convolute bedding in the *upper part*. (**s**) Convolute bedding and a slump structure in siltstone

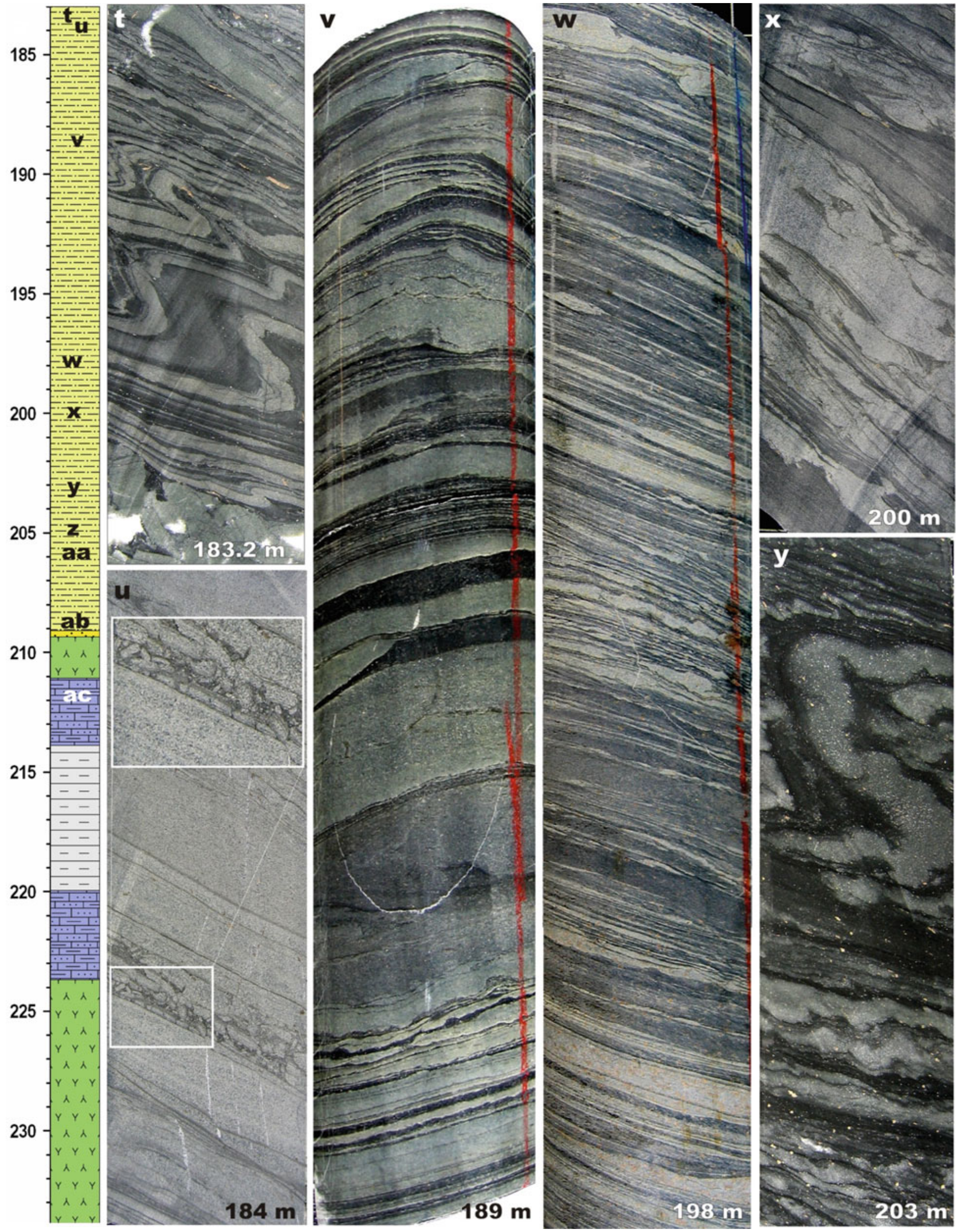

Fig. 6.27 (continued) (**t**) Synsedimentary, softly-deformed layers (in the *middle*) and a slump structure (in the *bottom*) in siltstone-shale. (**u**) Low-angle cross-laminated siltstone with disintegrated bed (*enlarged*) caused by slumping

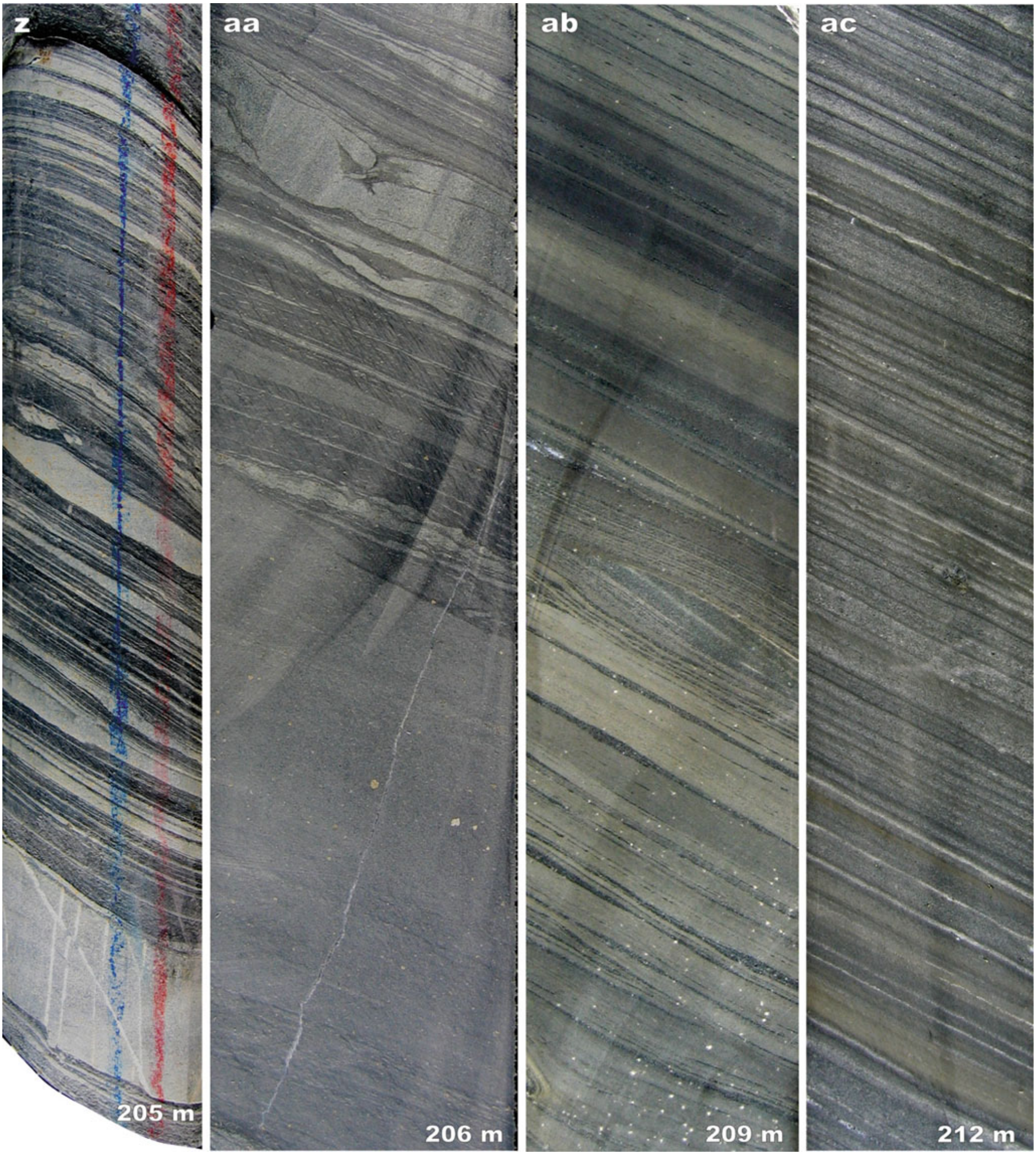

Fig. 6.27 (continued) (**v**) Sandstone-siltstone-shale showing parallel, wavy, and low-angle cross-lamination with a slump structure. (**w**) Thinly laminated sandstone-siltstone-shale with parallel and low-angle cross-lamination with slump structure. (**x**) Slumping in low-angle cross-laminated sandstone-siltstone-shale. (**y**) Synsedimentary folding in sandstone-shale. (**z**) Parallel-laminated sandstone-siltstone-shale with some layers showing wavy, lensoidal and low-angle cross-lamination. (**aa**) Indistinctly bedded siltstone erosively overlain by sandstone-siltstone-shale with wavy, parallel and low-angle cross-lamination; sandstone on the *top* shows a slump structure. (**ab**) Thinly-laminated sandstone-siltstone-shale with parallel and low-angle cross-lamination. (**ac**) Thinly, parallel-laminated dolostone-shale couplets (All photos by Victor Melezhik)

References

Borisov AE (1990) Volcanism and native copper occurrences in the early Proterozoic of the Kola Peninsula. Nauka (Science), Apatity, 70p, in Russian

Fedotov ZhA, Basalaev AA, Melezhik VA, Latyshev LN (1982) The Srel'na group. In: Gorbunov GI (ed) The Imandra/Varzuga zone of Karelids. Nauka (Science), Leningrad, pp 33–56, in Russian

Melezhik VA, Fallick AE (2005) The Palaeoproterozoic, rift-related, shallow-water, ^{13}C-rich, lacustrine carbonates, NW Russia – Part I: sedimentology and major element geochemistry. Trans R Soc Edinb Earth Sci 95:393–421

Melezhik VA, Predovsky AA (1982) Geochemistry of Palaeoproterozoic lithogenesis. Nauka (Science), Leningrad, 208p, in Russian

Sun S-S, McDonough WF (1989) Chemical and isotopic systematics of oceanic basalts; implications for mantle composition and processes. In: Saunders AD, Norry MJ (eds) Magmatism in the ocean basins, Geol Soc Spec Publ 42: 313–345. Blackwell Scientific Publications, Oxford/Boston

Suslova SN, Staritsyna GN, Dagelayskaya IN (1981) Nickeliferous ultramafic-mafic volcanic-intrusive complexes of the Karelia-Kola and North Siberian regions. Int Geol Rev 23:1135–1147

Winchester JA, Floyd PA (1977) Geochemical discrimination of different magma series and their differentiation products using immobile elements. Chem Geol 20:325–343

Zhangurov AA, Smolkin VF (1982) Mafic-ultramafic rocks of the middle and late Karelian and Caledonian stages. In: Gorbunov GI (ed) The Imandra/Varzuga zone of Karelids. Nauka (Science), Leningrad, pp 145–165, in Russian

6.1.4. Umba Sedimentary Formation, Sukhoj Section

Victor A. Melezhik

Scientific Targets

– Tectonic and depositional settings associated with the Lomagundi-Jatuli isotopic event
– Geochemical rock record during the global perturbation of the carbon cycle
– Influence of depositional setting on carbon and strontium isotopic composition of basinal water

The Sukhoj section is situated c. 40 km to the east along strike from FAR-DEEP Hole 4A (Fig. 6.3) and represents an insightful complementary exposure to that of the Umba Sedimentary Formation intersected by FAR-DEEP Hole 4A (Fig. 6.28 versus Fig. 6.20). The section is represented by several natural outcrops and a small quarry near the Sukhoj river in the central part of the Imandra/Varzuga Greenstone Belt. In contrast to the lithologies typifying the Umba Sedimentary Formation elsewhere, including those found in the drillcore, the Sukhoj section consists of resedimented carbonates intermixed with variably-altered mafic-ultramafic material in the form of carbonate-cemented ultramafic breccias (Figs. 6.29 and 6.30). The significant sedimentological difference of the Sukhoj section may raise a question whether or not it represents a stratigraphic equivalent to other logged sections of the Umba Sedimentary Formation. The possibility exists that it may be not entirely synchronous and represents a slightly younger dolostone unit with respect to other major carbonate subdivisions of the Umba Sedimentary Formation documented elsewhere within the Imandra/Varzuga Bel (for details see Chap. 4.1). However, it is robust to state that all measured sections, including Sukhoj, form parts of the same formation because they are all sandwiched in between two distinct suites of volcanic rocks, namely komatiitic basalts beneath and alkaline, highly oxidised lavas above. At any rate, the Sukhoj section offers great opportunity to assess the potential influence of local factors on the $\delta^{13}C_{carb}$ values of carbonate rocks deposited during the Lomagundi-Jatuli Isotopic Event. Apparent heterogeneity of the $\delta^{13}C_{carb}$ signal in contemporaneous carbonate units has been documented in the Imandra/Varzuga (Melezhik and Fallick 1996) and Pechenga (Melezhik et al. 2005) Greenstone belts, thus the comparative study of the Hole 4A and the Sukhoj sections has great potential for addressing the issue as to whether or not local depositional factors influenced $\delta^{13}C_{carb}$ of sedimentary carbonates within the same formation.

V.A. Melezhik (✉)
Geological Survey of Norway, Postboks 6315 Sluppen, NO-7491 Trondheim, Norway

Centre for Geobiology, University of Bergen, Allegaten 41, Bergen N-5007, Norway

Section Description

The exposed section is 74 m thick (Fig. 6.28) and likely represents a part of the Dolostone member. Although contacts with adjacent units are not exposed at this location, a direct contact of the Umba Sedimentary Formation with underlying mafic-ultramafic komatiitic lavas of the Polisarka Volcanic Formation has been reported from the study area (Melezhik and Predovsky 1982). The lowermost 16 m of the Sukhoj section is comprised of dolarenite, finely-crystalline (micritic) dolostone, and breccia containing ultramafic material. Each lithology defines a discrete unit and the three units have thicknesses of c. 4, 5 and 6 m, respectively (Fig. 6.28).

The middle part of the section (16–50 m) is only partially exposed and consists of a lower 1-m-thick dolostone conglomerate overlain by dolomicrite and ends with a c. 14-m-thick bed of dolarenite with a topmost bed, 0.5 m thick, of dolomicrite.

A 24-m-thick upper part of the succession (50–74 m) is comprised of interbedded finely-crystalline (micritic) dolostone and dolarenite with numerous beds of dolarenite-matrix mafic-ultramafic breccias, and a few dolostone conglomerate and breccia units (Fig. 6.28). All rock types are characterised by rapid lateral and vertical changes. Figure 6.31 demonstrates the main rock types and their sedimentological features throughout the logged section.

The dolomicrites are beige, tan, pink, white and variegated rocks throughout the section. Although the term "micritic" is used to describe this carbonate lithology, the rocks are, in fact, finely-crystalline dolostones closely resembling dolomicrite. These dolostones are mainly massive (Fig. 6.31c, i, j, r, z, ab, at, ax, az, bk, bl) with some beds showing parallel-laminated or horizontally bedded structures (Fig. 6.31bf). Dolomicrite beds may contain solitary and irregularly scattered dolostone clasts and channelised interlayers infilled by dolarenite.

The dolarenites are beige, buff, purple and variegated in colour, a result of differential post-depositional bleaching of the original red and pink beds (i.e. "red beds") by reducing fluids generating a spotty and patchy colouration (Fig. 6.31aa, bd, bh, bi, bn, bo). Some beds contain evidence that reducing fluids have migrated along brittle cracks (Fig. 6.31bi), thus postdating the lithification, and others are crosscut at a significant angle by overlying layers (Fig. 6.31bi), implying syndepositional deformation followed by subaqueous erosion. There is no evidence for phases of emergence prior to the deposition of the overlying bed. The dolarenites, similar

V.A. Melezhik et al. (eds.), *Reading the Archive of Earth's Oxygenation*, Volume 2: The Core Archive of the Fennoscandian Arctic Russia – Drilling Early Earth Project, DOI 10.1007/978-3-642-29659-8_2, © Springer-Verlag Berlin Heidelberg 2013

to other carbonate lithologies, have been affected by selective recrystallisation that has masked the original shape of clasts and cement types. The dolarenites are commonly characterised by a horizontal lamination (Fig. 6.31a, aa) and bedding (Fig. 6.31m, o, bd), although some beds are massive (Fig. 6.31k, l, ah, ao) or show a complex disrupted structural pattern (Fig. 6.31p, q, aq). A few beds contain low-angle cross-lamination (Fig. 6.31bh), whereas others a high-angle bimodal cross-stratification, implying reworking by tidal currents. Thin graded beds occurring in the form of rhythmites are a typical feature for both the lower and the upper parts of the section (Fig. 6.31bg, bh, bo). Another distinctive feature of the dolarenites is the presence of abundant sand- and grit-size rounded clasts of jasper, brown-coloured altered mafic-ultramafic rocks, and micritic dolostones. The clasts are cemented by white, isopachous dolomite and, combined, yield a distinctive dotted variegated colouration (Fig. 6.31l, m, o, ao). In many beds, red and purple colour is due to the presence of iron oxide phases formed as the result of alteration of ultramafic particles (Fig. 6.31p, q, ag, ah, an, bd). In rare cases, the dolarenite beds contain star-shape cracks resembling shrinkage feature (Fig. 6.31n).

The ultramafic breccias are comprised of dolomite-cemented fragments of ultramafic material. The breccia beds thin out over a distance of a few metres and exhibit rapid lateral facies changes as evidenced by abrupt interfingering within 10 m along strike at c. 60 m depth of the logged section (Fig. 6.27au–bb). The breccia contains clasts of variable sizes, partially or entirely dismembered lenses and beds, as well as, large fragments of ultramafic material cemented by isopachous dolomite (Fig. 6.31w, ac, ak–am, au–aw, ay, ba, bb, be). In many places fragments of ultramafic material form a fitted ('jig-saw-puzzle') fabric encased by carbonate cement (Fig. 6.31au, ay, bb). This implies that the lenses and clasts were disintegrated prior to cementation. The ultramafic material contains a significant concentration of Cr (2600 ppm) and Ni (600 ppm) (Melezhik et al. 1982), and is composed of chlorite, phlogopite, calcite and haematite (Fig. 6.31av), thus showing a considerable degree of alteration presumably by seafloor palaeoweathering. The only known source of such rocks is the underlying ultramafic rocks of the Polisarka Volcanic Formation.

The dolostone conglomerates are a distinctive lithology of the Sukhoj succession differentiating it from other sections of the Umba Sedimentary Formation. The conglomerates form several beds scattered throughout the section, with most of them occurring in its upper part (Fig. 6.28). The lowermost conglomerate (15.3–16.5 m) fills small-scale channels and consists of variably rounded, poorly sorted white dolomicritic pebbles set in a dolarenite matrix containing weathered ultramafic clasts (Fig. 6.31f–h). Both the pebbles and the smaller clasts in the matrix show a variable degree of dedolomitisation. Many sand-size dolomite clasts contain tiny grains of apatite; some dolomite clasts are partially replaced by quartz and barite.

The conglomerates at a depth of 51.5–52.5 m (Fig. 6.31s–y) occur as a stack of superposed small-scale channels, some of which are filled with pink and red dolarenites (Fig. 6.31t). Unlike all previously described conglomerates, these are mainly clast-supported. The fragments show a variable size with some appearing as blocks of bedded dolostones as large as 60 × 15 cm (Fig. 6.31u). Some large cobbles are composite consisting of reworked dolostone conglomerates (Fig. 6.31x) or even several fragments of conglomerates and gritstones incorporated into one cobble (Fig. 6.31y). This suggests an episode of erosion-cementation-erosion followed by redeposition. Some conglomerate cobbles exhibit surface dissolution features (Fig. 6.31x) implying a phase of emergence.

Several thin conglomerate beds occurring at a depth of 58–59 m are interlayered with dolarenites. These beds have erosive bases with irregular surfaces (Fig. 6.31ad–af) and contain rounded and angular pale pink and white dolomicritic clasts dispersed in a red and white dolarenite matrix. All the clasts are likely to have been locally derived; this is particularly the case for the angular clasts.

The 2-m-thick conglomerate bed at a depth of 63–64.5 m has an erosive base and contains a diverse clast assemblage (Fig. 6.31aq, ar, ap). Clasts are poorly sorted, dolarenite-matrix supported and variably rounded. They consist of purple and brown fine-grained, haematite-bearing calcitised dolostones (Fig. 6.31aq, ar) derived from an unknown source. Other clasts are much smaller in size and composed of ultramafic rocks, which have been intensively altered to chlorite-calcite-haematite-quartz mass. The clasts are encased in a grit-to sand-sized matrix consisting of pink, brown and purple haematite-bearing, partially dedolomitised dolomite, red jasper and weathered ultramafic material. Both the pebbles and the matrix clasts are cemented by white isopachous or drusy dolomite (Fig. 6.31ao, ar, as). These dolostone-pebble conglomerates contain a channel up to 0.5 m thick of unknown width filled with unsorted pebble to cobble polymict conglomerates (Fig. 6.31ap). Cobbles can reach sizes of 20 cm in diameter and consist mainly of weathered mafic and ultramafic volcanic rocks and minor dark brown dolostones, cherts and jaspers. Brown, purple and red carbonate clasts are enriched in iron-oxides and may have originally been ankerite and/or siderite. Many such clasts are partially replaced by barite. Barite is common in other measured sections of the Umba Sedimentary Formation where it also associate with jasper and silicified dolostone beds. This has $\delta^{34}S$ ranging between +27.8 and 34.2 ‰, and its origin has been linked to seafloor hydrothermal processes (Melezhik and Fetisova 1989; Grinenko et al. 1989).

A 0.25-cm-thick bed at a depth of c. 66 m is comprised of clast-supported conglomerates. It has an erosive base and the clasts are pale pink, rounded, unsorted fragments of dolomicrite emplaced into a white dolarenite matrix (Fig. 6.31bc), all cemented by white, isopachous dolomite. The clast colour, microfabrics and composition of the rock suggest a local source.

The top of the uppermost dolostone breccia at a depth of 73.5–74 m is not exposed and therefore its thickness remains unknown. This matrix-supported breccia consists of unsorted clasts of Fe-rich dolostone, altered ultramafic rocks and dolorudite cemented by white palisade dolomite. The matrix is comprised of sand- and grit-size, angular clasts of pink and purple dolostones, jasper and gritstones set in granular, white dolomite cement.

Depositional Framework

Reconstruction of the depositional environments is hampered by the incompleteness and lack of lateral continuity of the section. Another complication arises from the fact that many lithofacies are represented by resedimented clasts; thus their depositional setting and source area also need to be established. The latter can be deciphered from the lithology of the clasts.

The carbonate clasts are noteworthy for two reasons: the total absence of stromatolitic carbonates (which are common to all Jatuli group carbonates across the Fennoscandian Shield, Makarikhin and Kononova 1983; Melezhik et al. 1997), and the presence of clasts of carbonate conglomerates (Fig. 6.31f, h, x, y, bp). Combined with the observations that many of the carbonates are resedimented, that graded bedding occurs, clasts are both angular and rounded, textures exhibit both matrix- and clast-support and the overall fine grained character of the encompassing facies, it is envisaged that these rocks formed along a distally steepened ramp (e.g. Read (1982)).

In a vertical sequence, the initial finer-grained facies pass upward into lithofacies dominated by dolarenites with slumps and erosion channels, carbonate conglomerate and dolomite-cemented ultramafic breccia (Fig. 6.28) reasonably interpreted as debris flow deposits. The presence of mafic and ultramafic clasts indicates that synsedimentary faulting occurred to expose the Polisarka Formation ultramafic-mafic lavas.

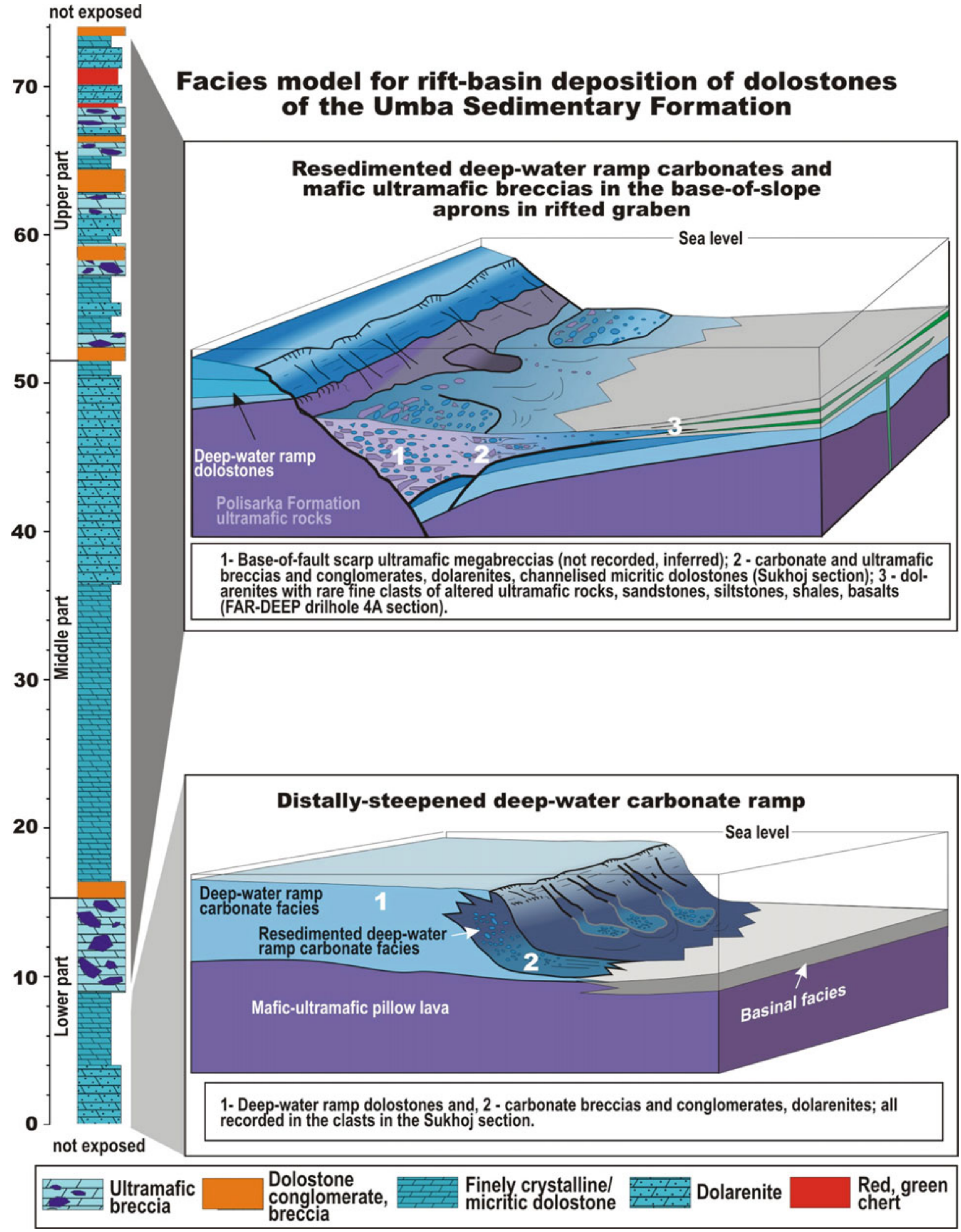

Fig. 6.28 The lithological column and suggested depositional environments of the Umba Sedimentary Formation at the Sukhoj section, Sukhoj River, central Imandra/Varzuga Greenstone Belt

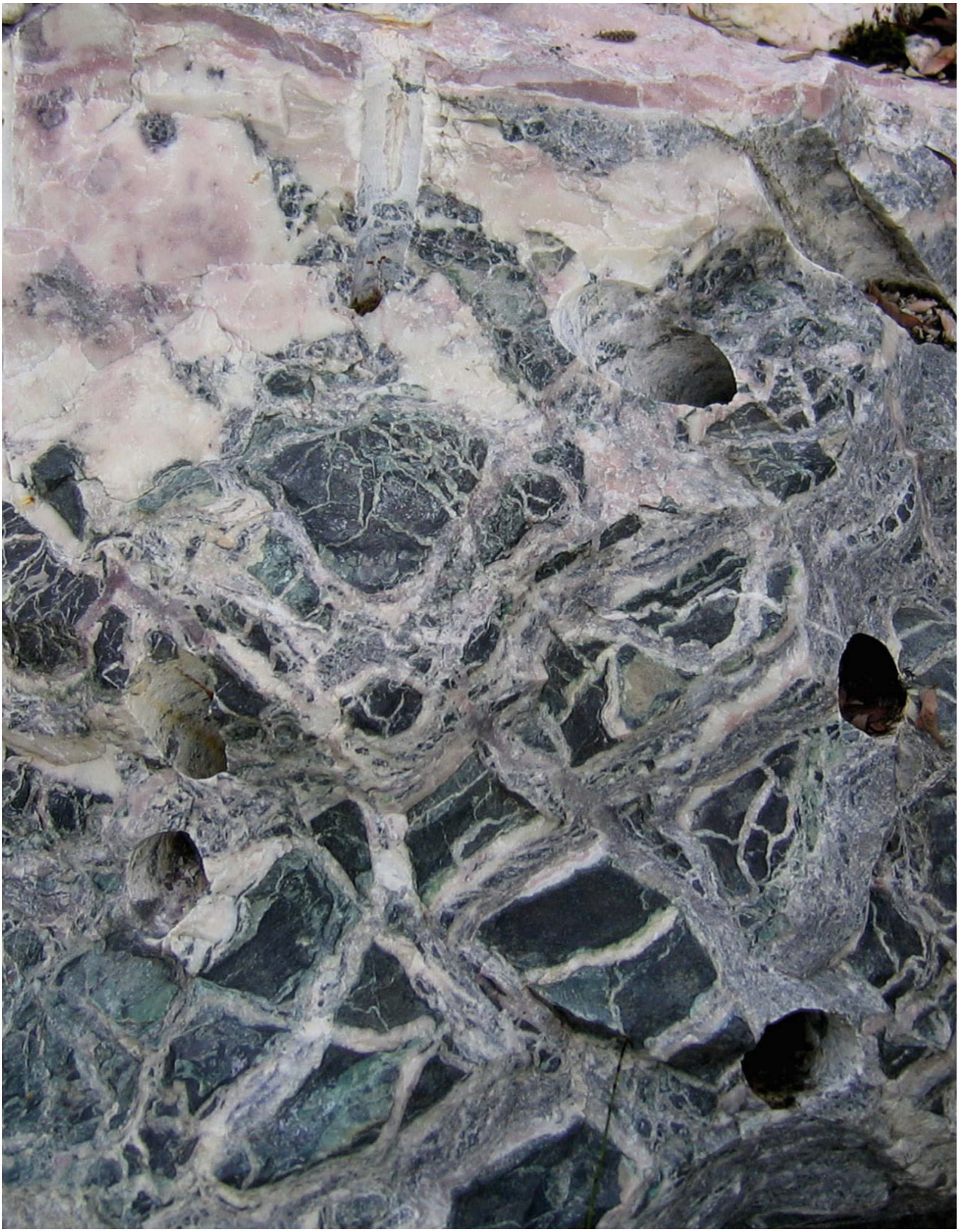

Fig. 6.29 Dolarenite-matrix ultramafic breccias are a peculiar feature of the Umba Sedimentary Formation at the Sukhoj section, central Imandra/Varzuga Greenstone Belt. They consist of angular clasts of altered ultramafic rocks in a dolarenite matrix. The ultramafic rocks have been altered to chlorite, calcite, quartz, and massive haematite. Width of the photograph is 50 cm (Photograph by Victor Melezhik)

Fig. 6.30 Dolarenite matrix-supported ultramafic breccia overlain erosively by dolostone conglobreccia. Dolostone clasts and fragments of ultramafic rocks. The latter appear as disintegrated "balls" (fragments of former pillows?) likely derived from older deep-water ramp dolostones and underlying ultramafic pillow lavas. The width of the photograph is 50 cm (Photograph by Victor Melezhik)

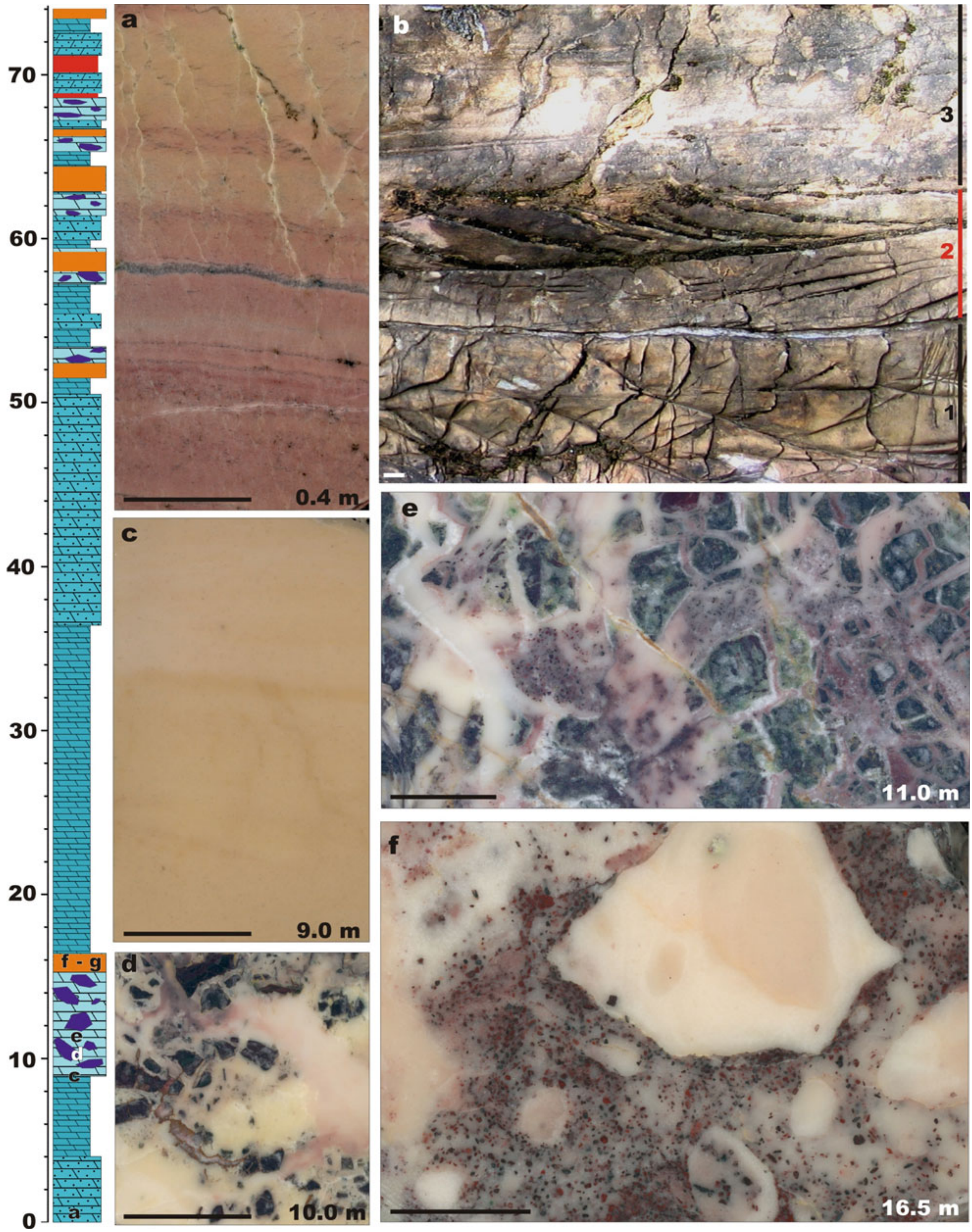

Fig. 6.31 Sedimentological features of carbonate rocks of the Umba Sedimentary Formation documented in the Sukhoj section. Scale bar in all images is 1 cm; all photographs by Victor Melezhik. (**a**) Polished slab of horizontally bedded dolarenite consisting of variably thick layers of alternating beige, tan and pale brown colours. (**b**) Exposed section of horizontally-bedded dolarenite (1) overlain by a dolarenite with bimodal (herringbone) cross-bedding (2), which is followed by a dolarenite with low-angle cross-bedding (3). (**c**) Beige dolomicrite showing no structures. (**d**, **e**) Intensively altered (weathered) angular clasts of ultramafic rock supported by variegated dolomite matrix. (**f**) Matrix-supported dolostone conglomerate; the matrix is composed of unsorted sand particles of micritic dolomite (*white*), Fe-rich carbonate (*brown*), altered ultramafic rock (*dark grey*) and jasper (*red*); note that the angular clast in the middle is a dolostone conglomerate suggesting several phases of erosion and redeposition

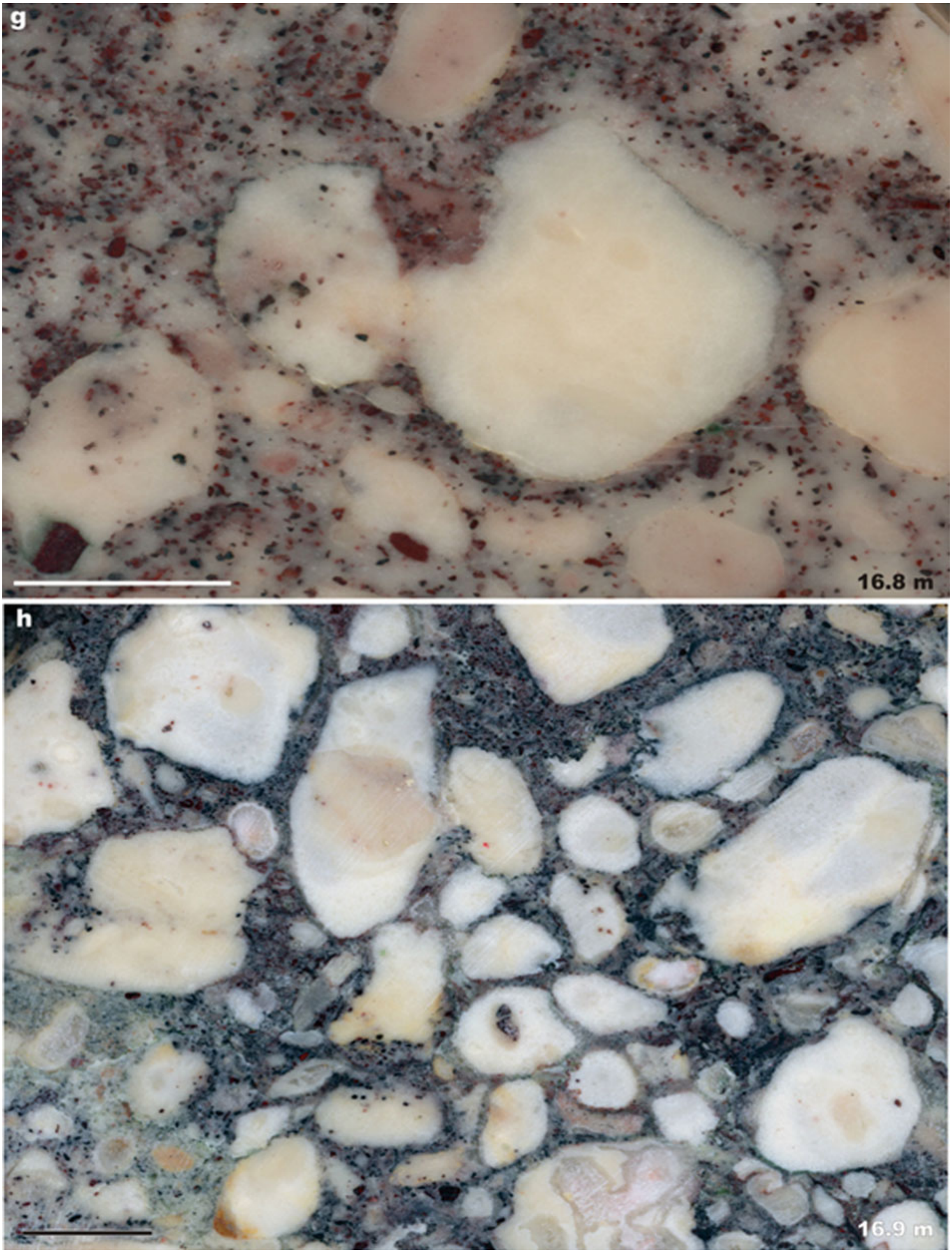

Fig. 6.31 (continued) (**g**, **h**). Matrix-supported dolostone conglomerate with matrix and clast composition similar to those described in (**f**); this demonstrates uniform lithology of the conglomerate bed through its entire thickness

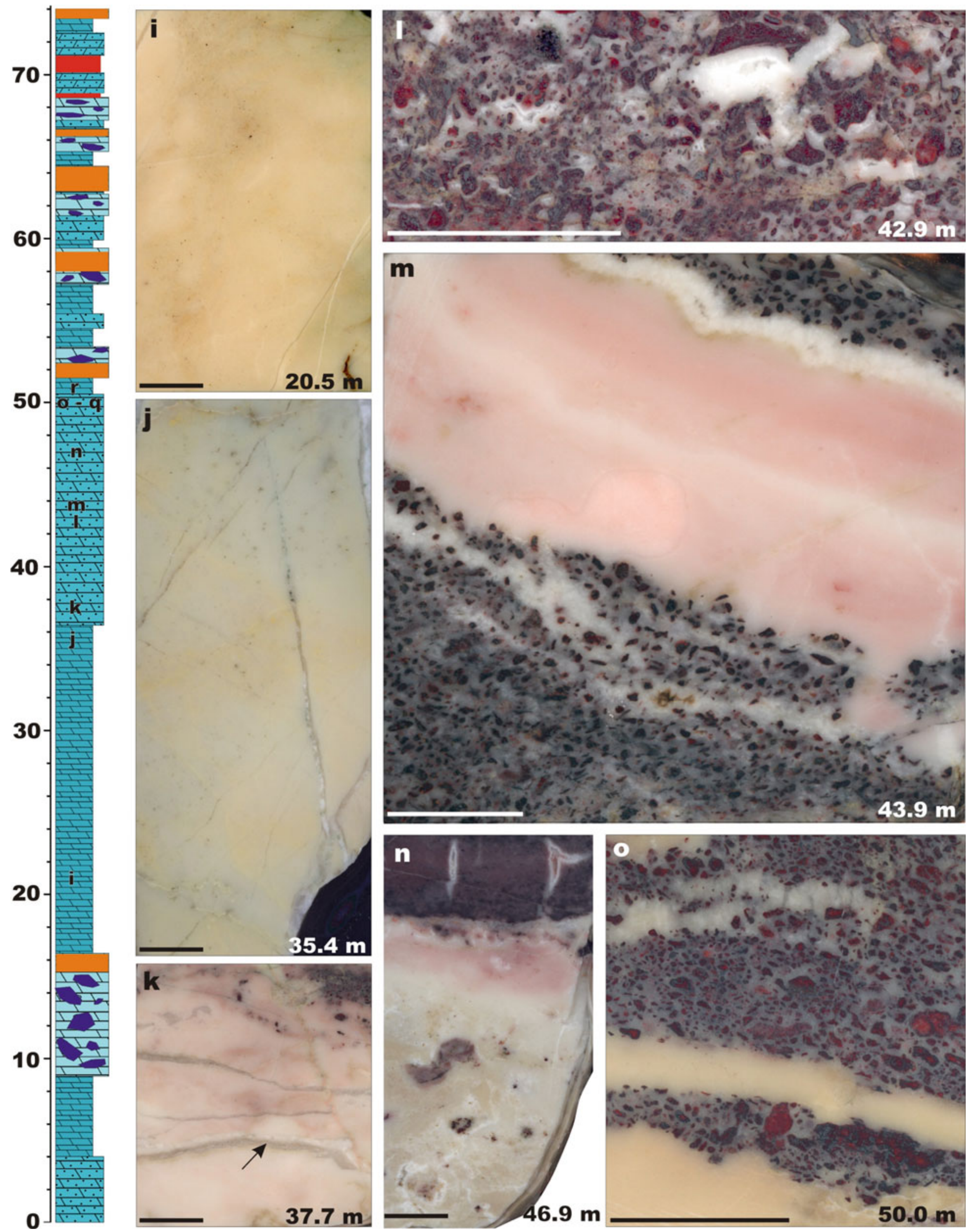

Fig. 6.31 (continued) (**i**, **j**) Beige and pale beige dolomicrite showing either massive or vague clotted structures. (**k**) Partially recrystallised dolarenite containing a grit-size dolomicrite clast (*arrowed*); dark particles in the right upper corner are comprised of weathered ultramafic material. (**l**) Dolomite matrix-supported dolorudite consisting of poorly sorted and variably rounded grains of Fe-rich carbonate (*red*) and altered ultramafic rock (*dark grey*). (**m**) Interbedded grainstone and finely crystalline (micritic?) dolostone both showing indistinct layering; grains are dolomite and altered ultramafic rocks (*dark*). (**n**) Vuggy, variegated dolostone capped by dark dolomarl showing star-shaped shrinkage cracks. (**o**) Interbedded pale beige, structureless, finely crystalline (micritic?) dolostone and grainstones containing poorly-sorted, variable-rounded clasts of Fe-rich carbonates (*red*) and altered ultramafic rock (*dark grey* and *brown*); the lower grainstone bed has an erosional base

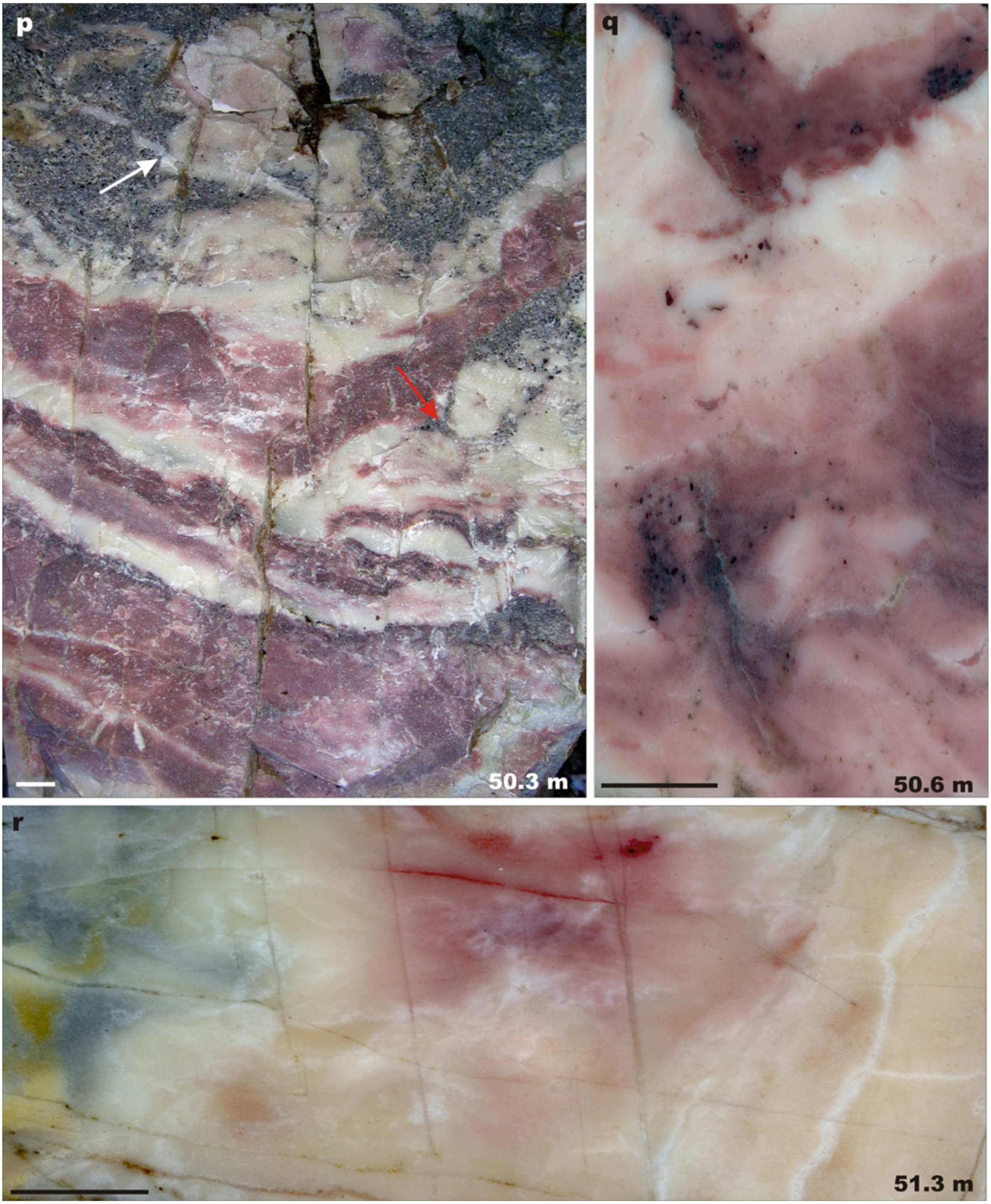

Fig. 6.31 (continued) (**p**) Variegated dolarenite with slump-associated, disrupted and partially-brecciated layers (*red arrowed*) overlain by grainstone containing sand- to grit-size particles of altered ultramafic material (*dark grey*) and large, fragmented, clast of beige dolostone (*white arrowed*). (**q**) Recrystallised, variegated, dolorudites and dolostone breccia with disrupted bedding. (**r**) Finely-crystalline (micritic) dolostone showing patchy, variegated colour

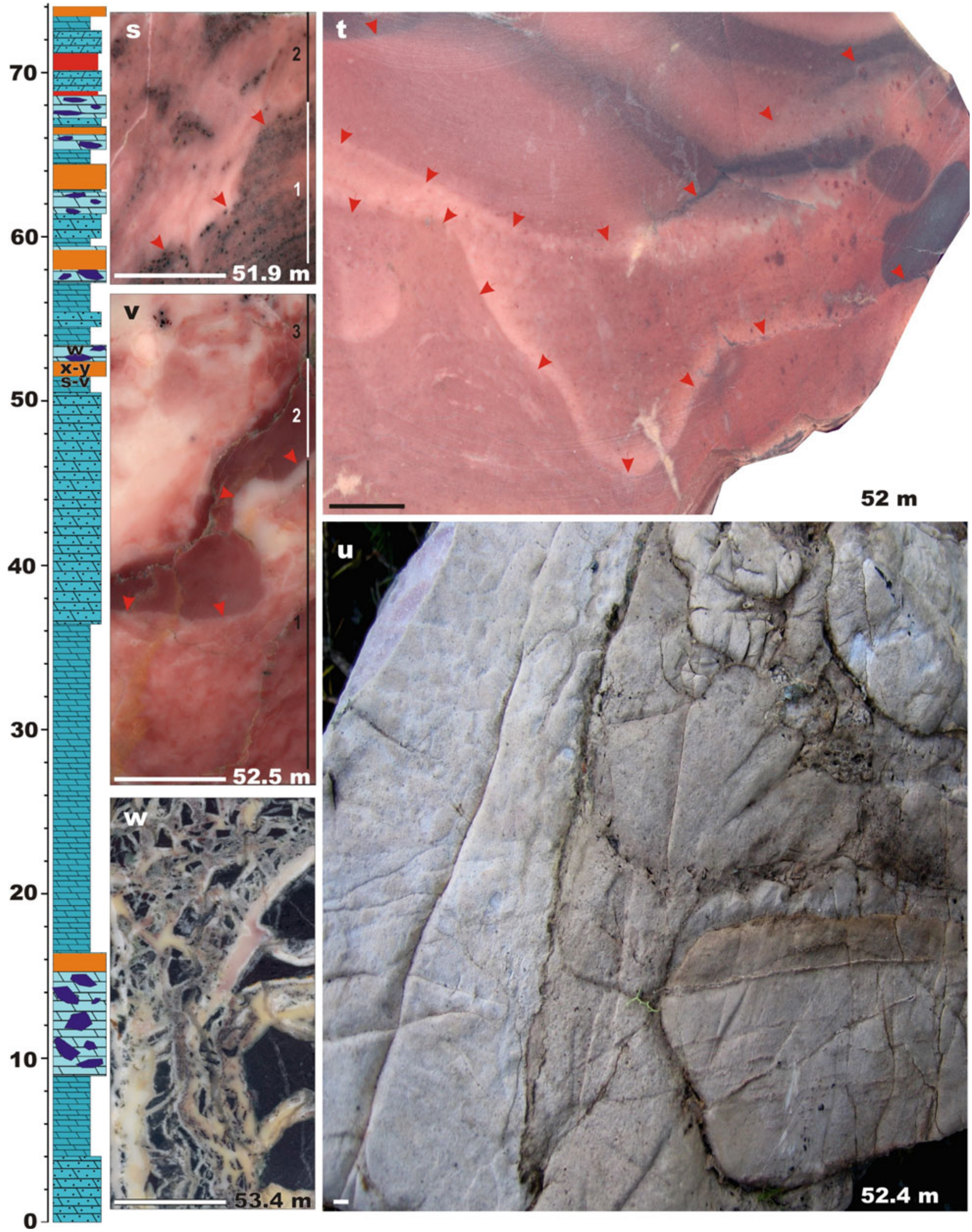

Fig. 6.31 (continued) (**s**) Pale pink dolostone matrix-supported breccia (2) erosively overlies dolarenite (1); erosion surface is arrowed. (**t**) Stack of small-scale channels filled with pink dolarenites containing scattered rounded pebbles of dolostones; channel surfaces are *red arrowed*. (**u**) Fragment-supported dolostone breccia; fragments are comprised of massive and parallel-bedded dolarenites and dolostone conglomerate (the *upper right corner*). (**v**) Fine-clast dolostone breccia (1) with erosive surface (*arrowed*) covered by brick-red coloured dolarenite (2), which is followed by unsorted, fine-pebble dolostone conglomerate (3). (**w**) Dolomicrite-cemented angular clasts of altered ultramafic rocks; many clasts can be reassembled if carbonate cement is removed suggesting that they were originally large fragments

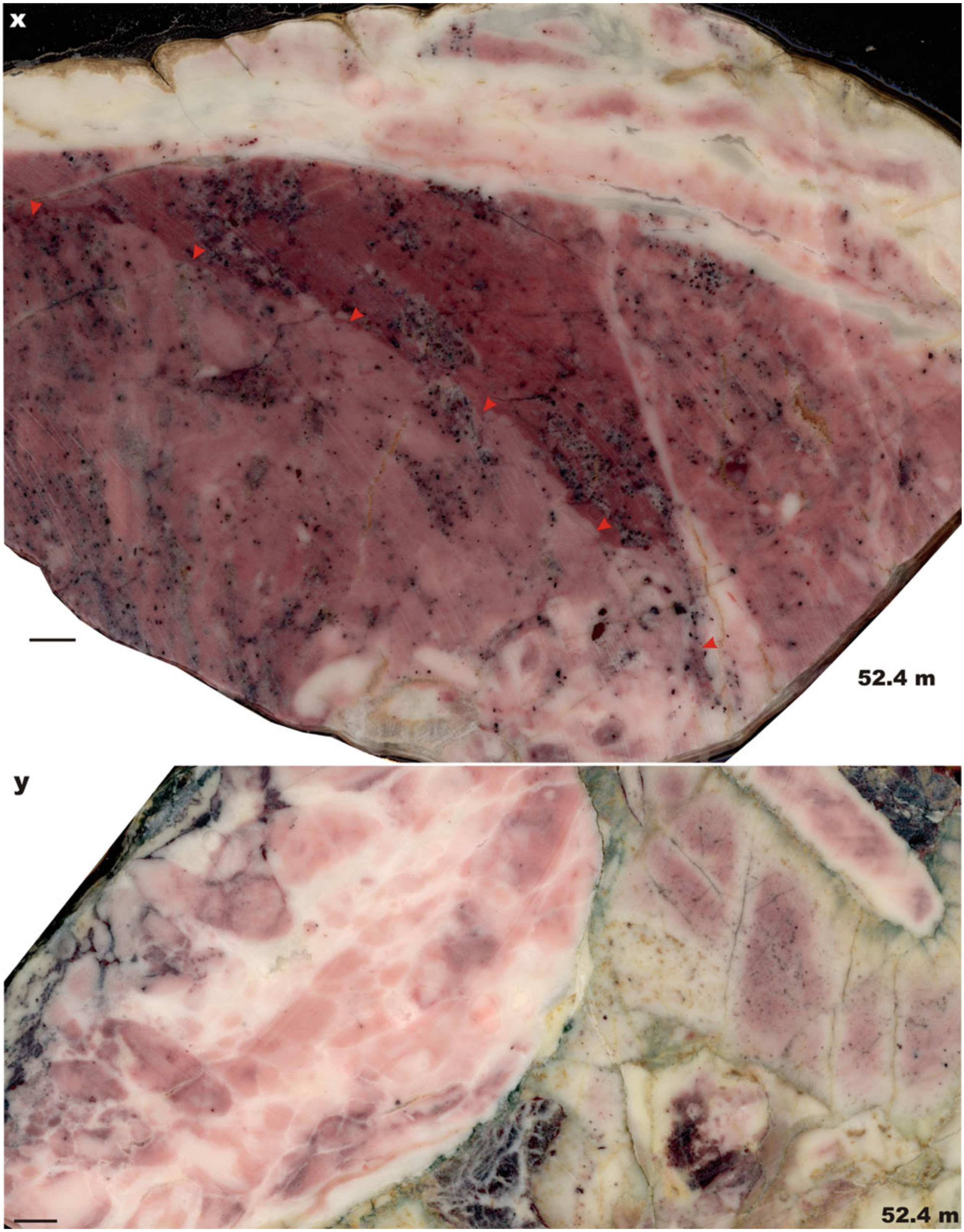

Fig. 6.31 (continued) (**x**) Eroded surface of a red dolostone conglomerate overlain by pale pink to beige dolostone with vague lamination developed parallel to the eroded surface; the conglomerate contains a composite cobble (*arrowed*) consisting of white rounded dolostone pebbles, and pink rounded and angular dolostone clasts; the whole pattern suggests multiple episodes of erosion and redeposition. (**y**) Unsorted, fragment-supported dolostone breccia containing a cobble of pale pink to white dolostone conglomerate; one surface (to the *left*) of the conglomerate cobble shows dissolution features and cavities filled with black haematite-rich muddy material; note that some pebbles in the cobble are fine-pebble dolostone conglomerate

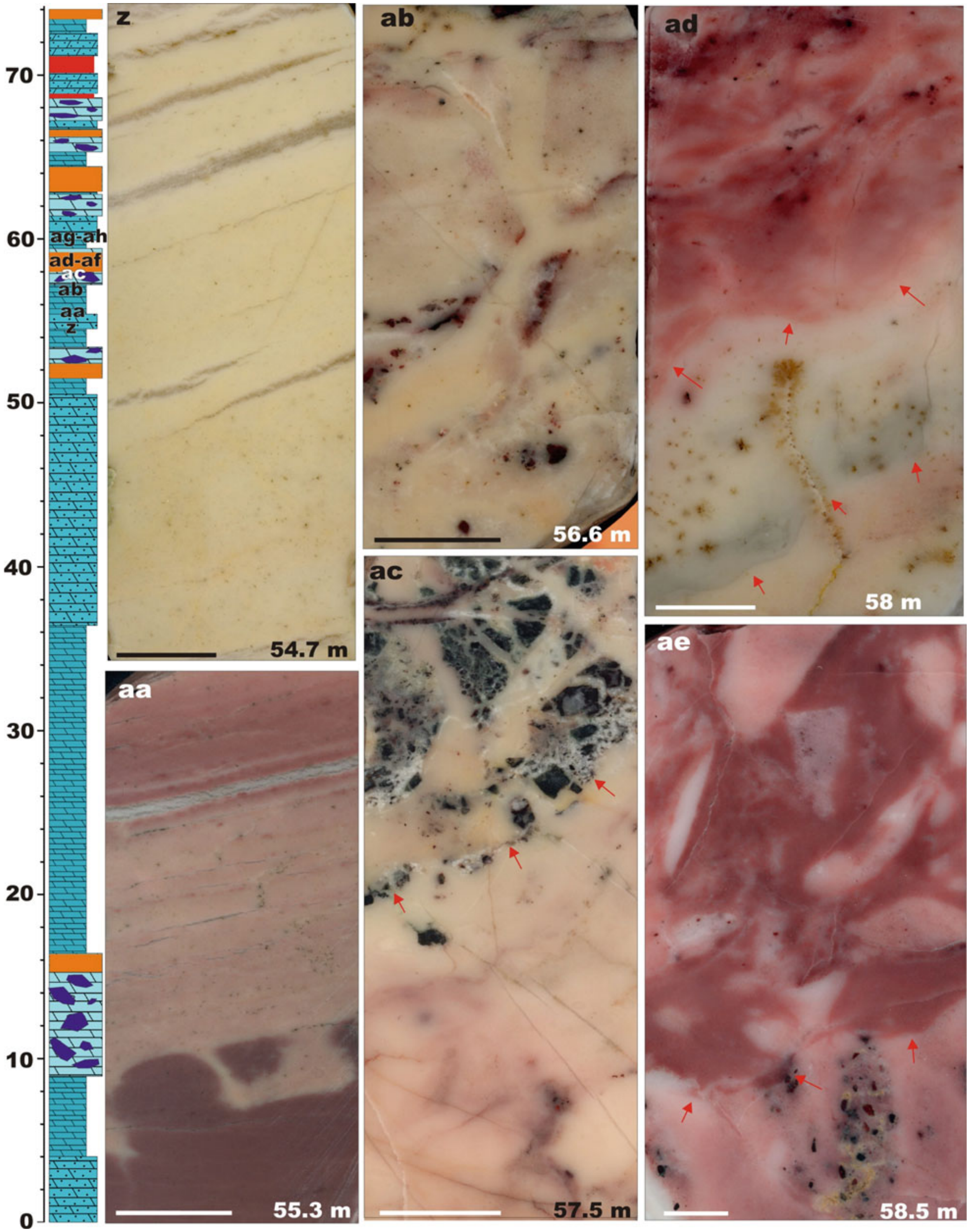

Fig. 6.31 (continued) (**z**) Beige, finely recrystallised (micritic) dolostone with a series of parallel extensional cracks filled with quartz. (**aa**) Variegated, parallel-bedded dolarenite; the upper part of lowermost brown layer was bleached suggesting that the beige colour of the middle and, apparently, upper layers is not primary and has been modified. (**ab**) Finely-crystalline (micritic) dolostone with scattered fine clasts of intensively altered ultramafic material causing red and brown staining of pale beige dolomicrite. (**ac**) Pale beige dolomicrite overlain by dolomite-matrix-supported ultramafic breccia (bedding surface is *arrowed*); clasts of altered ultamafic rocks show expansion features with expansion crack cemented by dolomite. (**ad**) Two dolarenite layers showing erosive surfaces (*arrowed*) overlain by a recrystallised pink dolostone conglomerate. (**ae**) Pale pink dolostone conglomerate with clasts containing sand-size ultramafic clasts (*black*) is overlain erosively by pink dolomite-matrix-supported breccia with clasts of white micritic dolostone

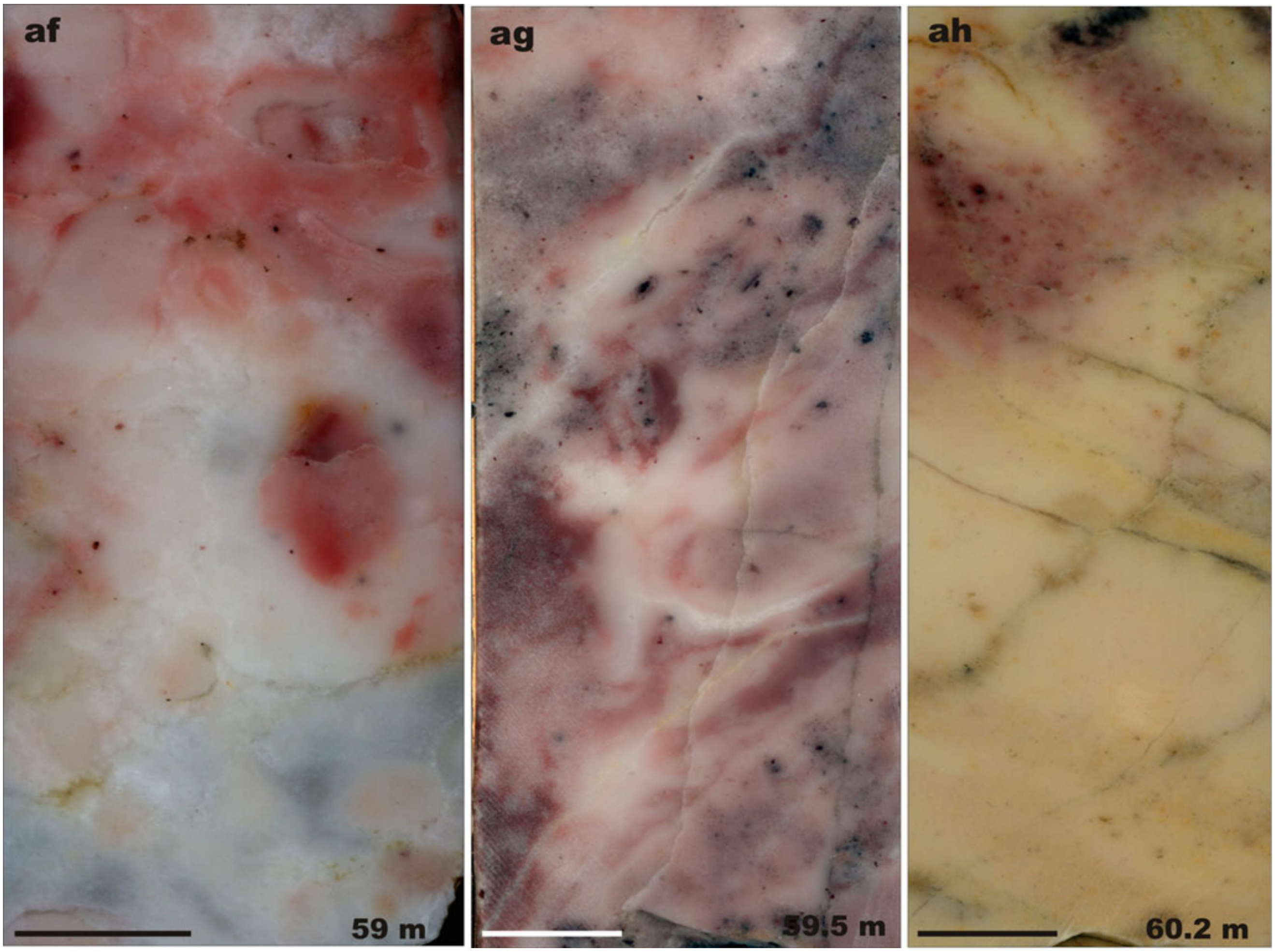

Fig. 6.31 (continued) (**af**) Recrystallised variegated dolostone conglomerate. (**ag**) Variegated dolarenite showing slump-related disrupted bedding. (**ah**) Variegated dolarenite with indistinct parallel bedding and extensional crack filled with dark grey quartz

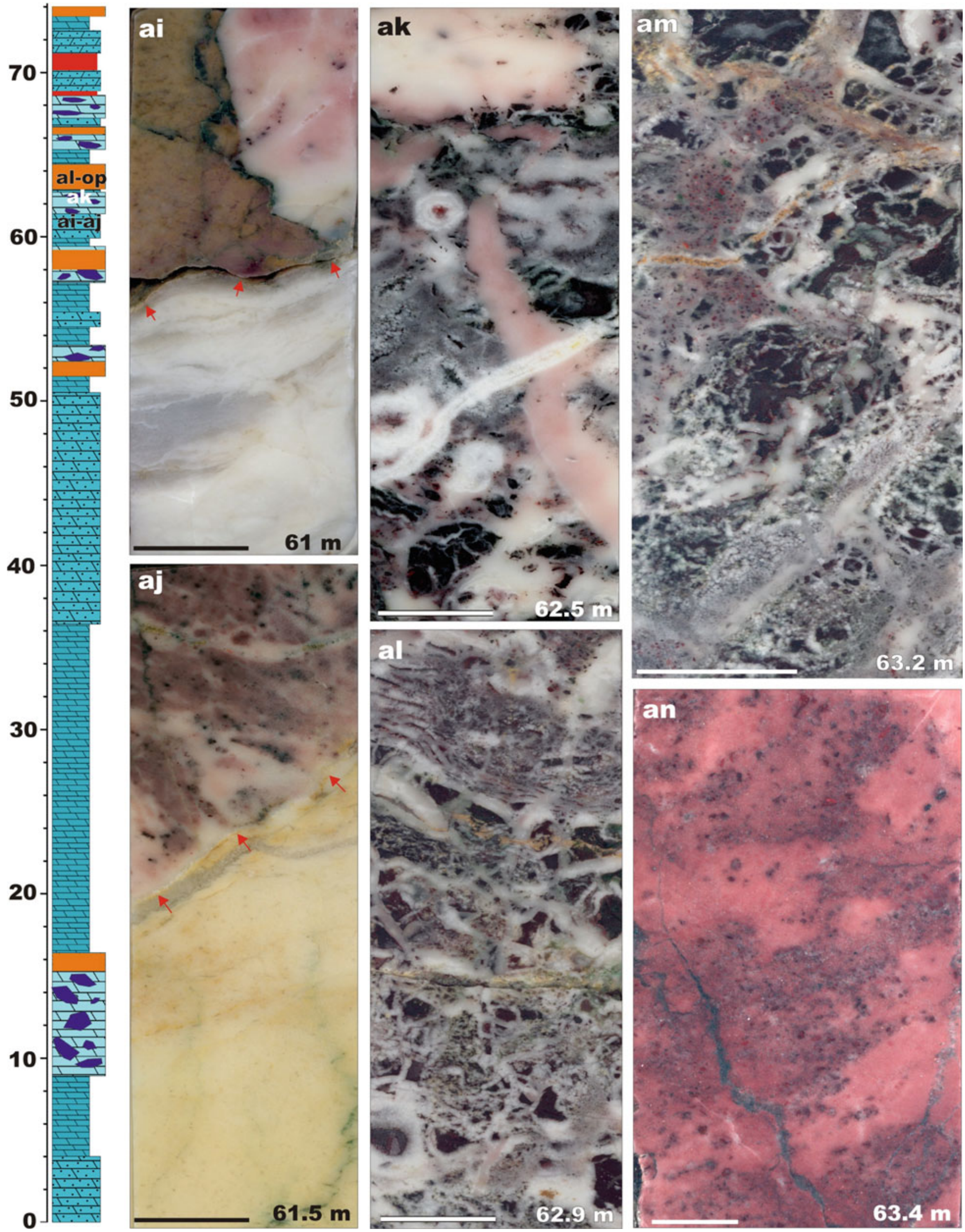

Fig. 6.31 (continued) (**ai**) White, silicified, finely crystalline dolostone overlain by breccia consisting of brown and pale-pink dolostone fragments; sharp erosion surface is *arrowed*. (**aj**) Pale beige, finely crystalline dolostone overlain by brown dolorudite with the contact modified by soft-sediment deformation. (**ak**) Polymict breccia containing angular, platy and rounded fragments of pale pink and white dolostone, and clasts of intensively altered ultramafic rocks (*black*) cut by a late dolomite vein. (**al**, **am**) Breccia consisting of angular fragments of altered ultramafic material cemented by dolomite. (**an**) Pink dolarenite with disrupted structure

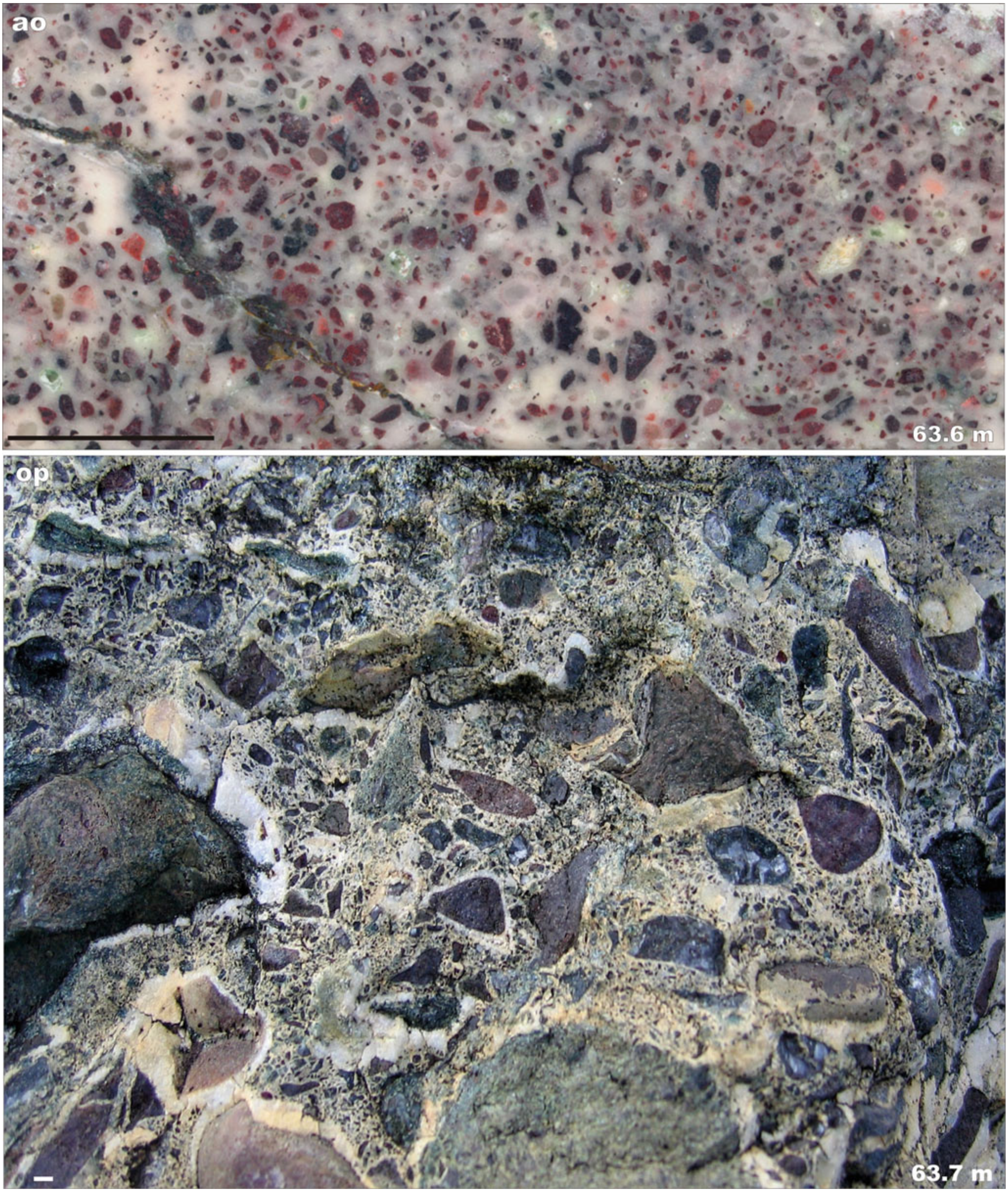

Fig. 6.31 (continued) (**ao**) Dolarenite consisting of rounded and angular fragments of Fe-rich carbonates (*brown*, *pink*, *red*), dolomite (*white*), and altered ultramafic material (*black*, *dark green*) cemented by white dolomite. (**ap**) Polymict breccia containing angular and variably rounded clasts of ultramafic rocks and lesser Fe-rich carbonates (*brown*) cemented by white dolomite

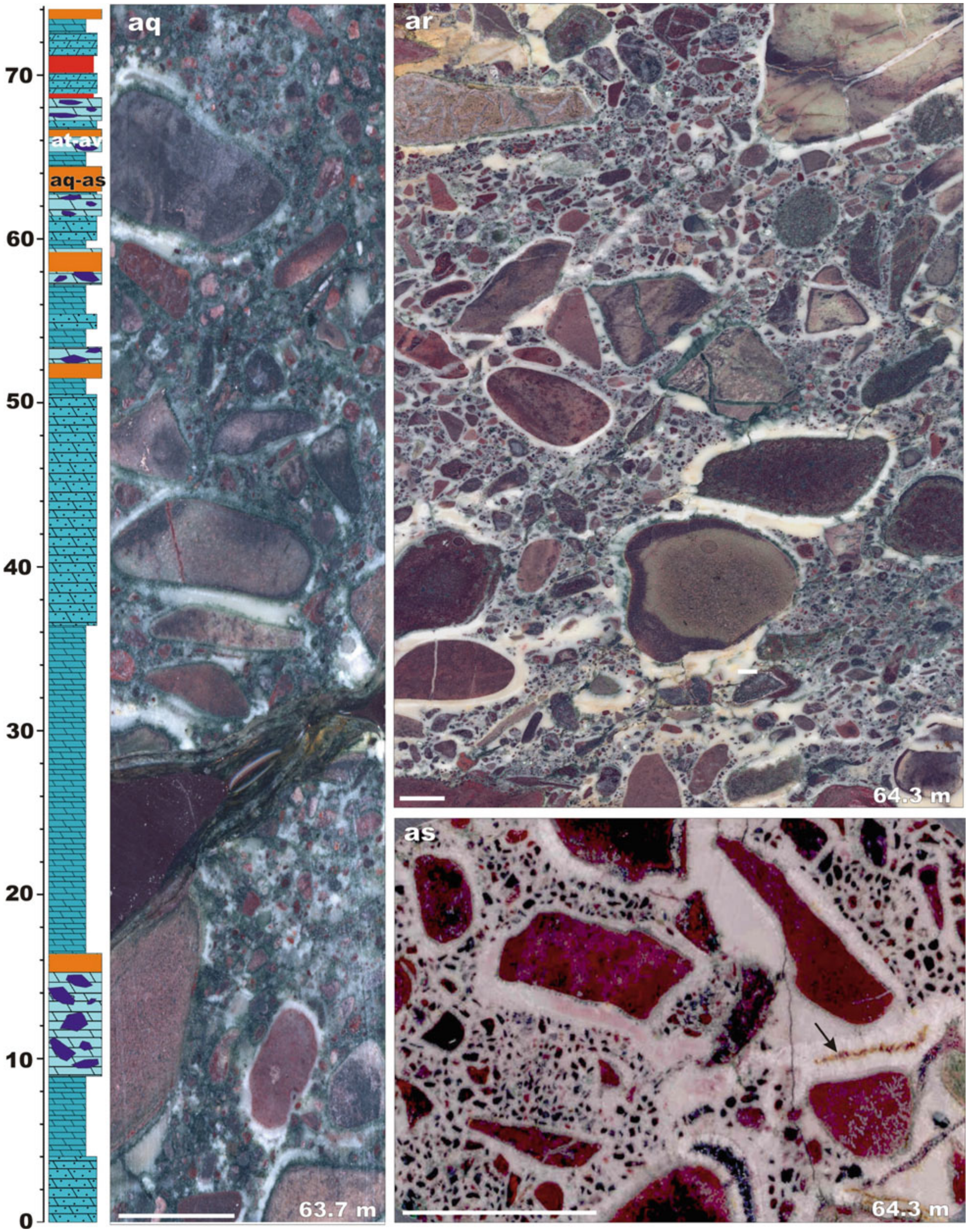

Fig. 6.31 (continued) (**aq**) Matrix-supported dolostone conglomerate comprised mainly of brown, Fe-rich carbonate pebbles; matrix is represented by smaller clasts of similar composition and intensively altered ultramafic material (*dark green*). (**ar**) Dolorudite matrix-supported dolostone conglomerate; pebbles of brown, Fe-rich carbonates are cemented by white dolomite druse. (**as**) Scanned polished thin section of matrix-supported dolostone conglomerate with dark brown-red fragments of Fe-rich dolostone cemented by white, columnar dolomite overgrown with white dolomite druse, and calcite spar (*pink*, stained by Alizarin-red, *arrowed*) filling remaining voids

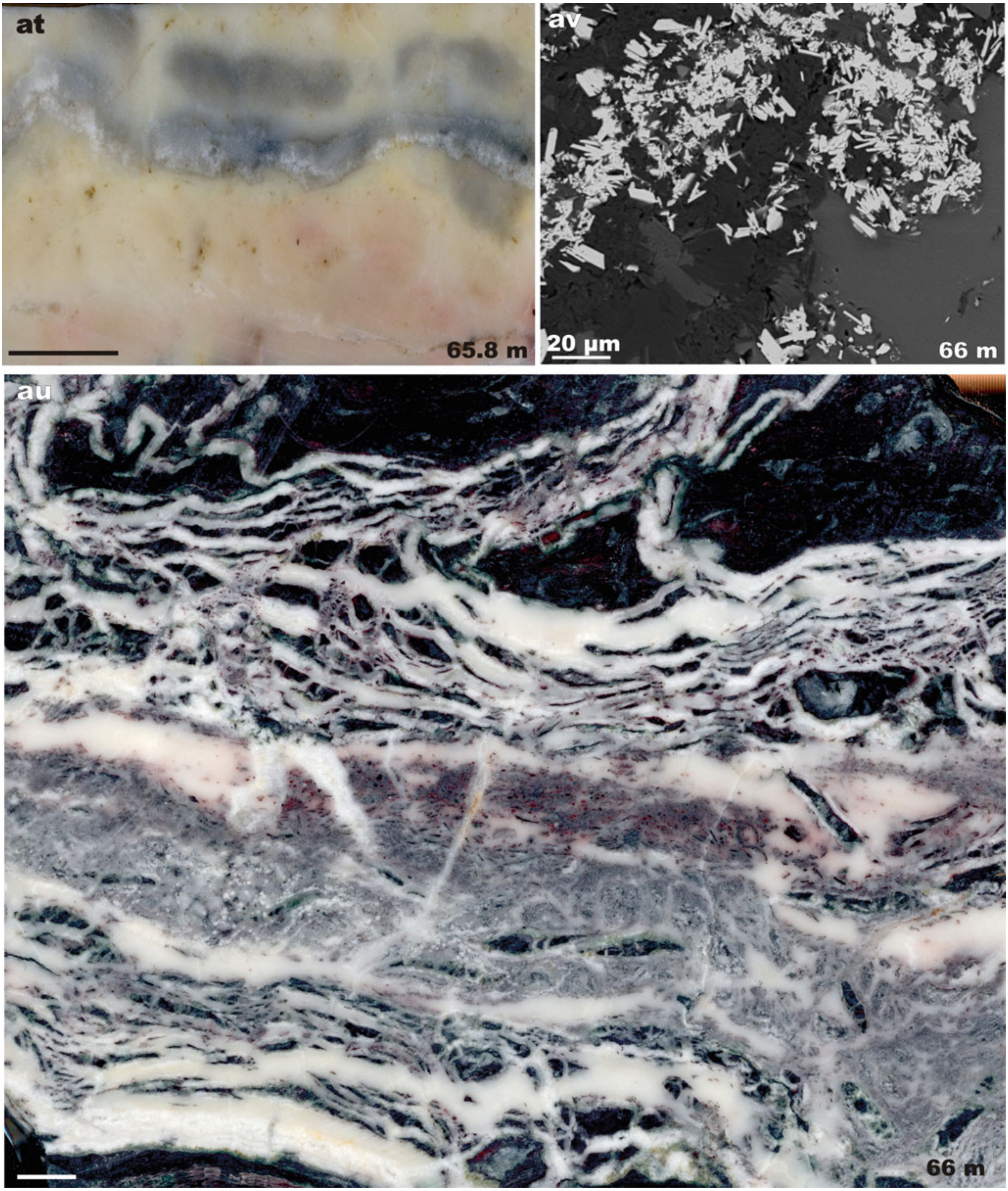

Fig. 6.31 (continued) (**at**) Beige, finely crystalline (micritic?) dolostone beds separated by an uneven bedding surface incrusted by white dolomite druse. (**au**) Bedded dolostone with angular, platy clasts of altered ultramafic rocks passing upward into dolomite-cemented ultramafic breccia. (**av**) Back-scattered electron image of altered ultramafic clast; grey – calcite, dark grey – Mg-chlorite, white – haematite crystals

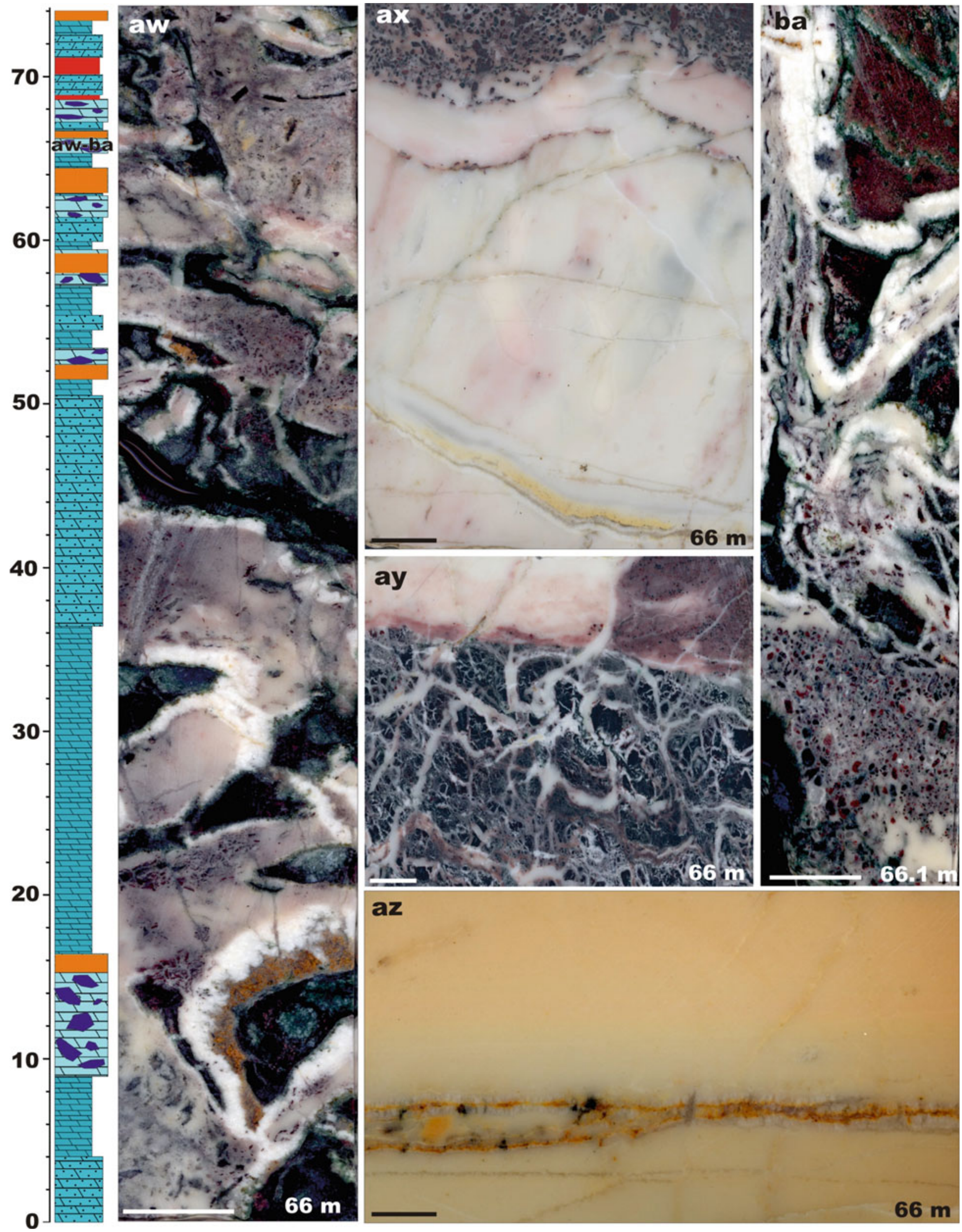

Fig. 6.31 (continued) (**aw**) Synsedimentary breccia composed of dolostone clasts and fragments of altered ultramafic rocks in white dolomite druse cement. (**ax**) Pale rose, finely crystalline (micritic?) dolostone overlain by volcaniclastic sandstone consisting of dark brown, altered clasts of ultramafic material emplaced into beige dolomite cement; these two lithologies occur as a thin dismembered layer in ultramafic breccia. (**ay**) Synsedimentary breccia consisting of tightly packed fragments of beige and dark violet dolostones, and an intensively cracked large fragment of altered ultramafic rock. (**az**) Tan, massive micritic dolostone occurring as a thin dismembered lens in ultramafic breccia. (**ba**) Synsedimentary breccia consisting of altered ultramafic rocks and a fragment of dolarenite (lower part) composed of dolomite-cemented particles of Fe-rich carbonates and altered ultramafic material; the ultramafic clasts are supported by white dolomite druse

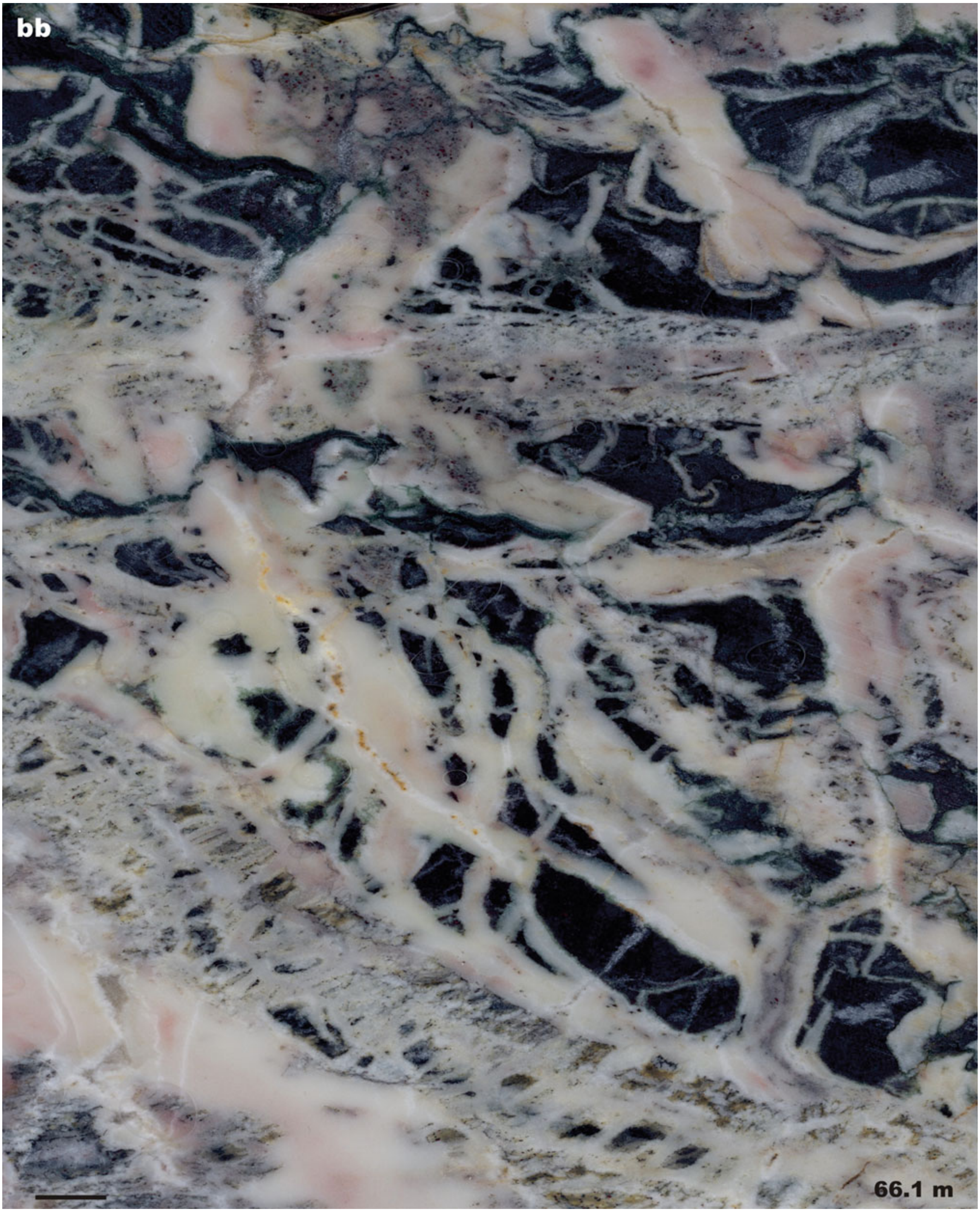

Fig. 6.31 (continued) (**bb**) Detailed image of dolomite-cemented ultramafic breccia illustrating several phases of brecciation and cementation; this implies a complex depositional history

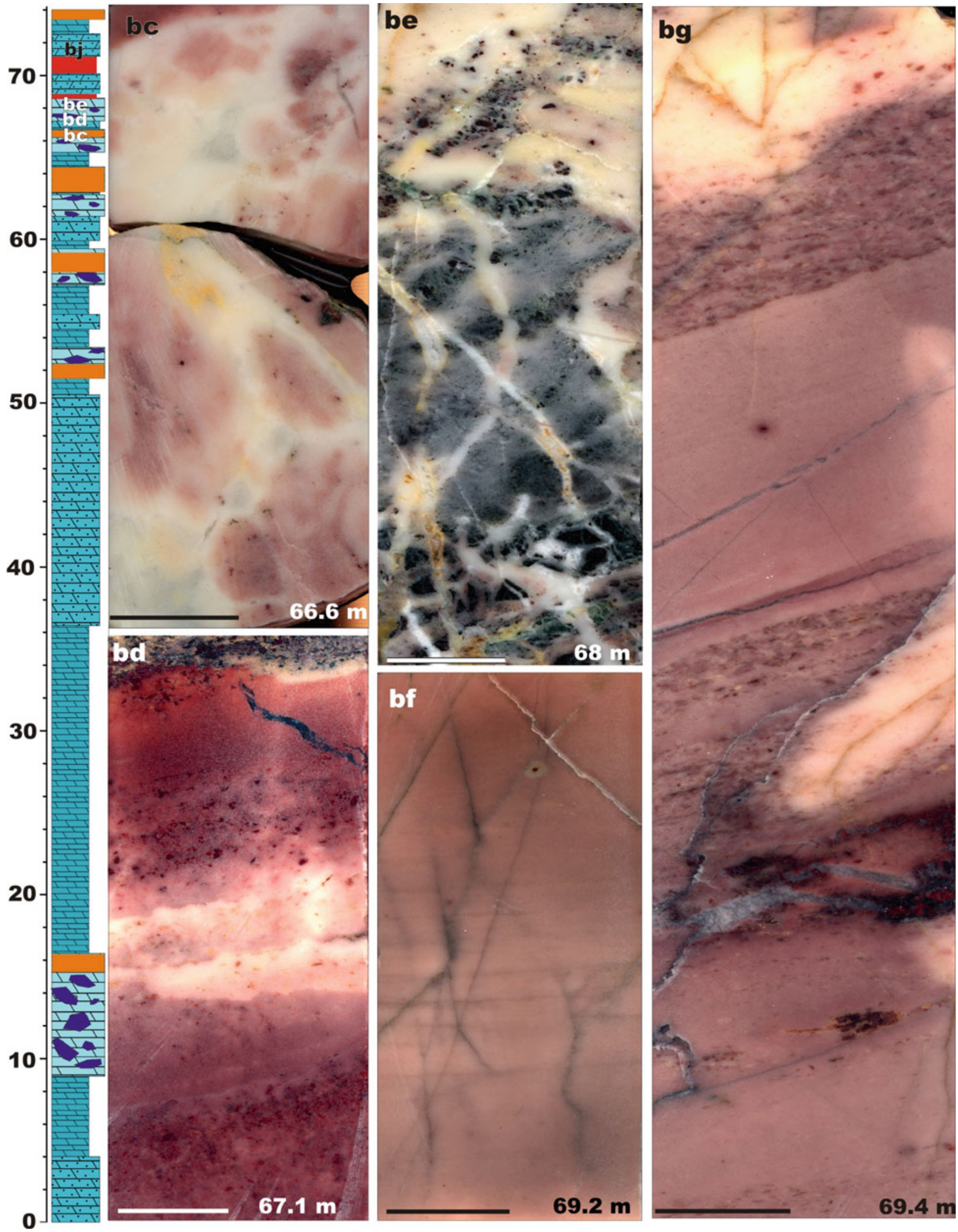

Fig. 6.31 (**bc**) Dolostone breccia consisting of rounded fragments of pale pink dolostone pebbles supported by white finely-crystalline dolomite matrix; fragment-matrix boundaries appear to be diffuse. (**bd**) Pink, parallel-bedded dolarenite; white zone in the middle caused by recrystallisation and formation of dolospar. (**be**) Dark to pale grey, fragmented, haematite- and magnetite-rich dolostone in beige microcrystalline dolomite with scattered particles of altered ultramafic material (*black*). (**bf**) Pink, massive and parallel-bedded dolomicrite occurring above a jasper bed. (**bg**) Pink, massive, fine-grained dolarenite interbedded with coarse-grained dolostone; note the pebble of pale pink dolostone in middle and that some layers appear to be graded

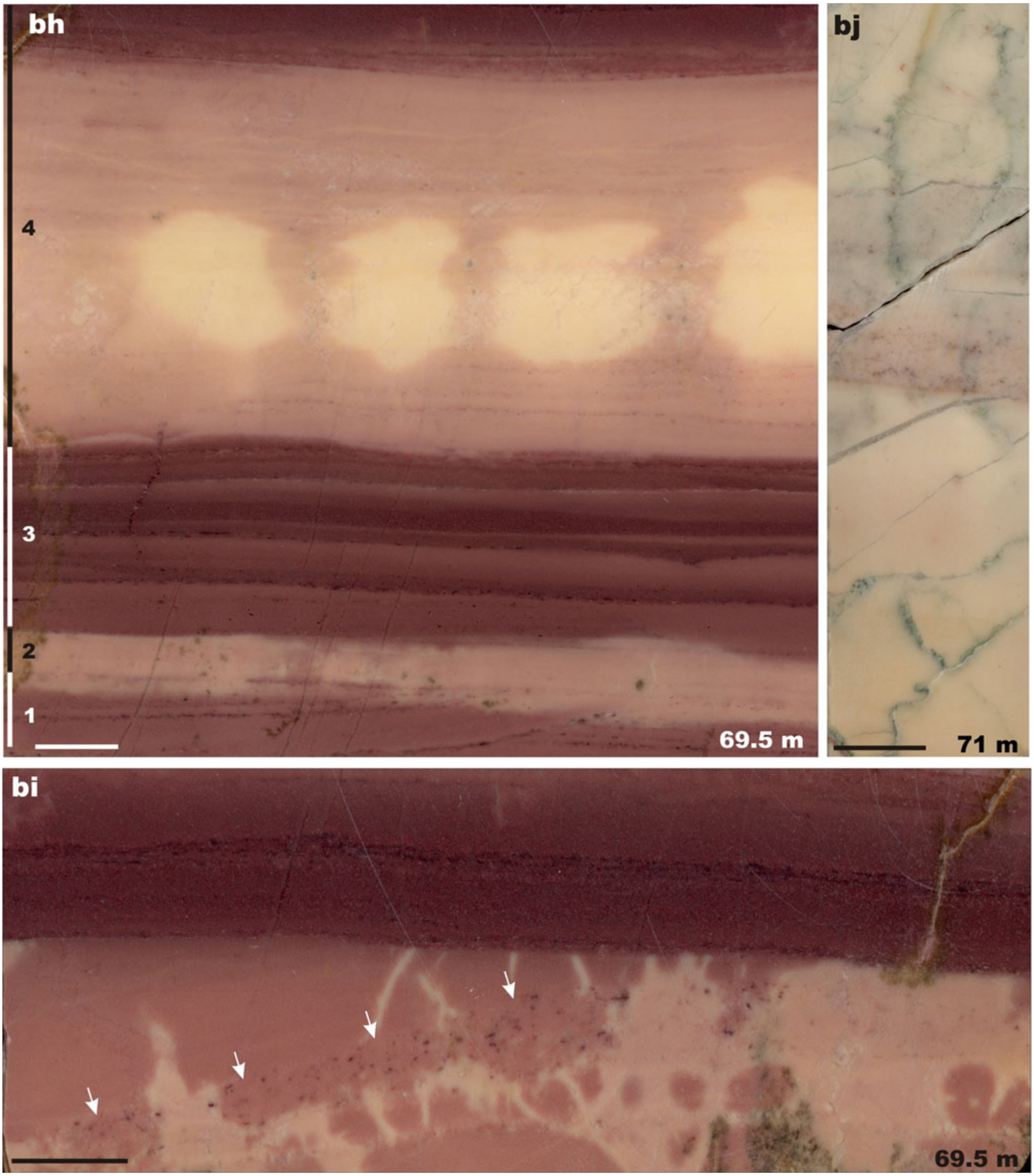

Fig. 6.31 (continued) (**bh**) Low-angle cross-bedded, purple dolarenite (1), overlain by pale pink, bleached bed (2), followed by a series of purple, graded dolarenite beds (3), capped by a thick, pale pink dolarenite with wavy and parallel lamination and patchy bleaching (4). (**bi**) Purple dolarenite cutting obliquely across bedding (*arrowed*) bleached zone and joints of underlying bed. (**bj**) Pale beige dolarenite showing indistinct bedding

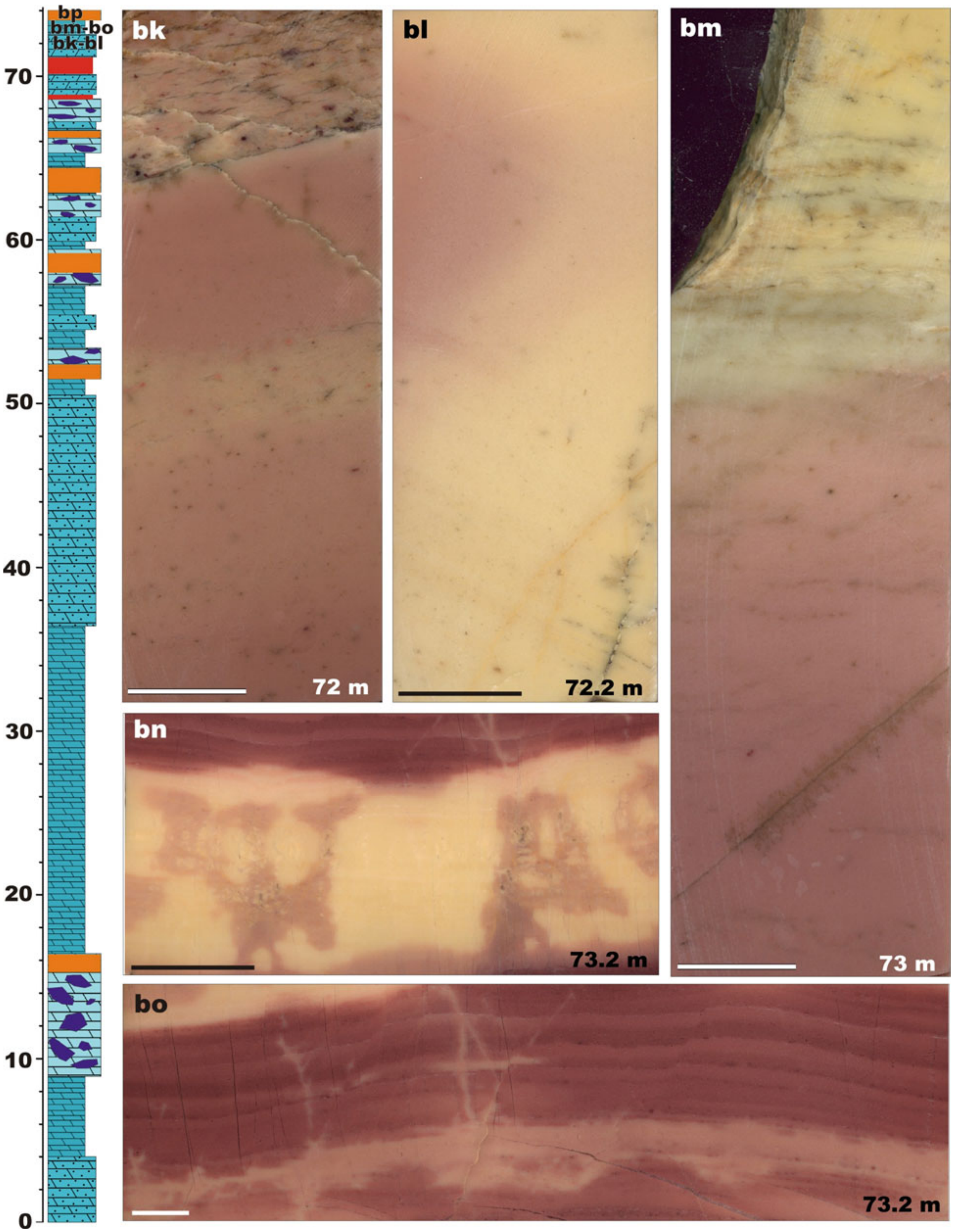

Fig. 6.31 (continued) (**bk**) Pale purple dolarenite showing indistinct bedding; the *upper part* has been sheared. (**bl**) Pale beige, massive, finely-crystalline (micritic?) dolostone; (**bm**) Indistinctly bedded, pale pink to beige, finely-crystalline (micritic) dolostone. (**bn**) Pervasive bleaching obliterating rhythmically laminated purple dolarenite. (**bo**) Graded-bedding in rhythmically bedded, purple dolarenite partially affected by bleaching

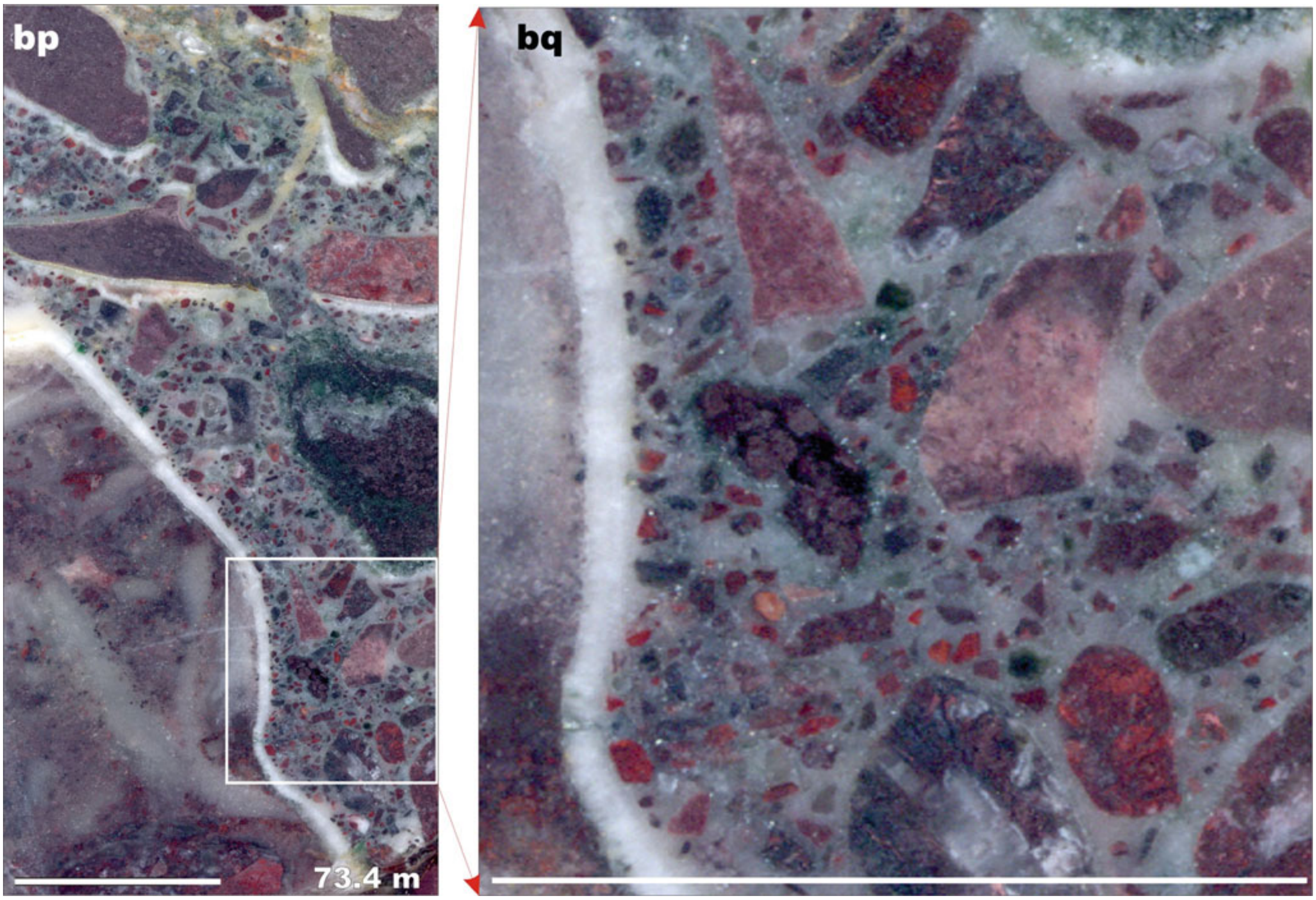

Fig. 6.31 (continued) (**bp**) Matrix-supported dolostone breccia; clasts of Fe-rich dolostone (*purple*), altered ultramafic rocks (*black*) and dolorudite (large clast in the *bottom left corner*) cemented by white palisade dolomite. (**bq**) Detailed image of the matrix composed of angular clasts of pink and purple dolostones, jasper (*red*) and gritstones cemented by white dolomite (All photographs by Victor Melezhik)

References

Grinenko LN, Melezhik VA, Fetisova OA (1989) The first finding of barite in Precambrian sedimentary rocks of the Baltic Shield. Dokl Trans USSR Acad Sci Mineral 304 (6):1453–1455, in Russian

Makarikhin VV, Kononova GM (1983) Early Proterozoic phytolites of Karelia. Nauka (Science), Leningrad, 180p, in Russian

Melezhik VA, Predovsky AA (1982) Geochemistry of early Proterozoic Lithogenesis. Nauka (Science), St. Petersburg, 208p, in Russian

Melezhik VA, Fetisova OA (1989) Discovery of syngenetic barium sulphates in Precambrian rocks of the Baltic Shield. Dokl Trans USSR Acad Sci Geol 307(2):422–425

Melezhik VA, Fallick AE (1996) A widespread positive $\delta^{13}C_{carb}$ anomaly at around 2.33–2.06 Ga on the Fennoscandian Shield: a paradox? Terra Nova 8:141–157

Melezhik VA, Fallick AE, Makarikhin VV, Lyubtsov VV (1997) Links between Palaeoproterozoic palaeogeography and rise and decline of stromatolites: Fennoscandian Shield. Precambrian Res 82:311–348

Melezhik VA, Borisov AE, Fedotov ZhA, Predovsky AA (1982) The Varzuga Series. In: Gorbunov GI (ed) The Imandra/Varzuga zone of the Karelides. Nauka (Science), Leningrad, pp 57–85, in Russian

Melezhik VA, Fallick AE, Kuznetsov AB (2005) The Palaeoproterozoic, rift-related, shallow-water, ^{13}C-rich, lacustrine carbonates, NW Russia – Part II: global isotope signal recorded in the lacustrine dolostones. Trans R Soc Edinb Earth Sci 95:423–444

Read JF (1982) Carbonate platforms of passive (extensional) continental margins: types, characteristics and evolution. Tectonophysics 81:195–212

6.2 The Pechenga Greenstone Belt

Victor A. Melezhik, Anthony R. Prave, Eero J. Hanski, Aivo Lepland, Paula E. Salminen, Alexander E. Romashkin, Dmitry V. Rychanchik, Anthony E. Fallick, Zhen-Yu Luo, Evgenii V. Sharkov, and Maria M. Bogina

6.2 The Pechenga Greenstone Belt

Victor A. Melezhik

Geology and stratigraphy of the Pechenga Greenstone Belt is described in detail in Chap. 4.2. The brief geological outline presented here provides a scientific context and background information for the FAR-DEEP implemented in this area.

The Pechenga Greenstone Belt (Fig. 6.1) forms the north-western part of a NW-SE-trending Palaeoproterozoic belt that extends for c. 800 km from Russia through Norway and Finland and then back into Norway. Because of its economic importance, it is the most intensely studied geological structure in the Kola Peninsula. The first detailed description of the geology of Pechenga dates back to the ore camps of the 1930–1940s (Väyrynen 1938). The stratigraphic subdivision of the Pechenga Greenstone Belt (Figs. 6.32 and 6.33) has remained essentially unchanged since Zagorodny et al. (1964) published the first general description of the regional geology, of what they called the Pechenga Series; later renamed the Petsamo Supergroup (Melezhik and Sturt 1994). The series/group was subdivided into the Northern Pechenga and Southern Pechenga subseries, later renamed the North Pechenga and South Pechenga groups, respectively (Melezhik and Sturt 1994; Melezhik et al. 1994). Each of the groups was further subdivided into numerous suites or formations that are shown on the simplified lithological column (Fig. 6.33).

A maximum depositional age of the North Pechenga Group is constrained by the presence of 2505 ± 1.6 Ma gabbro-norite pebbles in the basal Neverskrukk conglomerates (Fig. 6.33). The minimum age for the group is 1970 ± 5 Ma (U-Pb zircon, Hanski et al. 1990), obtained from felsic tuffs of the Pilgujärvi Volcanic Formation (Fig. 6.33). The age of sedimentation and volcanism of the South Pechenga Group remains largely unconstrained. Nevertheless, existing geochronological constraints indicate that the evolution of the Pechenga Greenstone Belt spans some 600 Ma of Earth history.

Six FAR-DEEP holes were drilled in the central part of the belt (Fig. 6.32) to recover rocks containing a record of a series of geological processes and global events. These include: (1) the Palaeoproterozoic perturbation of the global carbon cycle (the Lomagundi-Jatuli isotopic excursion) as recorded in lacustrine carbonates; (2) formation of the earliest know travertines and associated environmental conditions; (3) regional deep oxidation of terrestrial surfaces; (4) an apparent oxidation of the upper mantle; and (5) termination of the Lomagundi-Jatuli isotopic excursion.

V.A. Melezhik (✉)
Geological Survey of Norway, Postboks 6315 Sluppen, NO-7491 Trondheim, Norway

Centre for Geobiology, University of Bergen, Allegaten 41, Bergen N-5007, Norway
e-mail: victor.melezhik@ngu.no

V.A. Melezhik et al. (eds.), *Reading the Archive of Earth's Oxygenation*, Volume 2: The Core Archive of the Fennoscandian Arctic Russia – Drilling Early Earth Project, DOI 10.1007/978-3-642-29659-8_3, © Springer-Verlag Berlin Heidelberg 2013

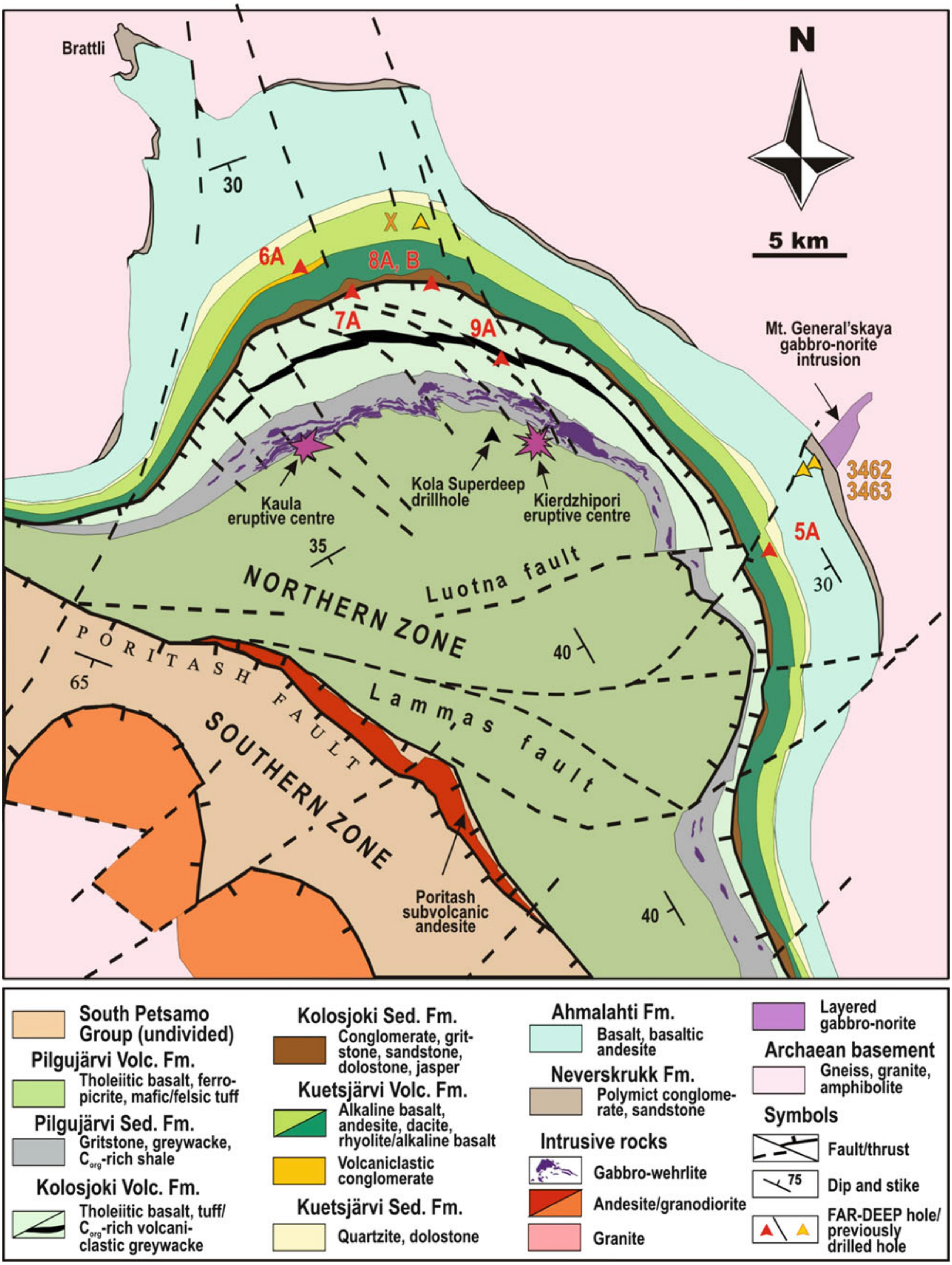

Fig. 6.32 Simplified geological map of the Pechenga Greenstone Belt (Modified from Zagorodny et al. 1964) showing the locations of FAR DEEP drill holes 5A, 6A, 7A, 8A, B and 9A

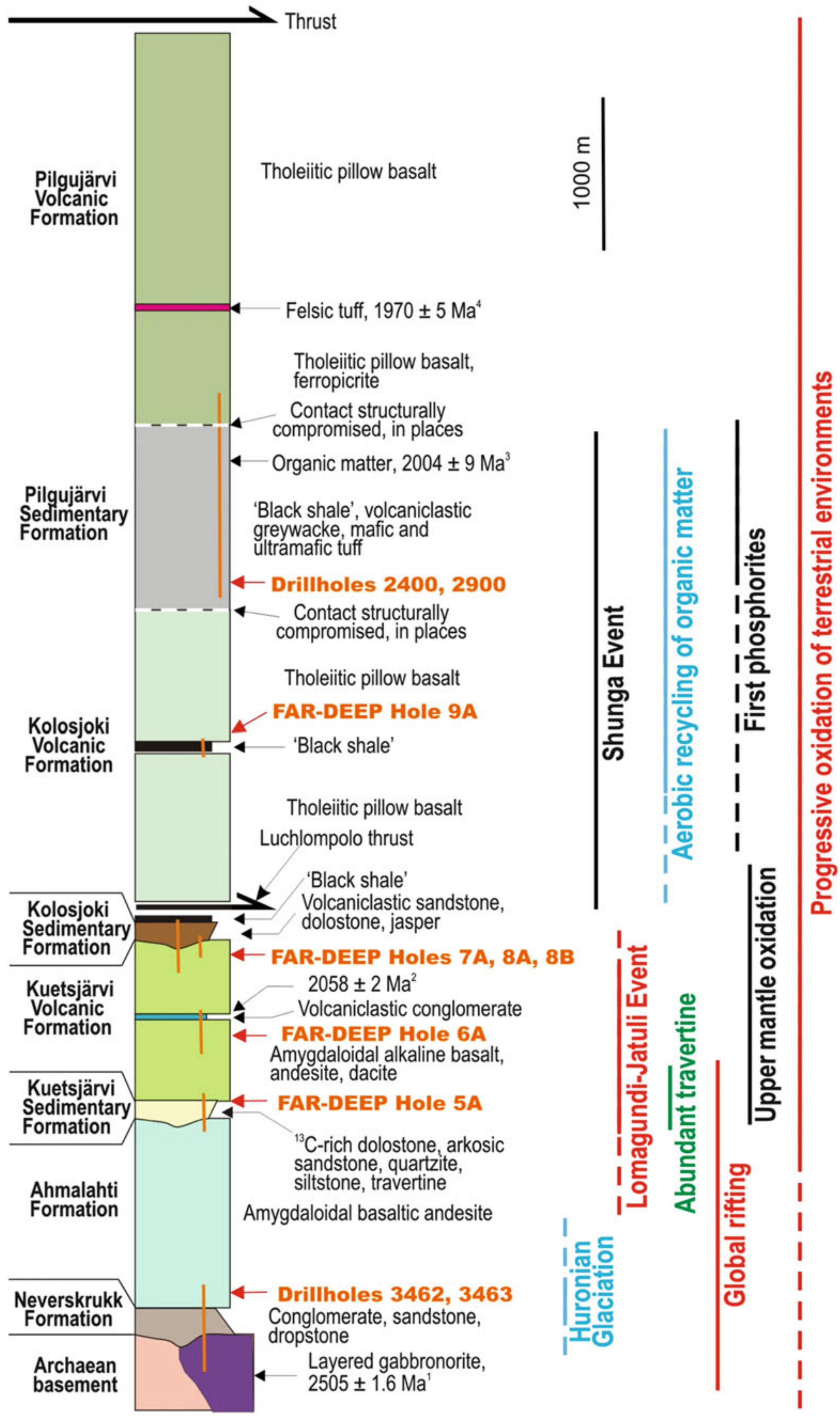

Fig. 6.33 Simplified lithological column of the North Pechenga Group, with positions of FAR-DEEP and other relevant drillholes. Also shown is how the evolution of the Pechenga Greenstone Belt is related to global palaeoenvironmental events. Superscripts denote radiometric ages from ([1]) Amelin et al. (1975), ([2]) Melezhik et al. (2007), ([3]) Hannah et al. (2004), and ([4]) Hanski (1992)

References

Amelin YuV, Heaman LM, Semenov VS (1995) U-Pb geochronology of layered mafic intrusions in the eastern Baltic Shield: implications for the timing and duration of Palaeoproterozoic continental rifting. Precambrian Res 75:31–46

Hannah JL, Stein HJ, Zimmerman A, Yang G, Markey RJ, Melezhik VA (2006) Precise 2004 ± 9 Ma Re-Os age for Pechenga black shale: comparison of sulfides and organic material. Geochim Cosmochim Acta 70:A228

Hanski EJ (1992) Petrology of the Pechenga ferropicrites and cogenetic, Ni-bearing gabbro-wehrlite intrusions, Kola Peninsula, Russia. Geol Surv Finland Bull 367:192p

Hanski EJ, Huhma H, Smol'kin VF, Vaasjoki M (1990) The age of the ferropicritic volcanics and comagmatic intrusions at Pechenga, Kola Peninsula, USSR. Bull Geol Soc Finland 62:123–133

Melezhik VA, Sturt BA (1994) General geology and evolutionary history of the early Proterozoic Polmak-Pasvik-Pechenga-Imandra/Varzuga-Ust'Ponoy Greenstone Belt in the north-eastern Baltic Shield. Earth Sci Rev 36:205–241

Melezhik VA, Sturt BA, Mokrousov VA, Ramsay DM, Nilsson L-P, Balashov YuA (1994) The early Proterozoic Pasvik-Pechenga Greenstone Belt: 1:200,000 geological map, stratigraphic correlation and revision of stratigraphic nomeclature. Norg Geol Unders Spec Publ 7:81–91

Melezhik VA, Huhma H, Condon DJ, Fallick AE, Whitehouse MJ (2007) Temporal constraints on the Paleoproterozoic Lomagundi-Jatuli carbon isotopic event. Geology 35:655–658

Väyrynen H (1938) Petrologie des Nickelerzfeldes Kaulatunturi-Kammikivitunturi in Petsamo. Bull Comm Géol Finlande 116, 198 p

Zagorodny VG, Mirskaya DD, Suslova SN (1964) Geology of the Pechenga sedimentary-volcanogenic series. Nauka (Science), Leningrad, 218p, in Russian

6.2.1 The Neverskrukk Formation: Drillholes 3462, 3463 and Related Outcrops

Victor A. Melezhik, Anthony E. Fallick, Anthony R. Prave, and Aivo Lepland

Scientific Targets

– Tectonic and depositional settings associated with onset of Huronian-age glaciation
– Geochemical rock record during the global icehouse event
– Mass-dependent and mass-independent sulphur isotope fractionation
– Provenance composition

Drillholes 3462 and 3463 are located in the northeast portion of the Pechenga Greenstone Belt, southwest of Mt. General'skaya (Figs. 6.1 and 6.32). These two holes (drilled for nickel exploration) intersected Ahmalahti Formation basaltic andesites and an entire thickness of the Neverskrukk Formation including the basal contact with the underlying 2505 ± 1.6 Ma (Amelin et al. 1995) Mt. General'skaya layered gabbro-norite intrusion (Fig. 6.32). The Neverskrukk Formation is the oldest unit in the Pechenga Greenstone Belt and is also a probable chronostratigraphic equivalent to the Huronian-age glacial deposits reported elsewhere. However, unlike its marine counterpart in the Imandra/Varzuga Belt, the Polisarka Sedimentary Formation, the Neverskrukk Formation is mainly composed of conglomerates (Fig. 6.34) with subordinate gritstones, sandstones and shales, and records deposition in fluvial and deltaic environments (Sturt et al. 1994).

The Archaean basement is comprised of a diverse assemblage of rocks including gneisses, amphibolites, crystalline schists, banded ironstones, diorites, granites and gabbro-norites; all can be found as clasts in the conglomerates and gritstones. Thus clast composition reflects a local derivation from underlying Archaean rocks. For example, at Brattli (Fig. 6.32), the conglomerates contain boulders of banded ironstones, which occur nearby and form several commercially exploited deposits. Another example is the conglomerates in the Mt. General'skaya (Fig. 6.32) area that contain pebbles and boulders derived directly from the layered gabbro-norite intrusion which they erosively overlie.

The conglomerates and sandstones fill palaeovalleys, and many sections demonstrate buried palaeotopography. At Brattli, several subvertical surfaces of the basement, up to 4 m high, form buttress unconformities which gently dipping sandstones and conglomerates abut against and eventually bury. A few kilometres further south, the conglomerates thin to zero and the surface is overlain by basaltic andesites. A general cross-section suggests that the original depth of this particular palaeovalley could have been >50 m (Sturt et al. 1994). In other places, fractures as much as 2 m deep can be seen to penetrate downward into the basement and are filled by angular fragments of fractured rocks and pale brown fine-grained massive or weakly laminated sandstones resembling a rockflour (Fig. 6.35). The cracks display irregular shapes with smaller branches and Sturt et al. (1994) interpreted these fractured basement rocks as a regolith. An alternative explanation is that they record ice-shattering, or possibly extensional jointing on uplifted rift shoulders. Drillholes 3462 and 3463 are separated by a distance of 800 m; the former intersected a 300-m-thick proximal section with respect to the latter, which is a thinner, c. 80-m-thick, more distal section. The formational thickness reported from the Kola Superdeep Drillhole, which is located 15 km SSW of Mt. General'skaya, is 7 m (Kozlovsky 1984). In combination with other drillholes from within the area, it can be shown that the Neverskrukk Formation quickly thins in both depositional dip and strike directions, laterally interfingering with associated volcanic rocks (Figs. 6.36, 6.37, and 6.38).

The Neverskrukk Formation, Drillhole 3462

Conglomerate Unit

The Neverskrukk Formation logged in hole 3462 is informally divided into five litho-units (Fig. 6.37). The lowermost is a 55-m-thick Conglomerate unit of clast-supported polymict boulder to pebble conglomerates resting sharply on the gabbro-norite basement, which shows no sign of weathering (Fig. 6.39ap). Conglomerates are massive or show crude stratification; a small channel has been observed in the upper part of the unit. Gabbro-norite pebbles and boulders in a gabbroic sand-size matrix (Fig. 6.39ai–ao) occur in the lower 40 m of the section. Above this the matrix is either greywacke or arkosic sand and a diverse suite of boulders occurs including diorites, gneisses, quartzites, crystalline schists and vein quartz (Fig. 6.39ad–an). Larger clasts are well rounded and poorly sorted, smaller clasts may be angular (Fig. 6.39ah, aj). Two 0.5-m-thick intervals of pebbly conglomerate with a calcite matrix are present at depths of 398.5 and 395 m (Fig. 6.39ae).

Gritstone Unit

The Gritstone unit lies above the boulder-pebble conglomerates. It is a 30-m-thick package dominated by

V.A. Melezhik (✉)
Geological Survey of Norway, Postboks 6315 Sluppen, NO-7491 Trondheim, Norway

Centre for Geobiology, University of Bergen, Allegaten 41, Bergen N-5007, Norway

V.A. Melezhik et al. (eds.), *Reading the Archive of Earth's Oxygenation*, Volume 2: The Core Archive of the Fennoscandian Arctic Russia – Drilling Early Earth Project, DOI 10.1007/978-3-642-29659-8_3, © Springer-Verlag Berlin Heidelberg 2013

polymict gritstones (Fig. 6.39ab–ad) with uncommon fine-pebble conglomerates; a small-scale sand-filled channel occurs close to the base (Fig. 6.37). Clasts are compositionally similar to the underlying *Conglomerate unit* though the matrix ranges from arkosic sandstone to greywacke. At a depth of 372 m, a 15-cm-thick interval of fine-pebble polymict conglomerate with a calcite matrix was intersected (Fig. 6.39ac). Some intervals contain sericite-muscovite plates and chips; these were originally mud chips.

Gritstone-Conglomerate-Sandstone Unit

The overlying Gritstone-Conglomerate-Sandstone unit is 125 m thick. It starts with a polymict conglomerate followed by a package of interbedded gritstones, conglomerates and sandstones (Fig. 6.37). Gritstones form beds 0.5 to 12 m thick, are pebbly, massive or crudely stratified, and are composed of angular, poorly-sorted clasts of plagioclase, microcline, quartz, quartzite, crystalline schist and amphibolite (Fig. 6.39r, x). Some beds contain numerous plates and rounded fragments of sericite-muscovite-biotite rocks that were originally mud chips (Fig. 6.39q, y). All gritstones between 330 and 315 m contain disseminated pyrite. Conglomerates occur in beds 1–20 m thick, are polymict, either clast- or fragment-supported, and contain rounded and poorly-sorted clasts (Fig. 6.39w, z–aa) similar in composition to those in the underlying units. Sandstones occur as channelised beds 0.1–2 m in thickness, are either massive or normally graded (Fig. 6.39v), and show either parallel bedding or low-angle cross-lamination. They range from clast-supported to matrix-supported (Fig. 6.39p, u) with clasts that are semi-rounded and poorly sorted. Some sandstones exhibit angular clasts of quartz floating in a sericite-muscovite-biotite (Al-rich) matrix (Fig. 6.39p). Many beds located between 360 and 292 m contain large muscovite chips, and some are partially or entirely pyritised (Fig. 6.39s, t). Some beds contain clusters of pyrite resembling small nodules (Fig. 6.39v).

Sandstone Unit

The Sandstone unit is 13 m thick. Apart from greywackes and rare arkosic sandstones it contains several intervals of polymict conglomerate and two thin layers of gritstones on top (Fig. 6.37). Sandstones show cross or plane-parallel bedding (Fig. 6.39k) and some beds contain pockets of pebbly material. Clasts of quartz, plagioclase and rare microcline are semi-rounded and angular and range greatly in size (Fig. 6.39j, l–n). Some beds contain plates and chips of fine-grained sericite-muscovite aggregate, again representing former mud chips (Fig. 6.39o).

Conglomerate-Sandstone Unit

The Conglomerate-Sandstone unit (c. 80 m) consists of alternating beds of thicker conglomerates (1–13 m) and numerous thin (0.1–0.9 m) sandstone layers (Fig. 6.37). The conglomerates (Fig. 6.39a–c, g) are similar in all characteristics to those described in the underlying units. Sandstones are either massive or show parallel and cross-lamination (Fig. 6.39k). Both massive and bedded varieties contain poorly-sorted, scattered clasts, and lonestones (Fig. 6.39d, e, h, i) which are characteristics strikingly similar to diamictites intersected by FAR-DEEP Hole 4A in the Polisarka Sedimentary Formation of the Imandra/Varzuga Belt (Fig. 6.19i–t in Chap. 6.1.2).

The Neverskrukk Formation, Drillhole 3463

The section intersected by drillhole 3463, 800 m down-dip from drillhole 3462, is 77 m thick (Fig. 6.38). In additional to the thinning, another principal difference is the presence of clayey siltstones (Fig. 6.40h) containing lonestones. These occur in the basal part of the drilled section and rest directly on the gabbro-norite substrate. The siltstones coarsen and thicken upward in three 1–5-m-thick cycles to gritstone grading to conglomerate (Fig. 6.38). Higher in the section, conglomerate units are interbedded with thin sandstones marked by layers of fine-grained sericite-muscovite-biotite (former clay material; Fig. 6.40e, f) containing numerous oversized clasts resembling dropstones (Fig. 6.40g). The rest of the section is similar in character to that described from hole 3462: the conglomerates are polymict, clasts are unsorted and poorly rounded with either clast- or matrix-supported textures (Fig. 6.40a–c) and small-scale channelised sandstones and gritstones contain scattered oversized clasts of cobbles and pebbles (Fig. 6.40d).

The Depositional Framework

The depositional framework of the Neverskrukk Formation was detailed in Sturt et al. (1994) based on mapping at Brattli (Fig. 6.32). The lowermost clast-supported cobble and pebble polymict conglomerates with oversized blocks were interpreted as debris flows that passed rapidly upward and southward into the fining-upward massive and cross-bedded gritstones and sandstones representing proximal alluvial fan through distal fan and braided fluvial depositional settings. Pebble imbrications (Fig. 6.34) and cross bedding suggest south-directed stream-flow.

The sedimentological features of the succession intersected by drillholes 3462 and 3463 suggest a similar, but more complete, sequence of depositional environments. The lowermost part of the section in drillhole 3463, which is comprised of multiple coarsening-up siltstone-conglomerate cycles (Fig. 6.38), can be interpreted as part of a distal braidplain and/or nearshore deltaic setting. The lower part of core 3462 is marked by a series of fining-upward cycles of cobble conglomerates through alternating conglomerate-gritstone into conglomerate-gritstone-sandstone and represents an upward transition from a fluvial into alluvial fan setting. The two coarsening-upward gritstone-conglomerate cycles followed by a fining upward conglomerate-sandstone cycle in the middle part of the section, and then the multiple thick-conglomerate – thin-sandstone cycles in the upper part of the section, reflect a retrogradational episode from alluvial fan through braided fluvial into braidplain environments.

A general reconstruction of the Neverskrukk basin is presented in Fig. 6.41. It is based on detailed mapping of the basal formation of the Pechenga Greenstone Belt (Sturt et al. 1994), logs of numerous drillholes in the Mt. General'skaya area (Fig. 6.36), and the section documented in the Kola Superdeep Drillhole (Kozlovsky 1984).

There are several features of the Neverskrukk Formation that deserve special attention and further research. The formation was deposited after 2505 Ma (the age of the underlying gabbro-norite) but prior to the onset of the Lomagundi-Jatuli carbon isotopic event (recorded in the overlying Kuetsjärvi Sedimentary Formation, Fig. 6.33). These constraints place deposition during the Huronian-time glaciation. The majority of the Neverskurukk Formation was deposited subaerially and contains no direct evidence of glacial sedimentation. However, lonestones in fine-grained sediments and the likelihood that some of the massive conglomerate-sandstone units (Fig. 6.39d, e, h) are diamictites should spur additional future research to assess a glacigenic influence on sedimentation.

Although deposition was largely within subaerial environments, some beds contain abundant disseminated and "nodular" pyrite (Fig. 6.39v). Pyritised sandstone beds are also known from surface outcrops at Brattli (Fig. 6.32) and the sandstone-filled joints in the Archaean basement contain finely disseminated pyrite as well. Some of the pebbles in the lower part of the fluviatile deposits at Brattli are composed of magnetite-pyrite ores and pyrite-rich skarns. These have been considered as the evidence of oxygen-low weathering conditions (Sturt et al. 1994) and the mud chips in core samples suggest *in situ* pyritisation (Fig. 6.39s, t). Sulphur isotopic compositions of different modes of pyrite from various rock types show somewhat similar values. A sizeable fractionation, and rather low values, indicates involvement of bacterial sulphate reduction (Fig. 6.42). However, the alluvial and thus freshwater, depositional environment would suggest a low sulphate concentration. Thus, the overall significance of such sulphides and their origin require further research.

There are a few beds of calcite-cemented conglomerates in the drilled succession (Figs. 6.39ac, ae and 6.43a). Similar conglomerates have been documented in surface outcrops at Brattli (Fig. 6.43b, c). The calcite cement fills the entire space between rounded pebbles, and thus the cementation was apparently an early phenomenon that occurred prior to burial. The calcite is depleted in ^{13}C ($\delta^{13}C = -4$ ‰, Melezhik and Fallick 1996). The nature of this calcite cement remains to be studied. It might have been precipitated from ground waters or washed in by surface waters as fine calcite particles. Resolving this may reveal the chemistry of ground or surface waters during the time of the Huronian glaciation.

Fig. 6.34 Polymict clast-supported conglomerate from the Neverskrukk Formarion in the Pasvik Greenstone Belt at Brattli. Poorly sorted and variably rounded cobbles and pebbles consist of gneiss, plagiogranite, amphibolite and vein quartz. Bar scale is 10 cm (Photograph by Victor Melezhik)

Fig. 6.35 Jointed and fragmented Archaean pegmatite (*white*) at the base of the Neverskrukk Formation in the Pasvik Greenstone Belt at Brattli, NE Norway. Joints are filled with pale brown sandstone. Such features can be assigned to either a fractured rift shoulder or ice-shattered basement rocks associated with Huronian glacial conditions. Sturt et al. (1994) interpreted the fracture infill as windblown sand. Photo width is 60 cm (Photograph by Victor Melezhik)

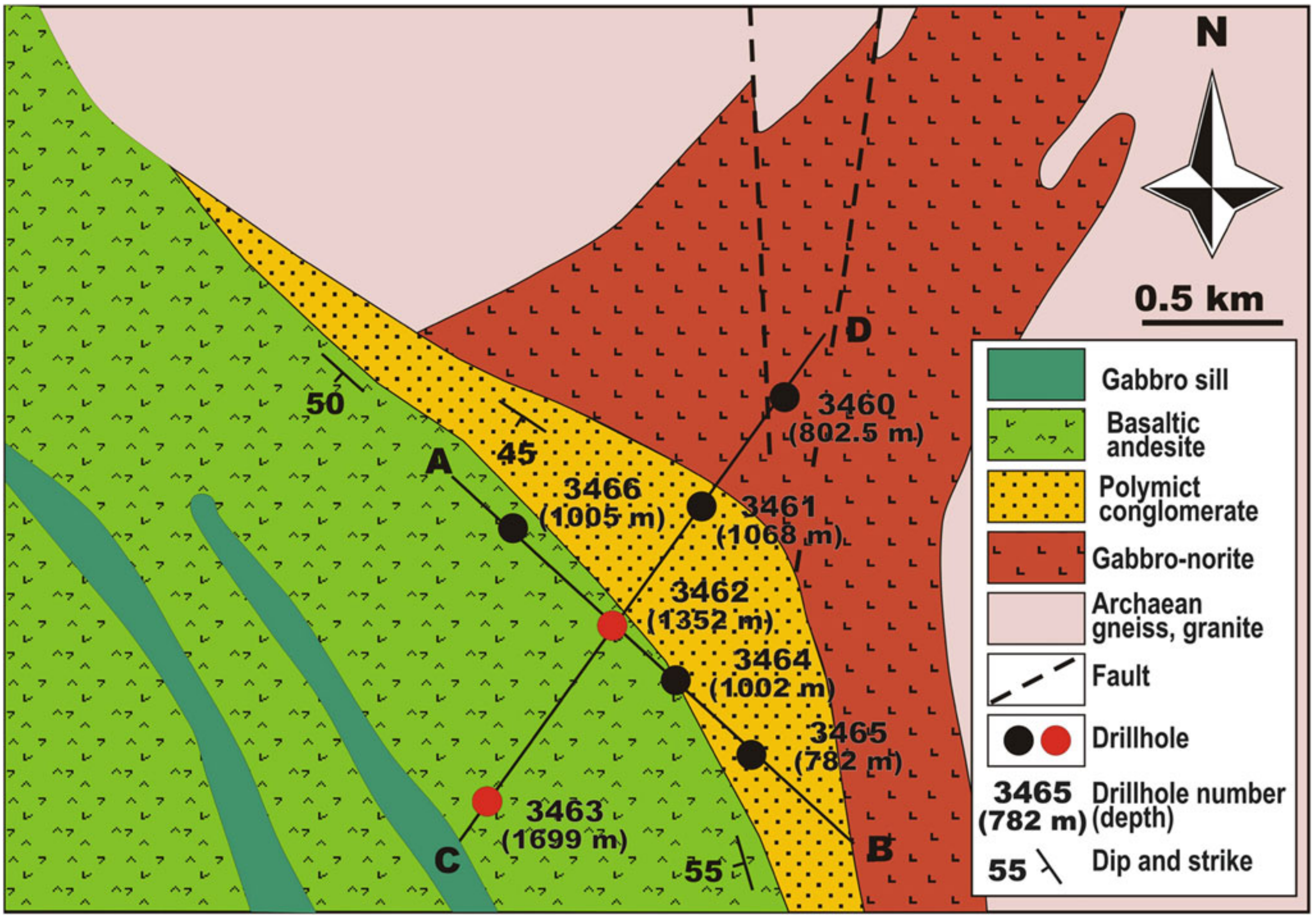

Fig. 6.36 A geological map showing basal Neverskrukk Formation conglomerates of the Pechenga Greenstone belt in the Mt. General'skaya area. The conglomerates rest unconformably on the 2505 Ga Mt. General'skaya layered gabbro-norite intrusion and are conformably overlain by Ahmalahti Formation basaltic andesites. Position of the studied drillholes shown by *red circles*. The Geological Survey of Norway database

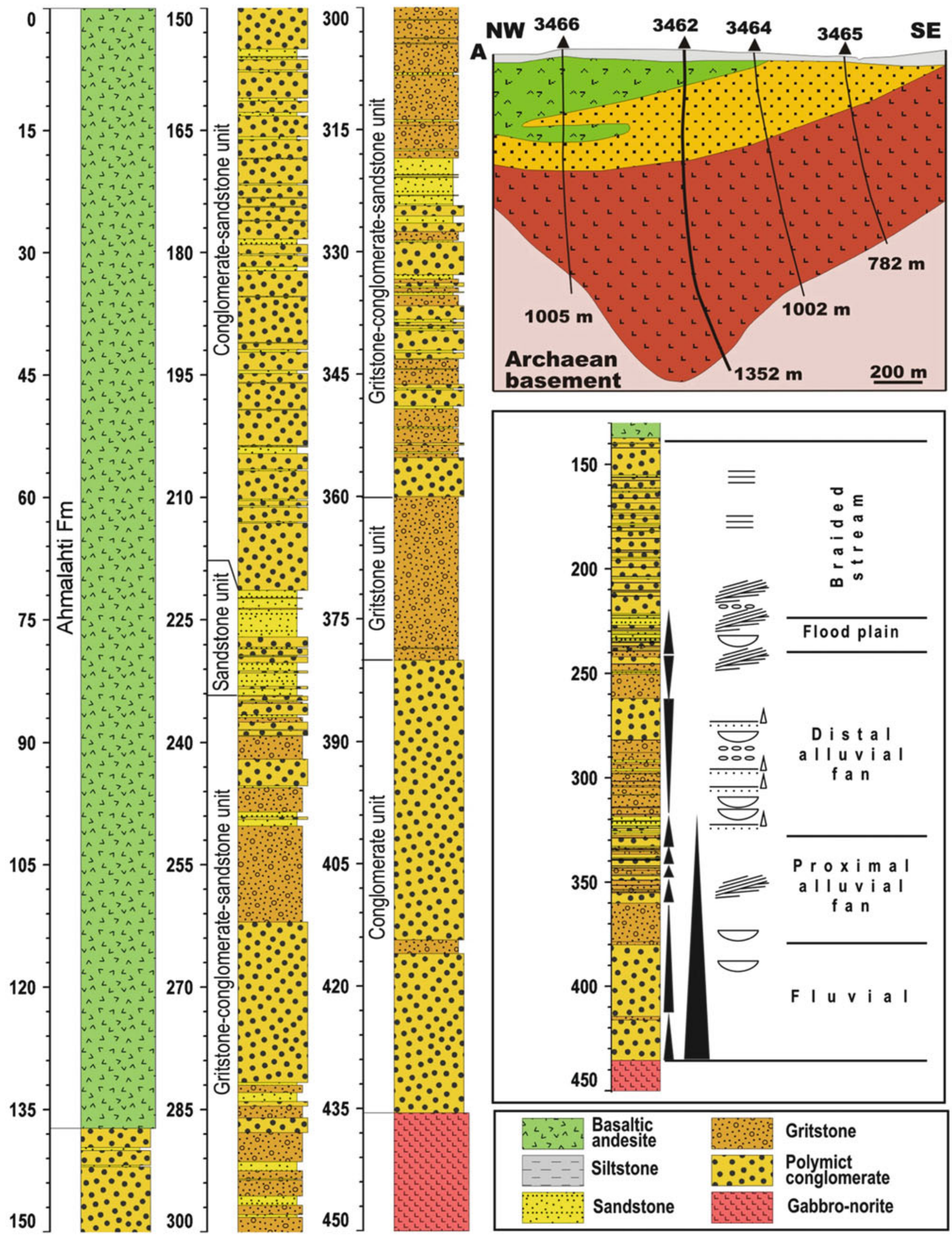

Fig. 6.37 Lithological section of the Neverskrukk Formation based on core log of drillhole 3462. V. Melezhik, unpublished data. Lithological symbols are explained in Fig. 6.6. Computer-generated log by Aivo Lepland

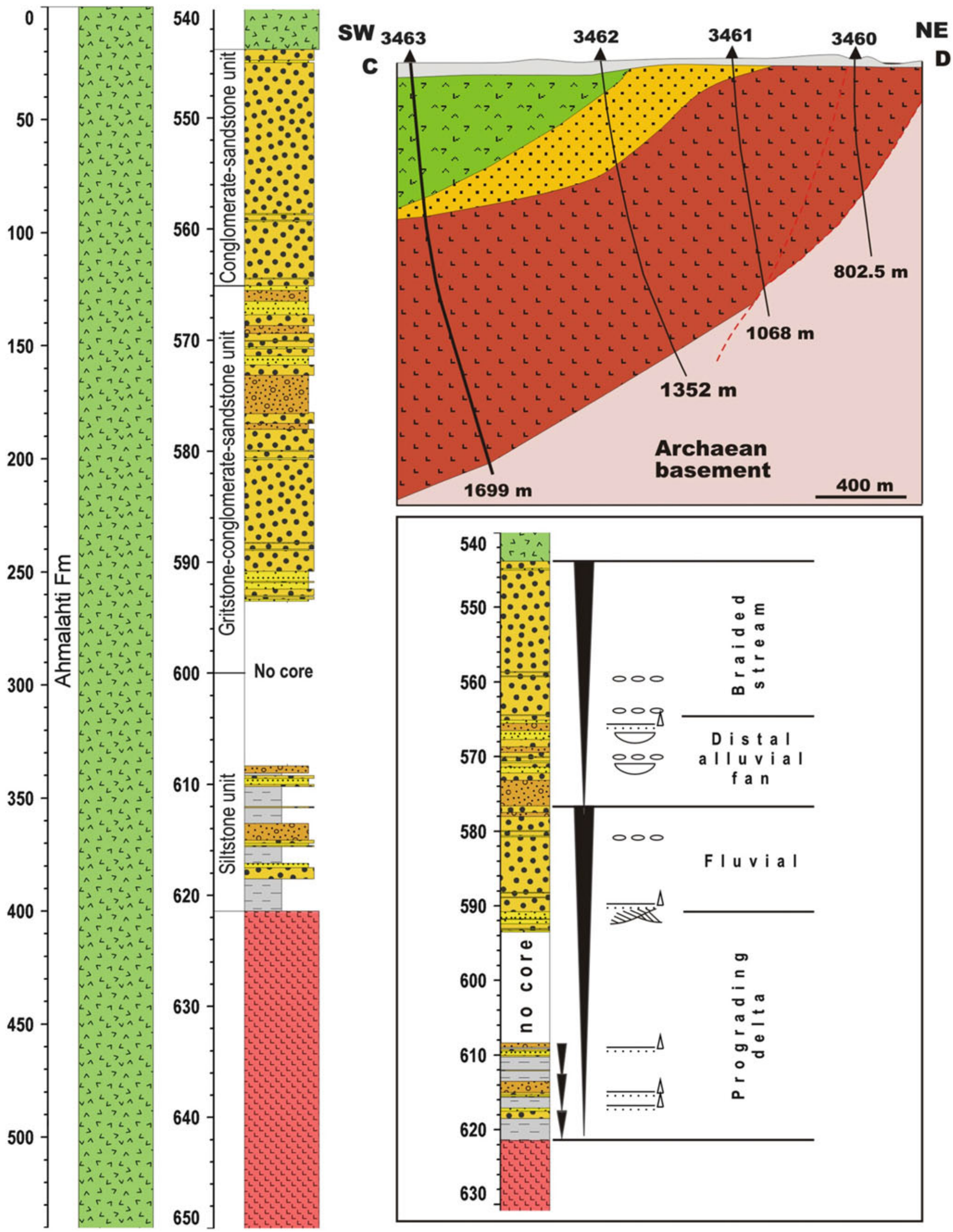

Fig. 6.38 Lithological section of the Neverskrukk Formation based on core log of drillhole 3463. V. Melezhik, unpublished data. Lithological symbols are explained in Fig. 6.6. Computer-generated log by Aivo Lepland

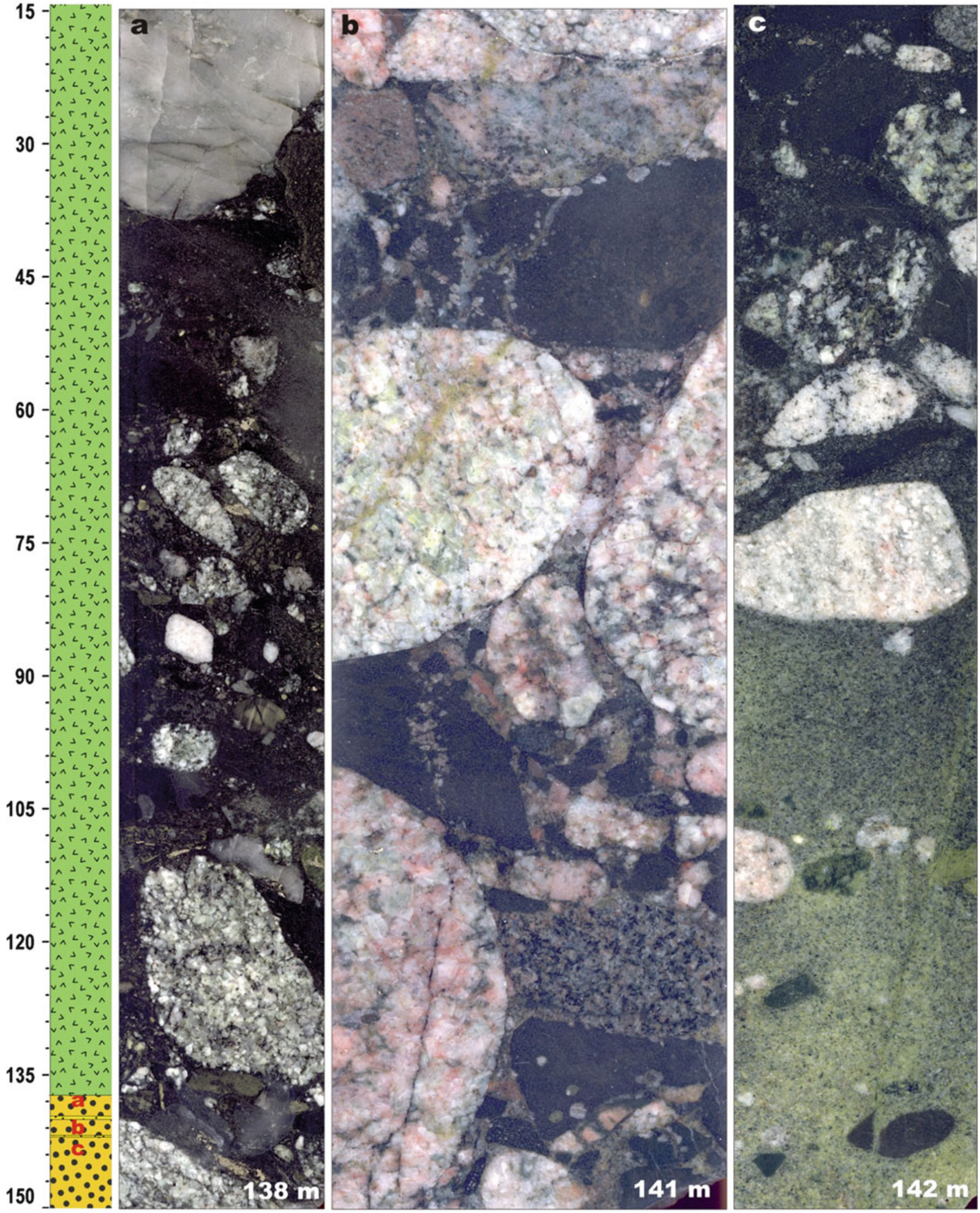

Fig. 6.39 Sedimentological features of main rock types of the Neverskrukk Formation in drillhole 3462. Core diameter in all figures is 42 mm. (Photographs by Victor Melezhik). (**a**) Polymict, greywacke matrix-supported conglomerate with plagiogranite pebbles of variable size; smaller clasts are vein quartz (*white*) and biotite schist (*dark green*). (**b**) Polymict, fragment-supported conglomerate with unsorted, rounded pebbles of microcline; smaller and variably rounded clasts are amphibolite (*black*). (**c**) Greywacke sandstone with scattered fragments of granite and amphibolite (*black*) overlain by polymict conglomerate; green colour caused by epidotisation

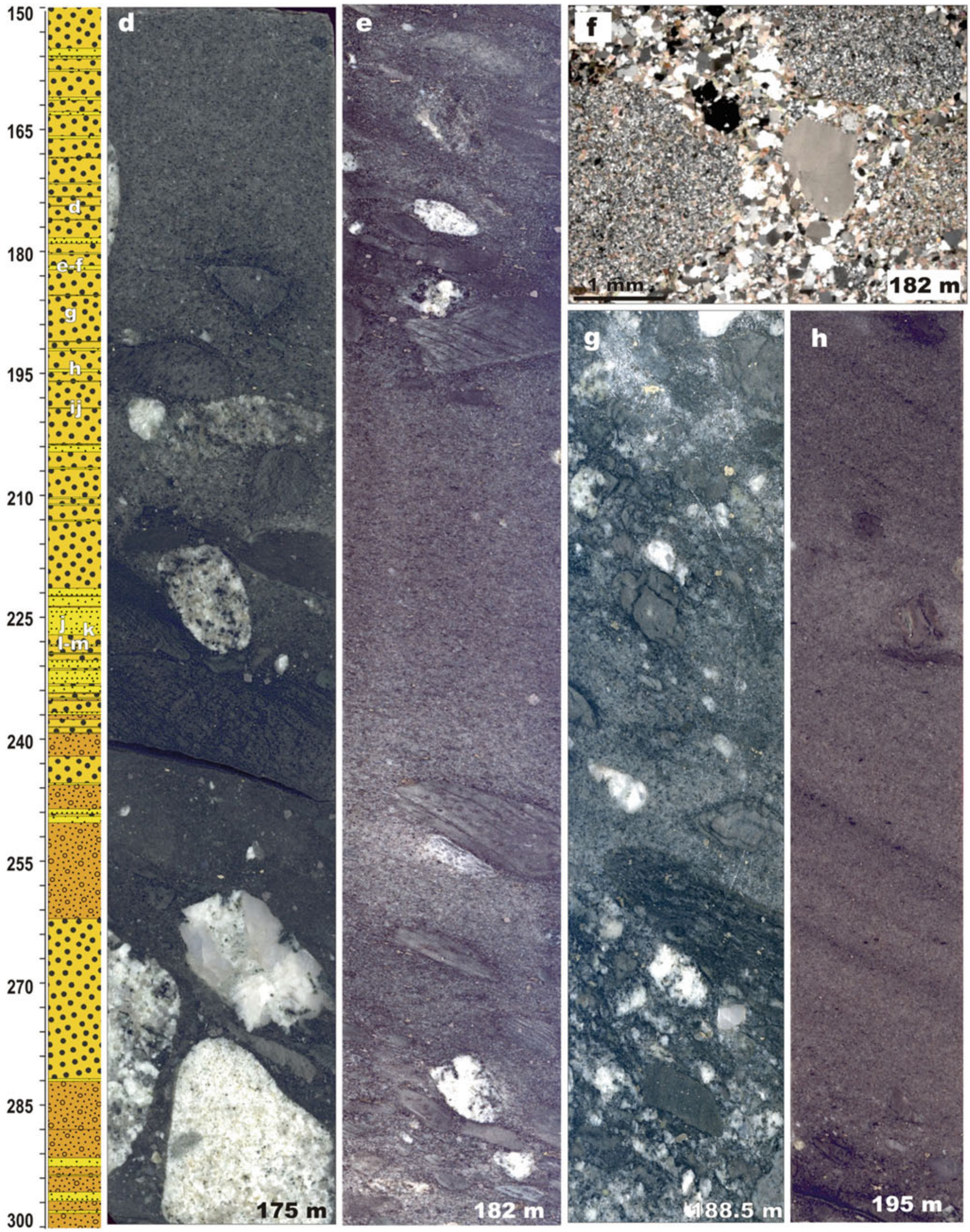

Fig. 6.39 (continued) (**d**) Matrix-supported conglomerate overlain by dark grey massive greywacke with scattered unsorted fragments of diorite and biotite schist. (**e**) Massive greywacke sandwiched between fragment-supported, fine-pebble polymict conglomerate. (**f**) Microstructure of the greywacke shown in "**e**"; rounded clasts of fine-grained sandstones and quartz (in the *middle*) in a fine-grained quartz-plagioclase sand matrix. (**g**) Fragment-supported, fine-pebble polymict conglomerate with pocket of sandstone (in the *middle*) with scattered pebbles. (**h**) Bedded greywacke with lonestone. (**f**) Microstructure of the greywacke shown in "**e**"; rounded clasts of fine-grained sandstone and quartz (in the *middle*) in a fine-grained quartz-plagioclase sand matrix. (**g**) Fragment-supported, fine-pebble polymict conglomerate with pocket of sandstone (in the *middle*) with scattered pebbles. (**h**) Bedded greywacke with lonestone

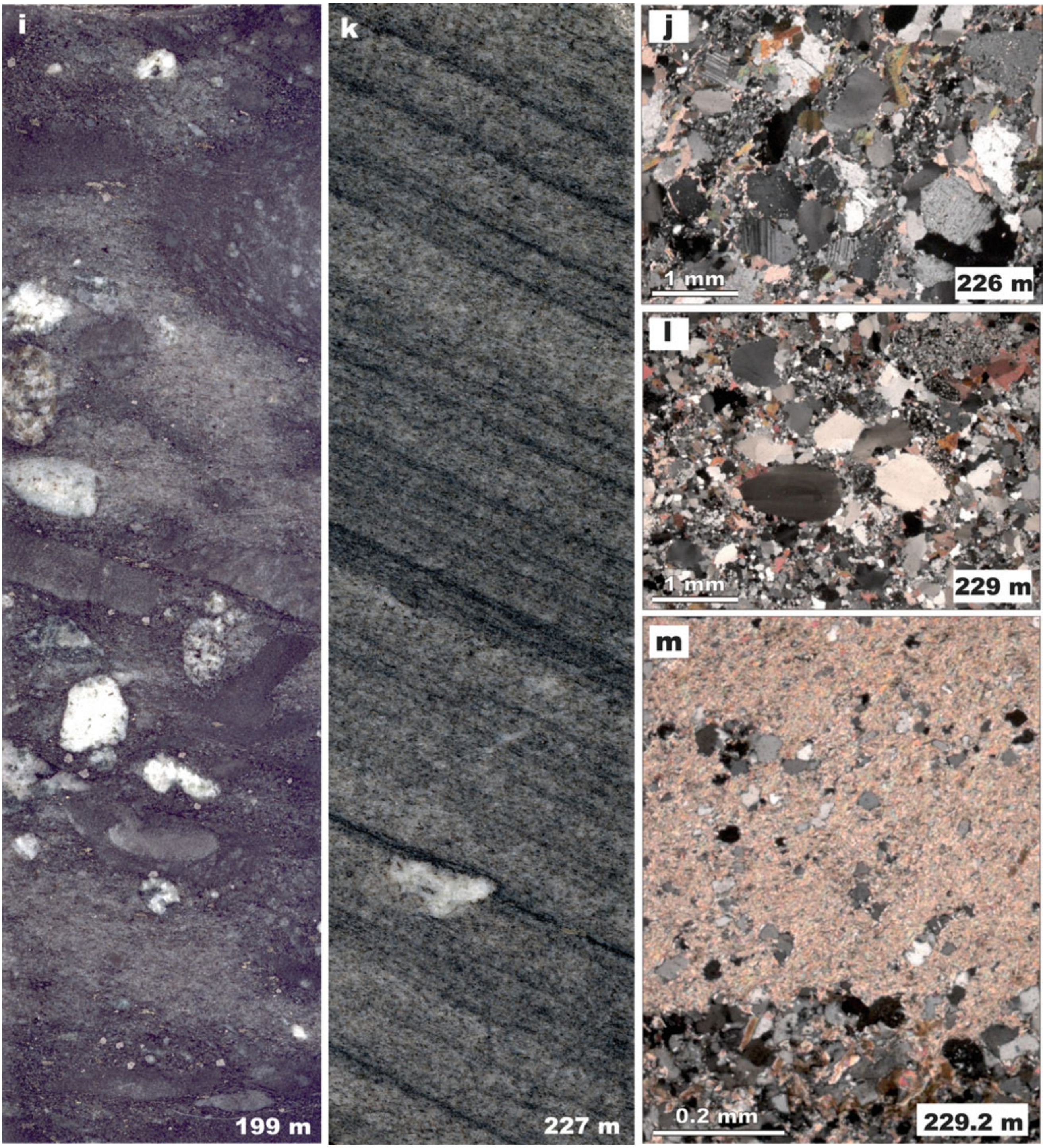

Fig. 6.39 (continued) (**i**) Massive greywacke with scattered clasts of diorite, mica schist and vein quartz. (**j**) Rounded clasts of quartz and plagioclase in a fine-grained quartz-plagioclase-sericite matrix. (**k**) Parallel-laminated greywacke with lonestone. (**l**) Photomicrograph in transmitted polarised light showing rounded quartz clasts supported by quartz-plagioclase-sericite matrix. (**m**) Photomicrograph in transmitted polarised light showing quartz-plagioclase siltstone overlain by sericite-rich layer with scattered grains of quartz and plagioclase. Photomicrographs (**f**, **j**, **l**, and **m**) in transmitted polarised light

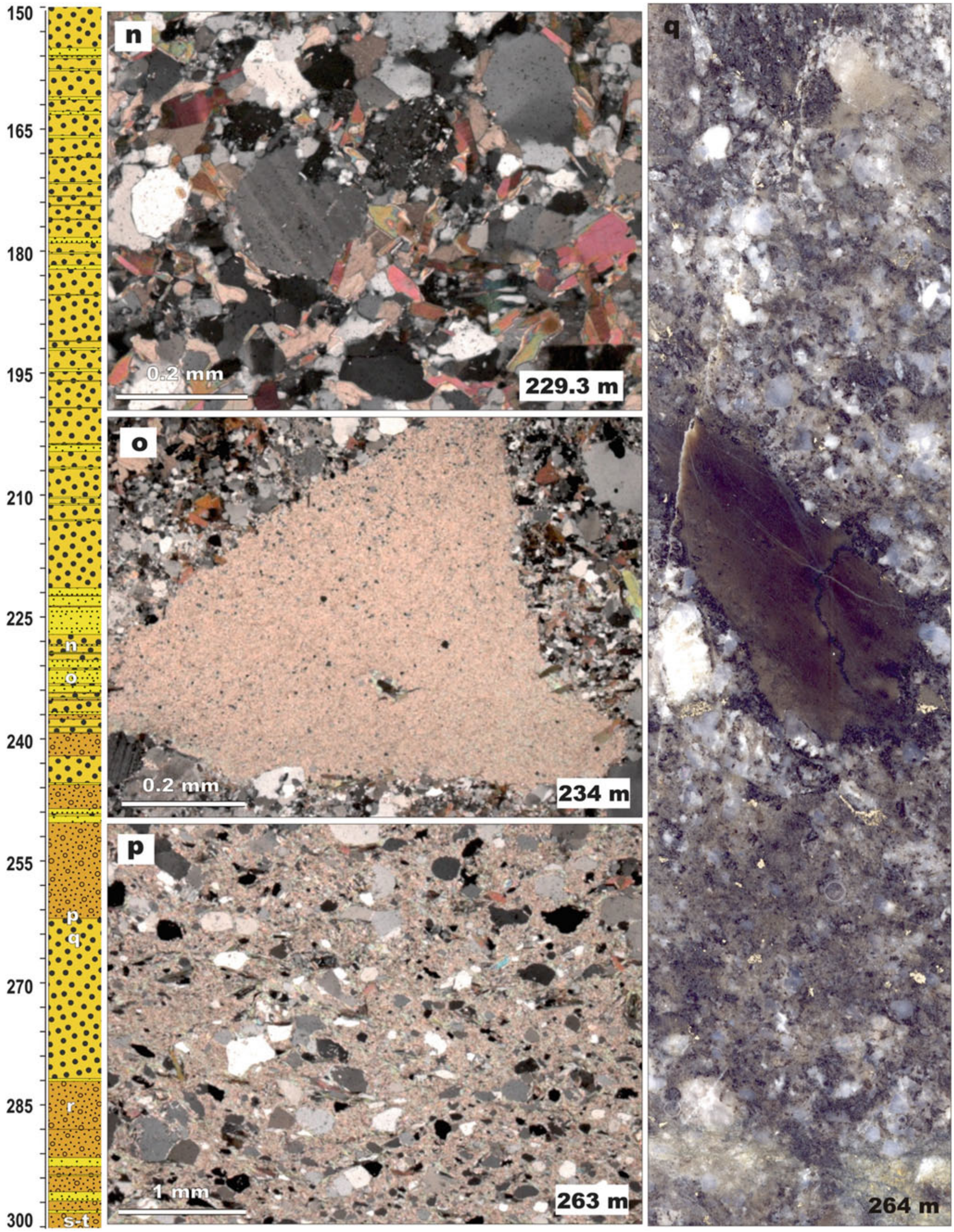

Fig. 6.39 (continued) (**n**) Sandstone consisting of rounded grains of quartz and plagioclase in quartz-plagioclase-sericite-calcite matrix. (**o**) Angular fragment of fine-flaky sericite aggregate (former clay fragment) in siltstone. (**p**) Angular siltstone-size clasts of quartz with minor plagioclase supported by sericite-matrix. (**q**) Unsorted gritstone with a large clast (*dark brown*) of fine-flaky sericite aggregate (former clay fragment). Photomicrographs (**n–p**) in transmitted polarised light

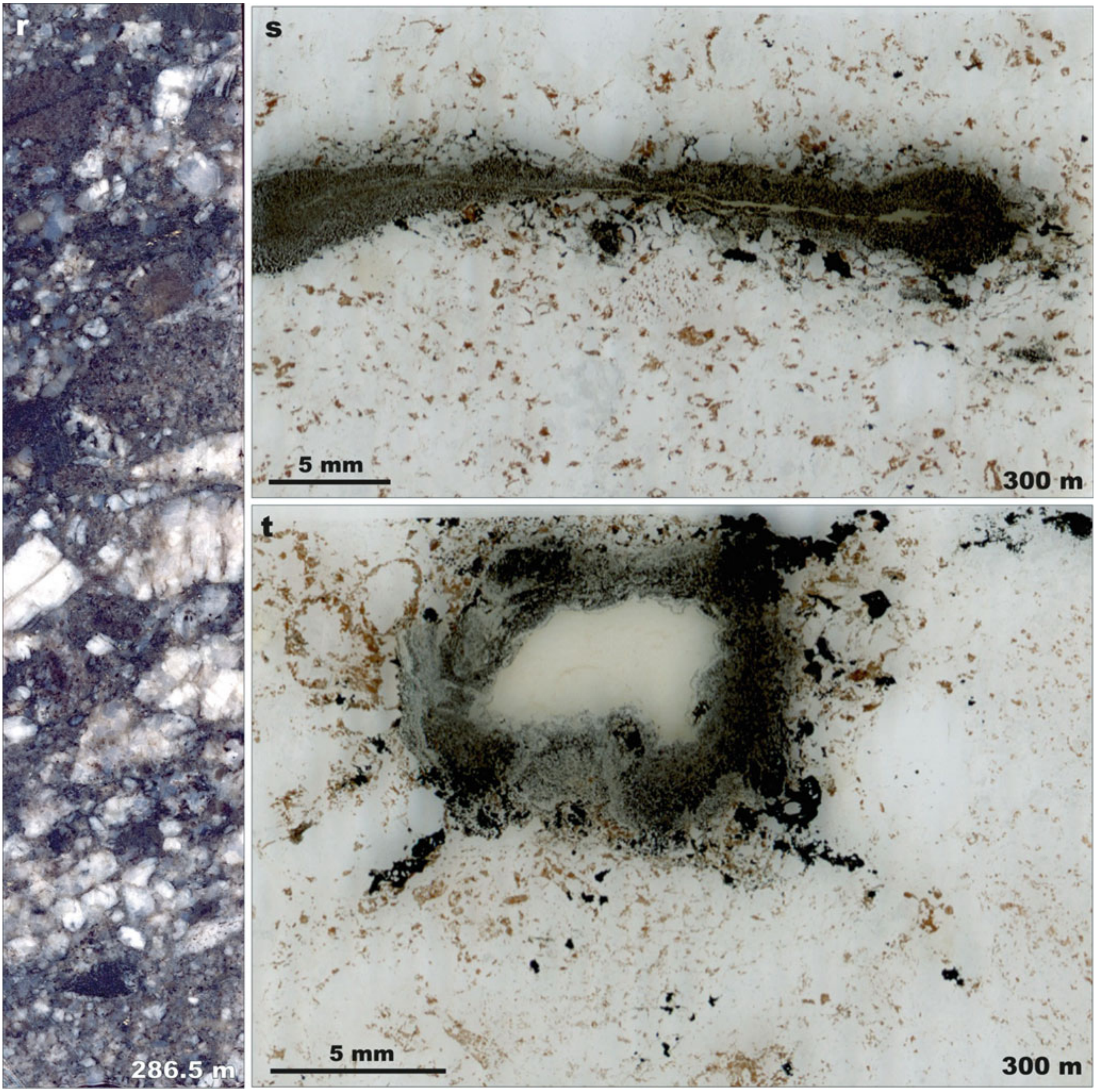

Fig. 6.39 (continued) (**r**) Angular, unsorted clasts of plagiogranite in unsorted gritstone matrix. (**s**) Flake of sericite (former clay) replaced by fine-grained pyrite (*black*) in the sandstone; note that the pyrite aggregate retains relict sericite in the middle (*pale grey*). (**t**) Flake of sericite (former clay) overgrown by fine-grained pyrite (black) in the sandstone. (**s**, and **t**) – scanned thin sections

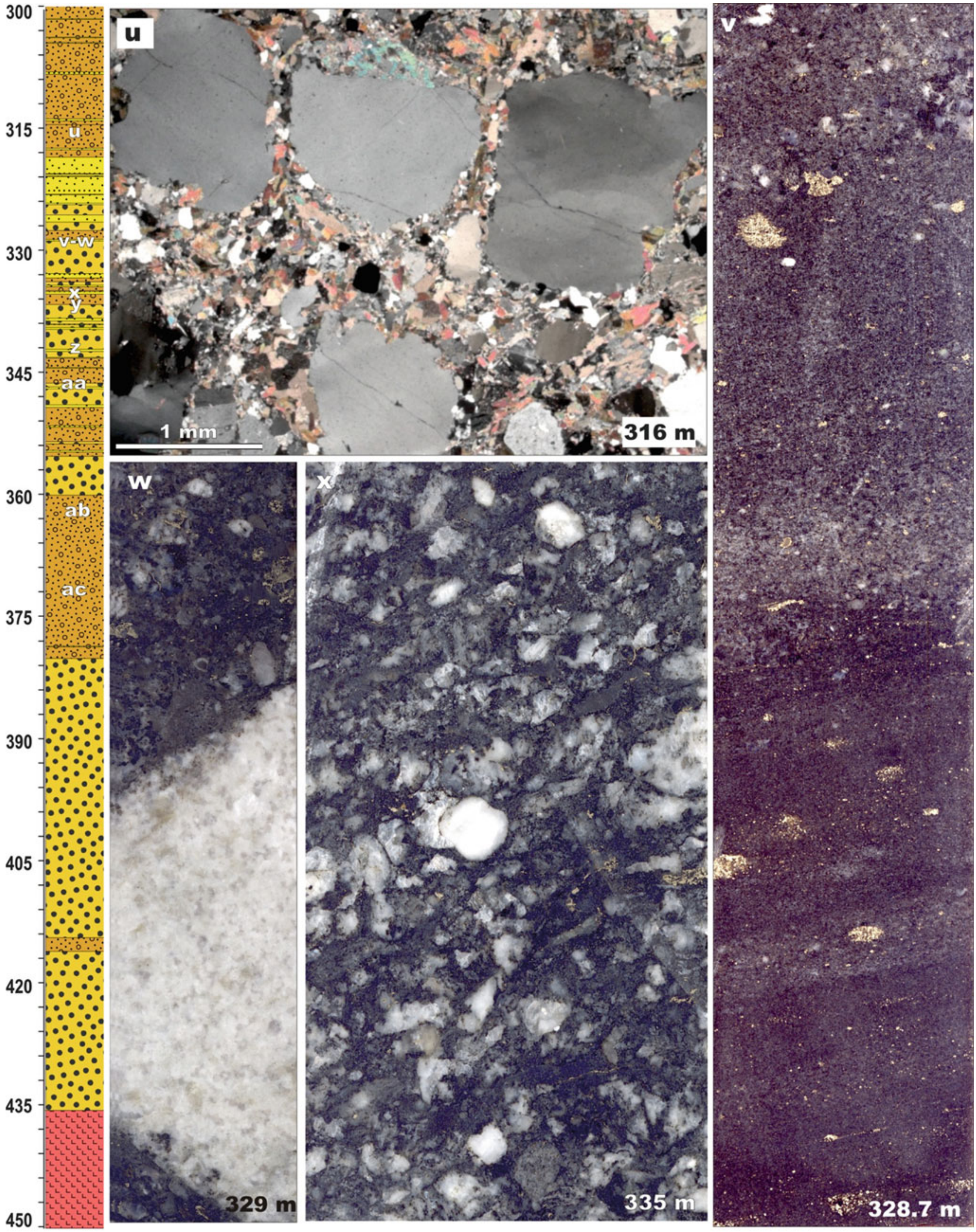

Fig. 6.39 (continued) (**u**) Sorted and rounded quartz clasts in fine-grained quartz-plagioclase-biotite-calcite matrix; photomicrograph in transmitted polarised light. (**v**) Graded sandstone with pyrite nodules (*pale yellow*). (**w**) Gritstone with oversized rounded clast of plagiogranite (*white*). (**x**) Gritstone composed of angular clasts of plagiogranite

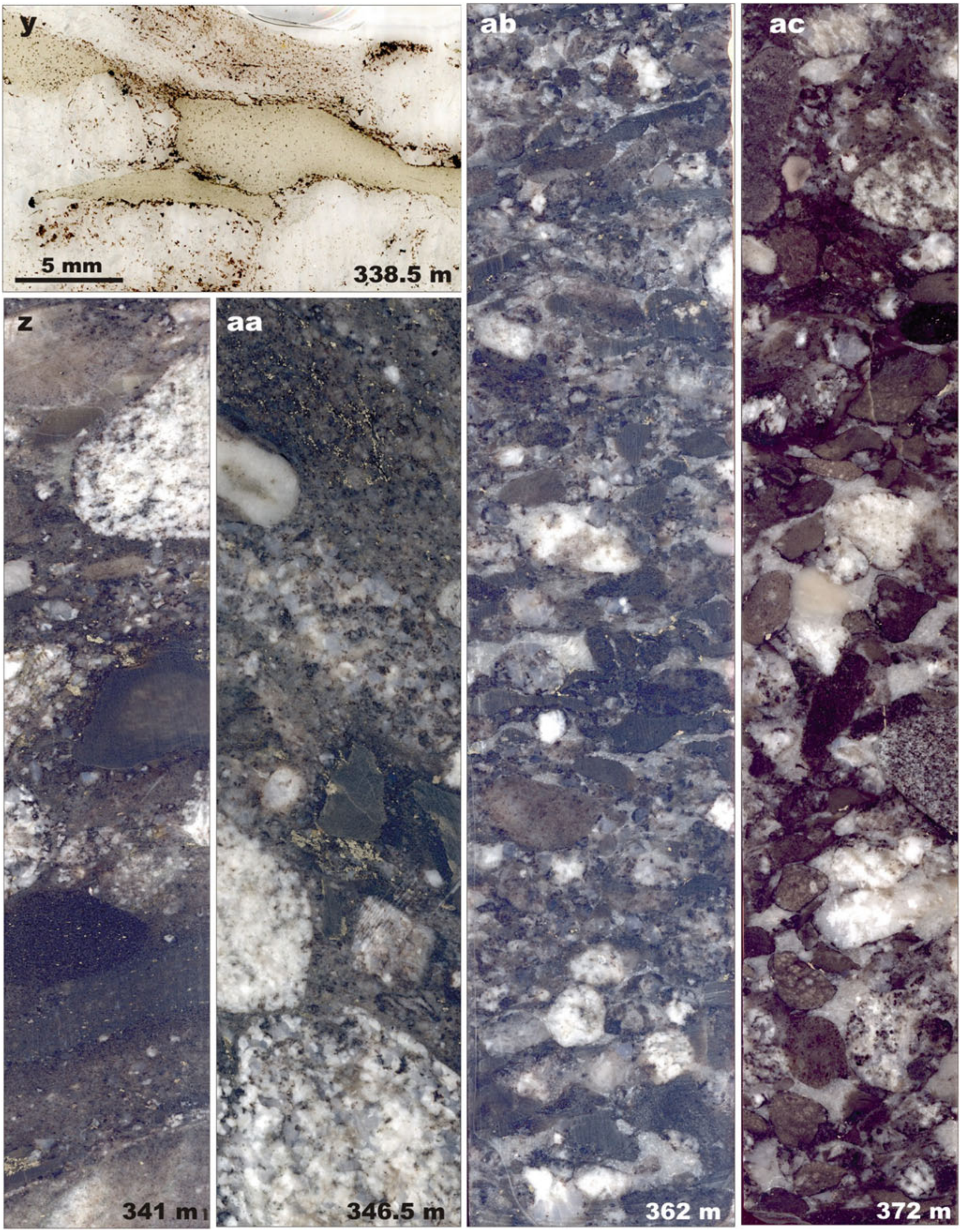

Fig. 6.39 (continued) (**y**) Gritstone consisting of clasts of plagiogranite (*white*) and fragments of fine-flaky sericite aggregate (*pale brown*); scanned thin section. (**z**, **aa**) Fragment-supported polymict conglomerate. (**ab**) Fine-pebble, clast-supported, polymict conglomerate showing normal grading. (**ac**) Fine-pebble, polymict, calcite-cemented (*middle* and *lower* parts) conglomerate

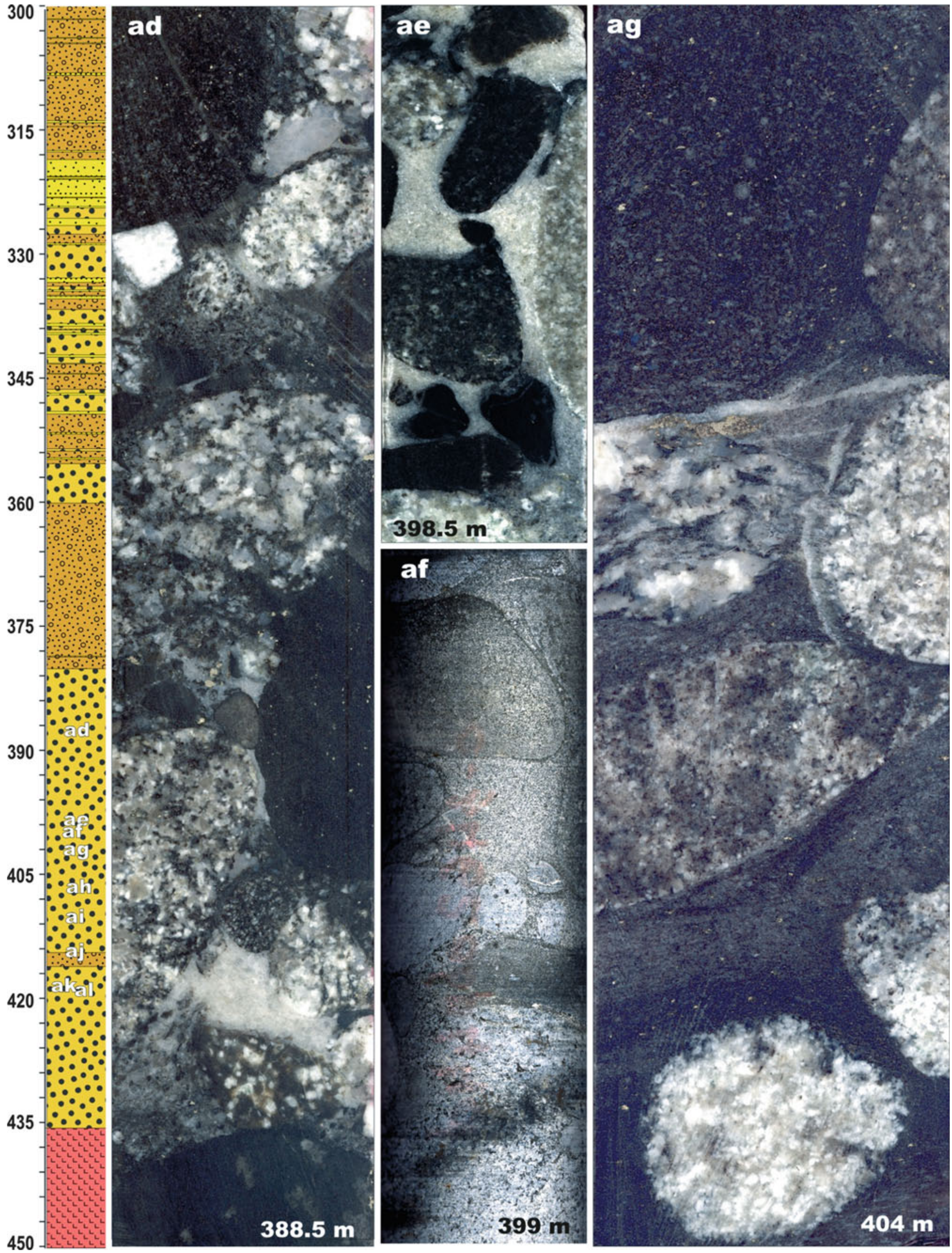

Fig. 6.39 (continued) (**ad**) *Rounded*, unsorted pebbles of diorite, amphibolite (*black*) and vein-quartz comprising fragment-supported conglomerate. (**ae**) Calcite (*white*) cementing amphibolite (*black*) and diorite pebbles. (**af–ag**) *Rounded*, unsorted pebbles of diorite, amphibolite (*black*) and fine-grained plagioclase-biotite schist in greywacke matrix

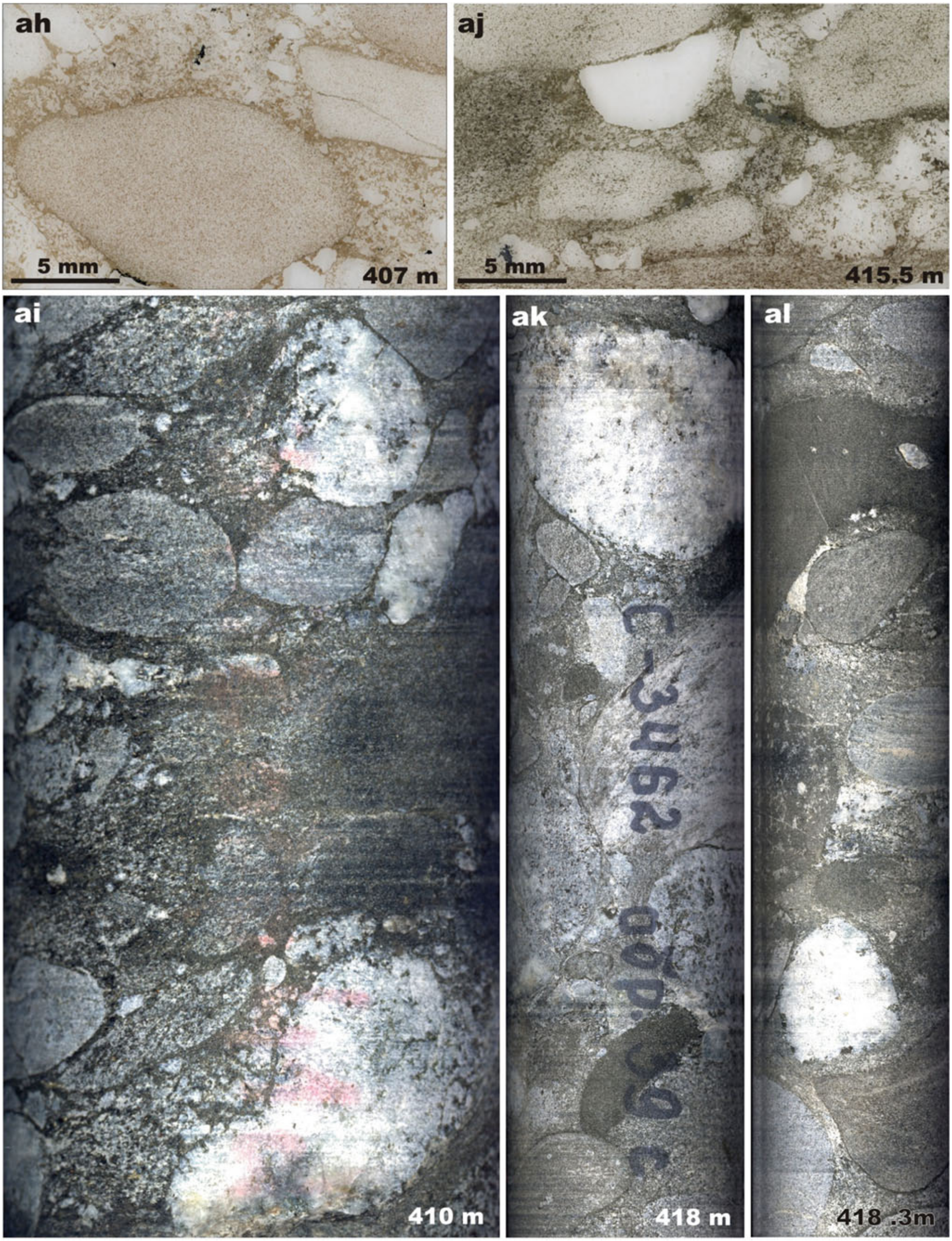

Fig. 6.39 (continued) (**ah**) Scanned thin section showing rounded and angular clasts in greywacke matrix of a polymict conglomerate. (**ai**) Polymict conglomerate comprised of well-rounded pebbles in gabbroic-sand matrix. (**aj**) Scanned thin section showing gabbroic-sand matrix supporting clasts of plagioclase-biotite schists and broken quartz pebble (*white*). (**ak–al**) Polymict conglomerate comprised of well-rounded, unsorted pebbles of amphibolites (*black*), plagioclase-biotite schist (*grey*) and granites (*white*) emplaced in gabbroic-sand matrix

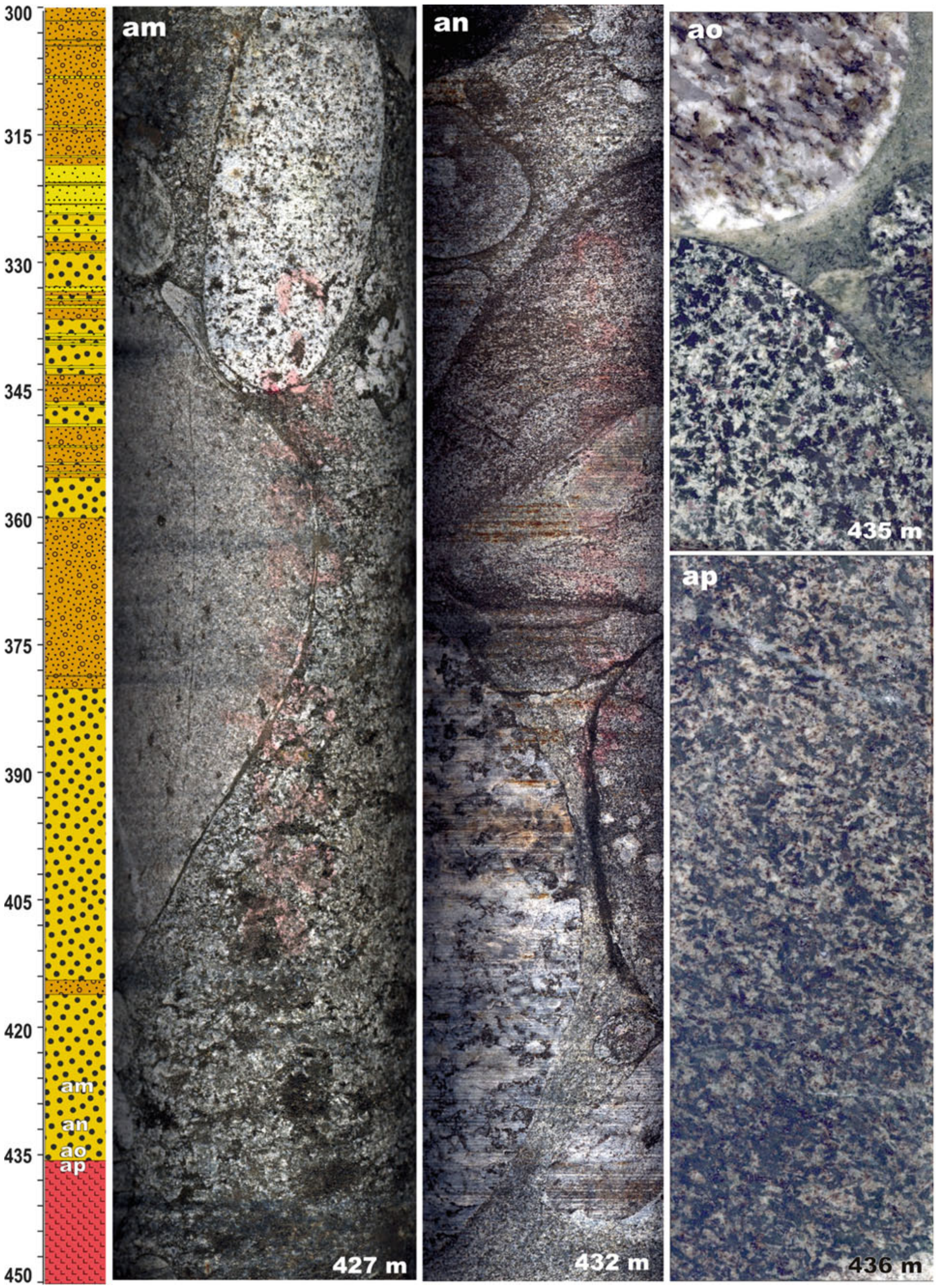

Fig. 6.39 (continued) (**am**) Well-rounded sandstone (*grey*) and granite (*white*) pebbles in gabbroic-sand matrix. (**an**) Polymict conglomerate comprised of well-rounded pebbles in a greywacke matrix. (**ao**) One plagiogranite and two gabbro-norite pebbles in gabbroic sand matrix. (**ap**) Gabbro-norite of the Mt. General'skaya intrusion

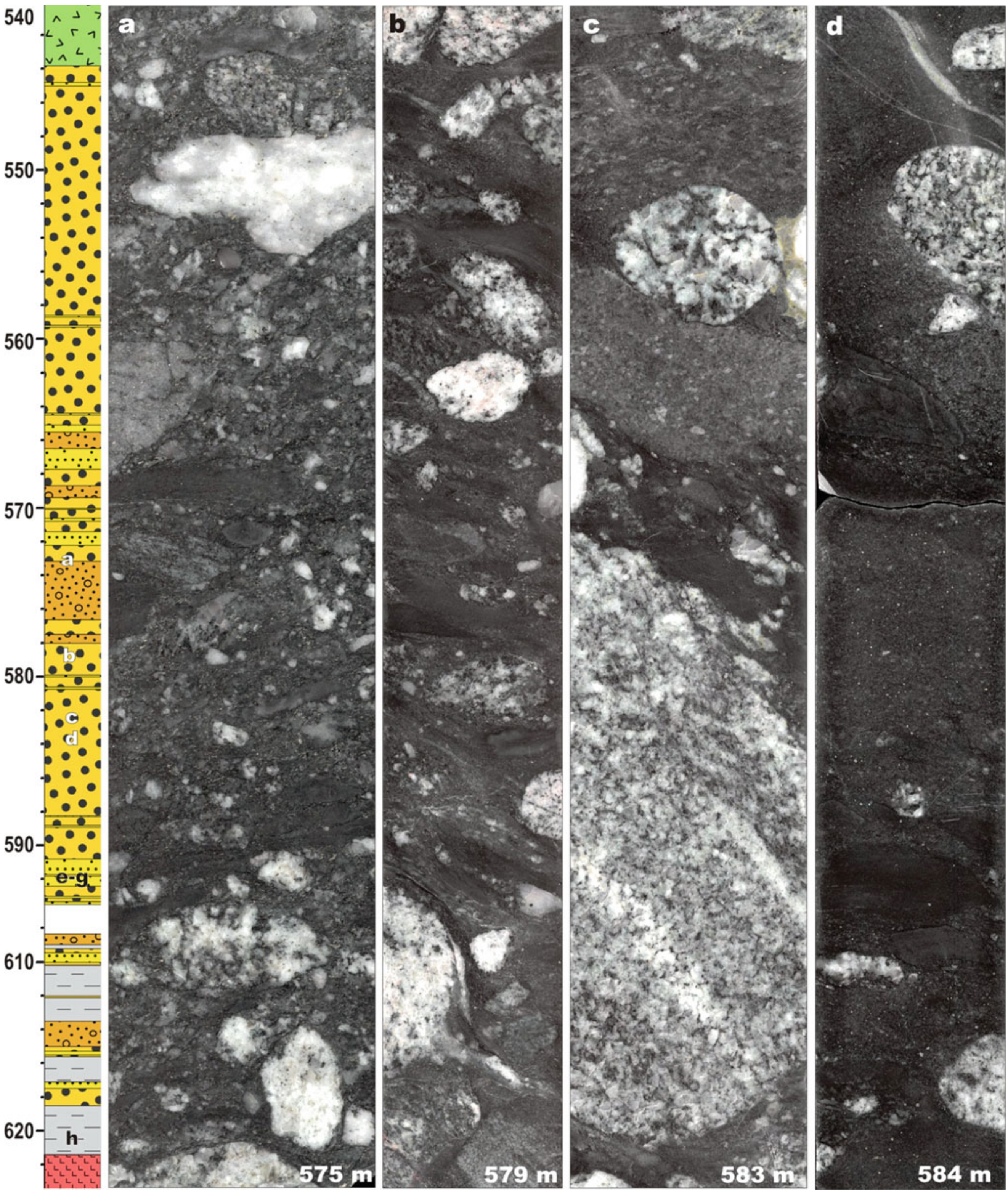

Fig. 6.40 Sedimentological features of the main rock types of the Neverskrukk Formation in drillhole 3463. (**a–d**) Polymict conglomerates composed of unsorted rock pebbles in a greywacke matrix; these types of conglomerates comprise most of the drilled section

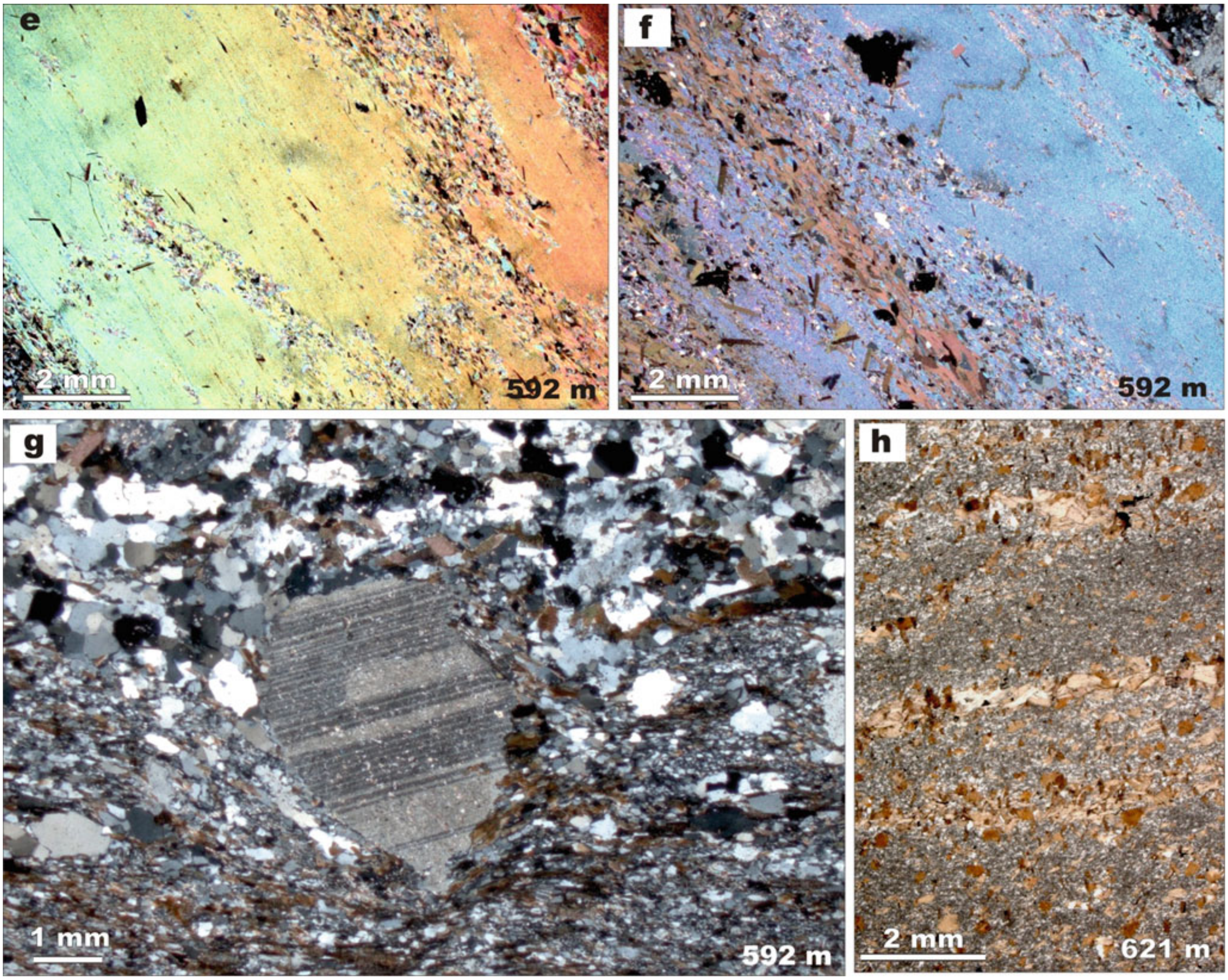

Fig. 6.40 (continued) (**e**) Sericite schist comprising thin layers in siltstone. (**f**) Interbedded siltstone and sericite schist. (**g**) Outsized clast piercing sandstone-siltstone layering. (**h**) Laminated siltstone-mudstone couplets comprising the base of the Neverskrukk Formation. Photomicrographs (**e–h**) in transmitted polarised light (Photograph by Victor Melezhik)

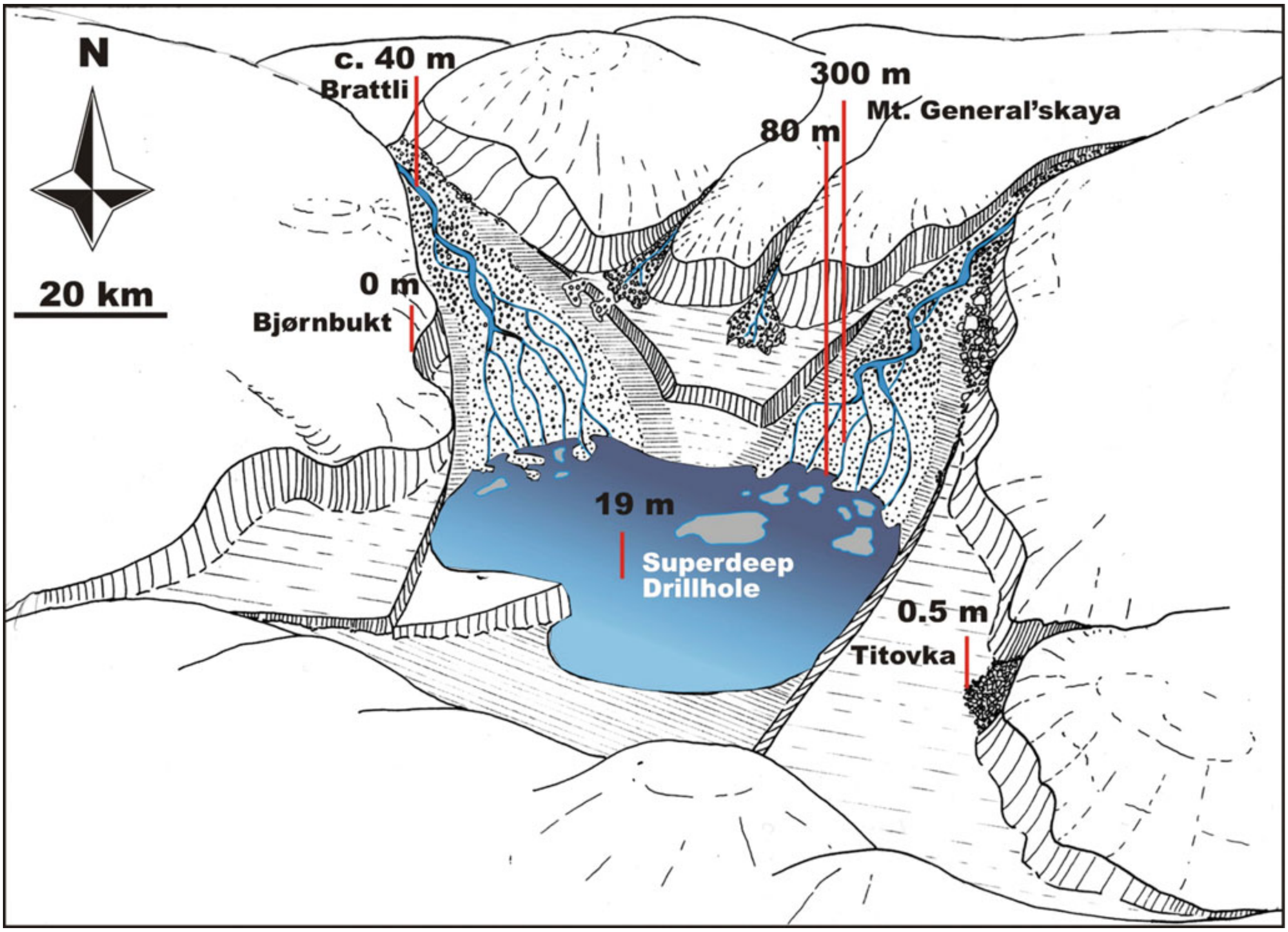

Fig. 6.41 A reconstruction of the Neverskrukk basin based on detailed mapping (Sturt et al. 1994) and drillhole logs. *Red lines* indicate positions of the logged sections, formational thicknesses and geographic names. Mt. General'skaya area includes drilholes 3462 and 3463 (V. Melezhik, unpublished data) (Data from the Kola Superdeep Drillhole are from Koslovsky (1994))

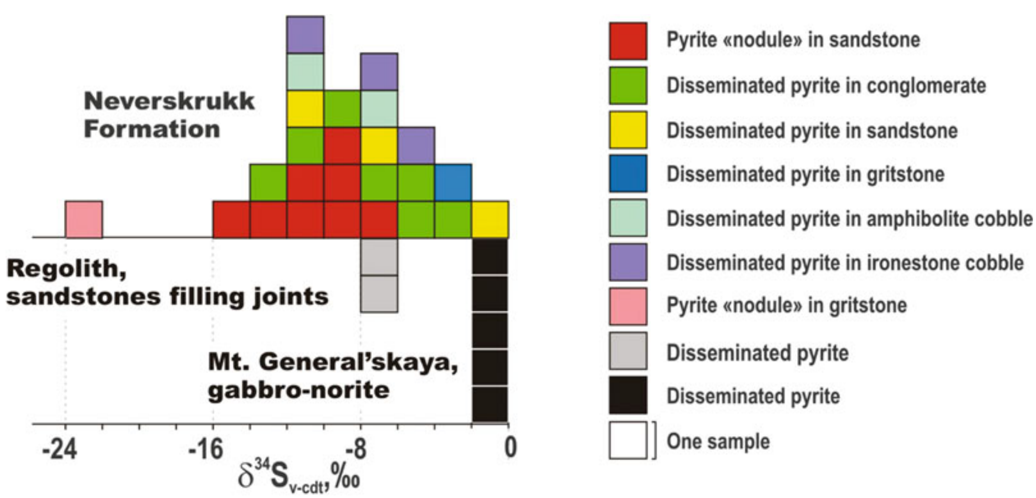

Fig. 6.42 Sulphur isotope composition of pyrite occurring in different rocks of the Neverskrukk Formation, the 2505 Ma gabbro-norite intrusion, and the regolith at the base of the Neverskrukk conglomerate. Note that the sulphur isotope composition of pyrite from regolith and sandstone filling joints represents an average for the majority of the Neverskrukk data. V. Melezhik and A. Fallick (unpublished data)

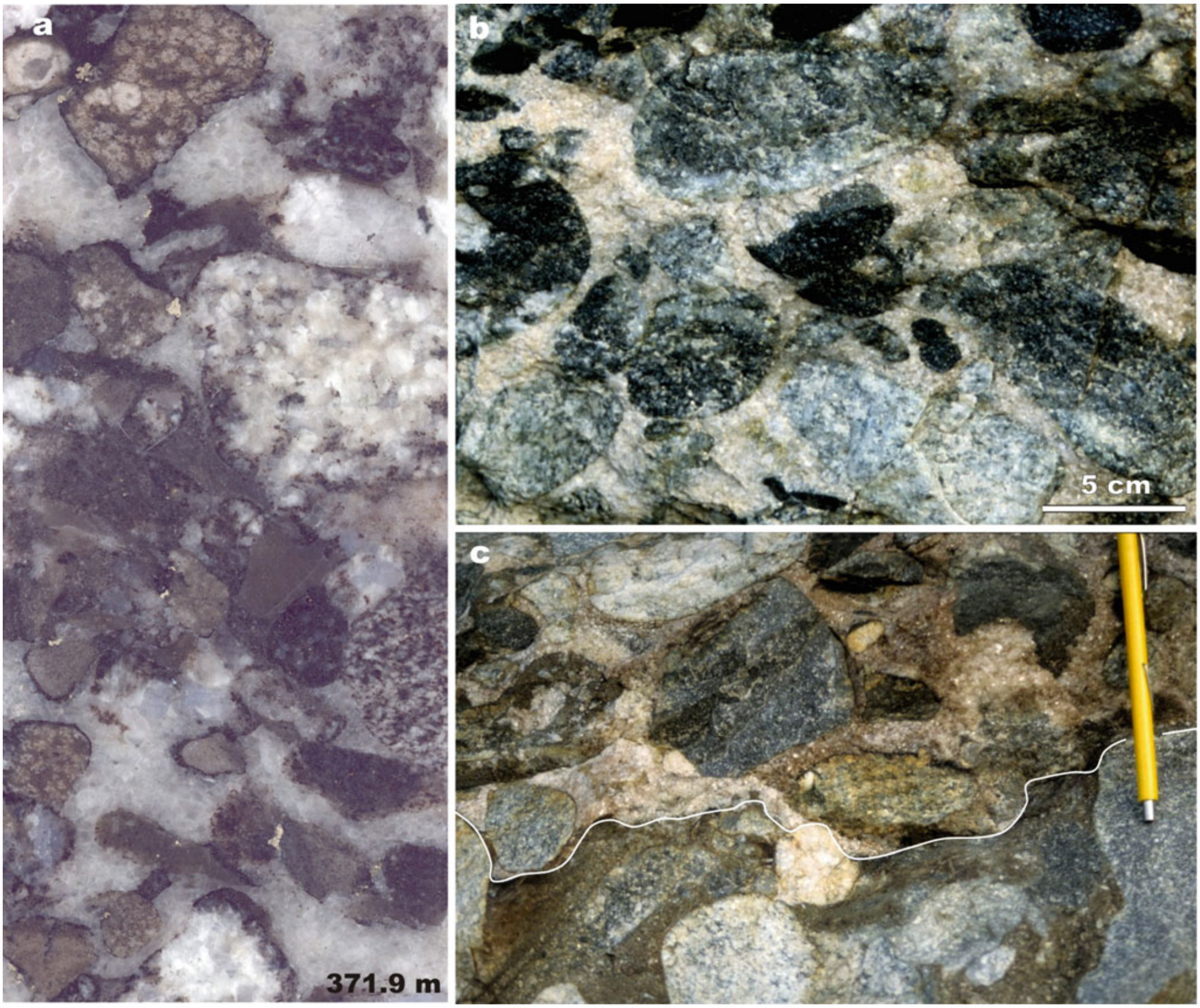

Fig. 6.43 Calcite-cemented polymict conglomerates. (**a**) Unsorted and *rounded* pebbles of different rocks cemented by sparry calcite in the core obtained from drillhole 3462. (b) Sparry calcite cement supporting pebbles of diorite and amphibolite as seen in surface outcrops at Brattli. (**c**) Greywacke matrix polymict conglomerate passing upward with a sharp boundary (enhanced by *white line*) into calcite-cemented conglomerate

References

Amelin YuV, Heaman LM, Semenov VS (1995) U-Pb geochronology of layered mafic intrusions in the eastern Baltic Shield: implications for the timing and duration of Palaeoproterozoic continental rifting. Precambrian Res 75:31–46

Kozlovsky YeA (ed) (1984) The superdeep well of the Kola Peninsula, Springer-Verlag, Berlin, 558 p

Melezhik VA, Fallick AE (1996) A widespread positive $\delta^{13}C_{carb}$ anomaly at around 2.33–2.06 Ga on the Fennoscandian Shield: a paradox? Terra Nova 8:141–157

Sturt BA, Melezhik VA, Ramsay DM (1994) Early Proterozoic regolith at Pasvik, NE Norway: palaeotectonical implications for the Baltic Shield. Terra Nova 6: 618–633

6.2.2 Kuetsjärvi Sedimentary Formation: FAR-DEEP Hole 5A, Neighbouring Quarry and Related Outcrops

Paula E. Salminen, Victor A. Melezhik, Eero J. Hanski, Aivo Lepland, Alexander E. Romashkin, Dmitry V. Rychanchik, Zhen-Yu Luo, Evgenii V. Sharkov, and Maria M. Bogina

Scientific Targets

- Tectonic and depositional settings associated with the Lomagundi-Jatuli isotopic event
- Geochemical rock record during the global perturbation of the carbon cycle
- Carbon, sulphur and strontium isotopic composition of ambient water
- Influence of depositional setting on carbon and strontium isotopic composition
- Geochemistry of travertine-precipitating hydrothermal water
- Provenance composition
- Microfossil record
- Radiometric age constraint on timing of deposition

Drillhole 5A intersected the Kuetsjärvi Sedimentary Formation (Figs. 6.44 and 6.45) in the eastern part of the Pechenga Greenstone Belt, Kola Peninsula, NW Russia (Figs. 6.1 and 6.32). The deposition of the Kuetsjärvi Sedimentary Formation occurred between 2505.1 ± 1.6 Ma and 2058 ± 2 Ma (Amelin et al. 1995; Melezhik et al. 2007). The latter age was obtained from volcanic rocks immediately overlying the Kuetsjärvi Sedimentary Formation and thereby provides a minimum age for its deposition (Fig. 6.33). The formation contains ^{13}C-rich dolostones recording the global Palaeoproterozoic positive $\delta^{13}C$ excursion of sedimentary carbonates (e.g. Karhu 1993; Karhu and Holland 1996; Melezhik and Fallick 1996). Several FAR-DEEP drillholes provide material from successions accumulated in open (Chaps. 6.1.3 and 6.1.4), restricted and partially restricted (Chaps. 6.3.1 and 6.3.2) marine environments, whereas Hole 5A intersected a succession, which is presently considered to represent a marine-influenced lacustrine system (Melezhik and Fallick 2005). Apart from chemically precipitated lacustrine dolomicritic and resedimented carbonates (Fig. 6.46), the Kuetsjärvi succession contains abundant hot-water travertines (Melezhik and Fallick 2001) and occurrences of caliche (Melezhik et al. 2004) (Fig. 6.47). It also contains lacustrine carbonate rocks and siliciclastic, fluvial "red beds" (Fig. 6.48), the latter being the first terrestrial "red beds" in the Pechenga Belt succession and evidence for an oxidising atmosphere. Consequently, Core 5A has multiple implications. Among them are foremost the carbon and sulphur cycles in a Palaeoproterozoic alkaline lake, interaction between hydrothermal, sea and lake waters, and consequences for isotopic compositions of carbon, sulphur and strontium.

The 158-m-long Hole 5A intersected the entire Kuetsjärvi Sedimentary Formation (24–145 m), 13 m of the underlying basalts of the Ahmalahti Formation (volcanic Unit A), and 15 m of the basalts of the overlying Kuetsjärvi Volcanic Formation (volcanic Unit C). The third magmatic body (Unit B), ferropicritic in composition, occurs between 92 and 97 m (Fig. 6.44). Figures 6.49 and 6.50 illustrate the main geochemical characteristics of the igneous rocks, while Fig. 6.45 shows stratigraphic profiles of selected major and trace elements and magnetic susceptibility. Chemical composition of the analysed samples is presented in Appendices 10–12. The core photos provide a detailed documentation of major lithological and structural features of sedimentary and igneous rocks through the stratigraphy (Fig. 6.51).

The Ahmalahti Volcanic Formation (Unit A)

The Ahmalahti Volcanic Formation was intersected at a depth of 145–158 m. The volcanic rocks are grey-green and ophitic, and compositionally tholeiitic low-Ti andesites and basaltic andesites (Appendices 10–11); these typify the Ahmalahti Formation (e.g. Predovsky et al. 1974). The basal part of the section is aphanitic with sparse vesicles filled with epidote. A part of the unit (145–149 m) is intensively chloritised. At the top of the formation is a c. 1-m-thick zone of intensely chloritised and calcitised rocks with calcite lenses and layers (Fig. 6.51bt). Similar rocks elsewhere in the Pechenga Belt have been interpreted as a remnant of palaeoweathered surface (Melezhik and Fallick 2005).

The basaltic andesites have high LREE/HREE ratios (Fig. 6.50a) and relatively low contents of HFSE relative to LILE, as exemplified by $(Ce/Nb)_{PM}$ ratios of 3.9–4.3 indicating an effect of interaction of the magma with the Archaean basement (cf. Fig. 6.50b). The levels of K_2O (1.9–2.6 wt.%) and Rb (44–65 ppm) are high due to potassic alteration. The magnetic susceptibility of unaltered basaltic andesites varies from 715 to 78,000 μSI (K* = 65–7,100 $\times 10^{-6}$ SI in Fig. 6.45) and decreases down to 180–2,000 μSI (K* = 30–180 $\times 10^{-6}$ SI in Fig. 6.45) in the uppermost chloritised and calcitised zone.

P.E. Salminen (✉)
Department of Geosciences and Geography, University of Helsinki, P.O. Box 64, Gustaf Hällströmin katu 2a, 00014 Helsinki, Finland

V.A. Melezhik et al. (eds.), *Reading the Archive of Earth's Oxygenation*, Volume 2: The Core Archive of the Fennoscandian Arctic Russia – Drilling Early Earth Project, DOI 10.1007/978-3-642-29659-8_3, © Springer-Verlag Berlin Heidelberg 2013

The Kuetsjärvi Sedimentary Formation

In the drillcore, the Kuetsjärvi Sedimentary Formation occurs as a siliciclastic-carbonate succession divided into four distinct lithological units termed the Arkosic, Lower Dolostone, Quartzite and Upper Dolostone members (Fig. 6.44). The contact of the formation with the Ahmalahti Formation (volcanic Unit A) at a depth of 145 m defines the formational base, whereas the formational top is placed at the contact with the Kuetsjärvi Volcanic Formation basalts (volcanic Unit C) at a depth of 24 m. Although the true intersected thickness of the formation is c. 110 m, the overall thickness variation documented in the Pechenga Belt is from 20 to 120 m (Predovsky et al. 1974).

The Arkosic Member

The formation starts with the Arkosic member at a depth of 144.7 m. The basal unit of the member comprises a c. 0.5-m-thick, sheared, banded, calcareous sericite-biotite-chlorite schist (Fig. 6.51bs); interpreted elsewhere as a weathering crust (e.g. Melezhik and Fallick 2005). This unit grades downward transitionally into the Ahmalahti Formation basalt, itself altered into calcareous sericite-chlorite-albite-biotite-actinolite schist (Fig. 6.51bt). The upper boundary of the member is defined by its contact with a ferropicritic rock of Unit B at a depth of 96.6 m. Thus, the total drilled thickness of the member is less than 50 m.

The member comprises mainly arkosic sandstones, interbedded shale-siltstone-sandstone, calcareous siliciclastic rock (marl) and minor calcarenite and limestone. The magnetic susceptibility of the rocks is generally monotonous and low, ranging between 22 and 1,100 μSI (K* = 2–100 $\times 10^{-6}$ SI in Fig. 6.45). The exception is red, iron-stained, arkosic sandstones at the depth interval of 131–128.6 m, showing much higher values and greater fluctuations (from 240 to 18,000 μSI; K* = 22–1,646 $\times 10^{-6}$ SI).

The lower part of the member (c. 145–141 m) comprises interbedded sandstone-siltstone-shale (Fig. 6.51bp–br) with thin calcareous sandstone layers. It is defined by irregular, though in places rhythmic, interbedding of light-coloured, arkosic sandstone beds (2–10 cm in thickness) and dark-coloured siltstone-shale units (1–5 cm in thickness). The sandstone beds are commonly graded, have an erosional base, and show low-angle cross-lamination, whereas the siltstone-shale units are parallel-laminated or exhibit low-angle cross-lamination (Fig. 6.51bp–br). The sandstones are arkosic in composition and typically carbonate-cemented. The calcareous sandstone contains 16.4 wt.% CaO and 7.8 wt.% MgO (Appendix 10).

The content of carbonate material increases upward, which defines the mineralogical composition of the subsequent unit occurring between 141 and 136 m. It comprises mainly interbedded limestone/dolostone-sandstone-siltstone with beds of highly siliceous (SiO_2 = c. 31 wt.%; sample 3107838 in Appendix 10) calcarenite and dolarenite up to 1 m thick. In addition, the dolarenite also contains talc and chlorite. All lithologies in this interval are intensely sheared. The best-preserved parts indicate combination of lenticular and low-angle cross-lamination. Some calcarenite/dolarenite beds are graded or cross-laminated.

The interval from 136 to 132.6 m is composed of indistinctly bedded greywacke beds, tectonically deformed, interlaminated sandstone-siltstone and intensely sheared shale units. The rocks have a dark colour. Some sandstone layers are carbonate-cemented. Where primary sedimentary features are partially preserved, the rocks exhibit mainly parallel bedding, though some beds show lenticular lamination and trough cross-bedding (Fig. 6.51bo).

The middle part of the member (132.6–106 m) is arkosic sandstone with a c. 1-m-thick greywacke bed in its upper part (Fig. 6.44). The arkosic sandstone unit has a sharp contact with the underlying siltstone (Fig. 6.51bn). The arkosic sandstone is defined by irregular intercalation of beds with a different colour (Fig. 6.51bj). Thicker (1–50 cm) and dark-coloured beds comprise haematite-bearing, fine- to medium-grained sandstone, whereas thinner (0.5–10 cm) and light-coloured units are composed of siltstone. Elsewhere in the belt, some arkosic beds exhibit "ball-and-pillow" structures (Fig. 6.51bk). On a smaller scale, the sandstone units are characterised by parallel lamination (Fig. 6.51bf–bh, bl) and low-angle, tabular cross-bedding (Fig. 6.51bi, bl). Graded beds (Fig. 6.51bf) and small-scale, sand-filled channels (Fig. 6.51bh) are present. There is a general stratigraphic trend from fine- and medium-grained sandstone to fine-grained sandstone.

The upper part of the Arkosic member (c. 97.5–106 m) comprises irregularly interbedded, fine-grained arkosic sandstone, siltstone and calcareous sandstone-siltstone with thin shale layers (Fig. 6.51az–be). The sandstone units exhibit parallel-lamination (Fig. 6.51be), low-angle, tabular cross-lamination (Fig. 6.51bc, bd), and trough cross-bedding (Fig. 6.51bb), whereas the calcareous sandstone-siltstones show parallel lamination (Fig. 6.51az, ba). Some siltstone-shale beds have lensoidal lamination (Fig. 6.51bb).

The analysed samples show that arkosic sandstones have a rather homogeneous chemical composition (Fig. 6.45; Appendices 10 and 11): SiO_2 = 70–77 wt.%, K_2O = 6.4–8 wt.%, Al_2O_3 = 8.6–11.7 wt.%. The rocks are low in Na_2O (0.43–1.2 wt.%), and some beds in the upper part of the member contain up to 0.28 wt.% P_2O_5. The shale contains 16.6 wt.% Al_2O_3 and 9.6 wt.% K_2O. The calcareous sandstone has 3.4 wt.% MgO and 6.4 wt.% CaO bound to the carbonate phase. All rocks are devoid of sulphur and organic carbon.

The Lower Dolostone Member

The Lower Dolostone member is c. 40 m thick (92–52.17 m). Its lower boundary is defined by a tectonically modified contact with the ferropicrite at a depth of 92 m (Fig. 6.44). The member consists of dolarenites and sparry dolostone, and finely crystalline (micritic) dolostones (Fig. 6.51v–x, ab, ac, ad–ai, al, ao, ap, au, av, ax, ay) with two thin beds of arkosic sandstone. Numerous travertine crusts occur throughout the member (Fig. 6.51w–y, aa, ab, ad, af, ai–an, ar–at, aw), and several intervals are injected by travertine veins (Fig. 6.51v, ac, ax).

The magnetic susceptibility of the Dolostone member rocks is generally invariable and stays below 20 µSI ($K^* < 2 \times 10^{-6}$ SI in Fig. 6.45) with two exceptions. One, a bed of pale grey dolostone located at a depth of c. 91 m (c. 1 m above the contact with the ferropicrite; Fig. 6.45), has a magnetic susceptibility of up to 80,300 µSI ($K^* = 7{,}300 \times 10^{-6}$ SI). The other, a dolarenite bed containing jasper fragments and located at a depth of 52.15 m (c. 2 m below the contact with the Quartzite member), records a value of 26,000 µSI ($K^* = 2{,}360 \times 10^{-6}$ SI in Fig. 6.45).

The dolarenites typify the lower part and sparry and micritic dolostones the upper part of the member, although both lithologies have been observed to be mutually interbedded within a decimetre-scale core specimen. This alternation may also include 1–3-cm-thick layers of dolomite-cemented, quartzitic sandstone (Fig. 6.51ao, ap, at).

All dolostone lithologies are characterised by irregular bedding (Fig. 6.51ay) that is in many places affected by erosional (Fig. 6.51ao, ap, au, av) and dissolution (Fig. 6.51v, ae) processes and complicated by travertine encrustation (Fig. 6.51af, ai, ak, an, aq, as, aw). The dolarenites commonly show crude parallel bedding (Figs. u, v, af, ai, ap, ax). In rare cases, micritic dolostones exhibit parallel lamination (Fig. 6.51ac, ad). All carbonate lithologies contain quartz either in the form of regularly scattered, sorted, angular and rounded clastic grains floating in a carbonate matrix (Fig. 6.51z, ah) or in the form of silcretes (Fig. 6.51al) and silica filling dissolution voids (Fig. 6.51ag).

Travertine occurs as thin crusts, small mounds and veinlets. The thickness of the travertine crusts varies from a centimetre to tens of centimetres. All travertine morphologies display variable colours ranging from white and pale grey through beige, tan and buff to pale pink and red (Fig. 6.51w–y, aa, ab, ai, am, an, aq–at, aw). The macrostructural pattern also varies from regularly laminated (Fig. 6.51ar–at, aw) to irregularly banded (Fig. 6.51aq). Travertine can occur as precipitate on a substrate with an uneven surface (Fig. 6.51ai) and shows complex banding and bending and cementation of surface rock fragments (Fig. 6.51am, an). Common phenomena in travertine crusts are enveloping of surface rock fragments (Fig. 6.51ak), cementing, and growing upwards, downwards and inwards while filling cavities. The remaining open space in travertine cavities is commonly filled with silica (Fig. 6.51aa, ab). When upper surfaces of travertine mounds or travertine crusts are exhumed, they display irregular clusters having a spheroidal structure (Fig. 6.51aj, am, an). Travertine veins and veinlets have irregular shapes and boundaries with numerous embayments into host rocks (Fig. 6.51v, x, af, ax).

All analysed samples from the Lower Dolostone member are highly siliceous ($SiO_2 = 4.6$–21 wt.%). All but one have moderate Mn (207–378 µg g^{-1}) and Fe (921–1,500 µg g^{-1}) contents, low Al_2O_3 (0.09–0.53 wt.%) and Sr (43–86 µg g^{-1}) abundances, and are devoid of sodium, sulphur and organic carbon (Fig. 6.45, Appendices 10–12). An exception is represented by white dolarenite, which is located immediately below the contact with the overlying Quartzite member (Fig. 6.51t). This dolarenite has higher Al_2O_3 (1 wt.%), Na_2O (0.17 wt.%), Fe (2,490 µg g^{-1}), and Mn (2,380 µg g^{-1}) concentrations.

The Quartzite Member

The member is a c. 12-m-thick unit (52.17–40.3 m) with a sharp lower contact on a pale pink dolarenite at a depth of 52.17 m (Fig. 6.51t). The member is mainly composed of quartzitic sandstone and minor greywacke. The magnetic susceptibility of the Quartzite member decreases upward from 70 to 850 µSI ($K^* = 6$–77×10^{-6} SI) to 0–90 µSI ($K^* = 0$–8×10^{-6} SI in Fig. 6.45).

The basal bed of the member (52.2–51.5 m) comprises interbedded dolarenite, dolorudite and greywacke containing resedimented carbonate rocks in the form of large dolostone fragments up to 5 × 5 cm (Fig. 6.51t). One dolarenite bed within this interval has rounded and angular clasts of dark-coloured jasper and shows an enigmatic structure (Fig. 6.51u), which may represent either inverted micro-stromatolites or cave deposits (micro-stalactites). The basal bed is sharply overlain by dark grey, parallel-laminated greywacke (Fig. 6.51s) gradually passing into beige and grey, parallel-laminated arkosic sandstone (Fig. 6.51q, r). This is followed by thickly interbedded, bright-coloured, massive or indistinctly laminated quartz sandstone (Fig. 6.51p) and dark-coloured, clayey sandstone (Fig. 6.51n). The uppermost, 1-m-thick bed comprises thin (0.5–1 cm), rhythmically bedded, mud-draped sandstone units and includes thin intervals with lenticular bedding (Fig. 6.51n, o).

The SiO_2 content in one analysed quartz sandstone sample is high (c. 95 wt.%). The contents of Al_2O_3 (1.2 wt.%), K_2O (0.8 wt.%) and Na_2O (0.2 wt.%) are low (Fig. 6.45, Appendices 10 and 11). Elevated concentrations of MgO (0.44 wt.%) and K_2O (0.77 wt.%) are due to the presence of dolomite and sericite in the cement. The quartzite is devoid of sulphur and organic carbon.

The Upper Dolostone Member

The Upper Dolostone member is c. 16 m thick and rests with a sharp contact on the sandstone-mudstone unit at a depth of 40.3 m (Fig. 6.51n). The upper contact with the overlying Kuetsjärvi volcanic rocks at a depth of 24 m is tectonically modified. The member comprises diverse lithologies, which include dolostone and limestone, dolarenite and calcarenite, stromatolitic dolostone, travertine, and calcareous sandstone, siltstone and shale. The micritic dolostone occurs predominantly in the lower part, stromatolitic dolostone and travertine in the middle part, whereas limestone and calcareous sandstone-siltstone are found in the upper part of the section (Fig. 6.44). There is a quartz sandstone layer at a depth of c. 28 m. All rocks have a low magnetic susceptibility, which ranges between 0 and 90 μSI ($K^* = 0\text{–}8 \times 10^{-6}$ SI in Fig. 6.45), though progressively and rapidly increasing from 100 to 77,000 μSI ($K^* = 9\text{–}7{,}000 \times 10^{-6}$ SI in Fig. 6.45) in calcareous sandstone-siltstone within the uppermost metre towards the contact with the overlying basalt.

All carbonate lithologies in the Upper Dolostone member have either pink or variegated colours with a mottled appearance. Bedding is irregular and disrupted by buckling, desiccation, formation of dissolution cavities and encrustation by travertine crusts (Fig. 6.51d–f, i, k). Crude, parallel bedding is a typical feature of micritic dolostone, dolarenite and calcareous sandstone-siltstone of the lower and upper part of the member (Fig. 6.51b–d, l). Some dolarenites in the upper part of the section show graded bedding (Fig. 6.51b). Calcareous shale comprising the uppermost part of the member is intensely sheared and does not retain primary structures (Fig. 6.51b).

The stromatolitic dolostone displays flat lamination and undulatory or weakly domed structures (Fig. 6.51g, h). They are commonly composed of 0.2–0.5-mm-thick, irregular laminae of micritic dolomite (primarily microbial mats), thicker layers of sparry dolomite containing carbonate intraclasts and quartz detritus, as well as silica-filled fenestrae and voids (Fig. 6.51g; see Chap. 7.8.2 for details).

The dolarenite contains both rounded and platy, unsorted intraclasts of micritic and stromatolitic dolostones and is affected by dissolution processes expressed by abundant micro- and macrocavities. All cavities, regardless of size, generally have a complex infill. Walls are veneered by white dolospar and travertine dolomite, with the remaining space occupied by silica (Fig. 6.51i–k). Larger cavities are commonly filled with sandy, allochemical dolostones, quartz sandstone or travertine dolomite (Fig. 6.51d, f).

All dolostone lithologies are associated with abundant travertine crusts and small-scale travertine mounds. The thickness of the travertine crusts varies from a few millimetres to tens of centimetres, and their fabric ranges from laminated to massive and clotted (for detail see Chap. 7.9.4). In many cases, the travertine crusts show both upward and downward growth (Fig. 6.51m). Some travertine crusts and mounds have been subject to syndepositional silicification, and many display upper surfaces veneered by silica sinters.

Two analysed samples represent highly siliceous dolarenite and silicified travertine (39.5 and 14.4 wt.% SiO_2, respectively). Both lithologies have similar Al_2O_3 (c. 1 wt.%), K_2O (c. 04 wt.%) and Mn (115–138 μg g^{-1}) contents (Appendices 10–12), but travertine shows slightly higher Sr content (139 μg g^{-1} versus 113 μg g^{-1}). Both are devoid of sulphur and organic carbon.

Igneous Bodies Within the Sedimentary Succession: Ferropicrite (Unit B)

The igneous body (Unit B) at interval c. 92–97 m is composed of ultramafic chlorite-biotite schist containing minor talc and pyrite, and is crosscut by quartz, dolomite and chlorite veinlets. Due to the high degree of schistosity and obscure contacts, it is unclear whether the protolith of this body represents a lava flow, dike-like intrusion or tuff layer. The magnetic susceptibility is high, approaching 80,000 μSI ($K^* = 7{,}300 \times 10^{-6}$ SI in Fig. 6.45). The unit has a high MgO content of 19.1 wt.% (Fig. 6.49), and elevated Cr (1360 ppm) and Ni (1000 ppm) concentrations (Appendices 10–11). It is also relatively high in FeO_T (14.2 wt.%) and TiO_2 (2.3 wt.%) and hence corresponds to ferropicrite in its chemical composition (cf. Hanski and Smolkin 1995). The chondrite-normalised REE spectrum is enriched in LREE compared to HREE (Fig. 6.50a), and the overall immobile trace element characteristics are similar to those of alkali basalts (Fig. 6.50b). The unit has an abnormally high K_2O content of 6.3 wt.%, which is interpreted to be a result of strong post-magmatic alteration.

The Kuetsjärvi Volcanic Formation (Unit C)

The igneous rocks in the interval 9–24 m (Unit C) at the top of the core belong to the Kuetsjärvi Volcanic Formation. The section contains six individual lava flows with thicknesses ranging from a few decimetres to c. 4 m. They have carbonate-filled amygdales close to the upper and lower contacts (Fig. 6.51a). Rocks are ophitic or aphanitic and in many places carbonatised. The magnetic susceptibility is high, and varies from 27,500 to 242,000 μSI ($K^* = 2{,}500\text{–}22{,}100 \times 10^{-6}$ SI in Fig. 6.45).

Two of the three analysed samples are from the upper part and one from the lower part of the volcanic pile. They are alkali basalts with MgO between 4.4 and 7.2 wt.% and relatively high contents of incompatible elements such as

LREEs, Nb (14–31 ppm), and TiO_2 (1.5–2.3 wt.%). Chromium concentration is also relatively high (210 and 500 ppm). The chondrite-normalised REE pattern, shown in Fig. 6.50a, is steeper than that of the Ahmalahti Volcanic Formation with La rising to a level of more than 300 times chondritic. The $(Ce/Nb)_{PM}$ ratio is variable (0.9–2.0), and the rocks have low P/Nd ratios indicating interaction with sialic crust (Fig. 6.50b). However, the contamination was likely not as severe as in the case of the underlying tholeiitic andesites of the Ahmalahti Volcanic Formation. Chemically the analysed alkali basalts are very similar to amygdaloidal basalts found from the basal part of the Kuetsjärvi Formation in the vicinity of the drilling site (Fig. 4.24b, Chap. 4.2).

Depositional Framework

The depositional framework presented below is based on the interpretation of sedimentary features documented in core from Hole 5A. The succession comprises three sandstone-carbonate cycles of uneven thicknesses (Fig. 6.44).

The first cycle is the thinnest of all (c. 9 m) and consists of two, similarly thick sub-cycles. The first sub-cycle is composed of immature arkosic arenite and siltstone, while the second sub-cycle comprises mainly calcareous sandstone-shale with minor calcarenite. The sandstone sub-cycle is characterised by a fine to medium grain size, combination of parallel and low-angle cross-lamination, trough cross-bedding and graded beds with some having an erosional base (Fig. 6.51bp–br). The overall sedimentological pattern can be best fit to a deltaic environment. The carbonate sub-cycle rocks were affected by tectonic reworking, which has masked the primary sedimentological features. What is in places preserved, is the combination of lenticular and low-angle cross-lamination, which may suggest influence of tides. Our tentative interpretation of the environment, acknowledging limited observations, is a tidally influenced delta-front setting.

The second cycle is the thickest (c. 80 m); it, too, contains two sub cycles. The first is a c. 30-m-thick, fining-upward succession from trough cross-bedded greywacke and parallel-laminated shale at the base that is overlain sharply by arkosic arenites that are at first fine- to medium-grained and become progressively finer-grained towards the top: an indication of the transition to a relatively lower energy environment. The sandstones are variegated in colour and occur as 1–50-cm-thick beds alternating with 0.5–10-cm-thick siltstone beds. Both lithologies show mainly parallel lamination and, less commonly, small-scale tabular and trough, low-angle cross lamination. Bedding surfaces are predominantly straight and sharp (Fig. 6.51bj). There is no evidence of tidal reworking. Hence, the overall sedimentological features suggest a prodelta environment within a lacustrine setting.

The transition to the overlying carbonate sub-cycle is gradual through a c. 10-m-thick unit of parallel-laminated, calcareous sandstone-siltstone (Fig. 6.51az) with sporadic beds of arkosic sandstone. The dominant feature of the carbonate sub-cycle is a high content of clastic quartz (Fig. 6.51z, ah), highly irregular, crude bedding or stratification (Fig. 6.51v–ay) with abundant evidence of repetitive subaerial erosional and dissolution processes (Fig. 6.51ae, ai, ao, ap, au, av, ax), redeposition of previously accumulated carbonate material, and formation of travertine crusts and mounds (Fig. 6.51v–y, aa, ab, af, ai–an, aq–at, aw). These features are inconsistent with marine settings and thus we infer them to have formed in a lacustrine environment. There is no indication of reworking by waves, apart from gentle, symmetrical sand-ripples covered by travertine crust (Fig. 6.51at). Hence, the lake was likely shallow.

The third cycle is c. 28-m-thick, with similar thickness of sandstone and carbonate sub-cycles (Fig. 6.44). The boundary with the underlying second cycle is marked by subaerial erosion followed by incorporation of the previously deposited dolostones as clasts into the base of the sandstone sub-cycle (Fig. 6.51t). The lower part of the sub-cycle comprises chemically immature, thinly laminated greywacke followed by parallel-laminated arkosic and, then, thickly bedded quartzitic sandstone (Fig. 6.51q–s). This defines a thickening-upward sequence. Higher up in the succession, the quartzitic sandstone becomes indistinctly bedded (Fig. 6.51p) and chemically mature (95 wt.% SiO_2) before being succeeded by a metre-thick interval of thinly interbedded sandstone-mudstone couplets, some showing lenticular bedding. The sedimentological features of the lower part of the sub-cycle suggest a flooding event followed by deposition of parallel-laminated and bedded sandstones in a delta-front and/or prodelta environment which, at the end, was influenced/reworked by tides.

The carbonate sub-cycle has a sharp contact with the underlying tidally influenced siliciclastic unit (Fig. 6.51n). The lowermost 0.5-m-thick bed comprises white, indistinctly bedded dolostone (Fig. 6.51n) that is rapidly succeeded by pale pink and variegated, crudely bedded dolostones incorporating a significant amount of reworked carbonate clasts (Fig. 6.51l). Circa 3 m above the base, there is the first occurrence of travertine (Fig. 6.44). The red colouration and the presence of travertine are consistent with dominance of subaerial, oxic conditions. Upward in the section, an episodic appearance of thin intervals with flat-laminated and desiccated stromatolites (Figs. 6.44 and 6.51g, h) corresponds with increasing amounts of thick travertine crusts (Figs. 6.44 and 6.51m). Associated with the stromatolites, there is a 3-cm-thick interval containing three dolarenite units with mud drapes (Fig. 6.51j). Crude bedding still prevails, intraclasts are abundant, composition remains impure (40 wt.% SiO_2), and dissolution voids progressively increase upward reaching dimensions of microkarst (>10 cm in height; Fig. 6.51f). The sub-cycle ends with crudely bedded dolarenite and calcarenite sharply overlain by calcareous shale buried under subaerially erupted amygdaloidal basalt (Fig. 6.51a, b). The overall sedimentological pattern of the carbonate sub-cycle suggests a shallow-water environment affected by frequent resedimentation and dissolution processes. Although initially deposited on apparently tidally influenced rocks, many features, such as stromatolite morphology, red colouration, and abundant travertine, are not readily attributed to a marine setting. Hence, a lacustrine environment is the most likely option. A few thin, mud-draped dolarenite layers in the middle of the sub-cycle may indicate that the lake was periodically influenced by tides, thus indicating a short-term intervention of seawater.

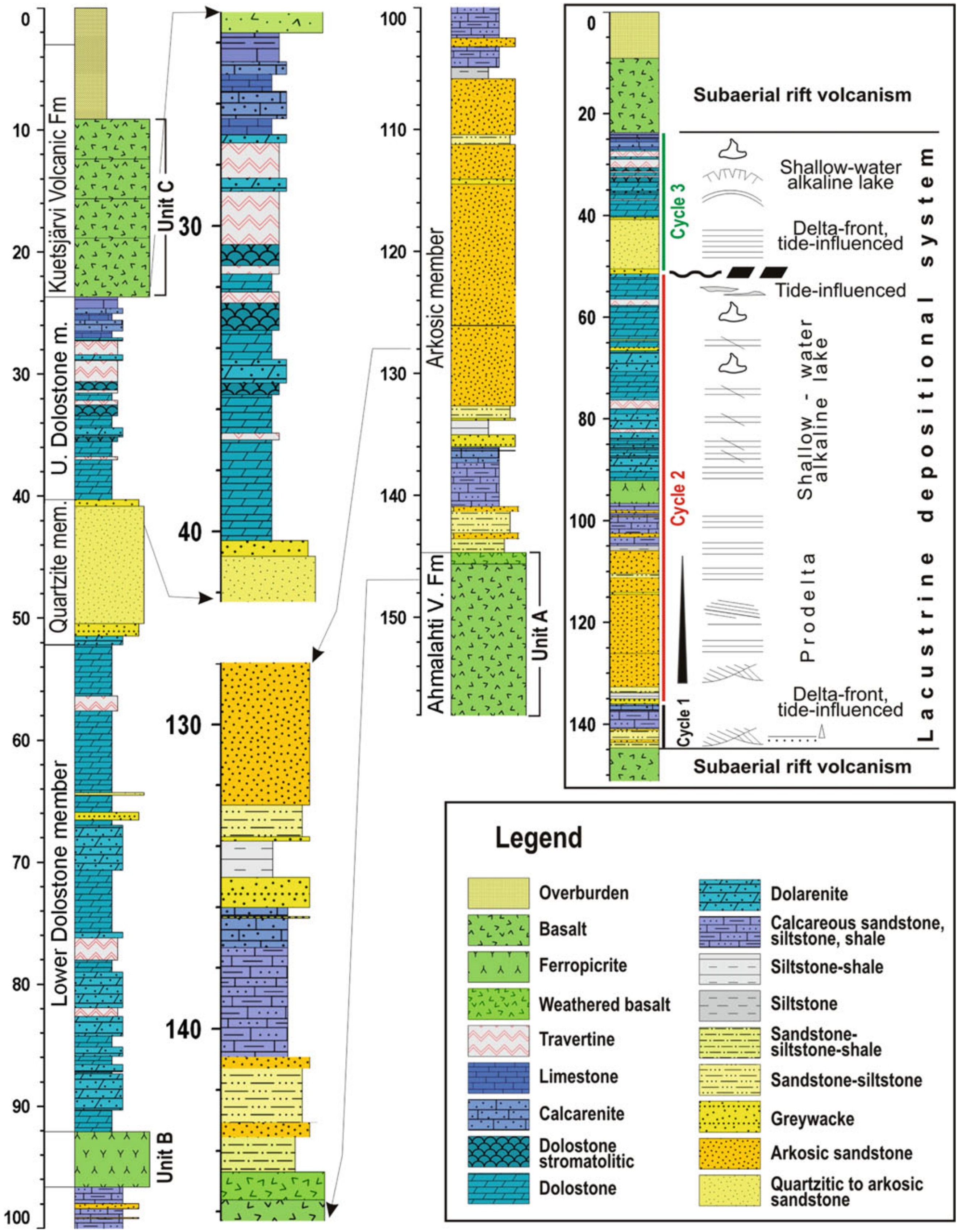

Fig. 6.44 Lithological section of the Kuetsjärvi Sedimentary Formation based on core log of Hole 5A and a tentative reconstruction of depositional environments based on core logging and sedimentological research in the vicinity of the drilling site. Lithological symbols are explained in Fig. 6.6

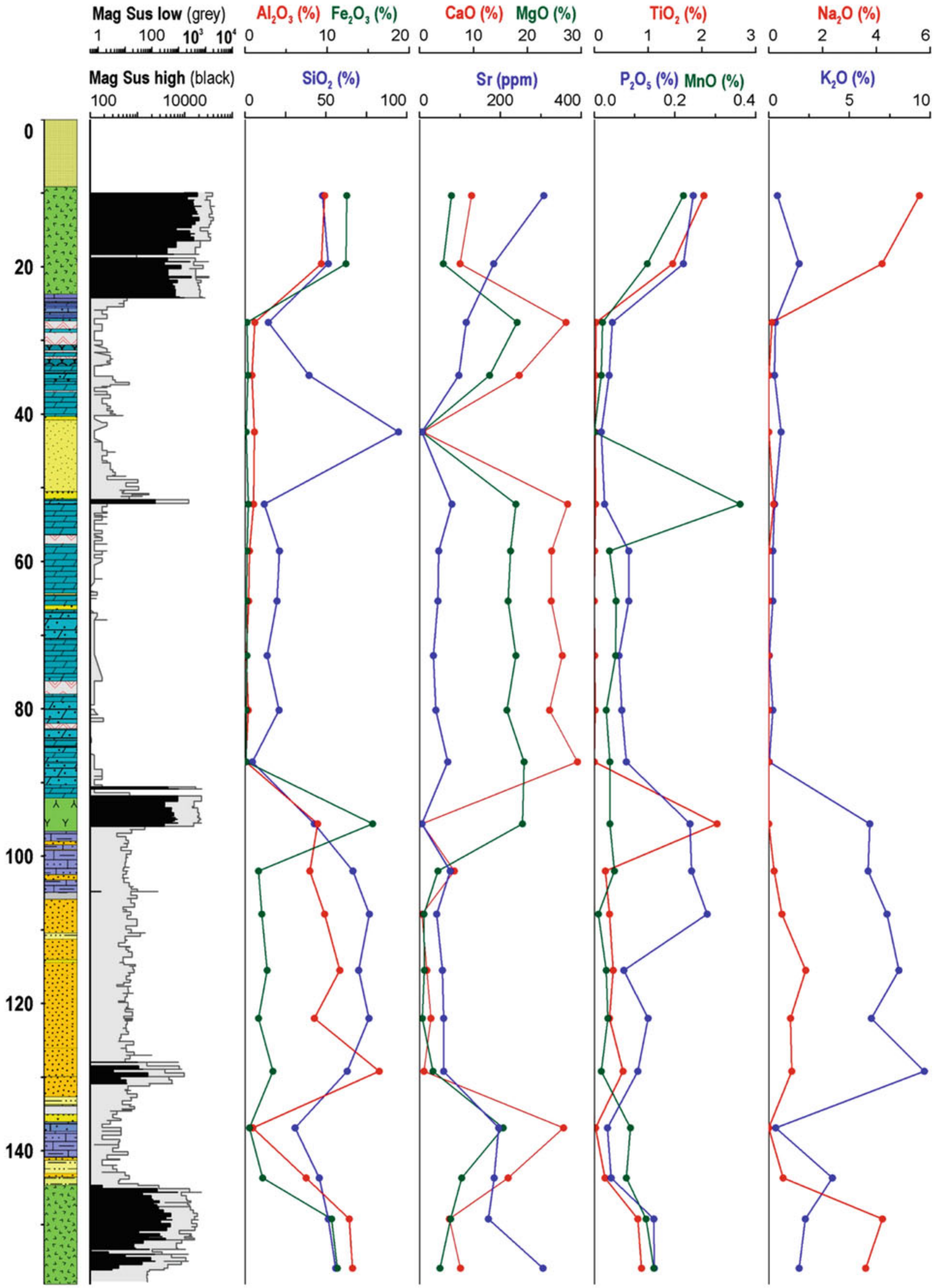

Fig. 6.45 Relative magnetic susceptibility (K*), and geochemical profiles of selected elements based on the archive samples collected with c. 8 m-spacing. For analytical techniques and data quality see **Part 5**

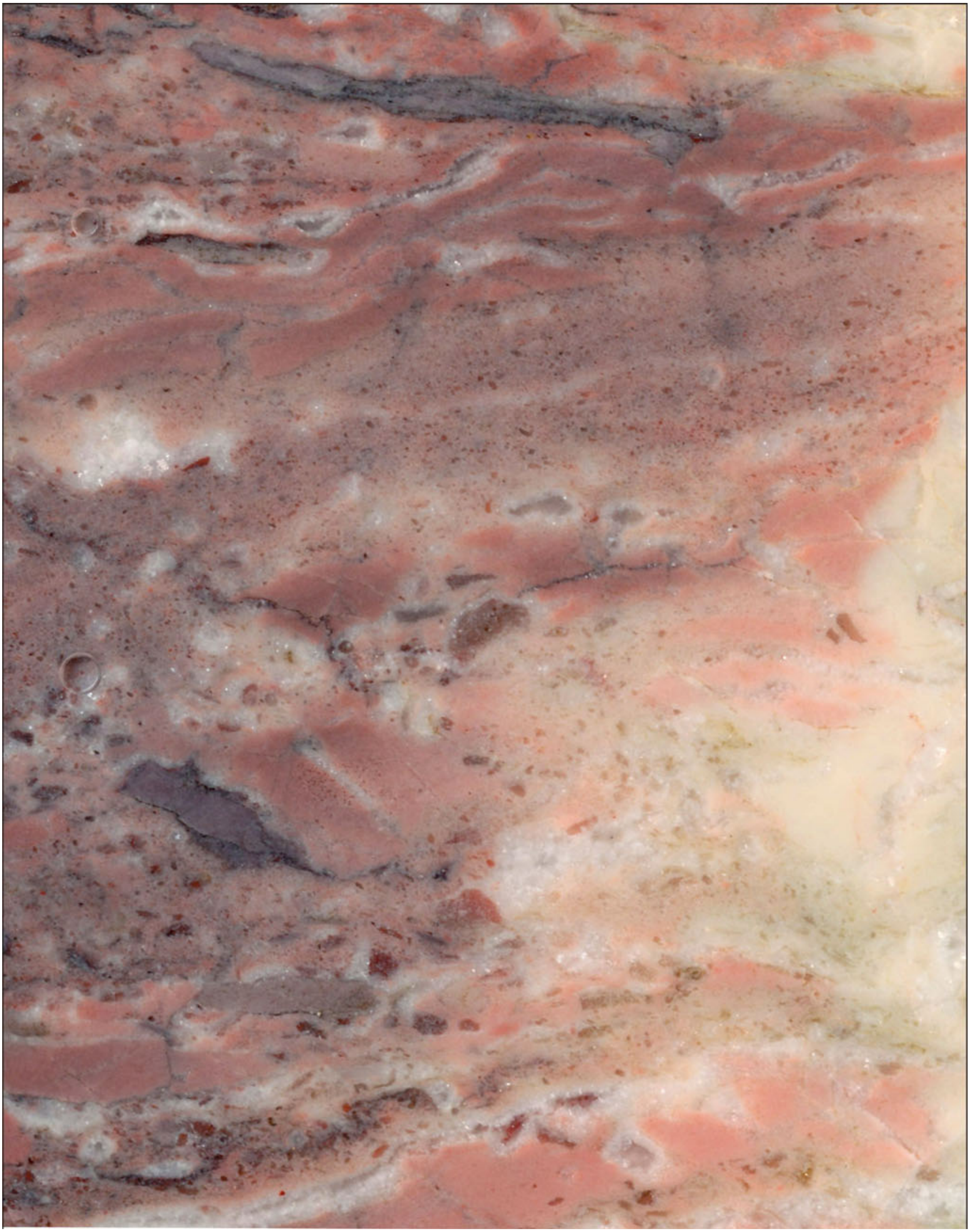

Fig. 6.46 Red, poorly sorted dolarenite with pink, “wavy” layers of dolomicrite (*upper* part). Resedimented carbonate material includes variably rounded and angular fragments of pink dolomicrite, brown and grey fragments of clayey dolostones and abundant sand-sized quartz grains. Note that both dolarenite and dolomicritic layers were affected by dissolution and formation of voids filled with late, white dolospar and quartz. Width of the photograph is 7 cm (The photograph was taken by Victor Melezhik from a quarry near the drilling site)

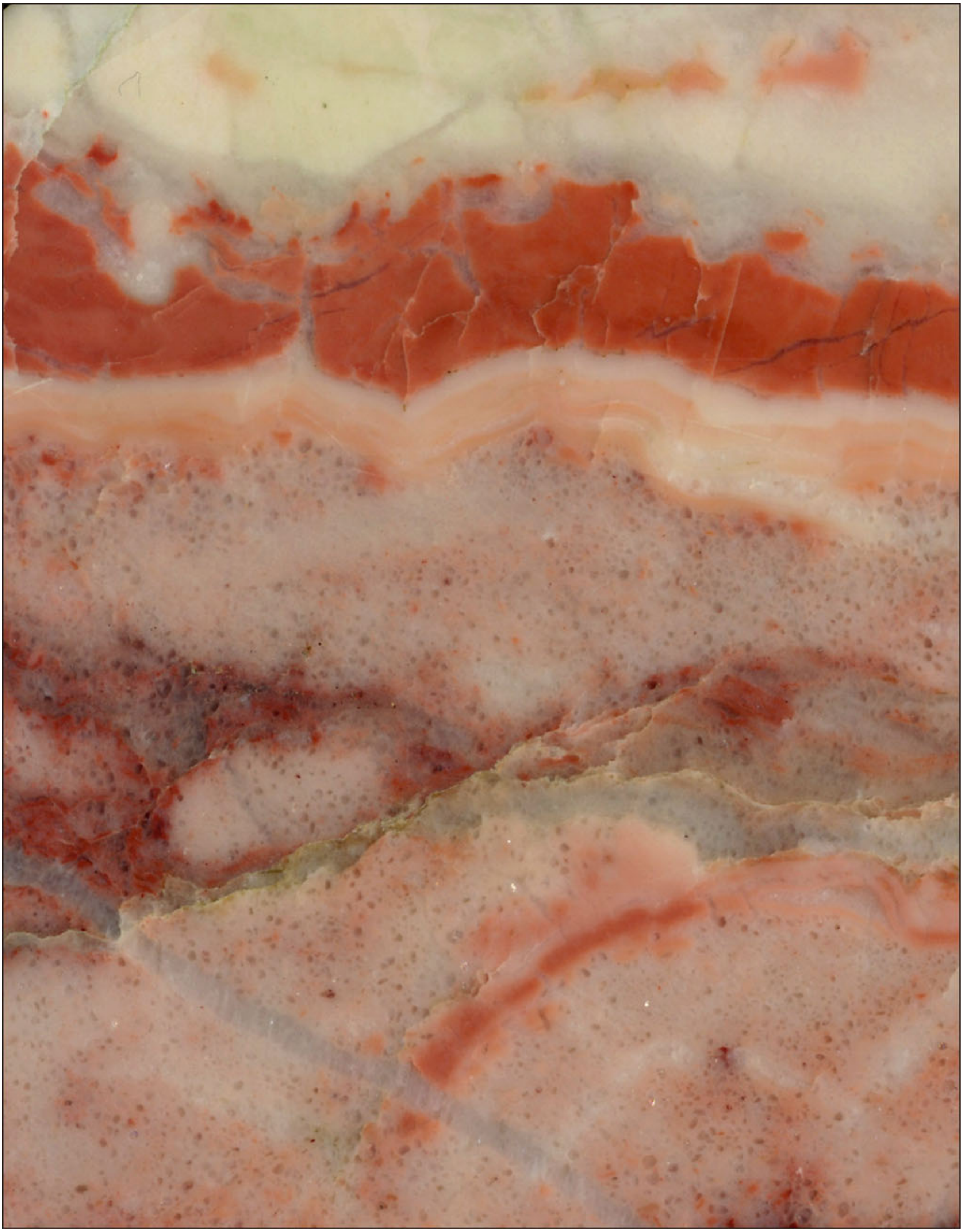

Fig. 6.47 Variegated, dolomite-cemented quartz sandstone overlain by thin, laminated travertine crust followed by red, haematite-stained, calichified, massive dolomicrite, and capped by white, dolomitic travertine. Note that dissolution voids in red, massive dolomicrite are filled with several generations of dolomite and silica cement. Such rock, containing several carbonate phases that represent diagenetic cementation of quartz sand, hydrothermal travertine dolomite, red pedogenic dolomicrite and dolospar and silica micronodules, has a great potential for addressing chemical and isotopic composition of various carbonate-precipitating fluids. Width of the photograph is 10 cm (The photograph was taken by Victor Melezhik from a quarry near the drilling site)

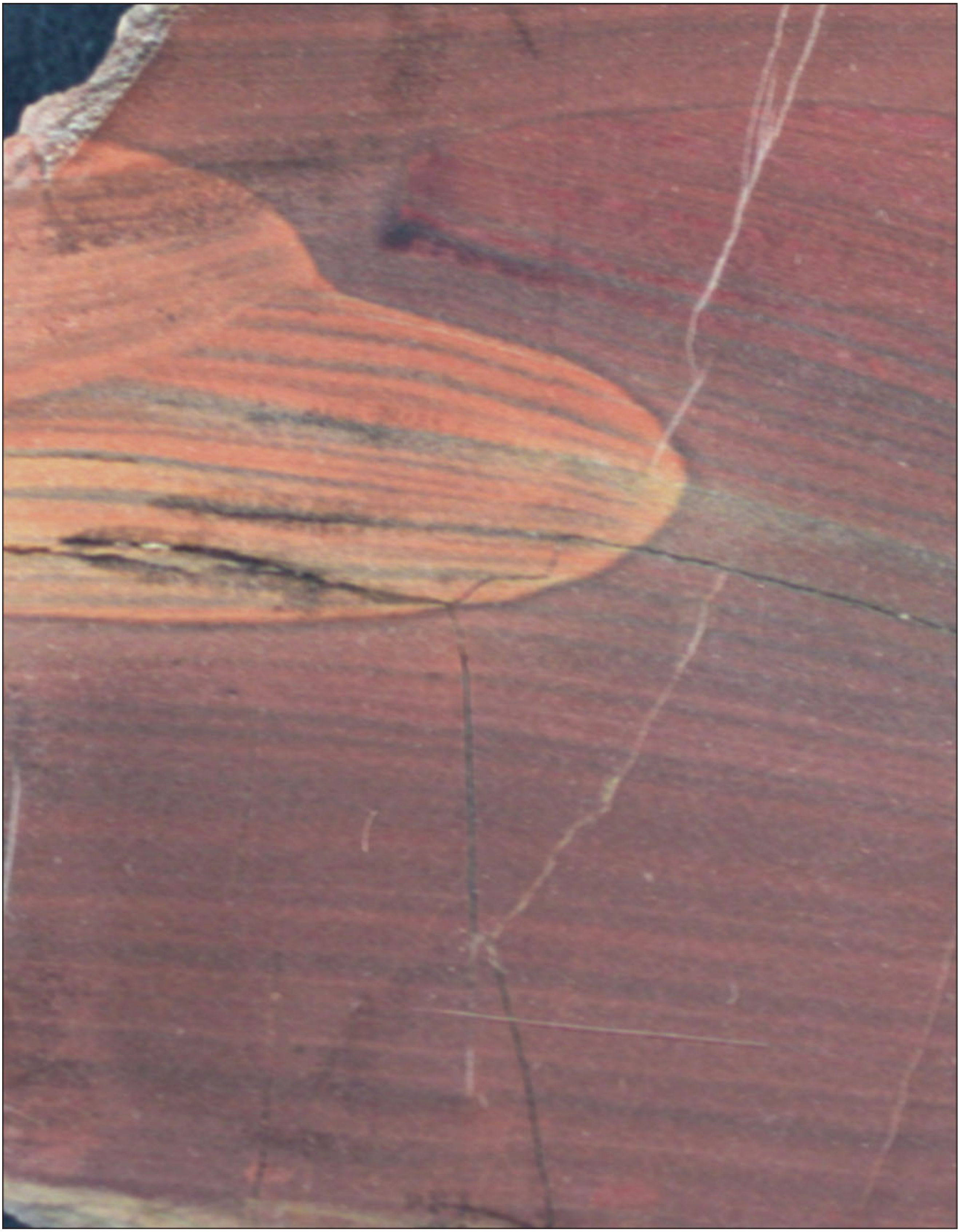

Fig. 6.48 Red, trough cross-bedded, arkosic sandstone with a superimposed pale pink “roll” structure caused by infiltration of reducing fluids which partially dissolved and flushed away iron oxides. Width of the photograph is 18 cm (The photograph was taken by Victor Melezhik from an outcrop located c. 15 km to the northwest of the drilling site)

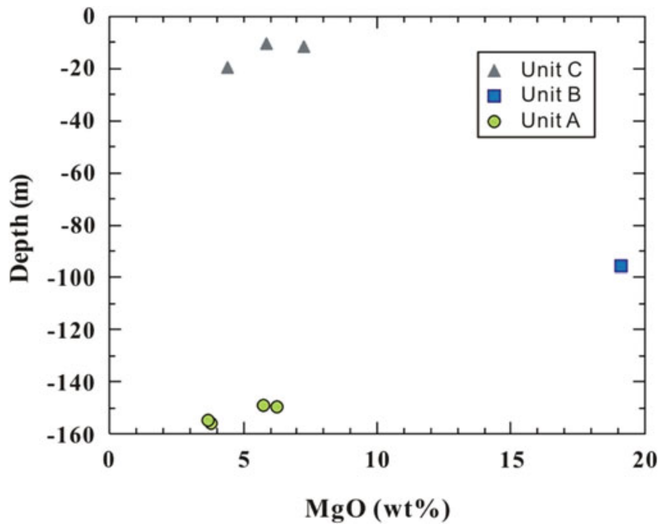

Fig. 6.49 MgO versus depth diagram for igneous rocks in core 5A

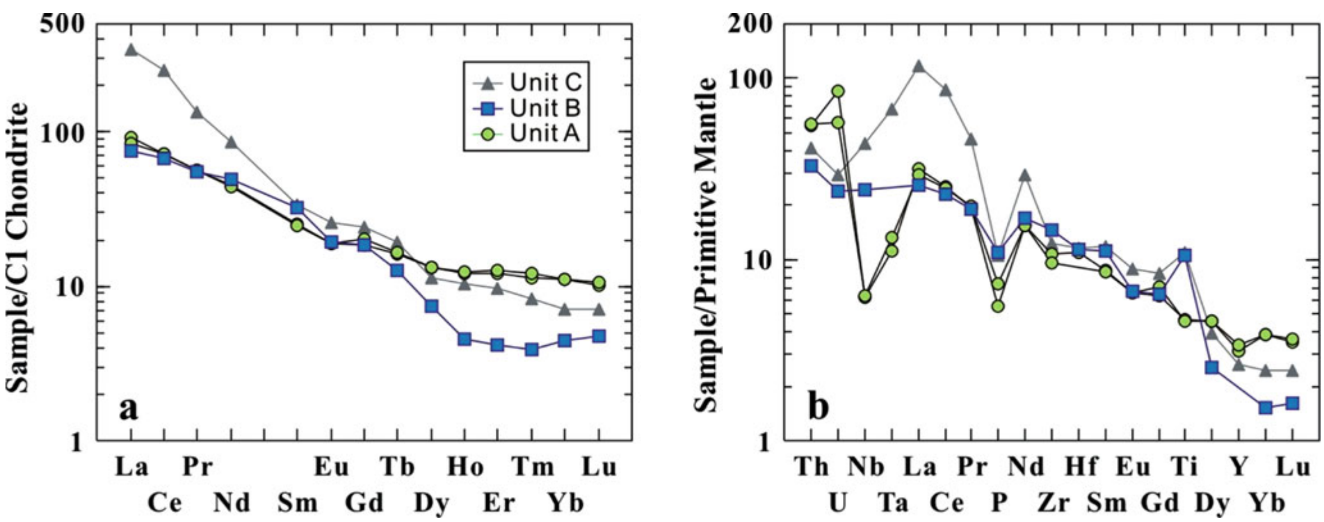

Fig. 6.50 Chondrite-normalised REE patterns (*left panel*) and primitive mantle-normalised trace element patterns (*right panel*) for igneous rocks in core 5A (Normalising values taken from Sun and McDonough (1989))

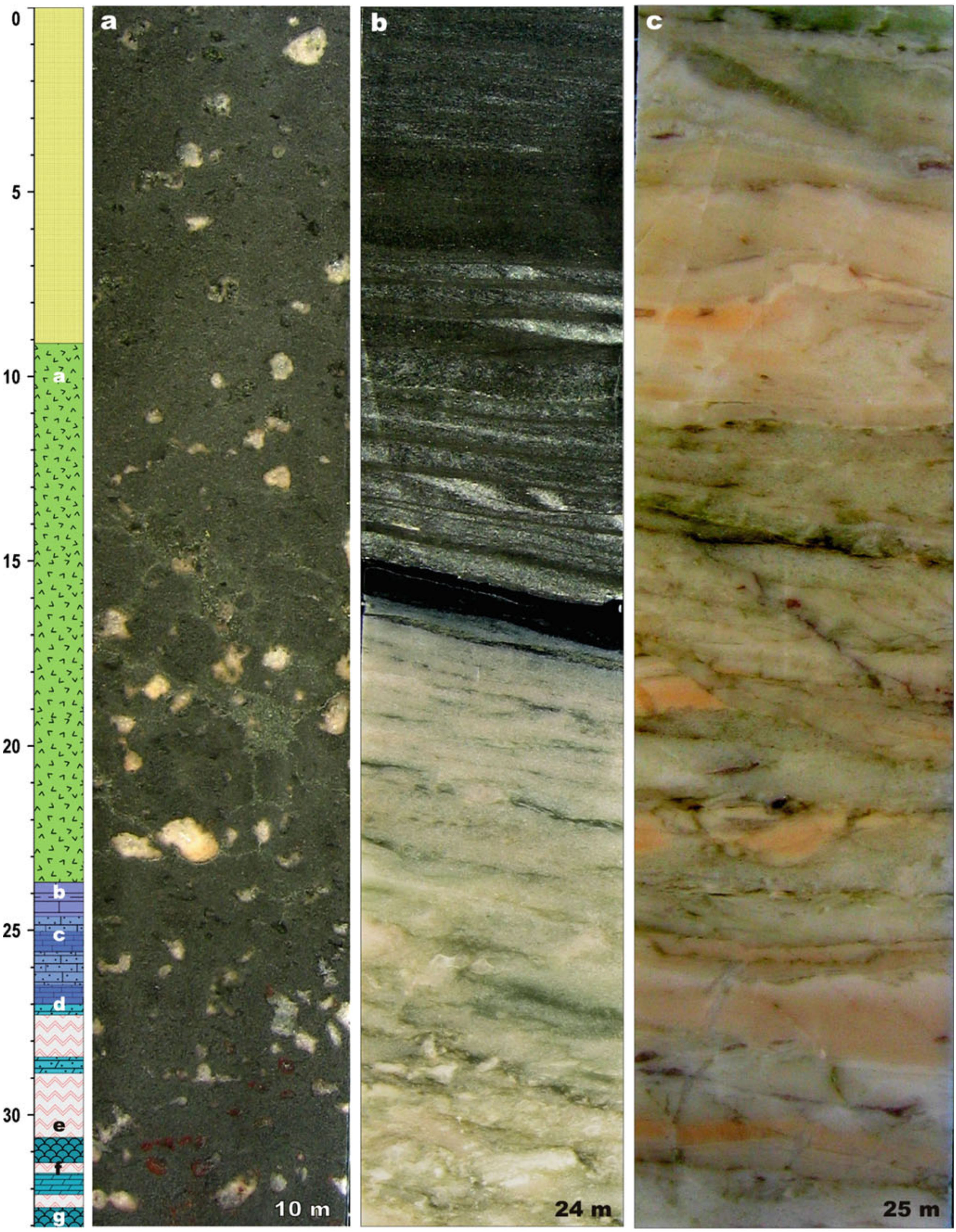

Fig. 6.51 Sedimentological and petrological features of the main rock types intersected by the Hole 5A and in the vicinity of the drilling site. Core diameter in all plates is 5 cm unless specified otherwise. (**a**) Amygdaloidal alkali basalt with quartz and calcite amygdales. (**b**) Graded, parallel-bedded calcarenite (bright) overlain by sheared, parallel-bedded, calcareous shale. (**c**) Beige, indistinctly bedded, clayey calcarenite

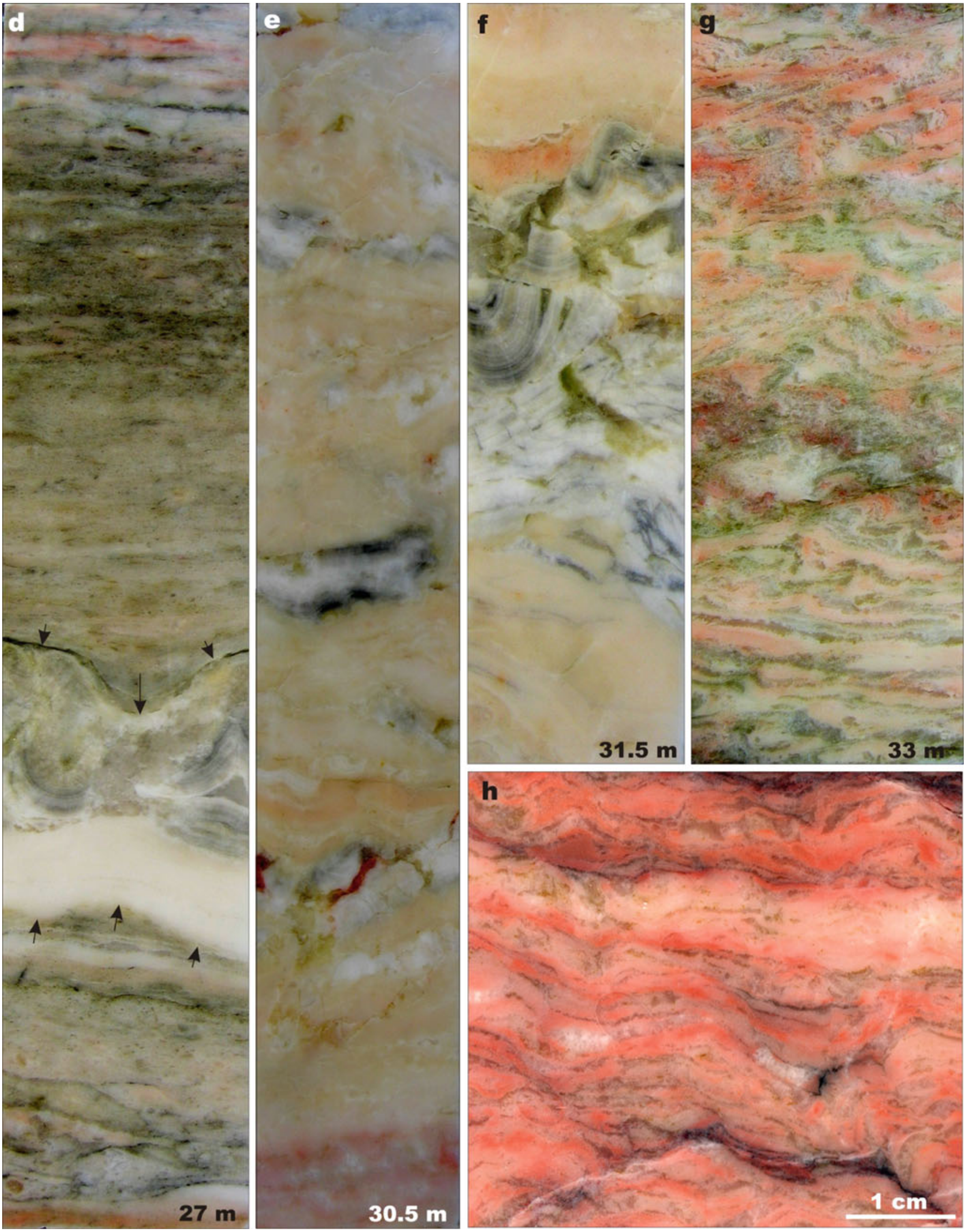

Fig. 6.51 (continued) (**d**) Variegated, clayey dolarenite with dissolution cavity floored by white travertine dolomite, whereas the roof is overgrown by travertine stalactites. (**e**) Buff and beige, indistinctly bedded, dolomitic travertine (*lower half*) overlain by buff travertine with a clotted microfabric. (**f**) White and grey, partially brecciated travertine stalactites filling cavity in beige, micritic dolostone. (**g**) Wavy-laminated and "curly" stromatolitic dolostone with dolospar and quartz-filled fenestrae. (**h**) Pink, wavy-laminated, stromatolitic dolostone with dolospar and quartz-filled fenestrae; sample collected from a quarry located near the drilling site

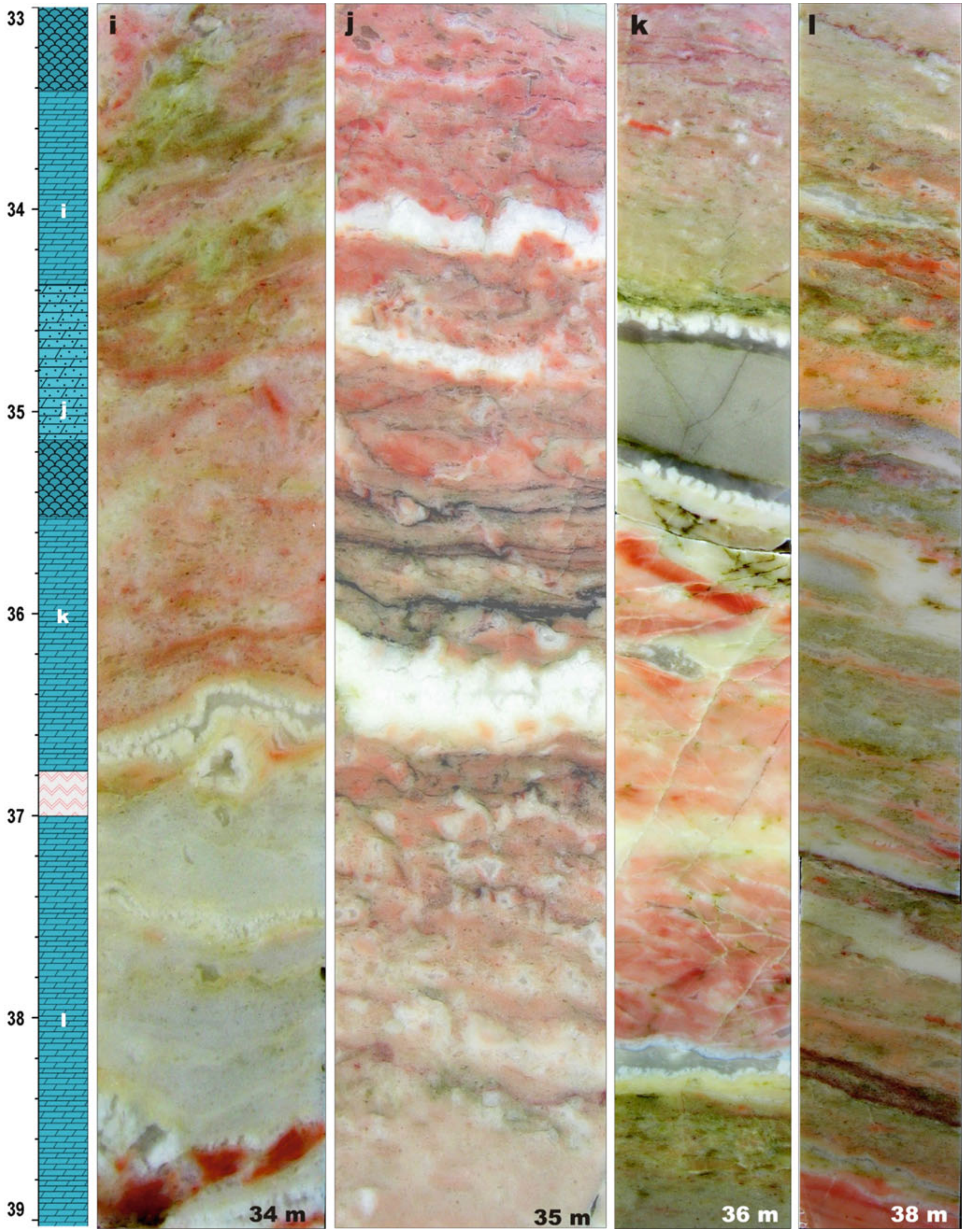

Fig. 6.51 (continued) (**i**) White travertine crust with red spots (at the *bottom*) overlain by pink, non-bedded dolarenite containing a dissolution cavity filled with white travertine dolomite and silica. (**j**) Pale pink, indistinctly-bedded dolostone with three mud-draped dolarenite layers (in the *middle*) and white, bedding-parallel, travertine veins; note abundant voids in the dolarenite filled with travertine dolomite and pale grey quartz. (**k**) Interbedded pink, red and beige, non-laminated, micritic dolostone and dolarenite with dissolution cavities filled with white travertine dolomite and silica quartz. (**l**) Variegated, parallel-bedded micritic dolostone and dolarenite with white travertine veins and quartz- and travertine-filled voids

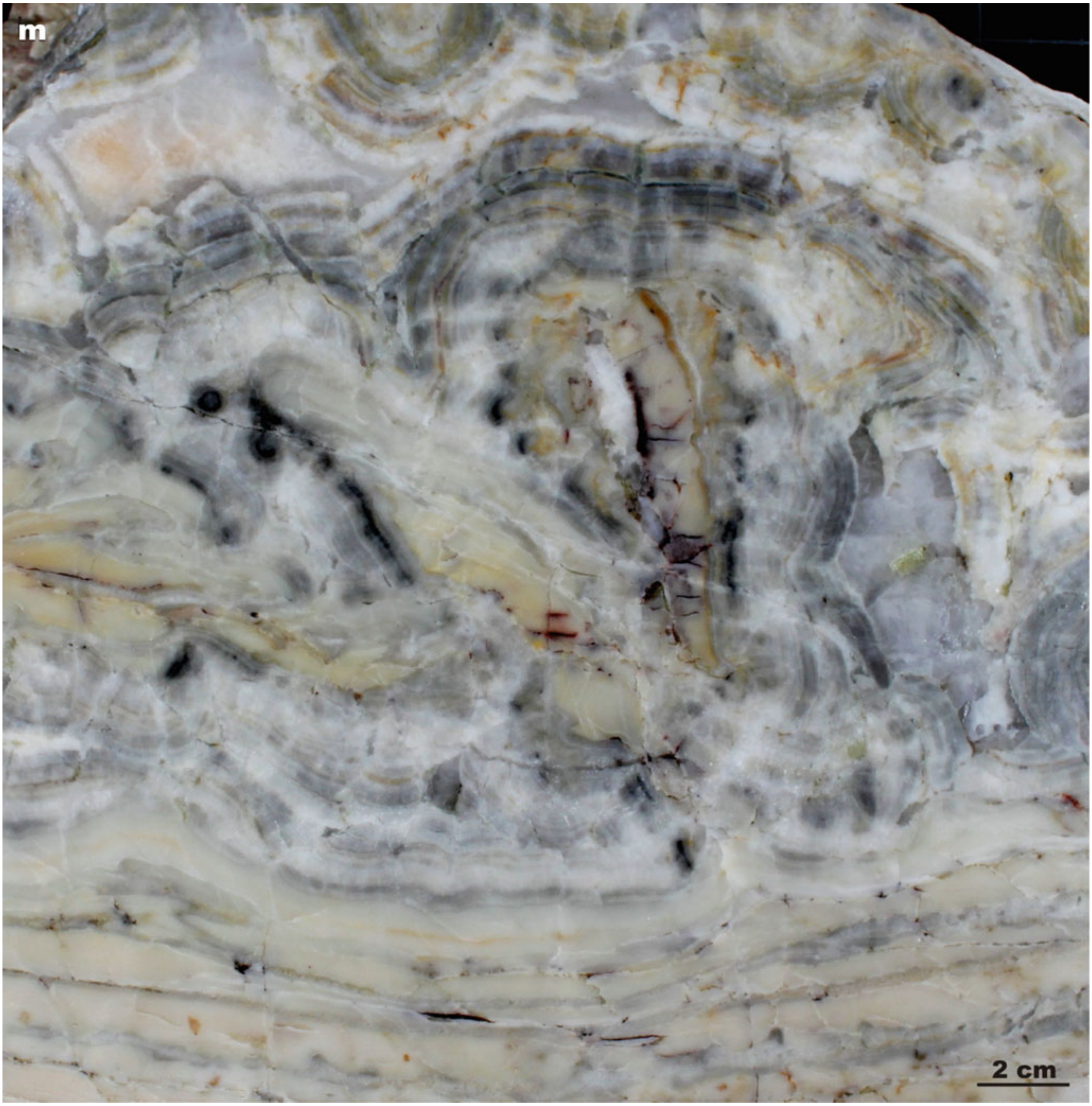

Fig. 6.51 (continued) (**m**) Beige, laminated, dolomitic travertine crust capped by syn-depositionally brecciated travertine mounds and stalactites; black coloration due to impregnation by finely disseminated haematite. Sample collected from a quarry located near the drilling site

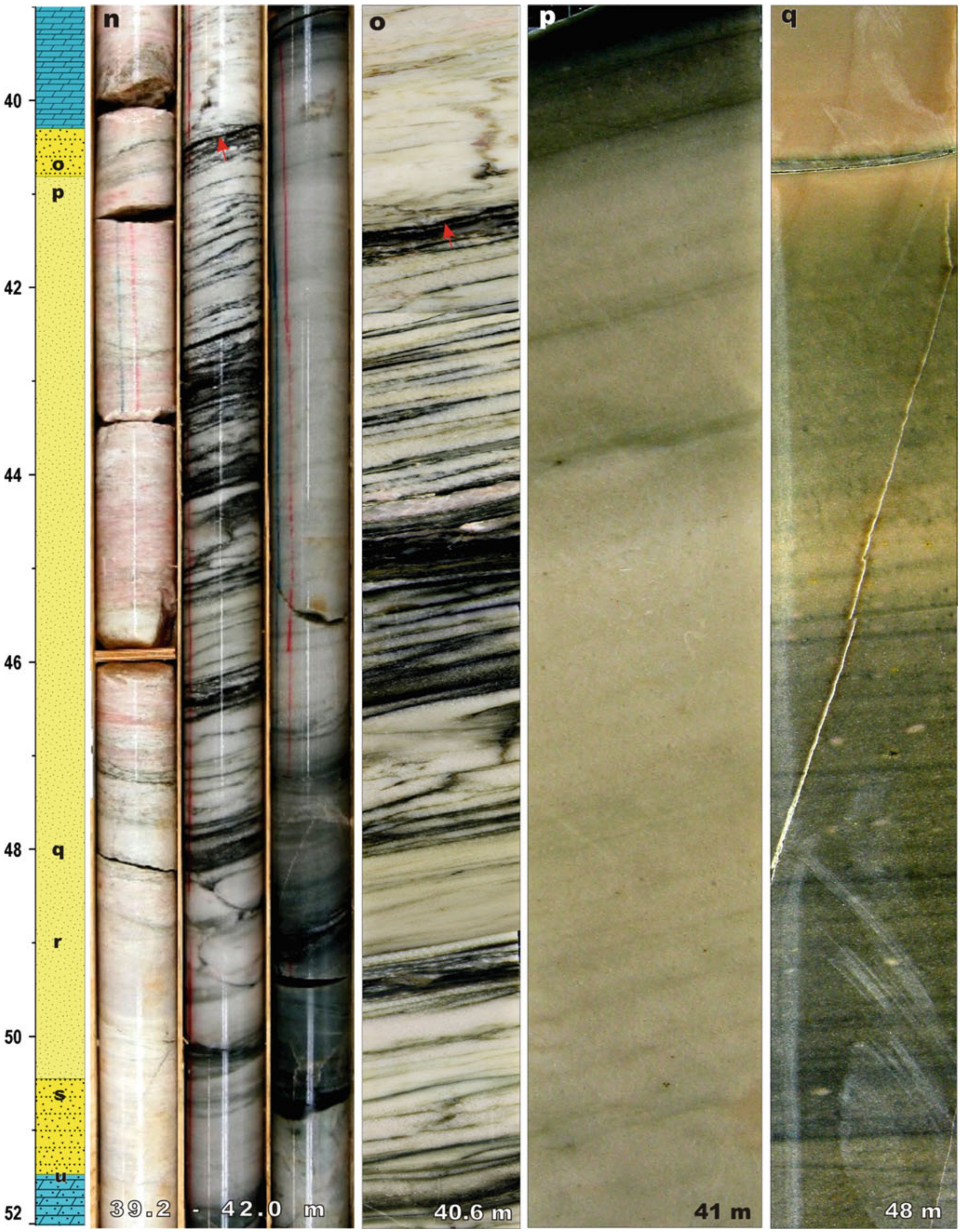

Fig. 6.51 (continued) (**n**) Selected core interval illustrating the transition and the contact (*arrowed*) between the Quartzite and *Upper* Dolostone members; thickly bedded, vaguely laminated, quartz sandstone passes upward into thinly bedded sandstone-mudstone couplets with intervals showing lenticular bedding; this is sharply overlain by white dolostone. (**o**) Close-up view of the photograph (**n**) detailing a structure of interbedded sandstone and dark-coloured mudstone layers; note, in the *middle* a c. 6-cm-thick, dark-coloured interval with lenticular bedding. (**p**) Light-coloured, indistinctly laminated, medium-grained quartz sandstone grading into black, clayey sandstone. (**q**) Grey, clayey, parallel and low-angle cross-bedded, arkosic sandstone grading into pink-grey, parallel-laminated and pink, massive, fine-grained quartz sandstone with siltstone layer

Fig. 6.51 (continued) (**r**) Parallel-laminated, fine to medium-grained, arkosic sandstone with thin siltstone layers grading into dark-coloured siltstone bed. (**s**) Parallel-laminated, medium-grained, dolomite-cemented greywacke. (**t**) Selected core interval illustrating the transition and the contact (*arrowed*) between the Lower Dolostone and Quartzite members; bright coloured dolarenite sharply overlain by interbedded silty breccia, dolorudites and dolomite-cemented, quartz sandstone containing large angular and rounded fragments of dolostone clasts. (**u**) Polymict breccia and bed with inverted stromatolites or travertine stalactites within white dolarenite (*top* and *bottom*); clasts in the breccia are jasper (*dark red*) and dolostone (*white*)

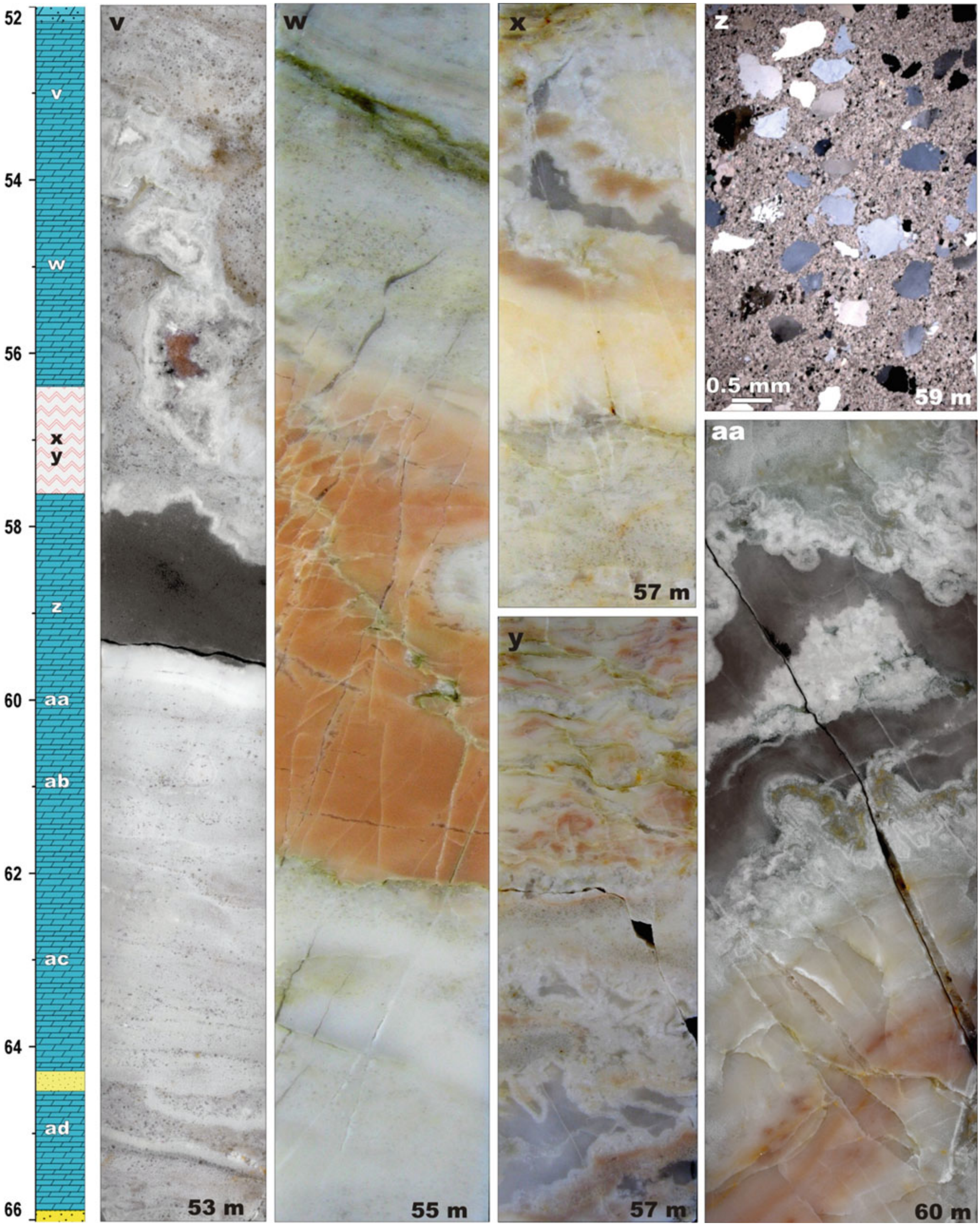

Fig. 6.51 (continued) (**v**) Indistinctly bedded, dolomite-cemented sandstone (*bottom*) separated from sandy dolostone (*bright*) by a grey, quartz-filled dissolution cavity; the dolostone is injected by a travertine vein. (**w**) White, non-bedded dolostone with an eroded *upper* bedding surface capped by pink, non-bedded, fractured travertine crust covered by dolomite-cemented quartz sandstone; the travertine crust contains a white dolarenite intraclast. (**x**) Dolarenite overlain by beige, micritic or travertine dolostone injected by a white travertine veinlet containing a void filled with grey silica. (**y**) Travertine with cavities filled by quartz (*pale grey*). (**z**) Photomicrograph in polarised light of dolostone containing floating, angular clasts of quartz. (**aa**) White, beige and buff, dolomitic travertine crust with quartz-filled cavities; note that travertine has grown inward from both sides of the cavity with the remaining space filled with grey silica

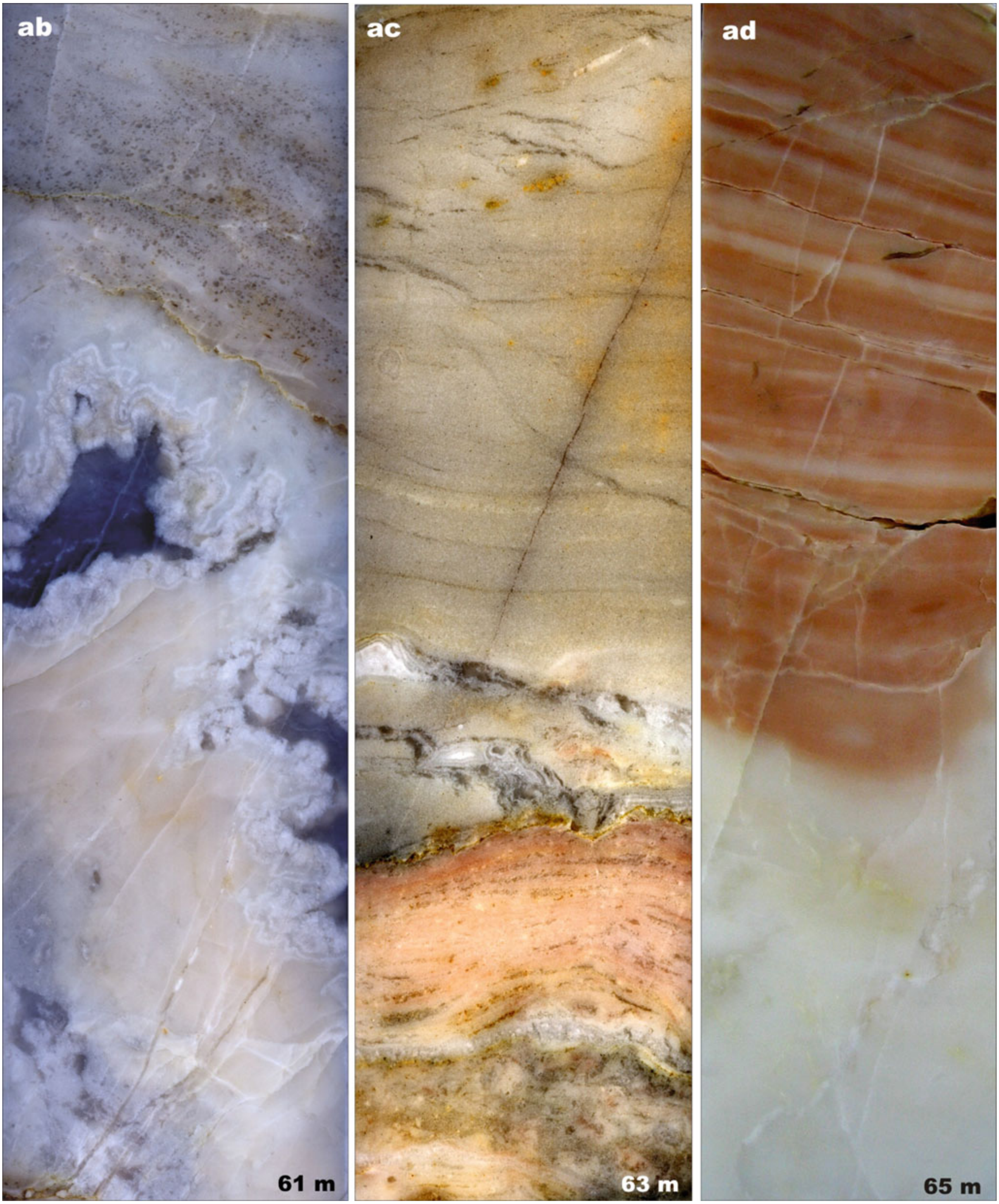

Fig. 6.51 (continued) (**ab**) White and beige, dolomitic travertine crust with a clotted microfabric and quartz-filled cavities overlain by dolomite-cemented quartz sandstone; note that travertine has grown inward from both sides of the cavity with the remaining space filled with grey silica. (**ac**) Travertine veinlets occurring in between pale pink and buff, parallel-laminated, micritic dolostone. (**ad**) White, massive, micritic dolostone overlain by pink, laminated dolostone

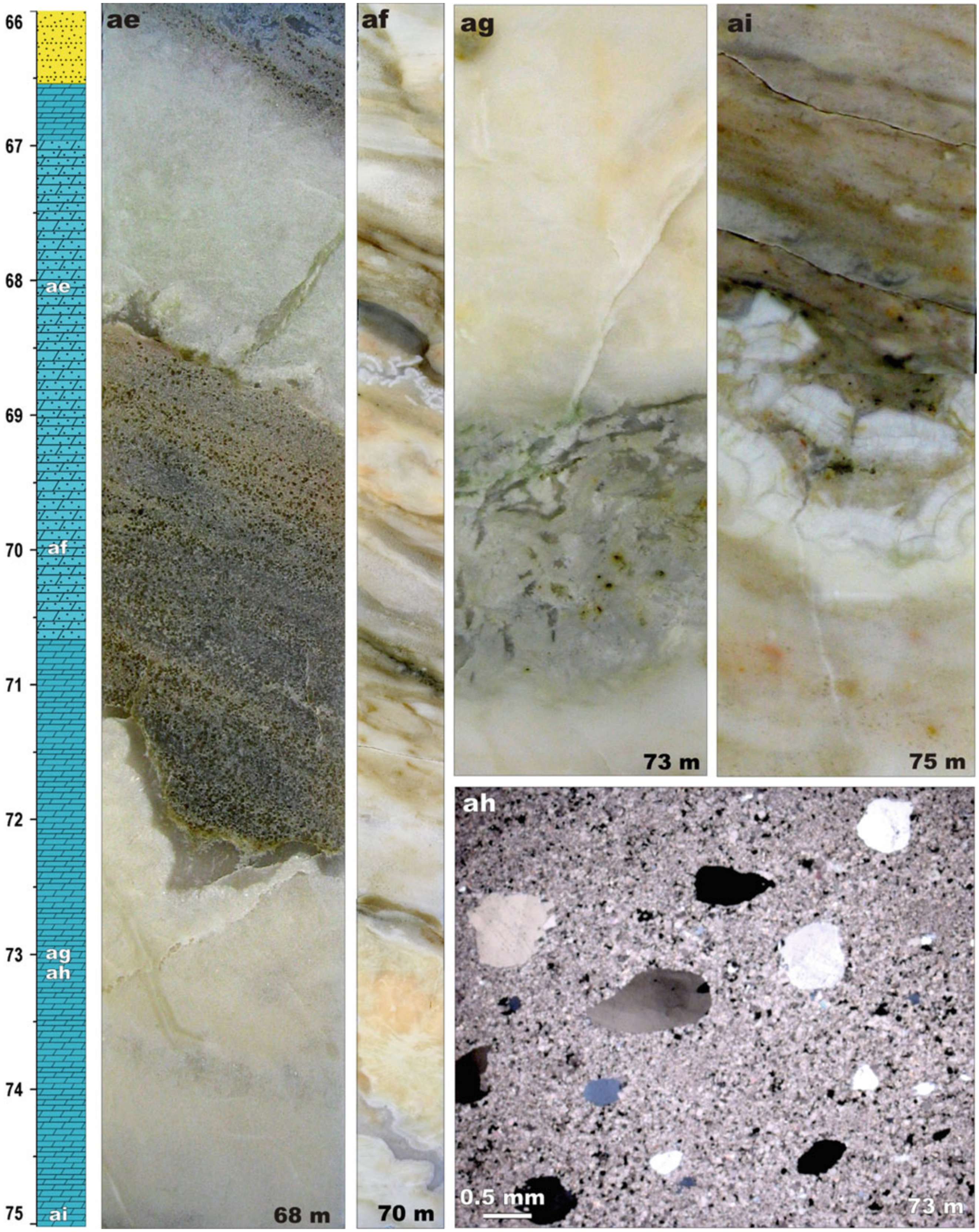

Fig. 6.51 (continued) (**ae**) White travertine crusts with an uneven *upper* surface veneered by silica sinter (*pale grey*) and covered by parallel-laminated quartz sandstone; this is in turn overlain by another travertine dolomite crust (bright) with quartz sandstone on *top* (*grey*). (**af**) Irregularly interbedded dolarenite, micritic dolostone, dolomite-cemented sericite-quartz sandstone, and white and beige dolomite travertine with quartz-filled cavities. (**ag**) Grey-coloured, siliceous dolostone with silica-filled voids overlain by beige, micritic dolostone. (**ah**) Photomicrograph in polarised light of micritic dolostone with scattered, variably rounded quartz clasts. (**ai**) Uneven surface on *top* of beige, sandy, micritic dolostone covered by a syn-depositionally brecciated travertine crust that is overlain by bedded dolarenite

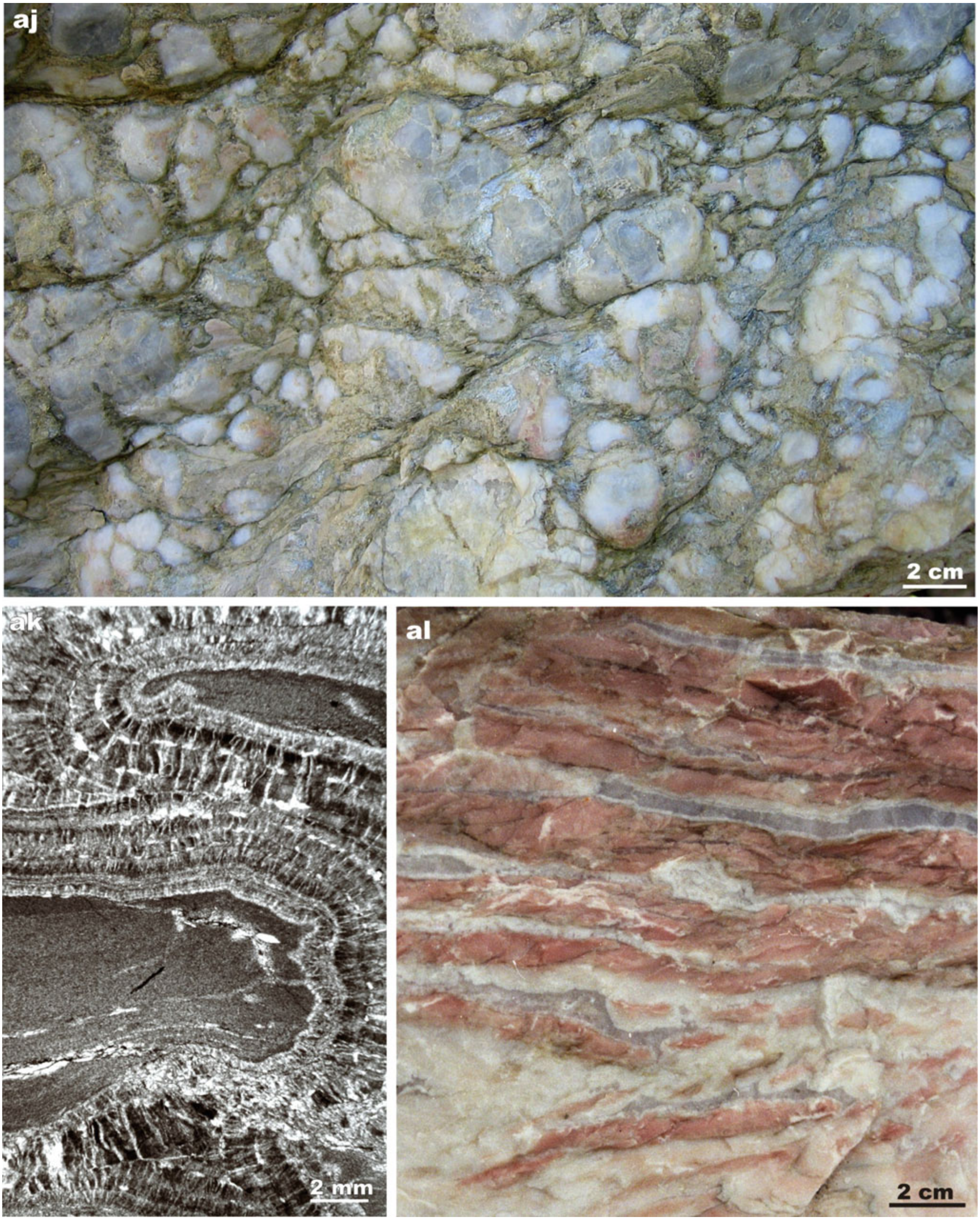

Fig. 6.51 (continued) (**aj**) Exhumed surface of travertine crust from a quarry adjacent to the drilling site. (**ak**) Photomicrograph in non-polarised light of dolomicrite fragments cemented by banded travertine dolomite; sample taken from drillcore X located c. 20 km northwest of Hole 5A. (**al**) A quarry wall showing pink, dolomicritic dolostone with white dolomite travertine and grey silcrete

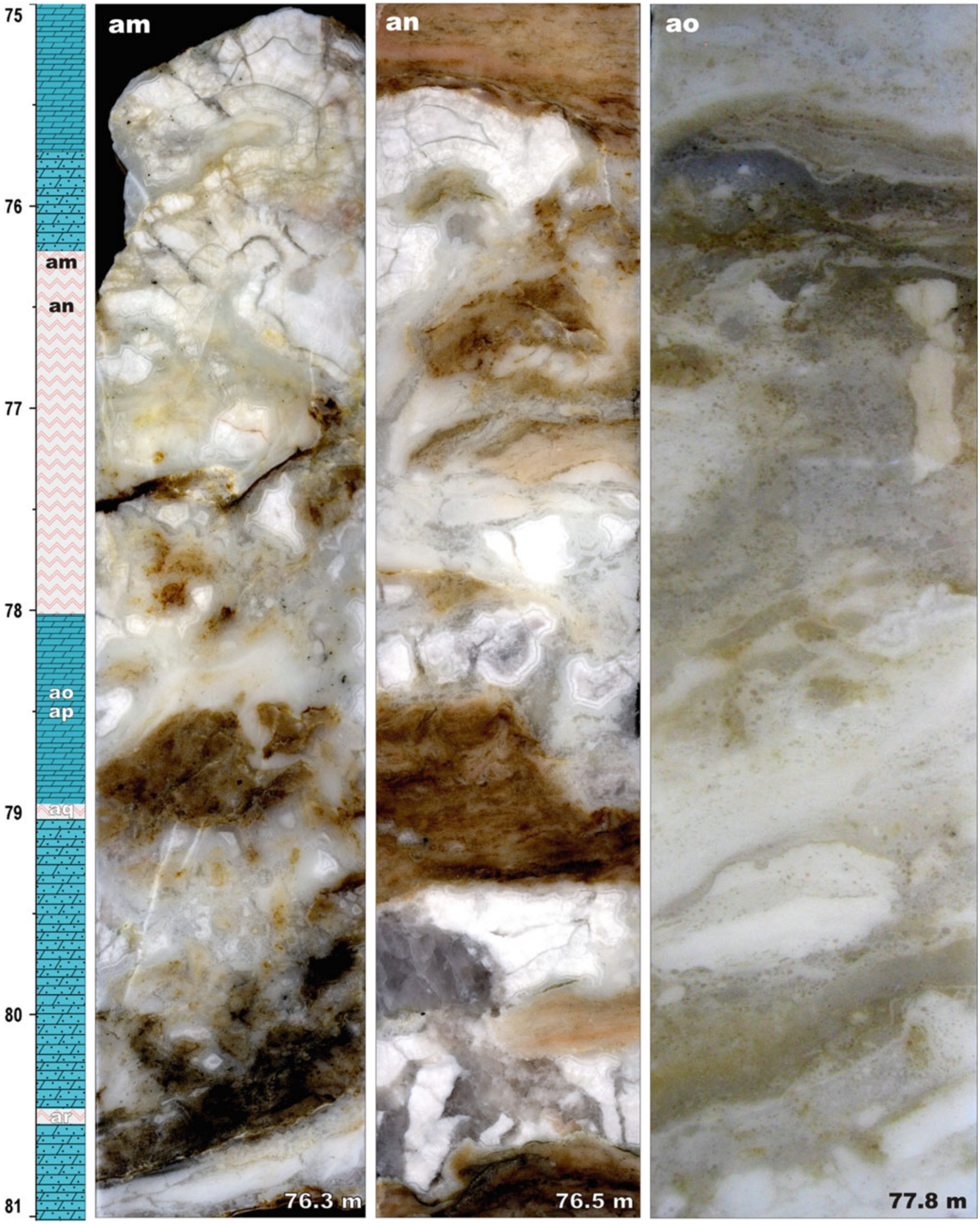

Fig. 6.51 (continued) (**am**) White, dolomitic travertine cementing brown, clayey siltstone; note that the *top* of the core demonstrates an "exhumed" *upper* surface of travertine mounds. (**an**) White, dolomitic travertine cementing brown, clayey siltstone and buff dolarenite; note that the *upper* surface of the travertine mound is covered by pale brown, dolomite-cemented sandstone. (**ao**) A series of erosive contacts between dolomite-cemented sandstone (*grey*) and in-situ-brecciated and soft-deformed, dolomicritic dolostones; note the thin layer of dark grey quartzitic sandstone in the *upper* part

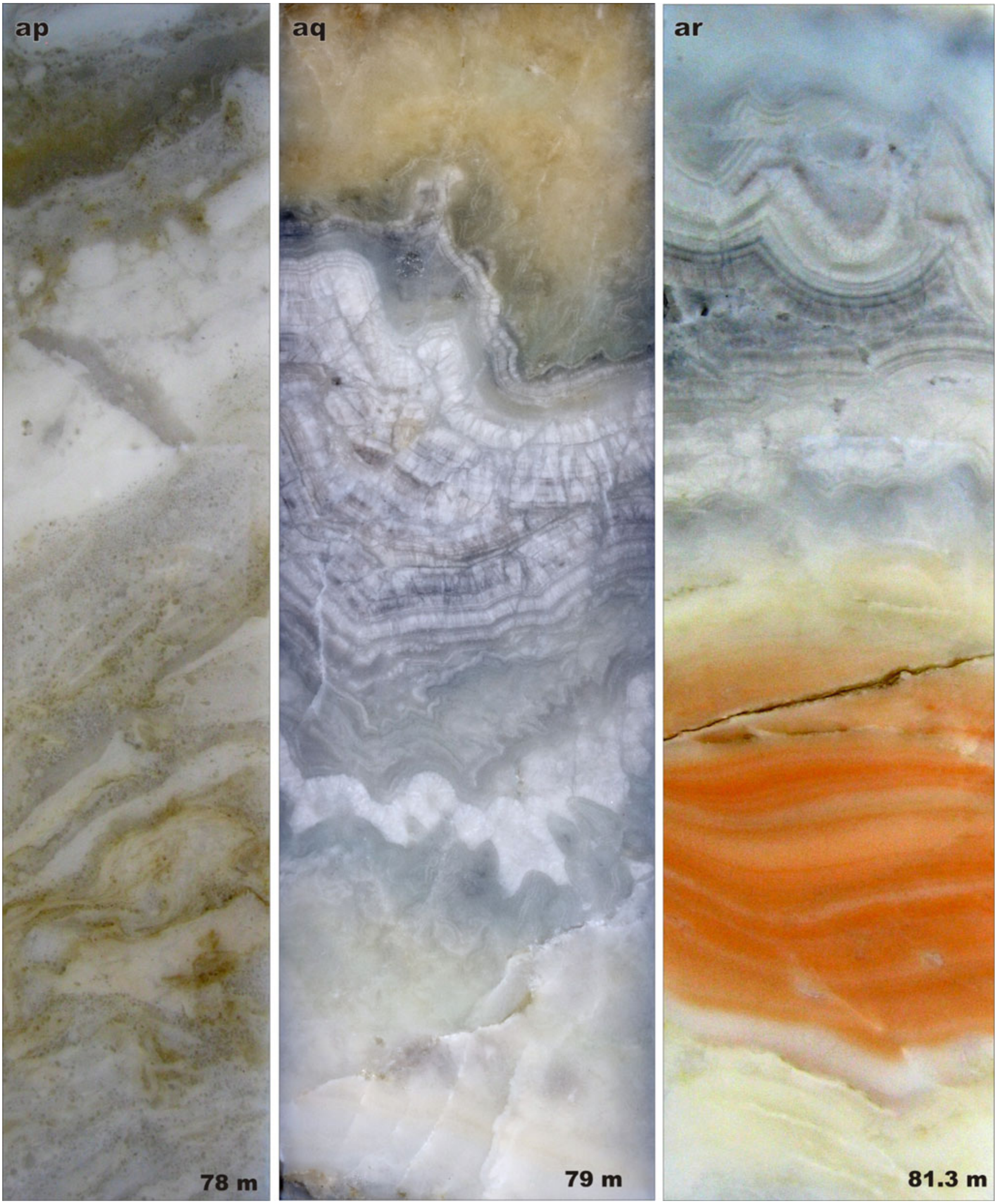

Fig. 6.51 (continued) (**ap**) Dolomite-cemented sandstone containing soft-deformed clasts of beige, micritic dolostone and in-situ-brecciated, white, dolomicritic bed; note the dark grey, quartzitic sandstone layer with an erosive base on *top*. (**aq**) White and grey, banded, dolomitic travertine crust overlain by yellowish, dolomitic travertine with a clotted microfabric. (**ar**) Red and white, banded, dolomitic travertine passing into white and grey travertine with a clotted microfabric, which is capped by a laminated travertine crust and travertine "stalactites"

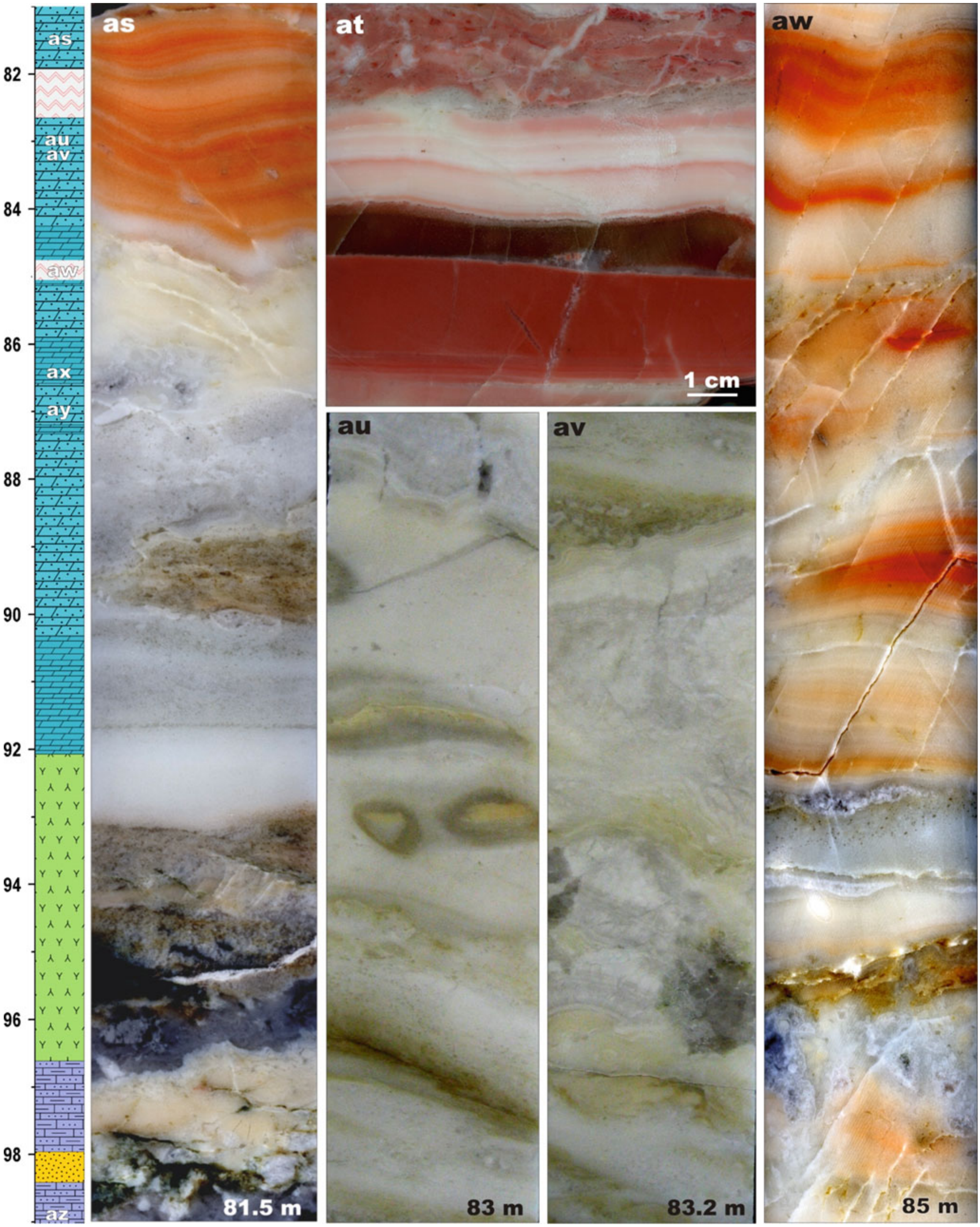

Fig. 6.51 (continued) (**as**) Dark-coloured dolarenite with dolostone fragments overlain by white, dolomicritic dolostone passing into light-coloured dolarenite, which is capped by pink, laminated dolomite travertine. (**at**) Red travertine layer overlain by dark grey quartzite with a rippled surface capped by white and pale-pink, laminated travertine and pink dolarenite; sample collected from a quarry adjacent to the drilling site. (**au**) Dolarenite with silica-rimmed, pale yellow dolomicrite clasts; note irregular bedding and a dolomite travertine crust on the *top*. (**av**) In-situ-brecciated dolarenite partially cemented by travertine (*white*); note the erosional surface on *top*. (**aw**) Variegated, banded travertine bed

Fig. 6.51 (continued) (**ax**) Indistinctly bedded dolarenite with travertine veinlets and thin crusts. (**ay**) Selected core intervals demonstrating irregular bedding in the Lower Dolostone member. (**az**) Parallel-laminated limestone-sandstone-siltstone

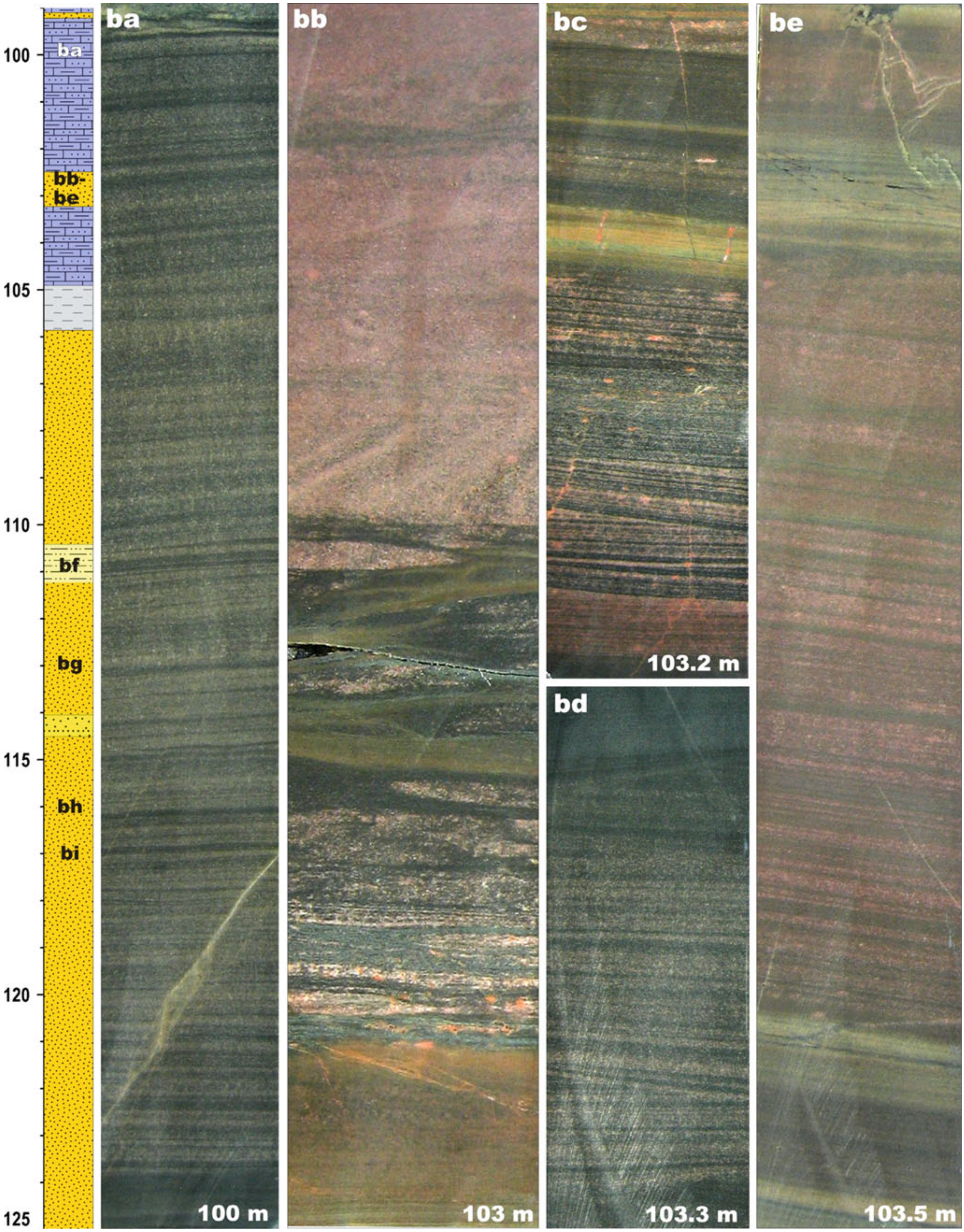

Fig. 6.51 (continued) (**ba**) Dark-coloured, parallel-laminated, calcareous sandstone-siltstone. (**bb**) Yellow-brownish, massive sandstone (*bottom*) overlain by variegated sandstone-siltstone-mudstone with lensoidal and low-angle cross lamination; this is followed by pink sandstone showing trough cross-bedding. (**bc**) Variegated, laminated sandstone-siltstone-mudstone with parallel and low-angle cross lamination; note that the light-coloured shale unit exhibits both parallel and low-angle cross-lamination. (**bd**) Dark grey, low-angle cross-laminated, thinly interbedded sandstone-siltstone. (**be**) Variegated, parallel-laminated, arkosic sandstone (*pink*) and siltstone-shale (light coloured)

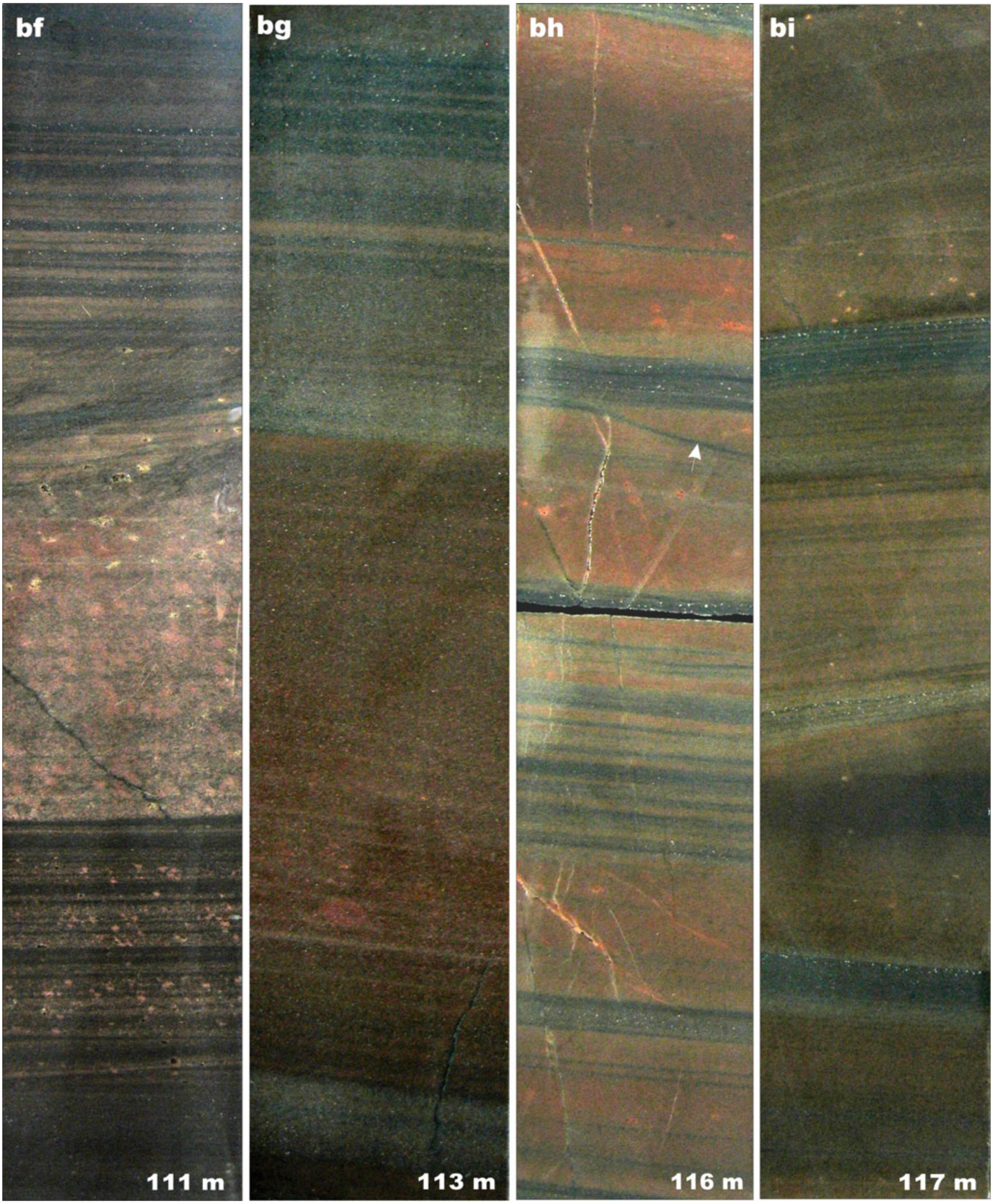

Fig. 6.51 (continued) (**bf**) Dark-coloured, parallel-laminated, sandy siltstone overlain by pinkish, carbonate-cemented, arkosic sandstone grading into cross-laminated sandstone-siltstone, which is overlain by parallel-laminated sandy-siltstone. (**bg**) Dark brown, parallel-laminated, medium-grained, arkosic sandstone overlain by dark green sandstone. (**bh**) Variegated, parallel-bedded, fine-grained, arkosic sandstone with dark-coloured siltstone layers; note the small-scale, sandstone-filled channel (*arrowed*). (**bi**) Variegated, fine-grained, arkosic sandstone with parallel lamination and low-angle, tabular cross-bedding; some sandstone beds grade into dark-coloured, haematite-rich siltstone

Fig. 6.51 (continued) (**bj**) Selected core that represents the arkosic sandstone unit; the general structural pattern is defined by irregular intercalations of thicker, dark-coloured, haematite-rich beds of arkosic sandstone and thinner, light-coloured, sericite-rich interlayers of clayey, arkosic sandstone

Fig. 6.51 (continued) (**bk**) Parallel-bedded arkosic sandstone with thin shale interlayers with "ball-and-pillow" structures in the overlying sandstone unit (Photograph was taken from an outcrop located c. 30 km northwest of the drilling site)

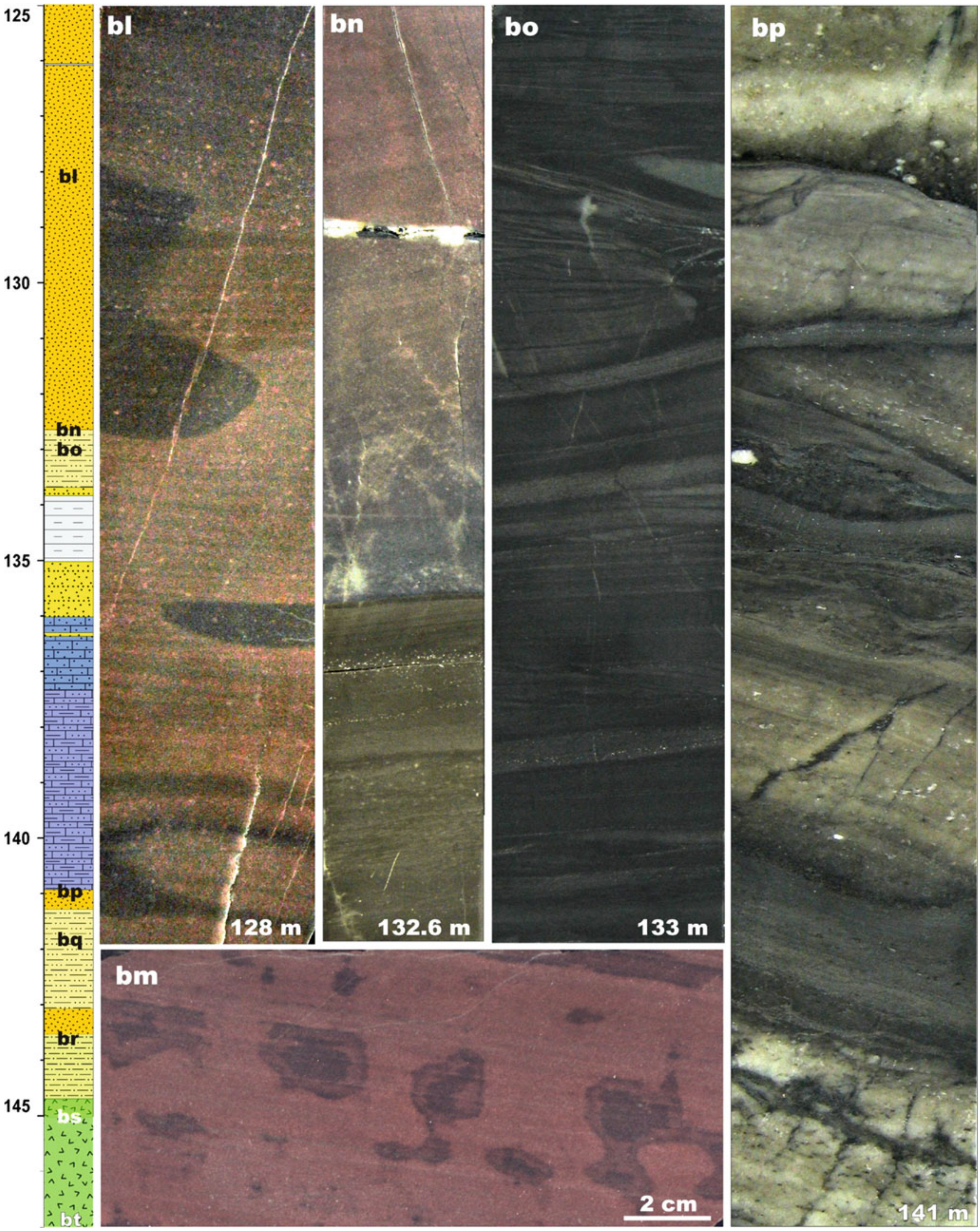

Fig. 6.51 (continued) (**bl**) Low-angle cross-laminated and parallel-laminated, fine- to medium-grained, mottled arkosic sandstone; note that the primary dark-brown colour was partially bleached by reducing catagenetic fluids. (**bm**) Parallel-laminated, mottled, arkosic sandstone; sample was collected 15 km northwest of the drilling site; note that the primary dark-brown colour was partially bleached by reducing catagenetic fluids. (**bn**) Dark-coloured siltstone overlain by grey and pale-brown arkosic sandstone; note gradual discolouration in the sandstone bed towards the siltstone. (**bo**) Trough cross-bedded, fine to medium-grained arkosic sandstone and siltstone; some sandstone layers are carbonate-cemented. (**bp**) Interbedded arkosic sandstone (bright) and siltstone-shale (dark-coloured) with parallel and low-angle cross-lamination; some sandstone units show graded bedding and have an erosional base

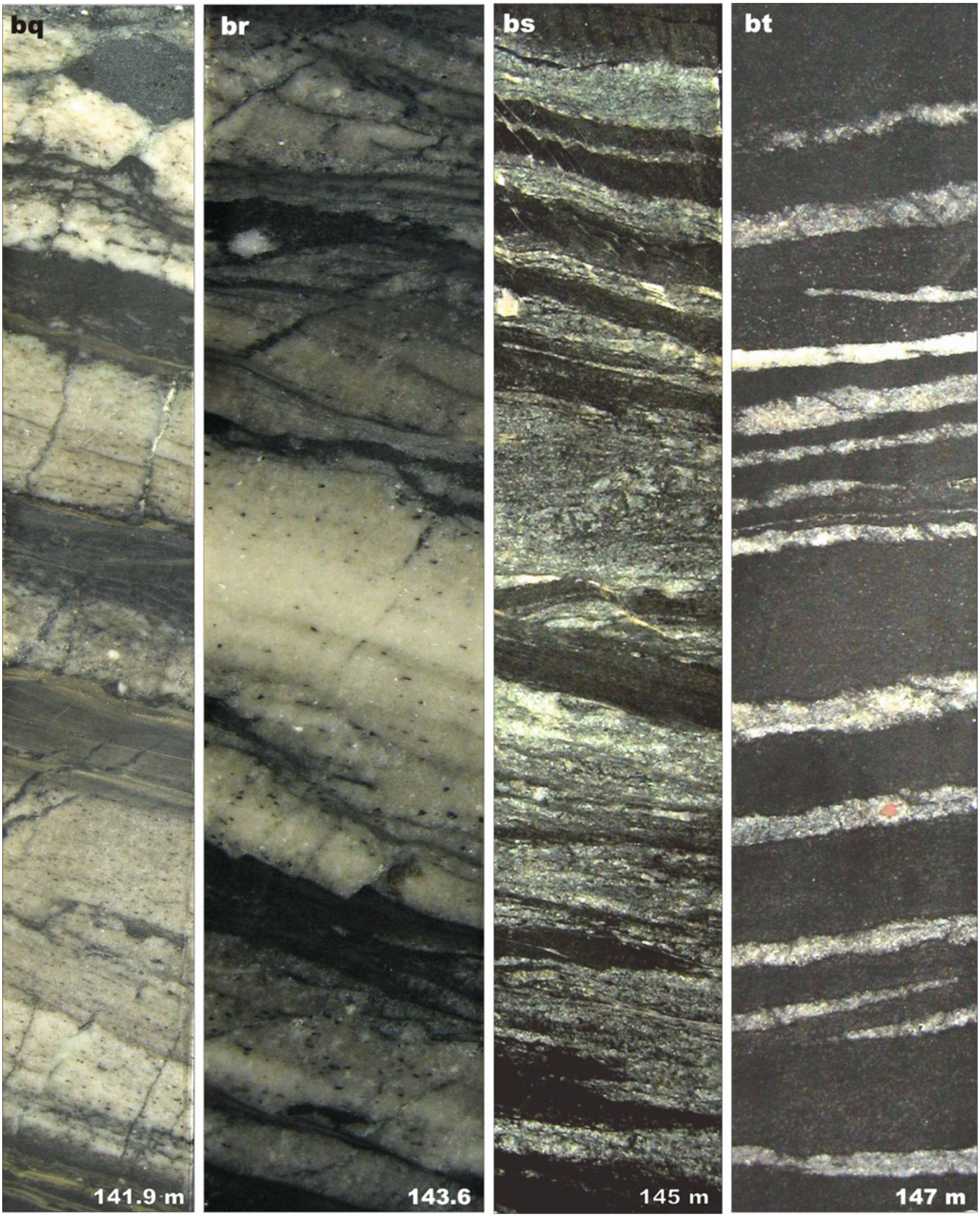

Fig. 6.51 (continued) (**bq**) Rhythmic interbedding of arkosic sandstone (bright) and clayey siltstone-shale showing slightly disrupted, parallel and low-angle cross lamination; some sandstone beds are graded. (**br**) Synsedimentary, disrupted trough cross-bedded, calcite-cemented, arkosic sandstone (light-coloured), clayey sandstone (*dark grey*) and mudstone (dark-coloured). (**bs**) Indistinctly bedded, calcite-albite-sericite-biotite-chlorite schist (redeposited weathering crust?) with well-developed rhythmic bedding in the *upper* part. (**bt**) Intensely altered Ahmalahti Formation andesite appearing as sericite-calcite-chlorite-albite-biotite-actinolite schist with chlorite-calcite bands (*white*); an ophitic texture is partially preserved (Photographs (**a–bt**) by Victor Melezhik)

References

Amelin YuV, Heaman LM, Semenov VS (1995) U-Pb geochronology of layered mafic instrusions in the eastern Baltic Shield; implications for the timing and duration of Paleoproterozoic continental rifting. Precambrian Res 75:31–46

Hanski EJ, Smolkin VF (1995) Iron- and LREE-enriched mantle source for early Proterozoic intraplate magmatism as exemplified by the Pechenga ferropicrites, Kola Peninsula, Russia. Lithos 34:107–125

Karhu JA (1993) Palaeoproterozoic evolution of the carbon isotope ratios of sedimentary carbonates in the Fennoscandian Shield. Bull Geol Surv Finland 371:1–87

Karhu JA, Holland HD (1996) Carbon isotopes and the rise of atmospheric oxygen. Geology 24:867–870

Melezhik VA, Fallick AE (1996) A widespread positive $\delta^{13}C_{carb}$ anomaly at around 2.33–2.06 Ga on the Fennoscandian Shield: a paradox? Terra Nova 8:141–157

Melezhik VA, Fallick AE (2001) Palaeoproterozoic travertines of volcanic affiliation from a ^{13}C-rich rift lake environment. Chem Geol 173:293–312

Melezhik VA, Fallick AE (2005) Palaeoproterozoic, rift-related ^{13}C-rich, lacustrine carbonates, NW Russia. Part I: sedimentology and major element geochemistry. Trans R Soc Edinb Earth Sci 95:393–421

Melezhik VA, Fallick AE, Grillo SM (2004) Subaerial exposure surfaces in a Palaeoproterozoic ^{13}C-rich dolostone sequence from the Pechenga greenstone belt; palaeoenvironmental and isotopic implications for the 2330–2060 Ma global isotope excursion of $^{13}C/^{12}C$. Precambrian Res 179:75–103

Melezhik VA, Huhma H, Condon DJ, Fallick AE, Whitehouse MJ (2007) Temporal constraints on the Paleoproterozoic Lomagundi-Jatuli carbon isotopic event. Geology 35:655–658

Predovsky AA, Fedotov ZhA, Ahkmedov AM (1974) Geochemistry of the Pechenga complex. Nauka (Science), Leningrad, p 139, in Russian

Sun SS, McDonough WF (1989) Chemical and isotopic systematics of oceanic basalts; implications for mantle composition and processes. In: Saunders AD, Norry MJ (eds) Magmatism in the ocean basins, vol 42, Geological Society special publication. Published for the Geological Society by Blackwell Scientific Publications, Oxford/Boston, pp 313–345

6.2.3 Kuetsjärvi Volcanic Formation: FAR-DEEP Hole 6A and Related Outcrops

Eero J. Hanski, Victor A. Melezhik, Aivo Lepland, Alexander E. Romashkin, Dmitry V. Rychanchik, Zhen-Yu Luo, Evgenii V. Sharkov, and Maria M. Bogina

Scientific Target

– Radiometric age constraint on timing of deposition
– Palaeomagnetic study
– Testing an upper-mantle oxidising hypothesis
– Groundwater chemistry (study of amygdaloidal infills)
– Geochemistry of palaeoweathered surfaces in response to the Great Oxidation Event

Hole 6A is located in the Pechenga Greenstone Belt (Fig. 6.1) and is one of the three FAR-DEEP drillholes transecting the Kuetsjärvi Volcanic Formation (Figs. 6.52 and 6.53). It intersects the middle part of the formation whereas the other two holes, 5A and 7A, intersect the lower and upper contacts of the formation, respectively. The depositional age of the Kuetsjärvi Volcanic Formation has been constrained to 2058 ± 2 Ma by dating zircons from volcaniclastic conglomerates interbedded with lavas, and detrital zircons from overlying fluvial and volcaniclastic sedimentary rocks in the basal part of the Kolosjoki Sedimentary Formation that were sourced from the Kuetsjärvi Volcanic Formation (Melezhik et al. 2007). This age places a younger limit to the Lomagundi-Jatuli positive carbon isotopic excursion of sedimentary carbonates recorded in the underlying Kuetsjärvi ^{13}C-rich carbonates (Fig. 6.33).

Hole 6A recovered more than 300 m of lavas (Fig. 6.54) and provides a valuable resource to address the evolution of the redox-state of iron oxide phases in magmatic, and post-volcanic hydrothermal processes, as well as oxidation/reduction by surface and groundwaters through the study of primary magmatic minerals, amygdaloidal infills, and vertical transects of individual lava flows. The Kuetsjärvi volcanic rocks have high Fe^{3+}/Fe_{total} ratios (0.6 on average), which are in sharp contrast to the lower ratios (<0.25) in the majority of all other volcanic formations of the Pechenga Greenstone Belt (for details see Chaps. 3.4 and 7.4). The oxidised nature of these volcanic rocks represents an unusual and as yet unexplained phenomenon. The rocks may represent either evidence for relatively oxidised mantle material (e.g. recycled banded iron formations; e.g. Kump et al. 2001) or a large-scale alteration of Earth's surface by oxic meteoric and/or groundwaters. Either outcome will represent a significant contribution to our knowledge on the oxygenation of terrestrial environments during the Great Oxidation Event. The predominantly intermediate to felsic composition of the volcanic rocks of the Kuetsjärvi Volcanic Formation, and diverse amygdaloidal mineralogy associated with the ancient surface and groundwater alterations (Fig. 6.55) offer an excellent opportunity to obtain geochronological data on the volcanism and post-volcanic hydrothermal and surface oxidation processes.

The Kuetsjärvi Volcanic Formation has a thickness of more than 1,000 m and is divided into two approximately equal parts, separated by a c. 30-m-thick unit of volcaniclastic conglomerate (for details see Chap. 4.2). Hole 6A starts 20 m above this conglomerate unit and intersects the entire formational thickness (313 m; Fig. 6.52). The drilled section has been tentatively subdivided into the lower Andesite-Rhyolite member, the middle Conglomerate member, and the upper Basalt member (Melezhik et al. 1994).

The 313.2-m-long Core 6A recovered mostly volcanic rocks with magma types varying from picritic through trachyandesitic to rhyolitic; one prominent sedimentary section (Conglomerate member) occurs at interval 22–50 m and consists entirely of volcaniclastic detritus. The sedimentary unit is underlain by a 264 m sequence of volcanic rocks of the Andesite-Rhyolite member. In order to facilitate core description and handling geochemical data, these rocks are informally divided into seven sections based on magma chemistry and defined as, from base to top, Units A to G (Figs. 6.55, 6.56, 6.57, and 6.58). The single volcanic unit overlying the Conglomerate member is assigned to Unit H, forming the lower part of the Basalt member.

Photos taken of core intervals and supplementary outcrops and thin section scans provide detailed documentation of the major lithological features (Fig. 6.60a–at) features. All primary mafic silicate phases are replaced by secondary minerals, mostly amphibole and chlorite. Nevertheless, the structural and textural preservation is very good and in places superb. Chemical compositions of the analysed archive samples are presented in Appendices 13 and 14, and Fig. 6.53 shows selected major and trace element distributions as a function of stratigraphic height.

The whole core displays a high degree of oxidation. This phenomenon is discussed elsewhere in more detail (Chaps. 3.4 and 7.4). It suffices to mention here that there is a general increase in the oxidation state upwards in the core until the appearance of the *Conglomerate member*, above which $Fe^{3+}/(Fe^{3+} + Fe^{2+})$ returns sharply to lower values. Figure 6.53 shows the variation of magnetic susceptibility in Core 6A as a function of stratigraphic height. The rocks are among the most magnetic recovered in FAR-DEEP drillcores, with magnetic susceptibility values in the range of 11,000–111,000 μSI ($K^* = 1{,}000–10{,}000 \times 10^{-6}$ SI units

E.J. Hanski (✉)
Department of Geosciences, University of Oulu, P.O. Box 3000, 90014 Oulu, Finland

V.A. Melezhik et al. (eds.), *Reading the Archive of Earth's Oxygenation*, Volume 2: The Core Archive of the Fennoscandian Arctic Russia – Drilling Early Earth Project, DOI 10.1007/978-3-642-29659-8_3, © Springer-Verlag Berlin Heidelberg 2013

in Fig. 6.53). There are two exceptions, the tholeiitic and picritic basalt sections at depths of 6.4–11.6 m and 66.0–77.7 m with values of 880–1,800, 440–2,900 μSI, respectively ($K^* = 80–160 \times 10^{-6}$ SI, $40–260 \times 10^{-6}$ SI, respectively). This is due either to a low content of oxides (tholeiite) or strong oxidation of iron (haematisation of picrite). The highest susceptibility (132,000–333,000 μSI; $K^* = 12,000–30,300 \times 10^{-6}$ SI) is shown by a single, 4-m-thick alkali basaltic lava flow in Unit E. The Conglomerate member also yielded mostly high but variable magnetic susceptibility 800–132,000 μSI ($K^* = 70–12,000 \times 10^{-6}$ SI in Fig. 6.53).

Andesite-Rhyolite Member

Unit A

Unit A (313.8–301.8 m) at the bottom of the core is composed of massive intermediate lava, which likely forms two flows of 5 and 7 m in thickness. Petrographically the rocks are microcrystalline, aphyric and non-vesicular, only containing sparse plagioclase microlites. As a result of variable total alkali contents, the analysed samples from Unit A can be classified as trachyandesite, mugearite or benmoreite, but the immobile trace element concentrations are approximately the same for all samples. This suggests that some disturbances have occurred in the major element compositions, particularly one sample which has MgO (<2 wt.%) lower than the others (4.8–5.7 wt.%). Nevertheless, the magma was originally mildly alkaline and we assume that all samples had a trachyandesitic primary composition. The alkaline affinity is indicated, for example, by high Nb/Y ratios of 0.75–0.92 (Fig. 6.56b). The rocks have low Ni and Cr contents (7–23 and 19–35 ppm, respectively), which demonstrate a relatively fractionated nature of the magma. The chondrite-normalised REE patterns exhibit a pronounced negative slope (Fig. 6.58a). The trace element data available for two samples are similar, with the exception of LREEs. The sample with higher LREE has negative Nb-Ta anomalies (Fig. 6.58b) and we assume that this sample is more representative of Unit A.

Unit B

Unit B at interval 301.8–252.7 m is a homogeneous, holocrystalline mafic body, which is free of amygdales and does not show any recognisable volcanic structures. The central part of this c. 50-m-thick unit is more coarsely crystalline than the upper and lower parts, but still remains fine-grained as the mineral size is equal to or less than 1 mm. The texture changes towards the margins from subophitic to aphanitic and originally the rock was composed of equal-sized pyroxene, plagioclase and ilmenomagnetite with the latest mineral exhibiting skeletal habits. It is noteworthy that internal differentiation led to crystallisation of quartz-feldspar intergrowths in the interstitial space between plagioclase and pyroxene (now amphibole) grains.

Chemically the analysed samples can be classified as basaltic andesites of tholeiitic affinity. Vertically the unit is rather homogeneous with MgO varying between 4.1 and 4.4 wt.%, excluding one altered sample that has MgO of 7.5 wt.% (Fig. 6.56a). Compared to the underlying unit (TiO_2 c. 1.8 wt.% and FeO_T 10–11 wt.%), Unit B has a relatively low TiO_2 content (1.3–1.4 wt.%), but is rich in iron (FeO_T 13.6–14.4 wt.%). Chemically Unit B is most easily distinguished from the rest of the core by its Nb/Y ratio, which is c. 0.25, the lowest in the entire Core 6A. Low Nb/Y is consistent with the subalkaline nature of the unit as opposed to the alkaline nature of underlying and overlying Units A and C. The original subalkaline affinity is also consistent with the presence of the aforementioned interstitial quartz and quartz-feldspar intergrowths. The magma had LREE/HREE higher than chondritic but the ratio was lower than in the adjacent units, as evident in the crossing trace element patterns in Fig. 6.58a, b. Because of the lack of evidence for a subaerial emplacement, and given its differing geochemical affinity compared to the rest of the core, we interpret Unit B as an intrusive body not belonging to the same stage of magmatism as the overlying and underlying volcanic rocks. However, in the overlying volcanic sections within Core 6A or 7A, or in the Kolosjoki and Pilgujärvi Volcanic Formations higher up in the stratigraphy, no chemically equivalent volcanic rocks are presently known for which Unit B could have acted as a feeder conduit.

Unit C

Unit C (252.7–206.3 m) contains eight microcrystalline, mafic lava flows with thicknesses ranging from c. 2 to 9 m, that are separated by six lava breccia interlayers having thicknesses between 2 and 5 m. Three lava flows are massive and free of macroscopic amygdales, one is only sparsely amygdaloidal and the rest are highly amygdaloidal. The size of the quartz-chlorite-filled amygdales varies from microscopic (<0.1 cm) to 2–3 cm in diameter, with one (filled with quartz) being >10 cm near the top of one of the lava flows (at 230.30 m). The fragmental interbeds contain irregular-shaped clasts up to c. 10 cm in size (Fig. 6.60as), which show a slight orientation roughly perpendicular to the core. Some clasts display a trachytoidal texture and many are amygdaloidal (Fig. 6.60at). They are composed of the same material as the lava flows and possibly represent surficial rubble of aa-type lava flows.

The present-day chemistry of the rocks classifies them as mugearites and trachyandesites. However, MgO has a large range between 1 and 6 wt.%; this variation is probably due to alteration and does not represent initial concentrations. Also SiO_2 varies widely (52.5–62.0 wt.%) and is decoupled from many other elements, potentially due to metasomatism by a silica-rich fluid, as shown by the presence of additional SiO_2 in amygdales. There is, though, good correlation between immobile, incompatible elements, which suggests a similar parental magma for all samples from this section of the core, including both fragmental rocks and lava flows. Cr and Ni contents are low (usually <20 ppm), indicating a fractionated nature of the magma. The Nb/Y ratio straddles the boundary between subalkaline and alkaline rocks (Fig. 6.56b). Chondrite-normalised REE patterns show a negative slope with the flat HREEs (Fig. 6.58c), and the spidergram shows distinct negative anomalies for Nb, Ta and P (Fig. 6.58d). Units A and C are very similar in their major and trace element characteristics (see Fig. 6.57b, for example), which lends support to the interpretation that the intervening Unit B is intrusive in nature.

Unit D

Unit D (206.3–101.4 m) is heterolithic, containing intermediate to felsic lavas and interfingering volcaniclastic rocks. The rocks are crypto- to microcrystalline and mostly aphyric, containing only erratic, small plagioclase phenocrysts. There are 11 breccia zones (Fig. 6.60n, q–r, t–v) with thicknesses of 1–4 m and c. 20 non-brecciated intervals 1–16 m in thickness. The lavas in the lower part of the section contain amygdales large enough to be seen by naked eye (Fig. 6.60ah), filled with various material including quartz, chlorite, albite, carbonate, biotite, haematite and jasper. Amygdales in the upper part are mostly microscopic. In the middle part of the section, even microamygdales are very rare. Figure 6.60ad–ar illustrate well-preserved amygdaloidal textures in the lower part of the section. Many of the amygdales show evidence of strain due to late-stage flow in the increasingly viscous lava, resulting in stretching out of gas bubbles. At a depth of c. 174–177 m, primary textures are perfectly preserved in amygdales, including concentric, cryptocrystalline, agate-like chalcedony-haematite banding (Fig. 6.60ae–af), demonstrating the low-degree of metamorphic recrystallisation and tectonic deformation of the rocks.

Flow banding structures are very common in lavas throughout the middle and upper parts of the unit (Fig. 6.60w–x, z, aa–ac), making this section different from the rest of the core. Secondary oxidation of iron (haematization) commonly follows and emphasises the banded structure (Fig. 6.60p). Similar banding is also present in breccia fragments (Fig. 6.60v), and it is likely that the brecciated intervals in the core do not represent distinct eruptions but were formed by breaking down of moving, partly solidified, viscous lava. Undulating flow banding and rock fragmentation have also been recognised in the outcrops of the drilling area (Fig. 6.60y). Another kind of fragmentation is associated with formation of polygonal contraction joints enhanced by syn- and post-volcanic haematisation (Fig. 6.60s).

The measured major element compositions of the rocks are variable, as indicated, for example, by the silica contents ranging between c. 55 and 70 wt.%, which make the rocks chemically similar to trachyandesites to rhyolites. However, in the lower part of the section, abundant quartz-bearing amygdales complicate the interpretation of the bulk rock chemical data. Also there exists a negative correlation between Na_2O and K_2O, which is likely not a magmatic feature of the rock suite. Therefore the rock names of Unit D (see Fig. 6.53) are assigned with caution. In the stratigraphic column, rocks displaying flow banding structures are considered most evolved and are termed rhyodacites while the massive, more-or-less amygdaloidal lavas are classified as trachydacites, though there are some discrepancies between major and trace element signatures (see below).

Despite the above mentioned complications, immobile elements show a systematic behaviour. For example, on a Nb/Y vs. Zr/TiO_2 diagram (Fig. 6.56b), the analyses plot in a restricted area, mostly in the field of trachyandesites, suggesting a similar parental magma for all samples. Nb/Y indicates a slightly alkaline nature of the magma, but Zr concentrations (220–400 ppm) are not as high as in trachyandesite-trachyte series in general. There is a good correlation between TiO_2 and Zr elsewhere in Core 6A, but a clear decoupling of these components in Unit D, as shown in the chemical profile of Fig. 6.53. Consequently, Unit D differs significantly from the other units in having very low Ti/Zr, from 14 to 32, while this ratio elsewhere in the core is ≥ 60 (Fig. 6.57a). This difference is due to both relatively low TiO_2 and high Zr in Unit D. There is some internal variation in Ti/Zr within Unit D, as the samples with a depth greater than 168 m have higher ratios (23–32), though being still unusually low relative to the other units of the core (Fig. 6.57a). The above-mentioned depth is the boundary between flow-banded and massive lavas. A very similar relationship to that seen in Fig. 6.57a is obtained if, instead of Ti/Zr, Ti/Th is plotted against depth (not shown): Ti/Th is much lower in Unit D (380–1,060) than in other units ($>2,100$). This is again due to both relatively low TiO_2 and high Th in Unit D (cf. Fig. 6.57b). The rocks of Unit D are also exceptional in plotting outside the 'normal' range of basalts from different geotectonic environments in the discrimination diagram of Pearce and Cann (1973) (Fig. 6.59a). With the exception of the subalkaline Unit B, the other volcanic units from Core 6A plot in the field of within-plate basalts in this diagram. A likely reason for the different behaviour of Unit D is that it is more evolved than the others; Ti/Zr tends to decrease with increasing crystal fractionation in the basalt-trachyte or basalt-rhyolite series (e.g. Mollel et al. 2009). Another geochemical feature that distinguishes Unit D (and also the two subunits from each other within

Unit D) is its V concentration or, to lessen the effects of secondary features such as quartz-bearing amygdales, the V/Al ratio (see Fig. 6.59b).

Figures 6.58c, d compare REE and other incompatible trace element characteristics of the rocks of Unit D and the underlying trachyandesitic rocks of Unit C. Abundances are higher in Unit D, but the shapes of the patterns are similar with the exception of the presence of slight negative Eu anomalies and a more pronounced depletion in Ti in Unit D.

One sample representing a fragmental rock at depth of 136.5 m is exceptionally rich in REEs: Ce 1680 ppm, Sm 31 ppm, and Nd 540 ppm. Otherwise the composition is similar to that of other samples in the interval. The high REE content is probably a result of incorporation of accidental secondary allanite into the bulk rock analysis. Allanite is a ubiquitous accessory mineral in Core 6A, occurring mostly in amygdales (for detail see Chap. 7.4).

Unit E

Unit E (101.4–77.6 m) is made up of three mafic lava flows with thicknesses between 3 and 12 m. They contain abundant, quartz-chlorite filled amygdales, up to 4 cm across, particularly close to the upper and lower contacts (Fig. 6.60k). The grain size of the lava is fine ($\leq$0.5 mm) but coarser than in the underlying Unit D. There is also a 2-m-thick fragmental layer, which is likely a volcaniclastic conglomerate containing lava fragments up to 12 cm in size (Fig. 6.60l, m). Some of the pebbles are cut by haematite banding similar to those found in clasts of the Conglomerate member proper (see below).

The lavas are alkali basalts with MgO between 4.2 and 6.2 wt.%, TiO_2 c. 2.2 wt.% and Cr and Ni abundances of 40–125 and 80–105 ppm, respectively. In terms of Ti/Zr, the boundary between Units D and E is as distinct as the boundary between Units C and D, as the ratio resumes the “normal” value of c. 70–80 in Unit E (Fig. 6.57a). In contrast to the negative Ti anomaly of Unit D, Unit E displays a slight positive Ti anomaly (Fig. 6.58f). Apart from Ti and Eu, the trace element characteristics are very similar to those in Units C, D and E (Fig. 6.58c–f).

Unit F

Unit F (77.6–63.3 m) represents the most primitive rocks of Core 6A and consists of two lava flows with thicknesses of c. 6 and 8 m. The flows are composed of fine-grained, olivine-phyric picritic basalt having carbonate- and quartz-filled amygdales up to 5 mm in diameter. Olivine phenocrysts reach 5 mm in size and are now replaced by chlorite $\pm$ haematite, quartz and carbonate. The unit contains cm-scale siltstone xenoliths (Fig. 6.60j). Four analyses of lava samples gave MgO contents from 10.5 to 12.9 wt.%, Ni concentrations between 290 and 360 ppm, and Cr concentrations from 850 to 1360 ppm. TiO_2 is c. 2.0 wt.% and FeO_T from 11.9 to 14.6 wt.%; the latter is lower than in the Pilgujärvi Volcanic Formation ferropicrites that occur higher in the stratigraphy (Fig. 6.33). Given the primitive character of the rocks, they are nevertheless relatively rich in incompatible trace elements such as LREEs (Ce 55–67 ppm), Nb (13 ppm), Zr (172–228 ppm), and P_2O_5 (0.3 wt.%), deviating only slightly from the abundances of the underlying more evolved unit E (Fig. 6.58e–f). Values of Nb/Y (0.64–0.76) indicate a slightly alkaline character of the magma, and $(Ce/Nb)_{PM}$ of 2.2 suggests some crustal contamination.

Unit G

Unit G (63.0–49.6 m) is separated from the underlying volcanic rocks by a 0.3-m-thick sandstone-siltstone layer, one of the rare sedimentary rocks in the core aside from the Conglomerate member. Unit G contains two fine-grained mafic lava flows, the lower one is 2 m and the upper one is 13 m thick. The latter is sparsely olivine-phyric with the phenocrysts now replaced by chlorite + haematite. There is an amygdale-rich contact zone (Fig. 6.60i) between the two lava flows, but the exact boundary cannot be determined accurately. The upper part of the section is devoid of macroscopic amygdales, which suggests that the original upper contact zone of the lava is not present in the core but was eroded before deposition of the overlying Conglomerate member. The upper flow contains abundant, a-few-mm-wide haematite bands (Fig. 6.60h), which can also form 5 to 15-cm-diameter rings (Liesegang rings). This banding is found within a vertical distance of 10 m from the palaeoweathering surface represented by the Unit G-Conglomerate member contact.

The two lava flows have variable silica content, which likely does not represent initial abundances. The rocks have an alkaline affinity, as evident by high Nb/Y of 0.72–0.81 (Fig. 6.56b) and originally were probably trachyandesites. The TiO_2 content is the highest within Core 6A (2.8–3.1 wt.%), and the FeO_T content is amongst the highest (14.4–17.1 wt.%). The rocks are enriched in LREE relatively to HREE (Fig. 6.58g) and exhibit strong negative P anomalies and slight positive Ti anomalies in the primitive mantle-normalised spidergram of Fig. 6.58h.

Conglomerate Member

The volcaniclastic Conglomerate member (49.61–19.9 m) is represented by five fining-upward cycles, all differing in thickness and composition (Fig. 6.52). The lowermost conglomerate (11 m)-siltstone (1.2 m) cycle, the thickest in the member, is followed by a sandstone (3.4 m)-siltstone (0.2 m), conglomerate (0.7 m)-gritstone (0.6 m), conglomerate (6.7 m)-siltstone (0.3 m) and finally by conglomerate (4.3 m)-sandstone (1.5 m) cycle.

All conglomerate units are clast-supported with a volcaniclastic sandstone matrix (Fig. 6.60c, g). Clasts are well-rounded, moderately-sorted fragments of lavas, ranging in size from 40 cm in the lowermost cycle to 15 cm in the uppermost cycle. A clast analysed from the lowermost conglomerate unit is chemically similar to the underlying Unit G lava. Some of the pebbles and cobbles are highly amygdaloidal, whereas others are massive, which indicates derivation from various depths of an eroded lava flow or lava flows. Moreover, clasts vary in composition from mafic to felsic (Fig. 6.60c) suggesting that the underlying volcanic pile has been eroded to a considerable depth. Several volcanic clasts display Liesegang rings formed by haematite banding (Fig. 6.60c, e), which are very similar to those found in the underlying Unit D volcanic rocks (Fig. 6.60h). This demonstrates that the banding in the underlying lava flows was formed prior to deposition of the conglomerate.

Gritstone is rare and comprises the upper unit in one thin conglomerate-gritstone cycle. Although the gritstone dominates in the unit, it is interbedded with grey to dark violet, haematite-rich, volcaniclastic sandstone-siltstone-mudstone layers with parallel lamination (Fig. 6.60d); several layers exhibit normal grading.

In the middle part of the Conglomerate member, volcaniclastic sandstones are the dominant lithology and comprise the lower unit of the sandstone-siltstone cycle. The sandstones are massive or indistinctly bedded with scattered, oversized, rounded clasts of lava. Another similar sandstone occurs in the upper member of the uppermost conglomerate-sandstone cycle. This sandstone is massive and has a gradational contact with the underlying conglomerate.

The two beds of siltstone comprising the upper units in conglomerate-siltstone cycles are similar and display distinct parallel-bedding emphasised by the irregular appearance of dark brown and dark violet, haematite-rich layers (Fig. 6.60b). However, some intervals in the lower and thicker siltstone unit contain fine-grained sandstone beds (Fig. 6.60f). In the three analysed siltstone interbeds, Cr is relatively high ranging between 395 and 416 ppm. This might indicate the presence of detrital material from the underlying picritic basalt of Unit F.

Basalt Member

Unit H

The uppermost part of the core, assigned to Unit H (19.9–0 m), is represented by a homogeneous, fine-grained, massive mafic lava, with large, ovoidal or more irregular amygdales in the top part of the core between depths 0 and 5 m (Fig. 6.60a); this is also observed in nearby outcrops (Fig. 6.55). The amygdales are variably filled with minerals including epidote, axinite, K-felspar, albite, quartz, chlorite and biotite. Red K-feldspar probably precipitated originally as a low-temperature potassic feldspar, adularia (Fig. 6.60a). In addition to an amygdale infilling, the violet Ca-Al-borosilicate axinite forms veinlets up to 2 cm in thickness. The outcrop observation suggests that Hole 6A starts from very close to the top of a lava flow with columnar joints, and Unit H represents a single lava flow. The analysed samples are basaltic in composition, having MgO in the range of 4.9–5.4 wt.%, TiO_2 c. 2.0 wt.%, and Ti/Zr of 76–77. The chemical affinity of Unit H is Fe-rich tholeiitic, unlike the mildly alkaline underlying volcanic Units C–G (Fig. 6.56b). The rocks of Unit H are less enriched in most incompatible elements than the rocks in Unit G, as shown by crossing trace element patterns in Fig. 6.58g–h, but the general incompatible trace element characteristics of the units are still comparable.

Depositional Framework

The data obtained from Hole 6A together with those from Holes 5A and 7A and other published data from the Kuetsjärvi Volcanic Formation (e.g. Predovsky et al. 1974; Skuf'in et al. 1986; Skuf'in and Yakovlev 2007) indicate that the formation is overwhelmingly composed of subaerially erupted lavas accumulated within an intraplate continental rift setting. Subaqueous deposition was rare and was associated with small-scale ephemeral lakes developed during erosional phase of the Andesite-Rhyolite member (for details see **Chap. 4.2**). Such ephemeral lakes have also been sites for accumulation of volcaniclastic sediments.

Despite the high lithological and chemical heterogeneities, the original nature of most volcanic rocks intersected by Hole 6A seems to have been alkaline but was disturbed to various extents by crustal contamination. On the other hand, outcrop samples from other parts of the formation also record basanitic/nephelinitic trace element signatures, probably representing less- or non-contaminated magmas (Hanski and Smol'kin (unpublished data)). Although plenty of analytical data are available from the Kuetsjärvi Volcanic Formation, low-Ti/Zr rocks characteristic of Unit D have not been reported previously.

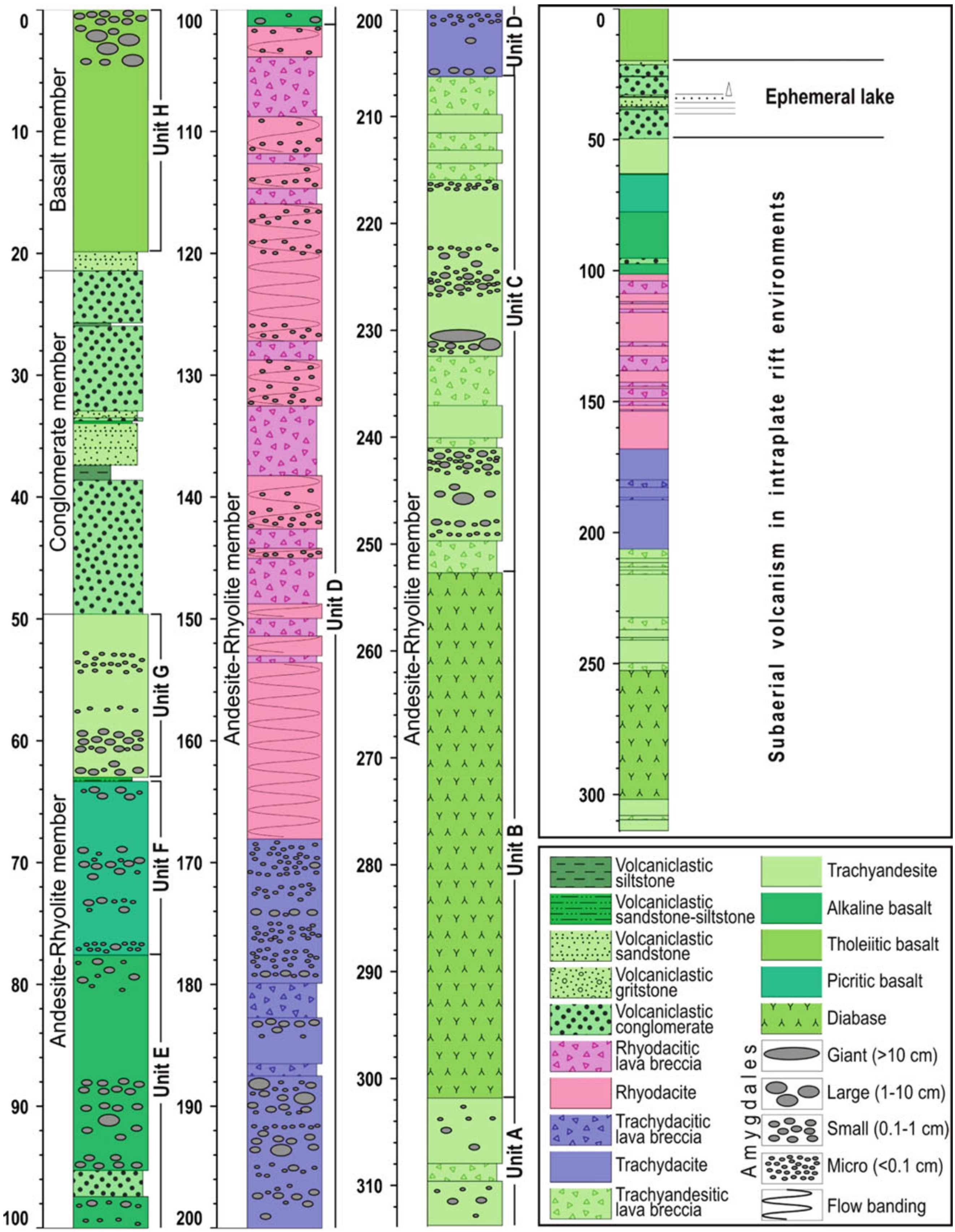

Fig. 6.52 Lithological section of the middle part of the Kuetsjärvi Volcanic Formation based on core logging of Hole 6A. Lithological symbols are explained in Fig. 6.6

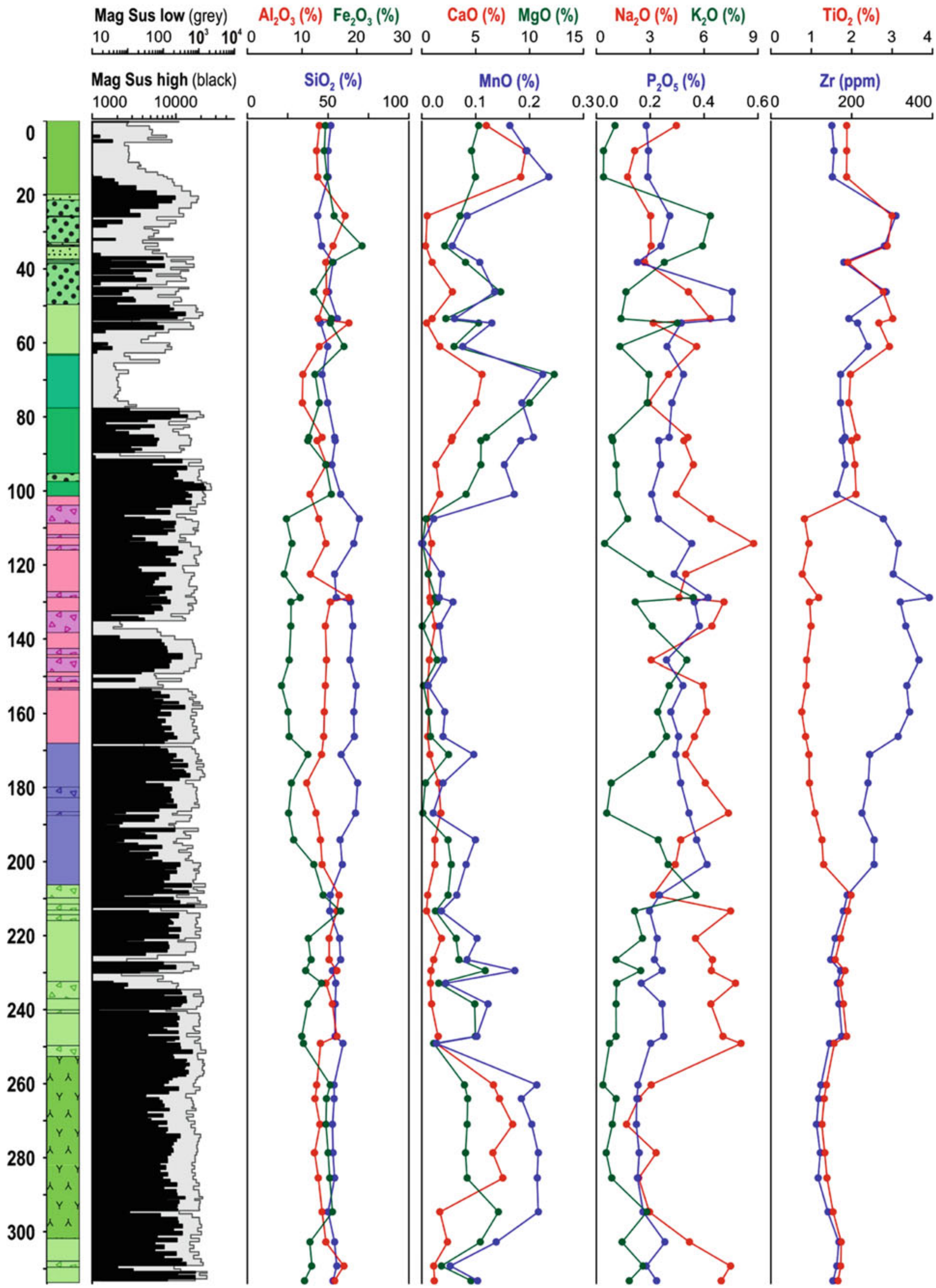

Fig. 6.53 Relative magnetic susceptibility (K*), and geochemical profiles of selected elements based on the archive samples collected with c. 8 m-spacing. For analytical techniques and data quality see **Part 5**

Fig. 6.54 Trachydacite fluidal lava with black haematite-magnetite-rich bands, and lava breccia with lava fragments separated by black haematite-magnetite-rich bands. This occurs on the top of the Kuetsjärvi Volcanic Formation beneath the Kolosjoki sedimentary rocks. The black "bands" contain up to 25 wt.% Fe_{tot}, apparently accumulated as the result of post-volcanic hydrothermal alteration or surface weathering or a combination of both. The rocks represent an attractive target to address chemistry of fluids modifying erosional surfaces. The rocks should also retain their primary magnetic properties and can be potentially used for palaeomagnetic studies as the oxide-rich bands are pre-metamorphic in origin. Width of the view is c. 1 m (Photograph by Victor Melezhik)

Fig. 6.55 Large, spherical amygdales filled with axinite (*violet*) and epidote (*green*) with minor chlorite, quartz and feldspar in a basalt flow with columnar joints extruded onto the Conglomerate member volcaniclastic sandstones. A complex mineralogical infill of amygdales can be used to track chemistry of groundwaters from which this mineral assemblage was precipitated. Width of view c. 20 cm (Photograph by Victor Melezhik)

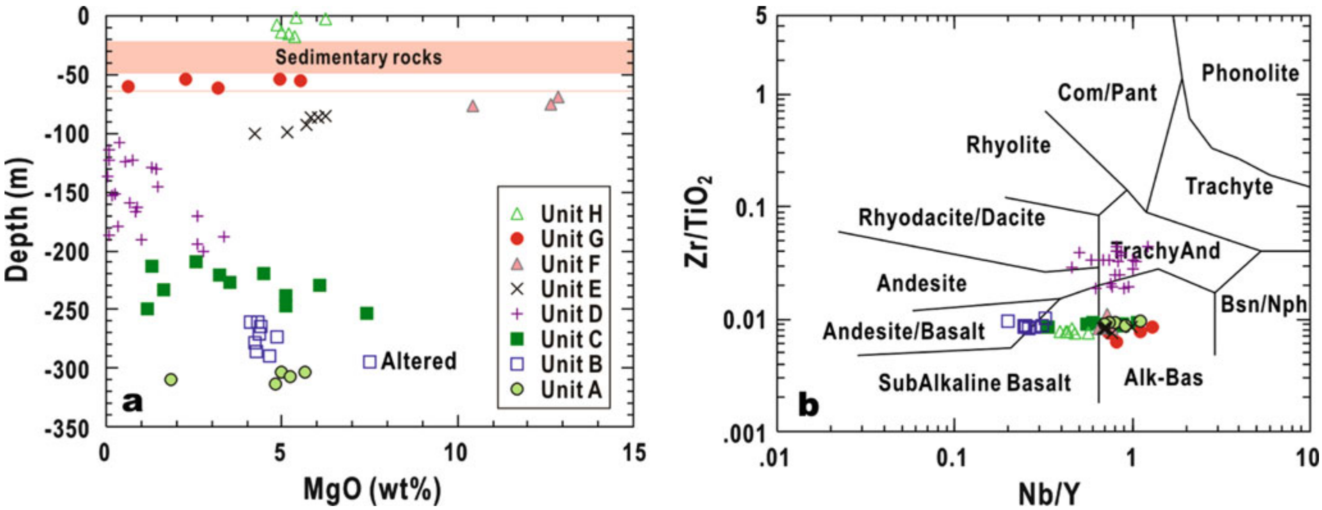

Fig. 6.56 MgO versus depth (**a**) and Nb/Y versus Zr/TiO_2 (**b**) diagrams for igneous rocks from Core 6A. Boundaries of the fields in (**b**) after Winchester and Floyd (1977)

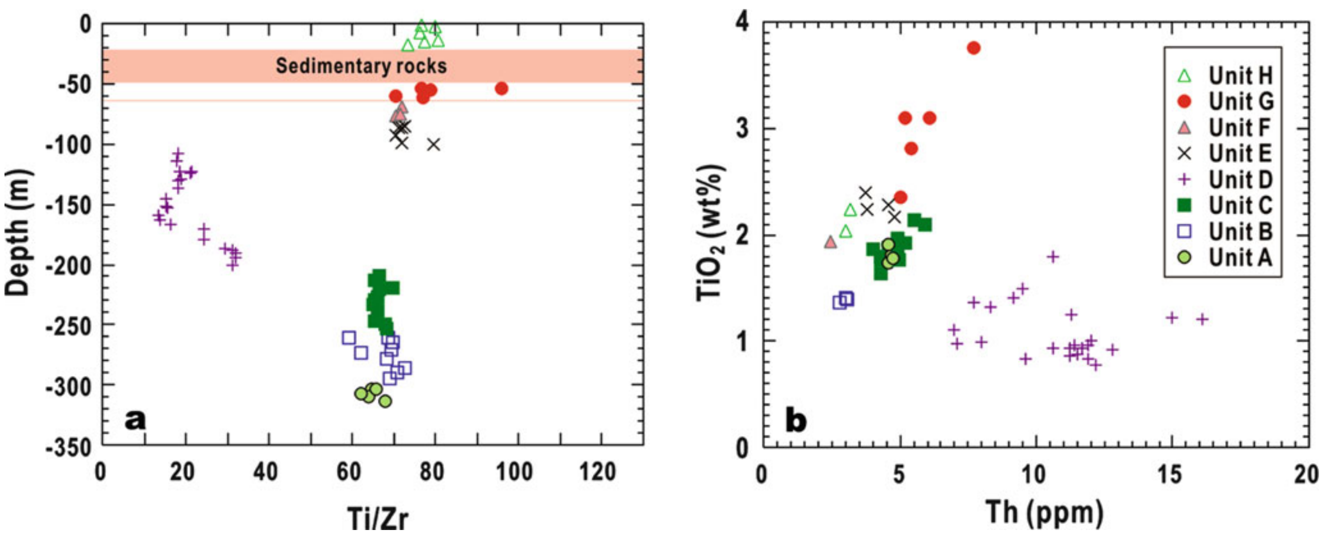

Fig. 6.57 Ti/Zr versus depth (**a**) and Th versus TiO_2 diagrams for igneous rocks from Core 6A

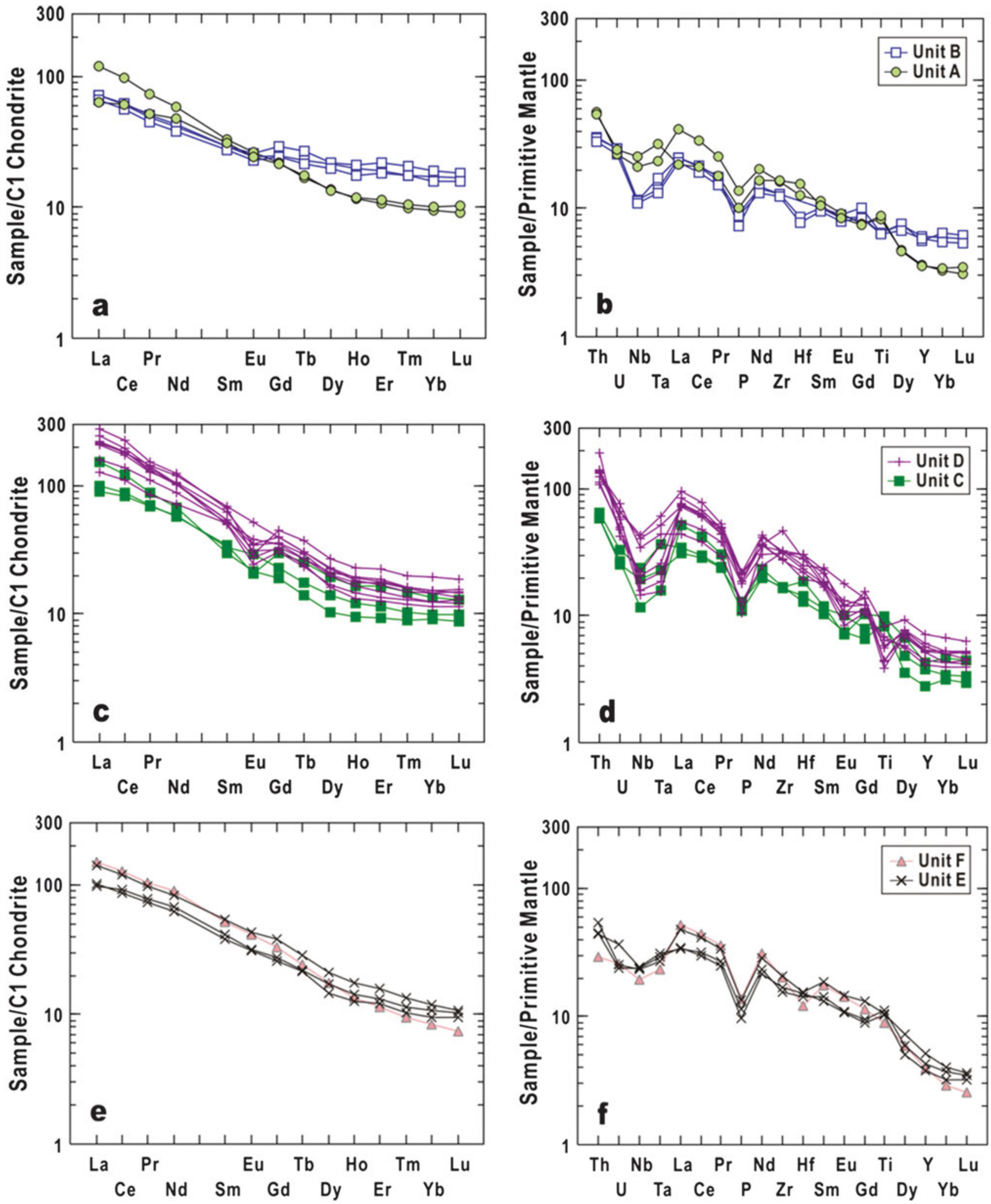

Fig. 6.58 (continued)

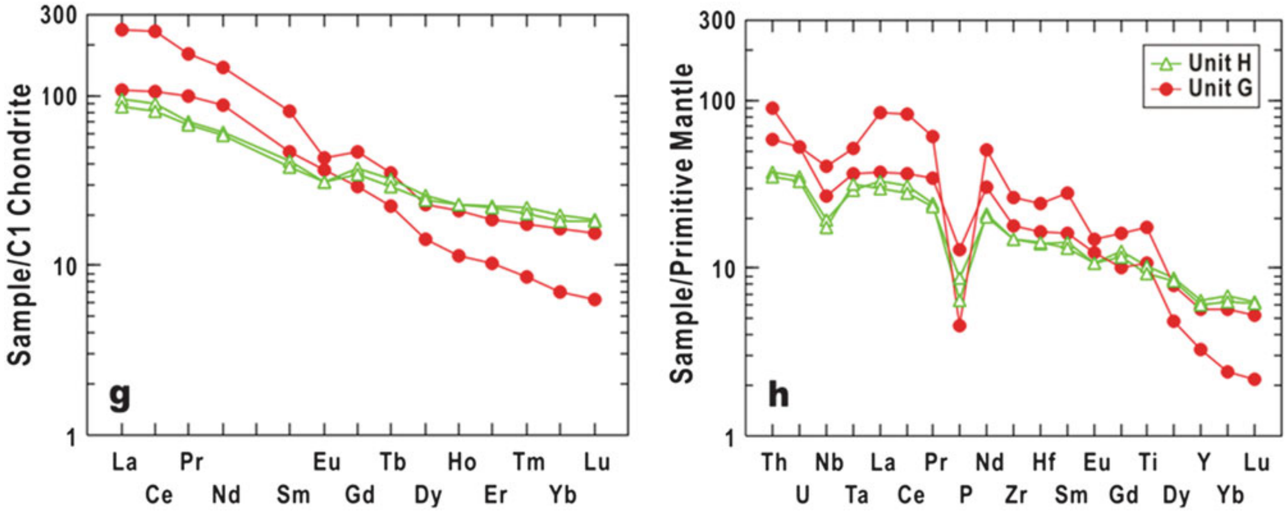

Fig. 6.58 Chondrite-normalised REE patterns (*left panels*) and primitive mantle-normalised trace element patterns (*right panels*) for igneous rocks from Core 6A. Normalising values taken from Sun and McDonough (1989). (**a**, **b**) Units A and B. (**c**, **d**) Units C and D. (**e**, **f**) Units E and F. (**g**, **h**) Units G and H

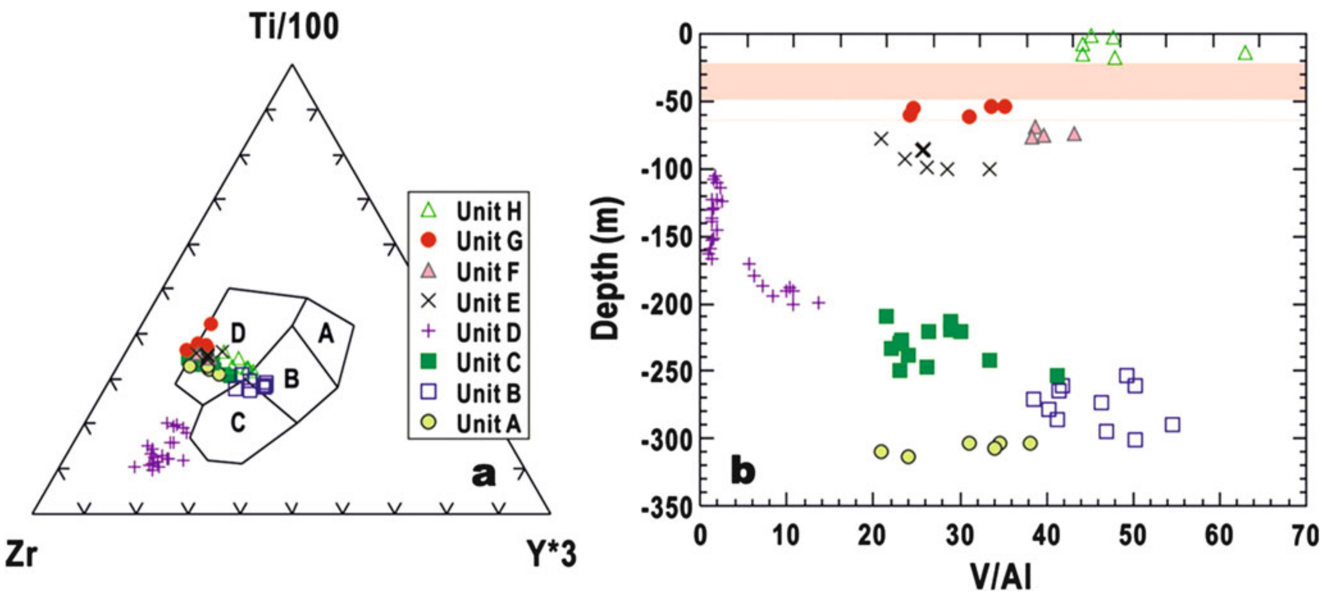

Fig. 6.59 (**a**) Analyses from Core 6A plotted on a discrimination diagram of Pearce and Cann (1973). Fields: A + B, low-K tholeiites; B, ocean-floor basalts; B + C, calc-alkali basalts; D, within-plate basalts. (**b**) Variation of V/Al with stratigraphic height

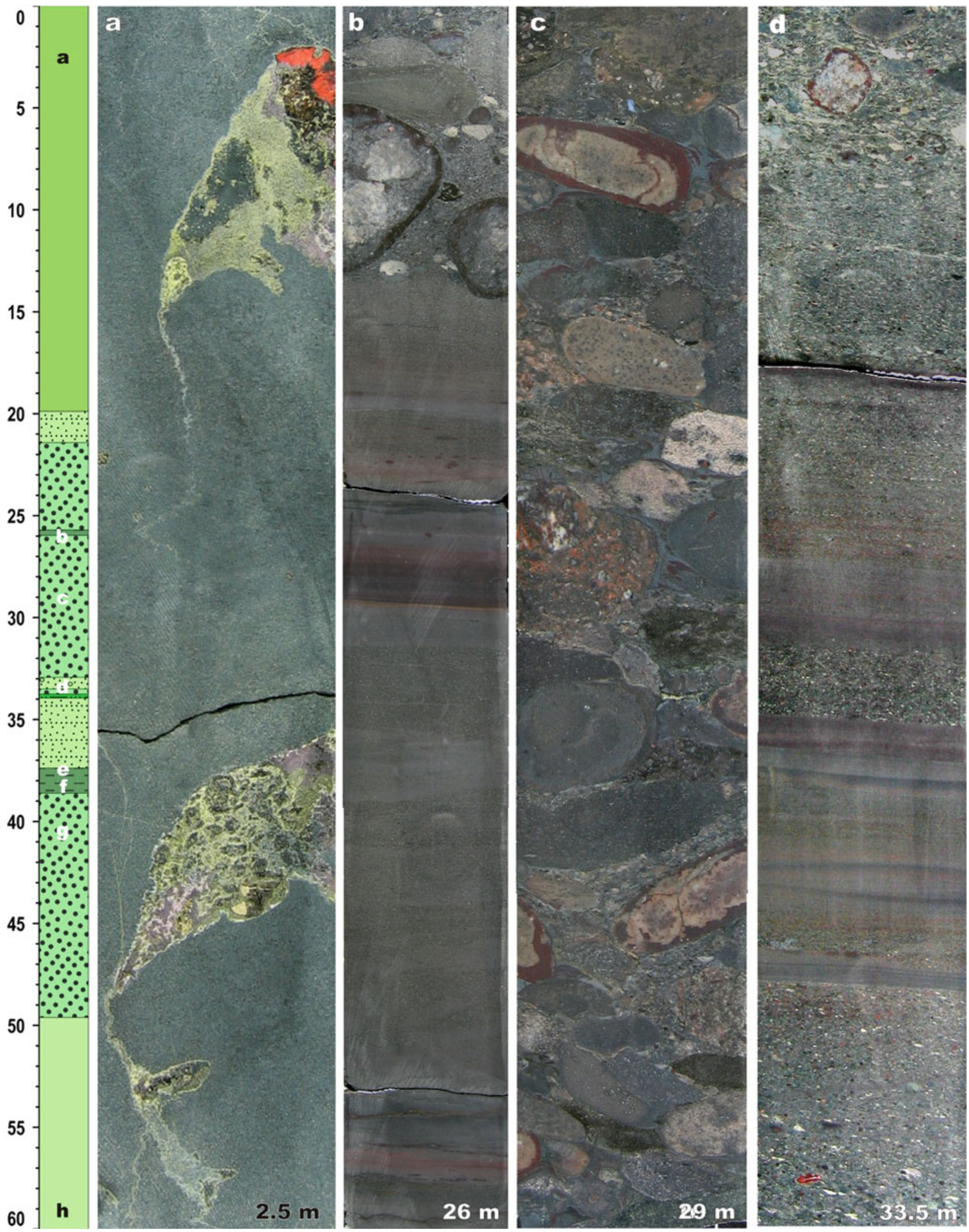

Fig. 6.60 Volcanic features of the main rocks types of the Kuetsjärvi Volcanic Formation based on core logging of Hole 6A and outcrops in the vicinity of the drilling site. Core diameter in all plates is 5 cm unless specified otherwise. (**a**) Tholeiitic basalt lava with large, irregular-shaped amygdales filled with violet axinite, pale green epidote, red K-feldspar, grey albite, dark green chlorite, and minor quartz and biotite; note that the both amygdales have thick feeder channels (conduit). (**b**) Parallel-bedded siltstone overlain by sandstone supported conglomerate; note several dark purple layers enriched in clastic haematite derived from underlying volcanic rocks, and implying that the haematite is pre-metamorphic. (**c**) Fragment-supported volcaniclastic conglomerate composed of well-rounded pebbles of trachyandesite, trachydacite and rhyolite; note that some pebbles have haematite-rich outer rims and internal bands implying pre-metamorphic origin of haematite. (**d**) Volcaniclastic gritstone interbeded with haematite-rich parallel-bedded siltstone

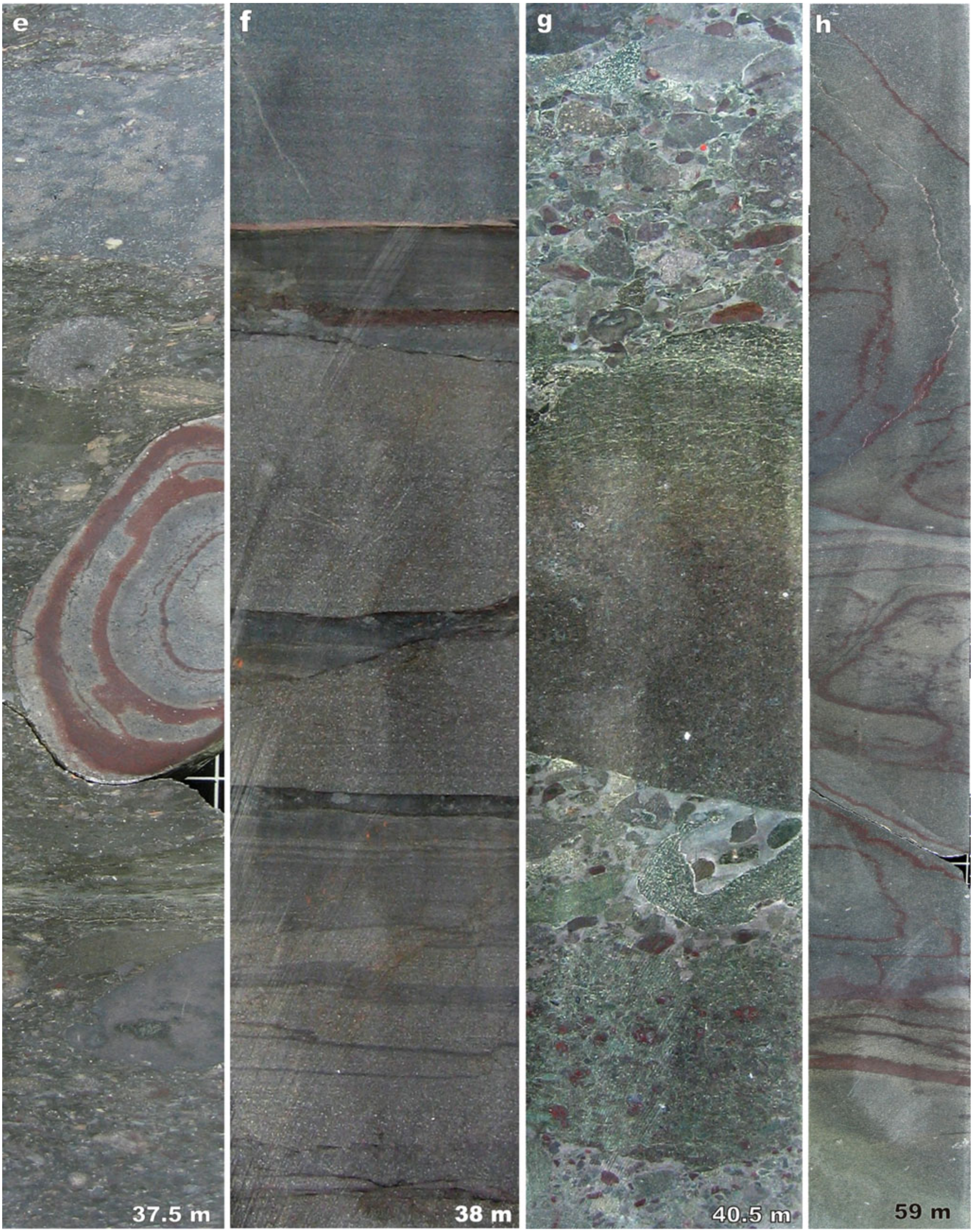

Fig. 6.60 (continued) (**e**) Bed of volcaniclastic gritstone-sandstone containing a cobble-sized, rounded dacite clast with concentric, Liesegang-type, haematite-rich bands, evidence that the haematisation was predepositional, not secondary, in origin. (**f**) Interbedded siltstone-sandstone showing parallel lamination and dark brown, haematite-rich layers. (**g**) Fine-pebble, volcaniclastic conglomerate with an outsized dacite fragment in the *middle*. (**h**) Trachyandesitic lava with haematisation banding

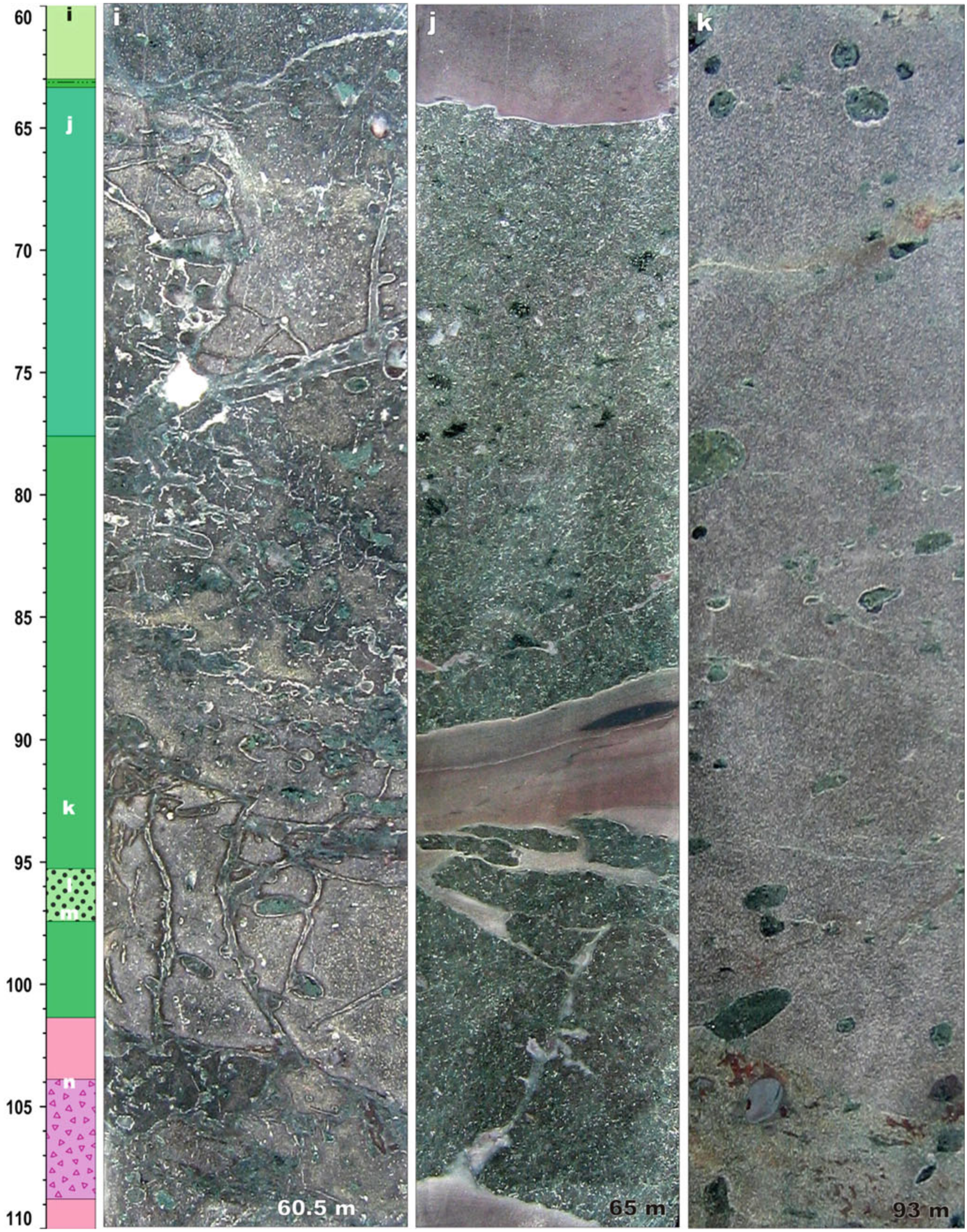

Fig. 6.60 (continued) (**i**) *Bottom*-flow, amygdaloidal lava breccia of trachyandesite. (**j**) Xenoliths of purple, haematite-rich, volcaniclastic siltstone in olivine-phyric picritic basalt. (**k**) Amygdaloidal alkaline basalt

Fig. 6.60 (continued) (**l**) Fragment-supported volcaniclastic conglomerate containing variably rounded polymict clasts of lava and tuff; note the oversized angular clast of rhyolite in the low *left* corner. (**m**) Interbedded volcaniclastic conglomerate and gritstone with a large amygdaloidal lava clast exhibiting haematised fracture-network. (**n**) Felsic lava breccia

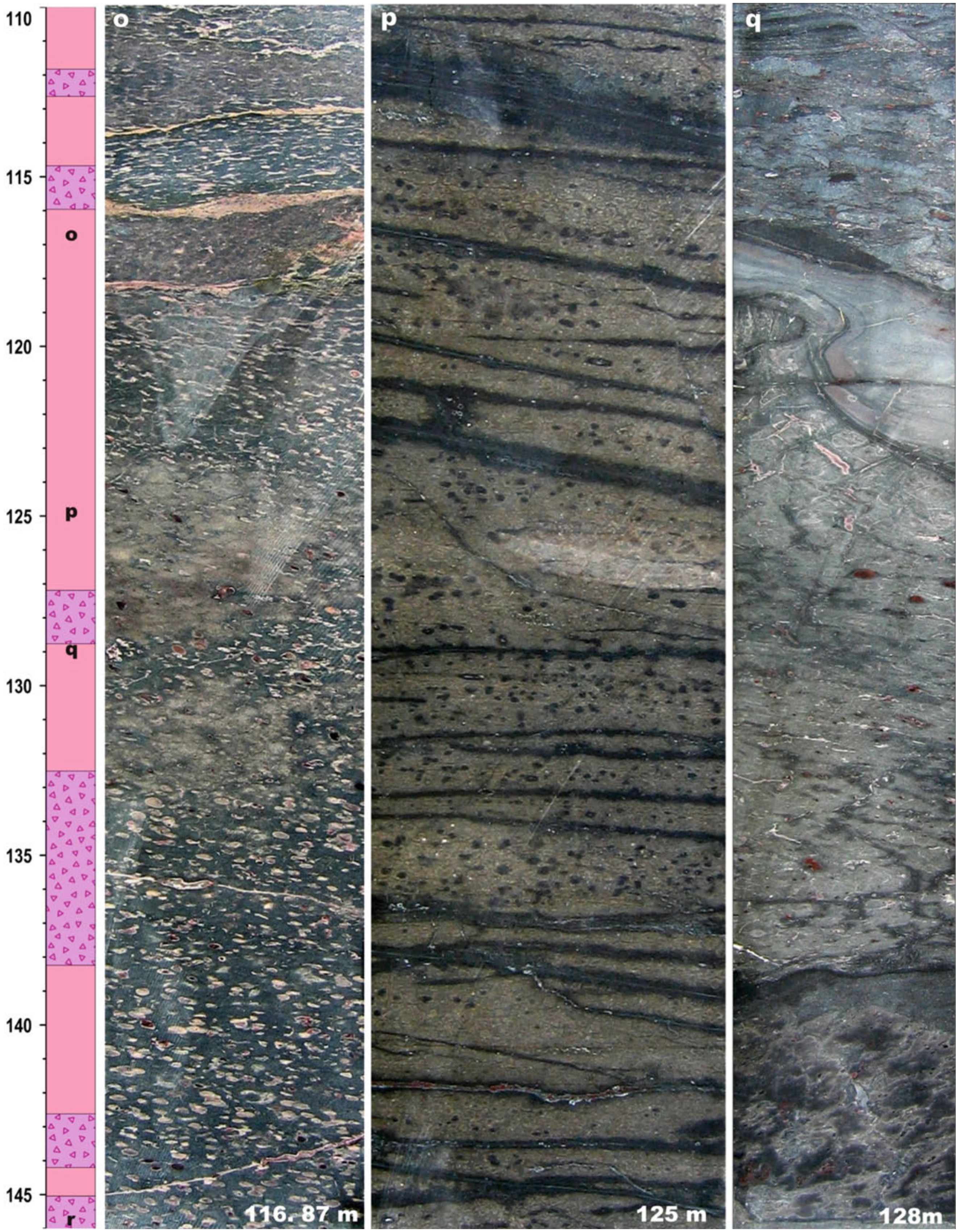

Fig. 6.60 (continued) (**o**) *Top*-flow, highly amygdaloidal, rhyodacitic lava. (**p**) Flow-banded (fluidal), microcrystalline felsic lava with the banded structure highlighted by black haematite pigment. (**q**) Rhyodacitic lava breccia with a bed of fluidal lava in the *middle*; note jasper-filled amygdales in the lava flow

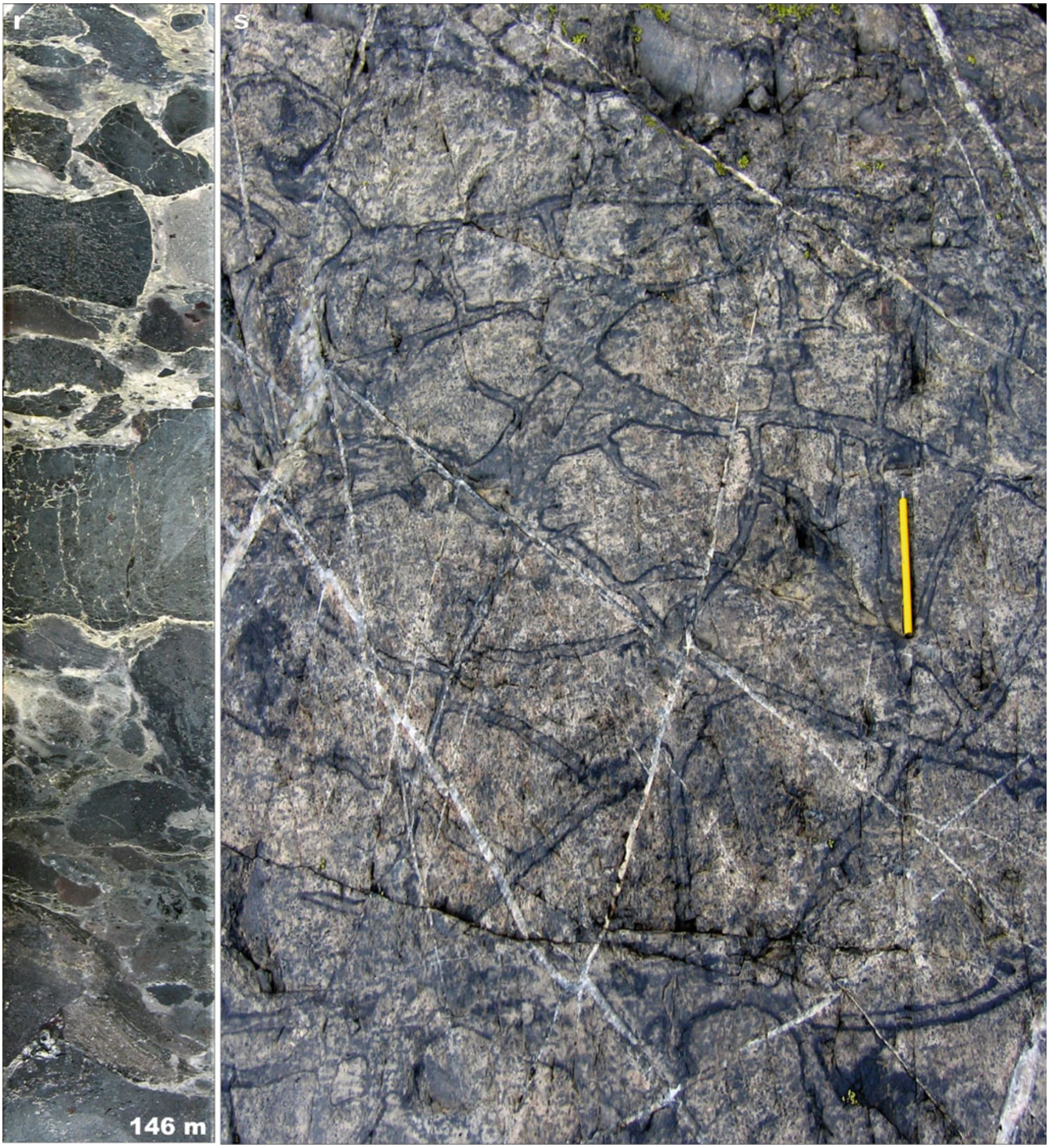

Fig. 6.60 (continued) (**r**) Rhyodacitic lava breccia. (**s**) Bedding surface of rhyodacitic fluidal lava flow exhibiting contraction (cooling) joints enhanced by a syn-volcanic haematitisation; note post-magmatic, white quartz veins

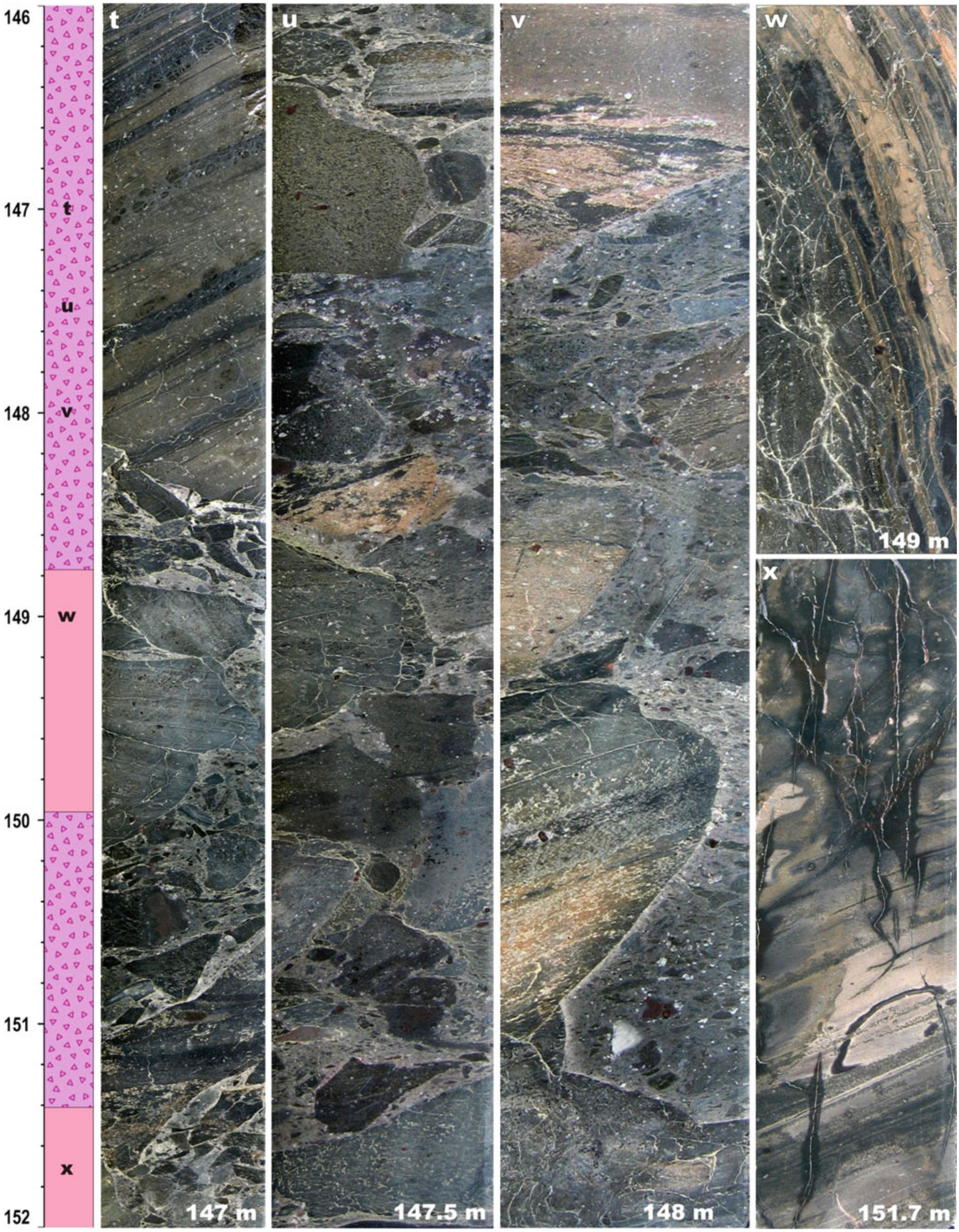

Fig. 6.60 (continued) (**t–v**) Rhyodacitic lava breccia. (**w–x**) Flow-banded (fluidal) rhyodacitic lava flow cut by a network of thin quartz veinlets

Fig. 6.60 (continued) (**y**) Outcrop view of flow-banded (fluidal) and brecciated felsic lava; note syn-volcanic folding

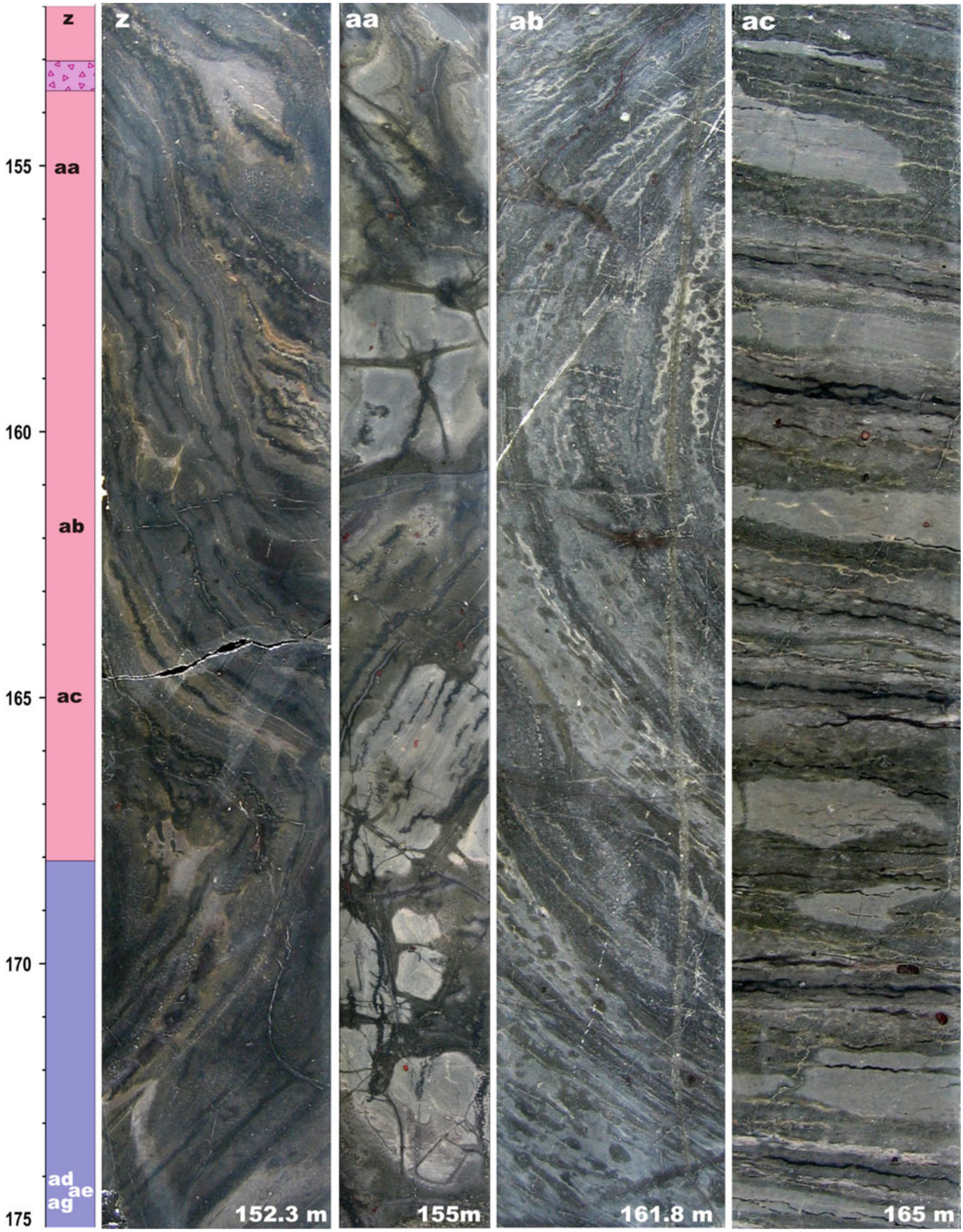

Fig. 6.60 (continued) (**z**) Syn-volcanic folding in flow-banded, oxidised (haematite-rich) rhyodacitic lava. (**aa**) Partial syn-volcanic brecciation in oxidised, flow-banded rhyodacitic lava flow. (**ab**) Syn-volcanic folding in oxidised, flow-banded rhyodacitic lava. (**ac**) Flow-banded, oxidised rhyodacitic lava

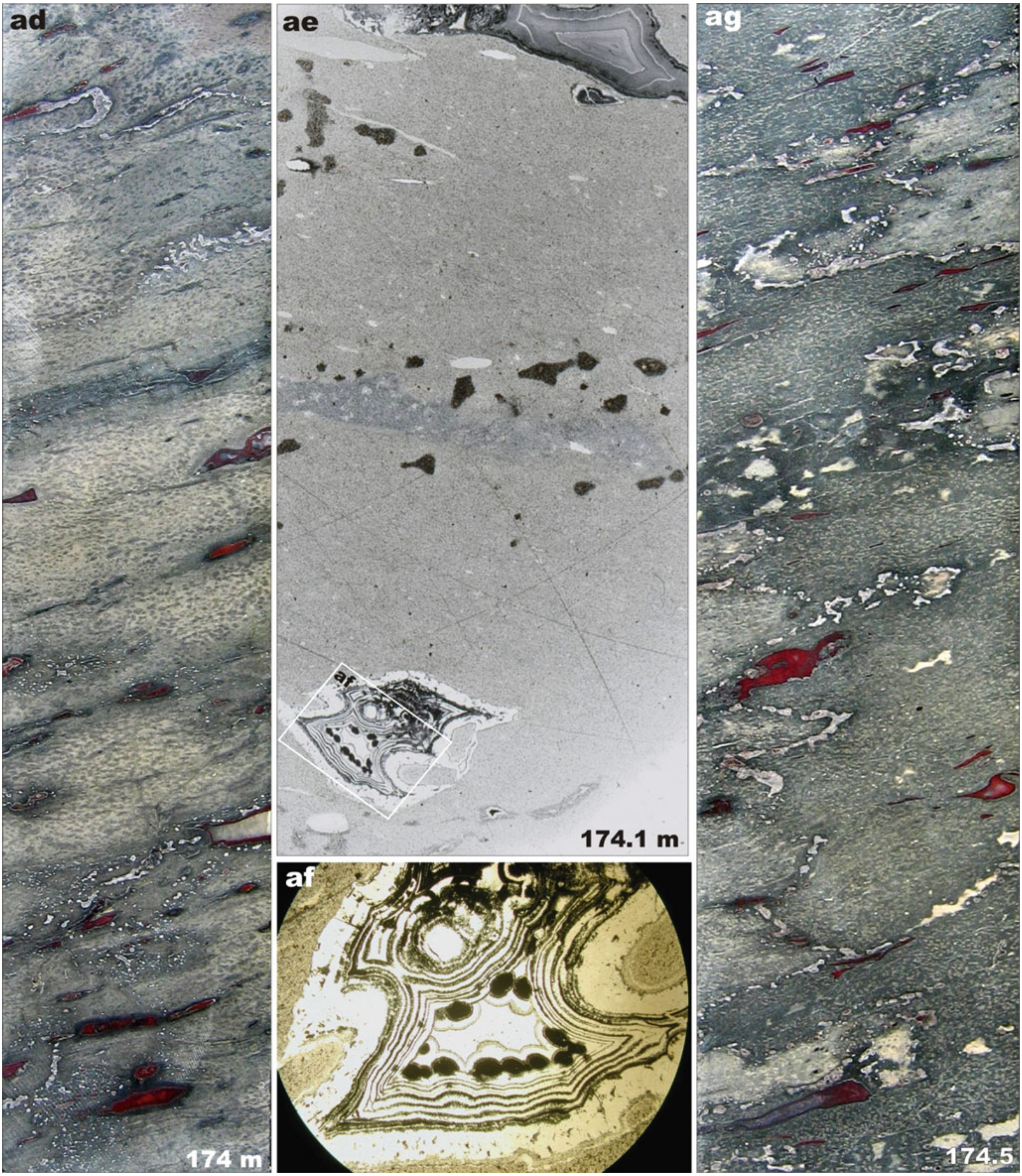

Fig. 6.60 (continued) (**ad**) Trachydacitic lava containing flattened vesicles filled with quartz and red jasper. (**ae**) Scanned thin section of cryptocrystalline, amygdaloidal trachyandesitic lava containing amygdales with well-preserved agate-like banding (*upper left* and *low left* corners); width of view 14 mm. (**af**) Photomicrograph in non-polarised, transmitted light illustrating detailed view of an amygdale from (**ae**), showing well-preserved concentric silica-haematite banding; width of view is 5 mm. (**ag**) Trachyandesitic lava with flattened amygdales filled with quartz and jasper (*red*)

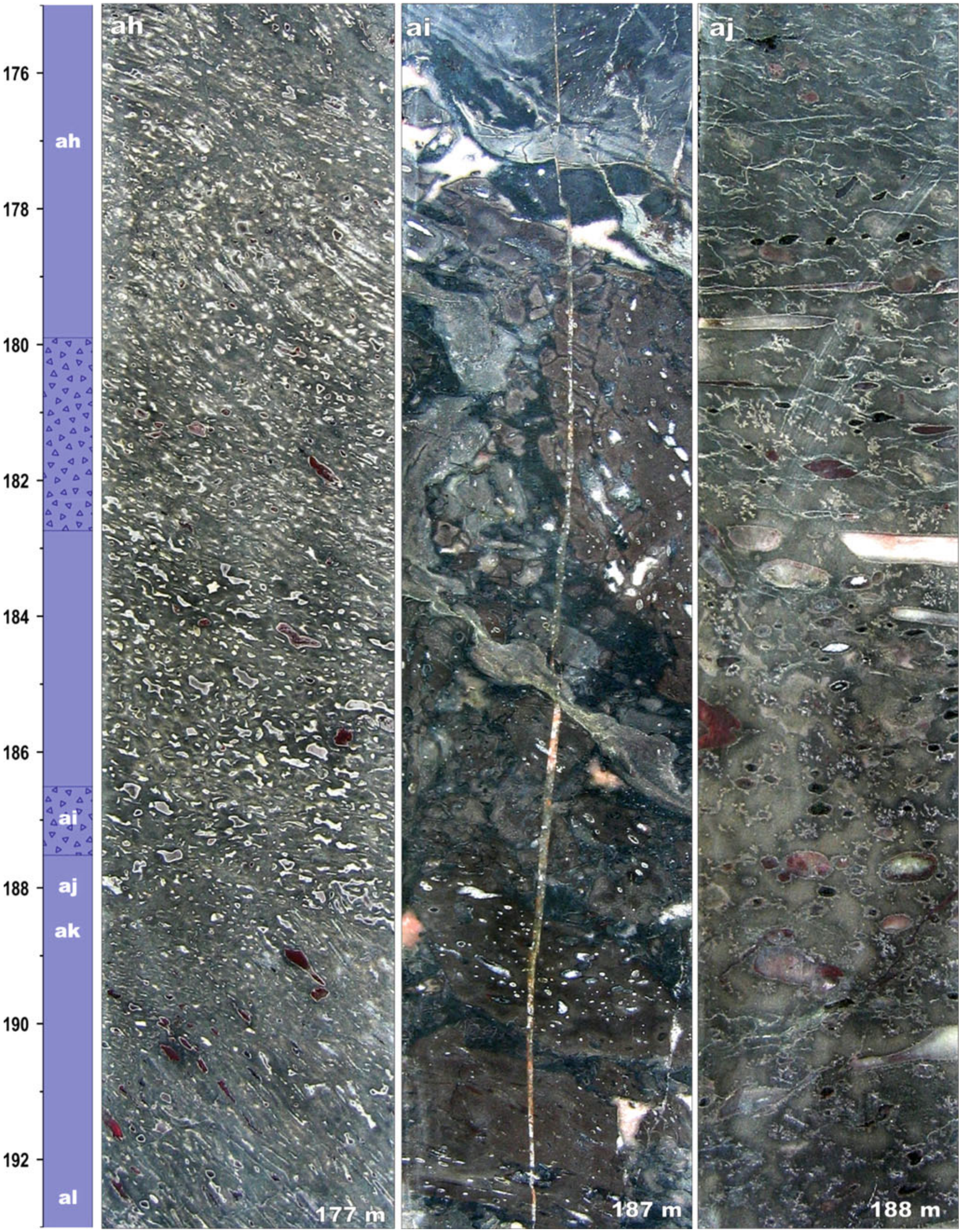

Fig. 6.60 (continued) (**ah**) Originally highly vesicular trachydacitic lava containing flattened amygdales filled with quartz and quartz-haematite (*red* jasper). (**ai**) Trachydacitic lava breccia. (**aj**) Originally highly vesicular trachydacitic lava containing amygdales filled with quartz and jasper

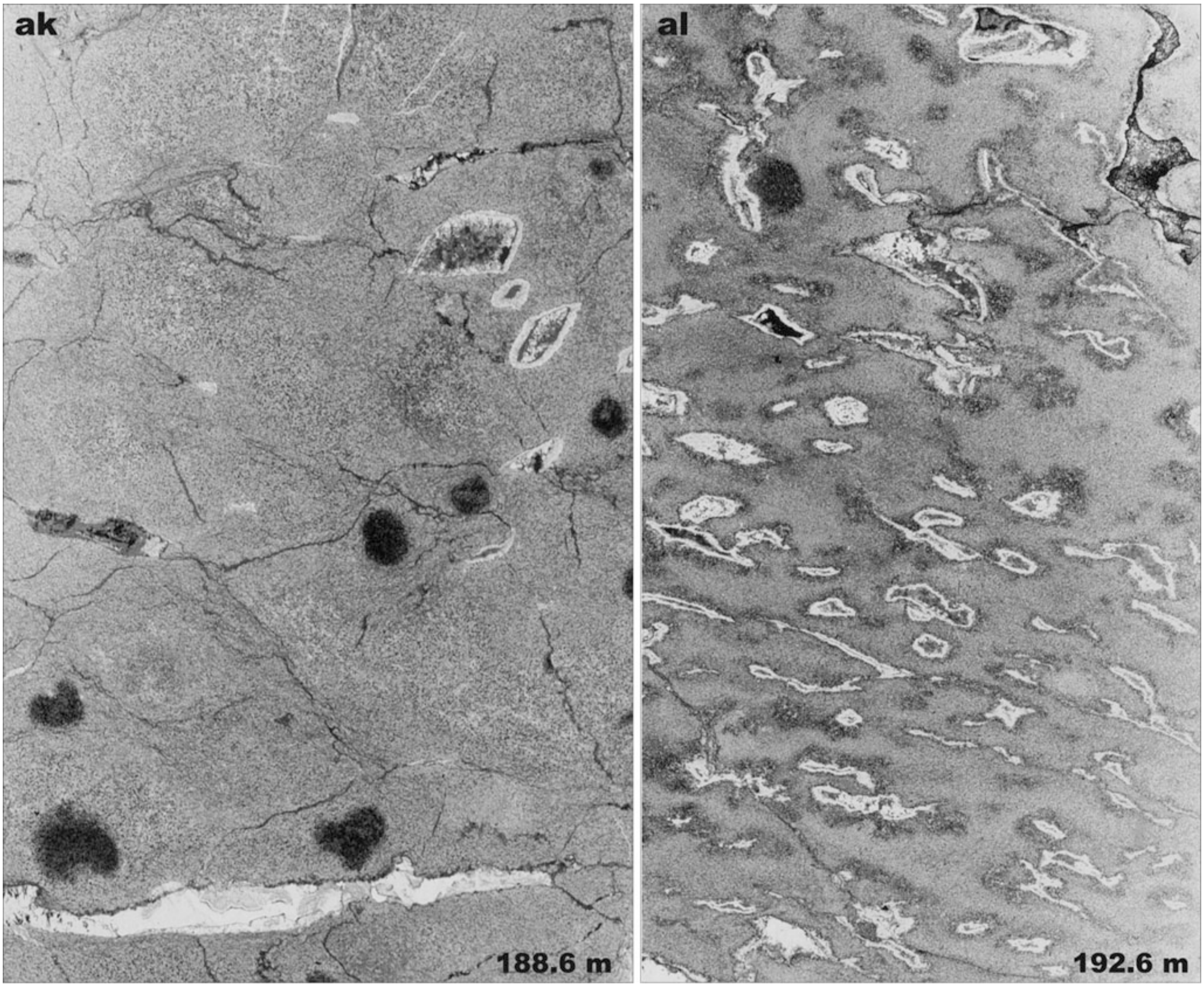

Fig. 6.60 (continued) (**ak**) Scanned thin section of microcrystalline, amygdaloidal trachydacitic lava with a long, horizontal amygdale filled with quartz; note thin pre-metamorphic, haematite-filled cracks and patchy haematisation in groundmass. (**al**) Scanned thin sections of microcrystalline, amygdaloidal trachydacitic lava with flattened and ameoboid-shaped amygdales filled with quartz (*white*), biotite (*brown*) and haematite (*black*); note thin pre-metamorphic haematite-filled cracks and patchy haematisation in groundmass. Width of both views is 20 mm

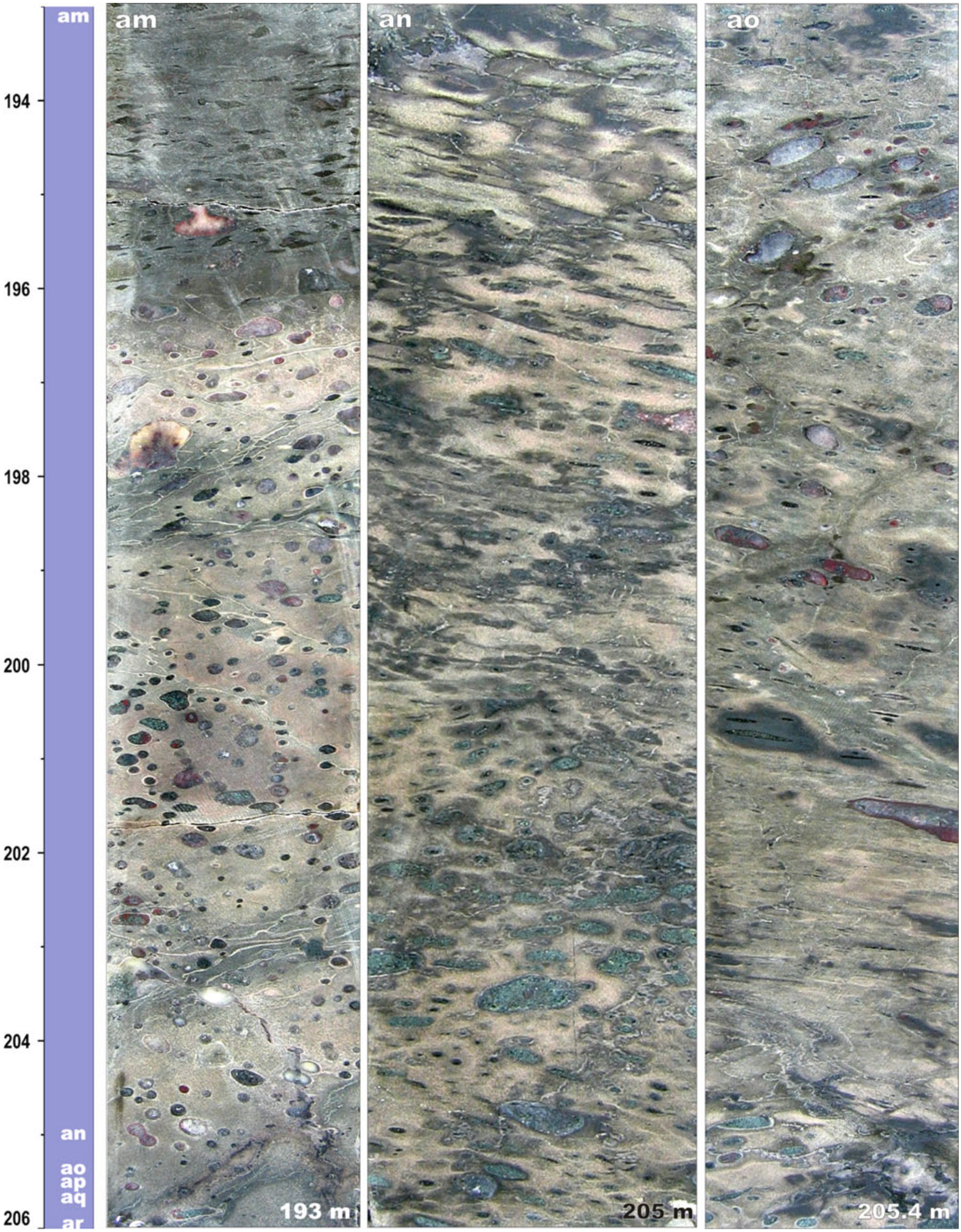

Fig. 6.60 (continued) (**am**–**ao**) Microcrystalline, highly-amygdaloidal trachydacitic lava with variably flattened amygdales filled with quartz, albite and carbonate (all *white*), chlorite (*green*), biotite (*brown*) and jasper (*red*)

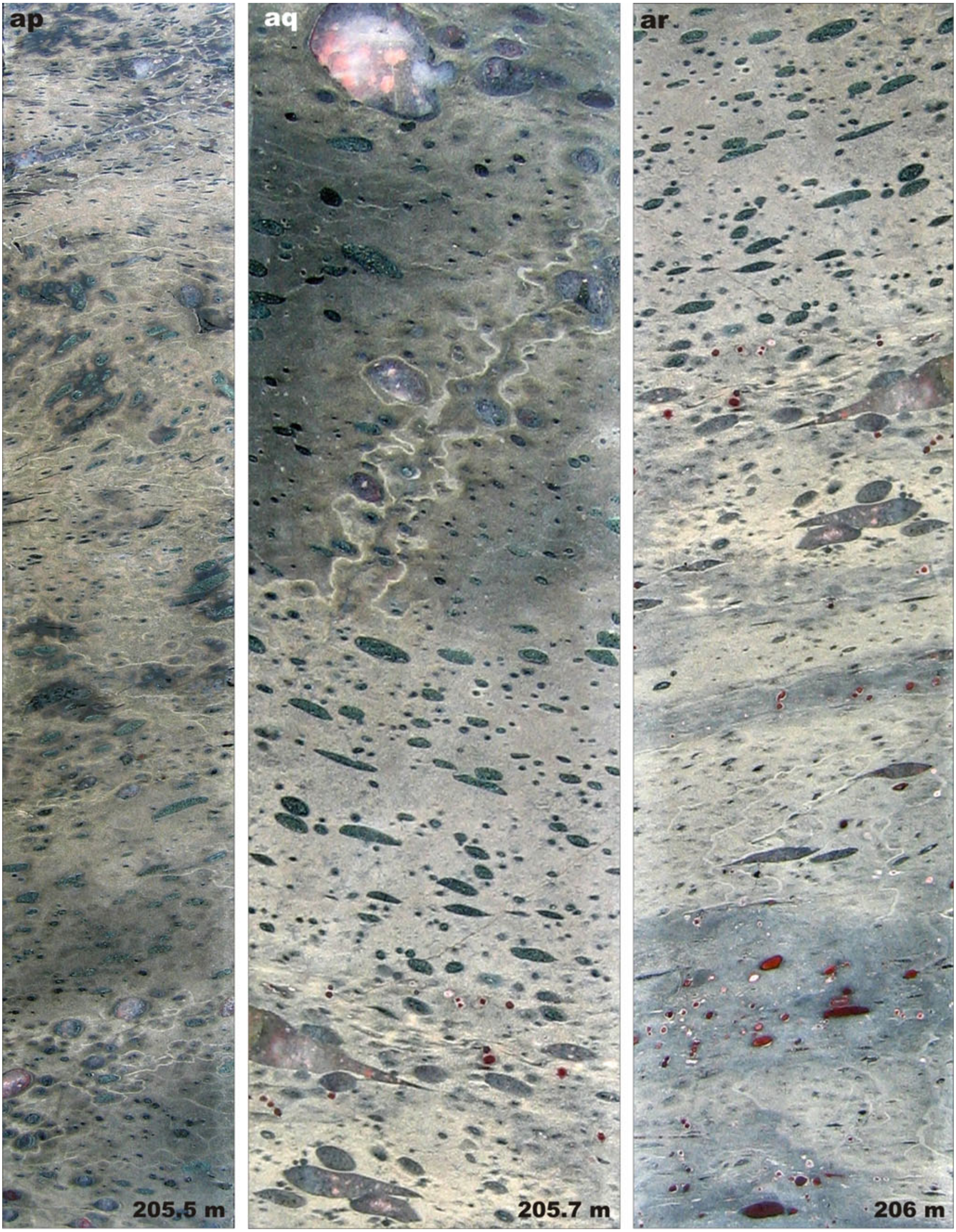

Fig. 6.60 (continued) (**ap**) Microcrystalline, amygdaloidal trachydacitic lava with variably stretched amygdales filled mainly with chlorite. (**ag**) Bright layer (*lower half*) of microcrystalline, amygdaloidal trachydacitic lava with variably stretched chlorite amygdales (*dark green*) intruding a darker layer of lava of the same composition but containing amygdales filled with chlorite, quartz, albite, carbonate and haematite. (**ar**) Microcrystalline, amygdaloidal trachydacitic lava with variably stretched chlorite and jasper-filled amygdales (*dark green*) whereas red jasper-filled amygdales exhibit a more spherical shape

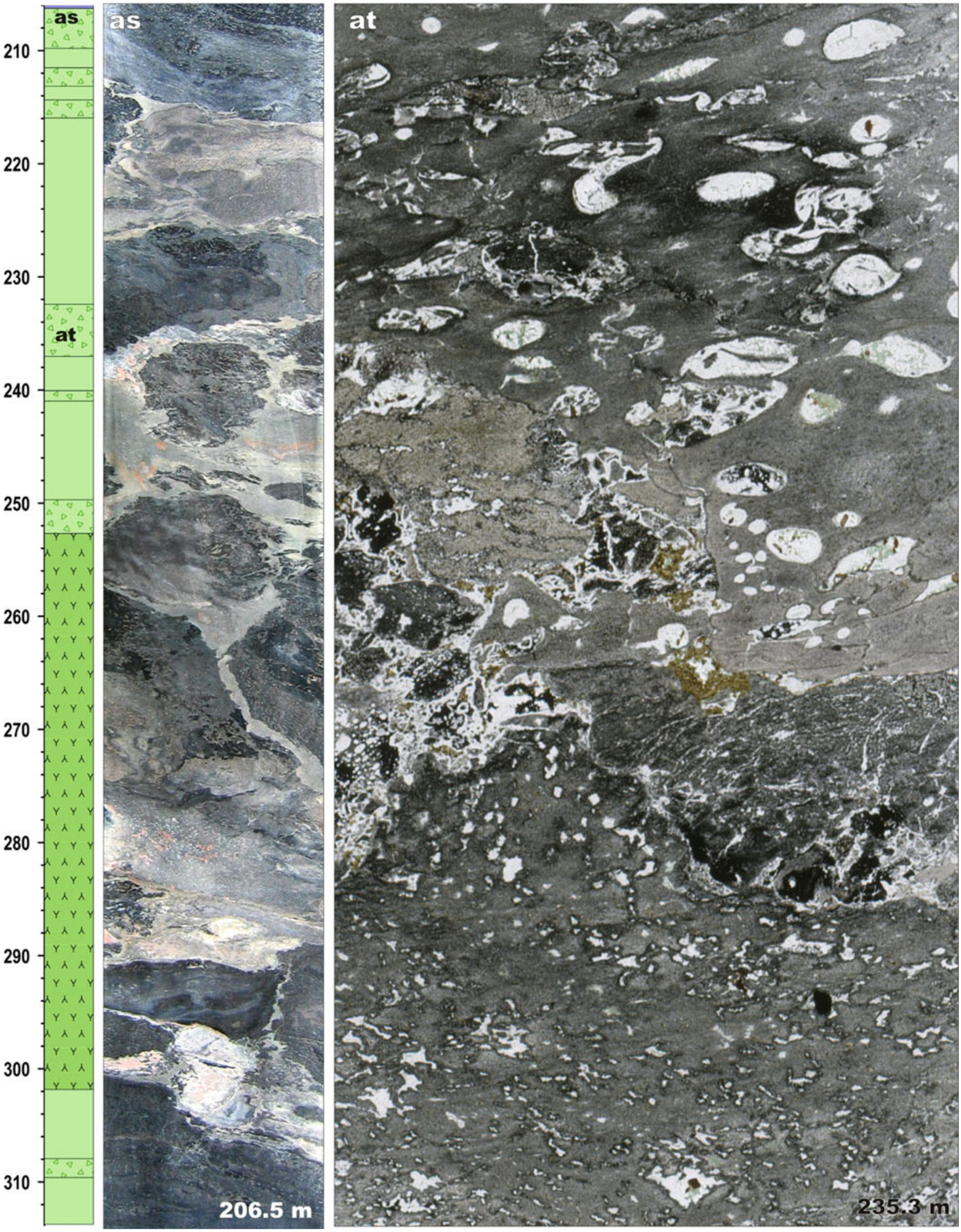

Fig. 6.60 (continued) (**as**) Trachyandesitic lava breccia. (**at**) Scanned thin section of volcaniclastite containing fragments of microcrystalline, amygdaloidal trachyandesite with amygdales filled with quartz (*white*), haematite (*black*), chlorite (*dark green*) and biotite (*brown*); width of view is 20 mm (Photograph (**a–ad**, **ag–aj**, **am–as**) by Victor Melezhik, photographs (**ae**, **af**, **ak**, **al**, **at**) by Eero Hanski)

References

Kump LR, Kasting JF, Barley ME (2001) Rise of atmospheric oxygen and the "upside-down" mantle. Geochem Geophys Geosyst 2: Paper No. 2000GC0114, p 10

Melezhik VA, Sturt BA, Mokrousov VA, Ramsay DM, Nilson L-P, Balashov YuA (1994) The early Palaeoproterozoic Pasvik-Pechenga Greenstone Belt: 1:200,000 geological map, stratigraphic correlation and revision of stratigraphic nomenclature. Norg Geol Unders Spec Publ 7:81–91

Melezhik VA, Huhma H, Condon DJ, Fallick AE, Whitehouse MJ (2007) Temporal constraints on the Paleoproterozoic Lomagundi-Jatuli carbon isotopic event. Geology 35:655–658

Mollel GF, Swisher CC III, McHenry LJ, Feigenson MD, Carr MJ (2009) Petrogenesis of basalt–trachyte lavas from Olmoti Crater, Tanzania. J Afr Earth Sci 54:127–143

Pearce JA, Cann JR (1973) Tectonic setting of basic volcanic rocks determined using trace element analyses. Earth Planet Sci Lett 19:290–300

Predovsky AA, Fedotov ZhA, Zhangurov AM (1974) Geochemistry of the Pechenga complex. Nauka (Science), Leningrad, p 139, in Russian

Skuf'in PK, Yakovlev YN (2007) Geological setting and petrogeochemical features of volcanic rocks from the Majärvi, Pirttijärvi and Orshoaivi suites in a section of the Kola Superdeep Well and near-surface zone. Bull Moscow State Tech Univ 19(2):173–197, in Russian

Skuf'in PK, Pushkarev YuD, Kravchenko MP (1986) Volcanic rocks of the mugearite-trachyte formation in the Pechenga volcano-plutonic palaeodepression. Proc USSR Acad Sci Geol Ser 1:18–29, in Russian

Sun S-S, McDonough WF (1989) Chemical and isotopic systematics of oceanic basalts; implications for mantle composition and processes. In: Saunders AD, Norry MJ (eds) Magmatism in the ocean basins, vol 42, Geological Society special publication. Published for the Geological Society by Blackwell Scientific Publications, Oxford/Boston, pp 313–345

Winchester JA, Floyd PA (1977) Geochemical discrimination of different magma series and their differentiation products using immobile elements. Chem Geol 20:325–343

6.2.4 Kolosjoki Sedimentary and Kuetsjärvi Volcanic Formations: FAR-DEEP Hole 7A

Eero J. Hanski, Victor A. Melezhik, Aivo Lepland, Alexander E. Romashkin, Dmitry V. Rychanchik, Zhen-Yu Luo, Evgenii V. Sharkov, and Maria M. Bogina

Scientific Target

– Radiometric age constraint on timing of deposition
– Palaeomagnetic study
– Testing an upper-mantle oxidising hypothesis
– Groundwater chemistry (study of amygdaloidal infills)
– Geochemistry of palaeoweathered surfaces in response to the Great Oxidation Event

Hole 7A is located in the Pechenga Greenstone Belt (Figs. 6.32 and 6.33). It is one of the three FAR-DEEP drillholes transecting the Kuetsjärvi Volcanic Formation and one of two holes intersecting the uppermost part of the Kuetsjärvi Volcanic Formation and its depositional contact with the overlying Kolosjoki Sedimentary Formation (Figs. 6.61 and 6.62). Thus the hole also provides core material from the basal part of the Kolosjoki Sedimentary Formation.

The depositional age of the Kuetsjärvi Volcanic Formation has been constrained to 2058 ± 2 Ma by dating zircons from volcaniclastic conglomerates interbedded with lavas in the middle part of the volcanic succession (Melezhik et al. 2007). This age places a younger limit to the Lomagundi-Jatuli positive carbon isotopic excursion of sedimentary carbonates recorded in the underlying Kuetsjärvi ^{13}C-rich carbonates (Fig. 6.33).

Hole 7A recovered totally c. 93 m of core and pierced a palaeoweathered surface developed on top of the Kuetsjärvi Volcanic Formation (Fig. 6.63). The potassium- and Fe^{3+}-rich rocks encountered among the uppermost volcanic units may represent evidence either for a surface hydrothermal alteration or a large-scale alteration of Earth's surface by oxic meteoric and/or groundwaters at c. 2060 Ma. Hole 7A also recovered more than 80 m of Kuetsjärvi lavas, which are known to have high Fe^{3+}/Fe_{total} ratios, in sharp contrast with the other volcanic formations of the Pechenga Greenstone Belt (for details see Chaps. 3.4 and 7.4). The volcanic rocks may represent evidence for relatively oxidised mantle material (e.g. recycled banded iron formations; e.g. Kump et al. 2001) and thus provide a resource to address potential causes for and conditions through the oxygenation of terrestrial environments during the Great Oxidation Event.

E.J. Hanski (✉)
Department of Geosciences, University of Oulu, P.O. Box 3000, 90014 Oulu, Finland

The predominantly intermediate composition of the drilled volcanic section and the diverse mineralogy of the amygdales, presumably associated with an ancient, near-surface groundwater alteration, offer an opportunity to obtain geochronological data on volcanism and post-volcanic hydrothermal and surface oxidation processes. Study of amygdaloidal infills (Fig. 6.64) and vertical transects of individual lava flows may reveal information on the evolution of the redox-state of iron oxide phases in post-volcanic hydrothermal processes, as well as on their change during oxidation/reduction by surface- and groundwaters.

The Kuetsjärvi Volcanic Formation

The Kuetsjärvi Volcanic Formation has a thickness of more than 1,000 m, and Hole 7A intersected the uppermost 80 m of it (Fig. 6.61). The drilled volcanic section is subdivided into four units designated, from base to top, as A, B, C and D. Each of these units probably represents a separate lava flow with a thickness between 9 and 34 m; hence they are referred to as Flows A to D in the following text. Photos taken from some core intervals are presented in Fig. 6.65. Chemical compositions of the analysed archive samples are presented in Appendices 15 and 16, and Fig. 6.62 shows selected major and trace element distributions as a function of stratigraphic height.

The entire core displays a high degree of oxidation, and this phenomenon is discussed in more detail in Chaps. 3.4 and 7.4. Figure 6.62 shows the variation of magnetic susceptibility in Core 7A as a function of stratigraphic height. The rocks exhibit a high, though variable, magnetic susceptibility ranging between 9,000 and 82,000 μSI ($K^* = 800–7,000 \times 10^{-6}$ SI in Fig. 6.62). One notable exception is the middle part of Unit A (c. 91–82 m), which shows much lower magnetic susceptibility of between 1,000 and 2,800 μSI ($K^* = 90–240 \times 10^{-6}$ SI in Fig. 6.62).

In all the recovered volcanic rocks, the primary mafic silicate phases are replaced by secondary minerals, mostly amphibole and chlorite. However, the rocks retain their primary structural and textural features. Unit A (93–59 m) is the lowermost, massive, mafic lava flow. It contains plagioclase phenocrysts, devitrified glass (Fig. 6.65p–q) and amygdales, 2–10 mm in size, filled with quartz, jasper, carbonates and chlorite. In addition, in the uppermost 2 m of the unit, near its upper contact, the lava contains cooling cracks and quartz-filled macroamygdales up to 25 cm in length (Fig. 6.65o). Another zone of macroamygdales is found in the middle part of the lava unit. Unit B, at interval 59–39 m, is an andesitic lava flow with a c. 5-m-thick,

V.A. Melezhik et al. (eds.), *Reading the Archive of Earth's Oxygenation*, Volume 2: The Core Archive of the Fennoscandian Arctic Russia – Drilling Early Earth Project, DOI 10.1007/978-3-642-29659-8_3, © Springer-Verlag Berlin Heidelberg 2013

fragmental upper part. In the upper part of the unit, beneath the fragmental zone, the lava flow contains amygdales of various size composed of quartz, jasper and red feldspar (Fig. 6.65l–n); some large quartz amygdales are up to 15 cm in size (Fig. 6.65l). Locally the flow contains glomerophyric clusters of plagioclase phenocrysts in a fine-grained groundmass (Fig. 6.65j–k). Unit C, at interval 39–21 m, is basaltic andesite with a massive appearance except the uppermost 5 m, which are fragmental. Amygdales up to 10 mm in size occur mostly below the fragmental zone. The uppermost Unit D (21–12 m) comprises a fine-grained, massive andesitic lava flow with sparse calcite- and chlorite-filled amygdales and has no top breccias, which implies erosion prior to the deposition of the overlying Kolosjoki sedimentary rocks (Fig. 6.61). There are several blotchy, 0.2–0.5-m-thick, reddish alteration zones at depth interval 12.6–14.8 m and one close to the bottom of the flow.

All the volcanic rocks are mafic to intermediate in composition (Fig. 6.66a), but their high FeO_T content (14–17.5 wt.%) suggests that they crystallised from a relatively evolved magma. They also show moderately high TiO_2 abundances of 2.1–2.9 wt.% and low Cr ($\leq$40 ppm) and Ni ($\leq$45 ppm). Constant ratios of most incompatible trace elements (Fig. 6.67) indicate that all volcanic units had a similar parental magma. Flow A is a tholeiitic basaltic andesite with MgO of 4.0–4.5 wt.% and relatively high TiO_2 of 2.3–2.7 wt.%. The original composition of the magma was probably mildly alkaline, and the present subalkaline nature of the rocks could be a result of crustal contamination, as suggested by their depletion in Nb relative to LREEs, e.g. $(Ce/Nb)_{PM}$ 1.8–2.2. The uppermost part of the lava flow with K_2O between 3–4 wt.% was apparently affected by moderate potassic alteration. Flow B is clearly more evolved than the underlying Flow A as revealed by its elevated trace elements concentrations. For example, Th and Zr contents reach 9.2 and 360 ppm, respectively (Fig. 6.67). This lava flow has the lowest Ti/Zr ratio (40–55), while in other samples of Core 7A, Ti/Zr ranges between 60 and 80. In terms of trace element abundances and ratios, Flow C is intermediate between Flows A and B (Fig. 6.67). The andesitic Flow D resembles Flow C in its fractionation state, but has the highest Ti/Zr (76–80) in Core 7A. The reddish patches in the uppermost part of the volcanic section (Flow D) have elevated K_2O contents (>12 wt.%), low FeO_T (5.6 wt.%) and very low Na_2O (<0.2 wt.%), relative to other igneous rocks in Hole 7A. They also have the highest proportion of trivalent iron (63–65 %) in Core 7A, thus being the most oxidised.

Vanadium behaves as a compatible element in the volcanic sequence, decreasing with decreasing Ni and increasing Zr and other incompatible elements, and shows the highest concentrations in Flows A and D and lowest in Flow B (Fig. 6.68). This feature indicates an important role of an oxide phase among the liquidus minerals. The REE and other incompatible trace element characteristics are very similar in all lava flows (Fig. 6.69a, b). All samples from the volcanic section have negatively sloping chondrite-normalised REE patterns and show negative anomalies at Nb and Ta. They differ essentially only in terms of trace element concentrations, which are related to the fractionation stage of the magma. Still there is one enigmatic feature: the decoupling of phosphorus and other trace elements. This is seen in Fig. 6.69b where the negative P anomaly is distinct in lava flow A. In contrast, the Unit B lava flow, which is most fractionated, has the highest concentrations of P (Fig. 6.66b) and other trace elements, and does not display any P anomaly.

The Kolosjoki Sedimentary Formation

In FAR-DEEP Cores 8A and 8B, the Kolosjoki Sedimentary Formation is informally subdivided into seven lithostratigraphic units, which are, from base to top: the Sandstone, Lower Greywacke, Gritstone, Haematite, Ferropicrite, Dolostone, and Upper Greywacke members (see Chap. 6.2.5). The Sandstone member – very distinct, massive, fine-grained sandstone – has not been documented in Core 7A. Only the Lower Greywacke member (12.3–11.2 m) and the lower part of the Gritstone member (11.2–1.5 m) were intersected by Hole 7A.

The lower 6 m of the Kolosjoki Sedimentary Formation inherit high magnetic susceptibility from the underlying Kuetsjärvi volcanic rocks; 8,500–605,000 μSI ($K^* = 730–5{,}179 \times 10^{-6}$ SI in Fig. 6.62). It decreases erratically up-section to as low as 2,000 μSI ($K^* = 170 \times 10^{-6}$ SI in Fig. 6.62).

The Lower Greywacke Member

The Lower Greywacke member is only c. 1 m thick (12.3–11.2 m) and rests with a sharp erosional contact on the underlying altered andesite. Strong potassic alteration affecting the andesite is not seen in basal sedimentary rocks, implying that the alteration predated the deposition of the Lower Greywacke member and is likely to have been synvolcanic in origin. Moreover, in contrast to the altered andesites, which are depleted in iron (Appendix 15), the basal bed of the Lower Greywacke member is considerably enriched in Fe_2O_{3tot} (c. 27 wt.%) due to incorporation of clastic haematite and magnetite (Fig. 6.65h, i). In terms of the iron content, the basal bed resembles dacitic lava breccias, having lava fragments separated by black, haematite-magnetite-rich (25 wt.% Fe_2O_{3tot}) bands (Fig. 6.63). Such lava breccia in the uppermost part of the Kuetsjärvi

Volcanic Formation is preserved in outcrop a few hundred metres to the west of the drilling site.

The greywackes are fine-grained rocks having irregular, millimetre-thick siltstone partings and display planar and trough cross-bedding. The greywackes are composed of angular clasts of quartz, microcline and rarely albite, fragments of intensively altered mafic to intermediate lavas, and particles of haematite, magnetite and leucoxene; all are embedded in a fine-grained matrix of similar composition but enriched in sericite. The degree of sorting and rounding are generally low.

Chemical composition of the Lower Greywacke member sandstone, based on one analysed sample, is presented in Appendices 15 and 16. The sandstone is rich in Fe_2O_{3tot} (c. 27 wt.%) and TiO_2 (>2 wt.%) and has a moderate K_2O content (c. 2 wt.%), which is significantly lower than the K_2O contents (5–7.6 wt.%) in the Lower Greywacke member rocks intersected by FAR-DEEP Hole 8B (Appendix 20). Interestingly, the sandstone is devoid of Na_2O.

The Gritstone Member

The drilled thickness of the Gritstone member is <10 m (11.2–1.5 m, Fig. 6.61). The member rests with a sharp contact on the underlying sandstones and its base is marked by a regionally developed polymict volcaniclastic conglomerate (see Chap. 4.2). This, together with two other beds of volcaniclastic conglomerate (2.3–0.5 m) interbedded with thinner intervals (0.5–0.3 m) of gritstone (Fig. 6.61), forms the lower part of the member. Combined with the interbedded sandstone-siltstone of the Lower Greywacke member, these lithologies define three coarsening-upward cycles (Fig. 6.61). A monotonous gritsone unit overlies the interbedded conglomerate-gritstone package.

The lowermost conglomerate bed is the thickest and is composed of poorly sorted, variably rounded and tightly packed clasts of weathered and oxidised dacite and andesite, and large quartz and jasper amygdales; all are derived from the Kuetsjärvi volcanic rocks (Fig. 6.65e–g). The conglomerate also contains scattered fragments of red K-feldspar. The amount of potassium-rich material (sericite and clasts of microcline) increases markedly in the two overlying conglomerate beds, occurring as large discrete lenses and as arkosic-gritstone matrix surrounding larger dacite and andesite clasts in conglomerates (Fig. 6.65c–d). Other sedimentological details of these volcaniclastic conglomerates are described in Chaps. 4.2 and 6.2.5.

The gritstones are commonly red in colour and massive (Fig. 6.65b). Where present, crude stratification is expressed by deposition of clastic haematite. The gritstones consist of semi-rounded clasts of quartz and K-feldspar (Fig. 6.65a) and accessory barite in the form of grains and intergranular veinlets. The gritstone contains c. 82 wt.% SiO_2 and is rich in Ba (1440 ppm) and low in Na_2O (0.8 wt.%) (Appendices 15 and 16).

The Depositional Framework

The data obtained from Hole 7A, together with those from Holes 6A and 8B and other published data from the Kuetsjärvi Volcanic Formation (e.g. Predovsky et al. 1974; Skuf'in et al. 1986; Skuf'in and Yakovlev 2007), indicate that the upper part of the formation is overwhelmingly composed of subaerially erupted lavas accumulated within an intraplate continental rift setting. The original nature of most volcanic rocks intersected by Hole 7A seems to have been mildly alkaline but was disturbed to various extents by crustal contamination. A well pronounced, intense potassic alteration associated with the uppermost part of Unit A, as well as with the base and the upper part of Unit D, is not seen in the overlying sedimentary units. This suggests a significant syn-volcanic surface hydrothermal alteration or surface palaeoweathering prior to the deposition of the overlying sedimentary rocks. The phenomenon represents an important topic for future research addressing environmental conditions during the Palaeoproterozoic oxygenation of terrestrial environments.

The Kolosjoki sedimentary rocks at the drilling site, similar to other locations (see Chap. 6.2.5), represent mostly fluvially influenced, non-marine sedimentation. The Lower Greywacke member (only 1 m thick) is inferred to be associated with broad palaeovalleys that are incised into the underlying Kuetsjärvi volcanic rocks. The sharply overlying Gritstone member has a wide variety of poorly sorted, volcaniclastic conglomerates and previous work in the vicinity of the drilling site showed that the member has tabular geometry and 'seals' the underlying palaeovalleys, in many places overstepping the Lower Greywacke units to rest on the Kuetsjärvi volcanic rocks (Melezhik 1992). The Gritstone member is typified by mostly massive rocks, but also contains wide conglomerate lenses with channel-shaped geometries at outcrop scale. Similar to other places (see Chaps. 4.2.2 and 6.2.5), a fluvially influenced depositional setting is inferred for the rocks comprising the Gritstone member. The abundant coarse material constituting reworked volcanic clasts is interpreted as an erosional 'lag'; the material reworked into the fluvial system from exposed, debris-mantled margins and upland areas surrounding the palaeovalley. Although most of the clastic material was derived from the underlying volcanic rocks, the source of large fragments of red K-feldspar remains enigmatic. This represents another important topic for future research, which may shed light upon the palaeogeographic history of the area.

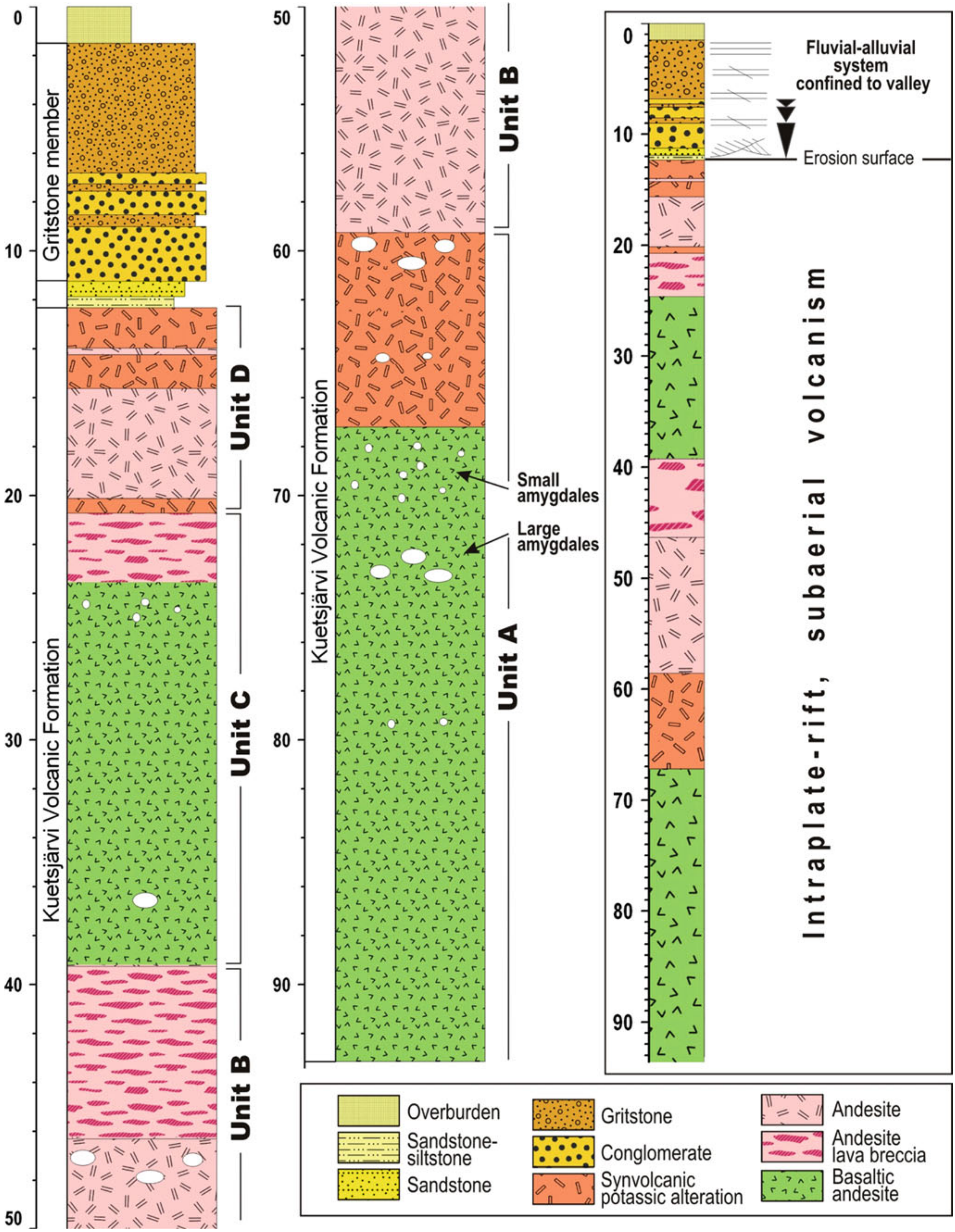

Fig. 6.61 Lithological section of the upper part of the Kuetsjärvi Volcanic Formation and the basal part of the Kolosjoki Sedimentary Formation based on core logging of Hole 7A, and a tentative reconstruction of depositional environments based on the core observations, geological mapping and sedimentological research in the vicinity of the drilling site. Lithological symbols are explained in Fig. 6.6

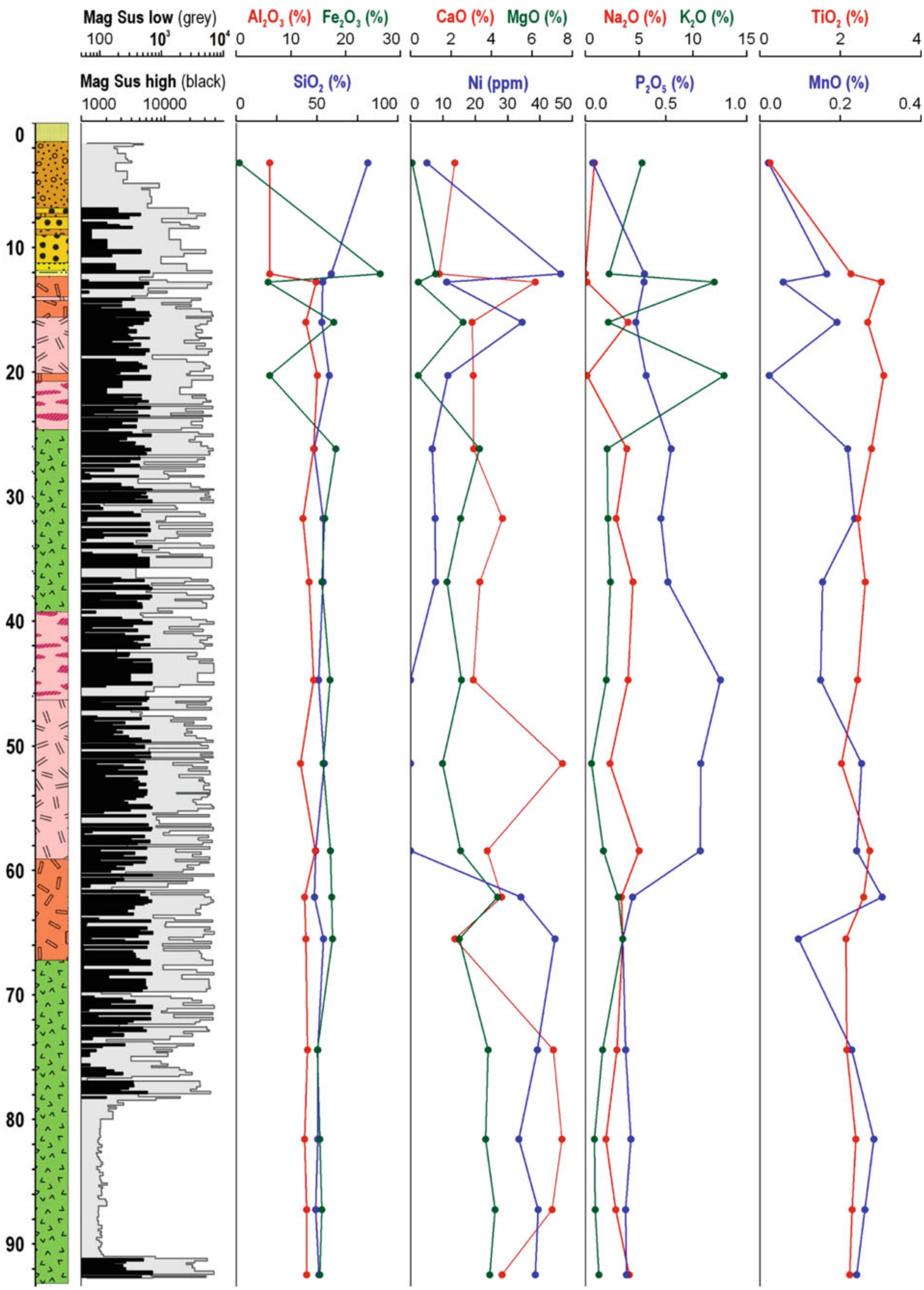

Fig. 6.62 Relative magnetic susceptibility (K*), and geochemical profiles of selected elements based on the archive samples collected with c. 8 m-spacing. For analytical techniques and data quality see **Part 5**

Fig. 6.63 The uppermost part of the Kuetsjärvi Volcanic Formation, immediately below the overlying Kolosjoki Formation. Where preserved, this part comprises potassium-rich (13 wt.% K_2O) dacitic lava breccia with fragments separated by black, haematite-magnetite-rich (25 wt.% Fe_{tot}) bands. Unusually high enrichment in K_2O and Fe_{tot} and highly oxidised state of Fe are indicative of either post-volcanic surface hydrothermal alteration or palaeoweathering processes. The rock represents valuable material for addressing palaeoenvironmental surface conditions during the Palaeoproterozoic oxidation event. Width of the image is 1 m (Photograph by Victor Melezhik)

Fig. 6.64 Large quartz amygdales in andesitic lava flows may preserve the original composition of oxygen isotopes and thus can potentially be used to track the chemistry and origin of fluids from which quartz was precipitated. Core diameter is 5 cm (Photograph by Victor Melezhik)

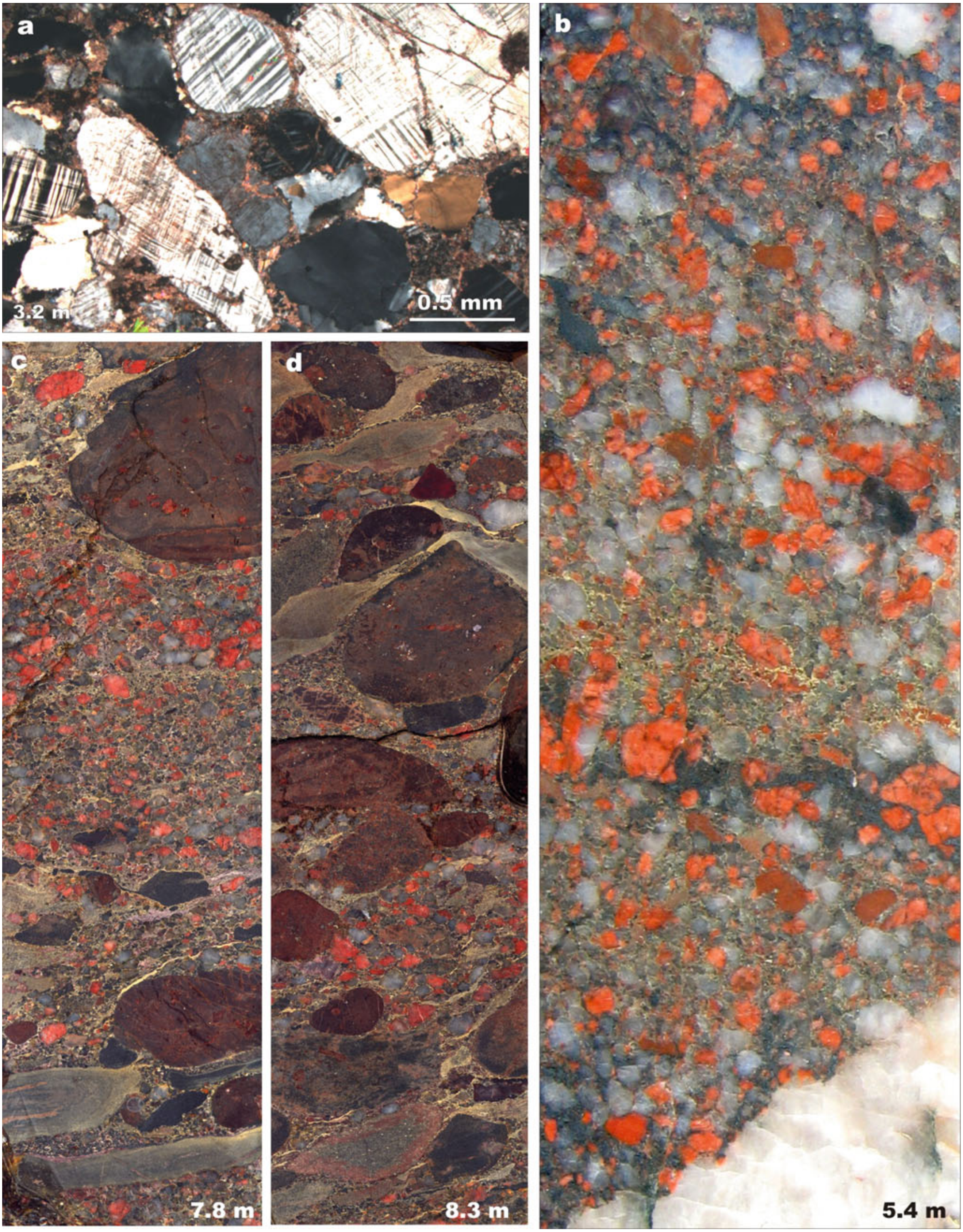

Fig. 6.65 Sedimentological features of the main rock types of the Kolosjoki Sedimentary and Kuetsjärvi Volcanic formations based on Core 7A and outcrops in the vicinity of the drilling site. In all core photographs, unless otherwise marked, the scale for the images is the core width of 5 cm. (**a**) Photomicrograph of a gritstone comprising semi-rounded clasts of quartz and K-feldspar; in transmitted, polarised light. (**b**) Arkosic gritstone composed of bright red microcline, brick-coloured dacitic lava, and reworked, white quartz amygdales; note a quartz vein in the *right lower corner*. (**c–d**) Volcaniclastic conglomerate composed of irregularly scattered fragments of dacite and andesite supported by arkosic-gritstone matrix

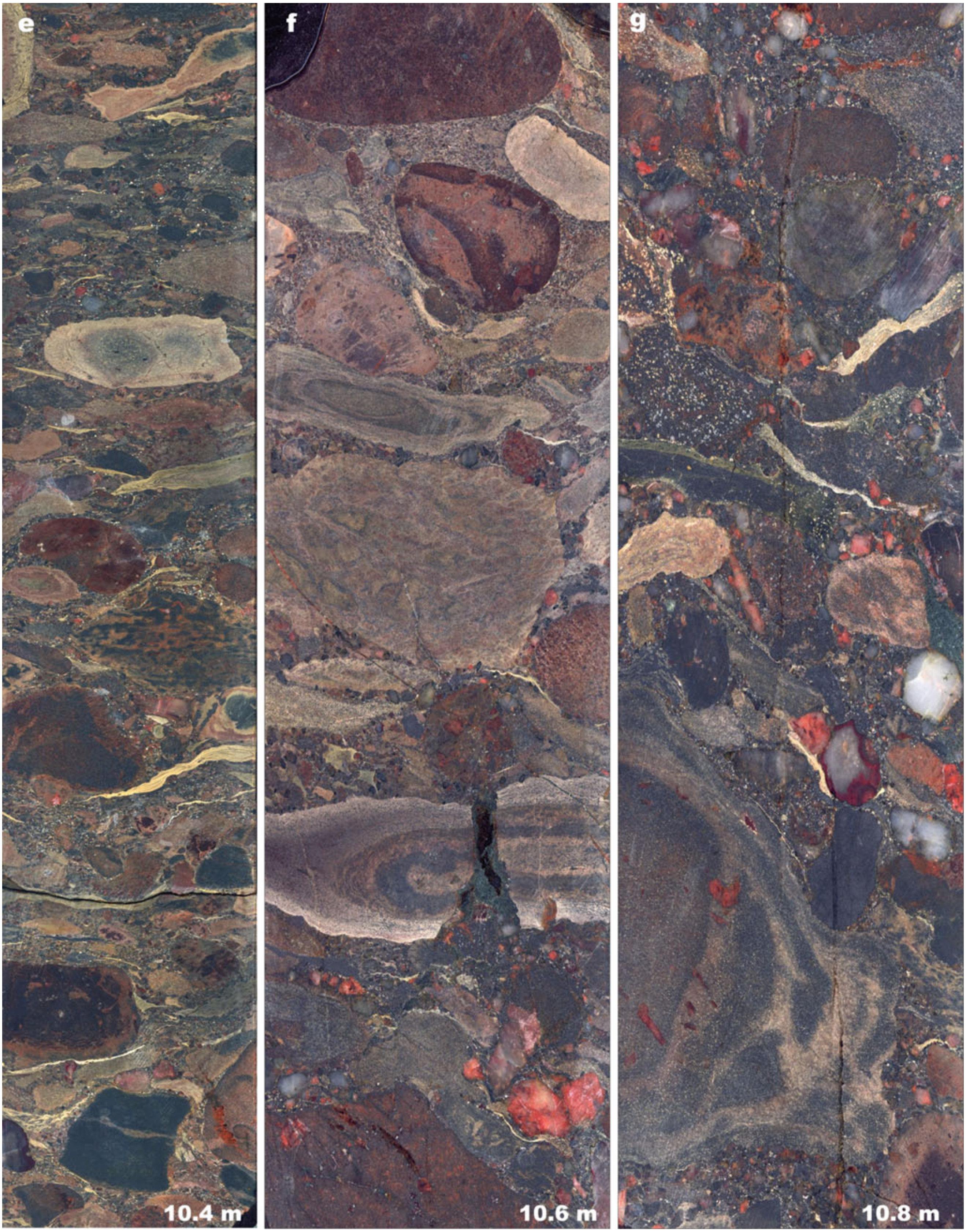

Fig. 6.65 (continued) (**e**–**g**) Volcaniclastic, clast-supported conglomerate containing highly oxidised fragments of intermediate to felsic volcanic rocks with several fragments showing concentric zoning enhanced by surface palaeoweathering

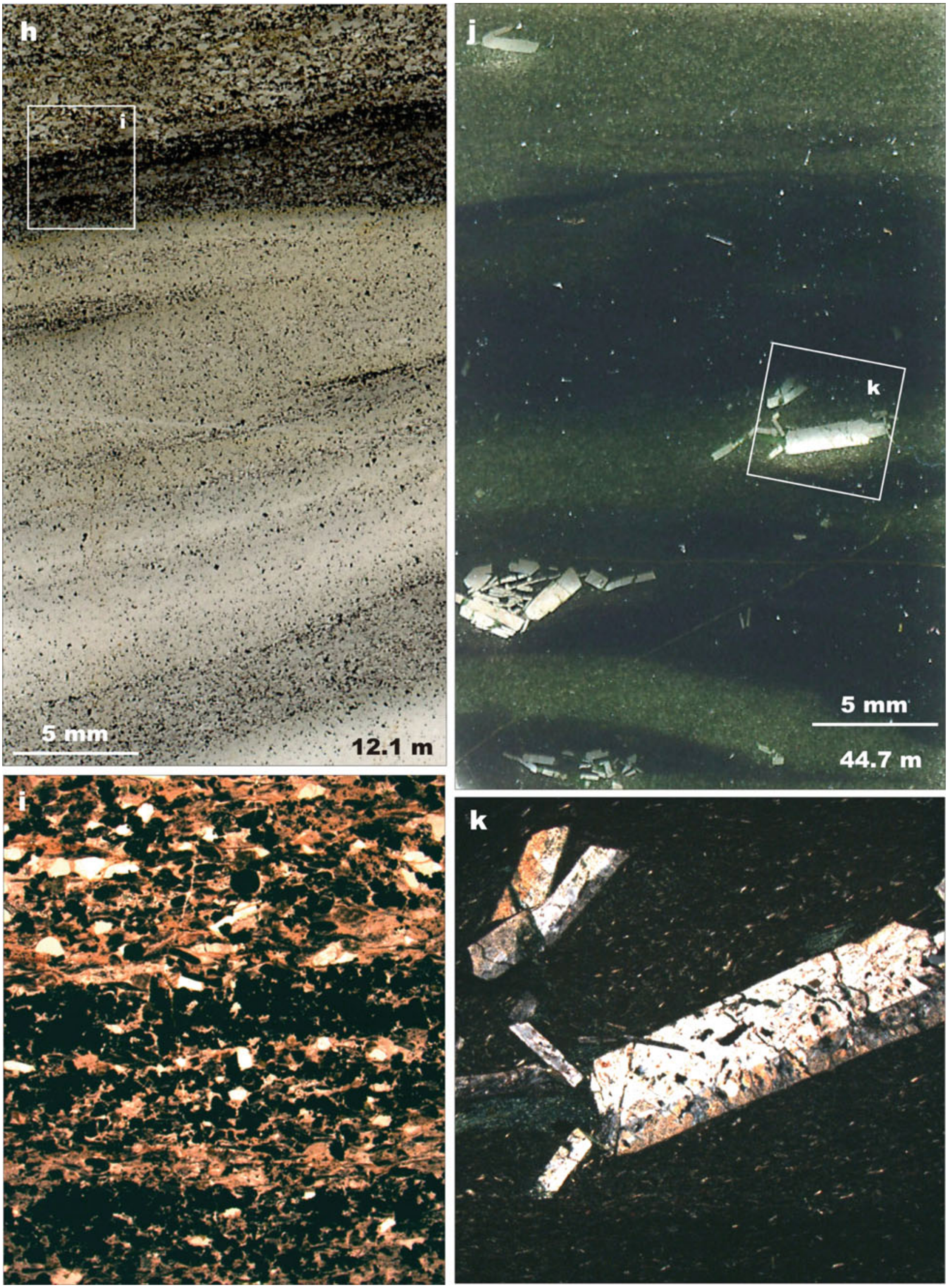

Fig. 6.65 (continued) (**h**) Scanned thin section of basal bed of the Lower Greywacke member enriched in clastic magnetite and haematite. (**i**) Close-up view showing distribution of clastic iron oxides (*black*); photomicrograph in transmitted, non-polarised light. (**j–k**) Closed clusters of equant plagioclase phenocrysts in an aphanitic/fine-grained groundmass with flow banding; scanned thin section (**j**) and photomicrograph in transmitted, polarised light (**k**)

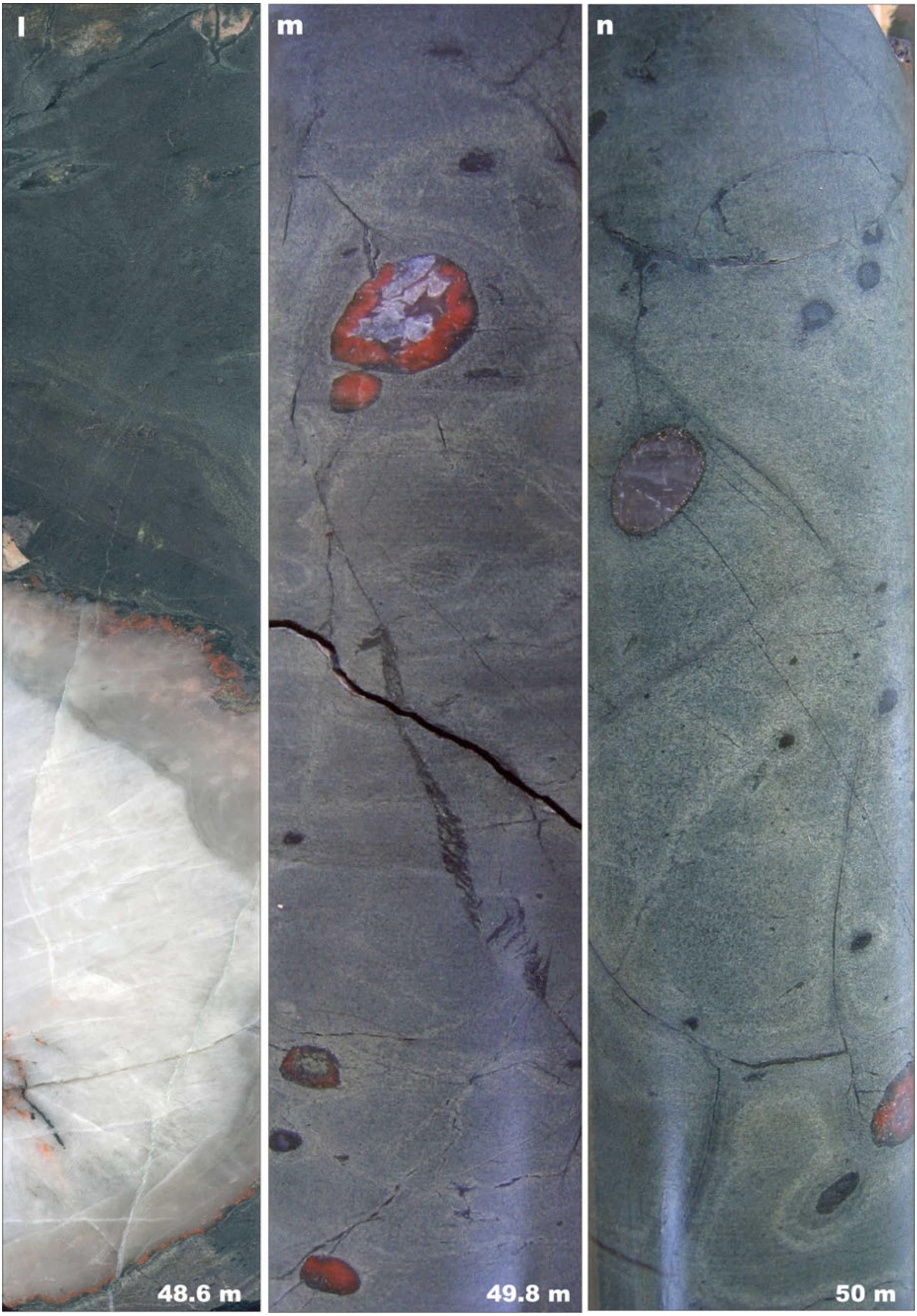

Fig. 6.65 (continued) (**l**) Large, zoned quartz amygdales in basalt. (**m**) Feldspar-filled amygdales (*red*) in andesite; note that some amygdales are zoned and have a quartz-chlorite core (**n**) Quartz (*dark grey*), jasper (*red*) and chlorite (dark coloured) amygdales in basaltic lava showing contraction joints

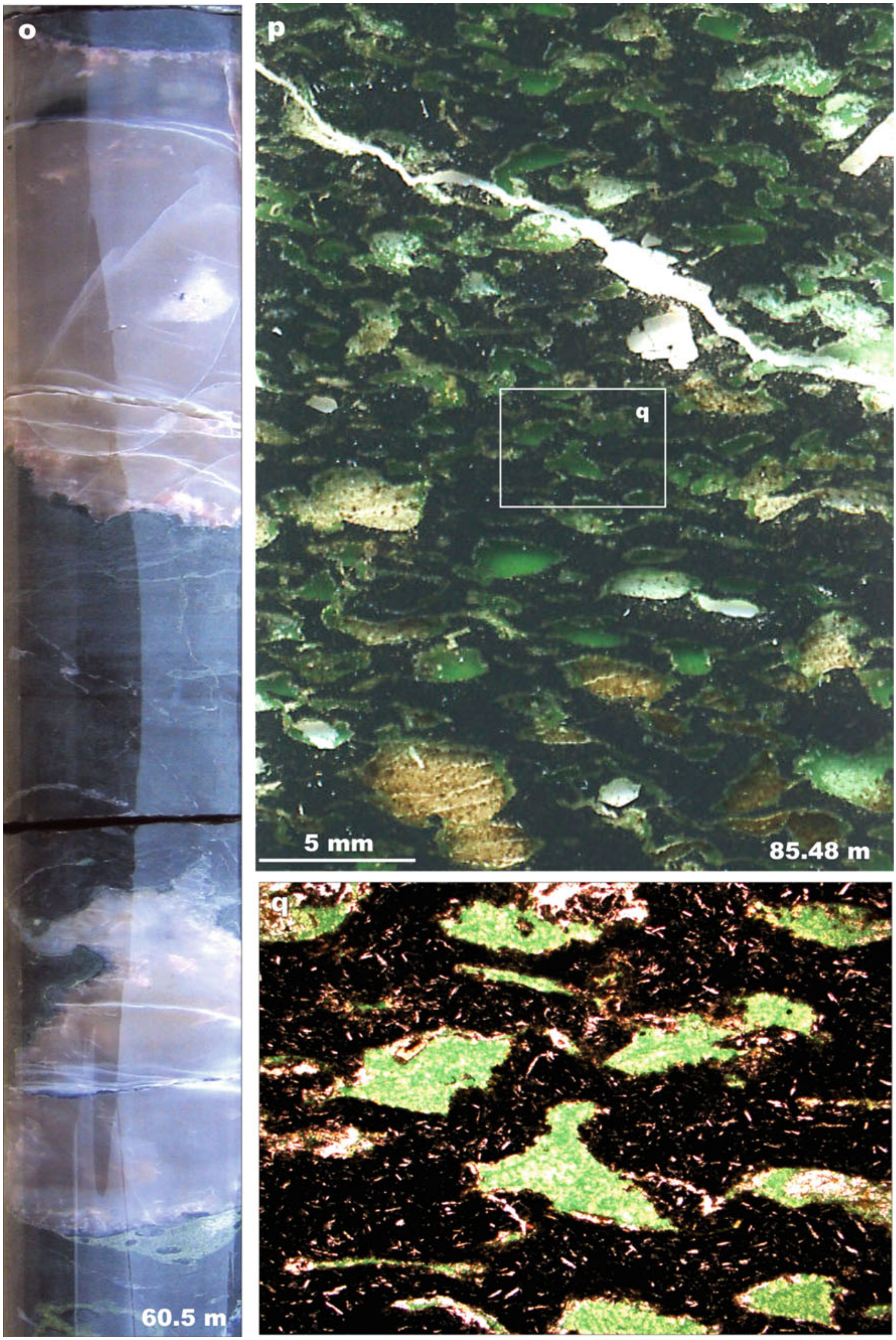

Fig. 6.65 (continued) (**o**) Large amygdales composed of microcrystalline quartz in basalt. (**p**) Scanned thin section of a fragmental, amygdaloidal mafic lava flow containing abundant fragments of devitrified glass (*green*). (**q**) Photomicrograph in transmitted, polarised light showing devitrified glass fragments replaced by green chlorite (All photographs by Victor Melezhik)

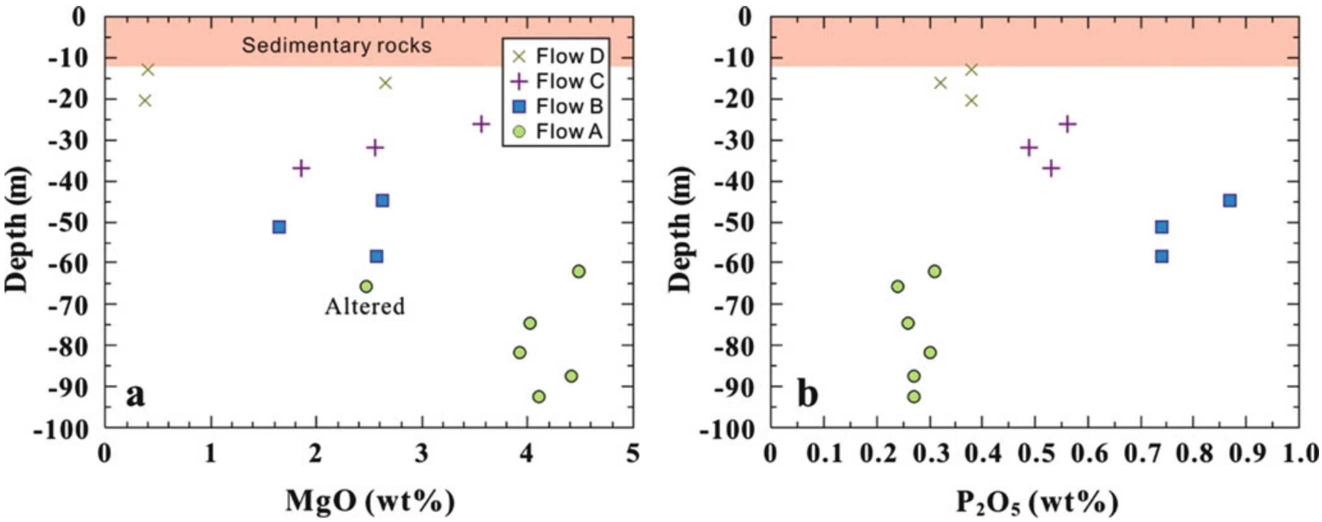

Fig. 6.66 (**a**) MgO versus depth, and (**b**) P_2O_5 versus depth cross-plots for igneous rocks in Core 7A

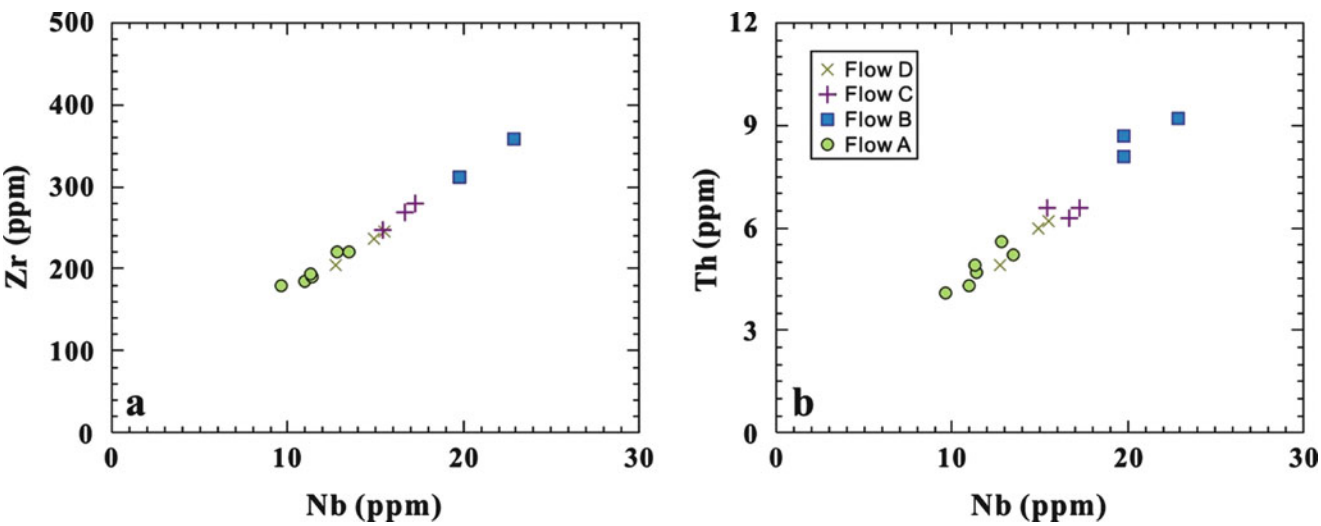

Fig. 6.67 (**a**) Zr versus Nb and (**b**) Th versus Nb cross-plots for lava flows from Core 7A, showing strong, positive correlation and indicating a similarity in the parental magmas

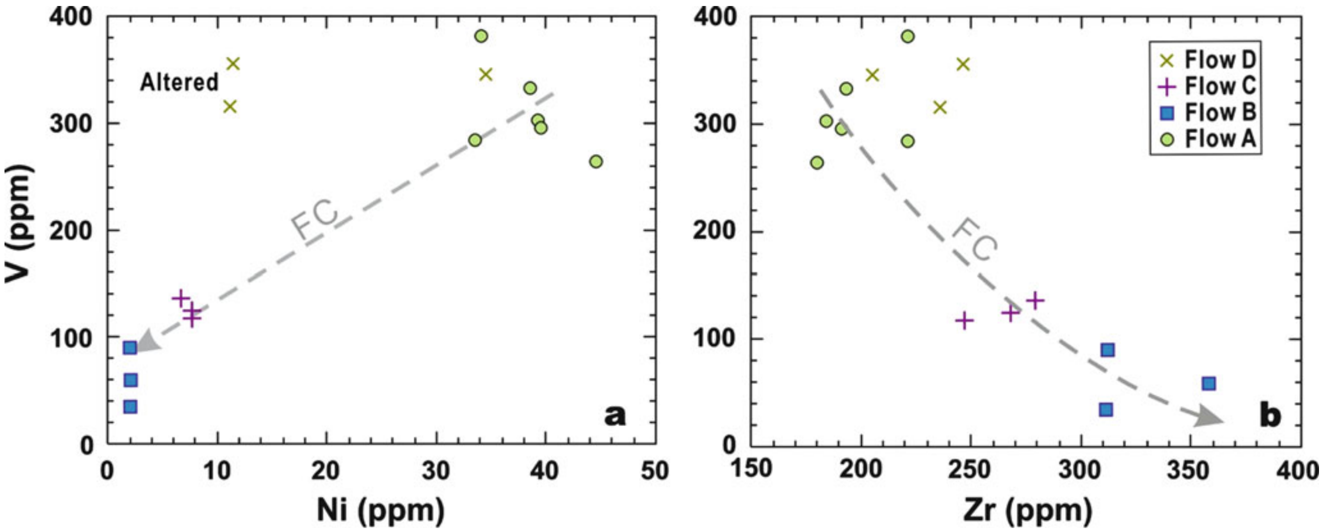

Fig. 6.68 (**a**) V versus Ni and (**b**) V versus Zr cross-plots showing positive V-Ni and negative V-Zr correlations caused by fractionation crystallisation (FC)

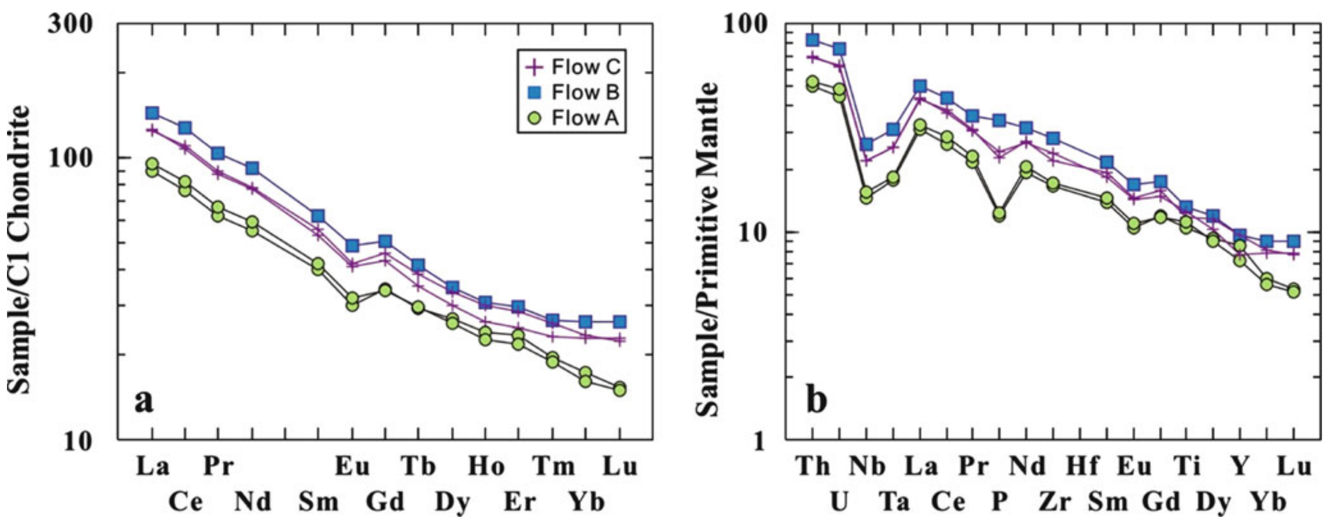

Fig. 6.69 (**a**) Chondrite-normalised REE patterns, and (**b**) primitive mantle-normalised trace element patterns for igneous rocks in Core 7A. Normalising values taken from Sun and McDonough (1989)

References

Kump L, Kasting JF, Barley ME (2001) Rise of atmospheric oxygen and the "upside-down" Archean mantle. Geochem Geophys Geosyst G3 2: Paper No. 2000GC000114, 10 p

Melezhik VA (1992) Early Proterozoic sedimentary and rock-forming basins of the Baltic Shield. Nauka (Science), St. Petersburg, p 258, in Russian

Melezhik VA, Huhma H, Condon DJ, Fallick AE, Whitehouse MJ (2007) Temporal constraints on the Paleoproterozoic Lomagundi-Jatuli carbon isotopic event. Geology 35:655–658

Predovsky AA, Fedotov ZhA, Zhangurov AM (1974) Geochemistry of the Pechenga complex. Nauka (Science), Leningrad, p 139, in Russian

Skuf'in PK, Yakovlev YuN (2007) Geological setting and petrogeochemical features of volcanic rocks from the Majärvi, Pirttijärvi and Orshoaivi suites in a section of the Kola Superdeep Well and near-surface zone. Bull Moscow State Tech Univ 19(2):173–197, in Russian

Skuf'in PK, Pushkarev YuD, Kravchenko MP (1986) Volcanic rocks of the mugearite-trachyte formation in the Pechenga volcano-plutonic palaeodepression. Proc USSR Acad Sci Geol Ser 1:18–29, in Russian

Sun S-S, McDonough WF (1989) Chemical and isotopic systematics of oceanic basalts; implications for mantle composition and processes. In: Saunders AD, Norry MJ (eds) Magmatism in the ocean basins, vol 42, Geological Society special publication. Published for the Geological Society by Blackwell Scientific Publications, Oxford/Boston, pp 313–345

6.2.5 Kolosjoki Sedimentary Formation: FAR-DEEP Holes 8A and 8B and Related Outcrops

Victor A. Melezhik, Anthony R. Prave, Aivo Lepland, Eero J. Hanski, Alexander E. Romashkin, Dmitry V. Rychanchik, and Zhen-Yu Luo

Scientific Targets

- Tectonic and depositional settings in the aftermath of the Lomagundi-Jatuli isotopic event
- Geochemical rock record in the aftermath of the global perturbation of the carbon cycle
- Carbon and strontium isotopic composition of basinal water
- Redox-state of the atmosphere and seawater
- Geochemical and mineralogical features of a palaeo-weathered surface
- Dissolution, transport and precipitation of iron oxides in low-temperature processes
- Provenance composition
- Microfossil record

Holes 8A and 8B intersected the Kolosjoki Sedimentary Formation (Figs. 6.70, 6.71, and 6.72) in the Pechenga Greenstone Belt (Figs. 6.32 and 6.33). The formation has a maximum depositional age of c. 2060 Ma and was deposited in the aftermath of the Lomagundi-Jatuli positive carbon isotopic excursion in sedimentary carbonates, which is recorded by the ^{13}C-rich carbonates of the Kuetsjärvi Sedimentary Formation (Melezhik et al. 2005, 2007). The Kolosjoki sedimentary rocks represent a varied suite of volcaniclastic "red beds" and haematite-rich lithofacies, and have a great potential to address low-temperature processes related to the mobilisation, precipitation, erosion and redeposition of iron oxides (Figs. 6.73 and 6.74). The drillhole intersected one of the rare successions that contain marine carbonates generated at the end of the Lomagundi-Jatuli isotopic event, and thus enables study of the global carbon cycle and ancient seawater chemistry in the aftermath of the greatest perturbation of the global carbon cycle.

Hole 8A recovered 47 m of the upper part of the sedimentary formation (Figs. 6.70 and 6.75) whereas the 336-m-deep Hole 8B intersected 319 m of the Kolosjoki Sedimentary Formation, and 13 m of volcanic rocks of the underlying Kuetsjärvi Volcanic Formation (Figs. 6.71 and 6.72). At the drilling site, the Kolosjoki Sedimentary Formation consists of greywackes, arkosic gritstones, haematite-rich siltstones and shales, dolostones and jaspers. The base of the formation is defined by an unconformity with a series of palaeovalleys deeply incised into the underlying Kuetsjärvi volcanic rocks (Fig. 6.75). This unconformity was intersected by Hole 8B at a depth of 323 m (Fig. 6.71). The formational top of the sedimentary unit was not intersected. It is defined elsewhere in the area by a major thrust-fault, which cuts out part of the formation and separates it from the overlying pillowed tholeiitic basalts of the Kolosjoki Volcanic Formation (Fig. 6.75). The thrust-fault, termed the Luchlompolo fault, represents one of the major seismic boundaries in the Pechenga Greenstone Belt (Kazansky et al. 1998; Sharov et al. 1998).

Chemical compositions of the analysed archive samples are listed in Appendices 20–22. Figure 6.72 shows major and trace element variations as well as magnetic susceptibility as a function of stratigraphic height, while Figs. 6.76, 6.77, and 6.78 exhibit geochemical diagrams with data from the volcanic intervals. The uppermost volcanic rocks of the Kuetsjärvi Volcanic Formation intersected by Hole 8B are characterised by a high magnetic susceptibility (up to 81,000 μSI; K* = 6,920 × 10^{-6} SI units in Fig. 6.72). The values stay high in the overlying greywackes to a depth of 295.5 m, and gradually decrease to 120–350 μSI (K* = 10–30 × 10^{-6} SI units in Fig. 6.72) at a depth of 230 m. Such values characterise the bulk of the remaining siliciclastic rocks, except arkosic gritstones (20–350 μSI; K* = 2–30 × 10^{-6} SI units in Fig. 6.72) and dolostones (−20–350 μSI; K* −2 to 12 × 10^{-6} SI units). Photos of core, natural outcrops and thin sections provide a detailed documentation of the major lithological features throughout the stratigraphy of Holes 8A and 8B (Figs. 6.70, 6.73, 6.74, and 6.79).

The Kuetsjärvi Volcanic Formation

The drilled 13.5-m-section at the bottom of Core 8B, belonging to the Kuetsjärvi Volcanic Formation, begins with 1.3 m of lava breccia with clasts of amygdaloidal lava; this likely represents the brecciated lava top of an underlying lava flow. The breccia is overlain by a massive, fine-grained, intermediate lava flow at interval 334.7–329.8 m. The remaining 7 m of this volcanic section, to the contact with the overlying sedimentary rocks (323 m), consists of fragmental rocks (Fig. 6.79fo–ft) representing the autoclastic upper part of the lava flow.

Three volcanic samples, one lava and two breccias, were analysed (Appendices 20 and 21; Fig. 6.76a). The andesitic lava sample (SiO_2 = 57.5 wt.%, MgO = 3.3 wt.%, TiO_2 = 2.5 wt.%) is more representative of the original magma composition than the breccia samples. The latter are lower

V.A. Melezhik (✉)
Geological Survey of Norway, Postboks 6315 Sluppen, NO-7491 Trondheim, Norway

Centre for Geobiology, University of Bergen, Allegaten 41, Bergen N-5007, Norway

V.A. Melezhik et al. (eds.), *Reading the Archive of Earth's Oxygenation*, Volume 2: The Core Archive of the Fennoscandian Arctic Russia – Drilling Early Earth Project, DOI 10.1007/978-3-642-29659-8_3, © Springer-Verlag Berlin Heidelberg 2013

in MgO (1.7, 2.0 wt.%) but also lower in silica (SiO_2 44.9, 47.9 wt.%). These low abundances are compensated by very high Fe (Fe_2O_{3tot} = 21–25 wt.%) and K_2O (5.4, 8.2 wt.%) contents, both due to strong alteration, complicating the chemical classification of the rocks. All analysed samples are relatively high in TiO_2 (2.2–3.6 wt.%), and low in Cr and Ni (7–65 ppm). Due to their low Nb/Y, the volcanic rocks plot in the subalkaline field in the Winchester and Floyd (1977) discrimination diagram (Fig. 6.76b), though the post-magmatic gain of alkalies makes the present chemical compositions alkaline.

Despite the above-mentioned alteration phenomena, immobile minor and trace element abundances can be utilised when comparing the Hole 8B volcanic rocks with their stratigraphic correlatives that have been recovered from Hole 7A. In Hole 7A, four lava flows have been identified (Flows A–D) differing from each other by their P_2O_5 contents. In terms of P_2O_5 and Nb abundances, the rocks from Hole 8B are comparable to the Flow C samples from Hole 7A (Fig. 6.77). Geochemical comparison and correlation of the volcanic rocks intersected by the two drillholes beneath the Kolosjoki Sedimentary Formation suggest that the uppermost Flow D was very likely eroded away at the site of Hole 8B prior to the accumulation of the overlying sedimentary rocks.

Outcrop observations show that the lavas exposed immediately below the Kuetsjärvi-Kolosjoki contact near site 8B are massive to fluidal, sparsely plagioclase-phyric rocks containing large jasper-filled amygdales and injected by numerous red K-feldspar veinlets and jasper veins (Fig. 6.79fu–fv). The jasper veins are also abundant in the cored lavas but have not been observed in the overlying Kolosjoki Sedimentary Formation rocks. Hence, the formation of these jasper veins is associated with post-volcanic hydrothermal activity and predates the deposition of the Kolosjoki Sedimentary Formation. Further, the K-feldspar veinlets are truncated by the unconformity and have not been seen to extend into the basal sedimentary rocks of the Kolosjoki Sedimentary Formation (Fig. 6.79fp). Similarly to Hole 7A, the uppermost 2 m of the volcanic unit exhibit numerous reddish patches and red K-feldspar veinlets (Fig. 6.79fp–ft) related to addition of K_2O, whereas most of CaO has been lost. The high total iron content (Fe_2O_{3tot} up to 25 wt.%) is likely connected to mobility of iron and haematisation. In contrast, loss of ignition, which is another index of alteration, is surprisingly low ($\leq$1.2 wt.%).

The Kolosjoki Sedimentary Formation

The Kolosjoki Sedimentary Formation is informally subdivided into seven lithostratigraphic units, which are, from base to top: the Sandstone, Lower Greywacke, Gritstone, Haematite, Ferropicrite, Dolostone, and Upper Greywacke members (Fig. 6.71).

The Sandstone Member

The Sandstone member fills palaeovalleys, and consequently its thickness varies greatly along strike (Fig. 6.75). In the logged core, the member has a thickness of c. 10 m (323–312.5 m, Fig. 6.71). It lies with a sharp contact on the underlying andesitic lavas (Fig. 6.79fo, fp), and is composed of pale pink, fine-grained, and locally coarse-grained to conglomeratic near the base, volcaniclastic sandstones (Fig. 6.79fj–fn). They are mainly massive, parallel laminated (Fig. 6.79fj) and normally graded (Fig. 6.79fk), with rare small-scale trough cross-beds (Fig. 6.79fn). The sandstones contain angular and well-sorted clasts of quartz, microcline, albite, particles of haematite, magnetite and leucoxene, and fragments of intensively altered volcanic rocks. A high magnetic susceptibility, similar to that of the underlying volcanic rocks, suggests a local clast source.

Chemical compositions of sandstone samples are presented in Appendices 20 and 21. They are rich in Fe_2O_{3tot} (9.6 wt.%), TiO_2 (1.2 wt.%), Ba (750 ppm) and Cu (570 ppm), and contain 5.4 wt.% K_2O and 1.2 wt.% Na_2O.

The Lower Greywacke Member

The Lower Greywacke member is 94 m thick (312.5–217.9 m), though in some measured exposed sections in the vicinity of the drilling site, the thickness is reduced to 20 m. In the core, the basal bed has a transitional contact with the underlying, indistinctly bedded sandstones. Elsewhere in exposed sections, it has been observed that the member has at the base a series of 0.5–5-m-deep and up to 20-m-wide channels filled with polymict conglomerate; the clasts are unsorted and variably rounded lava fragments, as well as, quartz and jasper amygdales (Fig. 6.79fm) weathered out from the underlying volcanic rocks (Fig. 6.79fu, fv). Basal beds of the member may contain abundant rip-up intraclasts of black haematite-rich mudstone (Fig. 6.79fl). The upper contact is defined by the first appearance of the pink arkosic gritstone unit at a depth of 218.7 m (Figs. 6.71 and 6.79ec–ee). The member contains volcaniclastic greywackes with a few beds of arkosic sandstone (0.9–5 m thick) and volcaniclastic conglomerate (0.5–3 m thick) (Figs. 6.79ae–fp).

The greywackes display planar and trough cross-beds occurring as varibaly thick cosets (Figs. 6.79el–es, ez, fb, fd, fg). In outcrop areas near the drilling site, they are stacked as 0.1–1.5-m-thick cosets having coarser material and intraclasts of black and pink mudrocks at their base (Figs. 6.79eo, eq, et–ev, fd–ff, fh). The cosets are commonly separated by well-developed erosional surfaces (Figs. 6.79eo, eq, ev). Mapping of exposed areas has shown that trough cross-beds pass laterally into channelized, tabular cross-beds (Fig. 6.79er), massive or normally graded gritstone-sandstone (Fig. 6.79fb), or sandstone-black mudstone beds. In places, both the trough and the tabular cross-beds contain overturned, soft-sediment deformed and slumped cross-bedding (Figs. 6.79en, eo, er). Some cross-beds show small-scale syndepositional folding and faulting (Fig. 6.79ff).

In the drillcore, syndepositional faulting is documented at the depth of 325.9–323.2 m as a matrix-supported autobreccia. From 278 m and upwards numerous laminae in cross-beds are "impregnated" by leucoxene, which resulted in pale yellow colouration (Figs. 6.79el–en, es). From c. 230 m upwards the cross-bedded greywackes pass gradually into "spotted", massive or indistinctly stratified varieties (Figs. 6.79ee–ej) with some intervals containing large clay fragments (Fig. 6.79eh).

The greywackes are composed of angular clasts of quartz, microcline, rare albite, fragments of intensively altered mafic to intermediate lavas, particles of haematite, magnetite and leucoxene; all embedded in a fine-grained matrix of similar composition but enriched in sericite. The degree of sorting and rounding does not show any clear stratigraphic trend. Black mudstones, which occur as drapes within the graded sandstones and intraclasts, are composed of similar but finer clastic particles and haematite. The "spotted" greywackes do not differ in mineralogy from their ordinary counterparts but generally contain laminae and layers enriched in leucoxene resulting in a yellowish colour (Figs. 6.79ee–eg). Black spots represent a haematite cement/matrix supporting clasts of quartz and feldspar.

The arkosic sandstones are scattered throughout the member as 0.9–1.5-m-thick beds but also form more extensive, up to 5-m-thick units in the upper part of the section. They are commonly massive or crudely stratified. The graded sandstones are associated with trough cross-beds ranging in thickness from centimetres to a few decimetres (Figs. 6.79ew–ey). Some are draped by black, haematite-rich mudstone units (Fig. 6.79fa) In places, graded-sandstone beds occur as sedimentary dykes injected into the overlying black mud units (Fig. 6.79fc). The volcaniclastic conglomerates form small channels and can be either matrix- or clast-supported (Figs. 6.79et, eu).

The arkosic sandstones are mainly composed of angular clasts of quartz, microcline and albite, contain particles of haematite, magnetite and leucoxene, all embedded in a fine-grained matrix of similar composition but enriched in sericite (Fig. 6.79fi). The volcaniclastic conglomerates consist exclusively of fragments derived from the underlying Kuetsjärvi Volcanic Formation (Fig. 6.79et, eu).

Chemical compositions of the rocks are presented in Appendices 20 and 21. The greywackes are rich in Fe_2O_{3tot} (7–13 wt.%), TiO_2 (1–3 wt.%) and Ba (up to 1700 ppm). With a few exceptions, they are rich in K_2O (5–7.6 wt.%) and low in Na_2O (0.1–0.5 wt.%). The exceptional samples are from the base of the member and contain up to 10 wt.% of calcite and 1.8 wt.% Na_2O, though the Ka_2O/Na_2O ratio remains high (3–5). The greywackes are devoid of organic carbon and sulphur.

The arkosic sandstones are rather similar in chemical composition to the greywackes but contain more SiO_2 (71–80 wt.%) and less Fe_2O_{3tot} and TiO_2 (Appendix 20). The Ba concentration ranges between 500 and 1200 ppm (Appendix 21).

The Gritstone Member

The Gritstone member is a 15-m-thick unit (217.9–203 m, Fig. 6.71) resting with a sharp contact on the underlying greywackes. The base of the member is defined by a thin, polymict volcaniclastic conglomerate developed basin-wide (Fig. 6.79ed). The contact with the overlying rocks is transitional. Sedimentological features of the member are presented in Figs. 6.79dm–ed.

The basal conglomerate contains unsorted fragments of lavas and large quartz and jasper amygdales derived from the Kuetsjärvi volcanic rocks. Similar conglomerates, though containing mainly fine pebbles and grading upward into gritstones, fill numerous small-scale channels throughout the member (Figs. 6.79dm, dv, dx, dy, ea, ab). They also contain lag deposits of clastic haematite, abundant large fragments of haematite "ores" (Figs. 6.79ea, eb), and large angular clasts of red K-feldspar (Figs. 6.79dm, dx). Earlier detailed studies on haematite "oolites" and "ores" have been conducted by Akhmedov (Predovsky et al. 1974; Akhmedov 1972a, b).

The gritstones are commonly red in colour and massive (Figs. 6.79dr, dz, ec). Crude stratification is expressed by deposition of clastic haematite (Figs. 6.79do, du), which also concentrates at the base of some gritstone beds (Fig. 6.79dn). Rare trough cross-bedding has been documented (Fig. 6.79dw). Numerous thin, parallel-laminated mudstone and claystone layers are present. Their amount gradually increases upward (Figs. 6.79dp, dq, dt) defining a transition to the overlying member. The gritstones consist of semi-rounded clasts of quartz and K-feldspar and accessory barite in the form of grains and intergranular veinlets. The gritstone contains c. 80 wt.% SiO_2, it is low in Na_2O (0.1 wt.%), rich in Sr (1150 ppm), and abnormally enriched in Ba (57700 ppm) (Appendices 20 and 21).

The Haematite Member

The Haematite member is 48 m thick (203–165.4 m, Fig. 6.71). The base of the member is defined by the first appearance of parallel-laminated sandstone-siltstone at a depth of 203 m (Fig. 6.71) followed by a 2-m-thick interval of interbedded sandstone-siltstone and gritstone-sandstone with a 1 m bed of marl on top. Figures 6.79bh–dl illustrate sedimentological features of the rocks.

The lowermost part of the member comprises thinly laminated siltstone units (Figs. 6.79db, dc, dl) interbedded with graded, greywacke/parallel-laminated siltstone couplets containing numerous small-scale gritstone channels. In some graded beds, the lowermost coarser units may contain large intraclasts of massive haematite “ore” (Figs. 6.79dh, di), whereas the uppermost units are massive beds composed of fine-grained haematite (Figs. 6.79dd–df). On the bedding plane, haematite beds may exhibit a wrinkled surface resembling elephant skin textures (Fig. 6.79dg). Some conglomerate channels contain abundant rounded, oolite-like clasts of haematite (Figs. 6.74, 6.79dk). Fine haematite particles are an important part of the sandstone and gritstone matrix (Fig. 6.79dj).

The succeeding rocks form a dolostone-jasper unit, which starts from 196.3 m (Fig. 6.71) with red, jasperised (SiO_2 = 52 wt.%, Fe_2O_{3tot} = 4.6 wt.%) dolostones (Fig. 6.79cw), dolorudite and dolarenite containing rounded particles of jasper, and probable small spheroidal stromatolites (Fig. 6.79da). In outcrops located close to the drilling site and farther to the east, jaspers have been seen to replace limestones and dolostones and form jasper beds with colloform structures (Figs. 6.79cx–cz).

The red dolostone-jasper unit is followed by a variegated, bedded, and channelised marl. The 0.7-m-thick channel is filled with polymict, rhythmically bedded breccia showing inverse grading (Figs. 6.79cu, cv). Fragments are silicified dolostones, greywackes, cherts, and probable stromatolitic dolostone. The breccia has a sharp contact with the overlying 33–m-thick succession of spectacular haematite-rich rocks, which make the Haematite member different from all other rocks of the Kolosjoki Sedimentary Formation. The haematite-rich rocks occur between depths 192 and 165 m. They are predominantly red, violet and brick-brown rocks with thin, parallel lamination marked by fine-grained sandstone couplets ranging from 3 mm to 4 cm in thickness and grading into siltstone (Figs. 6.79bh, bm, bo, bp, br, bs, bx–cb, ce, cl, cm); this lithofacies occurs over a thickness of c. 30 m. Many intervals show syn-depositional folding and slumping (Figs. 6.79bt–bw, cc, cd, cs). Ripples (Fig. 6.79bn), low-angle cross-lamination (Fig. 6.79bi) and small-scale, sand-filled channels (Figs. 6.79bq, cf) are present, but not common.

Several siltstone intervals contain jasper occurring either as 1-mm- to 2-cm-thick, well-defined layers with sharp contacts (Figs. 6.79co–cq) or as thicker beds with diffuse boundaries (Figs. 6.79ck, cn, cr). The former apparently represent hydrothermal Si-Fe precipitates, which form veneers across small-scale, uneven palaeorelief (Fig. 6.79bl). The thicker beds with diffuse boundaries apparently represent deposition of mixed clastic material and/or Si-Fe components chemically precipitated from a subaqueous hydrothermal source. Many graded sandstone beds contain angular and rounded jasper particles (Figs. 6.79bj, cg–cj, cn), whereas some beds with slump structures show larger jasper fragments with a clotted fabric (Fig. 6.79bk); all indicating syn-depositional erosion and resedimentation. Small-scale veinlets cross-cutting sandstone-siltstone rhythmites occur throughout the 190–165 m interval, with many having a ptygmatic appearance (Figs. 6.79be, cg, ch, cj) suggesting deformation in a plastic state.

The analysed samples show that the Haematite member rocks have diverse compositions. The carbonate rock is silicified (51 wt.% SiO_2) limestone (Mg/Ca = 0.21) with a high Mn (3300 ppm) and low Sr (68 ppm) concentrations (Appendices 20 and 22). The rhythmites show variable contents of SiO_2 (55–71 wt.%) and Al_2O_3 (8–14 wt.%), depending on the clast and matrix composition, though all have elevated Fe_2O_{3tot} (up to 14.5 wt.%) Cr (270–440 ppm) and Ni (55–130 ppm) contents (Appendices 20 and 21).

The Ferropicrite Member

The Ferropicrite member is a 72-m-thick unit (165.4–93 m) whose boundary with the underlying rocks is cryptic, but is placed at the first appearance of MgO, Cr and Ni-rich rocks at the depth of 165 m (Fig. 6.71). The member is composed of three main lithologies: (1) a massive, coarse-grained ferropicritic tuff with a clotted matrix (Figs. 6.79ap, av, aw, be); (2) an indistinctly bedded ferropicritic tuff (Fig. 6.79au) with a clotted structure (Fig. 6.79ax); and (3) parallel-laminated siltstones and rhythmically bedded sandstone-siltstone couplets (Figs. 6.79ba–bd, bf, bg), which are all apparently tuffites containing a variable degree of ferropicritic material. The bedded tuffites contain beds, lenses, layers and rip-up intraclasts of red, Fe-rich claystones (Figs. 6.79ay–bb, bd). Both the bedded and massive varieties contain thin jasper veinlets (Figs. 6.79bb–be). In some intervals, thickly bedded ferropicritic tuffs show reverse grading (Fig. 6.79bc).

The ferropicritic tuffs do not contain primary minerals and are composed of rock fragments replaced by serpentine, talc, phlogopite, apatite and magnetite (Fig. 6.79aw). The analysed samples have a rather homogeneous chemical composition (Appendices 20 and 21) and contain 42–45 wt.% SiO_2, 7.3–8.2 wt.% Al_2O_3, and 1–4 wt.% CaO (depending on the dolomite content). The rocks show high MgO (14.2–16.6 wt.%), Cr (722–1100 ppm) and Ni (690–1050 ppm) contents with good covariance (Fig. 6.78a). They are also high in total iron (mostly FeO_T >14 wt.%) and have elevated concentrations of high field strength elements (TiO_2 2.1–2.7 wt.%), which make them chemically similar to ferropicrites of the Pilgujärvi Volcanic Formation (cf. Hanski 1992). The tuffs are devoid of organic carbon and have low sulphur contents (<0.02 wt.%).

The four analysed tuffite samples consist of a mixture of ultramafic material (serpentine, talc, phlogopite and magnetite) with quartz and feldspar particles, and contain a significant amount of calcite (9–15 wt.% CaO, Appendix 20). They show lower MgO, TiO_2, FeO_T, Cr and Ni contents (marked as half-filled squares in Figs. 6.76 and 6.78). The values of loss-on-ignition vary within a wide range (2.0–18.4 wt.%), and correlate positively with CaO/Al_2O_3 (Fig. 6.78b). The latter ratio is either lower (<0.6) or higher (>1.4) than expected for magmatic values in ferropicritic lavas. The K_2O content (1.6–3.6 wt.%) is high for ultramafic rocks, having likely been added by fluids. Although the mobile elements occur in abundances far from the original magmatic values, the chemical characterisation of the tuffites as ferropicritic remains valid. The oxidation state of iron is very high as shown by the measured $Fe^{3+}/\Sigma Fe$ values of 0.88–0.92, which are comparable to the oxidation state of associated haematite-bearing sedimentary rocks. Given the high MgO content of the Ferropicrite member, the magnetic susceptibility of the unit is low ($<60 \times 10^{-6}$ SI), which is accounted for by the high degree of alteration and oxidation.

The Dolostone Member

The Dolostone member is a c. 40-m-thick (93–53.5 m) unit of interbedded clastic, microsparitic and stromatolitic dolostones, with rare limestones in the lower part, and several beds of greywacke, arkosic sandstone, conglomerate and breccia in the upper part. The thickness of the member logged in Core 8A is 33 m (Fig. 6.71). Sedimentological features of the main rocks comprising the member are presented in Figs. 6.70 and 6.79k–ao. The member has a sharp contact with the underlying ferropicritic tuff. However, elsewhere in outcrop areas, there are transitional beds composed of cross-bedded greywackes interbedded with greywacke matrix-supported breccia containing fragments of dolostones and cherts (Fig. 6.79aq–as).

The clastic, microsparitic and stromatolitic dolostones form 0.5–1.0-m-thick beds whose primary structures have been largely obliterated by recrystallisation and silicification processes. The clastic dolostones are massive (Figs. 6.70f, k and 6.79l, n, ah) or show crude horizontal and cross-bedding (Figs. 6.79p, aj) with small erosional surfaces (Fig. 6.79ao) and pockets of stone rosettes (Figs. 6.70h, i). In Hole 8A, the upper part of the member is composed of horizontally laminated dolarenite with some layers having mud drapes (Figs. 6.70a, b). Some dolorudite beds exhibit normal grading (Fig. 6.79o) whilst others contain angular jasper clasts (Fig. 6.79ah) or red oolites (Fig. 6.70d). Breccia beds are less than 1 m in thickness. They are either dolarenite or clay-supported. The former contain abundant chert and silicified dolostone fragments (Figs. 6.70j and 6.79q). The clay-supported breccias mainly contain dolostone fragments (Figs. 6.79r, t) and contacts with underlying and overlying carbonate beds appear to be irregular with numerous embayments (Figs. 6.79s, u); this is apparently a result from dissolution processes of evaporite-bearing beds (Fig. 6.79aq) or due to surface or subsurface karstification.

The microsparitic dolostones are generally recrystallised and appear to be massive (Figs. 6.70e, g and 6.79k, ab). Many beds are silicified (Figs. 6.70c and 6.79ac), though some show a relict horizontal lamination (Figs. 6.70f and 6.79am). Where the recrystallisation is less pervasive, wavy bedding is visible (Fig. 6.79ai).

The stromatolitic dolostones display numerous features of questionable biogenicity, such as convex-downward structures (Fig. 6.79an), which may represent tectonically inverted stromatolites, and irregular but non-wrinkly laminae (Fig. 6.79af) that could represent tufa or travertine deposits. Confidently identified microbial laminites include globular stromatolites (Figs. 6.79x–z) and other stromatolitic structures that are far too large to be robustly identified in the core (Figs. 6.79aa, ak, al). "Classic" columnar stromatolites are rare (Fig. 6.79v); they were first identified and described by Ljubtzov (1979). The arenitic rocks occurring in the upper part of the member are arkosic sandstones and greywackes with ripple-cross lamination (Fig. 6.79n) or low-angle cross-lamination (Fig. 6.79m)

All analysed carbonate samples are dolostones with the Mg/Ca weight ratio ranging between 0.50 and 0.62 (Appendices 19 and 22). The lower part of the member (93–80 m) is intensively silicified ($SiO_2 = 17–48$ wt.%) (Appendices 17 and 20). The dolostones have variable Mn (167–817 $\mu g\ g^{-1}$), Fe (890–7,500 $\mu g\ g^{-1}$) and Sr (23–110 $\mu g\ g^{-1}$) contents (Appendices 19 and 22).

The Upper Greywacke Member

The Upper Greywacke member is a c. 50-m-thick unit (53.5–3.6 m) with a sharp contact with the underlying Dolostone member. It is composed of interbedded shale, siltstone, greywacke, clayey greywacke and arkosic sandstone (Figs. 6.71). The main facies is parallel (Fig. 6.79a, b, g–i) and wavy (Figs. 6.79c, d) lamination with mud-draped sandstone layers (Fig. 6.79j). The laminae thicknesses vary from 1 mm to 1 cm. Rare gritstone beds are present and show a normal grading (Fig. 6.79e). The chemical composition of the analysed samples varies greatly depending on lithology (Appendices 17, 18, 20 and 21). Similarly to other silicate rocks of the formation, this member has high K_2O/Na_2O (up to 39), but lower iron and titanium contents. The upper contact of the member with the overlying Kolasjoki Volcanic Formation is tectonic, marked by the Luchlompolo thrust fault.

The Depositional Framework

The Kolosjoki sedimentary rocks can be assigned to two distinct depositional packages, those that represent largely fluvially influenced, non-marine sedimentation and those that record marine-influenced settings. The transition occurs between the Gritstone and Haematite members.

The lower two members of the Kolosjoki Sedimentary Formation (the Sandstone and Lower Greywacke members) are mostly associated with deep, steep-walled, canyon-like to broad-sided palaeovalleys that are incised into the underlying Kuetsjärvi volcanic rocks (see Fig. 6.75). The members are characterised by variably scaled sets and stacked cosets of trough to planar cross-bedded and flat-laminated intervals, many of which define decimetre to several-metre-scale lens to channel-shaped geometries. Between these units are thinner lenses and layers of mudstone, in places occurring as partings and drapes over individual foreset and set contacts. These finer-grained lithologies are eroded by the bases of overlying sandstone units and can be observed as angular intraclasts, many of which exhibit sharp, cuspate and upturned margins. The intraclasts are best interpreted as eroded desiccation mudchips. Thus, taken together, the most parsimonious interpretation of the lower two members is that they record a fine-grained (braided) fluvial-alluvial infill of previously cut and eroded valleys. The coarser-grained portions may represent small, alluvial fans that prograded from the mouths of narrow canyons. The shallow trough cross-beds record the down-channel migration of low-amplitude three-dimensional large ripples whereas the planar cross-bedded sets likely record large, two-dimensional ripples (sand bars/waves). Flat-laminated intervals are common in such settings and record upper-flow regime conditions, likely during flood and/or sheet flow events. The mudstone layers and partings represent ponded and/or slack-water areas, many of which dried up to provide the desiccation chips.

Sharply overlying these units is the Gritstone member. It has a tabular geometry in that it exhibits a relatively uniform thickness regionally, and 'seals' the underlying palaeovalleys, in many places overstepping the Lower Greywacke units to rest depositionally on the Kuetsjärvi volcanites. The Gritstone facies are typified by mostly massive, but also broad, shallow trough cross-bedded sets and cosets interlayered with flat to low-angle laminated units. These lithologies, like those of the underlying siliciclastics infilling the palaeovalleys, define wide lens and channel-shaped geometries at outcrop scale. Thus, we also infer a fluvially influenced depositional setting for rocks comprising the Gritstone member; this depositional system was widespread and not confined by the walls of palaeovalleys. The abundant coarse material comprised of reworked quartz amygdales and other volcanic clasts dispersed throughout the lower part of the Gritstone member formed as an erosional 'lag' that would have mantled the exposed margins and upland areas of the palaeovalleys, and which become reworked into the basal fluvial system of the Gritstone member.

Above this, the rocks of the Haematite and Ferropicrite members record an overall deepening or transgressive episode. The former exhibits centimetre to a few-decimeter-scale, well-defined tabular bedding (as observed in outcrop) arranged vertically as repetitively interlayered coarser and finer siliciclastics. Multi-directional ripple cross-lamination, abundant mudstone drapes, cyclical-appearing mudstone-siltstone couplets and an overall fining-upward trend from base to top of the Haematite member support this interpretation. Near the top of this member are jasperoid and dolostone beds–these likely represent deposition in shoreline and shallow-marine settings, perhaps influenced by hydrothermal activity. A continuation of the deepening trend is recorded in the largely fine-grained and finely laminated lithologies that comprise the majority of the Ferropicrite member, including the development of rhythmite intervals. These facies represent a low-energy, and presumably deep, water setting.

Thus, the overall pattern for the lower part of the Kolosjoki Formation is a progression from alluvial-fluvial settings confined to canyons and palaeovalleys (Sandstone and Lower Greywacke members) through to unconfined (likely braided) fluvial deposition (Gritstone member) and then to marine transgression marked by shoreline-deltaic-nearshore marine settings (Haematite member) that progressively deepened upward (Ferropicrite member).

A reversal in that trend, and a return to shallower conditions is marked by the uppermost part of the Ferropicrite member, which shows a systematic coarsening-upward pattern in the uppermost 20–30 m. Those rocks are sharply overlain by the Dolostone member. This unit bears many hallmark features of shallow-marine deposition, including the presence of oolites and oncolites, development of microbial lamination and stromatolites, and bed-scale interlayering between fine to coarse siliciclastics and carbonate rocks. Stone rosettes and abundant platy intraclasts suggest the influence of strong storm and tidal currents on deposition. The presence of potential karst surfaces, carbonate breccias and possible tufa and/or travertine deposits, indicates that the shallowing trend resulted in repeated episodes of subaerial exposure. Many of those lithologies are arranged in metre-scale shoaling cycles, arguably representing the classic peritidal cycles so common in many Phanerozoic shallow-marine/shoreline carbonate-dominated settings.

The Dolostone member is sharply overlain by the Upper Greywacke member. In the core, the contact is marked by a sandstone bed that contains angular carbonate-clasts and may well represent a sequence boundary. Unfortunately, this contact is not exposed in outcrop to assess its regional geometry (the Luchlompolo thrust fault transects this contact). Nevertheless, the observations from the core indicate that this member is typified by fine-grained, finely laminated to graded beds; cross-bedding (on any scale) and coarser facies are rare. Thus, we tentatively interpret these rocks as recording a return to a relatively low-energy, deep-water depositional setting. The tectonic contact at the top of the Kolosjoki Sedimentary Formation (Luchlompolo thrust fault) hinders any further assessment of the Kolosjoki's palaeoenvironmental framework.

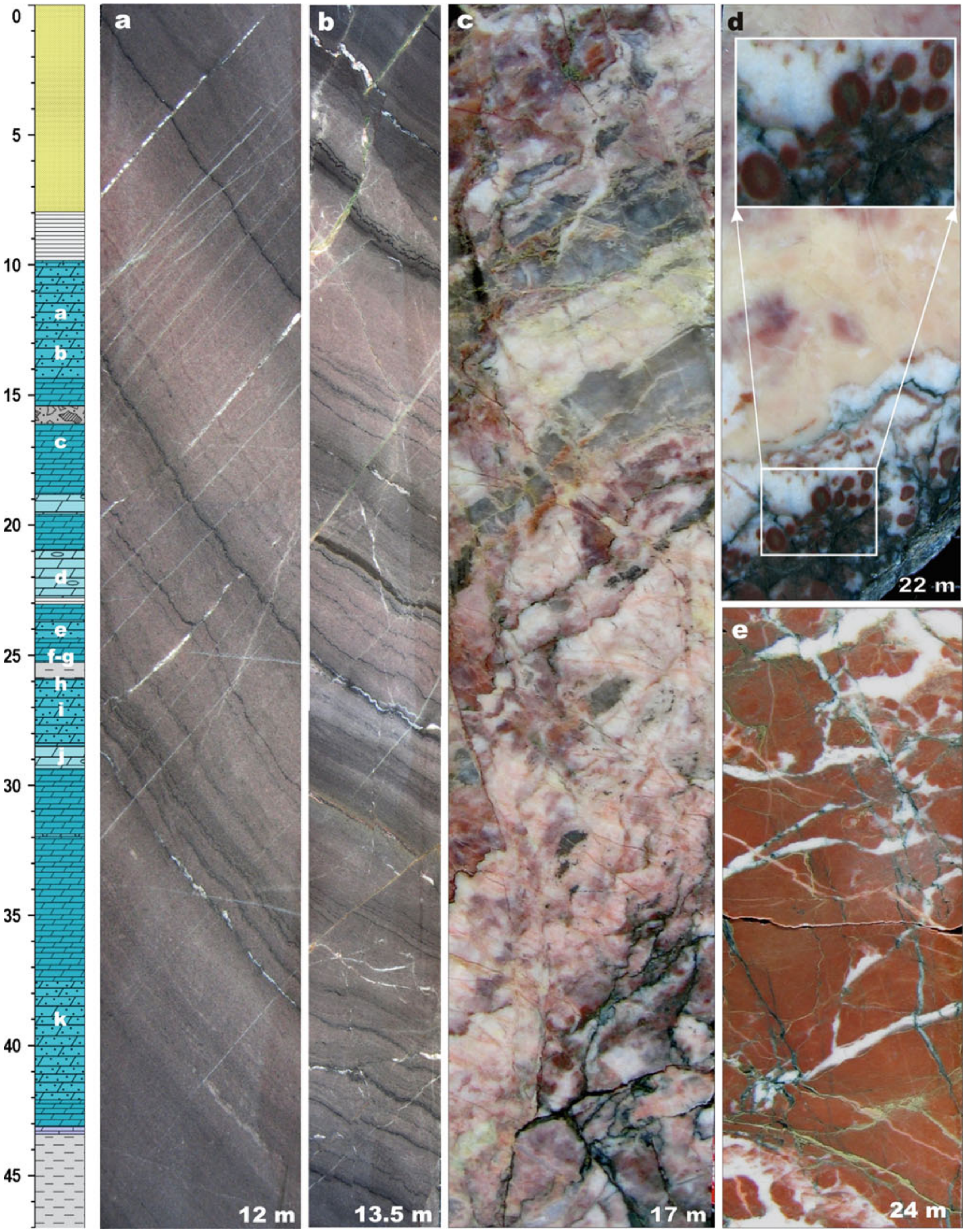

Fig. 6.70 Sedimentological features of the main rock types of the Kolosjoki Sedimentary Formation based on Core 8A. (**a**, **b**) Grey-purple, parallel-bedded, dolarenite; some dolarenite layers are draped by dark grey mudstone; white dolomite-filled cleavage cracks occur perpendicular to bedding. (**c**) Beige to pale pink, brecciated and silicified, microsparitic dolostone. (**d**) Dark-pink, dolomitic oolite embedded in white dolospar passing upward into beige dolorudite. (**e**) Brown, massive, microsparitic dolostone with extensional cracks filled with white dolospar

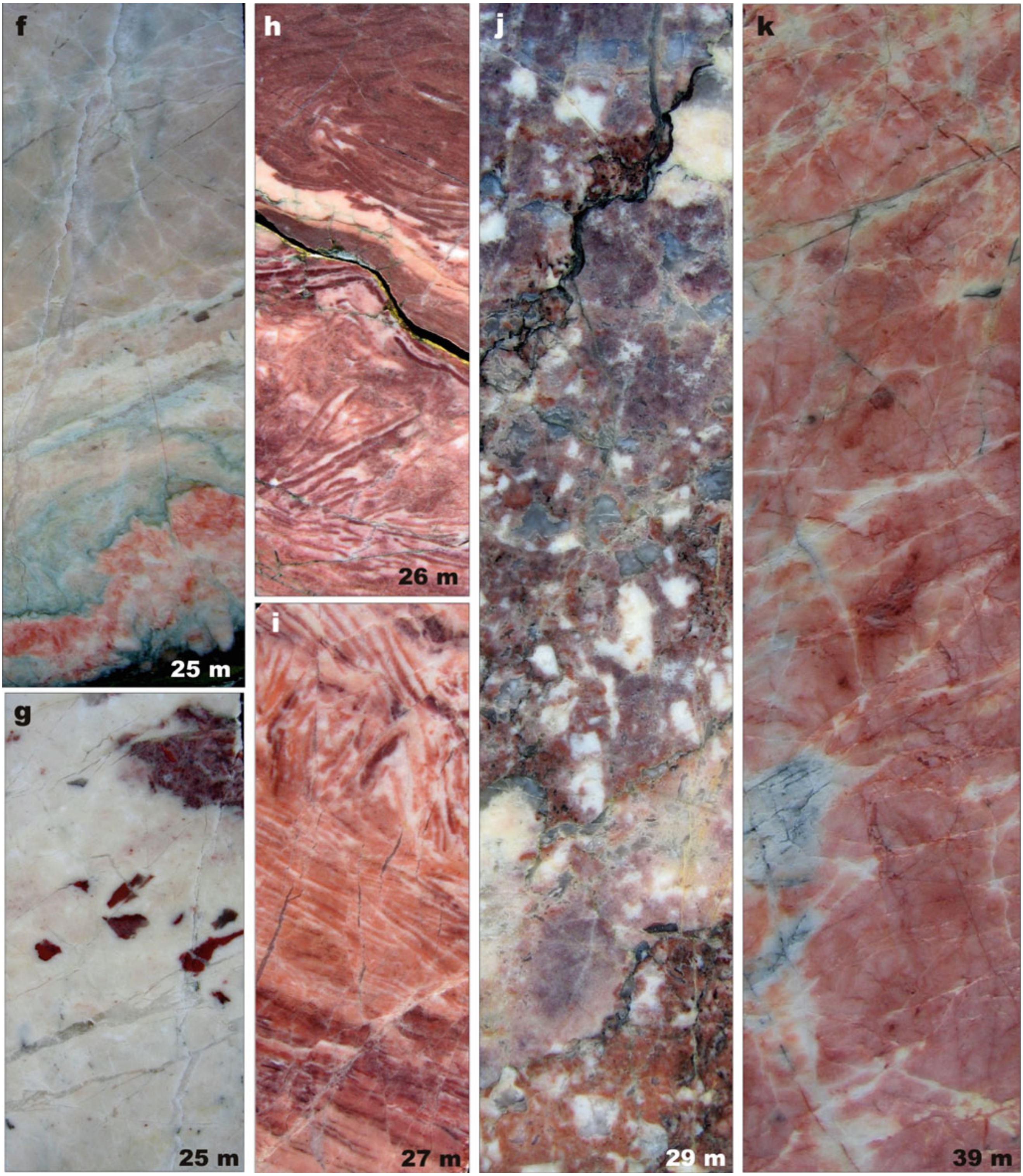

Fig. 6.70 (continued) (**f**) Pale pink dolarenite with a dissolution surface (near base) overlain by beige, horizontally bedded dolarenite passing into a massive variety; some dolarenite layers are graded. (**g**) White, massive, microsparitic dolostone with angular clasts of jasper. (**h**, **i**) Stone rosettes in bedded dolarenite. (**j**) Clast-supported breccia containing fragments of pale grey chert, and white and brown dolostone. (**k**) Pale pink, massive, tectonically brecciated dolarenite (Photographs by Victor Melezhik)

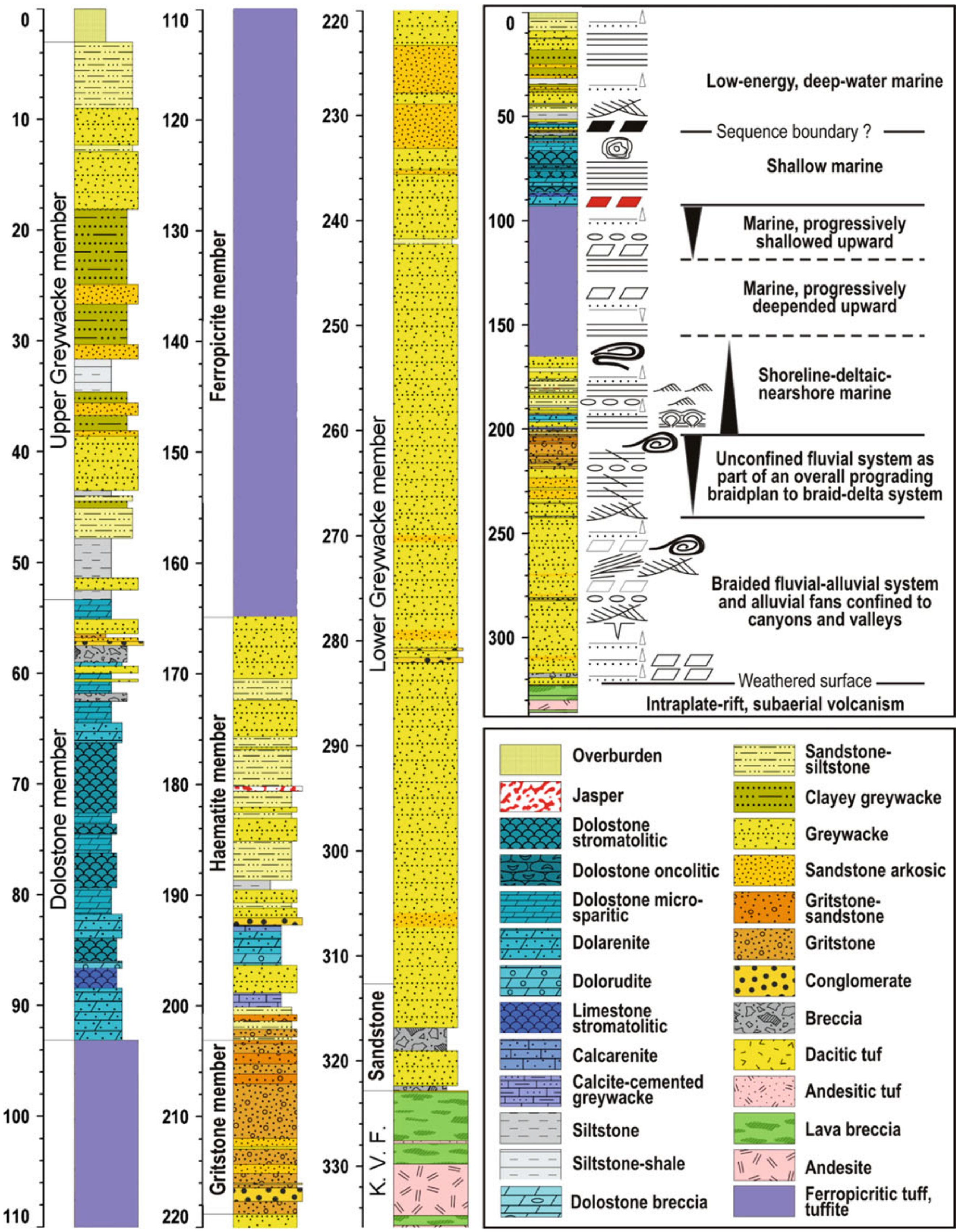

Fig. 6.71 Lithological section of the Kolosjoki Sedimentary Formation based on core logging of Hole 8B, and a tentative reconstruction of depositional environments based on the core observations, geological mapping and sedimentological research in the vicinity of the drilling site. Lithological symbols are explained in Fig. 6.6

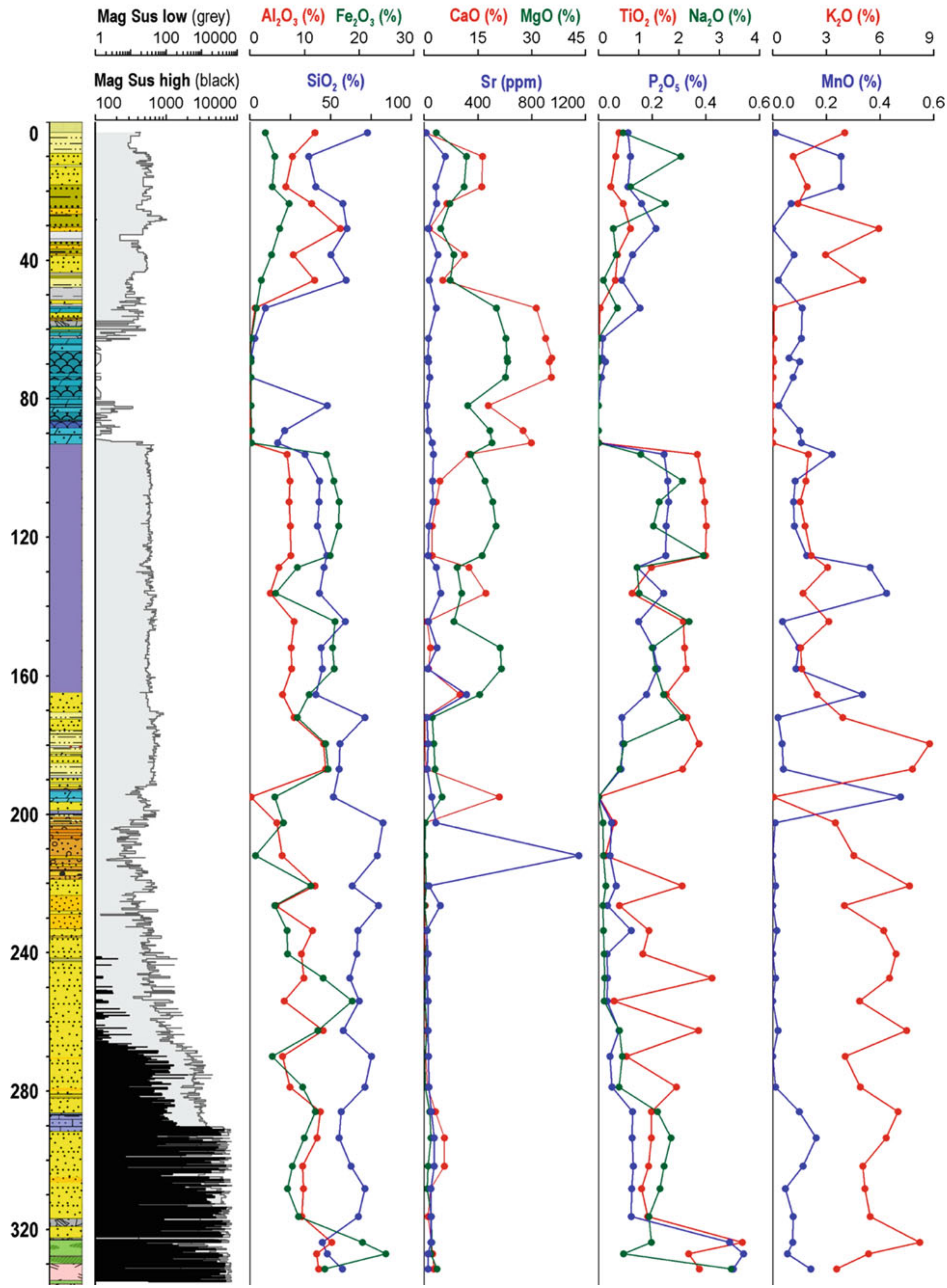

Fig. 6.72 Relative magnetic susceptibility (K*), and geochemical profiles of selected elements based on the archive samples collected from Core 8B with c. 8 m-spacing. For analytical techniques and data quality see **Part 5**

Fig. 6.73 FAR-DEEP Hole 8B intersected several intervals that contain c. 2060 Ma jasper. The jasper occurs in a large variety of modes, including amygdales and veins in volcanic rocks, layers, veinlets, and feeder veins in siltstone and dolostone beds. These, together with other occurrences of Fe-rich lithologies present in the drillcore, represent an apparent analogue of the latest Palaeoproterozoic banded-iron formations. Various occurrences of iron oxides and jasper reflect a complex history of fluid-migration and redox-alteration in a suite of processes linked to the Great Oxidation Event. The core offers an opportunity to address several questions related to the source, transport and deposition of iron oxides by subaerial and subaqueous hydrothermal systems. In addition, jaspers are known to harbour and preserve a specific form of microbial life. The photograph presents a composite image of three sawn core intervals from Hole 8B (182–190 m depth), each 5 cm in diameter (Photograph taken by Victor Melezhik)

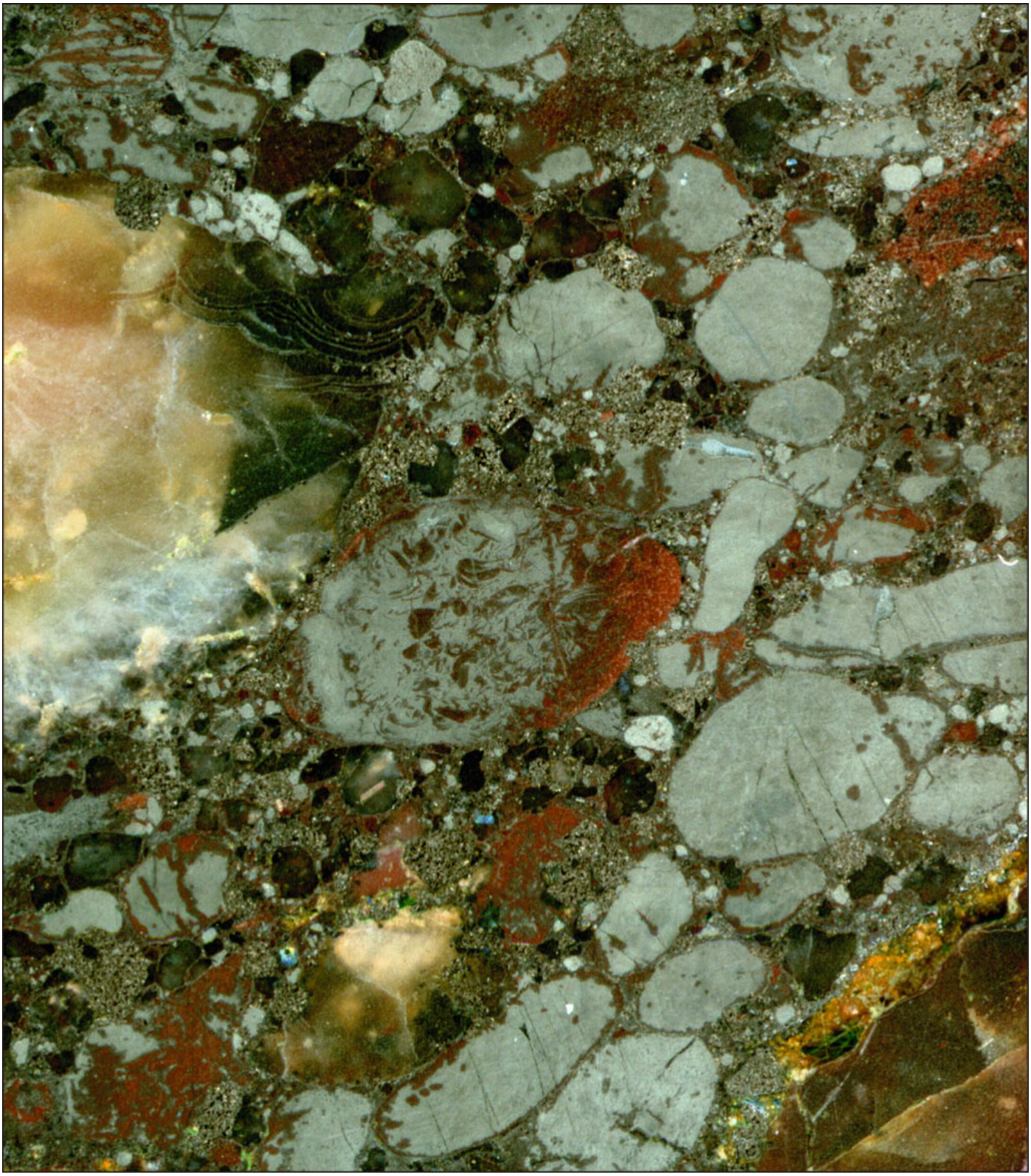

Fig. 6.74 The Kolosjoki Sedimentary Formation conglomerate containing rounded haematite-magnetite clasts (*pale grey*), weathered-out quartz amygdales (some with relict colloform fabrics), and fragments of rocks with red staining. Deposition, erosion, and redeposition of magnetite and haematite as clasts in fluvial, deltaic and marine sediments illustrate a complex history of the iron-oxide mineralogy and may provide new insights into the surface environmental conditions in the aftermath of the Lomagundi-Jatuli isotopic event (Photograph taken by Victor Melezhik)

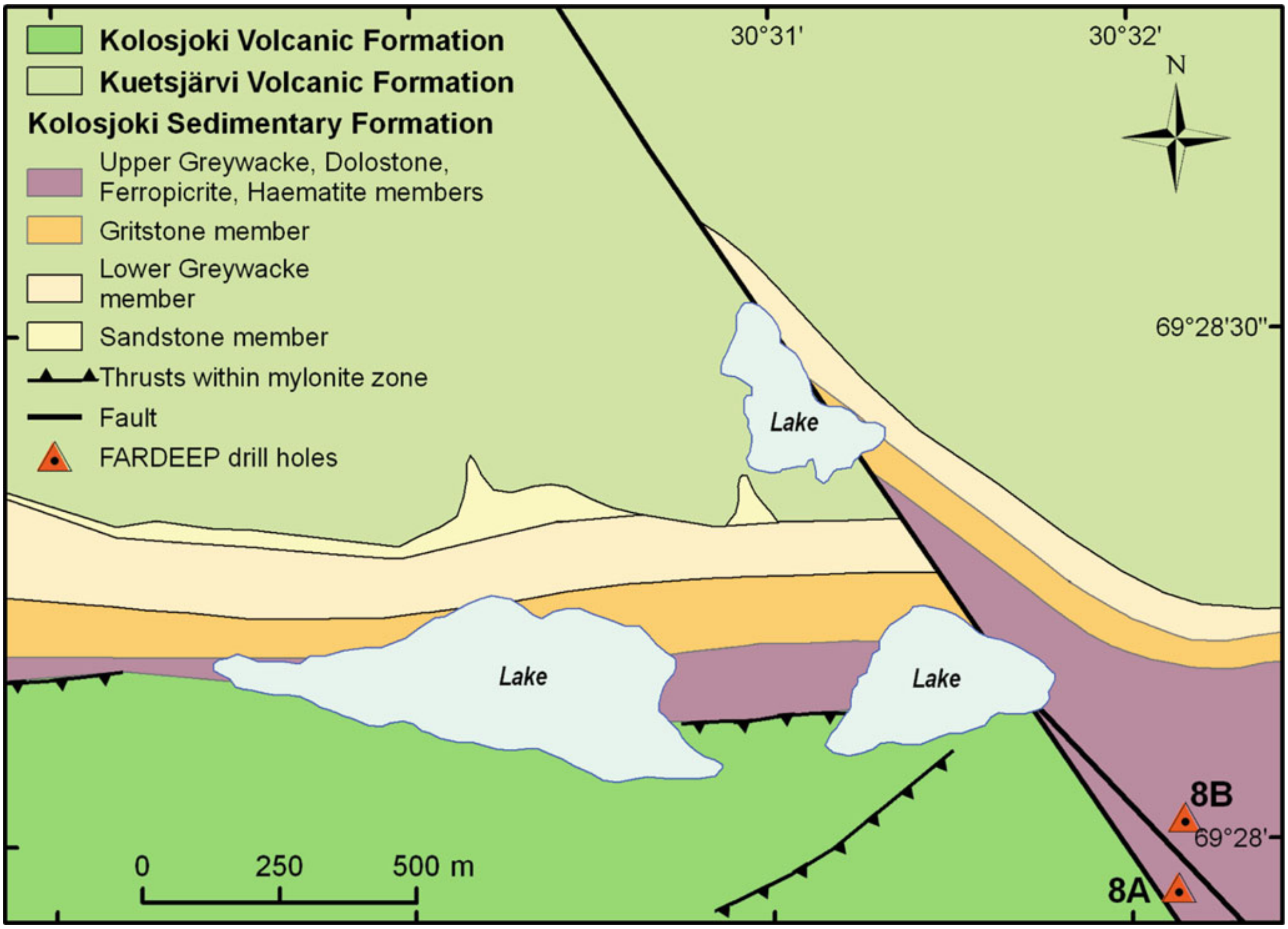

Fig. 6.75 Simplified geological map showing the stratigraphy of the Kolosjoki Sedimentary Formation and the positions of Holes 8A and 8B (Mapping by T. Prave and A. Lepland (unpublished data))

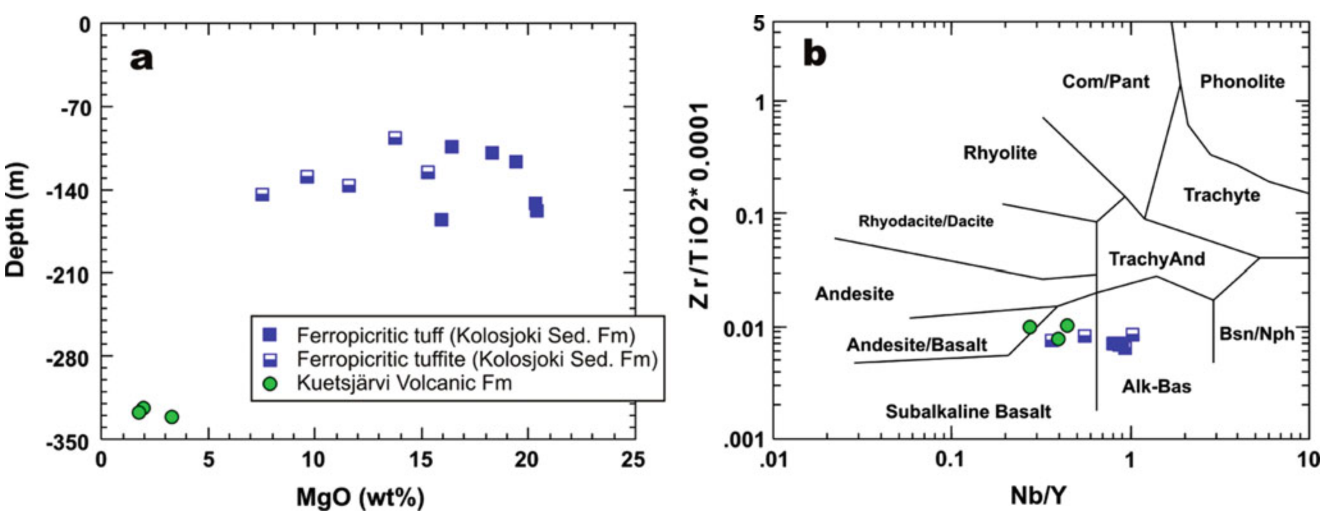

Fig. 6.76 (a) MgO (volatile-free) versus depth plot and (b) Nb/Y versus Zr/TiO_2 discrimination diagram for igneous rocks intersected by Hole 8B. In (b) boundaries between the rock types after Winchester and Floyd (1977)

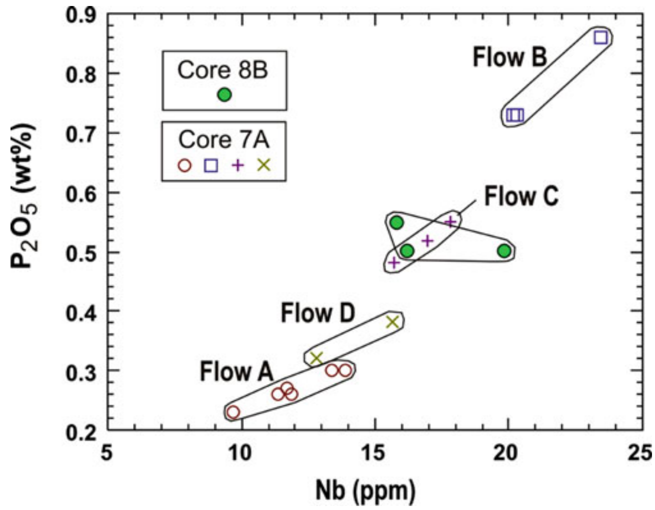

Fig. 6.77 Nb versus P_2O_5 diagram comparing the volcanic rocks in the uppermost part of the Kuetsjärvi Volcanic Formation as intersected by Holes 7A and 8B

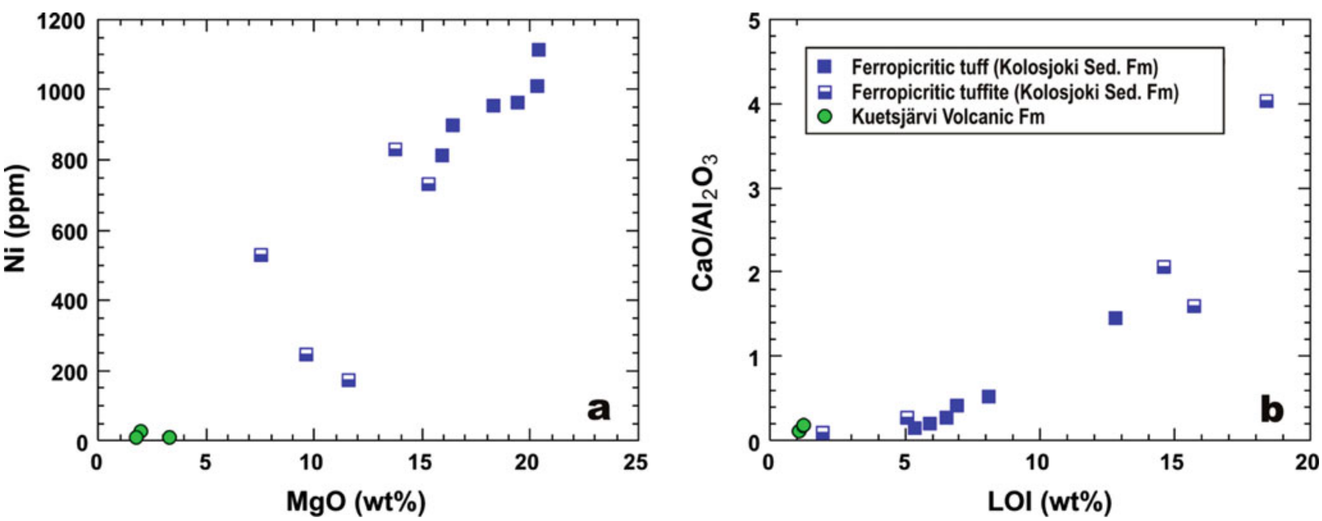

Fig. 6.78 (**a**) Ni versus MgO (volatile-free) and (**b**) CaO/Al_2O_3 versus LOI diagrams for the uppermost volcanic rocks of the Kuetsjärvi Volcanic Formation and the Ferropicrite member of the Kolosjoki Sedimentary Formation intersected by Hole 8B

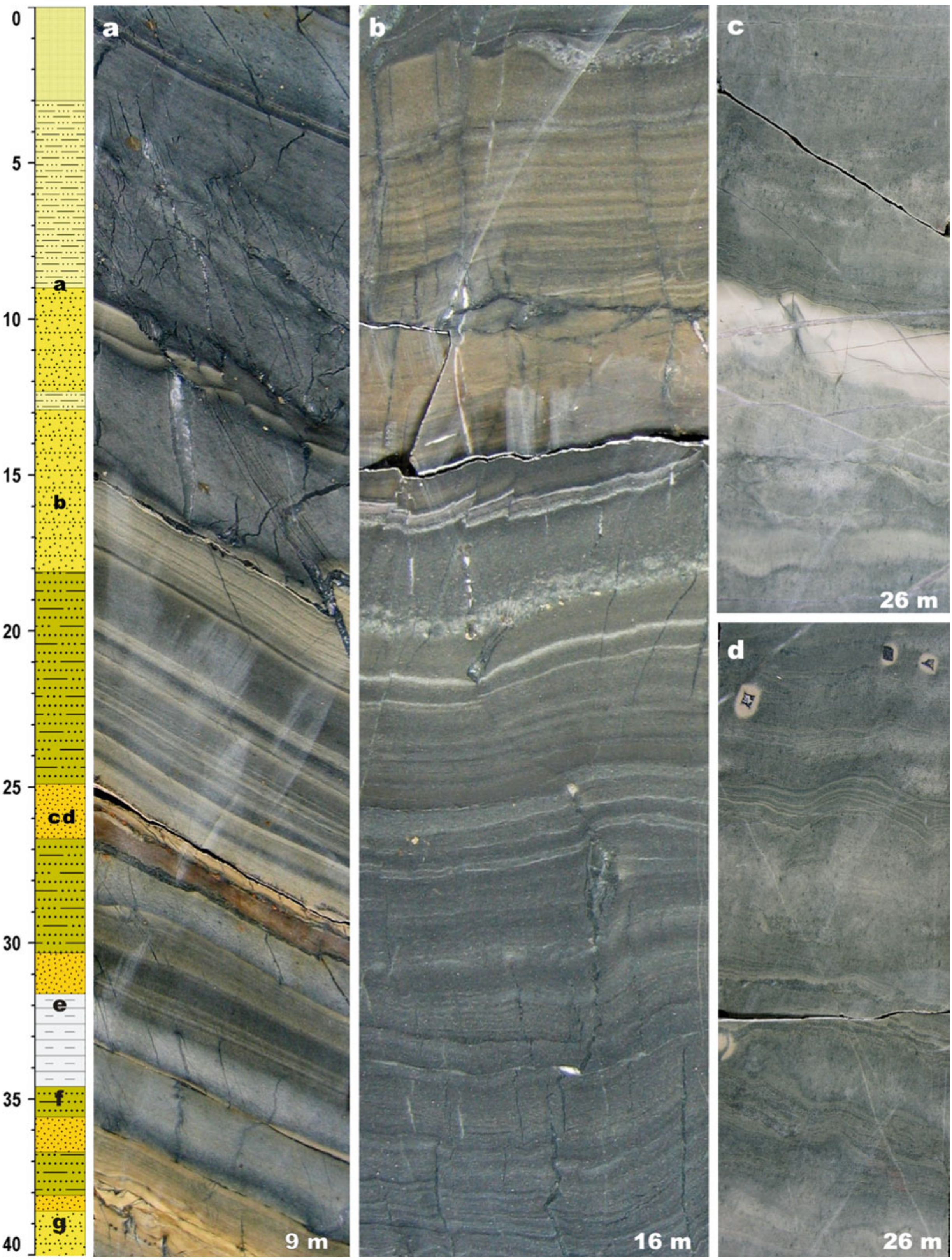

Fig. 6.79 Sedimentological features of the main rock types of the Kolosjoki Sedimentary Formation based on Core 8B and outcrops in the vicinity of the drilling site. In all core photographs, unless otherwise marked, the scale for the images is the core width of 5 cm. (**a**) Thinly alternating, horizontally bedded siltstone and arkosic sandstone overlain by dark grey, thickly bedded, clayey greywacke (*dark grey*). (**b**) Pale grey, parallel-laminated siltstone-greywacke couplets overlain by tan arkosic sandstone passing into laminated arkosic sandstone-siltstone couplets. (**c**) Pale grey, wavy and parallel-bedded arkosic sandstone overlain by indistinctly bedded greywacke. (**d**) Massive to wavy laminated greywacke with pyrite cubes surrounded by a bleached halo

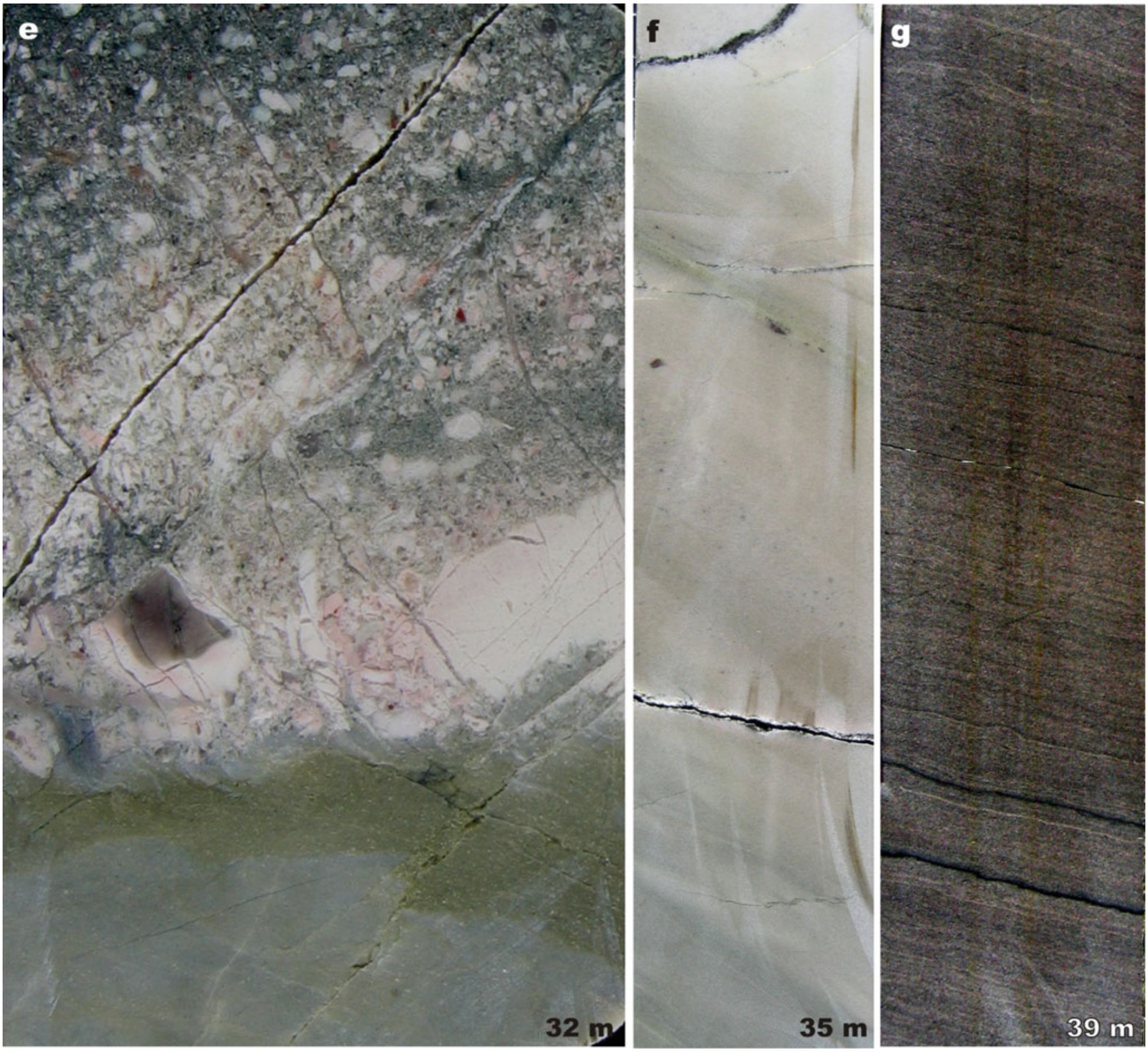

Fig. 6.79 (continued) (**e**) Normally graded volcaniclastic breccia erosively overlying massive, fine-grained greywacke. (**f**) Pale grey arkosic sandstone with indistinct cross-bedding. (**g**) Dark grey, parallel-laminated clayey greywacke

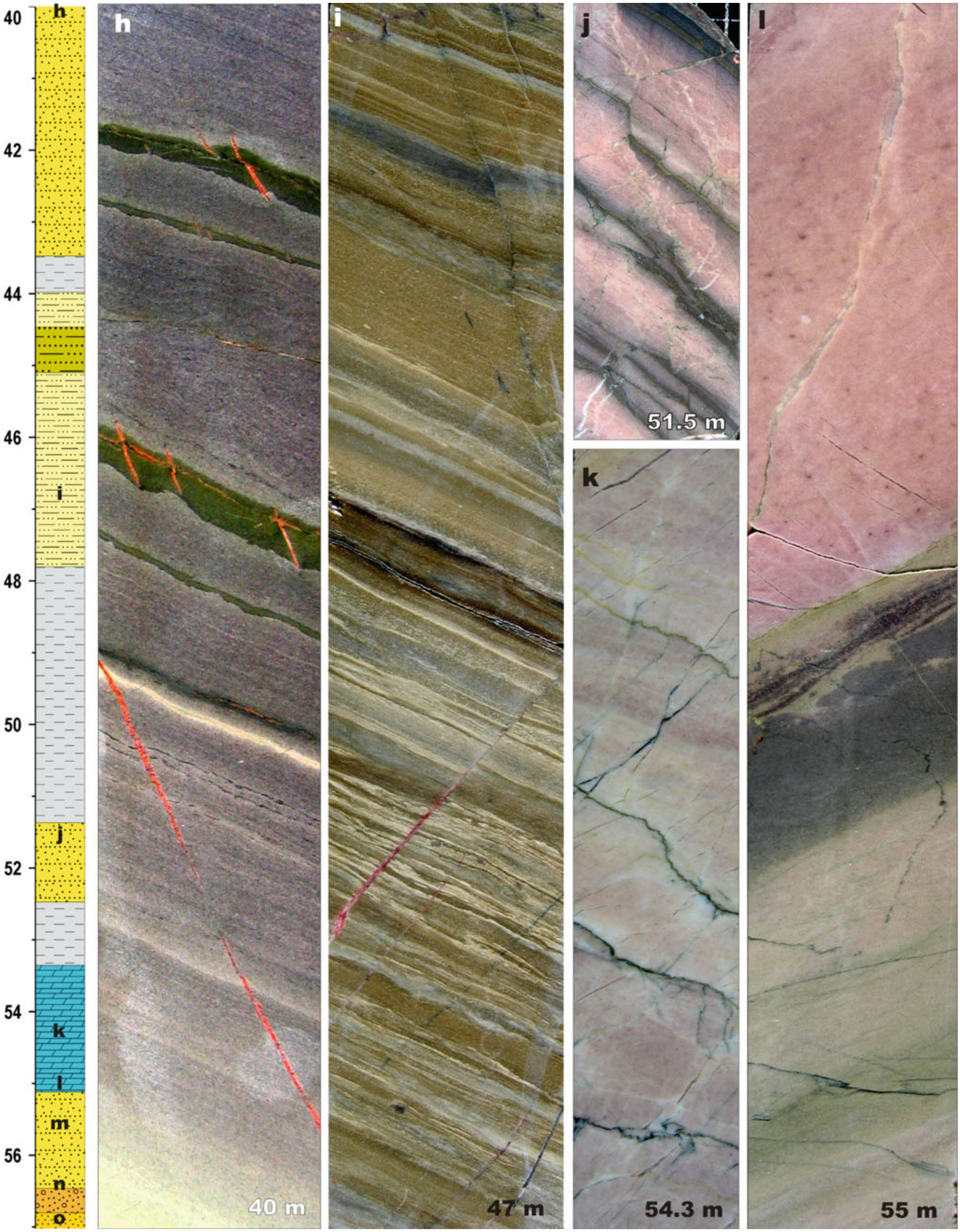

Fig. 6.79 (continued) (**h**) Light-coloured, parallel-laminated arkosic sandstone (*bottom*) passing upward into dark grey, haematite-bearing greywacke with dark green chlorite interlayers; extensional cracks are filled with red microcline. (**i**) Parallel- to wavy-laminated arkosic sandstone alternating with chlorite-rich layers (*dark green*). (**j**) Pink arkosic sandstone with dark grey mudstone drapes. (**k**) Variegated dolostone with indistinct parallel bedding; extensional cracks filled with chlorite. (**l**) Pale pink, parallel to wavy-bedded arkosic sandstone overlain by dark-grey clayey sandstone followed by pink, massive dolarenite

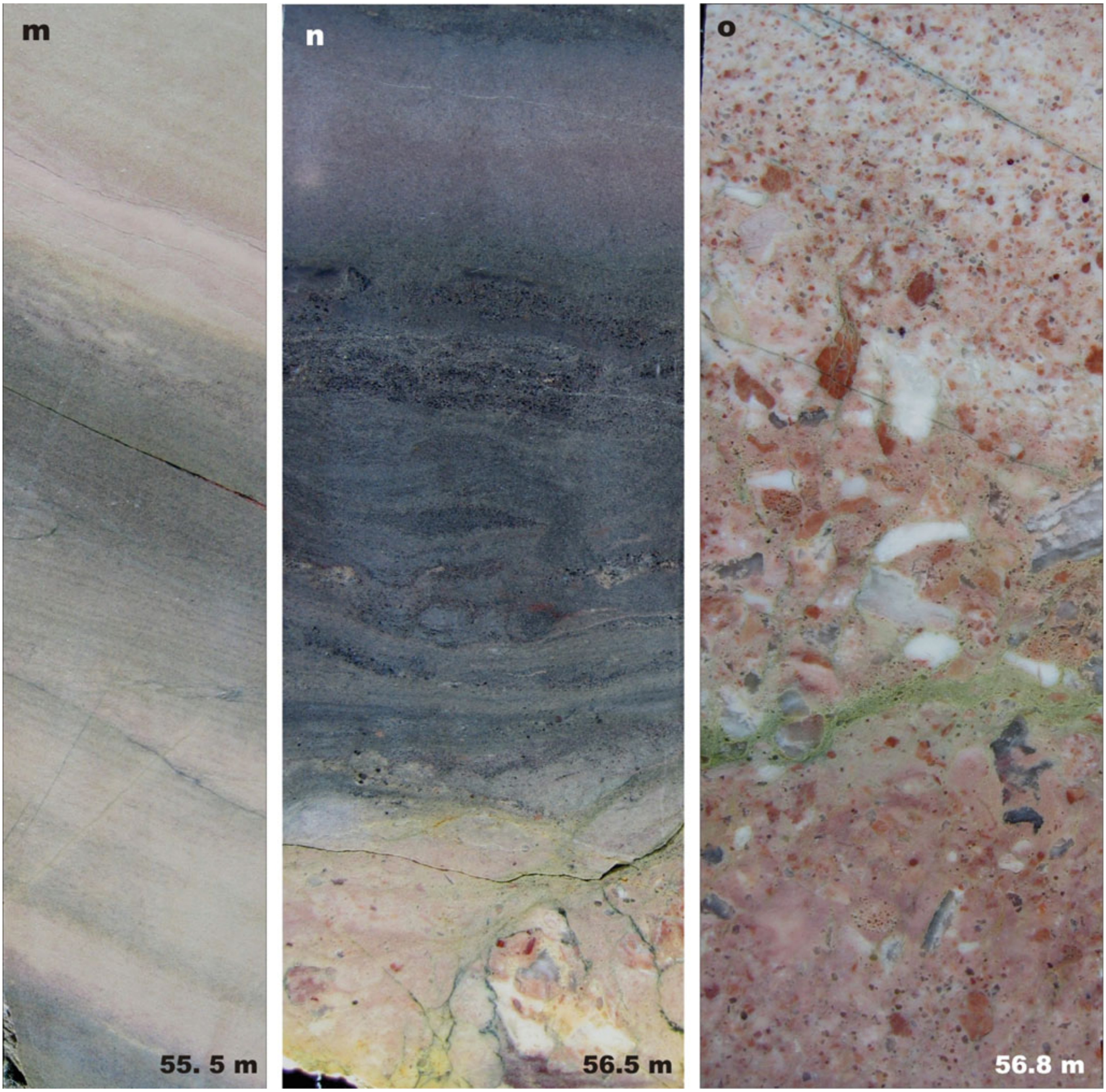

Fig. 6.79 (continued) (**m**) Variegated arkosic sandstone with low-angle cross-lamination. (**n**) Pale pink dolarenite erosively overlain by dark grey, fine-grained, wavy-laminated, clayey greywacke. (**o**) Pink dolarenite and dolorudite with white and pink, unsorted, angular clasts of dolostones

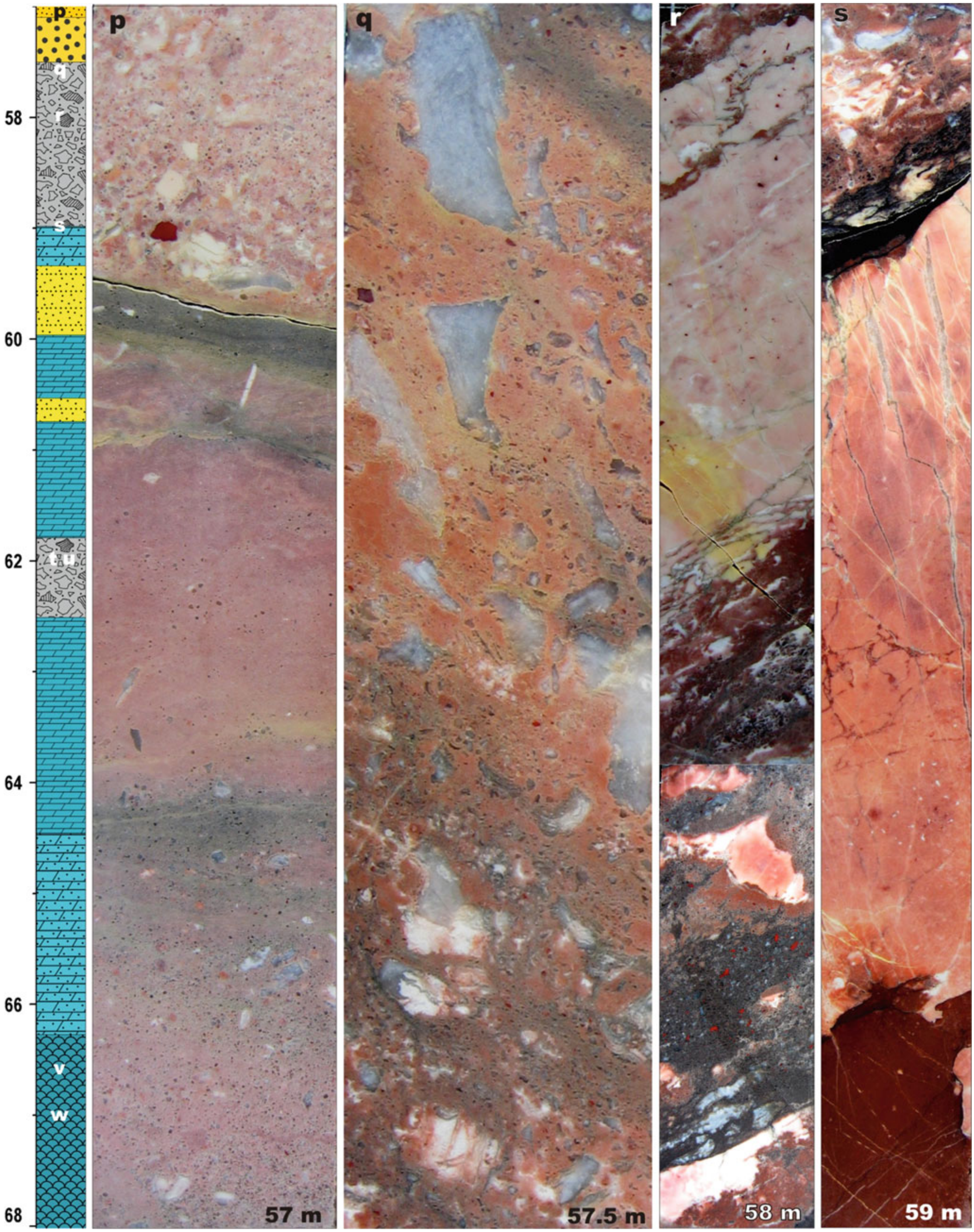

Fig. 6.79 (continued) (**p**) Pink dolarenite with grit-sized, angular, unsorted clasts overlain by pink, massive dolarenite with a dark grey mudstone drape followed by dolorudite showing crude normal grading. (**q**) Pink dolarenite with unsorted, angular chert clasts. (**r**) Matrix-supported dolostone- and chert-clast breccia overlain by beige dolarenite. (**s**) Brown, massive dolostone overlain by pink, massive dolostone capped by dolorudite with dark brown mudstone at the base

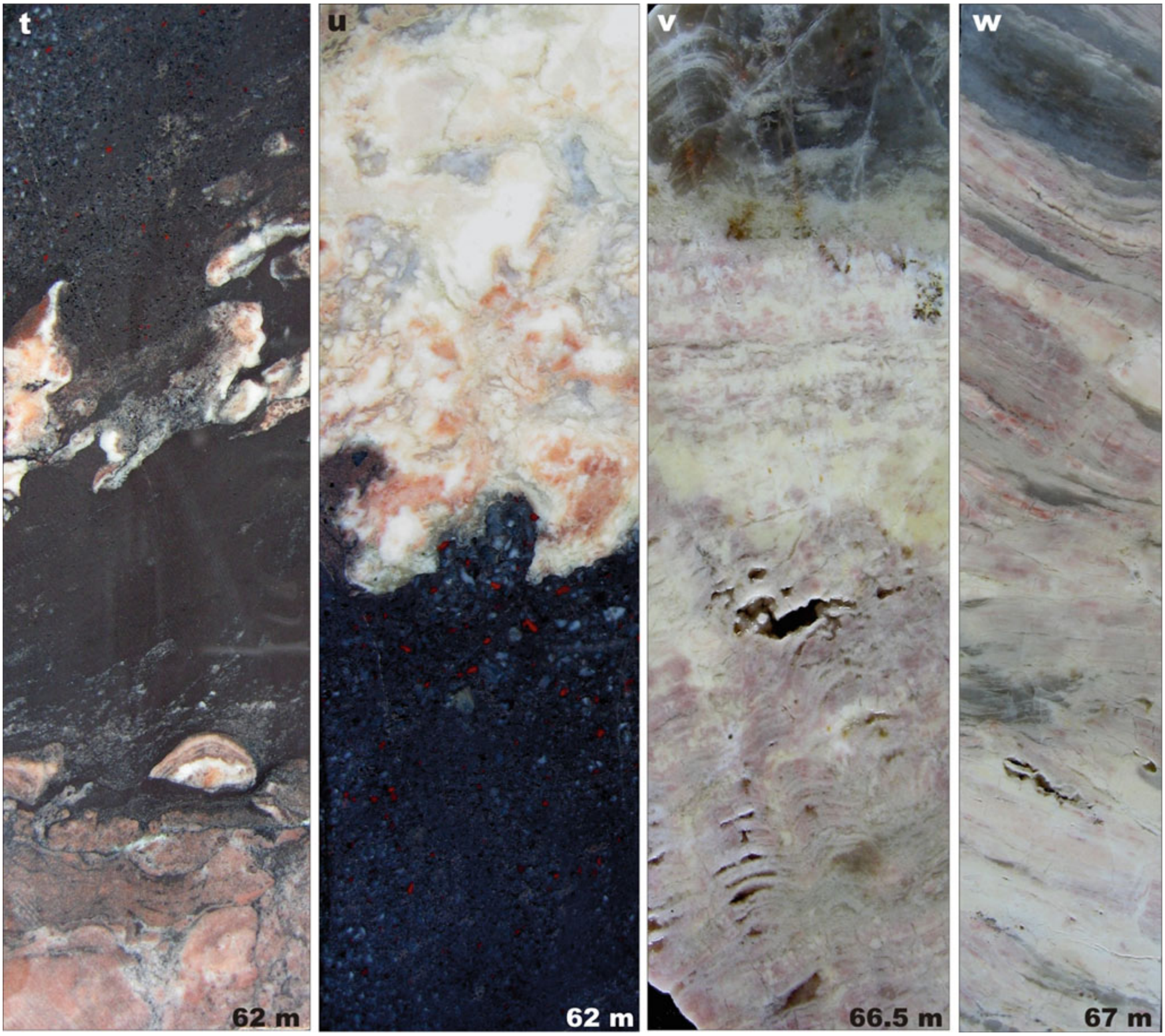

Fig. 6.79 (continued) (**t**) Pink, microbial dolostone overlain by dark brown claystone with scattered dolostone clasts and stromatolitic fragments. (**u**) Variegated dolorudite overlying the irregular palaeorelief of an eroded claystone surface. (**v**) Silicified stromatolitic dolostone with dissolution vugs. (**w**) Silicified microbial dolostone

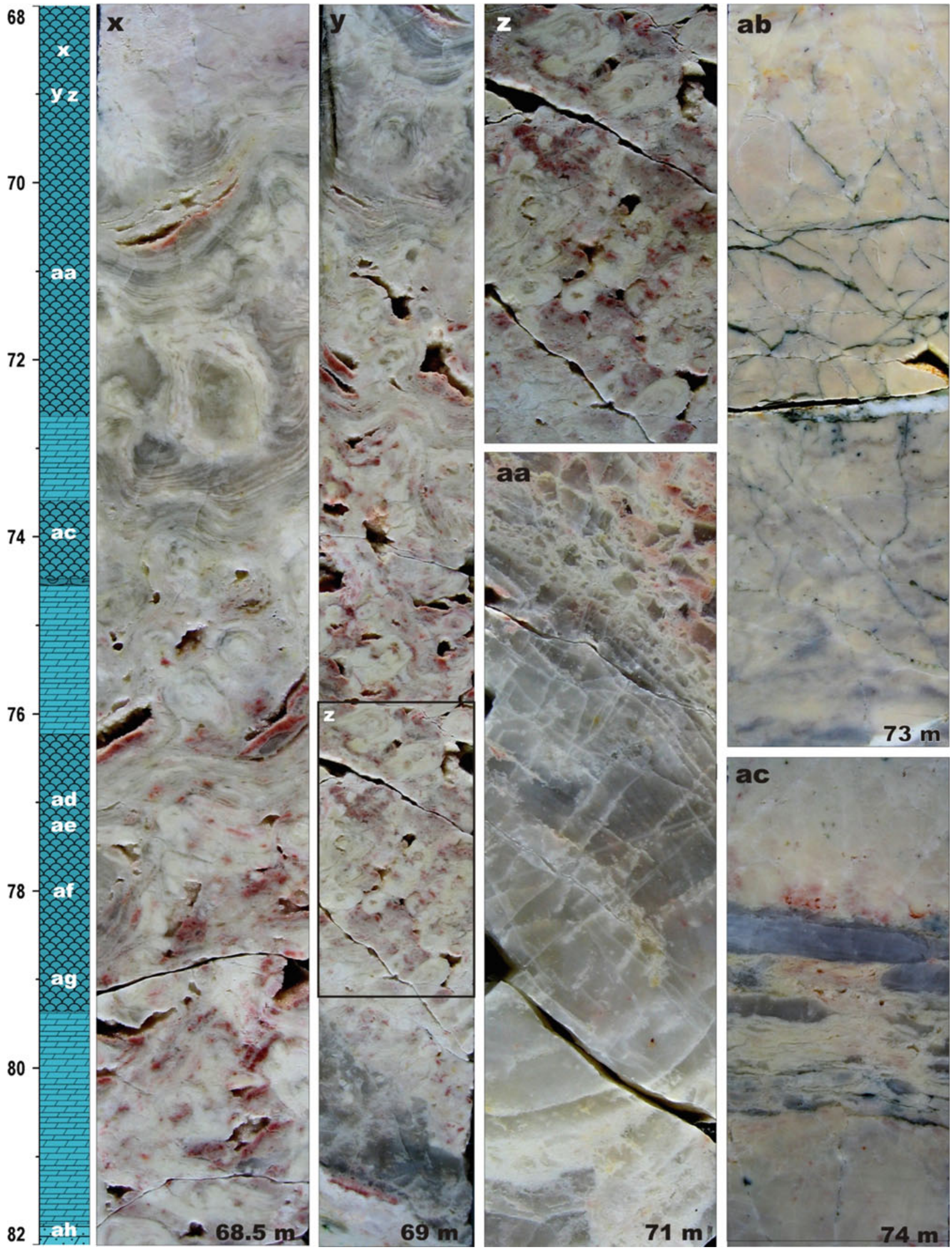

Fig. 6.79 (continued) (**x**) Spheroidal stromatolites in brecciated, fenestral dolostone framework. (**y**) Spheroidal stromatolites and oncolites passing upward into indistinctly columnar mini-stromatolites in a clotted, fenestral, microbial dolomite framework. (**z**) Enlarged image of oncolites shown in "**y**". (**aa**) Fragment of large columnar stromatolite; plan view. (**ab**) Brecciated, micritic dolostone. (**ac**) Grey chert lenses (concretions) in finely-crystalline dolostone

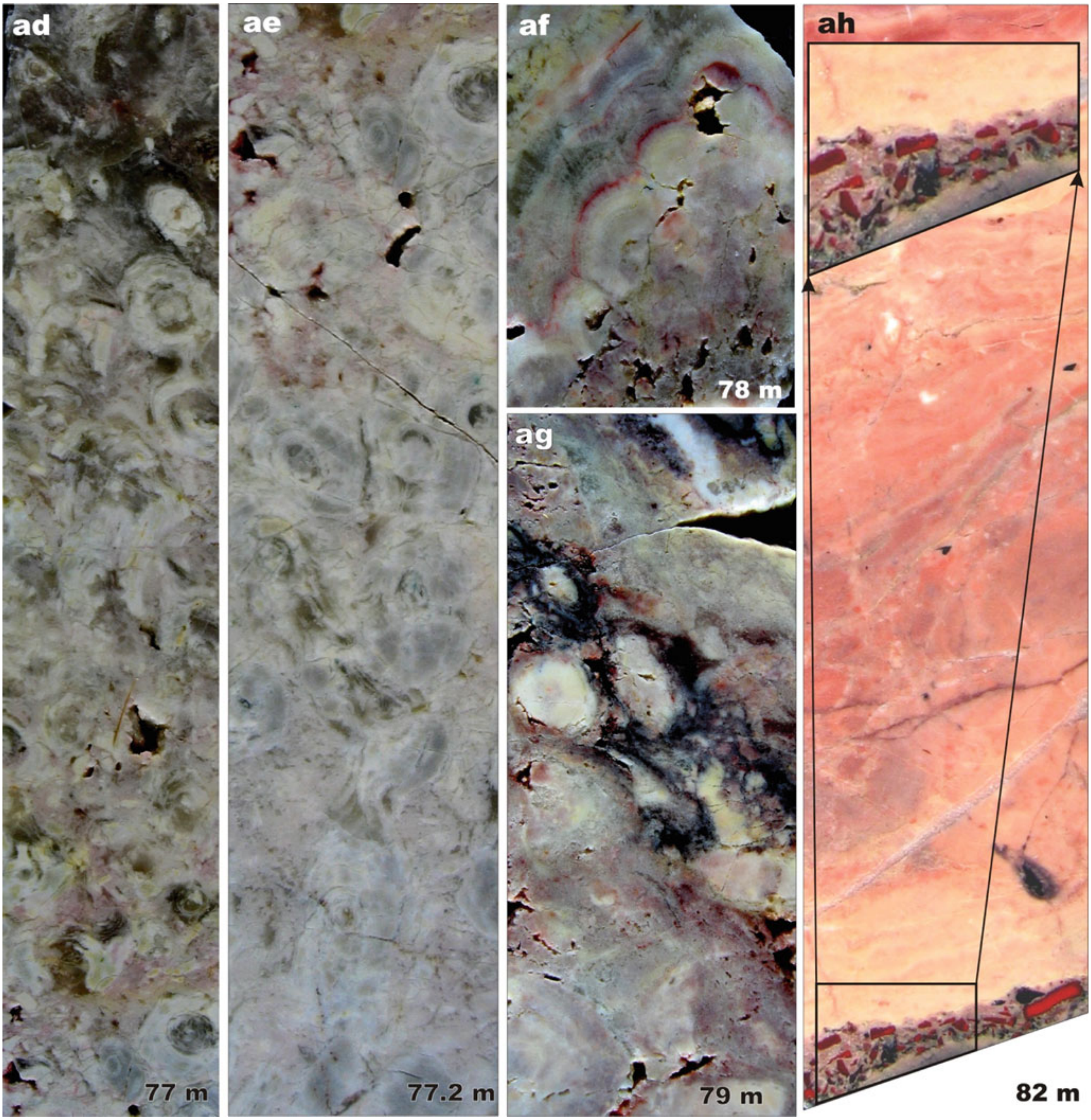

Fig. 6.79 (continued) (**ad**) Tightly packed oncolites and spherical stromatolites. (**ae**) Microbial dolostone with a clotted fabric passing upward into spherical stromatolites/oncolites. (**af**) Variegated, thinly laminated dolostone; note that the laminae show invariant thicknesses, which is atypical for stromatolites. (**ag**) Tightly packed, recrystallised oncolites or spherical stromatolites overlain by oncolite embedded in a black, haematite-rich mudstone matrix. (**ah**) Thin layer with dolarenite matrix-supported jasper gritstone at the base of pale pink dolorudite; part of the jasper gritstone layer is enlarged

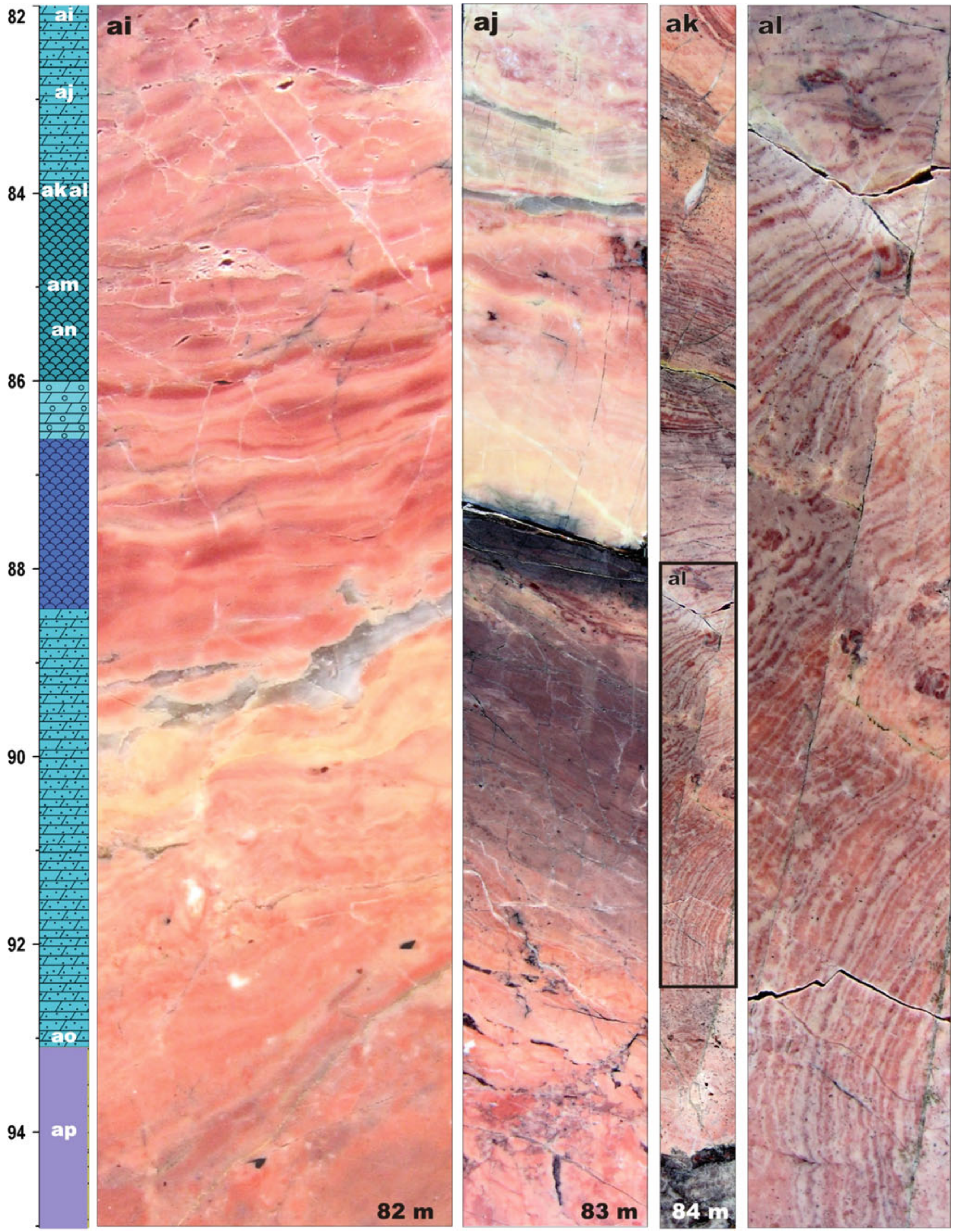

Fig. 6.79 (continued) (**ai**) Pale pink, redeposited dolostone with wavy lamination. (**aj**) Two variegated dolarenite beds separated by black, haematite-rich mudstone; the dolarenite shows crude horizontal layering and cross-bedding. (**ak**) Alternating pale pink and pink, slightly wrinkled dolomicritic bands of an uncertain origin; this can be interpreted as a stromatolite, tufa, or cave deposit. (**al**) Enlarged image of alternating bands shown in photograph (**ak**)

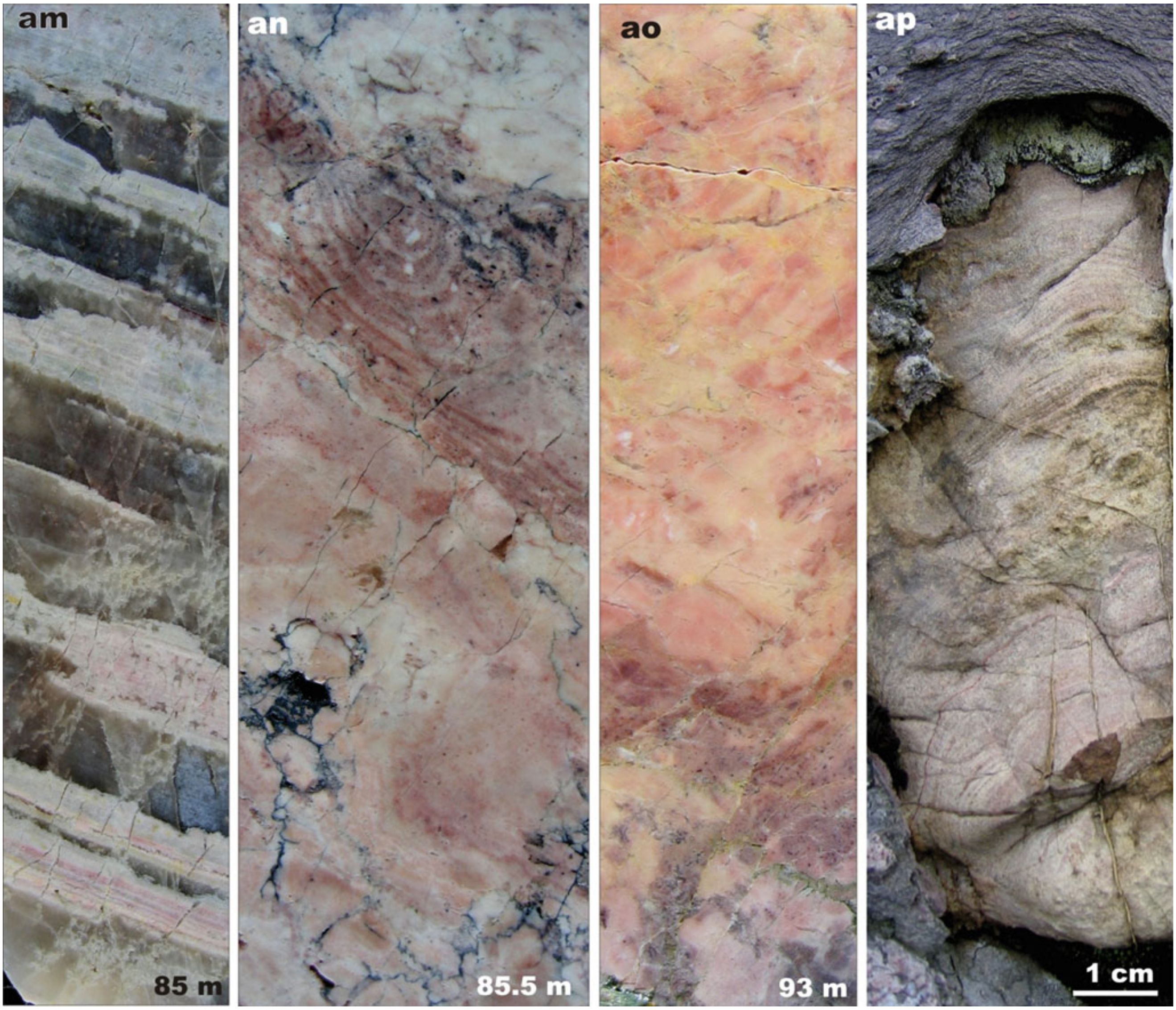

Fig. 6.79 (continued) (**am**) Pale pink, horizontally laminated dolostone showing intensive, bedding-parallel replacement by grey chert. (**an**) Pale pink and beige, brecciated dolostone containing a layer of inverted stromatolite or tufa/cave deposit. (**ao**) Two beds of massive dolorudite distinguished by different colour. (**ap**) A large dolostone fragment with alternating pale pink and beige bands of dolomicrite, which resembles banded dolostone shown in photographs (**ak**), (**al**) and (**an**)

Fig. 6.79 (continued) (**aq**) Cross-section view of massive dolarenite with quartz-pseudomorphs that were probably previously gypsum crystals; photograph was taken from an outcrop located c. 100 m away from drilling site. (**ar**) Cross-section view of interbedded dolostone and chert-breccia beds and cross-bedded calcareous greywacke (*grey*); photograph was taken from an outcrop located c. 700 m to the east-northeast of drilling site

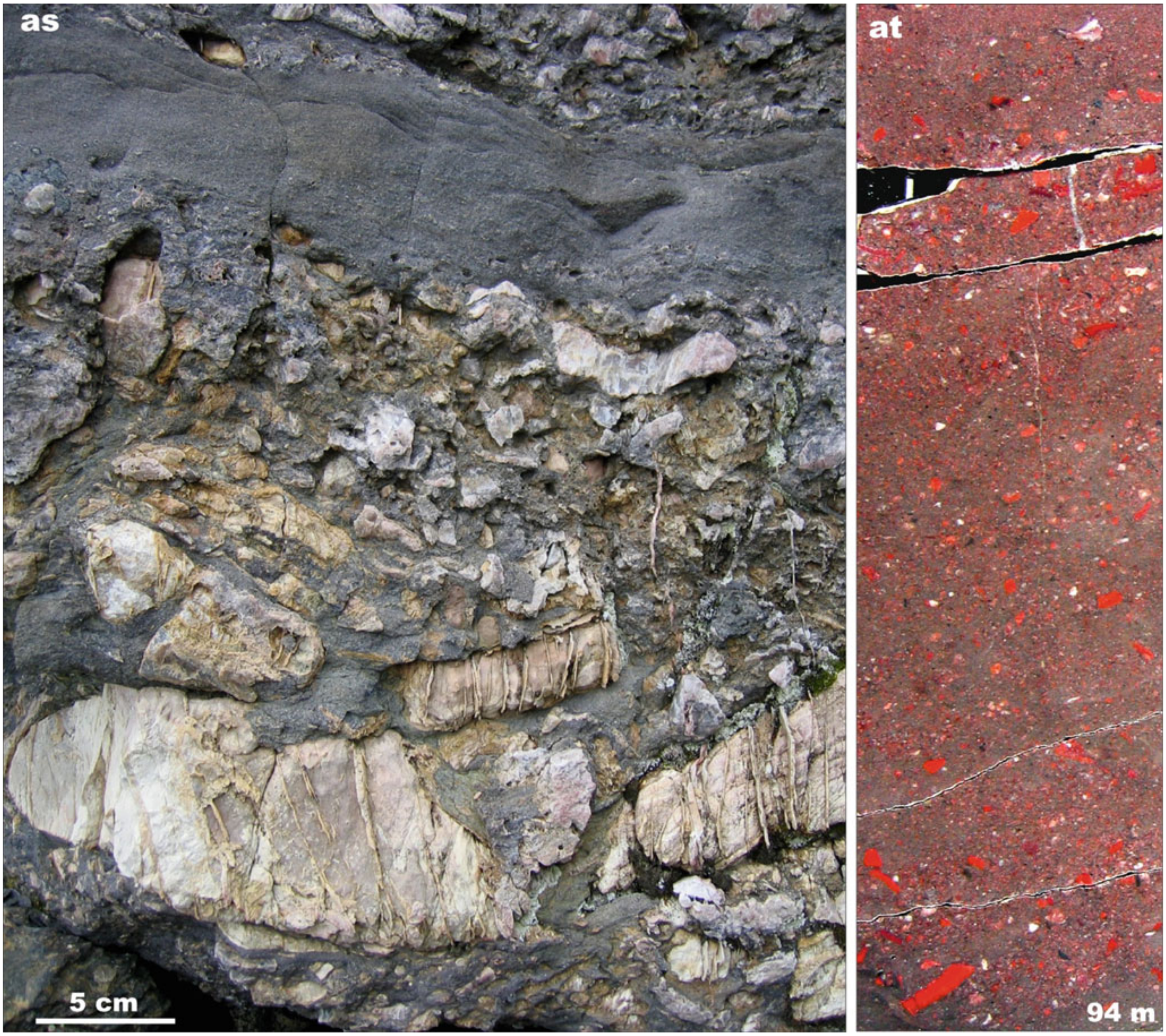

Fig. 6.79 (continued) (**as**) Cross-section view of greywacke-supported dolostone conglomerate overlain by greywacke with ripple-cross-bedding. (**at**) Massive, lithic ferropicritic tuff containing angular, poorly-sorted clasts of jasper

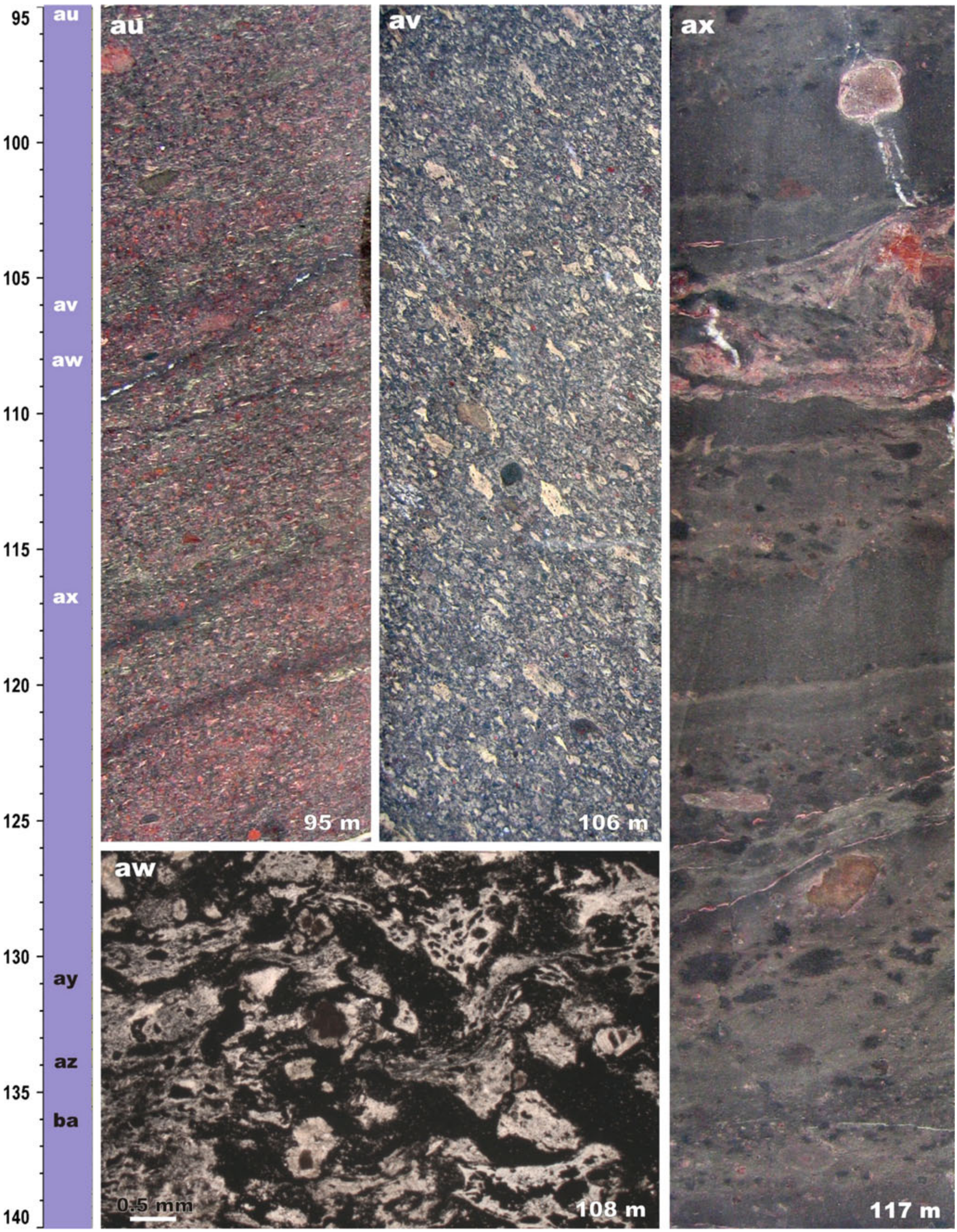

Fig. 6.79 (continued) (**au**) Crudely bedded, lithic ferropicritic tuff containing scattered, sand-sized clasts of jasper. (**av**) Massive, lithic ferropicritic tuff. (**aw**) Photomicrograph of massive ferropicritic tuff showing a clotted microfabric made of flame-shaped lithic particles and devitrified, intensively magnetitised glass (*black*); non-polarised transmitted light. (**ax**) Crudely bedded ferropicritic tuff with some layers exhibiting a clotted fabric

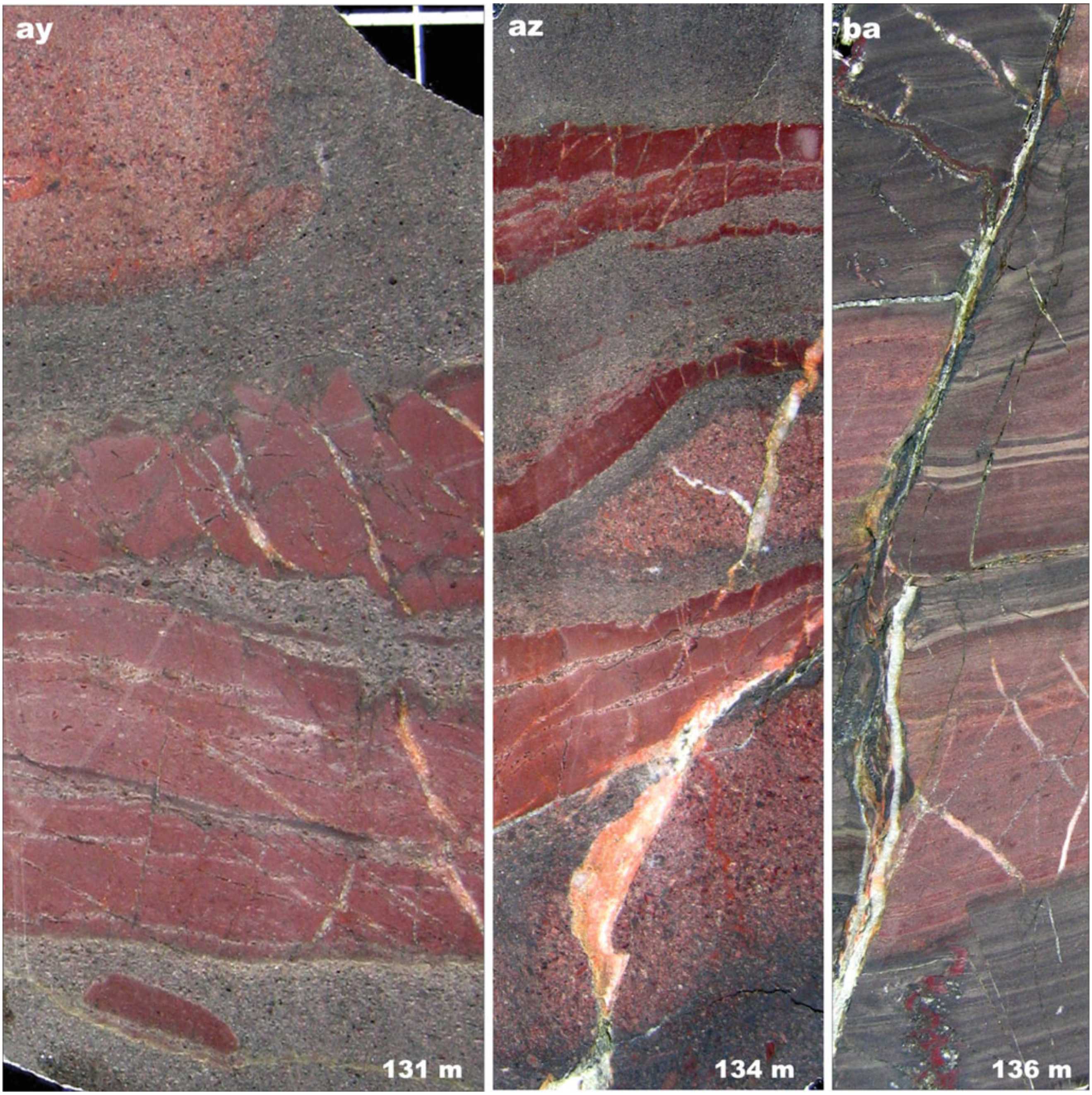

Fig. 6.79 (continued) (**ay, az**) Red, haematite-stained, partially desiccated claystone layers in ferropicritic psammitic tuffite with lenses enriched in red clayey material; extensional cracks are filled with quartz and haematite. (**ba**) Rhythmically laminated greywacke-siltstone couplets with extensional crack filled by quartz

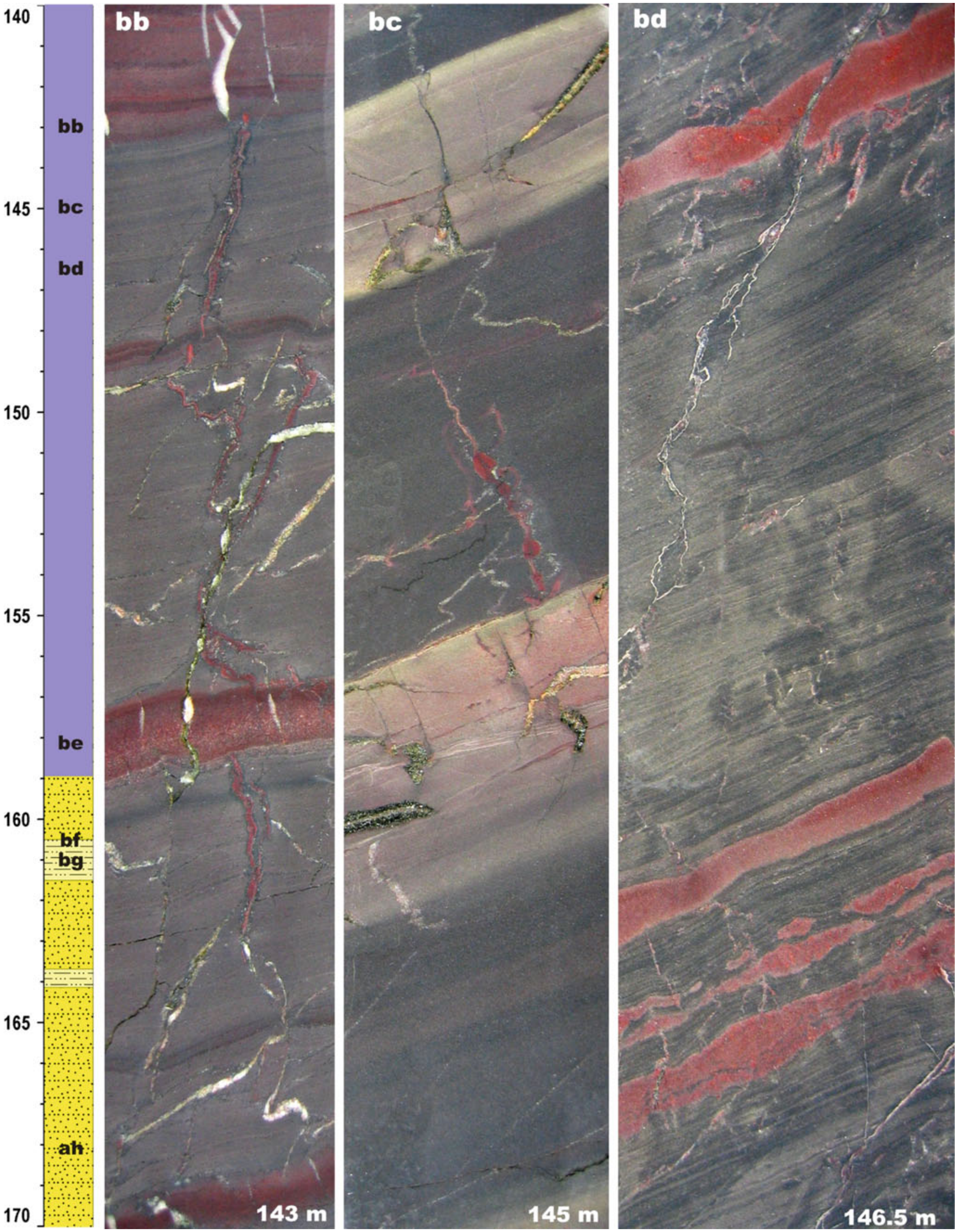

Fig. 6.79 (continued) (**bb**) Laminated siltstone with layers of brown, haematite-rich claystone cross-cut by jasper veinlets (*red*) with superimposed extensional cracks filled with white quartz. (**bc**) Many-cm-scale rhythmic bedding in haematite-rich siltstone with slight inverse grading. (**bd**) Dark grey, laminated siltstone with layers and lenses of red, haematite-rich claystone

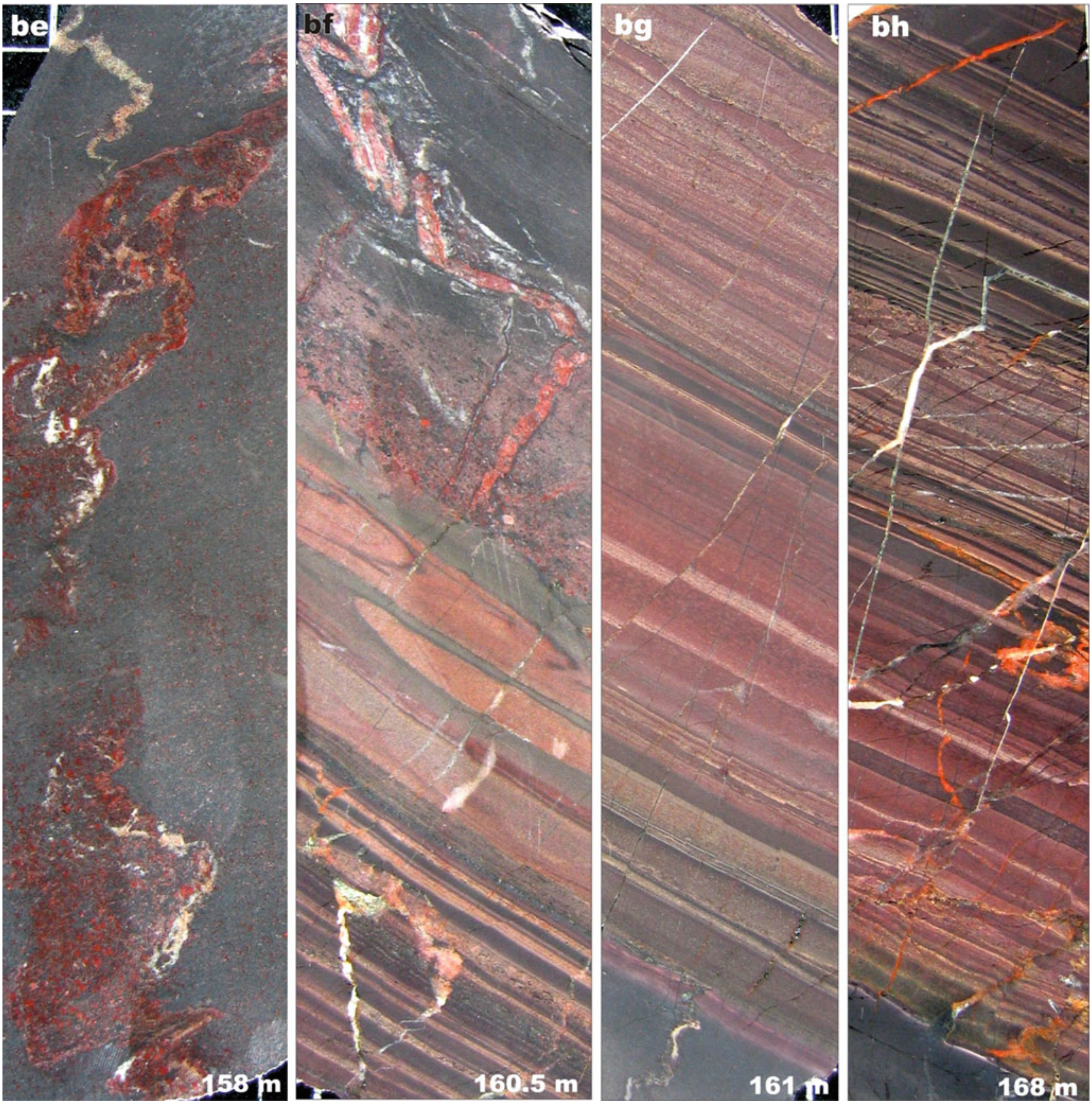

Fig. 6.79 (continued) (**be**) Massive ferropicritic tuff injected with a greywacke sedimentary dyke cemented by jasper. (**bf**) Thinly bedded greywacke-siltstone (*bottom*) followed by a bedded unit with small-scale slump structures (layer with isoclinal folding in the *middle*), passing into a graded greywacke bed with jasper clasts and injected by a ptygmatic jasper veinlet. (**bg**) Thinly bedded greywacke-siltstone couplets. (**bh**) Haematite-rich, rhythmically laminated greywacke-siltstone injected by jasper veinlets (*red*)

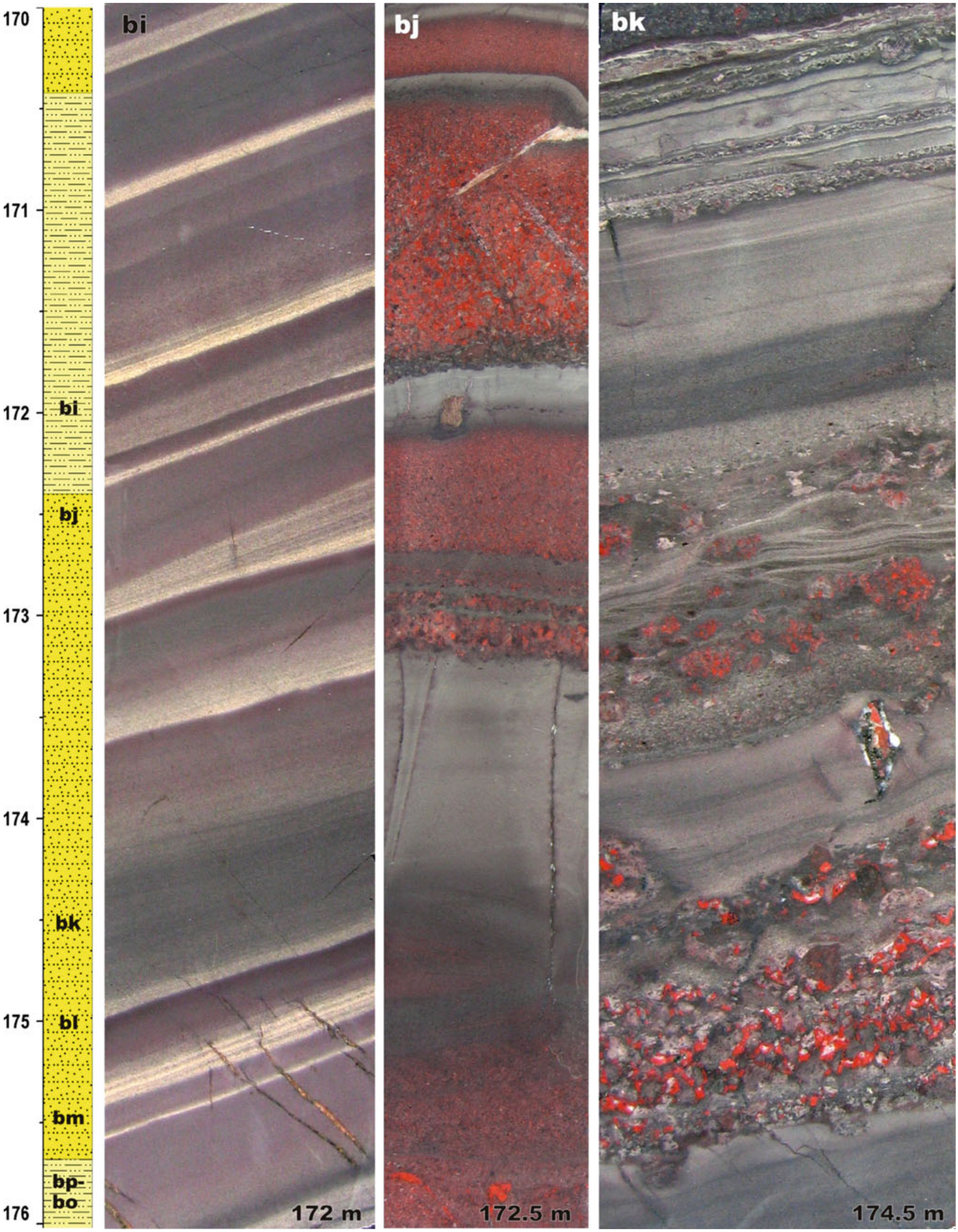

Fig. 6.79 (continued) (**bi**) Dark purple, haematite-rich, graded greywacke-siltstone couplets with parallel horizontal and low-angle cross-bedding. (**bj**) Several beds of red jasper-sandstone grading into grey siltstone. (**bk**) Parallel-bedded greywacke-siltstone with grit-sized jasper clasts (*red*)

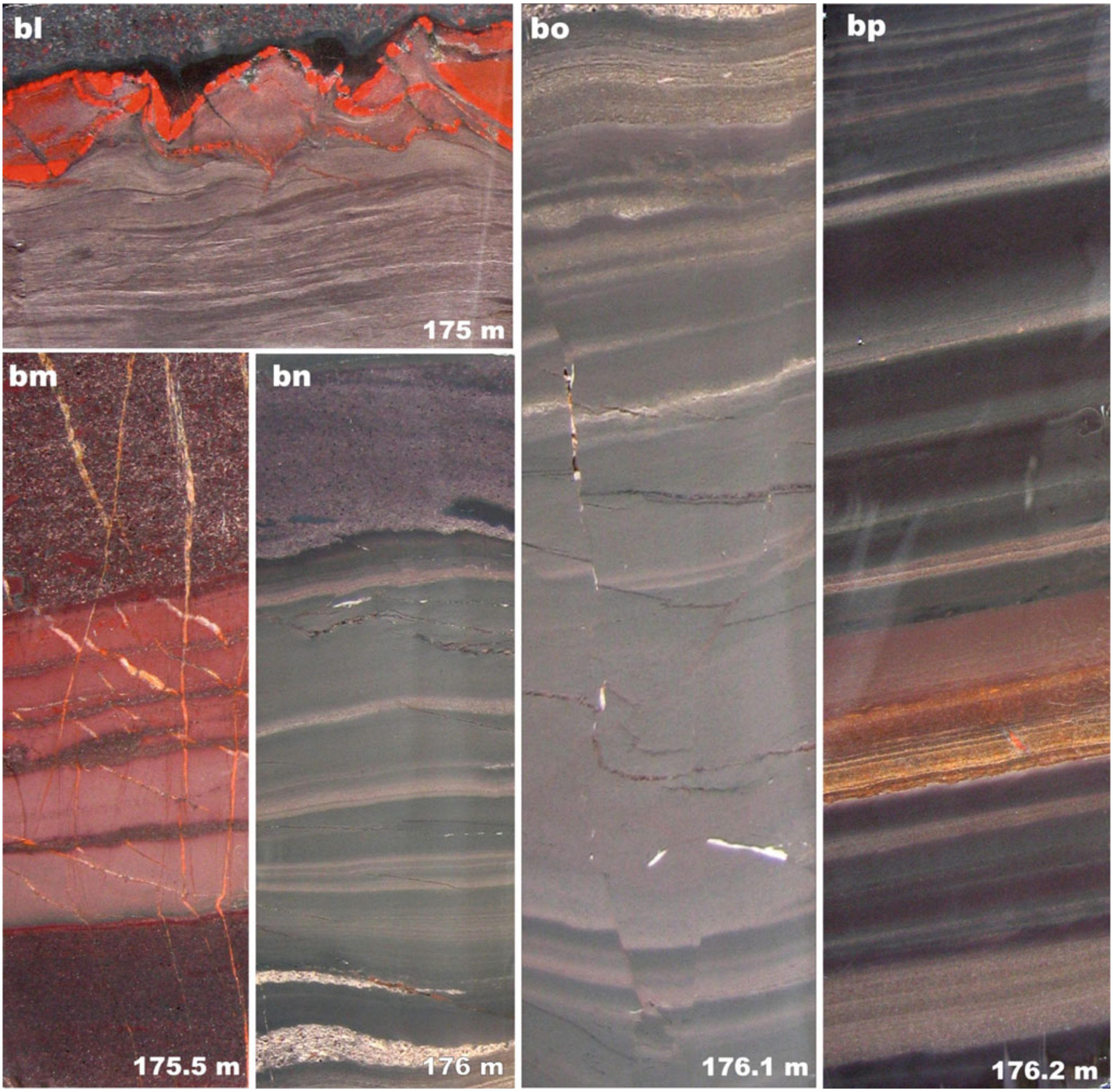

Fig. 6.79 (continued) (**bl**) Rippled, grey siltstone with the uppermost ripples encrusted with jasper. (**bm**) Bedded, haematite-rich sandstone-siltstone; extensional joints are filled with quartz and haematite (*pale pink*). (**bn**, **bo**) Dark tan, thin greywacke layers grading into grey, thicker siltstone units. (**bp**) Haematite-rich, horizontally-bedded, fine-grained sandstone-siltstone.

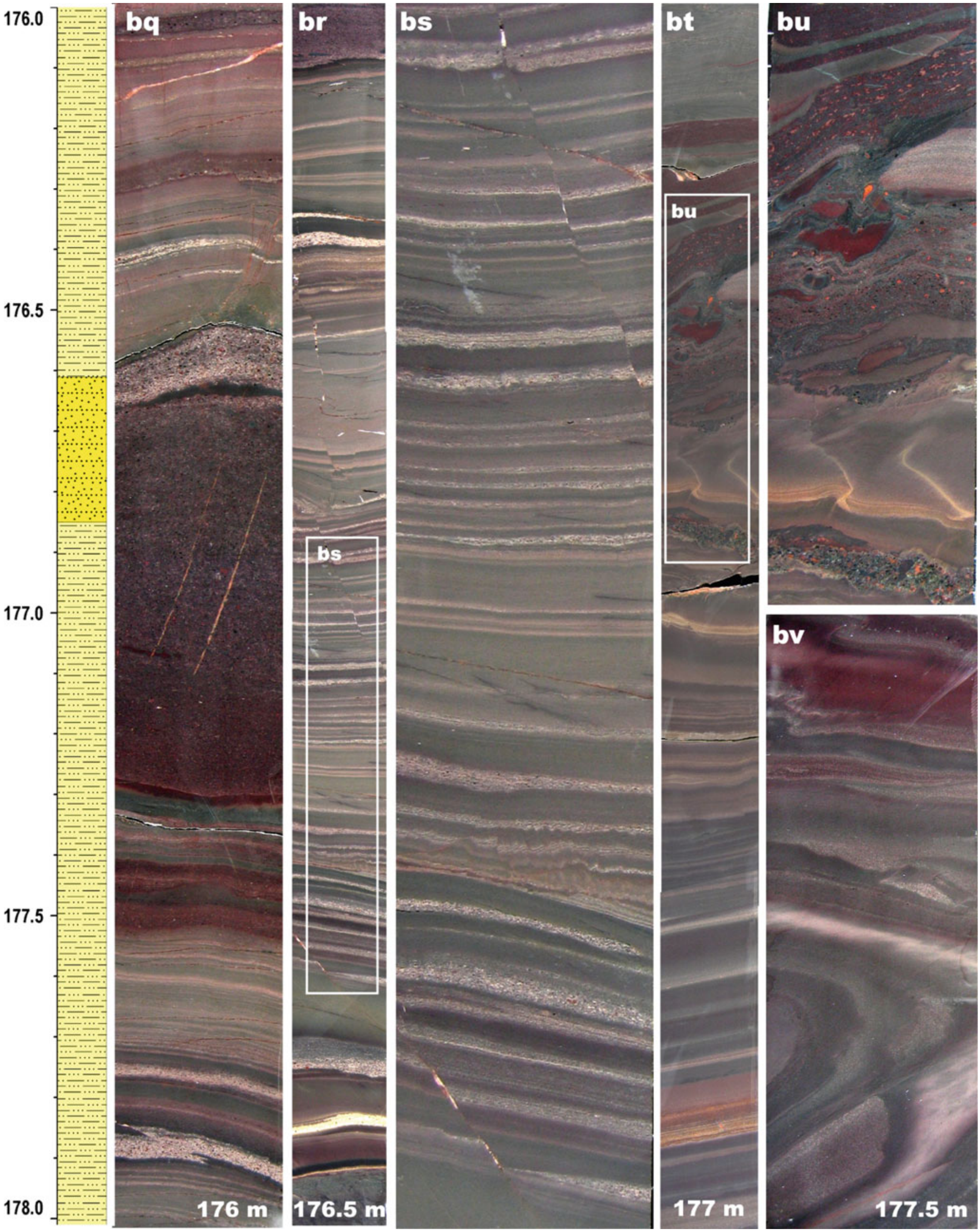

Fig. 6.79 (continued) (**bq**) Purple and grey, thinly-bedded, fine-grained sandstone-siltstone with a small-scale channel filled by crudely-bedded greywacke (in the *middle*). (**br**) General view, and (**bs**) close-up image of sandstone-siltstone couplets with thin, parallel and low-angle cross-lamination. (**bt**) General view of rhythmically bedded sandstone-siltstone couplets, and (**bu**) close-up image of slumped bed with syndepositionally folded layers and lumps of jasper and sandstone. (**bv**) Thinly-bedded, sandstone-siltstone with a slump fold

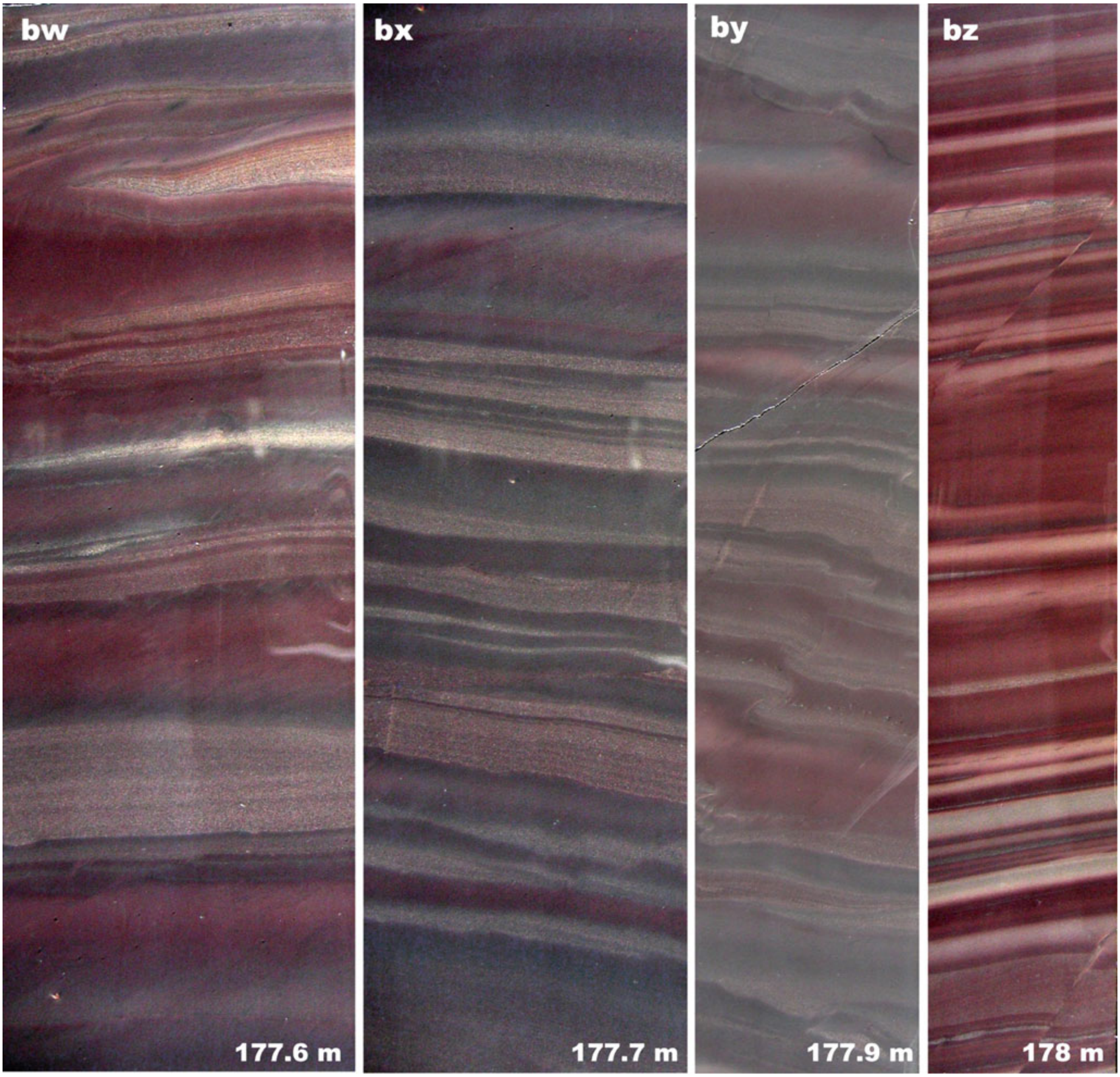

Fig. 6.79 (continued) (**bw**) Violet, haematite-rich, thinly bedded siltstone with an isoclinal slump fold on *top*. (**bx**, **by**) Dark violet, haematite-rich, rhythmically bedded siltstone. (**bz**) Pink, haematite-rich, thinly bedded sandstone-siltstone couplets

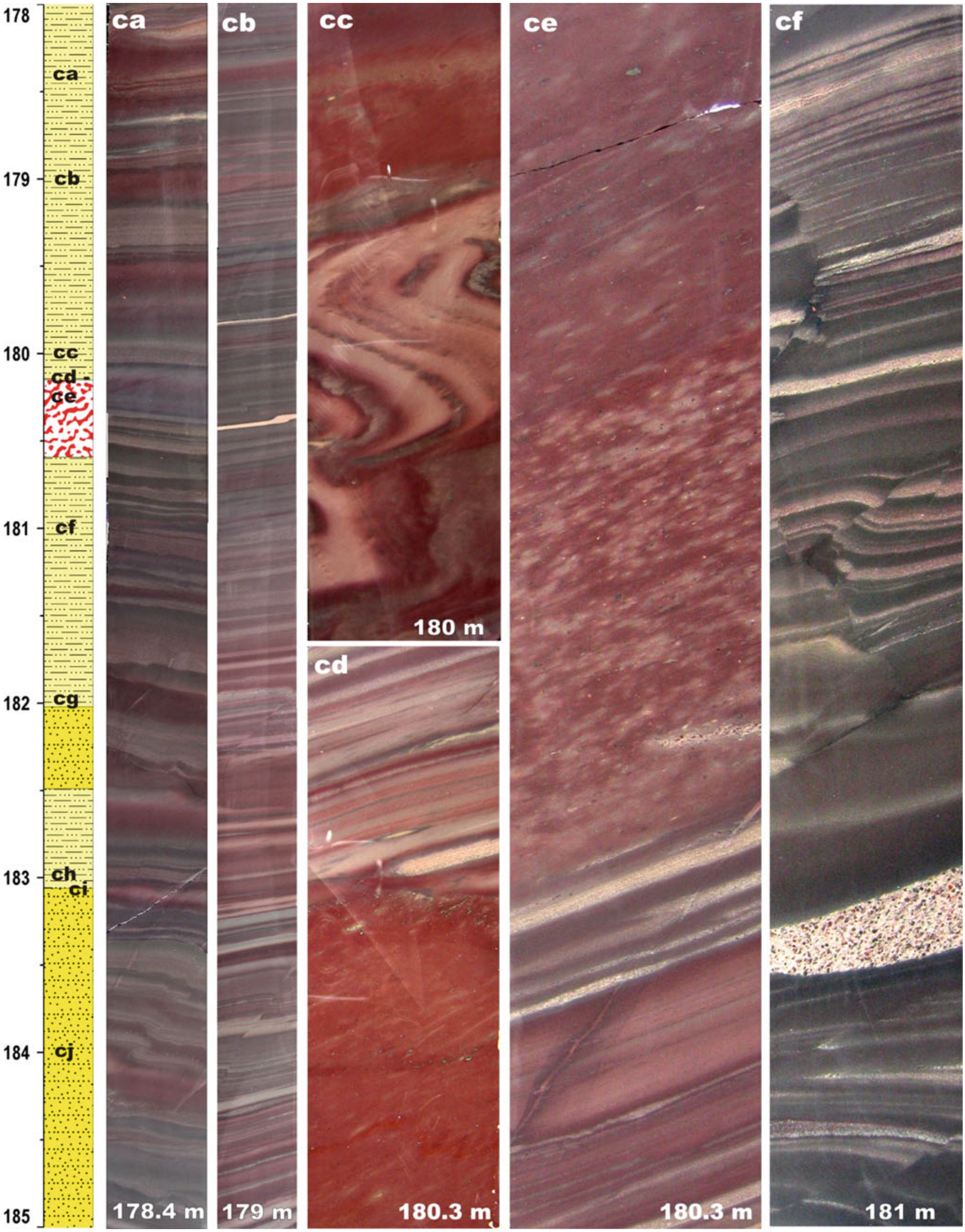

Fig. 6.79 (continued) (**ca**, **cb**) Dark violet, haematite-rich, rhythmically bedded siltstone. (**cc**) Slump folds in variegated, haematite-rich siltstone. (**cd**) Slumping-induced, discordant position of variegated, thinly bedded siltstone on red massive siltstone. (**ce**) Violet, haematite-rich, bedded siltstone overlain by semi-massive, gritty siltstone. (**cf**) Variegated, thinly bedded, fine-grained sandstone-siltstone couplets with a small-scale channel filled with beige, coarse-grained sandstone

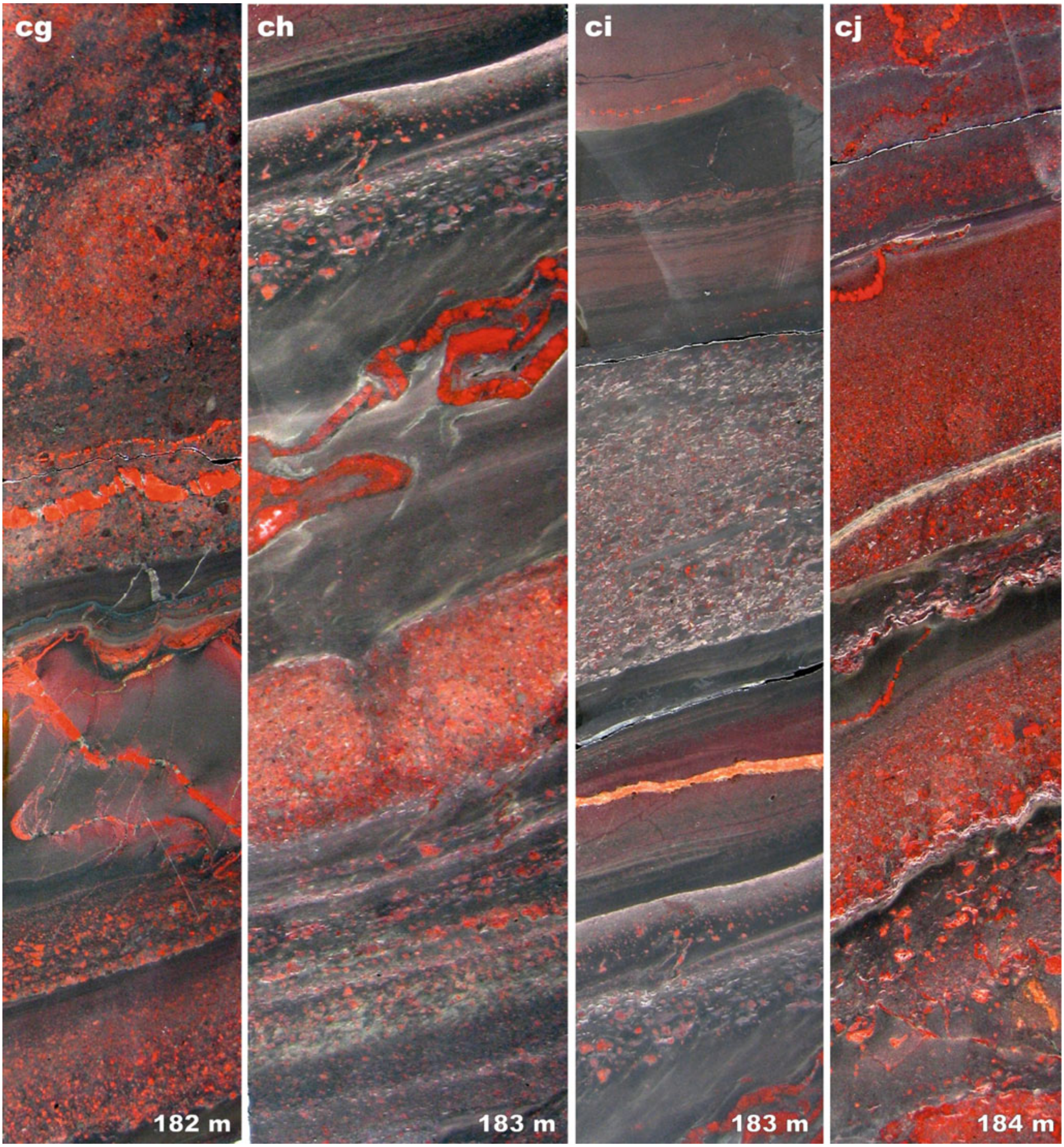

Fig. 6.79 (continued) (**cg**) Graded sandstone-siltstone beds containing jasper grains in the lower units; some beds have thin, fragmented jasper layers (crusts) whereas others are cross-cut by thin jasper veinlets. (**ch**) Brown, bedded siltstone with a bed of jasper sandstone, and plastically deformed jasper veinlet. (**ci**) Bedded, brown sandstone-siltstone with a jasper veinlet (*bottom*) and a thin, fragmented jasper veinlet (*top*). (**cj**) Jasper sandstone beds grading into brown siltstone; note several jasper veinlets

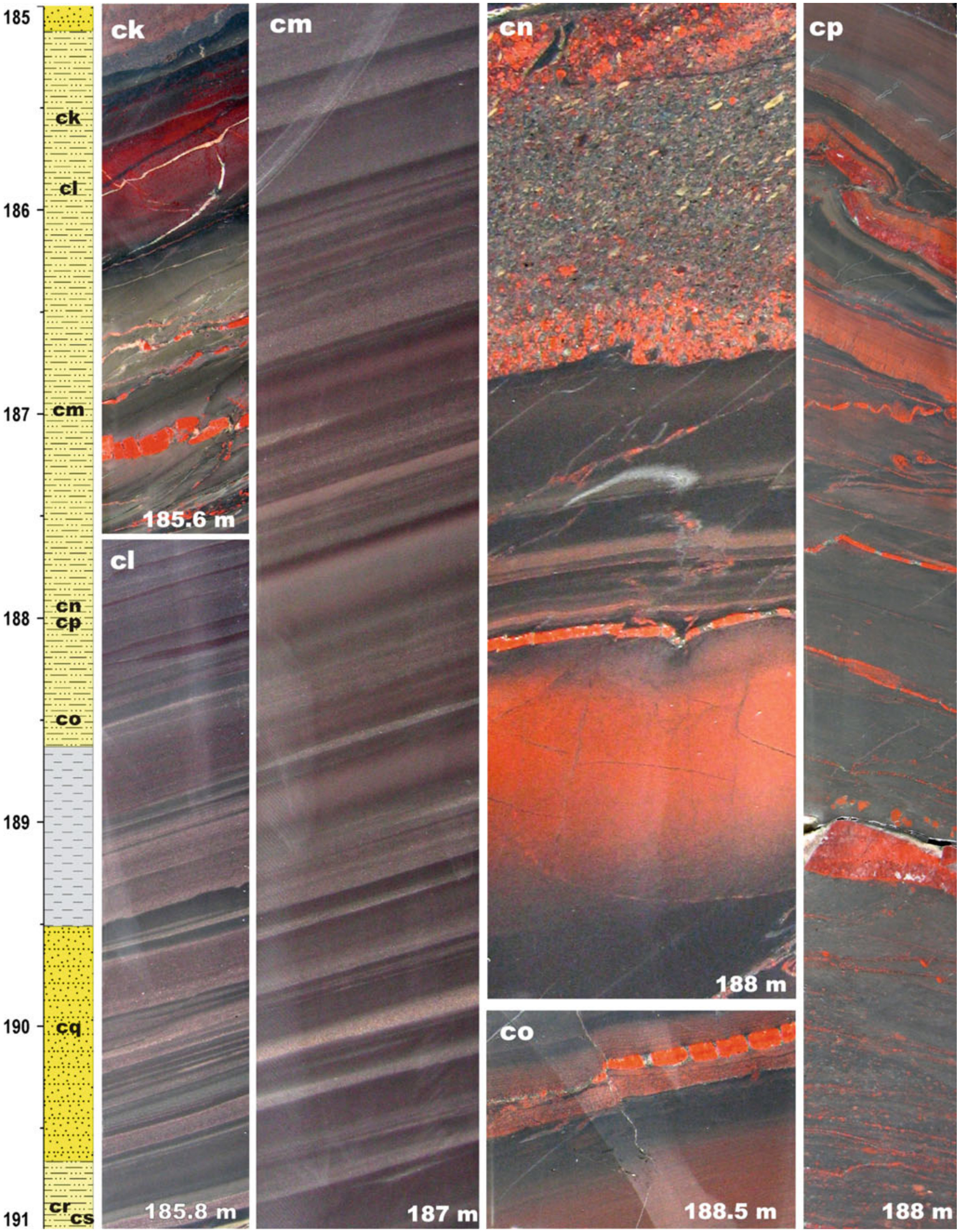

Fig. 6.79 (continued) (**ck**) Brown, bedded siltstone with several sub-parallel jasper veinlets; the thickest veinlet exhibits fragmentation and dismembering. (**cl**, **cm**) Dark brown, parallel-bedded, fine-grained sandstone-siltstone. (**cn**) Brown siltstone with a jasper-impregnated bed (*lower part*) that is veneered by a thin jasper crust, and graded sandstone beds with jasper clasts at their base (the *upper part*). (**co**) Dismembered jasper veneer in bedded siltstone. (**cp**) Jasper beds and veinlets in brown siltstone

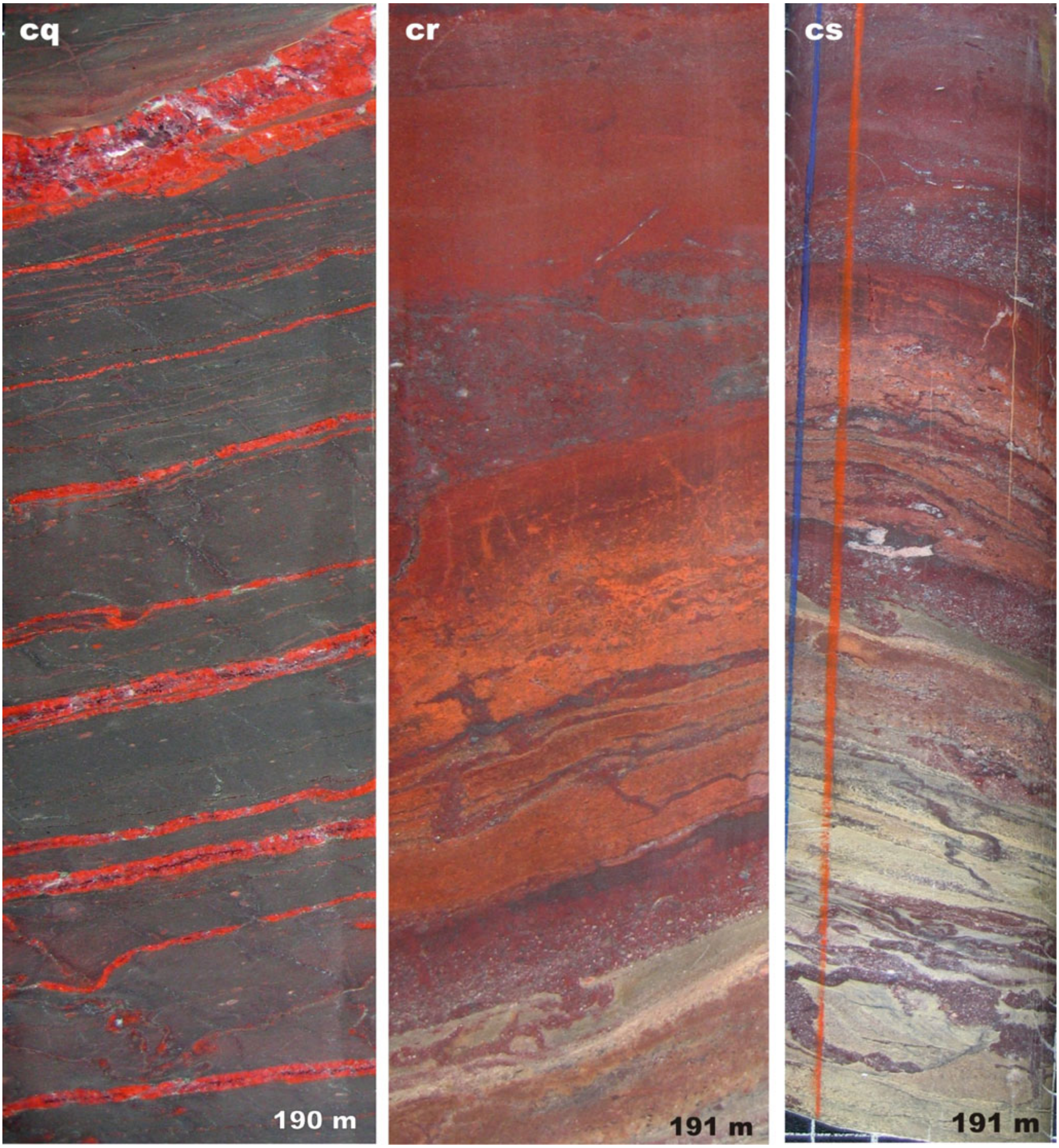

Fig. 6.79 (continued) (**cq**) Thin jasper layers rhythmically interbedded with brown siltstone. (**cr**) Jasper-impregnated, clayey siltstone with incipient slump features. (**cs**) Variegated silty claystone with slump structures

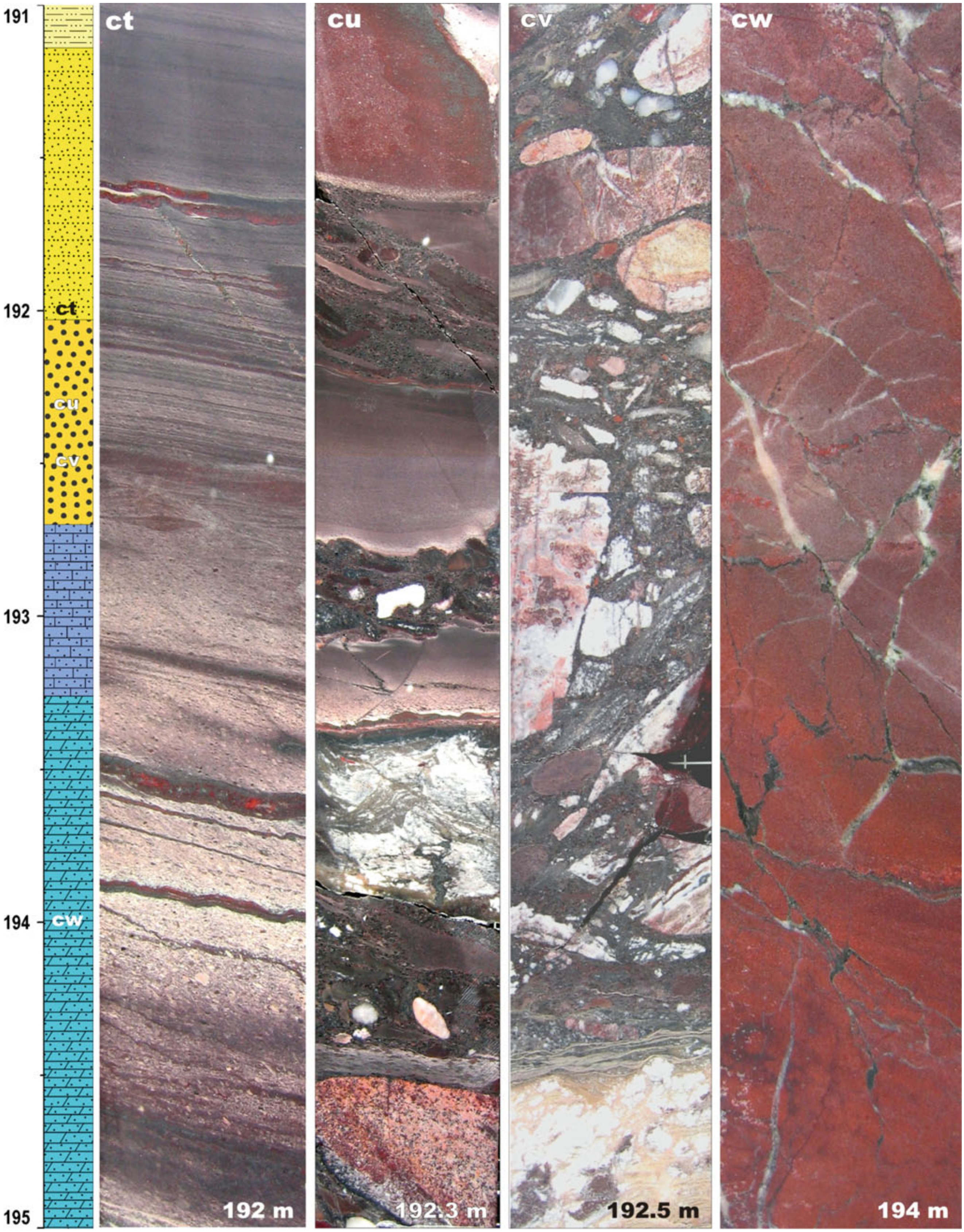

Fig. 6.79 (continued) (**ct**) Rippled, sandy and gritty siltstone passing into laminated siltstone. (**cu**) Thickly bedded siltstone with scattered polymict clasts of felsic volcanic rock; some beds exhibit an erosional base. (**cv**) Volcaniclastic conglomerate with unsorted clasts of felsic lava supported by a siltstone matrix. (**cw**) Jasperised dolostone

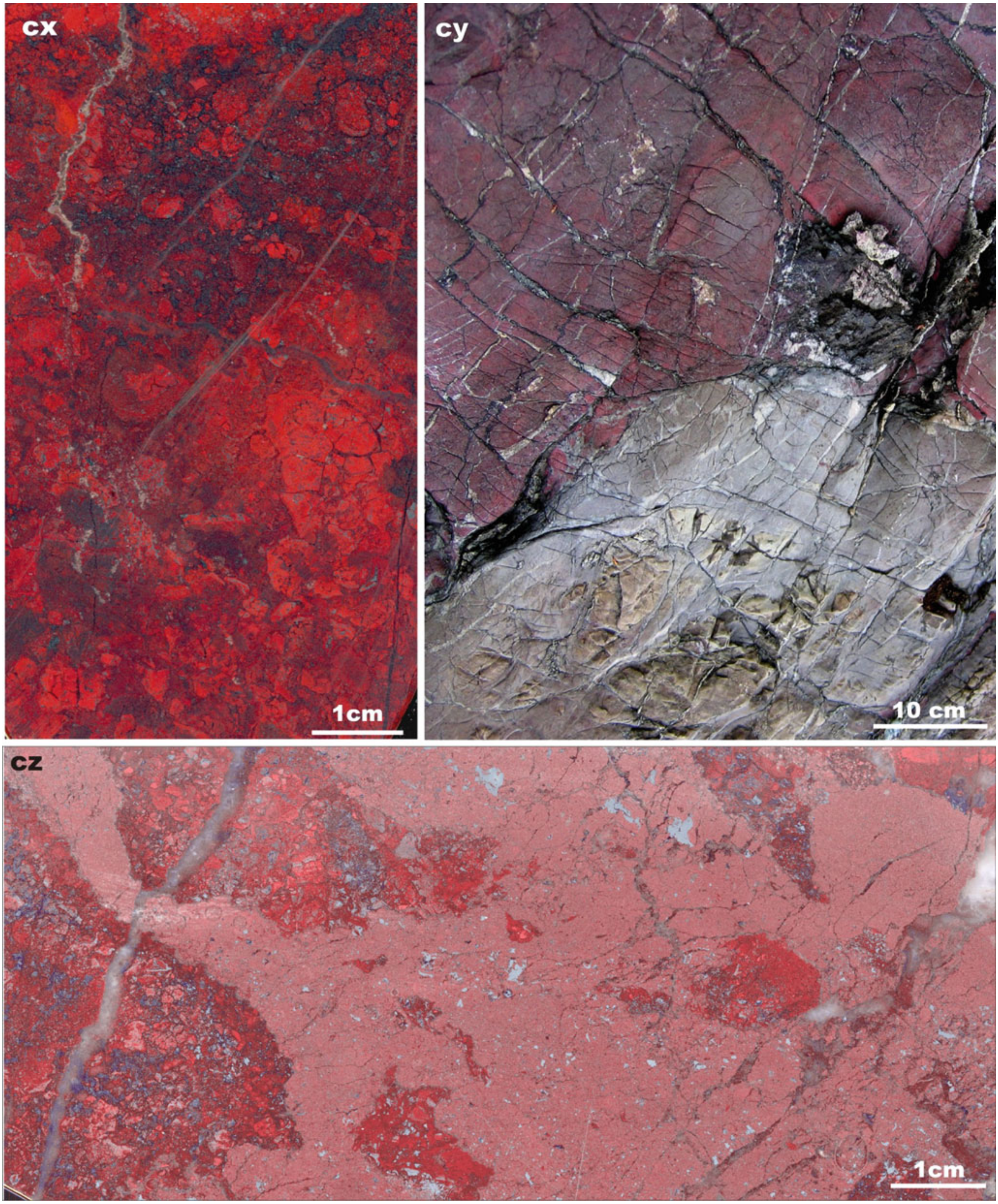

Fig. 6.79 (continued) (**cx**) Polished slab of jasper exhibiting colloform structure. (**cy**) Dark red, partially jasperised dolostone in contact with grey dolostone as seen on an exposed surface oblique to bedding. (**cz**) Pale pink, haematite-rich dolostone partially replaced by jasper (*red*)

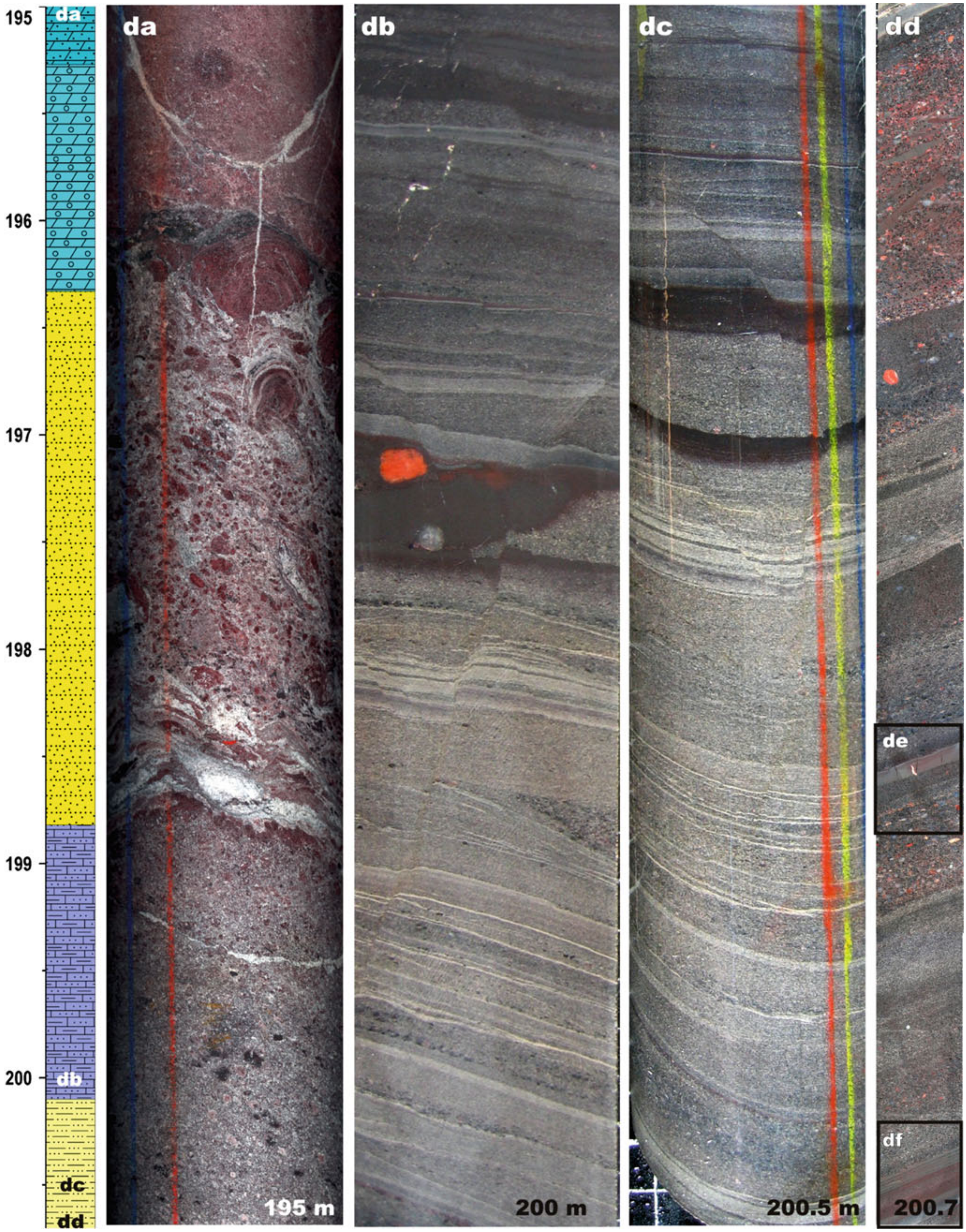

Fig. 6.79 (continued) (**da**) Fragments of brown stromatolite in a dolorudite bed sandwiched in dolarenite. (**db**) Grey, parallel- and low angle cross-bedded, fine-grained sandstone with a small-scale channel filled with black, haematite-rich mudstone containing clasts of quartz and red albite. (**dc**) Grey, laminated, fine-grained sandstone with black, haematite-rich mudstone beds. (**dd**) Interbedded volcaniclastic gritstone, sandstone and siltstone with haematite layers within rectangles marked by (**de**) and (**df**)

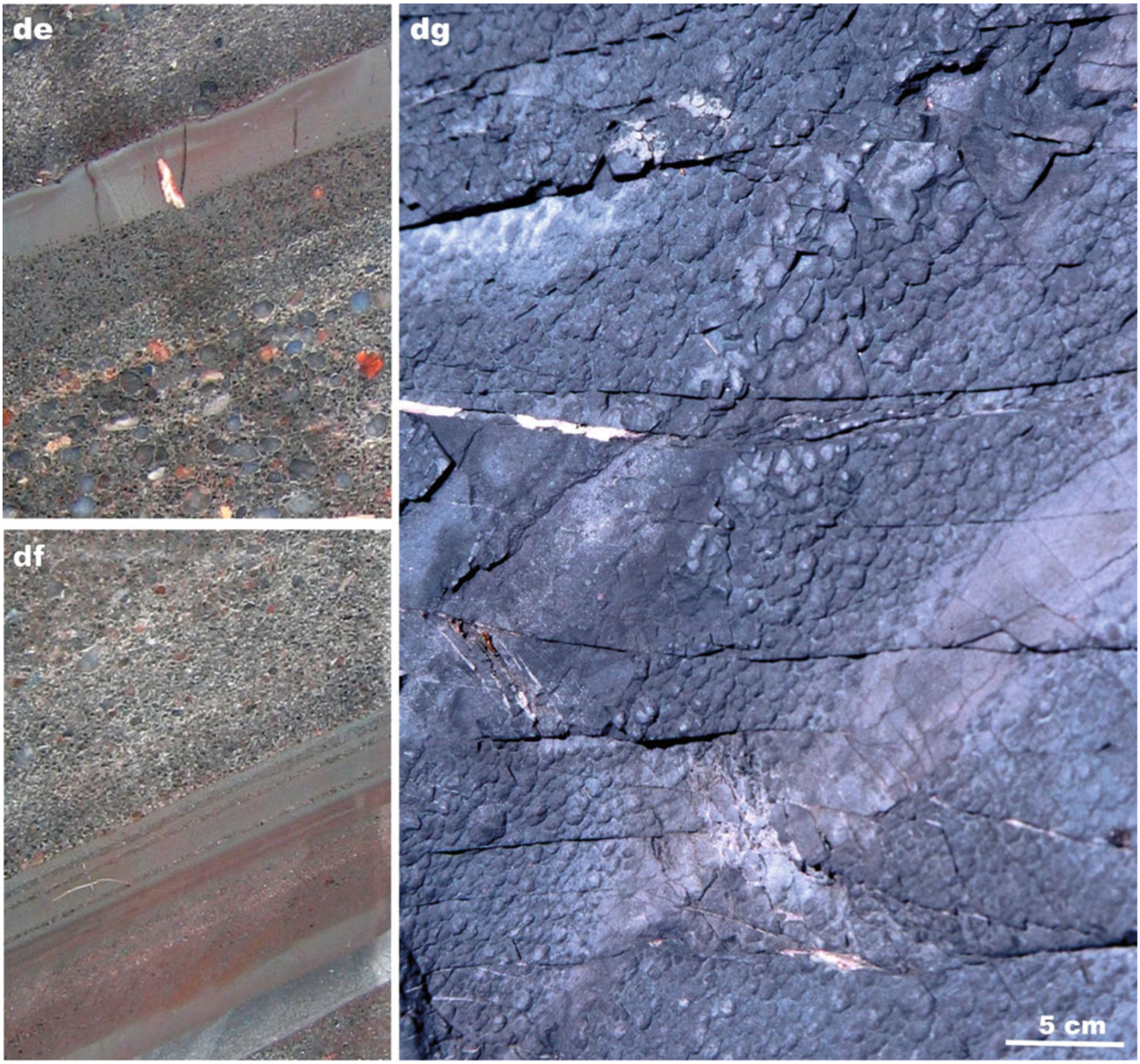

Fig. 6.79 (continued) (**de**) Massive haematite layer in interbedded volcaniclastic sandstone and gritstone. (**df**) Parallel-laminated haematite bed in volcaniclastic sandstone. (**dg**) A wrinkled surface of haematite bed resembling "elephant skin" texture

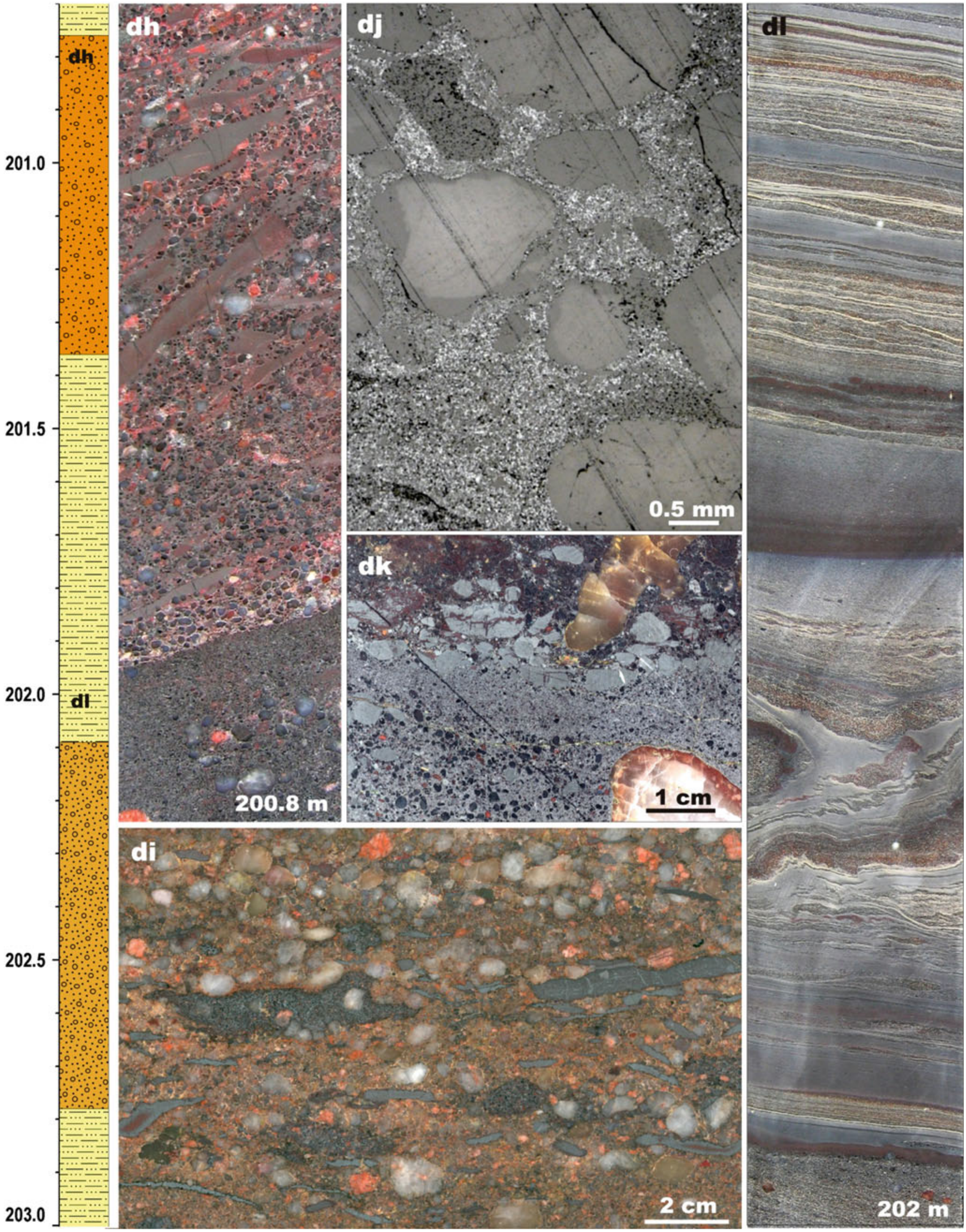

Fig. 6.79 (continued) (**dh**) Thickly bedded, volcaniclastic, coarse-grained sandstone with angular, platy rip-up clasts of fine-grained haematite layers. (**di**) Fine-pebble, volcaniclastic conglomerate with rip-up clasts of haematite layers (*black*). (**dj**) Photomicrograph of coarse-grained sandstone with a haematite-rich matrix (*white*); reflected light. (**dk**) Scanned polished slab of fine-pebble conglomerate containing rounded haematite particles and large, reworked quartz amygdales. (**dl**) Thinly-laminated siltstone with a small-scale slump structure

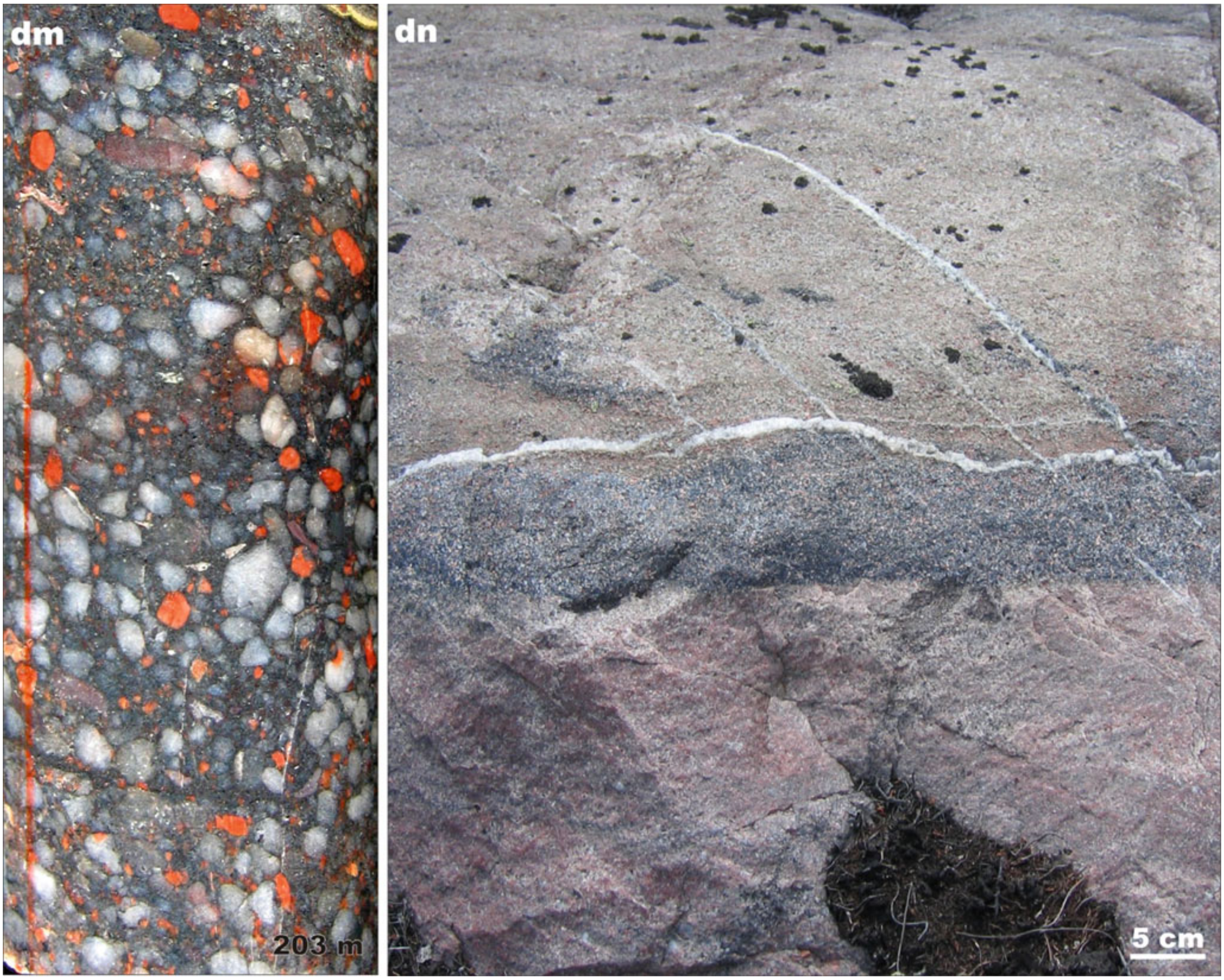

Fig. 6.79 (continued) (**dm**) Gritstone consisting of reworked quartz amygdales (*white*) and red microcline. (**dn**) Outcrop exhibiting massive, volcaniclastic greywacke hosting a haematite-rich gritstone bed (*dark grey*) similar to that shown in photograph (**dm**)

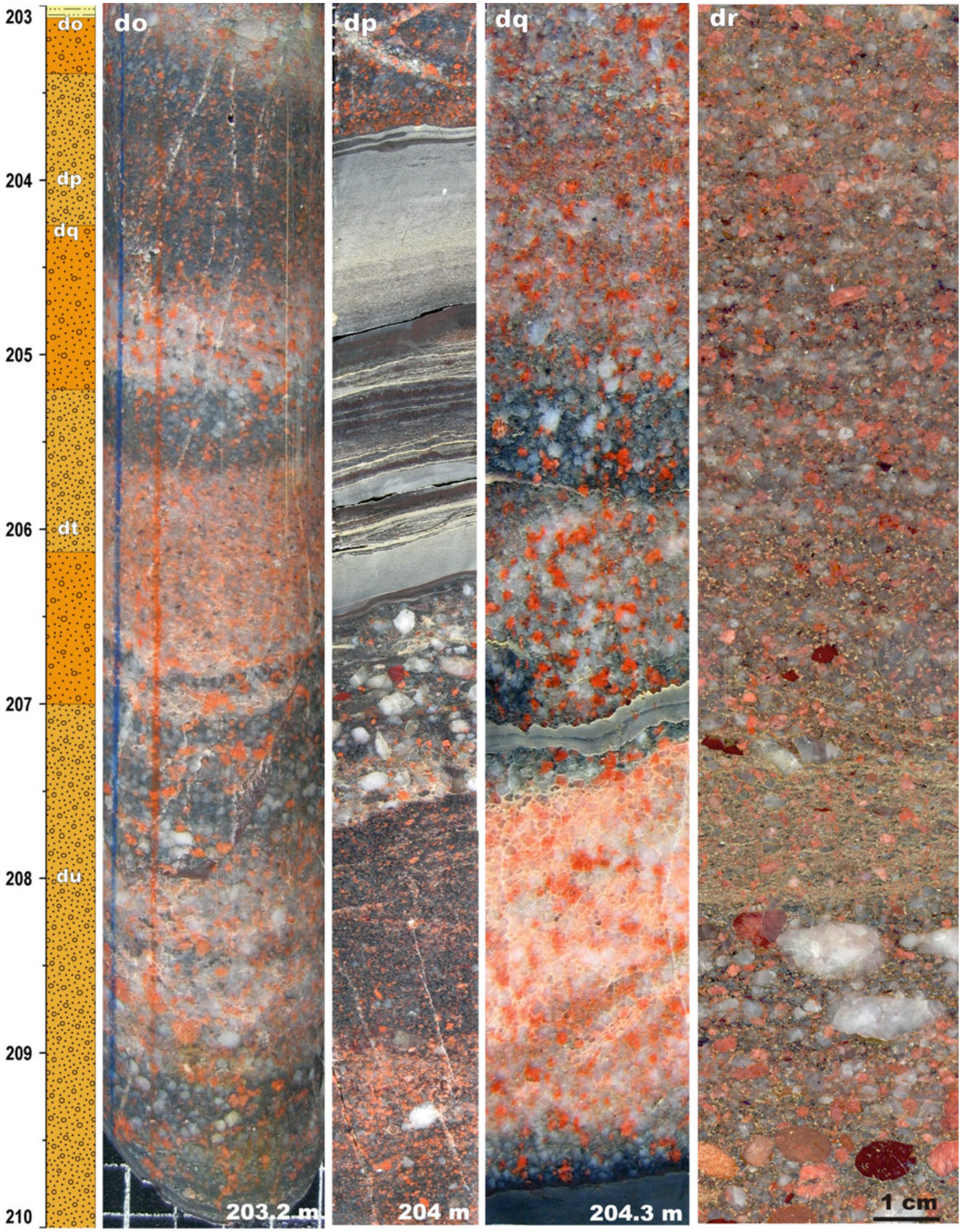

Fig. 6.79 (continued) (**do**) Crudely bedded arkosic gritstone with layers variably enriched in haematite (*dark grey*). (**dp**) Thickly bedded, haematite-rich, arkosic gritstone and sandstone with a bed of laminated, grey to brown siltstone-mudstone. (**dq**) Arkosic gritstone beds separated by black (*bottom*) and grey-yellowish (in the *middle*) claystone layers. (**dr**) Polished slab of arkosic gritstone containing in its lower part large clasts of pink microcline, brick-coloured felsic lava, and reworked white quartz amygdales

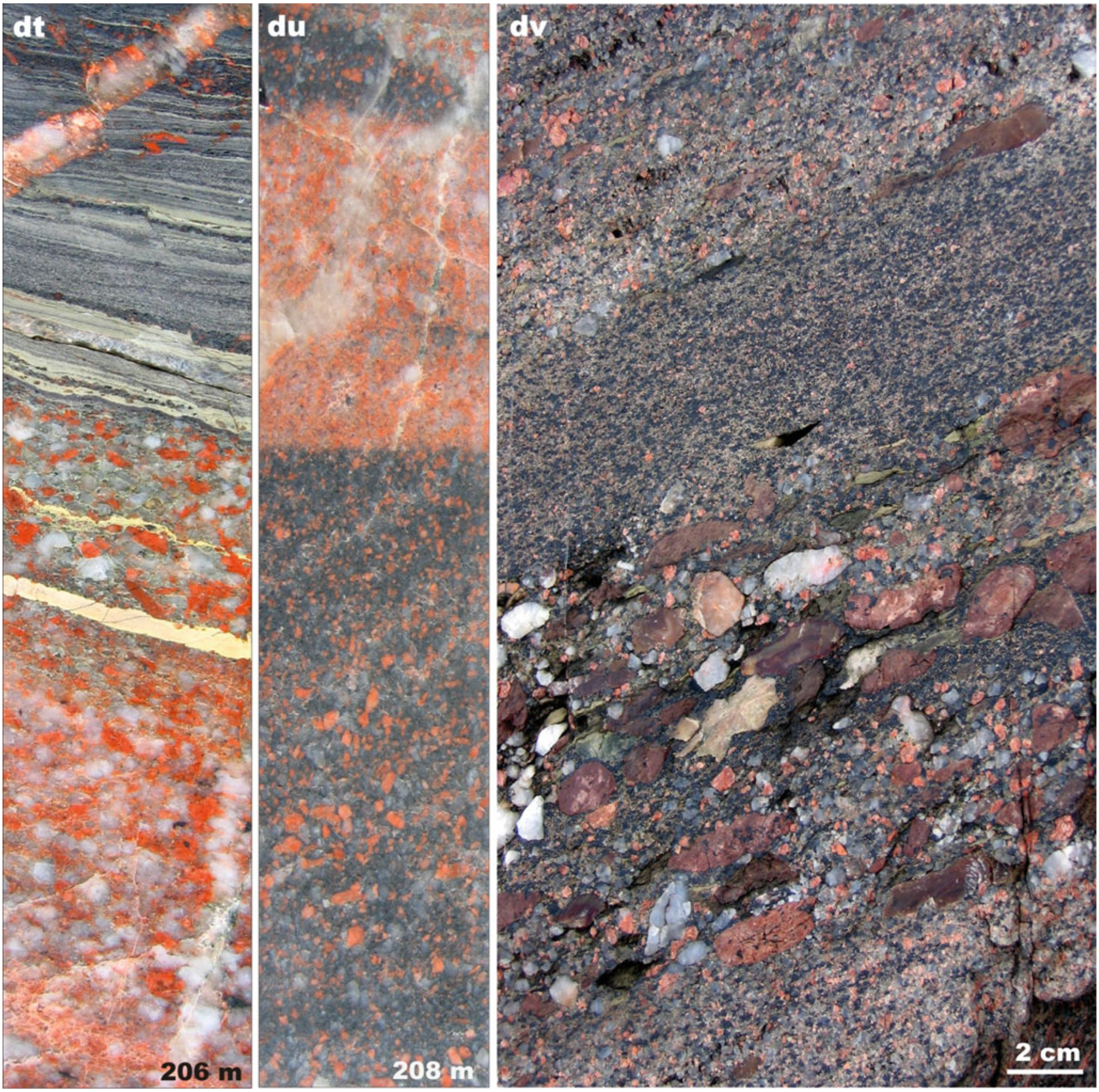

Fig. 6.79 (continued) (**dt**) Pink arkosic gritstone with yellow claystone (sericite) layers overlain by grey laminated siltstone. (**du**) Interbedded haematite-rich (*grey*) and haematite-free (*pink*) arkosic sandstone. (**dv**) Outcrop exhibiting volcaniclastic, haematite-bearing sandstone with a lens filled with fine-pebble, volcaniclastic, polymict conglomerate containing fragments of felsic lava and reworked quartz amygdales (*white*)

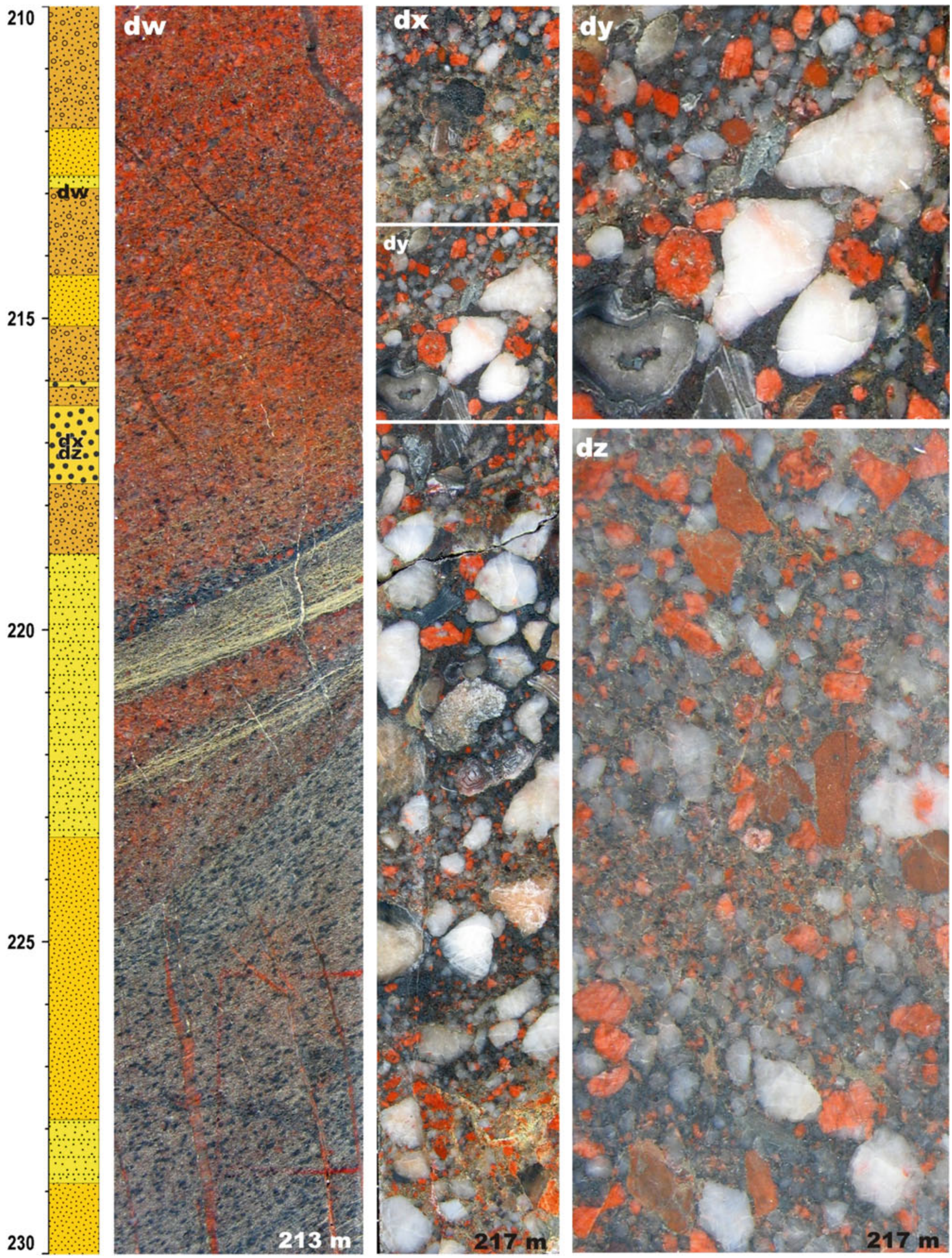

Fig. 6.79 (continued) (**dw**) Arkosic sandstone enriched in dark grey haematite (the *lower part*) and sericite (the *middle part*); the upper part is rich in red microcline. (**dx**) Volcaniclastic conglomerate containing mainly reworked quartz amygdales (*white*) and microcline clasts (*red*) in a haematite-rich sandstone matrix. (**dy**) Enlarged image of the photograph (**dx**) showing white reworked quartz amygdales and pink microcline clasts; note the zoned quartz amygdale in the lower-left corner. (**dz**) Arkosic gritstone composed of bright red microcline, brick-coloured felsic lava, and reworked, white quartz amygdales

Fig. 6.79 (continued) (**ea**) Cross-section view of grit-supported conglomerate grading upward into sandstone; clasts in the conglomerate are mainly reworked quartz amygdales and haematite "ore" (*black*). (**eb**) Fine-pebble conglomerate composed mainly of reworked quartz amygdales and rare clasts of haematite "ore" (*dark grey*)

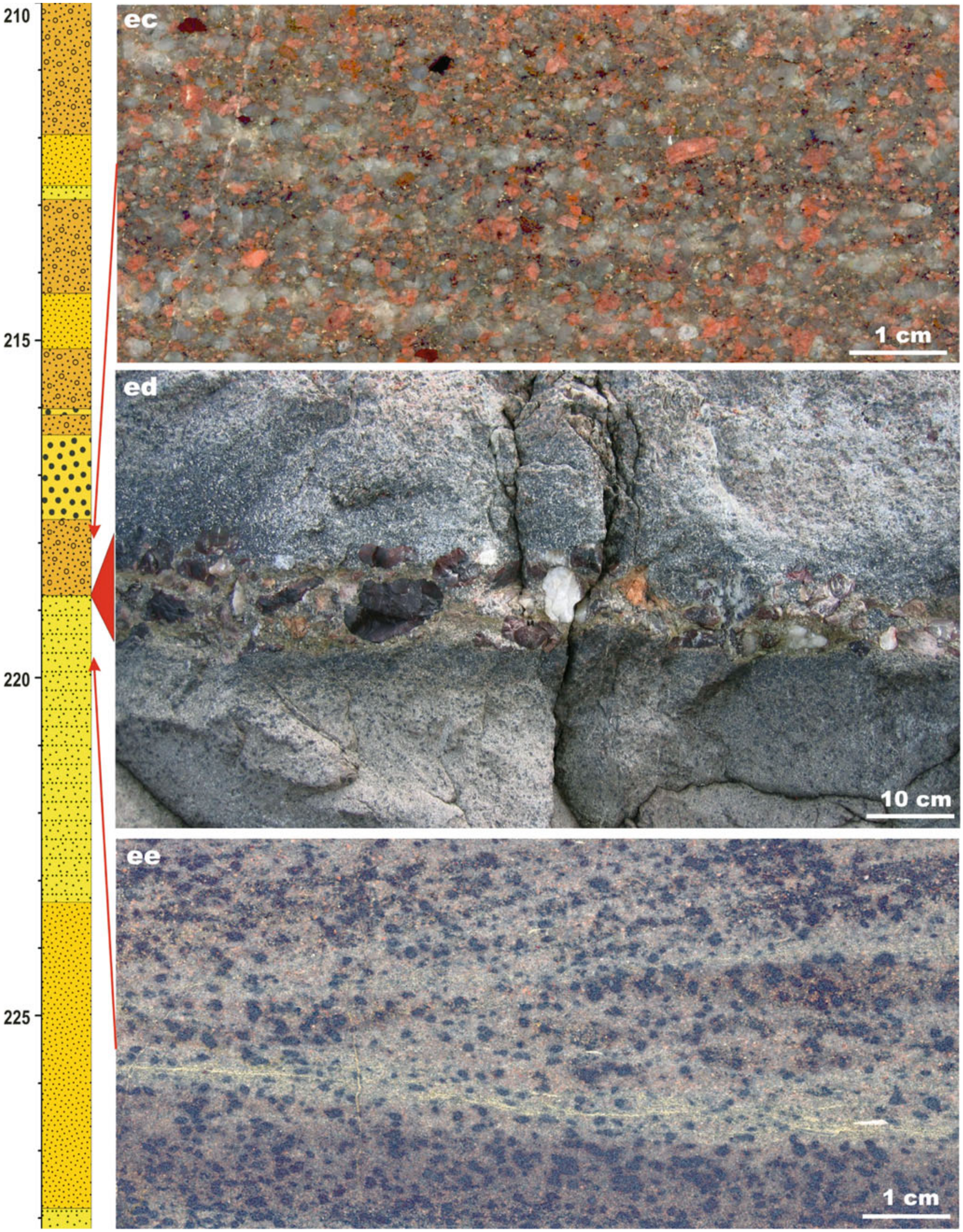

Fig. 6.79 (continued) (**ec**) Polished slab of arkosic gritstone composed of microcline (*bright red*), reworked quartz amygdales and felsic lava (*brown*). (**ed**) Cross-section through a thin layer of volcaniclastic conglomerate separating overlying arkosic gritstone (also detailed in photograph (**ec**)) from underlying greywacke detailed in photograph **ee**. (**ee**) "Spotted", low-angle, cross-bedded greywacke; yellowish colour is due to enrichment in leucoxene, whereas black spots are due to selective cementation by haematite

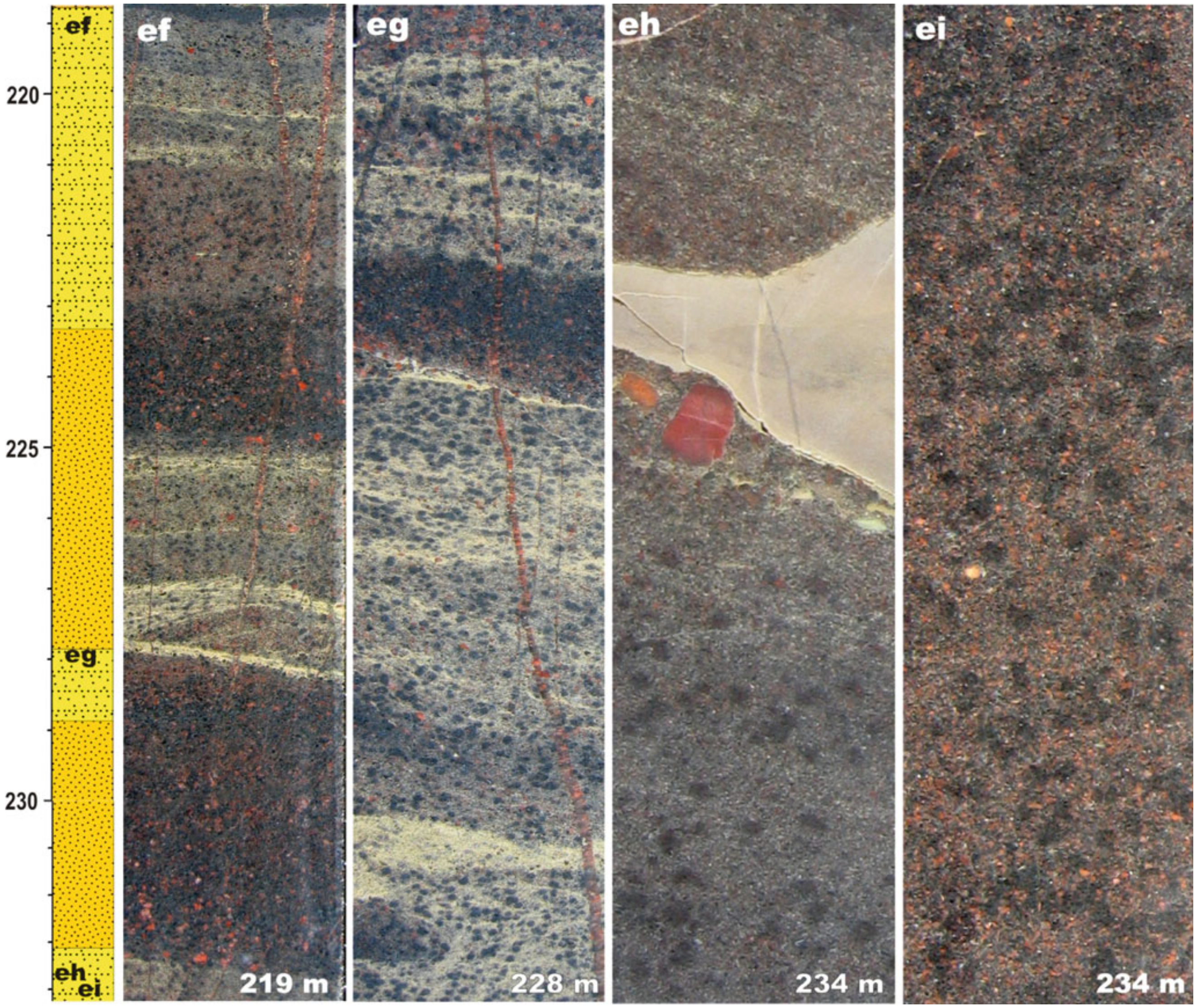

Fig. 6.79 (continued) (**ef**, **eg**) Low-angle cross-bedded greywacke with leucoxene-rich layers and matrix (*yellow*) and spotty cementation by haematite (*black*). (**eh**) "Spotted" greywacke with a clast of red felsic lava and a large, pale yellow claystone (sericite) fragment. (**ei**) "Spotted", massive, volcaniclastic greywacke; black spots due to selective cementation by haematite

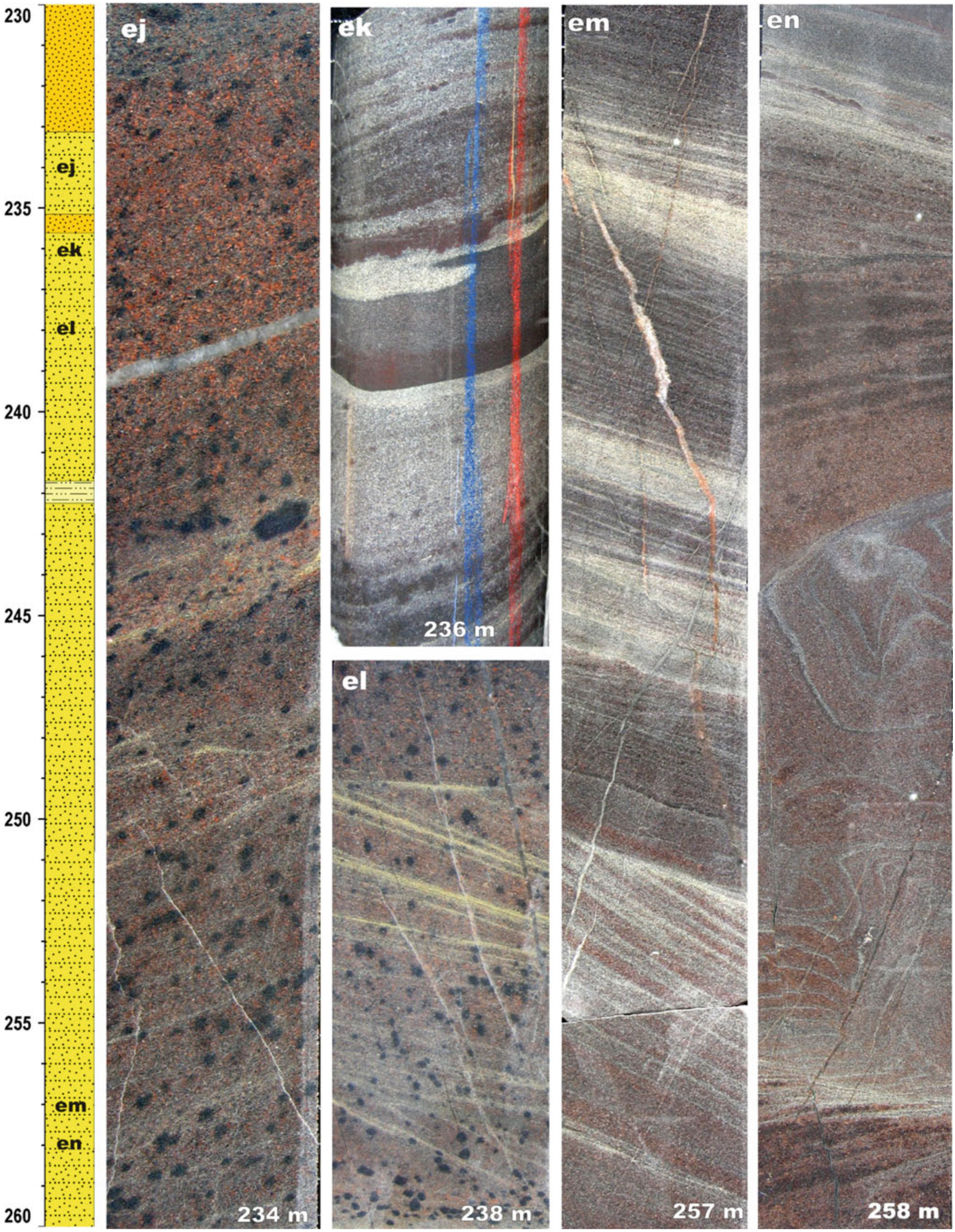

Fig. 6.79 (continued) (**ej**) Crudely-bedded, volcaniclastic greywacke with selective cementation by haematite resulting in a spotty appearance. (**ek**) Interbedded grey and brown siltstone with small-scale slump structures in the middle. (**el**) Cross-bedded, "spotted" greywacke. (**em**) Planar-cross-bedded greywacke. (**en**) Brown, cross-bedded greywacke with a syndepositional slump-fold in the middle bed

Fig. 6.79 (continued) (**eo**) Outcrop exhibiting trough cross-bedded, haematite-rich greywacke with rip-up clasts of black mudstone; note the erosional surface (above the yellow pen) and overturned cross-beds below the surface. Pen length is 13 cm

Fig. 6.79 (continued) (**ep**) Outcrop exhibiting trough and planar cross-bedded greywacke with scattered rip-up clasts of black mudstone; cavities are weathered-out carbonate-cemented lenses. Pen length is 13 cm

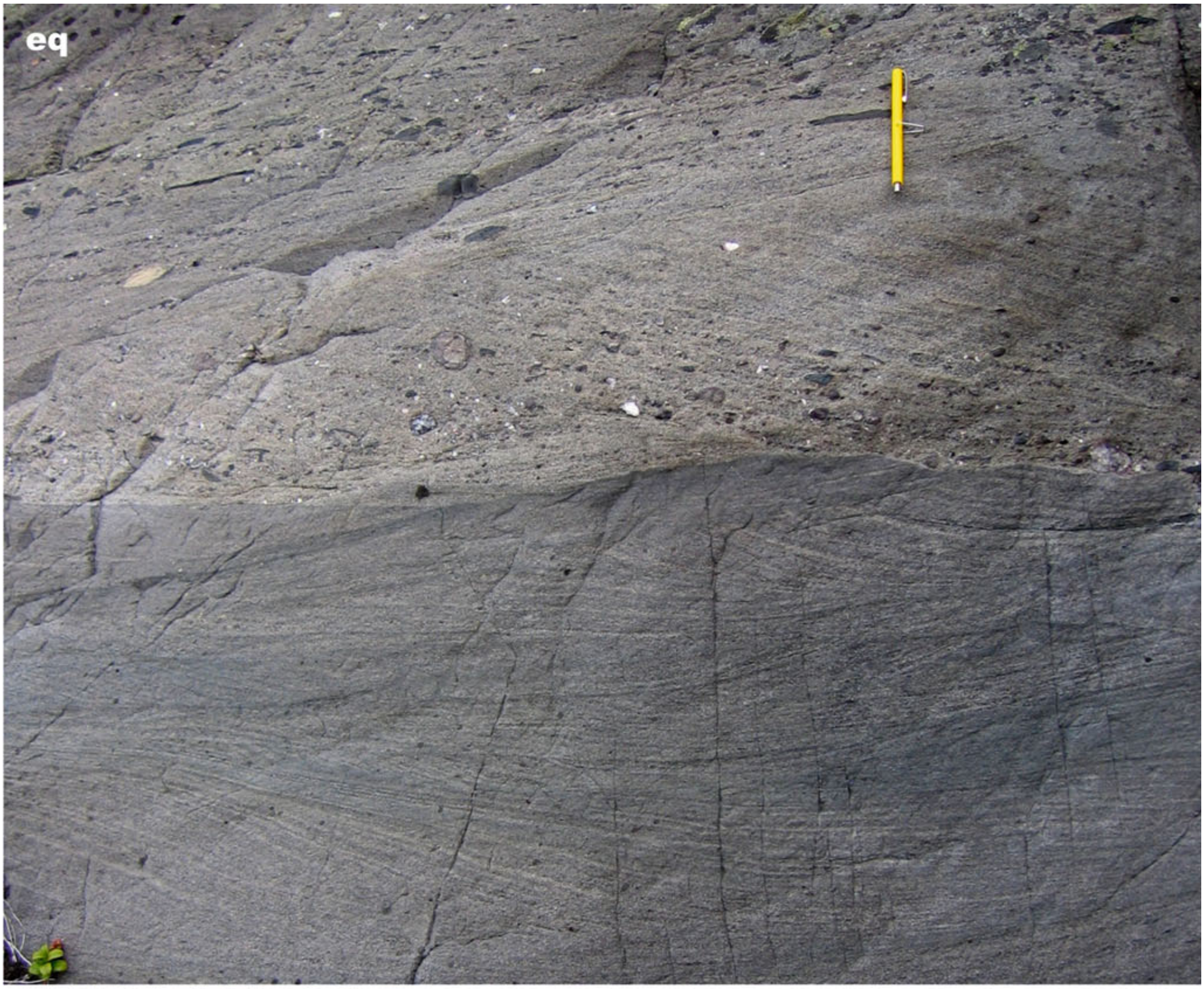

Fig. 6.79 (continued) (**eq**) Erosion surface separating cosets of small-scale through cross-bedded, fine-grained, volcaniclastic greywacke (*below*) and a large-scale trough cross-bedded, pebbly gritstone and greywacke; pen length is 13 cm. (**er**) Overturned cross beds overlain by planar to low-angle laminated volcaniclastic greywacke. Pen length is 12 cm

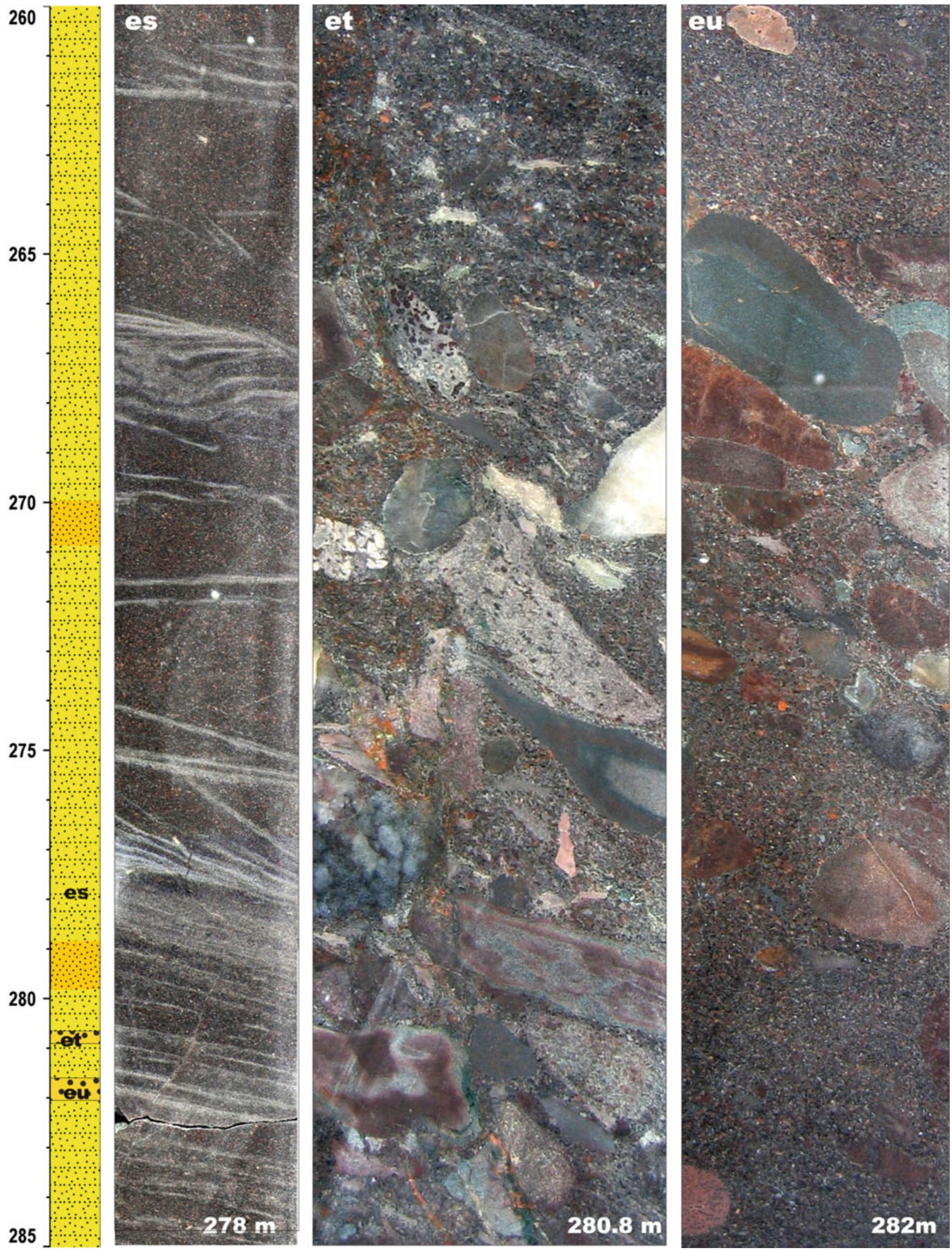

Fig. 6.79 (continued) (**es**) Dark brown, cross-bedded, volcaniclastic greywacke. (**et**) Volcaniclastic conglomerate comprising rounded fragments of alkaline dacite, andesite and basalt in a greywacke matrix. (**eu**) Massive, volcaniclastic greywacke with a pocket of well-rounded and unsorted pebbles of alkaline basalt and dacite

Fig. 6.79 (continued) (**ev**) Erosional surface separating cross-bedded greywacke (*below*) and unsorted, polymict, volcaniclastic conglomerate filling a channel at the base of another cross-bedded greywacke bed

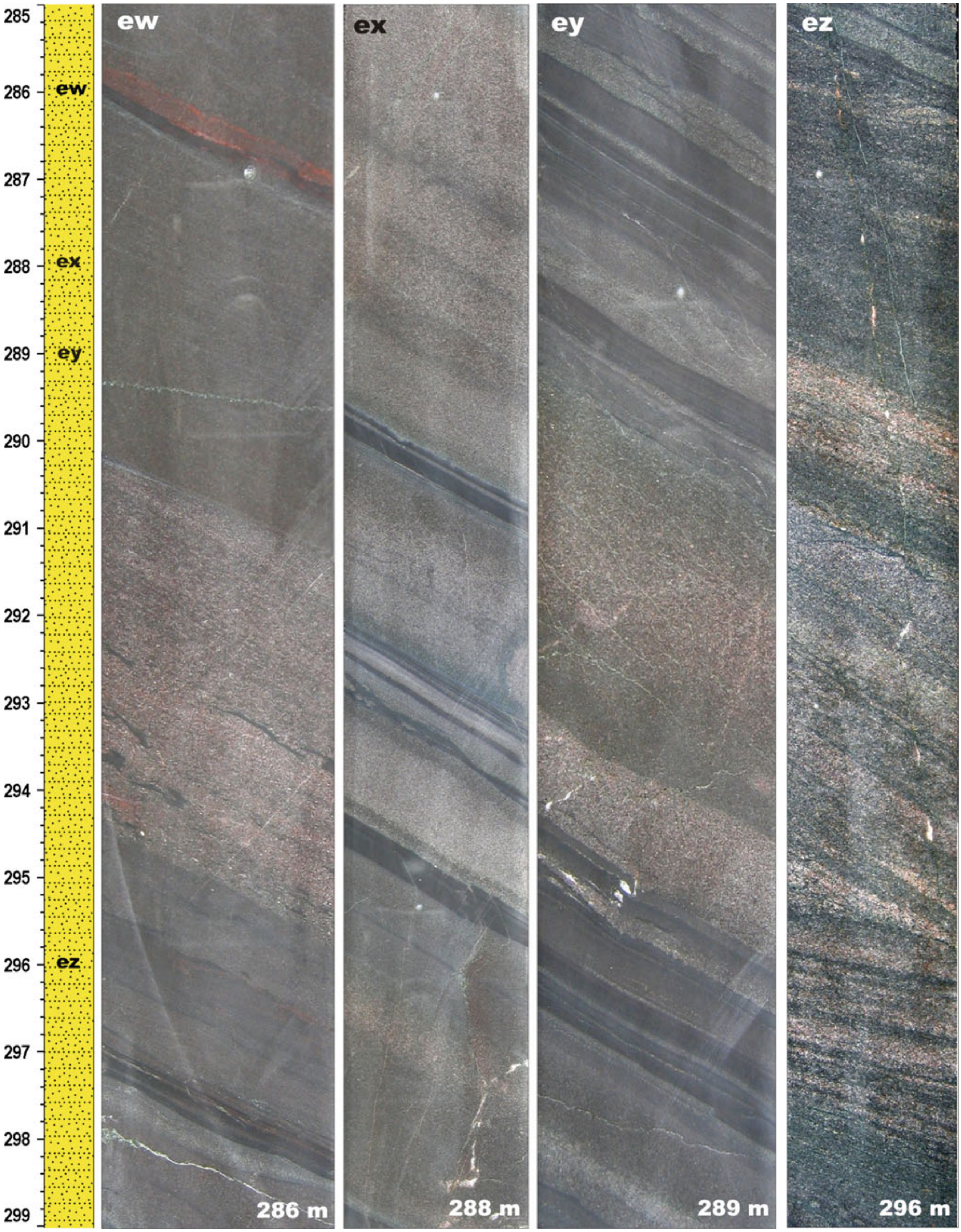

Fig. 6.79 (**ew**) Brown, thinly bedded to massive siltstone with a low-angle cross-bedded greywacke in the *middle*. (**ex**) Indistinctly bedded, fine-grained sandstone with several black mudstone-draped beds. (**ey**) Parallel- and low-angle cross-bedded sandstone-siltstone. (**ez**) Cross-bedded, clayey greywacke

Fig. 6.79 (continued) (**fa**) Graded arkosic sandstone beds draped with black, haematite-rich mudstone. (**fb**) Small-scale cross-beds in a grey sandstone-siltstone bed overlain sharply by gritstone grading into coarse-grained sandstone

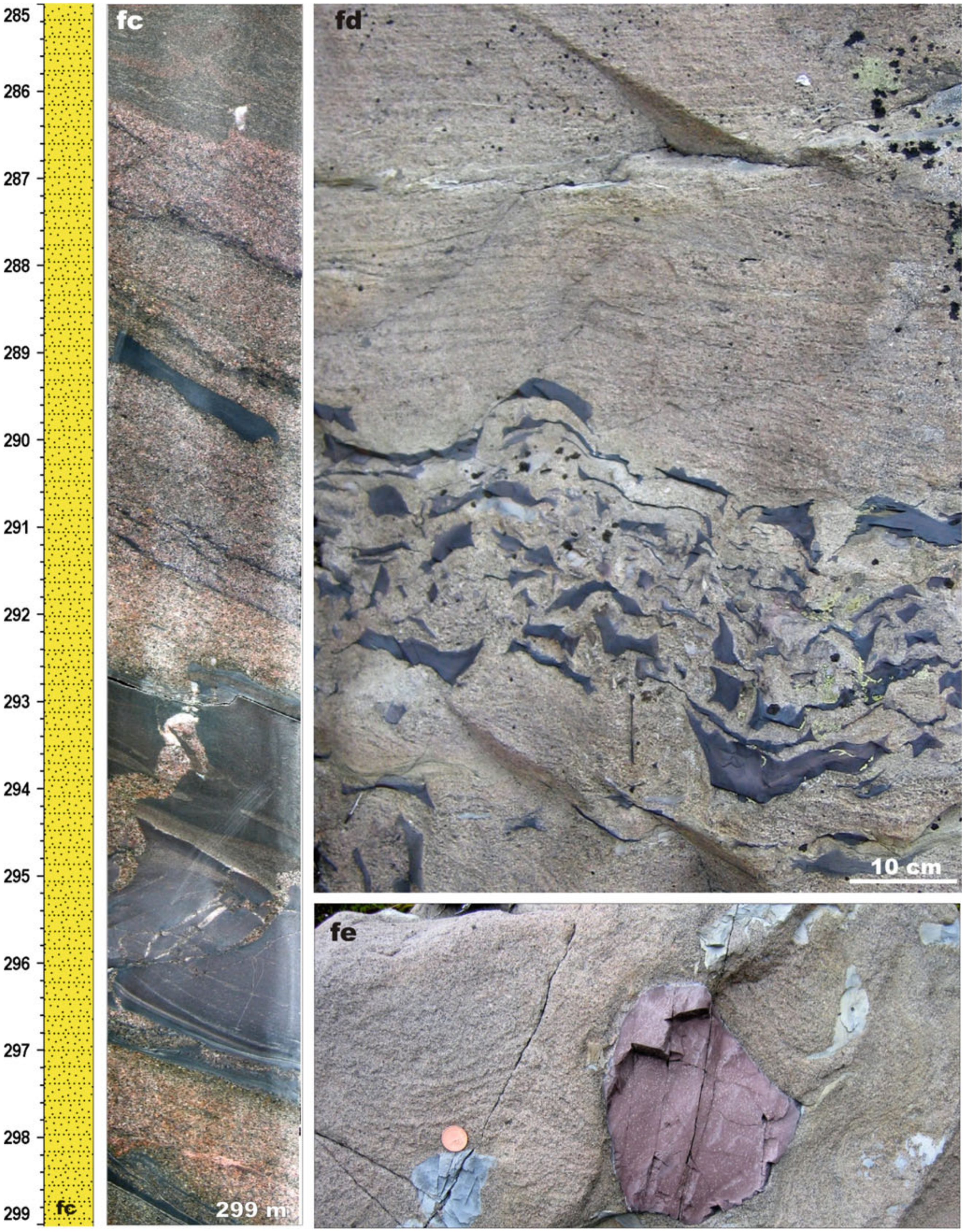

Fig. 6.79 (continued) (**fc**) Coarse-grained greywacke with black mudstone rip-up clasts and black, haematite-rich mudstone beds injected by a sand-dyke. (**fd**) Cross-bedded greywacke with a bed containing numerous, black, haematite-rich mudstone intraclasts. (**fe**) Cross-bedded greywacke with intraclasts of purple, bluish and pale grey mudstone; coin diameter is 1.5 cm

Fig. 6.79 (continued) (**ff**) Syn-sedimentary, folded and faulted, grey, thinly-bedded siltstone with a sandstone bed containing numerous, platy rip-up clasts of black mudstone

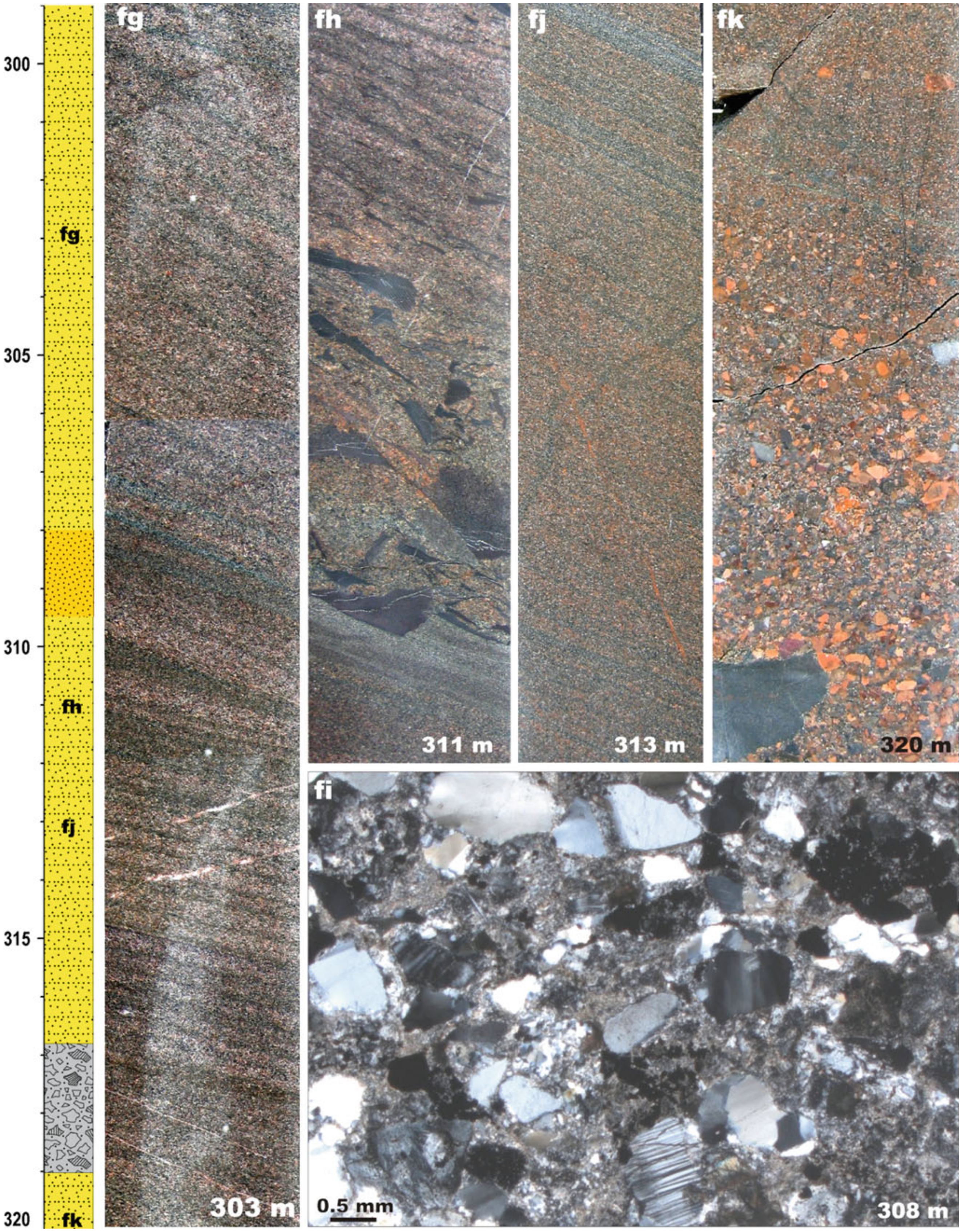

Fig. 6.79 (continued) (**fg**) Cross-bedded, volcaniclastic greywacke. (**fh**) Bedded, volcaniclastic greywacke with black mudstone rip-up clasts. (**fi**) Photomicrograph in polarised, transmitted light, showing matrix-supported, polymict, variably rounded and poorly sorted clasts of quartz, microcline and plagioclase. (**fj**) Laminated, fine-grained, volcaniclastic greywacke. (**fk**) Microcline-rich gritstone grading into fine-grained greywacke; note the oversized fragment of mafic lava in the gritstone

Fig. 6.79 (continued) (**fl**) Massive greywacke with black, haematite-rich mudstones fragments ripped off from formerly desiccated mudstone beds. (**fm**) Polymict conglomerate containing unsorted clasts of trachydacite, trachyandesite and weathered-out, large jasper amygdale supported by a volcaniclastic greywacke matrix; coin diameter is 1.5 cm. (**fn**) Cross-section view of indistinctly bedded, fine-grained, volcaniclastic greywacke at the base of the Kolosjoki Sedimentary Formation; length of the yellow pen is 13 cm

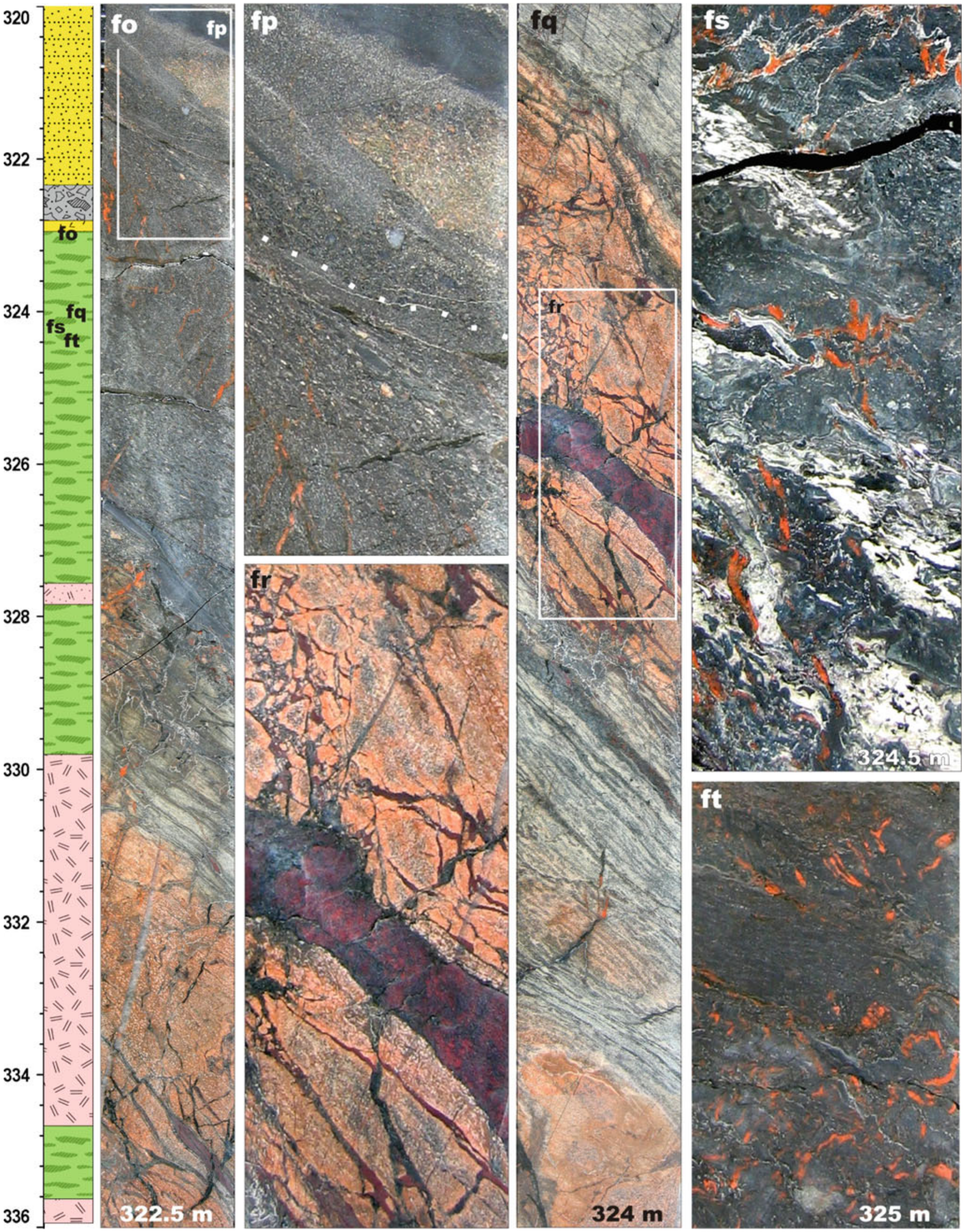

Fig. 6.79 (continued) (**fo**) Contact between Kuetsjärvi Volcanic Formation (pink felsic lava with grey tuff with red K-feldspar veinlets) and Kolosjoki Sedimentary Formation volcaniclastic greywacke; note dark red jasper vein in the lower part of the core interval. (**fp**) Contact (denoted by *dashed line*) details showing that Kuetsjärvi Volcanic Formation tuff is injected by red K-feldspar veinlets, whereas the greywacke of the overlying the Kolosjoki Sedimentary Formation is not. (**fq**) Fluidal flow-breccia with a fragment of pink felsic lava injected by a jasper vein. (**fr**) Detailed image showing a fragment of pink, felsic lava injected by a jasper vein; note that brecciated part of the lava fragment is cemented by jasper. (**fs**) Fluidal felsic lava injected by red K-feldspar veinlets. (**ft**) Aphyric dacitic lava with red K-feldspar veinlets

Fig. 6.79 (continued) (**fu**) Felsic lava with a large jasper-filled amygdale; coin diameter 1.5 cm. (**fv**) Zoned jasper vein in dacitic lava; coin diameter is 1.5 cm (All photographs by Victor Melezhik)

References

Akhmedov AM (1972a) Haematite oolites of the Pechenga complex. In: Bel'kov IV (ed) Data on mineralogy of the Kola Peninsula. Kola Science Centre, Apatity, pp 41–53, in Russian

Akhmedov AM (1972b) Iron-bearing metasedimentary rocks of the Pechenga complex, and their genesis. In: Bel'kov IV (ed) Data on geology and metallogeny of the Kola Peninsula. Kola Science Centre, Apatity, pp 125–131, in Russian

Hanski EJ (1992) Petrology of the Pechenga ferropicrites and cogenetic, Ni-bearing gabbro-wehrlite intrusions, Kola Peninsula, Russia. Bull Geol Surv Finland 367:192p

Ljubtzov VF (1979) Stromatolites of the Palaeoproterozoic Pechenga complex, Kola Peninsula. Trans USSR Acad Sci 247(2):419–421, in Russian

Kazansky VI, Kuznetsov AV, Lobanov KV, Kuznetsov OL, Pimanova NN, Cheremisina EN (1998) Local structures and deep structures of the Pechenga ore region. In: Orlov VP, Laverov NP (eds) Kola Superdeep. Scientific results and research experience. TECHNONEFTEGAZ, Moscow, pp 134–155, in Russian

Melezhik VA, Fallick AE, Kuznetsov AB (2005) The Palaeoproterozoic, rift-related, shallow-water, ^{13}C-rich, lacustrine carbonates, NW Russia – Part II: global isotope signal recorded in the lacustrine dolostones. Trans R Soc Edinb Earth Sci 95:423–444

Melezhik VA, Huhma H, Condon DJ, Fallick AE, Whitehouse MJ (2007) Temporal constraints on the Paleoproterozoic Lomagundi-Jatuli carbon isotopic event. Geology 35:655–658

Predovsky AA, Fedotov ZhA, Akhmedov AM (1974) Geochemistry of the Pechenga complex. Nauka (Science), Leningrad, p 139, in Russian

Sharov NV, Rispolozhensky YA, Karaev NA, Polyakova VA, Ronin AL, Lizinsky MD, Isanina EV, Yepinatieva AM, Galdin NE (1998) In: Orlov VP, Laverov NP (eds) Kola Superdeep. Scientific results and research experience. TECHNONEFTEGAZ, Moscow, pp 159–167, in Russian

Winchester JA, Floyd PA (1977) Geochemical discrimination of different magma series and their differentiation products using immobile elements. Chem Geol 20:325–343

6.2.6 Kolosjoki Volcanic Formation: FAR-DEEP Hole 9A

Eero J. Hanski, Victor A. Melezhik, Aivo Lepland, Alexander E. Romashkin, Dmitry V. Rychanchik, Zhen-Yu Luo, Evgenii V. Sharkov, and Maria M. Bogina

Scientific Targets

- Tectonic and depositional settings associated with the onset of the Shunga Event
- Geochemical rock record during enhanced global accumulation of organic matter
- Sulphur and organic carbon isotopic composition of seawater
- Seafloor bioalteration of mafic lava flows
- Microfossil record (organowalled and silicified)
- Provenance composition
- Radiometric age constraint on timing of deposition (Sm/Nd and Re/Os)

Drillhole 9A intersected the Kolosjoki Volcanic Formation (Figs. 6.80 and 6.81) in the eastern part of the Pechenga Greenstone Belt, Kola Peninsula, NW Russia (Figs. 6.32, 6.33). The deposition of the formation has been constrained between 2058 ± 2 Ma and 1970 ± 5 Ma (Melezhik et al. 2007 and Hanski 1992, respectively). The formation contains voluminous tholeiitic basalts with several interlayers of C-rich sedimentary rocks corresponding in age to the episode of enhanced global accumulation of organic matter in the Palaeoproterozoic, known as the Shunga Event (e.g. Melezhik et al. 2005; details are presented in **Chap. 7.6**).

Several FAR-DEEP drillholes (12A, 12B and 13A, Chaps. 6.3.3 and 6.3.4) provide material from successions accumulated in a marine environment within a volcanically active, intraplate rift setting developed on a continental margin. In contrast, Hole 9A intersected a succession which is presently considered to represent a marine basin within a "Red Sea" type setting and characterised by dominance of volcanic processes over sedimentary ones (for details see Chap. 4.2).

Apart from thick and monotonous tholeiitic basalts (Fig. 6.82) and "black shale" interbeds, the Kolosjoki volcanic succession contains sporadic occurrences of thin chert beds, some of which contain putative spheroidal microfossils (Ivanova et al. 1988; details are presented in Chap. 7.8.3). In addition, the Kolosjoki "black shale" contains ^{13}C-depleted limestone ($\delta^{13}C_{carb}$ at around −7.7 ‰; Melezhik and Fallick 1996), which might have been precipitated either from low-^{13}C ambient basinal water or formed from diagenetic, low-^{13}C fluids incorporating bicarbonate derived from oxidised organic carbon during the Shunga Event. Both scenarios have important implications for deciphering details of the carbon cycle. The Kolosjoki "black shale" also contains abundant disseminated sulphides with $\delta^{34}S$ ranging between +3.0 ‰ and +5.2 ‰ (V. Melezhik and T. Fallick (unpublished)).

Consequently, Core 9A has multiple implications. Among them are foremost carbon and sulphur cycles in a Palaeoproterozoic volcanically dominated basin, interaction between submarine microbial life and volcanic substrate (bioalteration processes) and hydrothermal processes (chert-hosted microfossils).

The 101-m-long Hole 9A was drilled in the middle part of the Kolosjoki Volcanic Formation (Fig. 6.33) and intersected a succession comprising nine individual lava flows, each separated by a sedimentary bed. Figures 6.80 and 6.81 show a lithological column, stratigraphic profiles of selected major and trace elements as well as magnetic susceptibility. The volcanic rocks show a lower magnetic susceptibility than the sedimentary rocks (Fig. 6.81). Chemical composition of analysed samples is presented in Appendices 23–25. Figures 6.83 and 6.84 illustrate main geochemical features of volcanic rocks. The core photos (Fig. 6.85) provide a documentation of major lithological and structural features of volcanic and sedimentary rocks through the stratigraphy.

The volcanic rocks of the Kolosjoki Volcanic Formation intersected by Hole 9A are characterised by a rather homogeneous magnetic susceptibility that averages around 1,100 μSI ($K^* = 1{,}000 \times 10^{-6}$ SI units in Fig. 6.81). The values are much higher in all greywacke beds averaging at 4,400 μSI ($K^* = 400 \times 10^{-6}$ SI units in Fig. 6.81) with some beds showing up to 55,000 μSI ($K^* = 5{,}000 \times 10^{-6}$ SI units in Fig. 6.81).

Volcanic Rocks

The lava flows are mostly massive (Fig. 6.85o), but some of them are amygdale-rich towards the top of the flow (5.80–39.15 m, 57.36–58.46 m; Figs. 6.85i–l). One of the flows has indications of a pillowed flow top, whereas another flow shows incipient pillows at the base (Figs. 6.85p, q). The lava flow at depth 35–53 m, between the thickest sedimentary interlayers (Fig. 6.80), is more coarse-grained than typical, displaying a subophitic texture with locally well-preserved clinopyroxene grains. Elsewhere primary pyroxene grains are replaced by amphibole pseudomorphs. All lava flows are chemically tholeiitic basalts. There are some

E.J. Hanski (✉)
Department of Geosciences, University of Oulu, Oulu, Finland

V.A. Melezhik et al. (eds.), *Reading the Archive of Earth's Oxygenation*, Volume 2: The Core Archive of the Fennoscandian Arctic Russia – Drilling Early Earth Project, DOI 10.1007/978-3-642-29659-8_3, © Springer-Verlag Berlin Heidelberg 2013

differences, which allow the lava flows to be divided into two chemical units, A and B (Fig. 6.83).

The lower Unit A (interval 21–101 m) consists of eight lava flows with thicknesses ranging between 5 and 18 m. The flows are composed of relatively primitive tholeiitic basalt, having MgO in the range of 6.3–9.7 wt.%, TiO_2 0.9–1.3 wt.%, and Cr $\leq$330 ppm. Two samples exhibit higher Mg# (57.6–60.4) (Fig. 6.83a) and higher Cr contents (c. 330 ppm) than other samples from Core 9A (Fig. 6.83c), indicating that they contain some cumulate components. In a Nb versus Ni diagram (Fig. 6.83d), analyses from Unit A have a different trend from those of Unit B, showing that the lavas from the two units were evolved from magmas having slightly different chemical compositions.

Unit B, in the uppermost part of the core (interval 1–21 m), represents a single lava flow. Compared to Unit A, it is more enriched in incompatible elements (e.g. LREEs, Fig. 6.84a). It is also slightly more evolved, having lower MgO (6.2–6.8 wt.%) and Cr (36–46 ppm), and higher TiO_2 (1.7–1.9 wt.%).

Taken together, the analyses exhibit a typical tholeiitic fractionation trend with a strong enrichment in iron (FeO_{tot} varies between 10.8 and 15.3 wt.%). Despite the above differences, the general chemical affinity of the samples is the same and their incompatible trace element ratios are similar. No distinct negative Nb-Ta anomalies, comparable to those in the underlying Ahmalahti and Kuestjärvi Volcanic formations, are seen in the Kolosjoki volcanic rocks. The most prominent feature in Fig. 6.84b is the negative P anomaly, which seems to be a rather common phenomenon in the Palaeoproterozoic volcanic rocks in the Kola Peninsula. Earlier published analyses from the Kolosjoki Volcanic Formation are more similar to our analyses from Unit A than Unit B, having a moderate enrichment in LREE compared to HREE, which renders the rocks akin to EMORBs (e.g. Hanski 1992).

Sedimentary Rocks

Sedimentary rocks occur in eight intervals forming discrete beds with thicknesses ranging from 0.2 to c. 8.5 m (Fig. 6.80). Rhythmically bedded, C_{org}- and S-bearing greywacke-siltstone-shale is the dominant lithology (Figs. 6.85a–h) and forms the thickest beds. Impure limestone interbedded with greywacke and siltstone-shale occurs in one thin interval, whereas marl forms another discrete bed separating two lava flows. Two other sedimentary beds are formed of chert.

The greywacke-siltstone-shale unit at a depth of 35.3–26.7 m, the thickest bed in the drilled succession, is characterised by parallel, rhythmic bedding (Figs. 6.85a–d) typical for sediments deposited from turbidity currents. The unit at a depth of 57.3–52.9 m is characterised by parallel lamination (Figs. 6.85e–h), and a few beds show erosional bases (Figs. 6.85e, f). The limestone bed exhibits thin parallel lamination (Fig. 6.85 m), whereas chert beds have rhythmic bedding or parallel lamination (Figs. 6.85p, r, s), and marl is thickly bedded (Fig. 6.85o).

Sedimentary rocks and volcanic flows show a variable relationship. C_{org}- and S-bearing rocks are commonly sheared and tectonically brecciated along the contact with lava flows (Figs. 6.85i, j, n), whereas marl and chert beds show only minor tectonic modification (Figs. 6.85o–q, s). In some examples where a lava flowed across a chert bed, the chert material was 'squeezed' into the interpillow space (Figs. 6.85p, q), suggesting that the siliceous substance was in a plastic, not lithified state.

Siliciclastic sedimentary rocks (SiO_2 = 53–62 wt.%) show elevated Al_2O_3 (12–17 wt.%), FeO_{tot} (10–15.5 wt.%), MgO (2–6.8 wt.%) and Na_2O (2–4.4 wt.%) contents implying a high proportion of altered mafic material. Both greywacke and siltstone-shale are enriched in organic carbon (0.2–2.3 wt.% total organic carbon) and sulphur (0.7–2.4 wt.%) (Appendices 23–24). The limestone is siliceous (SiO_2 = 11 wt.%), contains sulphur (0.22 wt.%) and organic matter (0.12 wt.%), and is low in Sr (116 μg g^{-1}) (Appendix 25).

Depositional Setting

The drilled section represents a small portion of the c. 2,000-m-thick Kolosjoki Volcanic Formation composed largely of tholeiitic basalts. The latter occur mainly as pillowed lava flows, thus implying a submarine depositional setting. The considerable volume and thickness of the subaqueously erupted volcanic rocks require accommodation space, hence very likely a marine basin. The observed thin bedding and parallel lamination and fine grain size with a high "mafic" component in interbedded sedimentary rocks displaying turbiditic features suggest a setting distal from shorelines and the Archaean basement. Chert beds might have been the result of seafloor hydrothermal activities.

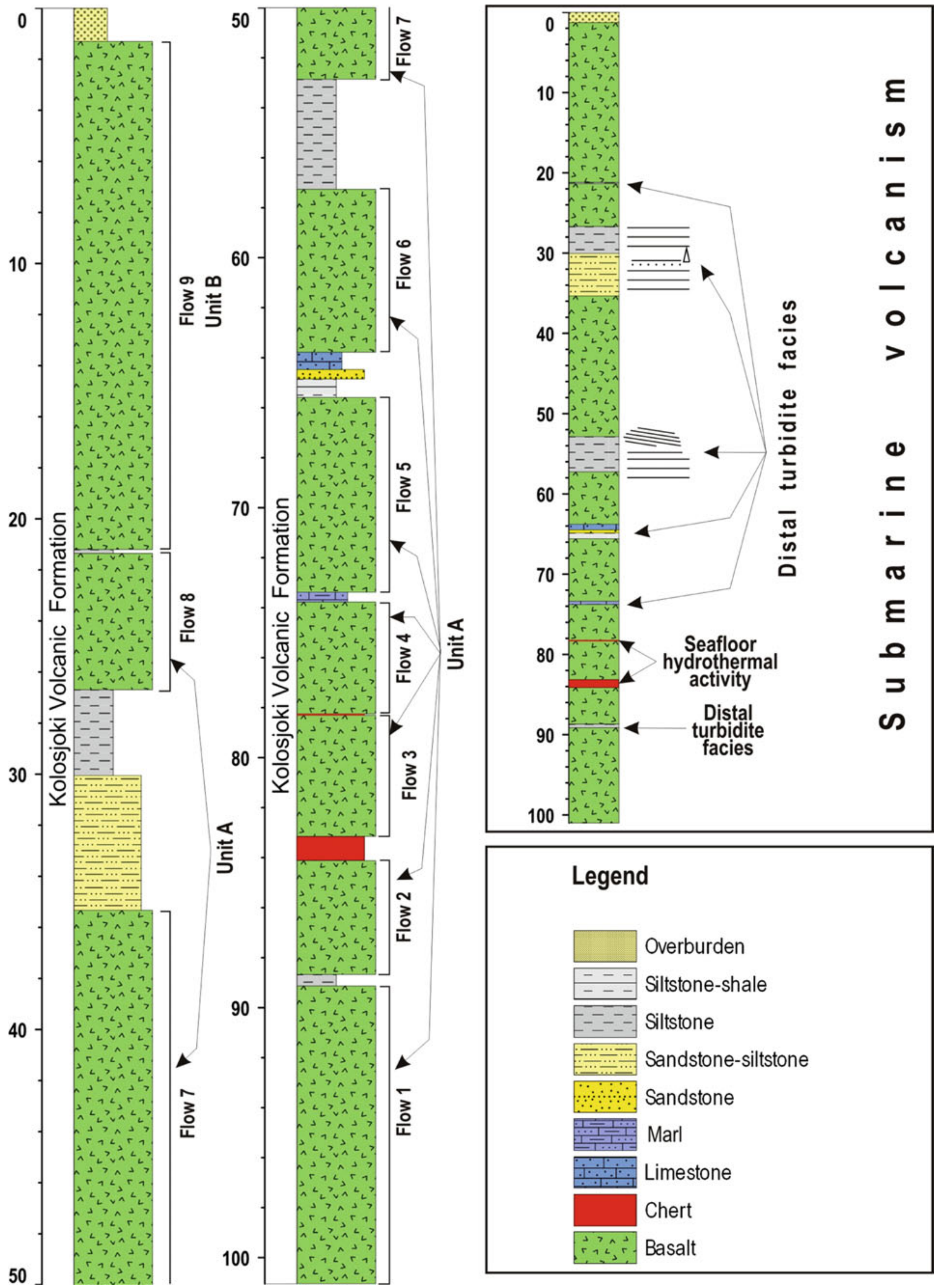

Fig. 6.80 Lithological section of the Kolosjoki Volcanic Formation based on core log of Hole 9A and a tentative reconstruction of depositional environments based on core logging and sedimentological research in the vicinity of the drilling site. Lithological symbols are explained in Fig. 6.6

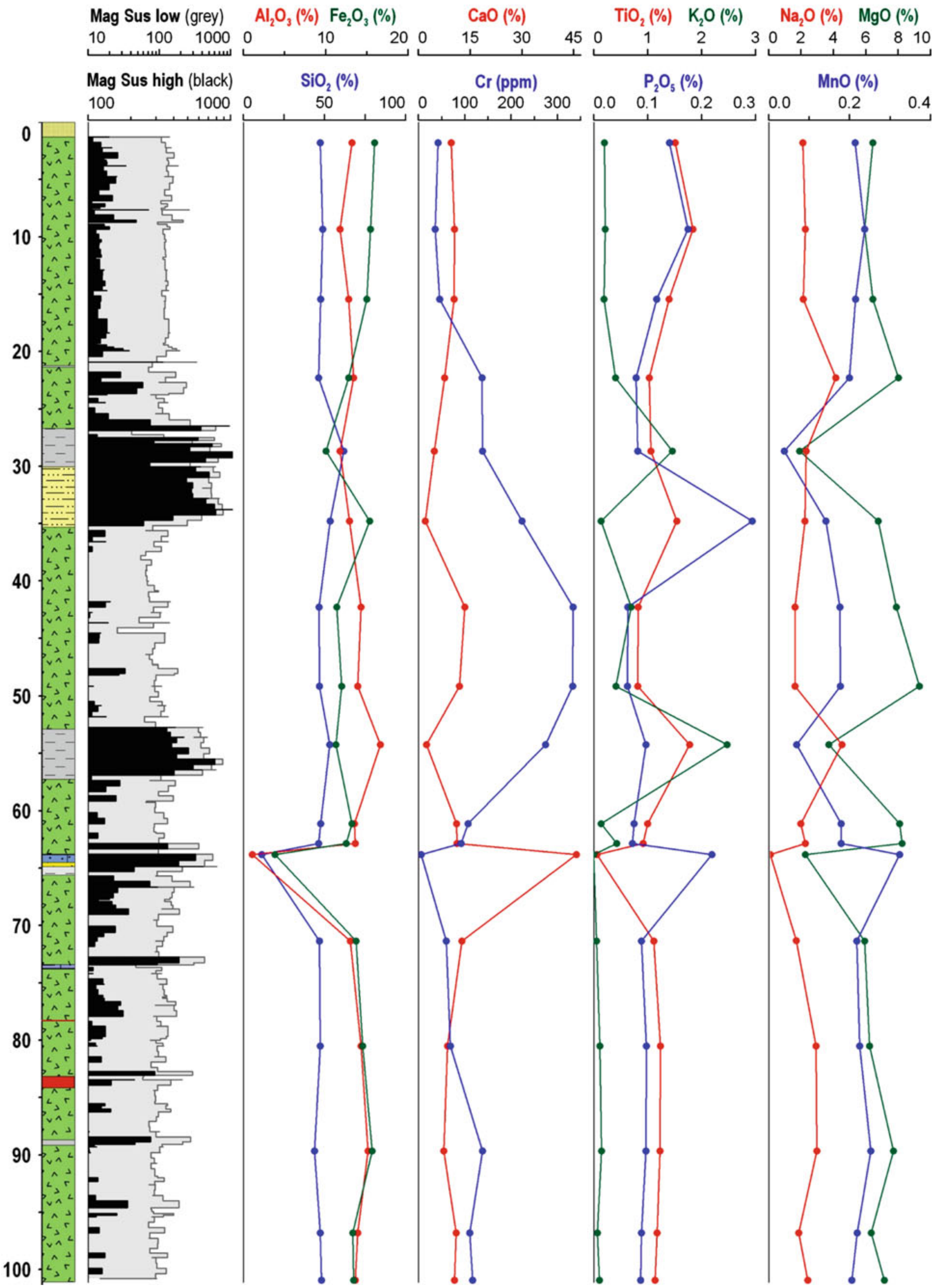

Fig. 6.81 Relative magnetic susceptibility (K*), and geochemical profiles of selected elements based on the archive samples collected with c. 8 m-spacing. For analytical techniques and data quality see **Part 5**

Fig. 6.82 Tholeiitic pillow lava represents the most common type of volcanic rocks of the Kolosjoki Volcanic Formation that reaches a thickness of 2,000 m (Photograph was taken by Victor Melezhik from an outcrop located c. 1 km to the south of the drilling site)

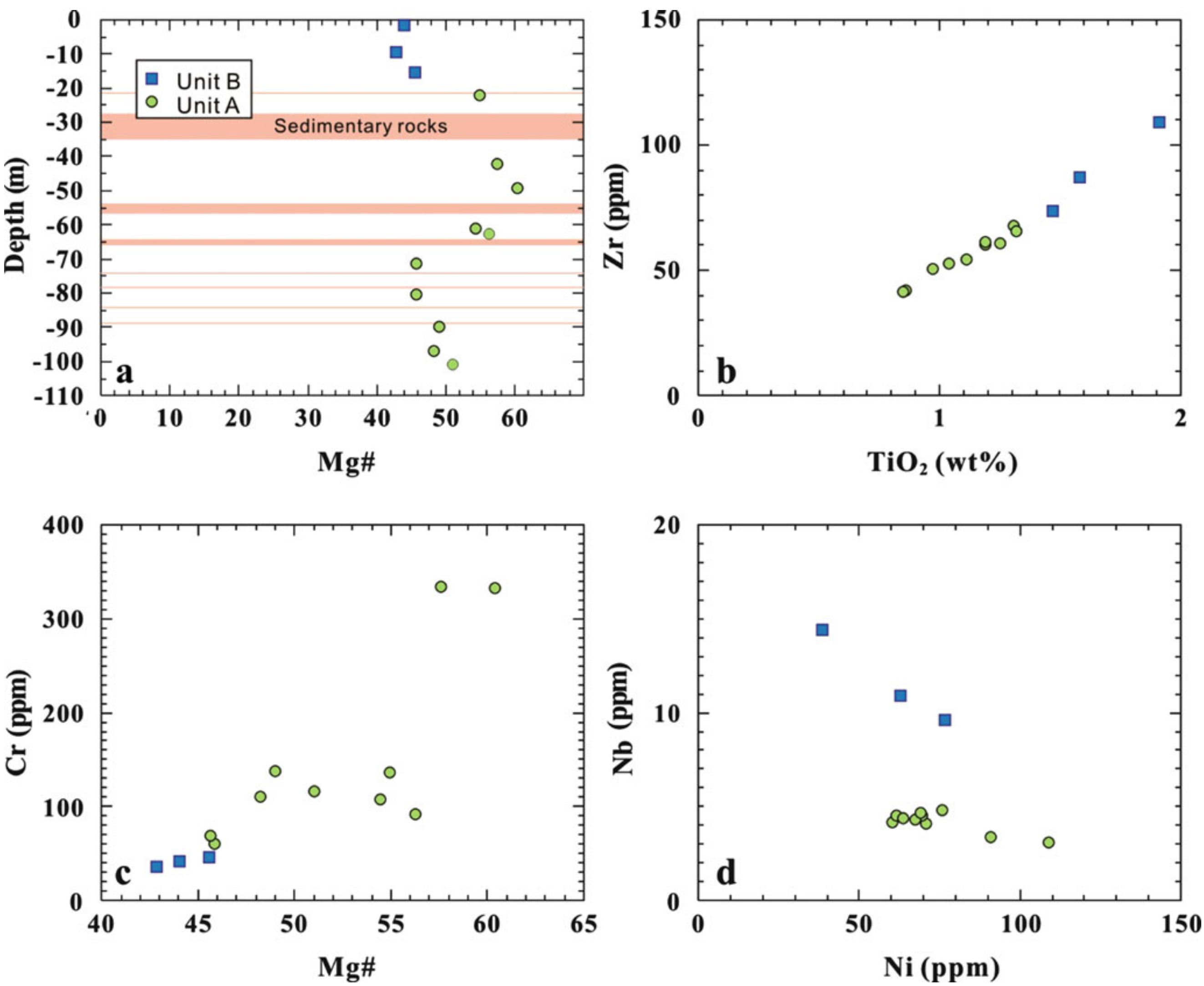

Fig. 6.83 Major geochemical features of volcanic rocks in Core 9A samples. (**a**) Mg# versus depth. (**b**) Zr versus TiO_2. (**c**) Cr versus Mg#. (**d**) Ni versus Nb

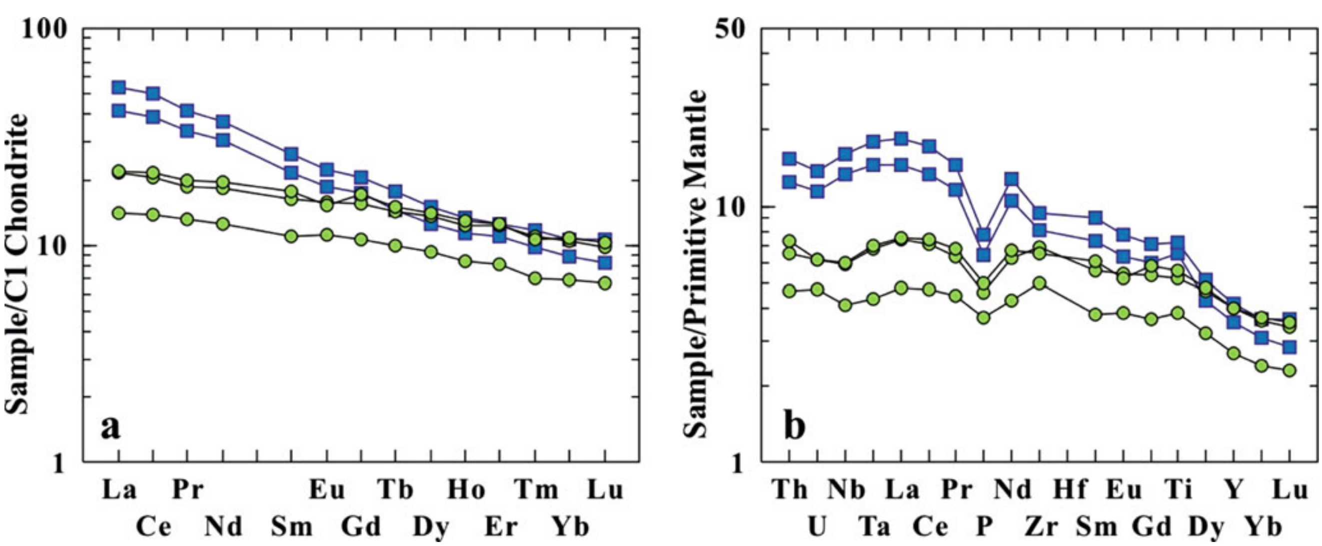

Fig. 6.84 Trace element geochemistry of volcanic rocks in Core 9A samples. (**a**) Chondrite-normalised REE diagram. (**b**) Primitive mantle-normalised spidergram. Normalising values from Sun and McDonough (1989)

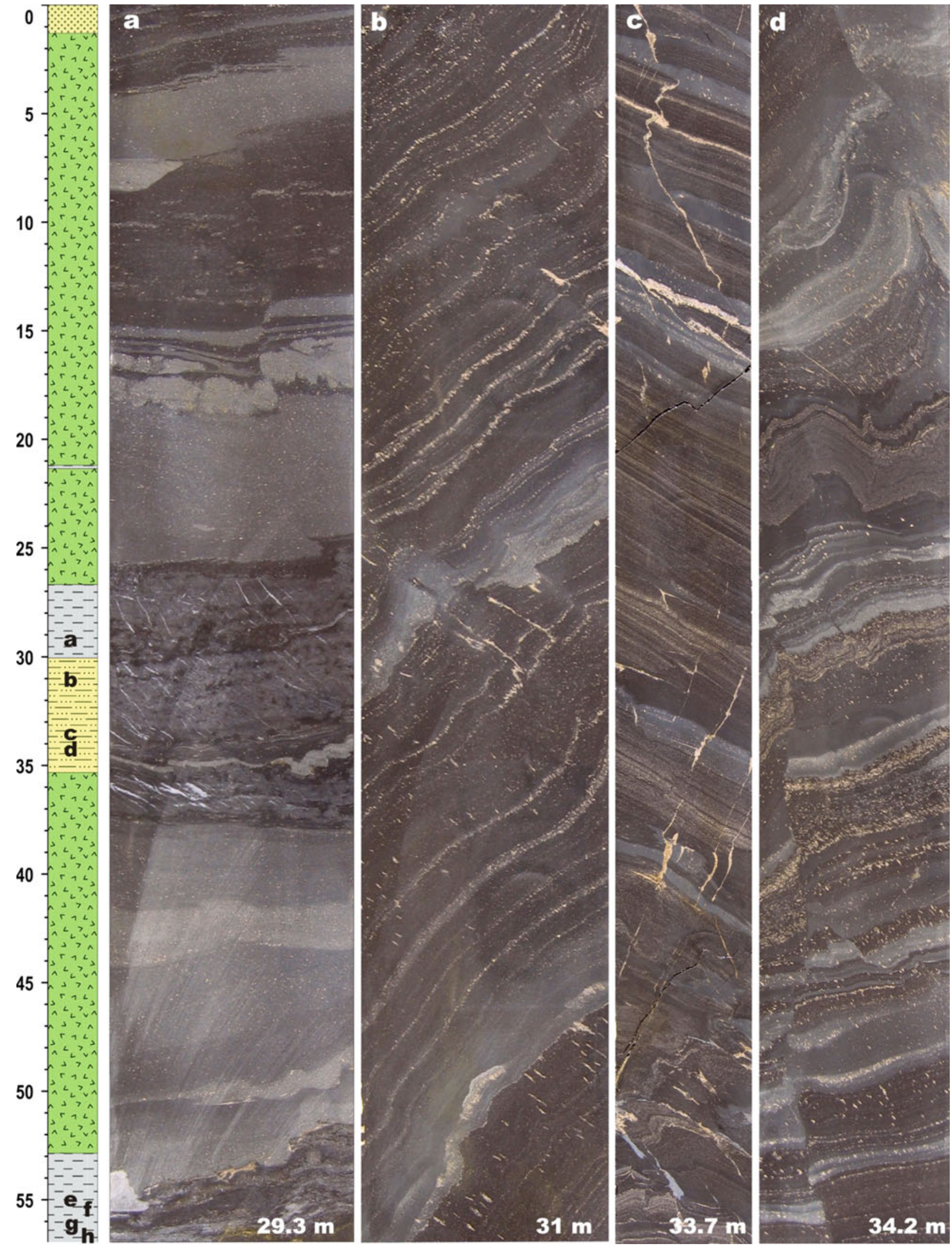

Fig. 6.85 Sedimentological and petrological features of the main rock types intersected by the Hole 9A. In all core photographs, unless otherwise marked, the scale for the images is the core width of 5 cm (**a**) Interbedded, C_{org}-bearing greywacke (*pale grey* and *grey*), siltstone (*dark grey*) and mudstone (*black*); note that the lowermost and uppermost greywacke beds have an erosional base. (**b**, **c**, **d**) Rhythmically bedded, C_{org} and sulphide-rich siltstone-mudstone

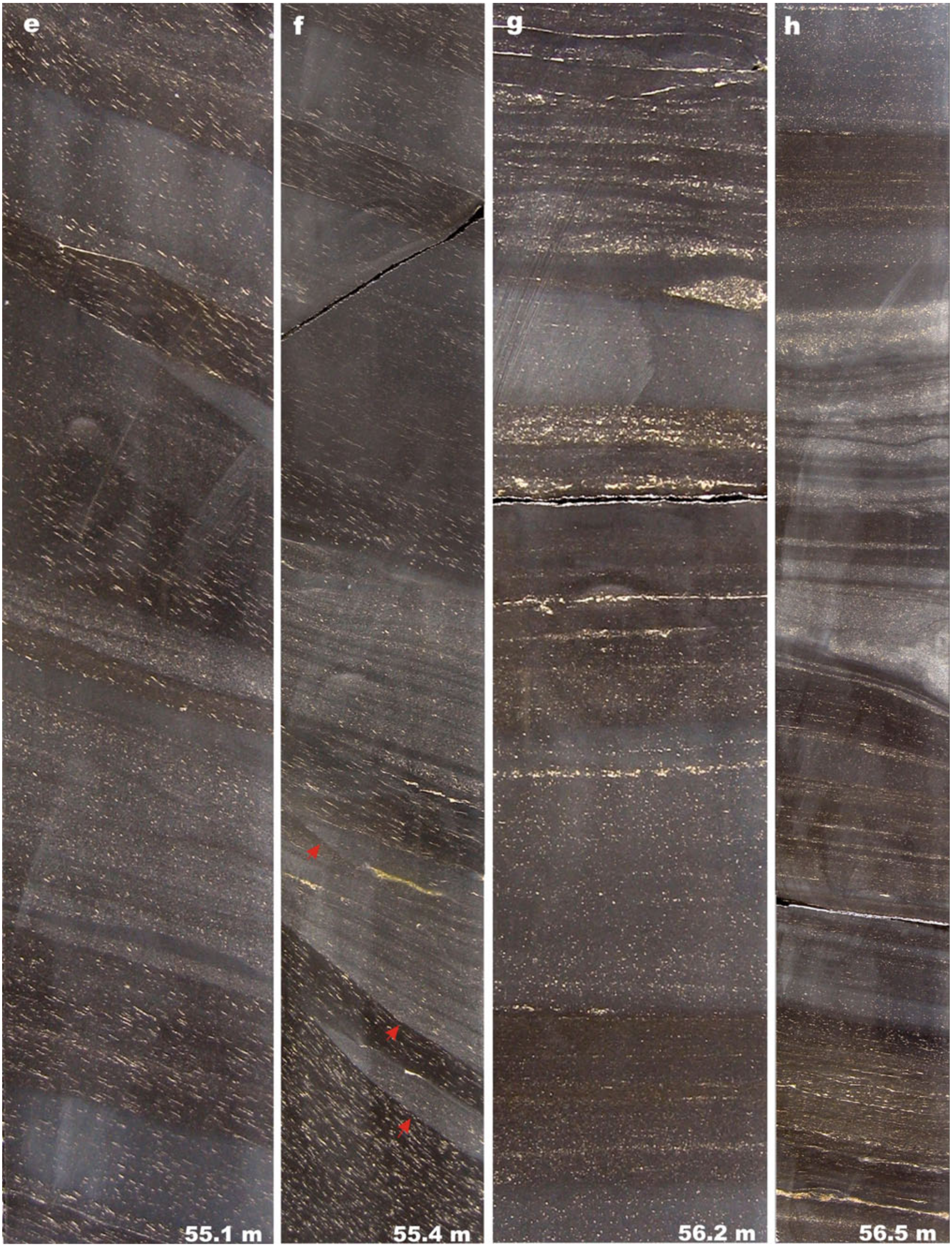

Fig. 6.85 (continued) (**e**, **f**) Laminated, C_{org}- and sulphide-rich siltstone-mudstone; note that coarser, and lighter coloured sandy siltstone beds have an erosional base (*arrowed*) and show lower-angle cross-lamination. (**g**) Parallel-laminated, C_{org} and sulphide-rich siltstone-mudstone. (**h**) Parallel-laminated, C_{org} and sulphide-rich siltstone-mudstone with interbeds of light-coloured sandy layers in the middle

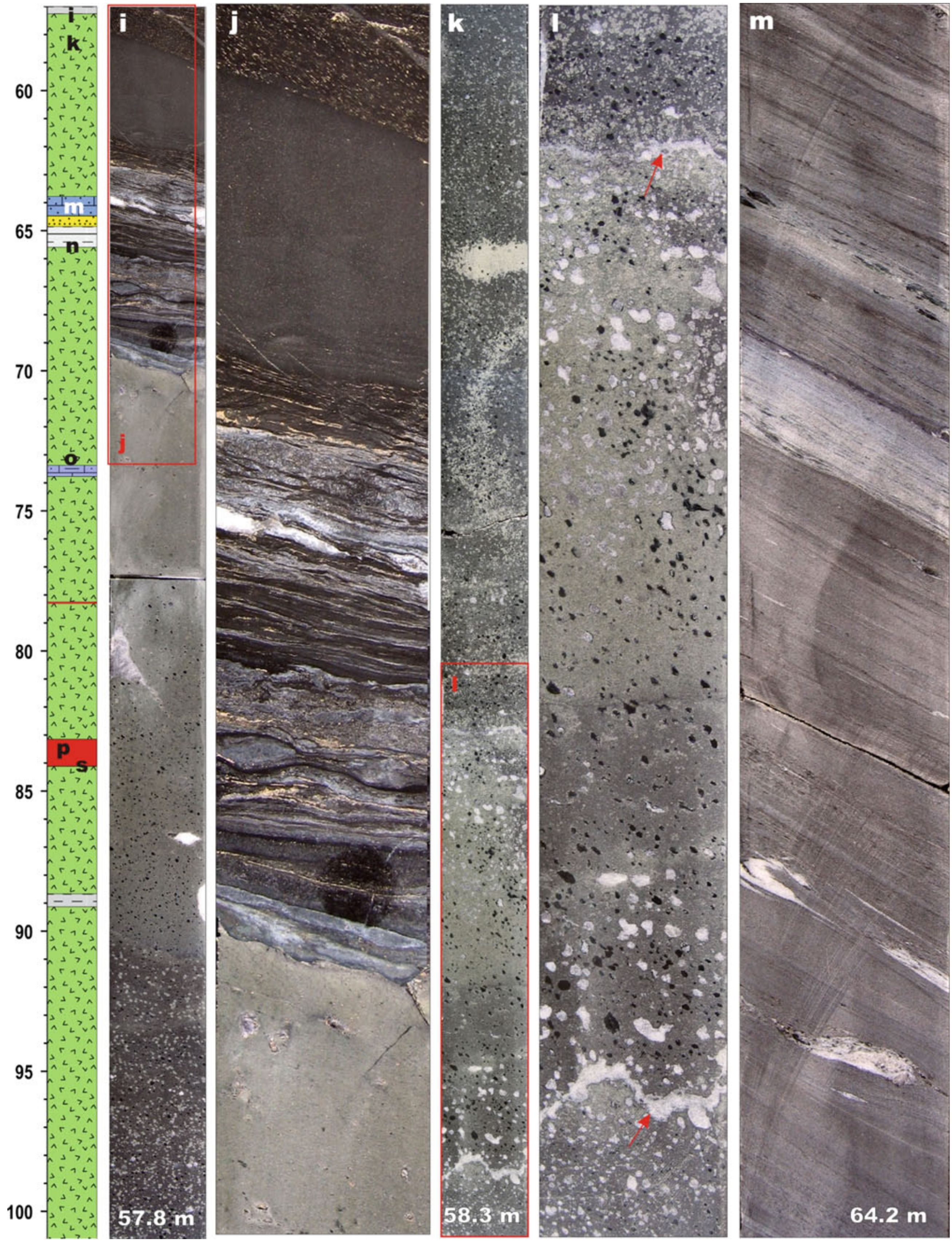

Fig. 6.85 (continued) (**i**) Flow top of amygdaloidal, tholeiitic, mafic lava in contact with overlying C_{org} and sulphide-rich siltstone-mudstone; note that the sedimentary rock is intensely sheared against the contact with the volcanic rocks. (**j**) Enlarged image of the contact zone between lava flow and overlying sedimentary rock; tectonically modified mudstone within a c. 12-cm-thick zone showing a sheared structure, remobilised sulphides and carbonatisation (*white*). (**k**) Mafic lava flow with ubiquitous amygdales. (**l**) Details of amygdaloidal lava flow showing layering marked by flow-parallel, elongated vesicles filled with white calcite (*arrowed*); subspherical vesicles are filled with chlorite (dark-coloured) and calcite (*white*). (**m**) Laminated limestone

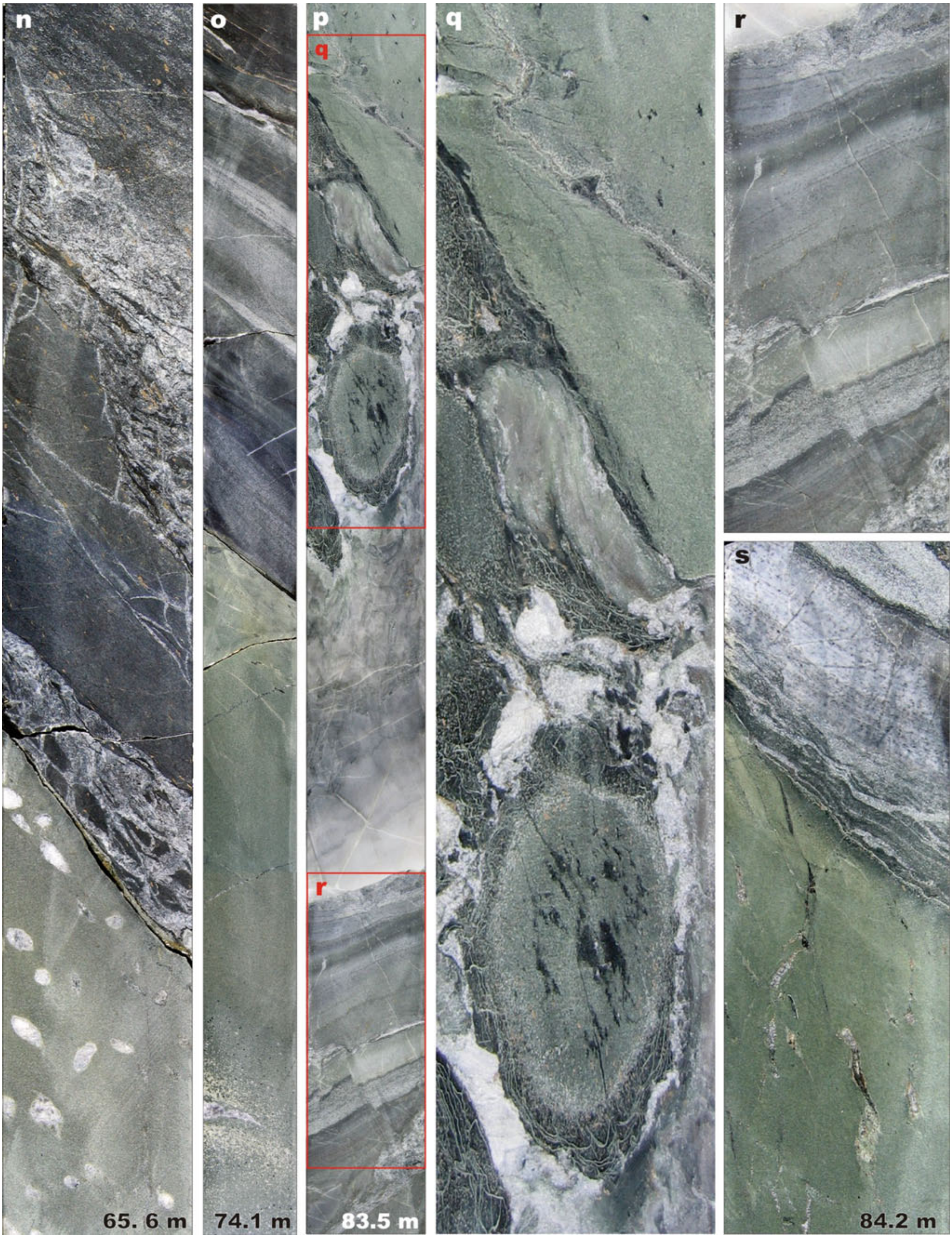

Fig. 6.85 (continued) (**n**) Contact between amygdaloidal mafic lava flow (*bottom*) and C_{org}-rich siltstone-mudstone; note that the mudstone is brecciated and carbonatised along the contact with the flow. (**o**) Contact between mafic lava flow and bedded marl. (**p**) Mafic lava flow extruded on bedded chert; note an incipient pillow at the bottom of the flow and incorporation of cherty material into the flow. (**q**) Detailed image of an incipient pillow and incorporated cherty material, implying that the latter was in a plastic state. (**r**) Detailed image of thinly bedded chert; layers have a variable colour due to the variable content of organic matter. (**s**) Contact of mafic lava flow and laminated chert

References

Hanski EJ (1992) Petrology of the Pechenga ferropicrites and cogenetic, Ni-bearing gabbro-wehrlite intrusions, Kola Peninsula, Russia. Bull Geol Surv Finland 367:192p

Ivanova LV, Chapina OS, Melezhik VA (1988) Discovery of coccoidal microfossils in early Precambrian metamorphosed cherts. Commun USSR Acad Sci 303:210–211, in Russian

Melezhik VA, Fallick AE (1996) A widespread positive $\delta^{13}C_{carb}$ anomaly at around 2.33–2.06 Ga on the Fennoscandian Shield: a paradox? Terra Nova 8:141–157

Melezhik VA, Fallick AE, Hanski E, Kump L, Lepland A, Prave A, Strauss H (2005) Emergence of the aerobic biosphere during the Archean-Proterozoic transition: challenges for future research. Geol Soc Am Today 15:4–11

Melezhik VA, Huhma H, Condon DJ, Fallick AE, Whitehouse MJ (2007) Temporal constraints on the Paleoproterozoic Lomagundi-Jatuli carbon isotopic event. Geology 35:655–658

Sun SS, McDonough WF (1989) Chemical and isotopic systematic of oceanic basalts; implications for mantle composition and processes. In: Saunders AD, Norry MJ (eds) Magmatism in the ocean basins, vol 42, Geological Society special publication. Published for the Geological Society by Blackwell Scientific Publications, Oxford/Boston, pp 313–345

6.3 The Onega Basin

Victor A. Melezhik, Alenka E. Črne, Anthony R. Prave, Aivo Lepland, Alexander E. Romashkin, Dmitry V. Rychanchik, Eero J. Hanski, Anthony E. Fallick, Pavel V. Medvedev, and Zhen-Yu Luo

6.3. The Onega Basin

Victor A. Melezhik

The main geological and stratigraphic features of the Onega Basin are discussed in Chap. 4.3. Given here is a brief geological outline to provide a scientific context and background information for the FAR-DEEP implemented in this area.

The Onega Basin is located in the southeastern part of the Archaean Karelian craton and represents one of the largest fragments of continental margin preserved on the eastern part of the Fennoscandian Shield (Fig. 6.1). The history of geological investigation of the Onega area dates back to the seventeenth century. A recently published summary book that has synthesised geological and geophysical data and the material from drilling exploration obtained over 50 years (Glushanin et al. 2011) provides comprehensive guidance through the stratigraphy and the more recent concepts of the deep crustal structure of the Onega Basin.

The Palaeoproterozoic volcano-sedimentary succession of the Onega Basin was subdivided into six lithostratigraphic units, from oldest to youngest: the Sumian, Sariolian, Jatulian, Ludicovian, Livian (or Kalevian) and Vepsian super-horizons (e.g. Sokolov 1987). The lowermost Sumian Super-Horizon rests unconformably on Archaean granites, gneisses and amphibolites. The six super-horizons have been subdivided further into a series of suites (e.g. Kulikov et al. 2011), which are termed formations in this 3-volume treatise (Figs. 6.86 and 6.87)

Currently, there is only one imprecise Pb-Pb age of 2090 ± 70 Ma, obtained from dolomite of the Tulomozero Formation, for the Jatulian Super-Horizon (Ovchinnikova et al. 2007). Two gabbro sills, one within the Jatulian Super-Horizon and the other within the Ludicovian Super-Horizon, have been dated by U-Pb (zircon)–Sm-Nd and Pb-Pb techniques at 1983.4 ± 6.5 and c. 1980 Ma, respectively (Philippov et al. 2007; Puchtel et al. 1992, 1998).

Six FAR-DEEP holes were drilled in the northern and central parts of the basin (Fig. 6.86) and recovered core from geological formations that archived information on: (1) the Palaeoproterozoic perturbation of the global carbon cycle (the Lomagundi-Jatuli isotopic excursion) as recorded in evaporitic marine carbonates; (2) formation of a sizable reservoir of marine sulphates; (3) termination of the Lomagundi-Jatuli isotopic excursion; (4) unprecedented accumulation of organic material; (5) a supergiant petrified oil field; and (6) the earliest know sedimentary phosphates.

V.A. Melezhik (✉)
Geological Survey of Norway, Postboks 6315 Sluppen, NO-7491 Trondheim, Norway

Centre for Geobiology, University of Bergen, Allegaten 41, Bergen N-5007, Norway
e-mail: victor.melezhik@ngu.no

V.A. Melezhik et al. (eds.), *Reading the Archive of Earth's Oxygenation*, Volume 2: The Core Archive of the Fennoscandian Arctic Russia – Drilling Early Earth Project, DOI 10.1007/978-3-642-29659-8_4, © Springer-Verlag Berlin Heidelberg 2013

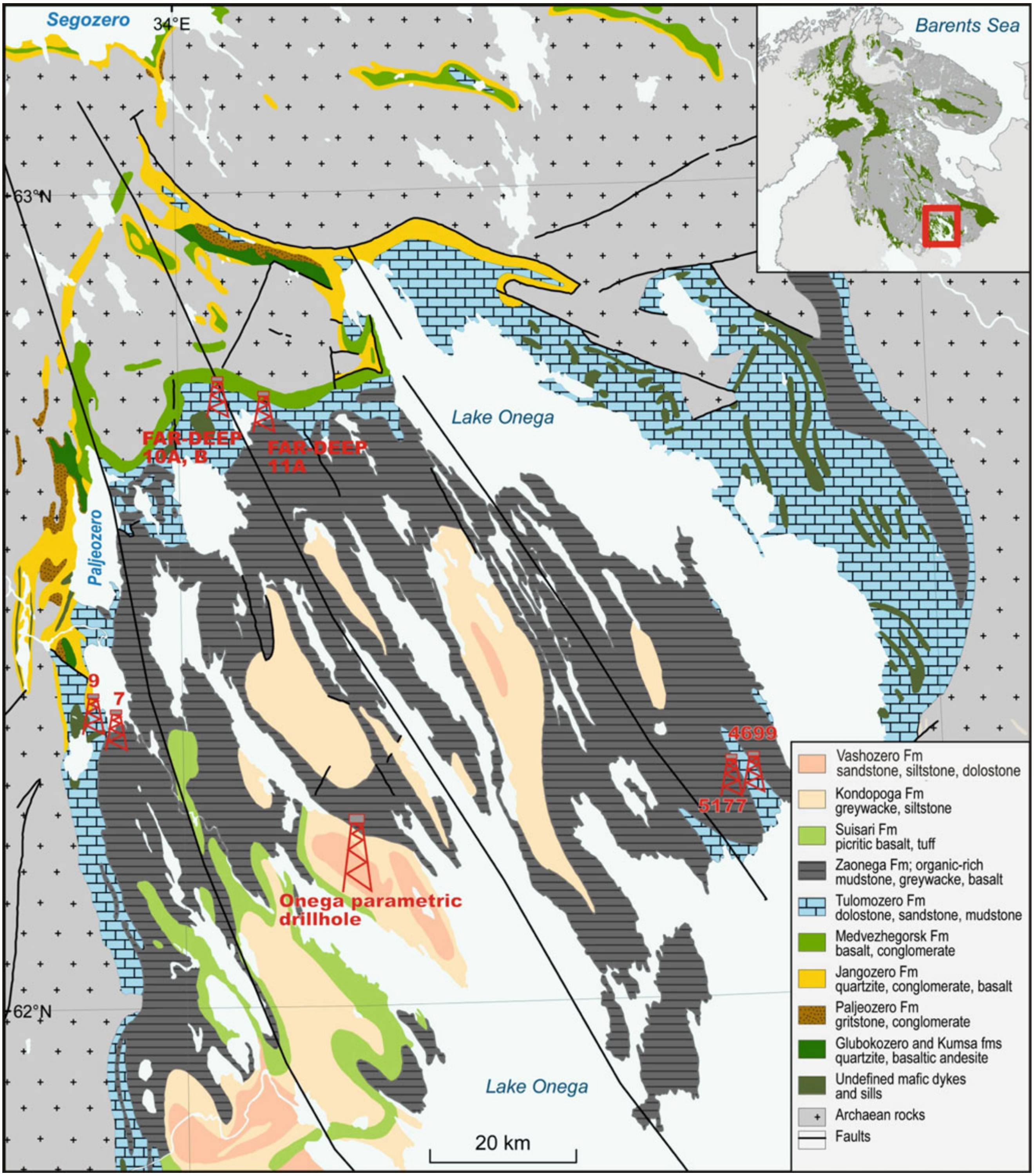

Fig. 6.86 Simplified geological map of the Onega Basin with drillhole locations (Based on Koistinen et al. (2001) with modification by Aivo Lepland)

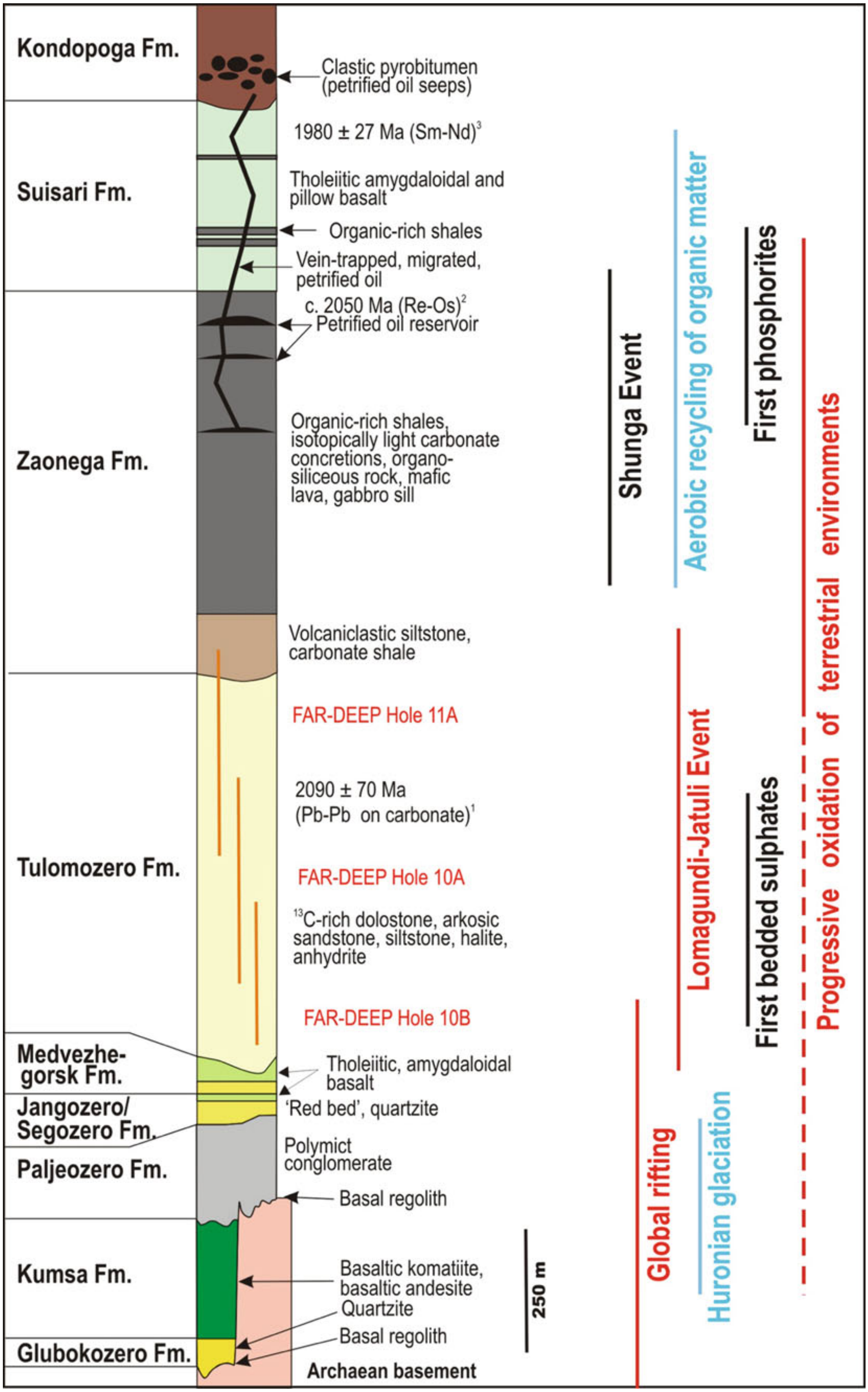

Fig. 6.87 Lithostratigraphic column of the Onega Basin and positions of FAR-DEEP drillholes intersecting the Tulomozero Formation. Also shown is how the evolution of the Onega Basin is related to global palaeoenvironmental events. Superscripts denote radiometric ages from (1) Ovchinnikova et al. (2007), (2) Hannah et al. (2008) and (3) Puchtel et al. (1992, 1998)

References

Glushanin LV, Sharov NV, Shchptsov VV (eds) (2011) Palaeoproterozoic onega structure (Geology, Tectonics, deep structure and mineralogeny). Karelian Research Centre, Petrozavodsk, p 431 (in Russian)

Hannah JL, Stein HJ, Zimmerman A, Yang G, Melezhik VA, Filippov MM, Turgeon SC, Creaser RA (2008) Re-Os geochronology of a 2.05 Ga fossil oil field near Shunga, Karelia, NW Russia, Abstract, the 33rd International Geological Congress, Oslo

Koistinen T, Stephens MB, Bogatchev V, Nordgulen Ø, Wennesträm M, Korhonen J (Comps) (2001) Geological map of the Fennoscandian Shield, Scale 1:2 000 000, Espoo, Trondheim, Uppsala, Moscow

Kulikov VS, Medvedev PV, Golubev AI (2011) Summary geological map of the Onega Structure. In: Glushanin LV, Sharov NV, Shchiptsov VV (eds) The Onega Palaeoproterozoic Structure (Geology, tectonics, deep structure and minerageny). Institute of Geology, Karelian Research Centre of RAS, Petrozavodsk, pp 19–23, (in Russian)

Ovchinnikova GV, Kusnetzov AB, Melezhik VA, Gorokhov IM, Vasil'eva IM, Gorokhovsky BM (2007) Pb-Pb age of Jatulian carbonate rocks: the Tulomozero Formation in southeastern Karelia. Stratigr Geol Correl 4: 20–33, (in Russian)

Philippov NB, Trofimov NN, Golubev AI, Sergeev SA, Huhma H (2007) New geochronological data on the Koikary-Svjatnavolok and Pudozhgora gabbro-dolerite intrusives. In: Golubev VI, Shchiptsov VV (eds) Geology and mineral resources of Karelia, Karelian Research Centre, Petrozavodsk, vol 10, pp 49–68, (in Russian with English abstract)

Puchtel IS, Zhuravlev DZ, Ashikhmina NA, Kulikov VS, Kulikova VV (1992) Sm-Nd age of the Suisarian suite on the Baltic Shield. Trans Russ Acad Sci 326:706–711, (in Russian)

Puchtel IS, Arndt NT, Hofmann AW, Haase KM, Kröner A, Kulikov VS, Kulikova VV, Garbe-Schönberg C-D, Nemchin AA (1998) Petrology of mafic lavas within the Onega plateau, Central Karelia: evidence for the 2.0 Ga plume-related continental crustal growth in the Baltic Shield. Contrib Mineral Petrol 130:134–153

Sokolov VA (ed) (1987a) Geology of Karelia. Nauka (Science), Leningrad, p 231, (in Russian)

6.3.1 Tulomozero Formation: FAR-DEEP Holes 10A and 10B

Victor A. Melezhik, Anthony R. Prave, A.T. Brasier, Aivo Lepland, Alexander E. Romashkin, Dmitry V. Rychanchik, Eero J. Hanski, Anthony E. Fallick, and Pavel V. Medvedev

Scientific Targets

- Tectonic and depositional settings associated with the Lomagundi-Jatuli isotopic event
- Geochemical rock record during the global perturbation of the carbon cycle
- Carbon, sulphur and strontium isotopic composition of ambient water
- Influence of depositional setting on carbon and strontium isotopic composition
- Provenance composition
- Microfossil record
- Radiometric age constraints on timing of deposition

Drillholes 10A and 10B intersected the Tulomozero Formation in the northern part of the Onega Basin, Karelia, NW Russia (Figs. 6.1 and 6.86). The formation contains ^{13}C-rich carbonates recording the global Palaeoproterozoic positive $\delta^{13}C$ excursion of sedimentary carbonates (e.g. Yudovich et al. 1991; Akhmedov et al. 1993; Karhu 1993; Tikhomirova and Makarikhin 1993; Karhu and Holland 1996; Heiskanen and Rychanchik 1999; Melezhik and Fallick 1996; Melezhik et al. 2005; Brasier et al. 2011). The depositional age of the Tulomozero Formation is imprecisely constrained to between 2090 ± 70 Ma and 1983.4 ± 6.5 Ma; the former is a Pb-Pb age of dolostone (Ovchinnikova et al. 2007) and the latter is a U-Pb age of zircon from a gabbro sill (Koikary-Svjatnavolok) intruded into the formation (Philippov et al. 2007).

The FAR-DEEP drillholes provide material from several time-equivalent successions that accumulated in different depositional settings. Hole 5A (see Chap. 6.2.2) intersected a succession deposited in a marine-influenced lacustrine system, whereas Hole 4A (see Chap. 6.1.3) recovered core from dolostones formed in an open-marine environment. In contrast, Holes 10A and 10B intersected a ^{13}C-rich succession, which is presently considered to represent restricted and partially restricted marine environments (Melezhik et al. 1999, 2000; Brasier et al. 2011).

The Tulomozero Formation shows a considerable lithofacies variation across the Onega Basin, from biohermal and biostromal stromatolitic dolostone and magnesite (Figs. 6.88 e.g. Makarikhin and Kononova 1983; Melezhik et al. 2001) to heterolithic sandstone-mudstone with abundant occurrences of evaporitic minerals including halite casts, pseudomorphed gypsum and anhydrite (Fig. 6.89 e.g. Melezhik et al. 2001; Brasier et al. 2011; Reuschel et al. 2012), and even thick halite and massive anhydrite deposits (Morozov et al. 2010; Krupenik et al. 2011a; Fig. 6.90). Such lithofacies variations reflect lateral changes in depositional environments from open marine to restricted marine and sabkha, and even to terrestrial playa. The formation also contains abundant dissolution-collapse breccias (e.g. Melezhik et al. 2000) suggesting that a significant volume of soluble evaporitic minerals underwent dissolution processes, apparently caused by percolation of fresh meteoric waters into the basin. Associated abundant shallow-marine and terrestrial carbonate and siliciclastic "red beds" are evidence for an oxidising atmosphere.

Holes 10A and 10B intersected a thick succession of marine and non-marine carbonates with abundant relicts of sulphates, hence the recovered core is particularly noteworthy in that it enables study of the Palaeoproterozoic carbon, sulphur and strontium cycles. Such studies will enhance our understanding of Palaeoproterozoic seawater, and associated interactions between fresh/meteoric and saline waters, and their influence on the carbon, sulphur and strontium isotopic compositions of carbonate and sulphate mineral phases. The cores are helping to refine understanding of the Palaeoproterozoic oceanic sulphate reservoir (e.g. Reuschel et al. 2012) and salinity of the Palaeoproterozoic ocean. The preserved abundant evaporite minerals could provide information on the chemistry of seawater and the precipitation sequences formed during the progressive evaporation of Palaeoproterozoic seawater.

The 432-m-long Hole 10A intersected the middle part of the Tulomozero Formation, whereas the 278-m-long Hole 10B penetrated its upper part. Siliciclastic and carbonate rocks comprise the entire section of Hole 10A, whereas the Hole 10 B section contains a c. 38-m-thick basaltic body (210.85–175.09 m) within a c. 242-m-thick unit of siliciclastic and carbonate rocks. Although the drilled sections are only a few hundred metres apart, their chrono- and lithostratigraphic correlations are not straightforward.

Several previous lithostratigraphic subdivisions of the Tulomozero Formation have been proposed (Perevozchikova 1957; Sokolov 1963; Negrutsa 1984; Akhmedov et al. 1993; Melezhik et al. 1999; Medvedev et al. 2011) (Fig. 6.91), which vary due to local differences in lithological composition and depositional environments. As a consequence, the existing subdivisions are difficult to use for making regional correlations. However, an

V.A. Melezhik (✉)
Geological Survey of Norway, Postboks 6315 Sluppen, NO-7491 Trondheim, Norway

Centre for Geobiology, University of Bergen, Allegaten 41, Bergen N-5007, Norway

V.A. Melezhik et al. (eds.), *Reading the Archive of Earth's Oxygenation*, Volume 2: The Core Archive of the Fennoscandian Arctic Russia – Drilling Early Earth Project, DOI 10.1007/978-3-642-29659-8_4,

amygdaloidal basalt present in several drillholes and natural exposures across the Onega Basin has been used as a chronostratigraphic marker in the upper part of the Tulomozero Formation (Fig. 6.92) (Satzuk et al. 1988; Krupenik et al. 2011a; Krupenik and Sveshnikova 2011; for details see Chap. 4.3). Using this basalt as a marker, we can infer that the 10A section occurs stratigraphically below the 10B section (Fig. 6.92).

$\delta^{13}C_{carb}$ stratigraphic trends also help to make correlations between the two sections (e.g. Reuschel et al. 2012), suggesting that the upper part of the 10A section either overlaps slightly (a few metres) with the lower part of the 10B section (Fig. 6.92), or not at all. The overall $\delta^{13}C_{carb}$ stratigraphic trend throughout the entire formation (e.g. cores 7 and 9 in Melezhik et al. 2005) apparently indicates that the lowermost part of section 10A corresponds to the middle part of Member B (Fig. 6.92), and also suggests that the c. 450 m of section 10A corresponds to c. 200 m, or less, of sections in Onega basin drillcores 7 and 9 (which are not part of the ICDP FAR-DEEP project) because Hole 10A was drilled at an oblique angle to the bedding plane.

Stromatolite morphologies offer another potential correlation tool (Makarikhin 1992; Medvedev et al. 2005). Figure 6.93 summarises stromatolite morphologies documented in Cores 10A, 10B and 11A and provides a visual basis for comparing them with columnar stromatolites described from well-studied reference sections (Fig. 6.94). Such an exercise can help to support correlations, providing that the detailed palaeontological description of the FAR-DEEP stromatolites is later accomplished.

Hole 10A

The lithological column of the cored section 10A is shown in Fig. 6.95, whereas Fig. 6.96 exhibits stratigraphic variation of selected major and trace elements and magnetic susceptibility. Chemical compositions of the analysed samples is presented in Appendices 26–28. Core photos presented in Fig. 6.97 provide detailed documentation of major lithological and structural features of the sedimentary rocks.

The Core 10A section is tentatively subdivided into several units (members) based on dominant rock types characterising the different parts of the section. This subdivision is not meant to replace previously suggested lithological subdivisions (Fig. 6.91); instead, it is used to facilitate core description. Where plausible correlation with the reference sections (core sections 7/9 and 5,177/4,699; for details see Chap. 4.3) can be made, this is acknowledged here explicitly.

Nine lithological units (members) can be informally recognised in the 10A section, being from base to top: member 1 (Lower Dolostone); member 2 (Siltstone-Sandstone-Breccia); member 3 (Dolostone-Dolomarl); member 4 (Dolomarl); member 5 (Siltstone-Dissolution Breccia-Magnesite); member 6 (Dolomarl-Dolostone-Siltstone-Sandstone); member 7 (Sandstone-Dolostone); member 8 (Siltstone-Sandstone); and member 9 (Dolostone-Sandstone-Dolomarl) (Fig. 6.95).

Member 1 (Lower Dolostone)

The Lower Dolostone member has a drilled thickness of 42 m (431.8–389.8 m). Its top is defined by the first appearance of dolostone breccias at a depth of 389.8 m (Fig. 6.95). The rocks have uniformly low magnetic susceptibility, between 0 and −15 µSI ($K^* = 0$ to -1.4×10^{-6} SI in Fig. 6.96). The member comprises rather massive dolarenite and dolorudite (Figs. 6.97gi–gs). The rocks appear pale grey and white when dry (Figs. 6.97gl, go, gr), but some intervals are variegated (beige, pale pink, pale brown) when the cores are sawn and polished (Figs. 6.97gi, gp, gs). Although the drilled section appears monotonous, at least seven fining-upward cycles can be recognised (Fig. 6.95). Most are c. 5 m thick and consist of two units: a lower unit of coarse-grained dolorudite (dolostone conglomerate) and an upper unit of medium-grained dolorudite (dolostone gritstone) and dolarenite (sandstone). Both units may contain several normally graded beds, each as much as a metre thick (Fig. 6.97gl). Some of the cycles are separated by erosion/dissolution surfaces (Fig. 6.97gi).

All carbonate lithologies have undergone moderate degrees of recrystallisation that have partially obliterated clast-matrix boundaries (Figs. 6.97gp, gq, gs). Rock fragments in clastic dolostones are mainly variably siliceous dolostone and rare quartz sandstone. The matrix, where not recrystallised, is composed of rounded and well-sorted dolomite grains supported by dusty, syntaxial, burial dolomite cement (Fig. 6.97gk).

All clastic dolostones of the member have uniform Mg/Ca elemental ratios ranging between 0.64 and 0.67 (Appendix 28), hence slightly elevated with respect to stoichiometric dolomite (0.62). The rocks contain 8.3–14.8 wt.% SiO_2, mainly as clastic quartz. In silicified intervals, the SiO_2 content ranges between 20.9 and 53.7 wt.% (Appendix 26). All carbonate lithologies are low in Al_2O_3 (0.12–0.33 wt.%) and K_2O (0.05–0.22 wt.%), devoid of measurable Na_2O, C_{org} and S (Appendix 27). Dolomite has low contents of Fe (46–86 µg g^{-1}), Mn (26–84 µg g^{-1}) and Sr (40–180 µg g^{-1}). All analysed archive samples from this member show high $\delta^{13}C$ values (+9.3 to +10.5 ‰, VPDB), while $\delta^{18}O$ fluctuates between 18.6 ‰ and 20.2 ‰ (VSMOW) (Reuschel et al. 2012).

Member 2 (Siltstone-Sandstone-Breccia)

This member is a c. 25-m-thick (389.8–364.9 m) succession of heterogeneous rocks (dolostone breccia, dolarenite or dolostone sandstone, polymict sandstone, siltstone, dolomarl and dissolution-collapse breccia). Its base is defined by the first appearance of dolostone breccias at 364.9 m depth, and the top appears as a sharp contact between siltstone and dolarenite (Fig. 6.95). Magnetic susceptibility tests reveal that the lower and middle parts of the member have low and homogeneous values similar to those obtained from member 1. In contrast, rocks from the uppermost part (371–365.4 m) have values ranging between 110 and 150 μSI ($K^* = 10–14 \times 10^{-6}$ SI in Fig. 6.96) with a few measurements around 0 μSI.

Dolostone breccia and dolarenite occur in the lower and middle part of the section where they form four fining-upward cycles (each 2–10 m thick) with dolostone breccia as a lower unit and dolarenite as an upper unit (Fig. 6.95). The uppermost part of the member comprises two compositionally different fining-upward successions of similar thickness. The lower succession is composed of polymict sandstone passing upward into dolarenite with a siltstone top. The upper succession is marked by a basal dissolution-collapse breccia that passes upward into dolarenite and then crystalline dolostone and siltstone with a dolomarl interbed (Fig. 6.95).

The dolostone breccias and dolarenites form the bulk of the section. The lowermost dolostone breccia sits on a c. 10-cm-thick interval of micritic dolomite with alternating white and beige concentric bands around a black mudstone core (Fig. 6.97gh); this may represent either a travertine or a cave deposit. The breccias are massive and clast-supported. Recrystallisation has partially obliterated primary features and masked the boundaries between clasts and the matrix. Clasts are mainly crystalline dolostone and up to 15 cm in diameter. The matrix is recrystallised dolarenite, with relicts of syntaxial overgrowth dolomite cement. In places, the cement comprises neomorphic, euhedral rhombs of dolomite containing mm-sized nodules of mosaic quartz.

Dolarenites are pale grey or variegated rocks with numerous stylolites. The bedding is wrinkled or highly disrupted due to syndepositional/diagenetic growth of sulphate crystals and nodules, now replaced by white dolospar (Figs. 6.97gd–gg). Where microstructures are preserved, dolarenites are composed of rounded quartz and dolomite grains overgrown with syntaxial dolomite cement.

Siltstone occurs in the uppermost part of the member as two discrete beds separated by dolomarl (Fig. 6.95). Both the siltstone and dolomarl are black (Fig. 6.97gc) due to impregnation by haematite, which is reflected in an elevated magnetic susceptibility (Fig. 6.96). The rocks have a laminated structure, which is disrupted by diagenetic growth of nodular sulphates replaced by quartz and white dolospar, and by veins filled with white, blocky dolomite and drusy dolomite spar (Fig. 6.97gc). The siltstone is composed of dolomite-cemented quartz, biotite, chlorite, and minor feldspar, and contains abundant euhedral prismatic crystals of metamorphic epidote. Smaller clasts are mostly formed from the silty groundmass whereas larger clasts are rounded, 0.5-mm-sized quartz grains that are evenly distributed in the groundmass. The dolomarl interbed has large, irregularly shaped inclusions resembling pseudomorphed nodules. Such inclusions are composed of drusy and blocky dolomite (Fig. 6.97gb) containing cm-sized clusters of pale pink quartz with micron-size relicts of anhydrite.

The dissolution breccia bed has a thickness of c. 1 m, a variegated colour, and sharp contacts with the overlying dolarenite and the underlying siltstone (Fig. 6.97gc). It is composed of angular fragments of variably silicified dolarenite, clayey dolostone, red sandstone and soft-sediment deformed shale clasts. Clasts are of variable size, tightly packed and embedded in black, haematite-rich shale or cemented by blocky and drusy dolomite.

The sandstone comprises a c. 80-cm-thick bed with sharp lower and upper contacts (Fig. 6.97gc). It has variegated colour and polymict composition, contains shale interbeds and exhibits highly deformed bedding.

All carbonate lithologies are dolomitic, with elemental Mg/Ca ratios ranging from 0.64 to 0.67. Dolostones contain 4.7–26.7 wt.% SiO_2, have low abundances of Al_2O_3 (0.1–0.56 wt.%) and K_2O (0.04–0.24 wt.%), and are devoid of measurable Na_2O, C_{org} and S (Appendices 26, 27). The dolomite contains little Fe (39–67 μg g^{-1}), Mn (63–93 μg g^{-1}) or Sr (53–100 μg g^{-1}) (Appendix 28). All analysed archive samples show a high $\delta^{13}C$ (+9.4 to 10.2 ‰, VPDB). $\delta^{18}O$ fluctuates between 19.4 ‰ and 20.2 ‰ (VSMOW) (Reuschel et al. 2012).

One analysed siltstone sample shows high MgO (13.8 wt.%) and CaO (5.4 wt.%) contents, a moderate K_2O (2.65 wt.%) concentration, low Na_2O (0.2 wt.%) abundance, and is devoid of measurable C_{org} and S. Its carbonate $\delta^{13}C$ value is high (+10.1 ‰, VPDB) with a low $\delta^{18}O$ value (17.5 ‰, VSMOW).

Copper and Zn contents show a distinct stratigraphic trend through the member irrespective of the lithological composition. The content of the former increases upward from <2 to 144 ppm, whereas the concentration of the latter varies from 8.9 to 36 ppm (Appendix 27).

Member 3 (Dolostone-Dolomarl)

Member 3 is c. 49 m thick (364.9–307 m) and is composed of dolarenite (dolostone sandstone), dolostone conglomerate, stromatolitic dolostone, dolomarl and carbonate-siltstone with minor dolostone breccia and siltstone (Fig. 6.95). A dolarenite bed sitting sharply on the siltstone of the underlying member 2 marks the lower boundary. The upper boundary is placed below the first thick dolomarl at a depth of 364.9 m.

Member 3 can be subdivided into three units of approximately equal thicknesses. The lower unit (364.9–349 m) comprises up to five, 1–6-m-thick, fining-upward cycles with the lower parts composed of dolorudite (dolostone conglomerate or gritstone) and the upper parts composed of dolarenite (Fig. 6.96). The middle unit (349–332.15 m) is composed of diverse carbonate lithologies including dolomarl, carbonate-sandstone-siltstone, dolarenite, fine-grained (micritic) dolostone and minor siltstone. The upper unit (332.1–307.5 m) consists mainly of dolarenite and stromatolitic dolostone with a few thin beds of dolorudite, carbonate-siltstone and carbonate-sandstone or -siltstone.

The member has a low, though variable, magnetic susceptibility ranging from slightly negative to values reaching 200 μSI ($K^* = -0.7$ to 18×10^{-6} SI in Fig. 6.96). All dolostone lithologies within the lower unit (364.9–347 m) show near zero or slightly negative values. The middle unit is characterised by magnetic susceptibility fluctuating between zero and 180 μSI ($K^* = 16 \times 10^{-6}$ SI). Dolarenites and stromatolitic dolostones occurring between 331.6 and 311.4 m show near zero or slightly positive values. The uppermost member unit (311.4–307 m) composed of interbedded dolarenite and carbonate-siltstone has a magnetic susceptibility in the range from zero to 200 μSI ($K^* =$ 0–18 $\times 10^{-6}$ SI in Fig. 6.96).

Carbonate rocks in the lower unit are variably recrystallised, mainly appear massive or crudely stratified, with a variegated colour and patchy texture (Figs. 6.97fv–fy). The rareity of stratification (Fig. 6.97ga) might reflect recrystallisation which obliterated depositional features and dolostone clasts - matrix boundaries, imparting the patchy dolorudite appearance (i.e. dolostone breccia, conglomerate and gritstone; Figs. 6.97fv, fx, fy) and the loss of primary microstructures in doloarenites (Fig. 6.97fw), though some beds may preserve stromatolitic fabrics (Fig. 6.97fz).

The middle unit of the Dolostone-Dolomarl member comprises diverse carbonate lithologies (Figs. 6.97ek–fu). The basal section of this middle unit (347–346 m) itself includes several lithofacies, beginning with a 0.6-m-thick bed of red, parallel-bedded marl, resting with a sharp contact on beige dolostone breccia. This is overlain by two graded beds of pale pink conglomerate, each draped by dark brown, haematite-rich siltstone (Fig. 6.97fu), and then a 0.3-m-thick bed of dolostone conglomerate (Fig. 6.97ft). The middle part of the section (346–345.4 m) is composed of interbedded pink dolarenite and finely crystalline (micritic) dolostone. Some intervals show rhythmic bedding expressed by 1–5-cm-thick dolostone beds with erosional bases and thin, brown-pink dolomarl drapes (Fig. 6.97fs).

The upper part (345.4–332.1 m) of the middle unit comprises a very distinct lithofacies: variegated dolarenite-siltstone (Figs. 6.97fm–fq) forming several, c. 1–2-m-thick, thickening-upward packages (Fig. 6.97fk). The lower part of each is composed of dark-coloured, thinly laminated siltstone passing into rhythmically bedded dolarenite-siltstone couplets that thicken upward into a unit of pink, massive, dolarenite (Fig. 6.97fk). Within the dolarenite-siltstone intervals, beds are commonly graded and display parallel and ripple-cross lamination (Figs. 6.97fg, fh, fk–fq). Some intervals contain dolomite- and quartz-pseudomorphed crystals of gypsum (Figs. 6.97fp–fr). From 340.9 m and upward, the pink dolarenites contain abundant dissolved surfaces, probable dissolution pipes, and larger dissolution cavities resembling karst (Figs. 6.97el–fj). The intensity of dissolution processes progressively increases up-section and culminates at a depth of 332.5 m where it is expressed as "a pothole" of unknown dimension but deeper than 40 cm (Fig. 6.97ek). The dissolution cavities are filled with brown, massive, indistinctly bedded and laminated siltstone and dolarenite. Some infil resembles "*terra rossa*" (Figs. 6.97ek, fj), whereas other examples contain abundant pseudomorphs after gypsum crystals (Figs. 6.97en–eo, ew–ey, fb, fc). At a depth of 332.3 m, there is evidence for two consecutive phases of dissolution and infill (Figs. 6.97el, em).

The upper unit of the Dolostone-Dolomarl member (332.1–307.5 m) has at its base a c. 3-m-thick interval of inter-bedded, pale pink dolomarl and dolarenite resting with a sharp contact upon the brown, clayey dolomitic siltstone filling the dissolution cavity. The dolomarl-dolarenite interval is sharply overlain by a unit of stromatolitic dolostones (328.7–324 m; Figs. 6.97ei, ej). That unit is composed of a series of tabular beds of pale pink, small-column stromatolites with thin, dark-coloured, haematite-rich, silty tops (Figs. 6.97ef–eh). It passes gradationally to overlying dolarenite through pale brown dolostone with wrinkled beds of flat-laminated stromatolites, and flaser bedding; in places there are asymmetric ripples draped by dark silt material (Fig. 6.97ee). The remaining part of the upper unit (324–307.5 m; Fig. 6.95) is largely dolarenite (Fig. 6.97ed), with a single bed of columnar stromatolites (Figs. 6.97eb, ec) and several thin beds of dolorudite, carbonate-siltstone and carbonate-sandstone-siltstone. The pale pink dolarenite shows parallel, slightly wavy bedding with thin mud drapes. The stromatolites have a divergent, columnar morphology and occur as a 70-cm-thick unit with sharp boundaries. The carbonate-siltstone and carbonate-sandstone-siltstone are characterised by a variegated colour and fine, parallel lamination, which is highly disrupted by growth of diagenetic minerals, primarily sulphates, found in the form of crystals and concretions now pseudomorphed by white dolospar.

All carbonate lithologies are dolomitic in composition with Mg/Ca ratios ranging between 0.64 and 0.67, hence identical to the ratios obtained from members 1 and 2. The micritic dolostone, dolarenite and gritstone contain 3.6–21.2 wt.% SiO_2, whereas the dolostone conglomerate has a SiO_2 content ranging between 24 and 58.5 wt.%. This is due to incorporation of sandstone clasts. The dolostones have a high Mn content (189–482 µg g^{-1}), a moderate Fe content (65–161 µg g^{-1}), and are low in Sr (65–118 µg g^{-1}) (Appendix 28). All rock types are devoid of measurable Na_2O, C_{org} and S (Appendices 26, 27). The content of CaO increases from 340.75 m upwards. This provides a dilution effect, resulting in decreasing abundances of several silicate-bound elements including Al_2O_3 (5.2 → 0.9 wt.%), Fe_2O_{3tot} (2.6 → 0.37 wt.%), TiO_2 (0.27 → 0.04 wt.%), Ba (140 → 143 ppm) Co (9.9 → <4 ppm), Cr (48 → 12 ppm) and Ni (36 → 6.3 ppm) (Appendix 27).

All analysed archive samples show high $\delta^{13}C$ values (+5.4 to +9.5 ‰, VPDB). $\delta^{18}O$ fluctuates between 18.8 ‰ and 20.4 ‰ (VSMOW) (Reuschel et al. 2012).

Member 4 (Dolomarl)

The Dolomarl member has a thickness of 38 m (307–269 m) and sharp contacts with both the underlying and overlying rocks. The member consists of dolomarls, three beds of dolarenites and two beds of siltstones, all of a variable thickness ranging from less than 0.5 m (siltstones) to more than 2 m (dolarenites) (Fig. 6.95).

Magnetic susceptibility measurements reveal that the member is characterised by low values ranging between −30 and 140 µSI (K* = −3 to 13 × 10^{-6} SI) (Fig. 6.96); dolomarls show an elevated magnetic susceptibility relative to that of dolarenites.

The dolomarls are mostly dark-coloured (rarely pale brown), massive or laminated rocks with numerous crystals, crystal rosettes, solitary and coalesced nodules, and layers of former sulphates (Fig. 6.97dj–du, dx, ea). Some intervals show desiccation (Fig. 6.97dq, dr). All forms of sulphate occurrence are partially replaced by white quartz, white dolospar or combinations of the two. Sulphates pseudomorphed by quartz commonly retain abundant relicts of Ca-sulphates (Fig. 6.97dy).

The concretionary sulphate ranges in size from 1 mm to 20 cm, is common throughout the section and can occur as dense clusters in 20–50-cm-thick intervals alternating with barren marls of somewhat similar thicknesses. In places, within half a metre of thickness, the density of scattered nodules can gradually increase and coalesce to form semi-massive nodular masses resembling chicken-wire anhydrite. The sulphate nodules are commonly associated with crystals and rosettes (Figs. 6.97dt, du, dx, ea). Several dolospar-pseudomorphed sulphate layers exhibit enterolithic layering as irregular, tight to open folds (Figs. 6.97dj, dk, dp).

Dolarenites occur as two discrete beds, with the thickest one in the middle of the section (292–288 m). The beds have sharp contacts with marls. The dolarenites are variegated in colour, show crude stratification (Figs. 6.97dv, dw) and display highly disrupted fabrics due to growth of evaporitic minerals.

Siltstones occur as two beds located below the main dolarenite bed and are separated from each other by dolomarl (Fig. 6.96); contacts are gradational. In contrast to the dark-coloured dolomarls, they are bright red and pink in colour (Fig. 6.97dz) and are laminated, though the lamination is diagenetically and tectonically modified. Similarly to dolomarls, the siltstones contain abundant sulphate nodules partially replaced by white dolospar.

Three analysed samples show Mg/Ca ratios of 0.64 (dolarenite), 0.59 and 0.70 (dolomarls), hence the dolomarls may contain minor calcite and magnesite. The dolomarls contain 34–48 wt.% SiO_2, 8.8–12 wt.% Al_2O_3, 3.7–4.6 wt.% Fe_2O_3, and 2.8–3.2 wt.% K_2O. They are devoid of measurable Na_2O, C_{org} and S (Appendices 26, 27). All carbonate lithologies have variable abundances of Fe (80–138 µg g^{-1}) and Mn (86–493 µg g^{-1}), and a low Sr content (29–107 µg g^{-1}) (Appendix 28). Three analysed archive samples show $\delta^{13}C$ of c. +9 ‰ and $\delta^{18}O$ at c. 19 ‰ (Reuschel et al. 2012).

One analysed siltstone sample has high SiO_2 (54 wt.%), MgO (8.6 wt.%) and CaO (9.9 wt.%), and is low in Al_2O_3 (6 wt.%) and devoid of measurable Na_2O, C_{org} and S.

Member 5 (Siltstone-Dissolution Breccia-Magnesite)

This member is c. 64 m thick (269–204.9 m) and consists of heterogeneous rocks. Siltstone, dissolution-collapse breccia and three magnesite beds occur as distinct units and distinguish this member from other units of the 10A section. A thick magnesite bed (269–265.3 m) defines the base of the member, and the top is placed at 204.9 m, below a siltstone-sandstone unit (Fig. 6.95). Thick beds of magnesite with dissolution-collapse breccia make this association lithologically similar to Member D of Melezhik et al. (1999; for details see Chap. 4.3).

Magnetic susceptibility of the member is marked by low values; dolostones and magnesites are characterised by values fluctuating around zero, whereas dolomarls show an elevated magnetic susceptibility up to 90 µSI (K* is up to 8 × 10^{-6} SI in Fig. 6.96). The siltstones have the highest magnetic susceptibility values of up to 150 µSI (K* is up to 14 × 10^{-6} SI in Fig. 6.96).

The lower magnesite bed is 3.7 m thick and is composed of monotonous, indistinctly bedded (Fig. 6.97di) or massive rocks, which gradually change their colour up-section from pale grey to pale brownish. The magnesite is fine-grained and contains clastic quartz. The other two beds at 224.7–222 m and 208.9–207.7 m are white and pale grey syndepositional breccias, whose original features were obliterated by pervasive recrystallisation. The breccias consist of angular, unsorted fragments of coarse-grained magnesite embedded in a crystalline magnesite matrix. Some clasts show relicts of rounded magnesite grains overgrown by syntaxial magnesite spar.

Siltstones occur as several thick units (Fig. 6.95), all having gradational contacts through alternation of cm- to dm-thick siltstone, dolarenite and dolomarl intervals. The siltstones have a dark grey (251.7–246.6 m), brown (229–224.7 m) or variegated colour. Their textures were highly disrupted by growth of sulphates in the form of nodules, individual crystals or clusters of rosettes (Fig. 6.97dc, dd).

Between 241 and 234.5 m is a unit of dissolution-collapse breccia composed of angular fragments of red and dark grey shale and siltstone, and white fragments of dolostone; all are cemented by white dolospar. Fragments are angular and unsorted, and larger clasts form a fitted fabric that can be easily assembled into the original shape. Stratification is defined by alternation of c. 1-m-thick intervals, each interval containing fragments of different rocks or colour (Fig. 6.97db). Contacts with encasing strata are gradational, with fragmentation progressively increasing from largely intact, to broken and jointed to, finally, brecciated.

The dolarenites are the next most abundant lithology, with the main portion occurring immediately above the lowermost magnesite body. This portion is c. 7.5 m thick with a thin interbed of dolostone breccia (Fig. 6.95). The dolarenites are pale grey, pale pink or variegated in colour with tectonically modified, indistinct ripple bedding and/or wrinkle lamination (Figs. 6.97dg, dh). Several other similar, but thinner (0.5–2-m-thick), intervals of dolarenite occur throughout the member in alternation with various carbonate lithologies and siltstones. The interval occurring above the uppermost magnesite bed displays soft-sediment deformed, rhythmically bedded, dolarenite-siltstone couplets. In places, fine lamination was modified/disrupted by diagenetic growth of sulphates, now replaced by white dolospar with a granular texture, whereas other intervals contain abundant quartz-pseudomorphed sulphate crystals (Figs. 6.97cl–cs).

Coarser clastic carbonate rocks such as dolorudites are also common and occur as 0.2–5-m-thick beds throughout the section (Fig. 6.95). They have sharp contacts with the variable host lithologies, appear as mainly massive rocks composed of tightly packed, poorly sorted, variably rounded clasts of dolostone that range in size from grit to pebble (Figs. 6.97cv–da). Some clasts show very little or no transport and can be readily re-assembled into an original bed (Figs. 6.97cv, cw). Stylolites are present in many places (Figs. 6.97cy, da).

Interbedded dolostone-siltstone and dolomarls occur as 0.5–2-m-thick beds in the middle and upper parts of the member. These lithologies are pale brown and brown, massive or bedded rocks containing talc and abundant nodules and crystal rosettes of sulphate partially replaced by white dolospar (Figs. 6.97ct, cu). Some intervals (234–233 m) show numerous dissolution cavities.

All carbonate lithologies are rich in SiO_2 (13–43 wt.%), low in Al_2O_3 (0.2–2.8 wt.%), and devoid of measurable Na_2O (with one exception at 0.3 wt.%), C_{org} and S (Appendices 26, 27). In all dolostones, Mg/Ca ranges between 0.64 and 0.67, hence slightly above 0.62 of stoichiometric dolomite. The magnesite has Mg/Ca ratios of 2.6–6.4 and thus contains a dolomitic component. The carbonate rocks have a low Fe content (42–75 μg g^{-1}, with one exception at 159 μg $g-^{1}$) and variable Mn abundance (43–330 μg g^{-1}). The Sr content in magnesite is low (33–43 μg g^{-1}), though it is highly variable in dolomitic rocks (64–253 μg g^{-1}) (Appendix 28). One dolorudite and one magnesite sample are enriched in Ba, containing 775 and 803 μg g^{-1}, respectively.

Irrespective of their compositions and stratigraphic positions, all analysed archive samples show high $\delta^{13}C$ values ranging between +7.4 ‰ and +9.2 ‰ (VPDB). $\delta^{18}O$ fluctuates between 18.4 ‰ and 19.8 ‰ (VSMOW) with one exception at 23 ‰. Reuschel et al. (2012) reported relicts of sulphate in marl and dolarenite samples (267.62 and 256.15 m) in a range of 126–172 ppm. These samples yielded $\delta^{34}S$ of 11.3 ‰ and 10.7 ‰ (VCDT).

Member 6 (Dolomarl-Dolostone-Siltstone-Sandstone)

The Dolomarl-Dolostone-Siltstone-Sandstone member occurs between 204.9 and 153.3 m (Fig. 6.95). The member is composed of dolomarls, dolorudites (dolostone gritstone) and dolarenites (dolostone sandstone), siltstones, sandstone and gritstones with subordinate micritic dolostone and heterolithic carbonate-siltstone (Figs. 6.95 and 6.97bi–ck). The base of the member is marked by a brown siltstone that rests with a sharp contact on the underlying dolarenite; its top is a grey siltstone bed (Fig. 6.97bj) overlain sharply by pale pink dolarenite (Fig. 6.97bi).

Magnetic susceptibility of the carbonate rocks is characterised by low positive and negative values. Dolomarls show a slightly elevated magnetic susceptibility reaching 120 μSI (K* as high as 11×10^{-6} SI in Fig. 6.96), whereas polymict conglomerates have the highest values up to 180 μSI (K* as high as 16×10^{-6} SI in Fig. 6.96).

The lowermost unit (202.2–198.3 m) is composed of homogeneous dark grey, massive dolomarl with abundant, evenly distributed rosettes of gypsum crystals that are partially replaced with white dolospar (Figs. 6.97cf–ch). The contact with the underlying siltstone is transitional, whereas the contact with the overlying dolarenite is sharp, although this bed may be over-turned (Fig. 6.97cf). The dolomarl is recrystallised, does not retain primary microstructures, and contains abundant tremolite laths; these features typify all dolomarl units throughout member 6.

The thickest dolomarl occurs between 183.1 and 174.9 m and is composed of dark grey, bedded rocks at the base passing upward into massive, monotonous rocks. The lower contact is marked by 10 cm of interbedded dolostone and dolomarl sitting sharply on dolarenite, and the upper contact into siltstone is transitional. The lower c. 0.5 m contains abundant dolomite-pseudomorphed nodules and layers of former sulphates. It is overlain by c. 1 m of bedded dolomarls and then dark brown, massive dolomarl. The latter contains casts of halite crystals at the base (Figs. 6.97bu, bv) and has three c. 10-cm-thick intervals of in situ breccias cemented by white dolospar that likely formed by dissolution collapse. There is also a c. 20-cm-thick interval of densely clustered, small sulphate crystals partially replaced by white dolospar and a c. 0.5 m-thick bed of dark brown, bedded sandstone in the middle of the section.

The uppermost dolomarl (155.5–154.2 m) appears as massive or thickly bedded, brown rocks resting on the underlying dolarenite. Its upper bedding surface shows irregular topography and apparent dissolution pipes, and is in sharp contact with the overlying dolarenite. One to four-cm-sized, sparsely distributed sulphate nodules partially replaced by white quartz and dolospar are present in this dolomarl (Figs. 6.97bj–bm).

Siltstones occur in three intervals (Fig. 6.95), are dark brown or red in colour and thickly bedded. All three contain scattered patches of rounded and sorted sand-sized quartz grains floating in silty matrices, and can be termed a "pudding" siltstone. The lowermost interval contains two thin sandstone beds, whereas the uppermost has a thin bed of dolorudite. The lower siltstone unit contains ubiquitous rosettes of sulphates partially replaced by white dolospar (Figs. 6.97cj, ck); adjacent beds differ in terms of the rosette size and density (Fig. 6.97ci). The middle unit comprises red, bedded siltstone and also contains dolospar-pseudomorphed nodules and crystals of apparent sulphates (Fig. 6.97by). The siltstones in the uppermost interval are dark brown, massive, and monotonous rocks crosscut by straight veins filled with white dolospar. The upper contact is transitional into the overlying variegated and parallel-laminated, heterolithic dolostone-siltstone rocks. The latter are partially affected by desiccation and contain quartz-pseudomorphed gypsum rosettes (Figs. 6.97bs, bt).

Dolorudites and dolarenites occur as two 8–10-m-thick units in the middle and upper parts of the member (Fig. 6.95). Both lithologies have sharp contacts with adjacent rocks (Fig. 6.97cf). Dolorudites and dolarenites have a white, grey, pink or variegated colour (Figs. 6.97bn, bp, bx, bz), and they show a massive (Figs. 6.97bn, bz) or thick-bedded structure and undulating, wrinkled or wavy bedding planes (Figs. 6.97bp, bx). Thin-bedded dolarenites are rare and commonly contain dark brown, thin mudstone laminae. One interval of thin-bedded dolarenite shows either in situ disintegrated beds or transported angular clasts composed of red dolospar. The rocks are variably recrystallised, but clast forms, primary microstructures and relicts of the cement can be readily identified. Where preserved, the clasts show diverse morphologies ranging from sub-spherical through angular to platy shapes (Fig. 6.97ca). In dolarenites, dolomite and minor quartz clasts are rounded and cemented with syntaxial dolospar overgrowth (Fig. 6.97bo). Silica cement is rare. Among the dolostones that occur in the middle part of the member, there is a c. 7-m-thick, massive bed composed of homogeneous, coarsely crystalline dolomite; beige, up to 2-cm-large dolomite crystals are tightly packed and cemented by white, dusty, syntaxial dolospar overgrowth (Fig. 6.97bw). Many crystals are xenomorphic, whereas others are rounded with dissolution embayments, or show perfect cubic shapes. Although this massive, crystalline dolostone was identified as dolomitic gritstone during visual core examination, its structural and textural features indicate that coarsely crystalline dolomite may represent halite or anhydrite replacement.

Sandstone and gritstone are minor rock types in member 6 and occur as 0.8–1.5-m-thick beds in the lower half of the section (Fig. 6.95). Clastic material in gritstone is poorly sorted and variably rounded quartz and dolostone (Figs. 6.97cb, cd). The sandstone is composed of well-rounded quartz and dolarenite clasts, which are unevenly distributed in a siltstone matrix. Both the sandstones and gritstones may contain soft-sediment deformed lenses of laminated siltstone (Fig. 6.97cc).

Dolomarls contain 26–40 wt.% SiO_2, 5–7 wt.% Al_2O_3, 15–20 wt.% MgO, and 11–16 wt.% CaO (Appendix 26), and have a sizable amount of Na_2O (c. 0.8 wt.%), though K_2O still dominates (2.6–3.8 wt.%). All types of dolostones (Mg/Ca = 0.69–0.67) have a variable SiO_2 content (9–23 wt.%) but the abundances of Al_2O_3 are very low (<0.1 wt.%), and the Fe_2O_3, TiO_2, and Na_2O contents are close to or below the detection limit. The rocks have a moderate Mn content (119–310 $\mu g\ g^{-1}$) and low Sr abundances (48–190 $\mu g\ g^{-1}$) (Appendix 28).

A single analysis of sandstone shows a high content of carbonate components (MgO = 15 wt.%, CaO = 13 wt.%) and is low in SiO_2 (38 wt.%) and Al_2O_3 (6 wt.%). The sandstone contains 2 wt.% K_2O, is devoid of measurable Na_2O and S, but contains up to 0.13 wt.% organic carbon (Appendix 27).

All analysed archive samples in this member show high $\delta^{13}C$ values (+7.4 to +8.2 ‰, VPDB). $\delta^{18}O$ fluctuates between 19.3 ‰ and 20.6 ‰ (VSMOW) with the highest value of 25.6 ‰ obtained from the dolomarl. Reuschel et al. (2012) reported 65 ppm of sulphate in dolorudite samples that yielded $\delta^{34}S$ of 8.8 ‰ (VCDT).

From c. 130 m and upward, tectonic folding compromises the stratigraphy and hence thicknesses are estimates and some intervals may, in fact, be structural repetitions. Hence, the lithostratigraphic subdivisions presented below should be treated with caution.

Member 7 (Sandstone-Dolostone)

The member spans 154.2–107.6 m (Fig. 6.95) and starts with a pale pink, massive dolarenite resting with a sharp contact on siltstone; the base of the dolarenite displays a structure resembling chicken-wire anhydrite (Fig. 6.97bi). The upper contact is placed at the top of a thick siliciclastic succession. The member comprises essentially two major lithofacies, clastic dolostone (dolarenite, dolorudite, breccias) and dolomite-cemented arkosic and quartzitic sandstone and gritstone with minor siltstone (Figs. 6.97ar–bi). All lithofacies have low magnetic susceptibility near zero with a few measurements reaching c. 60 μSI ($K^* = 5 \times 10^{-6}$ SI in Fig. 6.96).

Clastic carbonate rocks occur in the lower half of the section. The dolarenites are variegated, either massive or thick-bedded (Figs. 6.97be, bi) and commonly highly disrupted by syndepositional buckling, folding and brecciation (Fig. 6.97bh). Some dolarenites contain silica-filled dissolution vugs (Fig. 6.97be) and show eroded or dissolved bedding surfaces (Fig. 6.97be). Thin-bedded dolarenites are also common, with parallel layering to lensodial shapes (Fig. 6.97bg), and some beds at the base of the section contain chicken-wire anhydrite replaced by white dolospar (Fig. 6.97bi). Despite pervasive recrystallisation, the rocks retain relicts of rounded dolomite clasts and burial cement in the form of syntaxial dolospar overgrowths.

Dolorudites include dolostone gritstones and breccias (Figs. 6.97av–ax, bc, bd, bf) and are either massive (Figs. 6.97aw, ax, bf) or thick-bedded (Fig. 6.97av). Pervasive recrystallisation partially obliterated clast/matrix boundaries but, where primary depositional features are preserved, clasts of dolostone are unsorted in this member and angular in shape (Figs. 6.97av–ax, bd).

Sandstones are present throughout, but dominate the uppermost part of the section (Fig. 6.95). They are variegated, well-bedded and display sharp contacts with the encasing dolostone; the latter has eroded and/or dissolved surfaces (Fig. 6.97bb). Sandstones are commonly thin bedded and interbedded with thin layers of brown siltstone to form sandstone-siltstone couplets (Figs. 6.97au, ay, ba). Ripple lamination is present, and many sandstone beds have erosional bases (Fig. 6.97ba). In places, the interbedded sandstone-siltstone exhibits syndepositional deformation (Fig. 6.97az) and structures resembling small tepees (Fig. 6.97as). Sandstones are composed of well-rounded and sorted clasts of quartz, dolomite and rare microcline (Fig. 6.97at), and, locally, outsized angular rip-up clasts of dolostone (Fig. 6.97ba). Relicts of silica and dolomite burial cement are observed in the form of syntaxial overgrowths.

The member contains only one discrete, thin bed of siltstone occurring within the uppermost sandstone succession (Fig. 6.95). The siltstone is dark-coloured and shows fine lensoidal and flaser lamination (Fig. 6.97ar).

All carbonate lithologies of this member are dolomitic in composition with Mg/Ca of 0.66, with one outlier at 0.70. The rocks are siliceous containing 2–22 wt.% SiO_2, though having low abundances of Al_2O_3 (0.05–0.4 wt.%) and K_2O (<0.01–0.25 wt.%). The rocks are devoid of Na_2O, C_{org} and S (Appendices 26, 27). The dolomite has moderate contents of Fe (54–90 μg g^{-1}) and Mn (40–87 μg g^{-1}, with one outlier at 262 μg g^{-1}) (Appendix 28). There is a systematic stratigraphic increase in Zn (21→ > 100 μg g^{-1}) and Ba (2.5 → 17 μg g^{-1}) contents and decrease in Sr (142 → 65 μg g^{-1}). All carbonate lithologies show high $\delta^{13}C$ (+8.2 to +9.8 ‰, VPDB). $\delta^{18}O$ fluctuates between 19.1 ‰ and 20.4 ‰ (SMOW). Carbonate components of the sandstone show a similar range of $\delta^{13}C$ (+8.4 to +8.6 ‰, VPDB), whereas $\delta^{18}O$ (c. 18.5 ‰) is slightly depleted in ^{18}O. Reuschel et al. (2012) reported 310 ppm of sulphate in micritic dolostone that yielded $\delta^{34}S$ of 8.3 ‰ (VCDT).

Member 8 (Siltstone-Sandstone)

The Siltstone-Sandstone member occurs between 107.6 and 72.1 m (Fig. 6.95) and is gently folded (Figs. 6.97v–aq). It is composed mainly of siltstone with interbeds of marl, dolarenite, dolorudite, sandstone and dissolution breccias. Similarly to other members, the rocks of the Siltstone-Sandstone member show overall low magnetic susceptibility with most lithologies exhibiting values fluctuating near zero, whereas siltstones have values ranging between 0 and 180 μSI ($K^* = 0–16 \times 10^{-6}$ SI in Fig. 6.96).

The siltstones are rather similar throughout and are dark-coloured, either massive or laminated, and contain ubiquitous sulphates partially replaced by white dolospar and quartz (Figs. 6.97v–ad, af–an). Relicts of anhydrite over several tens of μm in diameter are present in the pseudomorphed sulphates, hence proving their primary composition. Lamination is commonly disrupted by the growth of sulphate nodules and rosettes, either by plastically deforming the sediment (Figs. 6.97an, aj) or piercing layering (Figs. 6.97z, ag). Several intervals contain chicken-wire and enterolithic fabrics (Fig. 6.97ak), the result of volume changes brought about by hydration of anhydrite to gypsum. Sulphate nodules, crystals and rosettes commonly cluster densely in layers, emphasising otherwise cryptic bedding (Figs. 6.97w, ah).

The siltstones have a bimodal texture. Silt-sized particles define a matrix that contains well rounded and sorted, sand-sized (0.3–04 mm) quartz grains. The latter are either irregularly distributed or form small, silt-matrix-supported lenses and pockets (Fig. 6.97aq).

The dolarenites, dolorudites and micritic dolostones occur throughout the member as discrete beds ranging in thickness from 0.5 to 5 m (Fig. 6.95) and having sharp contacts with the host siltstones. Where preserved, primary bedding appears as dolostone-siltstone rhythms, with wavy and buckled lamination (Fig. 6.97ap). All carbonate lithologies contain abundant dolospar- and quartz-replaced sulphate nodules, crystals and chicken-wire anhydrite whose formation has variably modified primary lamination and bedding (Figs. 6.97ac–ae, ao). A single bed of micritic dolostone is red in colour, and its original structure has been completely obliterated by massive growth of nodular masses of sulphate, replaced now by white dolospar.

There are several sandstone beds with the lowermost being brown-red in colour, mainly massive but in places displaying wavy and flaser bedding; it contains large dolospar-replaced sulphate nodules with mammillated surfaces. Sandstones in the middle part of the member are grey, massive or syndepositionally brecciated with some intervals showing wavy and parallel lamination. They contain few sulphate crystals and nodules, all replaced by white dolospar and quartz. Sulphates diminish up-section to almost none in the uppermost beds.

Three archive samples of the siltstones have variable SiO_2 (34–53 wt.%), Al_2O_3 (6–10 wt.%) and Fe_2O_3 (3–5 wt.%) contents due to the dilution effect by carbonate-bound components: 10–3 wt.% MgO and 5–12 wt.% CaO (Appendix 26). K_2O is present in abundances (3.8–4.7 wt.%) higher than those of Na_2O (<0.1–0.2 wt.%). The siltstones are devoid of C_{org} and S (Appendix 27).

All carbonate lithologies are dolomitic in composition (Mg/Ca = 0.67–0.70), though siliceous (7–27 wt.% SiO_2) and, for the first time, show an elevated content of Al_2O_3 (0.2–5 wt.%). The rocks are devoid of Na_2O, C_{org} and S (Appendices 26, 27), and have moderate Sr (135–202 μg g^{-1}) and low Fe (43–25 μg g^{-1}) contents. The Mn abundance systematically increases up-section from 79 to 101 μg g^{-1} (Appendix 28). All analysed archive samples show high $\delta^{13}C$ values (+8.7 to +9.5 ‰, VPDB). $\delta^{18}O$ fluctuates between 19.6 ‰ and 20.5 ‰ (VSMOW) (Reuschel et al. 2012).

Member 9 (Dolostone-Sandstone-Dolomarl)

The member spans 72.1 to c. 19.5 m (Fig. 6.95) and, with the exception of dolomarl and magnesite, includes all of the lithologies described in the underlying members. Magnetic susceptibility ranges between slightly negative to positive values, with sandstones and interlaminated dolostone-siltstone intervals being most magnetic (up to 170 μSI) (Fig. 6.96). Geochemical profiles show no obvious trends (Fig. 6.96).

Dolostones form the bulk of the section, occurring as numerous, thick intervals of micritic dolostone (Fig. 6.95) as well as microbial laminates and columnar stromatolites that distinguishes this member from the other in the 10A section (e.g. Figs. 6.97m–s).

The base of member 9 is marked by a c. 1-m-thick, grey, silty dolarenite in sharp contact with dark-coloured siltstone. Massive growth of sulphates obliterated primary structures and caused beds to become fragmented, rotated and even brecciated (Fig. 6.97u). The amount of sulphate decreases up-section, although some intervals in the middle part of the member appear as bedded dolarenite-siltstone with numerous dolospar-replaced sulphate rosettes.

Dolarenites occur as interbeds in dark-coloured, laminated dolomarl and siltstone and contain abundant dolospar-replaced sulphate rosettes whose growth obliterated primary bedding (Fig. 6.97i); several layers display dolomite-pseudomorphed chicken-wire fabrics forming clusters as much as 20 cm in thickness. In some intervals (Figs. 6.97a, r, t), there are domed structures resembling stromatolites and abundant dissolution vugs filled with white dolospar and silica that are reminiscent of fenestrae. These features interlaminate with thick dolostone beds having wavy and wrinkled lamination and abundant quartz- and dolospar-filled fenestrae (Figs. 6.97b, q, s). Detailed petrographic research is required to assess whether the dolostones are entirely stromatolitic (i.e., microbial). Stromatolites *per se* occur between 66 and 65 m (Fig. 6.95) and, although recrystallised, occur as small domes and large columnar forms (Figs. 6.97m, n). They are formed on top of beige or pale brown, massive to brecciated dolostones (Figs. 6.97i, o, p). There is some clotted fabric in the 53.4–47.1 m interval reminiscent of microbial, stromatolitic and oncolitic structures.

Sandstones are commonly variegated and bedded, dolomite-cemented, display ripples with dark-coloured siltstone drapes, and contain lenses of pale pink dolostone (Fig. 6.97e). The thickest bed in the middle part of the member is red-brown or variegated, massive or bedded (Fig. 6.97l). Red-brown, massive sandstones contain rosettes of dolomite-pseudomorphed gypsum (Fig. 6.97f). The amount of dolomite-pseudomorphed sulphates increases in the uppermost sandstone, which is brown, faintly bedded and has chicken-wire fabrics of former anhydrite.

One interval of dissolution-collapse breccia occurs beneath the middle sandstone bed. It rests with a sharp contact on beige dolostone (Fig. 6.97h) and is composed of angular fragments of mudstone in the lower part; sandstone fragments in the middle part; and beige dolostone clasts in the upper part. All fragments are angular and are cemented by white dolospar or drusy dolomite.

Gritstones and conglomerates are minor lithologies of the member and occur as beige beds draped by black, soft-sediment deformed mudstone and dolomarl. Some beds show normal grading (Figs. 6.97c, d, g) and are composed of variably rounded and unsorted clasts of dolostone and sandstone in a black, clayey siltstone matrix. In some places these rocks may represent reworked dissolution breccias.

The carbonate rocks here are dolomitic in composition (Mg/Ca = 0.64–0.67), show a variable content of SiO_2 (1.5–38 wt.%) and low abundances of Al_2O_3, Fe_2O_3 and K_2O, whereas Na_2O and S are below the detection limits; one sample shows 0.28 wt.% C_{org} (Appendices 26, 27). Similarly to dolostones of the other members, these examples are characterised by variable contents of Fe (81–308 μg g^{-1}), Mn (62–1390 μg g^{-1}) and Sr (36–196 μg g^{-1}) (Appendix 28). The heterolithic rock is rich in SiO_2 (48 wt.%), Al_2O_3 (12 wt.%) and K_2O (4 wt.%), although the content of Mn is low (46 μg g^{-1}). Carbonate components may contain some magnesite as suggested by a Mg/Ca ratio of 0.94. These analysed archive samples show high $\delta^{13}C$ values (+8.8 to +9.0 ‰, VPDB) with the uppermost sample having $\delta^{13}C$ of +7.2 ‰. $\delta^{18}O$ fluctuates between 18.6 ‰ and 20.6 ‰ (VSMOW) (Reuschel et al. 2012).

Fig. 6.88 Dolostone with quartz sand (*black*) overlain by a bed containing several sheets of probable dolomitic stromatolites separated by quartz-sandstone layers (dark-coloured). Uneven topography of the uppermost stromatolite bed is covered by coarse-grained sandstone with clasts of dolostone (*white*) and dolomite-cemented sandstones and grades upward into a dolarenite. Scanned thin section of core 7, depth of 298.7 m; width of the photograph is 2.5 cm (Photograph by Victor Melezhik)

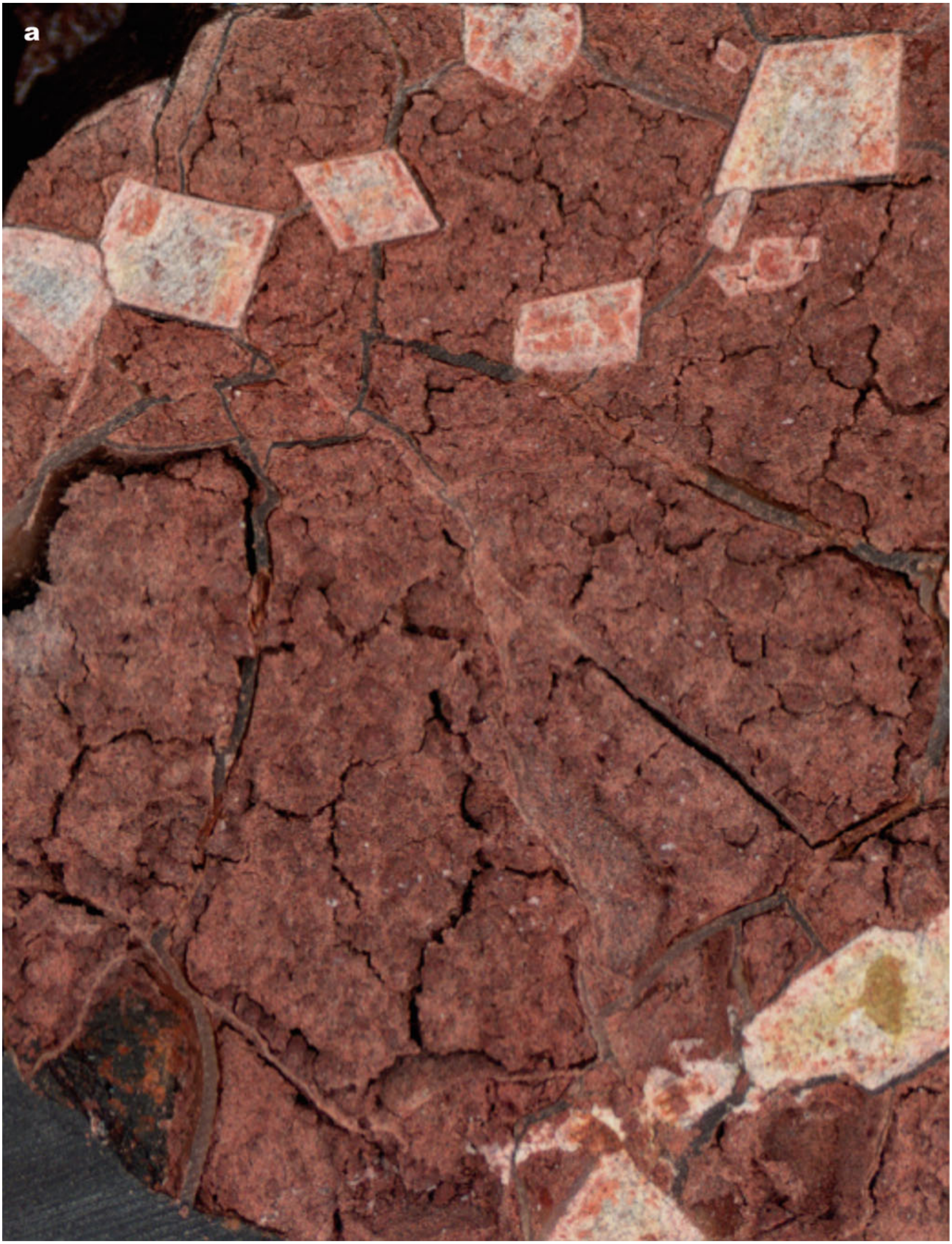

Fig. 6.89 Evaporitic features in the Tulomozero Formation. (**a**) Bedding surface of desiccated brown mudstone bed with dolomite-replaced probable halite crystals (bright). FAR-DEEP Core 10B, depth of 39.7 m. Width of the photograph is c. 3 cm (Photograph by Victor Melezhik)

Fig. 6.89 (continued) (**b**) Bedding surface of a desiccated dolomarl with dolomite-replaced probable halite crystals (bright). FAR-DEEP Core 10B, depth of 39.5 m. Width of the photograph is c. 3 cm (Photograph by Victor Melezhik)

Fig. 6.90 Halite with abundant inclusions of anhydrite (*white*) and a clast of magnesite (*buff yellow*, *centre left*). All clasts show a positive relief due to partial dissolution of the halite bed surface. Core from the Onega parametric drillhole; scale-bar in centimetres (Sample courtesy of the Geological Institute of the Karelian Science Centre. Photograph by Vladimir Makarikhin)

Akhmedov et al., 1993			Medvedev et al. (2011)		Melezhik et al. (1999) and current contribution	
Suite	**Sub-suite**	**Pile**	**Beds with *Lithophyta***	**Pile (Sokolov, 1963)**	**Member**	**Formation**
Tulomozero	Upper	Redbed-Dolostone	*Calevia ruokanensis*	Redbed-Dolostone	H	Tulomozero
		Oncolite-Dolostone	*Butinella*	Dolostone	G	
		Dolostone-Mudstone		Dolostone-Sandstone	F	
	Middle		*Omachtenia kintsiensis*	Volcanogenic		
		Haematite-Sandstone		Haematite-Sandstone-Mudstone	E	
		Pisolite-Dolostone		Chert-Dolostone	D	
		Siltstone			C	
		Stromatolite-Dolostone	*Sundosia*	Dolostone-Sandstone-Mudstone	B	
		Magnesite-Dolostone	*Nuclephyton*	Sandstone-Dolostone		
			Lukanoa	Limestone-Breccia-Mudstone		
		Phosphate-Dolostone			---?---	
		Limestone-Dolostone-Mudstone			A	
	Lower	Undivided		Conglomerate-Sandstone	Undivided	

Fig. 6.91 Various lithostratigraphic subdivisions of the Tulomozero Formation in the Onega Basin (Compiled by P. Medvedev and V. Melezhik)

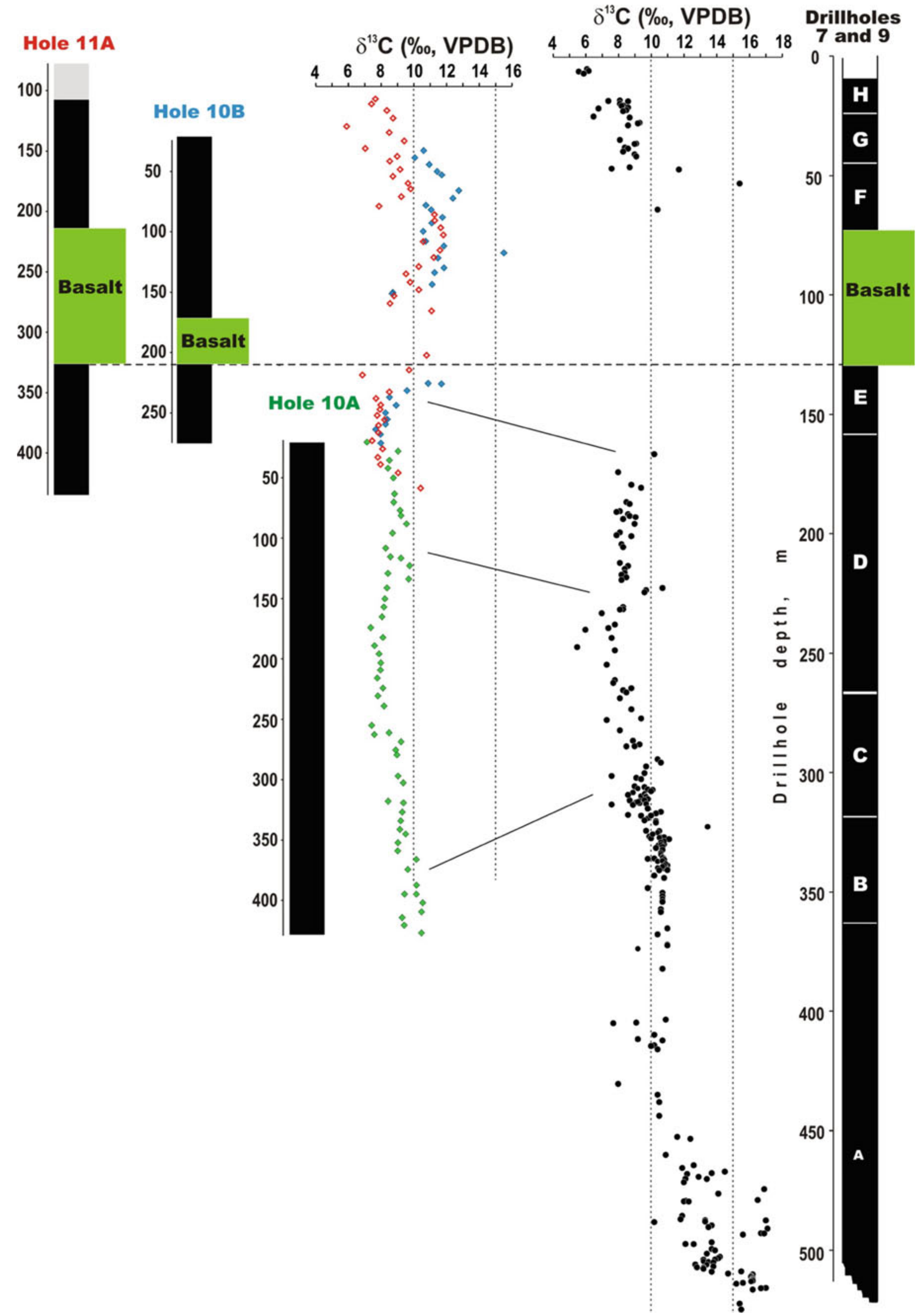

Fig. 6.92 Correlation of the drilled sections of the Tulomozero Formation using the basalt marker horizon and stratigraphical variation of $\delta^{13}C_{carb}$. Carbon isotope data are from Reuschel et al. (2012; Cores 10A, 10B and 11A) and Melezhik et al. (2005; core 7 and 9)

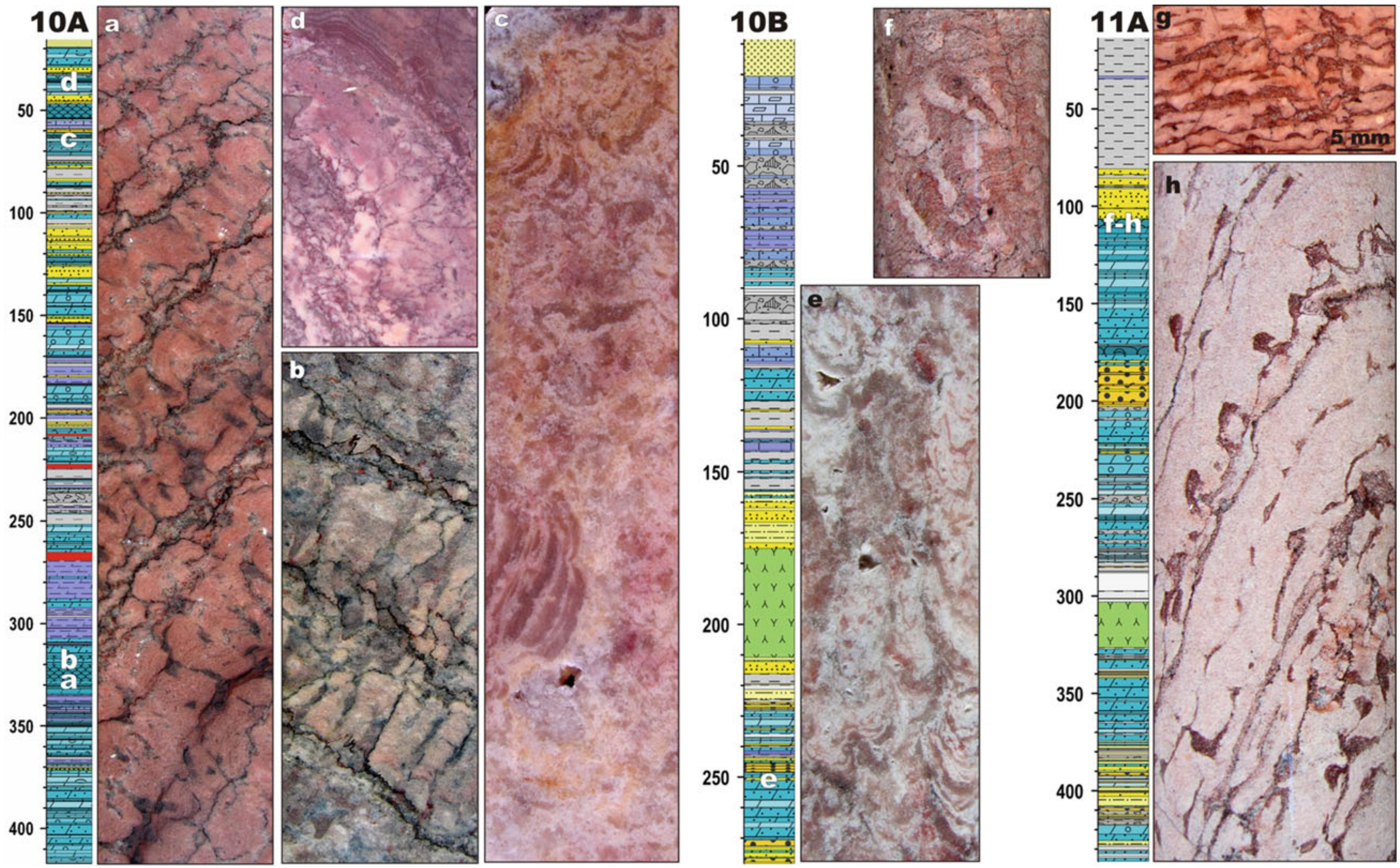

Fig. 6.93 Morphologies of stromatolites from the Tulomozero Formation in FAR-DEEP Cores 10A, 10B and 11A. Core diameter is 5 cm unless specified otherwise. (**a**) *Carelozoon metzgerii* Mak., 1983. (**b**) *Sundosia mira* Mak., 1983. (**c**) *Omachtenia kintsiensis* Mak., 1983. (**d**) *Stratifera janisjarvica* Mak., 1983. (**e**) *Omachtenia kintsiensis* Mak., 1983. (**f–h**) *Djulmekella sundica* Mak., 1983. Taxonomic classification is based on Makarikhin and Kononova (1983) (Photographs by Victor Melezhik (**a–c**, **e–h**) and Pavel Medevedev (**d**))

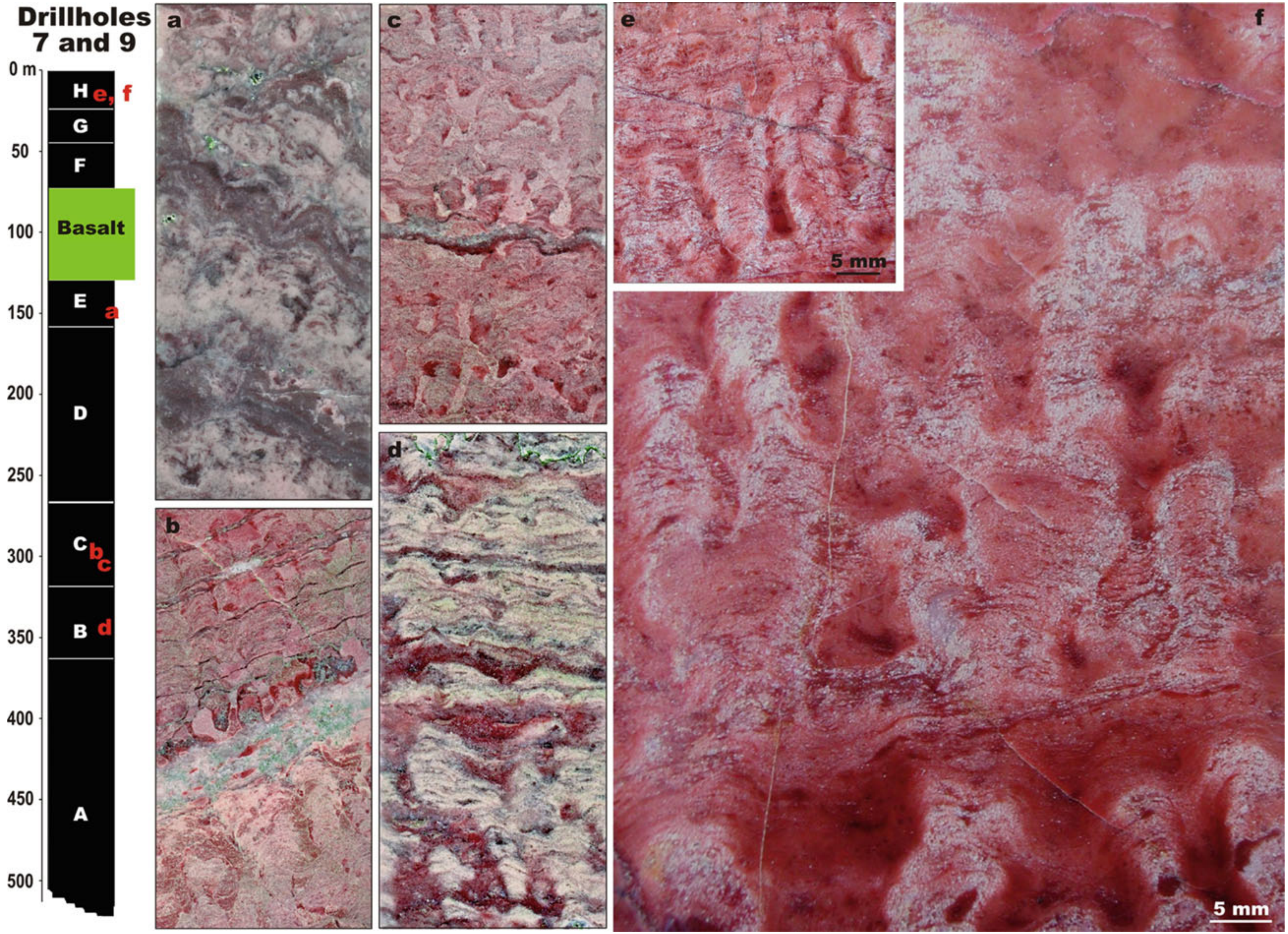

Fig. 6.94 Morphologies of columnar stromatolites from the Tulomozero Formation documented from cores 7 and 9 (not part of the ICDP FAR-DEEP project) in the reference section. Core diameter is 4 cm unless specified otherwise. (**a**) *Omachtenia kintsiensis* Mak., 1983 and *Stratifera janisjarvica* Mak., 1983 (**b**, **c**) *Sundosia mira* Mak., 1983. (**d**) *Carelozoon metzgerii* Mak., 1983. (**e**, **f**) *Djulmekella sundica* Mak., 1983. Taxonomic classification is based on Makarikhin and Kononova (1983) (Photographs by Pavel Medvedev)

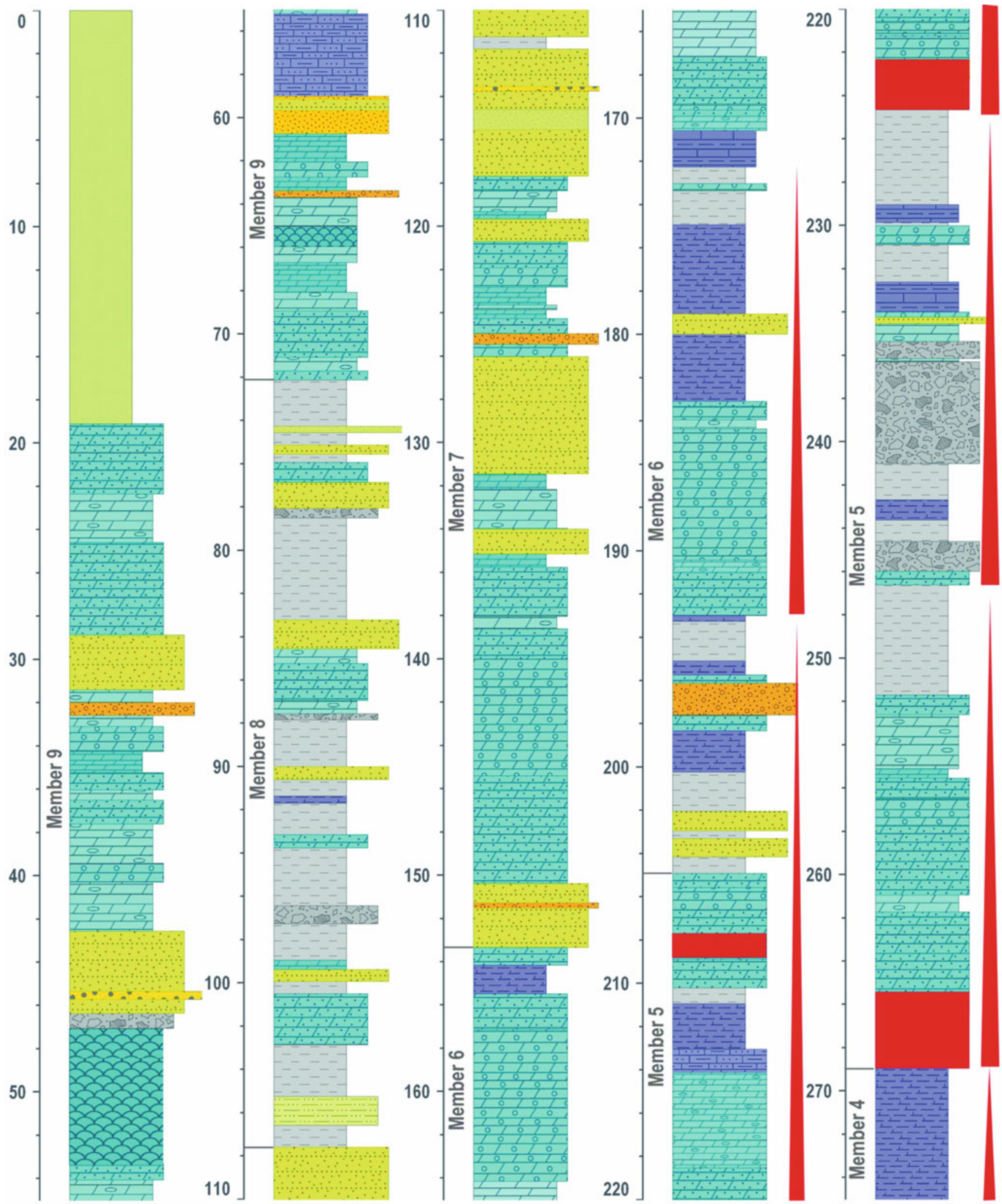

Fig. 6.95 Lithological section of the Tulomozero Formation based on core log of Hole 10A. Reconstructed depositional environments based on core logging, geological mapping and sedimentological research in the vicinity of the drilling site. Lithological symbols are explained in Fig. 6.6

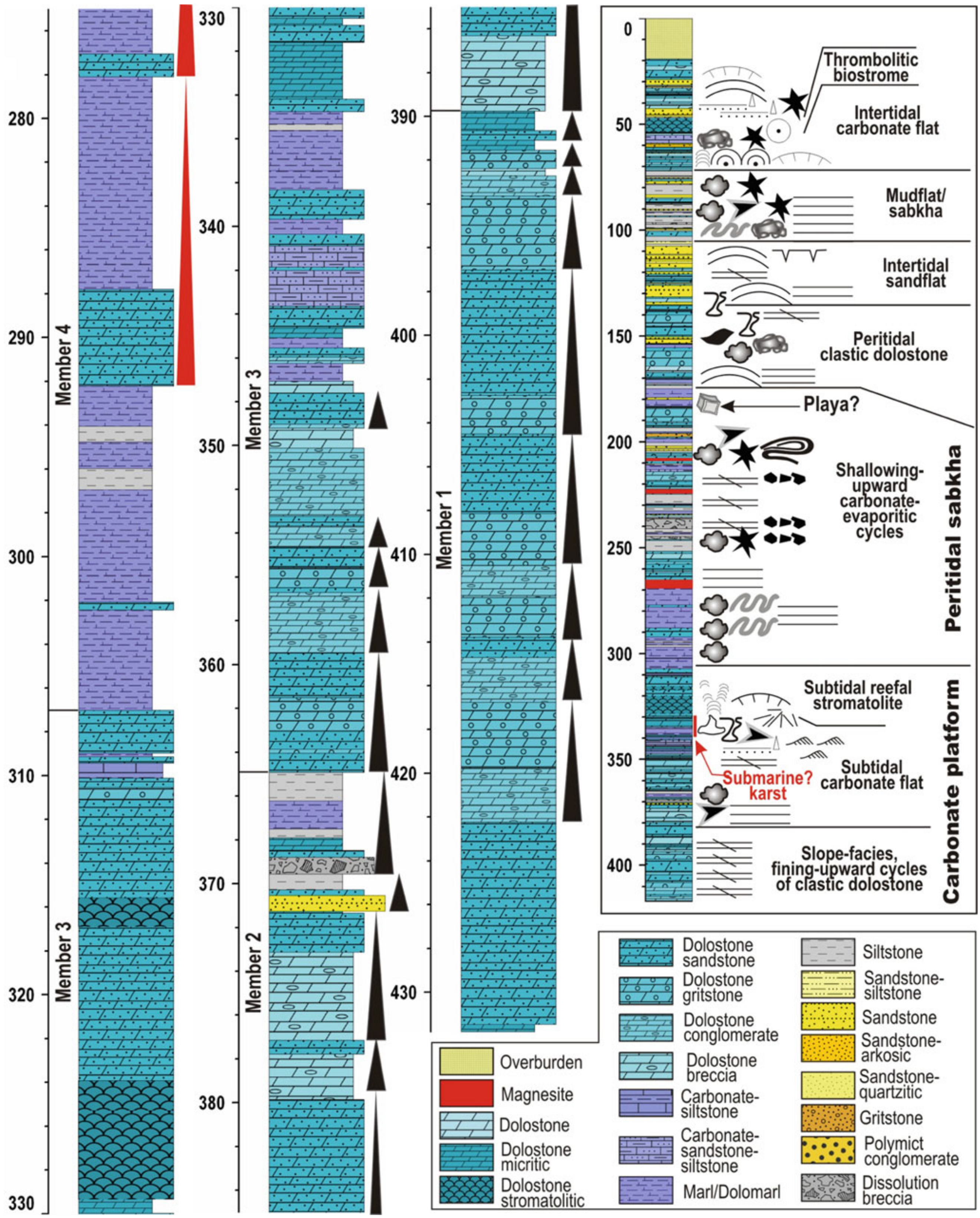

Fig. 6.95 (continued) Lithological section of the Tulomozero Formation based on core log of Hole 10A. Reconstructed depositional environments based on core logging, geological mapping and sedimentological research in the vicinity of the drilling site. Lithological symbols are explained in Fig. 6.6

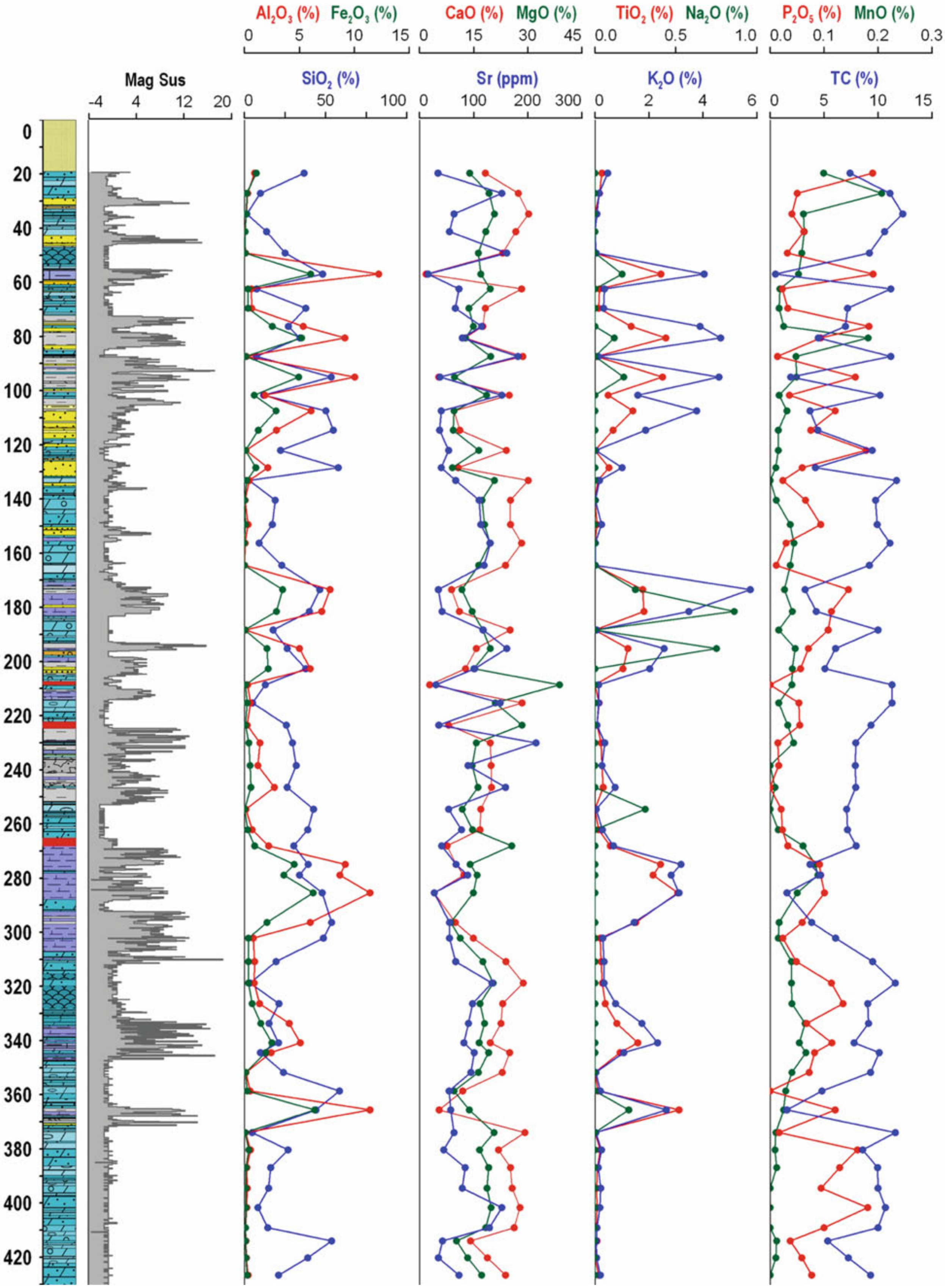

Fig. 6.96 Relative magnetic susceptibility (K*), and geochemical profiles of selected elements in Core 10A based on the archive samples collected with c. 8 m-spacing. For analytical techniques and data quality see Part 5

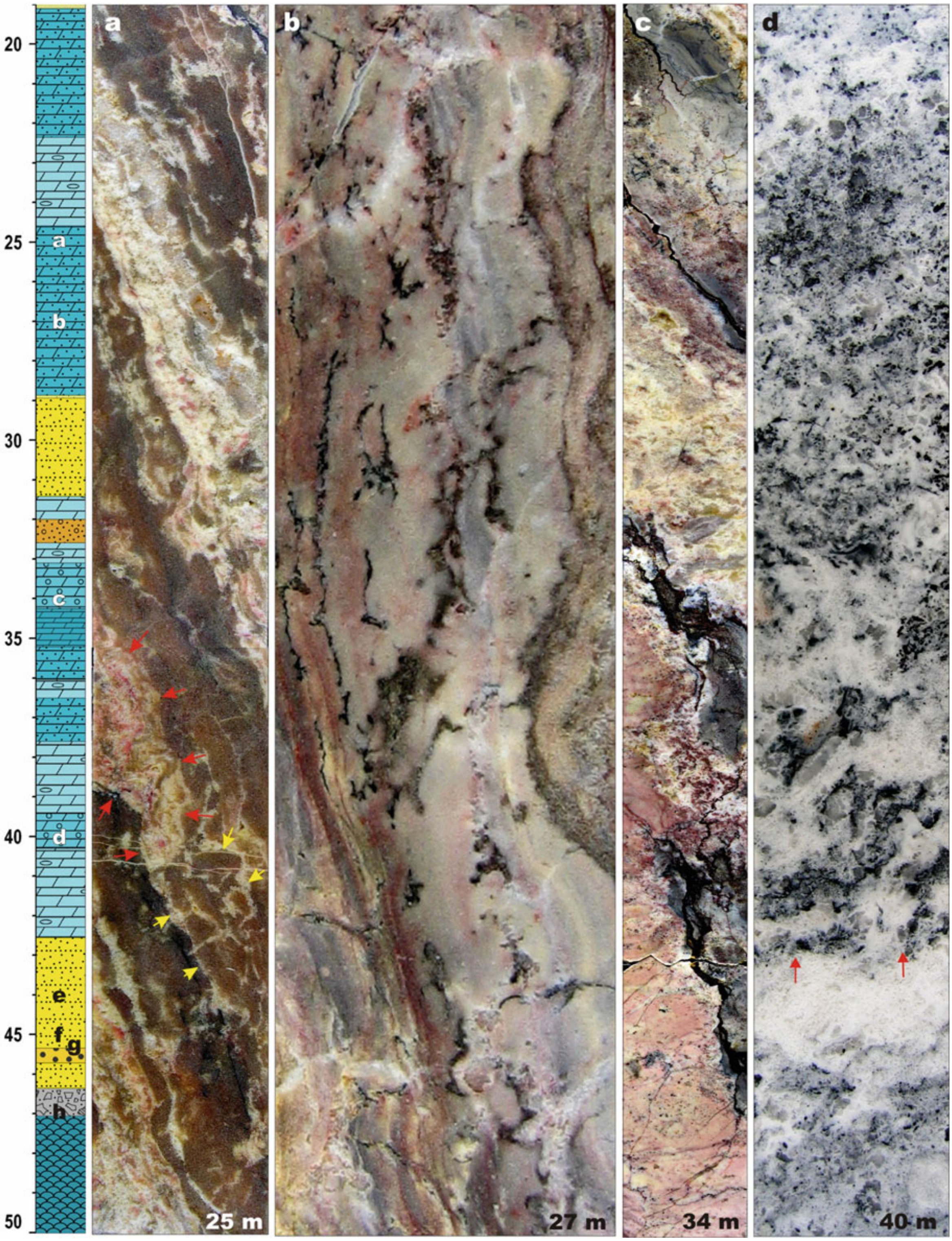

Fig. 6.97 Sedimentological features of main rock types of the Tulomozero Formation based on Core 10A. Core diameter in all plates is 5 cm unless specified otherwise. *Member 9 (Dolostone-Sandstone-Dolomarl)*: (**a**) Bedded dolostone composed of dark-coloured dolarenite and light-coloured dolomicrite with a crumbled and wrinkled structure apparently representing flat-laminated stromatolites; note that some apparent stomatolitic dolostone occurs as small-scale domed beds (*red arrows*), whereas the dolarenite adjacent to it shows in situ brecciation (*yellow arrows*). (**b**) Wavy-laminated dolostone with dismembered laminae of black mudstone; note the intense desiccation modifying primary bedding. (**c**) Thick-bedded dolostone gritstone composed of beige beds of gritstone draped by black, soft-sediment deformed mudstone and dolomarl. (**d**) Bedded dolostone gritstone; note the arrowed bed shows a grading from small-pebble dolostone conglomerate into dolarenite

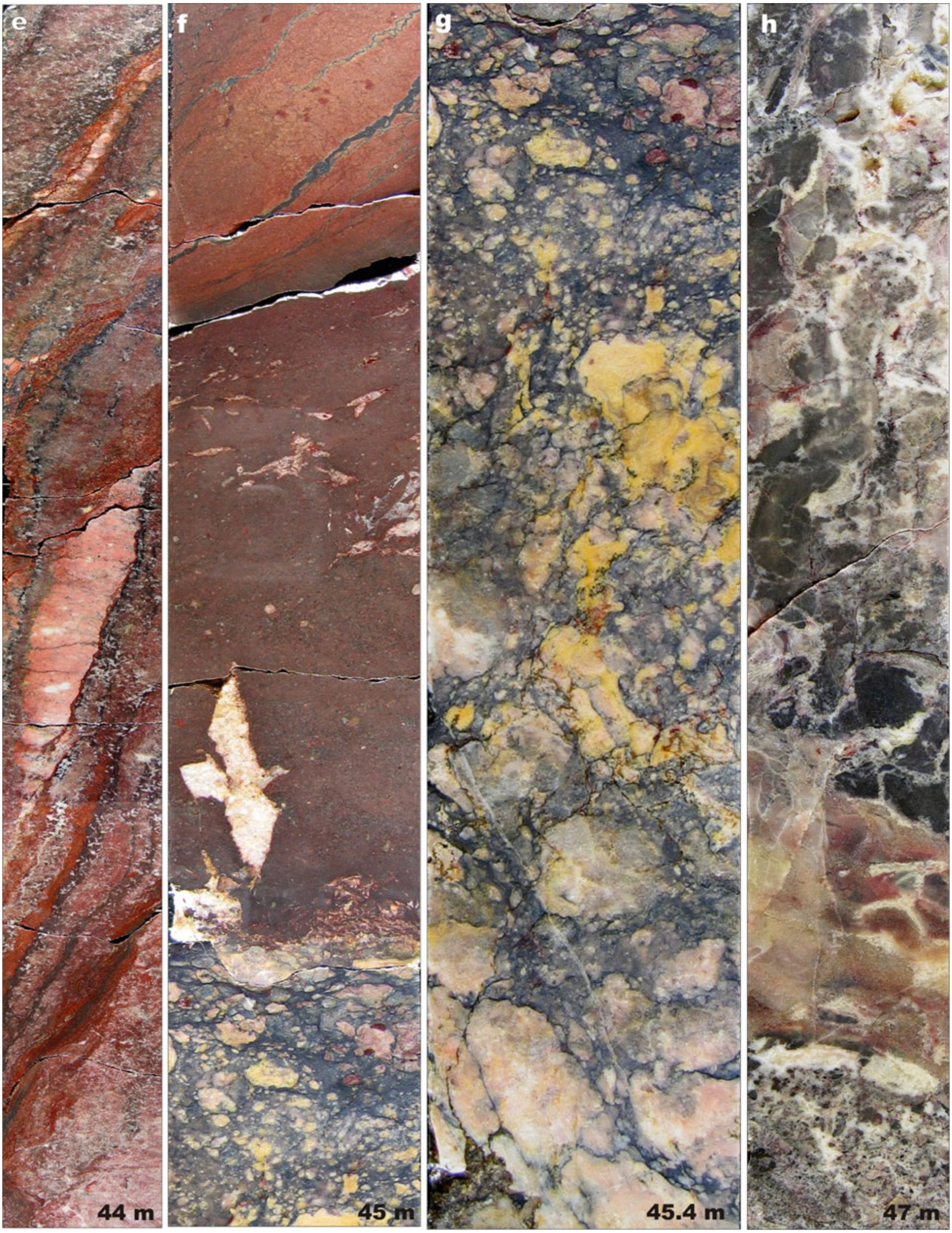

Fig. 6.97 (continued) (**e**) Bedded, dolomite-cemented sandstone with a lens of pale pink dolostone; note that some sandstone beds have dark-coloured drapes. (**f**) Mudstone-supported dolorudite overlain by red-brown, non-bedded sandstone with small and large crystals and rosettes of dolomite-pseudomorphed gypsum; note that some show swallow-tail twin morphology. (**g**) Normally graded conglomerate composed of dolostone, quartz sandstone and vein-quartz clasts supported by clayey gritstone matrix. (**h**) Apparent dissolution-collapse breccia composed of variably dismembered layers of black, beige and grey dolostone cemented by white dolospar

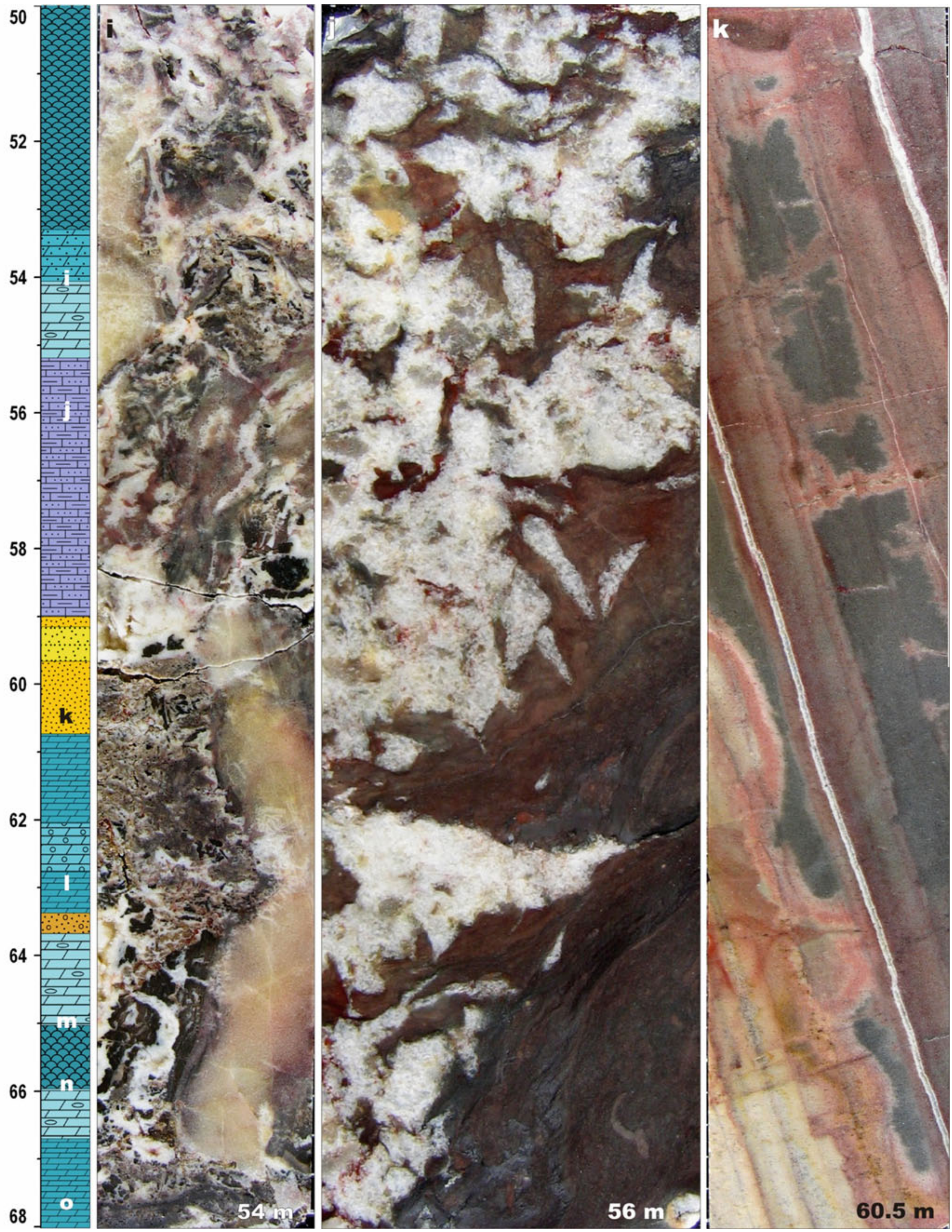

Fig. 6.97 (continued) (**i**) Core drilled sub-parallel to bedding, showing dolarenite-siltstone beds with crystal rosettes of sulphate partially replaced by white dolospar; note that primary bedding is obliterated by growth of sulphates. (**j**) Dark brown dolomarl with crystals of sulphates partially replaced by white quartz and dolospar. (**k**) Variegated, parallel-laminated sandstone; note that the primary dark colour was modified to brown and pale pink due to infiltration of oxidised fluids

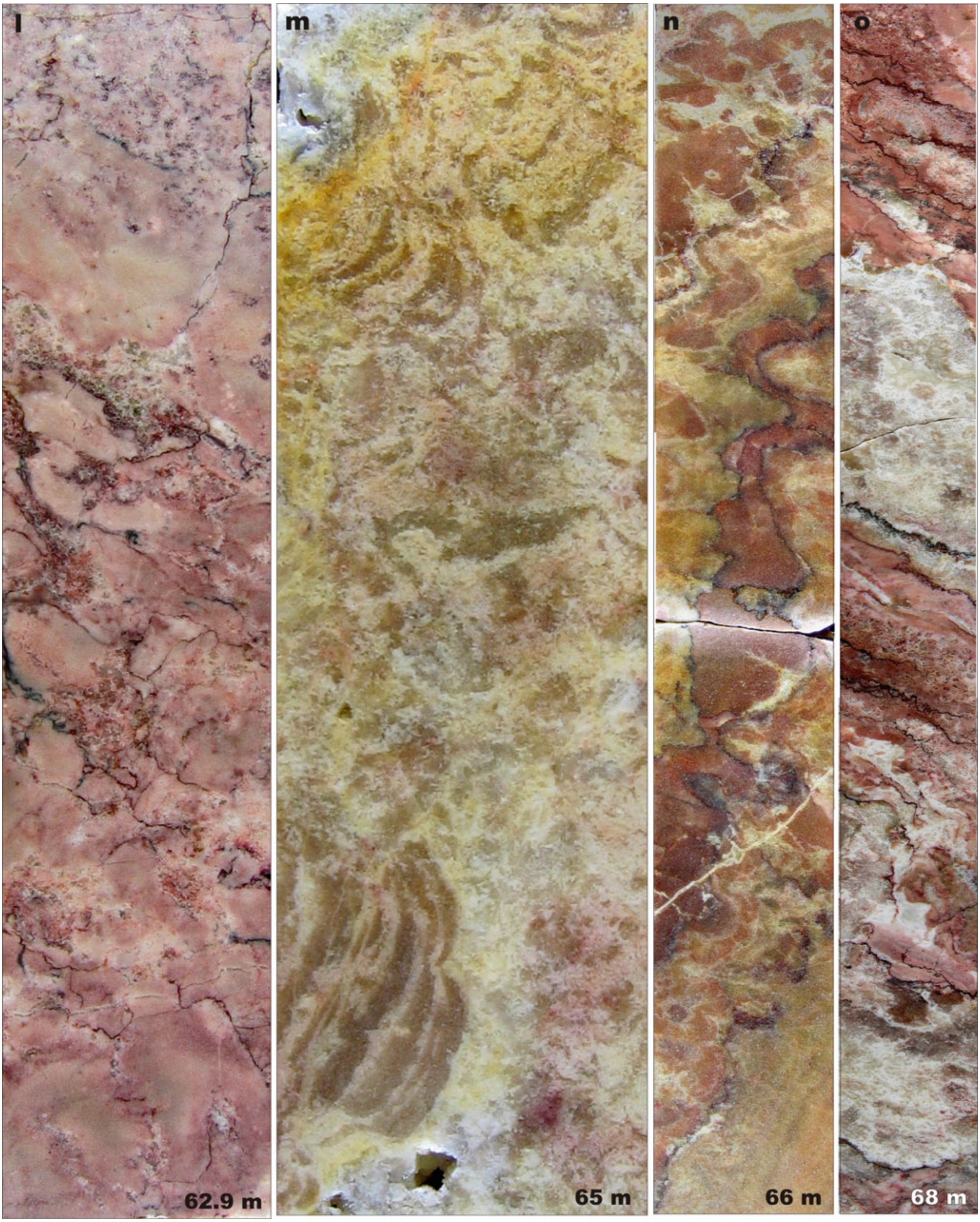

Fig. 6.97 (continued) (**l**) Beige, non-bedded micritic dolostone with syndepositional brecciation in the *middle* of the core. (**m**) Intensely recrystallised, over-turned columnar-layered stromatolites *Omachtenia sp*. (**n**) Intensely recrystallised columnar stromatolites *Omachtenia sp*. showing a variegated colour. (**o**) Variegated dolostone with wrinkled and irregular lensoidal bedding

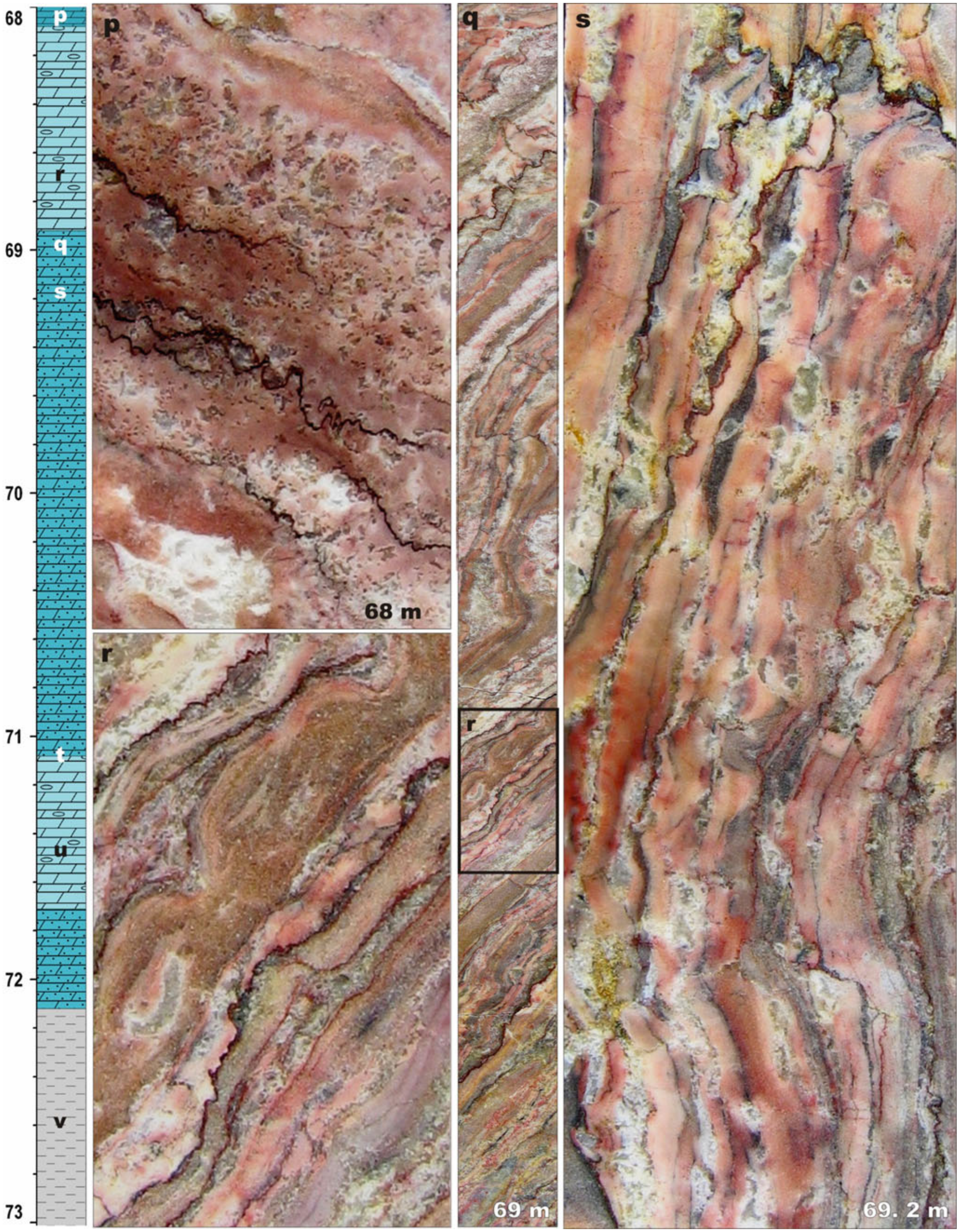

Fig. 6.97 (continued) (**p**) Irregularly bedded micritic dolostone with stylolites and quartz-pseudomorphed small crystals of sulphates. (**q**) Thin-bedded, variegated dolarenite with wavy, wrinkled lamination and soft-sediment deformation in the middle of the core. (**r**) Detailed view of wavy, wrinkled and domed lamination; the latter may represent small, cumulate stromatolite. (**s**) Details of wavy lamination in dolarenite; note the abundant voids (fenestrae?) filled with grey quartz and white dolospar

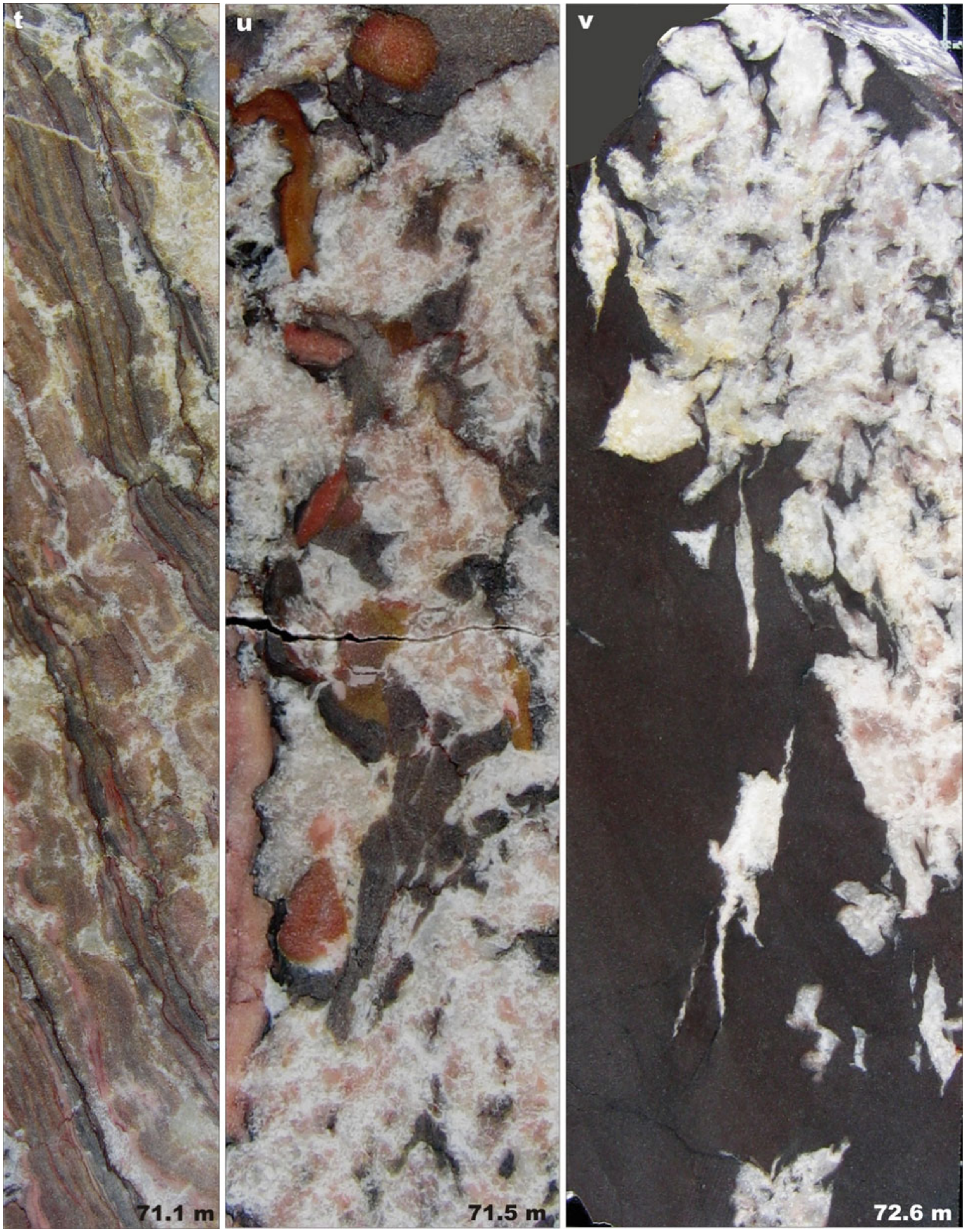

Fig. 6.97 (continued) (**t**) Interbedded beige dolostone and dark-coloured, laminated dolomarl-siltstone; note that the dolostone beds show an internal domed structure (stromatolite?) and intense dissolution joints and vugs filled with white dolospar and silica (**u**) Core drilled sub-parallel to bedding, showing dark-coloured dolarenite with rosettes and nodular masses of sulphates partially replaced by quartz and white dolospar; note that primary bedding was obliterated by growth of sulphates and the pale brown bed was dismembered into differently rotated fragments. *Member 8 (Siltstone-Sandstone):* (**v**) Dark-coloured, haematite-rich, muddy siltstone with gypsum rosette and solitary crystals partially replaced by white quartz and dolospar

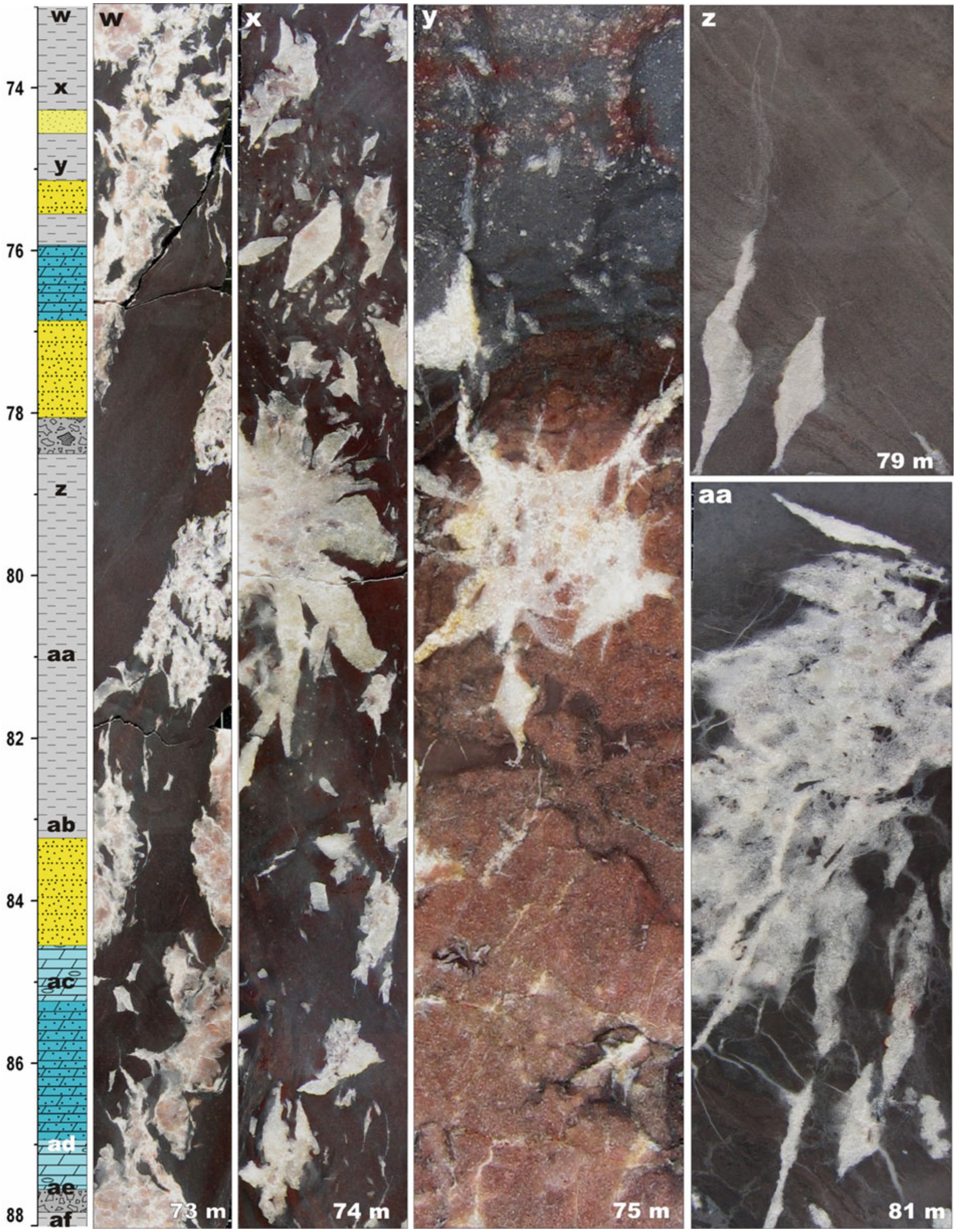

Fig. 6.97 (continued) (**w**) Indistinctly bedded, dark-coloured, haematite-rich, muddy siltstone with gypsum rosettes partially replaced by white quartz and dolospar; note that the rosettes were formed in three parallel bands emphasising primary bedding. (**x**) Dark-coloured, massive, muddy siltstone with rosette and crystals of gypsum partially replaced by white quartz and dolospar. (**y**) Pale brown dolomarl with large dolospar-pseudomorphed gypsum rosette overlain by dark-coloured siltstone with small gypsum crystals replaced by white dolospar. (**z**) Dark grey, laminated siltstone with two crystals of gypsum partially replaced by white dolospar. (**aa**) Dolospar-replaced gypsum rosette in dark-coloured siltstone

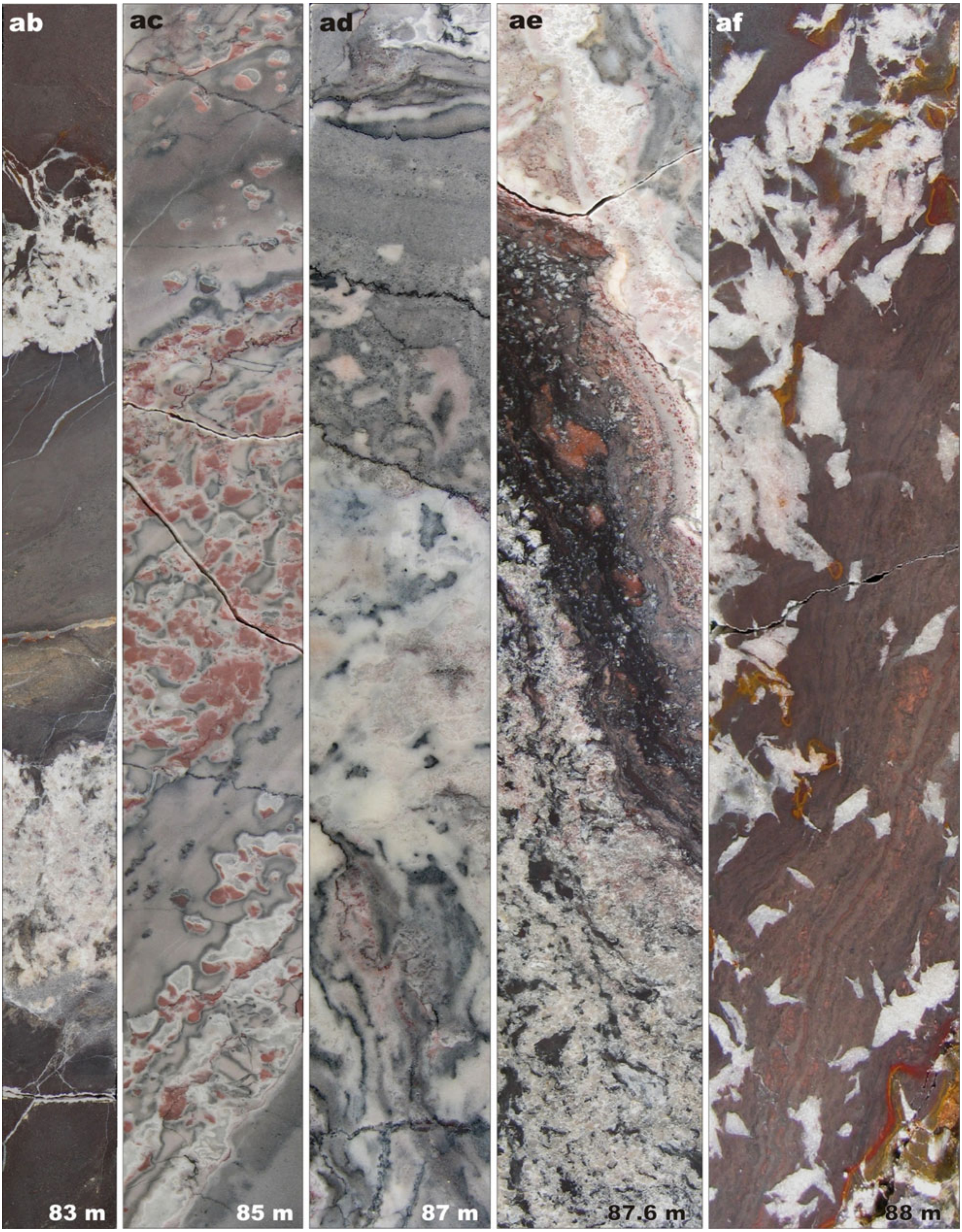

Fig. 6.97 (continued) (**ab**) Dark-coloured, massive, muddy siltstone with two nodular masses of sulphates partially replaced by white quartz and dolospar. (**ac**) Chicken-wire structure after pseudomorphed anhydrite in micritic dolostone. (**ad**) Quartz- and dolomite-pseudomorphed chicken-wire anhydrite and pale grey micritic dolostone. (**ae**) Dolomite-pseudomorphed dense cluster of gypsum crystals in dark-coloured dolomarl overlain by pale grey dolomicritic dolostone with white nodular masses of sulphates replaced by white dolospar. (**af**) Brown, laminate siltstone with abundant gypsum crystals partially replaced by white dolospar

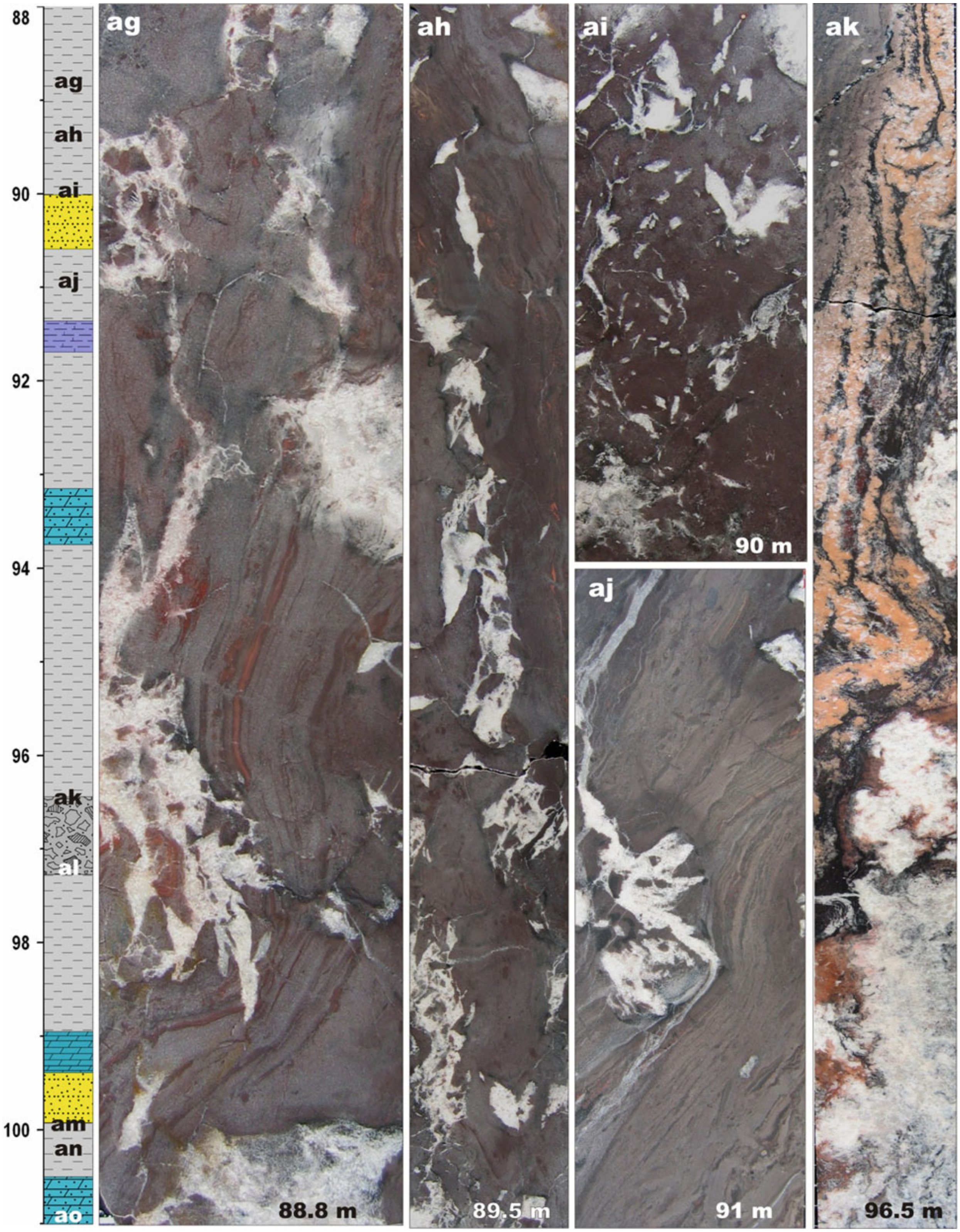

Fig. 6.97 (continued) (**ag**) Dolospar-pseudomorphed gypsum crystals and nodules in laminated siltstone; note how the growth of sulphate rosettes deformed primary lamination. (**ah**) Bedding-parallel bands with gypsum crystals and clusters in indistinctly bedded, muddy siltstone. (**ai**) Dark-coloured, massive, muddy siltstone with different-sized crystals of dolospar-pseudomorphed gypsum. (**aj**) Dolospar-pseudomorphed gypsum rosette modifying lamination in siltstone. (**ak**) Core drilled sub-parallel to bedding showing siltstone with white nodular masses of dolospar-pseudomorphed sulphates and orange beds with enterolithic folding

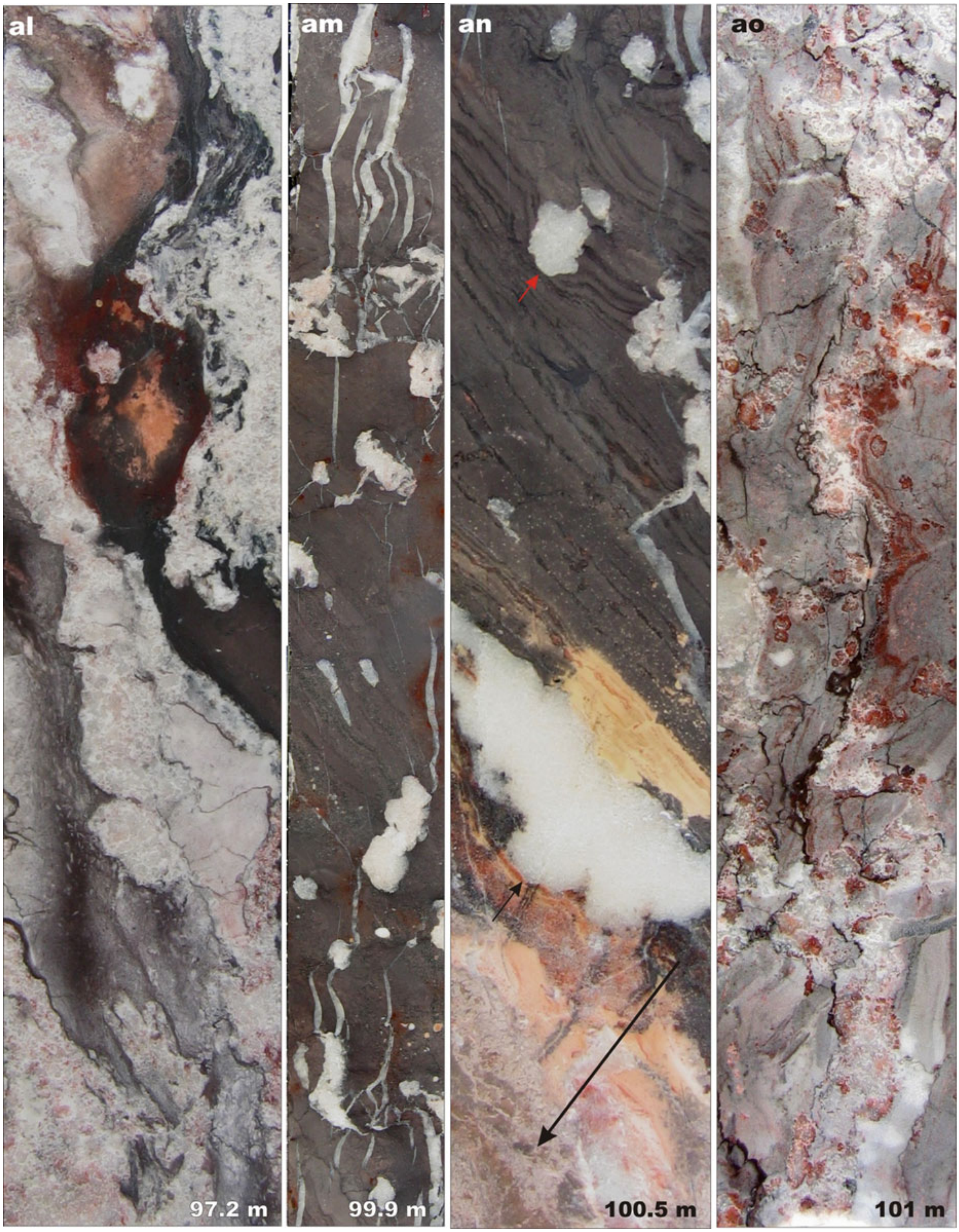

Fig. 6.97 (continued) (**al**) Nodular masses of quartz- and dolospar-pseudomorphed sulphates; note that primary bedding was completely obliterated by the growth of sulphate masses. (**am**) Crystals and nodules of dolospar-pseudomorphed sulphates in laminated, muddy siltstone; note the cleavage-parallel, dolospar-filled cracks extending from sulphate nodules and crystals into host siltstone. (**an**) Over-turned (*large arrow* points to stratigraphic top), dark-coloured, laminated siltstone-mudstone with nodular sulphates partially replaced by white dolospar overlain by beige, massive dolostone; growth of the small, spherical nodule (*red arrow*) deformed laminate whereas the large nodule grew upwards from a flat base (*black arrow*). (**ao**) Pale grey dolarenite whose primary structure was severely modified by growth of sulphates; the latter were replaced by white dolospar

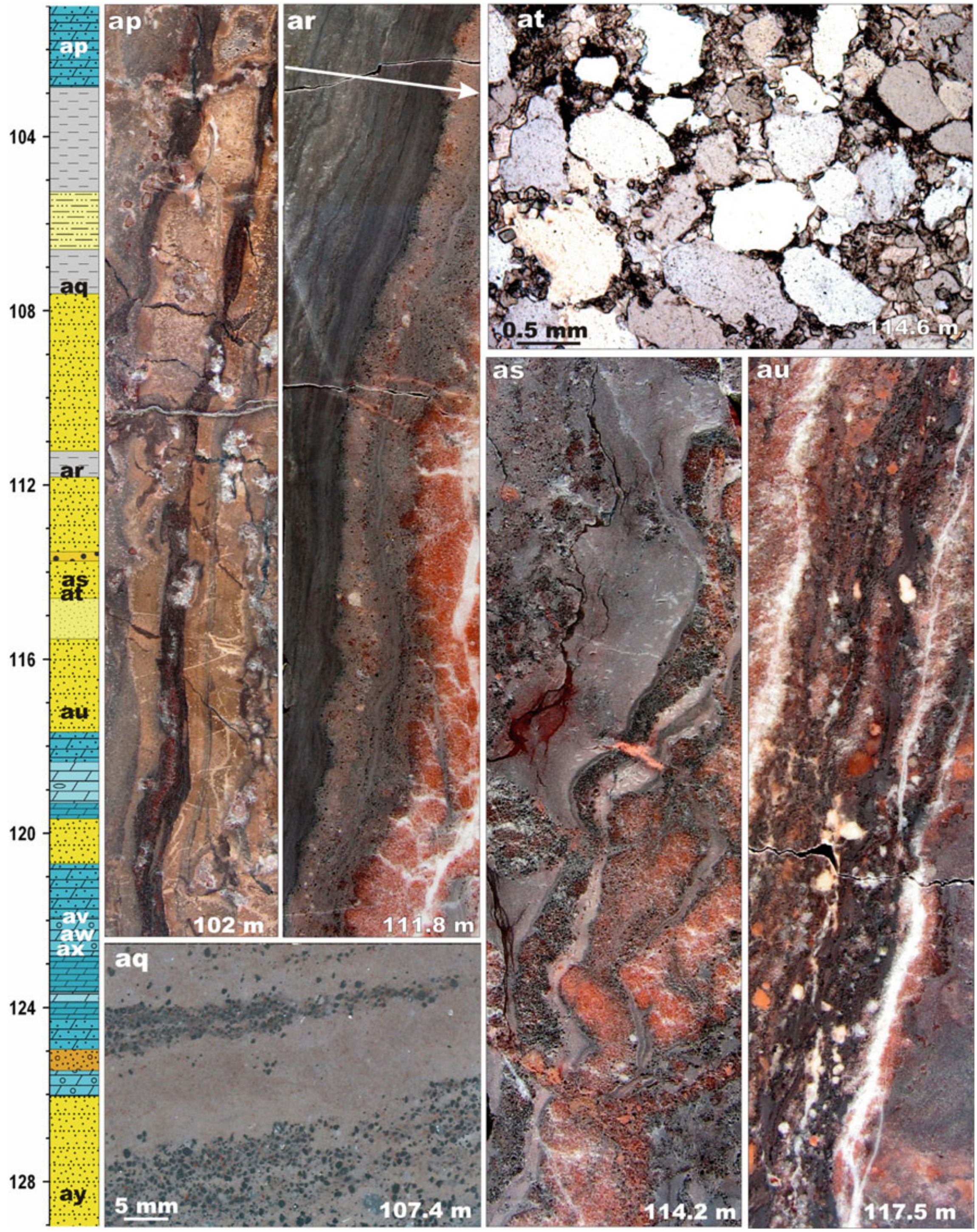

Fig. 6.97 (continued) (**ap**) Dolarenite-siltstone (dark-coloured) rhythmic bedding; note the wavy and buckled bedding planes and dolospar-replaced sulphate nodules. (**aq**) Scanned polished thin section showing sand particles (*grey*) in a pale pink siltstone matrix; quartz grains are well rounded and sorted. *Member 7 (Sandstone-Dolostone)*: (**ar**) Overturned section drilled sub-parallel to bedding (*large arrow* indicates stratigraphic top), showing dark-coloured, laminated siltstone overlain by coarse-grained sandstone grading into laminated siltstone covered by red, desiccated dolomarl; note flaser bedding at the base of lower siltstone and wrinkled bedding plane below the sandstone. (**as**) Heterolithic, variegated bed composed of red sandstone, pale brown siltstone and thin laminae of black mudstone; note that the heterolithic rocks show soft-sediment deformation and buckling apparently associated with evaporation (mini-tepee). (**at**) Photomicrographs in transmitted, non-polarised light showing microstructure of sandstone; note the well-rounded and sorted grains of quartz (bright) and dolomite (pale grey) in dolomite-rich matrix. (**au**) Heterolithic, variegated bed composed of interbedded arkosic sandstone and gritty siltstone (dark-coloured)

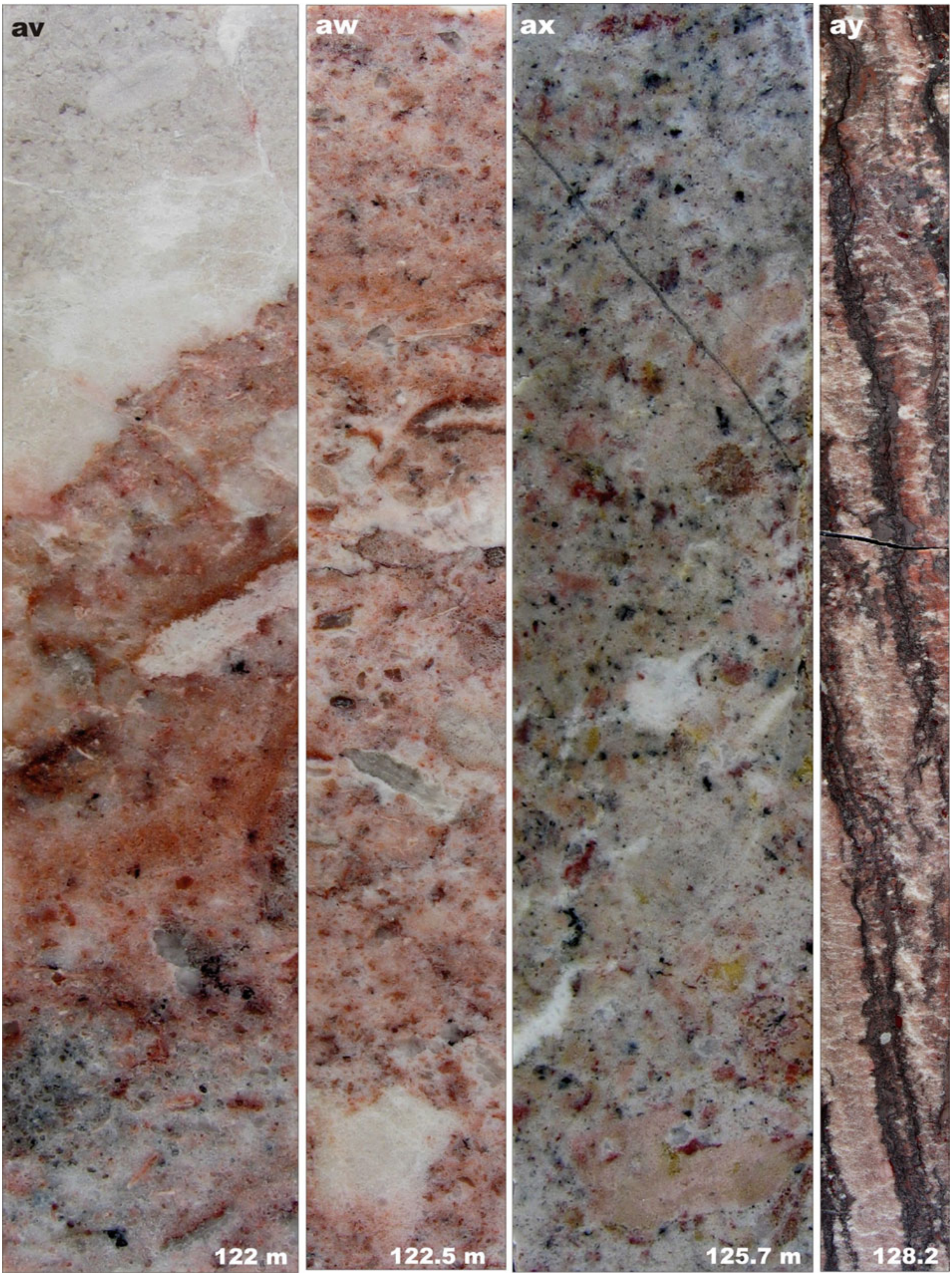

Fig. 6.97 (continued) (**av**) Thick-bedded dolorudite represented by pink and white varieties, both containing angular, unsorted clasts of quartz (grey) and dolostones (white, pale grey and pink) in a dolarenitic matrix. (**aw**) Pale pink, non-bedded dolorudite composed of angular, unsorted clasts of quartz (grey) and dolostones (white, pale grey and pink) in a dolarenitic matrix; the dolorudite shows indistinct normal grading. (**ax**) Variegated, massive dolorudite composed of clasts of red sandstone, pale pink dolarenite and small grains of quartz embedded into a dolarenitic matrix. (**ay**) Sandstone (pale pink)-mudstone (dark-coloured) rhythms with wavy and wrinkled bedding planes

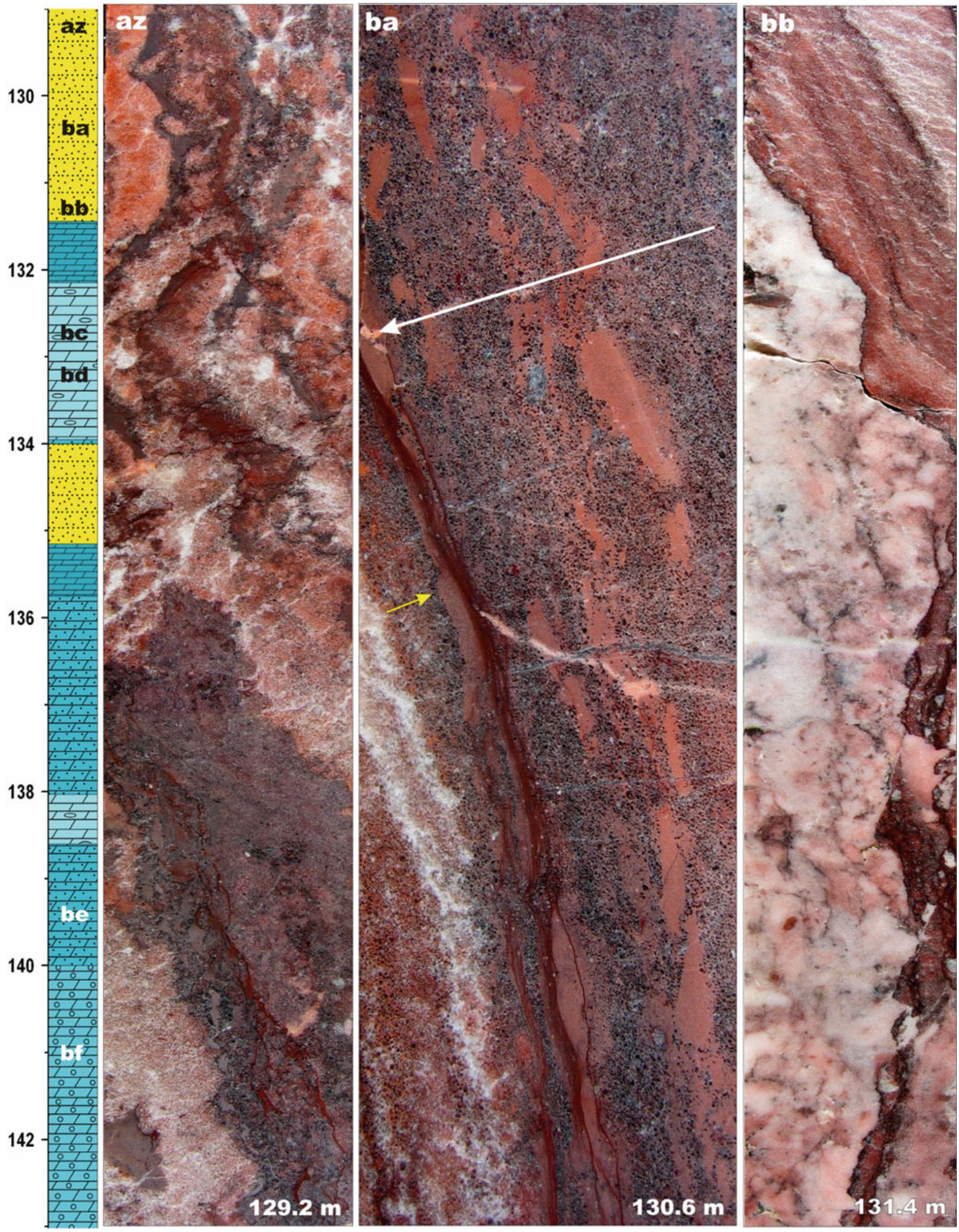

Fig. 6.97 (continued) (**az**) Interbedded pink, haematite-stained sandstone and brown siltstone showing soft-sediment deformation. (**ba**) Overturned section (*large arrow* indicates stratigraphic top) showing dark-coloured sandstone with outsized, angular rip-up clasts of pink dolostone with mudstone tops; note that the mudstone has ripple lamination and was partially eroded (*arrows*) by overlying sandstone. (**bb**) Light-coloured, variegated dolostone with an eroded or dissolved surface overlain by bedded sandstone

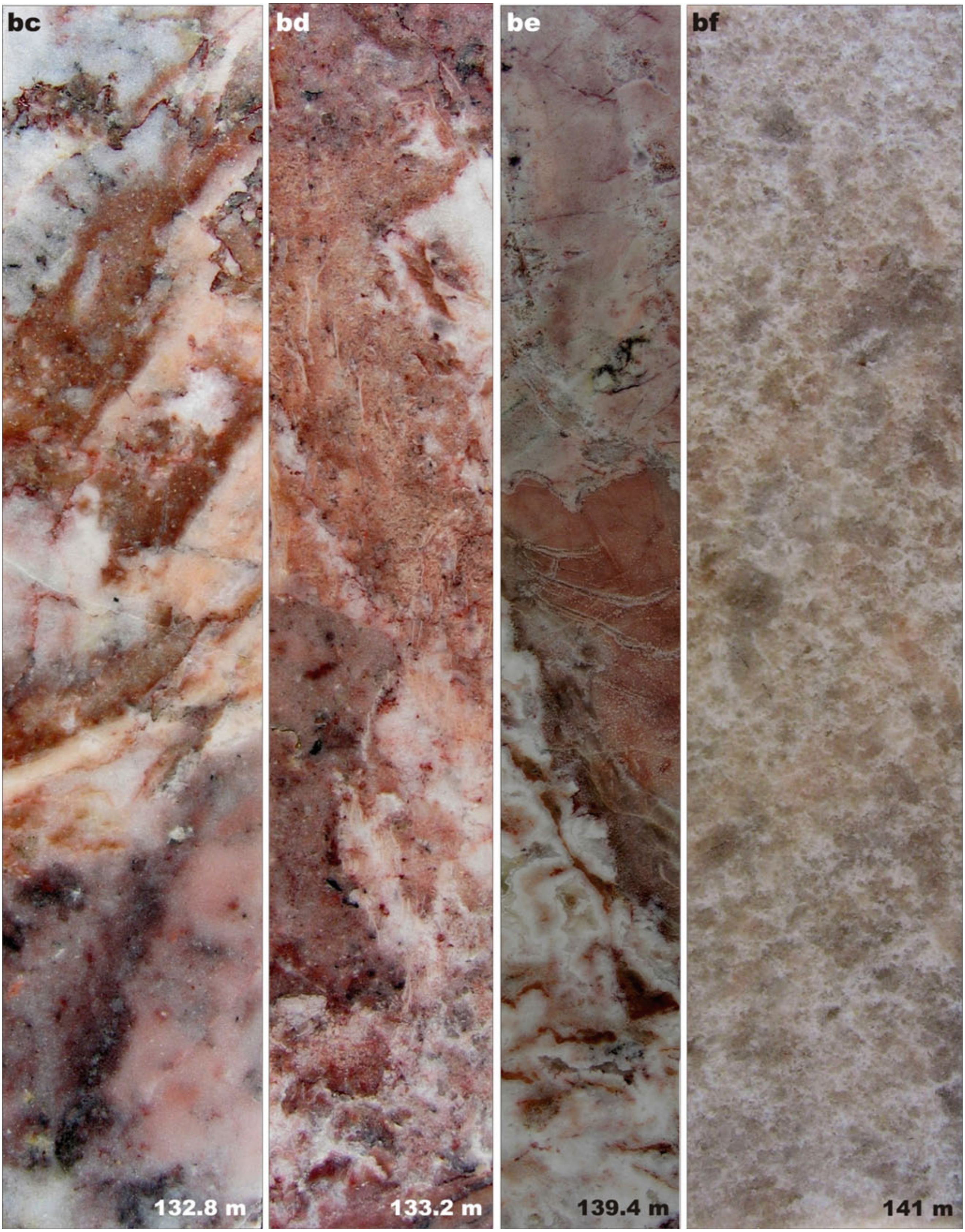

Fig. 6.97 (continued) (**bc**, **bd**) Partially recrystallised dolostone breccias composed of unsorted, angular fragments of dolostone embedded in a dolarenite matrix. (**be**) White, massive, vuggy dolostone overlain by red dolarenite, and then, by buff massive dolarenite; note that the dissolution vugs in the white dolostone are filled with quartz, and that the vuggy dolostone and red dolarenite show eroded/dissolved surfaces. (**bf**) Recrystallised, pale buff dolorudite (dolostone gritstone) composed of rounded clasts of dolostone cemented by white dolospar

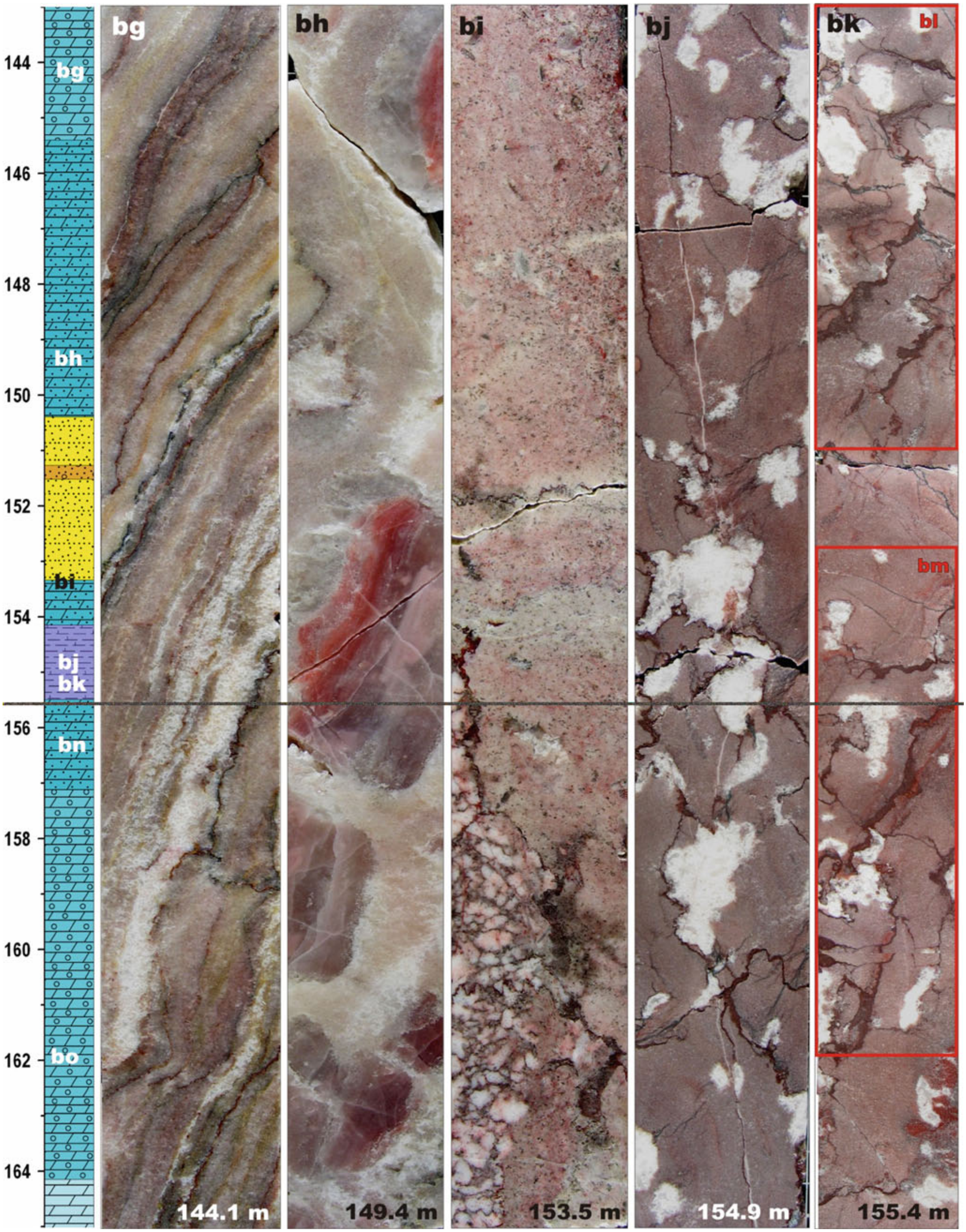

Fig. 6.97 (continued) (**bg**) Variegated dolarenite with irregular parallel and lensoidal bedding. (**bh**) Dismembered bed of pink-grey dolarenite embedded in white, massive dolostone. *Member 6 (Dolomarl-Dolostone-Siltstone-Sandstone):* (**bi**) Beige, massive dolarenite with a pocket of dolomitic gritstone. (**bj**, **bk**) Brown, non-bedded, nodular dolomarl with abundant sulphate nodules partially replaced by white quartz and dolospar

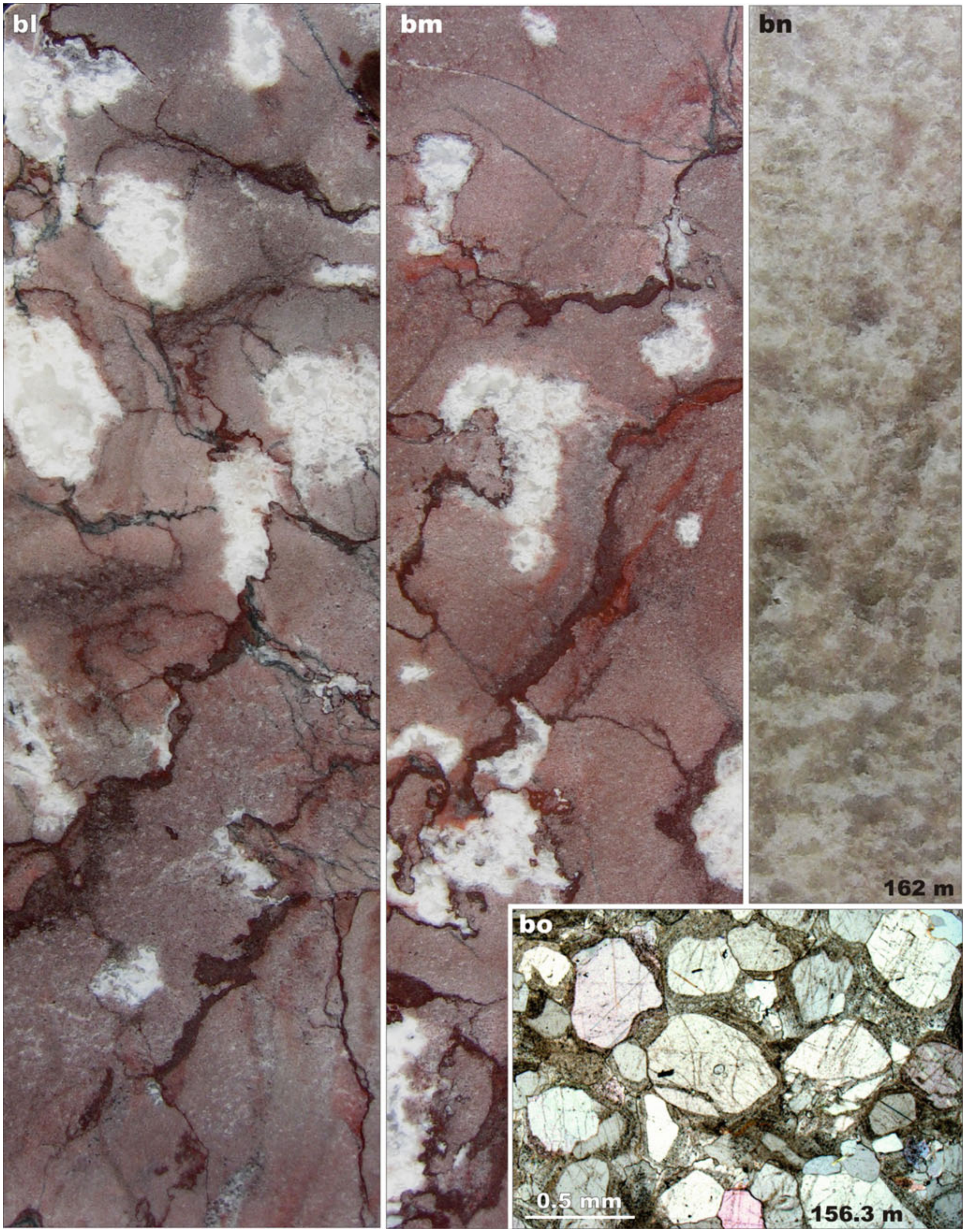

Fig. 6.97 (continued) (**bl**, **bm**) Detailed view of nodular dolomarl showing morphologies of dolomite-pseudomorphed sulphate nodules and their impact on the dolomarl structure. (**bn**) Partially recrystallised, white, massive dolarenite. (**bo**) Photomicrographs in transmitted non-polarised light of dolarenite composed of variably rounded dolostone clasts (bright) cemented by syntaxial, "dusty" dolospar (grey)

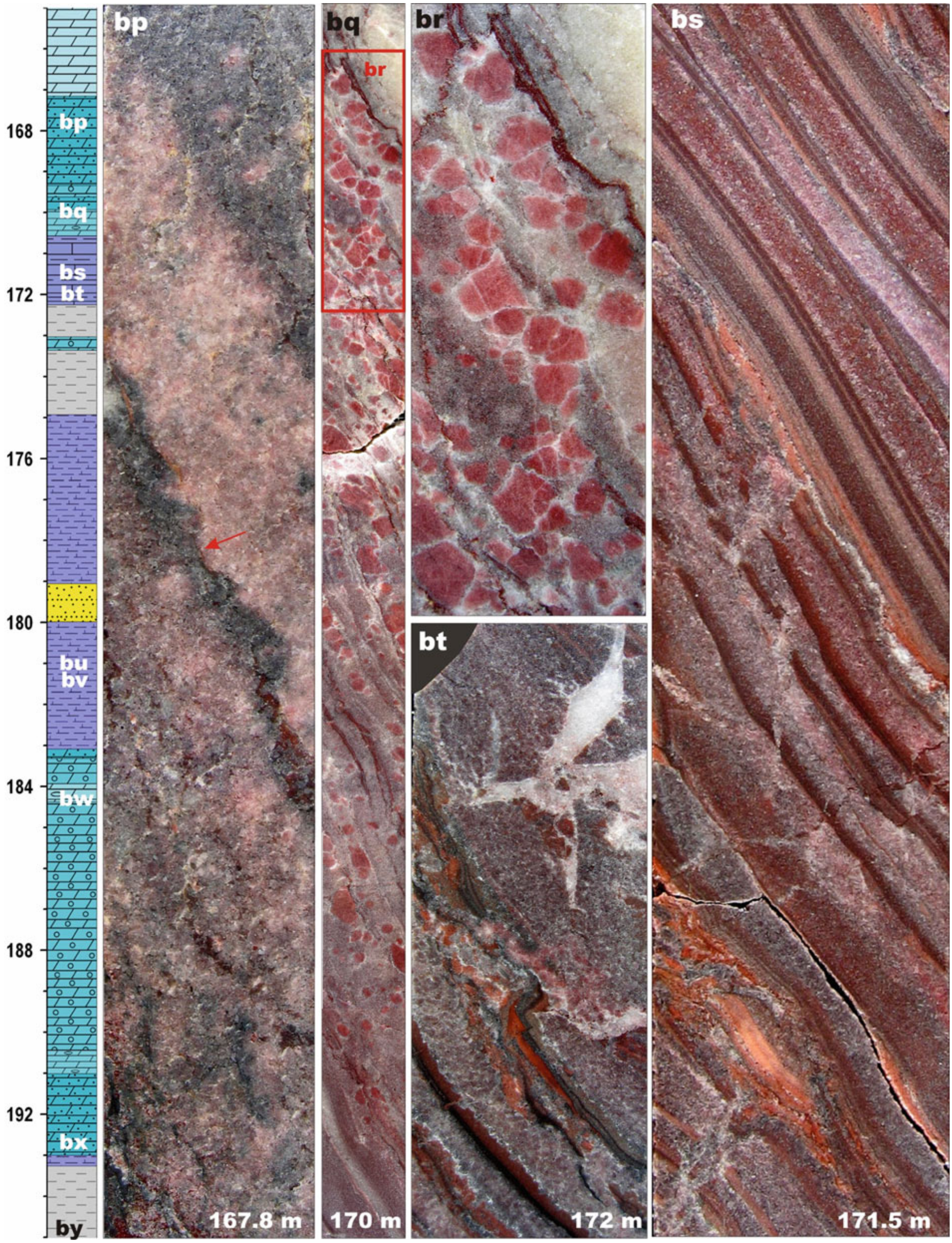

Fig. 6.97 (continued) (**bp**) Thick-bedded, variegated dolarenite; note the wavy/wrinkled bedding surface (*arrowed*). (**bq**) Thin-bedded, dolarenite with a few dark brown, thin mudstone laminae, and either in situ disintegrated beds or transported angular clasts composed of red dolospar. (**br**) Detailed view of red dolospar fragments embedded into fine-grained, bedded dolostone. (**bs**) Parallel-laminated, variegated dolostone-siltstone (dark brown) couplets; note that lamination in the lower part of the core was apparently affected by desiccation. (**bt**) Variegated dolostone-siltstone (dark brown, red and black) couplets; note the white quartz-pseudomorphed gypsum rosette in a thick dolostone bed

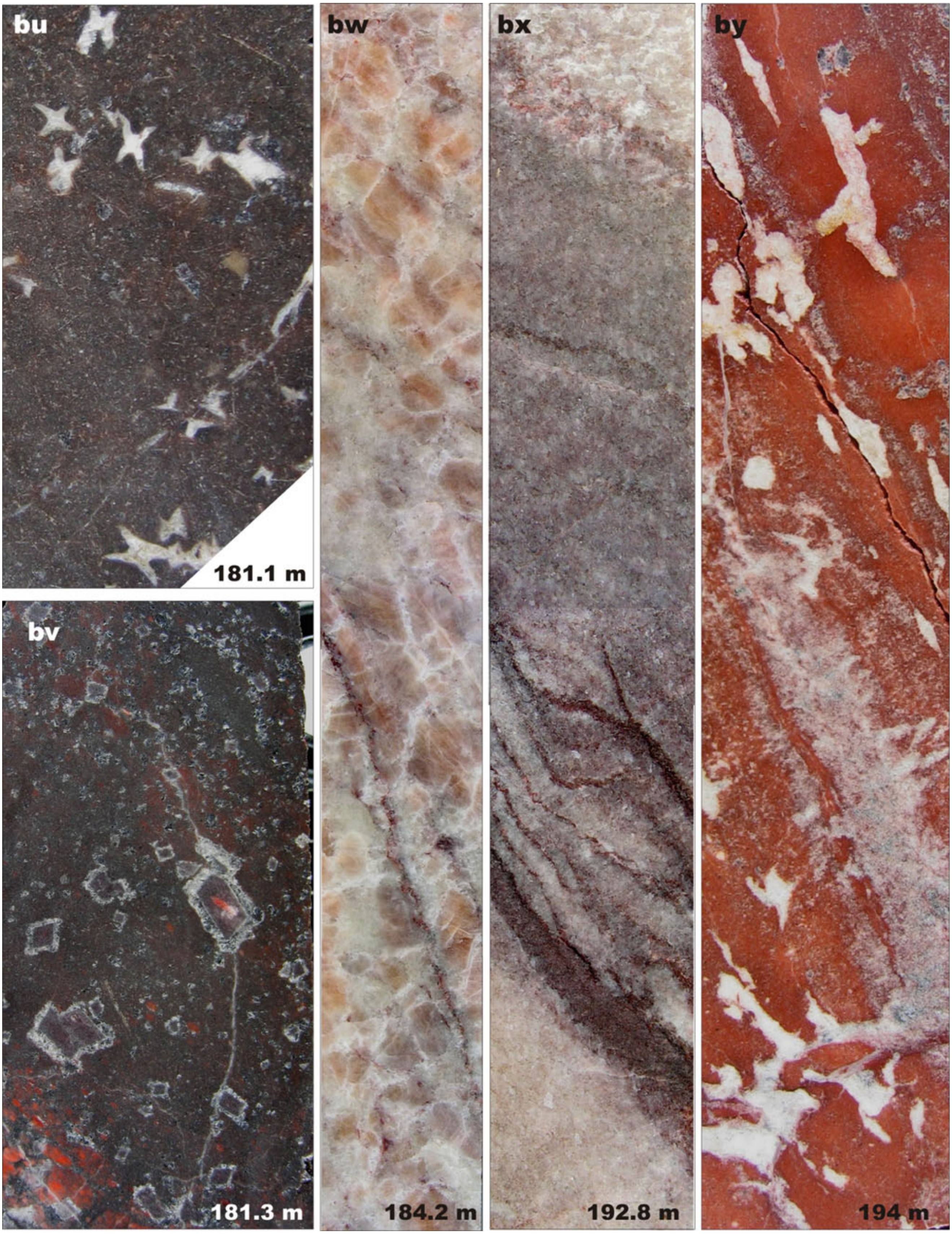

Fig. 6.97 (continued) (**bu**) Massive dolomarl with twins of halite (?) crystals pseudomorphed by dolospar. (**bv**) Massive dolomarl with casts of halite crystals. (**bw**) Recrystallised dolorudite composed of beige, large dolomite crystals cemented by white dolospar; dolomite-pseudomorphed crystalline halite or anhydrite is an alternative interpretation. (**bx**) Thick-bedded, white and grey dolarenite with interbeds of brown siltstone. (**by**) Red, bedded siltstone with nodules and crystals of sulphates partially replaced by white dolospar

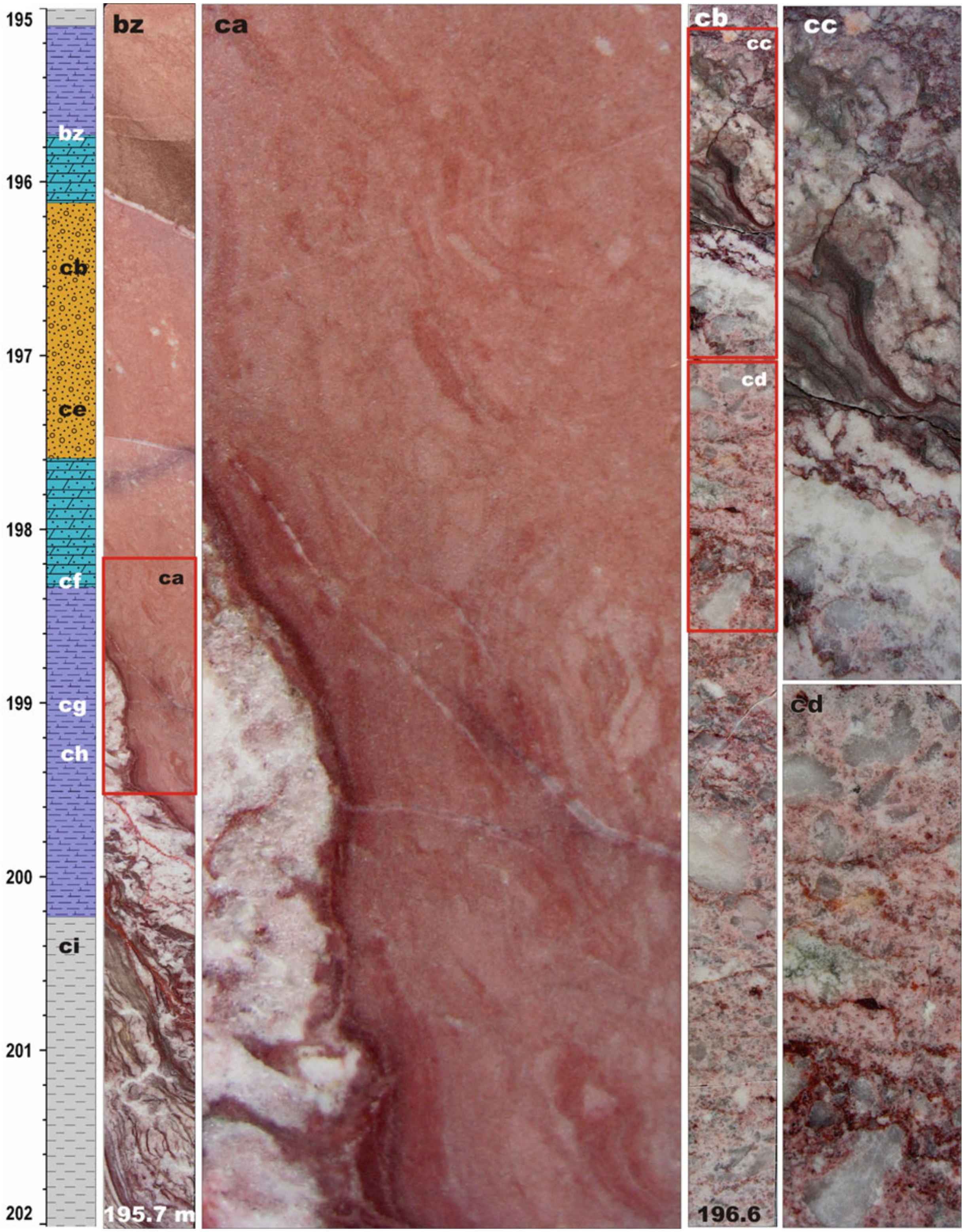

Fig. 6.97 (continued) (**bz**) Pale pink dolorudite overlying pale brown dolomarl with dolomite-pseudomorphed sulphate crystals and nodules (white). (**ca**) Detailed view of the dolorudite composed of platy fragments of micritic dolostone; note that the underlying bed contains sulphates partially pseudomorphed by white dolospar. (**cb**) Massive, gritty conglomerate composed of unsorted, variably rounded clasts of dolarenite and vein quartz. (**cc**) Detailed view of soft-sediment deformed, dark-coloured, laminated siltstone within gritty conglomerate. (**cd**) Detailed view of unsorted, variably rounded vein-quartz clasts supported by dolarenite matrix

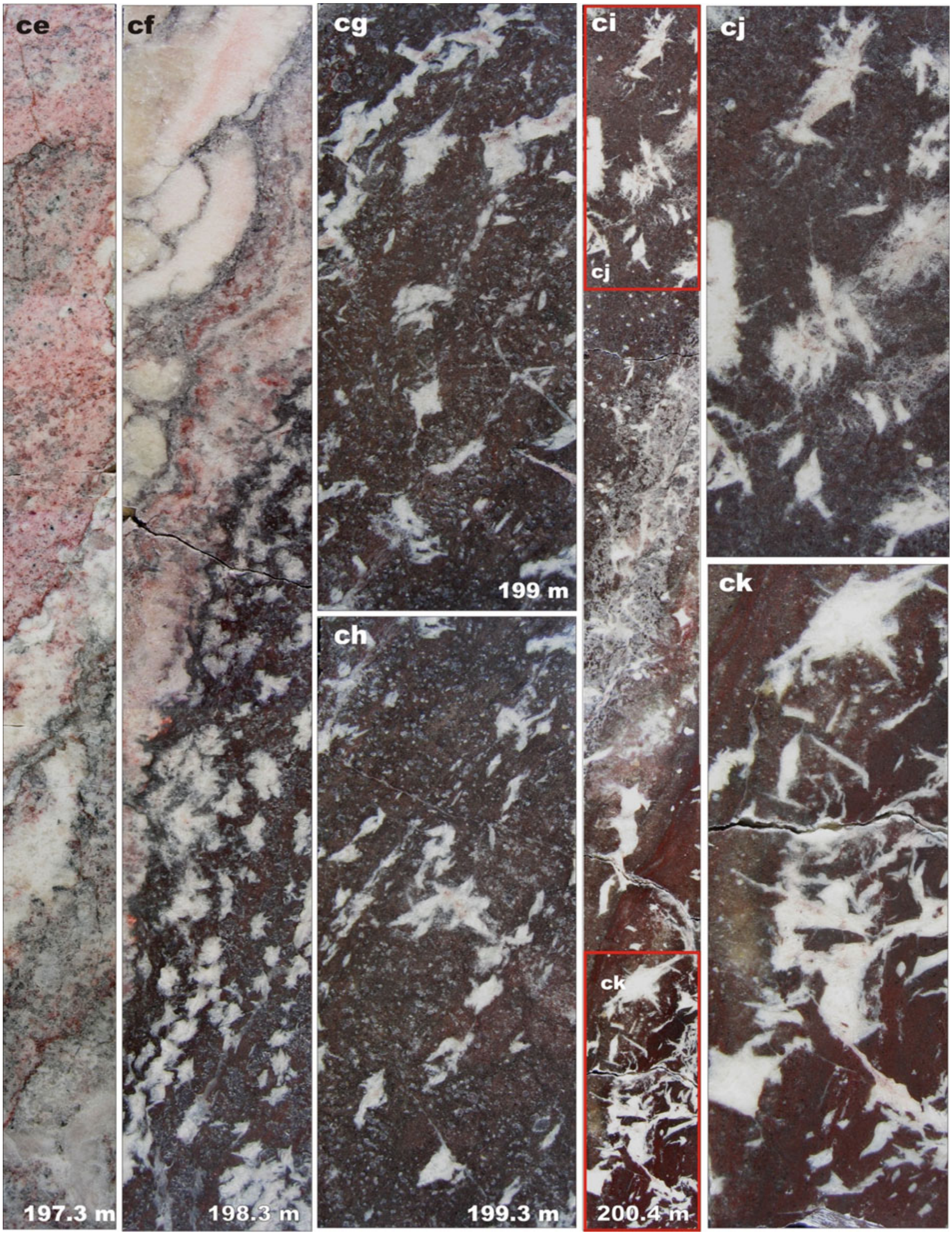

Fig. 6.97 (continued) (**ce**) Thick-bedded, variegated gritstone containing inclusions of white dolomite. (**cf**) Apparently over-turned section of white dolarenite with hummocky bedding overlain by clayey dolostone with red dolomite crystals, followed by dark-coloured marl with crystal rosettes of sulphates partially replaced by white dolospar. (**cg**, **ch)** Dark brown, massive dolomarl with gypsum rosettes replaced by white dolospar. (**ci**) Thick-bedded, brown siltstone with crystal rosettes of sulphates partially replaced by white dolospar; note that the adjacent beds differ in terms of the rosette size and their density. (**cj**, **ck**) Detailed view of morphologies of dolomite-replaced sulphate rosettes

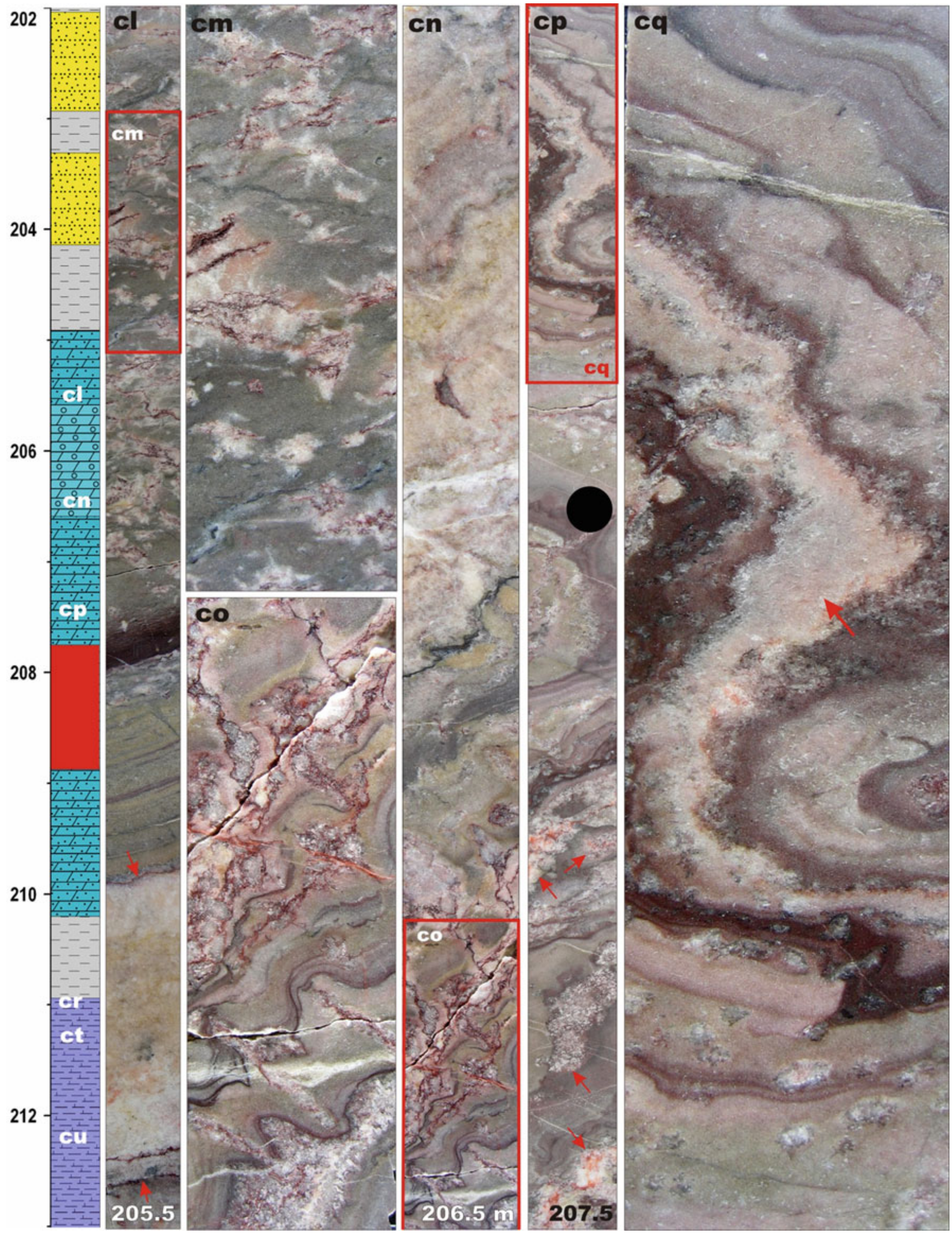

Fig. 6.97 (continued) *The Siltstone-Breccia-Dolostone-Magnesite member*: (**cl**) Parallel-bedded dolarenite overlain by dolostone, in which bedding was obliterated by diagenetic growth of probable sulphates; note that in the lower part of the core, a bed (*arrow*) of probable sulphate is now replaced by white and beige dolospar. (**cm**) Detailed view of grey-green dolostone with dolomite-replaced crystals of sulphate that obliterated primary bedding. (**cn**) Soft-sediment deformed, rhythmically bedded dolarenite-siltstone overlain by white and beige dolarenite. (**co**) Detailed view of soft-sediment deformed, laminated dolarenite; note that the lamination was modified by diagenetic growth of former sulphates replaced by white dolospar with granular texture. (**cp**) Soft-sediment deformed, rhythmically bedded dolarenite-siltstone; note the white lenses and clumps with a granular texture (*arrows*) apparently representing dolomite-replaced sulphates. (**cq**) Soft-sediment deformed, rhythmically bedded dolarenite-siltstone and probable sulphate (*arrow*); note the abundant quartz-pseudomorphed sulphate crystals in the lower part of the core

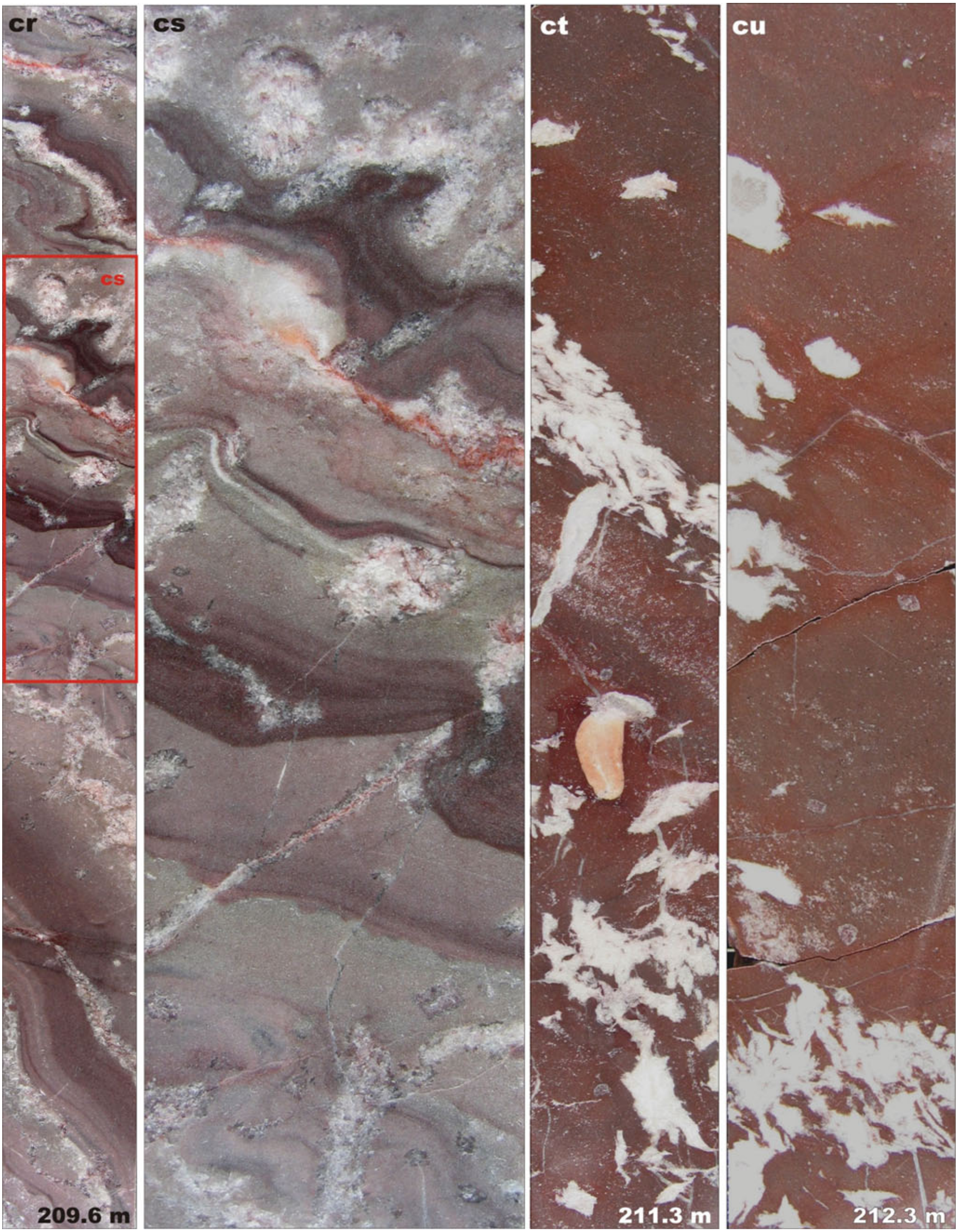

Fig. 6.97 (continued) (**cr**) Rhythmically bedded dolarenite-siltstone; note that fine lamination is disrupted by growth of former sulphate (white) in the form of nodules and crack infills. (**cs**) Detailed view of laminated, rhythmically bedded dolarenite-siltstone with dolospar-pseudomorphed sulphate nodules disrupting the lamination. (**ct**) Bedded, brown dolomarl with crystal rosettes of sulphate partially replaced by white dolospar. (**cu**) Massive, brown dolomarl with white nodules and crystal rosettes of sulphate partially replaced by white dolospar

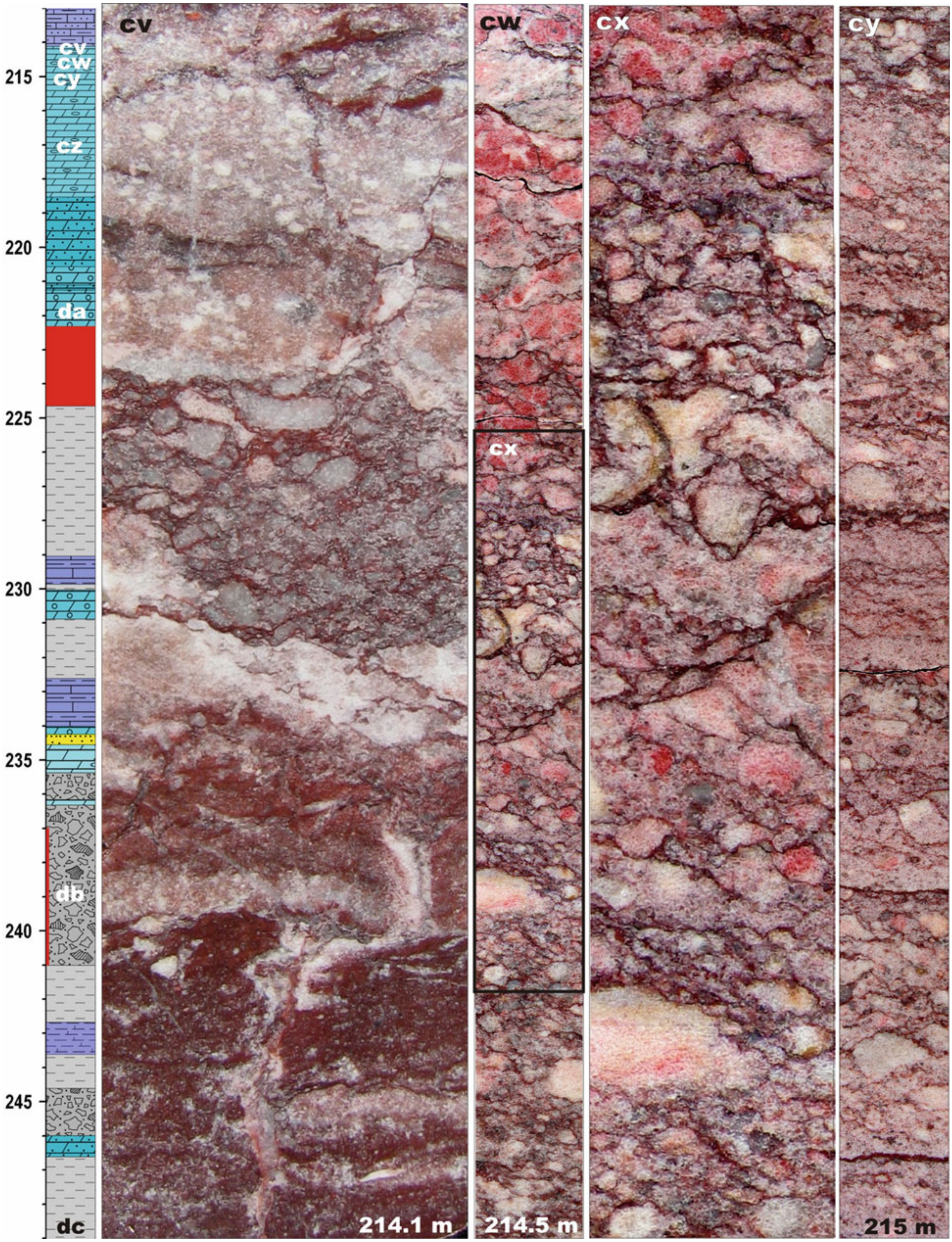

Fig. 6.97 (continued) (**cv**) Brown, clayey dolostone overlain by small-pebble conglomerate, which is capped by partially disintegrated dolostone bed. (**cw**) Massive conglomerate composed of tightly packed, poorly sorted, variably rounded clasts of dolostone; note that the clasts in the upper part show a fitted fabric and could be easily re-assembled into their original structure. (**cx**) Detailed view of clasts and matrix from dolostone conglomerate; clasts are mainly medium-grained dolostone with a few grains of grey quartz. (**cy**) Massive conglomerate composed of tightly packed, poorly sorted, variably rounded clasts of dolostone; dark brown, horizontal lines are thin stylolites.

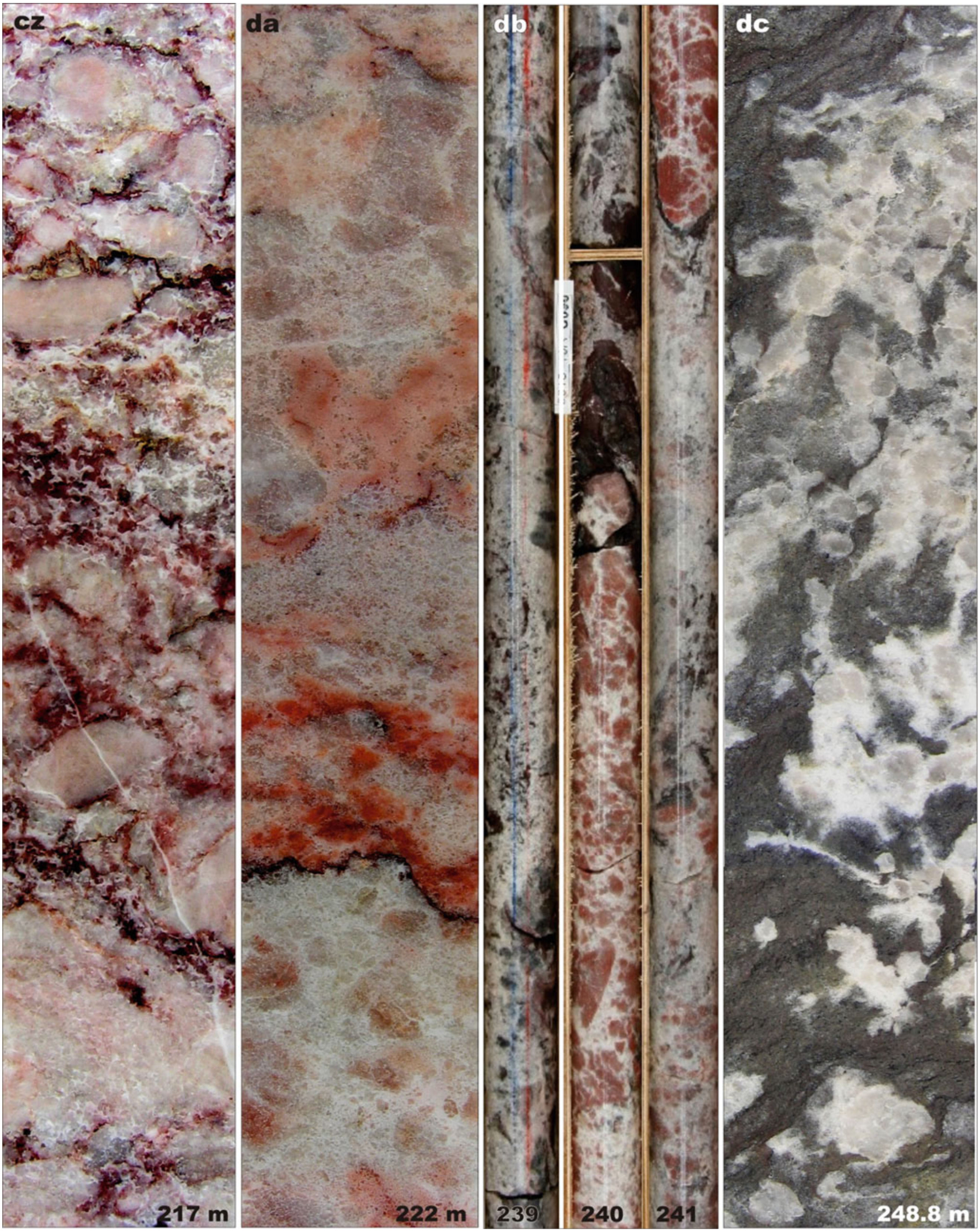

Fig. 6.97 (continued) (**cz**) Clast-supported dolostone conglomerate composed of rounded, unsorted fragments of beige, fine-grained dolostone in a brown, haematite-rich, clayey matrix. (**da**) Variegated dolostone conglomerate composed of rounded clasts of dolarenite, quartz sandstone in a dolarenitic matrix with syntaxial dolospar cement. (**db**) Continuous core showing a 3-m-thick interval of breccias composed of angular fragments of red and dark grey shale/siltstone supported by white dolospar cement. (**dc**) Dark grey siltstone with nodules, crystals and rosettes of sulphates partially pseudomorphed by white dolospar and beige quartz

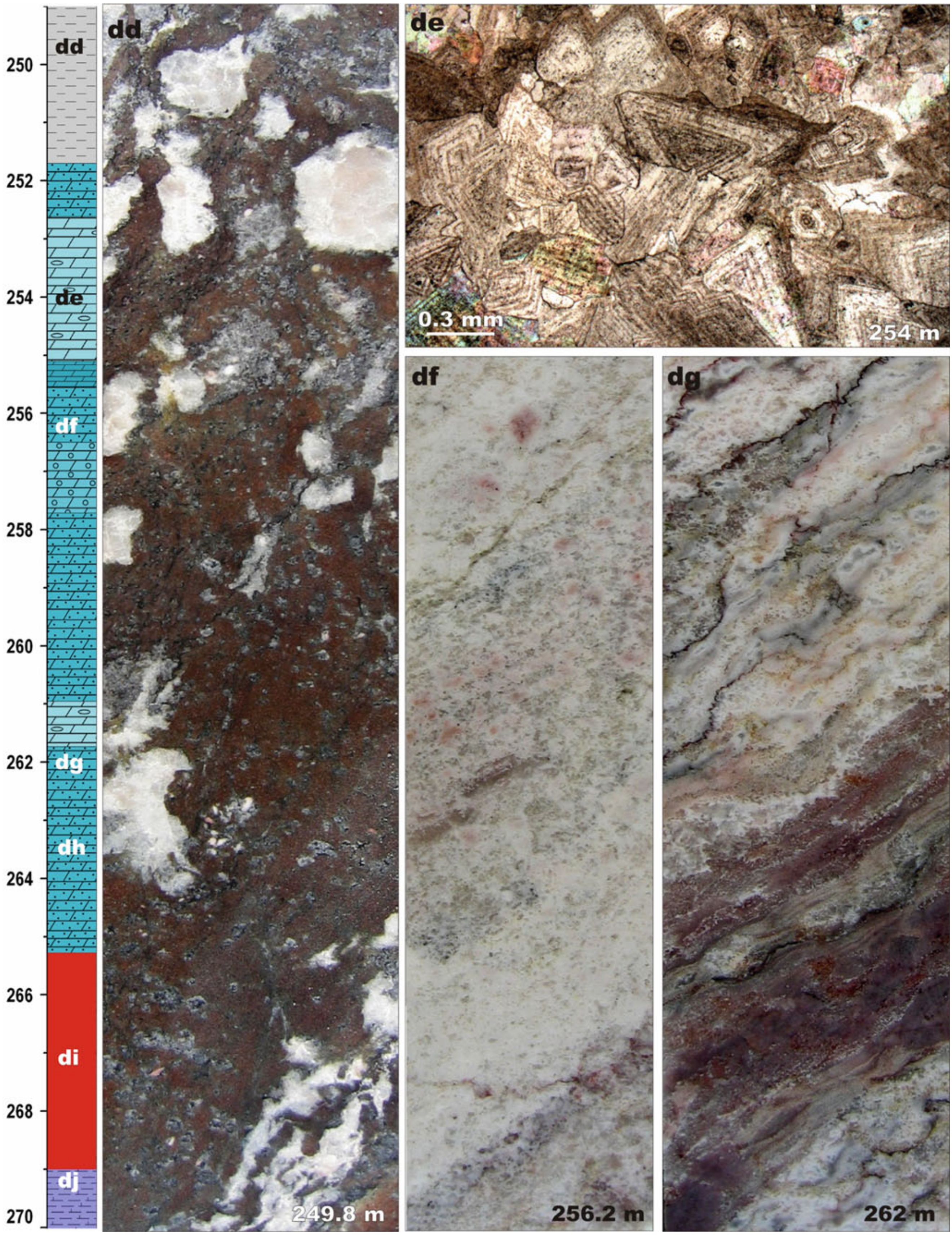

Fig. 6.97 (continued) (**dd**) Dark brown siltstone with a highly disrupted structure due to growth of sulphate nodules that are partially replaced by white quartz and dolospar. (**de**) Photomicrograph in transmitted, non-polarised light showing a drusy mosaic, dolospar, pore-filling cement. (**df**) Thick-bedded dolarenite. (**dg**) Variegated dolostone with wrinkled lamination and silica-cemented voids

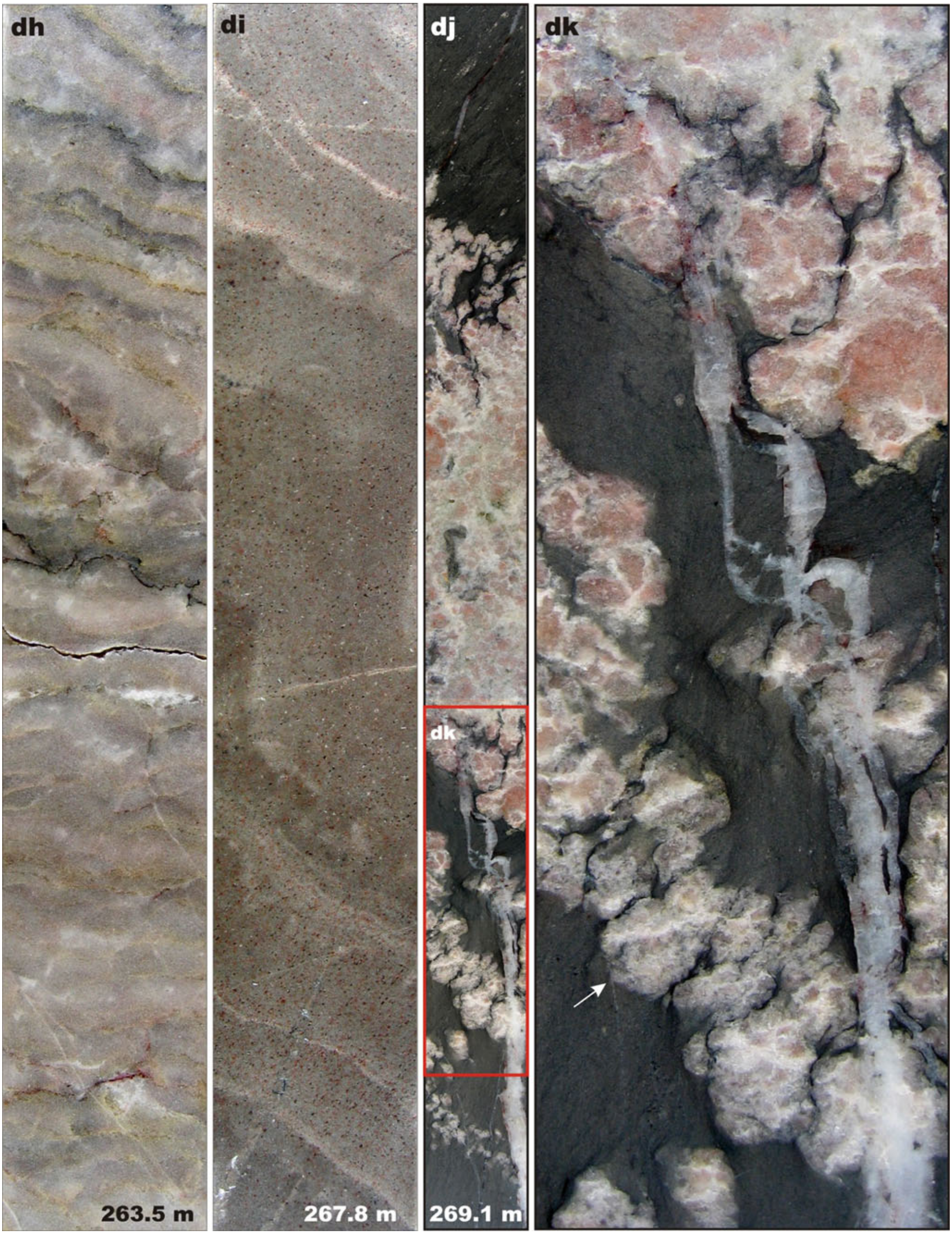

Fig. 6.97 (continued) (**dh**) Indistinctly bedded dolarenite with tectonically modified ripple bedding. (**di**) Thickly bedded, sandy, fine-grained magnesite. *The Dolomarl member:* (**dj**) Dark grey marl with quartz-pseudomorphed sulphates. (**dk**) Detailed view of quartz-pseudomorphed sulphates (white and pale pink) occurring as a series of coalesced nodules and as a layer with an enterolithic structure (*arrow*)

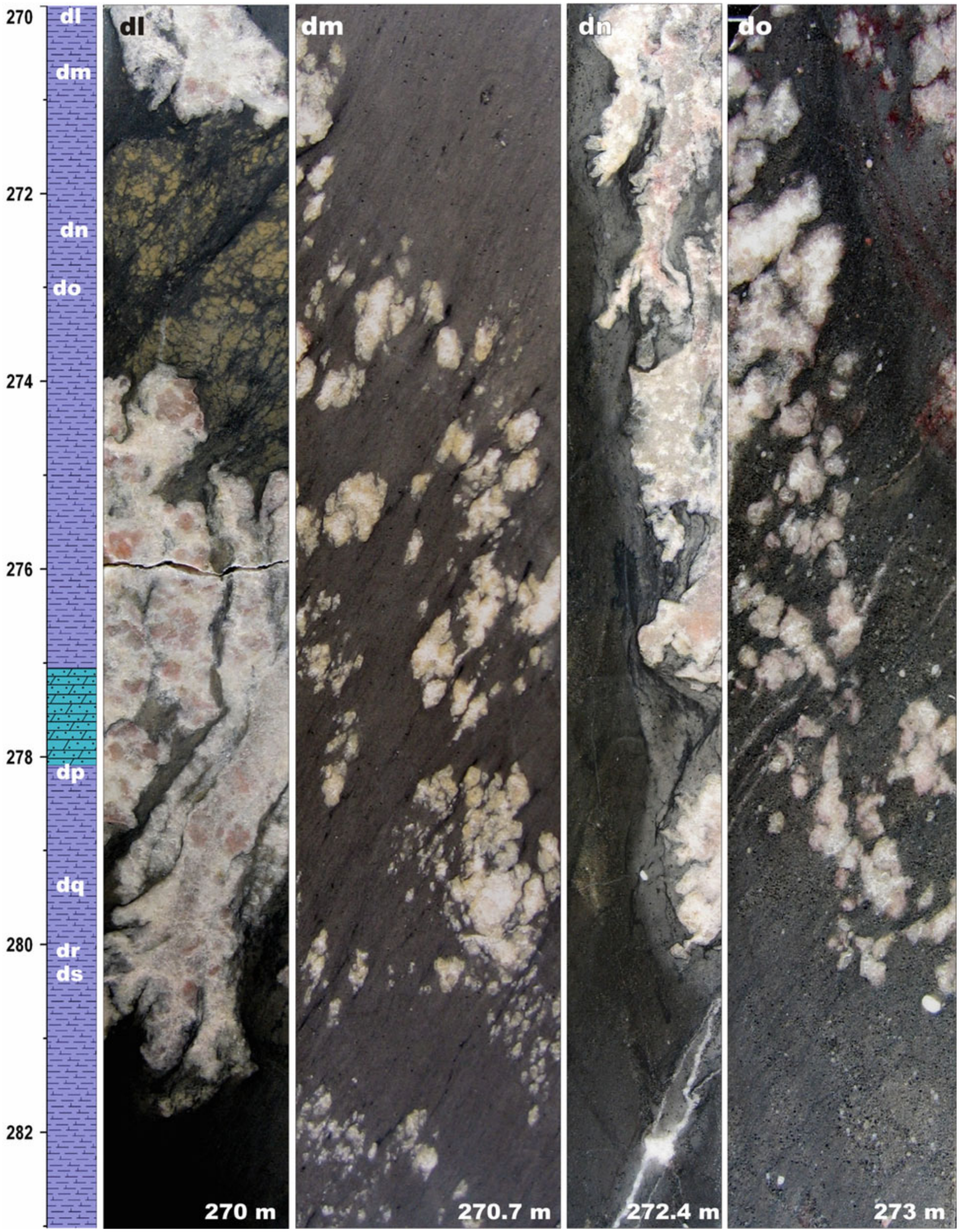

Fig. 6.97 (continued) (**dl**) Dolomarl with large nodular masses of sulphates partially replaced by white and pale pink quartz. (**dm**) Dark-grey, thinly laminated dolomarl with clusters of nodular sulphates partially replaced by white quartz and dolospar; note that primary bedding was intensely modified by cleavage. (**dn**) Bedding-parallel interval of coalesced sulphate crystals and nodules partially replaced by beige quartz and white dolospar; note that the hole was drilled subparallel to the bedding. (**do**) Bedding-parallel cluster of former sulphate nodules in dark grey, indistinctly bedded dolomarl; note that primary bedding was intensely modified by cleavage

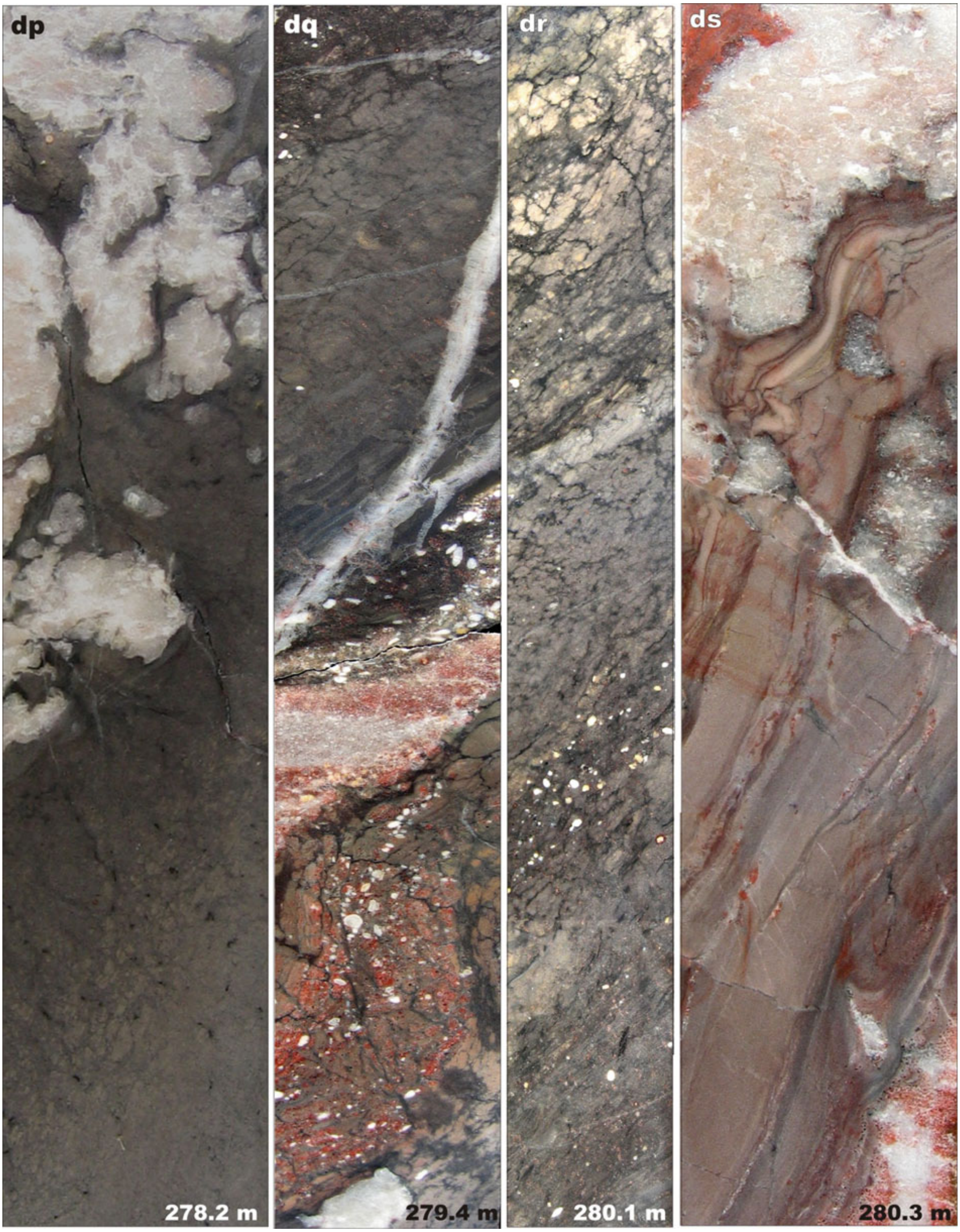

Fig. 6.97 (continued) (**dp**) Dark-coloured, massive dolomarl with former sulphate nodules and a layer showing an enterolithic structure. (**dq**) Variegated, desiccated dolomarl with granular fabrics and white, dolospar-pseudomorphed sulphate nodules overlain by grey, desiccated dolomarl with granular fabrics; the grey dolomarl is crosscut by a dolospar-filled vein, and the contact between the two beds is tectonically modified and recrystallised. (**dr**) Dolomarl with thin, parallel lamination (at *bottom*), which becomes up-section progressively affected by desiccation resulting in granular fabrics; the small bright spots are dolospar-pseudomorphed sulphate nodules. (**ds**) Pale brown, laminated dolomarl with dolospar-pseudomorphed nodule and crystals of sulphate; note that lamination was modified by growth of sulphates

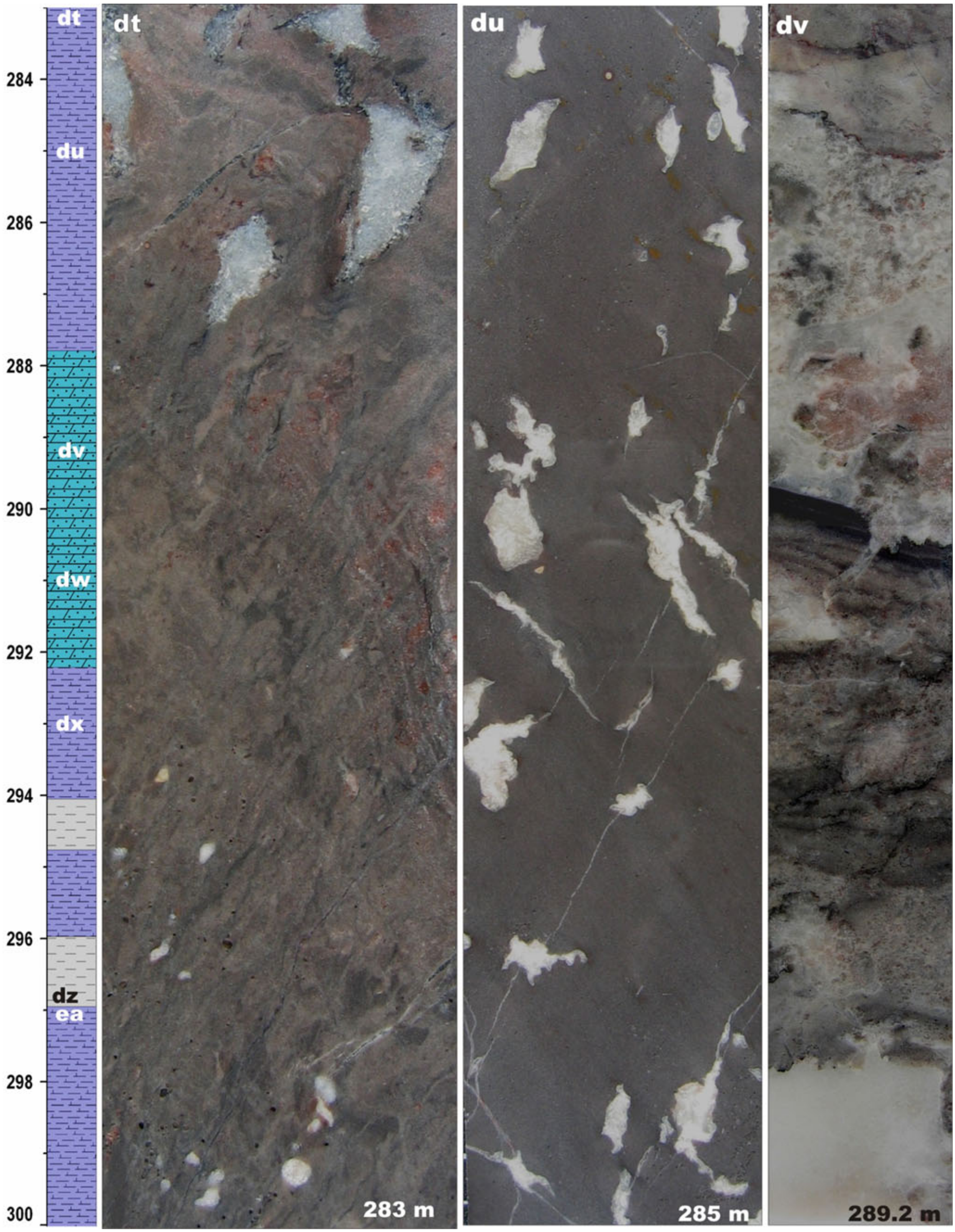

Fig. 6.97 (continued) (**dt**) Cleaved, dark-coloured, bedded dolomarl with sulphate crystals partially replaced by white quartz and dolospar; note that primary bedding was modified by cleavage. (**du**) Massive, grey-brown dolomarl with sulphate crystals partially replaced by white quartz and dolospar. (**dv**) Dolarenite with dark-coloured siltstone layer and a large sulphate nodule (at the bottom) partially replaced by white dolospar; note that bedding was disrupted by diagenetic growth of sulphates

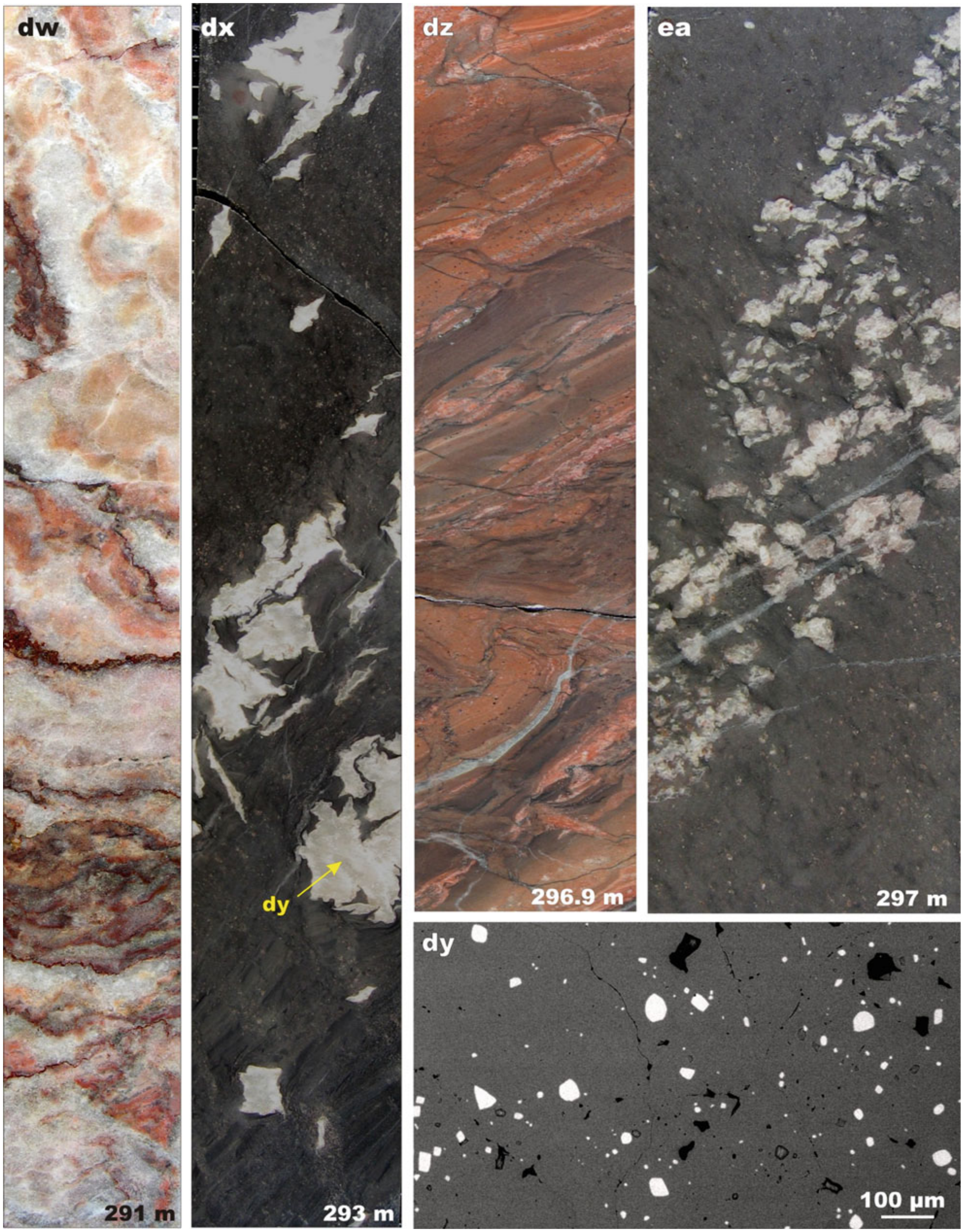

Fig. 6.97 (continued) (**dw**) Variegated dolarenite with highly disrupted bedding. (**dx**) Dark-coloured, laminated to massive dolomarl with crystals and crystal rosettes of sulphates partially replaced by white quartz. (**dy**) Back-scattered electron image of quartz-replaced sulphate rosettes shown in Fig. dx; the grey background mass is quartz, and the white spots are Ca-sulphate. (**dz**) Pink and brown siltstone with diagenetically and tectonically modified lamination. (**ea**) Dark-coloured, massive dolomarl with sulphate nodules and crystals partially replaced by white quartz and dolospar

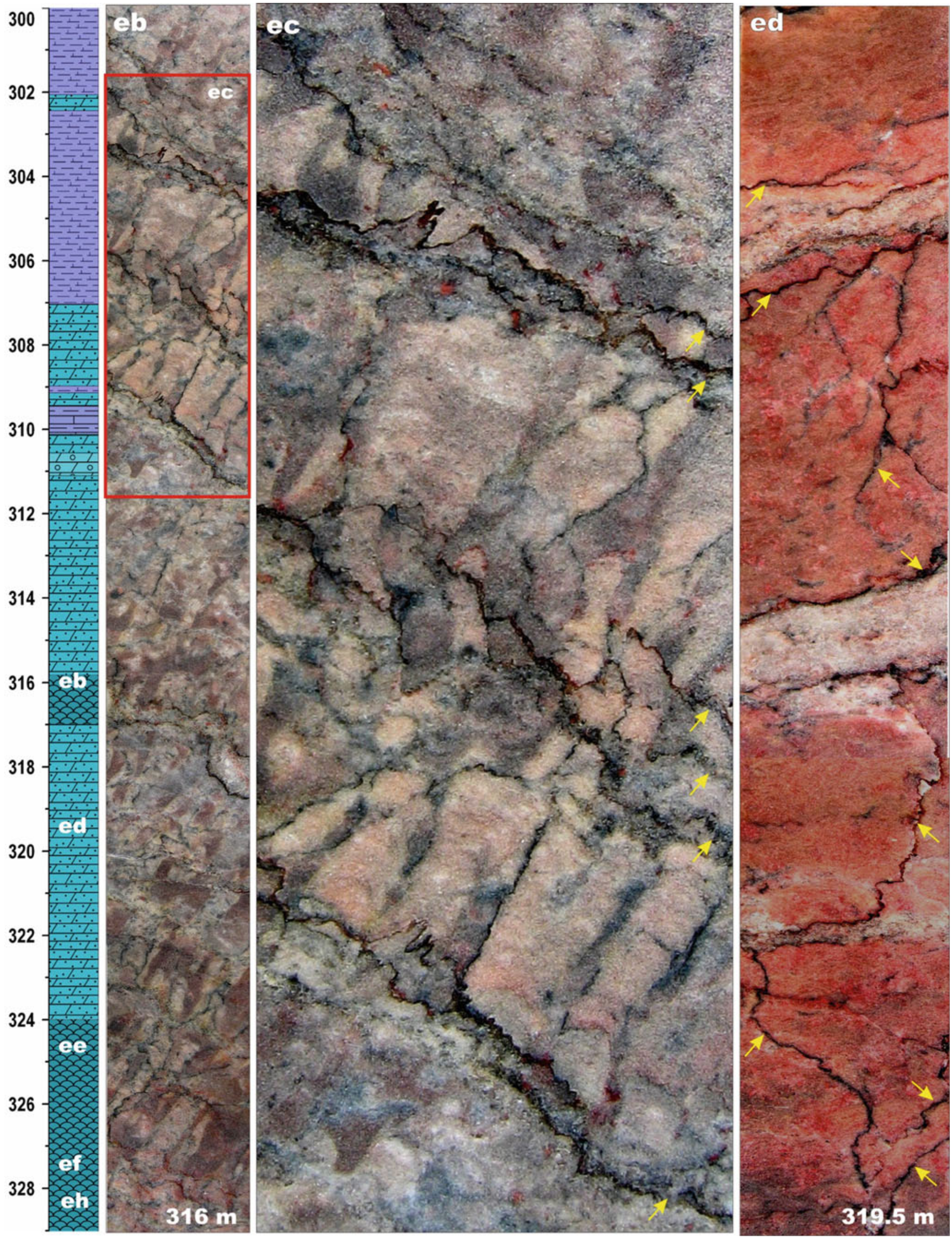

Fig. 6.97 (continued) *The Dolostone-Dolomarl member:* (**eb**) Series of tabular beds with columnar, dolomitic stromatolite *Sundosia sp*. (**ec**) Close-up view of columnar stromatolite *Sundosia sp*. showing their divergent morphology and separation by bedding-parallel stylolites (*yellow arrows*). (**ed**) Interbedded thick, pink, and thin, beige dolarenite with stylolites (*yellow arrows*)

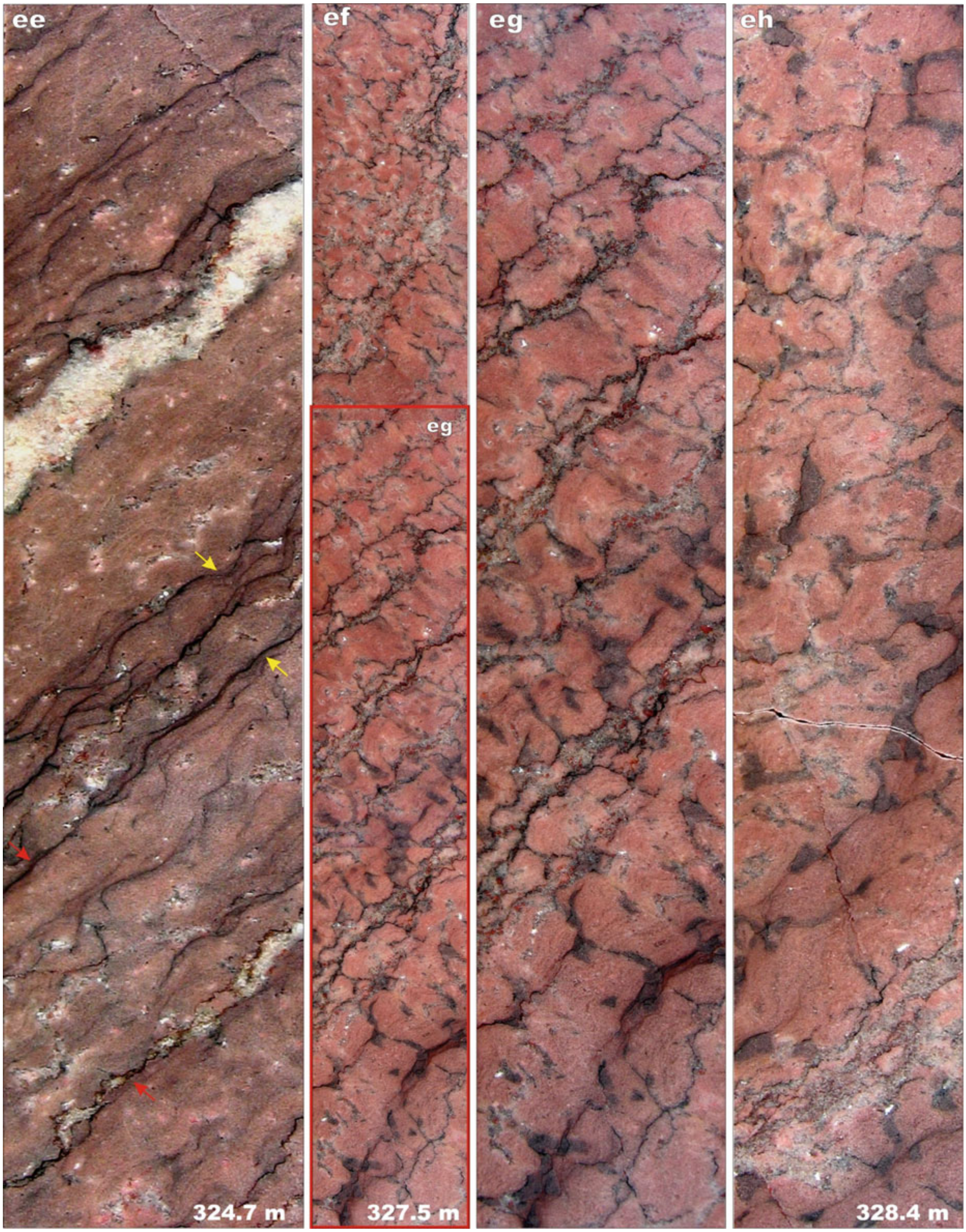

Fig. 6.97 (continued) (**ee**) Pale brown dolostone; wavy, irregular lensoidal, rippled or wrinkled bedding; the asymmetric lenses/ripples draped by dark silt material (*yellow arrows*) may represent flaser bedding, whereas the wrinkled beds (*red arrows*) may represent flat-laminated stromatolite. (**ef**) A series of tabular beds of pale pink, "clumpy" stromatolites *Carelozoon sp.*; each bed is separated by dark, haematite-rich silty material. (**eg**) Close-up view of "clumpy" stromatolites *Carelozoon sp.* showing their divergent morphology; individual beds have irregular topography which mimics the stromatolite morphology, and individual beds and stromatolite columns are separated by a dark-coloured, haematite silty or muddy material. (**eh**) Pink stromatolitic dolostone; note that the stromatolites *Carelozoon sp.* have an irregular morphology resulting in a "clumpy" textural pattern ("clumpy" stromatolite)

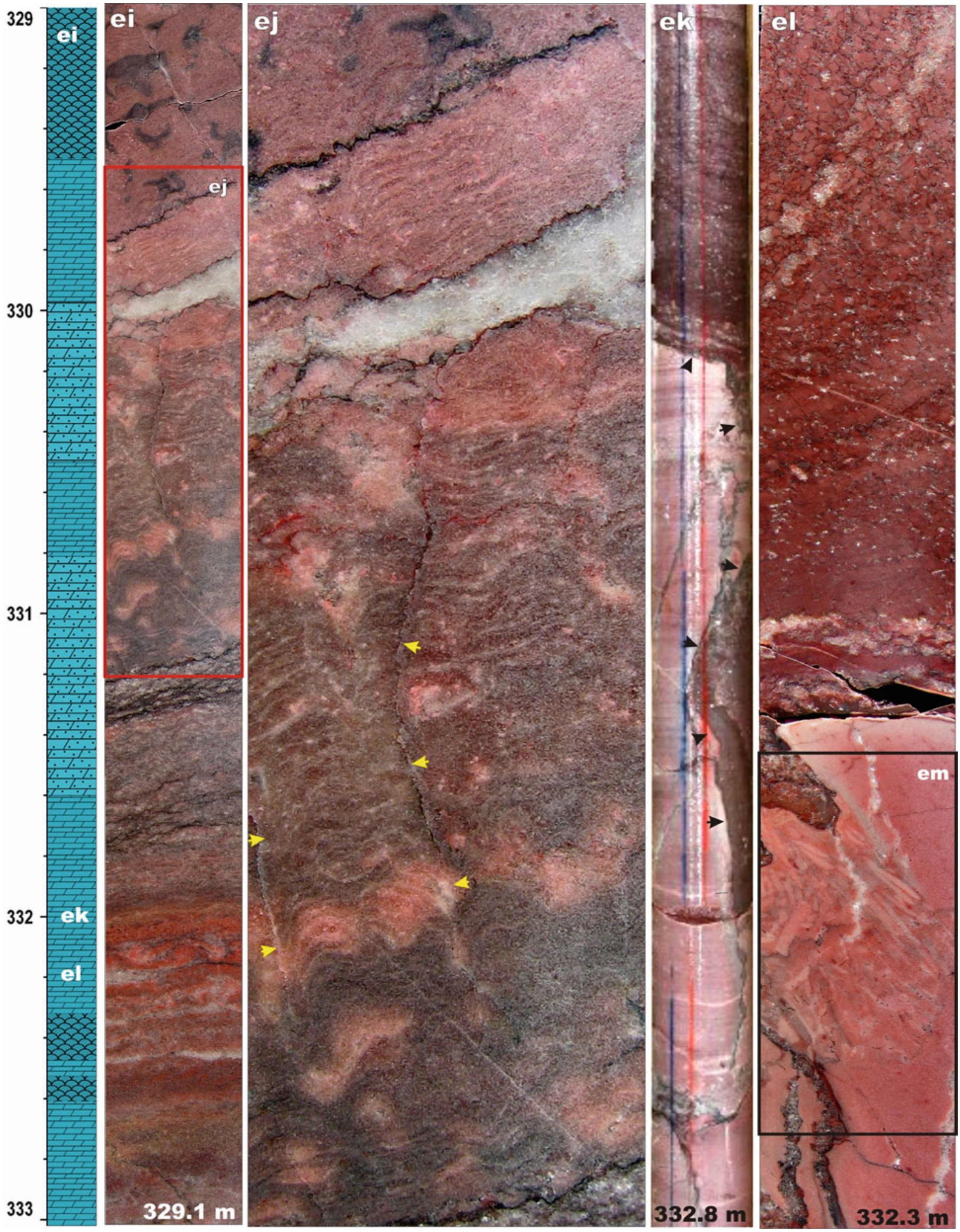

Fig. 6.97 (continued) (**ei**) Variegated dolostone overlain by columnar stromatolite (*red rectangle*) followed by "clumpy" stromatolite. (**ej**) Close-up view of variegated stromatolite; note that the two small, tightly packed columns are grown into one (*yellow arrow*). (**ek**) Dissolution cavity with a subvertical wall developed in pale pink, massive dolostone; the cavity is filled with brown, vaguely bedded, clayey dolarenite. (**el**) A bed of pale pink dolostone with dissolution surface covered by brown-red, haematite-rich, clayey dolarenite; note that sub-horizontal bedding in the dolarenite becomes steeply inclined

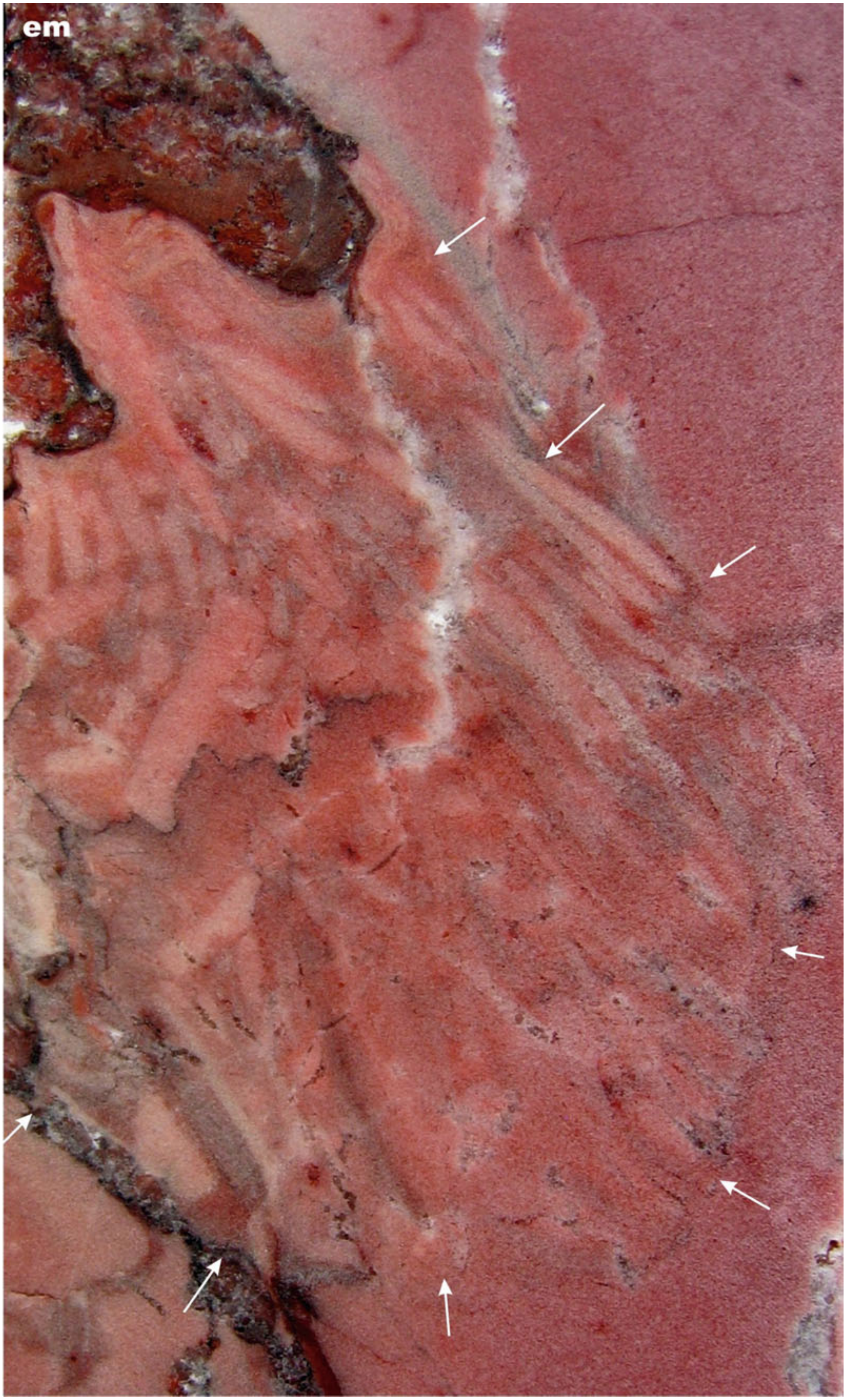

Fig. 6.97 (continued) (**em**) Close-up view of a dissolution surface in the pale pink dolostone bed covered by brown-red, haematite-rich dolarenite; below is another dissolution cavity (*white arrows*) filled with stone rosette containing platy intraclasts of pale pink dolostone

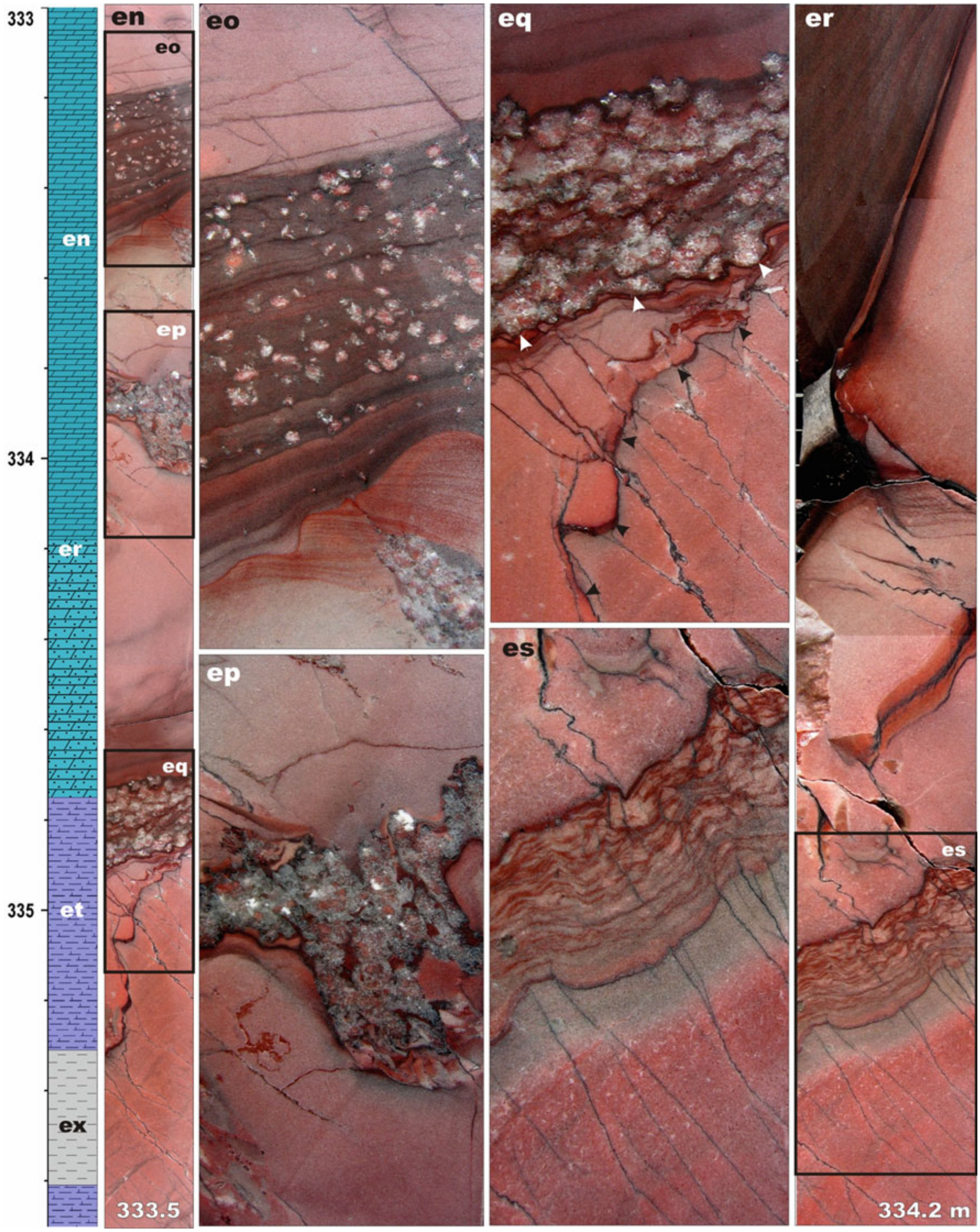

Fig. 6.97 (continued) (**en**) Dissolution surfaces/cavities in pale pink, non-bedded dolostone; the cavities and dissolution surfaces are filled with and/or covered by brownish, clayey dolostone with small crystals and crystal-rosettes of apparent gypsum pseudomorphed by white dolospar. (**eo**) Close-up view of dissolution surface on top of pale pink dolostone covered with brown, haematite-rich, laminated siltstone; note the small dissolution cavity in the lower right corner. (**ep**) Close-up view of a dissolution cavity in pink, massive dolostone that is filled with dark-pink-brown intraformational fragments in dark brown, haematite-rich siltstone/mudstone containing small, white, dolomite-pseudomorphed gypsum rosettes. (**eq**) Two dissolution surfaces in pink, massive dolostone; the first surface (*black arrows*) is covered by massive, pink dolarenite and the second one (*white arrows*) by brown siltstone/mudstone with pseudomorphs after apparent gypsum rosettes (bright). (**er**) Dissolution cavity in pink, massive dolostone filled with bedded, brown, haematite-rich siltstone. (**es**) Close-up view of the dissolution surface in pink, massive dolostone covered by dolorudite composed of intraformational, platy clast of pale pink dolostone; note discolouration beneath the dissolution surface

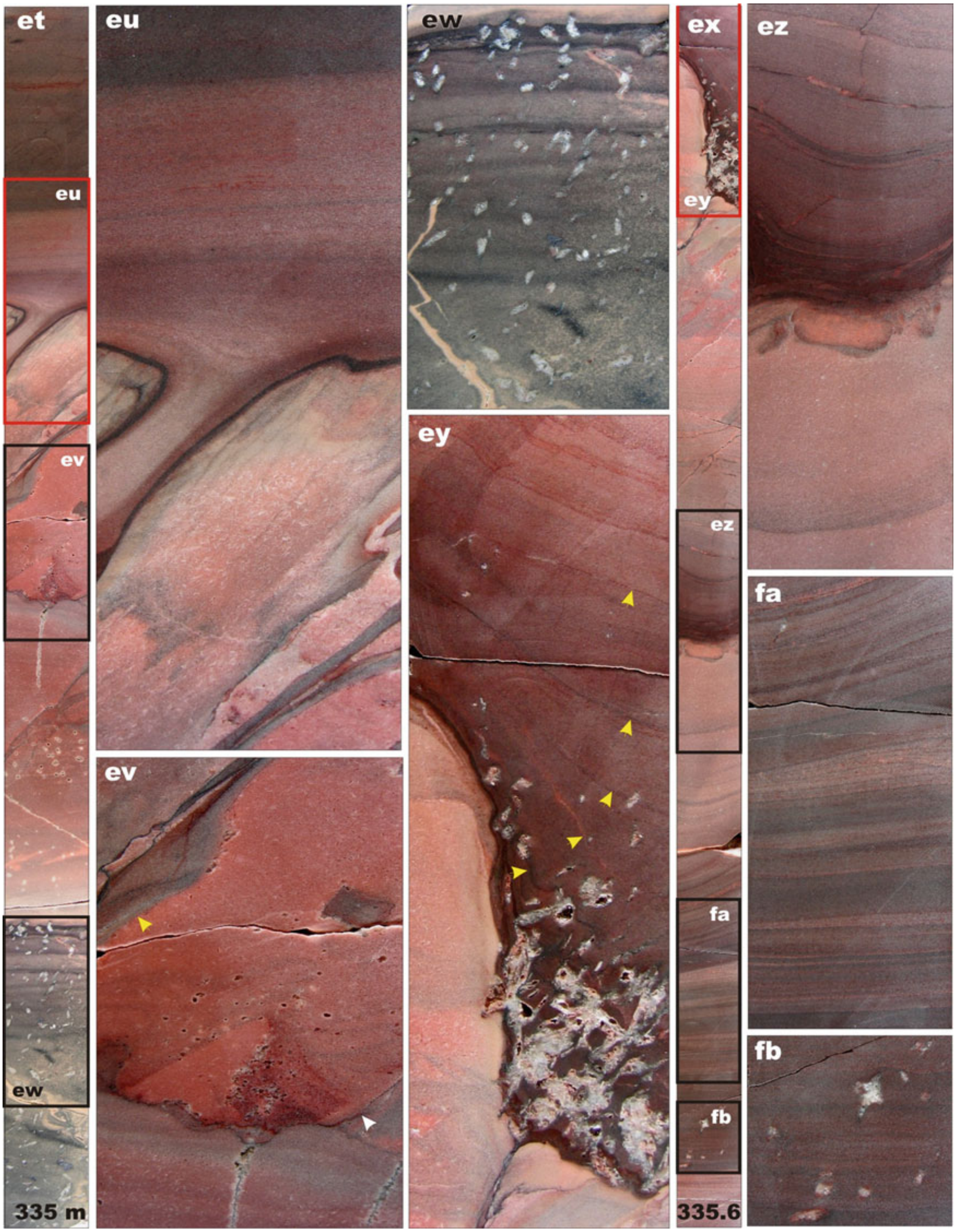

Fig. 6.97 (continued) (**et**) Pale grey, laminated dolomarl (bottom) sharply overlain by pale pink dolomarl with erosional/dissolution surfaces (detailed in Fig. eu and ev) and caped by brown laminated dolomarl. (**eu**) Detailed view of a dissolution surface with a dissolution pipe developed on a pale pink dolarenite bed; the dissolution pipe is filled with massive dolomarl passing upward into faintly laminated dolomarl. (**ev**) Two sets of erosional/dissolution surfaces (*white* and *yellow arrows*) in variegated dolomarl. (**ew**) Detailed view of the pale grey, laminated dolomarl with dolomite-pseudomorphed gypsum crystals (*white*). (**ex**) Variegated, bedded and massive dolomarls with erosional and dissolution surfaces detailed in Fig. ey, ez. (**ey**) Detailed view of a dissolution feature on a pale pink dolomarl bed; the dissolution cavity is filled with brown dolomarl with the former gypsum crystals replaced by white dolospar; the overlying bedded dolomarl shows gradual change in the bedding plane (*arrowed*) while progressively filling the cavity. (**ez**) Detailed view of the erosional feature on pale pink, massive dolomarl; the erosional surface is marked by a rounded dolomarl intraclast and covered by brown laminated dolomarl. (**fa**, **fb**) Close-up view of brown laminated dolomarl, and small, dolomite-pseudomorphed gypsum crystals

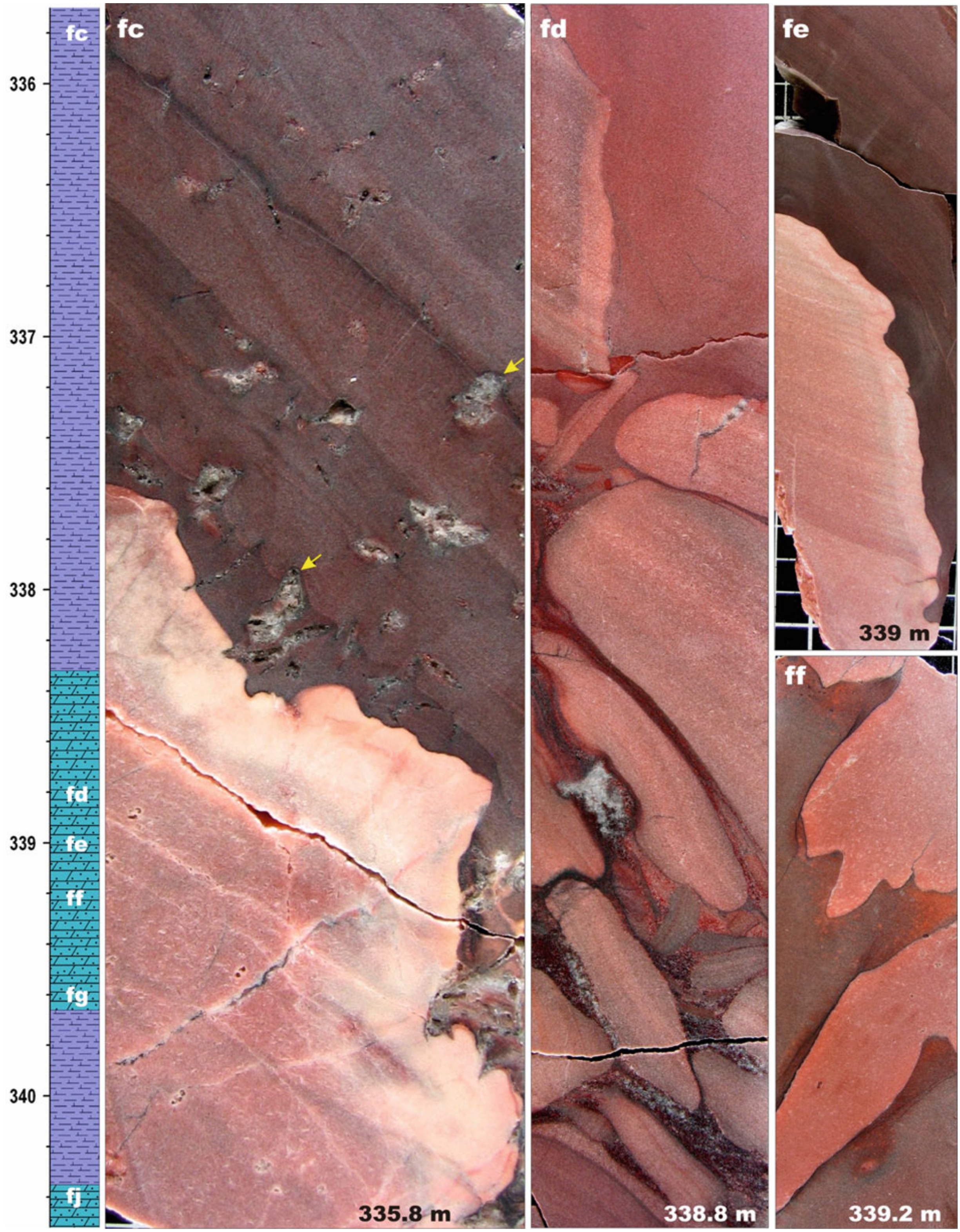

Fig. 6.97 (continued) (**fc**) Dissolution surface on a pale pink dolomarl bed; the dissolved surface is covered by brown, bedded dolomarl with dolomite-pseudomorphed gypsum crystals; some of these crystals pierce lamination (*arrow*) and hence were formed post-depositionally. (**fd**) Apparent dissolution cavity filled with rounded, pale pink, faintly bedded dolarenite intraclasts embedded in a brown siltstone and pink dolomarl matrix. (**fe**) Dissolution cavity in pale pink, faintly bedded dolarenite, filled by brown, massive and laminated dolomarl. (**ff**) Apparent dissolution cavity filled with pale pink, faintly bedded and massive, dolomarl intraclasts embedded in brown, massive dolarenite; note the irregular surface of the clasts caused by dissolution

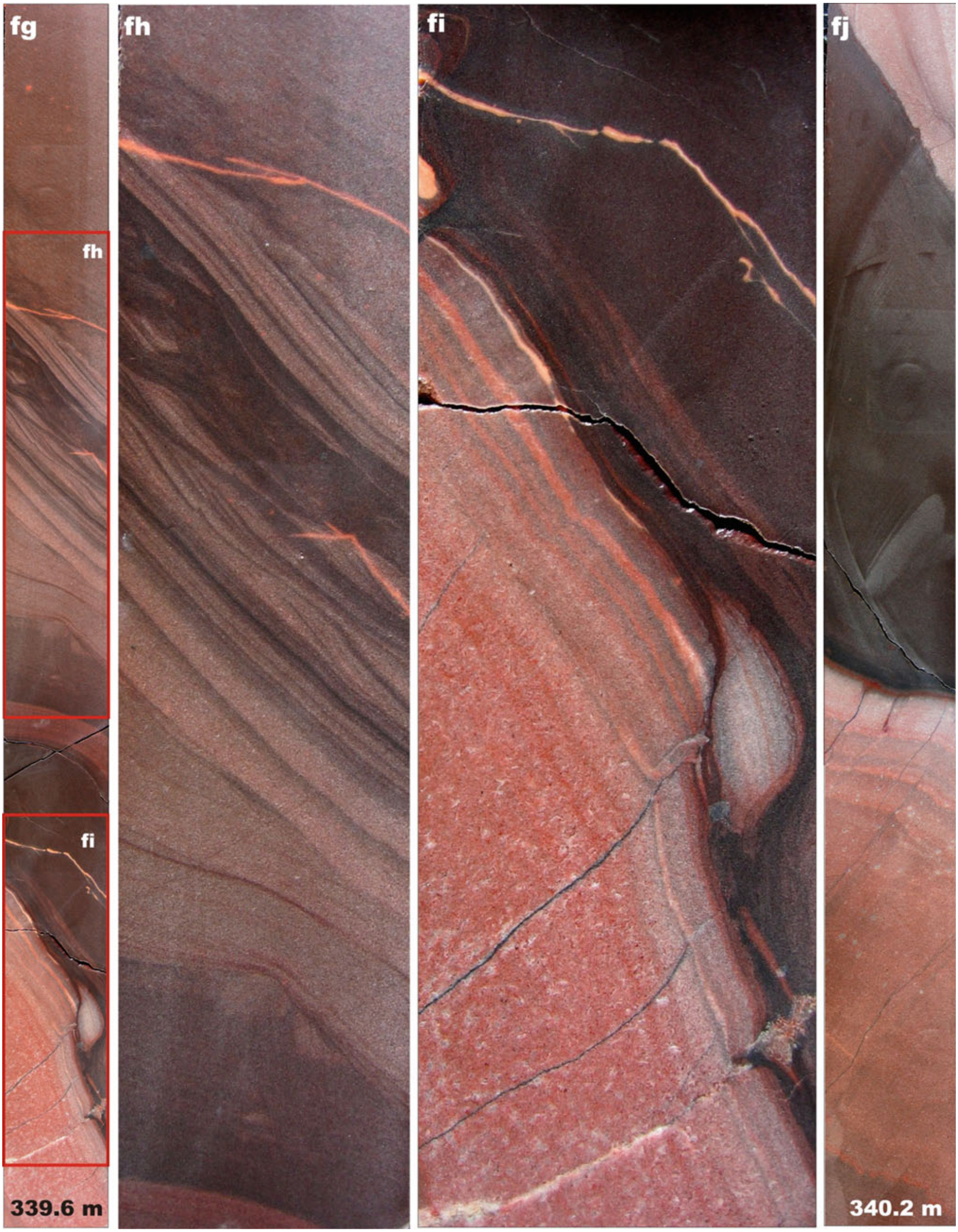

Fig. 6.97 (continued) (**fg**) Dissolution surface on pale pink, laminated dolarenite covered by brown, massive dolarenite passing upward into bedded and, then, into massive dolarenite. (**fh**) Detailed view of ripple-cross lamination in dolarenite. (**fi**) Detailed view of a dissolution or erosion surface on pale pink, laminated dolarenite covered by brown, faintly bedded siltstone. (**fj**) Probable dissolution cavity in pale pink dolarenite, filled with brown, massive, clayey siltstone ("*terra rossa*?")

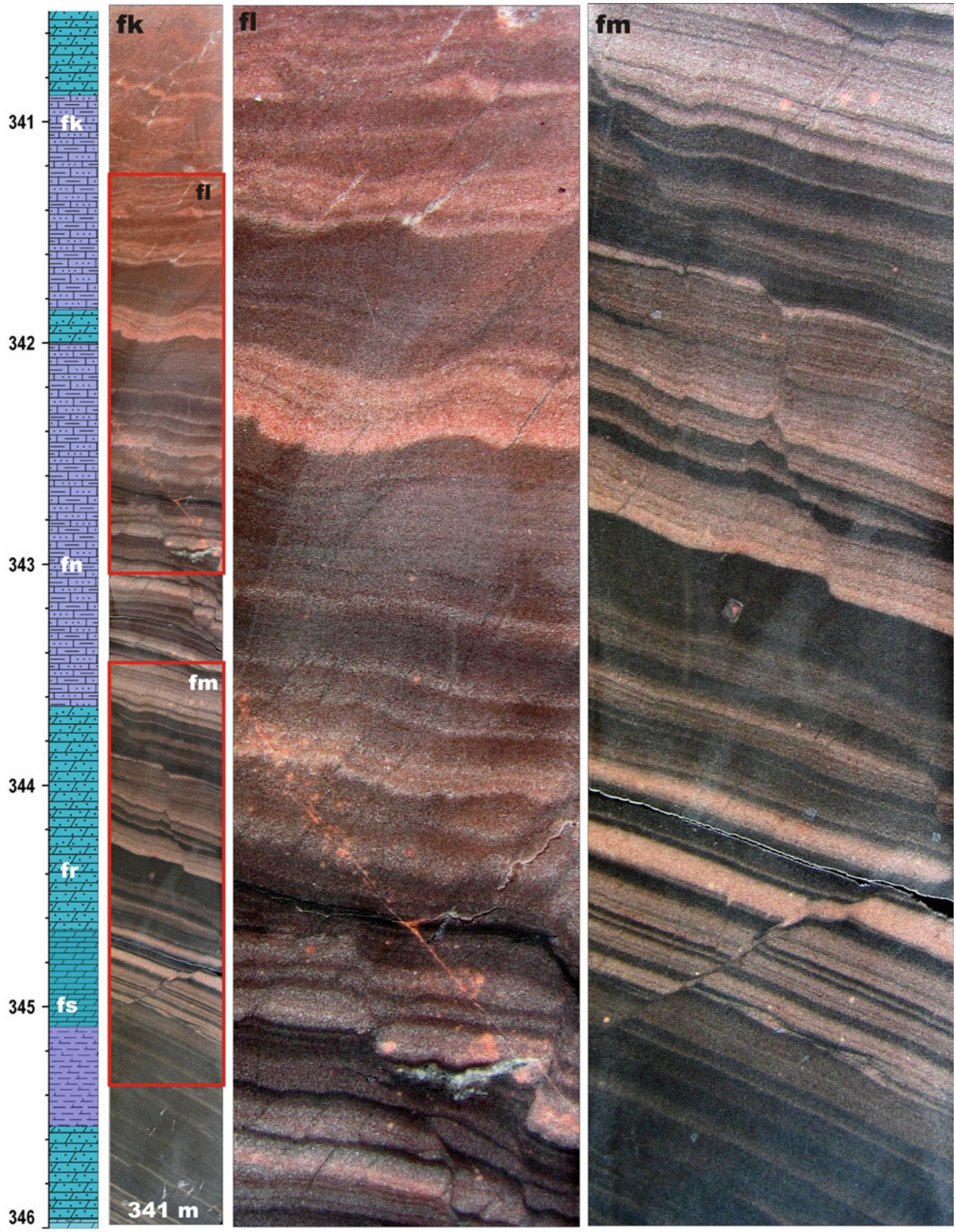

Fig. 6.97 (continued) (**fk**) Rhythmically interbedded pink dolarenite and brown siltstone; note the progressive thickening of the dolarenite beds to form a thick, massive unit on top. (**fl**) Details of the rhythmic bedding with graded beds; many pink dolarenite beds grade into brown siltstone forming dolarenite-siltstone couplets that comprise a thickening upward succession. (**fm**) Detailed view of interlaminated pink dolarenite and black siltstone beds with variable thicknesses

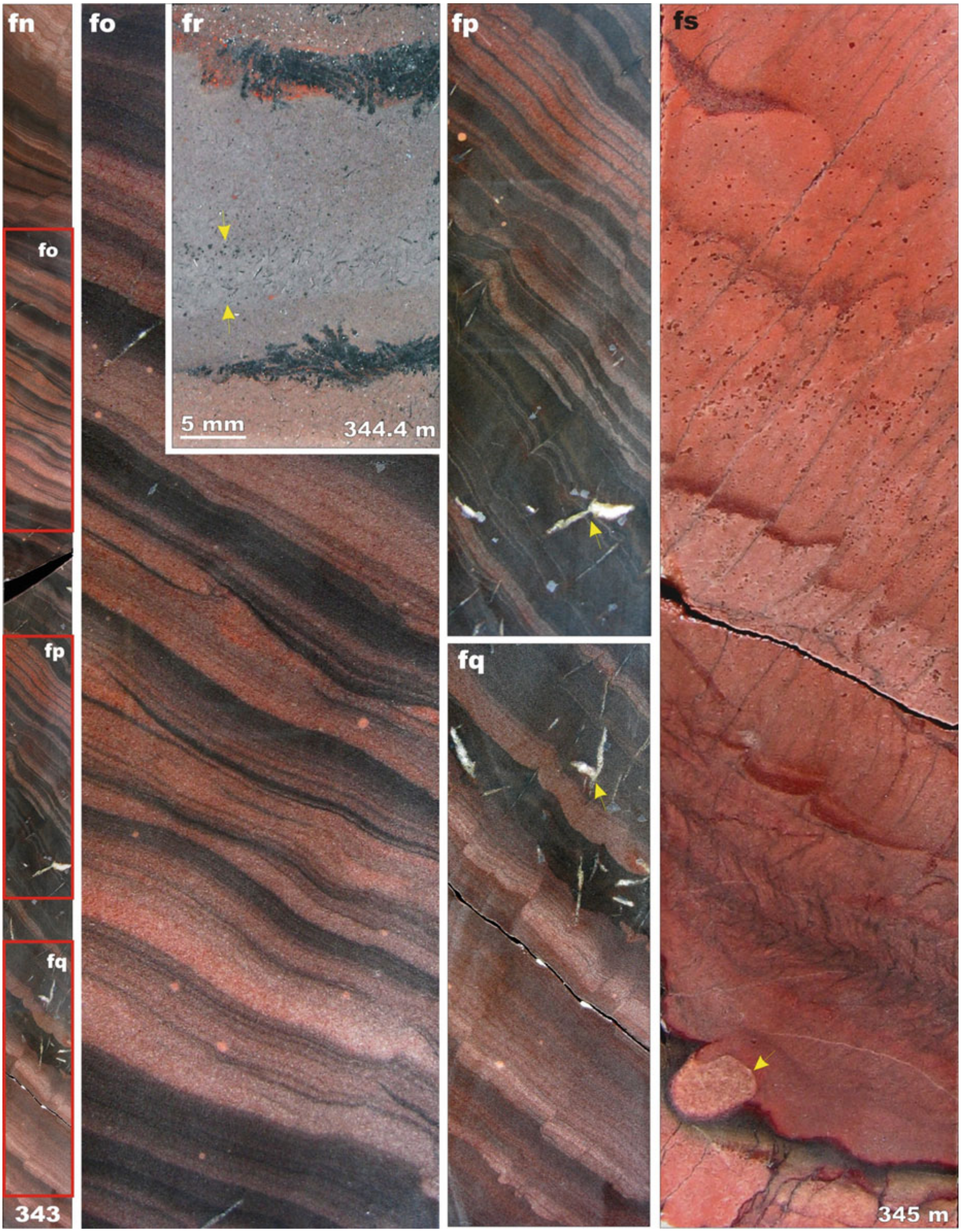

Fig. 6.97 (continued) (**fn**) Rhythmically interbedded pink dolarenite and black siltstone. (**fo**) Detailed view of parallel wavy and ripple-cross lamination in (**fp**, **fq**). Rhythmically interbedded pink dolarenite and black siltstone with dolomite-pseudomorphed, platy gypsum crystals, some with a swallow-tail-twin morphology (*arrows*). (**fr**) Scanned polished section of interbedded dolarenite and siltstone with quartz-replaced former gypsum rosettes (dark grey) developed along the bedding plane; note that the graded bed (*arrow*) contains tiny, platy crystal of former gypsum replaced by quartz. (**fs**) Intensely cleaved, pink dolostone beds with erosive bases and thin dark-coloured dolomarl drapes; note that the lowermost dolostone bed is draped by black mudstone, and the overlying pink dolostone has an erosive base and rounded intraclast (*arrow*)

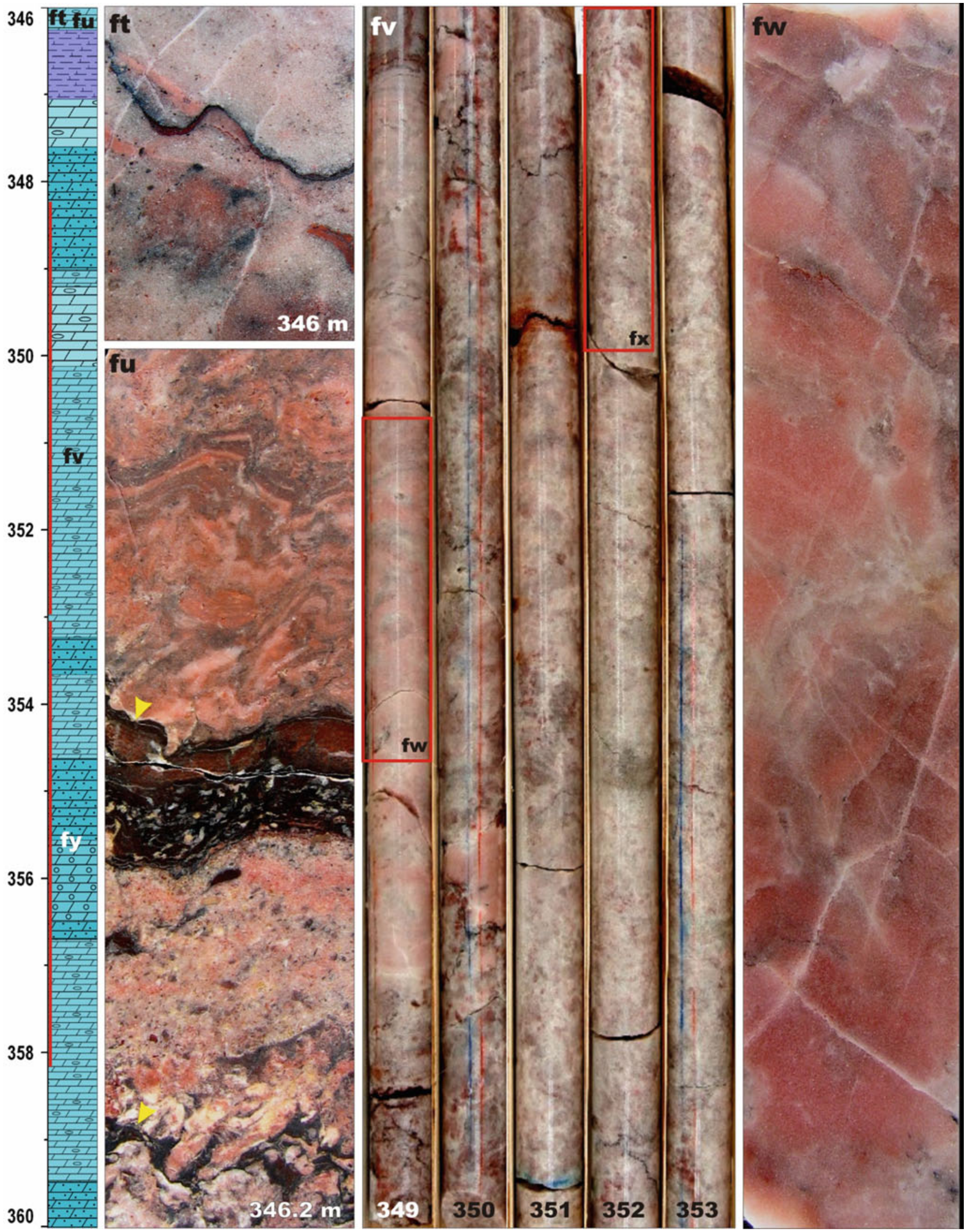

Fig. 6.97 (continued) (**ft**) Variegated, non-bedded dolorudite composed of rounded, unsorted, white, beige and pink dolarenite clasts. (**fu**) Pale pink, graded dolorudite beds with black and brown mudstone tops; each bed contains platy intraformational clasts and has an erosional base (*arrows*); note that the uppermost dolorudite bed shows soft-sediment deformation. (**fv**) Unsawn core showing a continuous dolarenite-dolostone breccia-dolorudite succession. (**fw**) Pale pink, non-bedded dolarenite

Fig. 6.97 (continued) (**fx**) Partially recrystallised dolorudite (dolostone conglomerate) showing a variegated colour; recrystallisation obliterated the contacts between clasts and matrix. (**fy**) Unsawn core showing a continuous section of interbedded dolorudite, dolarenite and dolostone breccia. (**fz**) Crudely bedded, variegated dolorudite; red bands may contain inverted, columnar stromatolites or cave deposits (arrows)

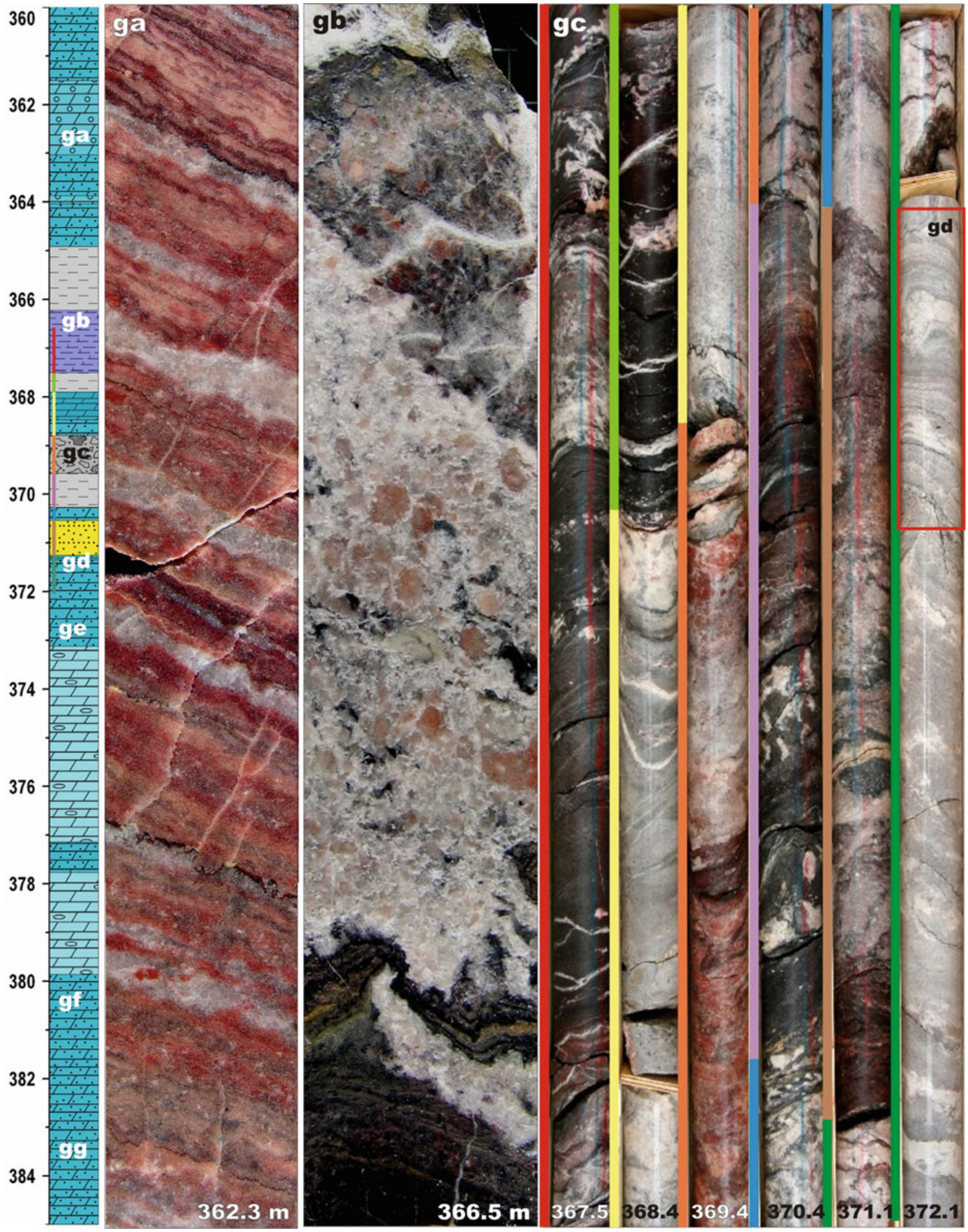

Fig. 6.97 (continued) (**ga**) Variegated dolostone gritstone (dolorudite) with wavy and wrinkled irregular bedding. *The Siltstone-Sandstone-Breccia member*: (**gb**) "Inclusion" of structureless dolomite in black, haematite-rich dolomarl; note that the dolomite inclusion contains pink quartz clusters apparently replacing Ca-sulphates. (**gc**) Continuous core through a succession of alternating white dolostone (*dark green line*), variegated sandstone (*brown line*), pale grey dolostone (*blue line*), dark-coloured, haematite-rich siltstone (*purple line*), pale pink breccia (*orange line*), pale grey dolostone (*yellow line*), black, haematite-rich siltstone (*green line*) and dark-coloured dolomarl (*red line*); note that bedding in all lithologies is highly disrupted due to growth of evaporitic minerals, primarily sulphates, which were consequently either partially dissolved or replaced by white dolospar and quartz containing relicts of anhydrite

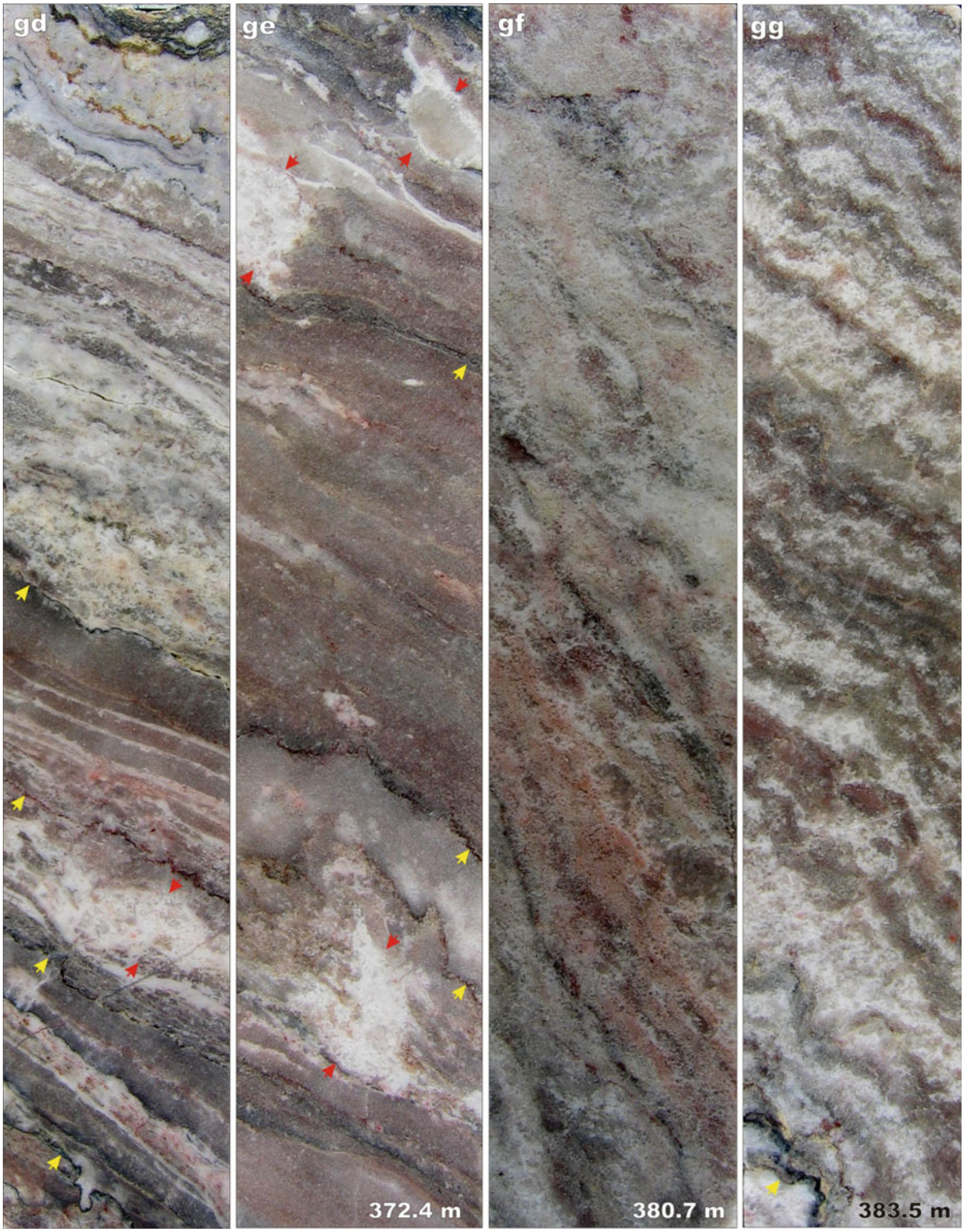

Fig. 6.97 (continued) (**gd**) Close-up view of the dolostone bed from Fig. gc, showing irregular alternation of white dolarenitic layers and grey beds of recrystallised dolostone; bedding is disrupted due to growth of evaporitic minerals, primarily sulphates, which were consequently replaced by white dolospar containing relicts of anhydrite; the *red arrows* mark nodular sulphate, now dolospar-pseudomorphed, and the *yellow arrows* mark stylolites. (**ge**) Indistinctly bedded, siliceous dolarenite with stylolites (*yellow arrows*) and white dolospar clumps replacing former sulphate nodules/crystals (*red arrows*). (**gf**) Variegated, siliceous dolarenite with disrupted wavy and wrinkled lamination; the grey layers are enriched in clastic quartz. (**gg**) Dolarenite with disrupted bedding and stylolite (*yellow arrow*); the grey bands are intensely silicified dolarenite; the silicification appears in micro-scale as spherical clusters of granular quartz resembling micronodules

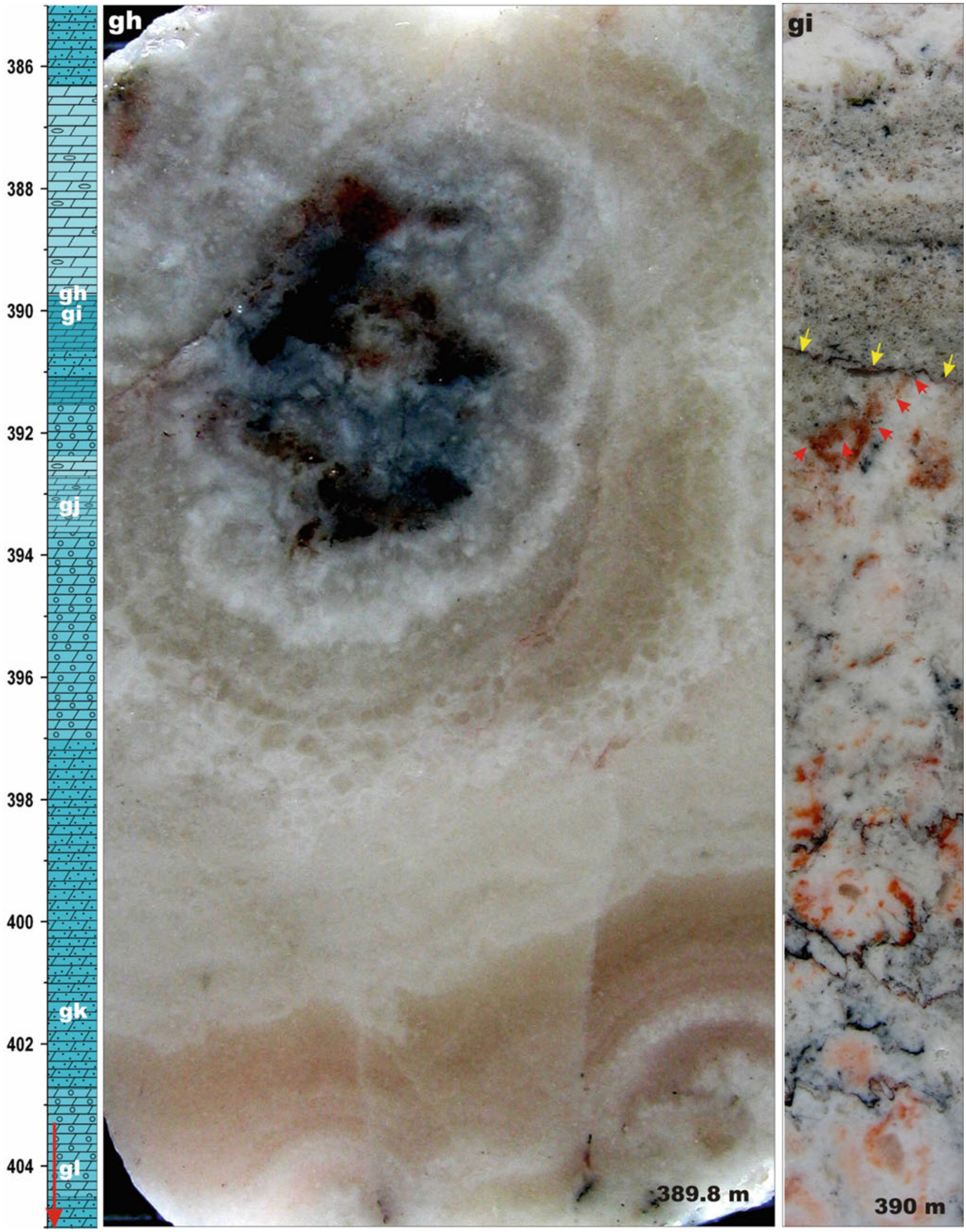

Fig. 6.97 (continued) (**gh**) Micritic dolomite with alternating white and beige concentric banding around a black mudstone centre; interpreted as either a travertine or a cave deposit. *The Lower Dolostone member:* (**gi**) Structureless, variegated dolostone with a "lumpy" appearance and thin, soft-sediment deformed, black mudstone laminae; the "lumpy" dolostone is overlain erosively (*red arrow*) by dolomite-cemented quartz sandstone; stylolite is marked by a yellow-arrow

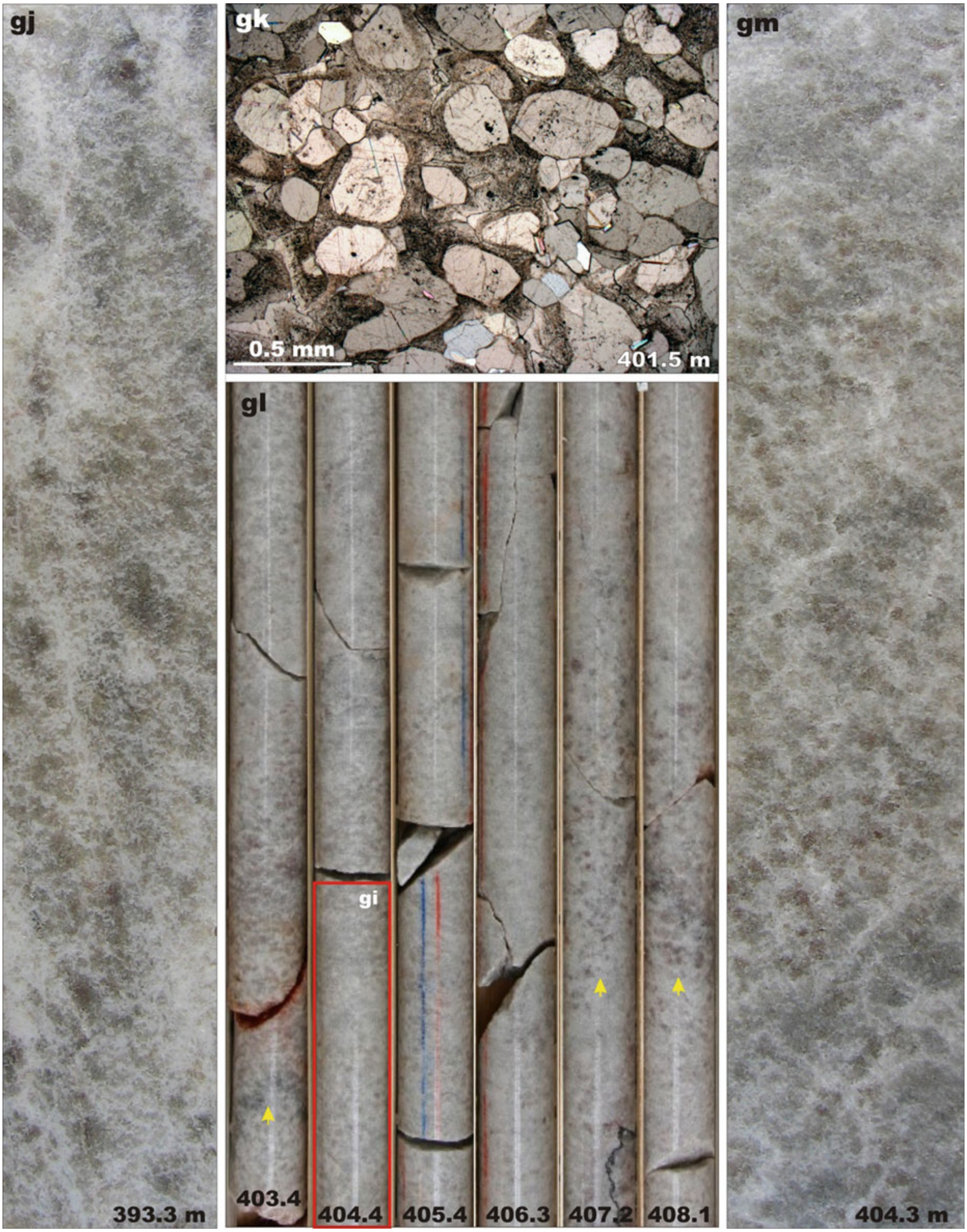

Fig. 6.97 (continued) (**gj**) Partially recrystallised, massive dolorudite; the pale grey patches with diffused boundaries are rounded dolarenite clasts, whereas the bright areas represent doloarenite matrix with syntaxial dolospar cement (see Fig. gk). (**gk**) Photomicrograph in transmitted, non-polarised light illustrating dolarenite with dusty, syntaxial, dolospar cement. (**gl**) Unsawn core showing a continuous dolorudite-dolarenite succession; note that several individual beds display upward grading from dolorudite (*yellow arrow*) to dolarenite. (**gm**) Partially recrystallised, massive dolorudite showing indistinct grading from a coarse-grained to fine-grained variety; the pale grey patches with diffused boundaries are rounded dolarenite clasts, whereas the bright areas represent doloarenite matrix with syntaxial dolospar cement (see Fig. gk)

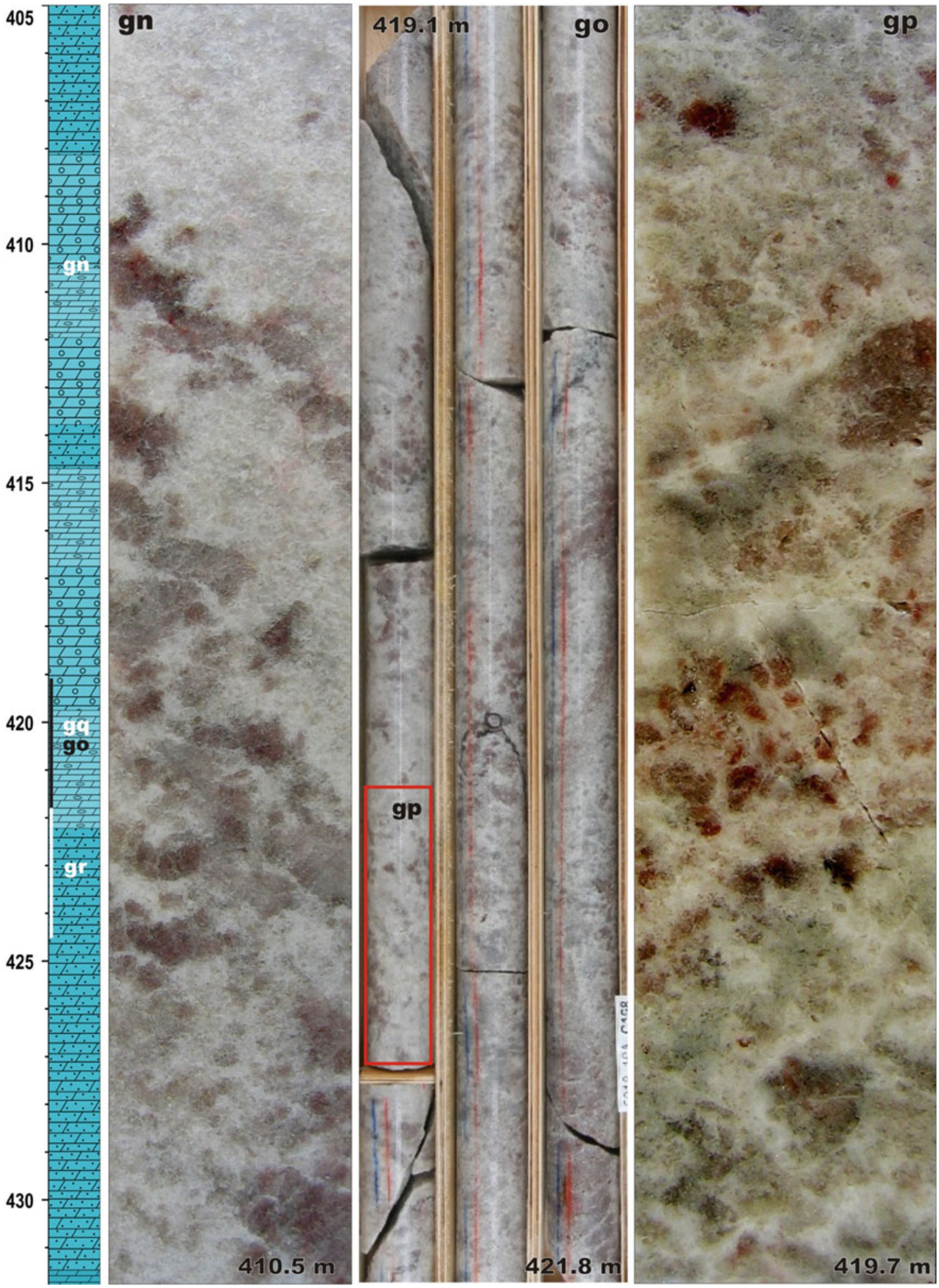

Fig. 6.97 (continued) (**gn**) White, massive dolarenite affected by recrystallisation that resulted in formation of grey patches of dolospar. (**go**) Unsawn core showing a c. 3-m-long, continuous interval of white, massive, partially recrystallised dolorudite and dolarenite. (**gp**) Close-up view of massive, partially recrystallised dolorudite; clasts of brown, grey and grey-green dolarenite, crystalline dolostone and rare quartzite are embedded in a dolarenite matrix with syntaxial dolospar cement

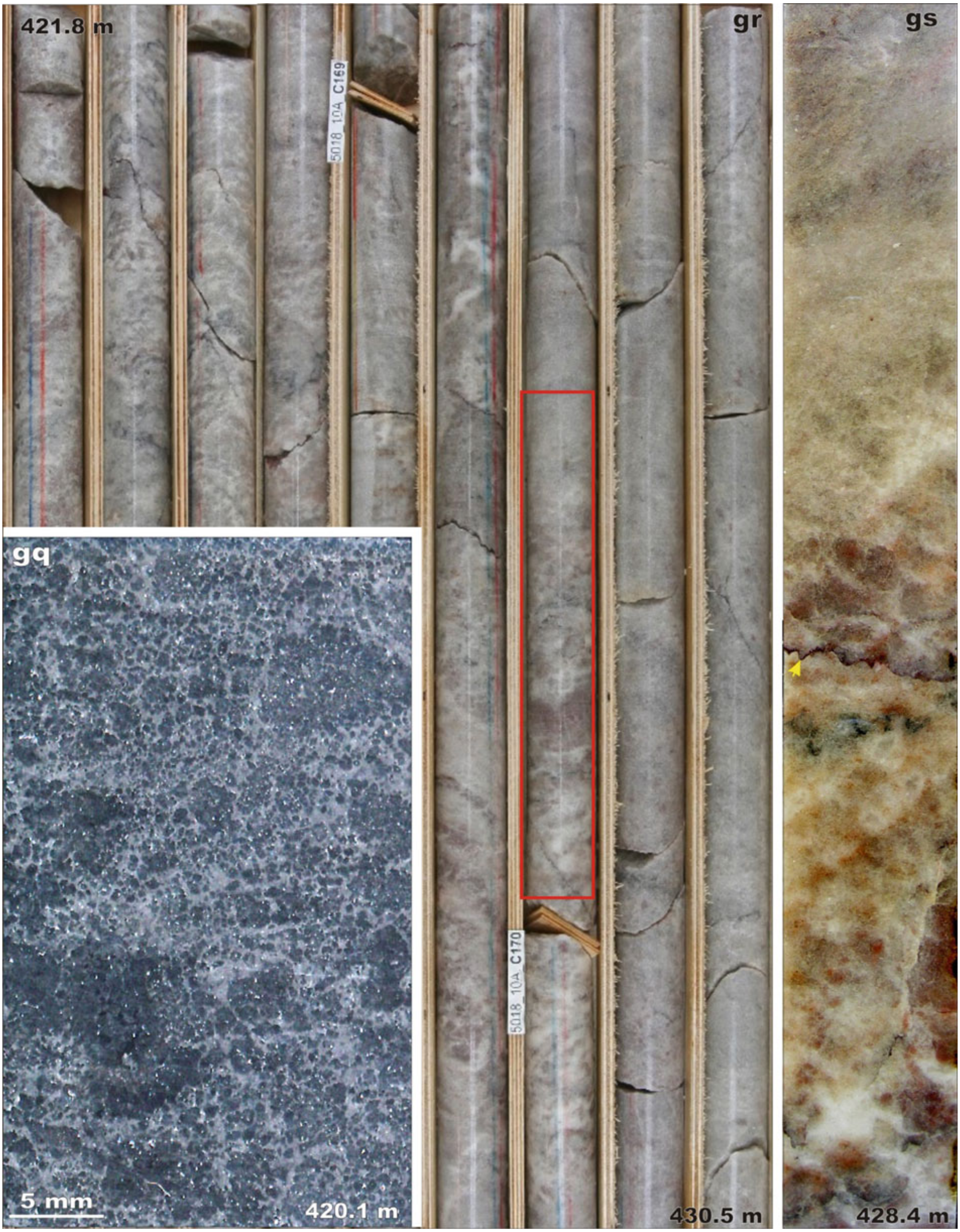

Fig. 6.97 (continued) (**gq**) Scanned thin section showing a structure of massive dolorudite; rounded clasts of dolarenite, crystalline dolostone and rare quartzite (all appear as grey patches) are embedded in a dolarenite matrix with syntaxial dolospar cement (bright). (**gr**) Unsawn core of a c. 6-m-long section of massive or indistinctly bedded, partially recrystallised dolarenite and dolorudite. (**gs**) Close-up view of variegated, partially recrystallised dolorudite overlain by beige dolarenite; stylolite is marked by *yellow arrow* (All photographs by Victor Melezhik)

Hole 10B

Hole 10B is 278 m long. The lithological column of the cored section is shown in Fig. 6.98 and profiles of selected major and trace elements and magnetic susceptibility are shown in Fig. 6.99. Chemical compositions of the analysed samples are presented in Appendices 29–32; Fig. 6.100 displays geochemical features of the mafic volcanic unit. Core photos provide a detailed documentation of major lithological and structural features of sedimentary rocks through the stratigraphy (Fig. 6.101).

A tentative correlation of the 10B and 10A sections based on carbon-isotopic profiles is shown in Fig. 6.92. This $\delta^{13}C$ correlation suggests that the two sections either do not overlap or do so only marginally. For the purpose of assisting the core description, the 10B section has been tentatively subdivided into several units (members) based on the dominant rock types. Due to considerable lithofacies variations across the Onega Basin, these subdivisions do not correspond to the previously identified lithological units (Fig. 6.91).

Six lithological units (members) have been recognised in the 10B section, being from base to top: member 10 (Dolostone-Conglomerate), member 11 (Sandstone-Basalt), member 12 (Siltstone), member 13 (Upper Dolostone), member 14 (Nodular Shale-Siltstone-Marl-Breccia) and member 15 (Shale-Dissolution Breccia) (Fig. 6.95). Brief descriptions of the stratigraphic units are presented below. Detailed characteristics of the distinct lithofacies are presented in Brasier et al. (2011).

Member 10 (Dolostone-Conglomerate)

Member 10 is a c. 51-m-thick succession (278.3–227 m) comprising diverse lithologies. These include thick packages of dolarenite, polymict and carbonate conglomerate and sandstone interbedded with thin intervals of siltstone, shale, dolarenaceous siltstone, stromatolitic dolostone and dissolution-collapse breccia (Fig. 6.98). The upper boundary is defined at c. 227 m where a coarse, non-bedded breccia-conglomerate passes gradually into bedded clastic rocks with finer clasts. The boundary is also marked by a change in magnetic susceptibility from 10–330 to 600–2,200 μSI ($K^* = 0.1$–30 to 50–200×10^{-6} SI in Fig. 6.99).

The dolarenites occur as three thick units in the lower half of the section (termed Units 1, 2 and 3) as well as numerous thinner interbeds throughout (Fig. 6.98). The lowermost Unit 1 (270.4–266.6 m) is composed of pale purple, thinly bedded dolarenite (Fig. 6.101di). In places the dolarenites show *in situ* brecciation and collapse structures (Fig. 6.101dh). Unit 2 (264.9–260.2 m) comprises pale purple dolarenites, which are massive or thickly-bedded in the lower part and thinly bedded in the upper part of the section (Figs. 6.101df–dg), with some brecciation and dissolution-collapse structures (Fig. 6.101de). Unit 3 (257.6–251.1 m) is composed of pink, bedded dolarenites, including a c. 2.5-m-thick interval with clotted fabrics and relicts of stromatolites (Fig. 6.101dc); orientation of the latter indicates local stratigraphic inversion due to structural deformation (e.g. tight folds).

Thin dolarenite interbeds exhibit sedimentological features similar to those observed in Units 1–3. They are pink, tan, pale brown, beige or variegated in colour. Commonly bedded, some intervals have sulphate nodules pseudomorphed by dolomite, dissolution vugs and dissolution-collapse structures (Figs. 6.101cp, ct, cu, cy, cz, db, dd, dk). The dolarenites in all units and intervals underwent pervasive recrystallisation. However relicts of rounded dolomite grains are preserved, with burial dolomite cement in the form of syntaxial overgrowths.

The conglomerates, breccias and gritstones are next in abundance. They occur as interbeds ranging in thickness from 0.5 to 1.5 m throughout the member (Fig. 6.98). These three lithofacies are characterised by gradual transitions between clast sizes and their roundness. The bulk of the clastic material is represented by dolostones, though some beds and intervals contain minor fragments of dolomite-cemented quartz sandstone, vein-quartz and shale/siltstone. All coarse-clastic sedimentary rocks of the member are non-bedded, unsorted, and commonly indicate very limited or no transport (Figs. 6.101ch–cj, cr–ct, cy–db, dj). The breccias at c. 233.6 and 257.7 m contain fragments of drusy dolomite with some retaining micron-sized cubes of dolospar, pseudomorphs of likely former halite crystals.

Sandstones occur in both the lower and upper parts of the member. They are pale brown, pale pink or variegated in colour, showing indistinct parallel bedding with some beds being graded. Although sandstones are composed of well-sorted quartz and microcline grains, many intervals contain outsized clasts of silicified dolostones, dolomite-cemented sandstone and vein-quartz (Figs. 6.101dm, dn). Primary depositional structures of many intervals were affected by dissolution and collapse processes (Figs. 6.101dm–do).

One notable dissolution-collapse breccia comprises a thin, discrete bed at 243.8–243.2 m (Fig. 6.98). This bed is composed of angular fragments of shale and dolostone floating in dolospar cement, although there are patches of tightly packed clasts (Fig. 6.101cx). Such dissolution and collapse structures are widespread in the member and have been observed in all lithofacies, including in dolarenites (Figs. 6.101cm, cq, db, dd, de, dh) and sandstones (Figs. 6.101dl–do), and are particularly well developed and widespread in dolarenaceous shales. Here, they appear as soft-sediment deformed fragments of shale chaotically floating in white spar or drusy dolomite cement (Figs. 6.101cv, cw).

The uppermost part of the member is marked by unusual, bright red, haematitic massive dolostones (Figs. 6.101ch–cl, cn–cp). They form three beds, as much as 30 cm thick, and are interbedded with conglomerates and dolarenites. Bright red dolomites can be observed as clasts in the overlying conglomerates (Figs. 6.101ch, cn), indicating that the impregnation by haematite is a depositional, not a late diagenetic, feature. The red dolomite is composed of large isometric and platy crystals. When the dolostone is brecciated, it appears as a mosaic of large dolomite monocrystals cemented by white dolospar (Figs. 6.101ci, cp). Large platy monocrystals show internal zoning expressed by abundant, euhedral (prismatic, bipyramidal, cubic morphologies) micron-sized, tartan-twinned microcline crystals. Given the crystal morphologies, it is evident that the microcline replaced an earlier mineral phase. When the platy crystals of bright red dolomite are tectonically dismembered and partially replaced by white dolospar, they leave a "residue" behind: a trail of prismatic, bipyramidal and cubic crystals of microcline embedded in dolospar.

All carbonate rocks of the member are dolomitic in composition (Mg/Ca = 0.64, with one exception at 0.68). They have a highly variable content of SiO_2 (6–28 wt.%, with one outlier at 40 wt.%), low abundances of Al_2O_3 (0.05–1.3 wt.%) and K_2O (0.2–0.74 wt.%), and are devoid of measurable Na_2O, C_{org} and S (Appendices 29, 30). However, one dolarenite contains 0.2 wt.% S, which might be bound to residual sulphate, and highly variable contents of Fe (82–273 $\mu g\ g^{-1}$) and Mn (71–1770 $\mu g\ g^{-1}$) and low abundances of Sr (54–117 $\mu g\ g^{-1}$) (Appendix 31). Analyses of ten archive samples show a stratigraphic increase in $\delta^{13}C$ from c. +8 to c. +11 ‰ (VPDB), whereas $\delta^{18}O$ varies independently from 19.5 to 20.8 ‰ (VSMOW) (Brasier et al. 2011).

Member 11 (Sandstone-Basalt)

This member is c. 100 m thick (227–155.8 m) and is composed mainly of sandstone and siltstone with a c. 34-m-thick volcanic unit in the middle of the section (Fig. 6.98). The lower boundary of the member is defined at a depth of 227 m, in the middle of a 0.5-m-thick conglomerate bed, gradually passing into sandstone. The upper boundary at a depth of 155.8 m is sharp, with the siltstone occurring directly on the underlying dolarenite (Fig. 6.98). The mafic volcanic unit shows rather homogeneous magnetic susceptibility, averaging at around 440 μSI ($K^* = 40 \times 10^{-6}$ SI) (Fig. 6.99). The siltstone-shale occurring below the volcanic unit shows a three-step decrease in magnetic susceptibility from 1,100 to 440, and then to c. 60 μSI (change in K* is from 100 to 40 and 5×10^{-6} SI; Fig. 6.99). The succession above the volcanic unit exhibits a monotonous decrease in magnetic susceptibility from 390 to 60 μSI (change in K* is from 35 to $<5 \times 10^{-6}$ SI; Fig. 6.99).

Sedimentary rocks from the base of the member upward to a depth of 219.5 m are mostly variegated, heterolithic sandstone-siltstone with one thin bed of polymict conglomerate (Figs. 6.101ca–cg). They are characterised by irregular planar, wavy and flaser bedding, and contain abundant irregularly scattered angular clasts of various intraformational rocks, especially black mudstone rip-ups (Figs. 6.101ce–cg). Small-scale loading structures, syndepositional tilting and soft-sediment deformation are common (Figs. 6.101cc, ce, cg). Quartz- and dolomite-replaced gypsum nodules and chicken-wire structures are also present (Figs. 6.101cb, cc). The heterolithic rocks are rich in Fe_2O_{3tot} (12.6 wt.%), K_2O (4.4 wt.%) and Cr (86 ppm), show a moderate concentration of SiO_2 (54 wt.%) and Al_2O_3 (11 wt.%) and have a low content of Na_2O (0.16 wt.%) (Appendices 29 and 30). The rocks contain a sizable amount of MgO (6.5 wt.%) and CaO (2.6 wt.%) bound to a carbonate phase. The rocks are devoid of measurable sulphur and organic carbon (Appendix 30).

The succession occurring above 219.5 m and below the volcanic unit (212.1 m) is represented by dark brown, haematite-rich, non-bedded siltstone with a spotted appearance (Fig. 6.101bz, 219.5–212.5 m), followed by chemically and mechanically mature red sandstones with flat, wrinkled and wavy lamination. They contain 94 wt.% SiO_2 and are composed of silica-cemented well-sorted quartz grains.

The mafic igneous unit (212.1–175 m) has sharp contacts with the host sedimentary rocks and is considered to be extrusive in origin, though it is mostly massive and contains amygdales only in the top and bottom parts of the body (Fig. 6.101by). The centre of the unit is medium-grained and becomes finer-grained towards the upper and lower margins. Chemically, all analysed samples are tholeiitic basalts with a high MgO (12.5–19.8 wt.%) content and TiO_2 abundances ranging between 1.2 and 1.6 wt.%. Nickel and chromium occur at levels of 91–136 and 150–165 ppm. Given the high MgO contents of the rocks, Cr and Ni concentrations are low and clearly below the level of komatiitic basalts with similar MgO (Fig. 6.100a). This, together with the lack of correlation between MgO and other elements, suggests that magnesium was added during post-magmatic alteration. Immobile incompatible trace elements, such as Nb (<1.6 ppm), Zr (50–59 ppm), and Ce (below the detection limit of XRF) show very low abundances indicating derivation from a depleted mantle source similar to that of the c. 2.1 Ga Jouttiaapa Formation basalts in the Peräpohja Belt (Huhma et al. 1990). Chemically, the basaltic member of Core 10B resembles the dolomite-associated mafic unit penetrated by FAR-DEEP Hole 11A (see Chap. 6.3.2) with both showing very low contents of incompatible elements compared to the mafic volcanic rocks encountered in Cores 12AB and 13A (Fig. 6.100b).

A c. 2 m thick (175.1–173.3 m) sedimentary bed overlying the volcanic unit consists of dark grey-greenish, massive or indistinctly bedded sandstone. The lower and upper parts of the bed contain large sulphate nodules partially replaced by pink, porous quartz (Fig. 6.101bx). The sandstone has a gradual contact with the overlying heterolithic rocks comprising a 6.8-m-thick unit (173.3–166.5 m). These are closely interbedded pink sandstone, grey siltstone and black mudstone with flaser, wavy, and lenticular bedding. Some beds are green (Figs. 6.101bs–bu), contain chlorite and actinolite, and may represent reworked mafic ash material. The heterolithic bedding is modified by desiccation cracks, small sedimentary dykes and gas/fluid escape structures (Figs. 6.101br–bw).

The heterolithic rocks pass gradually into a 10.8-m-thick succession (166.6–155.8 m) of sandstones and clastic dolostones (Fig. 6.98). All siliciclastic rocks are rich in haematite, have a variegated colour with a characteristic green hue (Figs. 6.101bj–bq), apparently due to the presence of reworked mafic ash material. The sandstones are commonly thickly bedded (Figs. 6.101bn–bq), though some intervals show small-scale lensoidal, wavy- and cross-bedding. Diagenetic growth of calcium sulphates in the form of nodules and chicken-wire structures, now partially replaced by pink, porous quartz and dolospar (Figs. 6.101bk, bl, bo–bq), disrupt layering. Interbedded intervals of heterolithic rocks have a larger proportion of black siltmudstone, hence lenticular bedding dominates over other types (Figs. 6.101bh–bj, bm). Similarly to the sandstones, the primary depositional features of the heterolithic rocks are considerably modified by desiccation and by evaporitic fabrics. Clastic dolostones occur as pale brown, structureless, porous dolarenite and dolorudite having sharp contacts with siliciclastic rocks (Figs. 6.101df, bg, bi).

The sandstones and heterolithic rocks occurring above the igneous body show a rather homogeneous content of SiO_2 (47.2–49.6 wt.%) and Al_2O_3 (11.2–14.3 wt.%). All lithologies have high abundances of Fe_2O_{3tot} (decreasing up-section from 15.3 to 6.6 wt.%; Fig. 6.99), TiO_2 (0.7–1.6 wt.%), K_2O (3.6–5.5 wt.%), Cr (88–148 ppm), Ni (50–86 ppm) and V (220–279 ppm). These geochemical features make the sedimentary rocks distinct from other lithologies in Hole 10B (Fig. 6.99; Appendices 29 and 30), but geochemically (with the exception of K_2O) similar to that in the underlying mafic body. This suggests that the sedimentary rocks contain material reworked from the underlying mafic rocks and/or incorporation of contemporary mafic ash material.

Member 12 (Siltstone)

This member is c. 29 m thick (155.8–126.9 m) and is composed mainly of calcareous and dolomitic siltstone with several thin intervals of dolarenite and sandstone (Fig. 6.98). A 5-cm-thick intraformational conglomerate, which rests on the pale brown, massive dolarenite of member 11, defines the base of the member (Fig. 6.101be). The upper boundary is placed at the contact between a variegated siltstone and a pale grey, massive dolostone at 126.9 m depth (Fig. 6.98). All these rocks are characterised by low magnetic susceptibility values, gradually decreasing upward from c. 300 to c. 40 μSI ($K^* = 30–4 \times 10^{-6}$ SI in Fig. 6.99).

The member C rocks are variegated, though dark grey and brown colours dominate (Fig. 6.101aj–be). A widely fluctuating carbonate content in siltstones/shale results in a suite of rocks ranging from calcareous and dolomitic siltstones/shales, through marls and dolomarls, to impure dolostones and limestones. Abundant pseudomorphed calcium sulphates partially replaced by pink and white quartz and dolospar are a prominent feature. These include crystals, concretions and chicken-wire structures, which obliterate primary depositional structures (Figs. 6.101al–ap, aw–be). Sulphate-poor and sometimes desiccated siltstones show thick, flat and lenticular bedding (Figs. 6.101aj, ak, aq, ar, at, au) or are massive (Fig. 6.101av). In many intervals the siltstones exhibit numerous subvertical, dolomite-filled veinlets connecting former sulphate nodules (Figs. 6.101bb–bd). Two sandstone beds occurring in the upper part of the member have a sharp contact with the enclosing siltstones. The lower bed is variegated with lenticular bedding or a massive structure, whereas the upper bed is brown and massive with sulphate nodules partially replaced by white, drusy dolomite.

The dolomitic siltstones (MgO = 13.3–16.8 wt.%, CaO = 17.9–19.3 wt.%) have a high SiO_2 content (26–33 wt.%). Two whole-rock analyses show a high MnO concentration, peaking at 1.6 wt.%, which represents the greatest concentration recorded by the Hole 10B section (Fig. 6.99). A high Mn content is also revealed in an acid-soluble component (9,230 μg g^{-1}; Appendix 31), hence probably in dolomite. Al_2O_3 and K_2O concentrations show a limited range between 2.6 and 3.7 wt.%, and 1.1 and 1.3 wt.%, respectively (Fig. 6.99, Appendix 29). Two samples yielded sulphur contents of 0.02 and 0.07 wt.% (Appendix 30), apparently bound to relicts of sulphate. The rocks are devoid of measurable organic carbon (Appendix 30). A single analysis of carbonate-poor siltstone shows a hight SiO_2 content (77.7 wt.%) (Fig. 6.99; Appendix 29). In all analysed samples, carbonate $\delta^{13}C$ increases up-section from +8.7 to +11.8 ‰

(VPDB). The oxygen isotopic ratio varies independently of carbon, between 18.4 ‰ and 20.4 ‰ (VSMOW) (Brasier et al. 2011).

Member 13 (Upper Dolostone)

The Upper Dolostone member is a c. 10-m-thick unit (126.9–116.6 m; Fig. 6.98) comprising crystalline dolostones with a c. 70-cm-thick shale interbed in the middle. The member has sharp contacts with both the underlying and overlying siltstones. The magnetic susceptibility of the dolostones decreases irregularly upward from c. 70 to c. 20 μSI ($K^* = 6$ to 0.2×10^{-6} SI in Fig. 6.98), while that in the shale interbed is as much as 130 μSI ($K^* = 12 \times 10^{-6}$ SI in Fig. 6.98).

The dolostone unit below the shale interbed (126.9–123.7 m) begins with grey and brown, non-bedded dolostones with abundant small crystals of gypsum replaced by white dolospar (Fig. 6.101ai). This is followed by a c. 60-cm-thick unit of variegated dolostone with deformed lamination and large dissolution cavities partially lined by white, drusy dolomite (Fig. 6.101ah). The unit ends with beige, non-bedded dolostone containing dissolution cavities and a dissolution surface overlain by laminated dolostone that passes upward into the overlying dark brown shale. The dolostone unit above the shale starts with a 1.5-m-thick, grey, non-bedded dolostone bed containing small crystals of gypsum replaced by white dolospar. This is followed by 0.5-m-thick interval of pink, massive dolostone (Fig. 6.101af) with a dissolution surface overlain by a 1.3-m-thick interval of pink dolarenite displaying wrinkled lamination and abundant vugs (Figs. 6.101ad, ae). The unit ends with a 2.5-m-thick bed of pink, massive dolostone with a distinctive micrognular texture (Fig. 6.101ac). This dolostone progresses upward from dissolution to seemingly in situ brecciation; the upper surface is marked by dissolution (Fig. 6.101ab).

One analysis of crystalline, siliceous (32 wt.% SiO_2), clayey (5.4 wt.% Al_2O_3, 2.6 wt.% K_2O) dolostone ($Mg/Ca = 0.6$) shows high abundances of Mn (1310 μg g^{-1}) and P (1020 μg g^{-1}), a moderate Fe content (214 μg g^{-1}), and a low concentration of Sr (38 μg g^{-1}) (Appendices 29, 31). The siliceous, clayey dolostone has $\delta^{13}C = +11.5$ (VPDB) and $\delta^{18}O = 20.5$ ‰ (VSMOW). One whole-rock analysis of the "granular" dolostone ($Mg/Ca = 0.64$) shows a low content of SiO_2 (5.2 wt.%) and Al_2O_3 (0.8 wt.%), and the abundances of Fe_2O_3 and K_2O are below 0.5 wt.% (Appendix 29). The dolostone has 600 μg g^{-1} Mn, 100 μg g^{-1} Fe, and 133 μg g^{-1} Sr (Appendix 31). This dolostone records a $\delta^{13}C$ value of +15.5 (VPDB). Whilst $\delta^{13}C$ reaches the highest documented values in Core 10B, $\delta^{18}O$ of 20.5 ‰ (VSMOW) represents an average value (Brasier et al. 2011).

Member 14 (Nodular Shale-Siltstone-Marl-Breccia)

The member has a lower boundary at a depth of 116.6 m expressed by the first appearance of siltstone lying on the dissolved surface of the "granular" dolostone (Figs. 6.98 and 6.101ab). The upper contact is placed at a depth of 57.2 m where a transition occurs from marl- to breccia-dominated rocks (Fig. 6.98). Based on visual core examination, several lithofacies have been recognised in this c. 60-m-thick member. These include marl, siltstone, shale, breccias, clastic carbonates and minor sandstone (Fig. 6.98). However, microscopic examination suggests a high degree of diagenetic modification (and metamorphic recrystallisation) of all carbonate rocks. The carbonate crystal morphologies do not resemble detrital grains, and it remains to be studied whether they mostly represent primary precipitates, resedimented carbonates or early diagenetic replacements. In the lithological column we retain the original rock names (Fig. 6.98); however, two non-genetic terms, namely crystalline dolostone and crystalline limestone, are used to characterise them in the following descriptions.

A wide fluctuation of the dolomite and calcite content in siltstones/shale, combined with a considerable degree of (early and/or late) recrystallisation, hampers reliable identification of, and distinction between, various carbonate-bearing siltstones/shales without examining geochemical data. All lithologies in the member contain massive occurrences of former calcium sulphates partially replaced by pink and white quartz and dolospar. The sulphates appear in the form of crystals, rosettes, concretions and chicken-wire structures that have modified considerably and, in many intervals completely obliterated the earlier primary structures and textures. Further, the sulphates experienced multiphase dissolution, reprecipitation, plastic deformation and injection resulting in a brecciated appearance of the rocks. Consequently, distinguishing soft-sediment deformation features with ubiquitous sulphates (Figs. 6.101e–x, z, ab) from dissolution-collapse breccias (Figs. 6.101y, aa) is not straightforward. Brasier et al. (2011) also acknowledged that, above 80 m, distinguishing between evaporate-rich siltstone and dissolution-collapse breccias is problematic. Some sulphate-nodule-rich siltstones can be easily confused with, and logged as, breccias.

Magnetic susceptibility of all rock types does not exceed c. 200 μSI ($K^* = 20 \times 10^{-6}$ SI in Fig. 6.99) and does not show any stratigraphic trend. Shales and siltsones have a higher magnetic susceptibility than that of the carbonate rocks (down to 3 μSI).

The carbonate rocks of the member are both calcitic and dolomitic. Crystalline limestones occur at the base and in the upper part of the member. The lowermost limestone bed (114–109 m; $Mg/Ca = 0.015$) contains a considerable volume of calcite-pseudomorphed sulphates in the form of coalesced nodules and chicken-wire aggregates. The limestone has a grey, patchy appearance due to abundant white pseudomorphs after sulphate nodules. The rock contains a shale component, as shown by its whole-rock composition: 18.4 wt.% SiO_2, 3.3 wt.% Al_2O_3, and 1.2 wt.% K_2O (Appendix 29). Acid-soluble components have moderate Fe (69 μg g^{-1}) and elevated Mn (701 μg g^{-1}) and P (772 μg g^{-1}) concentrations (Appendix 31). Primary features were obliterated due to formation of diagenetic sulphates, their dissolution and/or remobilisiation.

Five additional limestone beds occur in the upper part of the member (between 80.7 and 58.6 m). Four are compositionally and structurally similar to the lowermost bed: grey or variegated, with a patchy appearance caused by abundant white sulphate nodules, and chicken-wire textures pseudomorphed by white sparry calcite. They are porous, non- or indistinctly bedded and pervasively recrystallised; some intervals (c. 73 m) retain voids filled with baroque dolomite. The limestones (Mg/Ca = 0.008–0.04) are impure and contain c. 22 wt.% SiO_2, 2–4.5 wt.% Al_2O_3, 0.6–1.9 wt.% K_2O (Appendix 29). They have low Fe (c. 60 μg g^{-1}) and Sr (c. 110 μg g^{-1}) contents, and greatly variable Mn abundances (30–2080 μg g^{-1}).

The single limestone bed (80.7–77.9 m) has sharp contacts with both the lower and upper host breccias. The limestone (Mg/Ca = 0.04) is pale pink and beige in colour. It is crystalline, porous and non- to parallel-bedded and pure (4.8 wt.% SiO_2, 0.05 wt.% Al_2O_3). It is markedly enriched in Ba (24,900 ppm), Sr (650 ppm), and has a sizable amount of S (0.5 wt.%), apparently bound to barite. The acid-soluble component shows a high concentration of Mn (3,030 μg g^{-1}) and low Fe (41 μg g^{-1}) and Sr (182 μg g^{-1}) contents (Appendix 31).

Pale grey, crystalline, partially calcitised dolostone (Mg/Ca = 0.55) occurs as three beds (1.3, 1.5 and 0.8 m thick) intercalated with shale intervals in the middle part of the member (Fig. 6.98). They contain abundant dolomite-pseudomorphed sulphate nodules and chicken-wire structure, as well as dismembered, soft-sediment deformed layers of brown and pale grey shales. This results in great impurity, as reflected in the chemical composition of the rocks: the dolostones are siliceous (29 wt.% SiO_2), rich in Al_2O_3 (c. 4 wt.%), contain c. 1 wt.% K_2O (Appendix 29), have high Mn (7210 μg g^{-1}) abundances, and moderate Fe (124 μg g^{-1}) and low Sr (34 μg g^{-1}) contents (Appendix 31); they are devoid of measurable sulphur and organic carbon (Appendix 30).

Shales and siltstones comprise the lower half of the member, and marls the upper half (Fig. 6.98). The distinction between these three lithologies is not straightforward, and therefore they are considered here as a single lithological group. They are grey or brown in colour with abundant white patches of former gypsum nodules and chicken-wire anhydrite partially replaced by quartz, dolomite and calcite (Figs. 6.101u–x, z, ab).

Where the volume of the former sulphates increases, the siltstones/shales/marls appear as "breccias" composed of dismembered, soft-sediment deformed, grey, laminated shale embedded in chicken-wire anhydrite partially replaced by white, drusy calcite/dolomite and quartz (Figs. 6.101y, aa). In two such beds (between 101.6 and 92.4 m; Fig. 6.98), the former sulphates are replaced by dolomite and quartz, hence these "breccias" are termed dolomitic. In contrast, where sulphates are replaced by calcite and quartz (breccias beds above 83.4 m), they are termed calcitic breccias. Both types of breccias have a patchy, variegated colour and crude bedding expressed by dismembered layers of brown and grey siltstone/shale/marl. A whole-rock analysis of marl with a small amount of former sulphate nodules shows 38 wt.% SiO_2, 10 wt.% Al_2O_3, 2.7 wt.% MgO, 21 wt.% CaO and 4.2 wt.% K_2O (Appendix 29).

Reuschel et al. (2012) reported in one sample (100.84 m) 121 ppm of carbonate-associated sulphate that yielded a $\delta^{34}S$ value of 15.8 ‰ (VCDT). Carbonate components extracted from various rock types show enrichment in ^{13}C with $\delta^{13}C$ ranging between +10.6 ‰ and +12.7 ‰ (VPDB). $\delta^{18}O$ fluctuates between 21.2 ‰ and 22.9 ‰ (VSMOW) (Brasier et al. 2011). Major and trace elements do not exhibit any stratigraphic trends (Fig. 6.99).

Member 15 (Shale-Dissolution Breccia)

The Shale-Dissolution Breccia member (57.2–20.6 m) has a gradational contact with the underlying rocks. Although breccias, clastic limestones and shales have been logged in the member (Fig. 6.98), only shales can be confidently identified as depositional (Figs. 6.101j, k); all other lithologies only vary by their proportions of calcite cement and shale/calcite 'clasts' (Figs. 6.101a–i, l–t). All rock types show a low magnetic susceptibility ranging from 6 to 120 μSI ($K^* = 0.5$ to $<20 \times 10^{-6}$ SI in Fig. 6.99).

Abundant breccias formed by evaporite solution and collapse have been previously reported from the Tulomozero Formation by Melezhik et al. (2000). Brasier et al. (2011) attributed most of the rocks in the uppermost part of Hole 10B section to evaporite solution and collapse. In general, member 15 breccias include centimetre-sized (up to 30 cm) intraformational siltstone, shale and mudstone clasts cemented by calcite. Clasts are both angular and rounded, and some are soft-sediment deformed (Figs. 6.101a–i, l–m, p–t). In some intervals fragmentation likely resulted from extensive formation of sulphate nodules. In several cases siltstone layers still show a coherent layering even though they are dismembered and separated by nodules (Fig. 6.101c). Many large fragments are coherent clasts of pink sandstone-grey siltstone couplets (Fig. 6.101a).

Clastic limestone that appears in the member (Fig. 6.98) differs from breccias only by a larger volume of calcite cement and by the presence of small limestone clasts (Fig. 6.101o). In both breccias and clastic limestones, the clasts are coated by euhedral calcite cement. Dissolution cavities in calcite cement are partially lined by drusy calcite. Pervasive recrystallisation has masked original (depositional) textural characteristics.

Whole-rock analyses suggest breccias and clastic limestones are compositionally similar, with differences caused by the amount of siltstone clasts. Breccias (Mg/Ca = 0.006) contain 15–20 wt.% SiO_2, 3.4–5.2 wt.% Al_2O_3 and 0.8–1.6 K_2O; abundances of all these oxides are lower in the clastic limestones (Mg/Ca = 0.004); 12–18 wt.% SiO_2, 0.7–2.8 wt.% Al_2O_3 and 0.1–1.36 K_2O (Appendix 29). One sample of breccia shows the highest CaO content (58.4 wt.%) recorded by Hole 10B (Fig. 6.99). All rocks show similar abundances of Fe (18–53 $\mu g\ g^{-1}$), Mn (113–255 $\mu g\ g^{-1}$) and Sr (18–53 $\mu g\ g^{-1}$) (Appendix 31). Contents of sulphur and organic carbon are below the detection limits (Appendix 30). Major and trace elements do not exhibit any obvious stratigraphic trends (Fig. 6.99).

Reuschel et al. (2012) reported relicts of sulphate in two breccia samples (37.60 and 36.29 m) 348–556 ppm sulphate. These samples yielded $\delta^{34}S$ of 7.8 to 9.8 ‰ (VCDT). Carbonate components extracted from all rock types exhibit $\delta^{13}C$ ranging between +10.16 ‰ and +11.7 ‰ (VPDB). $\delta^{18}O$ clusters tightly between 22.1 ‰ and 22.9 ‰ (VSMOW) (Brasier et al. 2011).

Shales occurring in three intervals (Fig. 6.98) are dark brown, desiccated and contain individual and coalesced crystals of apparent halite pseudomorphed by calcite (Figs. 6.101j, k). All three beds have sharp contacts with the encasing breccias.

Depositional Settings Based on Core 10A and 10B Logs

Previous studies suggested that the Tulomozero Formation accumulated in a complex combination of coastal and shallow-marine evaporitic environments (Sokolov 1963; Sokolov et al. 1970; Melezhik et al. 2000, 2001, 2005; Akhmedov et al. 2004; Brasier et al. 2011). Sedimentological features of the rocks documented in Cores 10A and 10B and illustrated in Figs. 6.97 and 6.101 are consistent with these previous works. A broad depositional pattern as depicted from 10A and 10B cores includes several facies of a shallow-water carbonate platform evolving into evaporitic environments and associated with the establishment of a large epeiric sea (for details see Chap. 3.3). These reconstructed depositional environments are summarised in Figs. 6.95 and 6.98 and are described below in stratigraphic order from oldest to youngest.

Slope-facies, fining-upward cycles of clastic dolostones. The lowermost part of the Hole 10A section (432–c. 347 m) appears as a series of fining-upward cycles composed mainly of thick beds of massive, poorly-sorted, clastic dolostones (Figs. 6.97fv, fx, fy, gj, gl–gs) with minor and thin intervals of bedded dolarenites (Figs. 6.97ga, gd–gg), variegated siltstone (Fig. 6.97gc), and a single bed of apparent stromatolite (Fig. 6.97fz). The rocks do not display any features suggestive of subaerial exposure, and the sedimentological features suggest a slope setting, in which carbonate clasts were derived from the eroded margin of a nearby carbonate platform.

Subtidal carbonate flat and probable submarine karst. The overlying succession (c. 347–328.7 m; Fig. 6.95) of brown and pink, bedded dolarenite-siltstone couplets with ripple-cross lamination, lenticular and flaser bedding, tidal bundles and drapes (Figs. 6.97fh, fk–fq), and the absence of emergent features are best interpreted as recording deposition in a subtidal carbonate flat. Within the 340–332 m interval, several beds of pink, massive dolostones show large dissolution cavities and pipes reminiscent of karst (Figs. 6.97ek–ey, fc–fj). Some cavities/holes are packed with pink dolostones in a brown, dolomarl matrix (e.g. Fig. 6.97fd). Most, though, are filled with brown, laminated or rhythmically bedded dolomarls (e.g. Figs. 6.97eo, eu, ey, ex, fc, fe, ff), hence suggesting a subaqueous environment. Consequently, given the close association with inferred subtidal deposits, we infer that the dissolution processes occurred subaqueously as a submarine karst. Such a phenomenon, though on a larger scale, has been reported from the Straits of Florida, where submarine karst is formed by freshwater discharge along the edges of the Florida platform (Land and Paull 2000).

Subtidal reefal stromatolite. At a depth of 328.7 m (Fig. 6.95), the karstified dolostones are sharply overlain by a >2-m-thick stromatolitic dolostone followed by thick-bedded dolarenites (Fig. 6.97ed) and, at c. 317–307 m (Fig. 6.95), another stromatolite and dolarenite bed (Figs. 6.97eb, ec). These are interpreted as subtidal stromatolite lithofacies.

Shallowing-upward carbonate-evaporitic cycles. At a depth of c. 307 m (Fig. 6.95), the stromatolitic dolostones pass rapidly into variegated dolomarl-siltstone forming a c. 23-m-thick, shallowing-upward carbonate-evaporitic cycle, followed by four other cycles of similar thickness (Figs. 6.95 and 6.102a–c). The carbonate parts of these cycles comprise bedded dolostones with sparse microbial lamination (Figs. 6.97bx, bz, ca, df, dg, dh) and are interpreted as representing shoaling through the intertidal zone. Transitional to evaporitic parts of the cycles are dolostones and dolostone-siltstones with dolomite-pseudomorphed, displacive crystals and rosettes of calcium sulphates (Figs. 6.97cl–co, cr, cs). Some beds have enterolithic structures (Figs. 6.97cn–cq) that may represent beds of calcium sulphates now replaced by dolomite. Evaporitic *per se* parts of the cycles comprise black, grey, brown and red, homogeneous to laminated, siltstones and dolomarls with abundant gypsum and anhydrite in the form of displacive crystals, rosettes, nodules and chicken-wire aggregates, now partially pseudomorphed by dolomite and silica (Figs. 6.97by, cf–ck, ct, cu, dc, dd, dj, dl–do, dq–du, dx, ea). Any primary lamination in these lithofacies has been severely modified or completely obliterated by turbation during sub-surface gypsum and anhydrite growth. Some dolomarl beds show enterolithic structure, expressed by irregular, tight to open folds (Figs. 6.97dk, dp). Such structures commonly develop in evaporite sequences where they form by the swelling of anhydrite during its hydration to gypsum (Butler 1970; Butler et al. 1982). These sedimentological features suggest a sabkha depositional system.

The c. 7-m-thick, massive, homogeneous bed of coarse-crystalline dolomite at 190.4–183.1 m (Fig. 6.95) may also represent a former bed of massive sulphates. Up to 2-cm-sized dolomite crystals, tightly packed and cemented by white dolospar, is a texture (Fig. 6.97bw) that has not been reported from elsewhere in the Tulomozero Formation. Many crystals are xenomorphic, some rounded and partially dissolved, whereas others show cubic shapes. These rocks have been identified as recrystallised dolomitic gritstone during visual core examination. However, greenschist facies alteration cannot account for the formation of these large dolomite crystals, which, instead, may represent halite or anhydrite replacements; further detailed petrographic work is needed to assess this possibility.

Massive breccias occurring in some cycles suggest dissolution and collapse of evaporites. Clasts are intraformational siltstones or dolostones and commonly monomictic in each bed (Fig. 6.97db). The clasts are cemented by white, drusy dolomite, show no transport, and in places, can be easily assembled into their original layer (Fig. 6.97cw). Where dissolution-collapse breccias were reworked by currents, they appear as intraformational, monomict conglomerates (Figs. 6.97cu, cz).

Several shallowing-upward cycles documented through members 4–6 are variable in detail, as demonstrated in Figs. 6.95 and 6.102. Repetitions of such variable cycles are common in carbonate formations and reflect periodic flooding of platforms through transgressive events and suggest deposition in intertidal environments. In contrast, the nodular dolomarls and siltstone are similar to those described in peritidal sabkha sequences (e.g. Warren and Kendal 1985; Kendall 1992).

Playa dolomarl. At 183.1–172.2 m (Fig. 6.95), the uppermost carbonate-evaporitic cycle ends with a black, massive dolomarl showing several intensely desiccated and in situ brecciated intervals, and a c. 0.3-m-thick, dark brown, indistinctly bedded, fine-grained sandstone bed in the middle. The dolomarl contains both nodular sulphates and casts of halite crystals (Figs. 6.97bu, bv). Inclusion of the sand bed suggests a proximity to land, whereas other sedimentological features tentatively suggest an ephemeral playa lake developed in a coastal sabkha.

Sabkha magnesite. In recent evaporitic environments, gypsum, anhydrite and halite are the main minerals (Warren 2006); other minerals such as celestite and magnesite are precipitated in minor quantities (e.g. Bush 1973). Hence, the three magnesite beds associated with shallowing-upward carbonate-evaporitic cycles (Fig. 6.95) warrant a separate discussion. The thickest magnesite bed (3.7 m) is composed of monotonous, massive or indistinctly bedded, fine-grained magnesite (Fig. 6.97di). Two other beds, 2.7 and 1.2 m thick, comprise white and pale grey, syndepositional breccias composed of angular, unsorted fragments of coarse-grained magnesite embedded in a crystalline magnesite matrix with relicts of rounded magnesite grains and syntaxial magnesite spar overgrowths. A series of magnesite beds up to 15 m in thickness have been previously reported from drillcores 4699 and 5177 located c. 70 km to the southeast of Holes 10A and 10B (Fig. 6.86). These beds comprise micritic, stromatolitic and crystalline magnesite, and their formation was assigned to early diagenetic replacement of dolomite by mixed seawater-meteoric fluids in evaporitic sabkha or playa environments (Melezhik et al. 2001). We suggest a similar origin for the magnesite beds in Hole 10A.

Peritidal clastic dolostones. The sabkha-playa dolomarl passes rapidly into clastic dolostones (Figs. 6.97bb–bj, bn–bs) containing thin intervals of sandstones and a single bed of brown, nodular dolomarl (Figs. 6.97bj–bm). The lower part of this 40-m-thick succession (172.2–131.4 m; Fig. 6.95) comprises brown, parallel-bedded, dolarenite-siltstone couplets with rare dolomite-pseudomorphed gypsum rosettes (Figs. 6.97bs, bt). Wrinkled lamination in some dolostone beds implies the presence of microbial mats, and mud-drapes (Fig. 6.97bp), and lensoidal bedding (dolarenite ripples, Fig. 6.97bg) are suggestive of a lower intertidal setting. The overlying light-coloured, massive or thick-bedded dolarenite and dolorudite contain poorly sorted and variably reworked intraformational dolostone clasts with sizes varying from bed to bed (Figs. 6.97bf–bj, bn–br). Dismembered dolarenite beds embedded in a dolorenite matrix (Fig. 6.97bh) imply sediment-gravity flow processes, which suggest the presence of nearby steep slopes. The uppermost part of the succession shows several dissolution surfaces (Figs. 6.97bb, be) and increased deposition of pink dolostone breccias (Figs. 6.97bc, bd), which are all together interpreted as a phase of emergence. The overall sedimentological characteristics of the dolarenite/dolorudite-dominated lithofacies are consistent with clastic carbonates deposited in a peritidal setting adjacent to a carbonate platform, with local irregular subaqueous topography (to generate slopes for sediment-gravity flow deposits).

Intertidal sandflat. The phase of emergence was followed by the deposition of sandstone-dominated lithofacies through the 131.4–107.6 m interval (Fig. 6.95). Muddy, haematite-stained, thick-bedded sandstone with medium-scale bedforms shows low-angle lamination, small-scale scouring and/or channeling. Such bedforms and associated heterolithic facies (Figs. 6.97as–ay, ba) indicate deposition on a sandflat, under intertidal, low-flow regime conditions. All clasts observed in the sandstones (Figs. 6.97au, ba) can be attributed to intraformational sources. Rare desiccated mud-beds and buckling due to evaporation (Figs. 6.97as, au) indicate short-lived periods of emergence. Associated with the sandstones are clastic dolostones composed of unsorted, angular fragments of dolarenite (Figs. 6.97av–ax); these may have been sourced from a nearby eroded carbonate platform/shelf and transported across the intertidal sandflat by tides and waves.

Mudflat/upper intertidal heterolithic sabkha. The sandflat deposits pass transitionally into variegated sandstone-siltstone-mudstone rocks with heterolithic bedding modified by desiccation and sub-surface growth of sulphate nodules (Figs. 6.97ao–aq). The 107.6–72.1 m (Fig. 6.95) interval of siltstone/mudstone-dominated lithofacies with numerous small-scale beds of breccias, sandstone, dolarenite and marl is particularly noteworthy for its grey, brown and variegated colours and spectacular silica- and dolomite-pseudomorphed gypsum crystals, rosettes, nodules, and chicken-wire and enterolithic structures (Figs. 6.97v–ak). These features are typical of a mudflat in a sabkha setting.

Intertidal carbonate flat. The mudflat/sabkha lithofacies are overlain by dolostone whose bedding has been obliterated by turbation during sub-surface sulphate growth (now quartz-pseudomorphed chicken-wire fabrics; Fig. 6.97u). This dolostone forms the base for a c. 6-m-thick bed (71–65 m interval; Fig. 6.95) of interbedded small-scale domal, columnar and flat-laminated, fenestral stromatolites (Figs. 6.97m, n, r–t) with thin interlayers of micritic dolostone and intraclastic dolarenites (Figs. 6.97o, p). Intense desiccation and formation of diagenetic sulphates (Figs. 6.97p–s) are suggestive of supra- to intertidal settings and the stromatolitic dolostones are consistent with an associated lagoonal and/or shallow-marine setting.

The overlying mature sandstone with parallel bedding (Fig. 6.97k) was likely a beach swash face (60.7–59 m interval), followed by the next episode of sabkha deposition marked by marls (59–55.2 m interval) whose lamination was severely modified by growth of diagenetic gypsum and anhydrite (Figs. 6.97i, j).

Moving higher in the stratigraphy (to around 53.4 m), white, homogenous, massive dolostone with clotted, microbial, oncolitic and rare small-scale domal stromatolitic structures define a c. 6.3-m-thick interval (to around 47.1 m). The lack of lamination, the overall microstructures and massive macroappearance of this microbiolithic bed superficially resembles thrombolites (cf. Aitken 1967). If so, these provide a good indicator of deposition in shallow tidal-intertidal settings.

Breccias and dolorudites occurring above the subtidal thrombolytic interval (around 54–54.5 m) can be attributed to solution-collapse of evaporites (Figs. 6.97g, h) with the overlying brown mudstone with sulphate rosettes (Fig. 6.97f); this suggests a return to sabkha conditions. The following two sandstone-dolostone cycles (47.1–c. 19 m; Fig. 6.95) comprise variegated, coarse-grained, dolomite-cemented sandstones with lensoidal bedding and mud drapes (Fig. 6.97e), dolorudites (in places graded; Fig. 6.97d), dolarenites (in places with mud drapes; Fig. 6.97c), and microbial dolostones with desiccated fabrics (Fig. 6.97b) and rare small domal stromatolites (Fig. 6.97a). This lithofacies association is interpreted as an intertidal carbonate flat affected by fluxes of land-derived clastic material.

Supratidal, lagoonal, clastic dolostones. The exact relationship of the inferred lagoonal facies (Fig. 6.98) with intertidal carbonate flat sediments (Fig. 6.95) remains speculative due to uncertainties in correlation of Cores 10A and 10B. The lowermost 8 m of Core 10B (278.3–270.4 m) comprise interbedded siltstone, sandstone, conglomerate and dolarenite (Figs. 6.101dj–do). These different lithologies share several features: pinkish colour, massive structure, abundant and large dissolution cavities cemented by white, drusy dolomite and quartz grains. Intraformational clasts of carbonate rocks indicate minor transport and reworking. Rare dolarenite beds (e.g. at around 272. 6 m; Fig. 6.98) show bedding and former sulphate nodules partially replaced by quartz and drusy dolomite (Fig. 6.101dk). These features are compatible with supratidal-lagoonal settings.

Carbonate platform/shelf. Depositional environments associated either with an incipient carbonate platform or with the marginal part of a large carbonate platform/shelf are recorded in the lithofacies spanning the 270.4 to c. 251.5 m interval (Fig. 6.98). These include bedded dolarenite, dolorudite and columnar stromatolite (Figs. 6.101dc–di), which have been previously interpreted to represent shallow intertidal and the least-restricted environments observed in Core 10B (Brasier et al. 2011). However, some dolostone beds show *in situ* brecciation and collapse structures resembling incipient karst (e.g. Fig. 6.101dh). It is important to note that the stromatolites at a depth of 252 m and the overlying dolarenite-dolorudite at a depth of 248.8 m seem overturned, and hence the depositional sequence described above might be in reverse order.

Supratidal, evaporitic carbonate flat. The overlying facies association at 251.5–227 m (Fig. 6.98) comprises a variety of clastic dolostones (dolostone breccias, conglomerate, gritstone and dolarenite) with minor beds of shale and marl (Fig. 6.98). Several features are common in all lithologies: red-brown colour, in situ brecciation, lack of bedding, abundant dolomite-cemented dissolution cavities (Figs. 6.101ch–cx). Intraformational clasts of red-brown siltstone and dolostone are unsorted and show no or minor transport; some siltstone fragments are soft-sediment deformed (Figs. 6.101st–cw). The dolorudites composed of slightly reworked intraformational clasts (Figs. 6.101ci, cj, cy–db) may represent dissolution-collapse breccias redeposited by storm or large tides. Pendant vadose cements are found on the undersides of dolostone breccias clasts at 226 m (Brasier et al. 2011). Unusual crystalline dolostones at 230–227 m (Figs. 6.101ch–cl, co, cp) composed of large, bright red dolomite crystals may represent pseudomorphed calcium sulphate or even halite deposited in ponds on a sabkha surface. All these features can be attributed to an episodically exposed and reworked carbonate flat, solution-collapse of evaporites and formation of karst.

Low intertidal mud/sand flat. The carbonate-flat deposits pass rather abruptly into variegated, sandstone-siltstone-mudstone (227–166 m; Fig. 6.98) with parallel or heterolithic bedding. Small-scale bedforms, low-angle lamination in sandstone layers and the absence of significant scouring or channeling at the bases of sandstones (Figs. 6.101bx, bz–cg) indicate deposition under lower-flow regime conditions (Brasier et al. 2011), apparently in a lower intertidal flat. All clasts (e.g. Figs. 6.101ce–cg) are derived locally. The sandstones at 174.8–173.4 m contain large sulphate nodules partially replaced by pink, porous quartz (Fig. 6.101bx) suggesting an episode of evaporitic conditions. This phase of deposition was interrupted by the eruption and subareal deposition of mafic lavas (212.1–175 m). This volcanic phase can be recognised across the Onega Basin and forms an important marker in the Tulomozero Formation (e.g. Satzuk et al. 1988; Krupenik and Sveshnikova 2011).

Upper intertidal, evaporitic sand flat. Interlaminated siltstones and sandstones (particularly around 170 m; Fig. 6.98) with heterolithic structures, sand-mud couplets, tidal bundles and drapes (Figs. 6.101br–bw), and, in places, sand-filled desiccation cracks (Figs. 6.101br–bu) are evidence for deposition in evaporitic, sand-flat depositional environments. Up-section (around 166 m), these facies pass gradually into green-brown sandstone-mudstone (166.3–157.9 m) with sulphate nodules and chicken-wire anhydrite partially replaced by pale pink, porous quartz (Figs. 6.101bk–bq). These rocks are marked by an elevated content of non-carbonate MgO (13.3 wt.%, Appendix 29) and chlorite suggesting incorporation of partially decomposed mafic ash material, most likely linked to the episode of extrusion of mafic lavas.

Supratidal sabkha. The green-brown, nodular sandstones pass transitionally into a muddy siltstone with thin and rare interlayers of marl and dolarenite. This lithofacies occurs between 157.9 and c. 127 m (Fig. 6.98) and is distinctive because of a black and dark brown colouration and massive development of sulphates in the form of nodules and chicken-wire aggregates, now partially replaced by pink-brownish quartz and dolomite (Figs. 6.101aj–bi). Primary lamination has been largely obliterated by sub-surface growth of gypsum and anhydrite, but, where preserved, displays lenticular bedding (Fig. 6.101aq). These combined features indicate deposition mostly in supratidal settings.

Intertidal carbonate flat. The c. 10-m-thick (c. 127–116 m; Fig. 6.98) succession of pink and purple dolostones with massive structure and wrinkled (microbial?) lamination, and dissolution voids, marks a return to intertidal deposition. These dolostones are marked by the highest $\delta^{13}C_{carb}$ value of +15.5 ‰ (VPDB) (Brasier et al. 2011).

Supratidal sabkha. The overlying marl-shale-siltstone-breccia association was deposited on a dissolved surface of dolostone displaying dissolution features (Fig. 6.101ab). Small-scale, shallowing-upward carbonate-evaporitic cycles are present and are similar to, but thinner than, those documented in Core 10A (Fig. 6.102d). In addition, almost all lithologies occurring throughout the 116–20.6 m interval (Fig. 6.98) contain abundant displacive crystals, rosettes and nodules of gypsum, and chicken-wire anhydrite, now present as quartz and drusy dolomite pseudomorphs (e.g. Figs. 6.89 and 6.101j, k), and their growth has severly modified primary lamination (Figs. 6.101l–n, u–aa). Breccias consisting of angular siltstone and mudstone fragments in a porous, drusy calcite matrix (Figs. 6.101d–i, p–t) are attributable to solution-collapse of evaporites (Brasier et al. 2011). Other evaporite-related breccias are composed of soft-sediment deformed, brown and red siltstone-mudstone fragments set in porous, drusy calcite matrices. They represent extreme development of chicken-wire anhydrite (Figs. 6.101b, c, l–n). Nodular mosaic and chicken-wire anhydrites typically form in the shallow subsurface of sabkha where anhydrite displaces the host sediment during growth, or where anhydrite replaces gypsum during burial (Kendall 1992). It is difficult to discriminate between these two options here.

The lithofacies associations and interpreted depositional settings indicate that the Tulomozero Formation rocks recovered in Holes 10A and 10B consist of supratidal-intertidal carbonate-clastic and carbonate-evaporite cycles; slope clastic carbonates; reefal stromatolites; sabkha mudflats; and sand-flat environments. Depositional settings are typical of those associated with the establishment and growth of a shallow-marine carbonate platform. Several repeated carbonate-evaporite cycles (Fig. 6.102) record frequent fluctuation in sea-level, phases of exposure of the platform to supratidal-subaerial processes, deposition of sabkha evaporites, and karstification: a suite of characteristics that fits with models of epeiric sea carbonate platforms (cf. Irwin 1965).

All carbonates sampled during archiving of Cores 10A and 10B record the Lomagundi-Jatuli carbon isotopic excursion (Brasier et al. 2011; Reuschel et al. 2012; Fig. 6.92). Previous sedimentological and isotopic studies of the Tulomozero Formation carbonates inferred a significant role of local processes in ^{13}C enhancement, such as restricted/evaporitic settings and/or biological up-take and recycling of organic matter (e.g. Melezhik et al. 1999, 2005). Melezhik et al. (1999) further speculated that $\delta^{13}C$ of +4‰ was a global seawater signal.

Targetted research of Core 10B has reached the conclusion that the carbonates that accumulated in the least restricted environments exhibit the lowest $\delta^{13}C$ of +7.6‰ (VPDB), which may represent the closest approximation of the 'global' Lomagundi-Jatuli signal (Brasier et al. 2011). It was also concluded that there is no evidence that dolomite precipitation (or dolomitisation), calcium sulphate calcitisation and production of the high ^{13}C values were directly influenced by the activity of sulphate-reducing and/or methanogenic bacteria. The cause of the sharp deviation of $\delta^{13}C$, from +11 to +15.6‰, in the upper part of Core 10B remains to be explained. Interestingly, a sharp positive excursion of the same magnitude has been recorded in the upper part of drillcore 7; this also remains unexplained.

Even though carbonate- and quartz-pseudomorphed sulphate with abundant μm-sized anhydrite and barite relicts are widespread in the Tulomozero Formation, evidence for sulphate-reducing bacteria has not been detected. The formation also hosts a spectacular occurrence of thick, massive anhydrite beds recovered by a deep drillhole (Morozov et al. 2010; see Chap. 7.5). The study conducted by Reuschel et al. (2012) on Cores 10A and 10B identified measurable amounts of carbonate-associated (CAS) and breccia-associated sulphates (BAS) in a variety of lithologies. $\delta^{34}S$ obtained from these two proxies (10.9 ± 2.7 ‰ and 9.0 ± 1.1 ‰ (VCDT), respectively) show no distinct stratigraphic variations through middle and upper parts of the Tulomozero Formation, hence suggesting that the sulphur isotopic composition of the seawater sulphate remained constant during the time of deposition. However, fourteen $\delta^{34}S$ measurements from massive anhydrite beds comprising the base of the formation are lower, ranging between 4.8 ‰ and 5.7 ‰ (VCDT), though also showing no stratigraphic variation pattern (Krupenik et al. 2011b).

Ubiquitous pseudomorphs after Ca-sulphates with abundant μm-size anhydrite relicts documented through Cores 10 and 10B (e.g. Fig. 6.97dy) offer an opportunity for in situ measurement of sulphate sulphur isotopic compositions. The sulphate relicts preserved in silica- and carbonate-pseudomorphed concretions and crystals represent an independent proxy to address the seawater isotopic composition. This approach was shown to be viable by Reuschel et al. (2012) through the 270–300 m interval of Core 10A, thus offering an exciting research avenue for future studies.

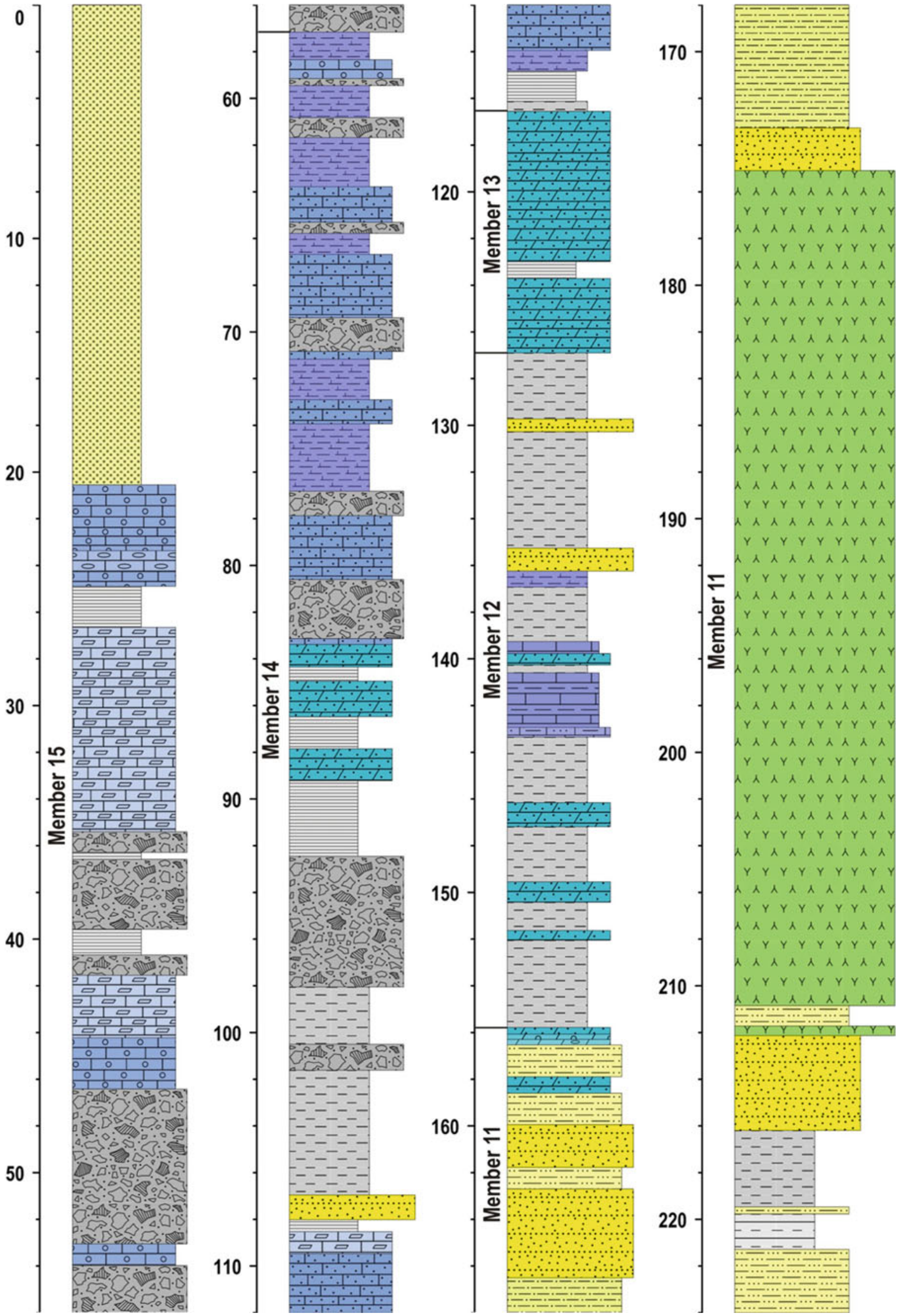

Fig. 6.98 Lithological section of the Tulomozero Formation based on core log of Hole 10B. Reconstructed depositional environments based on Brasier et al. (2011), core logging, geological mapping and sedimentological research in the vicinity of the drilling site

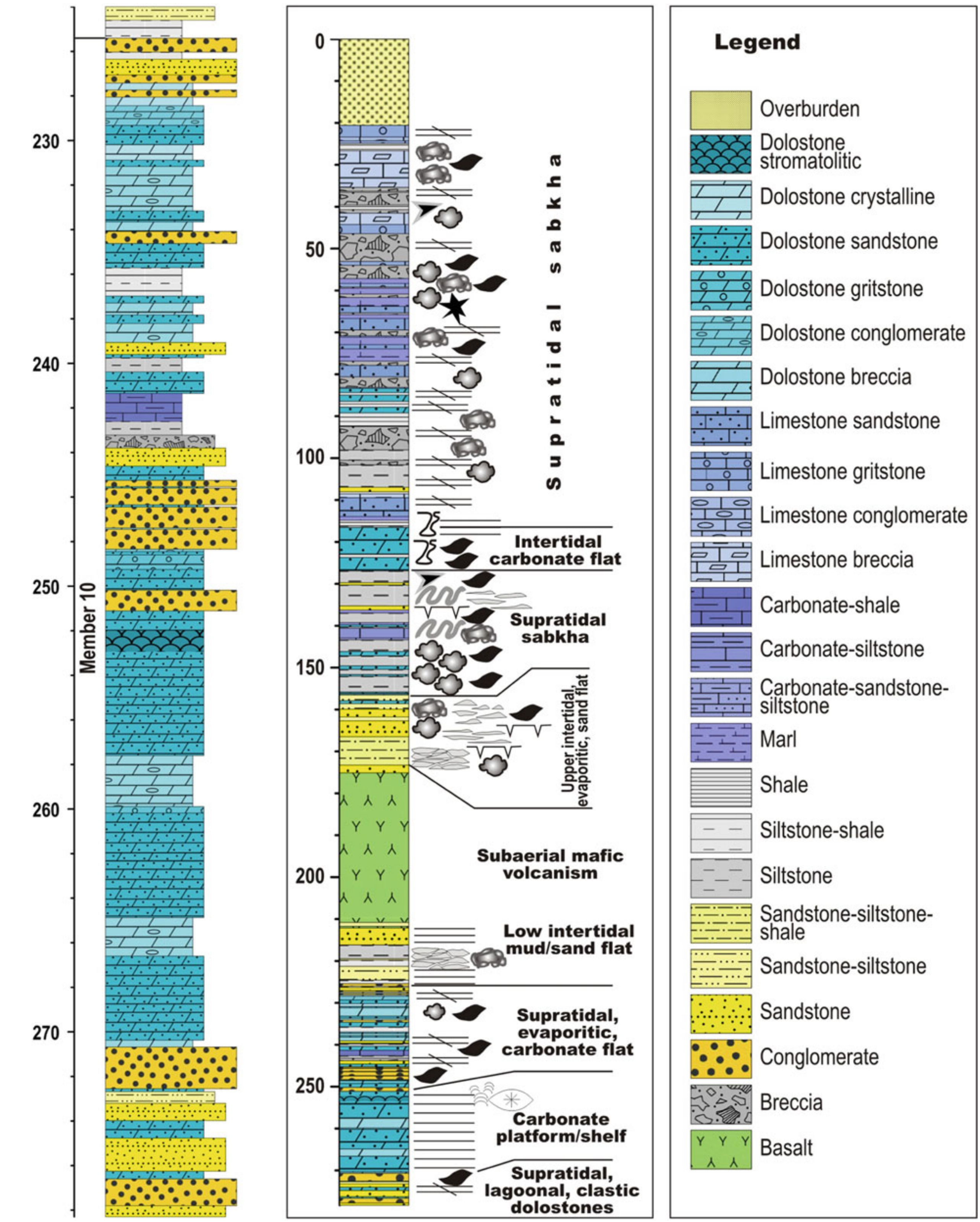

Fig. 6.98 (continued) Lithological section of the Tulomozero Formation based on core log of Hole 10B. Reconstructed depositional environments based on Brasier et al. (2011), core logging, geological mapping and sedimentological research in the vicinity of the drilling site. Lithological symbols are explained in Fig. 6.6

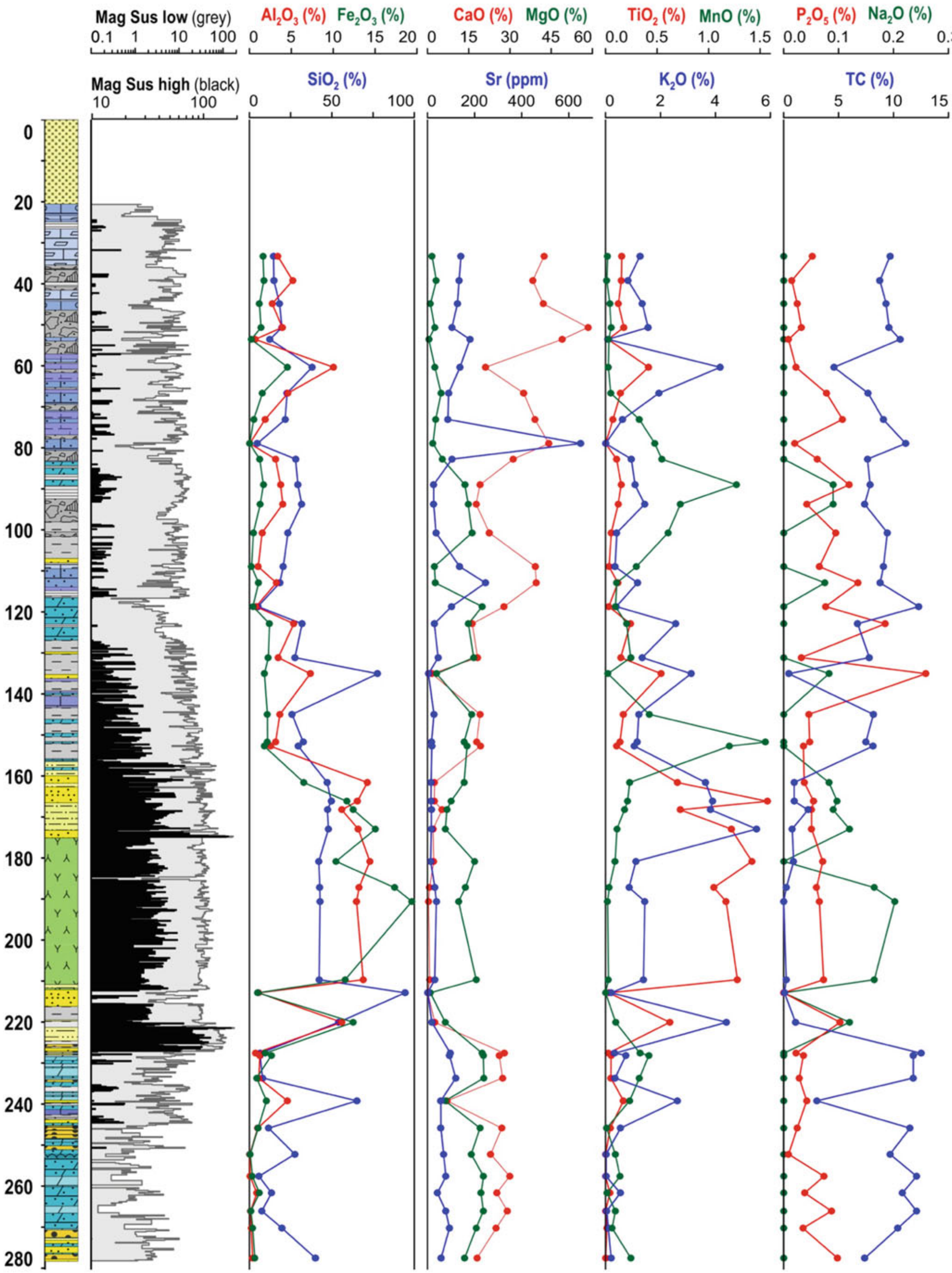

Fig. 6.99 Relative magnetic susceptibility (K*), and geochemical profiles of selected elements in Core 10B based on the archive samples collected with c. 8 m-spacing. For analytical techniques and data quality see Part 5

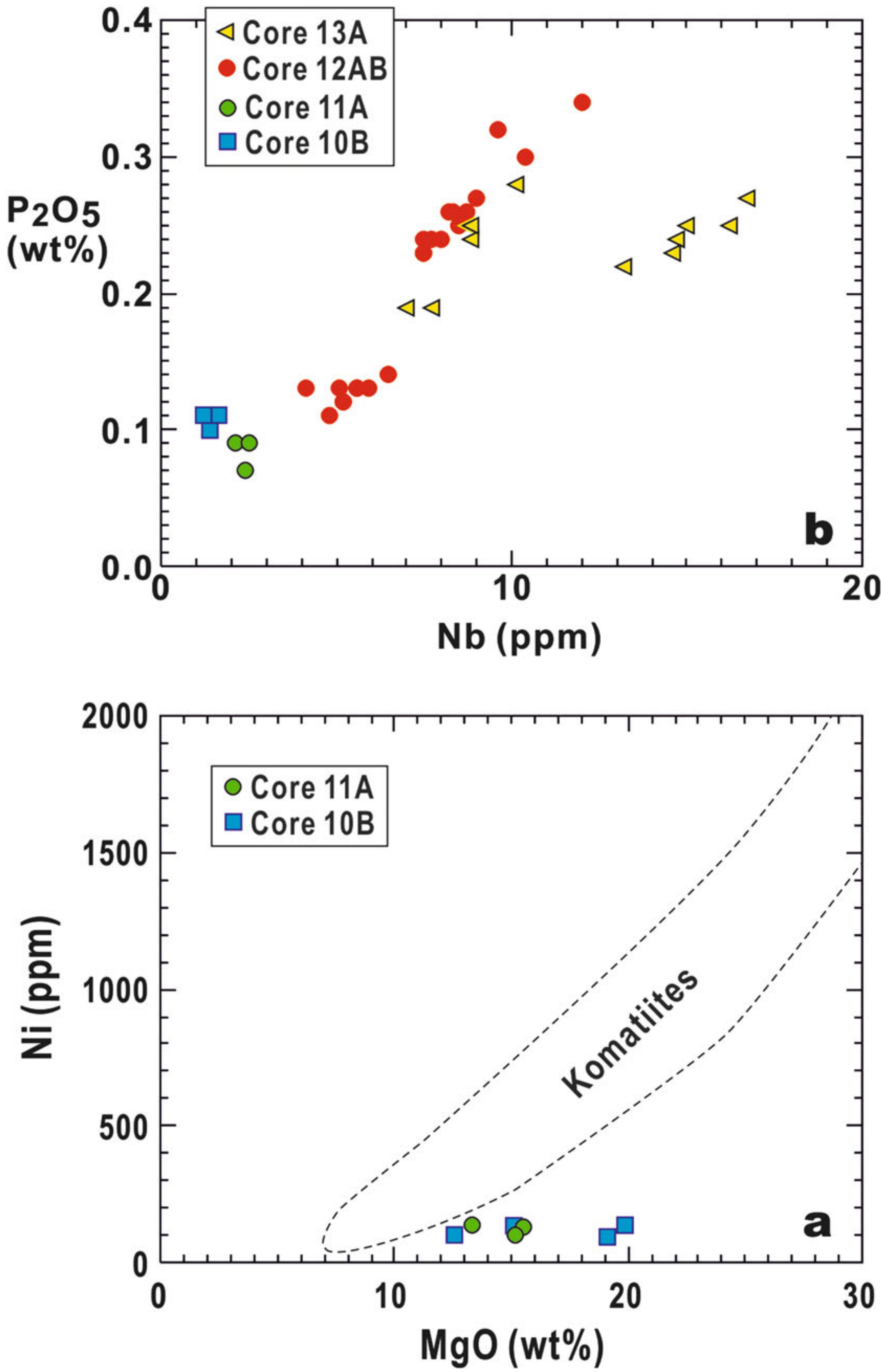

Fig. 6.100 (**a**) MgO versus Ni diagram for igneous rocks from Cores 10B and 11A. A comparative field is shown for komatiites from the literature. (**b**) Nb vs P_2O_5 diagram for basaltic rocks from the Onega Basin drillcores

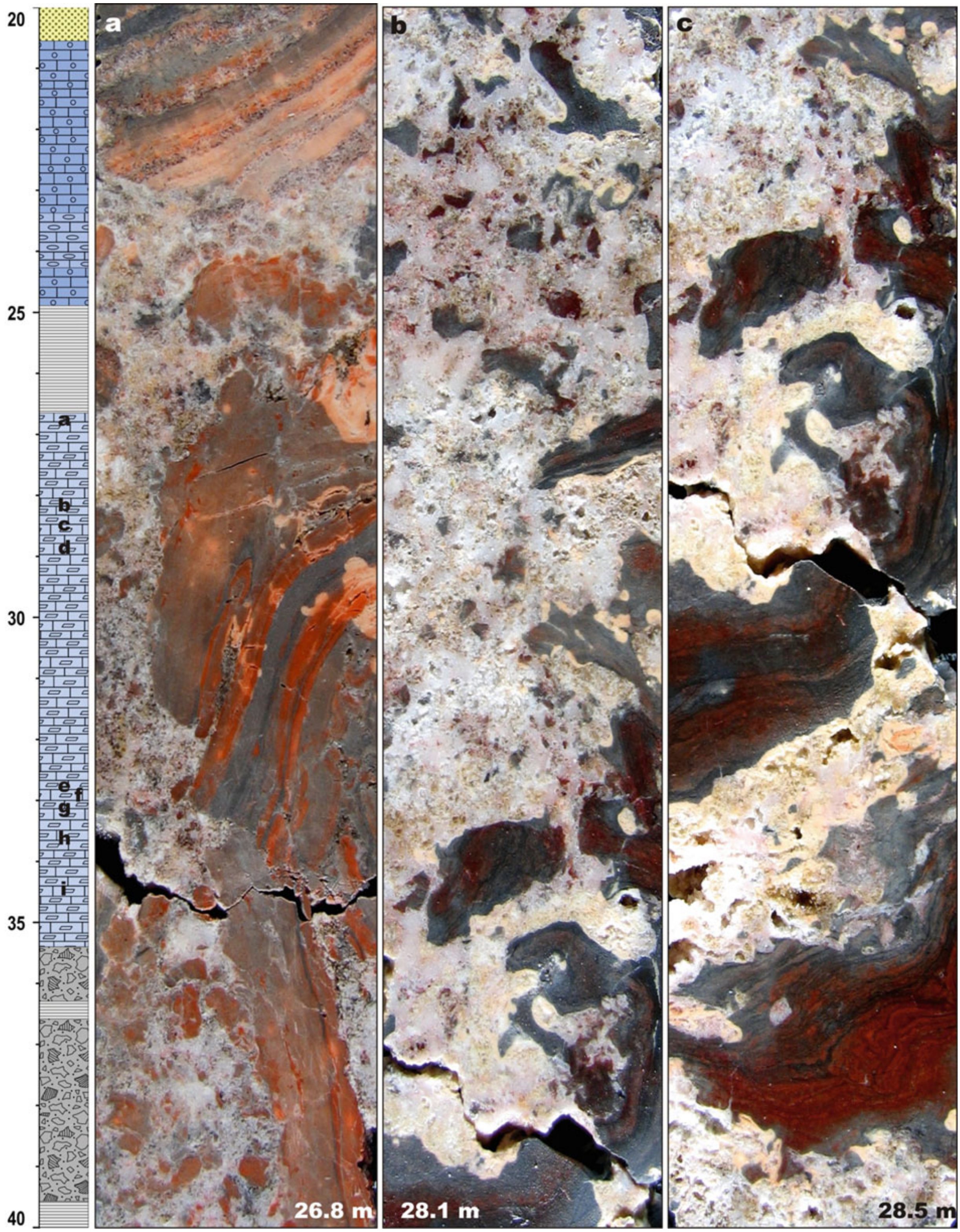

Fig. 6.101 Sedimentological features of main rock types of the Tulomozero Formation based on Core 10B. Core diameter in all plates is 5 cm unless specified otherwise. *Member 15 (Shale-Dissolution Breccia)*: (**a**) Dissolution-collapse brecccia composed of fragments of variegated, laminated shale cemented by white, drusy calcite; note that the size and shape of shale fragments vary greatly. (**b**, **c**) Dissolution-collapse breccia composed of fragments of brown shale and white, porous calcite cemented by white, drusy calcite; note that the shale fragments show soft-sediment deformation, while the fragments of porous calcite are affected by multiple dissolution, in situ fragmentation and cementation

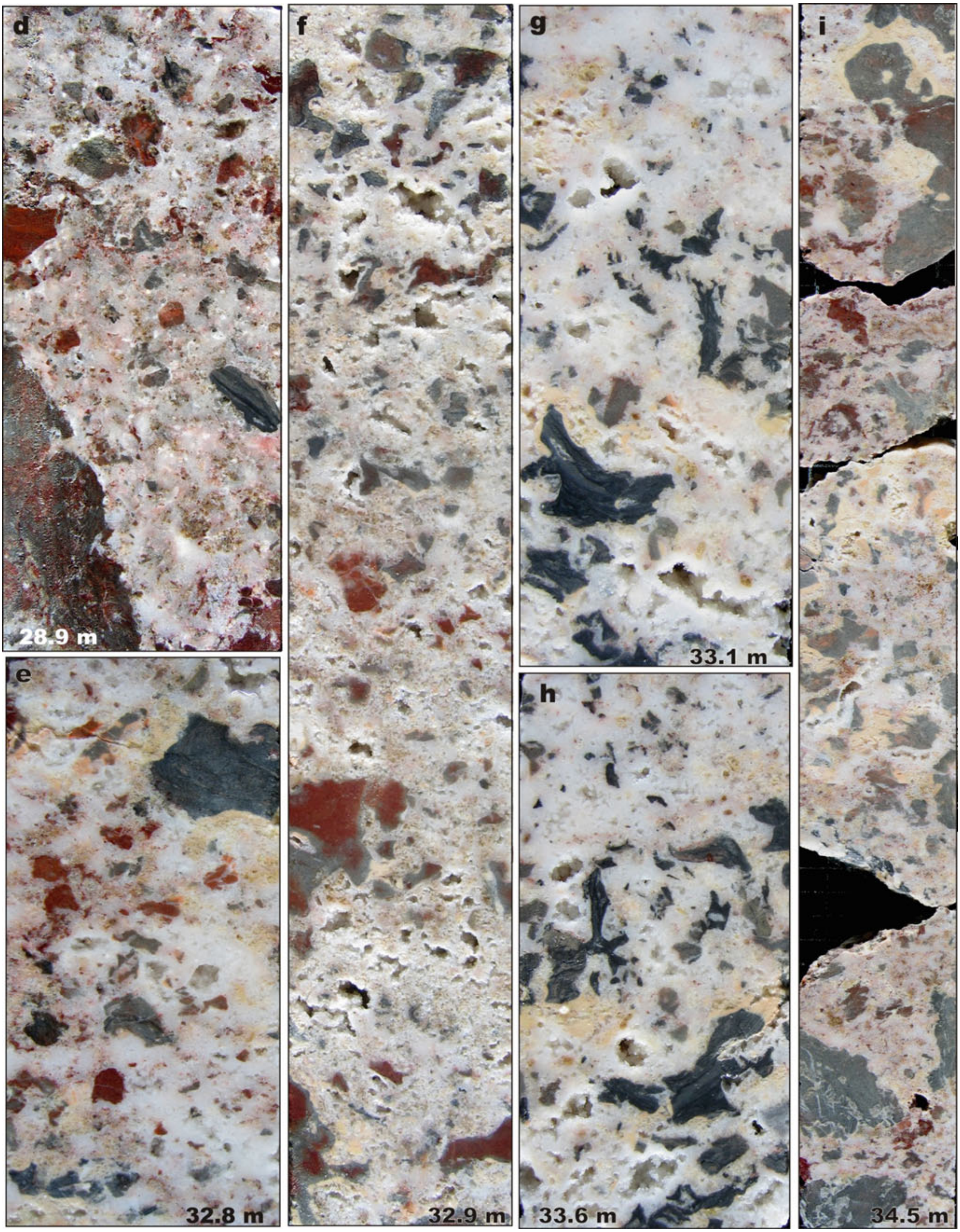

Fig. 6.101 (continued) (**d**–**i**) Dissolution-collapse breccia composed of fragments of vuggy, sparry calcite and dark brown, grey and red, massive shale cemented by white, drusy calcite; note that the fragments of vuggy, sparry calcite show multiple dissolution and cementation

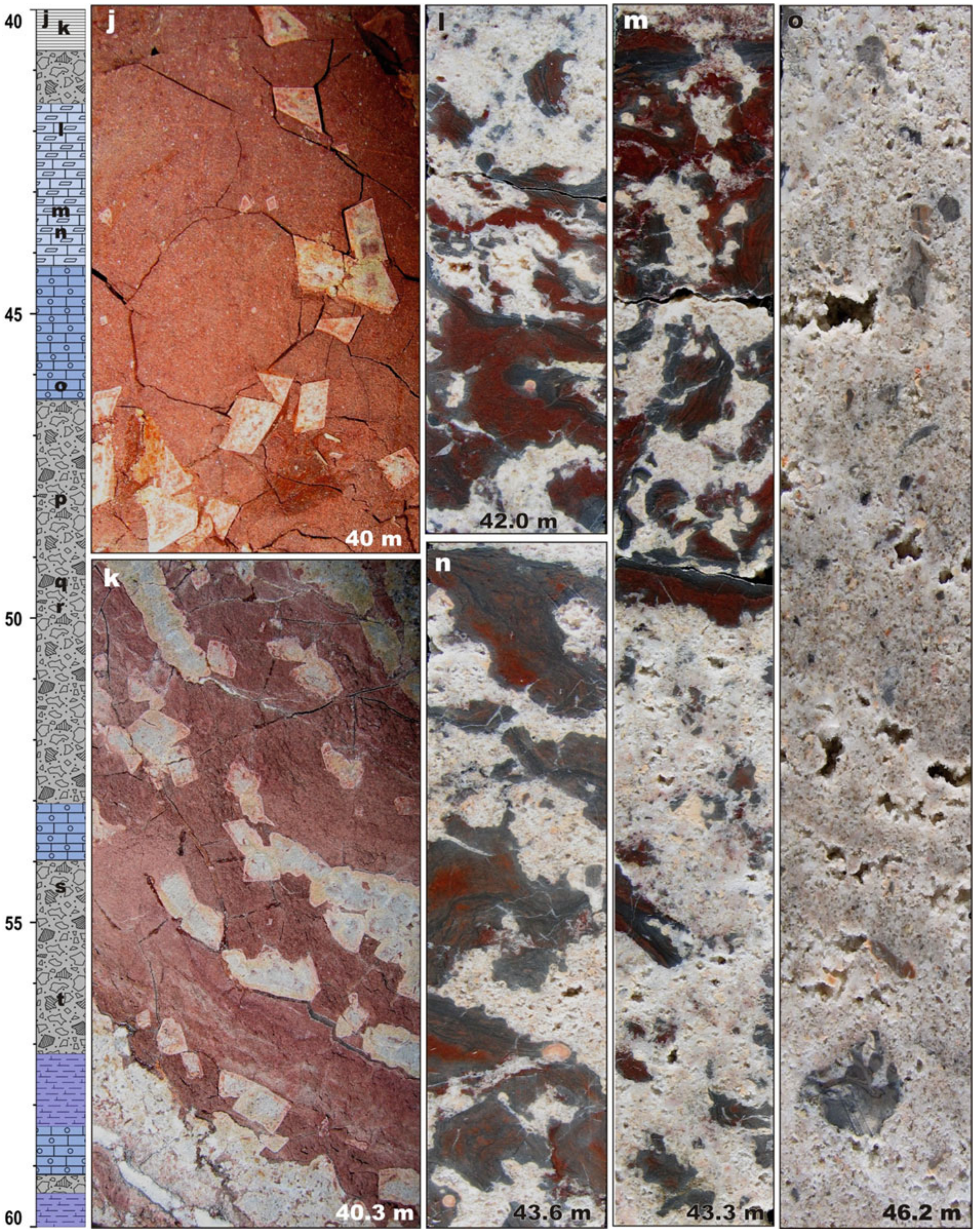

Fig. 6.101 (continued) (**j**) Brown mudstone with polygonal cracks and calcite-pseudomorphed apparent halite crystals. (**k**) Brown mudstone with individual and coalesced crystals of apparent halite pseudomorphed by calcite. (**l**) Soft-sediment deformed, dark brown shale with clumps of calcium sulphate partially replaced by white, drusy calcite. (**m**) In situ brecciated, white, vuggy, drusy calcite (former calcium sulphates) with scattered fragments of brown mudstone overlain by soft-sediment deformed, dark brown shale with clumps of calcium sulphate partially replaced by white, drusy calcite. (**n**) Soft-sediment deformed, dark brown shale with clumps of calcium sulphate partially replaced by white, drusy calcite. (**o**) White, porous, non-bedded limestone composed of small siltstone and limestone clasts set in calcite cement; note the dissolution cavities in the calcite cement

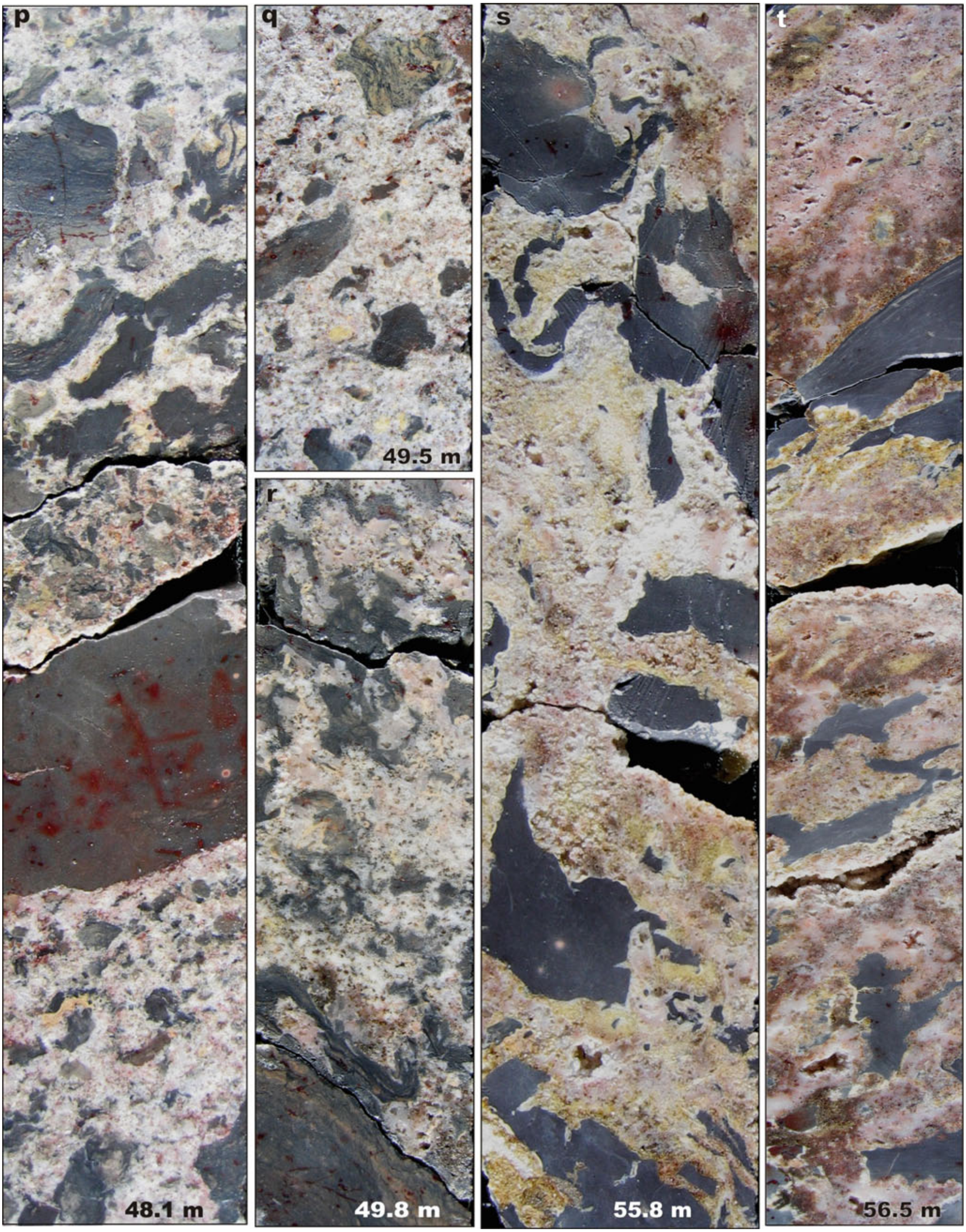

Fig. 6.101 (continued) (**p**–**t**) Fragments of dark brown, massive, soft-sediment deformed shale cemented by white, drusy calcite in dissolution-collapse-breccia

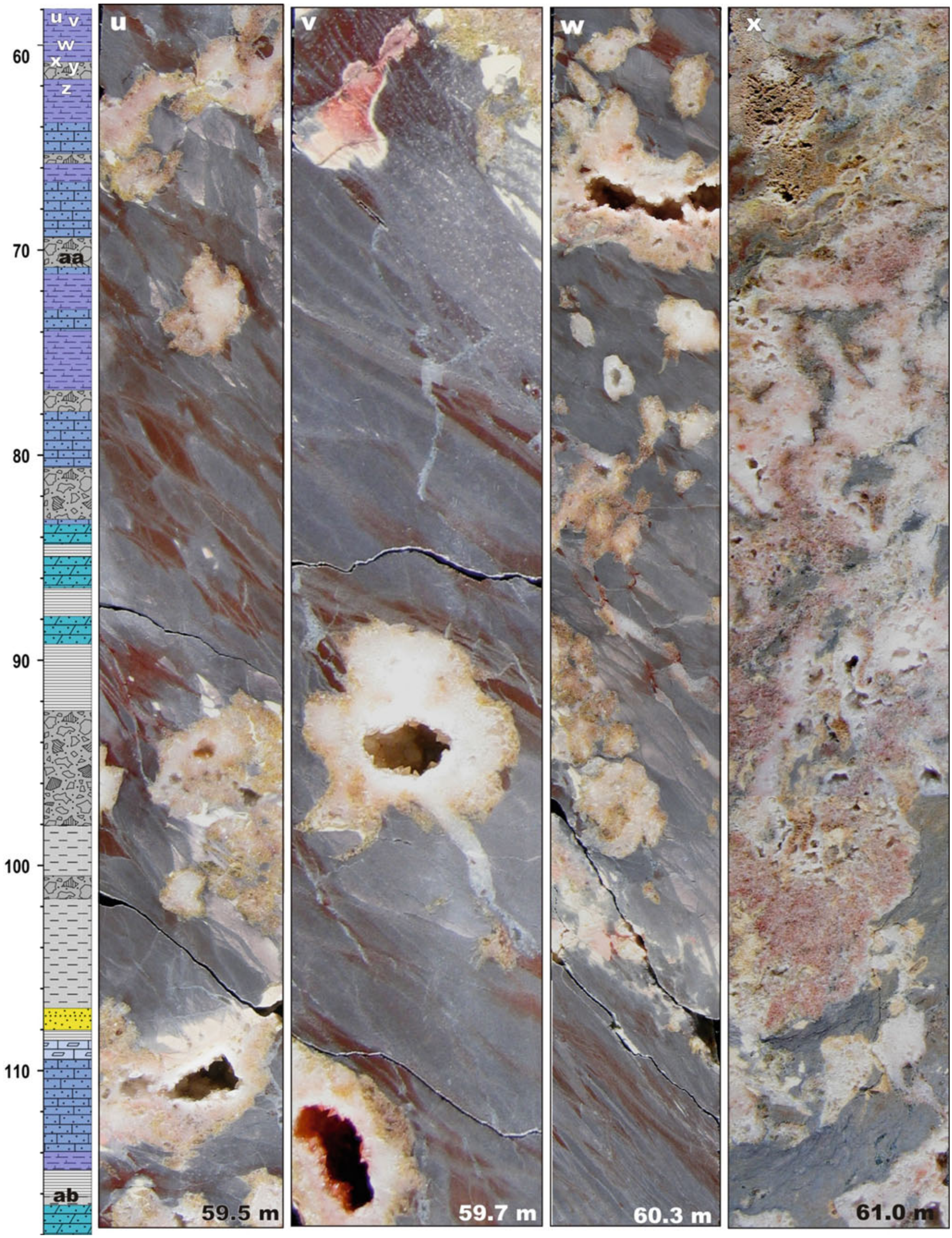

Fig. 6.101 (continued) *Member 14 (Nodular Shale-Siltstone-Marl-Breccia)* (**u**–**w**) Grey, laminated marl with lenses of brown shale and nodules of calcium sulphates; note that the nodules are partially replaced by white quartz and some of them have a hollow core. (**x**) Grey marl with chicken-wire anhydrite partially replaced by white, drusy calcite and pale brown quartz

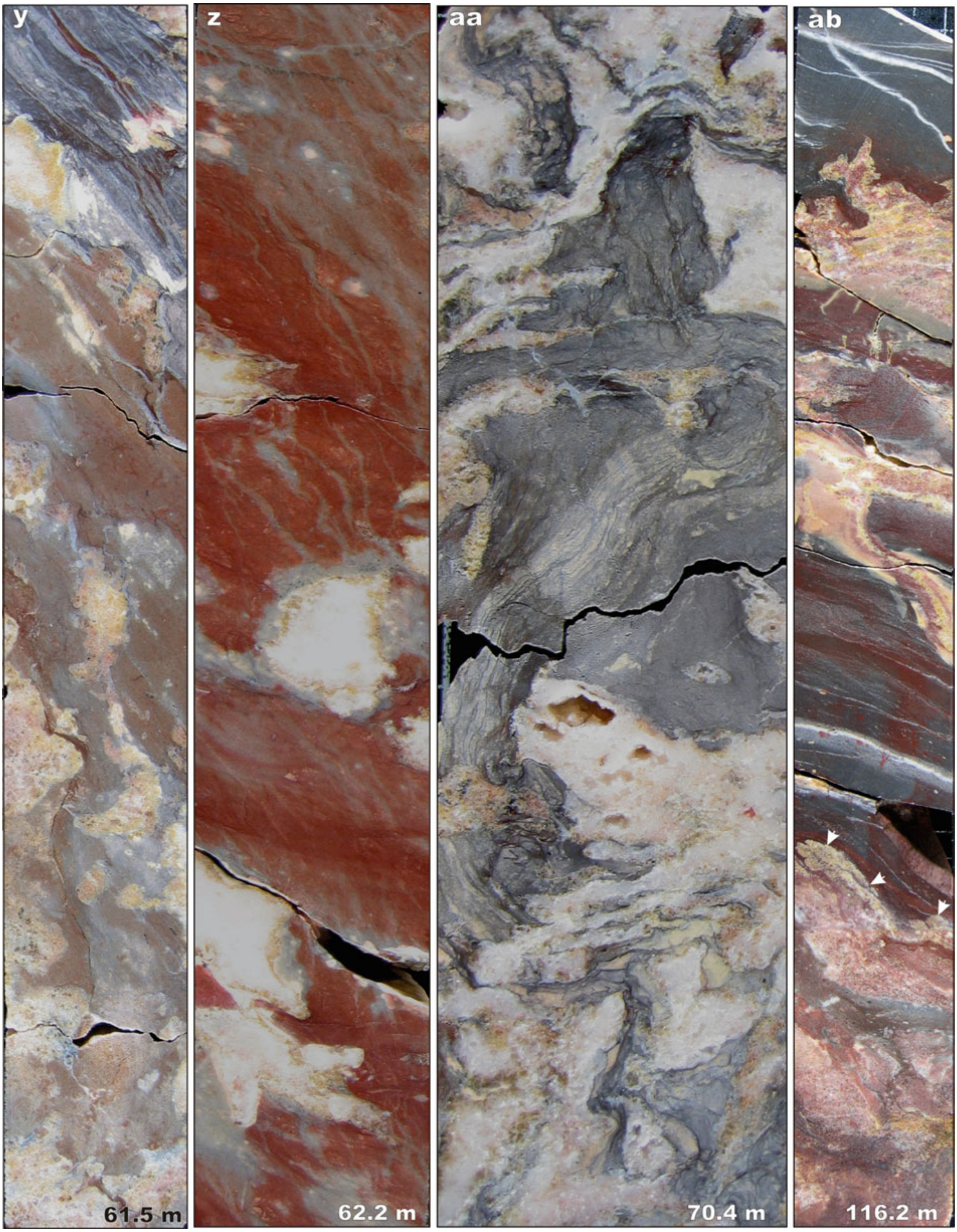

Fig. 6.101 (continued) (**y**) Grey laminated shale overlying pale brown breccias composed of soft-sediment deformed fragments of brown shale embedded in nodular calcium sulphates partially replaced by calcite and quartz. (**z**) Variegated marl with nodules and rosettes of calcium sulphates partially replaced by white quartz and drusy calcite. (**aa**) Soft-sediment deformed grey, laminated shale in chicken-wire anhydrite partially replaced by white, drusy calcite and quartz. (**ab**) In situ brecciated dolostone with a dissolved surface (*arrowed*) overlain by laminated shale with dolospar-pseudomorphed calcium sulphates (bright); note that the *arrowed* surface represents the boundary between Members 13 and 14

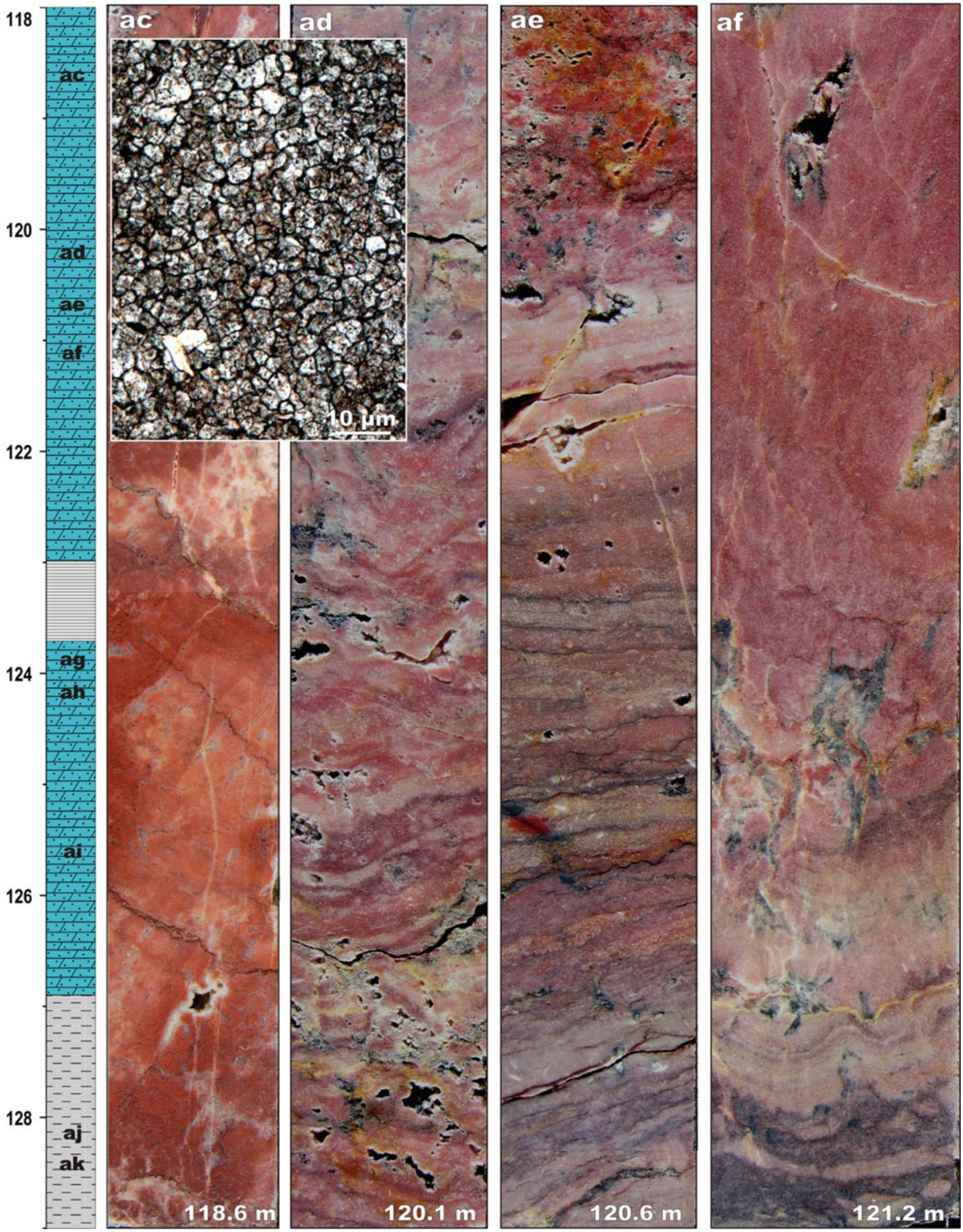

Fig. 6.101 (continued) *Member 13 (Upper Dolostone):* (**ac**) Red, non-bedded dolostone with a dense, microgranular texture shown by photomicrograph (see inset image) taken with transmitted, non-polarised light. (**ad**) Pale pink dolostone with wrinkled lamination and abundant vugs (*black*). (**ae**) Variegated, laminated dolarenite passing into pale pink and red, non-bedded dolostone with abundant vugs (*black*). (**af**) Dark grey and beige, laminated dolarenite passing into red, non-bedded dolostone

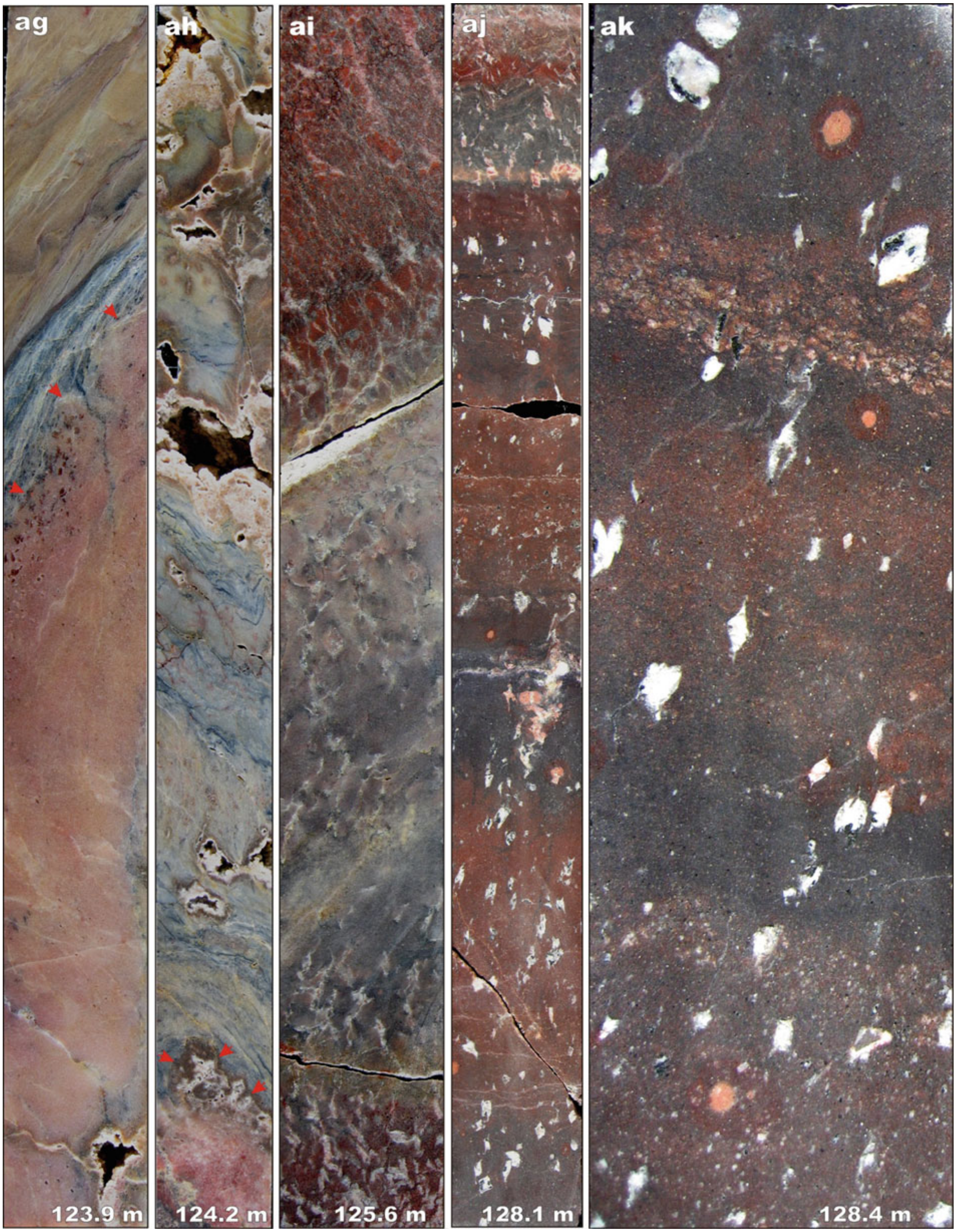

Fig. 6.101 (continued) (**ag**) Tan, massive dolostone overlain by clayey, laminated dolarenite; note that the contact between the massive and laminated dolostones represents a dissolution surface (*arrowed*). (**ah**) Pink dolostone with a dissolution surface (*arrowed*) overlain by variegated dolostone with deformed lamination and large dissolution cavities (*black*) partially filled with white, drusy dolomite. (**ai**) Recrystallised, brown, non-bedded dolostone overlying pale grey dolostone with abundant small crystals of gypsum replaced by white dolospar. *Member 12 (Siltstone):* (**aj**) Thickly bedded, brown siltstone with dolomite-pseudomorphed crystals of gypsum (*white*). (**ak**) Thickly bedded, brown siltstone with crystals of gypsum partially replaced by white dolospar

`

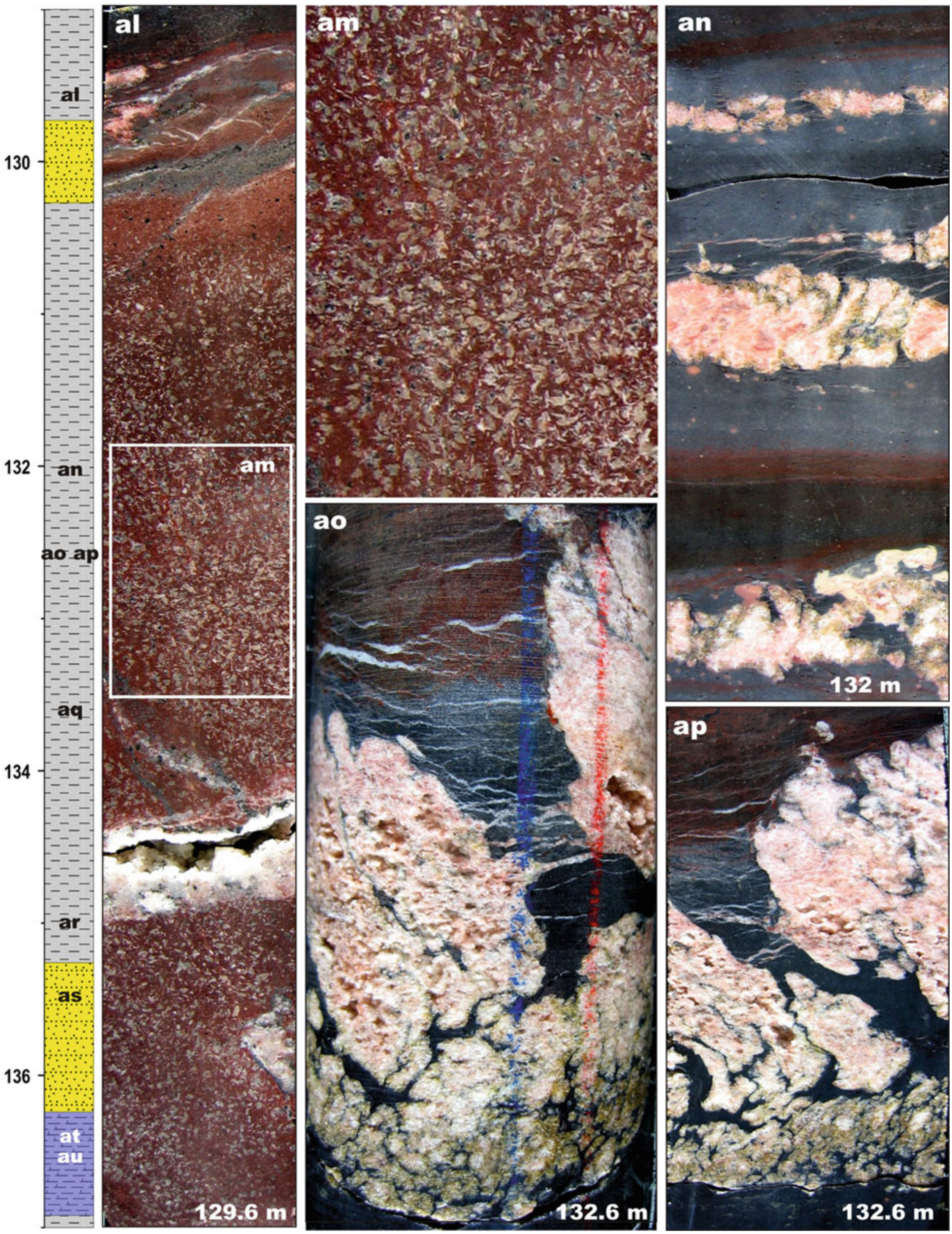

Fig. 6.101 (continued) (**al**) Variegated, bedded siltstone overlying brown, massive siltstone with a thin interval of calcium sulphate partially replaced by white, drusy dolomite. (**am**) Close-up view of brown, massive siltstone showing abundant gypsum crystals and rosettes replaced by white dolospar. (**an**–**ap**) Dark grey and brown siltstone with chicken-wire anhydrite partially replaced by white dolospar and quartz

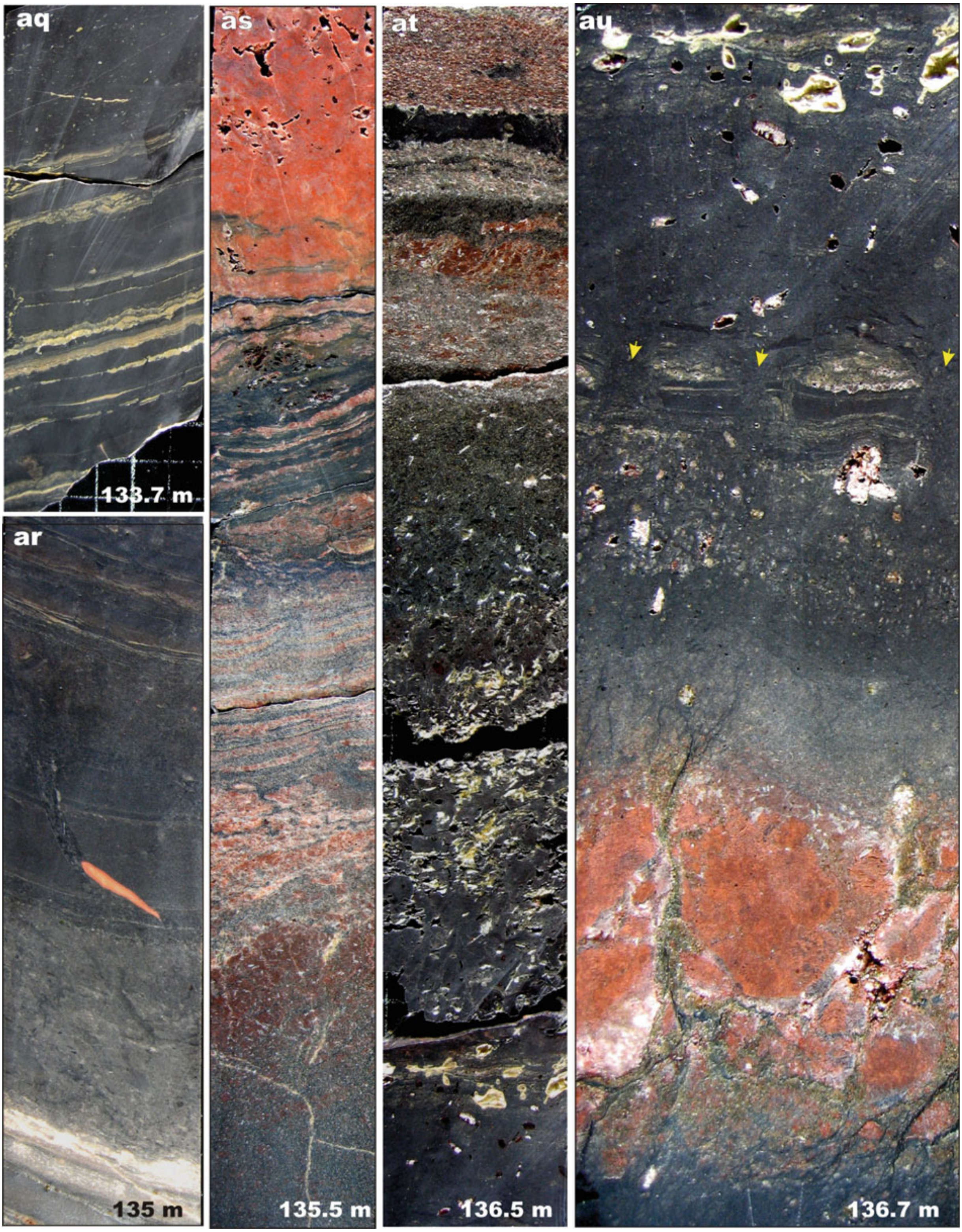

Fig. 6.101 (continued) (**aq**) Dark-coloured siltstone with thin lenticular bedding. (**ar**) Pale grey siltstone passing into dark-coloured, flat-laminated, clayey siltstone. (**as**) Variegated, massive to laminated sandstone passing into red, massive, quartz sandstone. (**at**) Variegated, bedded dolomarl overlying dark-coloured, non-bedded dolomarl with crystals and rosettes of gypsum partially replaced by white dolospar. (**au**) Dark-coloured dolomarl whose bedding was modified by growth of calcium sulphates partially replaced by pink quartz and white dolospar; note that the white, dolomite-replaced nodules of calcium sulphates have a hollow core; the yellow arrows denote desiccation cracks in c. 1-cm-thick mudstone-siltstone bed

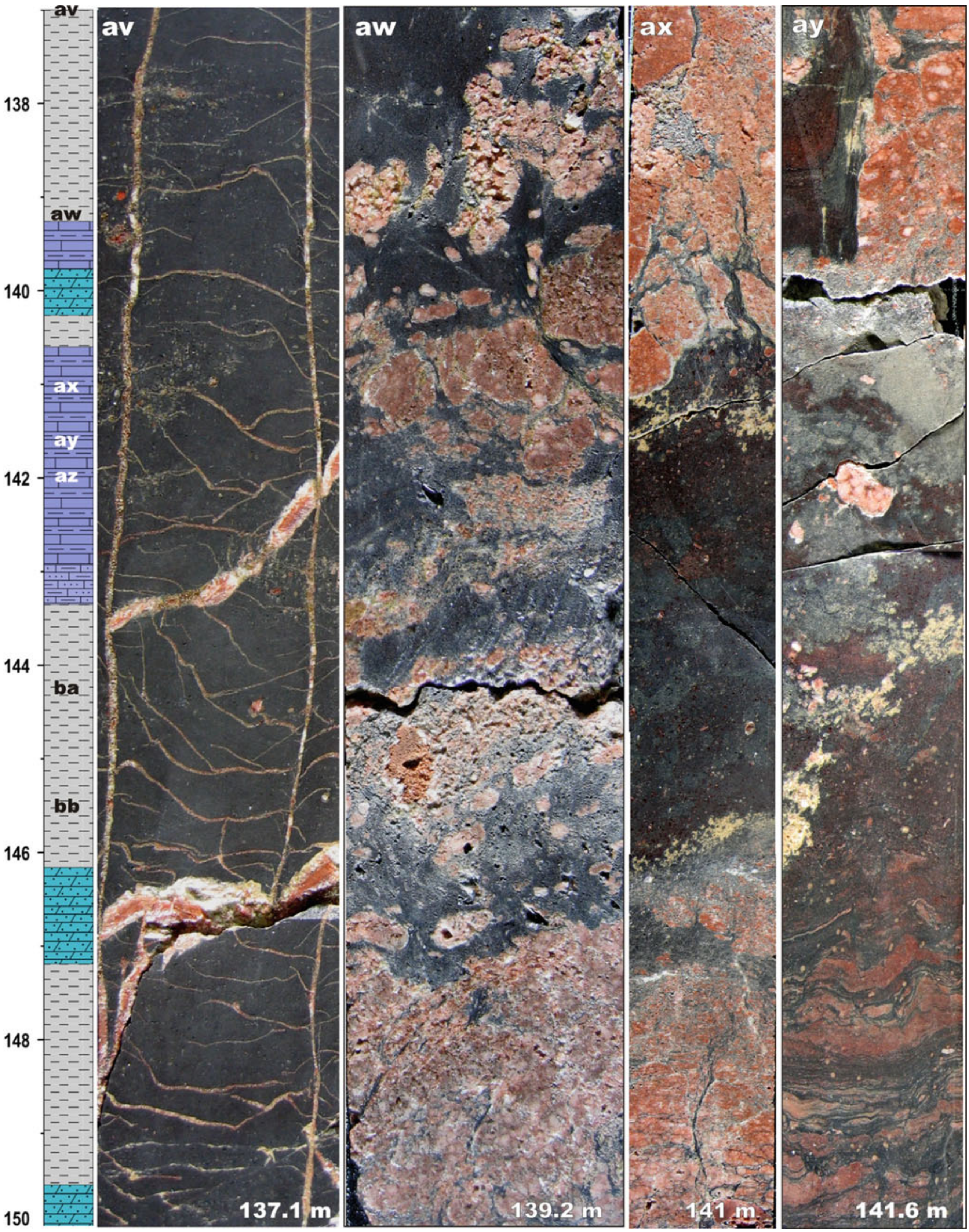

Fig. 6.101 (continued) (**av**) Black, massive siltstone with joints filled by white dolospar and pink quartz. (**aw**) Black siltstone with quartz-replaced nodular sulphates and chicken-wire anhydrite. (**ax**) Quartz-replaced calcium sulphates (*pale brown-pink*) in dark-coloured massive dolomarl. (**ay**) Dark-coloured marl with a lensoidal structure (*lower part*) overlain by brecciated siltstone and marl

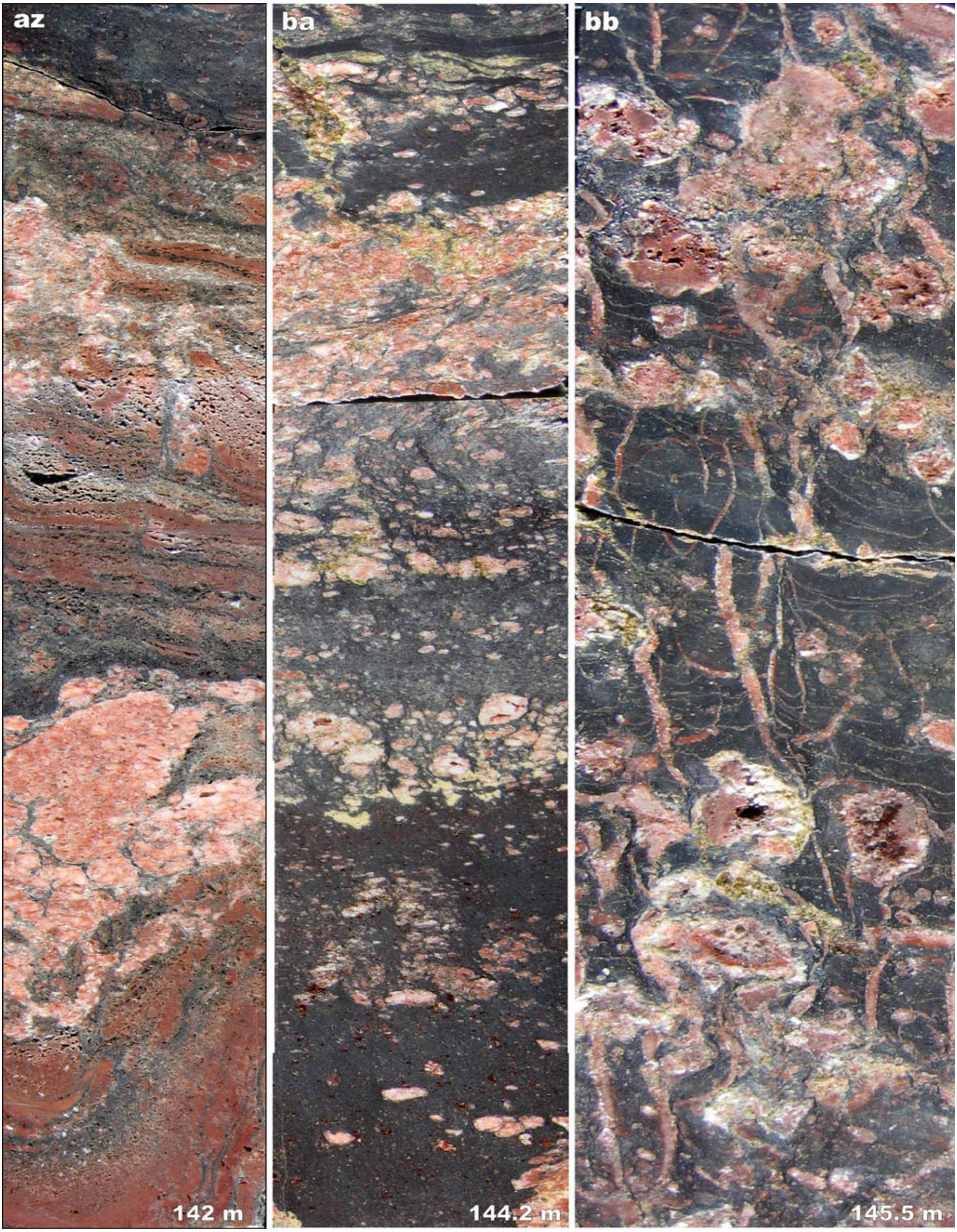

Fig. 6.101 (continued) (**az**) Brown, laminated marl with chicken-wire anhydrite partially replaced by pale pink-white aggregate of quartz and dolospar. (**ba**) Dark-coloured, non-bedded siltstone with chicken-wire anhydrite and abundant nodules of calcium sulphates partially replaced by white dolospar and pale pink quartz. (**bb**) Grey, non-bedded siltstone with abundant nodules of calcium sulphates partially replaced by pink dolospar; note the subvertical veinlets filled by dolomite

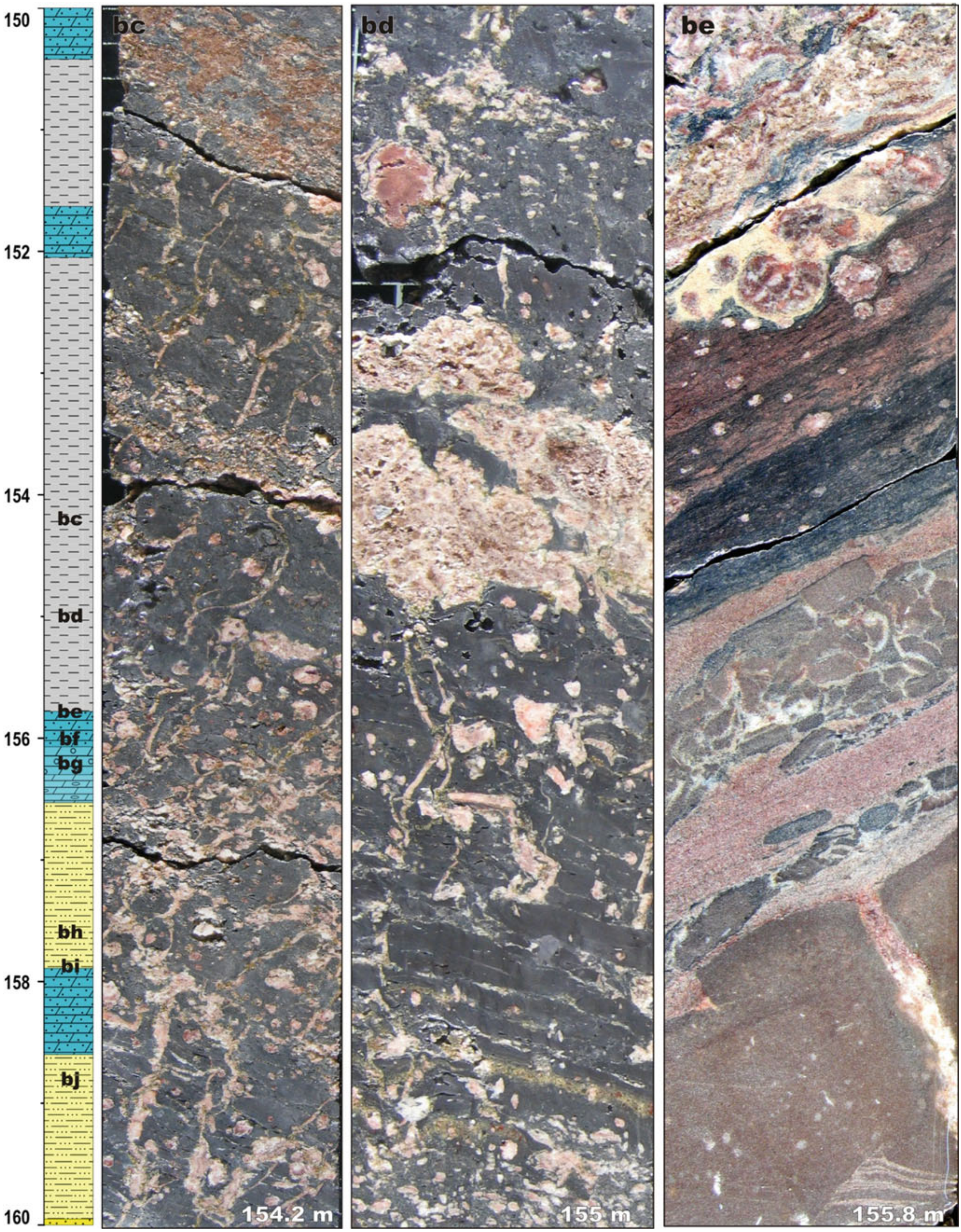

Fig. 6.101 (continued) (**bc**, **bd**) Grey, non-bedded siltstone with abundant nodules of calcium sulphates partially replaced by pink dolospar; note the subvertical veinlets filled by dolomite. (**be**) Pale brown, non-bedded dolarenite with two thin intervals of clast-supported intraformational conglomerate overlain by bedded siltstone with nodular mass of calcium sulphates that are partially replaced by white dolospar and pale pink quartz

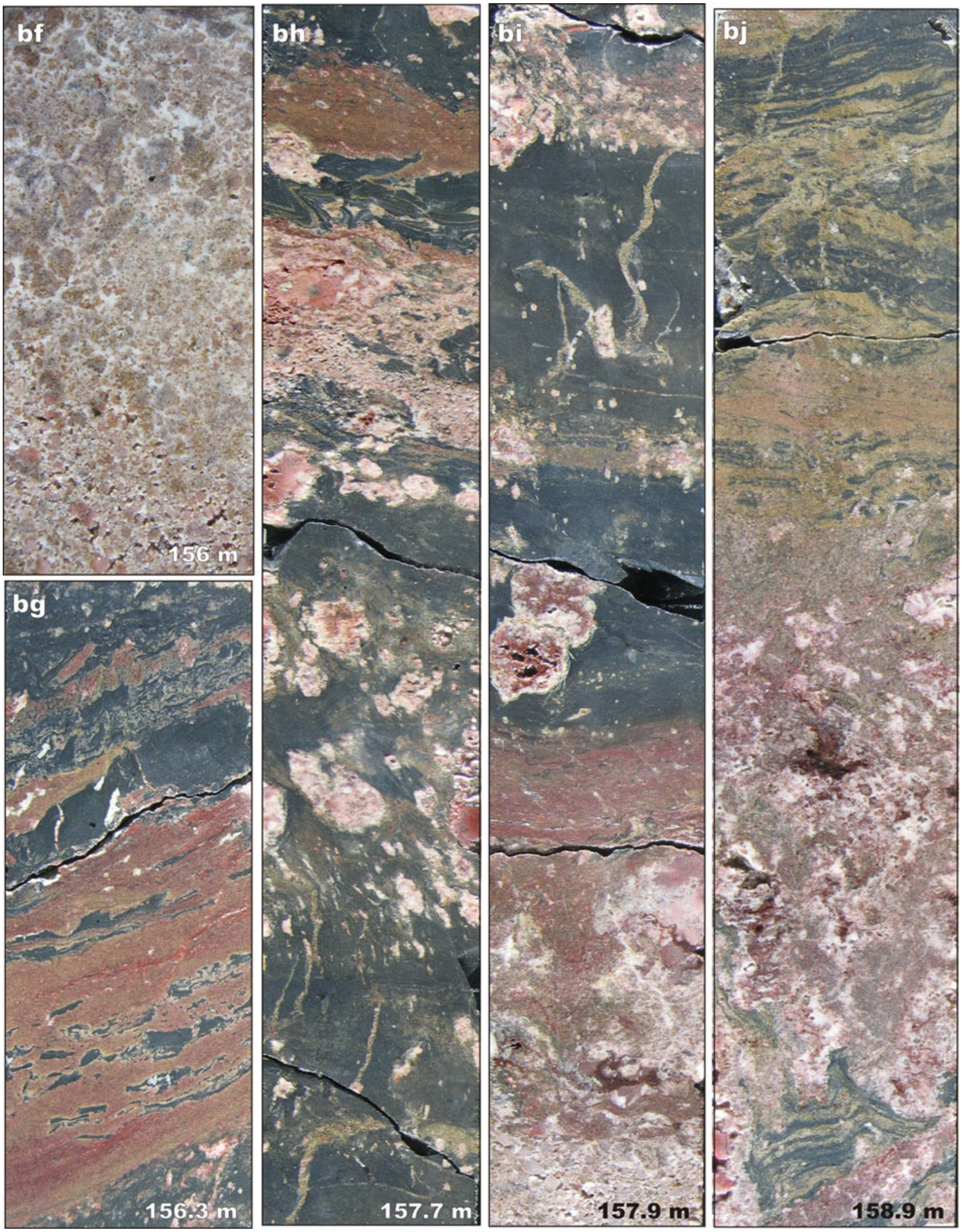

Fig. 6.101 (continued) *Member 11 (Sandstone-Basalt)*: (**bf**) Light-coloured dolarenite passing into dolorudite. (**bg**) Pale brown dolostone with dismembered layers of dark grey siltstone passing into dark-coloured siltstone with lenses of pale brown dolostone. (**bh**) Silty sandstone with nodules and chicken-wire anhydrite partially replaced by pale brown aggregate of quartz and dolospar. (**bi**) Pale brown dolostone with a clumped structure overlain by dark-coloured, bedded, silty sandstone with nodules, veins and chicken-wire anhydrite partially replaced by brown-white aggregate of quartz and dolospar. (**bj**) Sandstone-siltstone overlying pale brown, dolarenous, vuggy, non-bedded sandstone with fragments of soft-sediment deformed sandstone-siltstone

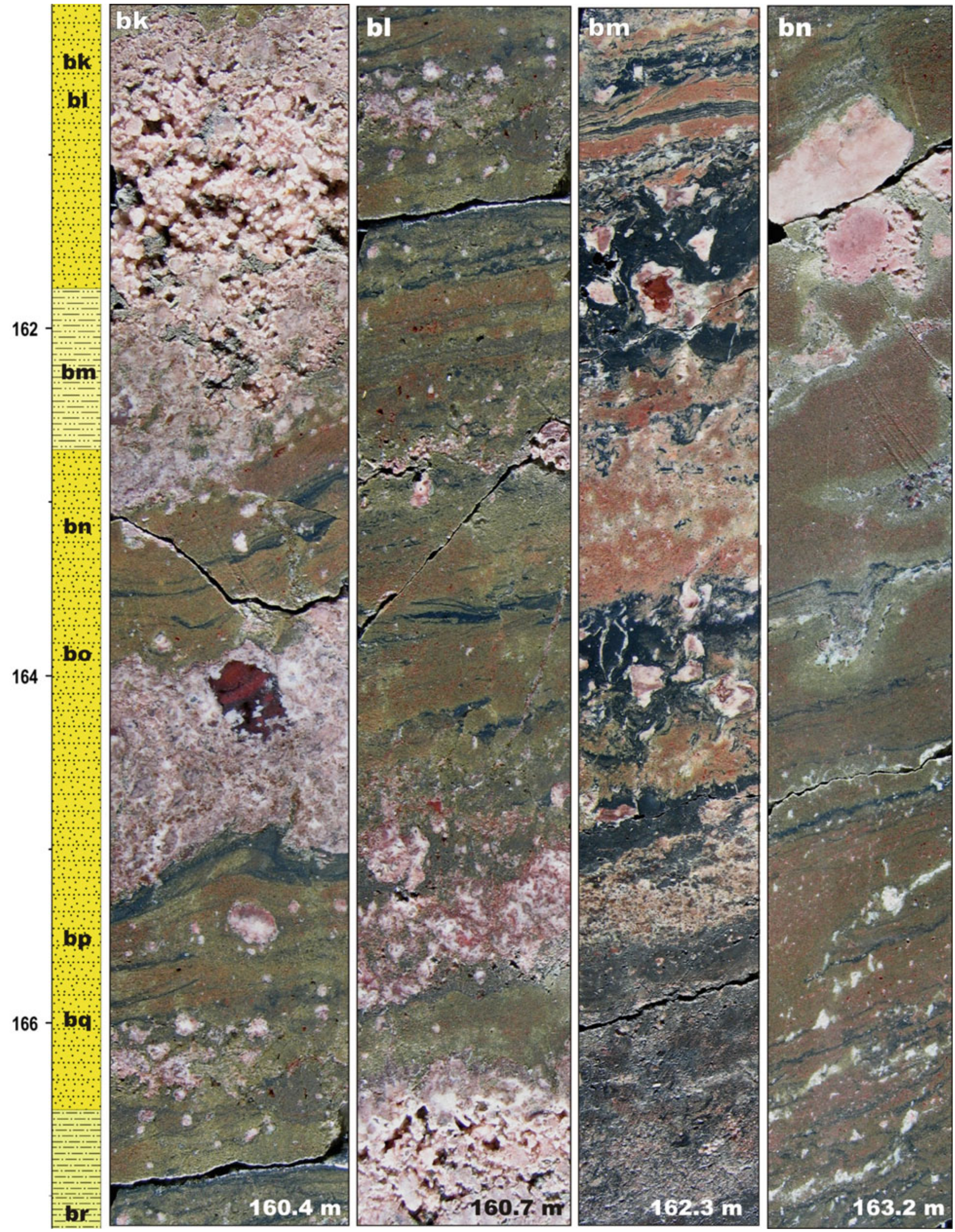

Fig. 6.101 (continued) (**bk**, **bl)** Brown-greenish, sandstone with lenticular and lensoidal bedding; note the dolomite-replaced nodules and porous chicken-wire anhydrite (bright) and the clast of red haematite-rich, bedded siltstone. (**bm**) Interbedded variegated sandstone and black, clayey siltstone; the latter shows desiccation cracks and contains abundant dolomite-replaced nodules of sulphates; note the clast of red, haematite-rich, bedded siltstone. (**bn**) Brown-greenish, thickly bedded sandstone with thin interlayers of black mudstone and sulphate nodules partially replaced by white dolomite and pale pink quartz

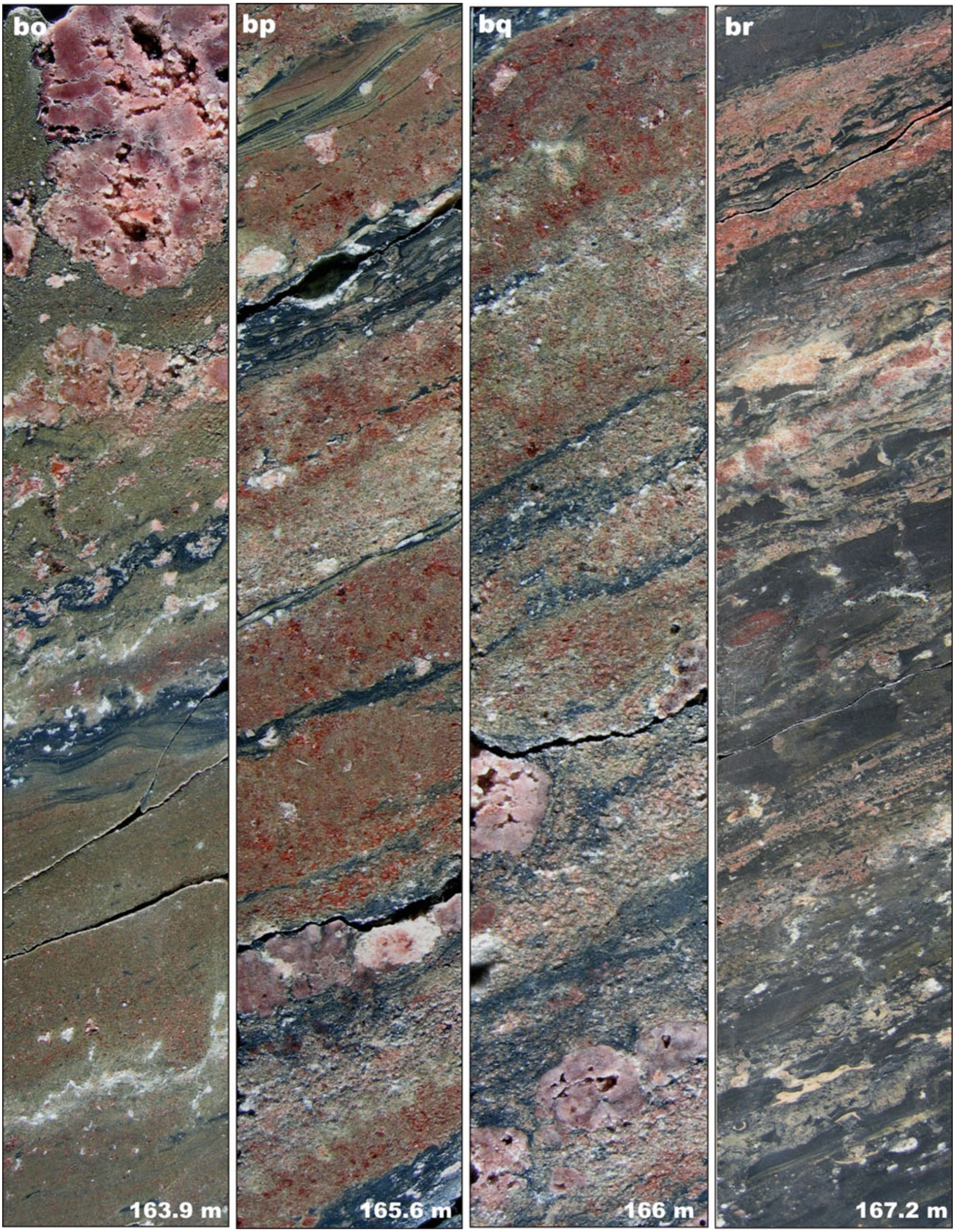

Fig. 6.101 (continued) (**bo**) Brown-greenish, thickly bedded sandstone with thin interlayers of black mudstone and porous sulphate nodules partially replaced by pale pink quartz; note the sand ripples in the middle part of the core. (**bp**, **bq**) Variegated, thickly bedded sandstone with thin interlayers of black mudstone and scattered sulphate nodules partially replaced by pale pink quartz. (**br**) Dark-coloured, clayey siltstone with thin, irregular interlayers of pink sandstone; note the irregular, wrinkled bedding and desiccation cracks in clayey siltstone

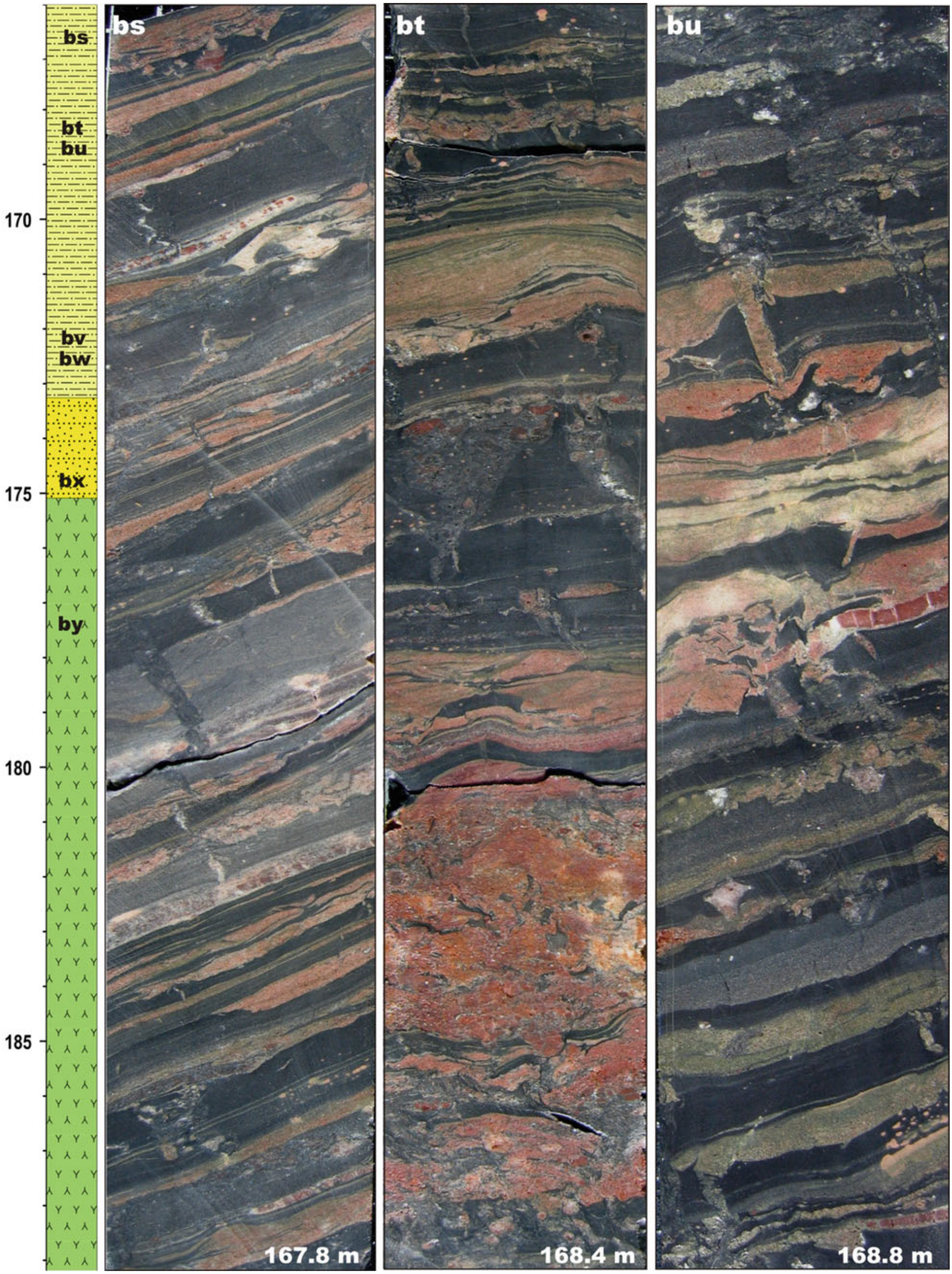

Fig. 6.101 (continued) (**bs**–**bu**) Variegated heterolithic unit composed of interbedded pink sandstone, grey siltstone and black mudstone with lenticular, wavy and flaser bedding; note desiccation cracks in grey siltstone and black mudstone; note that some sand-ripples have erosive bases

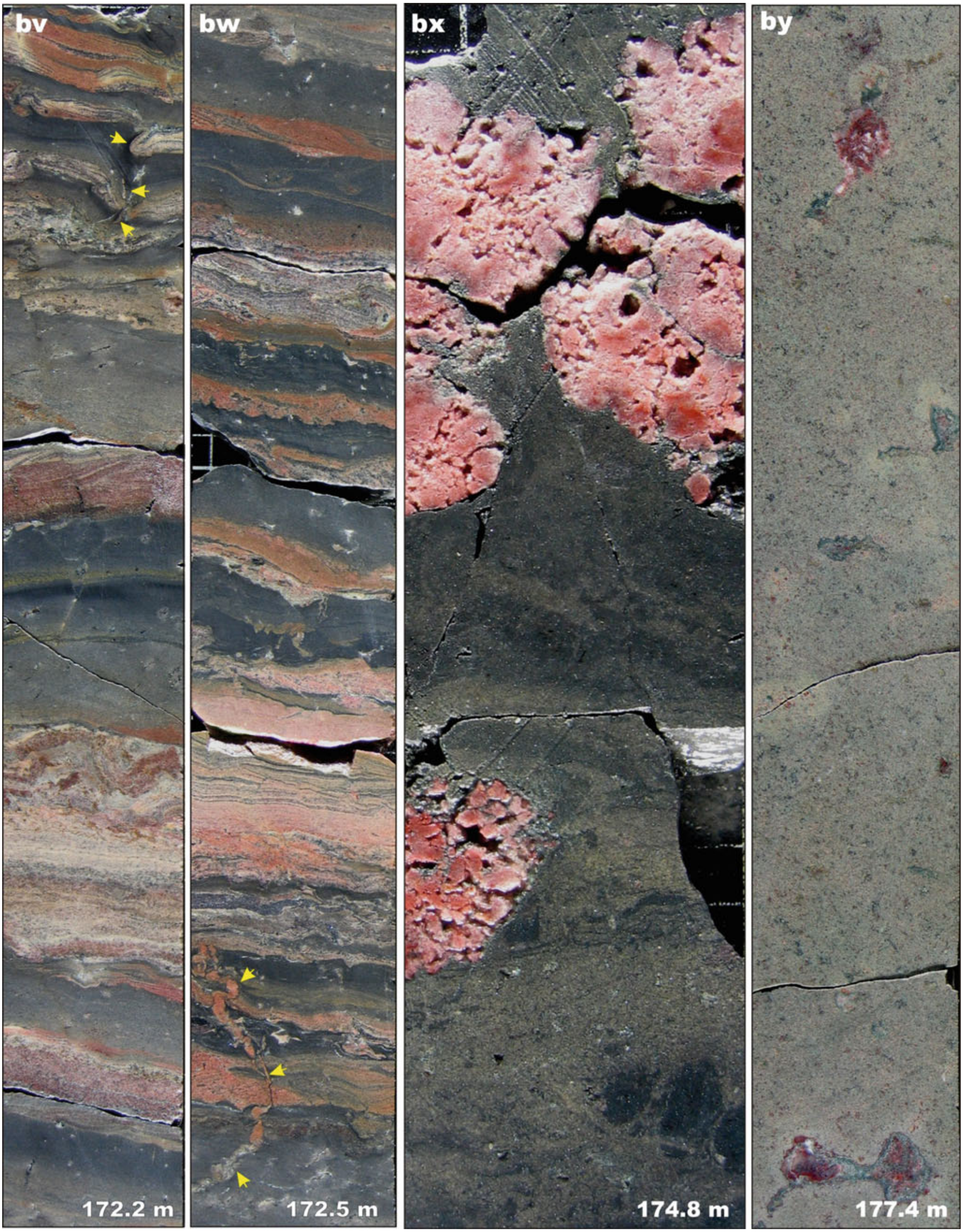

Fig. 6.101 (continued) (**bv**–**bw**) Variegated heterolithic unit composed of interbedded pink sandstone, grey siltstone and black mudstone with lenticular, wavy and flaser bedding; note the desiccation cracks, gas-fluid escape structure (*arrowed* in Fig. bv) and sedimentary dyke (*arrowed* in Fig. bw). (**bx**) Dark grey, indistinctly bedded sandstone with large sulphate nodules partially replaced by pink quartz. (**by**) Basalt with vesicles filled with green chlorite and pink haematite

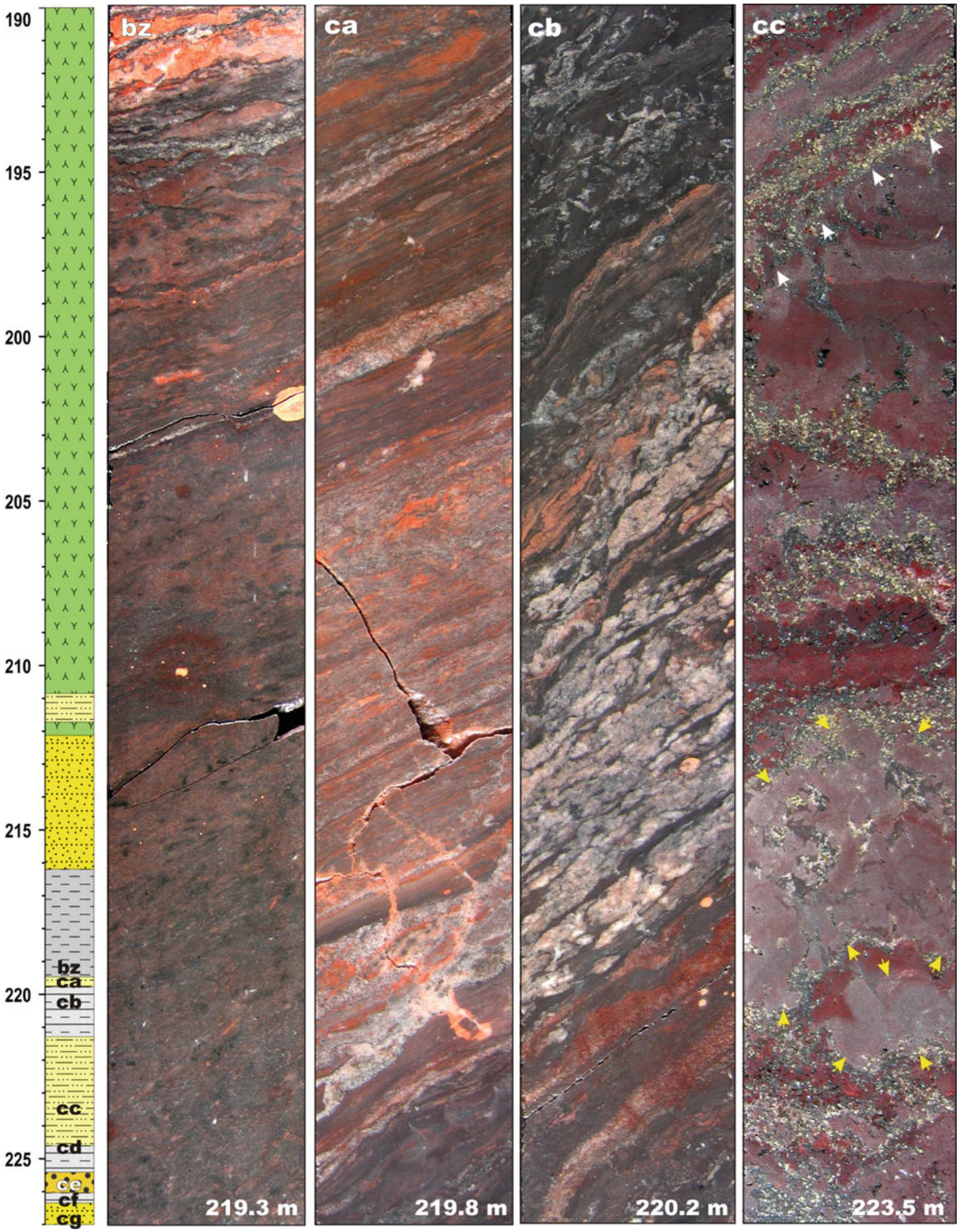

Fig. 6.101 (continued) (**bz**) Dark brown, non-bedded siltstone with a spotted appearance. (**ca**) Variegated sandstone-siltstone with flaser bedding and wrinkled lamination. (**cb**) Variegated siltstone with rippled and lensoidal bedding and chicken-wire anhydrite partially replaced by white dolospar. (**cc**) Variegated, bedded sandstone-siltstone; note the gypsum nodules replaced by pale purple quartz (*yellow arrowed*), and the erosional surface (*white arrowed*) followed by change in the bedding orientation

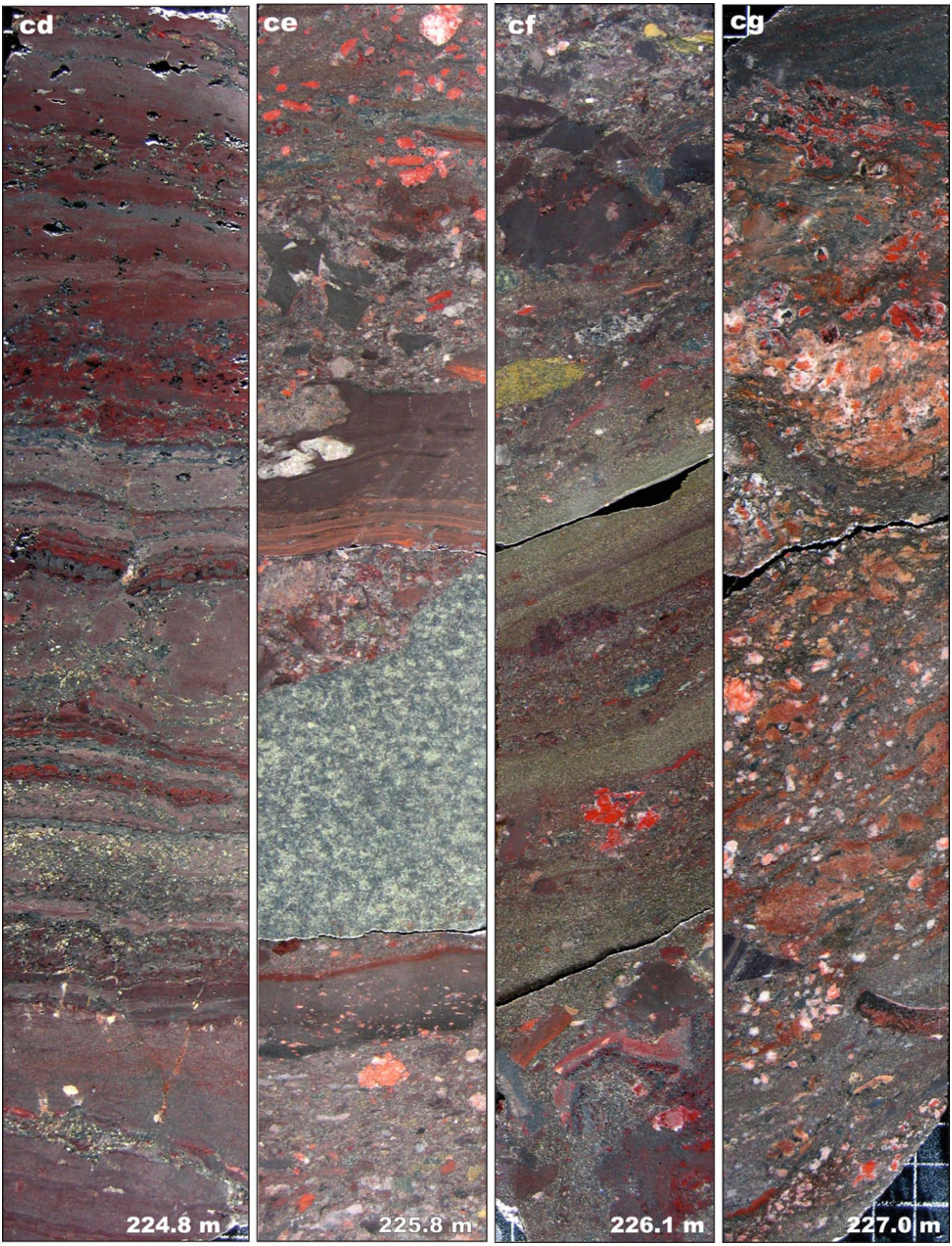

Fig. 6.101 (continued) (**cd**) Variegated sandstone-siltstone with irregular wavy bedding. (**ce**) Small-clast, polymict, non-bedded conglomerate with interbeds of brown and red laminated sandstone and siltstone intruded by a small gabbro dyke (*pale green*). (**cf**) Brown-green, bedded sandstone-siltstone in matrix-supported breccia composed of angular fragments of brown mudstone, sandstone and green-yellow sericite schist. (**cg**) Variegated, gritty, small-clast, unsorted, intraformational conglomerate composed of pale brown and pink clasts of mudstone and siltstone supported by coarse-grained sand material

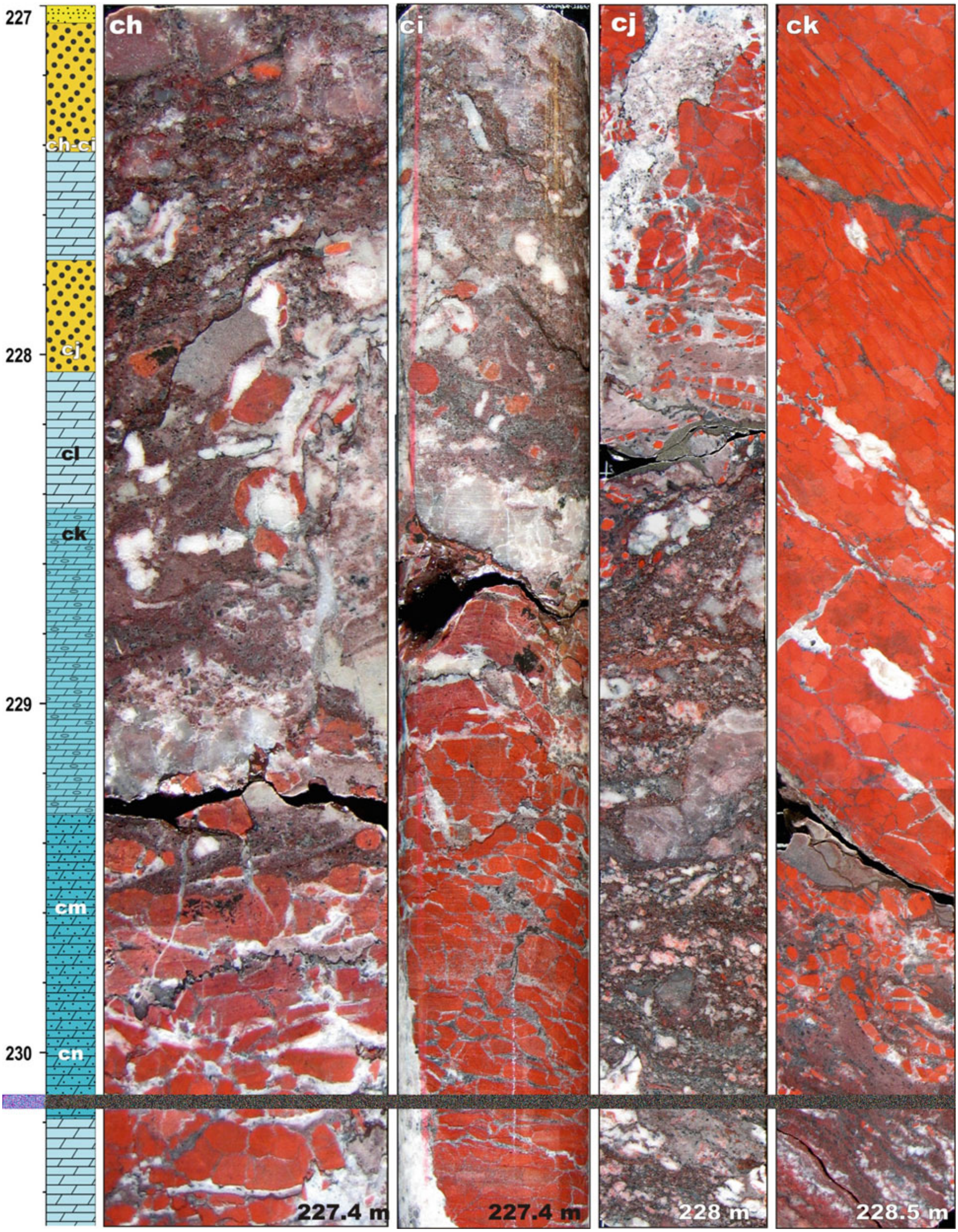

Fig. 6.101 (continued) *Member 10 (Dolostone-Conglomerate)*: (**ch**, **ci**) Sawn and unsawn core showing bright red, haematite-stained, coarsely crystalline dolostone erosively overlain by dolostone conglomerate with dissolution cavities filled by white dolospar; note that the red dolostone shows brittle deformation and abundant joints cemented by white dolospar. (**cj**) Non-bedded dolostone conglomerate overlain by intensely cracked, red, crystalline dolostone. (**ck**) Brecciated dolorudite overlain by bright red, massive, coarsely crystalline dolostone with dissolution cavities filled with white dolospar

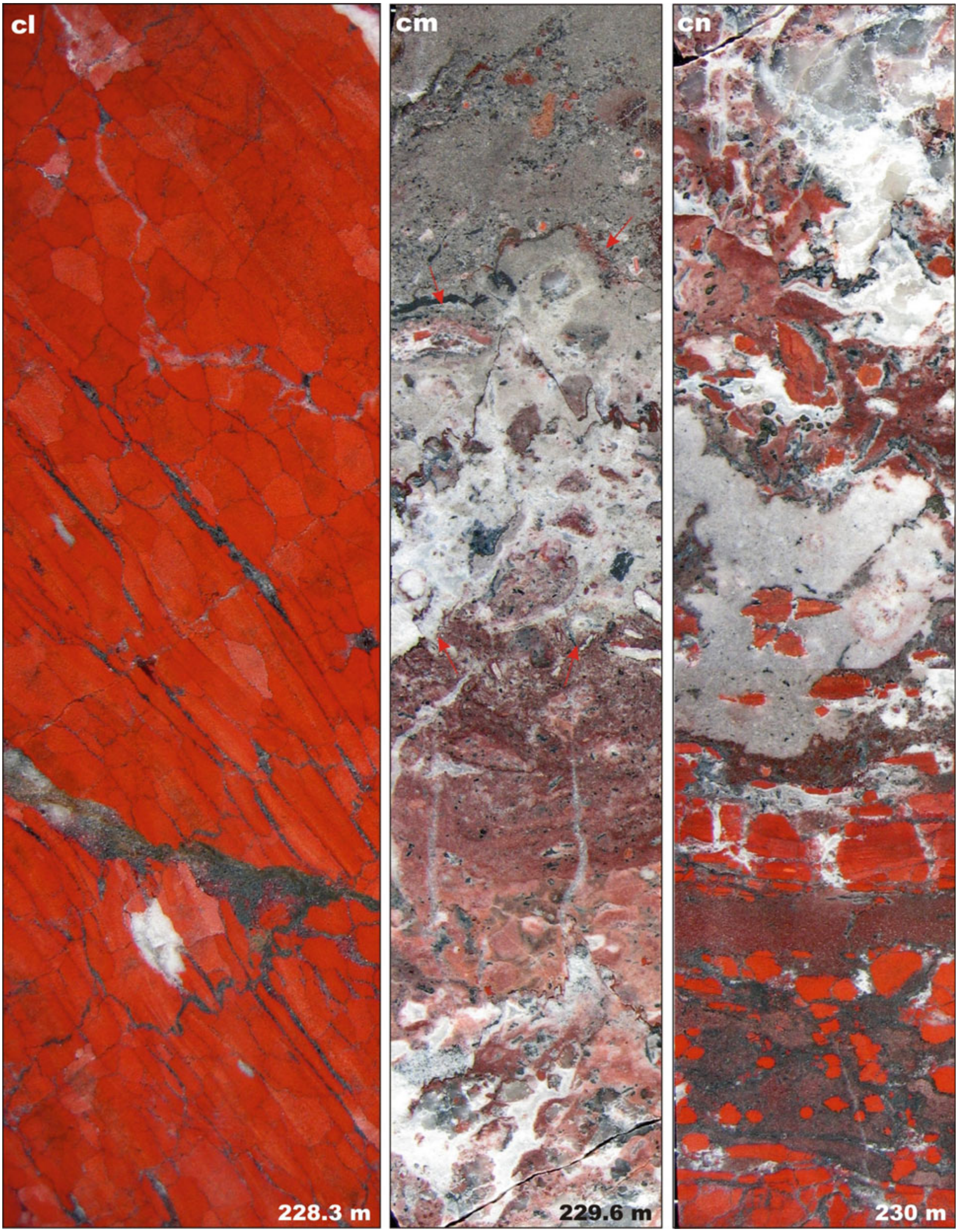

Fig. 6.101 (continued) (**cl**) Close-up view of red dolostone showing that the dolostone is composed of large, isometric and platy dolomite monocrystals that display a slightly different hue. (**cm**) Dolomite-cemented dissolution-collapse breccias (*arrowed*) developed along the contact between pale brown and grey, non-bedded dolarenite; the lower dolorenite contains dissolution cavities cemented by white, drusy dolomite. (**cn**) Brown dolarenite with clasts of bright red dolomite overlain by jointed bed of bright red dolostone followed by dissolution-collapse breccias

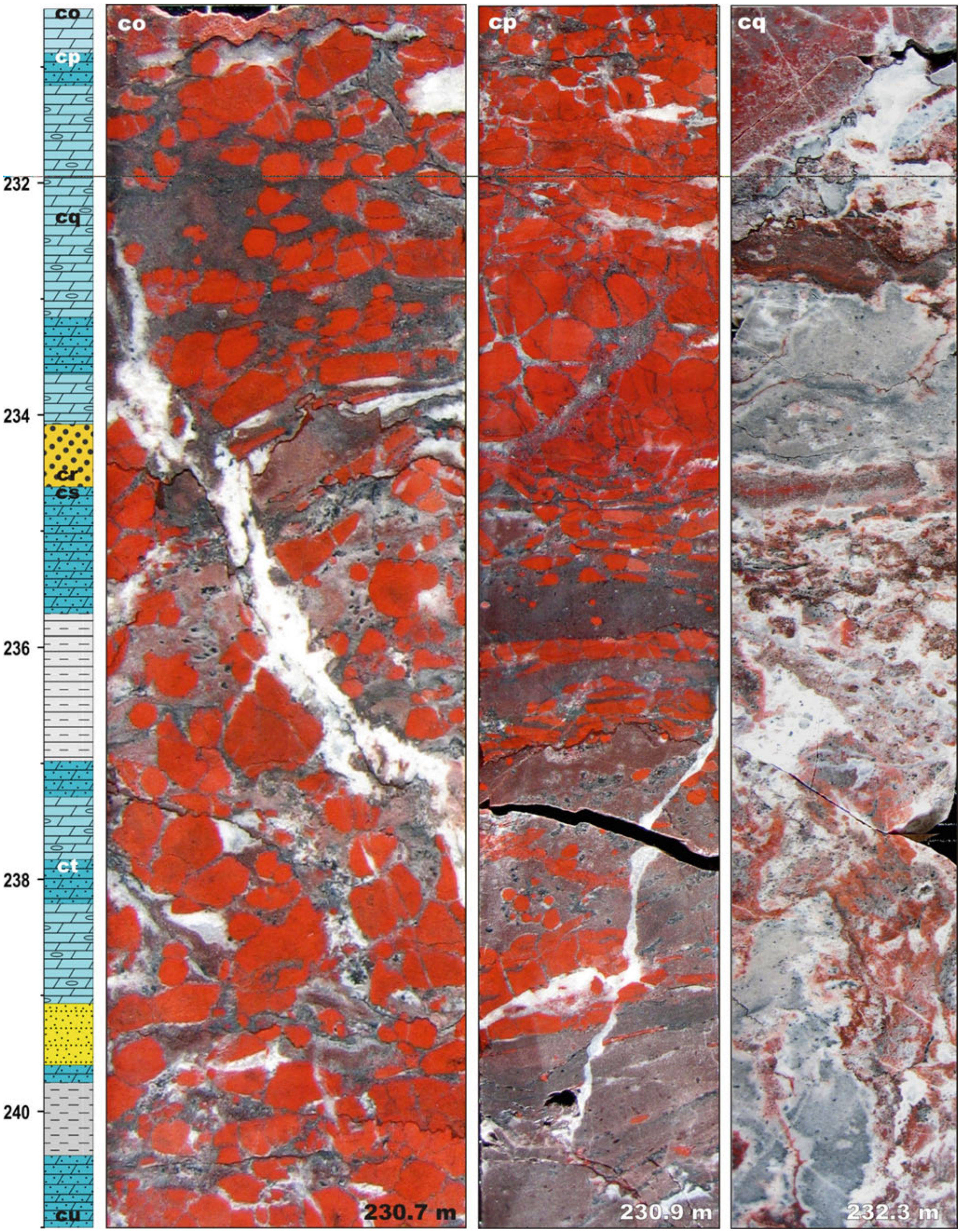

Fig. 6.101 (continued) (**co**) Fragments of bright red, coarsely crystalline dolomite in dark and pale brown dolarenite. (**cp**) Pale brown dolarenite with fragments of bright red, coarsely crystalline dolomite overlain by dark brown dolarenite passing upward into fragmented bright red, coarsely crystalline dolomite. (**cq**) Dissolution-collapse breccias composed of chaotically distributed and soft-sediment deformed clasts of dolostone and shale cemented by white, drusy dolomite

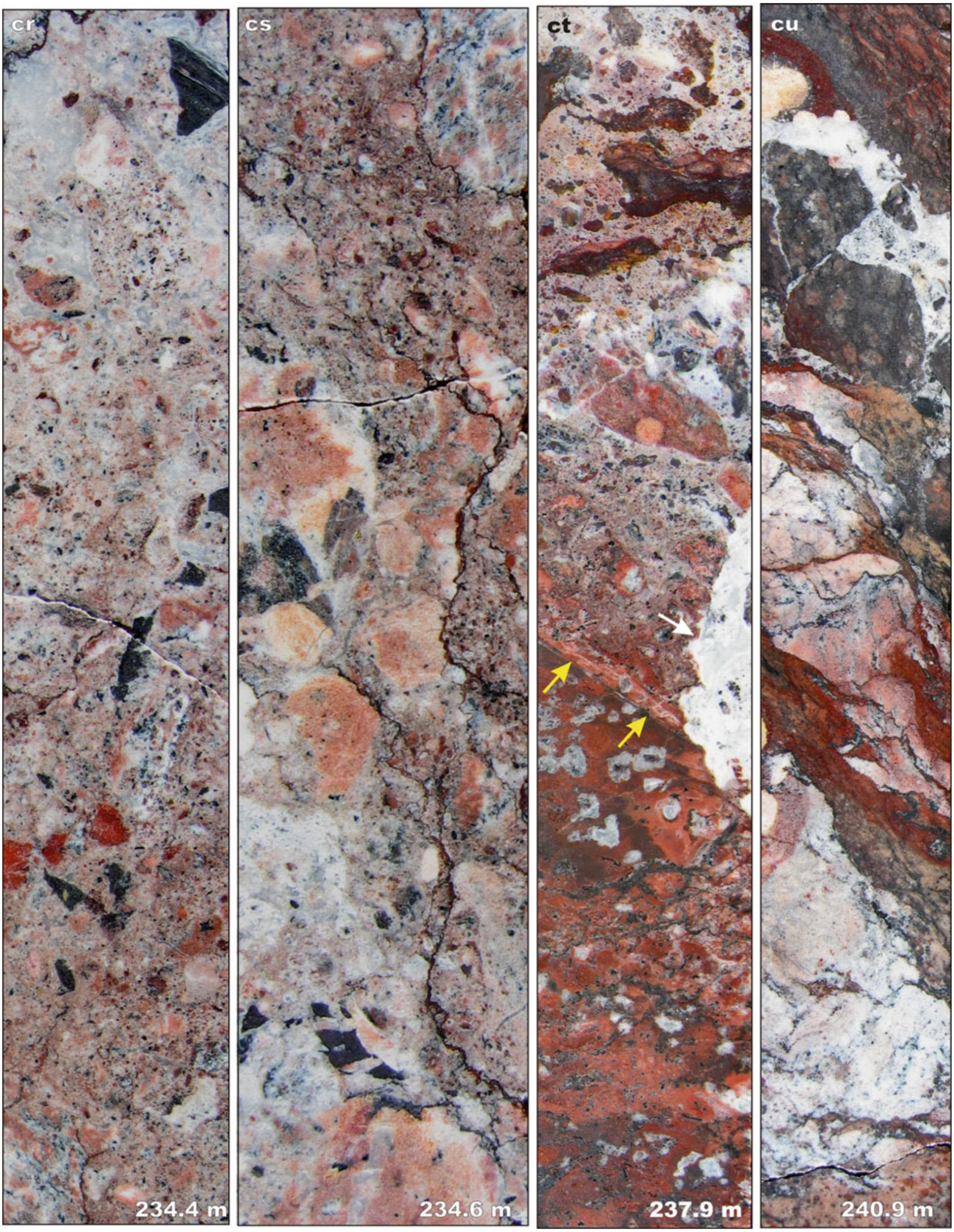

Fig. 6.101 (continued) (**cr**, **cs**) Non-bedded, gritty conglomerates composed of unsorted and rounded clasts of dolarenite and minor angular fragments of black mudstone. (**ct**) Contact (*yellow arrowed*) between dolorudite and underlying red dolarenite with dolospar-replaced small nodules of apparent sulphates; note the unsorted nature of clasts in dolorudite and the presence of soft-sediment deformed fragments of dark brown shale; a large, dolospar-infilled dissolution cavity cuts across the contact (*white arrow*). (**cu**) *In situ* brecciated, thickly bedded dolarenite with apparent outsized clasts of white dolostone

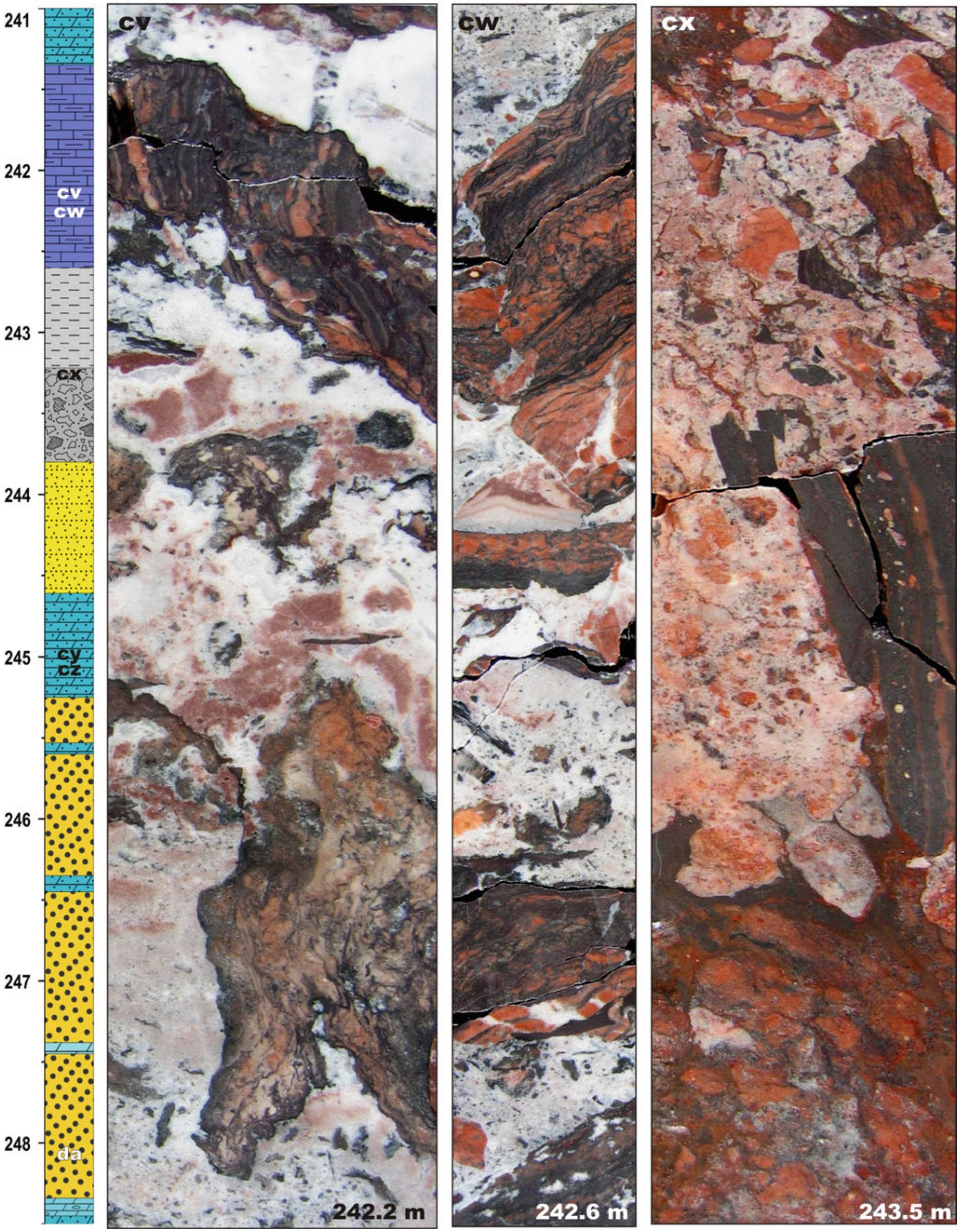

Fig. 6.101 (continued) (**cv**) Dissolution-collapse breccia composed of soft-sediment deformed fragments of variegated, dolarenaceous shale cemented by white, drusy dolomite. (**cw**) Brown-red dolarenaceous shale with solution and collapse structures. (**cx**) Dissolution-collapse breccias composed of shale (dark-coloured) and dolostone (*pale red*) clast cemented by dolospar; note that the lowermost interval is clast-supported, whereas the rest of the breccia is cement-supported

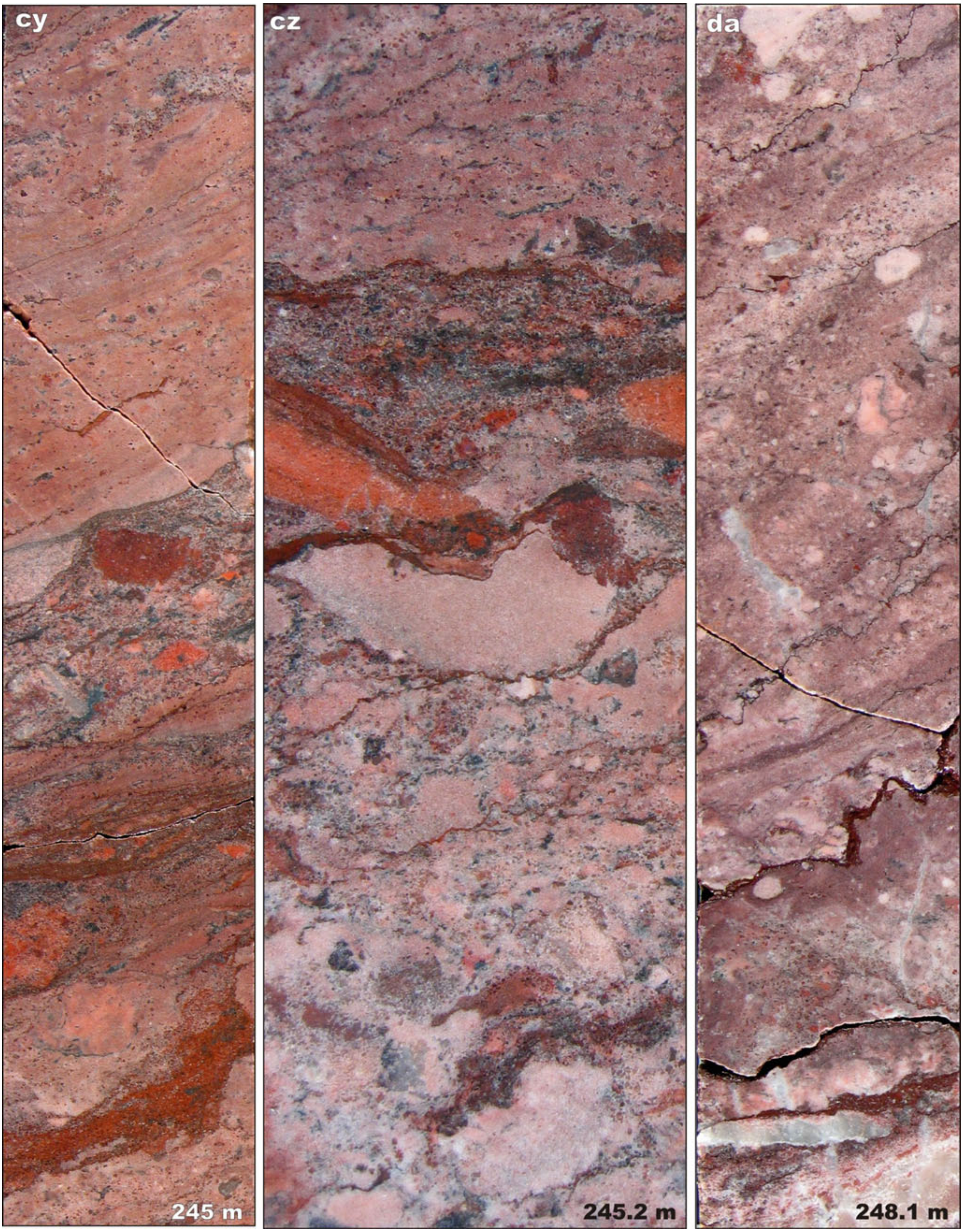

Fig. 6.101 (continued) (**cy**) Variegated, indistinctly bedded conglomerate overlain by tan, bedded dolarenite. (**cz**) Light-coloured, non-bedded dolorudite grading into dark-coloured dolarenite, which is overlain by pale pink, indistinctly bedded siliceous dolarenite. (**da**) Tan, gritty to sandy, non-bedded dolostone conglomerate with dark-coloured stylolites; note that the clasts are rounded but poorly sorted

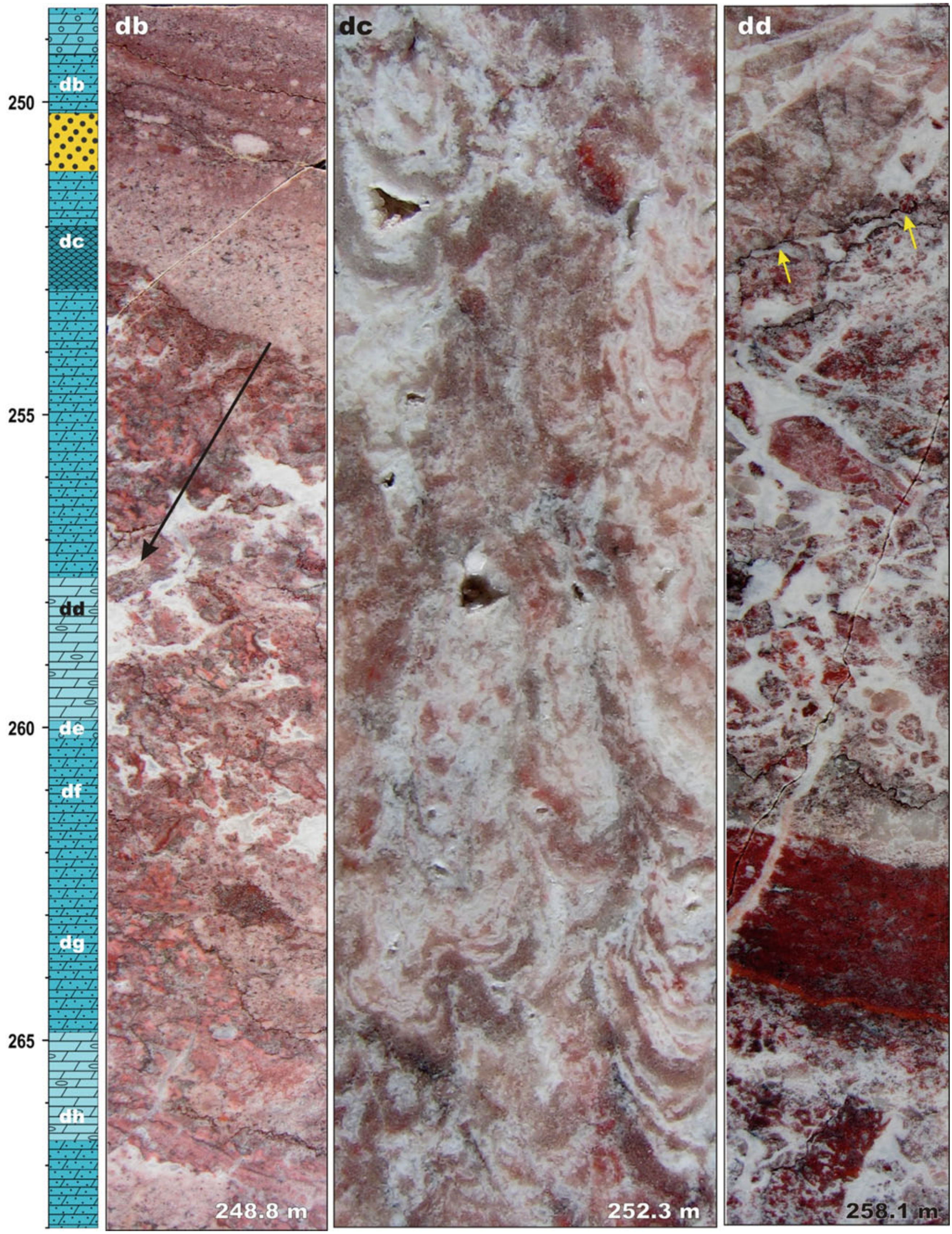

Fig. 6.101 (continued) (**db**) Overturned section (*arrow* indicates stratigraphic top) showing pale pink, normally-graded dolarenite bed erosively overlain by variegated, non-bedded dolorudite with dissolution cavities filled with white dolospar. (**dc**) Overturned columnar-layered stromatolites *Omachtenia kintsiensis* with dissolution cavities. (**dd**) Dolospar-cemented dolostone breccias with beds of pale beige (*yellow arrows*) and red dolarenite; note that the angularity of the dolostone clasts indicates very little or no transport

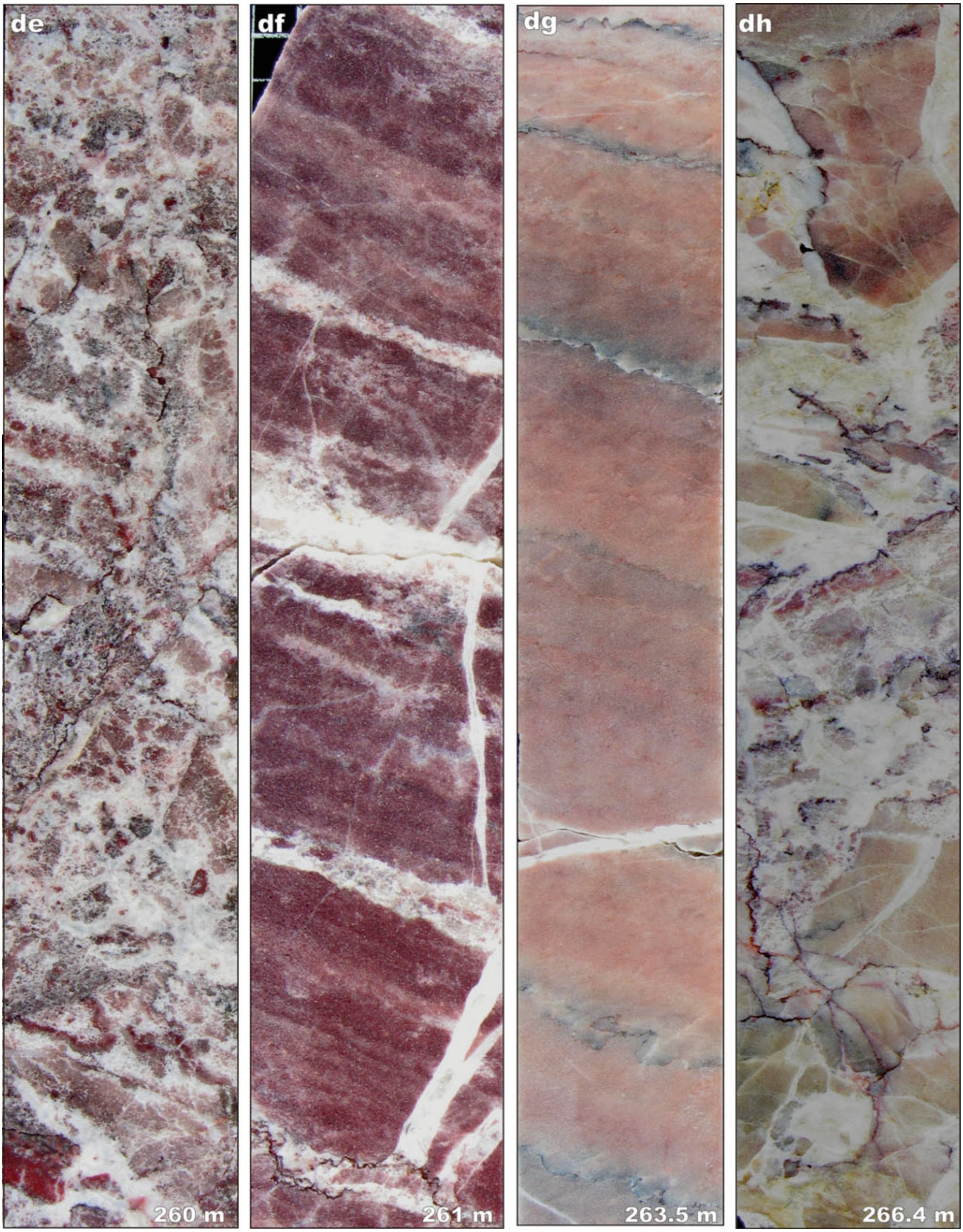

Fig. 6.101 (continued) (**de**) In situ brecciated (collapse breccias) dolarenite. (**df**) Pale brown, bedded dolarenite with cross-cutting and bedding-parallel veins of white dolospar. (**dg**) Tan, indistinctly bedded dolarenite. (**dh**) In situ brecciated dolarenite interpreted as dissolution-collapse breccias of a karstic origin (e.g. Brasier et al. 2011); all fragments are angular, implying no transport, and cemented by white, drusy dolomite

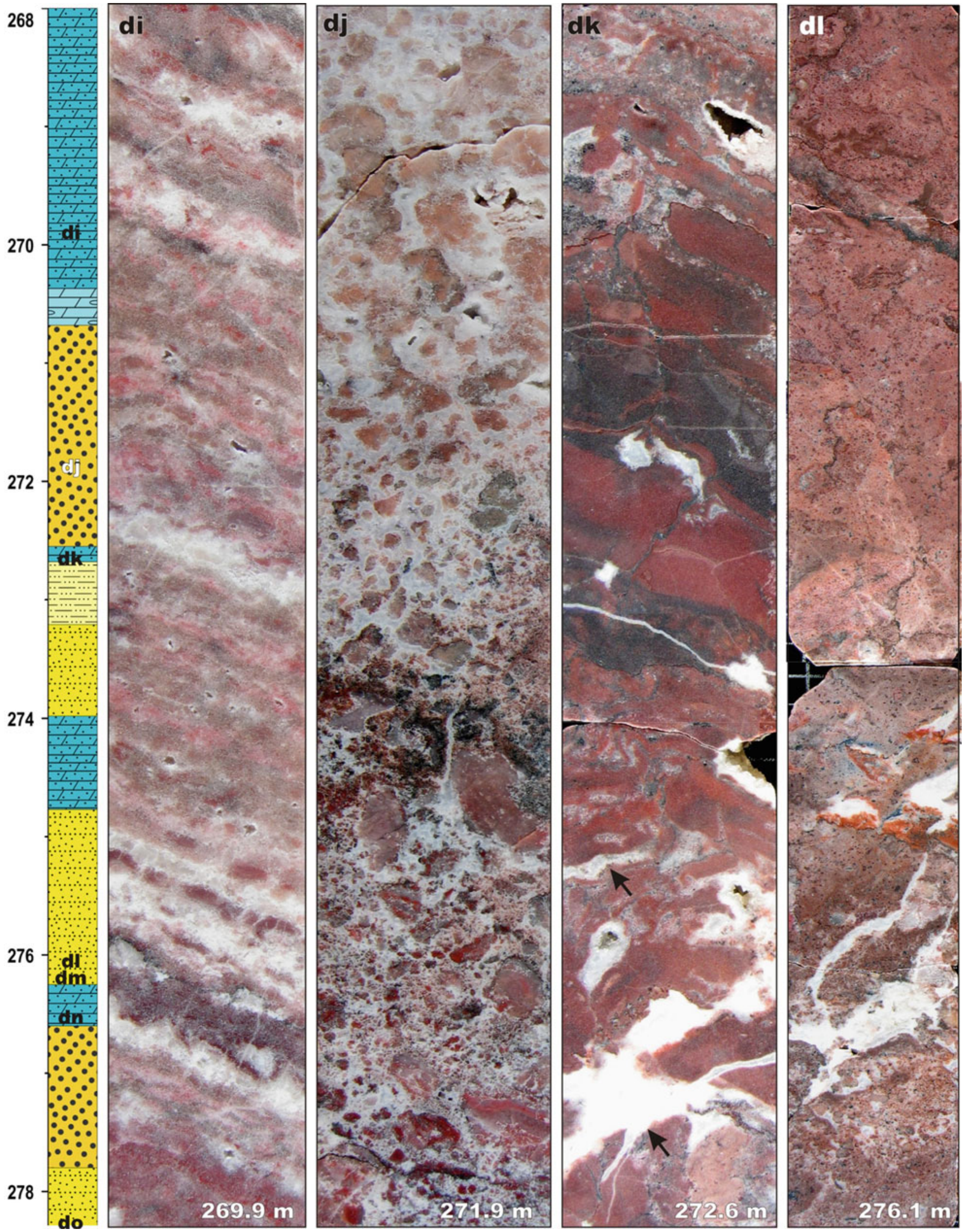

Fig. 6.101 (continued) (**di**) Variegated, indistinctly bedded dolarenite with small dissolution cavities. (**dj**) Gritty breccia composed of pale pink, angular dolostone clasts cemented by white, drusy dolomite; the clasts underwent no to very limited transport. (**dk**) Red dolostone with interlayers of black, Fe-oxide-rich mudstone; note the white, drusy dolomite replaced apparent sulphate nodules (some with hollow cores), and filled cavities after dissolved sulphates (*arrowed*). (**dl**) Pale brown sandstone with a clotted fabric and dissolution cavities filled by white dolospar

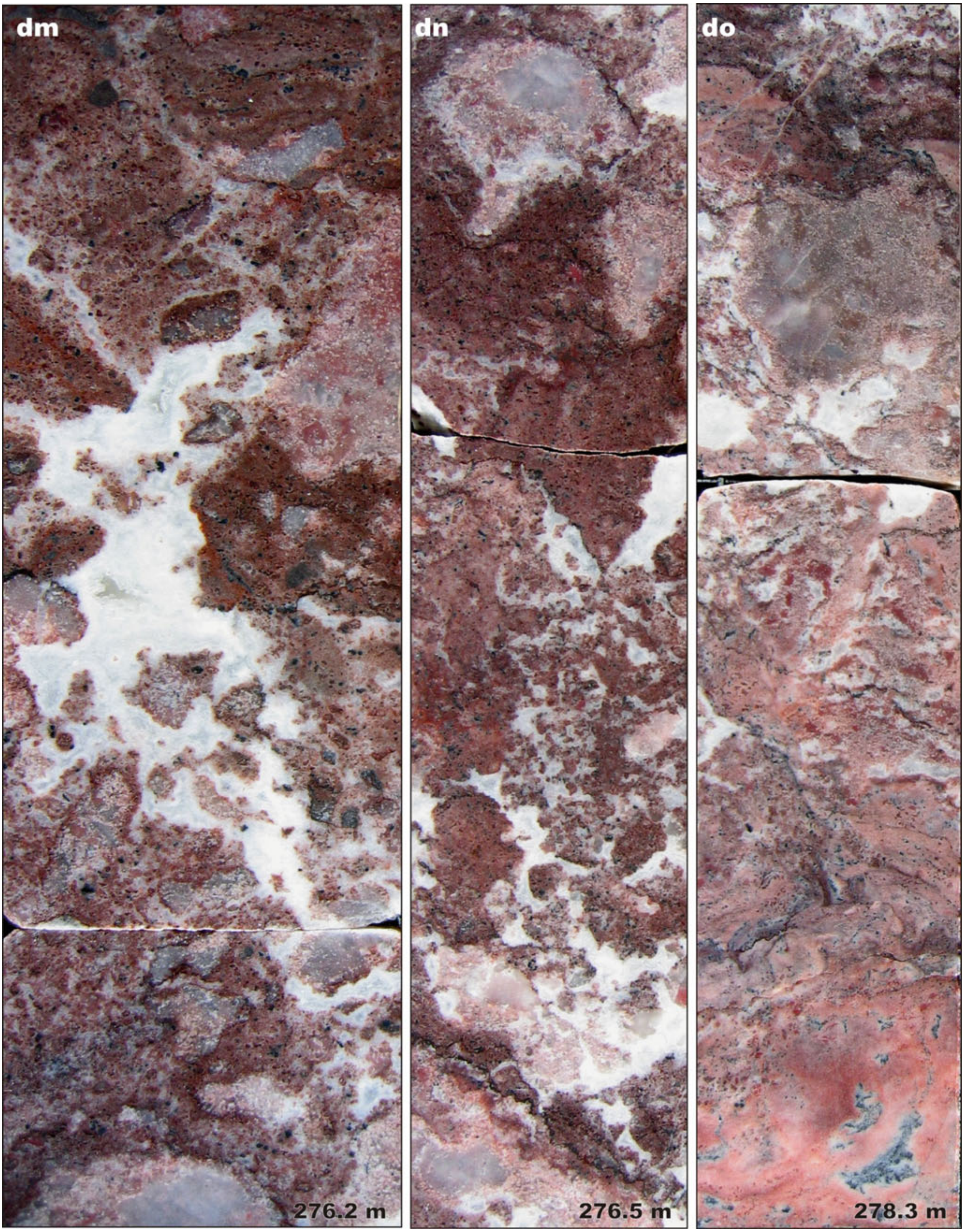

Fig. 6.101 (continued) (**dm**, **dn**) Brown, non-bedded sandstone containing outsized, rounded clasts of silicified dolostone, dolomite-cemented sandstone and vein-quartz; note the dissolution-collapse structure cemented by quartz and white, drusy dolomite. (**do**) Variegated sandstone with a dissolution-collapse structure; remaining cavities were cemented with dolomite (All photographs by Victor Melezhik)

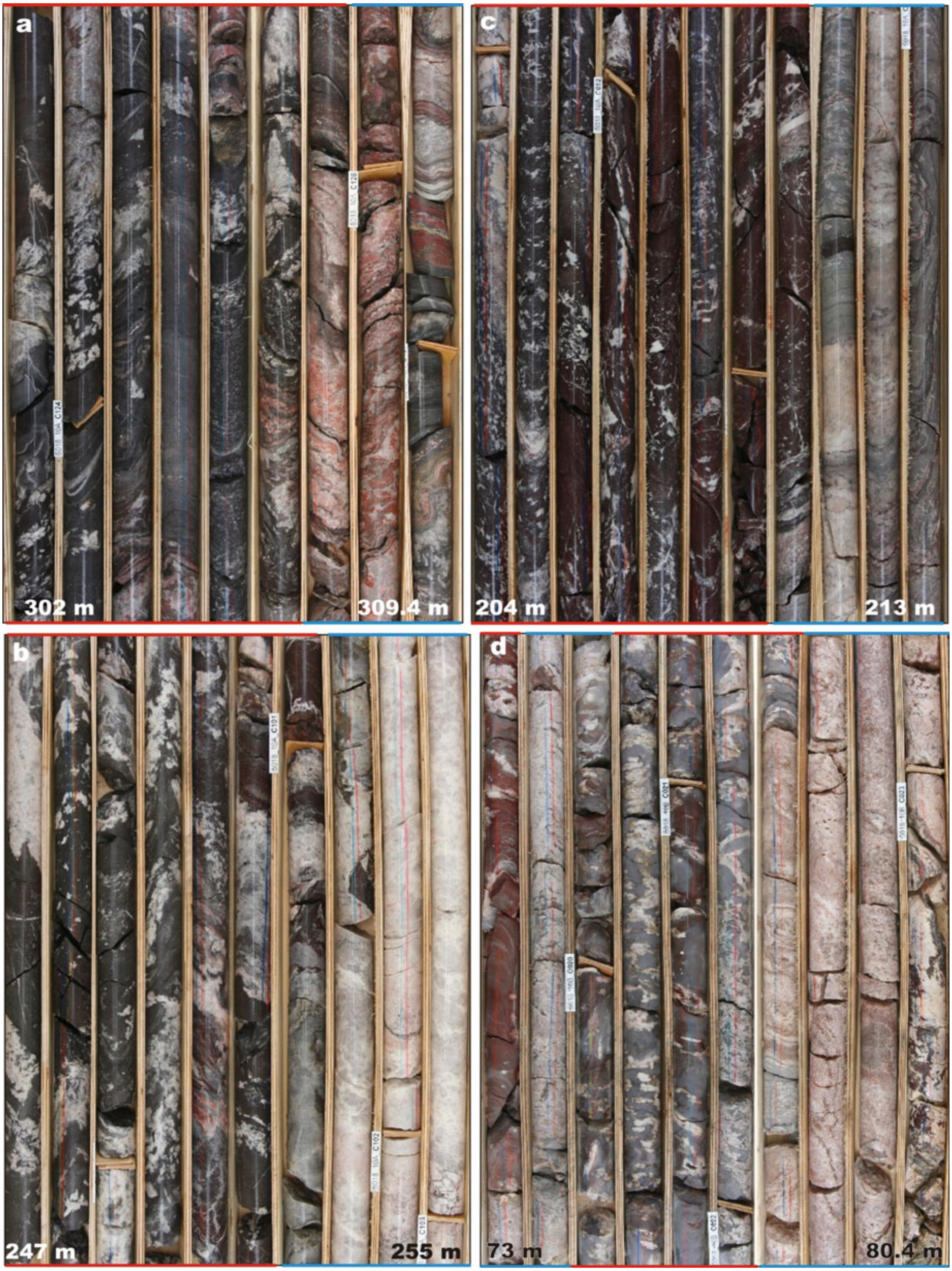

Fig. 6.102 Carbonate-evaporitic cycles in the Tulomozero Formation. *Core 10A*: (**a–c**) Unsawn core demonstrating transitions in thick cycles from dolostone-dominated beds (marked by *blue line*) to evaporitic-dominated layers of siltstones (marked by *red line*) with abundant pseudomorphs after sulphate crystals, rosette concretions and chicken-wire structures (*white*). *Core 10B:* (**d**) Unsawn core demonstrating thin carbonate-evaporitic cycles; the dolostone-dominated part of the cycles is marked by *blue line*, and the evaporitic, nodular siltstones (*grey* and *red*) are marked by a *red line* (Photographs of core are from the FAR-DEEP database (http://far-deep.icdp-online.org))

References

Aitken JD (1967) Classification and environmental significance of cryptalgal limestones and dolomites, with illustrations from the Cambrian and Ordovician of southwestern Alberta. J Sediment Petrol 37:1163–1178

Akhmedov AM, Krupenik VA, Makarikhin VV, Medvedev PV (1993) Carbon isotope composition of carbonates in Early Proterozoic sedimentary basins. In: Published report of the institute of geology. Institute of Geology, Karelian Research Centre of RAS, Petrozavodsk, p 56 (in Russian)

Akhmedov AM, Panova EG, Krupenik VA, Sveshnikova KY (2004) Early Proterozoic and Devonian arid palaeobasins from a joint zone of the Baltic Shield and Russian Platform. Trans St Petersburg Soc Natural 2 (86):1–140, (in Russian)

Brasier AT, Fallick AE, Prave AR, Melezhik VA, Lepland A, FAR-DEEP Scientists (2011) Coastal sabkha dolomites and calcitised sulphates preserving the Lomagundi-Jatuli carbon isotope signal. Precambrian Res 189:193–211

Bush P (1973) Some aspects of diagenetic history of the sabkha in Abu Dhabi, Persian Gulf, In: Purser BH (ed) The Persian Gulf. Springer-Verlag, Berlin, pp 395–407

Butler GP (1970) Holocene gypsum and anhydrite of the Abu Dhabi sabkha, Trucial Coast: an alternative explanation of origin, Third Symposium on Salt, North Ohio. Geol Soc 1:120–152

Butler GP, Harris PM, Kendal CG SC (1982) Recent evaporates from the Abu Dhabi coastal flats. In: Handford CR, Loucks RG, Davies GR (eds) Deposition and diagenesis spectra of evaporites, vol 3 Society of economic Paleontologists and mineralogists Core Workshop, pp 33–64

Hannah JL, Stein HJ, Zimmerman A, Yang G, Melezhik VA, Filippov MM, Turgeon SC, Creaser RA (2008) Re-Os geochronology of a 2.05 Ga fossil oil field near Shunga, Karelia, NW Russia, Abstract, the 33rd international geological congress, Oslo

Heiskanen KI, Rychanchik DV (1999) The Jatulian, Early Proterozoic carbonates with anomalously heavy carbon of the Baltic Shield. Stratigr Geol Correl 7(6):14–19, (in Russian)

Huhma H, Cliff RA, Perttunen V, Sakko M (1990) Sm-Nd and Pb isotopic study of mafic rocks associated with early Proterozoic continental rifting: the Peräpohja schist belt in northern Finland. Contrib Mineral Petrol 104:369–379

Irwin ML (1965) General theory of epeiric clear water sedimentation. Am Assoc Petrol Geol Bull 49:445–459

Karhu JA (1993) Palaeoproterozoic evolution of the carbon isotope ratios of sedimentary carbonates in the Fennoscandian Shield. Bull Geol Surv Finland 371:1–87

Karhu JA, Holland HD (1996) Carbon isotopes and the rise of atmospheric oxygen. Geology 24:867–879

Kendall AC (1992) Evaporites. In: Walker RG, James NP (eds) Facies models: response to sea level change. Geological Association of Canada, St John's, Newfoundland, pp 375–409

Koistinen T, Stephens MB, Bogatchev V, Nordgulen Ø, Wennesström M, Korhonen J (comps) (2001) Geological map of the Fennoscandian Shield, Scale 1:2 000 000, Espoo, Trondheim, Uppsala, Moscow

Krupenik VA, Sveshnikova KY (2011) Correlation of the Onega parametric hole with the reference sections of the Onega structure. In: Glushanin LV, Sharov NV, Shchiptsov VV (eds) The Onega Palaeoproterozoic structure (Geology, Tectonics, deep structure and minerageny). Institute of Geology, Karelian Research Centre of RAS, Petrozavodsk, pp 190–195, (in Russian)

Krupenik VA, Akhmedov AM, Sveshnikova KY (2011a) Structure of the section of the Onega structure based on the Onega parametric drillhole. In: Glushanin LV, Sharov NV, Shchiptsov VV (eds) The Onega Palaeoproterozoic structure (Geology, Tectonics, deep structure and minerageny). Institute of Geology, Karelian Research Centre of RAS, Petrozavodsk, pp 172–189, (in Russian)

Krupenik VA, Akhmedov AM, Sveshnikova KY (2011b) Isotopic composition of carbon, oxygen and sulphur in the Ludicovian and Jatulian rocks. In: Glushanin LV, Sharov NV, Shchiptsov VV (eds) The Onega Palaeoproterozoic structure (Geology, Tectonics, deep structure and minerageny). Institute of Geology, Karelian Research Centre of RAS, Petrozavodsk, pp 172–189, (in Russian)

Land LA, Paull CK (2000) Submarine karst belt rimming the continental slope in the Straits of Florida. Geo-Mar Lett 20:123–132

Makarikhin VV (1992) Lower Precambrian stromatolite associations of Karelia. In: Schidlowski M, Golubic S, Kimberley MM, McKirdy DM, Trudinger PA (eds) Early organic evolution. Springer, Berlin/Heidelberg/New York, pp 463–467

Makarikhin VV, Kononova GM (1983) Early Proterozoic phytolithes of Karelia. Nauka (Science), Leningrad, p 180, (in Russian)

Medvedev P, Bekker A, Karhu JA, Kortelainen N (2005) Testing the biostratigraphic potential of early Paleoproterozoic microdigitate stromatolites. Rev Esp Micropaleontol 37:41–56

Medvedev PV, Makarikhin VV, Golubev AI, Rychanchik DV, Trofimov NN (2011) The Jatuli. In: Glushanin LV, Sharov NV, Shchiptsov VV (eds) The Onega Palaeoproterozoic structure (Geology, tectonics, deep structure and minerageny). Institute of Geology, Karelian Research Centre of RAS, Petrozavodsk, pp 52–67, (in Russian)

Melezhik VA, Fallick AE (1996) A widespread positive $\delta^{13}C_{carb}$ anomaly at around 2.33–2.06 Ga on the Fennoscandian Shield: a paradox? Terra Nova 8:141–157

Melezhik VA, Fallick AE, Medvedev PV, Makarikhin VV (1999) Extreme $^{13}C_{carb}$ enrichment in ca. 2.0 Ga magnesite-stromatolite-dolomite-‘red beds’ association in a global context: a case for the world-wide signal enhanced by a local environment. Earth Sci Rev 48:71–120

Melezhik VA, Fallick AE, Medvedev PV, Makarikhin VV (2000) Palaeoproterozoic magnesite–stromatolite–dolostone–‘red bed’ association, Russian Karelia: palaeoenvironmental constraints on the 2.0 Ga positive carbon isotope shift. Nor Geol Tidsskr 80:163–186

Melezhik VA, Fallick AE, Medvedev PV, Makarikhin V (2001) Palaeoproterozoic magnesite: lithological and isotopic evidence for playa/sabkha environments. Sedimentology 48:379–397

Melezhik VA, Fallick AE, Rychanchik DV, Kuznetsov AB (2005) Palaeoproterozoic evaporites in Fennoscandia: implications for seawater sulphate, $\delta^{13}C$ excursions and the rise of atmospheric oxygen. Terra Nova 17:141–148

Morozov AF, Hakhaev BN, Petrov OV, Gorbachev VI, Tarkhanov GB, Tsvetkov LD, Erinchek YM, Akhmedov AM, Krupenik VA, Sveshnikova KY (2010) Rock-salts in Palaeoproterozoic strata of the Onega depression of Karelia (based on data from the Onega parametric drillhole). Trans Acad Sci 435(2):230–233, (in Russian)

Negrutsa VZ (1984) Early Proterozoic stages of evolution of the Eastern Baltic Shield. Nedra, Leningrad, p 270, (in Russian)

Ovchinnikova GV, Kusnetzov AB, Melezhik VA, Gorokhov IM, Vasil’eva IM, Gorokhovsky BM (2007) Pb-Pb age of Jatulian carbonate rocks: the Tulomozero formation in south-eastern Karelia. Stratigr Geol Correl 4:20–33, (in Russian)

Perevozchikova VV (1957) Proterozoic geology of Karelia. Mater Geol Miner Res Northwest USSR 1:25–51, (in Russian)

Philippov NB, Trofimov NN, Golubev AI, Sergeev SA, Huhma H (2007) New geochronological data on the Koikary-Svjatnavolok and Pudozhgora gabbro-dolerite intrusives. In: Golubev VI, Shchiptsov VV (eds) Geology and mineral resources of Karelia, vol 10. pp 49–68. Karelian Research Centre, Petrozavodsk, (in Russian with English abstract)

Puchtel IS, Arndt NT, Hofmann AW, Haase KM, Kröner A, Kulikov VS, Kulikova VV, Garbe-Schönberg C-D, Nemchin AA (1998) Petrology of mafic lavas within the Onega plateau, Central Karelia: evidence for the 2.0 Ga plume-related continental crustal growth in the Baltic Shield. Contrib Mineral Petrol 130:134–153

Puchtel IS, Zhuravlev DZ, Ashikhmina NA, Kulikov VS, Kulikova VV (1992) Sm-Nd age of the Suisarian suite on the Baltic Shield. Trans Russ Acad Sci 326:706–711, (in Russian)

Reuschel M, Melezhik VA, Whitehouse MJ, Lepland A, Fallick AE, Strauss H (2012) Isotopic evidence for a sizeable seawater sulfate reservoir at 2.1 Ga. Precambrian Res 192–195:78–88

Satzuk YI, Makarikhin VA, Medvedev PV (1988) Jatulian geology of the Onega-Segozero Watershed, Nauka (Science), Leningrad, p 96, (in Russian)

Sokolov VA (1963) Geology and lithology of middle Proterozoic carbonate rocks of Karelia. Nauka (Science), Moscow-Leningrad, p 196, (in Russian)

Sokolov VA, Galdobina LP, Ryleev AB, Satzuk YI, Heiskanen KI, (1970) Geology, sedimentology and palaeogeography of the Jatuli, Central Karelia. In: Proceedings of the institute of geology, Karelian Branch of Academy of the USSR Academy of Sciences. Issue 6, “Karelia”, Petrozavodsk, p 367, (in Russian)

Tikhomirova M, Makarikhin VV (1993) Possible reasons for the $\delta^{13}C$ anomaly of Lower Proterozoic sedimentary carbonates. Terra Res 5:244–248

Warren JK (2006) Evaporites: sediments, resources and hydrocarbons. Springer, Berlin, p 1035

Warren JK, Kendal CGSC (1985) Comparison of marine (subaerial) and salina (subaqueous) evaporites: ancient and modern. Bull Am Assoc Petrol Geol 69:1013–1023

Yudovich YE, Makarikhin VV, Medvedev PV, Sukhanov NV (1991) Carbon isotope anomalies in carbonates of the Karelian Complex. Geochem Int 28:56–62

6.3.2 Tulomozero Formation: FAR-DEEP Hole 11A

Victor A. Melezhik, Anthony R. Prave, Aivo Lepland, Alexander E. Romashkin, Dmitry V. Rychanchik, and Eero J. Hanski

Scientific Targets

– Nature of the geological boundary between the Tulomozero Formation (Lomagundi-Jatuli isotopic event) and the Zaonega Formation (the initiation of the Shunga event)
– Tectonic and depositional settings and geochemical rock record at the end of the Lomagundi-Jatuli isotopic event and initiation of the Shunga event
– Carbon, sulphur and strontium isotopic composition of ambient water
– Influence of depositional setting on carbon and strontium isotopic composition
– Provenance composition
– Microfossil record
– Radiometric age constraints on timing of deposition

The 436-m-long Hole 11A is in the northern part of the Onega Basin, Karelia, NW Russia (Figs. 6.1 and 6.86). It intersected 80 m of the lower part of the Zaonega Formation and c. 356 m of the upper part of the Tulomozero Formation, including a 24-m-thick mafic lava in the lower part of the formation; core recovery was 100 % through the contact between the two formations. Deposition of the Tulomozero Formation is imprecisely constrained to between 2090 ± 70 Ma and 1983.4 ± 6.5 Ma (Ovchinnikova et al. 2007; Philippov et al. 2007; for details see Chaps. 4.2 1 and 6.3.1). The core of the Tulomozero Formation contains carbonate rocks that record the global Palaeoproterozoic positive $\delta^{13}C$ excursion of sedimentary carbonates (e.g., Yudovich et al. 1991; Akhmedov et al. 1993; Karhu 1993; Tikhomirova and Makarikhin 1993; Karhu and Holland 1996; Heiskanen and Rychanchik 1999; Melezhik and Fallick 1996; Melezhik et al. 2005; Brasier et al. 2011) and also exhibit many features indicating that deposition occurred in restricted environments. Hence, there is good potential for studying the influence of evaporitic conditions on modification of the global $\delta^{13}C_{carb}$ marine signal. The presence of abundant dissolution-collapse breccias (Fig. 6.103) suggests that a significant volume of soluble evaporitic minerals underwent dissolution processes, apparently caused by percolation of fresh meteoric waters into the basin. Preserved relicts of evaporite minerals could inform on both the chemistry of Palaeoproterozoic seawater and the precipitation sequences formed during its progressive evaporation. Further, abundant terrestrial carbonate and siliciclastic "red beds" are evidence for an oxidising atmosphere.

The Zaonega Formation core (top 80 m) comprises a siliciclastic-dominated succession with minor carbonate beds. Similar beds were intersected by the 3,500-m-deep Onega parametric hole drilled in the southern part of the Onega basin and, occur in outcrops elsewhere. These rocks show a gradual decline in $\delta^{13}C_{carb}$ from values as high as +9 ‰ to +0 ‰ through c. 200 m (Krupenik et al. 2011), and thus contain valuable information on the termination of the Lomagudi-Jatuli isotopic excursion. In addition, post-depositional alteration of the Zaonega Formation rocks records the presence of fluids whose redox-state fluctuated from oxic (ascending fluids) to chemically-reducing (descending fluids), resulting in variegated colouration of the rocks (Fig. 6.104).

Figures 6.105 and 6.106 show a lithological column and stratigraphic profiles of selected major and trace elements as well as magnetic susceptibility. Chemical composition of analysed samples is presented in Appendices 32–34. Photos of core (Fig. 6.107) provide a detailed documentation of major lithological and structural features of the sedimentary rocks. Figure 6.108 shows some geochemical characteristics of the mafic volcanic rocks.

Although the drilled section is only less than 10 km away from Holes 10A and 10B (Fig. 6.86), the lithostratigraphic correlation is not straightforward. The basaltic marker (for details see Chap. 6.3.1) and $\delta^{13}C_{carb}$ trends suggest that the 11A section correlates with the 10B section (Fig. 6.92). Stromatolite morphologies offer another potential correlation tool (Makarikhin 1992; Medvedev et al. 2005), but this remains to be confirmed. Fig. 6.93 shows the stromatolites in drillcore 11A and constitutes a visual basis for comparison to those described from well-studied reference sections (Fig. 6.94).

The Tulomozero Formation

The Tulomozero Formation section intersected by Core 11A is subdivided into seven units (members) based on dominant rock types characterising the different parts of the section. This subdivision is used to facilitate core description and is not meant to replace previously suggested lithological subdivisions (Fig. 6.91). From base to top, the units are: member 1 (Dolostone-Siltstone-Shale); member 2 (Sandstone-Siltstone-Shale-Dissolution Breccia); member

V.A. Melezhik (✉)
Geological Survey of Norway, Postboks 6315 Sluppen, NO-7491 Trondheim, Norway

Centre for Geobiology, University of Bergen, Allegaten 41, Bergen N-5007, Norway

V.A. Melezhik et al. (eds.), *Reading the Archive of Earth's Oxygenation*, Volume 2: The Core Archive of the Fennoscandian Arctic Russia – Drilling Early Earth Project, DOI 10.1007/978-3-642-29659-8_4, © Springer-Verlag Berlin Heidelberg 2013

3 (Lower Dolostone); member 4 (Siltstone-Shale-Basalt); member 5 (Dolostone-Dissolution Breccia); member 6 (Conglomerate); and member 7 (Upper Dolostone) (Fig. 6.105).

Member 1 (Dolostone-Siltstone-Shale)

Member 1 has a drilled thickness of c. 19 m (436–417.3 m). Its top was defined by the first appearance of dolostone breccias at 417.3 m (Fig. 6.105). The rocks have a variable magnetic susceptibility ranging between 0 and 330 μSI (K* = 0 and 30 × 10^{-6} SI in Fig. 6.106). Clastic dolostone sandstone, siltstone and shale have been recognised and all show an essential degree of diagenetic and metamorphic modification. The preserved features suggest that both carbonate and siliciclastic rocks were affected by dissolution processes and in situ brecciation (Figs. 6.107eu–ex). Clastic fragments are mainly variably siliceous dolostone. Post-depositional processes have modified extensively clast-matrix boundaries but, where original features are preserved, clasts are well rounded, but poorly sorted, and cemented by syntaxial dolomite cement. Matrix in the *in situ* brecciated rocks consists of haematite-stained dolomite and minor talc whereas cements are white sparry and drusy dolomite. Some replacement dolomite has crystals with a cubic morphology indicating that at least part of the dissolved and replaced material could have been halite.

Only carbonate rocks were analysed during the archive process. All clastic dolostones of the member have a high SiO_2 content (10–22 wt.%), mainly as clastic quartz, and an elevated Al_2O_3 (2.6–3.7 wt.%) concentration (Appendix 32). They are low in K_2O (0.2–0.5 wt.%), devoid of any measurable Na_2O, C_{org} and S (Appendix 33). Acid-soluble components (Appendix 34) show dolomitic composition (Mg/Ca = 0.64), elevated concentrations of Fe (190–570 μg g^{-1}), Mn (490–790 μg g^{-1}) and P (c. 1,500 μg g^{-1}), and a low Sr content (64–89 μg g^{-1}). Two analysed archive samples from this member show high $\delta^{13}C$ (+9.0 to +10.4 ‰, VPDB) and $\delta^{18}O$ of 18.6 ‰ and 19.6 ‰ (VSMOW) (Reuschel et al. 2012).

Member 2 (Sandstone-Siltstone-Shale-Dissolution Breccia)

The member is c. 41 m thick (417.3–374.2 m), comprises diverse carbonate and siliciclastic lithologies and has several beds of dissolution-collapse breccias at the base and top (Fig. 6.105). The rocks show patchy, variegated colour (Figs. 6.107eb–et). All rocks, regardless of their lithological composition, have low magnetic susceptibility ranging between −22 and 165 μSI (K* = −2 and 15 × 10^{-6} SI in Fig. 6.106).

Siliciclastic rocks are dominant but contain a considerable amount of dolomite and, consequently, are termed dolomite-cemented conglomerate and sandstone (Figs. 6.107ei, eo, et), dolomitic siltstone and shale (Figs. 6.107eb, ec, ep, eq) and dolomarl (Fig. 6.107es). These rocks commonly show crude, irregular bedding that, in places, is disrupted by dissolution and collapse structures (e.g. Figs. 6.107eb, ec, ei, eq); regular, parallel bedding is rare (Fig. 6.107es).

Dissolution-collapse breccias are next in abundance and occur in several intervals within sandstone-siltstone and shale units (Fig. 6.105). They have a bizarre, variegated, spotted colour (Figs. 6.107ed–eg, eq, er), are clast-supported, non-bedded and composed of rounded and angular fragments of dolostone, mudstone and laminated dolomarl with spots and patches of diverse colour. Some breccias contain only partially disintegrated or collapse beds cemented by white drusy dolomite. The matrix is composed of haematite-containing clay and sand material with a variable content of talc and probable magnesite. Most of the breccia intervals resemble collapse structure after dissolved evaporites (Figs. 6.107ed–eg), whereas others are reminiscent of karst (e.g. Fig. 6.107er).

The dolarenites and crystalline dolostones occur as thin beds having sharp contacts with encasing siliciclastic rocks. The carbonate rocks do not retain their primary structures other than, in places, a crude stratification emphasised by lenses and layers of dark-coloured mudstone (Figs. 6.107em, en). Some dolostone beds show dissolution features, such as dissolution-enlarged cracks filled with debris of host rock in dark brown clayey material (Fig. 6.107eh), whereas others have probable dissolution pipes filled with black mudstone (Fig. 6.107en). The same beds contain dolomite-pseudomorphed nodules and crystals of apparent sulphate (e.g. Fig. 6.107en).

Conglomerates and sedimentary breccias are rare. The former are clast-supported and composed of poorly sorted and variably rounded fragments of quartz, dolostone and black mudstone (Fig. 6.107et). The latter are matrix-supported and contain angular clasts of white dolostone set in a polymict, sandy-gritstone matrix (Figs. 6.107ek, el).

Four analysed samples of conglomerate and breccia (Appendix 32) show variable contents of SiO_2 (12–38 wt.%) and Al_2O_3 (0.9–8 wt.%), and high concentrations of dolomite-bound CaO (11–26 wt.%) and MgO (16–21 wt.%); however, some MgO is partially associated with talc and magnesite. The dolomitic siltstones are rich in SiO_2 (28–48 wt.%) in the form of clastic quartz and also have high contents of dolomite-bound CaO (15–17 wt.%) and MgO (10–18 wt.%). All rocks of the member are devoid of any measurable C_{org} and S (Appendix 33). Carbonate components extracted from different lithologies (n = 6) show high $\delta^{13}C$ (+7.8 to +8.1 ‰, VPDB) and $\delta^{18}O$ between 18.8 ‰ and 19.1 ‰ (VSMOW) (Reuschel et al. 2012).

Member 3 (Lower Dolostone)

Member 3 is c. 47 m thick and consists of variegated, clastic dolostones and dolomarls with thin interlayers of sandstone, siltstone and shale that increase up-section (Fig. 6.105). The lower boundary of the member is placed at the base of the first thick dolarenite bed at 374.2 m (Fig. 6.105). The upper boundary is set at 327.4 m, the base of a siltstone-shale succession with a mafic volcanic body. Almost all rocks, regardless of their lithological composition, have a low magnetic susceptibility ranging between −16 and 110 µSI (K* = −1.5 and 10 × 10^{-6} SI in Fig. 6.106). The siltstone-shale unit at 332–330 m represents an exception with values up to 1,900 µSI (K* = 170 × 10^{-6} SI in Fig. 6.106).

The member comprises several shallowing-upward dolostone-shale cycles. The carbonate parts of the cycles range in thickness from 3 to 12 m, whereas the shales are thinner (0.3–6 m) with the thickest ones containing sandstone and breccia interbeds. Contacts between the carbonate-siliciclastic parts of the cycles are sharp. All carbonate rocks are variably recrystallised, although primary crude parallel bedding and stratification are preserved (Figs. 6.107dk–dg, do–dp, dr–ds, du–dy, ea). Well-pronounced parallel bedding is rare and is commonly emphasised by thin mud-clay laminae (Figs. 6.107dt, dz). In many dolostone beds mud fragments resemble rip-ups of desiccated mud layers (Figs. 6.107dm, dv, dw, dy). There are also desiccated dolostone beds (e.g. Fig. 6.107do) and dolostones with intensely desiccated and fragmented mudstone beds (e.g. Fig. 6.107dn). The former occur in the uppermost part of the member and display lensoidal bedding (Figs. 6.107dd, de) and thin intervals composed of dolarenite-shale couplets with lenticular and small-scale flaser bedding, and probable small-scale tepee structures (Figs. 6.107df, dg). However, primary depositional structures are commonly modified by dissolution and re-precipitation processes resulting in formation of dissolution surfaces, dolospar-filled cavities, "granular" and cryptic-brecciated fabrics, and in situ brecciation (Figs. 6.107dk–do). Dolomite- and quartz pseudomorphs after calcium sulphates have been observed on macro- and micro-scale (Figs. 6.107du, dy).

Four types of fabrics are recognised in the dolostones: commonly coarsely crystalline, rarely equigranular, granoblastic mosaic, and one case of pseudo-oolitic (Fig. 6.107ea). The coarsely crystalline microfabric is represented by zoned, euhedral dolomite rhombs overgrown by clear syntaxial cement. Zoning in the rhombs is commonly oscillatory and expressed by a variable content of finely dispersed, non-carbonate material, primarily haematite particles (e.g. the zoned crystals in Fig. 6.107eb).

The shale beds in the dolomarl-shale cycles are black or dark brown, thinly laminated rocks, which in most cases were considerably modified due to diagenetic growth of evaporitic minerals now replaced by white dolospar (e.g. Fig. 6.107eq). The uppermost shale unit at c. 331 m contains a thin interval of haematite-stained, matrix-supported breccias composed of angular fragments of grey siltstone embedded in a bright red gritstone-sandstone matrix (Figs. 6.107dh–dj).

Analyses of eight archive samples show that the carbonate rocks contain a variable amount of SiO_2 (3–44 wt.%), mostly in the form of clastic quartz and silica pseudomorphs after sulphates, small amounts of Al_2O_3 (1 wt.% on average) and K_2O (<0.1–0.15 wt.%), and are devoid of any measurable amount of Na_2O (Appendix 32). A few samples contain C_{org} (0.2 and 0.5 wt.%) and S (0.04 wt.%) (Appendix 33). Seven analyses of acid-soluble components show dolomitic composition (Mg/Ca = 0.60–0.65), a high P concentration (175–511 µg g^{-1}), moderate Mn (53–181 µg g^{-1}, with one outlier at 1,360 µg g^{-1}) and Fe (45–271 µg g^{-1}) contents, and low Sr abundances (11–69 µg g^{-1}, with one outlier at 252 µg g^{-1}) (Appendix 34). From 365.46 m in member 3 to 431.07 m at the base of member 1, acid-soluble Mn and P show a progressive increase from 53 to 794 µg g^{-1}, and from 205 to 1,510 µg g^{-1}, respectively (Appendix 34). Such a trend is not correlated with any systematic changes in the other analysed elements, and its cause remains to be studied.

All analysed archive samples from this member show a high $\delta^{13}C$ (+6.8 to +9.7 ‰, VPDB) and $\delta^{18}O$ between 18.6 ‰ and 19.8 ‰ (VSMOW) (Reuschel et al. 2012). The available isotopic data do not suggest any stratigraphic trend.

Member 4 (Siltstone-Shale-Basalt)

The siltstone-shale-basalt member is c. 45 m thick, but much of its thickness is occupied by a mafic lava unit (326.5–303 m) and thick quartz vein (297.5–288.1 m) (Fig. 6.105). The lava shows an elevated and rather homogeneous magnetic susceptibility averaging at 440 µSI (K* = 40 × 10^{-6} SI in Fig. 6.106), being similar in this respect to the potentially correlative basaltic unit in Core 10B (see Chap. 6.3.1) The siltstone-shale exhibits variation between 33 and 440 µSI (K* = 3–40 × 10^{-6} SI in Fig. 6.106).

The siltstone-shale is variegated with an essential dolomitic component. The section between the mafic lava and the quartz vein retains lenticular, flaser and wavy lamination (Fig. 6.107dc) whereas above the quartz vein, primary structures were modified severely by dissolution, cementation and diagenetic growth of evaporitic minerals. The latter occur now as quartz- and dolospar-pseudomorphed fabrics (Fig. 6.107da). This part of the section contains thin intervals of intraformational conglomerate (Fig. 6.107db) and pink dolostone with dolomite-cemented dissolution cavities (Fig. 6.107cz).

The lava has a tectonically modified lower contact and a gradational upper contact with the overlying siltstone-shale; the topmost 1 m of the lava shows intense reddening. Apart from rare chlorite amygdales, no other volcanic structures can be recognised and strong alteration has produced minerals like talc and chlorite. Chemically, this body shares many features with the mafic unit in Core 10B, including high MgO contents (13.3–15.5 wt.%) (Fig. 6.100) and relatively low contents of Ni (99–139 ppm), Cr (125–148 ppm) and very low abundances of immobile incompatible trace elements, such as Nb (2.1–2.5 ppm), Zr (52–58 ppm), and Ce (below the detection limit of XRF). As interpreted in the case of Core 10B, the rocks have gained extra MgO, potentially from surrounding dolomites (see Chap. 6.3.1). Along with MgO, they have also gained K, Rb, and U (Fig. 6.108).

The dolomitic siltstone overlying the mafic body in Core 11A is enriched in Ni (26 ppm), Co (35 ppm), Cr (111 ppm), V (1,329 ppm) and Fe_2O_{3tot} (12 wt.%), which is comparable to those from the underlying mafic body and distinguishes it from other rocks in Hole 11A (Appendices 32 and 34). It is noteworthy that similar geochemical characteristics are documented in the greenish sandstones and heterolithic rocks overlying the mafic body in Hole 10B (see Chap. 6.3.1). Thus, taken together, these characteristics suggest the igneous body was apparently affected by weathering and erosion allowing the overlying sediments to inherit some igneous geochemical features.

Member 5 (Dolostone-Dissolution Breccia)

Member 5 has a thickness of c. 77 m. Its lower boundary is placed at 282.2 at the base of the first dissolution breccias and its upper boundary is placed at the top of the last pink dolostone bed sharply overlain by talc- and magnesite-bearing conglomeratic breccias at 205.8 m (Fig. 6.105). Clastic dolostones and dissolution-collapse breccias form the bulk of the member, though minor conglomerate and shale intervals occur throughout the section (Figs. 6.107by–cy). Magnetic susceptibility of all rock types is low and fluctuates between −16 and 150 µSI ($K^* = -1.5$ to 14×10^{-6} SI in Fig. 6.106).

Numerous 0.5–10-m-thick dolostone-dissolution breccia cycles typify member 5 and show many similarities with those occurring in member 3. In both members, cycles have similar thicknesses, with the carbonate portions being thicker than the shale/breccia portions (Fig. 6.105). In contrast, though, the non-carbonate parts of cycles in member 5 comprise dissolution breccias (rather than shale, as per member 3) with minor shale and conglomerate intervals.

The carbonate beds in the cycles range in thickness from c. 1 m to c. 14 m, and their contact with breccias can be gradual, through partially brecciated or disintegrated carbonate rocks (e.g. Fig. 6.107cw), or sharp dissolution surfaces (e.g. Fig. 6.107cj). Some of the latter may represent large dissolution holes filled with debris of collapsed overlying beds (Fig. 6.107cx). Recrystallisation processes hamper distinguishing between chemically precipitated and redeposited carbonates and, although the visual core log indicates the dominance of clastic carbonate rocks (mainly dolarenite and dolorudite/gritstone), this should be viewed with caution. However, dolorudites can be confidently recognised, such as that shown in Fig. 6.107ci. Where the primary nature of the carbonate rocks is completely obliterated by recrystallisation, the rocks are termed ‘crystalline dolostone’.

All carbonate rocks are commonly light-coloured, pale brown and pale pink, massive and porous (Figs. 6.107cc, cd, cj), though crudely bedded and parallel-laminated varieties were also observed (e.g. Figs. 6.107ce, ci, cw). Both clastic and crystalline dolostones contain intraformational clasts of black mudstone (rip-ups) and outsized fragments of dolostone (Figs. 6.107cc, ce, ci). All fragments in dolorudites are intraformational dolostone. The clasts are poorly sorted and angular (e.g. Fig. 6.107ci). Clastic particles in dolarenites are commonly recrystallised beyond recognition.

The most common texture in all dolostone lithologies in the member is a groundmass composed of drusy, euhedral, dolomite crystals with oscillatory zoning (see the inset in Fig. 6.107eb as an example). This “drusy” groundmass contains abundant, mm-scale quartz pseudomorphs after crystals and nodules of gypsum/anhydrite (see the inset in Figs. 6.107co–cr as an example). The pseudomorphs contain plentiful µm-size inclusions of gas, fluid and relicts of anhydrite. Dolostone fragments in dolorudites appear microscopically as a combination of irregular “clumps” of dolomite with a granoblastic mosaic fabric; such “clumps” are cemented by drusy, euhedral dolomite crystals with oscillatory zoning. The relative proportion of these two modes of dolomite in clasts varies greatly. Dissolution vugs and cavities are also cemented by drusy euhedral, dolomite crystals with oscillatory zoning.

The carbonate rocks occurring between c. 238 and 219 m (Figs. 6.107cb–cd) show a peculiar mosaic of euhedral dolomite crystals, most having a cubic morphology (the inset in Fig. 6.107cd). This, together with the massive appearance of such dolostones, suggests that the dolomite might have been replacement of halite.

Another dolostone bed with unusual fabric occurs at c. 208 m. This is composed of red, discoidal, zoned, haematite-containing dolomite crystals floating in white, drusy dolomite cement (Figs. 6.107by, bz). Other components are large fragments of red and black laminated mudstone, pale pink dolostone and dark grey dolomarl. The discoidal, zoned dolomite crystals are interpreted to represent pseudomorphs after gypsum.

The dissolution breccias forming upper parts of the dolomite-siliciclastic cycles comprise beds that range in thickness from 0.3 to c. 4 m. Most (Figs. 6.107cf–ch, cj, ck, cn–cr, cx, cy) are composed of intraformational clasts of dark-coloured mudstone cemented by white, drusy dolomite; fragments of dolostone and marl are less abundant. Most of the clasts are angular, though soft-sediment deformed fragments are also present (e.g. Fig. 6.107ch). The breccias are commonly cement-supported, whereas clast-supported varieties are rare (e.g. Fig. 6.107cx). However, there are also dissolution breccias with no cement (Fig. 6.107ca), hence the dissolution process post-dates metamorphic recrystallisation. Some intervals contain thin beds of intraformational conglomerates, which may represent dissolution breccias reworked by waves or currents.

Many breccia beds contain thin intervals of laminated and desiccated dolomarl and limestone-mudstone, which still remain intact or show variable degrees of in situ disintegration (Figs. 6.107cf, cg, cl, cm). Some breccias host thicker (0.3–0.7 m) shale and dolomarl beds (Fig. 6.105). These are commonly variegated, parallel-laminated, or flaser-bedded and intensely desiccated. Some dolomarl-shale beds are soft-sediment deformed into complex open and closed folds resembling an enterolithic structure, and hence may originally represent shale-gypsum-dolomarl interbeds (Figs. 6.107cs–cv).

All clastic dolostones of the member have uniform Mg/Ca ratios ranging between 0.61 and 0.65 except one at 246.36 m that represents calcitised dolostone with a Mg/Ca ratio of 0.07. Clastic dolostones contain a high and variable amount of SiO_2 (10–32 wt.%), which in part is due to silicified sulphates. The content of other major and trace elements are either low or below the detection limits (Appendices 32 and 33). Acid-soluble components from the dolostones show low Fe (40–128 µg g^{-1}) and Sr (25–58 µg g^{-1}), and moderate Mn (46–446 µg g^{-1}) contents (Appendix 34).

All analysed archive samples of clastic dolostones in this member show high $\delta^{13}C$ (+8.5 ‰ to +11.6 ‰, VPDB) and $\delta^{18}O$ between 17.2 ‰ and 19.3 ‰ (VSMOW) (Reuschel et al. 2012). There is an erratic increase in $\delta^{13}C$ from +8.5 ‰ to +11.3 ‰ going up-section from 277 m. The calcitised dolostone has the lowest $\delta^{18}O$ (16.4 ‰) but $\delta^{13}C$ remains high (+10.3 ‰). The vein of white, crystalline dolomite (Fig. 6.107cb) shows the highest $\delta^{13}C$ (+11.8 ‰) but is comparable with that of the host dolostones (+11.6 ‰); $\delta^{18}O$ of 18.8 ‰ is also similar. Reuschel et al. (2012) reported 177 ppm of sulphate in dolorudite samples at a depth of 259.04 m, which yielded $\delta^{34}S$ of 10.4 ‰ (VCDT).

Member 6 (Conglomerate)

Member 6 is c. 23.5 m thick and composed of unusual polymict carbonate conglomerates that are markedly different (Figs. 6.107bk, bn–bx) from any other clastic rocks known within the Tulomozero Formation (see Chap. 4.3). The basal bed of dark grey, massive, gritty conglomeratic breccia at 205.8 m rests with a sharp contact on pink dolostone. The upper boundary is at 179.1 m, the top of the last bed of conglomerate (Fig. 6.105). Within this dominantly polymict conglomerate member are a few thin intervals of small-clast dolorudite and dolarenite. Magnetic susceptibility of all rock types is low, between −18 and 520 µSI ($K^* = -1.6$–47×10^{-6} SI in Fig. 6.106), averaging at 110 µSI.

The conglomerates consist of rounded clasts of carbonate rocks showing a variety of colours. Many clasts have irregularly curved surfaces suggesting leaching or dissolution. Clasts are tightly packed, unsorted and poorly to not cemented (e.g. Figs. 6.107bk, bn, bp, bw). The matrix is composed of sand-sized particles of dolomite surrounded by thick, bent talc plates. The conglomerates are massive rocks without even a hint of bedding. The associated small-clast dolorudite and dolarenite share with the conglomerates all compositional and structural characteristics and differ only by the size of the clasts.

Major element concentrations warrant caution in that some of the carbonate conglomerates may be confused with ultramafic rocks: 40 wt.% SiO_2, 10 wt.% Al_2O_3, 5 wt.% Fe_2O_{3tot}, 20 wt.% MgO, 6 wt.% CaO, 0.4 wt.% Na_2O and 0.07 wt.% K_2O (Appendix 32). Other varieties, having higher SiO_2 (50 wt.%) and Al_2O_3 (10–12 wt.%) abundances, may similarly suggest weathered or altered ultramafic components. However, contents of Co (15–20 ppm), Cr (40–50 ppm) and Ni (30–40 ppm) in the conglomerates are low, at the level of normal carbonates of members 1 and 2, and hence an ultramafic parentage can be ruled out. Alternative interpretations include reworked dissolution-collapse breccias or infill of deeply karstified surfaces; some of the conglomerates resemble "*terra rossa*" (Fig. 6.107bo).

Member 7 (Upper Dolostone)

This member is the only unit in Core 11A consisting almost entirely of dolostone (Figs. 6.107af–bj), although a c. 1-m-thick shale-breccia interval is present close to its base. It is also the only unit in Core 11A that contains oncolithic/oolithic and stromatolitic dolostones. The member is c. 77 m thick and rests with a sharp contact on dark brown, dissolution-collapse breccias at 179.1 m. The upper contact constitutes the boundary between the Tulomozero and Zaonega Formations. It is sharp and separates steeply dipping stromatolitic dolostones from flat-lying sandstones; this contact is detailed below in the description of the Zaonega Formation. The magnetic susceptibility of the Upper Dolostone member is the lowest among the rocks intersected by Hole 11A, never exceeding 110 µSI ($K^* = 10 \times 10^{-6}$ SI in Fig. 6.106).

The member starts with pale pink, recrystallised, porous, non-bedded dolostone. This gradually passes into a 7.3-m-thick unit of bedded rocks composed of mm-size, irregular spheres of dolomite rimmed by haematite-rich clayey material and cemented with quartz and dolomite (Fig. 6.107bj). The spheres resemble oolites or oncolites. The oolitic/oncolitic dolostone is sharply overlain by a thin interval of slumped shale dolomarl (Fig. 6.107bi) capped by 0.5-m-thick, dark brown, clast-supported, dissolution-collapse breccia. The rest of the member, to 111.2 m, is composed of three dolostone varieties: (1) non-bedded rocks with a patchy, variegated colour (e.g. Fig. 6.107ay); (2) buff, microcrystalline, mainly massive rocks with thin interbeds of brown, laminated dolomarl and abundant dissolution holes of karstic origin filled with dolostone and collapsed beds of laminated dolomarls (Figs. 6.107as–ax, az–be, bg); and (3) parallel-laminated dolostone (Figs. 6.107an, ar, bf, bh). The first two varieties constitute the bulk of the member. The bedded and laminated dolostones are rare, occur as thin intervals in different parts of the section and have gradational contacts with massive dolostones displaying a variegated, patchy colouration. Microstructural preservation of all above-listed dolomite varieties is poor; they show either a granoblastic mosaic, finely crystalline or xenomorphic structure.

At 111.2 m, non-bedded dolostone with abundant, unfilled dissolution cavities is overlain by a c. 5-m-thick unit of pink, stromatolitic dolostones. This unit comprises two deepening-upward cycles of similar thicknesses with flat-laminated stromatolites at the base and small, columnar stromatolites on the top (Figs. 6.107af–am). The thicknesses of both members are approximately equal, and the contacts between the members and the cycles are sharp (Fig. 6.107ak). The microfabric of stromatolitic dolostones has been considerably recrystallised. Stromatolitic laminae within both laminated and columnar stromatolites show a dark red colour due to staining by haematite, and contain more clay material relative to microcrystalline dolomite, which occurs between the microbial laminae and between the columns (Figs. 6.107af–am).

All carbonate rocks are dolomitic in composition (Mg/Ca = 0.63–0.66). The oncolitic/oolitic and stromatolitic dolostones contain higher abundances of SiO_2 (7.7–28.6 wt.% vs. <0.5–6.5 wt.%), Al_2O_3 (0.8–2 wt.% vs. <0.2–0.33 wt.%) and Fe_2O_{3tot} (0.7–1.2 wt.% vs. 0.02–0.25 wt.%) (Appendix 32). They also show a relative enhancement in Co (5–8 ppm vs. <4 ppm), Cr (9–14 ppm vs. <4 ppm) and Ni (5–16 ppm vs. <2 ppm); the oncolitic/oolitic dolostones are also enriched in Cu (160–300 ppm) with respect to other dolostones of the member (7–81 ppm) (Appendix 33). Acid-soluble components suggest that all dolostones are similar in Sr abundances (44–133 $\mu g\ g^{-1}$), but the stromatolitic and oncolitic/oolitic types contain more Mn (236–410 $\mu g\ g^{-1}$ vs. 60–171 $\mu g\ g^{-1}$) and Fe (174–3,610 $\mu g\ g^{-1}$ vs. 80–313 $\mu g\ g^{-1}$) (Appendix 34). From 129.4 m, the Fe content increases up-section from 80 to 3,610 $\mu g\ g^{-1}$ whereas upward from 116.2 m, the Mn content increase from 60 to 410 $\mu g\ g^{-1}$.

All analysed archive samples from this member show high $\delta^{13}C$ (+7.4 ‰ to +9.6 ‰, VPDB) and $\delta^{18}O$ between 17.1 ‰ and 19.2 ‰ (VSMOW) (Reuschel et al. 2012). From c. 220 m and upward, there is a systematic decrease in $\delta^{13}C$ from +11.8 ‰ to +7.6 ‰; $\delta^{18}O$ does not display a similar trend.

The Zaonega Formation

The lower contact of the Zaonega Formation was documented in various places, but interpretation of its nature remains controversial (e.g. Negrutsa 1984; Galdobina 1987). Two conflicting interpretations are currently available, including: (1) an erosional surface implying a significant hiatus in the geological record (e.g. Negrutsa 1984); (2) a conformable, transitional, stratigraphic contact (Medvedev et al. 2011).

Hole 11A intersected the contact between the Tulomozero and Zaonega formations at 106.3 m (Fig. 6.105). The Zaonega Formation starts with red, flat-laminated and cross-bedded sandstones (Figs. 6.107aa–ac). The basal sandstone shows flat, horizontal lamination (perpendicular to the core axis) and has at its base a c. 5-cm-thick bed of rusty conglomerate that rests with a sharp contact on steeply to subvertically dipping, pink stromatolitic dolostones (Figs. 6.107ad, ae). If this dip discordance were tectonic, then such a relationship would imply deformation and erosion of the Tulomozero rocks prior to deposition of the Zaonega Formation; this is discussed in more detail in the section of *Depositional settings*.

The drilled section of the Zaonega Formation comprises sandstone, siltstone, and minor dolomarl and dolostones. Two members have been defined: member 1 (Sandstone-Siltstone-Dolomarl) and member 2 (Siltstone). The magnetic susceptibility measurements reveal that the lower half of member 1 has low values, which insignificantly increase in its upper half up to 220 μSI ($K^* = 20 \times 10^{-6}$ SI in Fig. 6.106), and then fluctuate around 200 μSI throughout member 2 with a gradual decline to c. 160 μSI within uppermost 10 m ($K^* = 15 \times 10^{-6}$ SI in Fig. 6.106).

Member 1 (Sandstone-Siltstone-Dolomarl)

The member is 25 m thick (106.3–80.8 m; Fig. 6.105) and composed of fine-grained sandstone with thin intervals of shale and dolomarl forming several fining-upward cycles (Fig. 6.105). All cycles start with thicker sandstone units passing transitionally into thinner siltstone units.

The sandstones are commonly red-brown in colour, produced by post-depositional (catagenetic or epigenetic) oxidation (Figs. 6.107r, t–ac); original grey-green colours are rarely preserved (e.g. Figs. 6.107w–z). Further, secondary reddening also commonly obliterated primary bedding and lamination (Figs. 6.107r, aa), but, where preserved, both thin, parallel lamination (Figs. 6.107t, ac) and large cross-beds can be observed (Figs. 6.107u, ab). At 91–92 m, the sandstone consists of nicely developed thin graded beds forming irregular rhythmic bedding (Figs. 6.107v–z).

The siltstones and dolomarls tend to retain better the primary grey-green colour (Fig. 6.107s), due to their lower permeablity. However, the primary colour in thinner siltstones, i.e. those forming the upper parts of sandy graded beds, was also overprinted by secondary oxidation (Fig. 6.107u).

Clastic material in all sandstones and siltstones is well sorted and mainly quartz with minor albite. The rocks are rich in sericite, resulting in elevated contents of Al_2O_3 (up to 18 wt.%) and K_2O (up to 6 wt.%). The sandstones and siltstones may contain a significant amount of dolomite cement resulting in gradual transitions between dolomite-cemented, fine-grained siliciclastic rocks and dolomarls. The latter contain up to 12 wt.% MgO and 17 wt.% CaO (Appendix 32). All rocks are devoid of any measurable amount of C_{org} and S, with one exception (0.2 wt.% S) (Appendix 33).

Member 2 (Siltstone)

The Siltstone member has a drilled thickness of 70 m (80.8–2.8 m). It is a monotonous succession of siltstones with two thin intervals of dolostone and one thin bed of dolomarl (Fig. 6.105). The siltstones retain their original grey-green colour (Figs. 6.107a–j, l–n) with the exception of the lowermost strata (Figs. 6.107k, o–q). The siltstones contain pyrite (e.g. Fig. 6.107g) and show an erratic increase in the sulphur concentration up-section from <0.01 to 0.34 wt.% (Appendix 33).

The siltstones display small- to larger-scale cross bedding (Figs. 6.107e, h, j, l, m, q), rhythmic bedding and parallel lamination (Figs. 6.107d, f). Channelised beds, and load, scour and slump structures are common (Figs. 6.107a, c, e–g, n). Clastic material in the siltstones is well sorted and mainly quartz, though albite is also present in some beds (up to 2.3 wt.% Na_2O; Appendix 32). The siltstones are rich in sericite, as reflected in Al_2O_3 (12–17 wt.%) and K_2O (3–5 wt.%) contents. The P_2O_5 content increases gradually up-section, from 0.15 to 0.43 wt.% (Fig. 6.106).

Two dolostone beds (MgO/CaO = 0.68), one occurring close to the base and the other in the middle of the section, are gradational with the encasing siltstone and are not readily distinguishable from them in the core. The lower dolostone was affected by secondary reddening, though it still retains relicts of parallel lamination (Fig. 6.107p), whereas the upper one has a primary grey-green colour and is massive. Both are composed of fine-grained (micritic) dolomite and contain a significant amount of clastic quartz (8 and 19.6 wt.% SiO_2) and sericite (2–4 wt.% Al_2O_3). The upper bed contains scattered pyrite cubes (0.03 wt.% S).

Depositional Settings

The depositional environment for the Tulomozero Formation rocks intersected by Hole 11A is summarised in Fig. 6.105. Although diverse depositional settings are inferred based on the core log, the overall depositional trend includes alternating supratidal, sabkha and intertidal environments punctuated by several episodes of subaerial exposure and karstification, eventually culminating in the development of a subtidal carbonate platform. If the contact is indeed an angular unconformity, it implies a period of uplift, tectonic deformation and subsequent erosion, prior to the deposition of the overlying Zaonega Formation.

Peritidal, evaporitic, carbonate flat. The lower part of the drilled succession (members 1 and 2 at 436–374 m) includes variegated dolomitic siltstone, shale, dolomarl and dolostone with irregular or indistinct bedding or a massive structure (Figs. 6.107eb–ex), and *in situ* brecciation and soft-sediment deformation due to post-depositional growth of sulphates as well as dissolution of evaporitic minerals. These facies are organised typically into 0.2–2.5-m-thick dolostone-dolomarl/shale, and partially dolostone-evaporite, cycles (e.g. Fig. 6.109). Combined, these sedimentological features suggest accumulation within an intertidal zone, hence fit a setting of a peritidal carbonate flat.

Low intertidal carbonate flat. The overlying c. 44-m-thick succession (member 3 at 374–327.4 m) consists of light-coloured and variegated dolarenite and dolorudite interbedded with thinner intervals of dolomarls, shales and mudstones (Figs. 6.107dk–ea), minor apparent oolitic dolostone at the base (Fig. 6.107ea), and red dolarenite with thin intervals of interlaminated dolarenite-shale couplets in its upper part. Lensoidal (sand ripples), lenticular and flaser bedding (Figs. 6.107dd–df) are present in places. Elsewhere, the bulk of the carbonate rocks are clastic dolostones that have massive, crudely bedded, irregular laminated and *in situ* brecciated structures. Desiccated beds (Figs. 6.107dk, dn, do), rip-up clasts, dissolution surfaces (Fig. 6.107do), dolomite-pseudomorphed nodular masses of sulphates (Fig. 6.107du), and quartz-pseudomorphed gypsum crystals (Fig. 6.107dx) occur rarely in the succession, hence suggesting limited subaerial exposure. Interbedded dolomarls, shales and siltstones show microlensoidal and flat lamination and contain cavities filled with white, drusy dolomite (Figs. 6.107dq, ea).

Similar to the underlying peritidal sequence, this succession is marked by numerous, but thicker, dolostone-dolomarl/shale, shallowing-up cycles that show less evidence for formation of evaporitic minerals (Fig. 6.110). These combined features suggest limited subaerial exposure, hence a setting compatible with deposition along the lower part of intertidal flats.

Low intertidal mud flat. The lower half of member 4 (327.4–297.5 m) displays thinly interbedded siltstone-shale with a variegated colour and lensoidal and wavy lamination, a typical feature of tidal sediments (Fig. 6.107dc). Considering that desiccated beds have not been documented, the combined sedimentological features suggest accumulation within a mud flat that was apparently located below the level of the lowest tide. In contrast, the upper part of member 4 (288–282 m) contains siltstone-shale units modified by dissolution and cementation, as well as rare pseudomorphs after sulphate crystals (Fig. 6.107da). This likely indicates the onset of intertidal conditions.

The accumulation of the siltstone-shale lithofacies was interrupted by the emplacement of c. 20-m-thick body of mafic lava with a large areal extent (e.g. Satzuk et al. 1988; Krupenik et al. 2011). In the drilled section, the extrusive body shows a "diffuse" contact with the overlying siltstone-shale lithofacies through a c. 1-m-thick, greenish, structureless shale bed. The transitional bed is enriched in Ni, Co, Cr, V and Fe_2O_{3tot}, with the abundances of these elements being comparable to those in the underlying mafic body. These characteristics are suggestive of subaerial weathering and erosion of the mafic lava and incorporation of the weathered material into the overlying sediments. An alternative interpretation would be emplacement of the flow subaqueously followed by submarine weathering.

Supratidal sabkha. The intertidal siltstone-shale is overlain sharply by dolostones and dissolution-collapse breccias of member 5 (282 to c. 203 m) that define numerous 0.5–10-m-thick dolostone-breccia cycles. Most of the dolostones represent redeposited carbonates composed of poorly sorted and angular intraformational clasts (e.g. Fig. 6.107ci) with abundant rip-ups of black mudstone (Figs. 6.107cc, ce). Throughout the section, the dolostones contain abundant, mm-sized, quartz-pseudomorphed sulphate nodules and twinned crystals after gypsum. In places there are mosaics of cubic, euhedral dolomite crystals (the inset in Fig. 6.107cd) that may represent replaced halite beds, and the uppermost beds are locally saturated with dolomite-replaced, discoidal crystals of gypsum (Figs. 6.107by, bz). Even many of the clasts in the breccia beds contain abundant, mm-sized quartz-pseudomorphed crystals and nodules of gypsum or anhydrite (the inset in Figs. 6.107co–cr). There are intensely desiccated dolomarl and limestone-mudstone beds, some with enterolithic structures of former anhydrite beds (Figs. 6.107cs–cv), as well as dissolution surfaces (e.g. Fig. 6.107cw), some of which appear as large solution holes filled with debris of collapsed overlying beds (Fig. 6.107cx). Consequently, the dolostone-breccia cycles are interpreted as a stack of shallowing-up carbonate-evaporite cycles deposited in a sabkha-like environment.

Karst deposits. The dolostone-evaporite sabkha deposits are overlain by the peculiar polymict, clast-supported carbonate conglomerates with a talc-rich matrix. (Figs. 6.107bk, bn–bx); one interval superficially resembles "*terra rossa*" (Fig. 6.107bo). These lithofacies occur throughout the 203–179 m interval and have not been documented previously in the Tulomozero Formation (see Chap. 4.3). The nature of these rocks remains enigmatic. The talc-rich matrix might have formed through quartz-dolomite reaction under greenschist metamorphic conditions or even diagenetically (e.g. Tosca et al. 2011). The roundness of the clasts suggests physical/mechanical reworking. However, the conglomerates show neither bedding nor stratification, thus do not bear any signs of reworking by currents or waves. We infer that they are karstic collapse breccias after dissolved evaporites and were partially reworked by currents and/or waves. This would explain the absence of stratification and the uniquely localised occurrence of these unusual rocks in the Tulomozero Formation.

Sub- to intertidal carbonate flat. The 179–c. 160 m interval is the only succession in Core 11A section that contains oncolithic/oolithic dolostones (Fig. 6.107bj). This interval is mostly dolostone with a c. 1-m-thick slumped shale-dolomarl (Fig. 6.107bi) capped by dissolution-collapse breccia in the middle. Hence, we interpret this as a thin interval recording deposition in shallow, subtidal through intertidal flat settings.

Karstified carbonate platform. Between depths 160 and 120 m occurs a succession of dolostones, the bulk of which are buff and microcrystalline with layers of brown, laminated dolomarl. Typifying this interval are solution-enlarged cracks (Fig. 6.107az), as well as abundant large cavities (e.g. Figs. 6.107as–ax, ba–be, bg) in places filled with red, clay-rich, intraformational breccia (Fig. 6.107ao, ap). Primary depositional characteristics of the dolostones, namely parallel lamination (Figs. 6.107ar, bf) and a limited clastic input (low SiO_2 and Al_2O_3 contents; Appendix 32), suggest accumulation in relatively tranquil settings away from terrigenous influx. However, the cracks and cavities are indicative of karst, and the red-clay-rich breccias superficially resemble "*terra rossa*". Thus, we interpret this as an interval of karstification. It is not possible to assess the size of the inferred karstic cavities or holes from the core alone, but they must have been considerable given their development through the 20-m-thick interval (Fig. 6.105). If this is subaerial (rather than subaqueous dissolution) karst, it would be interesting to determine if the dissolution phenomenon represents the karst *per se* or perhaps other surficial forms like karren (e.g. Bogli 1980).

Subtidal carbonate platform. The karsified interval is followed by non-bedded to laminated dolostones (e.g. Fig. 6.107an) devoid of any dissolution features. At c. 111 m, these are overlain by two deepening-upward cycles of flat-laminated and columnar stromatolites (Figs. 6.107af–am), apparently forming a large biostrome or bioherm. The stromatolite microfabric does not suggest exposure and desiccation, and the entire succession is interpreted to represent a platformal carbonate formation accreted under subtidal conditions.

At 106.3 m (Fig. 6.105) there is a sharp contact above which occur cross- and parallel-bedded sandstones of the Zaonega Formation (Figs. 6.107ab, ac). Immediately beneath this contact, the Tulomozoero stromatolites exhibit steep to subvertical bedding (Figs. 6.107ad–ag). These could be the steep margins of large bioherms or, alternatively, this contact could define an angular unconformity. The latter interpretation implies a period of deformation, uplift and erosion of the pre-Zaonega rocks.

The latter interpretation is supported by the observation that in Holes 10A, 10B, 12A, 12B and 13A (Chaps. 6.3.1, 6.3.3, and 6.3.4), the Tulomozero rocks contain evidence for structural inversions and tight folds whereas the overlying Zaonega Formation rocks are devoid of such structures. This apparent structural discordance is also suggested from outcrops in the region of the Onega Basin. There, in several places, pre-Zaonega strata exhibit tight folding and variable strike and dip orientations whereas the Zaonega and younger units are typically only broadly folded. However, in some places, the transition from the Tulomozero Formation upward into the Zaonega Formation appears to be conformable and gradational. Assessing correctly the nature of this contact has far-reaching implications for the tectonostratigraphic evolution of the Karelian craton, and hence additional research is required before drawing robust conclusions.

Low-energy (non-marine?) siliciclastic basin. The carbonate platform is overlain by a succession composed of several dm- to m-scale, fining-upward sandstone-siltstone/dolomarl cycles that pass up-section into clayey siltstones with minor dolostone and dolomarl. Depositional features include alternation of parallel-bedded (Figs. 6.107t, ac) and small- to large-scale cross-bedded rocks (Figs. 6.107h, i, l, m, q, u, ab), rhythmically bedded and graded sandstone-siltstone beds (Figs. 6.107f, g, v–z), slump and loading structures (Figs. 6.107a, c, g, n, c), and even varve-like siltstones (Fig. 6.107d). Such features, though, may suggest either relatively deep marine (below storm wave base) or lacustrine environments. Consequently, the available sedimentological observations offer non-unique interpretations. However, if the inferred episode of uplift and erosion of the underlying marine dolostones is correct, then at least the initial phase of sedimentation likely represents non-marine (probably fluvial) accumulation. Further, it is noteworthy that the overlying and major part of the Zaonega succession is devoid of wave- and/or tide-influenced sedimentary structures. Thus the most parsimonious inference, given the existing data, is that the overall characteristics suggest deposition in a relatively low-energy, siliciclastic-dominated setting, likely to be deep lacustrine; future work should confirm or reject this interpretation. The original grey-green colour of the sediments was considerably modified or obliterated by secondary oxidation. The rocks overlying the Tulomozero-Zaonega formational contact were the most affected by the secondary reddening (Figs. 6.107aa–ac). This (dis)colouration vanishes gradually up-section (Fig. 6.111) suggesting that the oxidising fluids ascended from the Tulomozero red bed succession.

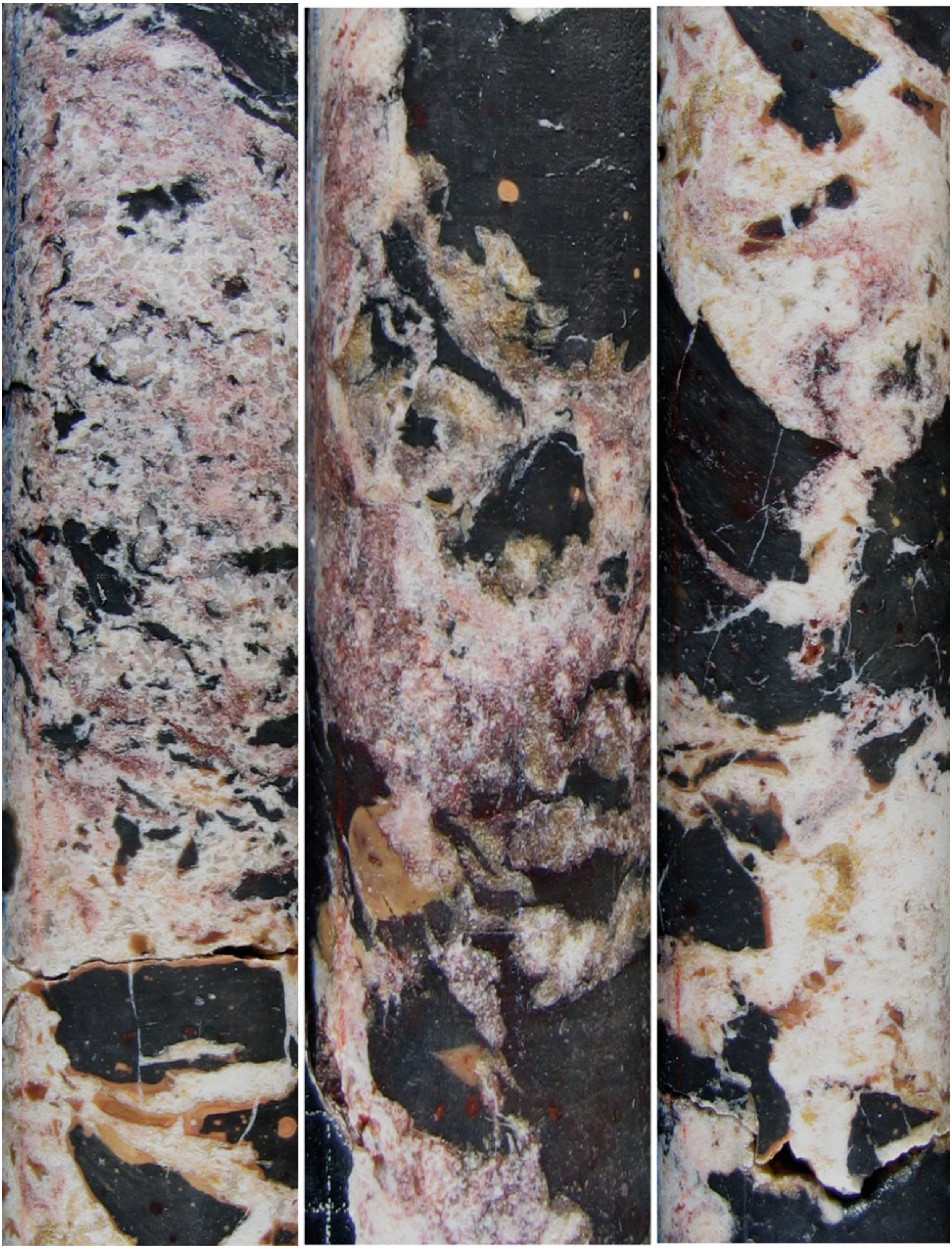

Fig. 6.103 An essential part of the Tulomozero section intersected by FAR-DEEP Hole 11A comprises collapse breccias after dissolved sulphates and halite, indicating a considerable accumulation of evaporitic minerals. Despite near-complete dissolution of those minerals, the breccias still retain traces of sulphates that can be extracted and measured for sulphur isotopes (e.g. Reuschel et al. 2012) and used as a proxy for isotopic composition of seawater. Core 11A, depth of c. 275 m, core diameter is 5 cm (Photographs by Victor Melezhik)

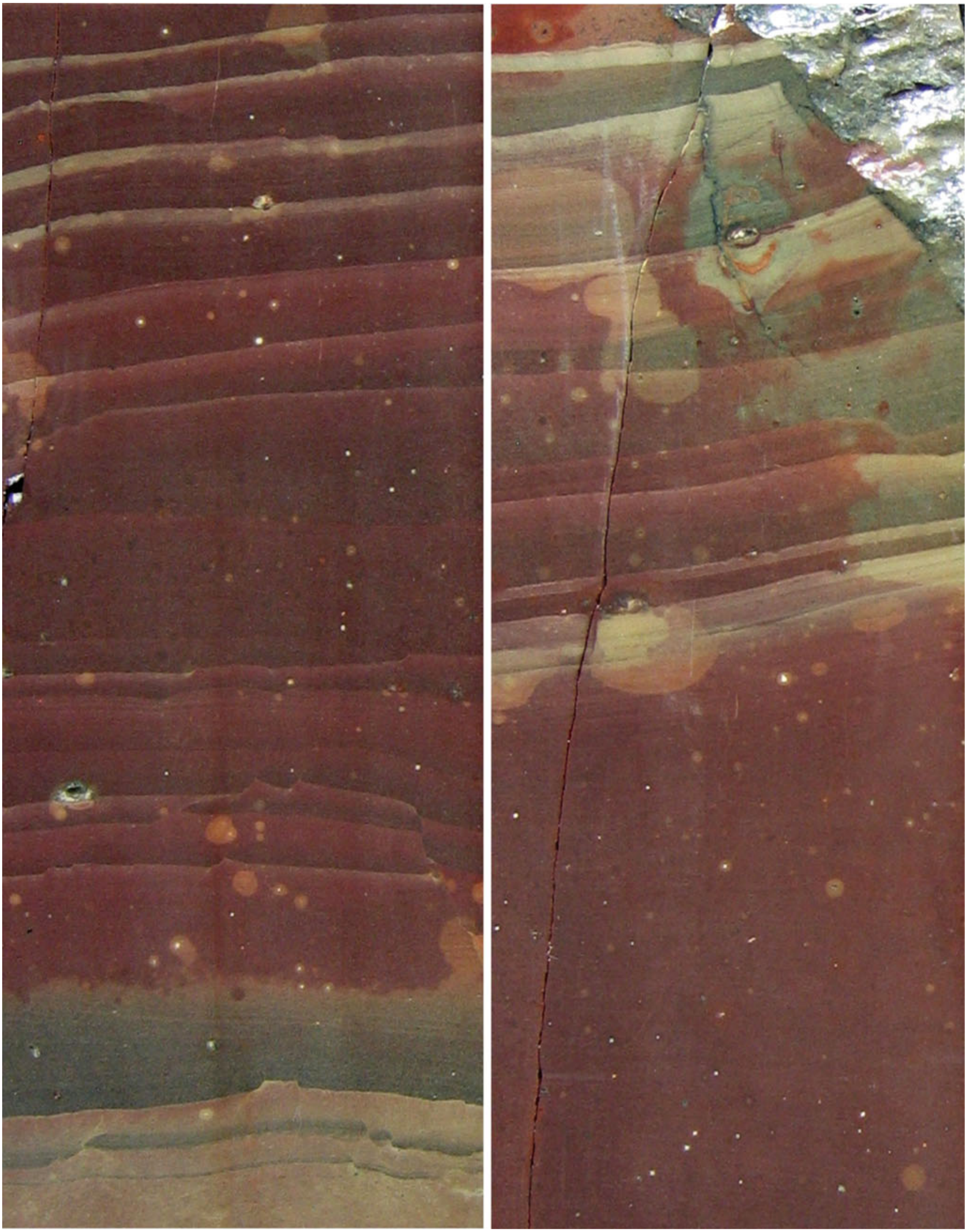

Fig. 6.104 Variegated, rhythmically bedded greywackes record a transition from Jatulian-Lomagundi-age "red beds" to Shunga-age "black shales". These turbiditic greywackes were originally deposited as pyrite-bearing "grey shales" but were altered to brown colours by to post-depositional oxidising fluids; such features inform on the nature of interactions from deposition in chemically reduced environments to subsequent modification by later oxidising fluids. Core 11A, depth of c. 91 m, core diameter is 5 cm (Photograph by Victor Melezhik)

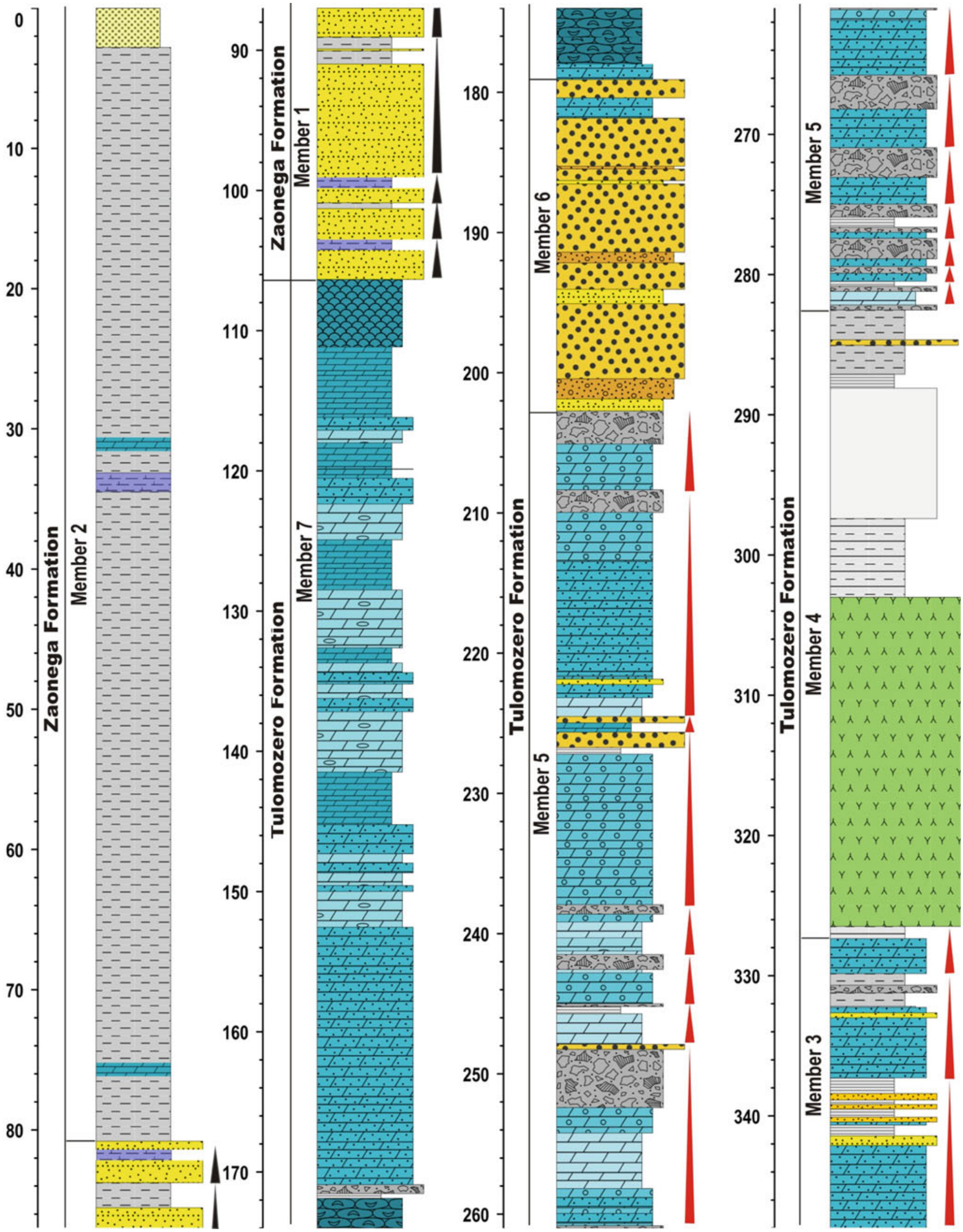

Fig. 6.105 Lithological section of the Zaonega and Tulomozero formations based on core log of Hole 11A. Reconstructed depositional environments based on core logging, geological mapping and sedimentological research in the vicinity of the drilling site

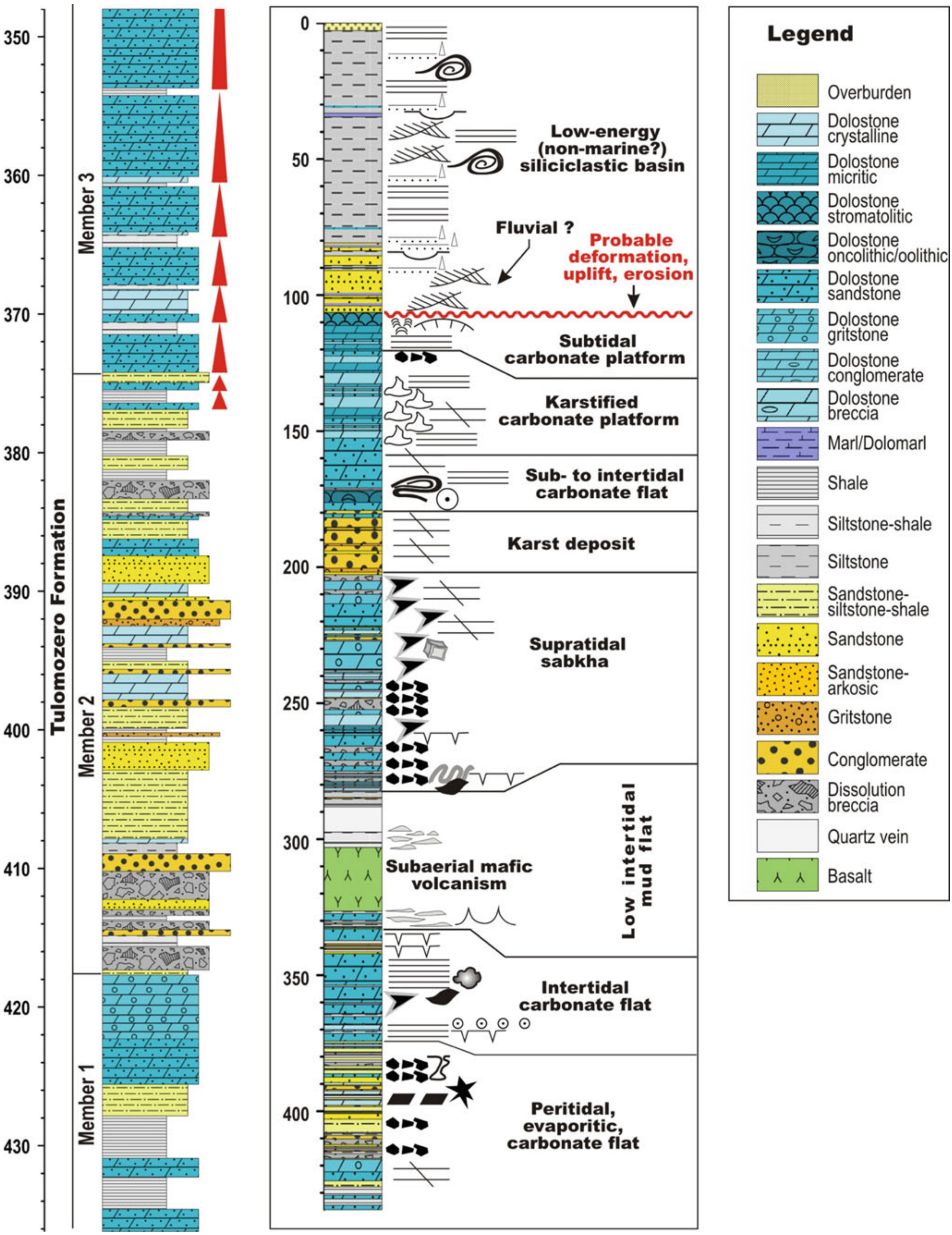

Fig. 6.105 (continued) Lithological section of the Zaonega and Tulomozero formations based on core log of Hole 11A. Reconstructed depositional environments based on core logging, geological mapping and sedimentological research in the vicinity of the drilling site. Lithological symbols are explained in Fig. 6.6

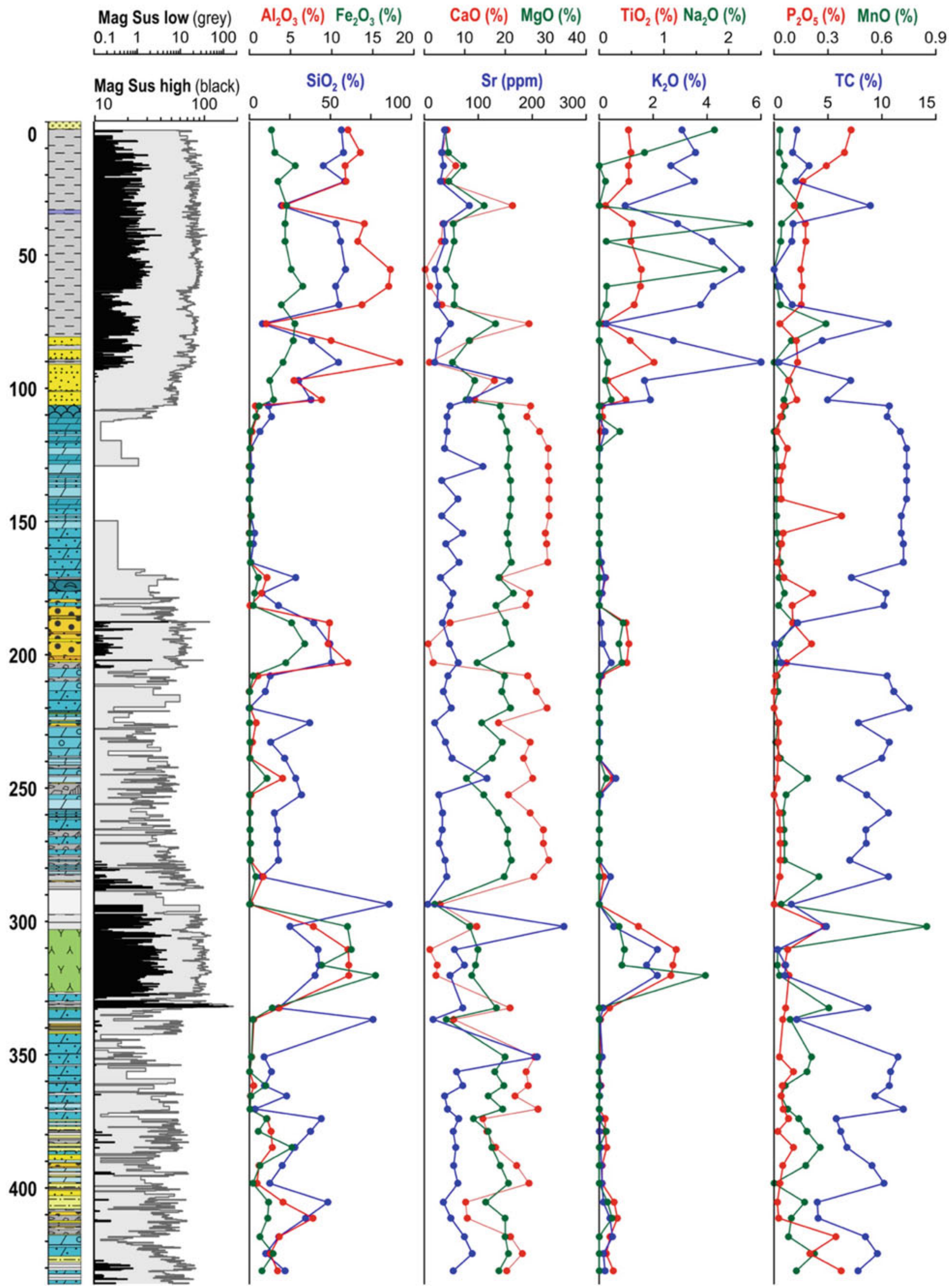

Fig. 6.106 Relative magnetic susceptibility (K*), and geochemical profiles of selected elements in Core 11A based on the archive samples collected with c. 8 m-spacing. For analytical techniques and data quality see Part 5

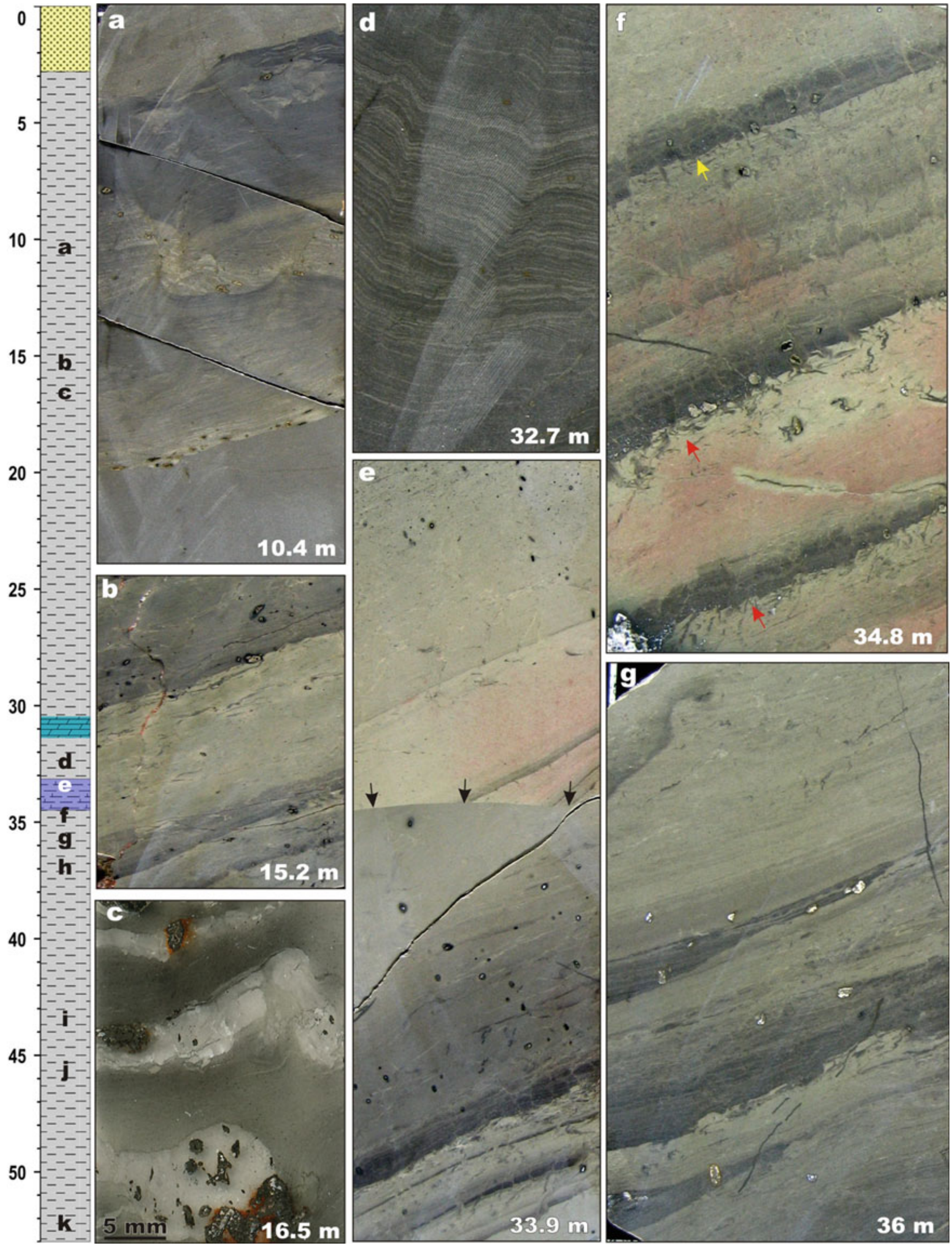

Fig. 6.107 Sedimentological features of main rock types of the Zaonega and Tulomozero formations based on Hole 11A cores. Core diameter in all plates is 5 cm unless specified otherwise. ***The Zaonega Formation,*** *member 2*: (**a**) Bedded greywacke-siltstone with a small-scale slump structure. (**b**) Bedded siltstone-mudstone. (**c**) Scanned thin-section showing a slump structure in interbedded dolomarl and dolarenite (bright); black crystals are oxidised pyrite cubes. (**d**) Laminated, varve-like dolomarl. (**e**) Graded beds with the erosional contact (*black arrows*) overlain by cross-bedded siltstone or, alternatively, by tilted bed of flat-laminated siltstone. (**f**) Rhythmically bedded, dark green siltstone and pale green and yellow-pinkish mudstone; the yellow arrow denotes cracked mudstone layer whereas the red arrows mark mudstone beds with granulated surface; both features might have been caused by loading or earthquake. (**g**) Interbedded dark green, fine-grained siltstone and pale green mudstone with scattered pyrite crystals (bright specks) and small-scale channel and scour structures

Fig. 6.107 (continued) (**h**) Pale grey siltstone erosively overlain by grey-green, cross-bedded, muddy siltstone; an erosional surface is marked by *black arrows*. (**i**) Bedded and laminated, muddy siltstone. (**j**) Intercalated parallel-bedded and cross-bedded, muddy siltstone. (**k**) Siltstone whose primary structure and colour was obliterated by post-depositional (catagenetic) oxidising and chemically reducing fluids that caused red-brownish colouration and bluish spots; an erosional surface is marked by *black arrows*

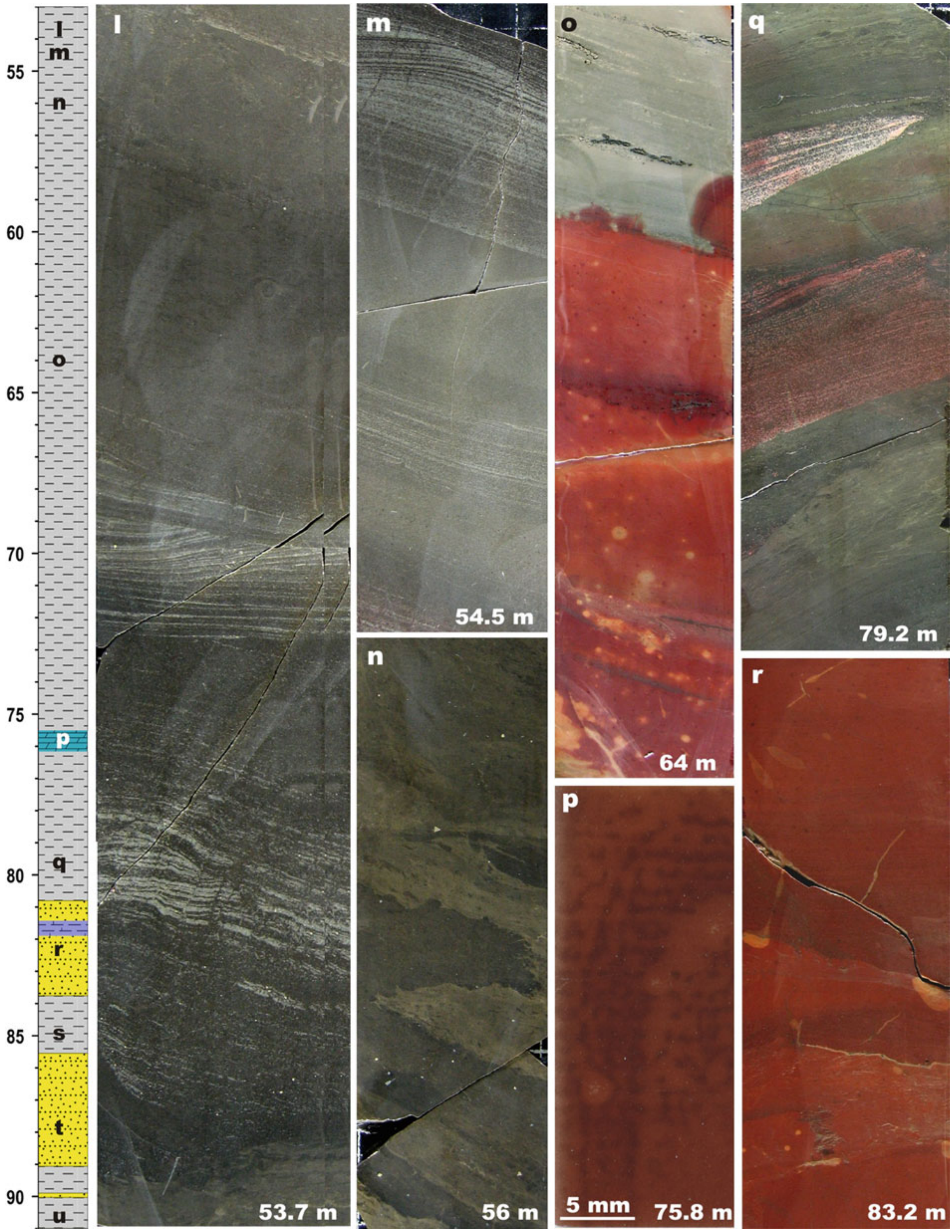

Fig. 6.107 (continued) (**l**) Interbedded massive, muddy siltstone and cross-bedded dolomarl. (**m**) Laminated, muddy siltstone and dolomarl. (**n**) Slumped structure in interbedded muddy siltstone and mudstone. (**o**) Pale green, laminated, muddy siltstone affected by secondary red colouration. (**p**) Scanned thin-section of dolostone with parallel lamination considerably obliterated by secondary red colouration. (**q**) Variegated, cross-bedded, muddy siltstone whose variegated colour was caused by infiltration of oxidising fluids. *Member 1*: (**r**) Former grey-green greywacke whose primary colour and structure were obliterated by secondary oxidation

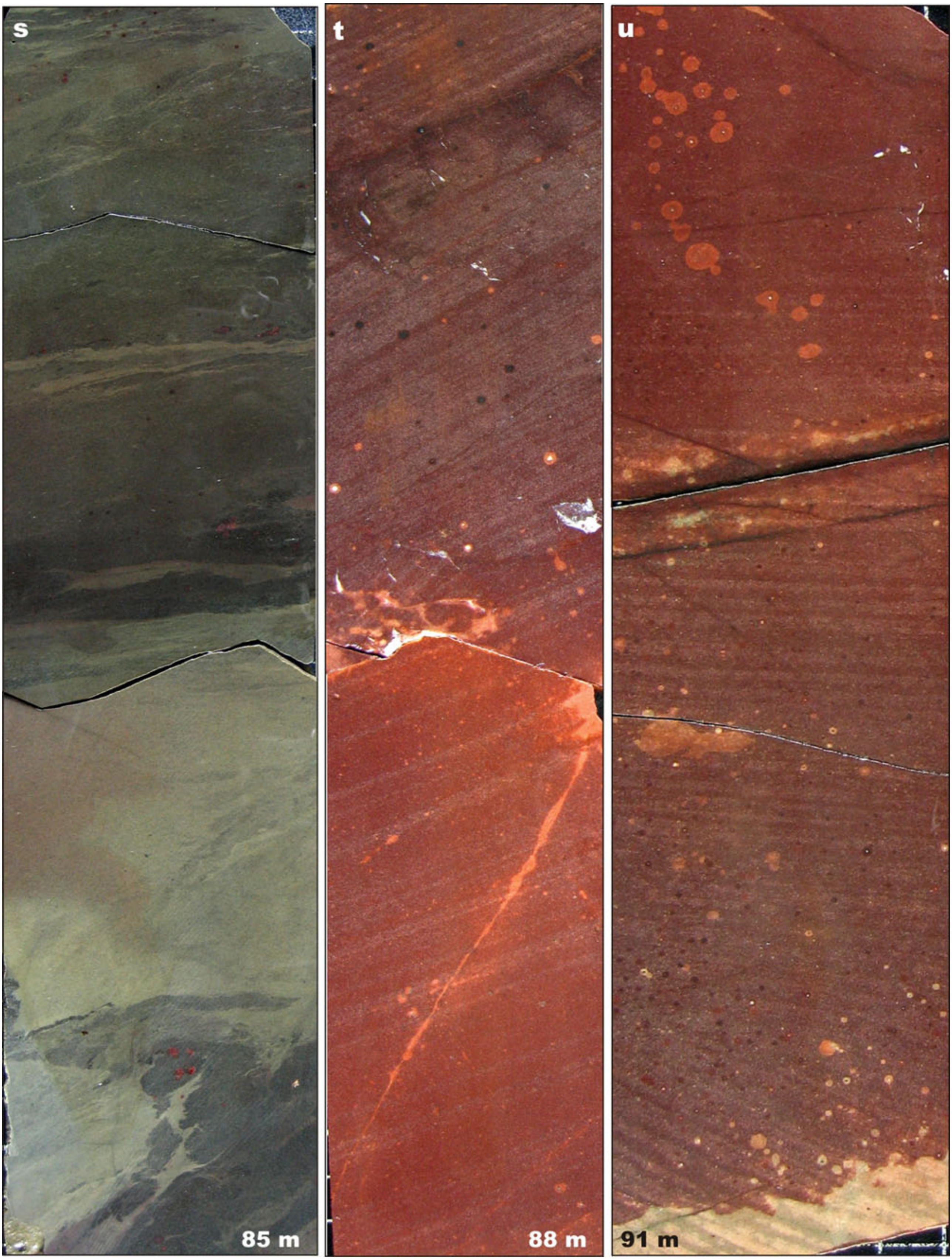

Fig. 6.107 (continued) (**s**) Muddy siltstone with a slump structure. (**t**) Bedded greywacke whose primary grey colour was modified by secondary oxidation; black specks are oxidised pyrite cubes. (**u**) Cross-bedded siltstone passing upward into massive siltstone; note the secondary red-brown colour and bright spots around oxidised pyrite crystals

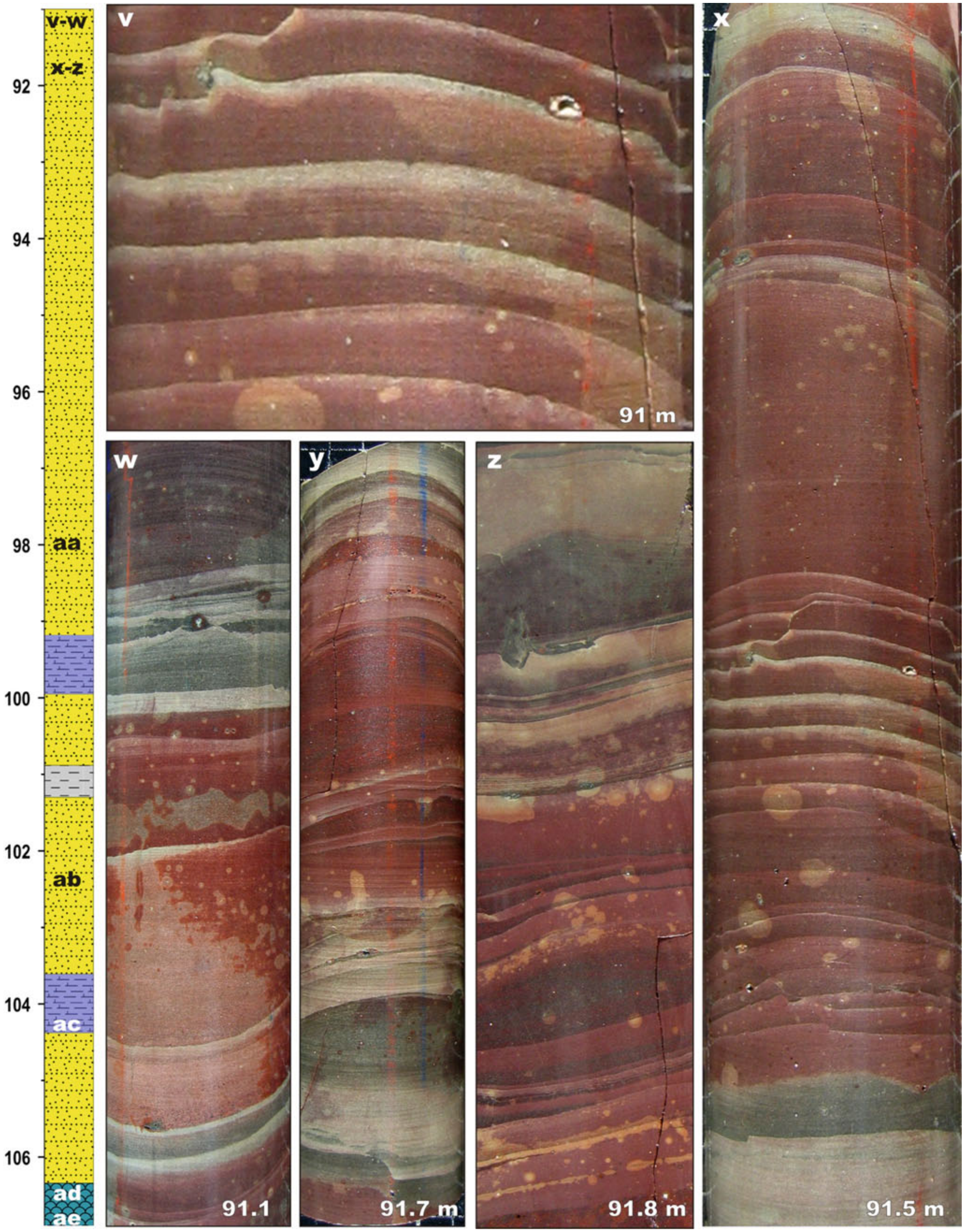

Fig. 6.107 (continued) (**v–z**) Rhythmically interbedded, graded sandstone-siltstone whose primary grey-green colour was considerably overprinted by catagenetic oxidising fluids

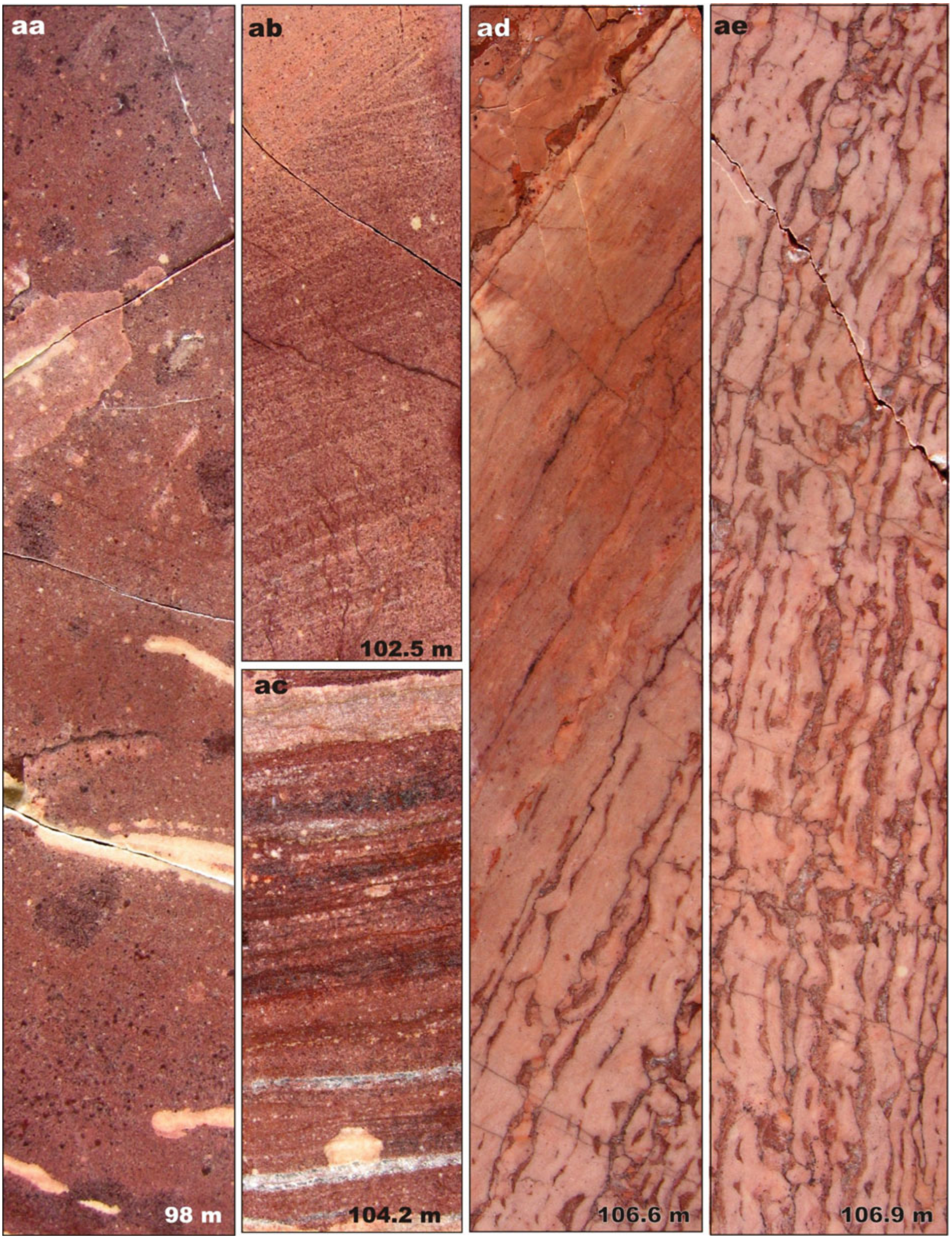

Fig. 6.107 (continued) (**aa**) Massive sandstone whose primary grey-green colour was obliterated by secondary oxidation with superimposed bright and pale brown spots. (**ab**) Cross-bedded sandstone whose primary grey-green colour was overprinted by secondary oxidation. (**ac**). Laminated dolomarl whose primary grey-green colour was overprinted by secondary oxidation; note that the bedding is subhorizontal. ***The Tulomozero Formation,*** *member 7*: (**ad**, **ae**) Pale pink dolostone with red-brown stromatolitic laminae; note that the bedding is steep or subvertical immediately below the contact (106.3 m) with the overlying and horizontally bedded Zaonega sandstones

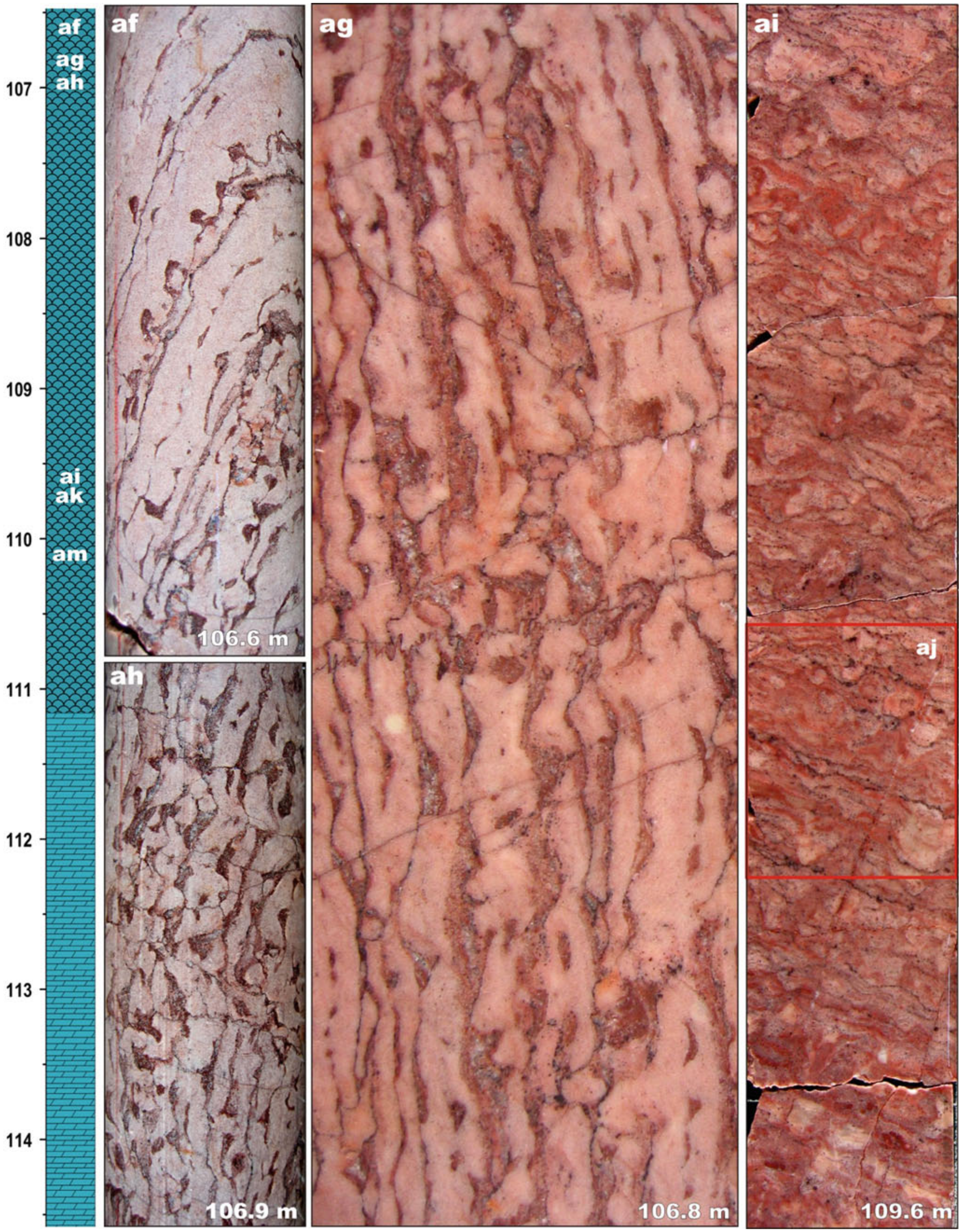

Fig. 6.107 (continued) (**af–ah**) Pale pink dolostone with red-brown layers of small-scale domal stromatolites. (**ai**) Red, stromatolitic dolostone with a clotted fabric

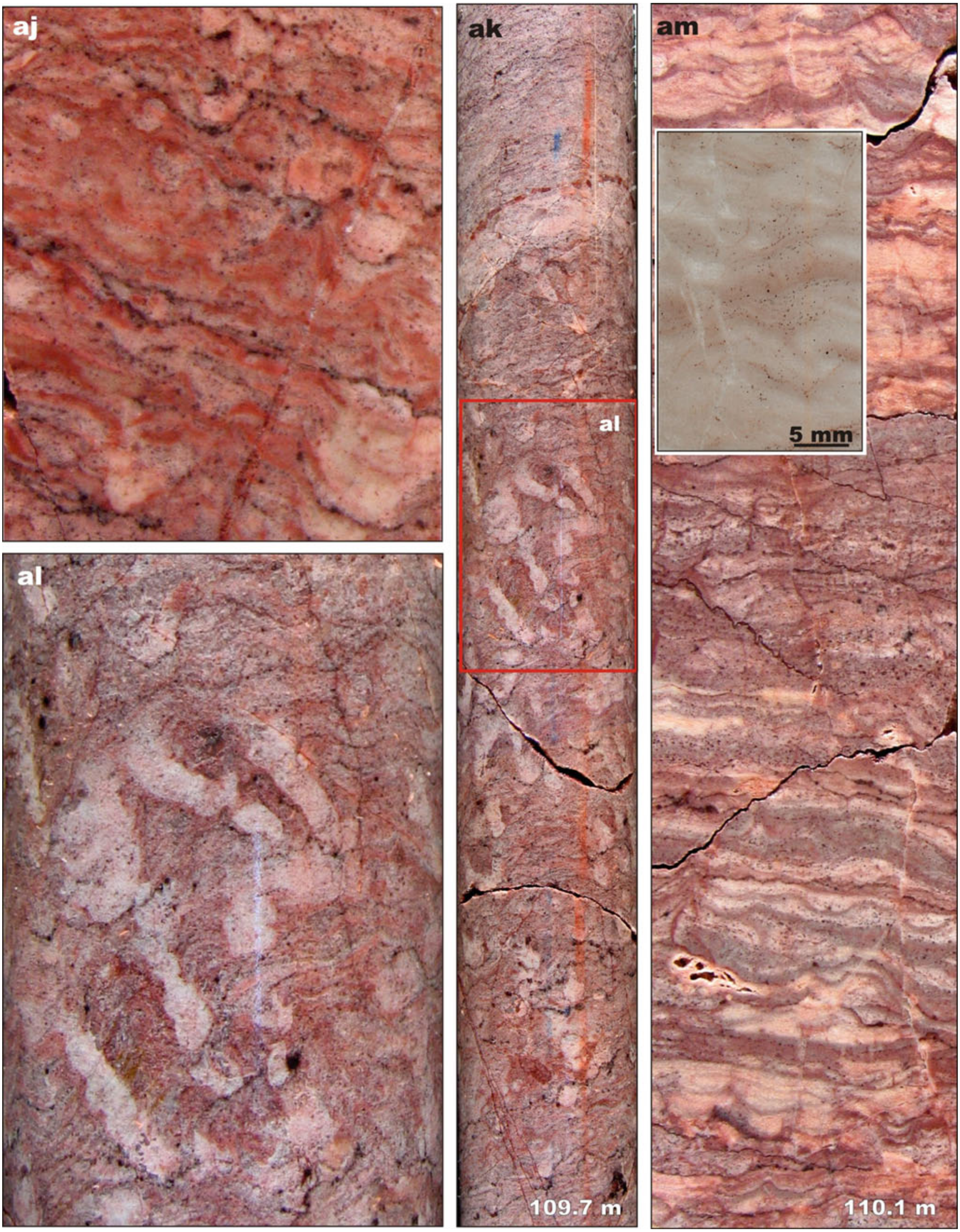

Fig. 6.107 (continued) (**aj**) Detailed view of stromatolitic dolostone with a clotted fabric. (**ak**) Small-columnar stromatolite overlain by flat-laminated stromatolite. (**al**) Detailed view of stromatolitic dolostone composed of small, divergent, columns (*dark red*) with the inter-column space filled with pale pink, sandy dolomite. (**am**) Variegated dolostone with intervals of flat-laminated stromatolites; the inset with scanned thin-section shows details of the stromatolitic lamination

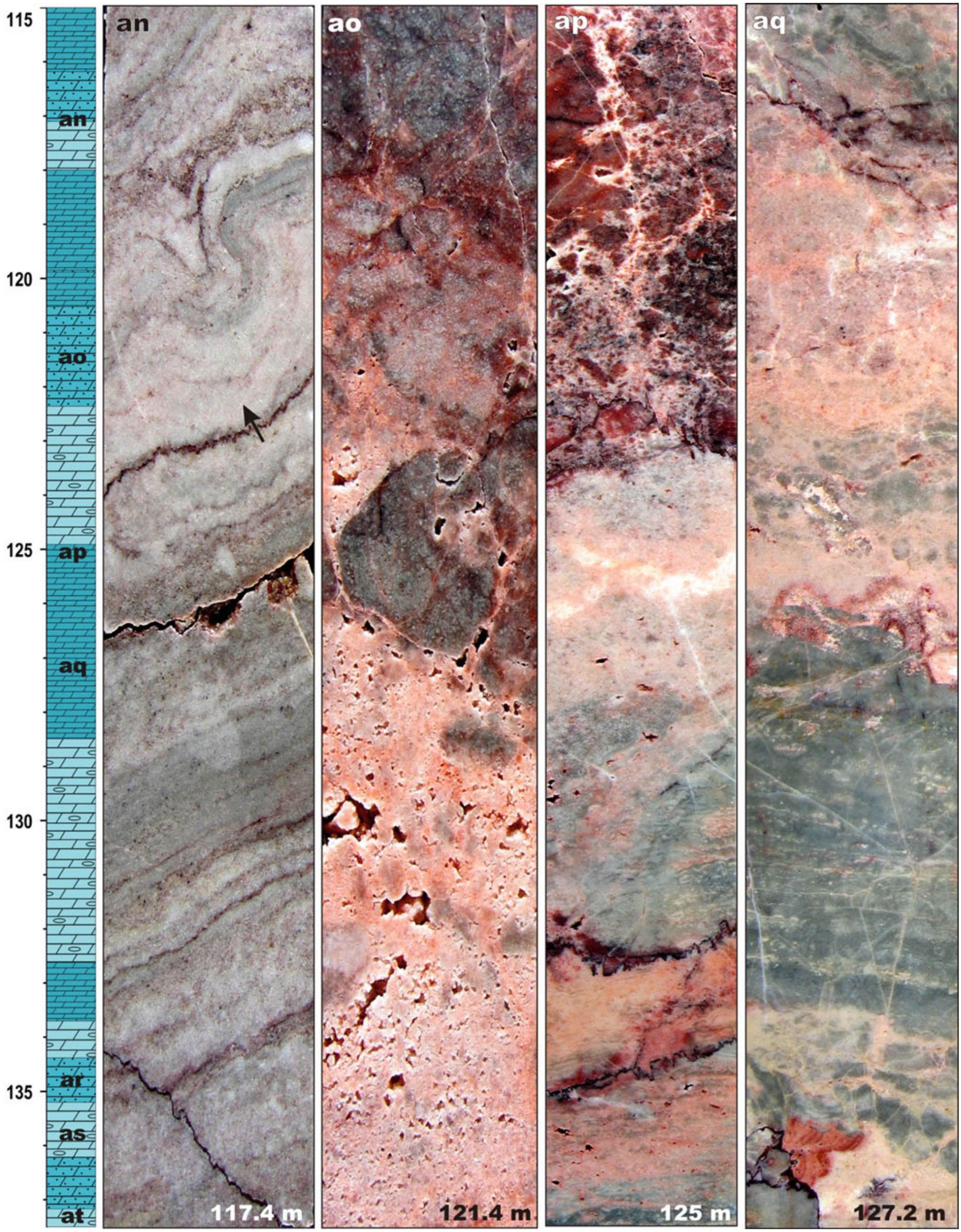

Fig. 6.107 (continued) (**an**) Pale grey, parallel-bedded dolarenite with apparent soft-sediment defomation (*black arrow*) (**ao**) Pale pink dolarenite passing into dissolution-collapse breccias; note the dissolution cavities in the dolarenite. (**ap**) Variegated, massive dolostone overlain sharply by dissolution-collapse breccia; note the stylolites (*brown*) in the dolostone. (**ag**) Variegated, indistinctly bedded dolostone

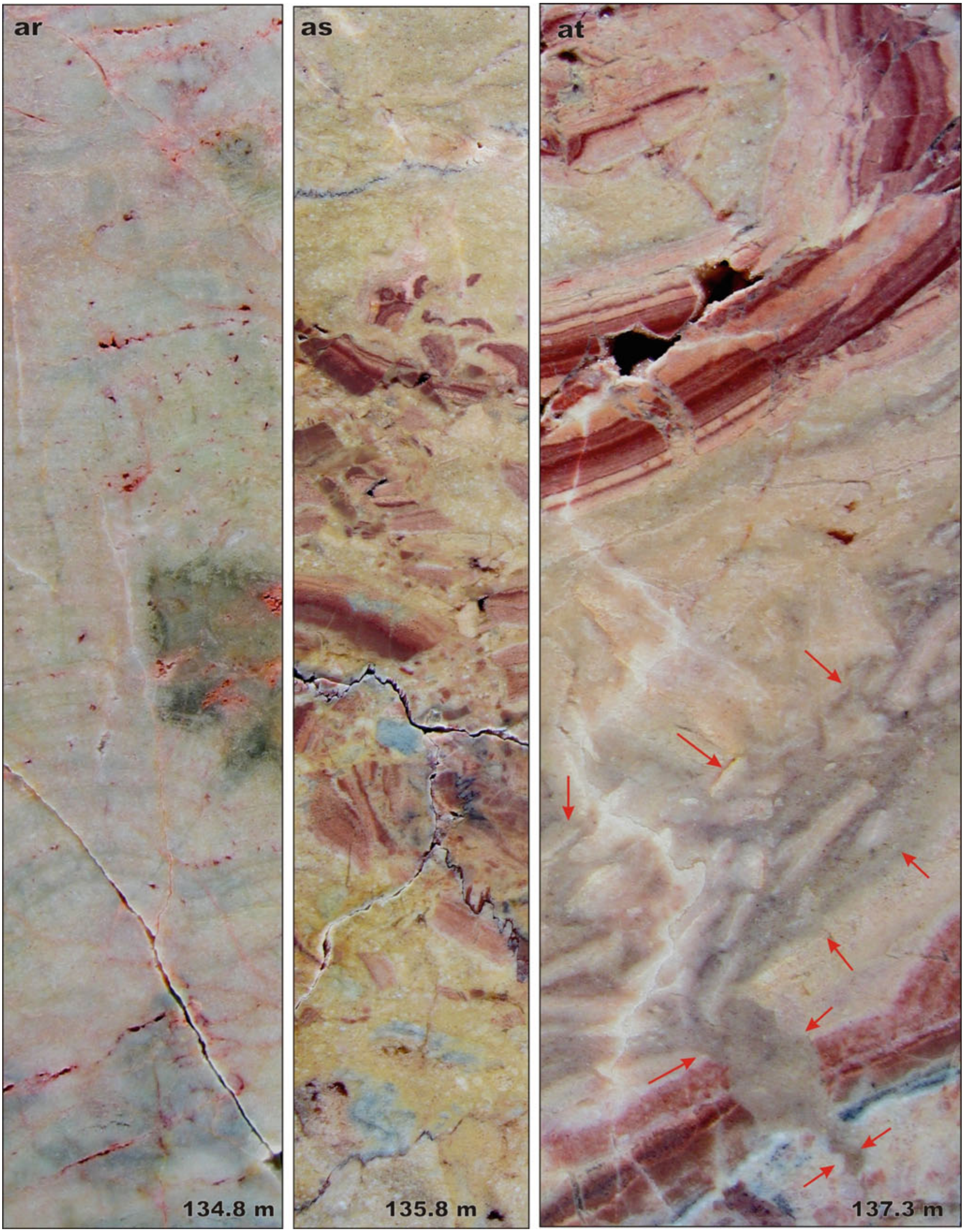

Fig. 6.107 (continued) (**ar**) Variegated dolostone with indistinct wavy bedding. (**as**) Beige dolostone with an interval of dissolution-collapse structure represented by collapsed bed of red, laminated dolomarl. (**at**) Beige dolostone containing dismembered and deformed beds of brown-red, laminated dolomarl and an apparent dissolution pipe (*red arrows*) filled with platy dolostone fragments set in a dolarenite matrix

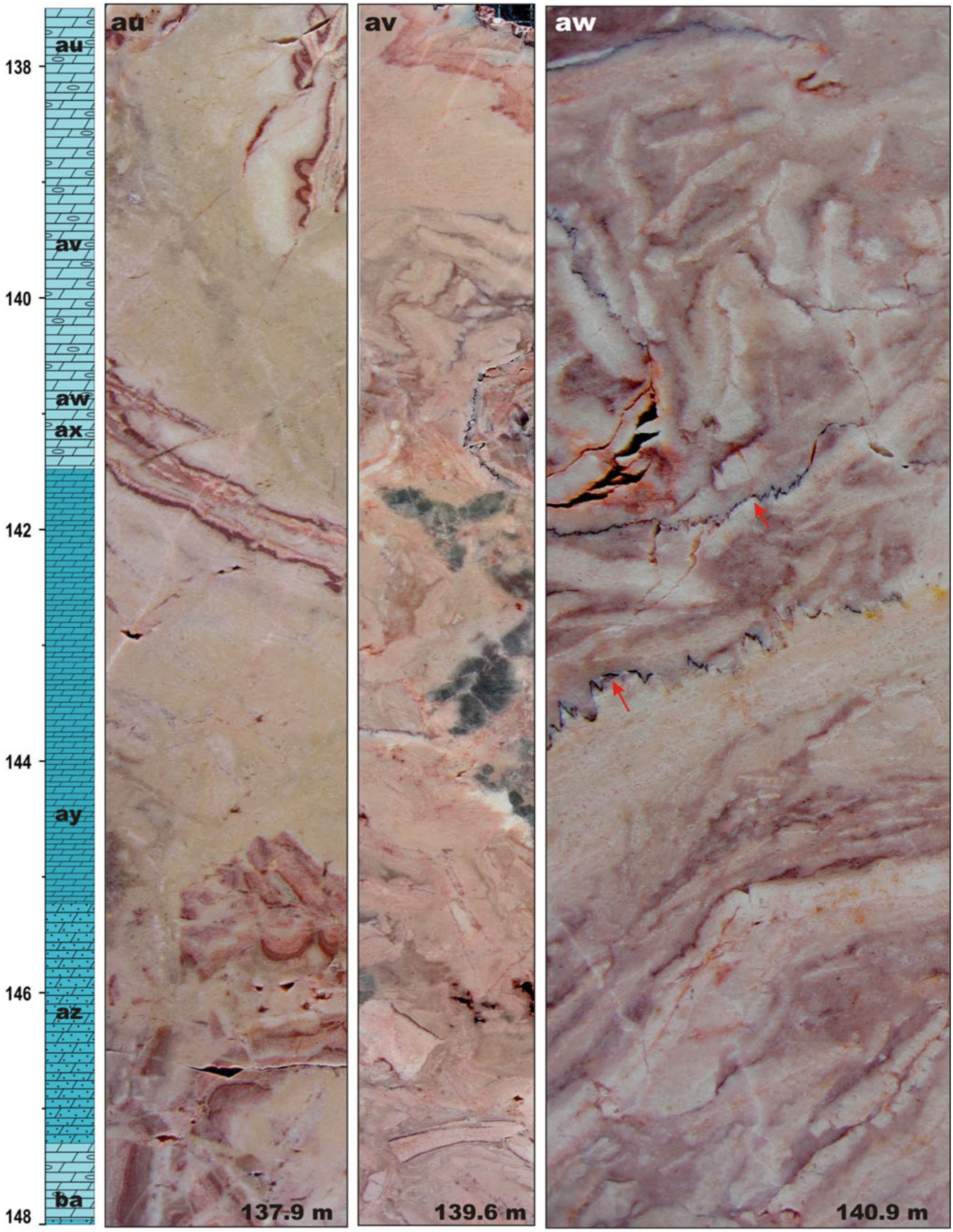

Fig. 6.107 (continued) (**au**–**aw**) Beige, buff and tan dolostone with solution cavities and dissolution-collapse structures resembling karst. Red arrows in (**aw**) identify stylolites

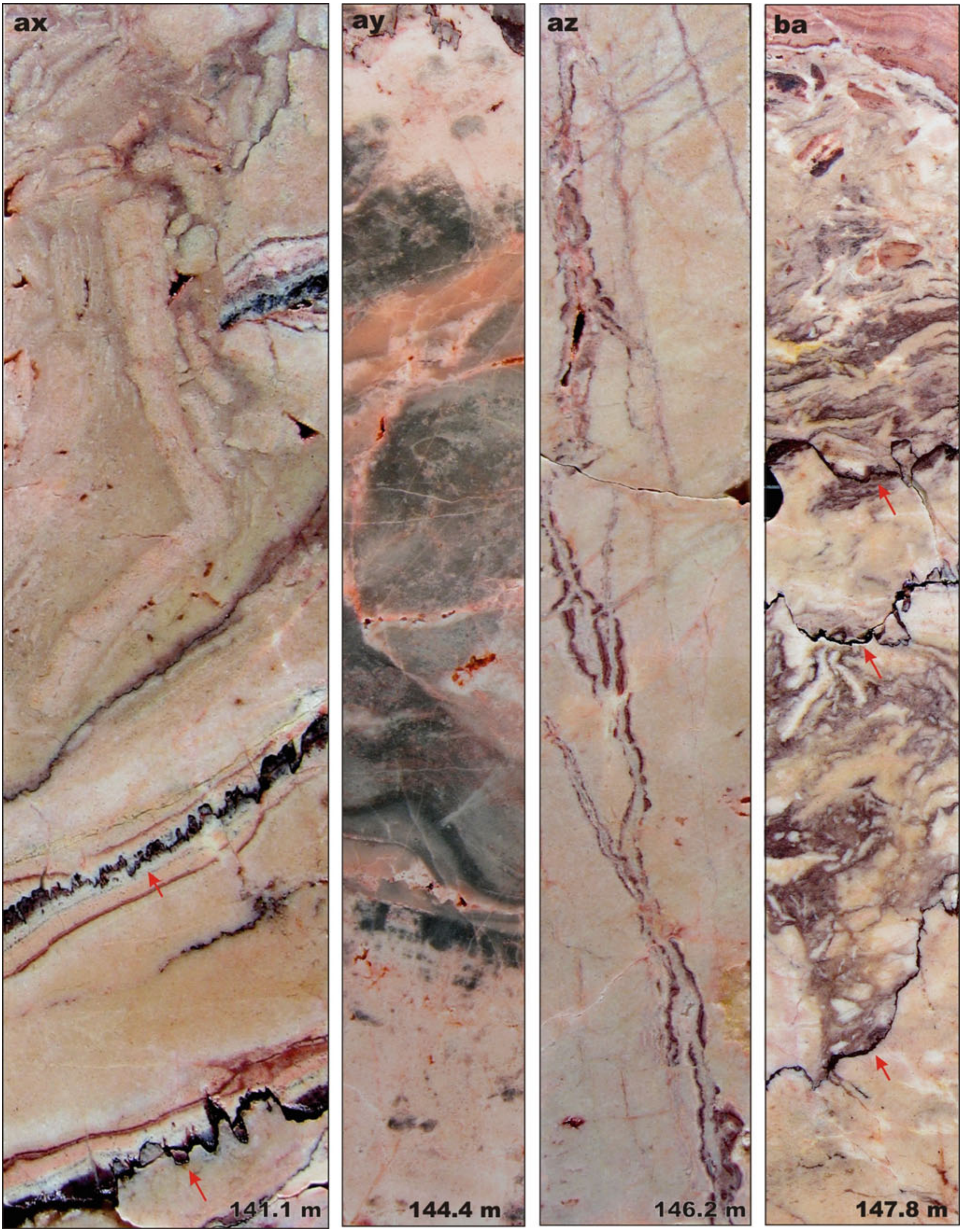

Fig. 6.107 (continued) (**ax**) Beige, bedded dolostone with dissolution hole (*red arrows*) filled with collapse dolostone beds. (**ay**) Massive, variegated dolostone with a patchy colouration. (**az**) Subvertical, dissolution-enlarged cracks (dissolution pipes) in beige, indistinctly bedded dolostone; the dissolution pipes are filled with red clay material, while the remaining space is cemented by drusy dolomite. (**ba**) Dissolution-collapse structure (karst) in dolarenite; stylolites are marked by *red arrows*

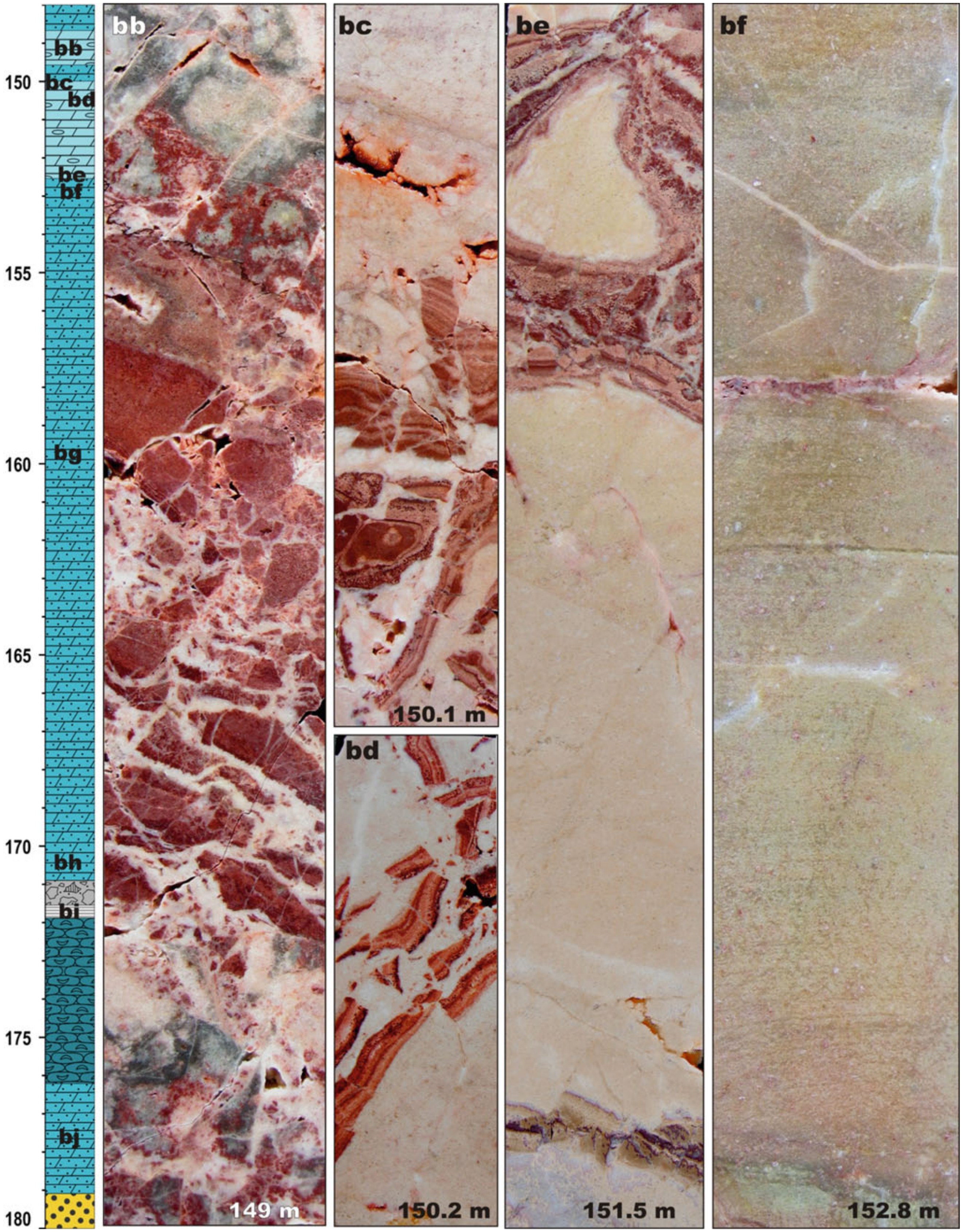

Fig. 6.107 (continued) (**bb–be**) Dissolution-collapse structures (karst) in dolarenites and dolorudites. (**bf**) Pale tan dolarenite with indistinct parallel bedding

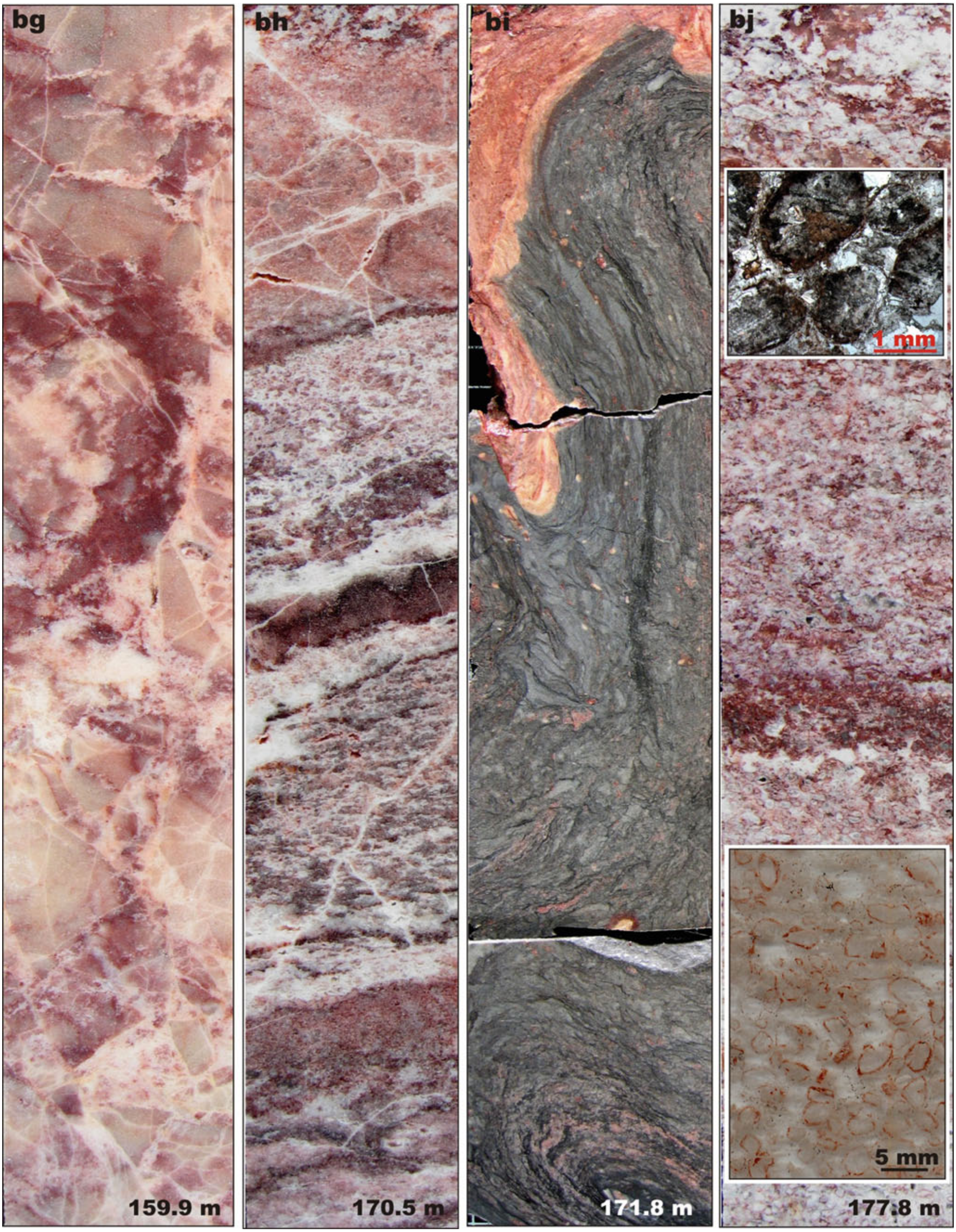

Fig. 6.107 (continued) (**bg**) In situ brecciated dolarenite. (**bh**) Thick-bedded, variegated dolarenite-dolorudite. (**bi**) Grey shale and pink dolomarl that are soft-sediment deformed into isoclinals folds. (**bj**) Recrystallised, indistinctly bedded oncolitic or oolitic dolostone; the upper inset photomicrograph in transmitted, non-polarised light shows recrystallised oolites or oncolites; the lower inset is a scanned thin-section showing that oolites/oncolites have haematite-rich coating (red rims)

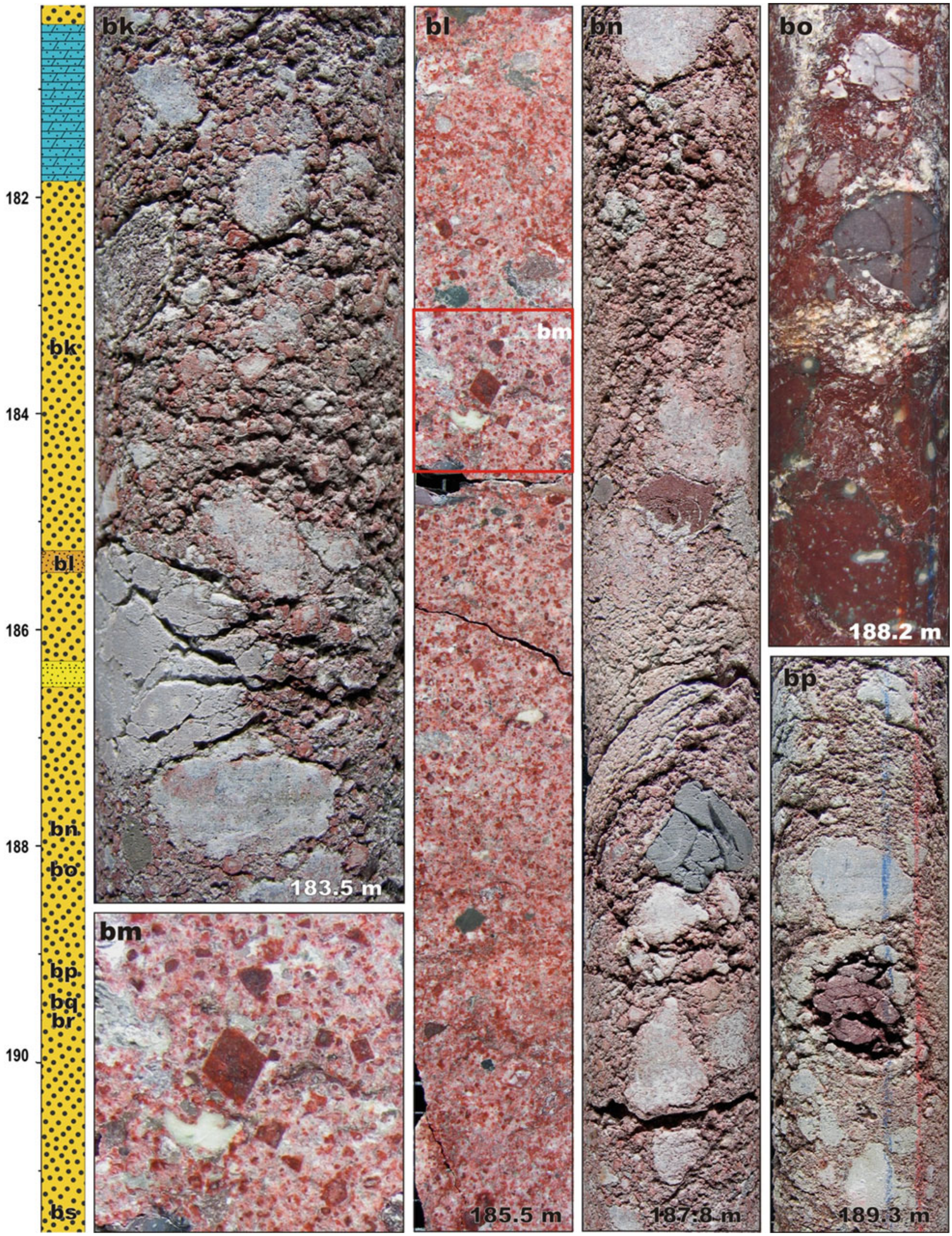

Fig. 6.107 (continued) *Member 6:* (**bk**) Fragment-supported, dissolution-collapse, conglomeratic breccias composed of unsorted dolomarl fragments; note that the cement was largely dissolved. (**bl**) Pinkish, dolomite-cemented gritstone with polymict clasts; note the rhombs of red dolomite. (**bm**) Detailed view of red dolomite crystals in dolomite-cemented, polymict gritstone. (**bn**–**bp**) Fragment-supported, dissolution-collapse, polymict, conglomeratic breccias composed of unsorted intraformational clasts of dolostones and dolomarls; note that the cement is partially dissolved

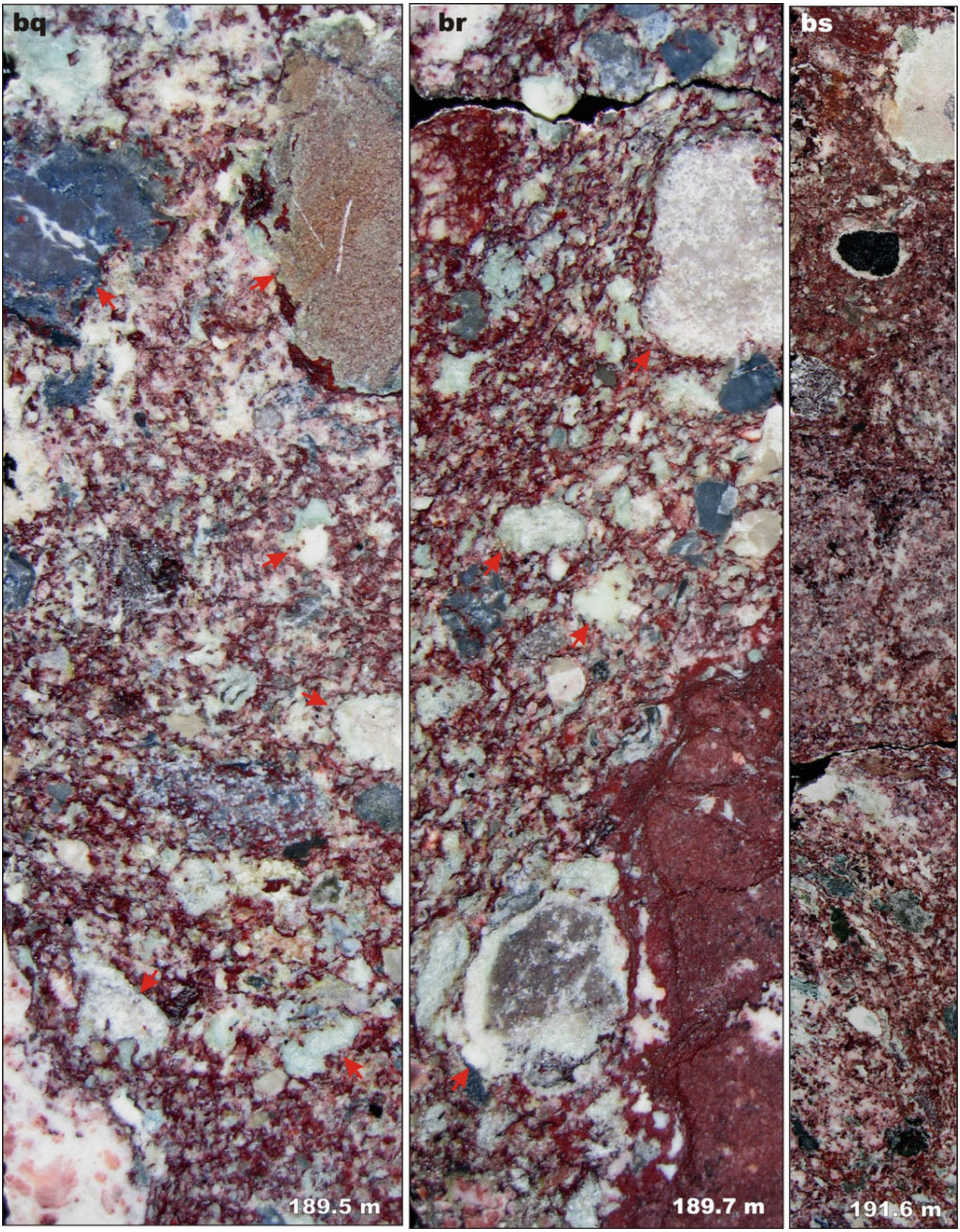

Fig. 6.107 (continued) (**bq**–**bs**) Non-bedded, fragment-supported, polymict conglomerates (redeposited dissolution-collapse breccias?) composed of unsorted intraformational clasts of dolostones, dolomarls and magnesite (?) in a talc-rich matrix; note that some clasts in (**bq**) and (**br**) show a dissolved/leached surface (*red arrows*)

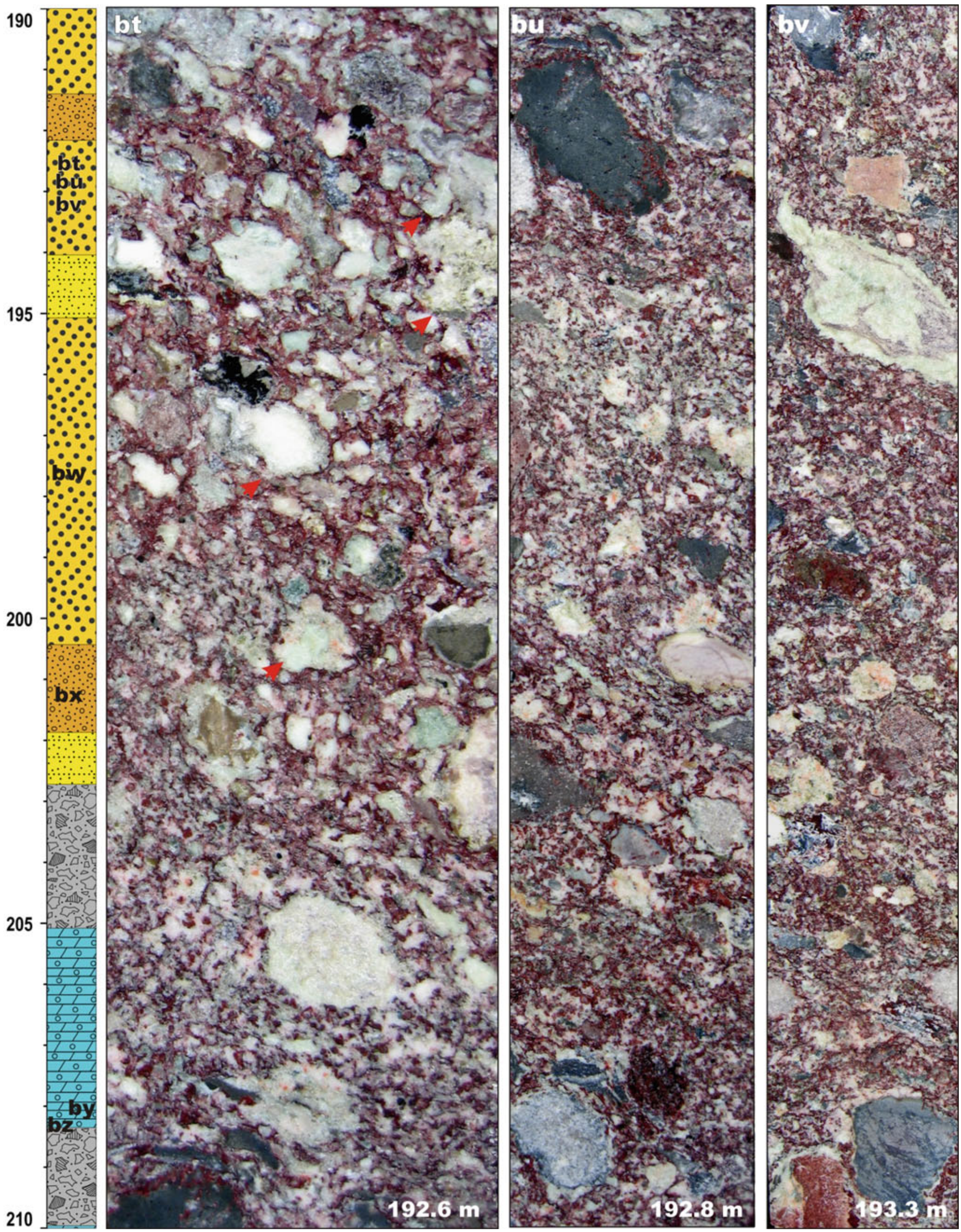

Fig. 6.107 (continued) (**bt**–**bv**) Fragment-supported, dissolution-collapse, polymict conglomerates (redeposited dissolution-collapse breccias) composed of unsorted intraformational clasts of dolostones, dolomarls and magnesite (?) in a clay-talc matrix; note that some clasts in (**bt**) show a dissolved/leached surface (*red arrows*)

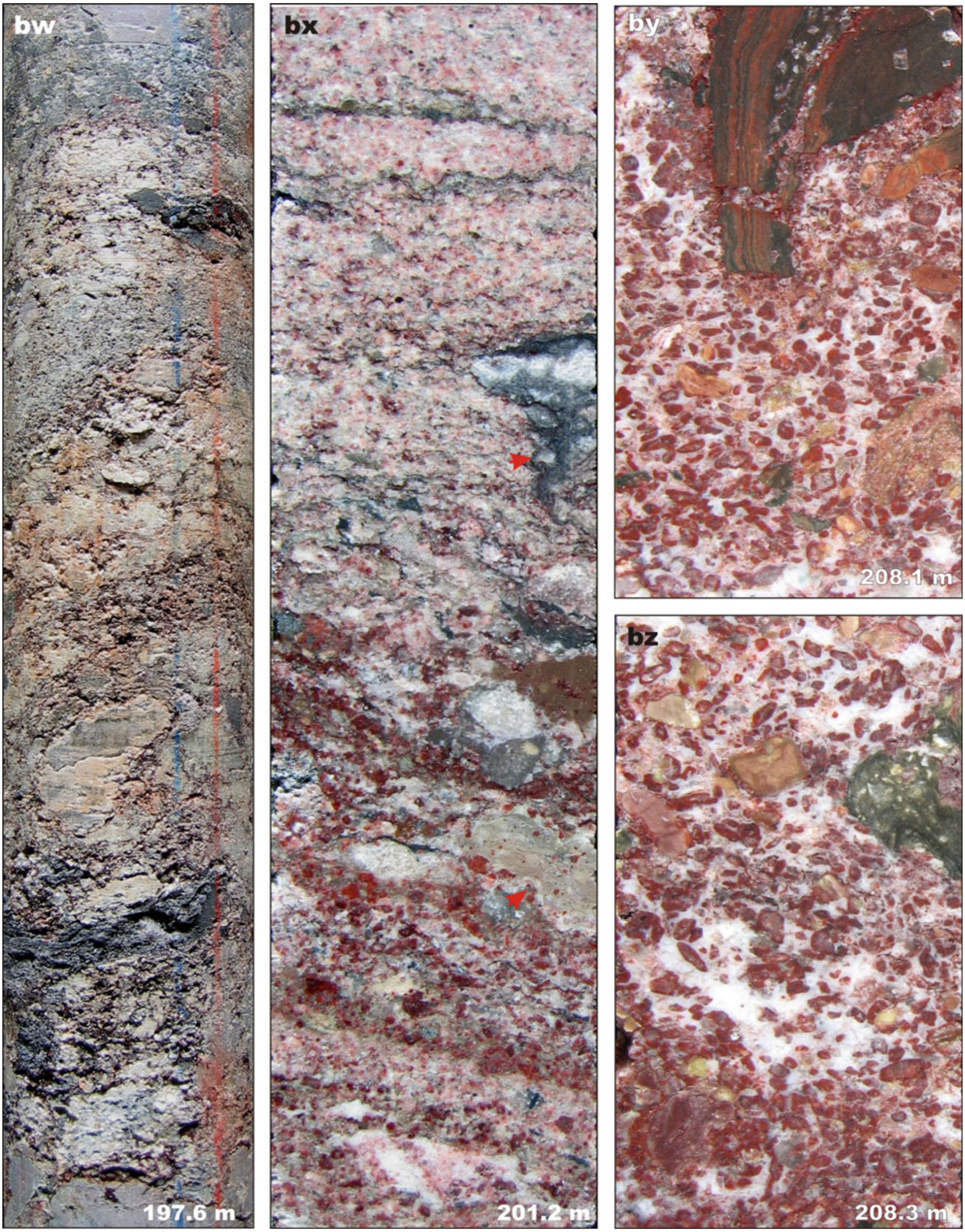

Fig. 6.107 (continued) (**bw**) Dissolution-collapse breccia composed of tightly packed, unsorted mudstone fragments in a clay matrix. (**bx**) Crudely bedded dolarenite-dolorudite containing intraformational clasts of mudstone, dolostone and dolomarl; note that some clasts show a dissolved/leached surface (*red arrows*). *Member 5:* (**by**, **bz**) Variegated rocks composed of red, discoidal dolomite crystals and large fragments of red and black, laminated mudstone, pale pink dolostone and dark grey dolomarl in white, drusy dolomite cement; the zoned, discoidal dolomite crystals apparently represent pseudomorphs after gypsum

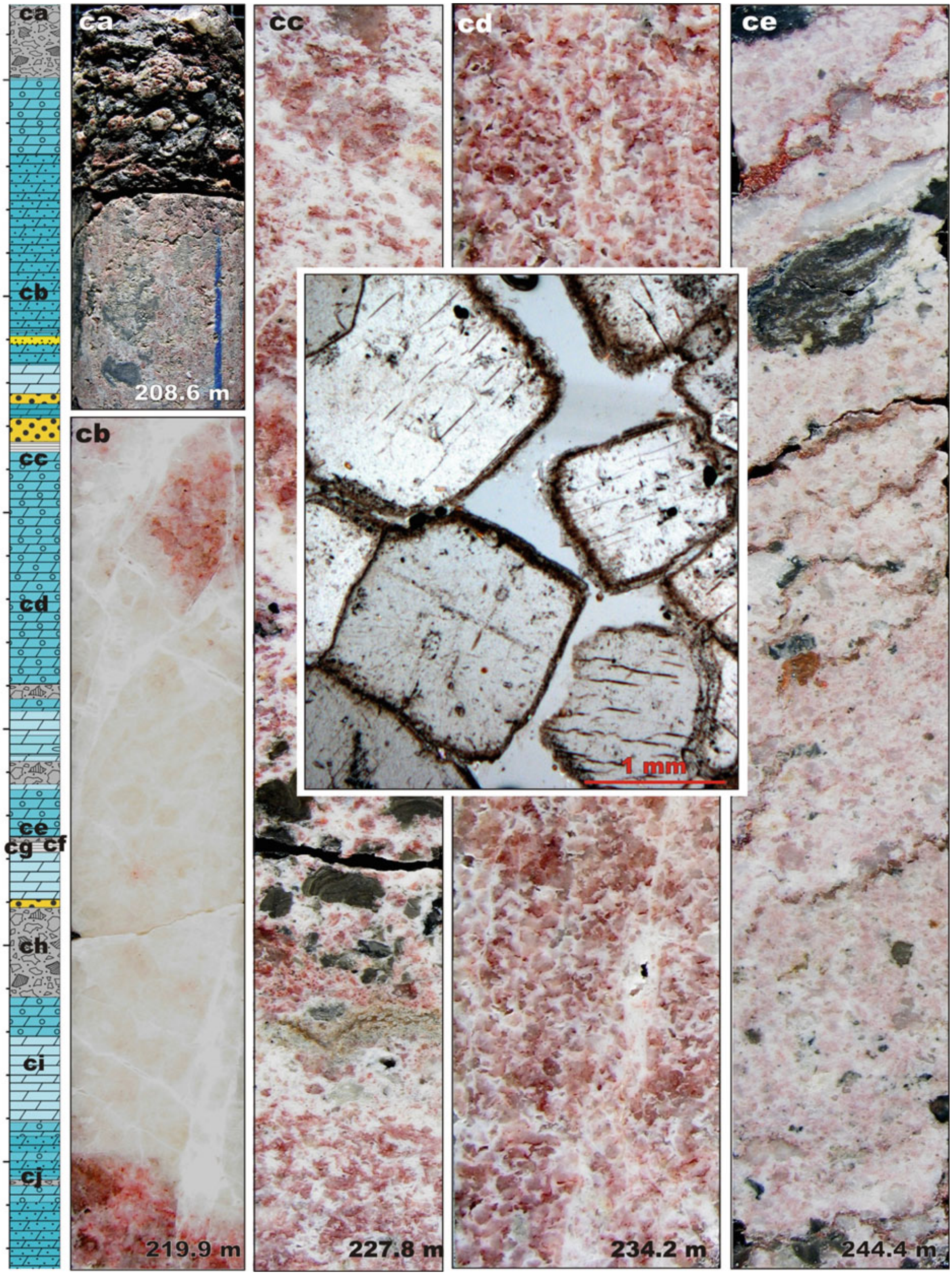

Fig. 6.107 (continued) (**ca**) Massive, dolomite-cemented intraformational breccia overlain by collapse breccia left after dissolved sulphate/halite; note that the upper breccia is not cemented. (**cb**) Vein of white, crystalline dolomite with patches/relicts of preserved pink precursor dolarenite. (**cc**–**ce**) Massive or crudely bedded, vuggy dolostone composed of pale pink, "granular" dolomite crystals and oversized fragments of black siltstone cemented by white, drusy dolomite; the inset photomicrograph in transmitted, non-polarised light shows that many "granular" dolomite crystals have a cubic shape

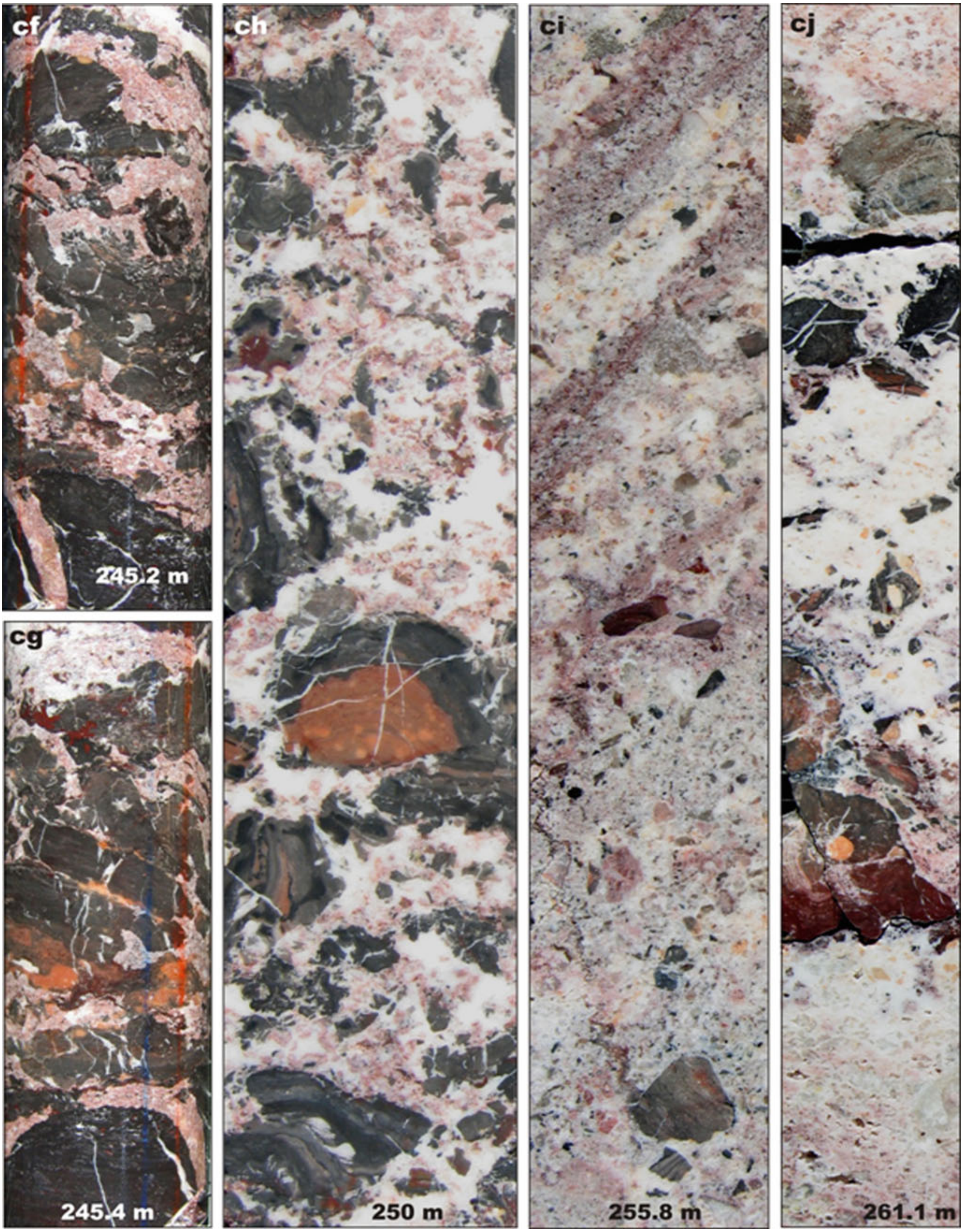

Fig. 6.107 (continued) (**cf**–**ch**) Dissolution-collapse breccias composed of angular, unsorted, and cracked fragments of black and pink dolomarl cemented by white, drusy dolomite. (**ci**) Crudely bedded dolorudite with oversized, angular and unsorted fragments of dolomarl and dolostone. (**cj**) White, massive dolarenite covered by dissolution-collapse breccias composed of black and brown dolomarl fragments embedded in white drusy cement

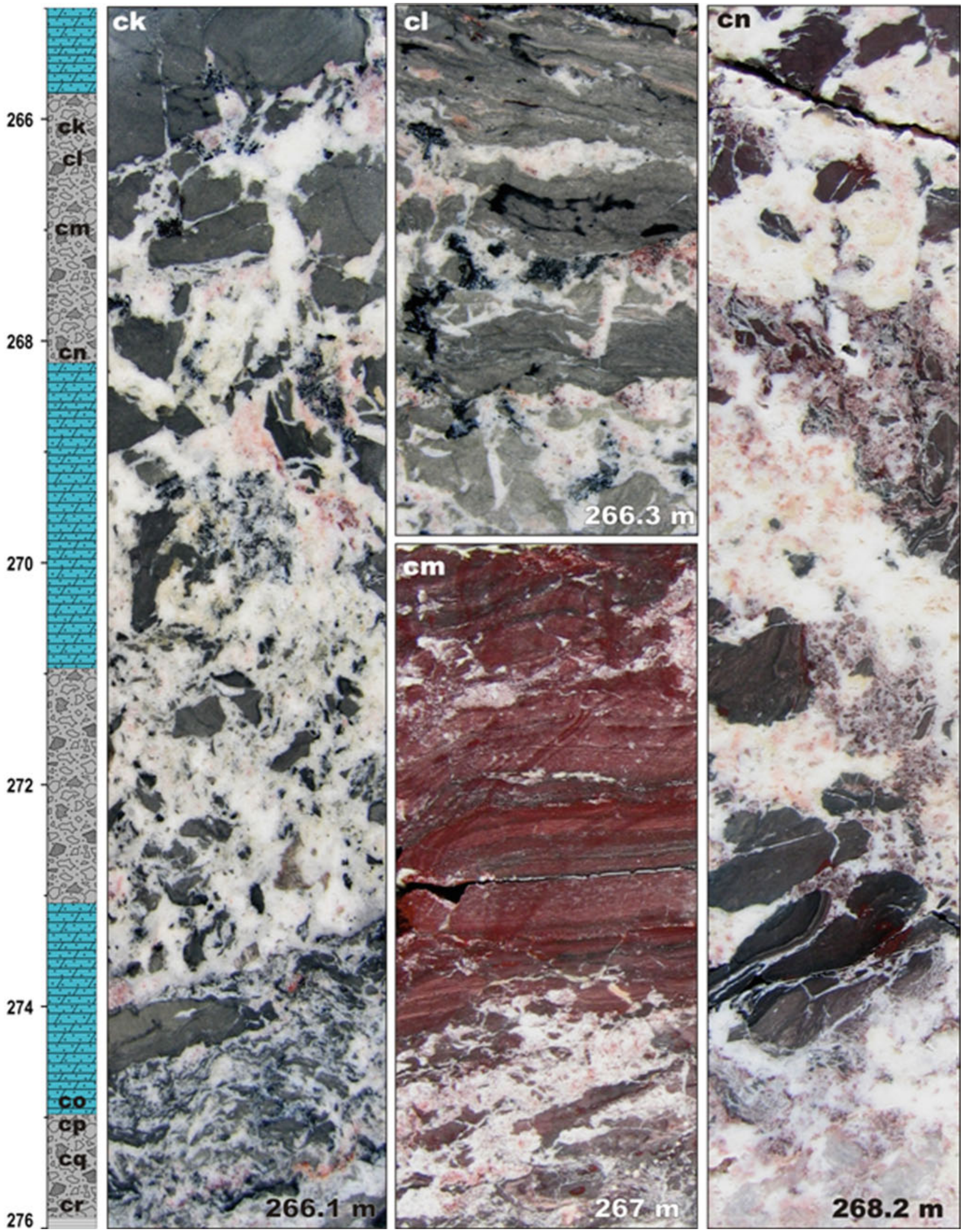

Fig. 6.107 (continued) (**ck**) Dissolution-collapse breccias composed of angular, unsorted fragments of dark grey dolomarl floating in white, drusy dolomite cement. (**cl**) Grey, laminated dolomarl with intensive vertical and bedding-parallel, sheet-cracks cemented by white dolospar. (**cm**) Cement-supported dissolution-collapse breccia passing into red, laminated siltstone/mudstone. (**cn**) Dissolution-collapse breccias composed of unsorted fragments of dark grey dolomarl floating in white, drusy dolomite cement

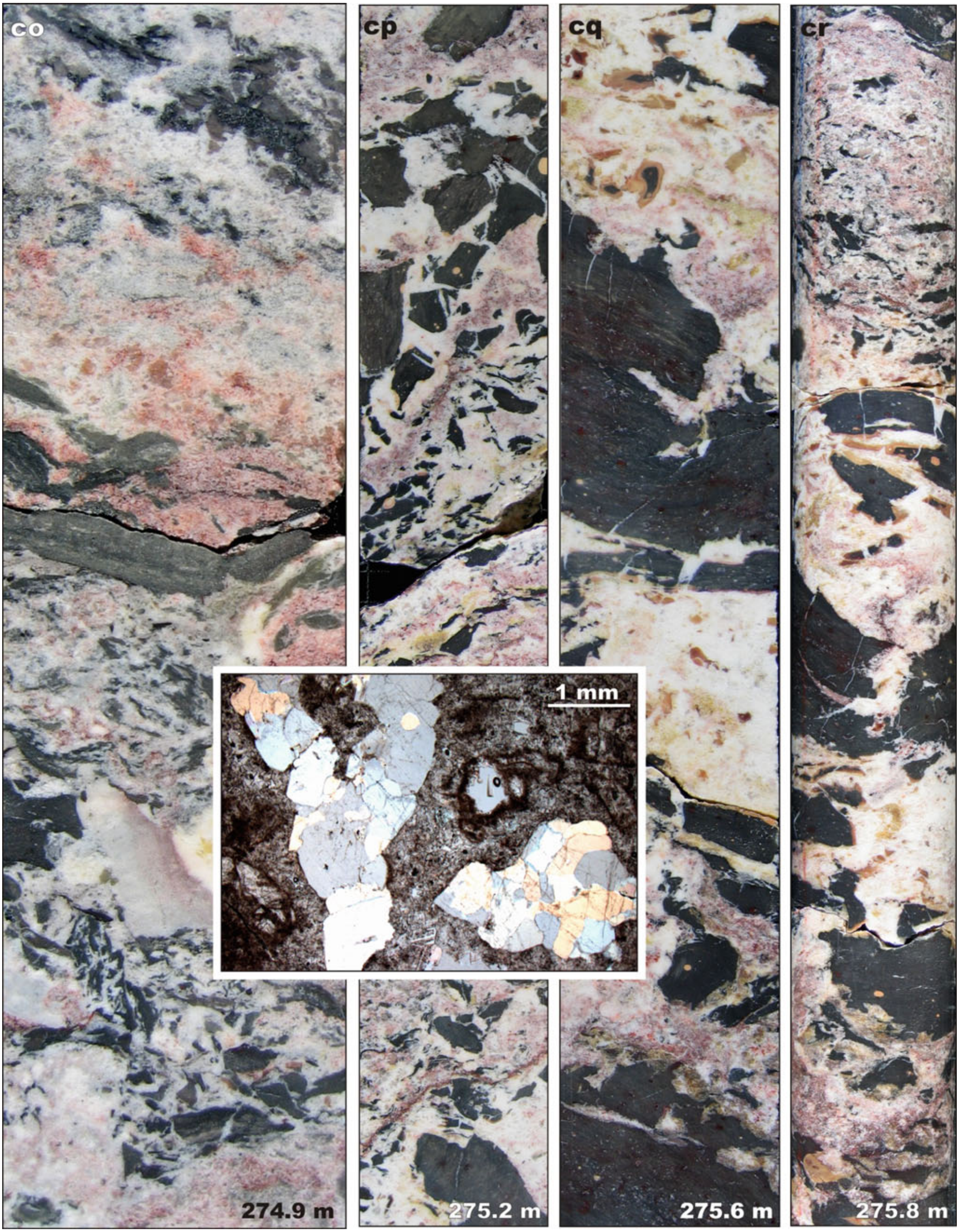

Fig. 6.107 (continued) (**co**–**cr**) Sawn and unsawn core demonstrating dissolution-collapse breccias composed of angular, unsorted clasts and partially intact beds of grey and black dolomarl, pale pink and white dolostone embedded in white, drusy dolomite; the inset photomicrograph in transmitted, non-polarised light shows a quartz-pseudomorphed sulphate nodule and twinned gypsum crystal in white, dolostone clasts

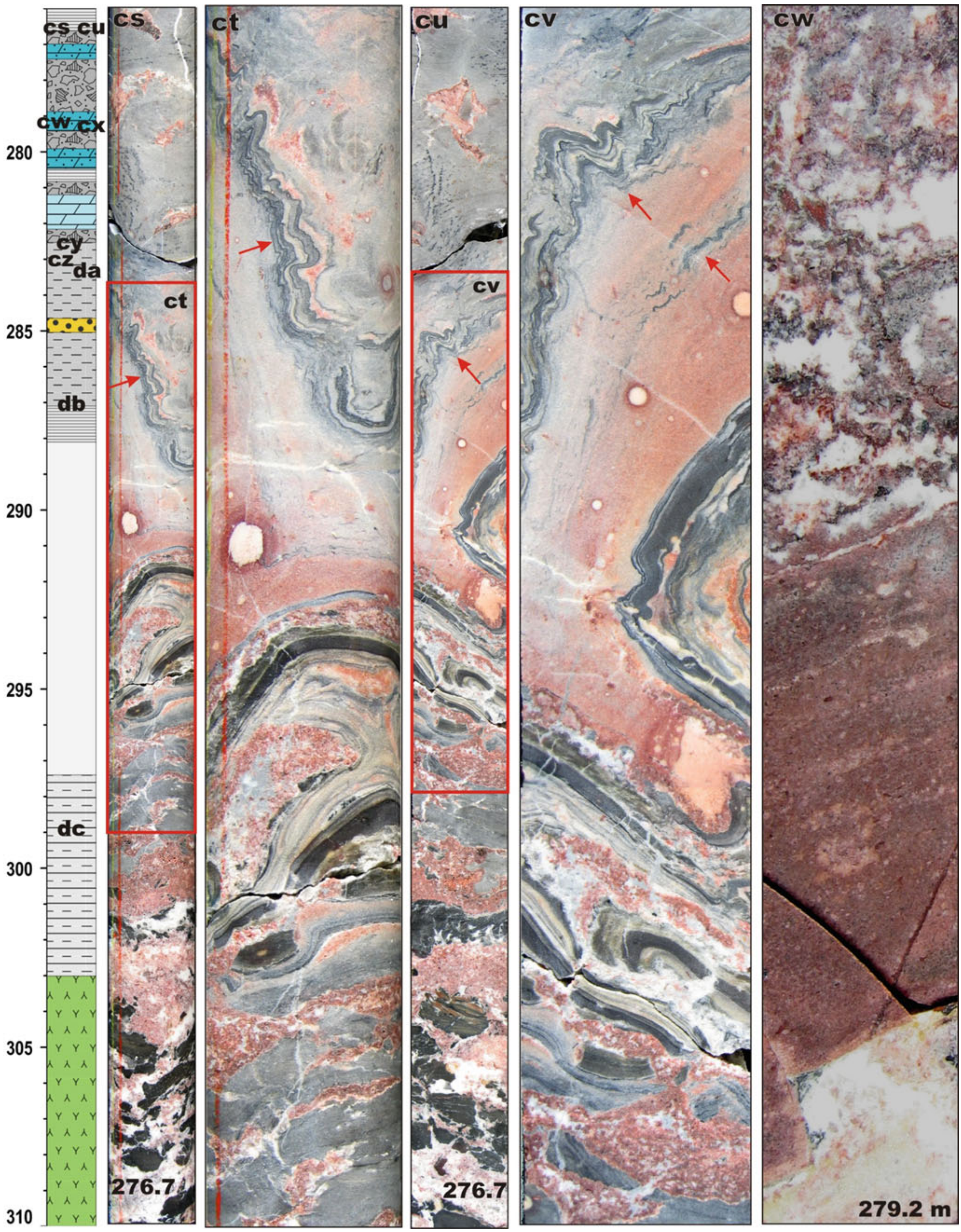

Fig. 6.107 (continued) (**cs**–**cv**) Sawn and unsawn core demonstrating interbedded pale pink/white dolostone and laminated grey and black mudstone; note that the interbedded rocks are soft-sediment deformed into tight folds, and laminated mudstones are desiccated and partially dismembered; some layers show an enterolithic structure (*red arrows*); note that the desiccated mudstone beds are cemented by white dolospar and pink dolomite with a granular fabric. (**cw**) White and pink, crudely bedded dolarenite passing upward into small-clast dolorudite

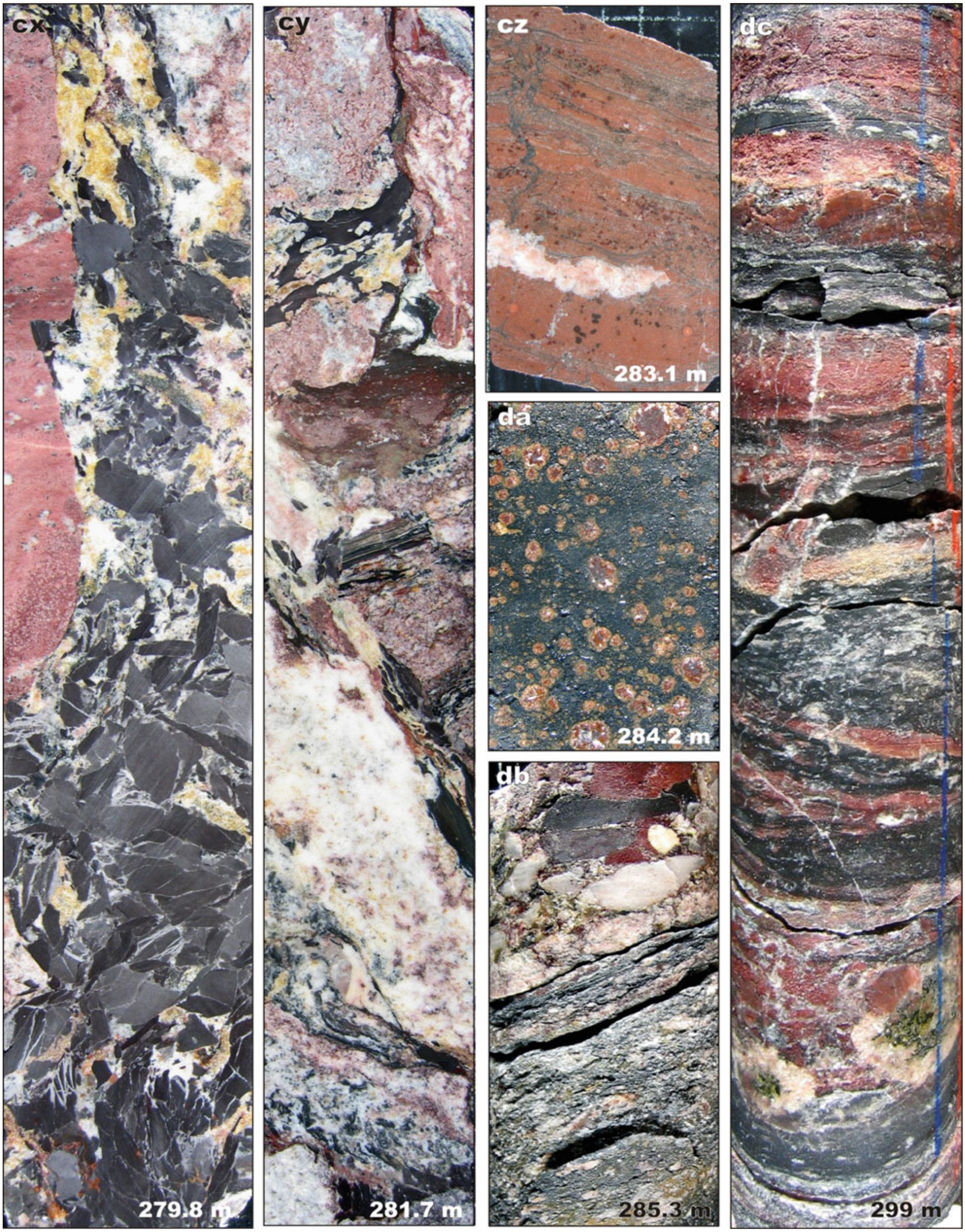

Fig. 6.107 (continued) (**cx**) Dissolution hole in pink dolostone filled with tightly packed, angular fragments of black dolomitic mudstone cemented by white dolospar. (**cy**) Clast-supported dissolution-collapse breccia composed of large fragments and fragmented and rotated layers of dolostone and black mudstone. *Member 4*: (**cz**) Pink dolostone with a dissolution cavity cemented by white dolospar. (**da**) Quartz-dolomite pseudomorphs (bright brown) after sulphate (?) in mudstone. (**db**) Gritty mudstone sharply overlain by clast-supported conglomerate. (**dc**) Interbedded siltstone-shale with a variegated colour and lensoidal and wavy lamination

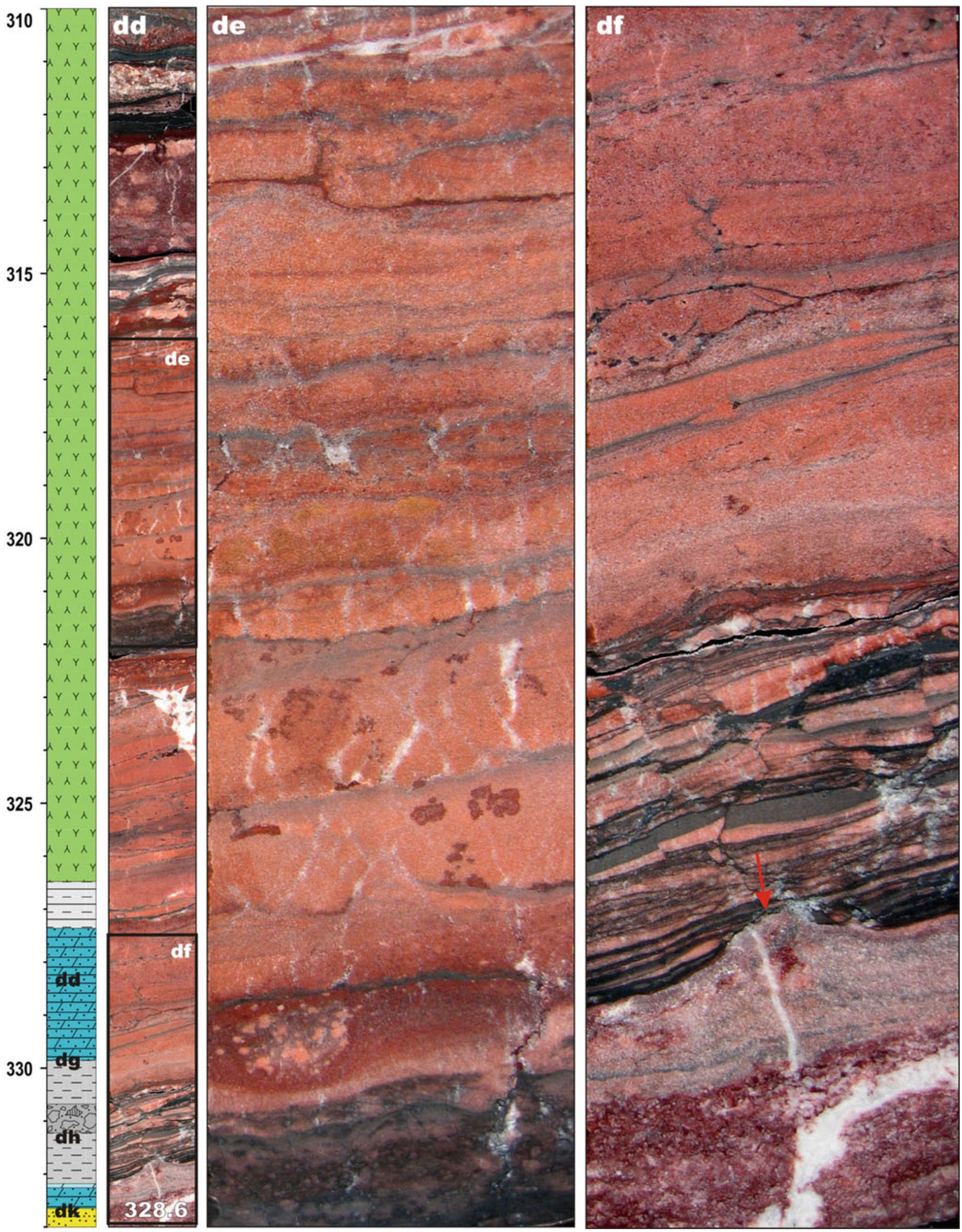

Fig. 6.107 (continued) *Member 3* (**dd**) Red, bedded dolarenite with thin intervals of interlaminated dolarenite-shale. (**de**) Structural details of red dolarenite with lensoidal bedding and black shale at the base. (**df**) Close-up view of interlaminated, pale pink dolarenite and black shale occurring as a thin interval in red dolarenite with lensoidal bedding; note the lenticular and small-scale flaser bedding in the dolarenite-shale couplets; the *red arrow* points to a buckled bed above massive, gritty dolarenite resembling a small-scale tepee

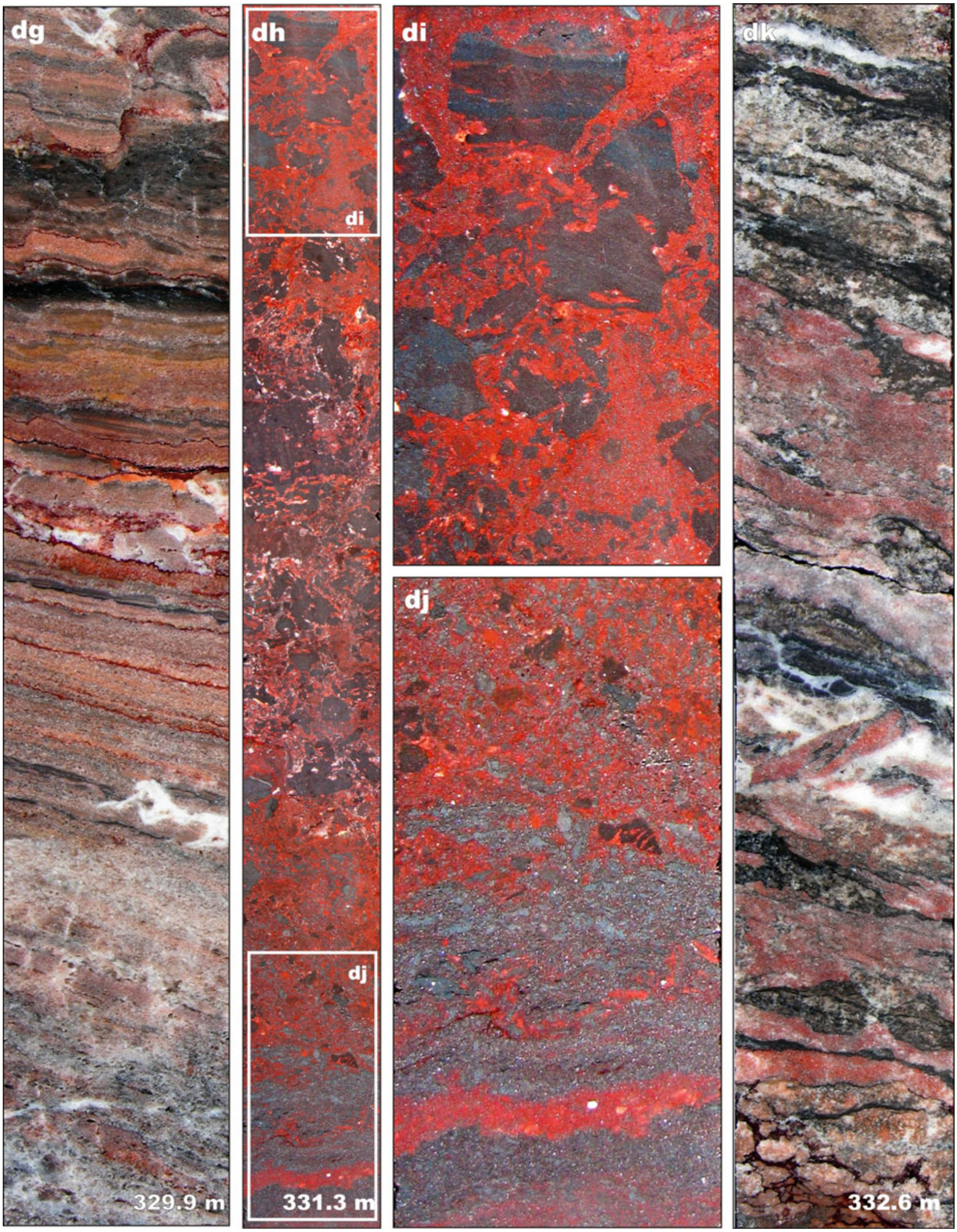

Fig. 6.107 (continued) (**dg**) Fining-upward succession; it starts with light-coloured, coarse-grained, laminated dolarenite followed by pale pink, laminated dolomarl with shale laminae, then passing into interlaminated dolomarl-shale. (**dh**) Massive, matrix-supported, haematite-stained breccias composed of large, angular fragments of grey siltstone embedded in a red gritstone-sandstone matrix. (**di**) Detailed view of angular siltstone clasts floating in a red sandstone matrix. (**dj**) Structural details of the transitional contact between variegated, gritty siltstone and red, haematite-stained gritstone. (**dk**) Desiccated and in situ brecciated succession of interbedded dolarenite, dolomarl and siltstone

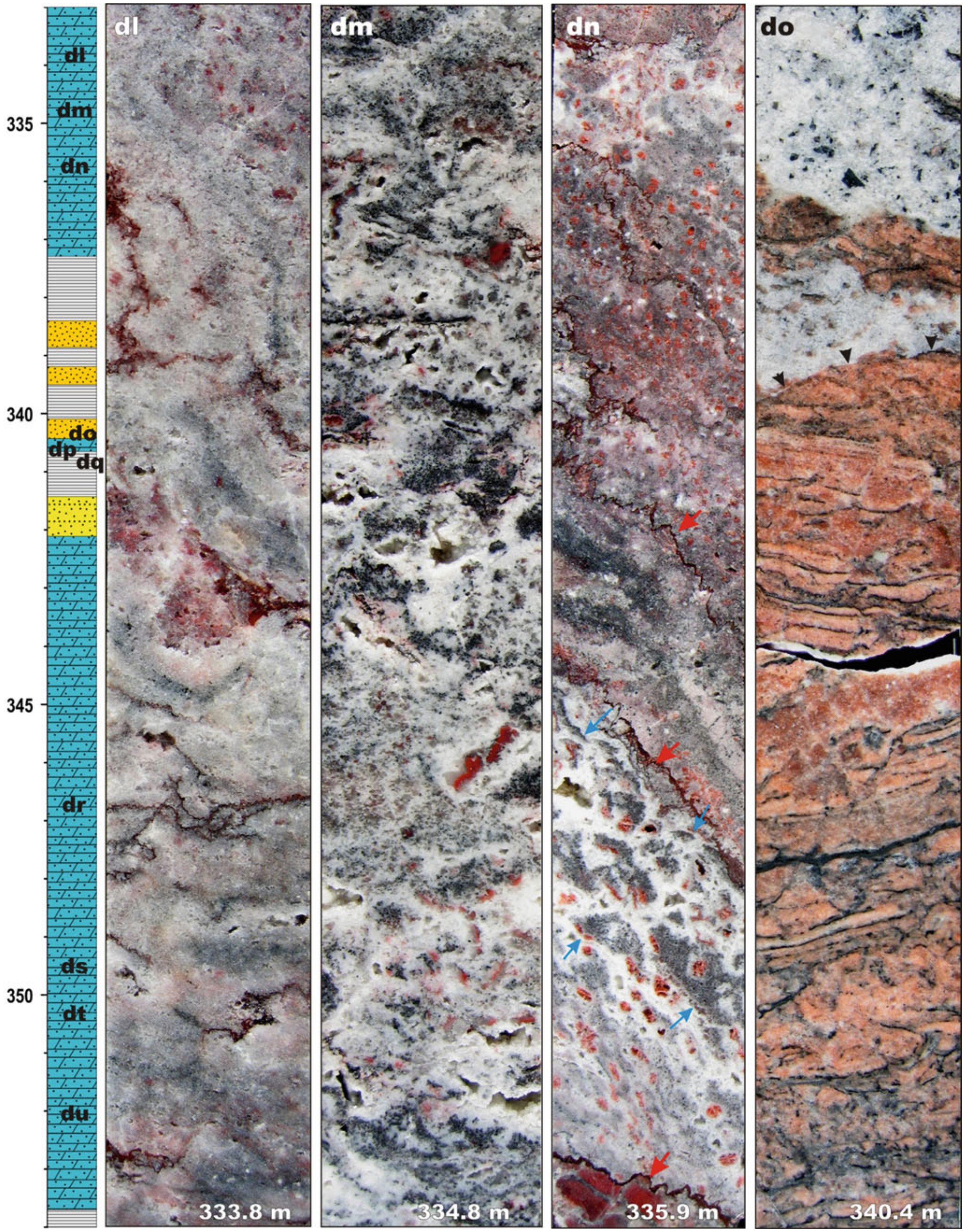

Fig. 6.107 (continued) (**dl**) Light-coloured dolarenite with a cryptic brecciated fabric and relicts of deformed mudstone laminae. (**dm**) Massive dolarenite with abundant small, angular fragments of black mudstone rip-ups and dissolution cavities. (**dn**) Crudely bedded, variegated dolarenite with stylolites (*red arrows*) and a desiccated mudstone bed at the base (*blue arrows*). (**do**) Pink, desiccated and in situ brecciated dolomarl with a dissolved upper surface (*black arrows*) covered by cement-supported dissolution-collapse breccia

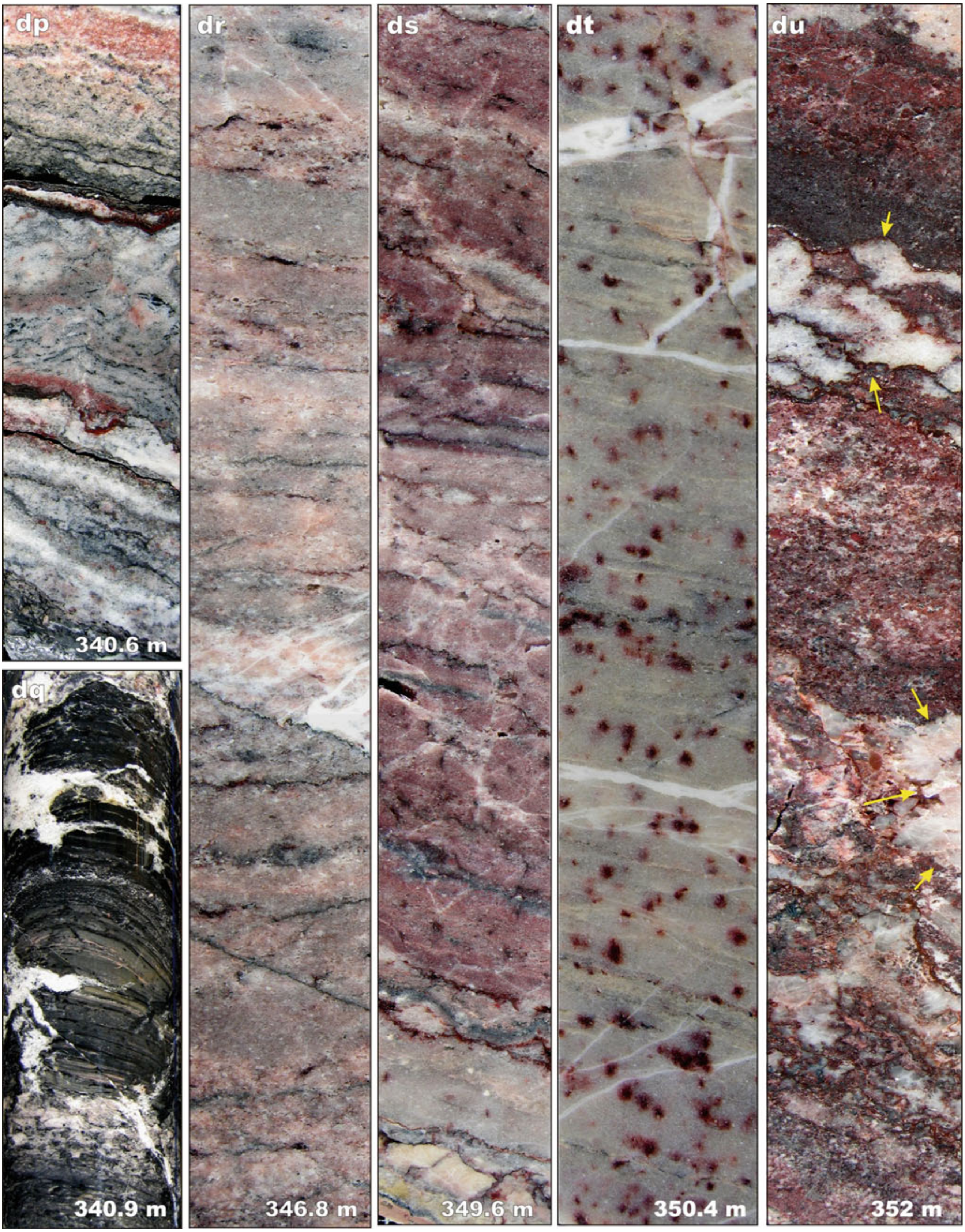

Fig. 6.107 (continued) (**dp**) Dolarenite with mudstone interlayers (black), lensoidal bedding and in situ brecciation. (**dq**) Flat-laminated shale with dissolution cavities filled with white, drusy dolomite. (**dr**–**dt**) Partially recrystallised, bedded dolarenites with thin dolomarl laminae (dark-coloured) and haematite spots in (dt). (**du**) Haematite-stained, crudely bedded, muddy dolarenite-dolorudite with in situ brecciated intervals and dolomite-pseudomorphed nodular masses of probable sulphates (*yellow arrows*)

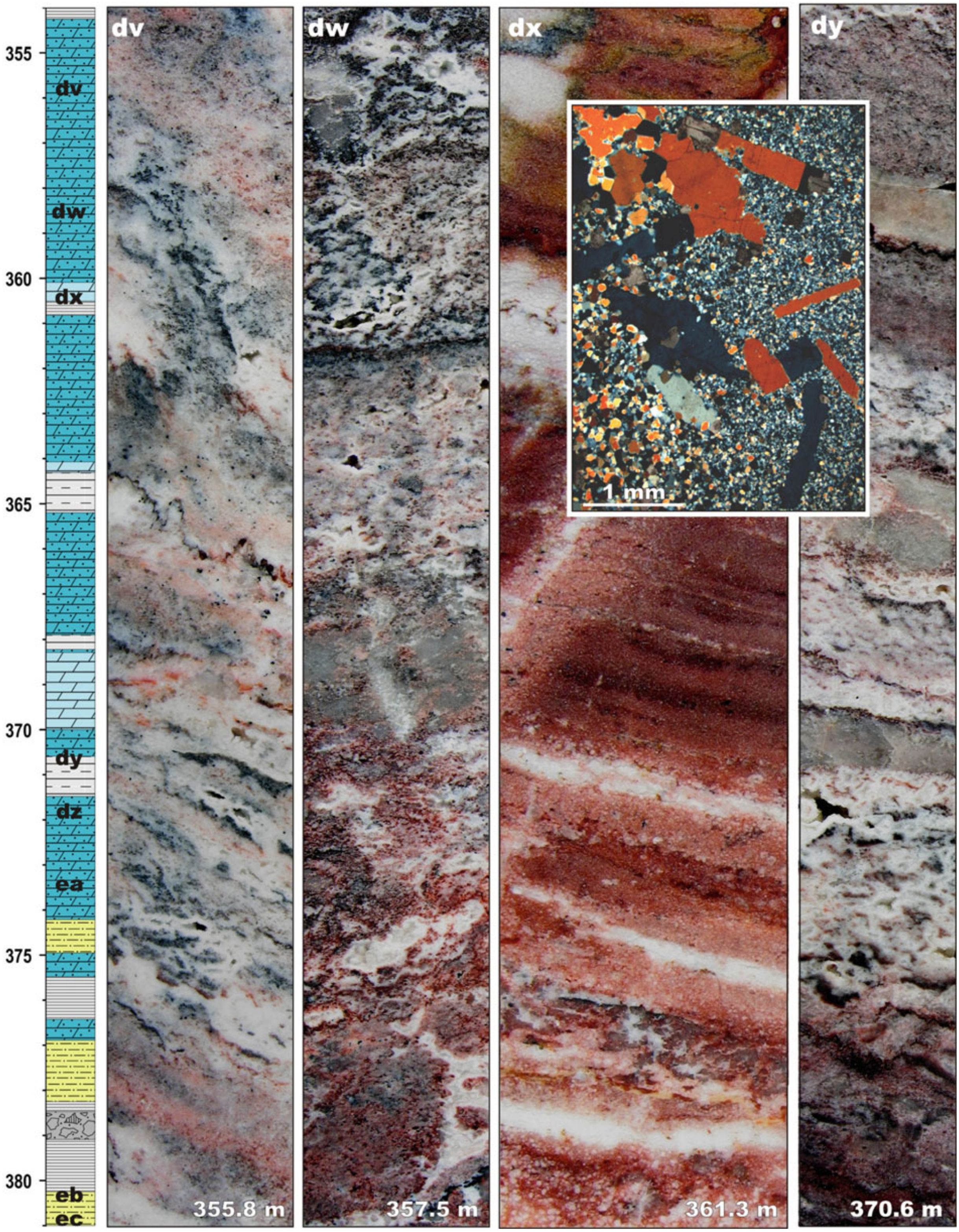

Fig. 6.107 (continued) (**dv**) Variegated, crudely bedded dolarenite with cryptic microbrecciation and platy, flame-shaped fragments of black mudstone. (**dw**) Variegated, crudely bedded dolarenite-dolorudite with intensely desiccated, disintegrated and dolospar-cemented black mudstone (the uppermost bed), and dissolution cavities filled with white dolospar. (**dx**) Red dolomarl affected by recrystallisation and formation of white crystalline dolomite. (**dy**) Interbedded dolarenite and dolorudite containing abundant small rip-ups of black mudstone; note the "granular" fabric caused by solution and re-precipitation processes; the inset photomicrograph in transmitted polarised light shows platy, rectangular and discoidal crystals (red, black and pale grey) of former evaporitic minerals now pseudomorphed by quartz

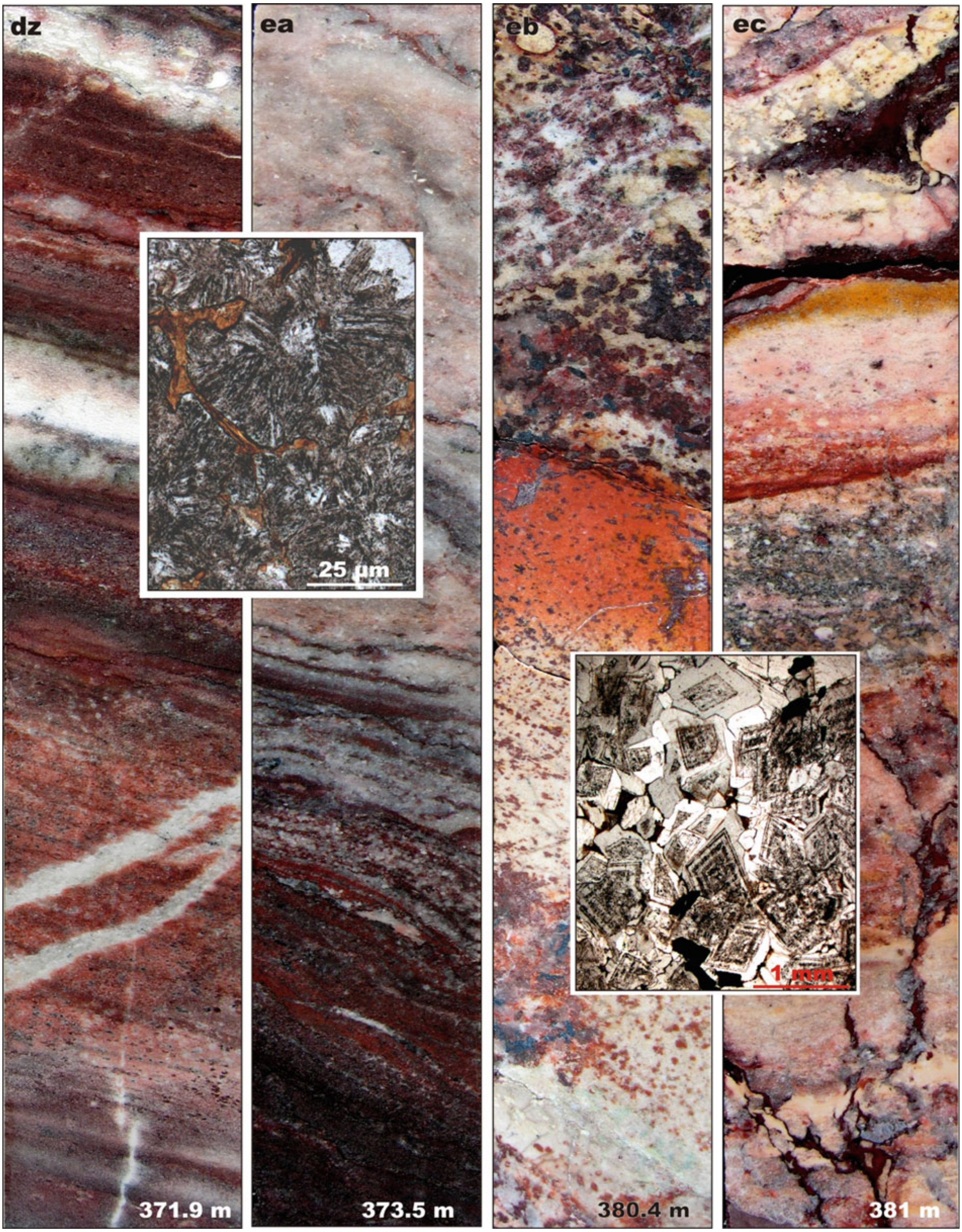

Fig. 6.107 (continued) (**dz**) Red, flat-laminated dolarenite affected by recrystallisation and formation of white, crystalline dolomite. (**ea**) Dark-coloured mudstone with micro-lensoidal lamination overlain by bedded dolomarl passing upward into white, massive dolostone; the inset photomicrograph in transmitted light shows pseudo-oolite in white, massive dolostone: a spherical dolomite particle with light core and radiating fabric encased in brown clayey material. *Member 2:* (**eb**) Variegated, parallel-bedded, dolomitic siltstone sharply overlain by dissolution-collapse breccias composed of small mudstone fragments cemented by white dolospar; the inset photomicrograph in transmitted light shows zoned dolomite crystals that line large cavities and fill veinlets in dolomitic siltstone. (**ec**) Pale pink to red, in situ brecciated dolomitic siltstone with mud-filled cracks overlain by graded beds of dolorudite-dolarenite with collapse breccias on top

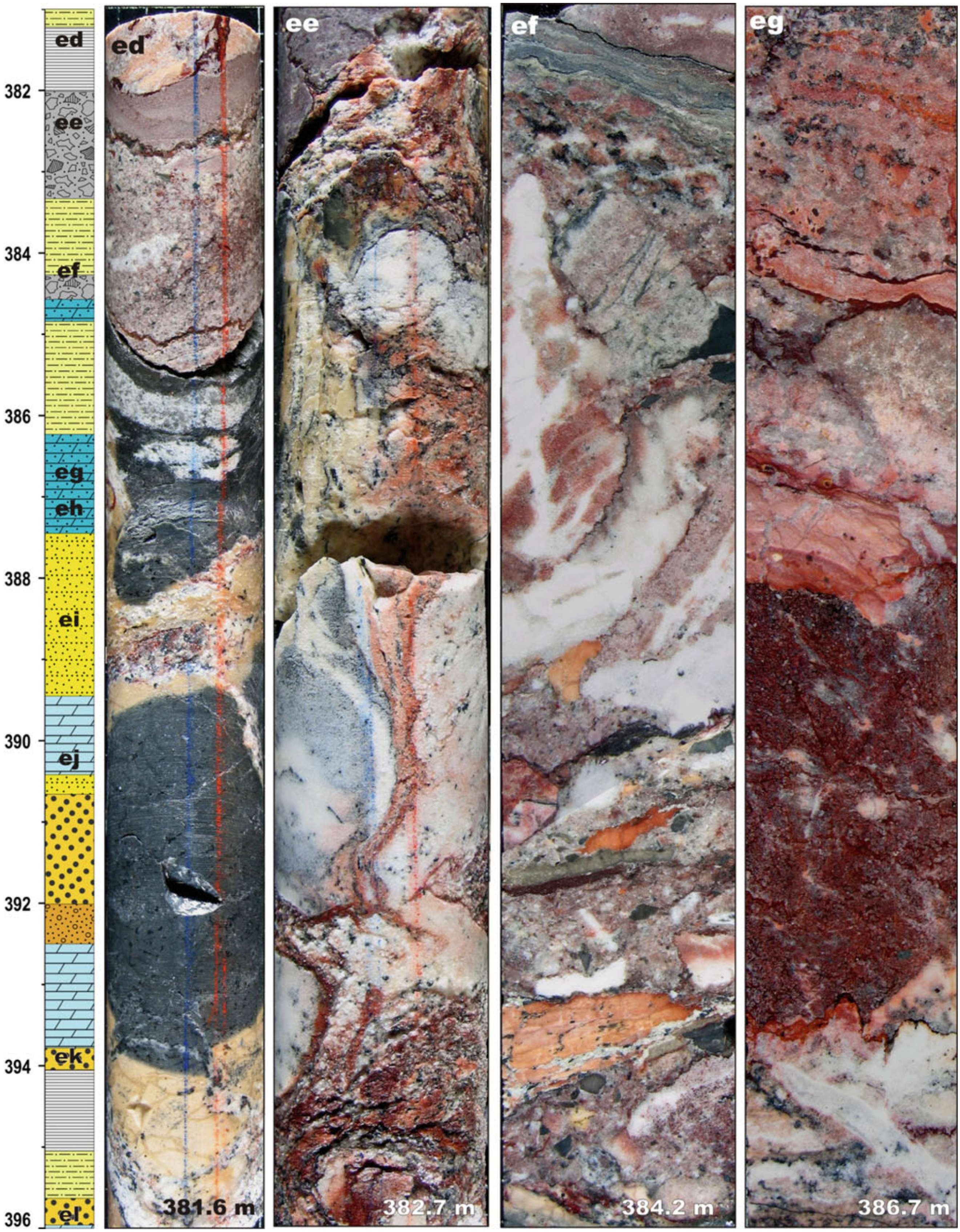

Fig. 6.107 (continued) (**ed–eg**) Clast-supported, non-bedded dissolution-collapse breccias composed of rounded and angular fragments and partially disintegrated beds of variegated dolostone, black mudstone and laminated dolomarl

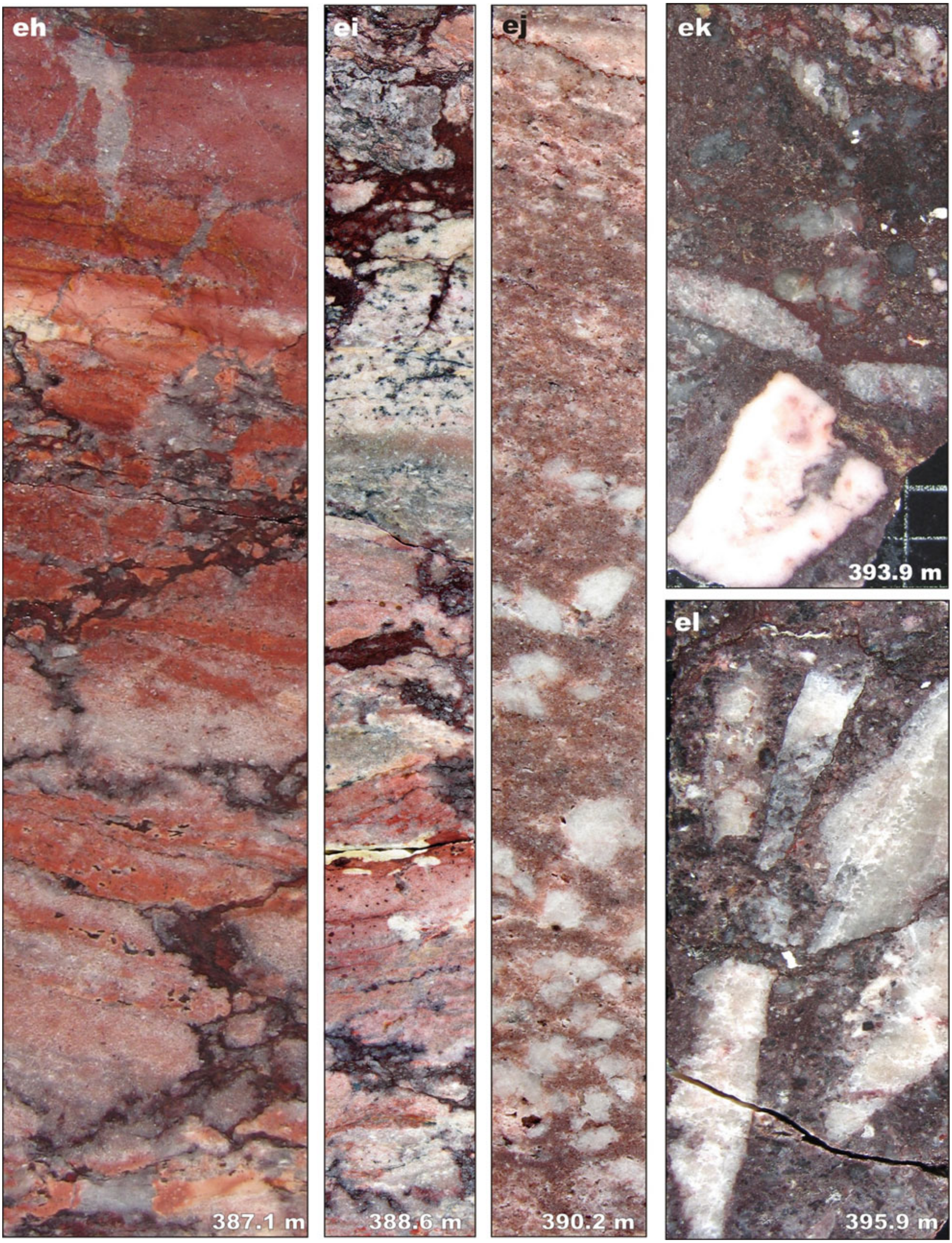

Fig. 6.107 (continued) (**eh**) In situ disintegrated, red dolarenite with irregular open joints filled with debris of host rock set in dark brown, clayey material. (**ei**) In situ brecciated, partially disintegrated sandstone with dissolution-collapse breccia on top. (**ej**) Crudely bedded to massive dolarenite with dolomite-pseudomorphed sulphate crystals. (**ek**, **el**) Matrix-supported breccia containing angular clasts of white dolostone set in a polymict gritstone matrix

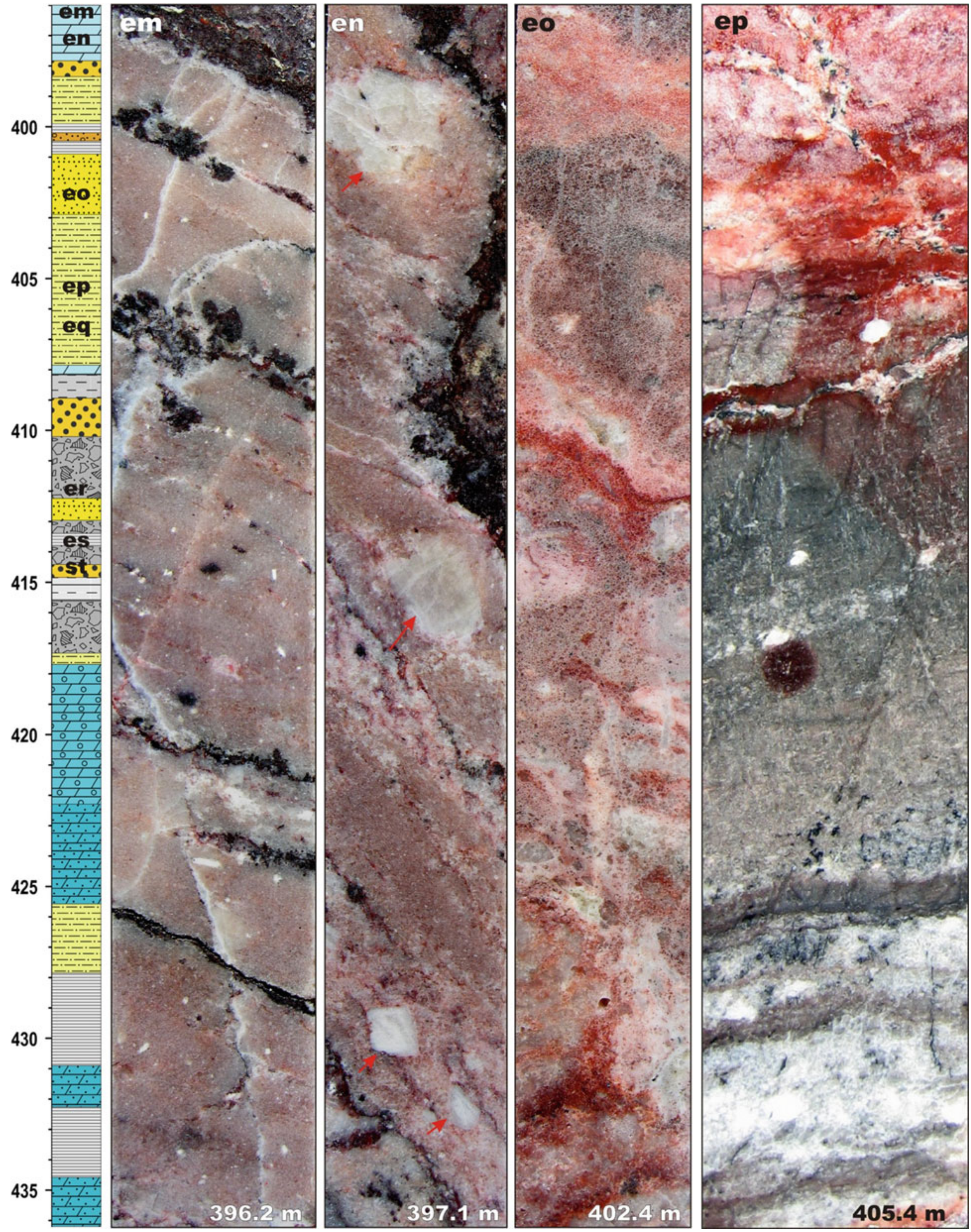

Fig. 6.107 (continued) (**em**) White, fine-grained dolostone whose bedding is expressed by sparse laminae, lenses and patches of black mudstone. (**en**) Bedded dolostones with a dissolution pipe filled with black mudstone; note the dolomite-pseudomorphed nodules and crystals of apparent sulphate (*red arrows*). (**eo**) Crudely bedded, dolomite-cemented sandstone whose primary structure was modified by dissolution and cementation processes. (**ep**) Recrystallised, variegated, bedded dolomitic siltstone with dolomite-cemented dissolution cavities

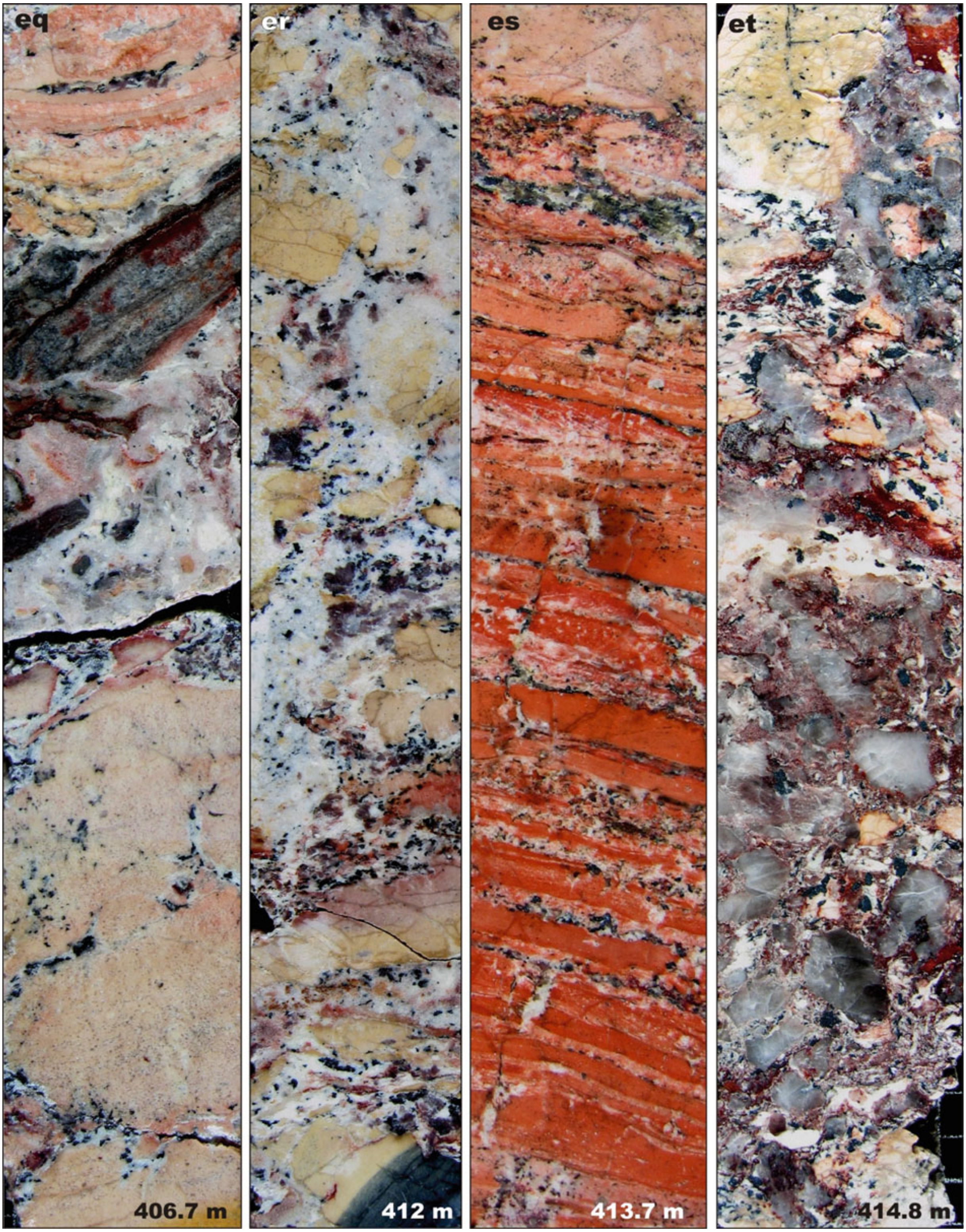

Fig. 6.107 (continued) (**eq**) Beige, massive dolomitic siltstone with dissolution-collapse breccias on top. (**er**) Cement-supported dissolution-collapse breccias composed of angular and rounded clasts, and partially disintegrated beds of yellow, pale pink and black dolostone set in white, drusy dolomite cement. (**es**) Flat-laminated, red dolomarl with small rip-ups of black mudstone; note the network of dissolution voids and cracks that are cemented by white dolospar. (**et**) Polymict, clast-supported conglomerate showing no bedding; clasts of quartz, dolostone and black mudstone are poorly sorted and variably rounded

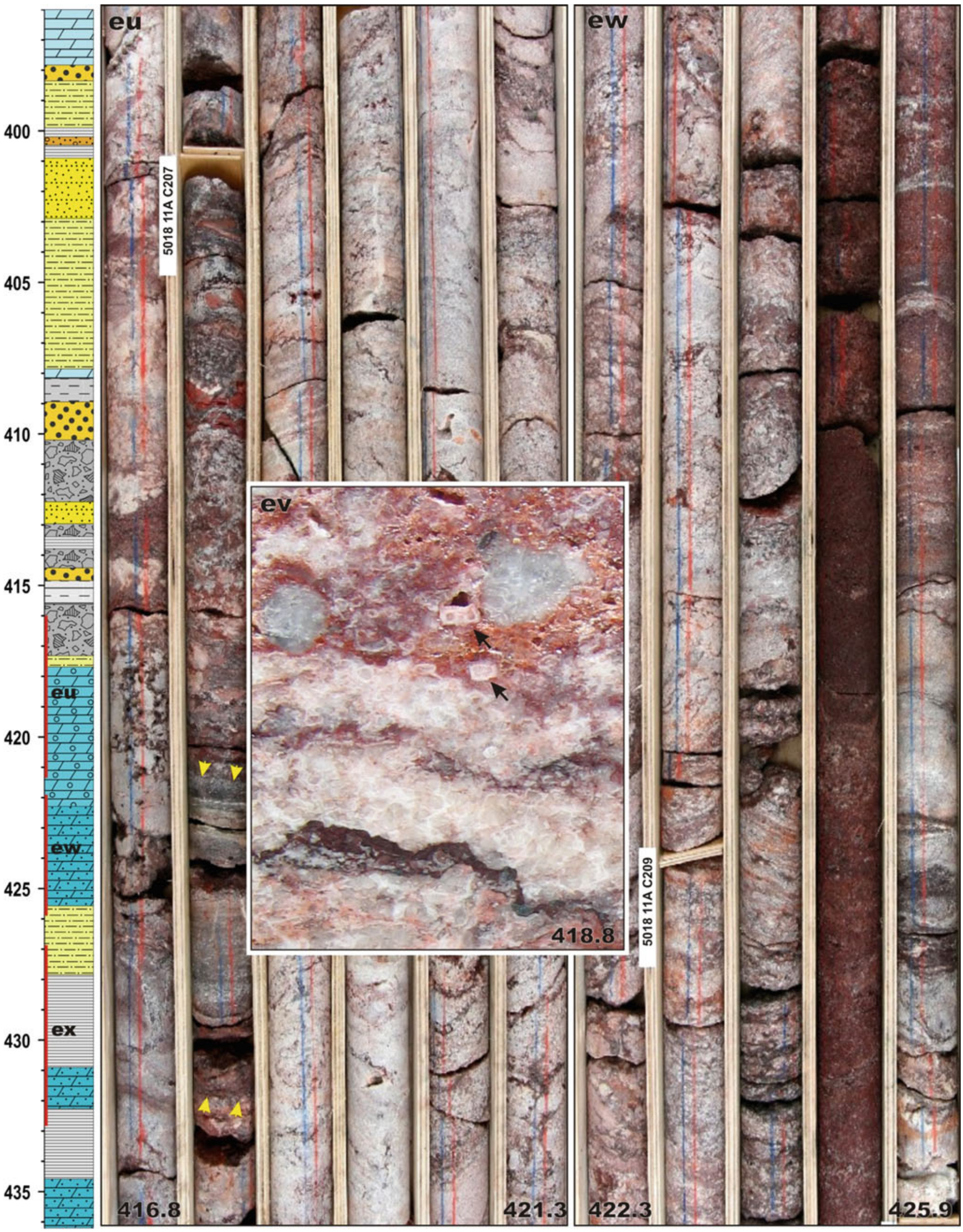

Fig. 6.107 (continued) *Member 1*: (**eu**) Continuous, unsawn core through variegated dissolution-collapse breccias (first and second sections), a shale unit (between *yellow arrows*) and indistinctly bedded or massive dolostones; note that the dolostones show dissolution cavities, in situ brecciation and a considerable degree of recrystallisation. (**ev**) Detailed view of replacement fabrics in the dolostones; note that some dolomite crystals have a cubic morphology and may represent replacements after halite. (**ew**) Continuous, unsawn core through light-coloured and dark brown, haematite-stained dolarenite with indistinct bedding or a massive structure, *in situ* brecciation and a considerable degree of recrystallisation

Fig. 6.107 (continued) (**ex**) Continuous, unsown core through variegated dolomitic siltstone, shale, dolomarl and dolostone with indistinct bedding or a massive structure, *in situ* brecciation and a considerable degree of recrystallisation

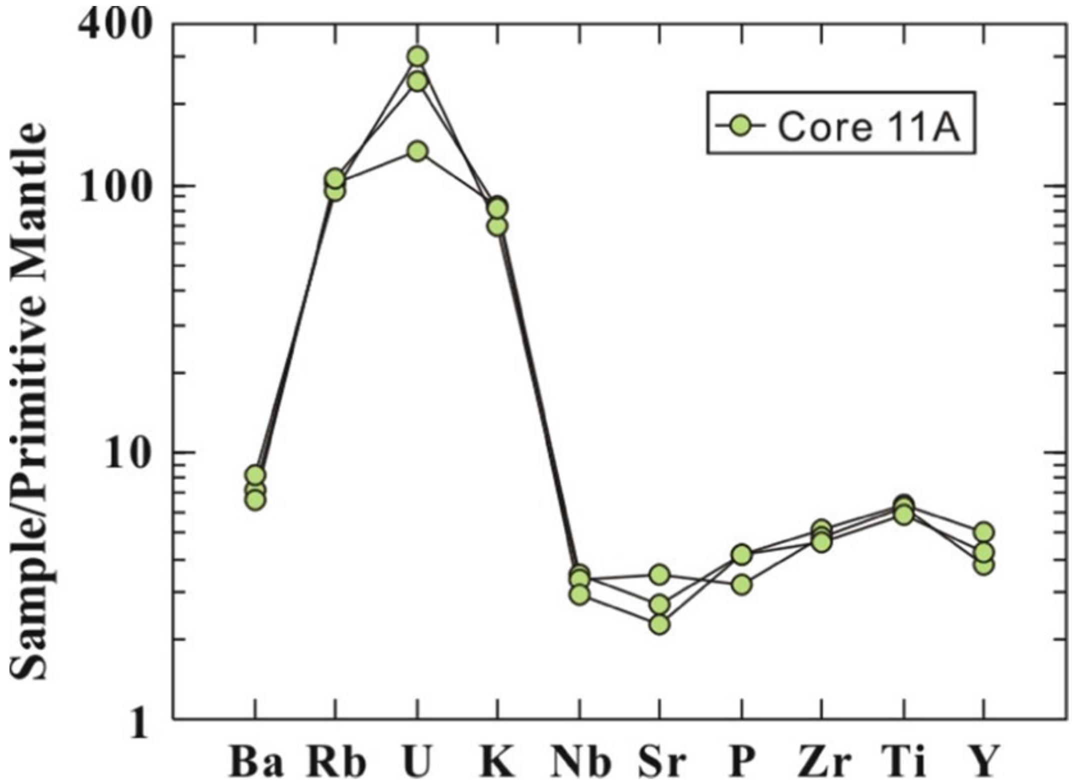

Fig. 6.108 A primitive mantle-normalised trace element diagram for samples from the mafic igneous unit in Core 11A, indicating abnormally high K, Rb and U concentrations due to alteration. The diagram is based on XRF analyses. Normalising values taken from Sun and McDonough (1989)

Fig. 6.109 Dolostone-dolomarl/shale, and partially dolostone-evaporite, cycles. The dolostone forms thicker parts of the cycles and appears as massive, indistinctly bedded or *in situ* brecciated (collapse breccias) rocks. The siliciclastic parts of the cycles are commonly thinner and comprise black or dark brown, muddy siltstone whose primary bedding was modified considerably by syngenetic and diagenetic growth of gypsum concretions and chicken-wire anhydrite now replaced by white dolospar and drusy dolomite

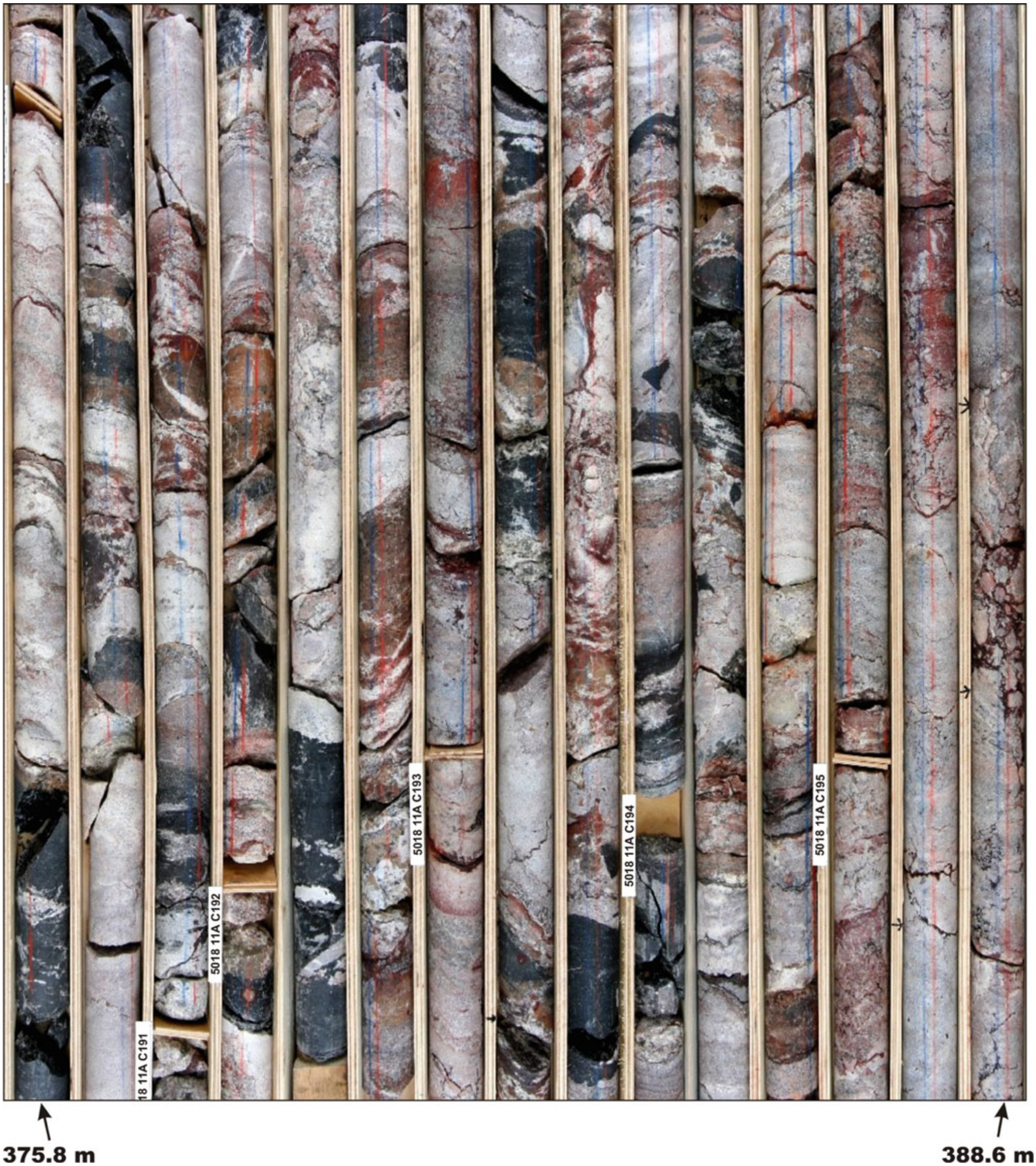

Fig. 6.109 (continued) Dolostone-dolomarl/shale, and partially dolostone-evaporite, cycles (Photographs from FAR-DEEP data base (http://far-deep.icdp-online.org))

Fig. 6.110 Dolostone-dolomarl/shale cycles. The dolostone forms thicker portions of the cycles and appears as indistinctly bedded or massive rocks. The siliciclastic parts of the cycles are commonly thinner and comprise mainly black siltstone/mudstone; in places primary bedding was modified by diagenetic growth of gypsum crystals and concretions, now replaced by white, drusy dolomite or quartz

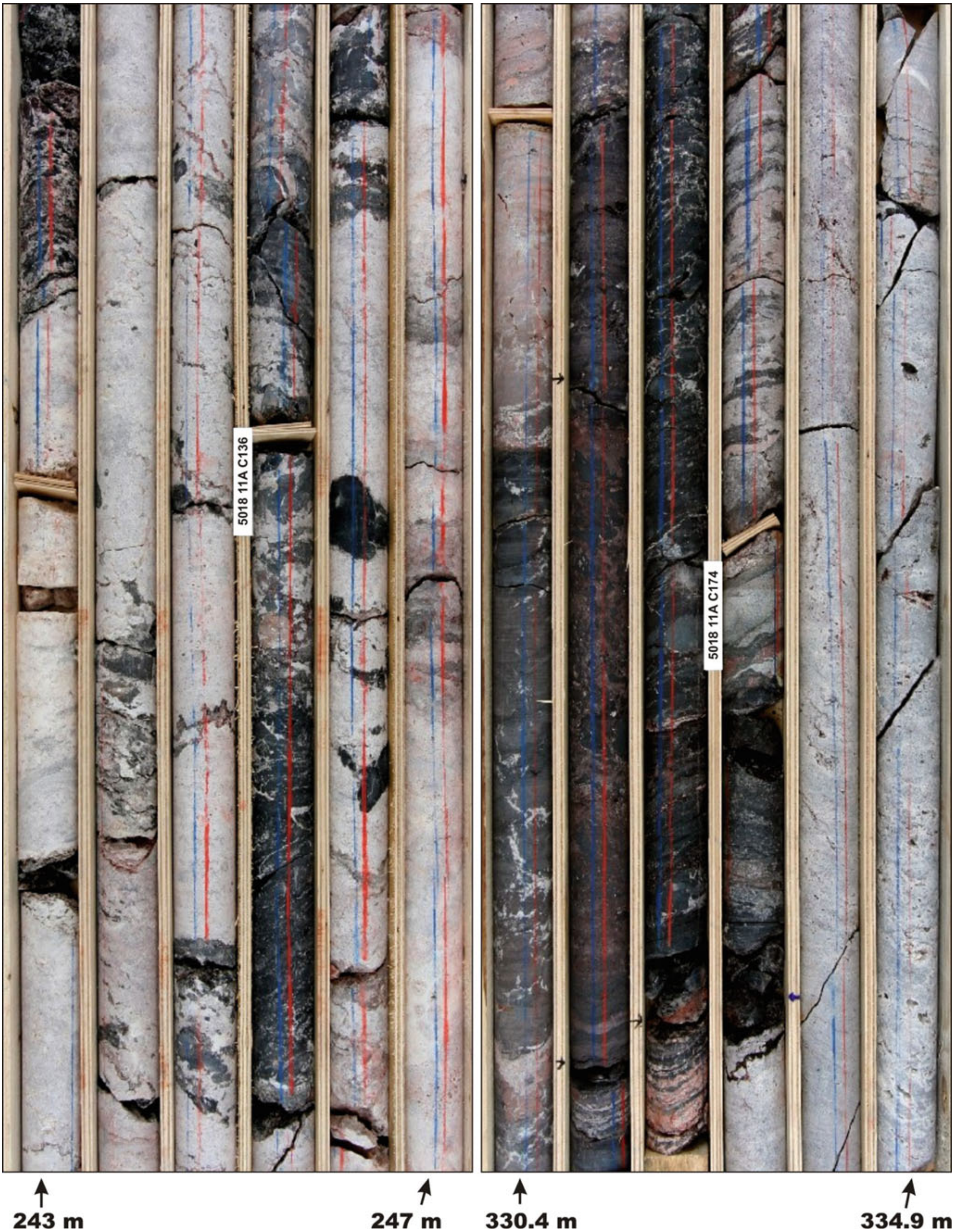

Fig. 6.110 Dolostone-dolomarl/shale cycles (continued) (Photographs from the FAR-DEEP data base (http://far-deep.icdp-online.org))

Fig. 6.111 Greywackes of the Zaonega Formation showing erratic, progressive oxidation and reddening towards the contact with the underlying Tulomozero "red beds" (Photographs from the FAR-DEEP data base (http://far-deep.icdp-online.org))

References

Akhmedov AM, Krupenik VA, Makarikhin VV, Medvedev PV (1993) Carbon isotope composition of carbonates in Early Proterozoic sedimentary basins. In: Published report of the institute of geology. Institute of Geology, Karelian Research Centre of RAS, Petrozavodsk, p 56, (in Russian)

Brasier AT, Fallick AE, Prave AR, Melezhik VA, Lepland A, FAR-DEEP Scientists (2011) Coastal sabkha dolomites and calcitised sulphates preserving the Lomagundi-Jatuli carbon isotope signal. Precambrian Res 189:193–211

Bogli J (1980) Karst hydrology and physical speleology. Springer-Verlag, Berlin, p 285

Galdobina LP (1987) The Ludicovian Super-Horizon. In: Sokolov VA (ed) Geology of Karelia. Nauka (Science), Leningrad, pp 59–67, (in Russian)

Heiskanen KI, Rychanchik DV (1999) The Jatulian, Early Proterozoic, carbonates with anomalously heavy carbon of the Baltic Shield. Stratigr Geol Correl 7(6):14–19, (in Russian)

Karhu JA (1993) Palaeoproterozoic evolution of the carbon isotope ratios of sedimentary carbonates in the Fennoscandian Shield. Bull Geol Surv Finland 371:1–87

Karhu JA, Holland HD (1996) Carbon isotopes and the rise of atmospheric oxygen. Geology 24:867–879

Krupenik VA, Akhmedov AM, Sveshnikova KY (2011) Isotopic composition of carbon, oxygen and sulphur in the Ludicovian and Jatulian rocks. In: Glushanin LV, Sharov NV, Shchiptsov VV (eds) The Onega Palaeoproterozoic structure (geology, tectonics, deep structure and minerageny). Institute of Geology, Karelian Research Centre of RAS, Petrozavodsk, pp 172–189, (in Russian)

Makarikhin VV (1992) Lower Precambrian stromatolite associations of Karelia. In: Schidlowski M, Golubic S, Kimberley MM, McKirdy DM, Trudinger PA (eds) Early organic evolution. Springer, Berlin, pp 463–467

Medvedev P, Bekker A, Karhu JA, Kortelainen N (2005) Testing the biostratigraphic potential of early Paleoproterozoic microdigitate stromatolites. Rev Esp Micropaleontol 37:41–56

Medvedev PV, Makarikhin VV, Golubev AI, Rychanchik DV, Trofimov NN (2011) The Jatuli. In: Glushanin LV, Sharov NV, Shchiptsov VV (eds) The Onega Palaeoproterozoic structure (geology, tectonics, deep structure and minerageny). Institute of Geology, Karelian Research Centre of RAS, Petrozavodsk, pp 52–67, (in Russian)

Melezhik VA, Fallick AE (1996) A widespread positive $\delta^{13}C_{carb}$ anomaly at around 2.33–2.06 Ga on the Fennoscandian Shield: a paradox? Terra Nova 8:141–157

Melezhik VA, Fallick AE, Rychanchik DV, Kuznetsov AB (2005) Palaeoproterozoic evaporites in Fennoscandia: implications for seawater sulphate, $\delta^{13}C$ excursions and the rise of atmospheric oxygen. Terra Nova 17:141–148

Negrutsa VZ (1984) Early Proterozoic stages of evolution of the eastern Baltic Shield. Nedra, Leningrad, p 270, (in Russian)

Ovchinnikova GV, Kusnetzov AB, Melezhik VA, Gorokhov IM, Vasil'eva IM, Gorokhovsky BM (2007) Pb-Pb age of Jatulian carbonate rocks: the Tulomozero Formation in south-eastern Karelia. Stratigr Geol Correl 4:20–33, (in Russian)

Philippov NB, Trofimov NN, Golubev AI, Sergeev SA, Huhma H (2007) New geochronological data on the Koikary-Svjatnavolok and Pudozhgora gabbro-dolerite intrusives. In: Golubev VI, Shchiptsov VV (eds) Geology and mineral resources of Karelia, vol 10. pp 49–68, Karelian Research Centre, Petrozavodsk, (in Russian with English abstract)

Reuschel M, Melezhik VA, Whitehouse MJ, Lepland A, Fallick AE, Strauss H (2012) Isotopic evidence for a sizeable seawater sulfate reservoir at 2.1 Ga. Precambrian Res 192–195:18–88

Satzuk YI, Makarikhin VA, Medvedev PV (1988) Jatulian geology of the Onega-Segozero Watershed. Nauka (Science), Leningrad, p 96, (in Russian)

Sun S-S, McDonough WF (1989) Chemical and isotopic systematics of oceanic basalts: implications for mantle composition and processes. In: Saunders AD, Norry MJ (eds) Magmatism in the ocean basins. vol 42, Geological Society special publication. Published for the Geological Society by Blackwell Scientific Publications, Oxford [Oxfordshire]/ Boston, pp 313–345

Tikhomirova M, Makarikhin VV (1993) Possible reasons for the δ13C anomaly of Lower Proterozoic sedimentary carbonates. Terra Res 5:244–248

Tosca NJ, Macdonald FA, Strauss JV, Johnston DT, Knoll AH (2011) Sedimentary talc in Neoproterozoic carbonate successions. Earth Planet Sci Lett 306:11–22

Yudovich YE, Makarikhin VV, Medvedev PV, Sukhanov NV (1991) Carbon isotope anomalies in carbonates of the Karelian Complex. Geochem Int 28:56–62

6.3.3 Zaonega Formation: FAR-DEEP Holes 12A and 12B, and Neighbouring Quarries

Alenka E. Črne, Victor A. Melezhik, Anthony R. Prave, Aivo Lepland, Alexander E. Romashkin, Dmitry V. Rychanchik, Eero J. Hanski, and Zhen-Yu Luo

Scientific Targets

- Tectonic and depositional settings associated with enhanced accumulation of organic matter
- Cause-and-effect relationship between the Lomagundi-Jatuli and Shunga Events
- Geochemical rock record during the Shunga Event
- Petrified oil field: oil generation and migration
- Source rocks and carbon-isotope composition of primary biomass
- Pathways in recycling of organic matter
- Carbon, sulphur and strontium isotopic composition of seawater
- Provenance composition
- Microfossil record
- Search for biomarkers
- Radiometric age constraint on timing of deposition
- Geochemical interaction between igneous rocks and C_{org}-rich sediments
- Anomalous fractionation of sulphur isotopes during thermochemical sulphate reduction

Holes 12A and 12B are located in the Palaeoproterozoic Onega Basin (Figs. 6.1 and 6.86) and targeted the Zaonega Formation, which is c. 900-m-thick and consists of immature siliciclastic rocks, limestones, dolostones, cherts, mafic tuffs and basalts, all of which are intruded by gabbroic sills. There is also abundant diagenetic carbonate, some in the form of ^{13}C-depleted concretions that provide evidence for the onset of modern recycling of organic matter (Fallick et al. 2008). The most remarkable feature, though, is an exceptionally high accumulation of organic material (Galdobina 1993; Filippov 1994; Fig. 6.112) in the form of C_{org}-rich rocks that record the global Shunga Event (Melezhik et al. 1999, 2009) and one of the geologically earliest and most volumetrically significant generation of petroleum in the form of a petrified oil field (Melezhik et al. 2009). The depositional age of the Zaonega Formation remains poorly constrained and is currently bracketed by a Pb–Pb isochron date of 2090 ± 70 Ma for dolomite of the underlying Tulomozero Formation (Ovchinnikova et al. 2007) and a Sm-Nd age of 1980 ± 27 Ma obtained from a mafic-ultramafic sill intruding Zaonega Formation volcanic rocks (Puchtel et al. 1992, 1998, 1999). Consequently, it remains unresolved whether or not the Shunga Event may partially overlap in time with the Lomagundi-Jatuli positive isotopic excursion of carbonate carbon (reviewed in Melezhik et al. 1999; Fig. 6.87), the end of which has been constrained to c. 2060 Ma in the Fennoscandian Shield (Karhu 2005; Melezhik et al. 2007).

The cored material offers a unique opportunity to investigate the conditions leading to enhanced accumulation of organic matter, and to assess possible mechanisms and processes of petroleum generation and migration. The carbonate- and S-rich rocks have potential for reconstruction of isotopic composition of Palaeoproterozoic seawater, whereas abundant diagenetic carbonates in the form of cements and concretions enable addressing the Palaeoproterozoic carbon cycle with emphasis on recycling of organic matter. High abundances of organic matter (up to 50 wt.%; Melezhik et al. 1999) in a variety of deposits including detrital sediment and chemical precipitates, combined with a low-grade metamorphic alteration under greenschist-facies conditions (Volodichev 1978), could represent conditions that preserve primary biomarkers. Providing a better depositional age constraint is obtained, the causative relationship between the Shunga and Lomagundi-Jatuli events may be resolved. Numerous gabbro bodies intruded into C_{org}-rich sediments may have triggered extensive hydrothermal circulation resulting in interaction between organic matter in sediments and sulphate-rich hydrothermal fluids. Hence, the anomalous fractionation of sulphur isotopes during thermochemical sulphate reduction observed in a laboratory experiment (Watanabe et al. 2009) could perhaps be tested in a natural environment.

The stratigraphy and geochemistry of the Zaonega Formation has been the subject of extensive previous research (reviewed in Filippov 1994, 2002; Melezhik et al. 1999, 2004). The Zaonega Formation has been divided into a lower part dominated by shales (Galdobina 1987) and an upper part, which has been further subdivided into Members A, B and C (Melezhik et al. 1999). Member A comprises rocks rich in albite and chlorite, therefore named as 'sodic series', Member B contains rock rich in quartz, sericite and biotite, therefore named as 'potassic series' (Filippov 1994; Melezhik et al. 1999), and Member C contains rocks rich in quartz, biotite and chlorite (Galdobina 1987). It has been reported that Members A and B contain nine C_{org}-rich horizons ranging in thickness from 8 to 120 m (Galdobina 1987). Three horizons (1–3) are located in Member A, whereas member B contains six horizons (4–9). The sixth, and thickest, horizon, is also known as the 'Productive horizon' as it contains commercially exploited organic- and silica-rich rocks locally termed "maksovite".

A.E. Črne (✉)
Geological Survey of Norway, Postboks 6315 Sluppen, NO-7491 Trondheim, Norway

V.A. Melezhik et al. (eds.), *Reading the Archive of Earth's Oxygenation*, Volume 2: The Core Archive of the Fennoscandian Arctic Russia – Drilling Early Earth Project, DOI 10.1007/978-3-642-29659-8_4, © Springer-Verlag Berlin Heidelberg 2013

The Zaonega Formation is known worldwide for its C_{org}-rich rocks, which have been termed “shungite” (Filippov 1994; Buseck et al. 1997; Melezhik et al. 1999; Kovalevski et al. 2001; Melezhik et al. 2004). However, this term has been defined and used differently by various researchers; some have restricted its usage to fossilised migrated bitumen (Inostranzev 1885, 1886; Melezhik et al. 2004) whereas others have applied it to all C_{org}-bearing rocks in the Zaonega and Kondopoga Formations (Borisov 1956). Filippov and Melezhik (2007) devised a more specific definition, largely limited to the rocks in the eponymous type area. Thus the term “shungite” is not used herein. Instead, the common term 'C_{org}-rich rocks' has been utilised for rocks consisting of residual kerogen and migrated bitumen mixed in various proportions.

The Zaonega Formation

Holes 12A and 12B are 99.57 m and 411.46 m long, respectively. They overlap at a depth interval of 92.80–99.57 m, resulting in a total stratigraphic thickness of 504 m (Fig. 6.113). Although the cores obtained from these two holes represent by far the most complete, continuous record of the Zaonega Formation, neither the lower nor the upper formational contacts have been intersected. However, the lower 106-m-thick succession of the formation and its contact with the underlying Tulomozero Formation have been retrieved by Hole 11A (see Chap. 6.3.2). Consequently, more than 600 m of the Zaonega section are available for research.

The combined section of Holes 12A and 12B (in the following Hole 12AB and correspondingly Core 12AB) has been conventionally subdivided into four lithostratigraphic members, from bottom to top: Greywacke (499.07–250 m), Dolostone–Greywacke (250–179.7 m), Mudstone–Limestone (179.7–9.3 m), and Dolostone–Chert (9.3–1.6 m) members (Fig. 6.113). The succession is intruded by gabbro and contains a series of mafic lava flows. Four intervals with massive to indistinctly laminated rocks enriched in total C_{org} (analysed as total organic carbon; 23–41 wt.%) have been identified at depths of 489.48–487.2 m, 413.6–403.5 m, 156–132.9 m, and 56–31 m (Fig. 6.113).

Chemical composition of all analysed archive samples is presented in Appendices 35–40, and Fig. 6.114 shows stratigraphic profiles of selected major and trace elements as well as magnetic susceptibility. Most sedimentary rocks within the Greywacke member are characterised by a moderate magnetic susceptibility of 2,644 μSI on average (average $K^* = 226 \times 10^{-6}$, Fig. 6.114). High values of up to 44,472 μSI ($K^* = 3{,}801 \times 10^{-6}$ in Fig. 6.114) are only present below and above the large gabbro body (493–484 m; 414–405 m) and low values with an average of 34 μSI ($K^* = 2.9 \times 10^{-6}$) occur within the uppermost metres of the member (262–250 m). Other sedimentary rocks in Core 12AB, except for the middle part of the Dolostone-Greywacke member (maximum of 6,283 μSI; $K^* = 537 \times 10^{-6}$ in Fig. 6.114), have low magnetic susceptibility. Figure 6.115 illustrates the main geochemical features of the igneous rocks. Core photos provide detailed documentation of the major lithological features of sedimentary and volcanic rocks (Fig. 6.116).

The Greywacke Member

The lower contact of the Greywacke member has not been recovered, and the lowermost part of the core in Hole 12B (504–498 m) is an igneous mafic body (defined as magmatic Unit A). The member is 178 m thick (498–250 m; excluding a 70-m-thick gabbro body defined as magmatic Unit B), and consists mostly of rhythmically interbedded greywacke and mudstone. Also present are calcareous greywackes, sandy limestones, minor intraformational matrix-supported conglomerates and breccias, and some cherts. Black, C_{org}-rich, massive to indistinctly laminated rocks occur at 489.5–487.2 and 413.6–403.4 m. Thicker magmatic bodies are present as both intrusions and lava flows and are identified as separate magmatic units (a gabbro intrusion comprises Unit B whereas mafic flows constitute Units A and C; Fig. 6.113).

Rhythmically interbedded and interlaminated greywackes and mudstones, with bed thicknesses ranging from thin laminae to several decimetres, are the dominant lithology (Figs. 6.116di, dl, do, ds–dz, ee, ef, eh, ei, ep, es, et). Bed contacts are commonly flat and sharp, very rarely locally channelised (Fig. 6.116eo). The greywacke beds are mostly fine-grained and rarely medium-grained (Fig. 6.116ek) and typically normally graded (Figs. 6.116dl, ds). The lowermost 5-m-thick interval of greywackes (at a depth of 498 m) is distinctive in that they are thinly laminated (Figs. 6.116fx–ga). Mudstones are dark-grey to black and range in thickness from partings (Figs. 6.116dy, et) to as much as 0.5 m, with many of the thicker beds displaying flat laminae (Figs. 6.116di, dm, ft, fu, fw). Some mudstones contain up to 10 wt.% $CaCO_3$, in places in the form of fine- to medium-sized grains of calcite (Fig. 6.116ew). In general, the thickness and abundance of mudstone increases up-section in the upper part of the Greywacke member and at two depth intervals, 493–484 and 255–250 m, mudstones dominate. For the majority of the member, though, the greywackes and the mudstones occur as thin, fining-up beds with the ratio of greywacke to mudstone usually 1:1 or higher. In some places, greywacke beds are amalgamated and form packages as much as 80 cm thick.

Some greywacke layers and beds are enriched in calcite and are termed calcareous greywackes ($10 \leq$ wt.% of $CaCO_3 < 50$), whereas beds with higher carbonate content are termed sandy limestones ($50 \leq$ wt.% of $CaCO_3 < 90$). The former mostly occur as the basal part of greywacke-mudstone beds (Figs. 6.116dn, do). In places, calcareous greywackes and sandy limestones form individual beds up to 30 cm thick (Figs. 6.116eu, ez–fc, fe, fg), which can be either massive, flat laminated or, very rarely, low-angle cross-laminated and locally amalgamated to form intervals as much as 3 m thick. Thicker beds of sandy limestones (Fig. 6.116da) are more abundant within the uppermost part of the member.

Several intervals of intraformational, matrix- and clast-supported conglomerates have been documented at various depths. The lowermost interval appears as an intraformational, matrix- to clast-supported breccia at 409–403.4 m. It contains a variety of clasts (carbonate rocks, mudstones, C_{org}-rich rocks, and completely pyritised clasts; Figs. 6.116fb–fd, fi–fk, fl) embedded in a massive C_{org}-rich (up to 27 wt.% C_{org}) matrix.

Another interval of fragmental rocks occurs at 305.9–304.1 m. Here, two thick superposed greywacke beds contain unsorted, angular, intraformational clasts of greywacke, mudstone and calcareous greywacke, as much as a few centimetres in size, floating within a finer greywacke matrix (Figs. 6.116dw, dx). The lower bed is 88 cm thick and the other one is 23 cm thick and both are capped by black, cross to parallel-laminated mudstone; the lower bed displays an erosional lower contact.

From 295.9 to 290.6 m, intraformational, matrix-supported conglomerates (individual beds are 0.6–1.1 m thick) occur interbedded with greywacke-mudstone units (Figs. 6.116dq, dr). These beds have gradational lower contacts with the underlying greywackes and contain soft-sediment-deformed (Fig. 6.116dq), rounded to irregularly shaped, elongate clasts up to a few centimetres in size (Fig. 6.116dr). Clasts of greywacke, calcareous greywacke, pyrite grains and pyritised rocks float in a sandy mudstone matrix. From 254 to 250 m, four discrete mudstone beds (5–60 cm thick) occur, in which angular clasts of intraformational mudstones, C_{org}-rich mudstones and/or angular clasts of greywackes and sulphide concretions are scattered in a brownish (Fig. 6.116cz) or black, C_{org}-rich matrix.

Two intervals of C_{org}-rich rocks are worth highlighting. One, at 489.5–487.5 m, is 2 m thick and characterized by a massive structure. It has no direct contact with the 70-m-thick gabbroic body igneous body that occurs 3.5 m above, but contains possible peperite (Fig. 6.116fv) and has gradational contacts with encasing laminated mudstones (Figs. 6.116fu–fw). The other interval is at 413.6–403.4 m, is 10.1 m thick, displays a massive structure and has a sharp contact with the gabbro beneath it; pyrobitumen-rich veins cross-cut both the massive, C_{org}-rich rock and the gabbro (Figs. 6.116fn, fo). The lower 4.6 m of this interval is massive with some intervals exhibiting pyritised, polygonal cracks (Fig. 6.116fm), whereas the overlying portion is breccia alternating with bedded sandy limestones, calcareous greywackes and greywackes (Figs. 6.116fb–fd, fi–fk, fl); the breccia has a massive, C_{org}-rich matrix.

Other minor lithologies of the member include chert occurring irregularly throughout the section (mostly as a few-cm to as much as 50-cm-thick layers alternating with interbedded greywackes and mudstones), and a 55-cm-thick tuff bed at 401.4 m with irregular and sharp lower and upper contacts.

The overall rhythmically bedded pattern of the Greywacke member rocks is disturbed by abundant soft-sediment deformation features. Numerous beds display sliding and slumping structures (Figs. 6.116ej, en), broken and disrupted laminae (Figs. 6.116eb, ec), and convolute laminations (Figs. 6.116ea, ei, el, em). Loading structures and sedimentary dykes have also been observed (Figs. 6.116er, fg, fh), as well as incipient and advanced diagenetic and/or sedimentary boudinage affecting mudstone-hosted calcareous greywacke beds (Figs. 6.116dd, df). In many instances, the intensity of soft-sediment deformation features in all lithologies increases with stratigraphic proximity to the magmatic units.

Structural expression of diagenetic modification of the Greywacke member sediments is recorded in abundant diagenetic carbonate concretions (particularly in the uppermost part of the member), some as much as 35 cm across (Figs. 6.116dg, dh, dj, dk), and layers (Figs. 6.116ex, ey, ez). Diagenetic chert nodules are present within the uppermost metres of the member. Diagenetic disseminated sulphide, sulphide laminae (Figs. 6.116de) and centimetre-size sulphide concretions, some showing soft-sediment deformation (Figs. 6.116db, dc), are common throughout the member.

Migration of oil through partially compacted sediments is recorded in ptygmatic, pyrobitumen-rich veins. They are most abundant in sedimentary rocks immediately above the upper C_{org}-rich interval (403.4–395 m; Figs. 6.116ew, ez, fa), and within the mudstone packages of the upper part of the member (280–250 m; Figs. 6.116df, di, dm, do, dp). Later generations of veins have sharp side-walls and a composite infill composed of calcite, biotite, albite, quartz, sulphide and pyrobitumen. Different generations of sulphides and carbonates, including sulphide porphyroblasts and numerous calcite seams (Figs. 6.116dt, du, eq, ff), are abundant throughout the member.

Bulk analyses of greywackes and interlaminated greywackes and mudstones (Appendices 38–40) show variable SiO_2 (38.1–46.1 wt.%), Al_2O_3 (13.2–17.1 wt.%) and MgO (6.2–12.2 wt.%) contents. They are rich in Fe_2O_{3T} (14.5–20.4 wt.%) and Na_2O ($Na_2O/K_2O = 4.6$) and contain from 0.3 to 4 wt.% of C_{org}. Albitised greywackes occurring within the lowermost metres of the member show a Na_2O content reaching 7.7 wt.%. Mudstones contain 1–6.3 wt.% Al_2O_3 and are extremely enriched in C_{org} (5.4–27.1 wt.%). These rocks were affected by silicification (SiO_2 = 54–77.4 wt.%) or, alternatively, they represent clayey cherts. One analysed sample of pure chert (SiO_2 = 80.8 wt.%; Al_2O_3 = 1 wt.%) contains 5.7 wt.% C_{org}. Intraformational, matrix-supported conglomerates are geochemically similar to greywackes (Al_2O_3 = 13.8 wt.%; Fe_2O_3 = 16.1 wt.%; MgO = 9.7 wt.%), but have a higher C_{org} content (6.5 wt.%). Limestones and sandy limestones contain 45–90 wt.% of $CaCO_3$ (IC = 5.6–11 wt.%), with the rest being comprised of silica (3.6–24 wt.%), aluminium (1–8 wt.%) and magnesium (1.2–2.9 wt.%). Apart from high amounts of SiO_2 (39.7 wt.%) and C_{org} (34.6 wt.%), the rocks of the upper C_{org}-rich interval contain 9.6 wt.% Al_2O_3, 4.9 wt.% Fe_2O_{3T}, 3.9 wt.% Na_2O and 1.6 wt.% MgO.

The Dolostone-Greywacke Member

This member is 70 m thick (250–179.7 m) and begins with the first occurrence of dolostone; in the core this is a 70-cm-thick bed that is massive except for being laminated in its lowermost part. The main lithologies of the member are dolostones, sandy dolostones, and commonly rhythmically interbedded greywackes and mudstones. Also present are calcareous greywackes, marls, a bed of intraformational, matrix-supported conglomerate at 201.3 m and a mafic tuff bed at 234.9 m.

Dolostones and sandy dolostones occur as several-metres-thick, flat-laminated layers (Figs. 6.116ct, cu, cx) or as metre-thick, massive beds (Figs. 6.116co, cp, cv, cw, ct); the latter have gradational contacts with underlying mudstone (Fig. 6.116cx). Dolostones and sandy dolostones are the dominant lithology within the lower part of the member, and their thickness and abundance decrease up-section. In the middle and upper part of the member dolostone beds (up to 50 cm thick) are sporadically present; mostly they are massive, but also faintly parallel laminated (Figs. 6.116bp, bq, bv).

Rhythmically interbedded and interlaminated greywackes and mudstones contain thicker, generally normally graded beds of greywackes (Figs. 6.116cf, cg, ch) and flat laminated mudstones. Amalgamated, yellowish and brownish greywacke beds form up to 50-cm-thick packages (Figs. 6.116ci–cn). Greywackes are mostly flat-laminated, rarely cross-bedded, and commonly contain mm-scale carbonate-rich patches (Figs. 6.116bs, ci, cm). Rhythmically interbedded and interlaminated greywackes and mudstones are rare in the lower part of the member, but their abundance increases up-section and they are the dominant lithology in the upper part of the member (Figs. 6.116ce, cf). Thicker packages of mudstones are present in the lowermost part of the member where they alternate with massive dolostones. Otherwise, the abundance and thickness of mudstone generally increase up-section with the thickest mudstone intervals being present at the top of the member (Figs. 6.116bn, bm).

Some greywacke layers and beds are enriched in calcite and therefore termed calcareous greywackes. Beds of calcareous greywackes are up to 50 cm thick, normally graded, and typically interbedded with mudstones (Figs. 6.116bw–bz, cq–cs). Together with marls, calcareous greywackes are more abundant in the upper part of the member (Figs. 6.116bo, bp, br–bu).

The intraformational, matrix-supported conglomerate bed at 201.3 m has a sharp, erosional contact with the underlying greywackes. It contains various unsorted, angular to rounded clasts, from a few mm to more than 10 cm in size, that are composed of greywackes, mudstones, sandy limestones and C_{org}-rich rock; these float in a mudstone matrix (Figs. 6.116bz–cd).

A single bed of mafic tuff documented at a depth of 234.9 m is more than 1 m thick and topped by a cross-laminated mudstone bed.

Similarly to the Greywacke member, the rhythmically bedded pattern of the greywacke-mudstone within the Dolostone-Greywacke unit is disturbed by soft-sediment deformation throughout the section; these features are mostly due to synsedimentary faulting (Figs. 6.116cj, bn, bo) and slumping (Fig. 6.116cn). Oil migration in partially compacted rocks is manifested by ptygmatic, pyrobitumen-rich veinlets and veins; they are particular abundant within sections of dolostones and sandy dolostones (Figs. 6.116bp, bq, bu, bv, co, cp). Different generations of sulphides are abundant throughout the Dolostone-Greywacke member and occur as diagenetically formed disseminations and concretions (Figs. 6.116bm–bo, bt, bx, by, co–cq). Later generations of sulphides, in the form of straight veinlets, are mostly present in the lower and upper parts of the member.

Dolostones and sandy dolostones have a Mg:Ca ratio ranging from 0.43 to 0.63 and contain from 73 to 89 wt.% $MgCa(CO_3)_2$ (IC = 9.5–11.6 wt.%), some SiO_2 (2.6–11.6 wt.%) and Al_2O_3 (0.4–4.2 wt.%), and C_{org} (0.2–4.3 wt.%). Greywackes contain 48.9–62.6 wt.% SiO_2 and show variable contents of Al_2O_3 (9.2–18.5 wt.%), MgO (4.3–7.6 wt.%), K_2O (1.4–4.7 wt.%) and Na_2O (1.1–3.5 wt.%). The total iron content shows a limited variation ranging between 10.1 and 13.8 wt.% Fe_2O_{3T}. Greywackes contain a sizable amount of C_{org} (0.1–2.3 wt.%), but less than that of the greywackes of the Greywacke member, and, relative to that member, are relatively enriched in potassium but depleted in sodium. The mudstones (SiO_2 = 45.4–58.7 wt.%; Al_2O_3 = 6.8–11.4 wt.%) are calcareous, contain up to 28 wt.% $CaCO_3$ (IC = 1.1–3.3 wt.%) and are C_{org}-rich (5.8–11.6 wt.%).

The Mudstone-Limestone Member

This member is 170 m thick (179.7–9.3 m). Its lower contact with the Dolostone–Greywacke member is gradual and defined where mudstones become the dominant lithology. The main lithologies are mudstones, sandy limestones and calcareous greywackes. Also present are rhythmically interbedded greywackes/calcareous greywackes/sandy limestones and mudstones/calcareous mudstones, marls, and sandy dolostones. Other rock types include a breccia bed at 19.2 m, an intraformational, matrix-supported conglomerate at 9.4 m, and few cherts intervals. Black, C_{org}-rich massive to indistinctly laminated rocks occur at 156–132.9 and 56–31 m. Igneous rocks are represented by mafic lava flows comprising two units (D and E) in the middle part of the member at depths of 119–113 and 95–45 m.

Mudstones are the dominant lithology (Figs. 6.116ac, ao, aq, as, at, bh) and occur as thin laminae to 11-m-thick, flat-laminated packages that contain minor beds (up to 6 cm thick) of greywacke, some of them with dolomite or calcite grains. Within the uppermost 17 m of the member (26–9.3 m) mudstones become brownish, flat-laminated (Figs. 6.116c, g, i–k), pyrobitumen-rich (Figs. 6.116r) and contain chert layers and nodules as much as 16 cm in size (Figs. 6.116p, q, s–v, x), soft-sediment deformed greywacke laminae and layers (Figs. 6.116h–j).

Sandy limestones (Figs. 6.116w, y–aa, aw), calcareous greywackes (Figs. 6.116ax, ay) and rare sandy dolostones are typically a few decimetre-thick and indistinctly laminated, but can also be massive with predominantly gradational contacts with the encasing mudstones and carbonate mudstones (Figs. 6.116ab, ad); a few sharp contacts also exist (Figs. 6.116l, ap, ax). Thicker sandy limestones (Fig. 6.116ap) are more abundant in the uppermost part of the member (31–9.7 m; Figs. 6.116l, n, w, y–aa), and a few beds have gradual upper contacts with mudstones, defining a sandy limestone-marl-mudstone rhythm (Fig. 6.116bi). Greywackes (Figs. 6.116ar, ay), calcareous greywackes (Fig. 6.116ad) and sandy limestones (Fig. 6.116m, ax) are commonly rhythmically interbedded on a centimetre to decimetre scale with mudstones or calcareous mudstones.

Rhythmically interbedded greywackes/calcareous greywackes/sandy limestones and mudstones/calcareous mudstones are common in the lower and middle part of the member. Greywackes, calcareous greywackes and sandy limestones are commonly flat-laminated; only few greywacke beds are cross-bedded (Fig. 6.116ar). Numerous ‘clay balls’ up to 2 cm in size occur within several thin greywacke beds in the lowermost 20 m of the member (Figs. 6.116bf, bg).

A 1-m-thick breccia bed is present at 19.2 m, and an intraformational conglomerate of a similar thickness occurs at 9.4 m. The breccia is clast-supported and mostly contains large (typically greater than 10 cm) angular fragments of limestones (Figs. 6.116n–p) and subordinate mudstone clasts and chert nodules, all in a brownish C_{org}-rich matrix. The contact of the breccia with the overlying laminated limestone, which is intersected by pyrobitumen veinlets, is gradual with the amount of matrix gradually decreasing up-section.

The intraformational conglomerate is matrix-supported and occurs at the top of the member. It contains mostly angular clasts of greywacke (some as large as 5 cm), some with deformed and broken laminae, and subordinate angular fragments of mudstone (up to 1 cm in size), all floating within a brownish, C_{org}-rich matrix (Figs. 6.116d–f). The upper and lower contacts are gradational with the encasing brownish, laminated, C_{org}-rich mudstones – the proportion of clasts and the degree of deformation of greywacke laminae gradually increases at the lower contact and decreases at the upper contact.

Chert occurs as white or black layers and beds up to 16 cm thick (Figs. 6.116p, q, t, u) and as black nodules (Figs. 6.116s, v, x) within the uppermost 17 m of the member.

Two C_{org}-rich intervals are worth highlighting (156–132.9 and 56–31 m). The lower interval is marked by a massive structure, whereas the upper one has indistinct lamination and a less massive structure. The lower interval (Figs. 6.116az–be) is 23.1 m thick (156–132.9 m) and consists of three different occurrences of C_{org}-rich rocks, described below in stratigraphical order, from bottom to top.

The first occurrence is represented by massive, C_{org}-rich rock forming the lowermost 17.2 m of the interval. It is in sharp contact with the underlying limestone-bed (Fig. 6.116be) and contains several rounded, pyrobitumen-rich intraclasts, up to a few centimetres in size, and clasts of siltstones a few millimetre in size (Fig. 6.116bd).

The second occurrence is in a 2.9-m-thick unit as several layers of brecciated, C_{org}-rich rock (18–55 cm thick). They consist of irregular, soft-sediment deformed, C_{org}-rich clasts surrounded by a mudstone matrix (Fig. 6.116bc) and alternate with soft-sediment deformed, laminated mudstones (a few cm to 50 cm thick, Figs. 6.116bb, bc). Contacts between C_{org}-rich rock and mudstones are sharp and depositional. Some mudstone beds contain pyrobitumen-rich clasts typically a few centimetres in size (Fig. 6.116ba). The uppermost bed of brecciated, C_{org}-rich rock at 136 m is overlain by a laminated mudstone (Fig. 6.116az), passing up-section gradually into rhythmically bedded mudstones and greywackes.

The third occurrence (133.70–132.90 m) is an 80-cm-thick vein (the thickest vein within the drilled Zaonega Formation) of massive, C_{org}-rich rock. This vein cross-cuts the rhythmically bedded mudstones and greywackes and marks the topmost part of the lower C_{org}-rich interval.

The upper C_{org}-rich interval (56–31 m; Fig. 6.116ae–al) is 25 m thick and is in sharp contact with the underlying 37-m-thick lava flow (Fig. 6.116al). This interval consists of indistinctly laminated (Fig. 6.116af), in places massive (Fig. 6.116ae, aj) or brecciated (Fig. 6.116ak), C_{org}-rich rocks alternating with lava flows and a few thin limestone beds. The uppermost contact of the interval with the overlying C_{org}-rich mudstones is gradual.

Abundant soft-sediment deformation features characterise the Mudstone-Limestone member in the uppermost metres. These consist of slumps (Fig. 6.116f), broken greywacke laminae (Figs. 6.116h, j) and loading structures (Fig. 6.116s) within a brownish-blackish, C_{org}-rich mudstone. Migration of oil in partially compacted rocks is manifested by ptygmatic, pyrobitum-rich veinlets. They are abundant within the thicker sandy limestones and mudstones of the upper part of the member (Figs. 6.116l, w, y). Bedding-parallel, pyrobitumen-rich seams are also present (Fig. 6.116r). Both pyrobitumen-rich (Fig. 6.116r) and composite veinlets commonly have sharp side-walls. Diagenetic, disseminated sulphides are pervasive in places (Fig. 6.116ah), and diagenetic sulphide concretions (Figs. 6.116ab, ac, ap) occur throughout and especially in the lower part of the member (Figs. 6.116bh–bk).

Mudstones and calcareous mudstones (Al_2O_3 = 4.4–14.1 wt.%; SiO_2 = 50.8–66 wt.%) contain up to 13 wt.% $CaCO_3$ (IC = 0.1–1.6 wt.%) and are rich in C_{org} (7.4–25.3 wt.%). Calcareous greywackes and sandy limestones contain from 38 to 67 wt.% $CaCO_3$ (IC = 4.6–8 wt.%; Mg/Ca = 0.09), and sandy dolostones from 63 to 80 wt.% $CaMg(CO_3)_2$ (IC = 8–10.4 wt.%; Mg/Ca = 0.4–0.5); both rock types are characterised by variable abundances of C_{org} (0.1–10.9 wt.%). Sandy limestones contain a significant amount of SiO_2 (17.2–31 wt.%) and MgO (3.7−9.3 wt.%) and a moderate amount of Al_2O_3 (1.7–3.3 wt.%). In contrast, the sandy dolostones contain less SiO_2 (8–13.1 wt.%) and Al_2O_3 (0.7–1.2 wt.%).

Marls (up to 48 wt.% $CaCO_3$; IC = 4.9–5.8 wt.%) are very siliceous (SiO_2 = 27–32.2 wt.%) and rich in C_{org} (6.5–10.8 wt.%) with the Al_2O_3 content ranging between 1.4 and 4 wt.%.

The lower C_{org}-rich interval includes rocks with high contents of C_{org} (32.8–40.7 wt.%) and SiO_2 (33.6–42.5 wt.%) and moderate concentrations of Al_2O_3 (5–8 wt.%) and Fe_2O_3 (2.5–6.9 wt.%). K_2O content fluctuates between 1.8 and 3 wt.% and that of MgO between 0.8 and 2.4 wt.%. In contrast, the rocks of the upper C_{org}-rich interval contain less C_{org} (23–26.7 wt.%) and more SiO_2 (57–62.8 wt.%). However, concentrations of Al_2O_3 (4.1–5.4 wt.%), Fe_2O_3 (0.8–6.4 wt.%), K_2O (1.2–2.6 wt.%) and MgO (0.9–1.1 wt.%) are rather similar in the rocks of both intervals.

The 80-cm-thick, C_{org}-rich vein shows high abundances of several trace elements: 376 ppm Mo, 53.3 ppm U, 1,730 ppm V and 510 ppm Ni. Their contents are more than ten times higher than in any other rocks within the Zaonega Formation.

The Dolostone-Chert Member

This member forms the uppermost part of the Hole 12AB section and its intersected thickness is 7.7 m (9.3–1.6 m). The lower contact with the Mudstone-Limestone member is sharp and is placed at the first massive dolostone bed. The lithologies present in the drillcore include dolostones, cherts, and a bed of dolostone breccia at 4 m.

The dolostone units range in thickness from 0.76 to 3.3 m. The rocks are massive, except for the lowermost layer which is laminated at its base (Fig. 6.116c). This layer is cut by pyrobitumen-rich veinlets (Fig. 6.116c). Massive dolostones are interbedded with massive black cherts of similar thickness (1.05–1.72 m; Fig. 6.116b). The 0.5-m-thick dolostone breccia contains clasts of white dolostone and carbonate-mica spherules within a grey dolostone matrix (Fig. 6.116a). The breccia bed exhibits a gradational contact with the surrounding dolostones as the amount of clasts diminishes away from the lower and upper contacts.

An analysis of dolostone yielded 96 wt.% $CaMg(CO_3)_2$ (IC = 12.9 wt.%, Mg/Ca = 0.65), 2.9 % SiO_2 and 2.8 wt.% C_{org}, while that of chert gave 91 wt.% SiO_2 and 4.5 wt.% C_{org}.

Magmatic Units

Five mafic magmatic units, separated from each other by sedimentary rocks, are distinguished in Core 12AB and termed Units A, B, C, D and E (Fig. 6.113).

Unit A (504–498 m) occurs at the bottom of the core. The recovered 6-m-thick section is composed of mafic, medium-grained, massive rocks. The nature of the upper contact with the overlying rocks is not clearly seen in the core. We tentatively interpret the section to represent part of a lava flow.

Unit B (484–414 m) starts with a 1.1-m-thick, fine-grained mafic dyke (Figs. 6.116fr, fs), and is overlain by a 0.5-m-thick, sulphide-bearing sediment or tuff (Figs. 6.116fq, fr). The remaining 68 m consist of homogeneous mafic rocks that are medium-grained in the central part of the unit and become finer-grained towards the margins. A few, cm-scale black shale xenoliths are found in the uppermost part of the body. There are no clear volcanic structures in the unit, except for some uncertain amygdales in the uppermost zone. We tentatively interpret it as intrusive.

Chemically, Units A and B (interval 484–414 m) are similar and relatively primitive, having MgO in the range of 6.5–8.6 wt.% and Cr up to 230 ppm. These mafic rocks have a tholeiitic affinity, and moderate FeO_T and TiO_2 contents of 11.8–13.0 wt.% and 1.3–1.6 wt.%, respectively. There is a moderate degree of asymmetrical, vertical chemical fractionation within Unit B, with MgO (Fig. 6.115a) and Ni decreasing upwards and incompatible elements increasing upwards, suggesting *in-situ* differentiation of a horizontally emplaced, sill-like magmatic body.

Unit C (367–315 m; Figs. 6.116ed, eg, ei) is divided into three lava flows separated by two, c. 2-m-thick sedimentary interlayers (Figs. 6.116eg–ei). All three flows are slightly coarser textured in the central parts relative to the margins and contain a few amygdales close to their upper contact (Fig. 6.116ed).

Unit D (119–113 m; Figs. 6.116as–av) is formed by a single, 6-m-thick lava flow and exhibits the highest average value of the magnetic susceptibility compared with the other four igneous units. Small chlorite- and carbonate-filled vesicles are found in the upper part of the lava flow (Figs. 6.116au, av).

Unit E (95–45 m), the uppermost igneous section, is composed of six extrusive bodies separated by thin beds of C_{org}-rich rocks (Figs. 6.116ae–ag, aj–an). The most voluminous of the lava flows has a thickness of c. 37 m and contains a pillowed flow top and an amygdaloidal uppermost part. The other lava flows have smaller thicknesses ranging between 0.2 and 2.2 m. The flow top at 53.5 m is cut by a vertical crack filled with organic material (Figs. 6.116am, an).

Rocks comprising Units C, D and E are chemically evolved, tholeiitic, high-Ti basalts and basaltic andesites with MgO in the range of 4.4–5.6 wt.%. All lava flows from these units have high FeO_T, TiO_2, and V contents and differ in this respect from the underlying Units A and B. FeO_T and TiO_2 are highest in Unit C (16.6–17.5 and 2.6–3.1 wt.%, respectively), while in Unit E, FeO_T is 15.0–17.0 wt.% and TiO_2 ranges between 2.0 and 2.3 wt.%. As shown in Fig. 6.115b, the V content in Unit C is also very high (400–570 ppm) having no overlap with the V content of Unit E (300–400 ppm). Nb/Y is relatively low in all igneous samples from Core 12AB, falling in the range of 0.16–0.21 for Units A, C, D and E and 0.22–0.25 for Unit B (see Fig. 6.121), which is consistent with a subalkaline affinity of the rocks. The ratios are lower than those (0.56–0.72) published by Puchtel et al. (1998) for Zaonega Formation mafic lavas from the upper part of the Formation, indicating vertical geochemical heterogeneity of volcanic rocks in the Zaonega Formation. This also seems to apply for REE characteristics (see Chap. 3.4), though published REE data are limited.

Depositional Environment and Postdepositional Alteration

The lower part of the drilled Zaonega Formation corresponding to the Greywacke member is dominated by rhythmically interbedded, fine-grained greywackes and mudstones. These are interpreted as turbiditic Bouma sequences consisting of a normally graded greywacke base (Bouma T_a) and, rarely, cross-laminated, calcareous greywackes (Bouma T_c) passing into parallel-laminated mudstone tops (Bouma T_d). The fine-grained character of the rocks records turbidity current deposition either in a distal portion of the basin or reflects the fine-grained nature of sediments in the provenance. Thicker packages of mudstones, on the other hand, may represent background sedimentation.

The few matrix-supported, intraformational conglomerates and breccias, together with greywackes and mudstones containing angular clasts, are interpreted as debrites. These deposits, together with the slumped beds, loading structures, sedimentary dykes, and sedimentary/-diagenetic boudinage within the Greywacke member, could be taken as evidence for rapid sedimentation on an unstable slope. Slumped beds and debrites could also have been generated by earthquakes. Their increased frequency of appearance below and above mafic lava flows within the Greywacke member (Fig. 6.113) favours the latter interpretation and its association with submarine volcanism.

The origin of the carbonate associated with the Greywacke and Dolostone-Greywacke member remains currently unresolved due to pervasive recrystallisation. However, thick packages of laminated dolostone and sandy dolostone beds at the base of the Dolostone-Greywacke member are best explained as being sedimentary in origin. Calcite and dolomite may represent contemporaneously shed carbonate from a nearby carbonate platform. Alternatively, clastic carbonate particles might have been transported into the basin from a nearby eroded older Palaeoproterozoic carbonate sequence. In addition, carbonate is present as diagenetic cement and could also be of a metasomatic/hydrothermal origin. Progressive decrease in thickness and abundance of dolostone and sandy dolostone beds up-section within the Dolostone-Greywacke member is concomitant with an increase in mudstone. This lithological change continues throughout the overlying Mudstone-Limestone member and is interpreted as recording a transgressive trend.

A distinctive characteristic of dolostone beds within the Dolostone-Chert member is their massive structure. Such massive dolostones were previously interpreted as diagenetic megaconcretions (Melezhik et al. 1999). Alternatively, their massive appearance could be the result of pervasive recrystallisation. In such a case, they might have the same origin as dolostones of the Dolostone-Greywacke member, i.e. contemporaneous carbonate shedding from a productive carbonate platform or clastic carbonate transported into the basin from an eroded carbonate sequence. More work employing detailed petrographic and isotopic studies is required in order to better determine the origin of these dolostones.

The two lowermost (489.5–487.5 and 413.6–403.4 m) and the uppermost (56–31 m) massive to indistinctly laminated, C_{org}-rich rocks are either in close proximity to, or in direct contact with the magmatic bodies. This suggests a plausible link between mobilisation and migration of organic material and emplacement of the igneous bodies. Obliteration of primary sedimentary structures in the massive C_{org}-rich rocks (i.e., horizon at 413.6–403.4) might have been caused by recrystallisation due to thermal effects and hydrothermal circulation associated with the emplacement of the gabbroic body. Subsequent cooling of massive, bituminous rocks/sediments resulted in formation of columnar contraction joints (Figs. 6.116fm, fp). Multiple breccias in the upper interval are either debrites or represent injection of organic-rich mud into sandy limestones; further work is required to resolve this. The uppermost C_{org}-rich interval (56–31 m) in places also contains massive or brecciated C_{org}-rich rocks alternating with lava flows. This further implicates an influence of thermal/hydrothermal processes on mobilisation/migration of organic material and formation of C_{org}-rich rocks with a massive structure.

In contrast, the C_{org}-rich rocks within 156–132.9 m interval are not associated with igneous bodies. The lowermost 17.2-m-thick, massive layer has depositional contacts with the under- and overlying C_{org}-poor sediments (Fig. 6.116be). The contact relationship suggests formation of these rocks through deposition on the seafloor (see Chap. 7.6 for details). Alteration of *in-situ* brecciated C_{org}-rich rock and soft-sediment deformed, laminated mudstones indicates multiphase generation of C_{org}-rich material contemporaneous with deposition of mudstones. Post-depositional migration of C_{org}-rich material is indicated by the 80-cm-thick, C_{org}-rich vein injected into the laminated mudstone.

Post-depositional history of the Zaonega succession has been recorded in formation of abundant diagenetic carbonates in the form of cement and concretions, and diagenetic disseminated sulphides, pyrite nodules and layers. Although several chert layers could represent primary chemical precipitates, the occurrence of massive cherts and chert nodules are evidence of post-depositional mobilisation of silica. Additional evidence for post-depositional silica mobility is provided by the presence of silicified mudstones. Abundant pyrobitumen-rich veinlets are witness to oil migration. The presence of ptygmatic and straight, cross-cutting, pyrobitumen-rich veins and bedding-parallel, pyrobitumen-rich seams, and veinlets with diffuse and sharp walls collectively reflect a prolonged period of oil migration (for details see Chap. 7.6).

Significant diagenetic modifications of chemical composition as well as structural and textural patterns of the sediments were further overprinted by metasomatic alteration in some intervals (i.e. albitisation of some Greywacke member rocks) associated with emplacement of gabbroic bodies. Porphyroblasts, large crystals and their clusters, veinlets and veins of sulphides and carbonates are evidence of metamorphic recrystallisation and mobilisation of sulphides and carbonates; these are ubiquitous throughout the Zaonega succession.

New information obtained through sedimentological and geochemical study of Hole 12AB contributes to our understanding of the depositional setting of the Zaonega Formation in general. Melezhik et al. (1999) previously suggested a shallow-water basin for the lowermost part of the Zaonega succession (not intersected by Hole 12AB, and discussed in Chap. 6.3.2), and a lagoonal, brackish-water environment for the middle and upper parts of the succession. The inference of the brackish-water conditions was based on a low S/C ratio in sediments (prevalence of S-poor, C_{org}-rich rocks, Melezhik et al. 1999). Such inference may have been caused by biased sampling of very C_{org}-rich rocks and is not corroborated by the study of Hole 12AB cores; S-rich sediments are abundant throughout the drilled section. A sizeable fractionation of sulphur isotopes ($\delta^{34}S = -22$ to +31 ‰, Shatsky 1990) suggests bacterial reduction of sulphate, which in combination with abundant sulphides is consistent with sulphate-rich basinal water, hence marine.

Voluminous mafic volcanism, which occurred contemporaneously with the predominantly clastic sedimentation from turbidity currents, has a geochemical and isotopic signature indicating a contribution from continental lithosphere (Puchtel et al. 1998). This suggests either an active continental margin or an intraplate rift setting. Indications for seafloor hydrothermal activity, enhanced production and preservation of the organic matter, early oil generation (caused by enhanced heat flow; for details see Chap. 7.6) indicate a rift setting as the most probable depositional system.

The co-occurrence of thick successions of chemically immature siliciclastic sedimentary rocks formed by turbiditic currents and several-metre-thick intervals of both massive and bedded dolostone and limestones, if sedimentary in origin, implies that the Zaonega succession represents a mixed siliciclastic-carbonate depositional system with a putative contemporaneous carbonate platform adjacent to the deeper-water basin.

Fig. 6.112 Zaonega Formation rocks exemplifying an episode of enhanced accumulation of organic matter in the Palaeoproterozoic, an episode known as the Shunga event. (**a**) C_{org}-rich rock (c. 55 wt.% total organic carbon) containing authochthonous kerogen and migrated bitumen from an old adit at the type locality near Shunga village. The rock superficially resembles anthracite and was mined in the 1930's as a coal substitute, though it does not burn due to very low O and H contents. This anthracite-like substance represents one of the rock types of the Palaeoproterozoic petrified oilfield in the Onega Basin. Width of the image is c. 50 cm

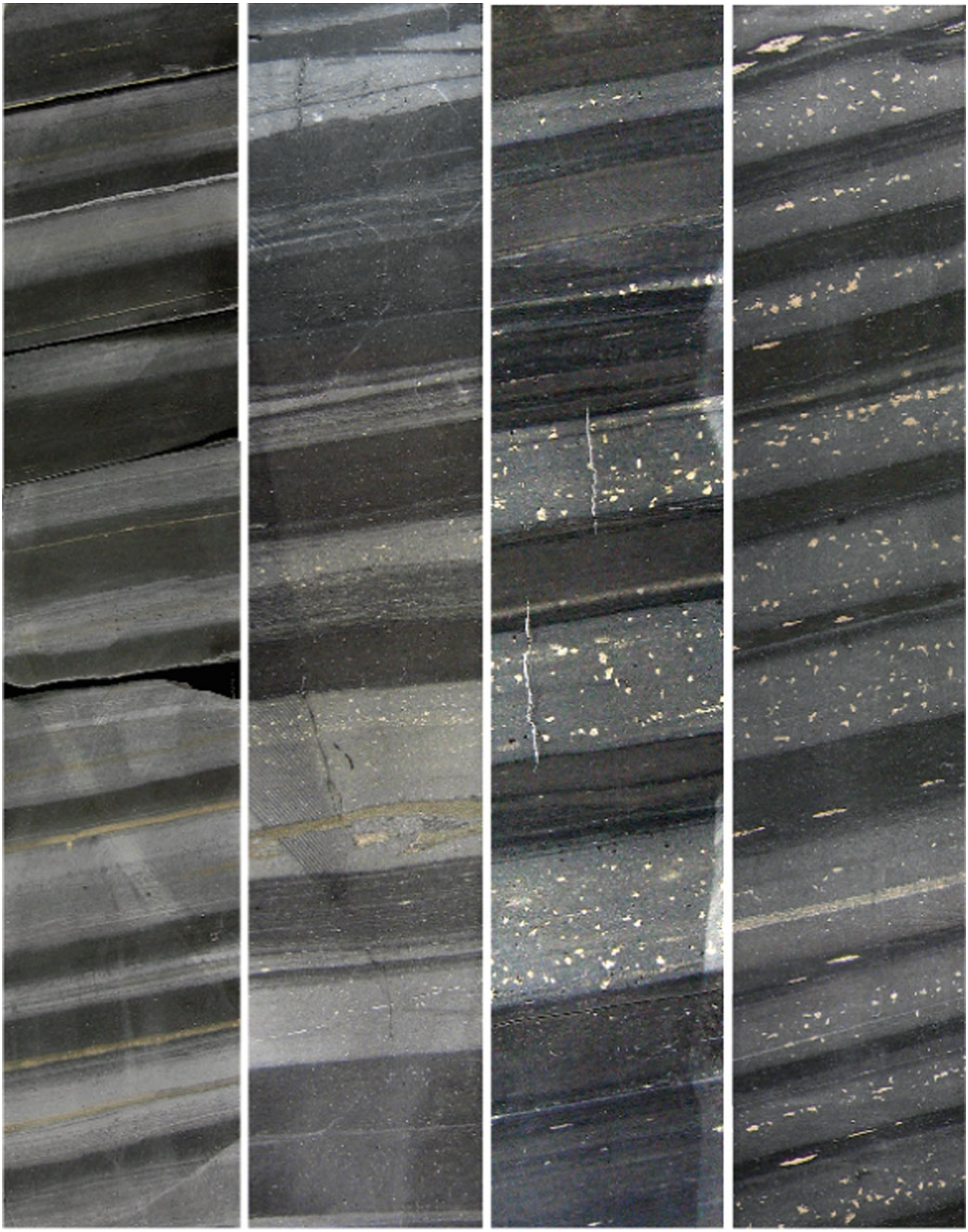

Fig. 6.112 (continued) (**b**) Sawn core of rhythmically bedded, C_{org}-bearing greywackes and mudstones with disseminated sulphides (bright). These rocks were deposited from turbidity currents and represent the most common lithology of the Zaonega Formation and are apparent source rocks for the Onega petrified oilfield. Having been metamorphosed under low-temperature greenschist facies conditions, the rocks have a great potential to preserve primary geochemical and isotopic characteristics of organic matter and sulphides, which would contribute to understanding the causes of the Shunga event. Core diameter is 5 cm (Photographs by Victor Melezhik)

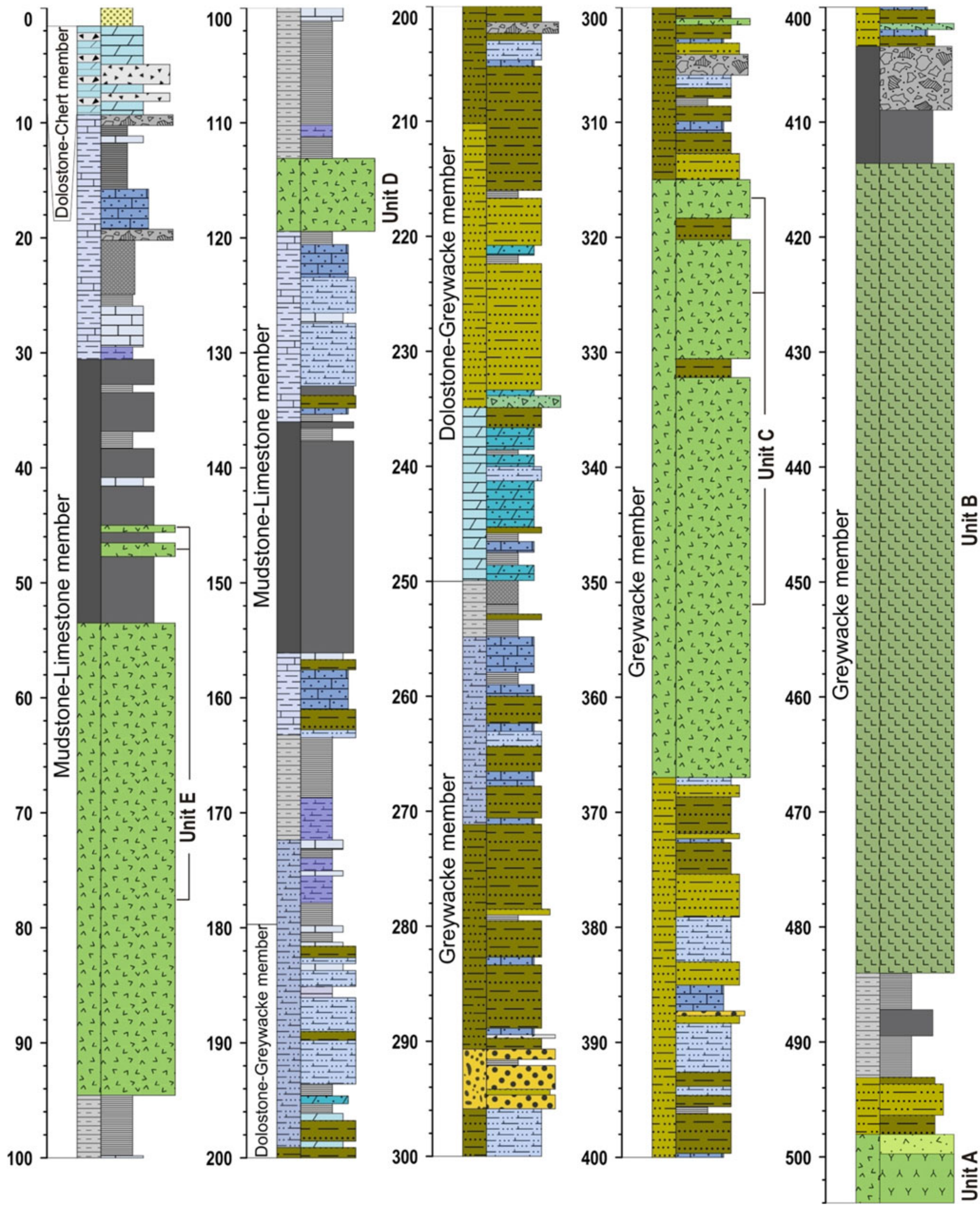

Fig. 6.113 Lithological section of the Zaonega Formation in FAR-DEEP Hole 12AB, and tentative reconstruction of depositional environments based on the core observations and previous sedimentological research in the vicinity of the drilling site. Note that lithological section is presented in two forms; whereas the left, narrow lithocolumn is simplified (used in Fig. 6.119), the right, wider lithocolumn provides more details on lithology

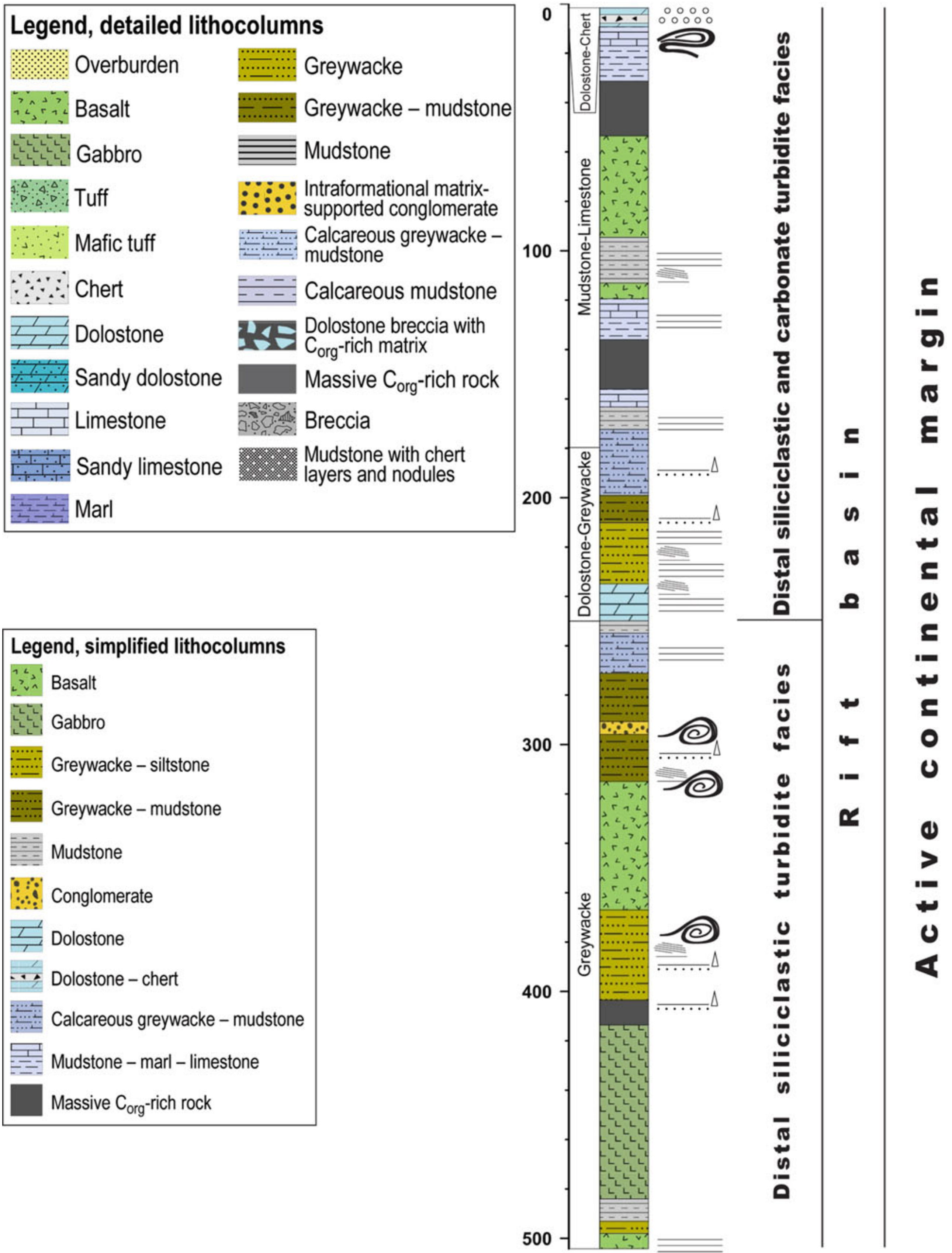

Fig. 6.113 (continued) Lithological section of the Zaonega Formation in FAR-DEEP Hole 12AB, and tentative reconstruction of depositional environments based on the core observations and previous sedimentological research in the vicinity of the drilling site. Lithological symbols are explained in Fig. 6.6

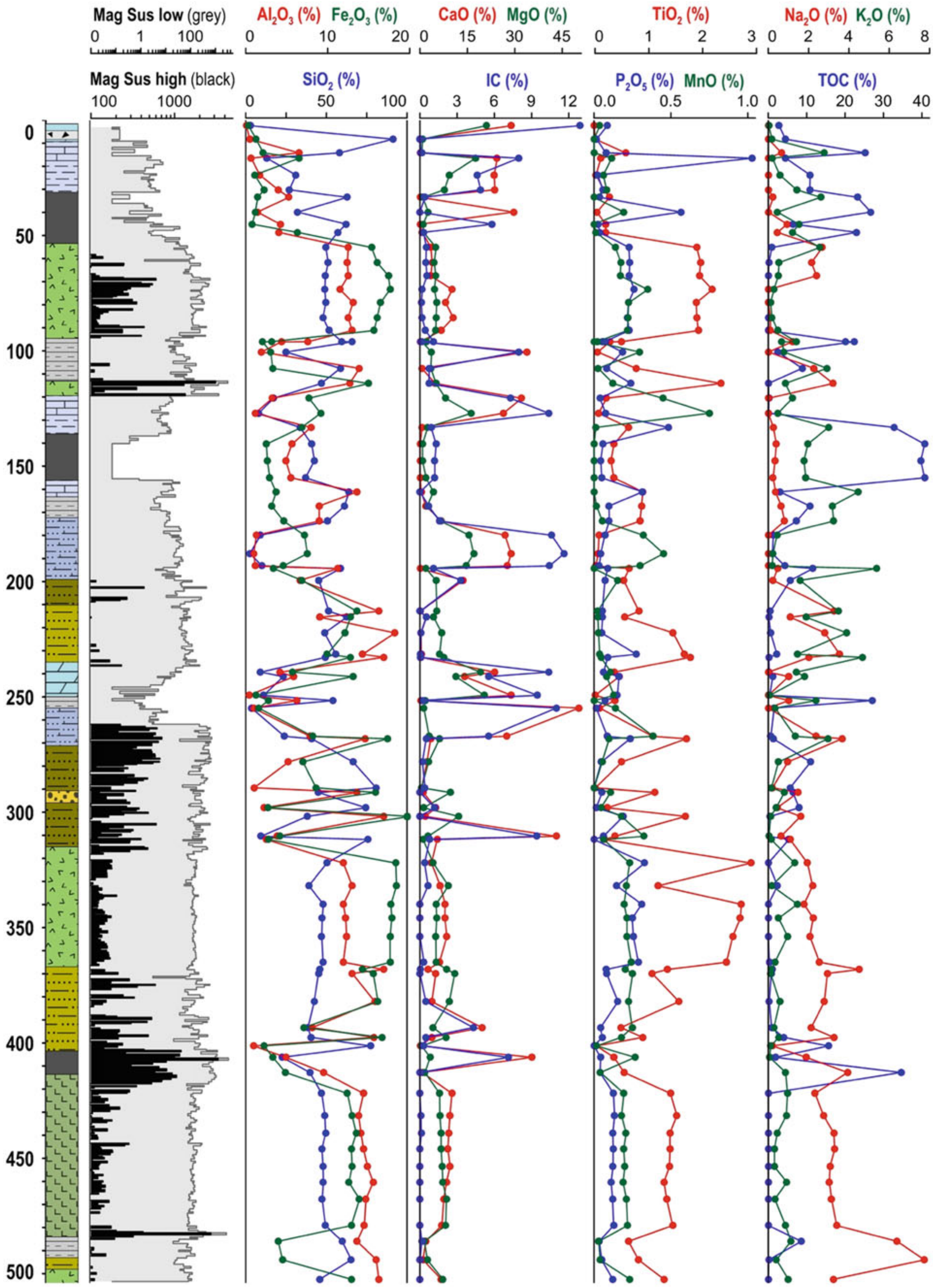

Fig. 6.114 Relative magnetic susceptibility (K*), and geochemical profiles of selected elements based on the archive samples collected with c. 8 m-spacing. For analytical techniques and data quality see Part 5

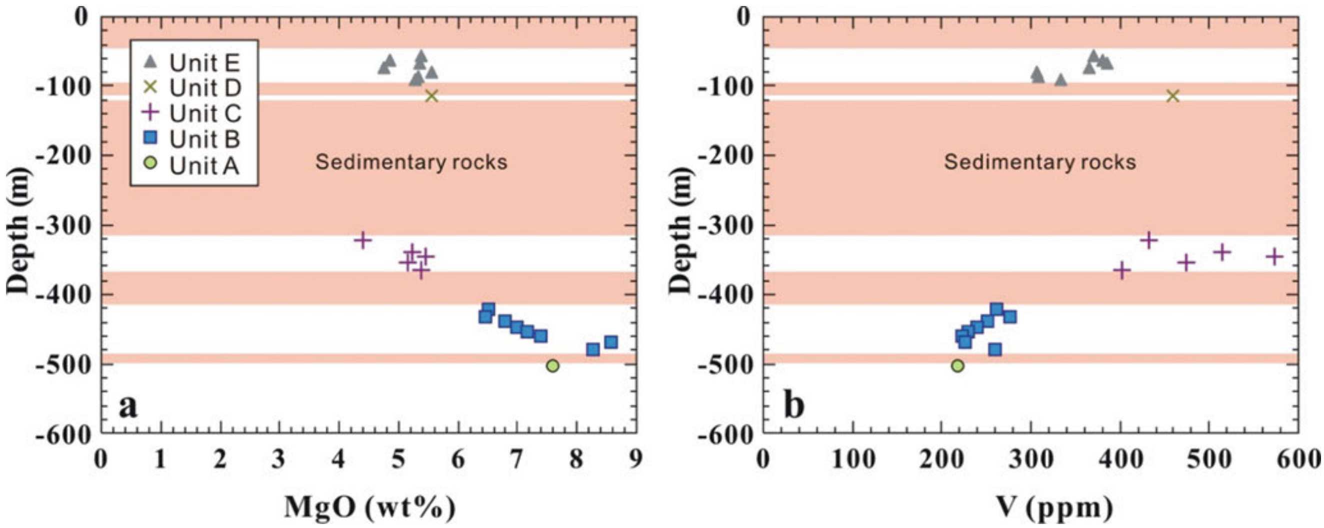

Fig. 6.115 MgO versus depth (**a**) and V versus depth (**b**) diagram for igneous rocks in Core 12AB

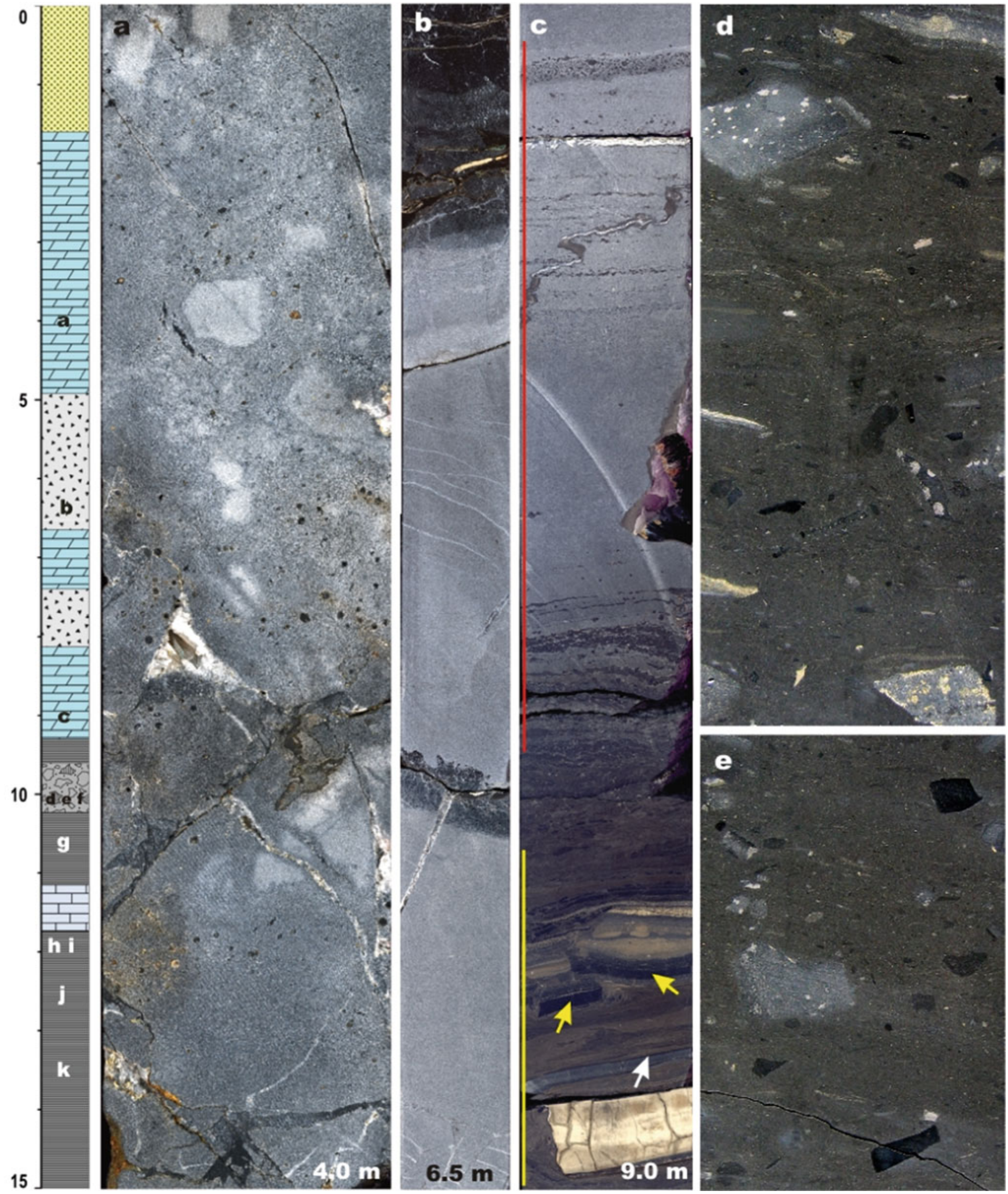

Fig. 6.116 Sedimentological and petrological features of the main rock types intersected by Holes 12A and 12B. (**a**) Dolostone breccia containing angular dolostone clasts and carbonate-mica spherules (*black*) within a dolostone matrix. (**b**) Massive dolostone bed with a chert interlayer and thin calcite veins, overlain by black, massive chert. (**c**) Bedded, *brownish* mudstone (*yellow bar*) with broken layers of sulphides (*bright* and *yellowish*), broken (*yellow arrowed*) and intact (*white arrowed*) black, siliceous mudstones; this is overlain by massive to bedded dolostone (*red bar*) containing black, siliceous mudstone layers at the *bottom* and pyrobitumen-rich veinlets in the top. (**d,e**) Close-ups of Fig. 6.121f showing angular clasts of greywackes (*pale grey*) and mudstones (black) floating in C_{org}-rich matrix. Core diameter here and in the following images is 5 cm unless specified otherwise

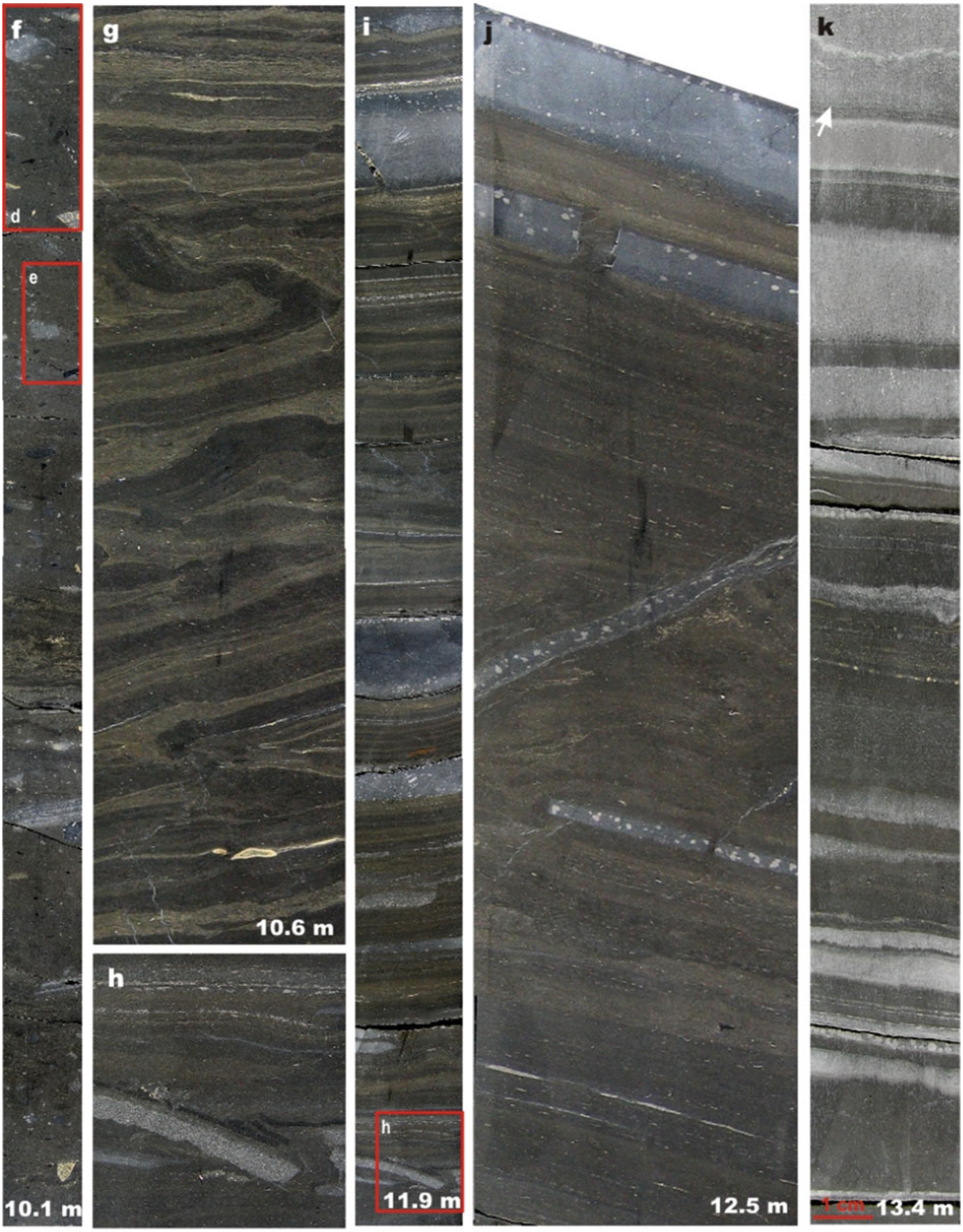

Fig. 6.116 (continued) (**f**) Matrix-supported, polymict breccia; large, angular clasts of greywacke (up to a few cm in size), some pervasively sulphidised mudstones and siliceous mudstones floating in massive, C_{org}-rich matrix. (**g**) Laminated, organic-rich mudstone with synsedimentary folds. (**i**) Laminated, pyrobitumen-rich mudstone containing greywacke layers that are, in places, broken and rotated. (**h**) Close-up of Fig. 6.121i showing broken and displaced greywacke lamina within C_{org}-rich mudstone. (**j**) Laminated, pyrobitumen-rich mudstone containing broken and rotated greywacke layers. (**k**) Interbedded C_{org}-rich mudstone and greywacke overlain by sandy limestone (*arrowed*)

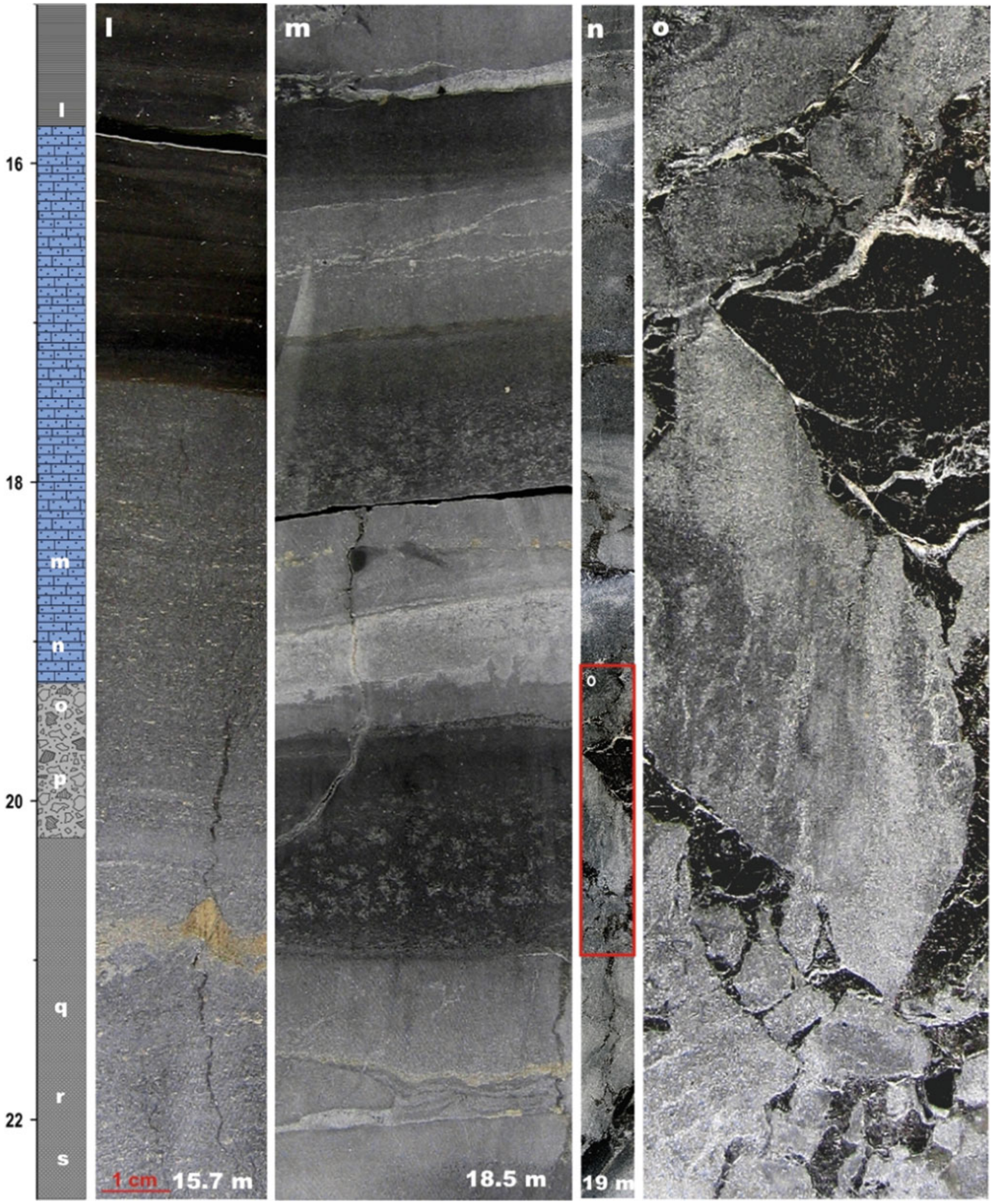

Fig. 6.116 (continued) (**l**) Sandy limestone with a partially sulphidised layer, overlain by dark, C_{org}-rich mudstone. (**m**) Alternation of sandy limestones and calcareous mudstones (dark coloured). (**n**) Breccia containing large, up to 10 cm in size, sandy limestone clasts and few small, angular, siliceous mudstone clasts in C_{org}-rich mudstone matrix. (**o**) Detail of Fig. 6.121n showing small, angular, siliceous mudstone clasts in C_{org}-rich matrix

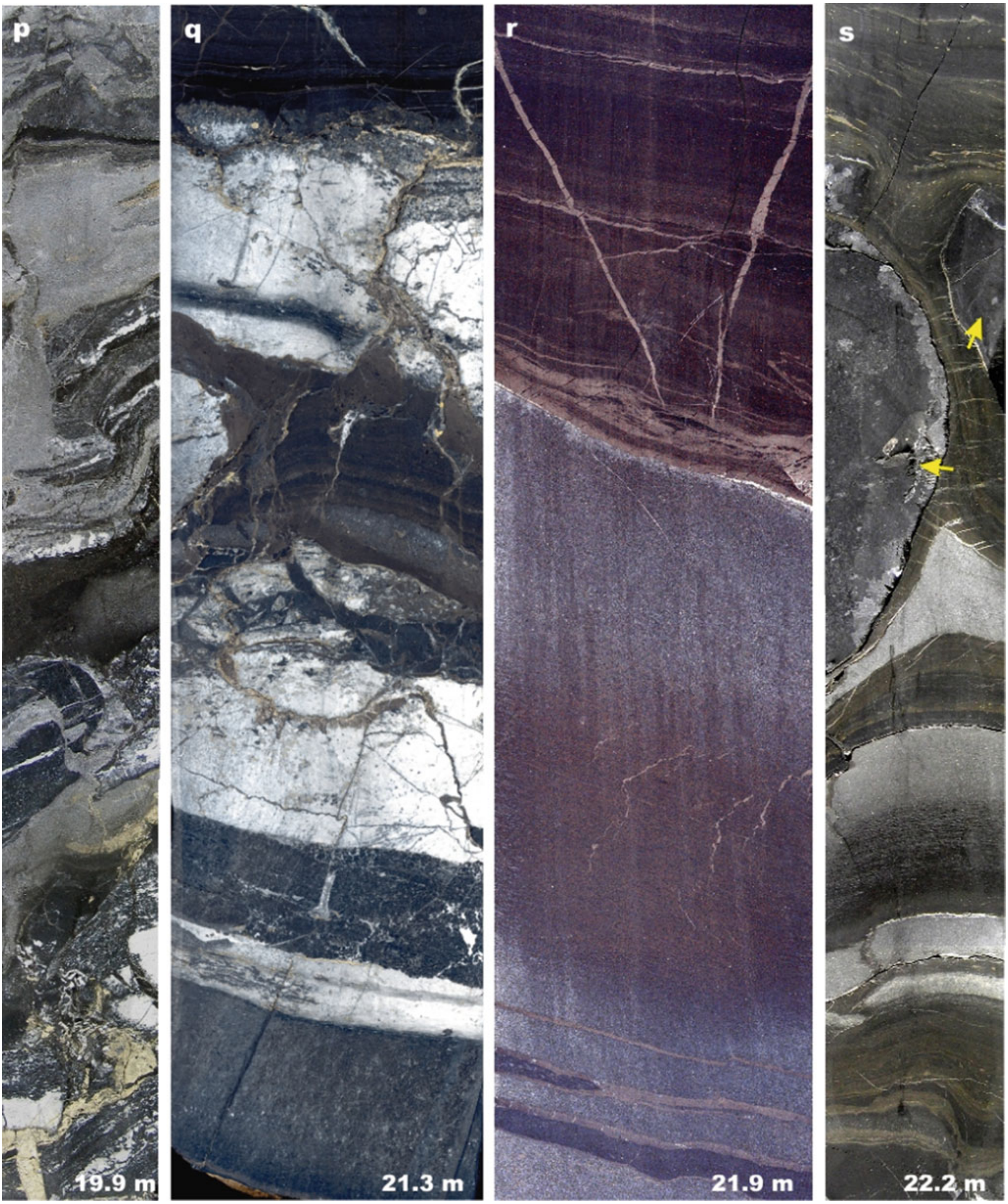

Fig. 6.116 (continued) (**p**) Massive, soft-sediment deformed layers of sandy mudstone (*pale grey*) with a black mudstone layer and intervals of breccia containing broken layers of black and white chert, a broken chert nodule, and sulphide-rich layers. (**q**) Brecciated and intact, white and dark grey, massive chert interbedded with laminated, dark-coloured, C_{org}-rich mudstones; note that cracks within chert layers are filled with black, sulphide- and C_{org}-rich mudstone. (**r**) Grey, sandy limestone and overlying black mudstone with bedding-parallel, pyrobitumen-rich seams and veinlets (*pale grey-brownish*). (**s**) Interbedded sandy limestone (bright) and laminated, dark-coloured, C_{org}-rich mudstone with nodules of dark grey chert (*yellow arrowed*)

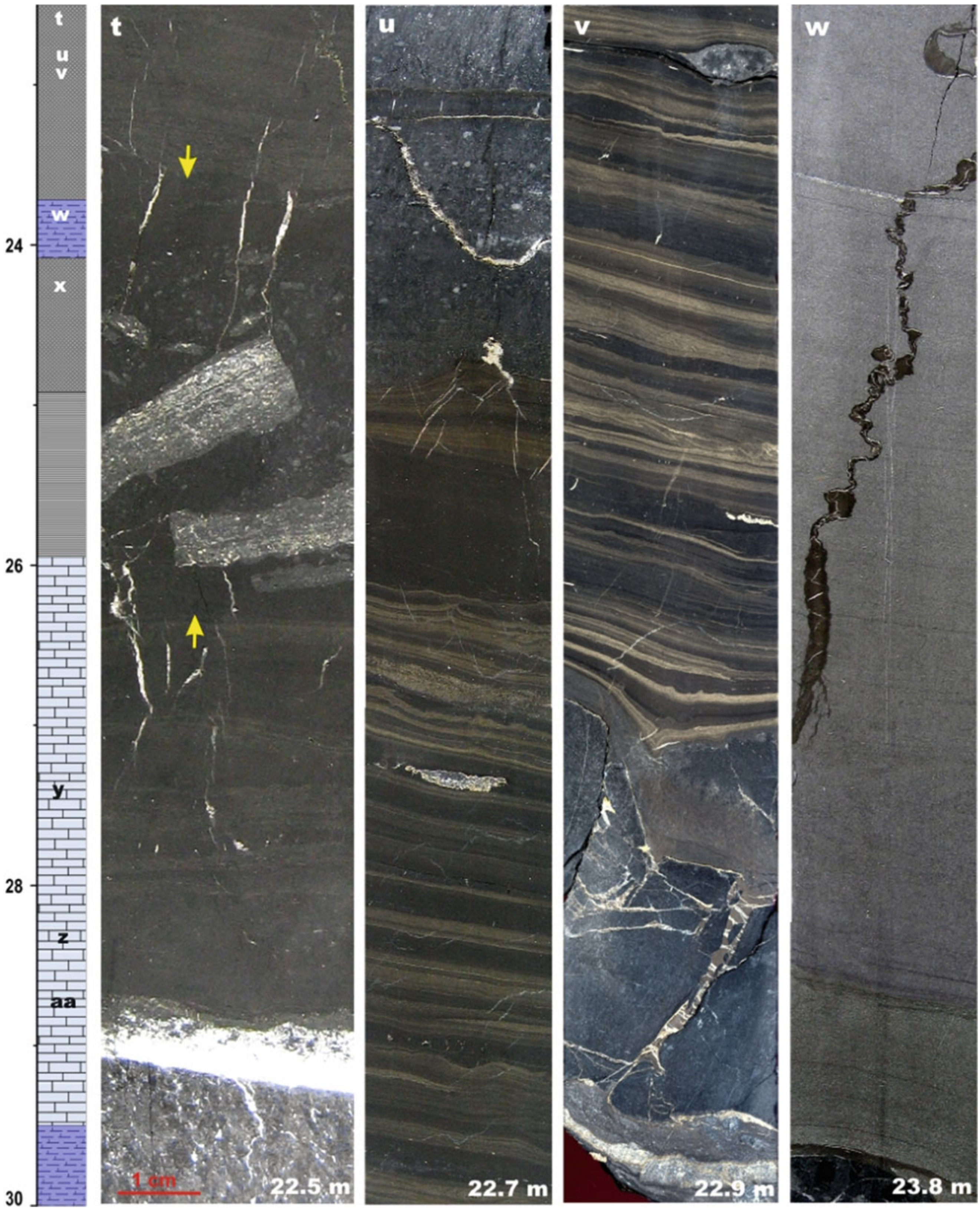

Fig. 6.116 (continued) (**t**) Grey chert overlain by dark-coloured, C_{org}-rich, bedded mudstone containing a breccia layer (*yellow arrowed*) with broken layers and small angular clasts of greywacke. (**u**) Dark coloured, laminated, C_{org}-rich mudstone containing chert layers or nodules (top part of the photo). (**v**) Dark-coloured, laminated, C_{org}-rich mudstone with broken layer or nodule of dark-grey chert and a small chert nodule (at the top). (**w**) Laminated marl (at the base) passing gradually upward into massive to laminated, sandy limestone (upper part of the bed), which is injected with black, ptygmatic, pyrobitumen-rich vein

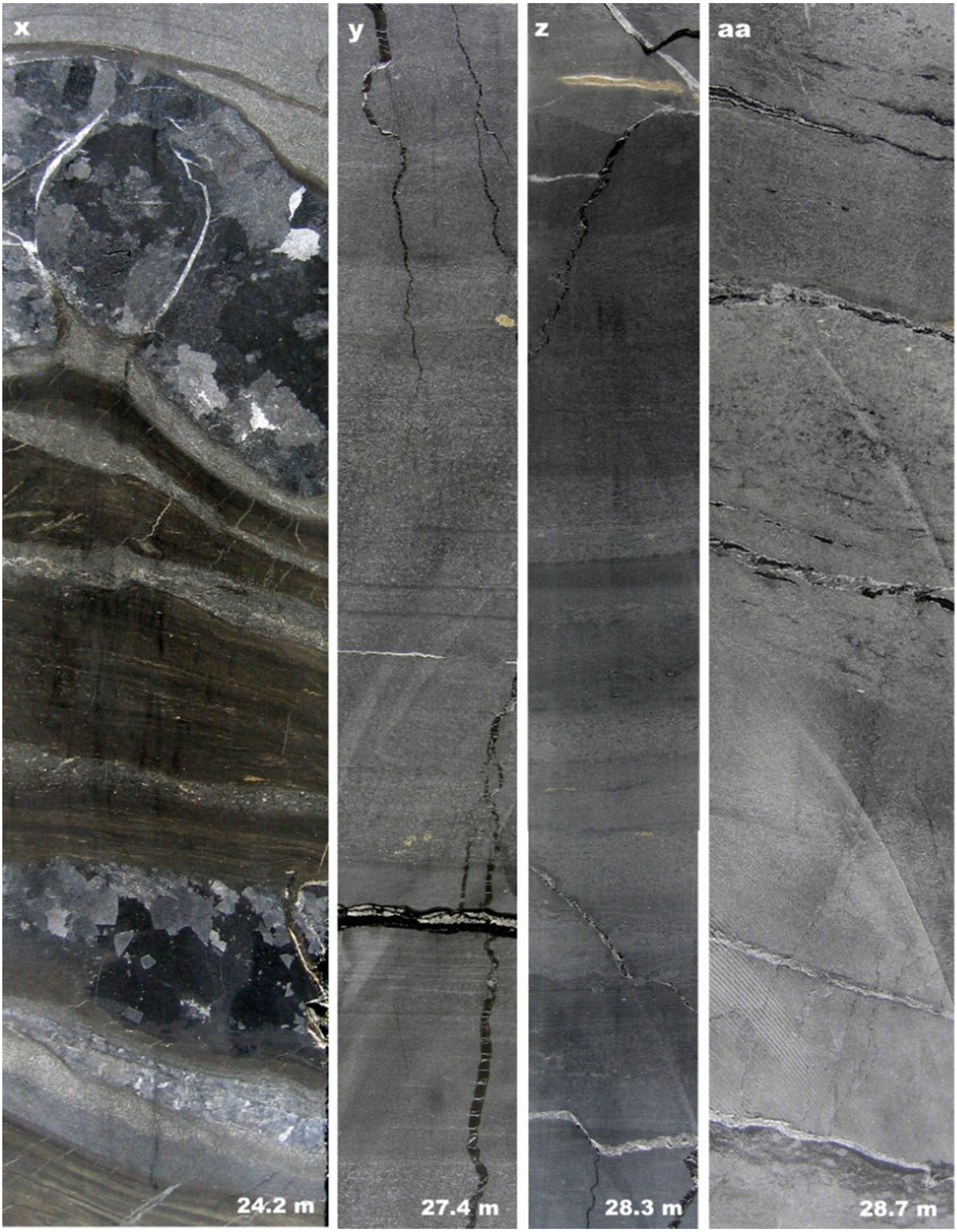

Fig. 6.116 (continued) (**x**) Interbedded dark-coloured, laminated, C_{org}-rich mudstone and sandy limestone (*pale grey*) containing layers of coarsely crystalline chert. (**y**) Massive to laminated, sandy limestone with black, pyrobitumen-rich veins and a bedding-parallel seam and few sulphide concretions. (**z**) Sandy limestone (*grey*) and marl (*dark grey*) with black, pyrobitumen-rich, and white, calcite veins, and few sulphide concretions. (**aa**) Massive to laminated sandy limestone with bedding-parallel calcite (bright) and pyrobitumen-rich (black) seams

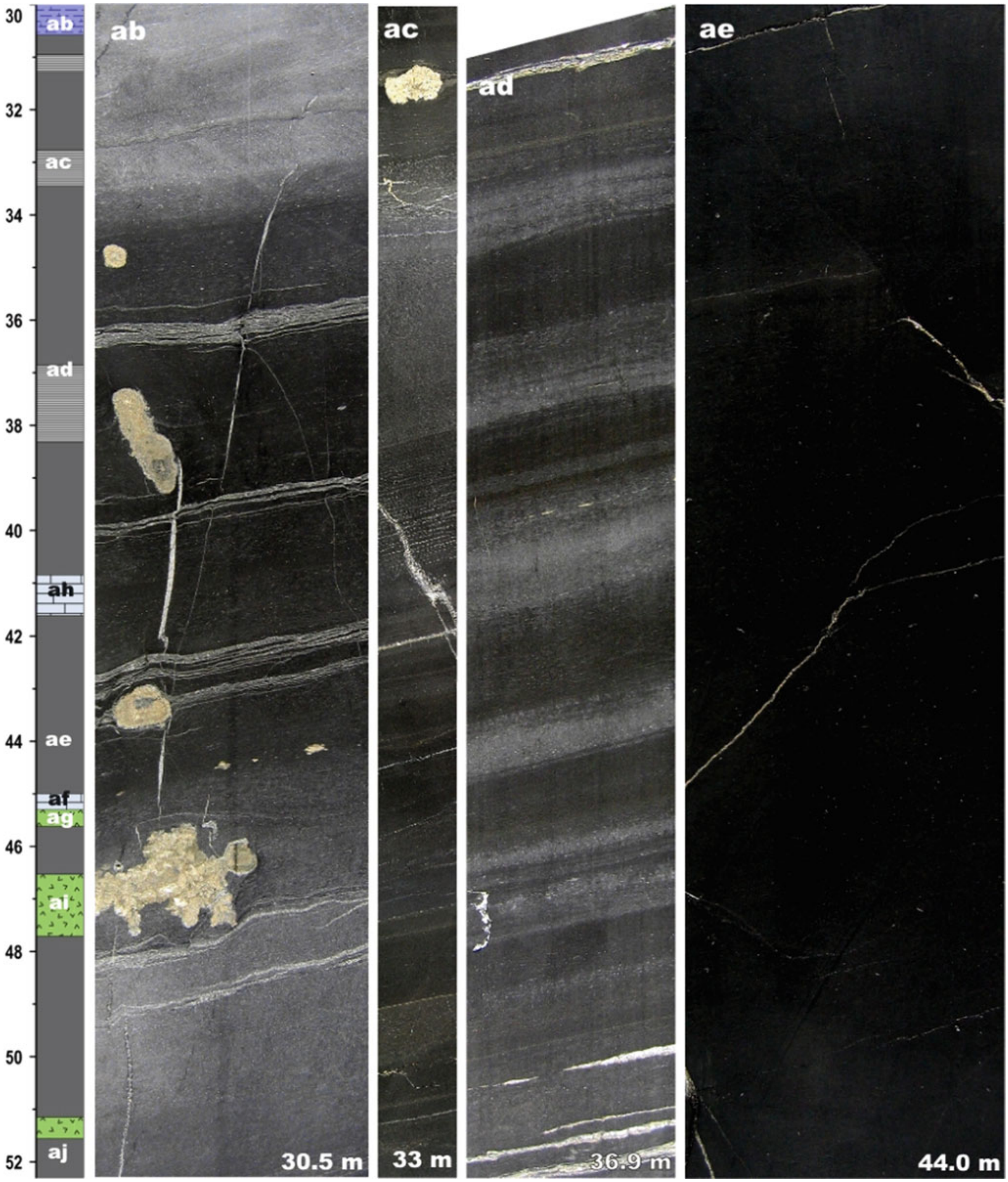

Fig. 6.116 (continued) (**ab**) Interbedded massive to laminated marl (*light grey*) and mudstone (*dark grey*) with sulphide concretions, thin horizontal seams and vertical veinlets of calcite. (**ac**) Interbedded black mudstone and grey calcareous mudstone containing sulphide concretions and composite veinlets. (**ad**) Rhythmically interbedded sandy limestones and mudstones with bedding-parallel calcite (*bottom*) and sulphide (*top*) seams. (**ae**) Massive, C_{org}-rich rock with sulphide veinlets

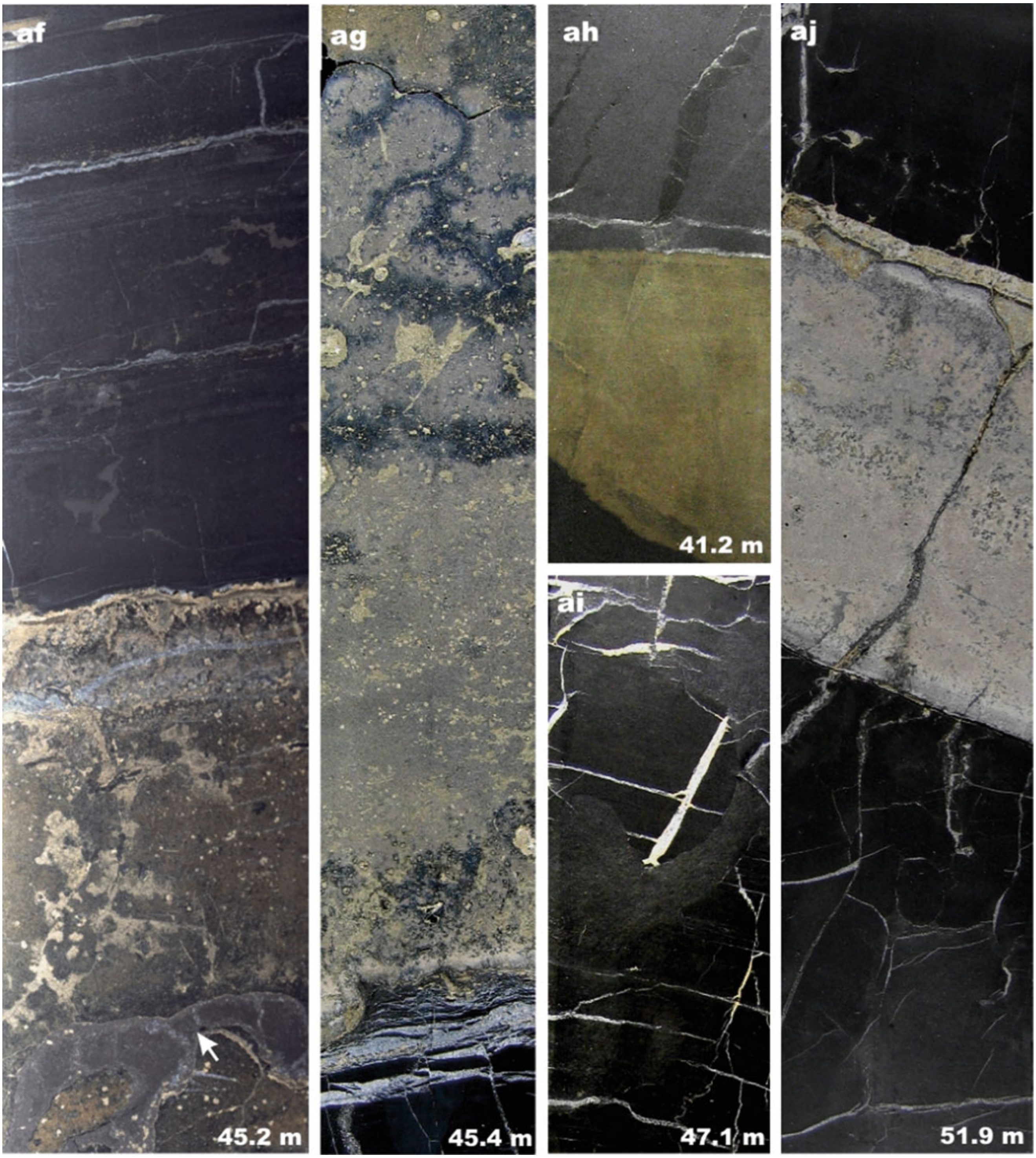

Fig. 6.116 (continued) (**af**) Contact of a mafic lava flow with carbonate mudstones containing pyrobitumen veinlets; uppermost part of the lava flow is pervasively sulphidised and contains a horizontal, irregular vein filled with C_{org}-rich mudstone (*arrowed*). (**ag**) Massive, C_{org}-rich rocks (lowermost part) overlain by a mafic lava flow with incipient pillows; note the intense calcite veining of the mudstone directly at the contact. (**ah**) Large sulphide nodule in sandy limestone with pyrobitumen-rich veins. (**ai**) Two generations of massive, C_{org}-rich rock differing in colour (*black* and *dark grey*) with calcite and sulphide-filled cracks. (**aj**) Thin mafic lava flow within massive, C_{org}-rich rock; note that top of the lava flow is intensely sulphidised

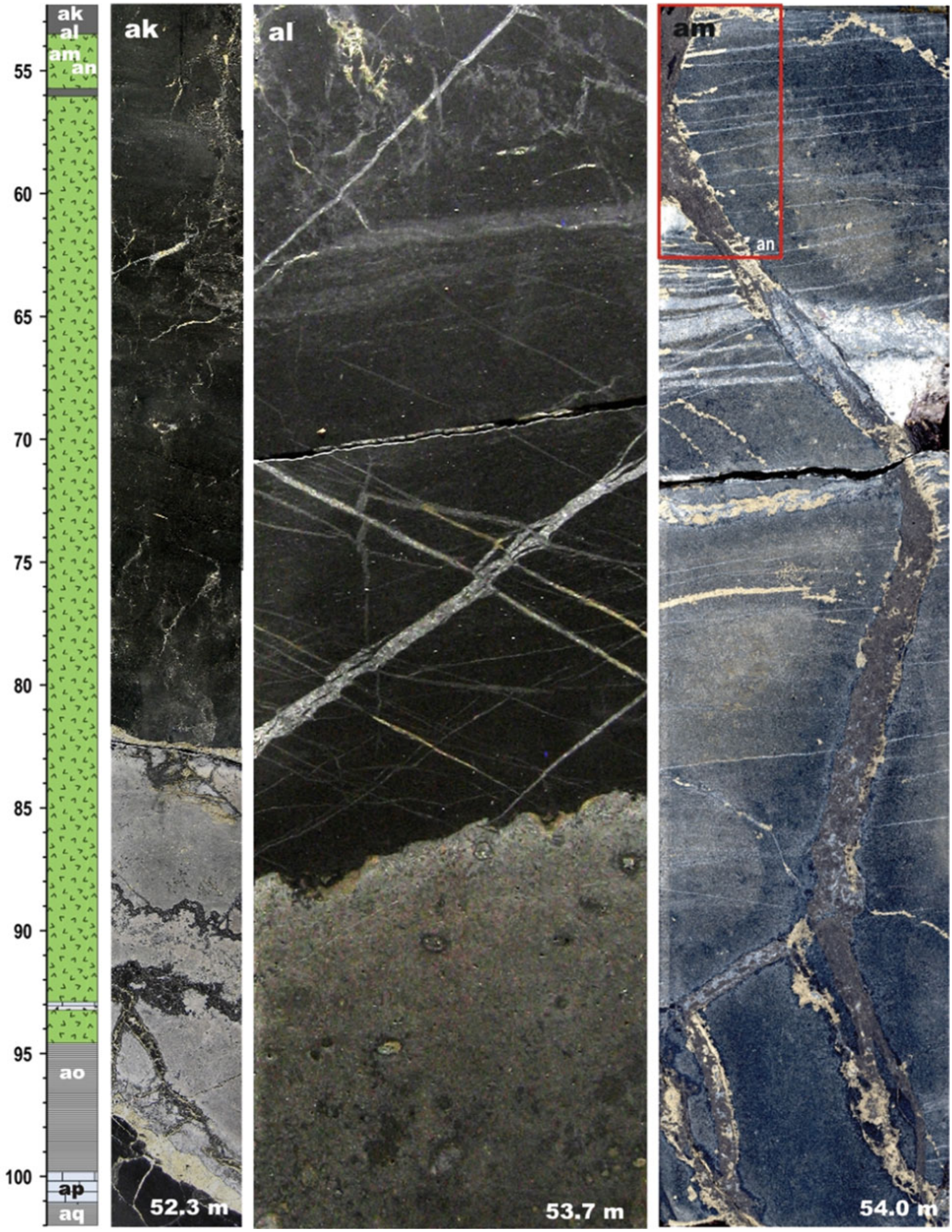

Fig. 6.116 (continued) (**ak**) Thin mafic lava flow within a massive, partially brecciated, C_{org}-rich rock; note that the flow is sulphidised along both contacts and affected by internal disintegration, separation and chloritisation (dark coloured). (**al**) Amygdaloidal lava flow with an irregular upper surface overlain by massive, C_{org}-rich rock with numerous calcite veins. (**am**) Mafic lava flow with abundant horizontal sulphide-calcite veinlets, which are all affected by extensional joints filled by pyrobitumen-rich, sulphidised veins

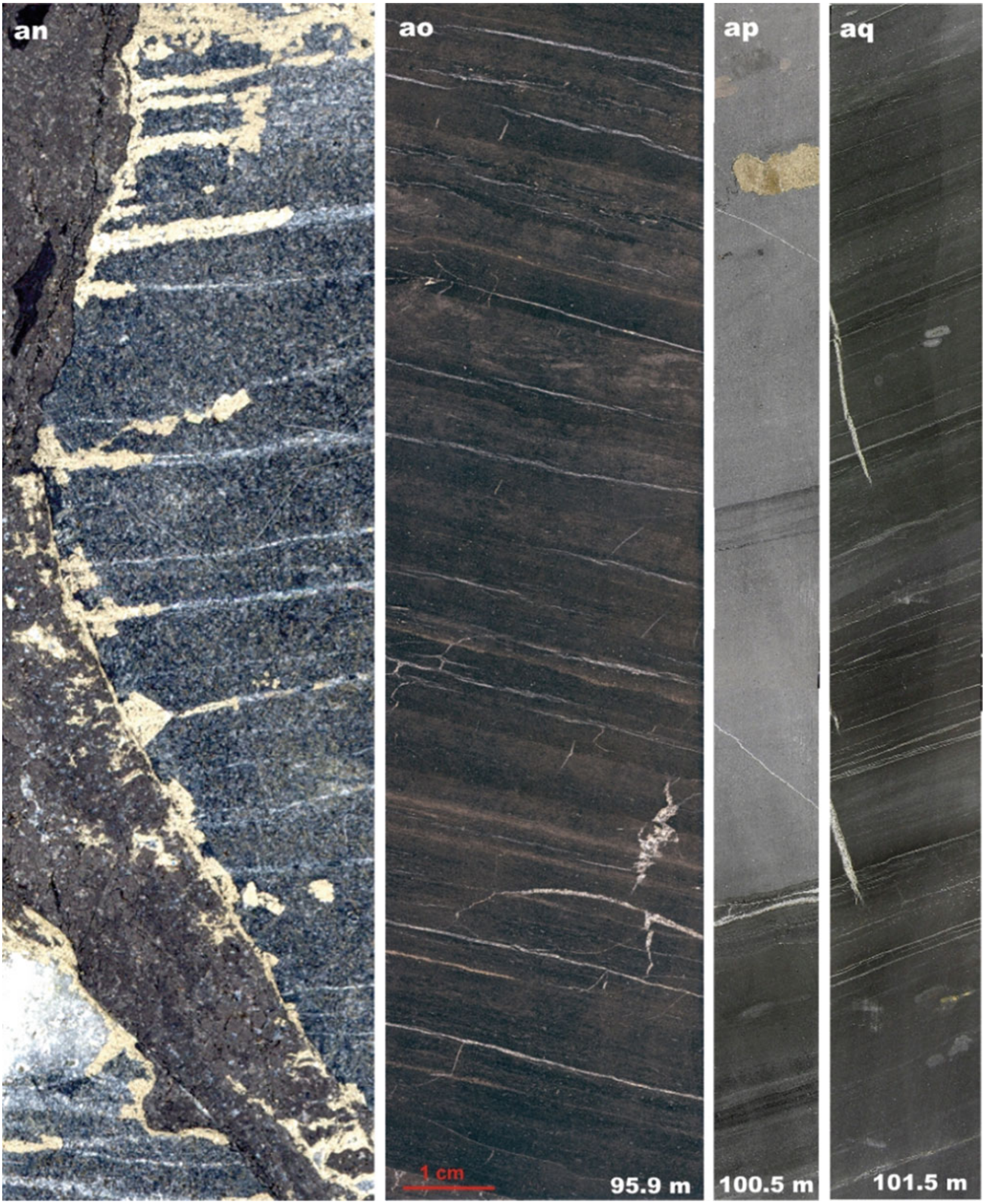

Fig. 6.116 (continued) (**an**) Details of Fig. 6.116am showing intensively sulphidised margins of the pyrobitumen-rich vein and sulphide-replacement of calcite veinlets in areas adjacent to the pyrobitumen-rich vein. (**ao**) Laminated, dark-coloured, C_{org}-rich mudstone with horizontal calcite and sulphide seams. (**ap**) Dark-coloured, calcareous mudstone overlain by massive to laminated, sandy limestone with sulphide nodule. (**aq**) Parallel-laminated, dark-coloured, C_{org}-rich mudstone

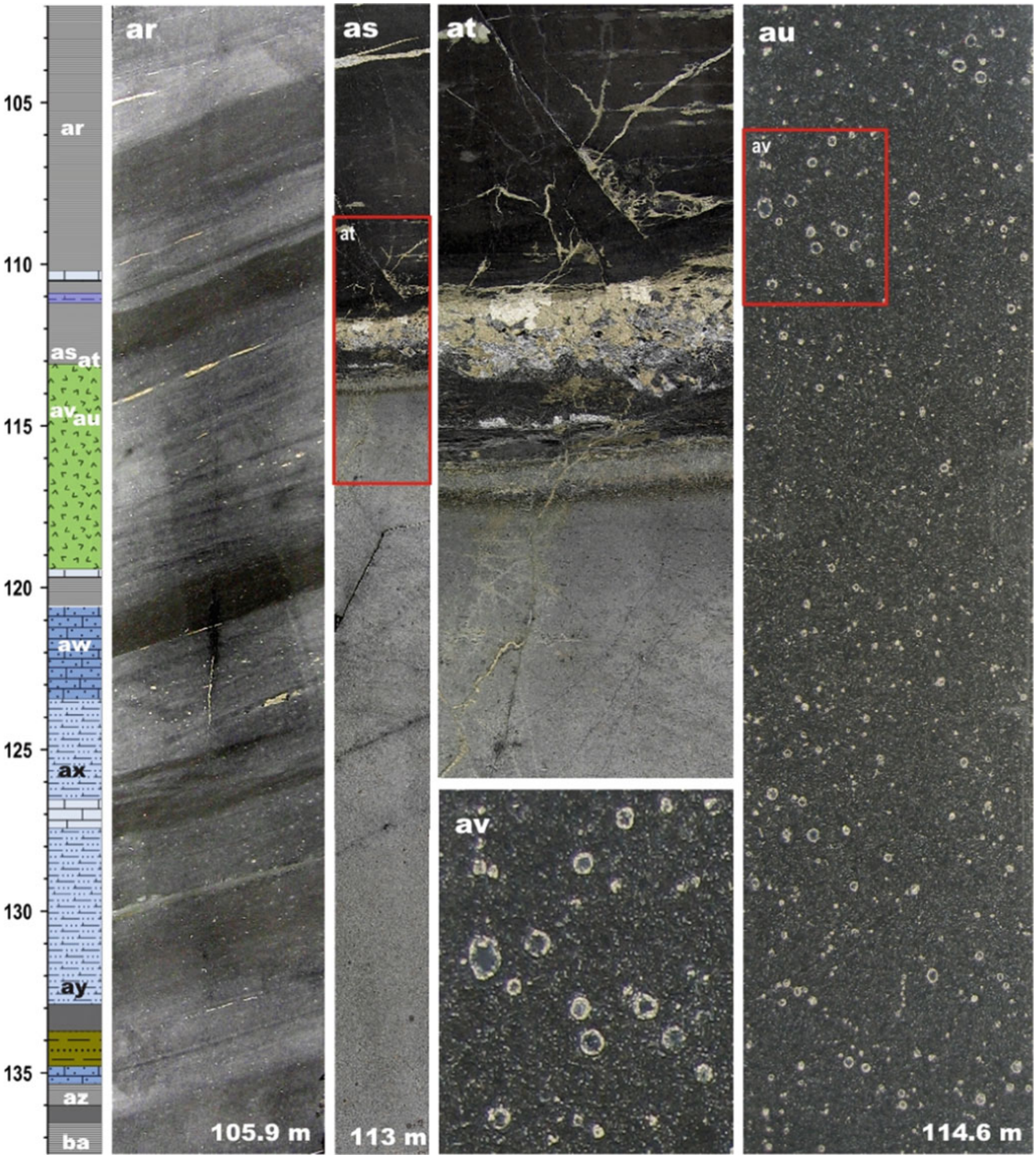

Fig. 6.116 (continued) (**ar**) Rhythmically interbedded, dark grey greywackes and dark-coloured mudstones with sulphide impregnations; note that the greywackes show parallel and low-angle, small-scale cross lamination, whereas the mudstones are massive or indistinctly laminated. (**as**) Mafic lava flow in contact with the overlying massive, C_{org}-rich rock. (**at**) Close-up of Fig. 6.116as showing intensive pyritisation and calcitisation of the massive, C_{org}-rich rock in the proximity to the lava flow. (**au**) Upper part of the lava flow containing abundant zoned, sulphide-chlorite amygdales. (**av**) Close-up of Fig. 6.116av showing details of zoned, sulphide-chlorite amygdales

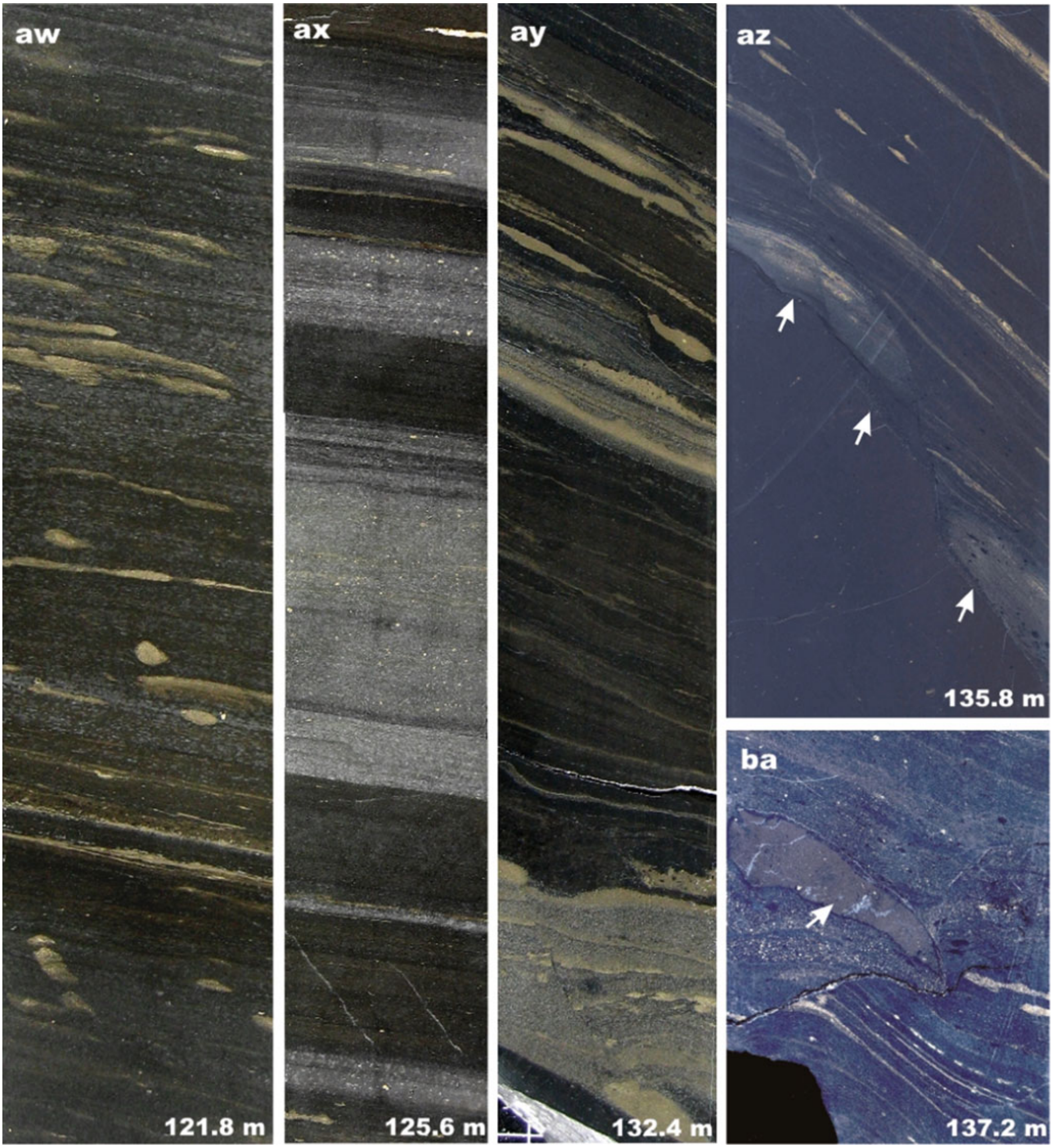

Fig. 6.116 (continued) (**aw**) Sandy limestone with abundant small sulphide concretions and concretionary layers. (**ax**) Rhythmically interbedded, grey, parallel-laminated, sandy limestones and black mudstones. (**ay**) Greywacke bed (at the *base*) with distorted bedding and an uneven surface overlain by black, laminated mudstone with sulphide nodules and concretionary layers. (**az**) Upper depositional contact of massive, C_{org}-rich rock (*arrowed*) with the overlying laminated mudstone containing abundant sulphide laminae. (**ba**) Elongated and irregularly shaped pyrobitumen-rich clast (*arrowed*) within the laminated sulphide-rich mudstone

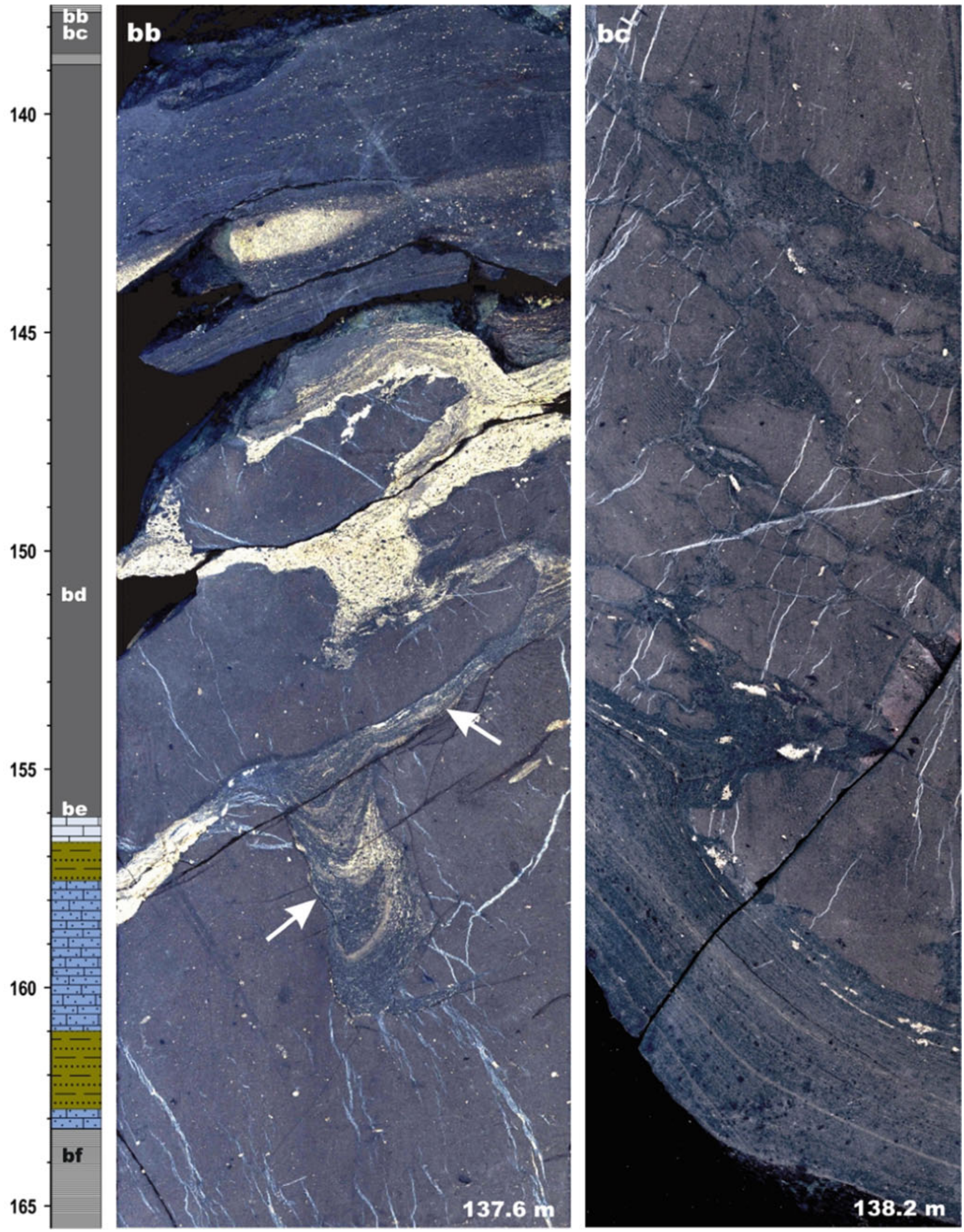

Fig. 6.116 (continued) (**bb**) Black, massive, C_{org}-rich rock with sulphide layers/lenses (bright) and inclusions of soft-sediment deformed siltstone (*arrowed*) overlain by laminated mudstones with a sulphide nodule. (**bc**) Laminated mudstones overlain by soft-sediment brecciated, C_{org}-rich rock with black mudstone matrix; note the mm-sized, clay "balls" (*black*) in the laminated mudstone

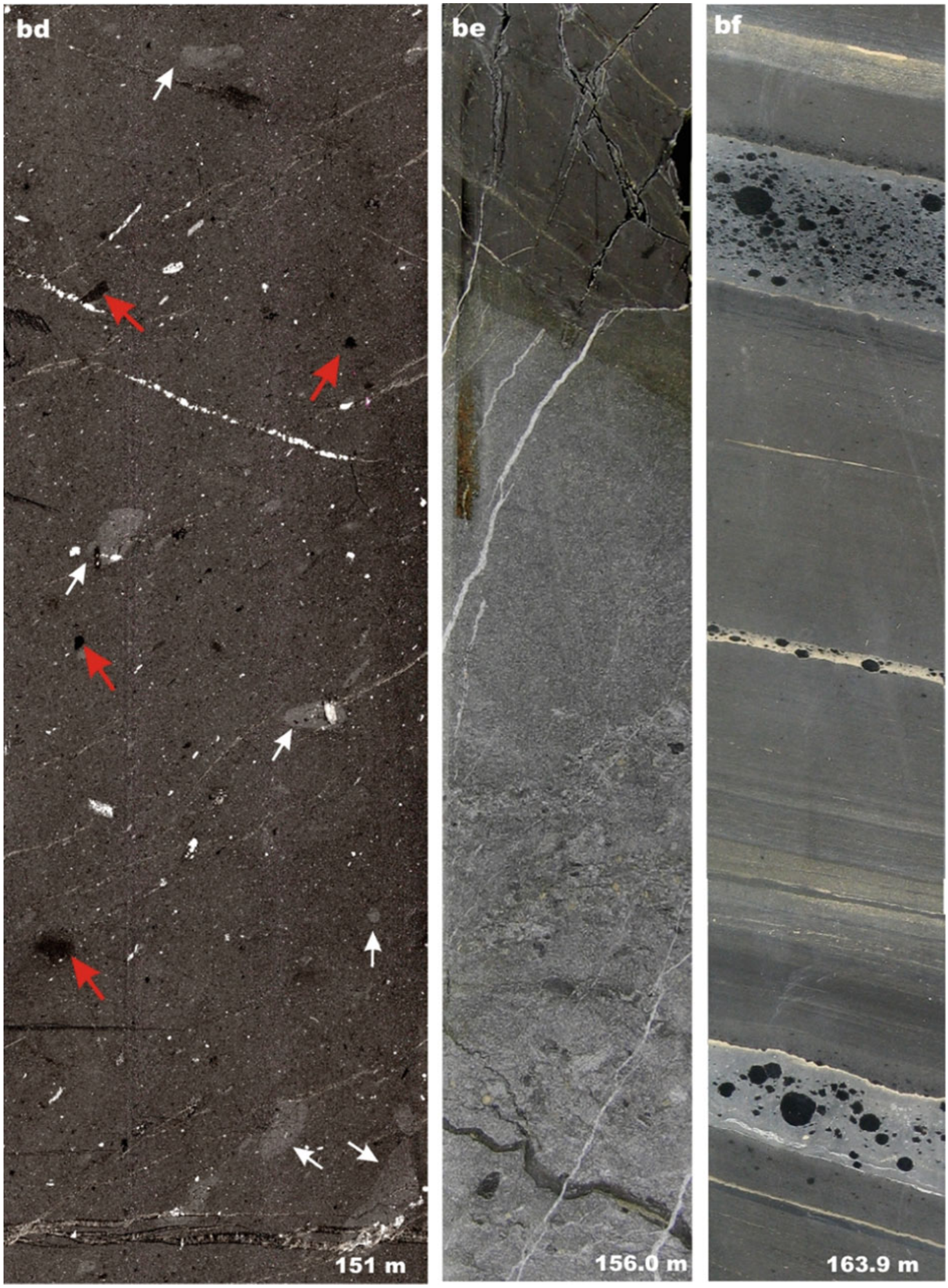

Fig. 6.116 (continued) (**bd**) Massive, C_{org}-rich rock containing pyrobitumen-rich intraclasts (*white arrows*), and clasts of mudstone (*red arrows*) and sulphides (bright). (**be**) Lower contact of massive, C_{org}-rich rocks with an underlying sandy limestone containing several intraclasts and pyrobitumen-rich veinlets. (**bf**) Parallel-laminated and massive, grey mudstones with three thin, massive greywacke beds (*pale grey*) containing abundant black, C_{org}-rich clay balls; bright phase is sulphide

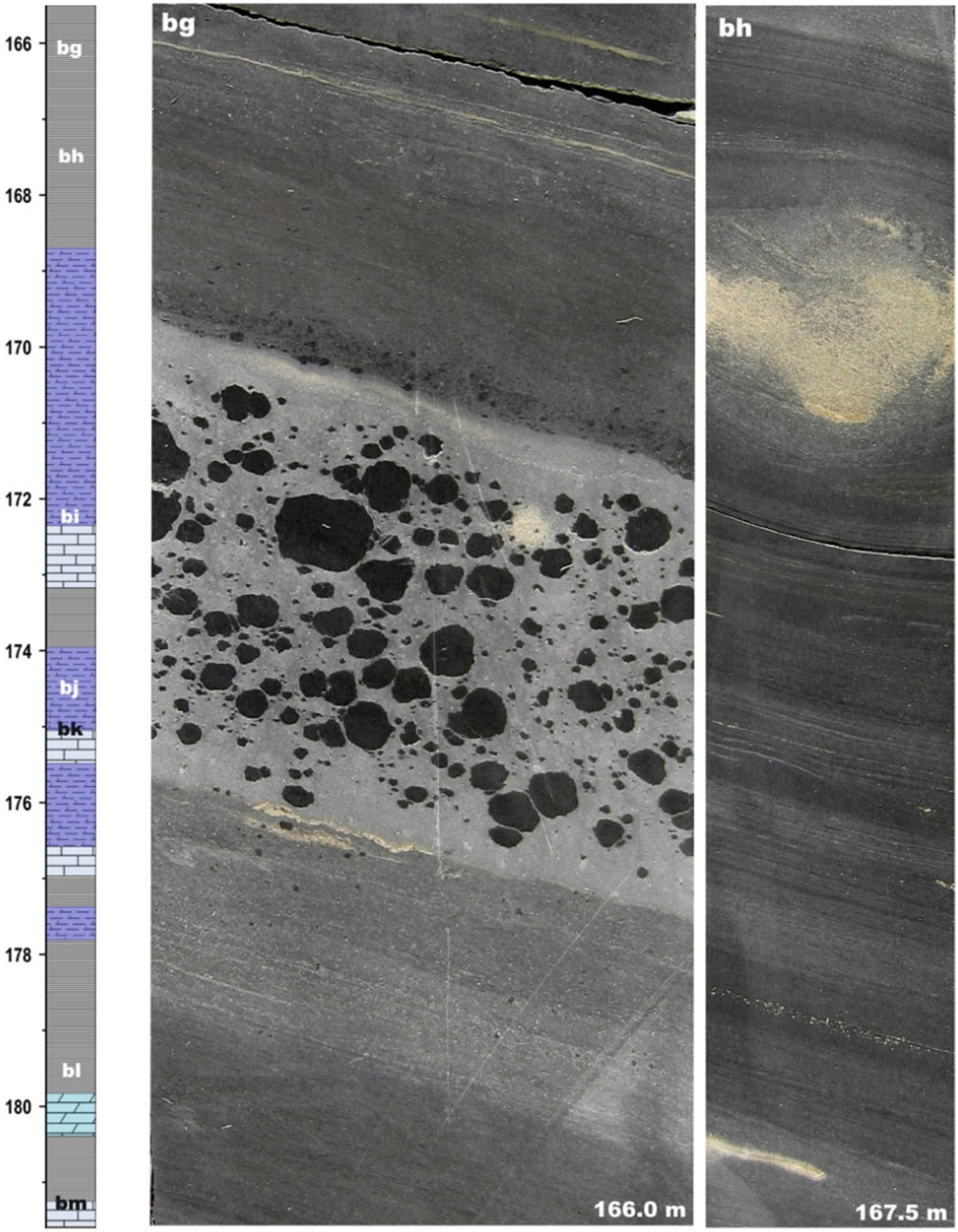

Fig. 6.116 (continued) (**bg**) Parallel-laminated mudstone with a bed of light grey greywacke containing abundant black, C_{org}-rich clay balls. (**bh**) Parallel-laminated, calcareous mudstone with sulphide impregnations

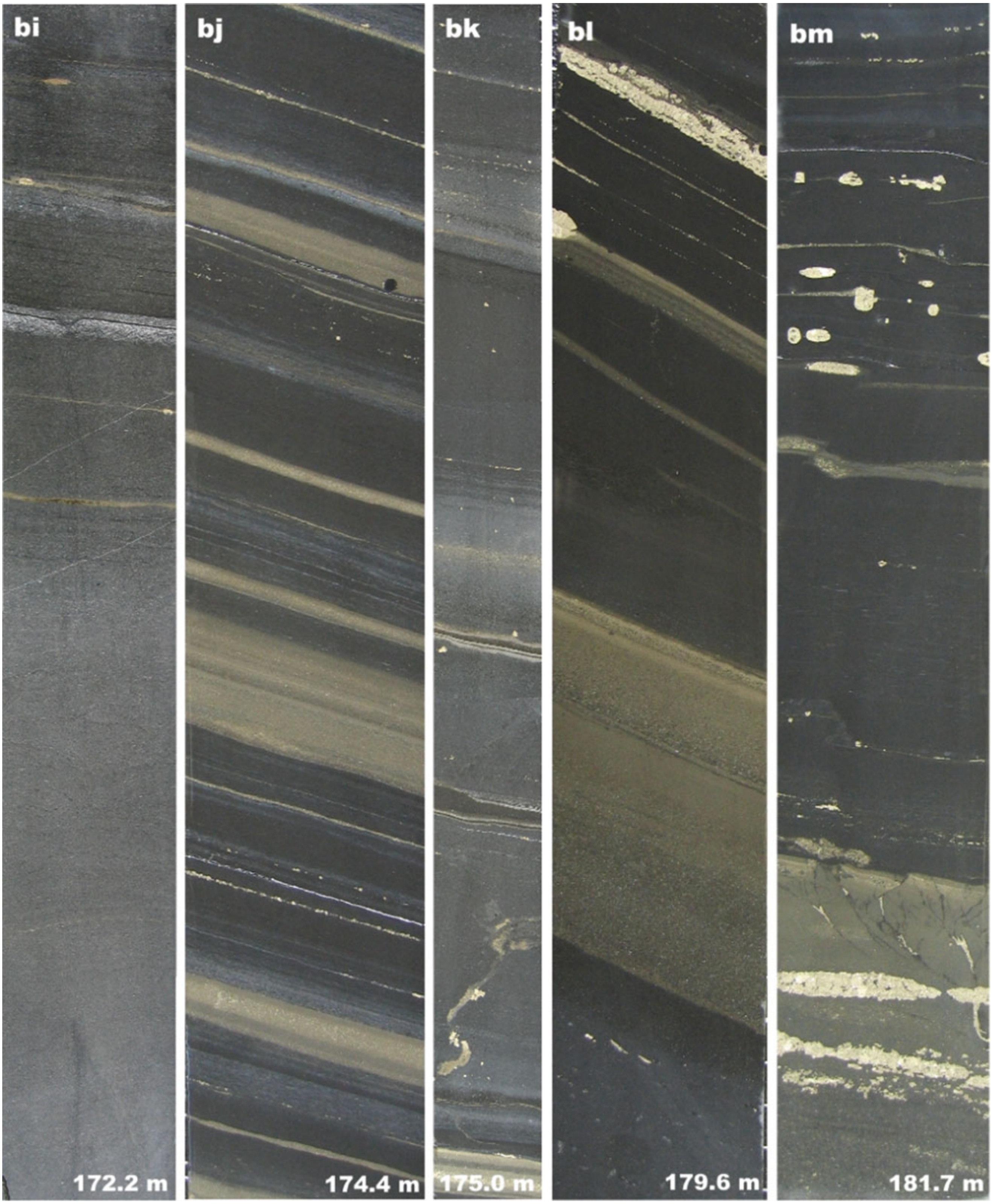

Fig. 6.116 (continued) (**bi**) *Grey*, massive, sandy limestone gradually passing into marl and laminated calcareous mudstone. (**bj**) Black and dark grey, thinly laminated mudstone interbedded with yellow-grey, sandy limestone; thin sulphide laminae are bright. (**bk**) Interbedded grey, sandy limestones and dark grey, massive marls with thin intervals of black mudstone; bright phase is sulphide layers and small nodules. (**bl**) Black, massive, sandy limestone (*lowermost* part of the photo) overlain by normally graded greywacke (*middle* part of the photo) and mudstone (*uppermost* part of the photo) containing sulphide nodule and layers (bright). (**bm**) Greywacke with abundant sulphide concretions and a syn-depositionally faulted surface overlain by black, massive, mudstones with sulphide concretions

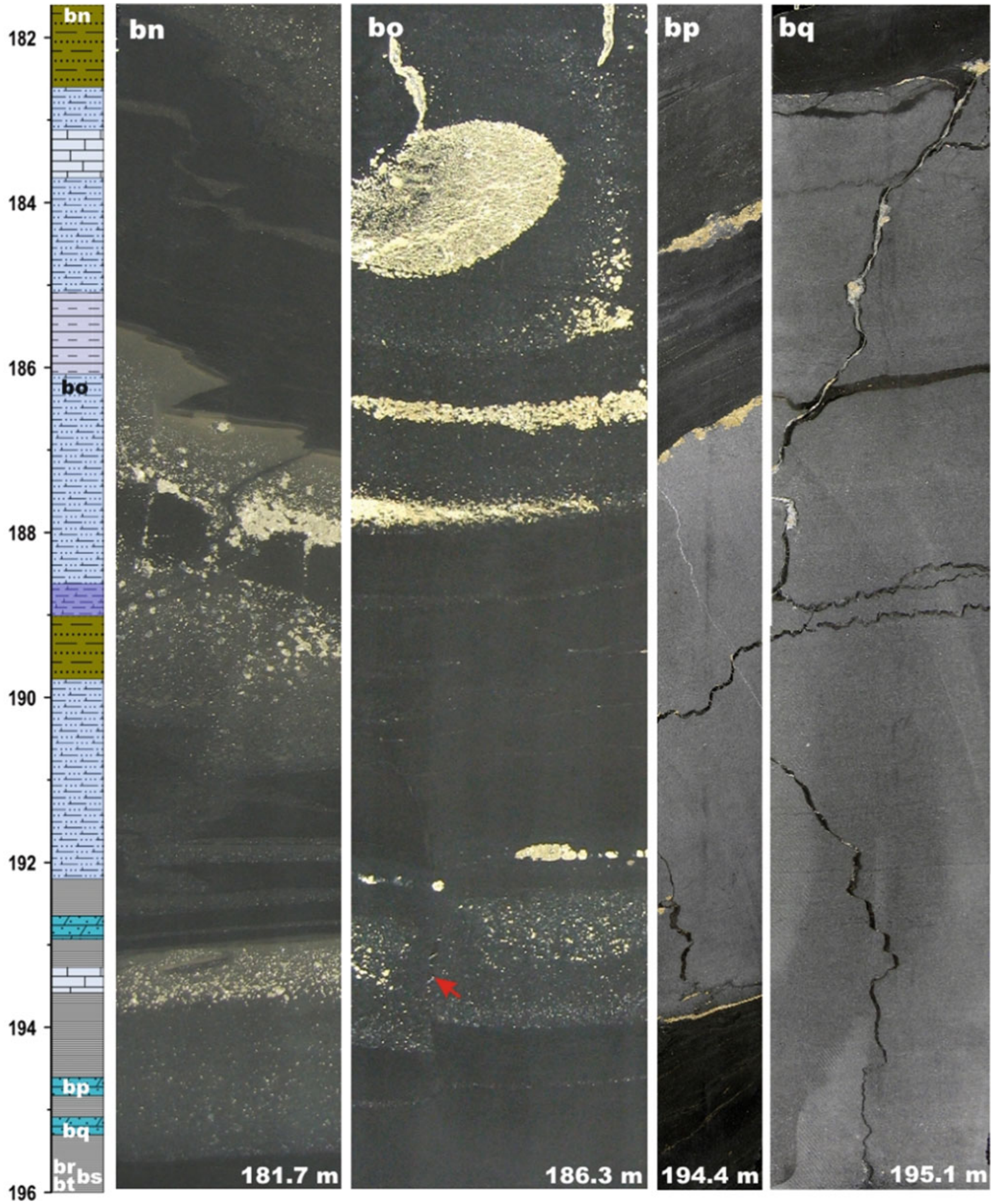

Fig. 6.116 (continued) (**bn**) Interbedded black mudstone and greywacke with abundant sulphide impregnations; note the syn-depositional deformation of the greywacke-mudstone contact. (**bo**) Interbedded greywackes and black mudstones with abundant sulphide impregnation and a large sulphide concretion; the lower greywacke bed was fractured with a displacement joint filled by a pyrobitumen-rich veinlet (*red arrowed*). (**bp**) *Grey*, massive, sandy dolostone within black mudstones; dolostone contains pyrobitumen-rich veins and sulphide impregnations at the contacts with mudstones. (**bq**) Grey, massive to indistinctly laminated dolostone bed with cross-cutting and bedding-parallel pyrobitumen-rich veinlets, in places containing sulphides; the dolostone is overlain by black mudstones

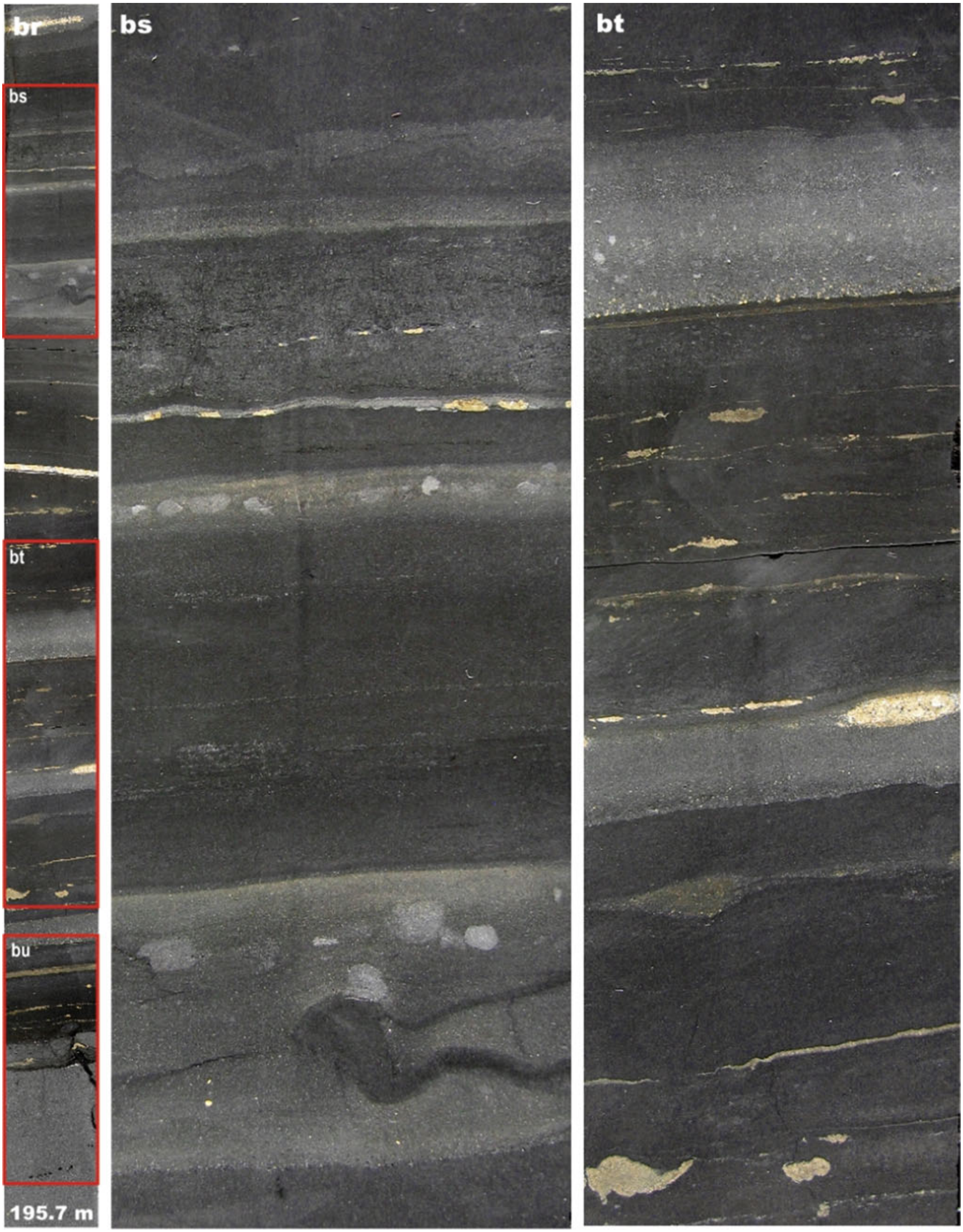

Fig. 6.116 (continued) (**br**) A grey dolostone bed overlain by rhythmically interbedded black mudstones and greywackes containing abundant sulphide laminae and small concretions. (**bs**) Close-up of Fig. 6.116br showing greywackes (with *pale grey* carbonate patches) interbedded with black mudstones; note the mud injection into the lowermost greywacke layer. (**bt**) Close-up of Fig. 6.116br showing abundant sulphide concretions and laminae in black mudstones interbedded with graded beds of greywacke

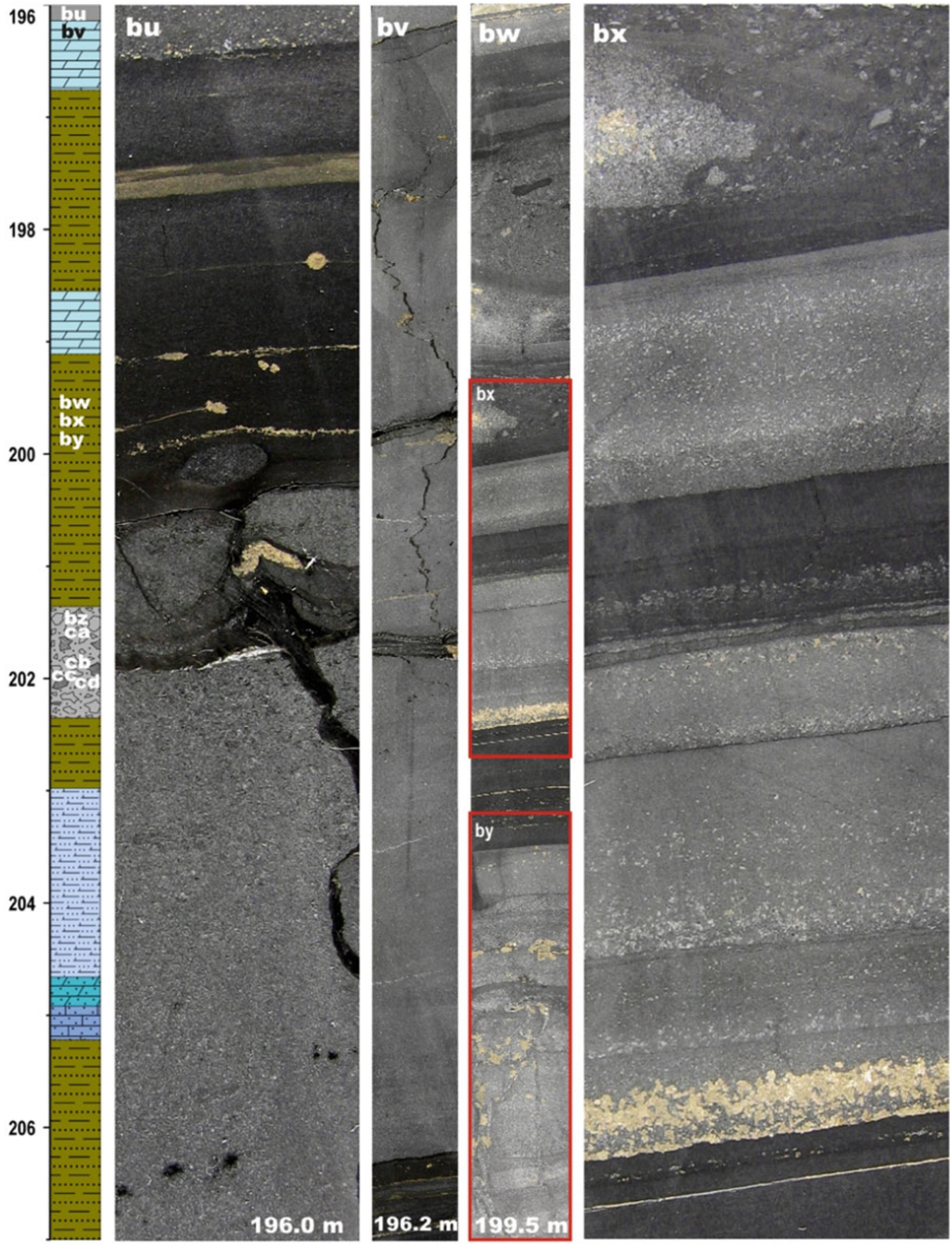

Fig. 6.116 (continued) (**bu**) Close-up of Fig. 6.116br showing contact of dolostone bed with the overlying black mudstones; note that the contact is disrupted by the injection of a pyrobitumen-rich vein. (**bv**) *Grey*, massive dolostone beds separated by thin interlayers of black, laminated, C_{org}-rich mudstones; dolostones contain ptygmatic, pyrobitumen-rich veins apparently sourced from mudstone interlayers. (**bw**) Greywackes and calcareous greywackes rhythmically interbedded with black mudstones and overlain by a bed of matrix-supported, intraformational conglomerate (*uppermost* part of the photo); note that two beds of the greywacke in the middle are graded. (**bx**) Close-up of Fig. 6.116bw showing normally-graded beds of sulphide-bearing greywackes and calcareous greywackes rhythmically interbedded with mudstones; the intraformational conglomerate (*uppermost* part of the photo) is composed of matrix-supported, mm-sized grains of greywacke and mudstone and larger irregular fragments of greywacke

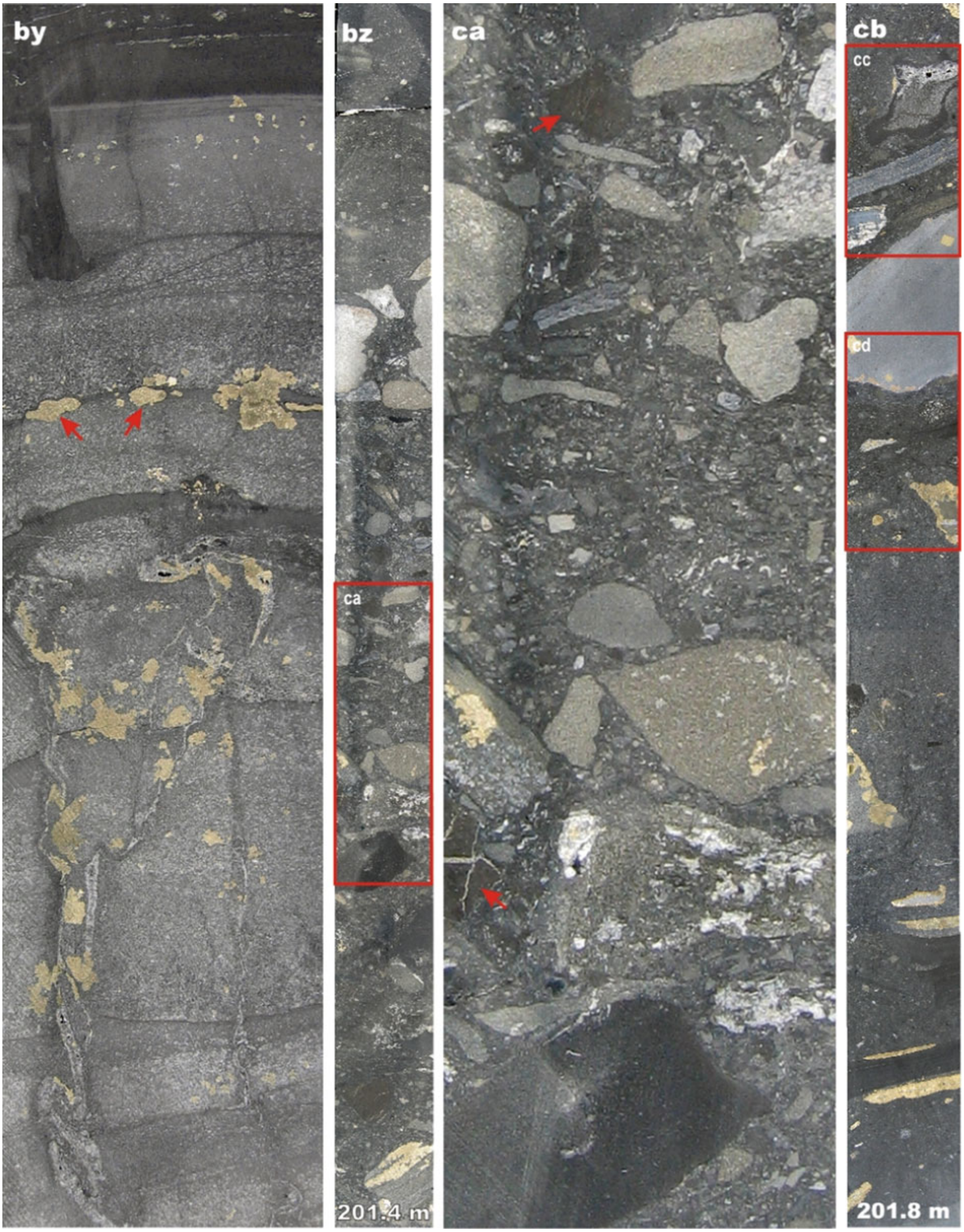

Fig. 6.116 (continued) (**by**) Close-up of Fig. 6.116bw showing thin bedded greywackes and calcareous greywackes containing sulphide concretions (*red arrowed*) and porphyroblasts and intersected by calcite veinlets. (**bz**) Intraformational, matrix-supported conglomerate containing various unsorted, angular to rounded clasts from a few mm to more than 10 cm in size. (**ca**) Close-up of Fig. 6.116bz showing clast composition of the intraformational conglomerate: clasts of greywackes and sandy limestones (*grey*), mudstones (*black*) and pyrobitumen-rich mudstones (*red arrowed*) floating within a mudstone matrix. (**cb**) Intraformational, matrix-supported conglomerate containing angular and variably rounded clasts of greywacke, sandy limestone, resedimented sulphide concretions and intensely sulphidised rocks

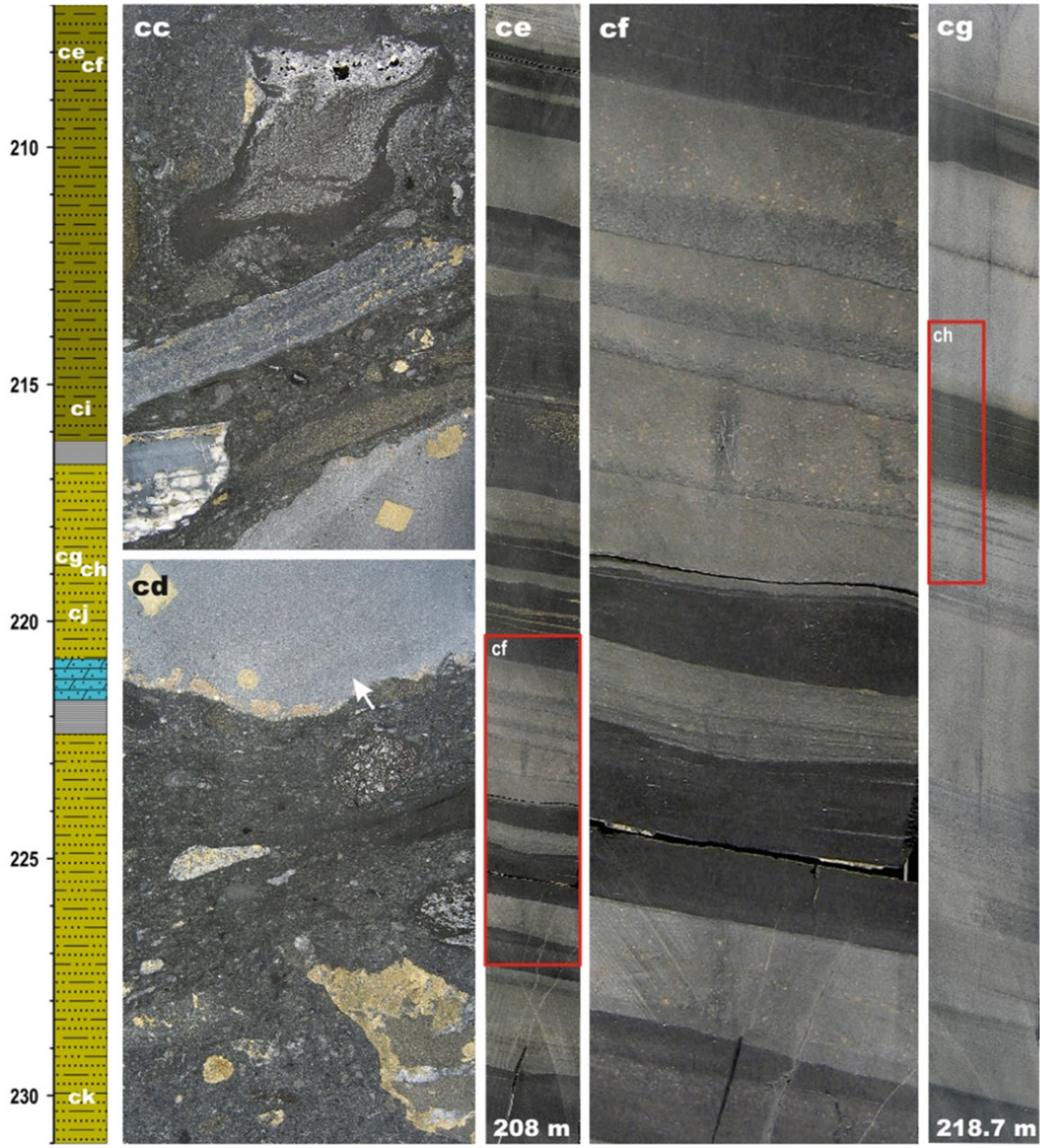

Fig. 6.116 (continued) (**cc**) Close-up of Fig. 6.116cb showing intraformational, matrix-supported conglomerate containing soft-sediment deformed, black mudstone, a broken greywacke layer, angular dolostone clast with pyrite cubes and numerous mm-sized greywacke grains. (**cd**) Close-up of Fig. 6.116cb showing intraformational, matrix-supported conglomerate containing rounded and angular clasts of sulphidised greywacke (*lower* part of the photo) and either a clast or a soft-sedimentary deformed layer of sandy limestone with abundant sulphides (*arrowed*). (**ce**) Rhythmically interbedded greywackes and mudstones. (**cf**) Close-up of Fig. 6.116ce showing normally graded and flat-laminated greywackes interbedded with black mudstones. (**cg**) Interbedded flat-laminated grey and dark-coloured greywackes

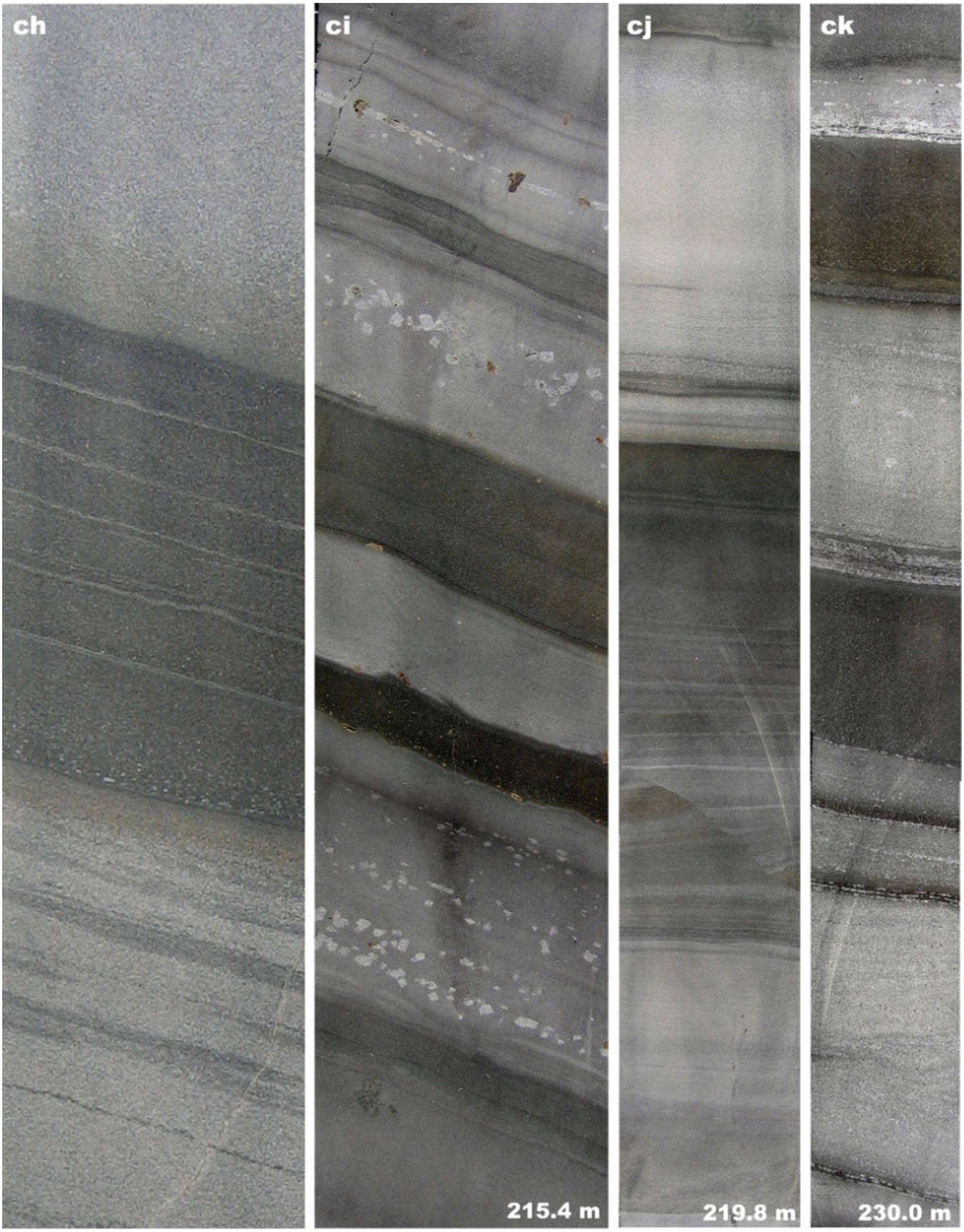

Fig. 6.116 (continued) (**ch**) Close-up of Fig. 6.116cg showing normal grading in thin beds of dark-coloured greywackes. (**ci**) Rhythmically interbedded grey and dark-coloured greywackes; grey greywackes contain abundant calcite crystals. (**cj**) Interbedded grey, indistinctly bedded to massive greywackes and dark-coloured, flat-laminated greywackes. (**ck**) Interbedded grey, laminated and dark-coloured, massive and flat-laminated greywackes; note the small-scale slumping in the lower bed

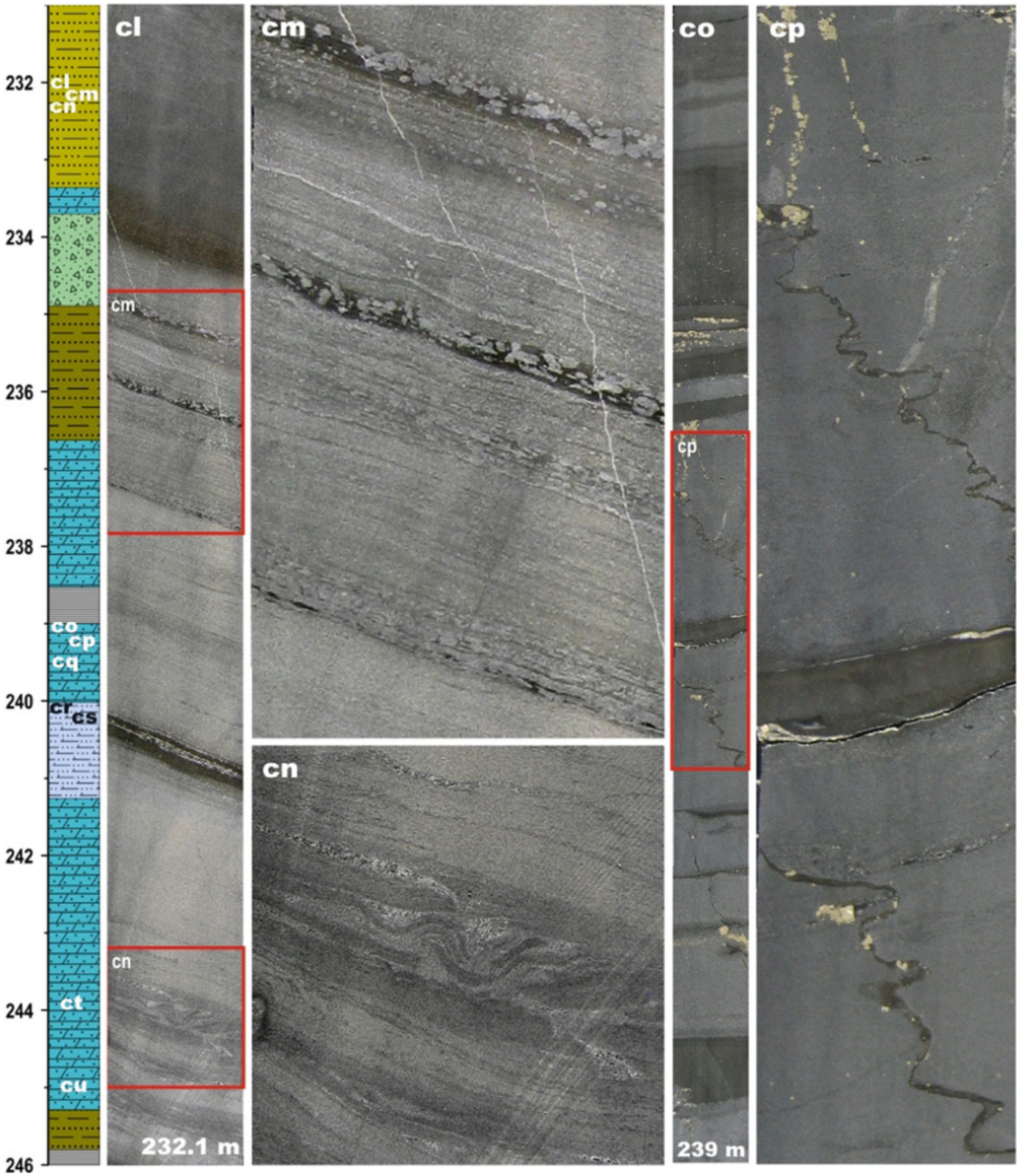

Fig. 6.116 (continued) (**cl**) Interbedded grey and dark-coloured, flat-laminated greywackes. (**cm**) Close-up of Fig. 6.116cl showing thinly laminated, grey greywackes with dark-coloured greywacke layers containing abundant calcite crystals. (**cn**) Close-up of Fig. 6.116cl showing a small-scale slumping structure involving both light and dark grey greywacke laminae; some laminae contain small calcite crystals. (**co**) Grey, massive, sandy dolostone alternating with dark-coloured mudstone. (**cp**) Close-up of Fig. 6.116co showing ptygmatic pyrobitumen veins and sulphides (*pale yellow*) within the sandy dolostone beds

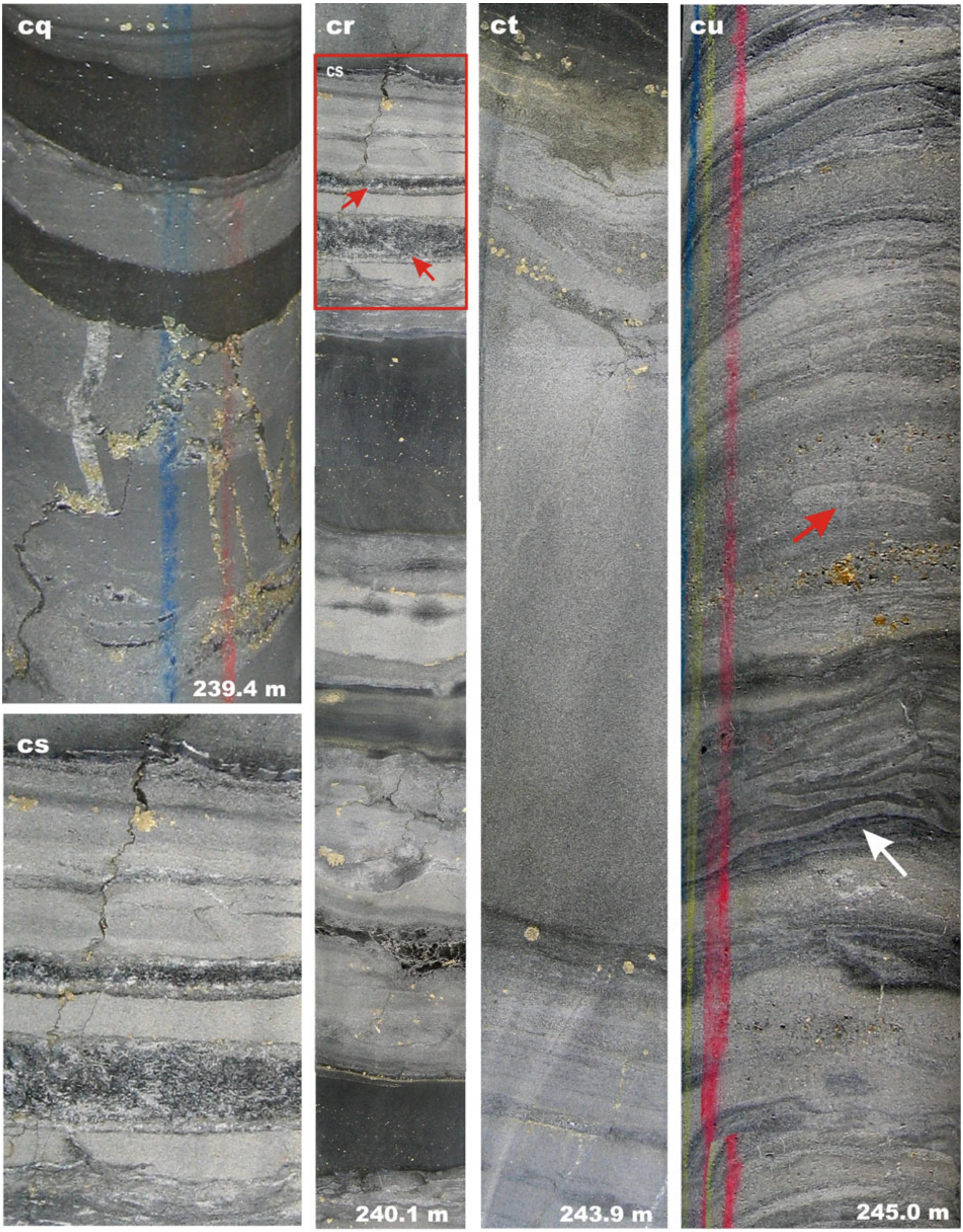

Fig. 6.116 (continued) (**cq**) Uncut core showing sandy dolostone interbedded with black mudstone; the dolostone contains a ptygmatic, pyrobitumen-rich veinlet, sulphide concretions and vertical calcite-sulphide veins terminating at the black mudstone bed. (**cr**) Interbedded sandy dolostones, calcareous greywackes and mudstones; note the bedding-parallel seams containing pyrobitumen-rich material and calcite (*red arrowed*). (**cs**) Close-up of Fig. 6.116cr showing details of the subvertical, pyrobitumen-rich veinlet and bedding-parallel seams with pyrobitumen and calcite. (**ct**) Pale grey, laminated dolostone (*lowermost* part of the photo) overlain by massive limestone passing into soft-sediment deformed limestone-marl interbeds. (**cu**) Uncut core of bedded dolostone with a dolostone intraclast (*red arrowed*) and distorted ribbon structure in a dark grey bed (*white arrowed*)

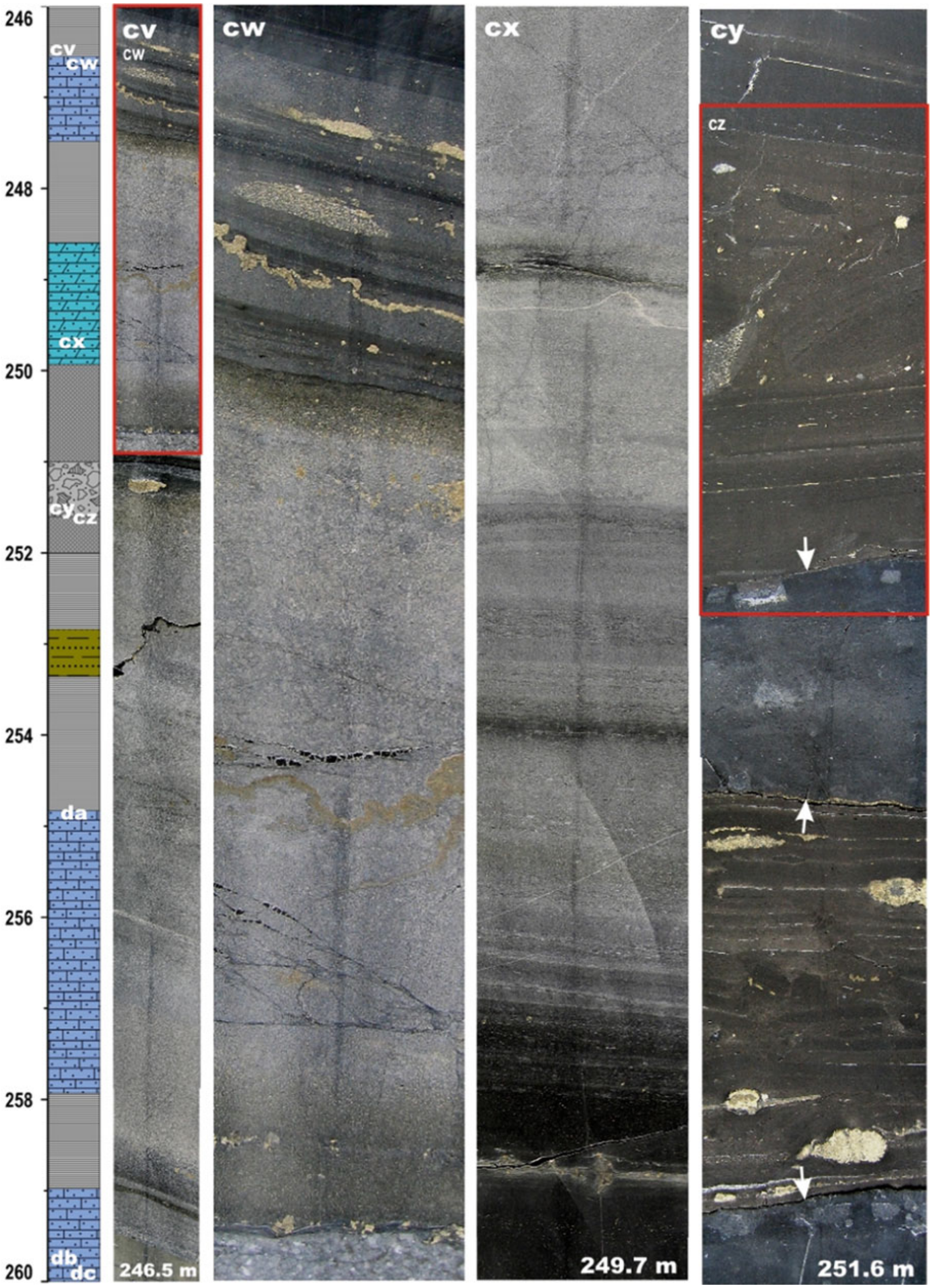

Fig. 6.116 (continued) (**cv**) Sandy limestone containing mudstone laminae, pyrobitumen veinlets and sulphide concretions, overlain by mudstone rich in sulphides. (**cw**) Close-up of Fig. 6.116cv showing the upper contact of massive sandy, limestone with overlying sulphide-rich laminated mudstone; note the thin interval composed of sparry calcite at the *bottom*. (**cx**) Gradual contact of mudstone with overlying dolostone; the latter is flat-laminated at the *bottom* and massive at the *top*. (**cy**) Pyrobitumen-rich mudstone containing chert nodules (*arrowed*) and sulphides in the form of spherical concretions, thin laminae and dissemination

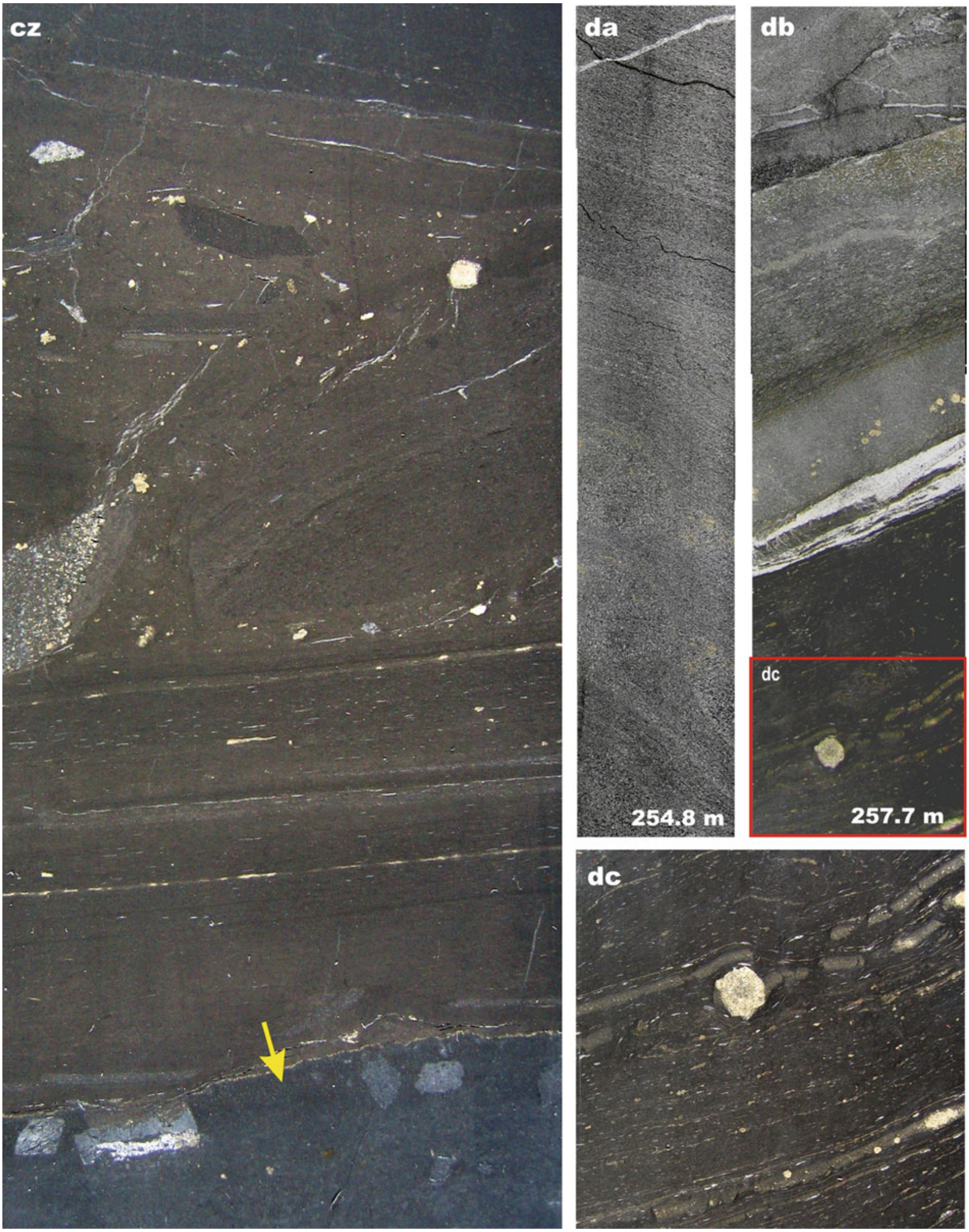

Fig. 6.116 (continued) (**cz**) Close-up of Fig. 6.116cy showing structural details of pyrobitumen-rich mudstone. Parallel-laminated mudstone is overlain with a sharp boundary by intraformational, matrix-supported conglomerate that passes into parallel-laminated mudstone. Laminae within the upper mudstone bed are at an oblique angle with respect to the lamination in the lower bed. A chert nodule at the bottom is *yellow-arrowed*. (**da**) Flat-laminated, sandy limestone containing bedding-parallel, pyrobitumen-rich veinlets and cut by a white calcite veinlet. (**db**) C_{org}-rich mudstone overlain by grey, bedded sandy limestone; note the calcite veins at the contact. (**dc**) Close-up of Fig. 6.116db exhibiting C_{org}-rich mudstone with a spherical, zoned sulphide nodule and synsedimentary sulphide layers affected by diagenetic boudinage causing dismembering

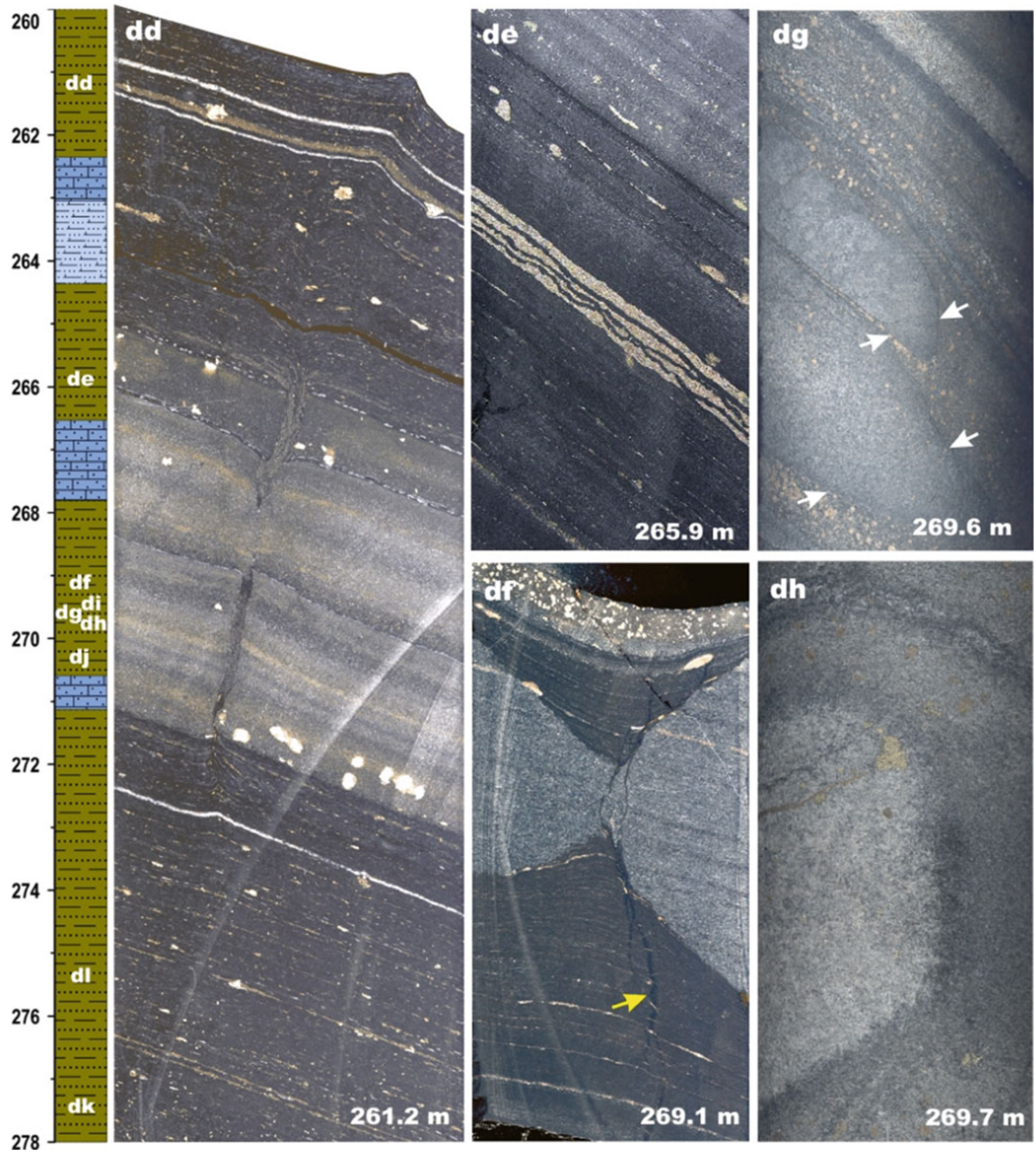

Fig. 6.116 (continued) (**dd**) Laminated, grey greywacke and dark grey, C_{org}-rich mudstone with abundant sulphides in the form of disseminations, thin, bedding-parallel laminae, and spherical micronodules; note the partial separation of the greywacke bed by injected mudstones from either side (interpreted as incipient sedimentary boudinage). (**de**) C_{org}-rich mudstone overlain by calcareous mudstone, both containing disseminated sulphides; note the package of sulphide laminae in the mudstone. (**df**) Grey, flat-laminated sandy limestone bed, partially dismembered (interpreted as sedimentary boudinage) in black, C_{org}-rich mudstone; note the vertical pyrobitumen-rich veinlets crosscutting the lower mudstone bed (*yellow arrowed*) and the attenuated part of the limestone bed. (**dg**) Two lensoidal calcite concretions (*arrowed*) in laminated greywacke-mudstone containing disseminated sulphides. (**dh**) Spherical calcite concretion in massive greywacke

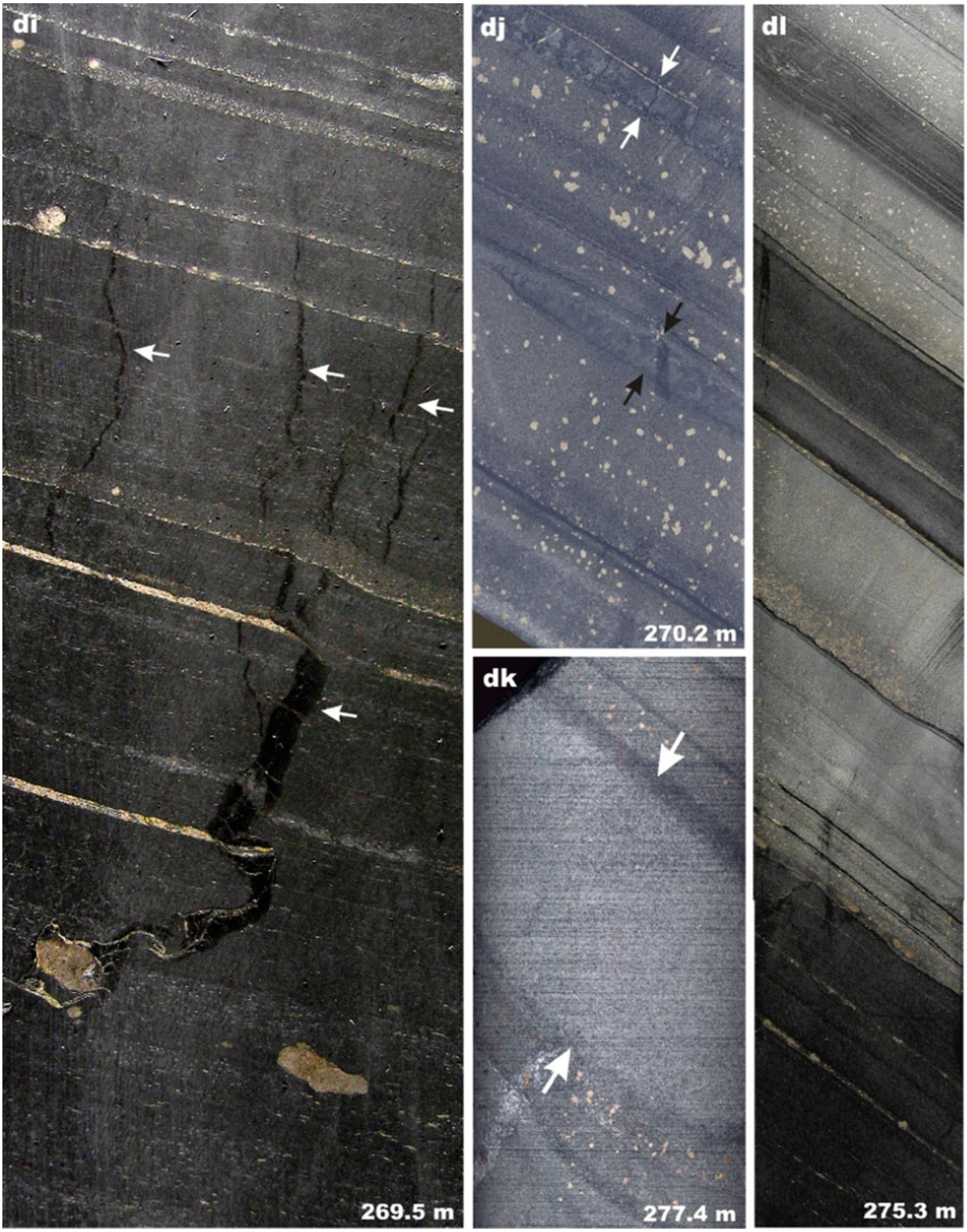

Fig. 6.116 (continued) (**di**) Black, C_{org}-rich mudstone with a few fine-grained greywacke laminae (*grey* and enriched in disseminated sulphides); note the two subspherical sulphide concretions, two sulphide laminae, and sub-vertical, branching upward, pyrobitumen-rich veinlets (*arrowed*). (**dj**) Lensoidal calcite concretion (*black arrowed*) and concretionary layer (*white arrowed*) in parallel-bedded greywacke with disseminated sulphides. (**dk**) Calcite concretion (*arrowed*) in parallel-bedded greywacke with disseminated sulphides. (**dl**) Interbedded greywacke and black, C_{org}-rich mudstone, both showing parallel lamination and containing disseminated sulphides; note that some sandstone beds are graded

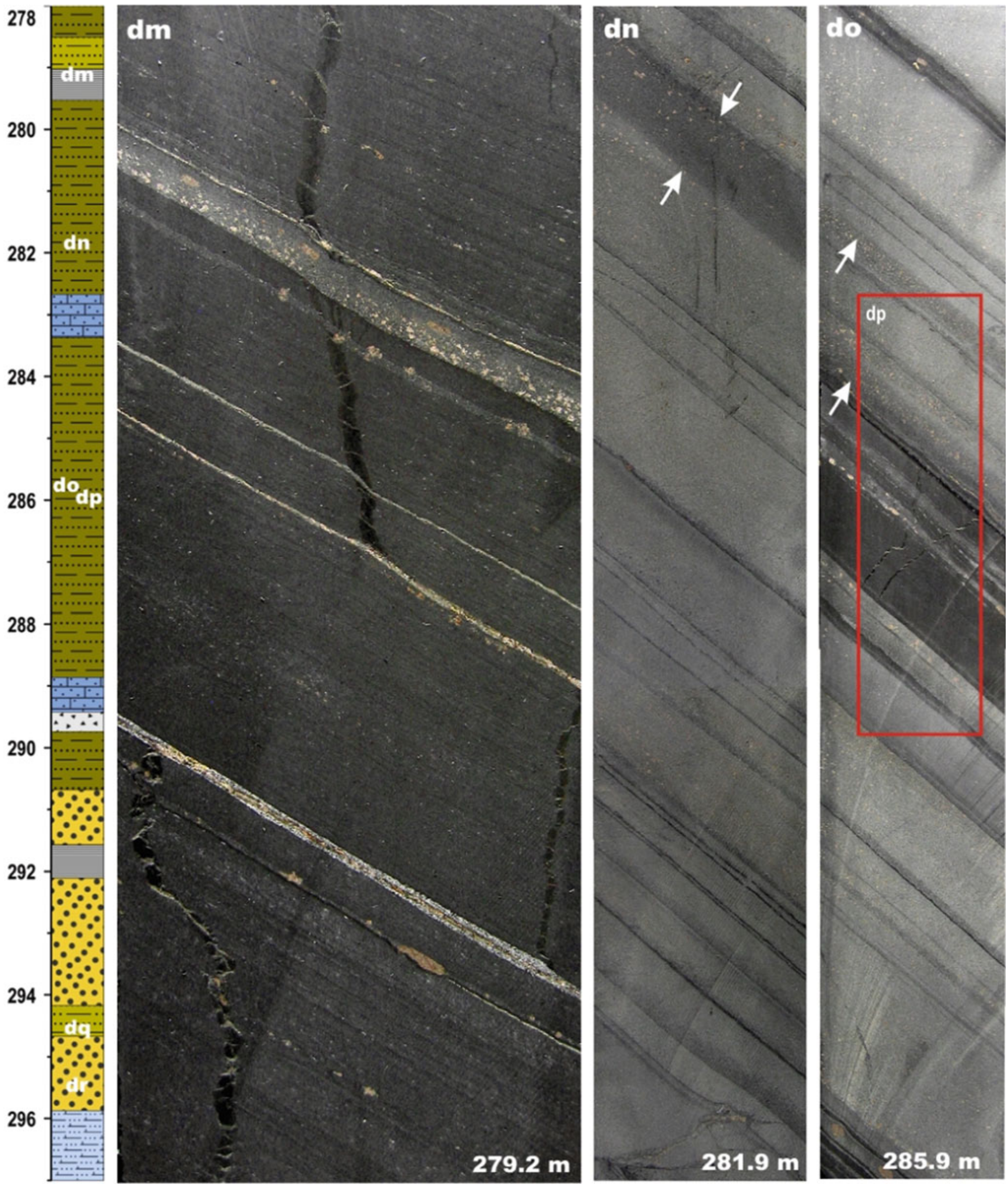

Fig. 6.116 (continued) (**dm**) *Black*, C_{org}-rich mudstone containing sulphide-rich greywacke lamina; sub-vertical, pyrobitumen-rich veinlets (*arrowed*) are displaced along bedding-parallel, shear-zones cemented by calcite, sulphide and mica (bright). (**dn**) Interbedded greywackes (*grey*) and calcareous greywacke (*dark grey*) with a mudstone bed (*arrowed*). (**do**) Interbedded greywacke (*grey*) and mudstone (*black*); calcareous greywacke layers are arrowed

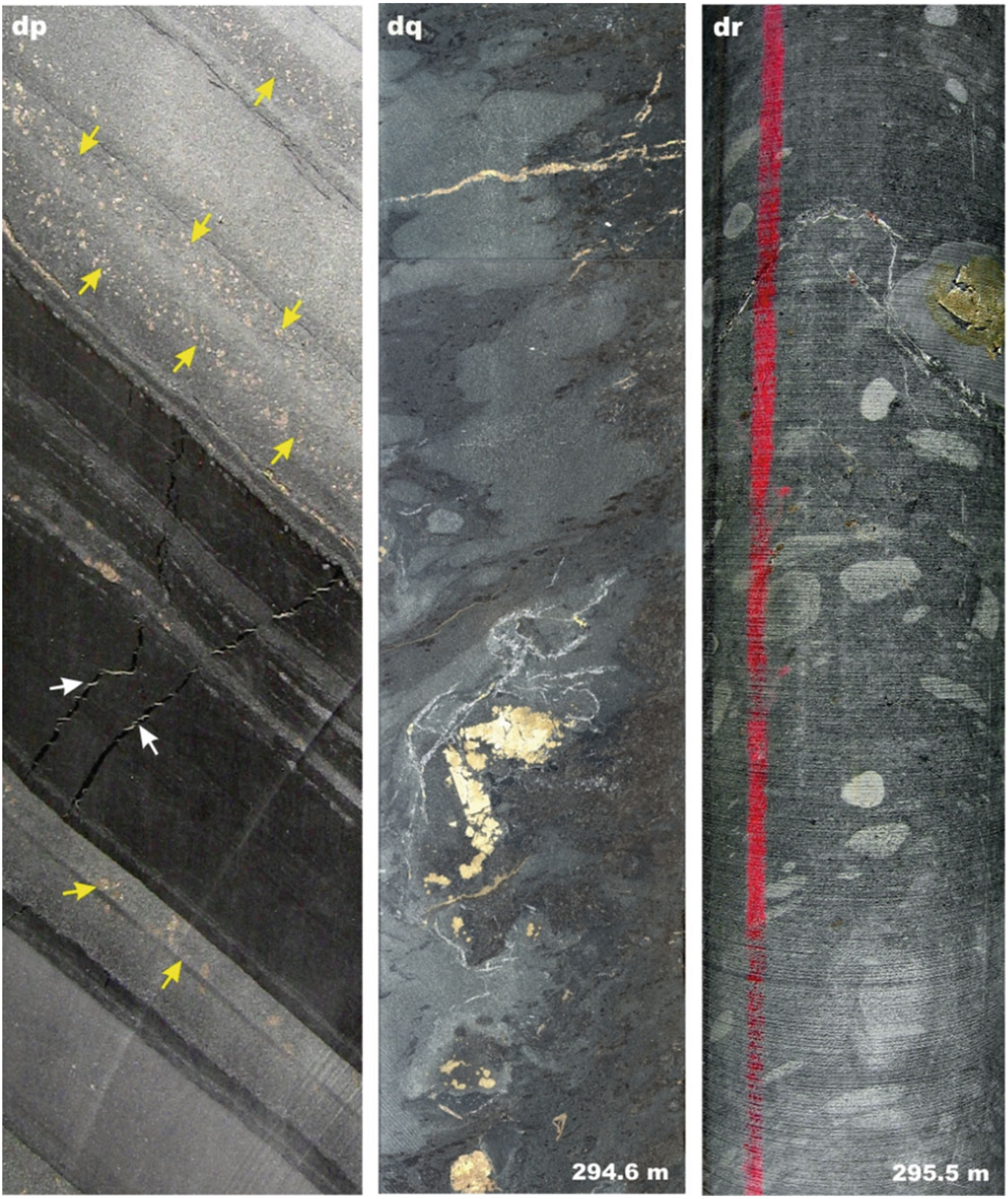

Fig. 6.116 (continued) (**dp**) Close-up of Fig. 6.116do showing parallel lamination in both greywackes and black, C_{org}-rich mudstone; note the sub-vertical, pyrobitumen-rich veinlets (*white arrowed*) in the mudstone layer and abundant disseminated sulphides in calcareous greywacke layers (*yellow arrowed*). (**dq**) Uppermost part of intraformational, matrix-supported conglomerate containing distinct, individual intraclasts and soft-sediment deformed greywacke and black mudstone layers with disrupted bedding; sulphide clasts or concretions, thin sulphide and calcite veinlets are also present. (**dr**) Lower part of intraformational, matrix-supported conglomerate containing mostly rounded and elongated greywacke clasts and some sulphide nodules

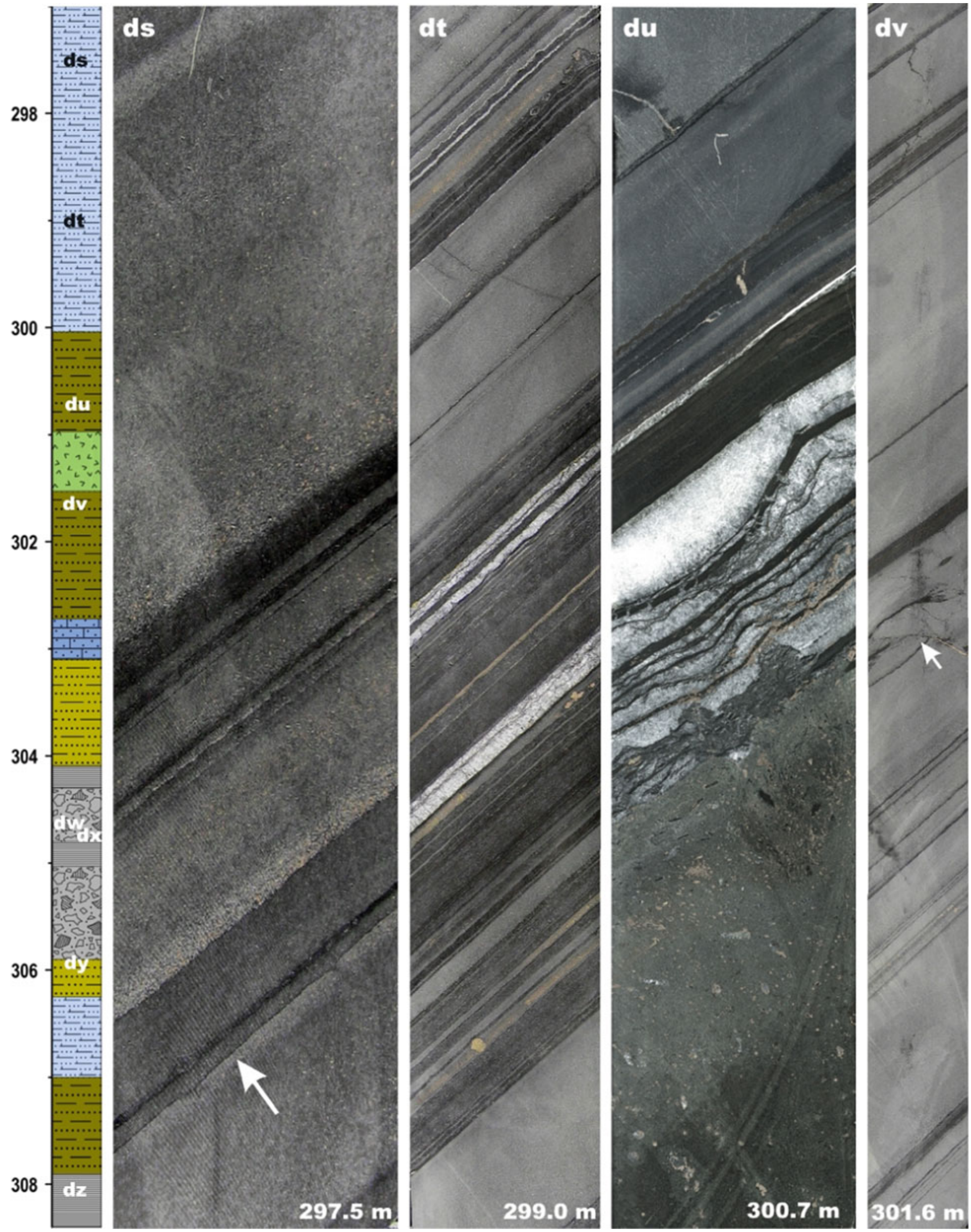

Fig. 6.116 (continued) (**ds**) Calcareous greywackes and greywackes alternating with black mudstone; note both inverse (*arrowed*) and normal grading in some greywacke beds. (**dt**) Interlaminated greywacke, black mudstone and calcareous mudstone with bedding-parallel calcite and sulphide veins/seams (bright). (**du**) Uneven contact of a mafic lava flow with the overlying black, C_{org}-rich mudstone and greywacke; note the alternation of bedding-parallel, white calcite veins/seams and black mudstone laminae between the basalt and greywacke-mudstone. (**dv**) Thicker beds of greywacke alternating with thinner mudstone layers; note the small-scale, synsedimentary fault (*arrowed*) in the middle of the section

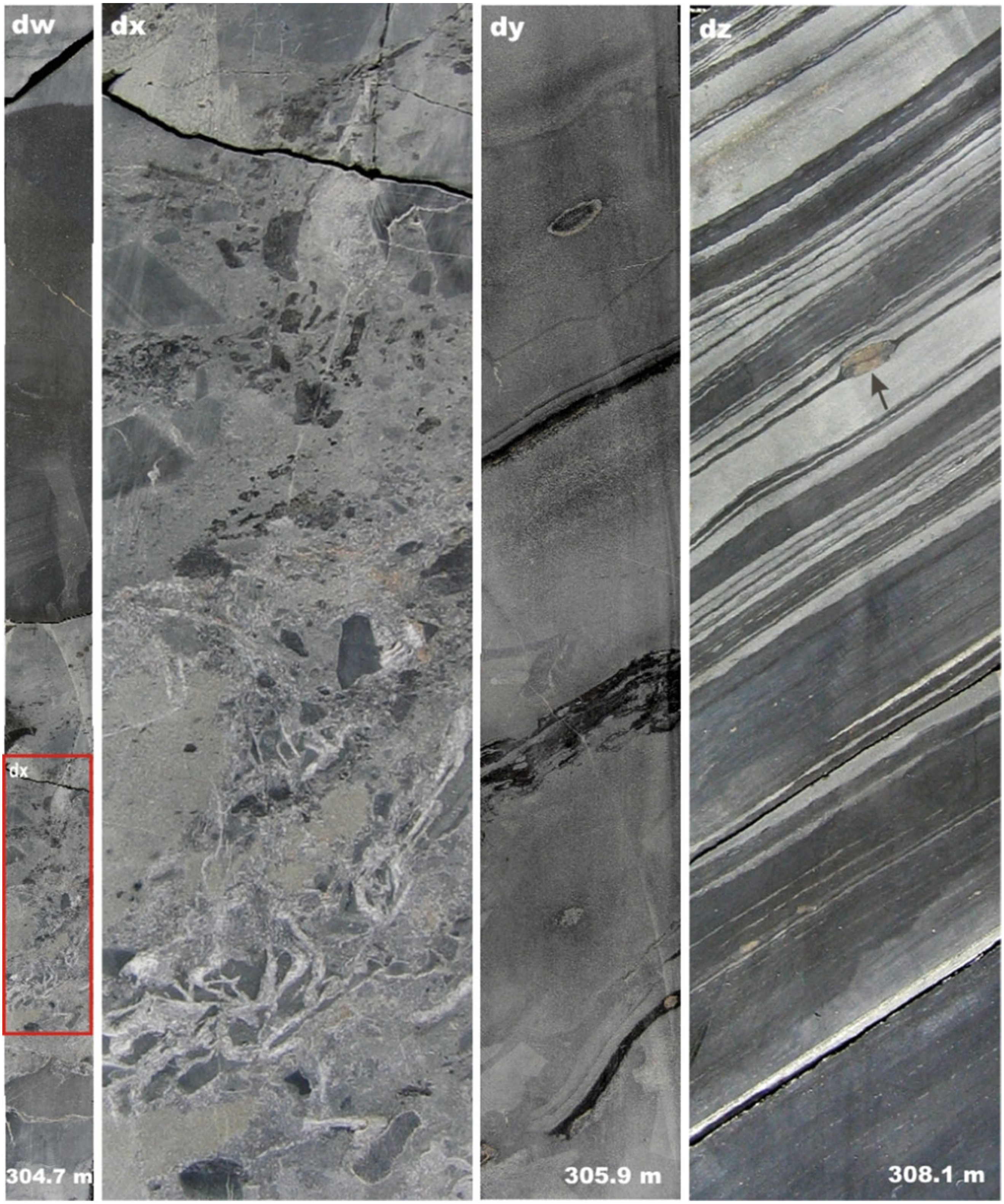

Fig. 6.116 (continued) (**dw**) Brecciated greywacke overlain by massive, black, C_{org}-rich mudstones. (**dx**) Close-up of Fig. 6.116dw exhibiting details of the brecciated greywacke bed with angular, dark grey clasts of mudstone in soft-sediment deformed greywacke matrix; note the network of thin *white* calcite veinlets separating some clasts. (**dy**) Interbedded thick greywackes and thin mudstone beds; note the synsedimentary deformation and brecciation at the base of two greywacke beds and partial dismembering of mudstone layers. (**dz**) Finely interlaminated greywackes and mudstones containing a small sulphide concretion (*arrowed*)

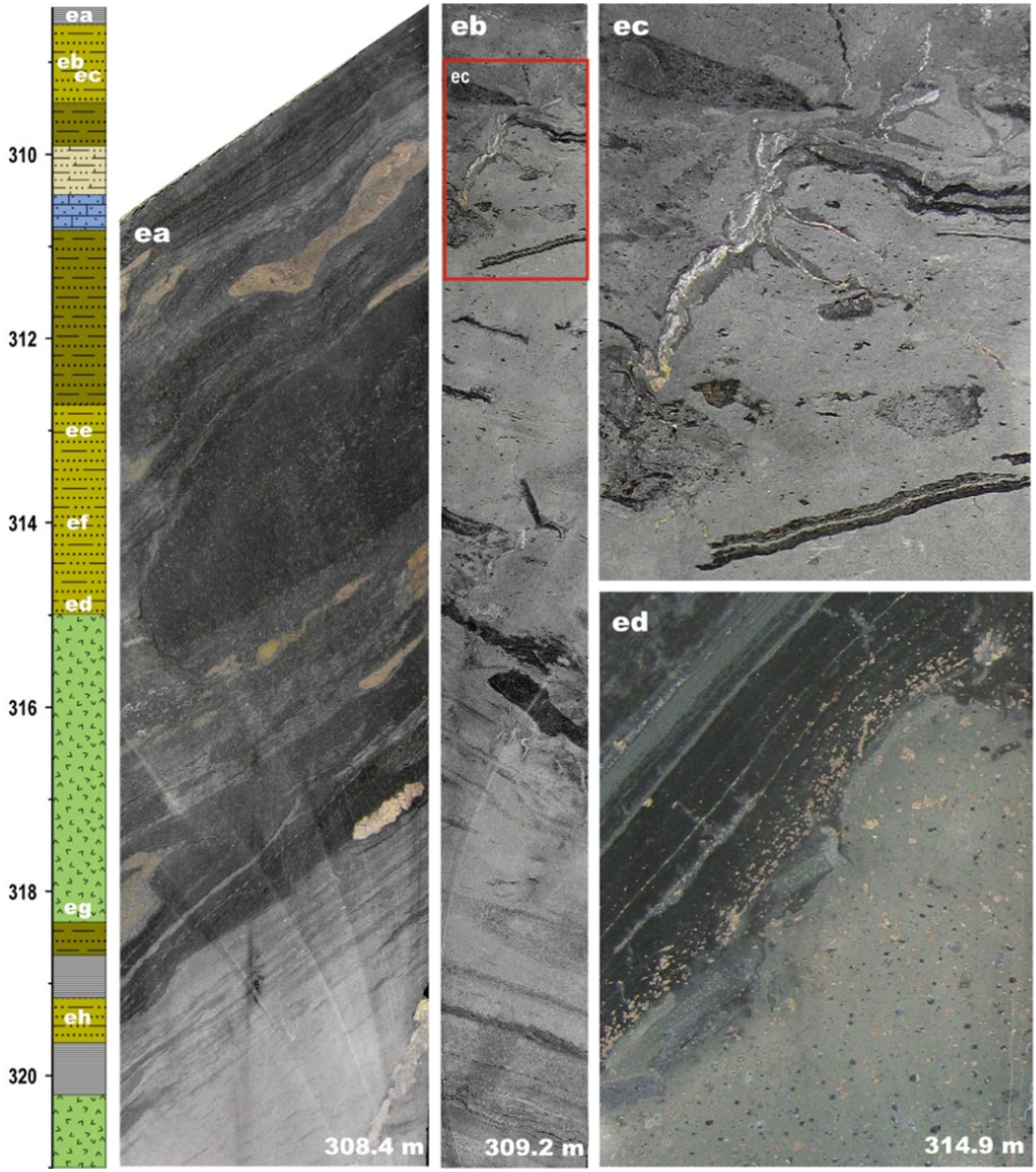

Fig. 6.116 (continued) (**ea**) Slumped, interlaminated greywacke and dark grey, C_{org}-rich mudstone; note the large, rounded mudstone clast and softly-deformed and dismembered sulphide layers. (**eb**) Variably disrupted layers of black mudstone, some of which become distinct, elongate or platy intraclasts in a greywacke matrix. (**ec**) Close-up of Fig. 6.116eb detailing variably disrupted and dismembered mudstone layers; note the apparent gas- or fluid-escape structure filled with white calcite. (**ed**) Contact of a mafic lava flow with the overlying interlaminated greywacke and black, C_{org}-rich mudstone; note the irregular relief of the contact, abundant sulphides above it and small lava fragments in the basal mudstone bed

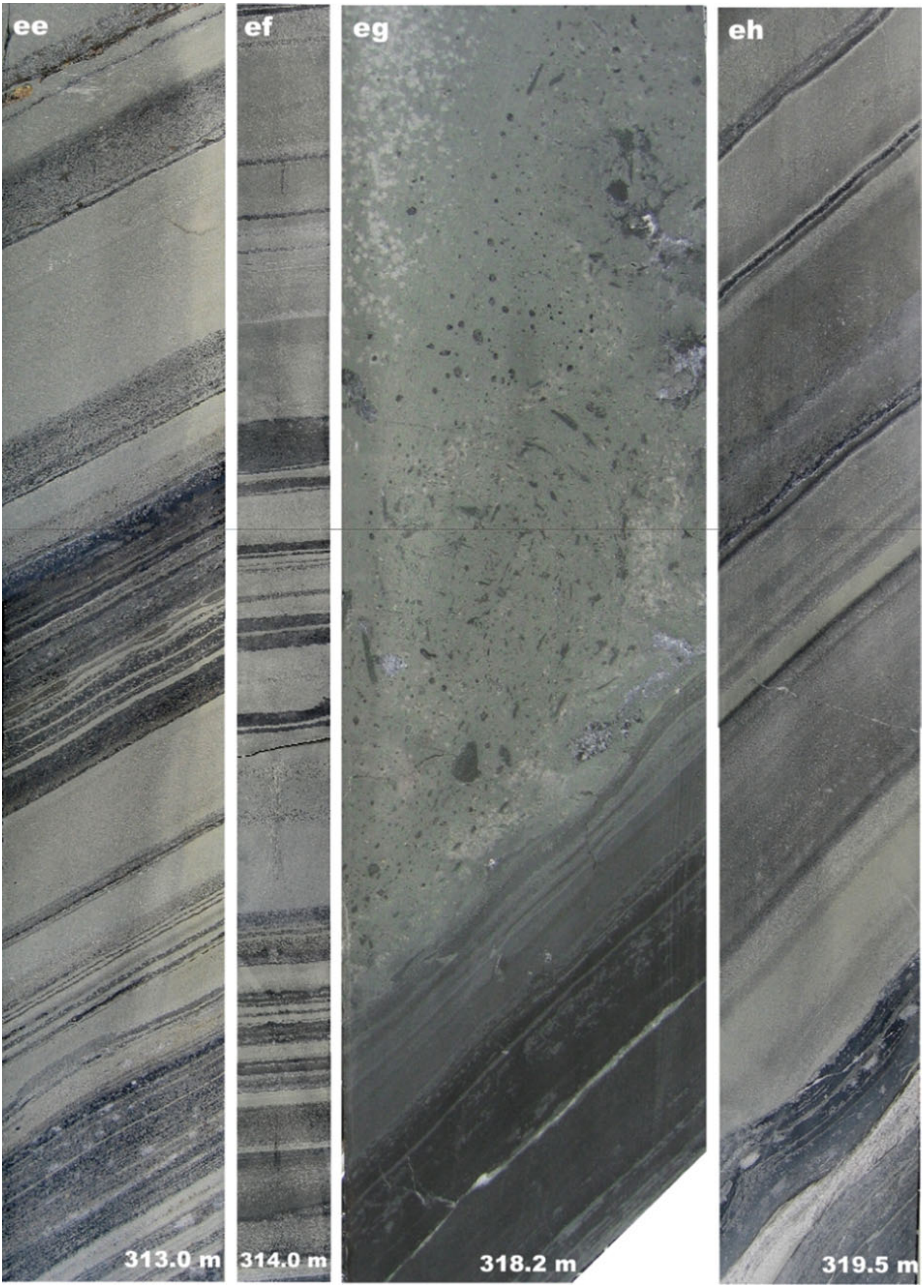

Fig. 6.116 (continued) (**ee**) Finely interbedded greywacke and black, C_{org}-rich mudstone impregnated with small calcite crystals. (**ef**) Interbedded greywacke, black, C_{org}-rich mudstone and calcareous greywacke; such intercalations are interlayered with basaltic lava flows similar to one shown in Fig. 6.116eg. (**eg**) Contact of a black, laminated, C_{org}-rich mudstone with the overlying mafic lava flow; note the abrasive nature of the contact. (**eh**) Interbedded, pale grey greywacke and black mudstone; such lithology occurs between mafic lava flows

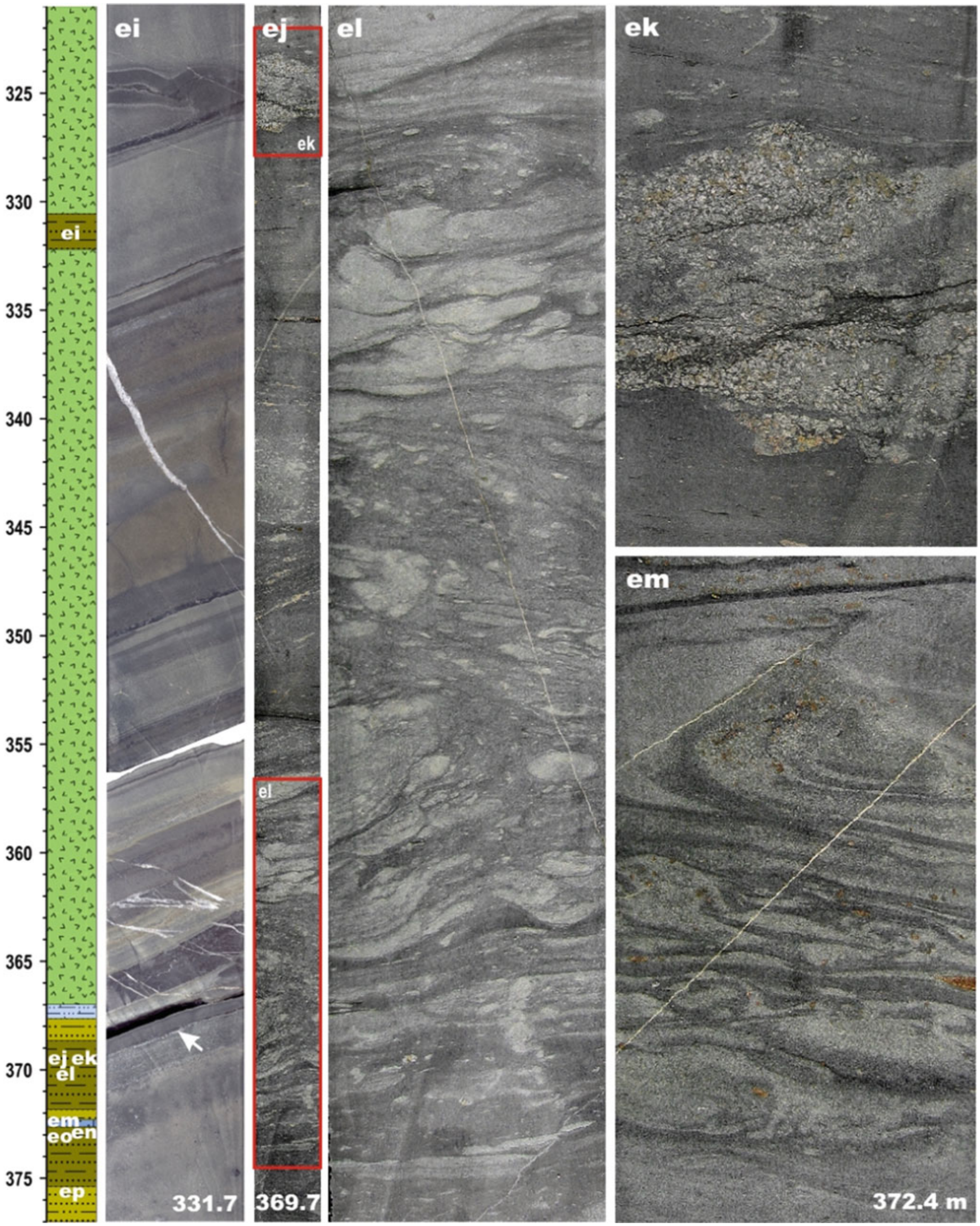

Fig. 6.116 (continued) (**ei**) Interbedded greywacke and dark grey mudstone layers forming a unit between mafic lava flows; the contact with the underlying basalt is *arrowed*. (**ej**) Slumped, interlaminated greywacke and black mudstone. (**ek**) Close-up of Fig. 6.116ej showing soft-sediment deformed, carbonate-rich greywacke (bright) in mudstone. (**el**) Close-up of Fig. 6.116ej showing soft-sediment deformed and dismembered greywacke and mudstone beds. (**em**) Convolute lamination in interbedded greywacke and mudstone

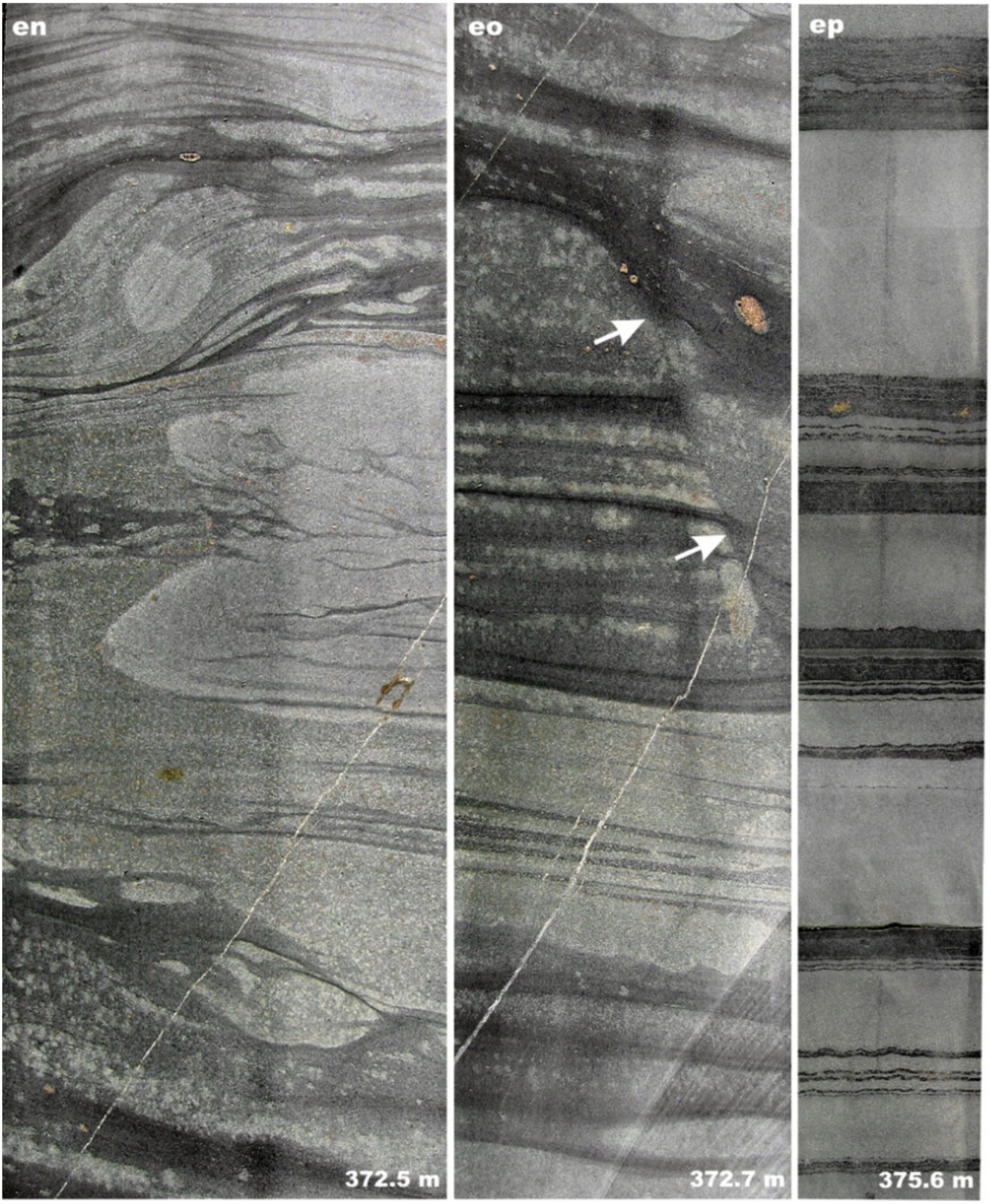

Fig. 6.116 (continued) (**en**) Soft-sediment deformed, interlaminated greywacke and mudstone; note the convolute lamination in light grey greywacke (*middle* part). (**eo**) Interlaminated greywacke and black mudstones; note locally channelized bed (*arrowed*). (**ep**) Interbedded massive greywackes and black, C_{org}-rich, laminated mudstones; the bottommost part of the beds are calcareous. Flat-laminated mudstones contain sulphide micronodules (*dark yellow*)

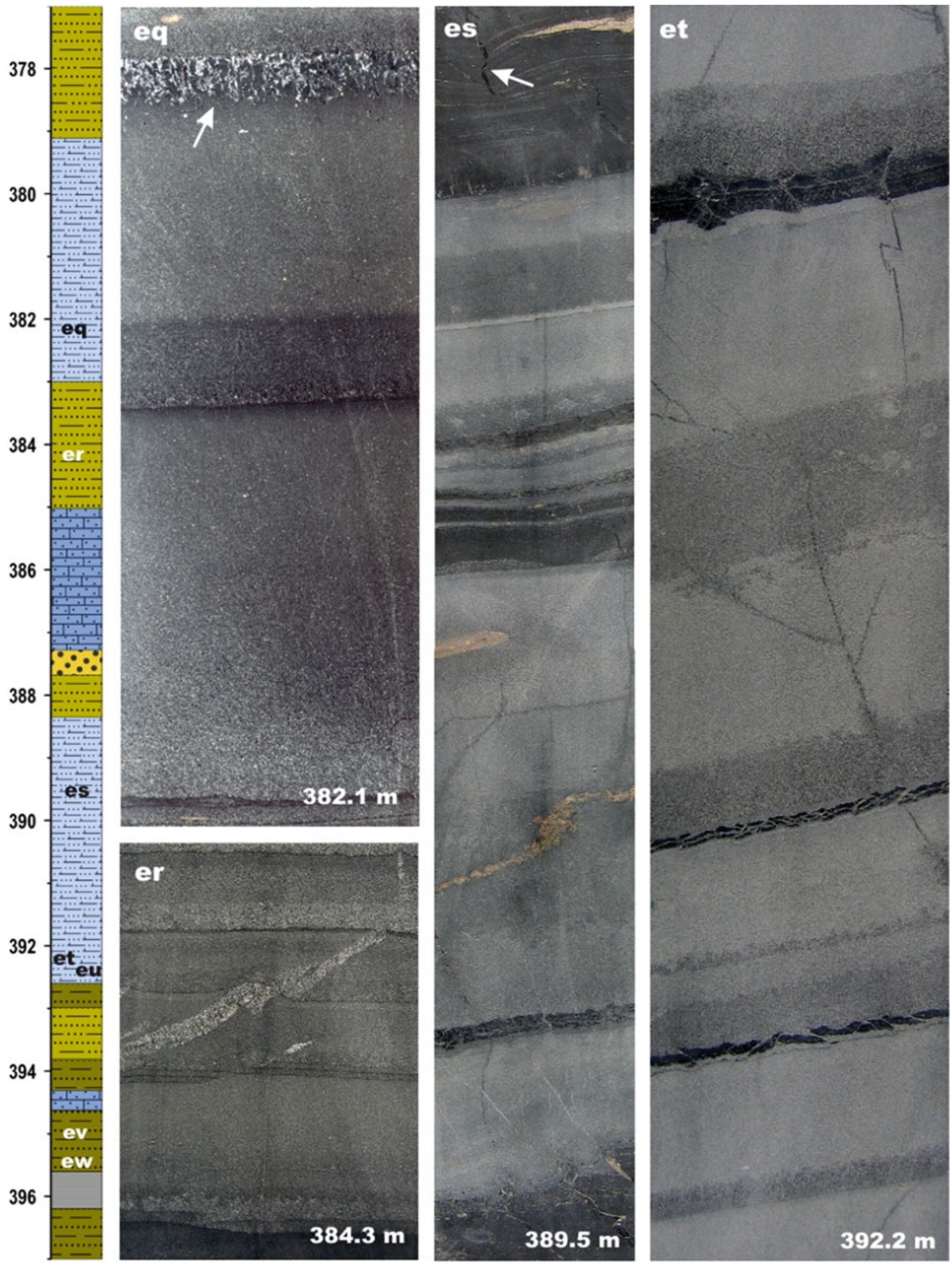

Fig. 6.116 (continued) (**eq**) Normally graded greywacke beds with calcareous bottommost parts; note the 1-cm-thick mudstone lamina (*arrowed*) that is cut by small, anastomosing calcite veinlets. (**er**) Interbedded greywacke and mudstone cross-cut by a tectonically-modified sedimentary dyke. (**es**) Interbedded greywacke (*grey*), calcareous greywacke (*pale grey*) and black, C_{org}-rich mudstone with a sulphide concretion and veinlets; note the vertical, pyrobitumen-rich veinlet within the uppermost mudstone layer (*arrowed*). (**et**) Interbedded calcareous greywacke (*pale grey*), greywacke (*grey*) and black, C_{org}-rich mudstone; note that all mudstone units are fractured and slightly displaced

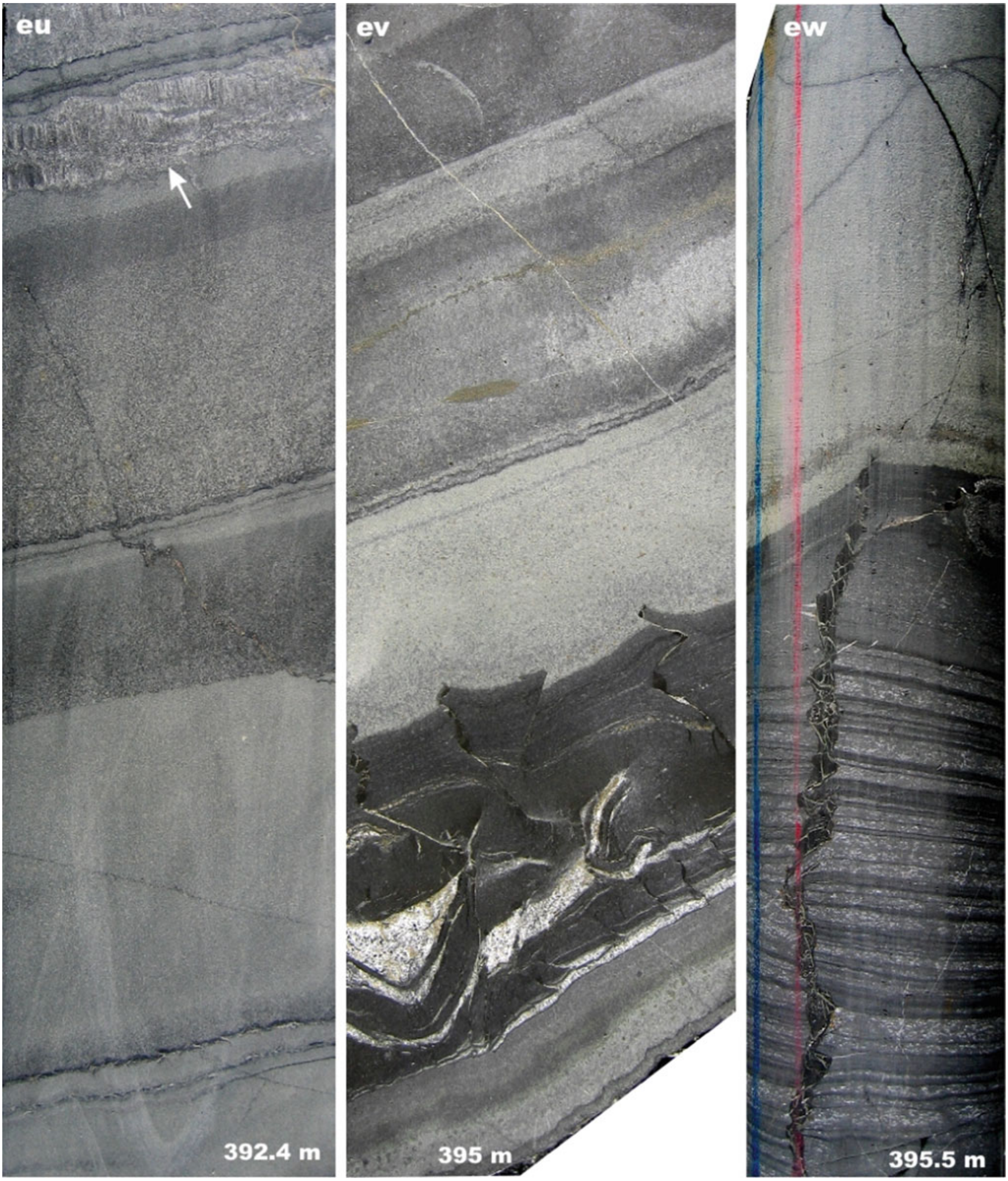

Fig. 6.116 (continued) (**eu**) Bedded greywacke (*dark grey*), calcareous greywacke (*pale grey*) and thin mudstone layers (*black*); note the bedding-parallel, cleaved vein (*arrowed*) composed of fibrous calcite and mica. (**ev**) Bedded greywacke (*grey*) and calcareous greywacke (*pale grey*) with a thick, black, C_{org}-rich mudstone layer, which is deformed and fractured, and interpreted as a loading structure; note the white calcite seams and veinlets, as well as a series of thin pyrobitumen-rich veinlets developed along the cracks within the mudstone layer. (**ew**) Dark grey, flat-laminated, calcareous mudstone cross cut by a pyrobitumen-rich vein, and overlain by a massive greywacke

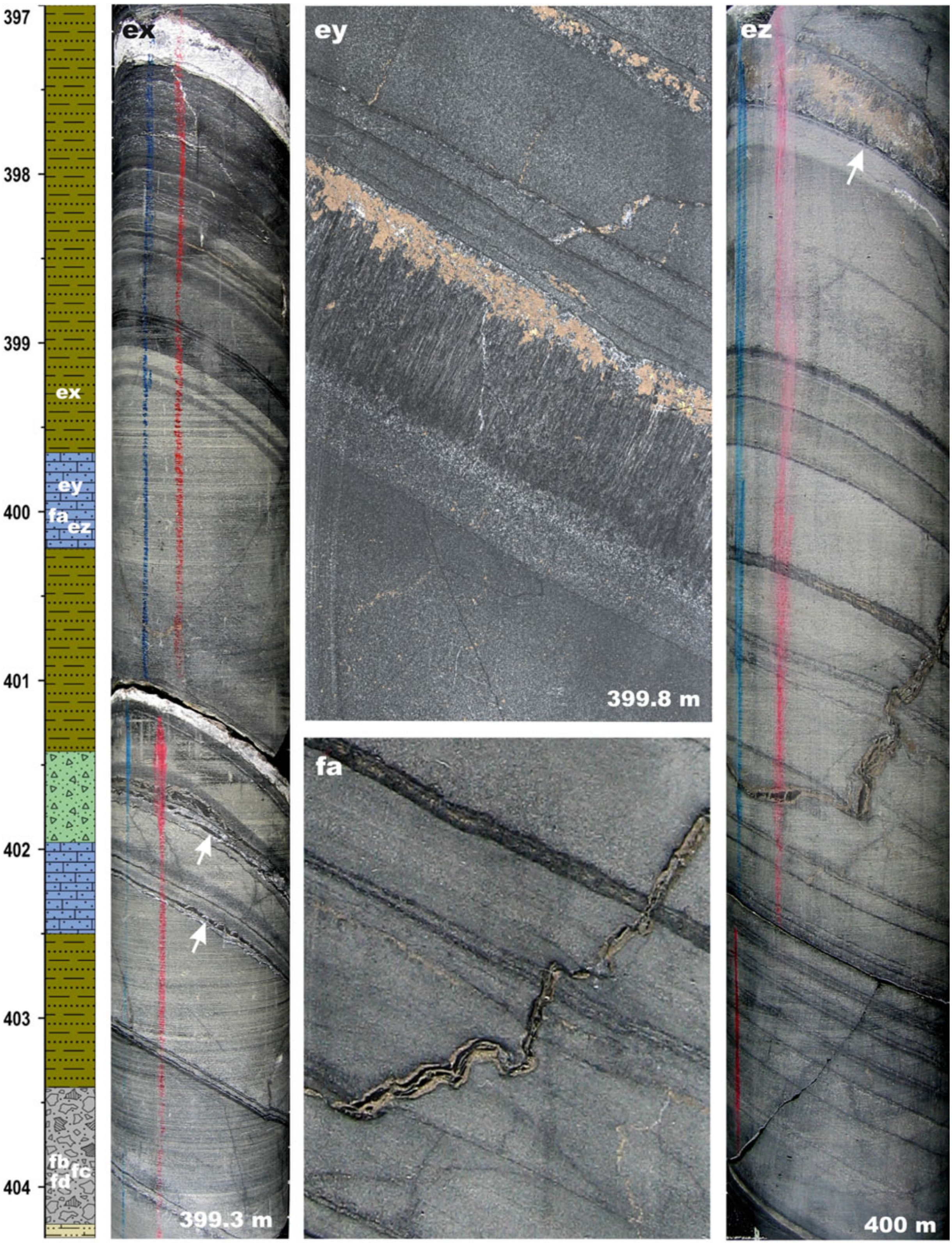

Fig. 6.116 (continued) (**ex**) Light grey greywacke beds with calcareous bottommost part and thin, black mudstone tops overlain by dark grey, laminated mudstone with bedding-parallel white calcite vein; note the thin, bedding-parallel calcite-pyrobitumen seams/veinlets within the greywacke bed (*arrowed*). (**ey**) Two layers (concretions?) of fibrous calcite in bedded greywacke; note the abundant sulphides occurring along the upper contact of the thicker layer. (**ez**) Sandy limestone (*pale grey*) alternating with thin, dark grey mudstone units; note the thin, ptygmatic vein filled with pyrobitumen and sulphides, and a thicker "layer" (concretion?) filled with fibrous calcite and sulphides (*arrowed*). (**fa**) Close-up of Fig. 6.116ez detailing the ptygmatic vein filled with pyrobitumen and sulphides

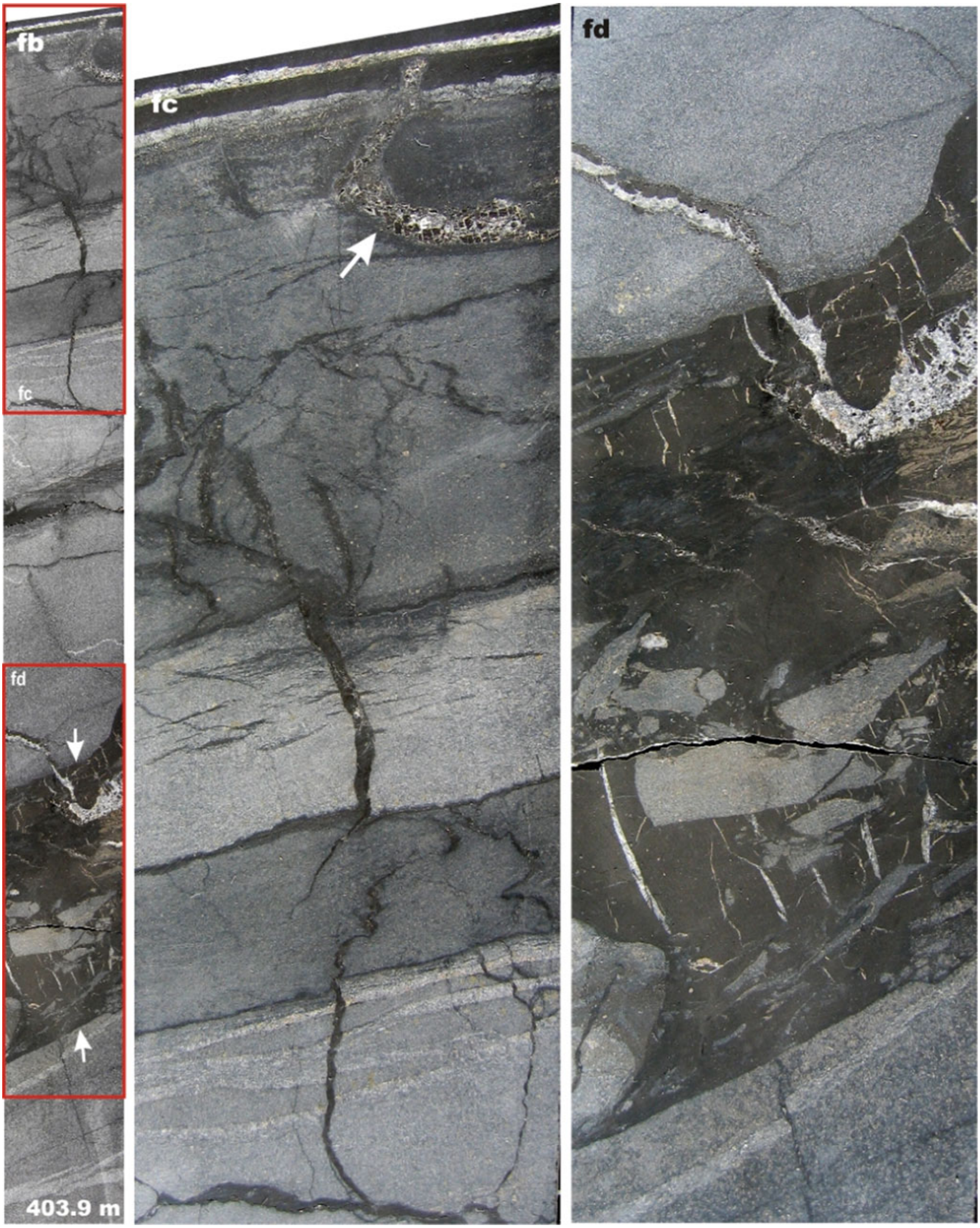

Fig. 6.116 (continued) (**fb**) Bedded, grey, sandy limestone, which is cracked on top and contains a dark coloured layer of intraformational, matrix-supported breccia (*arrowed*) composed of sandy limestones clasts floating in a dark coloured, C_{org}-rich matrix. (**fc**) Close-up of Fig. 6.116fb showing jointed, sandy limestone with pyrobitumen-rich (*black*) veinlets and calcite vein (*arrowed*) with fragmented pyrobitumen (*black* specks). (**fd**) Close-up of Fig. 6.116fb detailing the breccia composed of angular clasts of sandy limestone emplaced in pyrobitumen-rich matrix; brittle extensional cracks are filled with white calcite

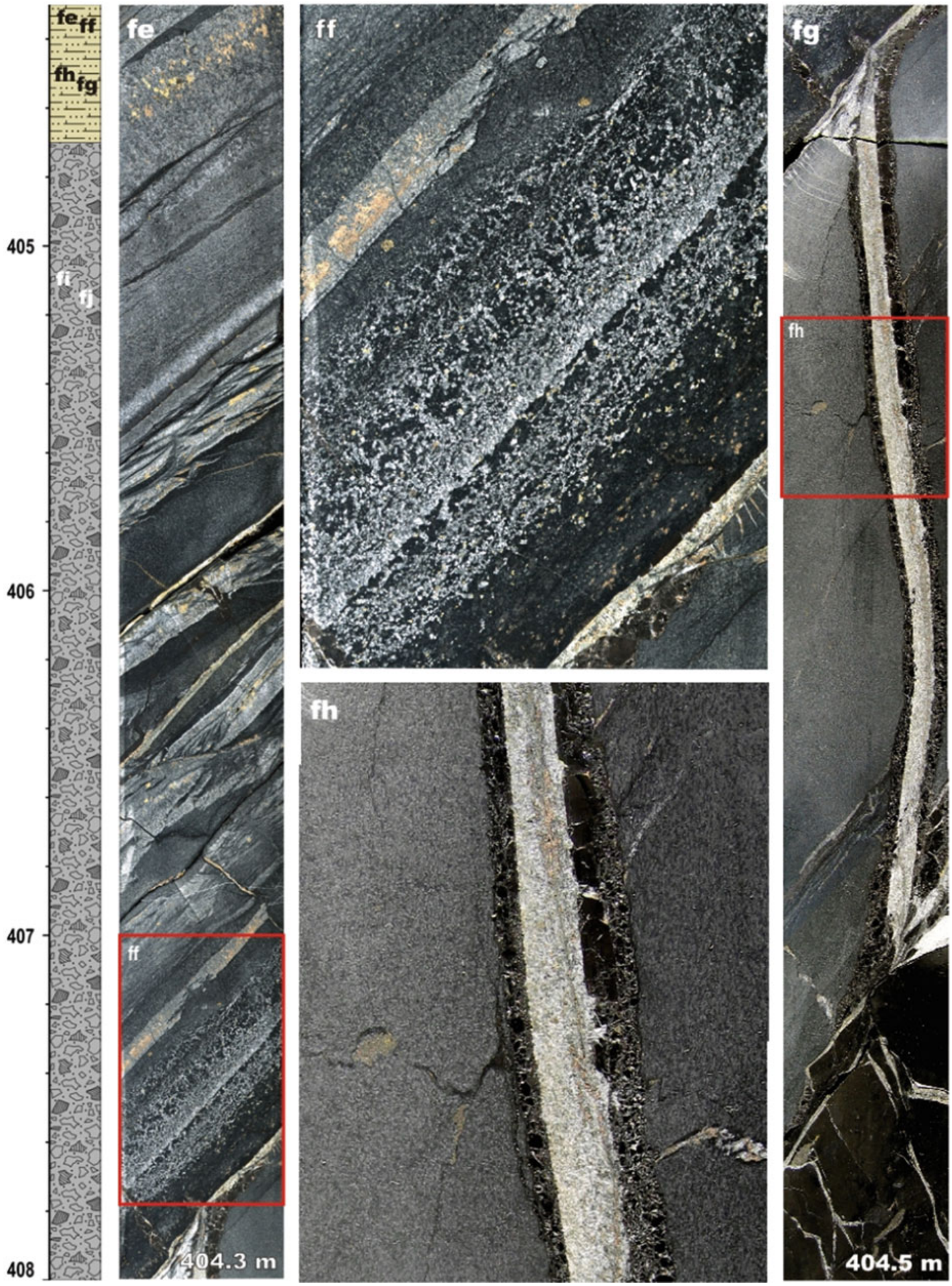

Fig. 6.116 (continued) (**fe**) Interbedded greywacke and dark grey, C_{org}-rich mudstone (*lower* half) overlain by interbedded sandy limestone and calcareous mudstone; all lithologies are intensely calcitised. (**ff**) Close-up of Fig. 6.116fe showing a dense impregnation of the mudstone layer by calcite. (**fg**) Black, C_{org}-rich layer (*bottom*) overlain by a bed of massive sandy limestone cut by a 1.5-cm-thick, extensional crack filled with a zoned vein. (**fh**) Close-up of Fig. 6.116fg detailing the zoned vein composed of white calcite with pyrobitumen fringes (*black*) and minor mica

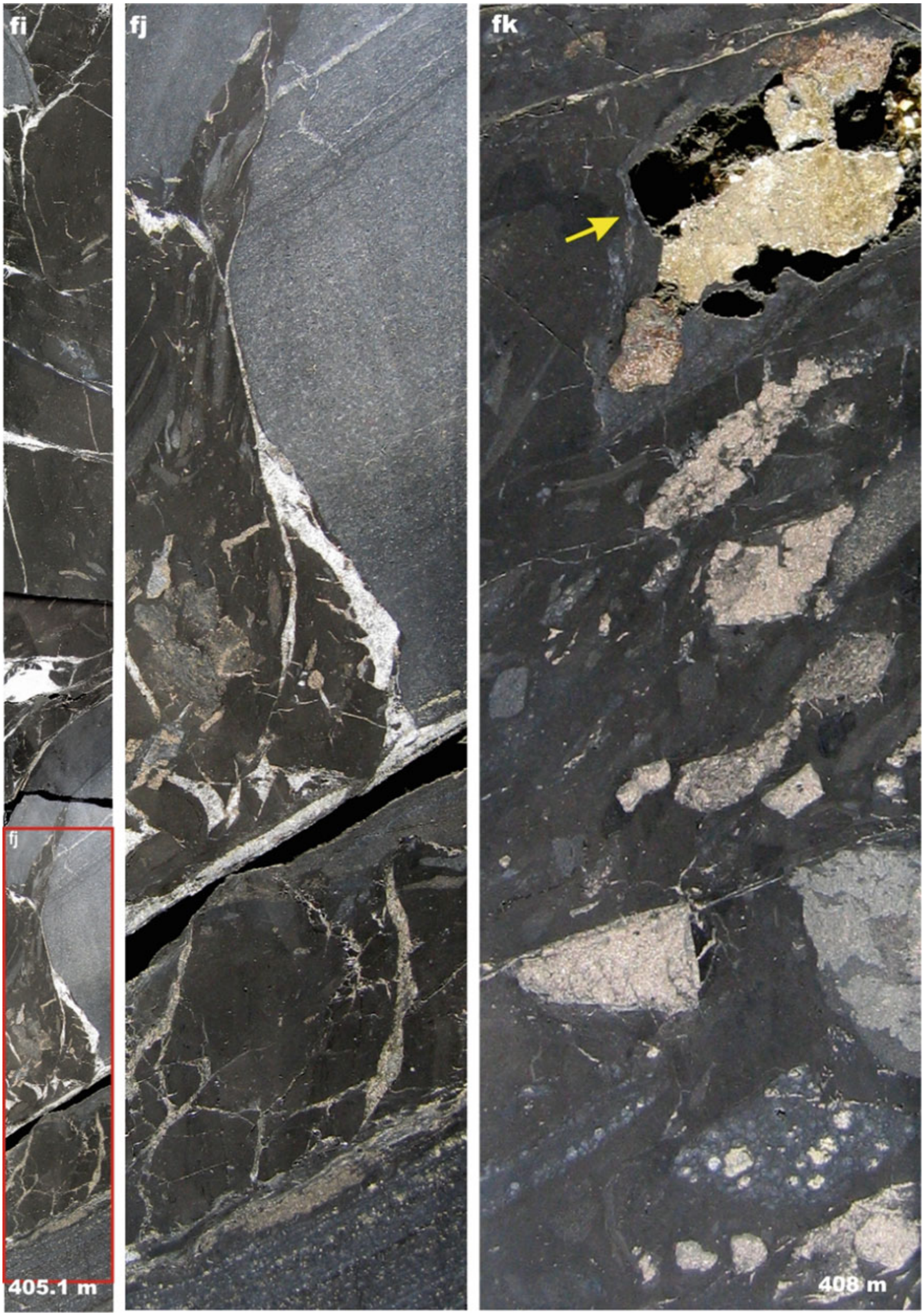

Fig. 6.116 (continued) (**fi**) Laminated, sandy limestone (lowermost part of the photo) overlain by breccias containing clasts of sandy limestone floating in C_{org}-rich matrix. (**fj**) Close-up of Fig. 6.116fi breccia affected by intensive brittle deformation and abundant extensional cracks cemented by calcite and sulphide. (**fk**) Close-up of Fig. 6.116fl detailing an intraformational breccia composed of angular clasts supported by black, C_{org}-rich matrix; clasts are sandy limestone (*grey*), intensely sulphidised rocks (bright), sulphide-pyrobitumen aggregate (*yellow arrowed*), and various C_{org}-rich lithologies (*black*)

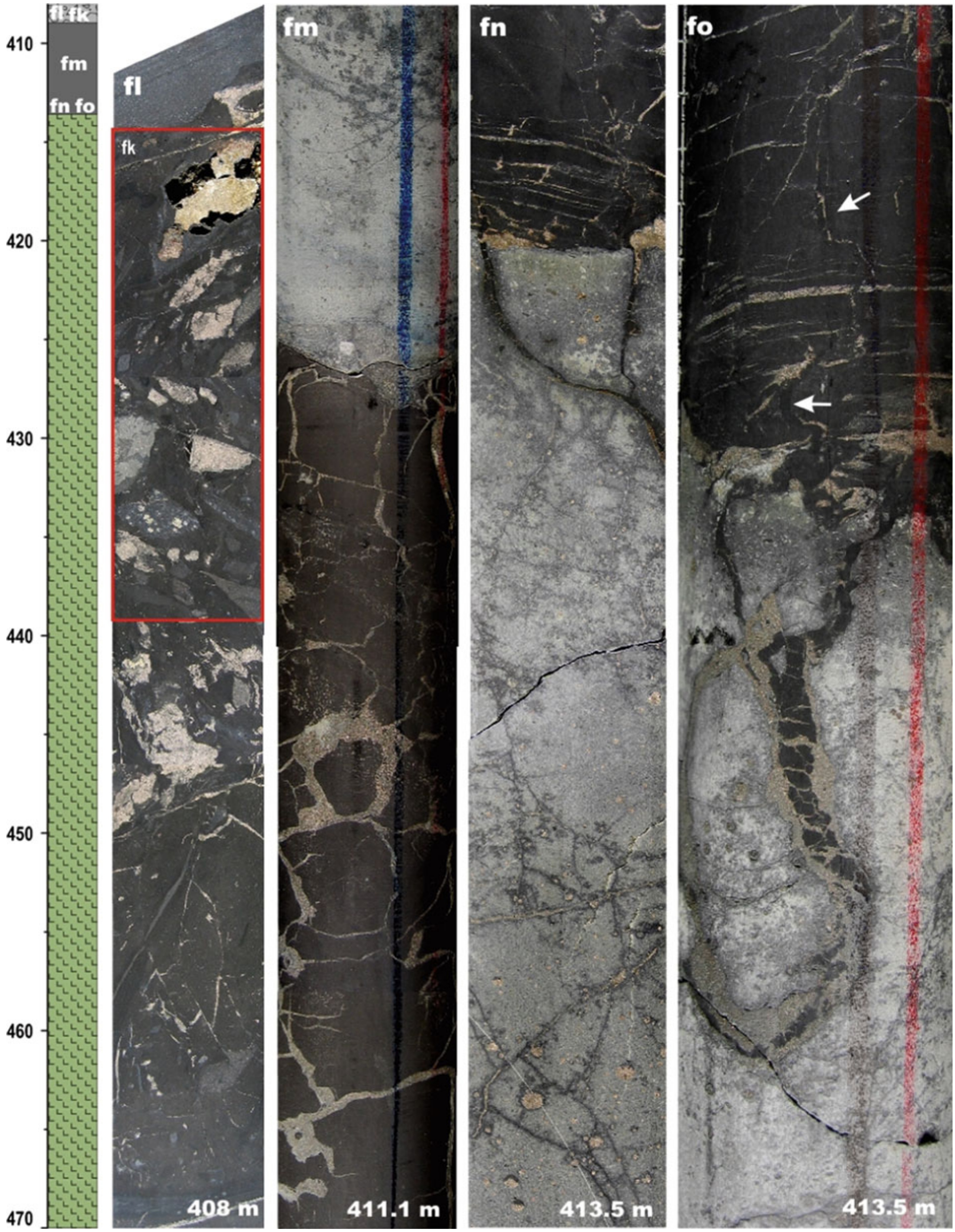

Fig. 6.116 (continued) (**fl**) Intraformational, matrix-supported breccia containing polymict clasts floating in pyrobitumen-rich matrix. (**fm**) Gabbro inclusion (*uppermost* part of photo) in contact with massive, C_{org}-rich mudstone with polygonal cracks (columnar joints in three-dimensional space) filled with sulphide. (**fn**) Contact of gabbro with the overlying massive, C_{org}-rich rock; note the two thin pyrobitumen veinlets cross-cutting both lithologies through the contact, and that the gabbro contains vesicles filled with sulphides (*bottom*). (**fo**) Detailed view of the contact between the gabbro and massive, C_{org}-rich rock cross-cut by pyrobitumen vein (*arrowed* within the organic-rich rock); note that within the diabase, the same pyrobitumen vein has wide sulphide fringes and joints filled with sulphide

Fig. 6.116 (continued) (**fp**) Contraction cracks (columnar joints in three-dimensional space) in massive, C_{org}-rich rock from the Maksovo quarry located c. 3 km to the south of the FAR-DEEP Holes 12AB outcrop; image view is c. 0.5 m

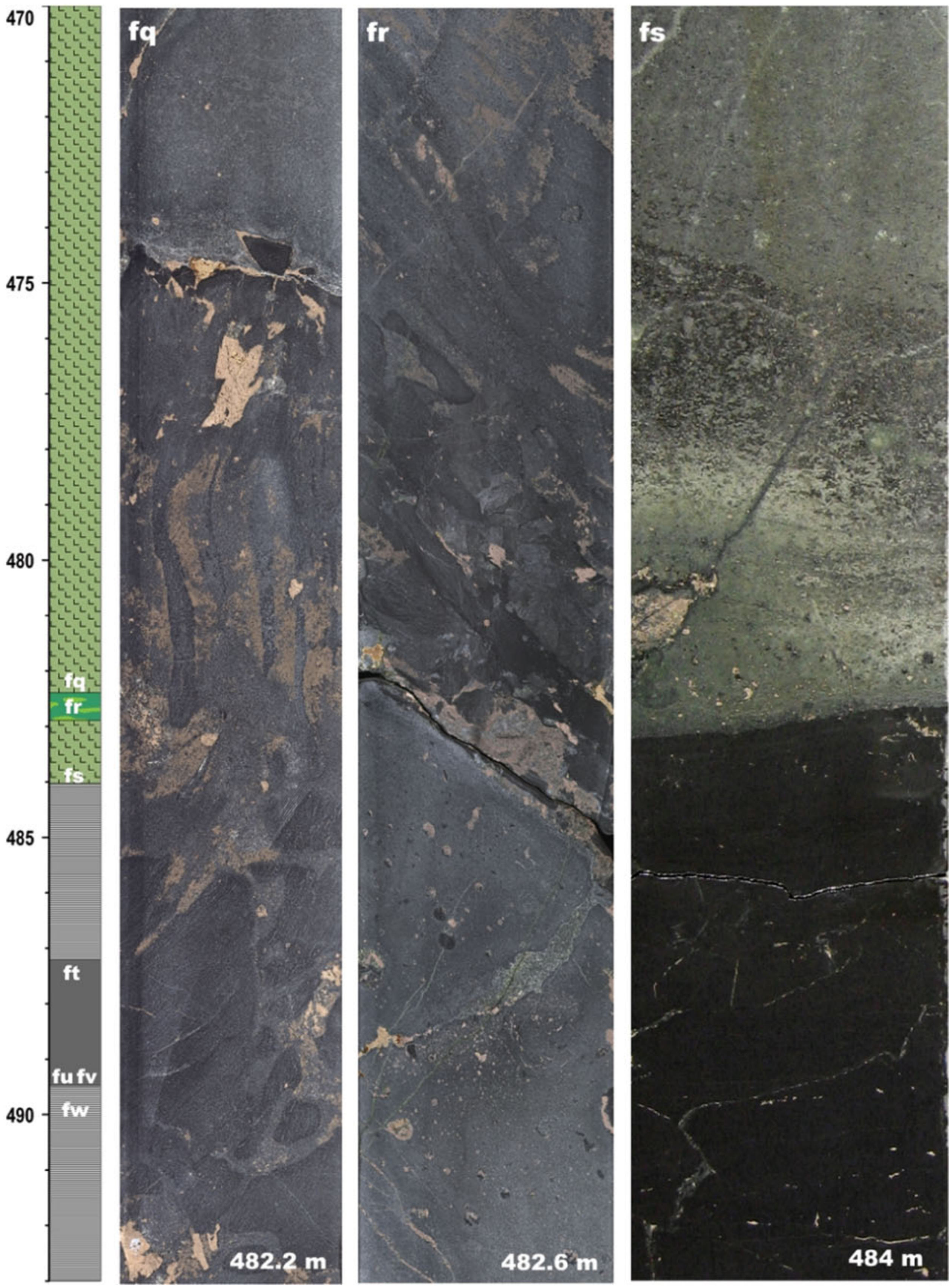

Fig. 6.116 (continued) (**fq**) Lower contact of a gabbroic body with the underlying brecciated sedimentary rock or tuff, which contains rounded and angular clasts; note the linear structure (fluid or gas escape structure?) oriented perpendicular to the contact. (**fr**) Fine-grained mafic lava flow or mafic dyke overlain by brecciated sedimentary rock or tuff; the vesicles are filled with sulphides and chlorite. (**fs**) Contact of black, massive, C_{org}-rich mudstones with the overlying mafic lava flow

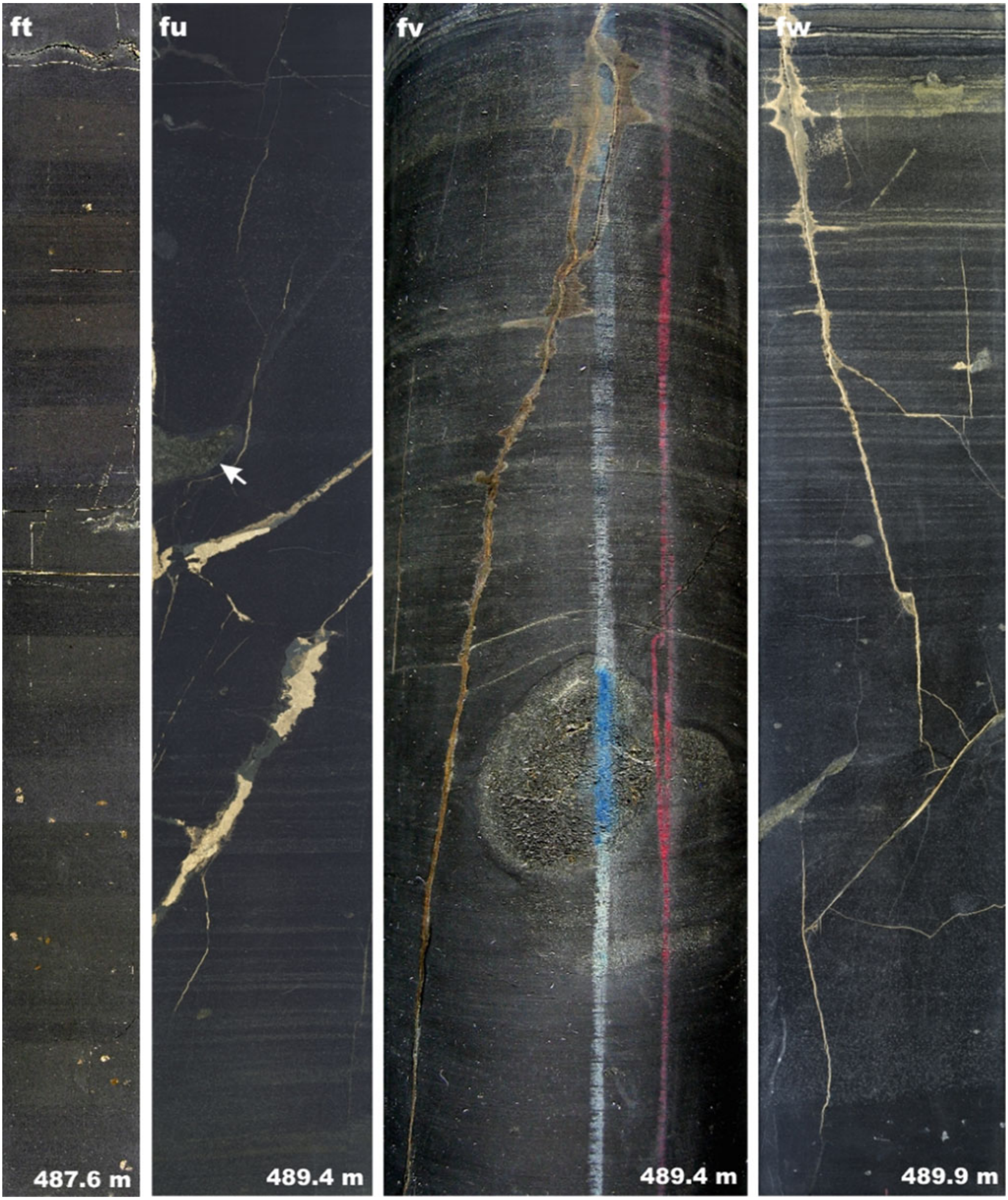

Fig. 6.116 (continued) (**ft**) Alternation of black and slightly lighter, C_{org}-rich mudstone layers forming indistinct rhythmical bedding. (**fu**) Massive, C_{org}-rich rock containing an inclusion of mafic igneous rock (*arrowed*); note the sulphide veins cutting through the C_{org}-rich rock. (**fv**) Uncut core showing the same interval as in Fig. 6.116fu and exhibiting a mafic igneous inclusion (possibly injected material, hence peperite) in C_{org}-rich mudstone cross-cut by sulphide veinlet; note that sedimentary layering conformably envelops the mafic inclusion (emplacement in plastic sediment). The inclusion has a fine-grained chilled margin. (**fw**) Black, massive, C_{org}-rich mudstone passing gradually upward into laminated mudstones; note the sulphide veinlet, which in places expands/widens along bedding surfaces

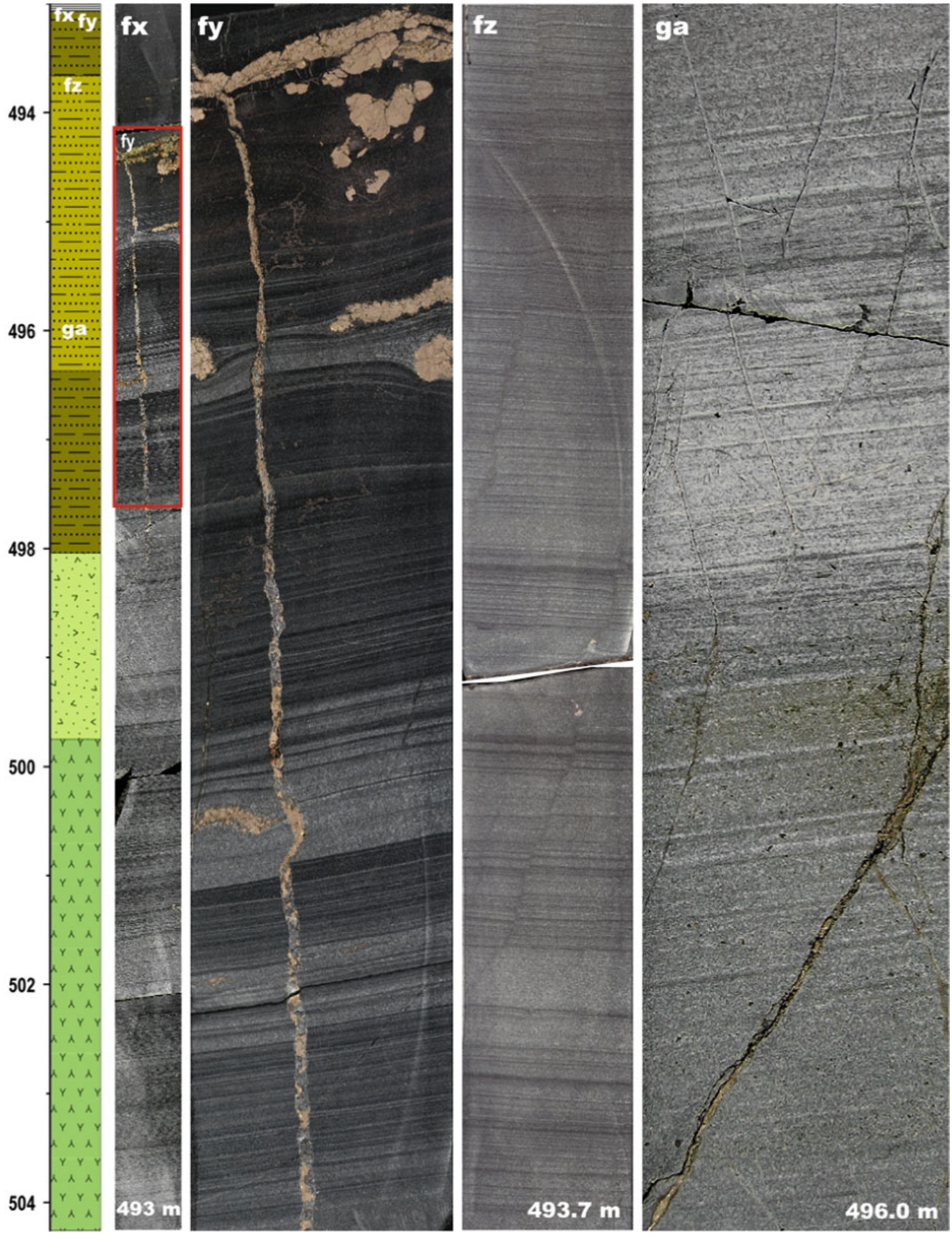

Fig. 6.116 (continued) (**fx**) Parallel-laminated, albitised greywacke gradually passing upward into albitised mudstones. (**fy**) Close-up of the upper part of Fig. 6.116fx detailing transition from the flat-laminated, albitised greywacke to the *black*, massive rock containing possible recrystallised sulphide concretions, bedding-parallel clusters of sulphide and a cross-cutting sulphide-silicate vein. (**fz**, **ga**) Rhythmical, parallel lamination in albitised greywacke (Photographs by Alenka Črne (**a–c**, **q**, **v**, **af**, **am–ao**, **az–bc**,,**bn**, **dd**, **df–dh**, **dj**, **dk**, **dq**, **du**, **ei**, **ey**, **fe**, **ff**, **fq**, **fr**, **fu**, **fw**, **fy**, **fz**) and Victor Melezhik (**d–p**, **r–u**, **w–ae**, **ag–al**, **ap–ay**, **bd–bm**, **bo–dc**, **de**, **di**, **dl–dp**, **dr–dt**, **dv–eh**, **ej–ex**, **ez–fd**, **fg–fp**, **fs**, **ft**, **fv**, **fx**, **ga**))

References

Borisov PA (1956) Karelian Shungites. Karelia, Petrozavodsk, p 96, (in Russian)

Buseck PR, Galdobina LP, Kovalevski VV, Rozhkova NN, Valley JW, Zaidenberg AZ (1997) Shungites: the C-rich rocks of Karelia, Russia. Can Mineral 35:1363–1378

Fallick AE, Melezhik VA, Simonson BM (2008) The ancient anoxic biosphere was not as we know it. In: Dobretsov N, Kolchanov N, Rozanov A, Zavarzin G (eds) Biosphere origin and evolution. Springer, New York, pp 169–188

Filippov MM (ed) (1994) The organic matter of Karelian Shungite rocks (Genesis, evolution and the methods of study). Kola Science Centre, Petrozavodsk, p 208, (in Russian)

Filippov MM (2002) Shungite rocks of the Onega structure. Karelian Science Centre, Petrozavodsk, p 280, (in Russian)

Filippov MM, Melezhik VA (eds) (2007) Atlas of textures and structures of Shungite-Bearing rocks of the Onega Sinclinorium. Karelian Science Centre, Petrozavodsk, p 80, (in Russian)

Galdobina LP (1987) The Ludikovi superhorizon. In: Sokolov VA (ed) Geology of Karelia. Nauka (Science), Leningrad, pp 59–67, (in Russian)

Galdobina LP (1993) Shungite rocks. In: Schiptsov V (ed) Precambrian industrial minerals of Karelia (Russia), Karelia. Karelian Research Center, Institute of Geology, Petrozavodsk, pp 45–50, (in Russian)

Inostranzev AA (1885) Geology. General lecture course for students of the St. Petersburg University, 2E, vol 1, St. Petersburg University, Russia, (in Russian)

Inostranzev AA (1886) Once more on shungite. Mining J 2:35–45, (in Russian)

Karhu JA (2005) Paleoproterozoic carbon isotope excursion. In: Lehtinen M, Nurmi PA, Rämö OT (eds) Precambrian geology of Finland: key to the evolution of the Fennoscandian Shield. Elsevier, Amsterdam, pp 669–680

Kovalevski VV, Buseck PR, Cowley JM (2001) Comparison of carbon in shungite rocks to other natural carbons: an X-ray and TEM study. Carbon 39:243–256

Melezhik VA, Fallick AE, Filippov MM, Larsen O (1999) Karelian shungite: an indication of 2.0-Ga-old metamorphosed oil-shale and generation of petroleum: geology, lithology and geochemistry. Earth Sci Rev 47:1–40

Melezhik VA, Filippov MM, Romashkin AE (2004) A giant Palaeoproterozoic deposit of shungite in NW Russia: genesis and practical applications. Ore Geol Rev 24:135–154

Melezhik VA, Huhma H, Condon DJ, Fallick AE, Whitehouse MJ (2007) Temporal constraints on the Paleoproterozoic Lomagundi-Jatuli carbon isotopic event., Geology 35:655–658

Melezhik VA, Fallick AE, Filippov MM, Lepland A, Rychanchik DV, Deines YE, Medvedev PV, Romashkin AE, Strauss H (2009) Petroleum surface oil seeps from a Palaeoproterozoic petrified giant oilfield. Terra Nova 21:119–126

Ovchinnikova GV, Kuznetsov AB, Melezhik VA, Gorokhov IM, Vasil'eva IM, Gorokhovskii BM (2007) Pb-Pb age of Jatulian carbonate rocks: the Tulomozero Formation of Southeast Karelia. Stratigr Geol Correl 15:359–372

Puchtel IS, Zhuravlev DZ, Ashikhmina NA, Kulikov VS, Kulikova VV (1992) Sm–Nd age of the Suisarian suite on the Baltic Shield. Trans Russ Acad Sci 326:706–711, (in Russian)

Puchtel IS, Arndt NT, Hofmann AW, Haase KM, Kröner A, Kulikov VS, Kulikova VV, Garbe-Schönberg C-D, Nemchin AA (1998) Petrology of mafic lavas within the Onega plateau, central Karelia: evidence for 2.0 Ga plume-related continental crustal growth in the Baltic Shield. Contrib Mineral Petrol 130:134–153

Puchtel IS, Brügmann GE, Hofmann AW (1999) Precise Re–Os mineral isochron and Pb–Nd–Os isotope systematics of a mafic–ultramafic sill in the 2.0 Ga Onega plateau (Baltic Shield). Earth Planet Sci Lett 170:447–461

Shatsky GV (1990) Isotope composition of sulphides from the Zazhogino shungite deposit. Lithol Miner Res 1:20–28, (in Russian)

Volodichev OI (1987) Metamorphism. In: Sokolov VA (ed) Geology of Karelia. Nuka (Science), Leningrad, pp 152–175, (in Russian)

Watanabe Y, Farquhar J, Ohmoto H (2009) Anomalous fractionations of sulphur isotopes during thermochemical sulfate reduction. Science 324:370–373

6.3.4 Zaonega Formation: FAR-DEEP Hole 13A

Alenka E. Črne, Victor A. Melezhik, Anthony R. Prave, Aivo Lepland, Alexander E. Romashkin, Dmitry V. Rychanchik, Eero J. Hanski, and Zhen-Yu Luo

Scientific Targets

– Tectonic and depositional settings associated with enhanced accumulation of organic matter
– Cause-and-effect relationship between the Lomagundi-Jatuli and Shunga Events
– Geochemical rock record during the Shunga Event
– Petrified oil field: oil generation and migration
– Source rocks and carbon-isotope composition of primary biomass
– Pathways in recycling of organic matter
– The earliest phosphogenesis
– Carbon, sulphur and strontium isotopic composition of seawater
– Provenance composition
– Microfossil record
– Search for biomarkers
– Radiometric age constraint on timing of deposition
– Geochemical interaction between igneous rocks and C_{org}-rich sediments
– Anomalous fractionation of sulphur isotopes during thermochemical sulphate reduction

FAR-DEEP Hole 13A was drilled in the northeastern part of the Palaeoproterozoic Onega Basin (Fig. 6.1), c. 25 km northwest of FAR-DEEP Hole 12AB and c. 100 m east from the world famous type locality of shungite at Shunga village (Fig. 6.86) first described by Inostranzev (1885, 1886). Hole 13A targeted the uppermost part of the Zaonega Formation; study of these rocks is complementary to, and should be considered with, work undertaken on Holes 12AB (see Chap. 6.3.3). The drillhole intersected the thickest accumulations of cherts and dolostones with the objective to assess their genesis and establish geochemical and sedimentological criteria for distinction between sedimentary, diagenetic and hydrothermal varieties. The aim is to: (1) understand the genesis and significance of enigmatic massive C_{org}-rich rocks; (2) provide information on seawater chemistry; and (3) decipher the style of diagenesis and remineralisation of organic matter. The drillhole also intersected an interval containing diagenetic phosphates (Fig. 6.117a), one of the earliest in the geological record (Fig. 6.87), and, consequently, the recovered core has potential to address the causes of phosphogenesis.

Hole 13A was drilled in close proximity to an adit near the village of Shunga, where is exposed the thickest known interval of semilustrous shungite with layers and veins of lustrous varieties (Figs. 6.117b, c). Hence, the obtained cores may provide new details of this remnant of a petrified ancient oil reservoir, the generation and migration of Precambrian oil, and the associated fractionation of carbon and nitrogen isotopes.

The Zaonega Formation

Drillcore 13A is 240 m long and intersects the upper part of the Zaonega Formation containing sedimentary rocks and series of mafic lava flows. The latter are assigned to Units A, B and C (Fig. 6.118) and the 13A section is divided conventionally into a lower Siliciclastic-Carbonate member (240–76.6 m) and an upper Dolostone-Chert member (76.6–1.6 m).

Chemical composition of all analysed archive samples is presented in Appendices 41–43. Figure 6.119 shows stratigraphic profiles of selected major and trace elements as well as magnetic susceptibility. Magnetic susceptibility is high (maximum of 22,000 μSI; $K^* = 2{,}006 \times 10^{-6}$ SI) in sedimentary rocks above the lowermost mafic flow at 195–150 m depth (Fig. 6.119). Above 150 m, the magnetic susceptibility decreases irregularly to 275 μSI ($K^* = 25 \times 10^{-6}$ SI in Fig. 6.119) and then fluctuates between 10 and 100 μSI ($K^* = 1$–10×10^{-6} SI in Fig. 6.119) from 90 to 25 m, increasing to 1,000 μSI ($K^* = 10 \times 10^{-6}$ SI) in the upper 20 m of section. The lower volcanic Unit A has a magnetic susceptibility of around 22,000 μSI ($K^* = 2{,}000 \times 10^{-6}$ SI in Fig. 6.119); successive units show decreases to 10,000 μSI ($K^* = 2{,}000 \times 10^{-6}$ SI in Fig. 6.119) in Unit B and 7,700 μSI ($K^* = 700 \times 10^{-6}$ SI) in Unit C.

Figures 6.120, 6.121, and 6.122 illustrate the main geochemical features of the igneous rocks. Core photos provide a documentation of the major lithological features of the sedimentary and volcanic rocks (Fig. 6.123).

The Siliciclastic-Carbonate Member

The member is 163.4 m thick (240–76.6 m) and contains mudstones commonly interbedded with greywackes, calcareous greywackes, and sandy limestones. Also present are rare intervals of intraformational, matrix-supported conglomerates, as well as breccias, cherts and peperites. Mafic lava flows of Unit A occur at 240–197 m, of Unit B at 129–115 m and Unit C at 109–91 m.

Mudstones and greywackes are generally rhythmically interbedded on a cm- to dcm-scale (Figs. 6.123bb, bg, bx,

A.E. Črne (✉)
Geological Survey of Norway, Postboks 6315 Sluppen, NO-7491 Trondheim, Norway

V.A. Melezhik et al. (eds.), *Reading the Archive of Earth's Oxygenation*, Volume 2: The Core Archive of the Fennoscandian Arctic Russia – Drilling Early Earth Project, DOI 10.1007/978-3-642-29659-8_4, © Springer-Verlag Berlin Heidelberg 2013

by, ca, cc, cf). Mudstones (Figs. 6.123bh, bt, bu) are black to dark grey and typically flat-laminated with the bed thickness ranging from thin laminae to layers as thick as 2 m. Mudstones containing more than 10 wt.% $CaCO_3$ are termed calcareous mudstones. Greywackes are fine-grained and mostly thin-bedded. Within the lower part of the member (from 197 to 180 m), the greywacke beds are thicker, up to 30 cm, and normally graded. A 24-m-thick interval (183–159 m) is marked by several greywacke beds containing black 'clay balls' that can be a few-mm in diameter (Fig. 6.123bs). Apart from being interbedded with greywackes, mudstones occur as thick packages dominating three intervals; a 10-m-thick interval in the lower part (180–170 m) and two thinner intervals within the upper part (90–87 and 83.8–81 m) of the member.

Calcareous greywackes (Fig. 6.123ba) and sandy limestones (Fig. 6.123bf) occur either as thin beds, interbedded with mudstones, or packages as much as 3.5 m thick, comprised of consecutive carbonate-rich beds. Some calcareous greywackes and sandy limestones are flat-laminated (Figs. 6.123bp, bu, bw, cb). The abundance of consecutive thick-bedded calcareous greywackes and sandy limestones is highest from 164 to 154 m.

Intraformational, matrix-supported conglomerates occur within a 5-m-thick interval (157–152 m) as a-few-cm- to 20-cm-thick beds containing rounded clasts of greywackes, mudstones and intensely sulphidised rocks that can be as large as 2 cm in cross-section. The conglomerate beds alternate with beds of greywackes of similar thickness (Fig. 6.123br) within the lowermost metre of the interval. The thickness and occurrence of intraformational, matrix-supported conglomerates decreases upsection within the conglomerate-greywacke interval.

An interval located between 112 and 91 m is worth highlighting due to the presence of C_{org}-rich rocks, which occur as up to 1-m-thick, black interlayers within basalts (Fig. 6.123ap). The C_{org}-rich rocks are mostly massive, but in places where there are abundant cm-thick, sulphide-rich veins, they have a brecciated appearance (Fig. 6.123aq). At 106.2 m, the massive C_{org}-rich rock contains inclusions of basalt (Fig. 6.123at) and is therefore considered to be a peperite. Peperites are also present below magmatic unit C (111.1–108.6 m) and in the uppermost part of the member (86.6–84.6 m). The former is composed of sub-angular basalt inclusions floating within a matrix of black, massive, C_{org}-rich rock (Fig. 6.123au). The second peperite interval is similar, but it additionally contains mudstone fragments and white clasts of bleached basalt(?) and has been affected by sulphidisation (Fig. 6.123al).

Breccias and cherts are minor lithologies of the member. The breccias are present within the uppermost metres of the member (81.6–78 m) and contain mostly angular, but also well-rounded clasts up to a few cm in size; clasts are sandy limestones, mudstones and cherts within a mudstone matrix. Breccia intervals alternate with sandy limestones, cherts and mudstones and can be as much as 0.4 m thick. Cherts are black and occur as dm-thick layers within the uppermost metres of the member.

The parallel-bedded character of the greywacke-siltstone-mudstone sequence is commonly disrupted by synsedimentary deformation, mostly in the form of slumping, and is most abundant above the interval containing intraformational, matrix-supported conglomerates (Figs. 6.123av, bc, bi, bj, bl–bn). Fine-grained sand dykes, injected upward into mudstone layers, are also common (Figs. 6.123by, cc, ce).

Iron sulphides are ubiquitous and occur in different forms. The most abundant are as disseminated and micronodular sulphides in rhythmically bedded greywacke-mudstone, calcareous greywacke and sandy limestone (Figs. 6.123be, bg, bh, br, bs, bv, bw). Other forms occur as concretions, some up to 5 cm in length, and a significant differential compaction of layers around the concretions suggests they formed early in diagenetic growth (Figs. 6.123az, bt). Thin, mm-thick lenses and layers of iron sulphides are also common (Figs. 6.123bh, bk–bm, bo, bs). Some sulphide layers show dismembering caused by sedimentary/diagenetic boudinage (Fig. 6.123bu), similarly indicating early diagenetic origin of sulphides. Some sulphides were resedimented and incorporated as clasts into intraformational conglomerates (Fig. 6.123bq). Intensive sulphidisation of the tops of volcanic flows (Fig. 6.123an) and peperites (Figs. 6.123ar, as, at) indicates synvolcanic sulphidisation. Large pyrite porphyroblasts in greywacke are superimposed on sedimentary structures (Fig. 6.123ay), suggesting episodes of intensive sulphidisation postdating sediment compaction. Remobilised sulphides are abundant and occur as veins and veinlets (Figs. 6.123bp, bt, bz, cb, cd).

Analysed archive samples do not reveal any stratigraphic trend in geochemical composition of the Siliciclastic-Carbonate member (Fig. 6.129). Most of the siliciclastic rocks have a K_2O/Na_2O ratio >1. Whole-rock analysis of the greywacke shows SiO_2 and Al_2O_3 contents of c. 66 and 5.3 wt.%, respectively (Appendix 41); greywacke also contain considerable amounts of CaO (7.6 wt.%) and MgO (2.5 wt.%), low contents of Na_2O (1.8 wt.%), K_2O (1.0 wt.%) and inorganic carbon (1 wt.%). Mudstones contain variable amounts of SiO_2 (43–67 wt.%), Al_2O_3 (3.8–16.1 wt.%), MgO (1.6–13.3 wt.%) and K_2O (1.0–5.9 wt.%), but are rich in C_{org} (1.7–31.7 wt.%). Sandy limestones and calcareous greywackes (45 wt.% $CaCO_3$, 5.4 wt.% IC and Mg/Ca of 0.06, on average) contain 1.1–2.1 wt.% C_{org} and variable amounts of SiO_2 (26–30 wt.%) and MgO (9.7–12.7 wt.%). A single analysis of chert shows 86 wt.% SiO_2 and 5.3 wt.% C_{org}.

The Dolostone-Chert Member

The member is 75 m thick (76.6–1.6 m) and begins with the first thick (1.4 m) package of chert. The main lithologies are dolostones, sandy dolostones and limestones, cherts and breccias. Also present are intraformational, matrix-supported conglomerates, mudstones and greywackes, which are all commonly interbedded with marls.

Dolostone and sandy dolostone beds are mostly around 1 m thick, commonly massive (Figs. 6.123e, x, ab, aj), and very few are flat-laminated (Figs. 6.123c, f, g, aa). While dolostones are the dominant lithology within the main part of the member, there are only a few dolostone beds within the uppermost 15 m. Spherical, mm-size particles are present in three intervals: they occur abundantly at 67 and 27 m (Figs. 6.123j, k, ac, ad), and a few were seen at 71 m. Spherical particles are zoned, have concentric fractures and are composed of phlogopite and calcite (Huber et al. 2011). Dolostones and sandy dolostones also contain a-few-mm-thick, phosphate-rich layers (Figs. 6.124a–c) in which phosphates occur as in-place concretionary precipitates and cements (Figs. 6.124c, d; see Chap. 7.7 for details). Cherts are black, commonly massive (Figs. 6.123m, n, ag–ai), but in places show faint parallel lamination and a concentric structure (Figs. 6.123m, n). Up to 6-m-thick packages of black, massive chert dominate two intervals, from 76.6 to 68.2 m, and from 41.7 to 30.5 m. Additionally, chert occurs as thin (up to a few-cm-thick) layers within the lower part of the member, but is absent within the uppermost 20 m.

Breccias are restricted to the lower part of the member, with the uppermost breccia occurring at 42.5 m. Breccias reach a thickness of 1.7 m and are mainly composed of sub-angular to rounded dolostone clasts from a few mm to more than 10 cm in size, supported by a brownish-blackish, massive, pyrobitumen-rich matrix (Figs. 6.123w, y–z, ag–aj); also present are rounded clasts of mudstones and angular and sub-angular clasts of black chert (Figs. 6.123ae, af, ag). In some breccias, the clasts have been brecciated in situ and show no transport (Fig. 6.123aj). Few breccia intervals contain more dolostone clasts in the lower part than in the upper part. Some breccias are composed of dolostone clasts supported by a sandy dolomite matrix (Fig. 6.123s).

Intraformational, matrix-supported conglomerates are less abundant with respect to breccias and are present within a thin interval from 47.5 to 45.4 m. The conglomerates are composed of rounded to angular greywacke clasts supported by a greywacke matrix (Figs. 6.123o–r, t, u). Both the clasts and the matrix commonly show soft-sediment deformation.

Rhythmically interbedded greywackes and mudstones are scarce, but represent the dominant lithology at two intervals: below the upper chert bed (49–43 m) and within the uppermost 15 m (Fig. 6.123a). The greywackes are commonly synsedimentary deformed (Fig. 6.123v) and contain slumped beds of sandy limestone (Figs. 6.123o–q). In the vicinity of the 13A drilling site near Shunga village, coarse-grained greywackes and some mudstones contain either concretions or soft-sediment deformed phosphatic clasts (Figs. 6.124e, f; see Chap. 7.7 for details). A few m-thick packages of brownish, parallel-laminated mudstones occur from 25 to 20 m. They contain thin interlayers of marls (Figs. 6.123h, i).

Iron sulphides occur irregularly throughout the member and in different morphological and genetic forms. Diagenetic sulphides are represented by concretions and fine impregnations, generally involved in soft-sediment deformation and redeposition (Figs. 6.123o, p, q, u, v, ak). Post-diagenetic sulphides occur as dense impregnations (Figs. 6.123d, e), porphyroblastic pyrite cubes (Fig. 6.123b), and sulphides filling shrinkage cracks in a pyrobitumen-rich material (Figs. 6.123ae, af).

The member bears information on oil migration processes in the form of pyrobitumen-rich veins and veinlets. These features have mostly sharp-sided walls and occur in dolostones and sandy dolostones (Figs. 6.123i, l, ab). Some breccia intervals have a pyrobitumen-rich matrix.

Carbonate rocks contain from 77 to 92 wt.% dolomite component and have a Mg/Ca ratio ranging between 0.43 and 0.59, which is only slightly lower than stoichiometric dolomite (0.62). Hence, the carbonate constituents represent dolomite with an admixture of calcite. Carbonate rocks are low in SiO_2 (1.5–7.0 wt.%) (Appendix 41), contain a variable amount of C_{org} (0.4–4.6 wt.%) and a low content of S_{tot} (<0.01–0.2 wt.%; one outlier with 1.5 wt.%). The carbonate rocks are characterised by high abundances of Mn (519–4,030 $\mu g\ g^{-1}$) and Fe (572–55,000 $\mu g\ g^{-1}$ Appendix 43) and a low Sr content (70–136 $\mu g\ g^{-1}$). Some intervals show a high P_2O_5 concentration up to 1.3 wt.% (Appendix 41).

Cherts (77–94 wt.% SiO_2) are rich in C_{org} (3–9.3 wt.%) and were locally termed lydites (Galdobina et al. 1982). They have low abundances of Al_2O_3 (0.08–2.2 wt.%) and K_2O (0.04–1 wt.%) and are devoid of Na_2O. Mudstones contain variable amounts of SiO_2 (36–66 wt.%) and Al_2O_3 (8–14 wt.%) and mostly a high amount of C_{org} (1.6–28 wt.%). The content of K_2O (3.3–4.7 wt.%) is higher than that of Na_2O (0.2–1 wt.%), and the S_{tot} concentration ranges between 1.1 and 6.6 wt.%.

Magmatic Units

Three magmatic bodies, Units A, B and C, are distinguished in Core 13A (Fig. 6.120). Unit A (197–240 m) at the bottom of the core is a more than 40-m-thick, massive, medium-grained mafic body with no recognisable volcanic structures; it is likely a diabase sill. Chloritisation is a common alteration phenomenon. There are several C_{org}-rich (Figs. 6.123cg, ch), calcite-veined inclusions up to 20 cm in length. The 14-m-thick Unit B (115–129 m) is also massive with no discernible volcanic structures. Both the top and bottom parts are fine-grained (Figs. 6.123aw, ax) and darker than the central part; these are arguably chilled margins, hence Unit B may also be a sill. In contrast, Unit C (91–109 m) contains six individual lava flows varying in thickness from 0.6 to 5.7 m and having thin intercalations of C_{org}-rich rock (Figs. 6.123am–ar, at). The thickest lava flow has a massive major part and pillowed uppermost part. In Units B and C, secondary biotite is abundant and carbonate is locally present due to strong alteration.

Chemically, all analysed magmatic rock samples from Core 13A are tholeiitic high-Ti evolved basalts or basaltic andesites with relatively low MgO contents in the range of 3.3–6.8 wt.%, and low Ni and Cr contents (≤52 and ≤84 ppm). Units A and B have a high FeO_T content (13–19 wt.%), while in Unit C, FeO_T falls below 10 wt.%. The low-Fe samples have likely lost iron, as their Ti and V contents are comparable with those of other samples from the core. Units B and C have also suffered from other alternation phenomena including gain of silica, Na_2O and K_2O, and loss of CaO. The magma type was similar in all units in terms of major elements, but there is a significant difference in Nb/Y: Unit A has a low Nb/Y ratio of 0.2, whilst Units B and C have ratios of 0.35–0.45. The $(Ce/Nb)_{PM}$ ratio reaches values up to 1.8, indicating some crustal contamination.

Comparison of the igneous geochemistry in the relatively closely placed Cores 12AB and 13A shows that, in terms of their Ce/Y and Nb/Y ratios (Fig. 6.121), the lowermost Unit A of Core 13A is chemically similar to the Fe-rich Units D and E, and particularly Unit C, in Core 12AB. For Units B and C of Core 13A, there are no counterparts in Core 12AB. Using Cr as an index of fractionation, and plotting Cr against Nb for all igneous rock samples from the FAR-DEEP cores of the Onega region, the samples can be divided into four compositional groups (Fig. 6.122). The mafic lavas of group I, occurring in Cores 10B and 11A, are very low in Nb and other incompatible elements, while group IV in Core 13A is highest in Nb. There is thus a considerable variation in the chemistry of the Zaonega Formation magmatism and more so, if the earlier study of Puchtel et al. (1998) on the Angozero area basalts, is taken into account. The latter differ from the FAR-DEEP hole samples in being higher in Zr/Y, for example (Fig. 6.122b). Incompatible trace element-depleted volcanic rocks similar to group I are rare in the Karelian formations, but can be found among the MORB-like tholeiitic basalts of the Jouttiaapa Formation in the Peräpohja Belt, Finland (Huhma et al. 1990). The strong Mg-metasomatism (see Chaps. 6.3.1 and 6.3.2), though, complicates the interpretation of the chemistry of group I, but, nevertheless, immobile trace element concentrations and ratios suggest that it forms a magmatic pulse of its own.

Correlation of Holes 12AB and 13A

The main lithological change within Core 13A occurs at 76.6 m, where mudstones interbedded with greywackes are overlain by dolostone breccias, cherts and dolostones. This corresponds to the boundary between the Siliciclastic-Carbonate and the Dolostone-Chert members. Comparable lithological change occurs in Core 12AB at 9.3 m, where the Mudstone-Limestone member is in contact with the Dolostone-Chert member. The Dolostone-Chert member is nearly identical in Cores 13A and 12AB. Considering the main lithological change to be time equivalent within the basin, a direct correlation between the two drillholes is possible (Fig. 6.118). The Siliciclastic-Carbonate member of Core 13A is therefore a lateral equivalent of the Mudstone-Limestone member in Core 12AB; the interval of "clay ball" occurrence within the lower part of the Siliciclastic-Carbonate member in Core 13A (183–159 m) is correlative to the interval from 180 to 160 m within Core 12AB, where black "clay balls" are also abundant.

It should be noted that the correlation presented in Fig. 6.118 is not as straightforward when it comes to the igneous rocks. The uppermost two igneous units in both cores, D and E in Core 12AB, and B and C in Core 13A, are part of the sections that are shown as correlative in Fig. 6.118. However, as shown in Fig. 6.121, the two uppermost igneous units in Core 13A have high Nb/Y, forming their own chemical group IV in Fig. 6.122, and do not have corresponding chemical equivalents among igneous rocks in Core 12AB. On the other hand, the lowermost igneous unit (A) in Core 13A belongs to group III together with the units C, D and E of Core 12AB, but the former is massive and interpreted to be a sill while the latter three represent volcanic eruptions.

Depositional Environment and Postdepositional Alterations

The main lithologies of the Siliciclastic-Carbonate member are mudstones commonly interbedded with greywackes. While thicker packages of mudstones are interpreted to have been formed from background water-column sedimentation, the greywackes are assumed to have been deposited from turbidity currents. In comparison to the correlative Mudstone-Limestone member of Hole 12AB, the Siliciclastic-Carbonate member contains coarse-grained deposits in the form of intraformational, matrix-supported conglomerates, and a higher abundance of greywackes.

Consequently, it is possible that the deposition of the Siliciclastic-Carbonate member occurred in a more proximal position to sediment-routing sources than the correlative member of Hole 12AB. Nevertheless, thick, normally-graded greywacke beds of the lowermost part of the Siliciclastic-Carbonate member are overlain by a 10-m-thick interval of mudstones (180–170 m), suggesting a decrease in sediment flux possibly linked to a transgressive phase of basinal development, consistent with a similar trend observed in the 12AB section. Although not diagnostic of a particular palaeoenvironmental setting, the abundance of sand-dykes (Figs. 6.123by, cb, ce) indicates frequent liquefaction of high water-content sediments, and this is likely linked to seismic disturbances, implying sedimentation was occurring during a phase of tectonic instability (cf. Audemard and de Santis 1991; Peterson 1997; Ettensohn et al. 2002).

Several peperite intervals (Figs. 6.123al, ao, ar–au) are present in the uppermost part of the Siliciclastic-Carbonate member in association with massive C_{org} rocks. This may indicate a genetic link between peperites and massive C_{org}-rich rocks through the interaction of magmatic bodies with unconsolidated wet sediments. Interlayers of black, massive, C_{org}-rich rocks present within basalts (Fig. 6.123ap) may also owe their origin to a similar process of thermal modification of unlithified, C_{org}-rich sediment.

The origin of carbonates within Core 13A is currently unresolved. Both limestones and dolostones could be either of sedimentary (re-sedimented from a nearby carbonate shelf), diagenetic (remineralisation of organic material), hydrothermal (processes on the seafloor or within the sedimentary column) or metasomatic origin. The varying textures and sedimentary structures perhaps hint at a multigenetic origin and that all of the above processes were responsible for forming the carbonate rocks in Core 13A.

The lowermost part of the Dolostone-Chert member in Core 13A, unlike its assumed correlative strata in Core 12AB consisting of massive dolostone and black chert, is a breccia consisting of angular clasts of those two lithologies encased in a pyrobitument-rich matrix. This is consistent with an origin by *in situ* brecciation of the host rock (Fig. 6.123aj). The presence of pyrobitumen-rich material cross cutting chert (Figs. 6.123ag, ai) similarly indicates injection into an already lithified host rock. On the other hand, some breccia intervals are normally graded, and/or contain rounded clasts, which show that these beds were formed by normal sedimentary processes of transport and settling. It is thus probable that two different processes governed the formation of breccias, one as injection of C_{org}-rich material into the host rock (injection breccias) (Figs. 6.123ae–aj) and the other by mass-flow transport (Fig. 6.123w). However, it is important to note that, in the instances where the breccias contain a considerable amount of pyrobitumen as a matrix, their origin was more likely due to the former, possibly linked to expulsion/explosion events associated with peperites, because the formation of such breccias as mass-flows would require erosion of a previously deposited succession to the depth of the "oil window"; this is an unlikely scenario, unless the oil widow was at a very shallow depth. The upper part of the Dolostone-Chert member is marked by intraformational, matrix-supported conglomerates together with interbedded mudstones and greywackes. This may indicate a high input of siliciclastic material resulting in rapid deposition, enabling mass-flows on an unstable slope.

Phosphate-rich sedimentary intervals in Core 13A are among the oldest known phosphorites appearing in the Palaeoproterozoic rock record (Papineau 2010). The typical co-occurrence and intergrowth of phosphate precipitates with calcite indicates a co-formation of these phases that was likely triggered by diagenetic decomposition of organic matter (see Chap. 7.7 for details). Multiple generations of iron sulphides, including disseminations, nodules, impregnations, veins and porphyroblasts record a complex depositional and post-depositional history of sulphur in the Zaonega succession. These remain to be studied. The presence of pyrobitumen-rich material occurring in various morphological forms (clasts, matrix of breccias, veins) records several stages of oil generation and migration; these deposits, too, are prime candidates for further investigation. Lastly, the formation of chert looks equally complicated and remains understudied. Some thick chert intervals with parallel, rhythmic lamination might be primary seafloor precipitates, while those with a massive structure and concentric laminations may be diagenetic products or formed as a result of hydrothermal silicification.

In summary, the lithologies observable in Core 13A indicate deposition in a deep-water setting. Interbedding of graded greywackes and shales, intraformational breccias, the presence of peperites and abundant soft-sediment deformation features imply an environment in which sediment-gravity flow processes were occurring coeval with magmatism and tectonic instability. The exact origin of C_{org}-rich rocks, in the variety of forms seen in Core 13A, and the association of those rocks with carbonate rocks, remains unresolved and thereby represent exciting targets for future research.

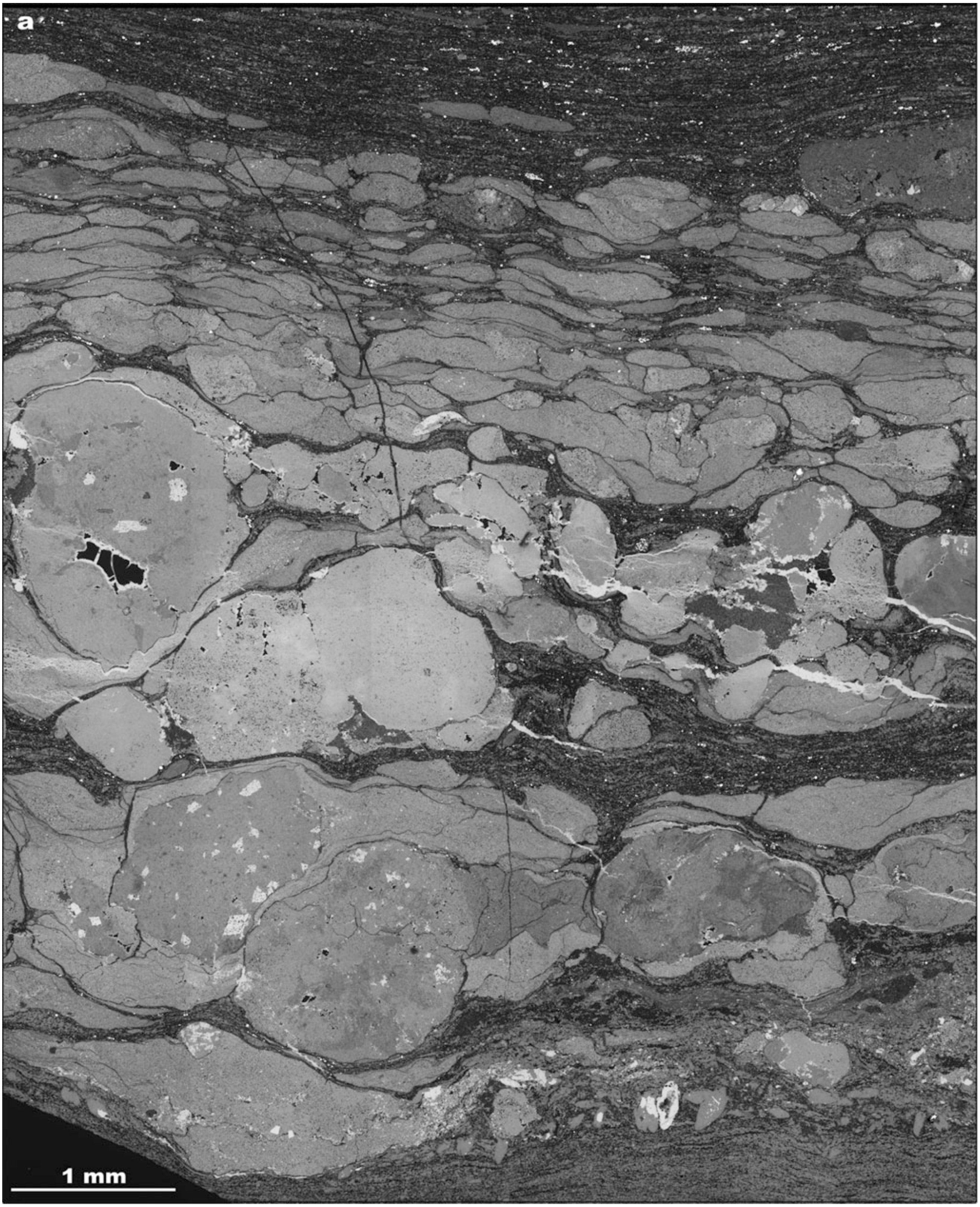

Fig. 6.117 C_{org}-rich and phosphate-bearing rocks from the adit at the type locality at Shunga, nearby to FAR-DEEP Hole 13A. (**a**) Back-scattered electron image of nodular phosphates in C_{org}-rich mudstone from an outcrop at the type locality at Shunga. Note that extensional cracks are filled with apatite (bright), and some voids in concretions are occupied by black desiccated pyrobitumen

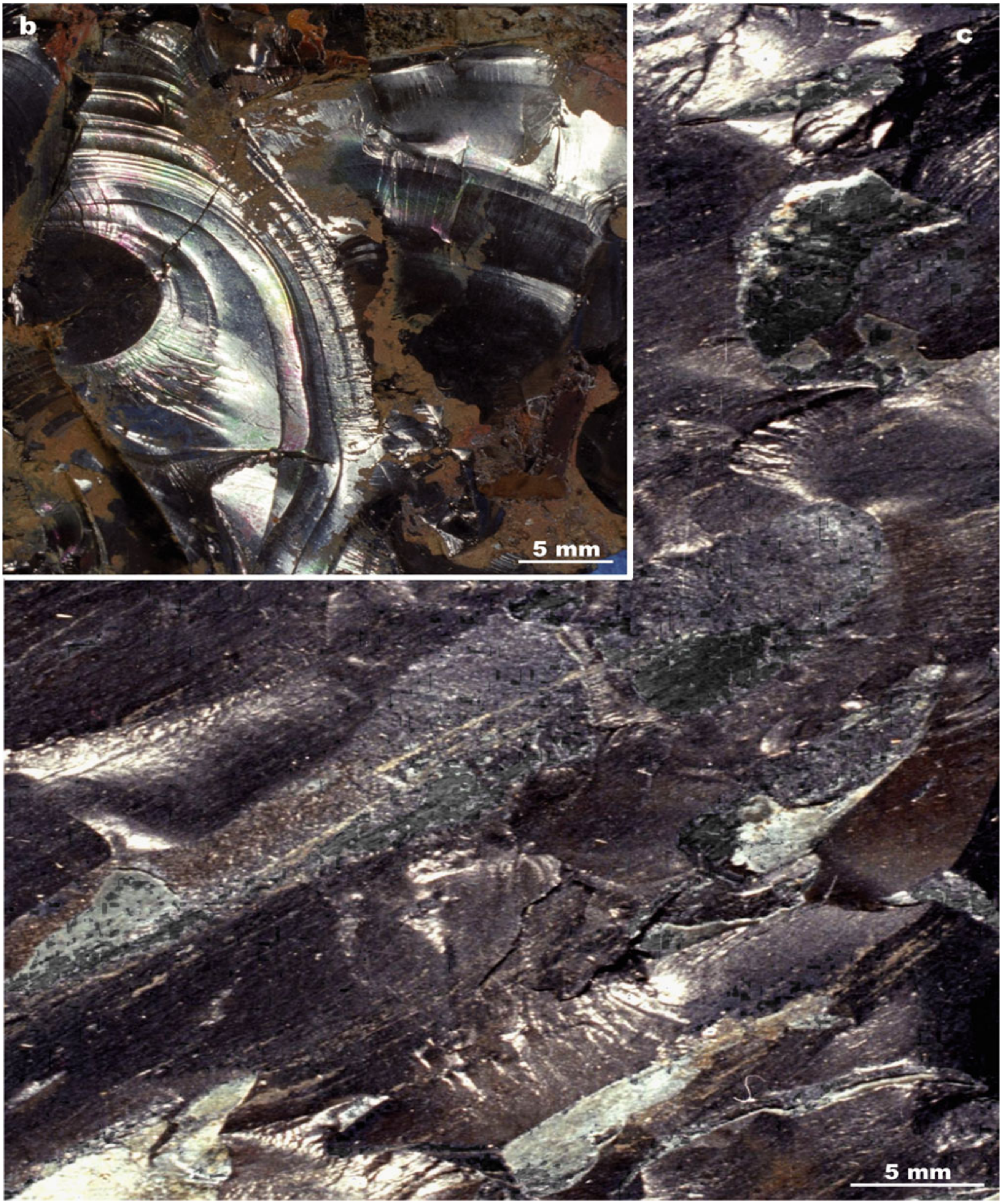

Fig. 6.117 (continued) (**b**) A hand specimen of lustrous pyrobitumen (shungite) containing 99 wt.% total organic carbon and representing metamorphosed oil, which was trapped in an interbed opening. (**c**) A hand specimen of semilustrous, massive rock rich in migrated pyrobitumen and residual kerogen (c. 65 wt.% total organic carbon) with faint bedding (*Back*-scattered image by (**a**) by Aivo Lepland. photographs (**b**, **c**) by Victor Melezhik)

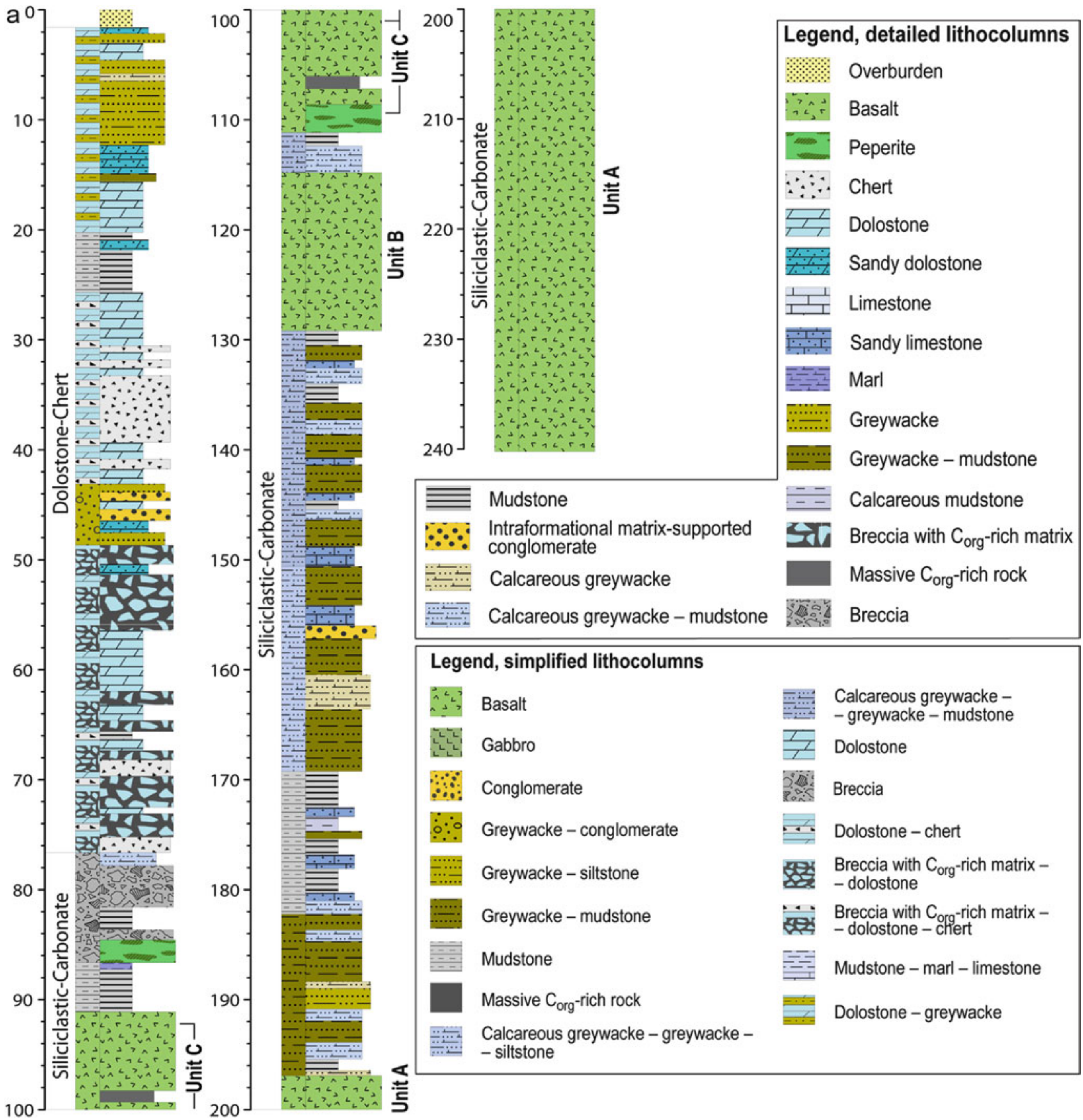

Fig. 6.118 Lithological section of the Zaonega Formation within FAR-DEEP Hole 13A (**a**), correlation to Hole 12AB (**b**), and tentative reconstruction of depositional environments (**c**) based on the core observations and previous sedimentological research in the vicinity of the drilling site. Note that lithological section is presented in two forms in Fig. 6.118a; while the left, narrow lithocolumn is simplified, the right, wider lithocolumn provides more details on lithology

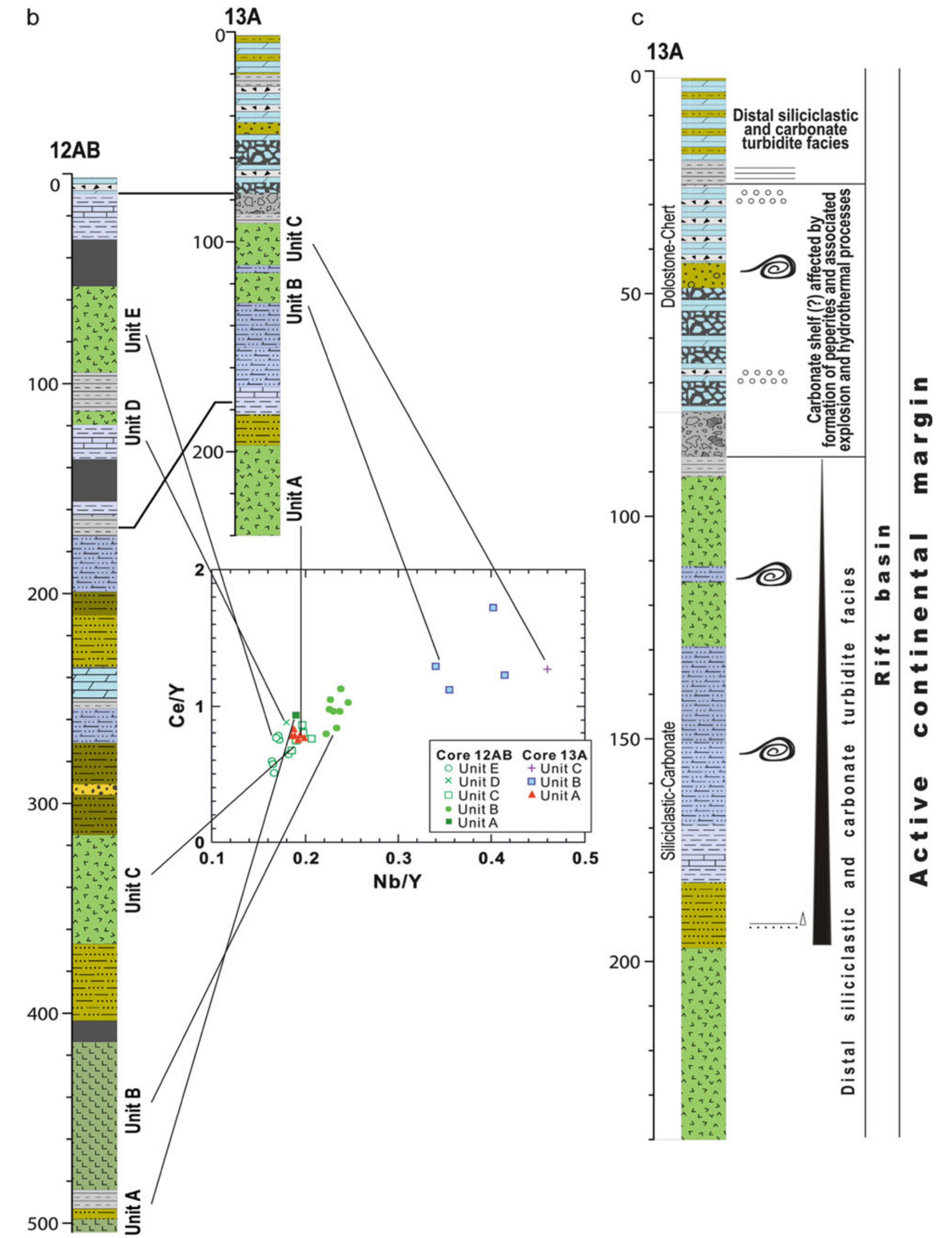

Fig. 6.118 (continued) Lithological section of the Zaonega Formation within FAR-DEEP Hole 13A (**a**), correlation to Hole 12AB (**b**), and tentative reconstruction of depositional environments (**c**) based on the core observations and previous sedimentological research in the vicinity of the drilling site. Lithological symbols are explained in Fig. 6.6

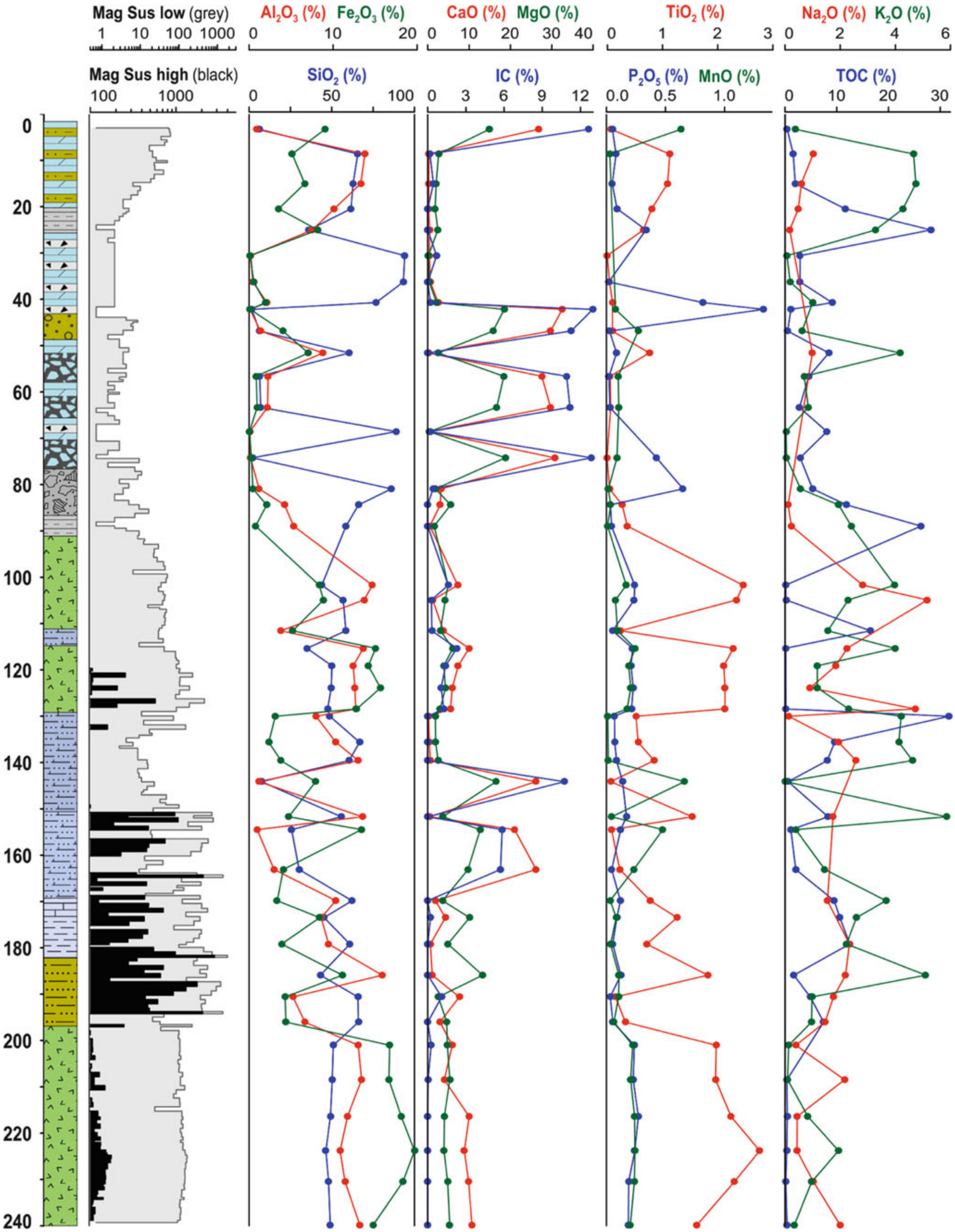

Fig. 6.119 Relative magnetic susceptibility (K*), and geochemical profiles of selected elements in Core 13A based on the archive samples collected with c. 8 m-spacing. For analytical techniques and data quality see Part 5

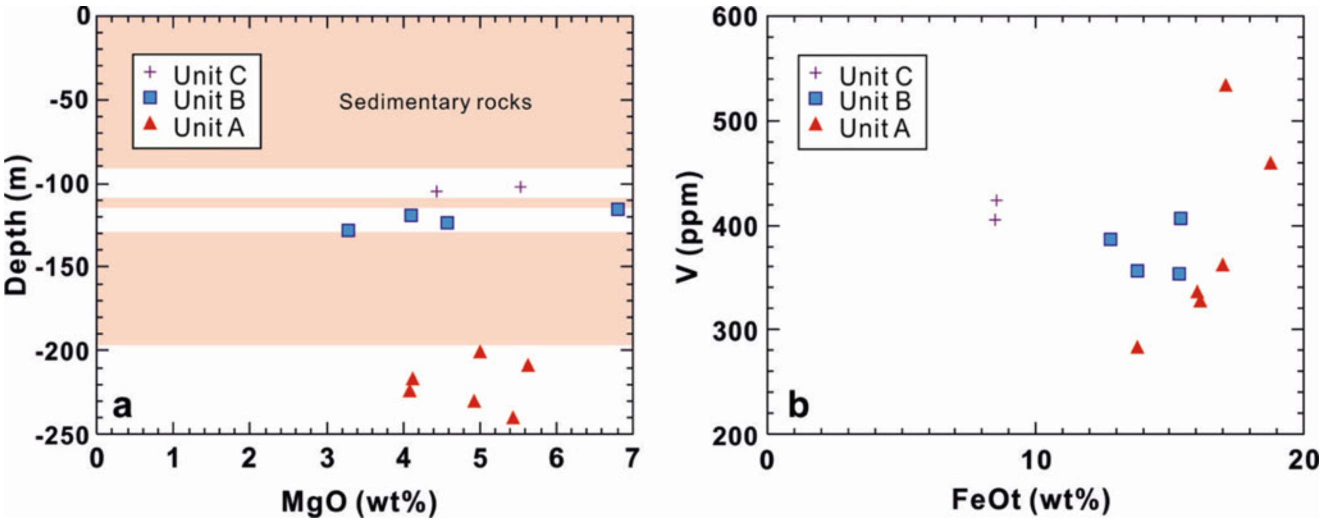

Fig. 6.120 (**a**) MgO versus depth diagram for igneous rocks in Core 13A. (**b**) FeO_t versus V diagram for igneous rocks in Core 13A

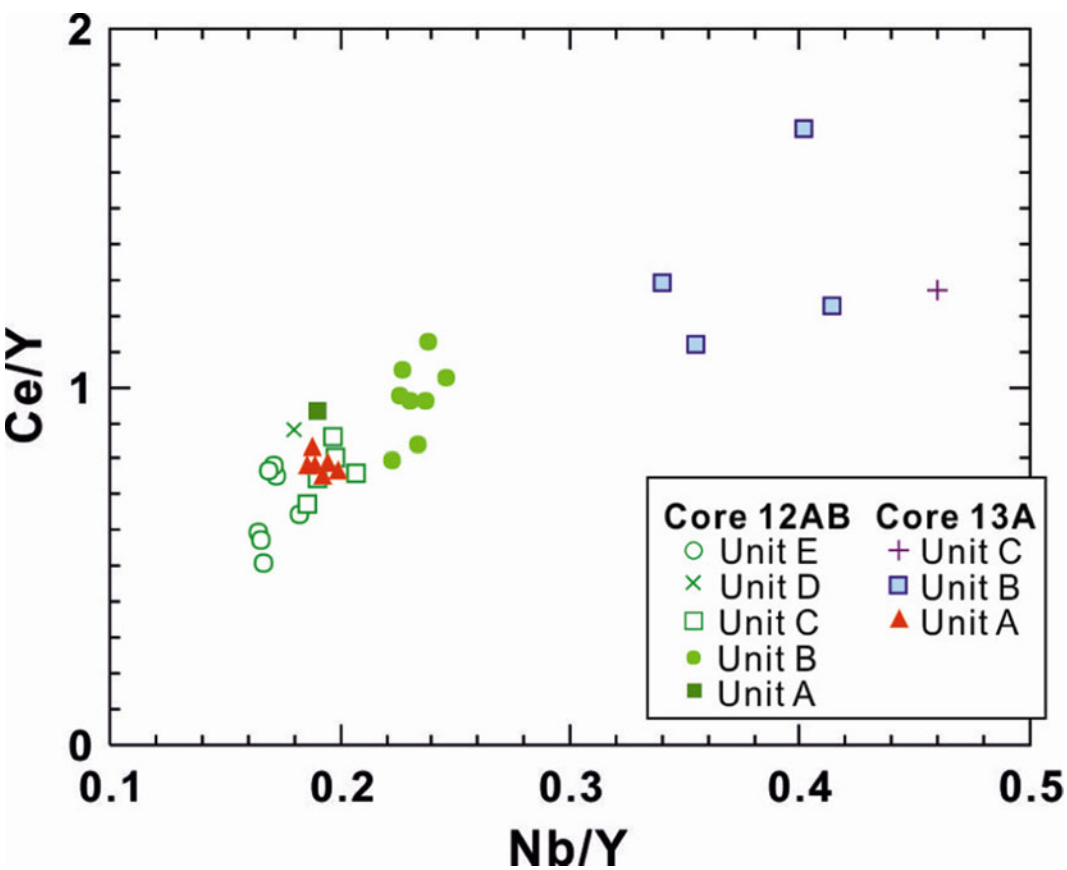

Fig. 6.121 Comparison of Ce/Y and Nb/Y ratios in igneous rocks from Cores 12AB and 13A

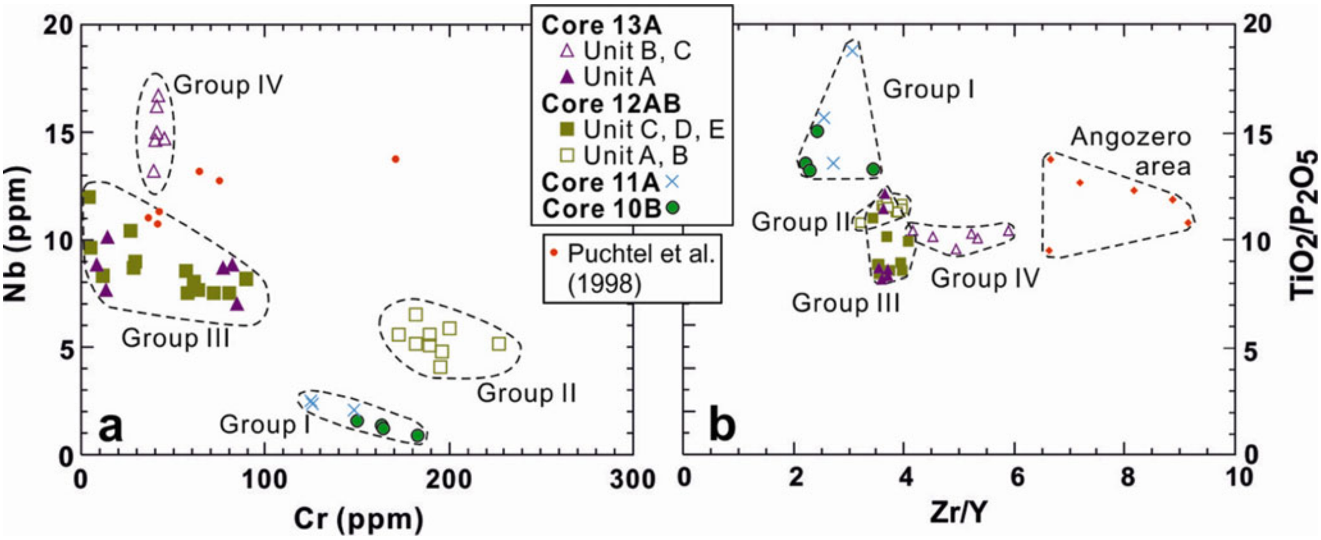

Fig. 6.122 Relationship between Cr and Nb concentrations (**a**) and Zr/Y and TiO_2/P_2O_5 ratios (**b**) in igneous rock samples from Cores 10B, 11A, 12AB and 13A obtained from the Onega region. Also shown are analytical data on Zaonega Formation basalts from the Angozero area published by Puchtel et al. (1998)

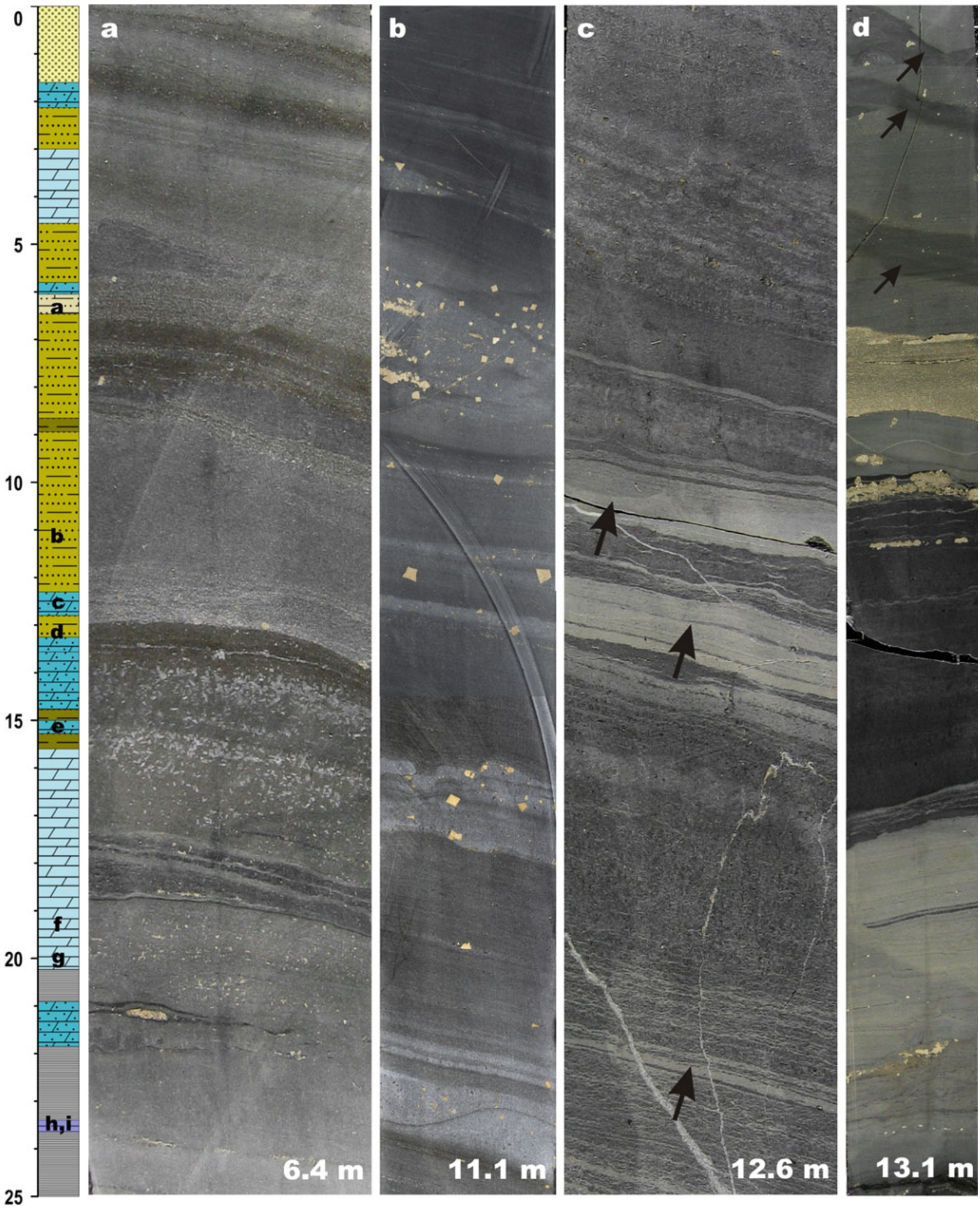

Fig. 6.123 Sedimentological and petrological features of the main rock types intersected by Hole 13A. Core diameter is 5 cm. (**a**) Bedded greywacke with thin siltstone interlayers (dark-coloured) containing carbonate porphyroblasts/grains (middle part of the photo). (**b**) Rhythmically bedded greywacke and mudstone containing pyrite porphyroblasts. (**c**) Laminated dolostone with thin greenish greywacke laminae (*arrows*). (**d**) Interbedded mudstone and greywacke, the latter impregnated by sulphides; note that three dark grey bands (*arrows*) cross-cut the lamination and are the result of post-depositional alteration (fluid infiltration?)

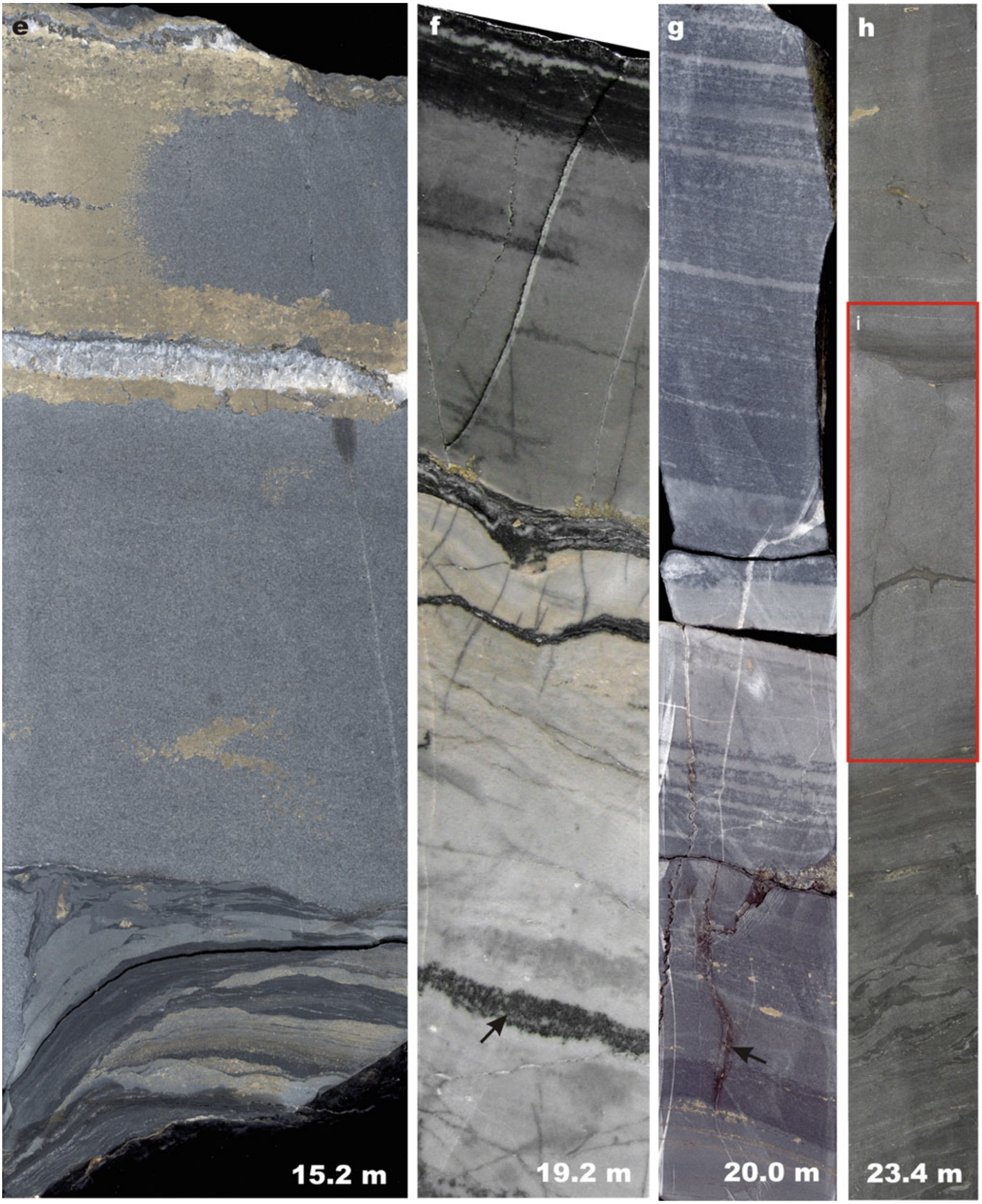

Fig. 6.123 (continued) (**e**) Greywacke and mudstone with disturbed bedding (*lowermost* part of the photo) overlain by massive dolostone with calcite veins (bright) and sulphide impregnation. (**f**) Indistinctly bedded, pale and dark grey dolostone with dark grey, silicified mudstone laminae (*arrow*), and a mudstone *top*. (**g**) Laminated dolostone with pale grey, semi-massive middle part; note the pyrobitumen-rich vein (*arrow*). (**h**) Dark grey marl with disturbed lamination passing upward into massive limestone; topmost faintly bedded marl has an erosive base

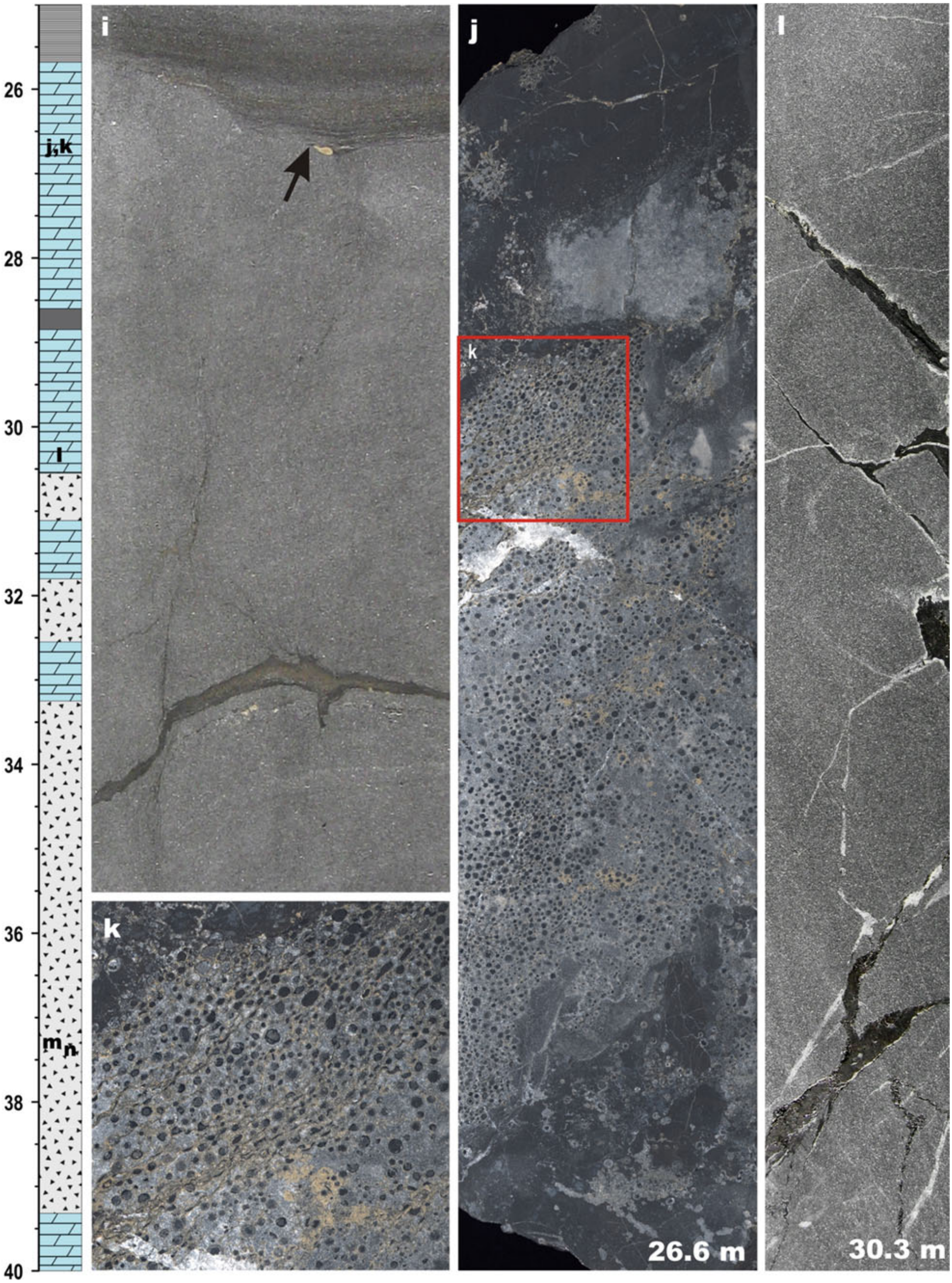

Fig. 6.123 (continued) (**i**) Close-up view of Fig. 6.123h showing a pyrobitumen-rich vein in massive limestone with eroded top (*arrow*). (**j**) Spherule-rich interval within a dolostone layer, which is under- and overlain by brecciated and massive mudstone. (**k**) Close-up view of Fig. 6.123j showing details of the spherule-rich interval. (**l**) Massive dolostone intersected by black, pyrobitumen-rich veins and white calcite veins

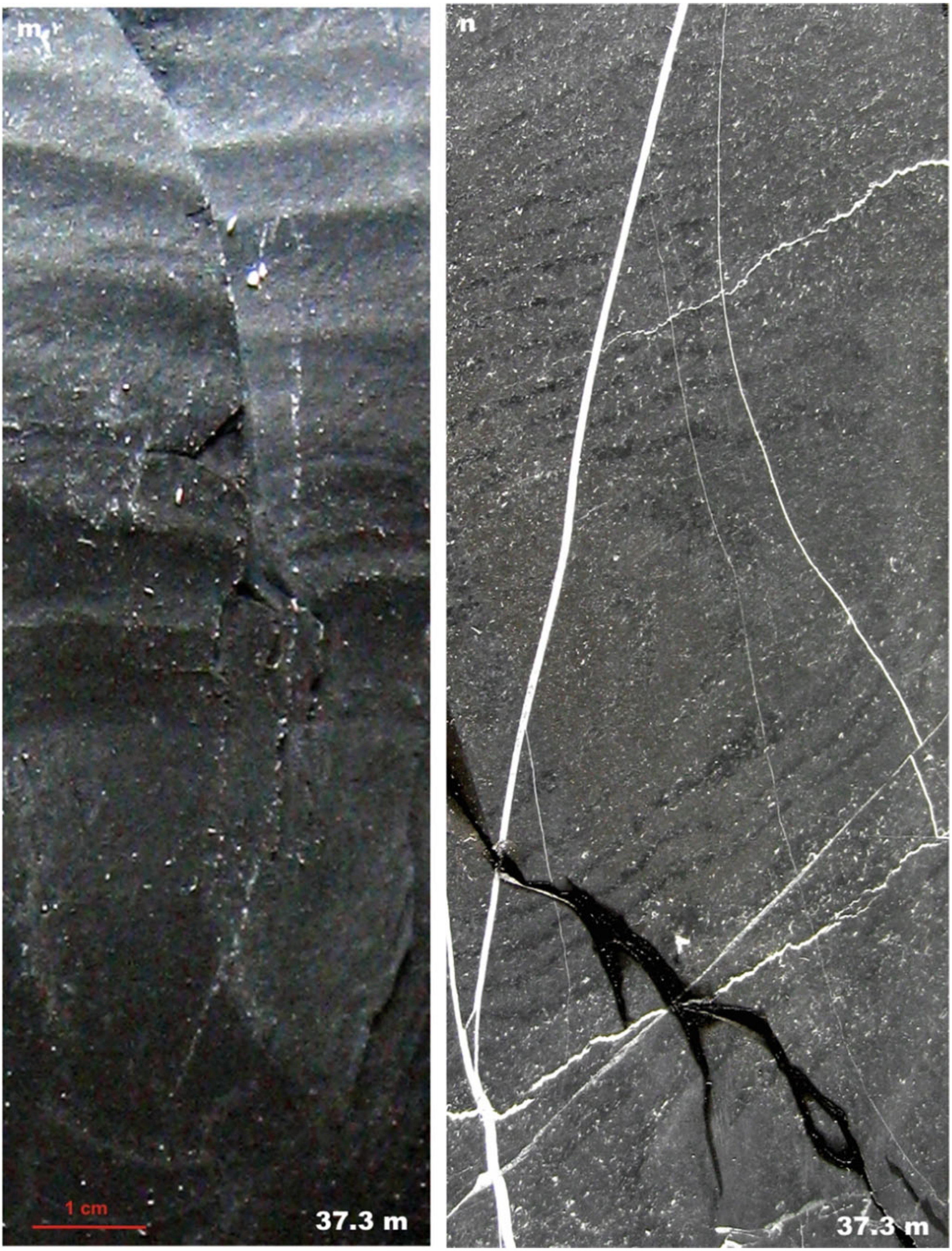

Fig. 6.123 (continued) (**m**) Massive chert passing into rhythmically laminated chert. (**n**) Rhythmic, concentric layering in a dark grey chert

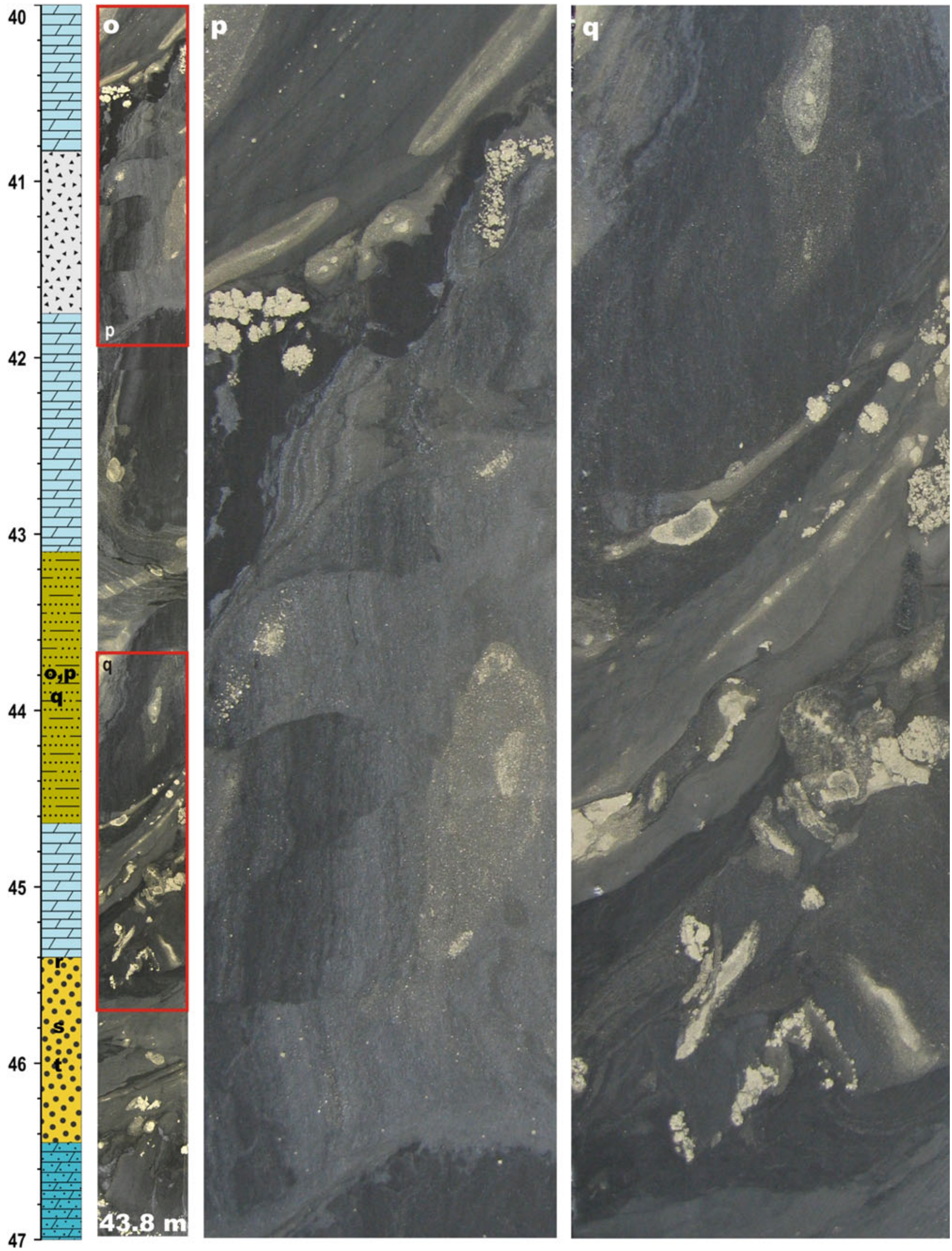

Fig. 6.123 (continued) (**o**) Slumped, sandy limestone beds containing abundant sulphides. (**p, q**) Close-up views of Fig. 6.123p showing details of synsedimentary deformation caused by slumping; note that dismembered pyritised layers and nodular sulphides are involved in slumping indicating their early diagenetic origin

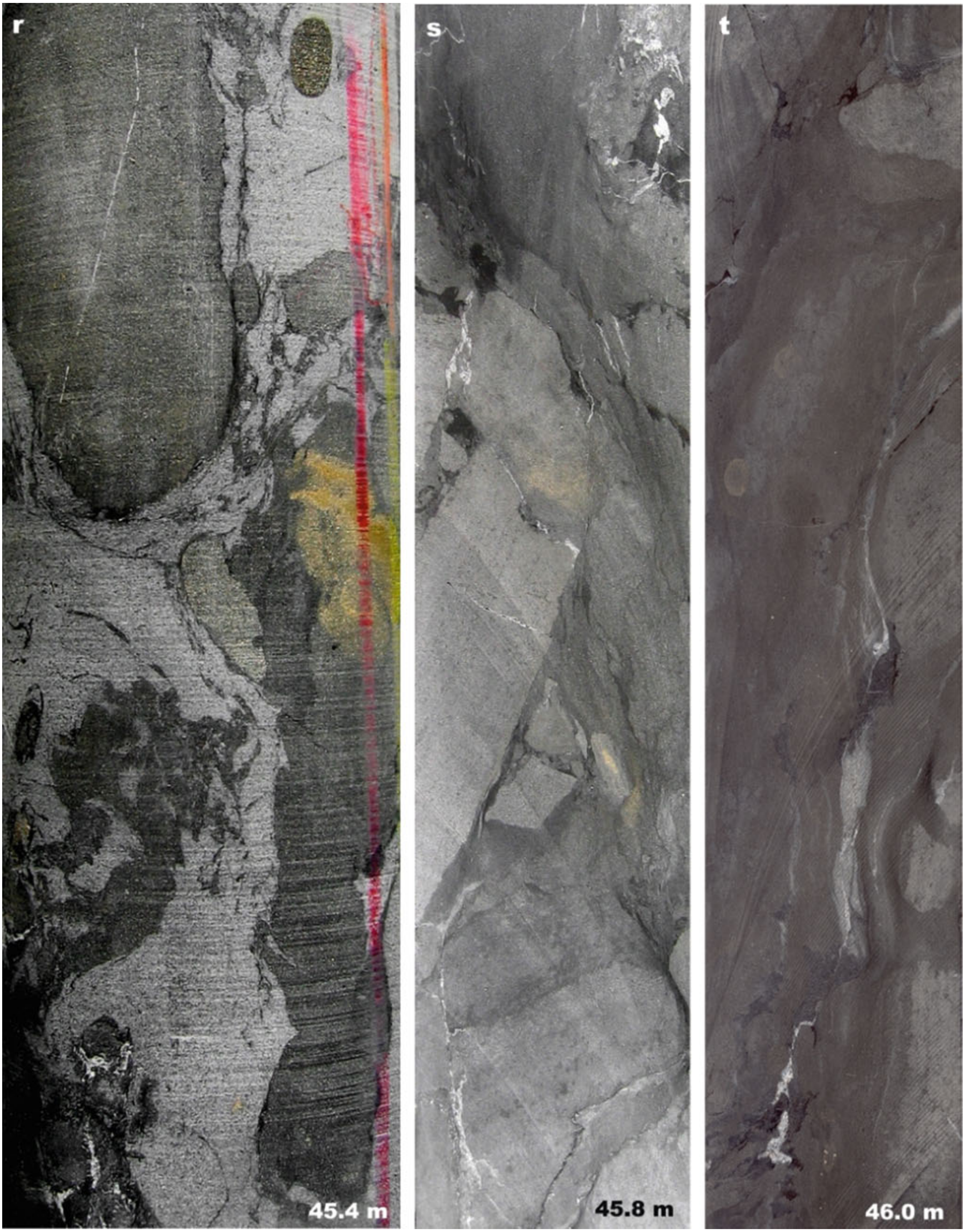

Fig. 6.123 (continued) (**r**) Intraformational, matrix-supported conglomerate containing rounded and soft-sediment deformed greywacke clasts supported by sandy limestone matrix. (**s**) Intraformational breccia containing angular and synsedimentary deformed clasts of dolostone with a sandy dolostone matrix. (**t**) Greywacke with a slumped structure and scattered fragments of pale grey dolostone

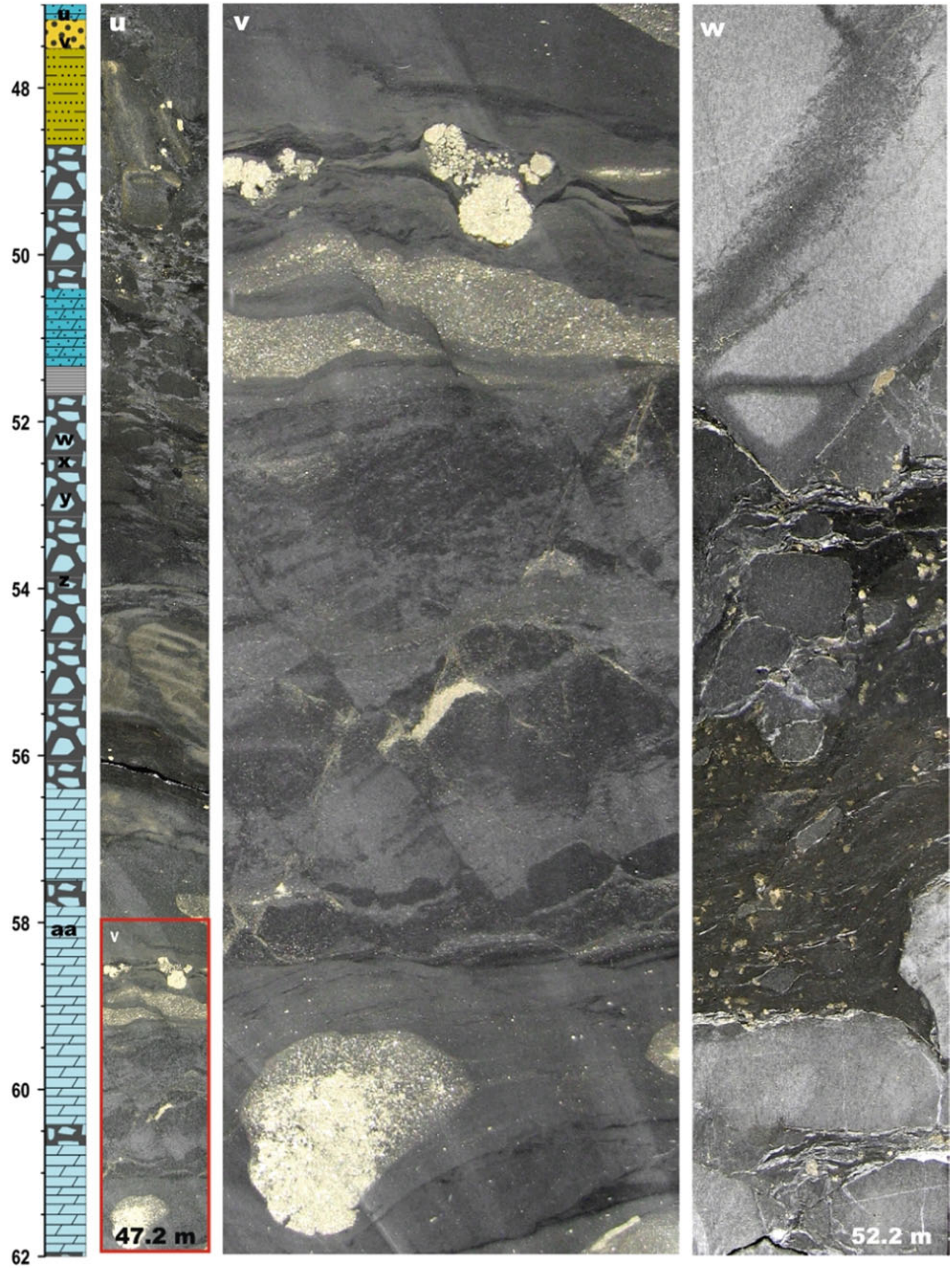

Fig. 6.123 (continued) (**u**) Intraformational conglomerates containing unsorted and variably rounded greywacke clasts supported by carbonate matrix; note the abundance of sulphides. (**v**) Close-up view of Fig. 6.123t showing synsedimentary deformation and brecciation; note that sulphide-impregnated clasts are affected by soft-sediment deformation and are involved in slumping together with nodular sulphides. (**w**) Breccia containing clasts of massive dolostone and pyrobitumen-rich matrix with sulphides

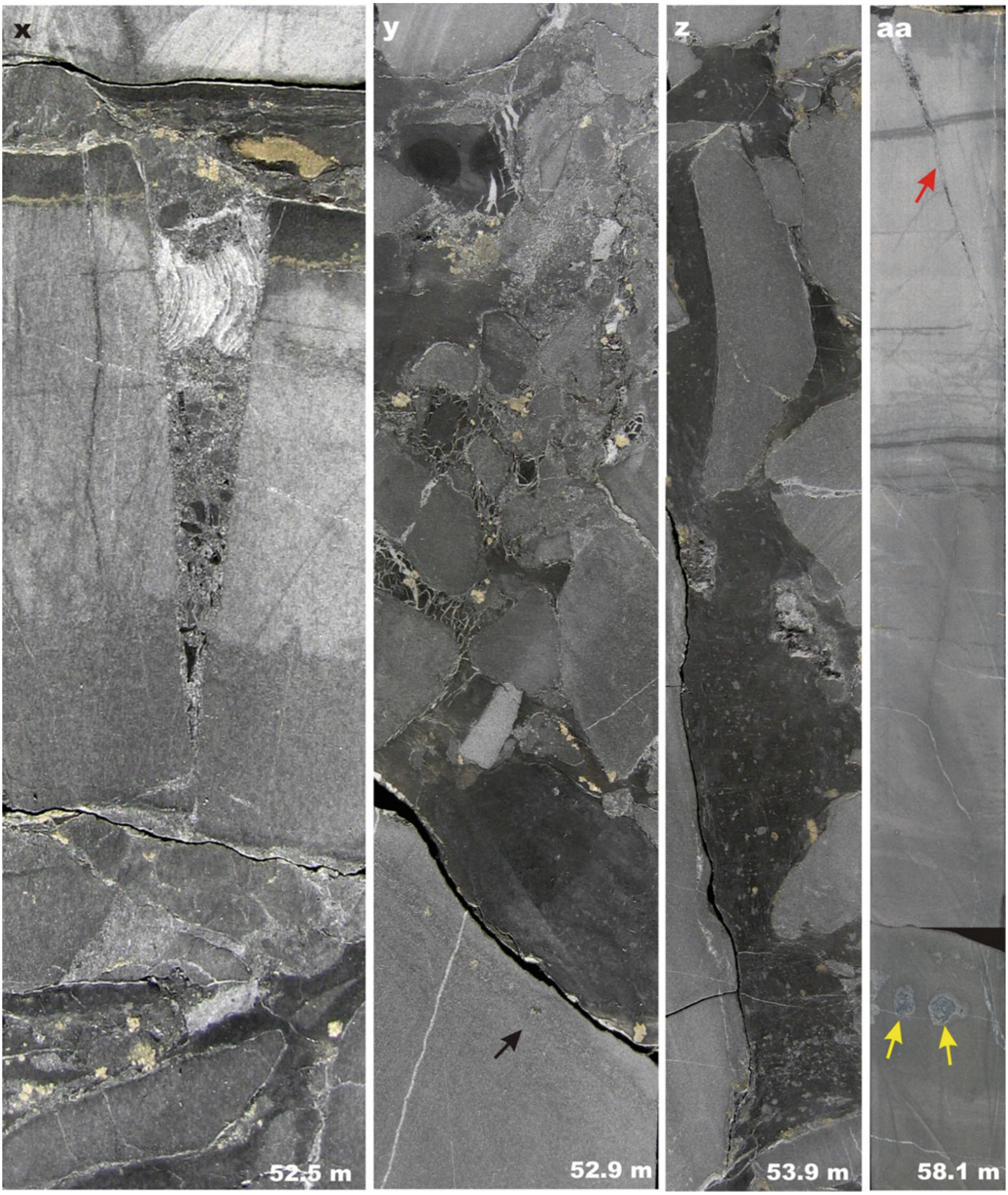

Fig. 6.123 (continued) (**x**) Breccia with clasts of massive dolostone and C_{org}-rich matrix, overlain by dolostone containing a vertical fracture, which is filled with small fragments of greywacke and mudstone cemented by calcite. (**y**) Massive dolostone (lowermost part of the photo) overlain by a breccia, which contains dolostone and limestone clasts within a pyrobitumen-rich matrix. (**z**) Breccia containing variably rounded clasts of massive dolostone embedded into pyrobitumen–rich matrix. (**aa**) Pale grey and grey, indistinctly-laminated dolostone; within the lowermost part of the photo calcite infilled voids are present (*yellow arrowed*); note the fracture filled with pyrobitumen-rich material and calcite in the upper part of the dolostone bed (*red arrowed*)

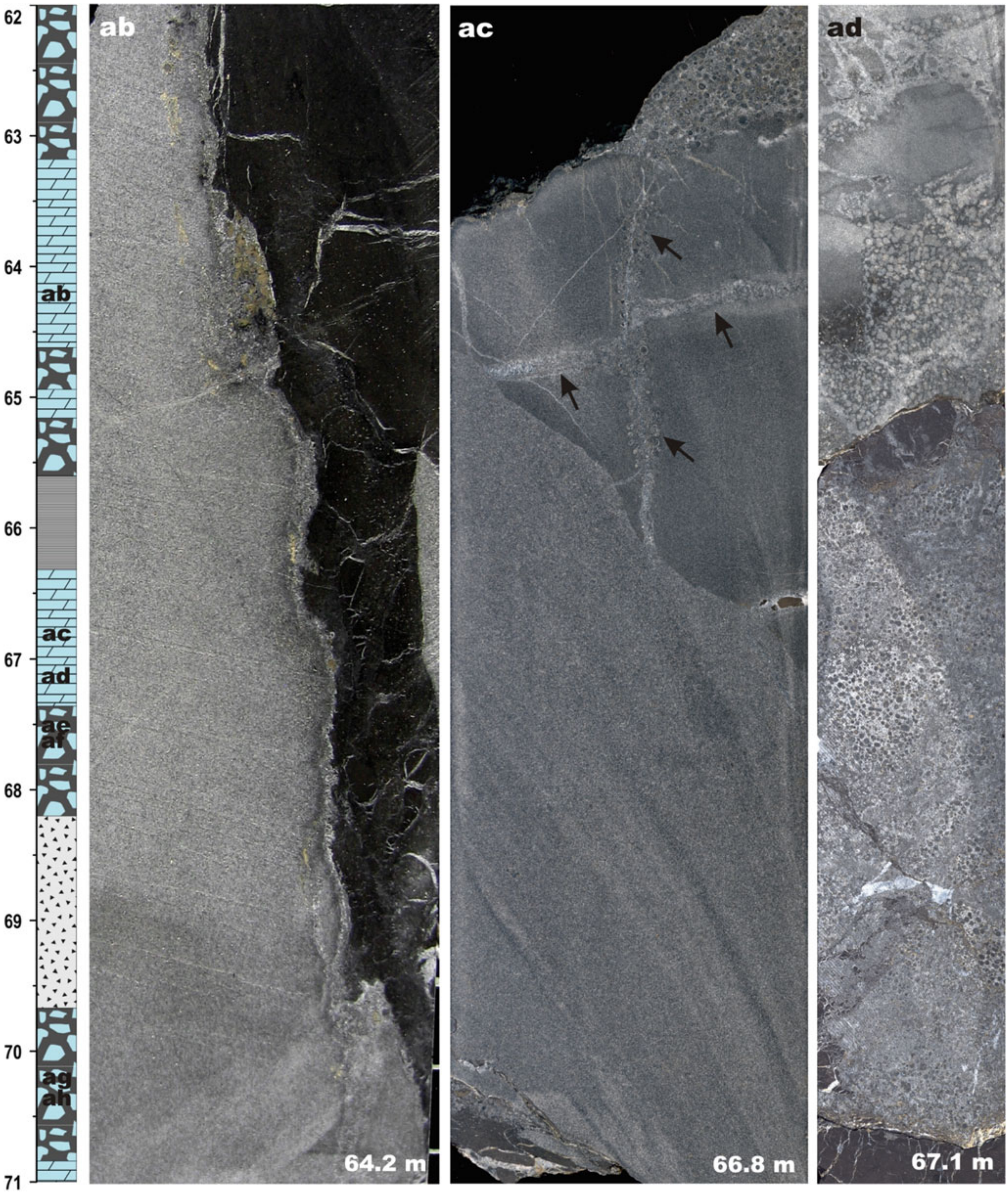

Fig. 6.123 (continued) (**ab**) Massive dolostone intersected by a wide fracture filled with pyrobitumen-rich material. (**ac**) Dolostone containing carbonate-phlogopite spherules, which fill narrow vertical and horizontal fractures (*arrows*). (**ad**) C_{org}-rich rock overlain by a fractured dolostone bed containing abundant calcite (bright)

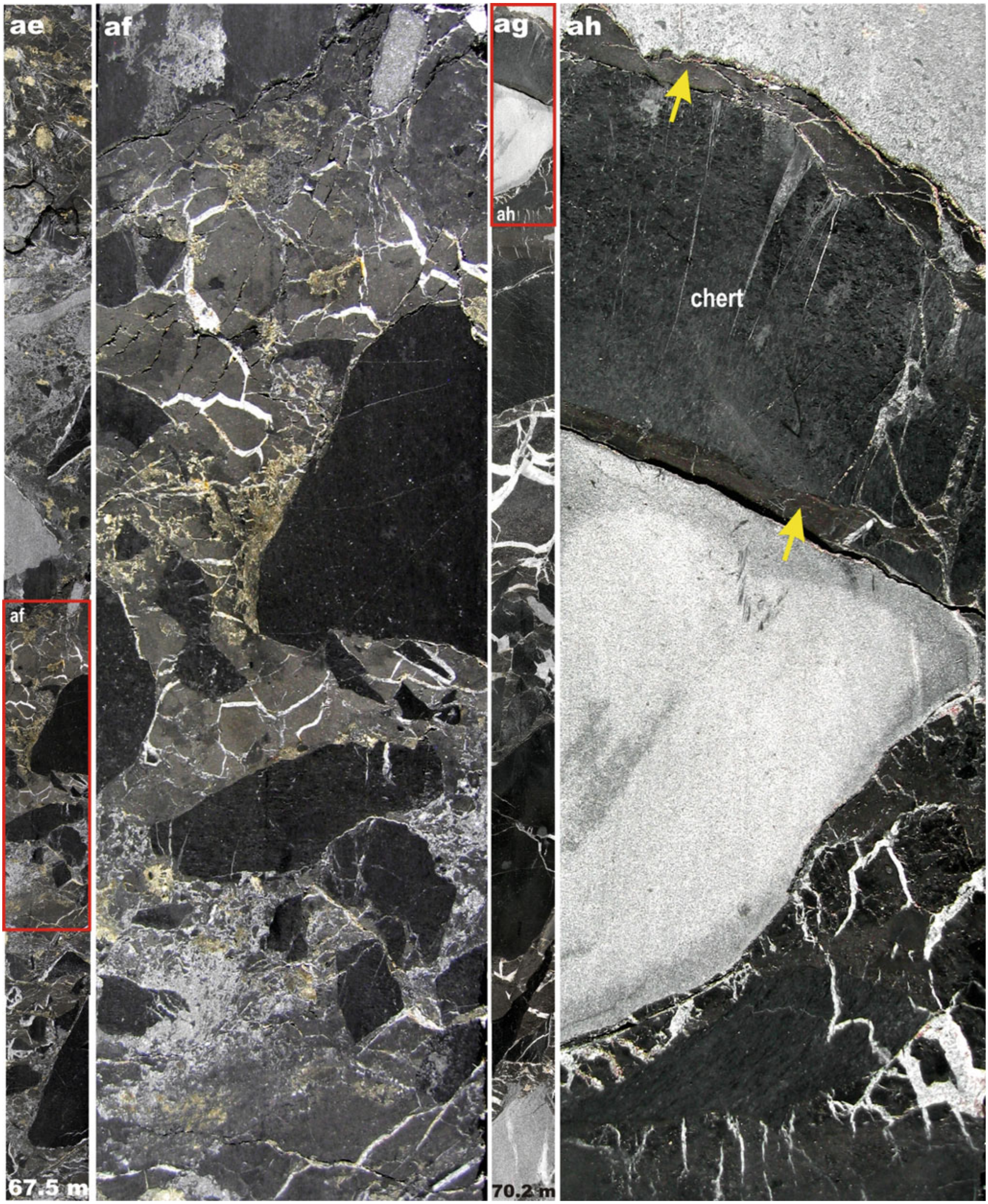

Fig. 6.123 (continued) (**ae**) Breccia mostly containing clasts of chert (*black*), but also clasts of dolostone and limestone (*gray*) embedded into pyrobitumen-rich matrix. (**af**) Close-up view of Fig. 6.123af showing details of chert clasts and pyrobitumen-rich matrix; note that the matrix shows polygonal joints cemented by sulphide and white calcite. (**ag**) Chert layers (*black*) with up to 20-cm-wide fractures filled with breccia containing clasts of siliceous mudstone, dolostone, and limestone embedded into pyrobitumen-rich matrix; joints in the matrix are filled with white calcite. (**ah**) Close-up view of Fig. 6.123ag showing rounded dolostone clast (*white*) embedded into pyrobitumen-rich matrix (*arrows*) containing chert. Joints within chert are filled by white calcite

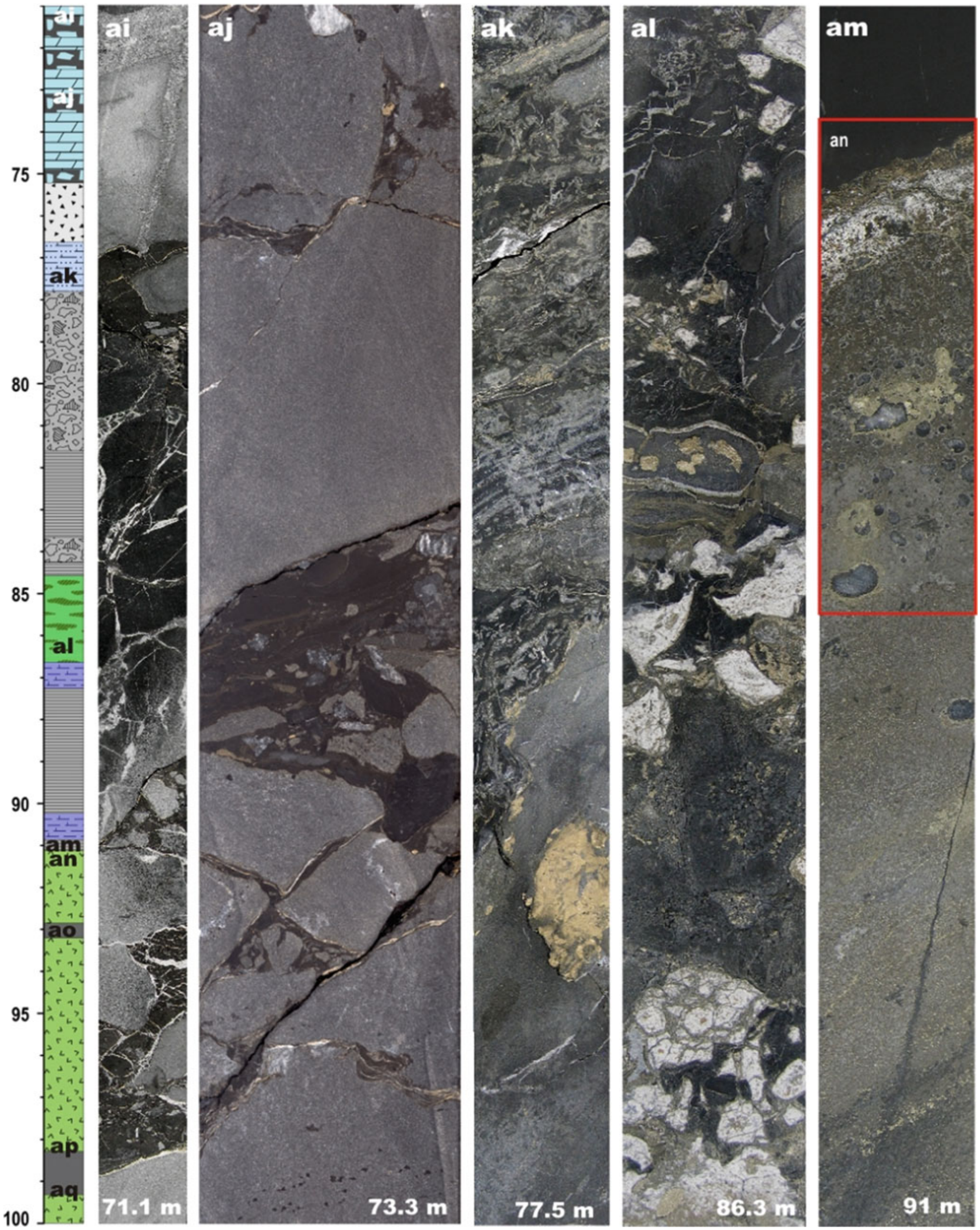

Fig. 6.123 (continued) (**ai**) Brecciated massive dolostone with pyrobitumen-rich matrix overlain by brecciated black chert followed by a grey, massive dolostone bed with calcite vein. (**aj**) Brecciated, massive dolostone with pyrobitumen-rich matrix and thin pyrobitumen-rich veins. (**ak**) Non-bedded limestone with a sulphide concretion and a scoured upper surface; the overlying mudstone shows intensive fracturing and calcite cementation. (**al**) Peperite containing variably rounded and angular clasts of sulphidised mudstones and inclusions of "bleached" basalt (light-coloured) embedded into pyrobitumen-rich matrix. (**am**) Top of amygdaloidal lava flow overlain by black, massive, C_{org}-rich rock

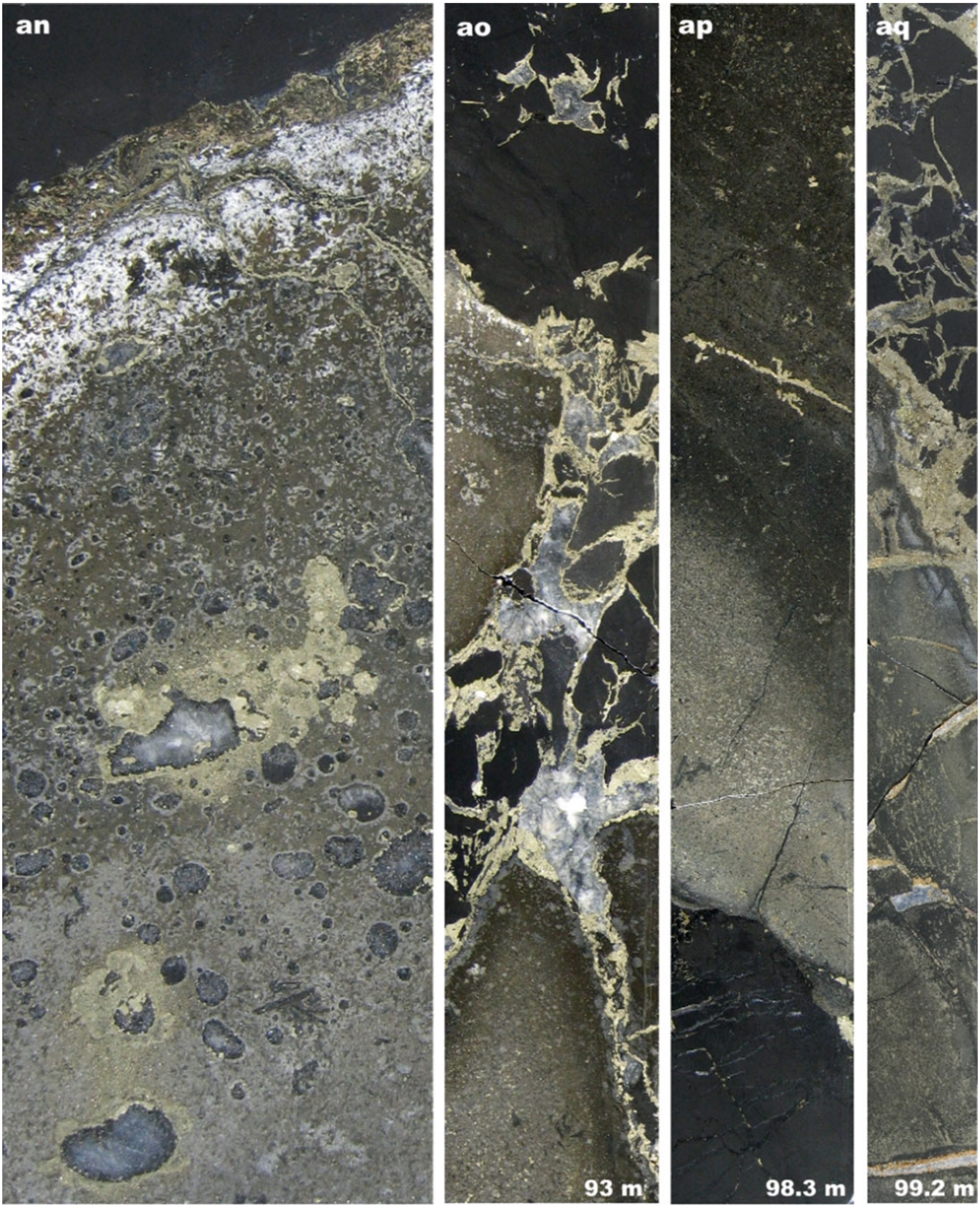

Fig. 6.123 (continued) (**an**) Close-up view of Fig. 6.123am showing the uppermost part of a basalt flow containing abundant vesicles filled with calcite and surrounded by sulphides; note the intensive sulphidisation of the basalt and calcitisation (bright) of its upper part. (**ao**) Basalt lava flow (peperite?), intensively veined, and overlain by massive, C_{org}-rich rock; fractures within the basalt are filled with pyrobitumen-rich material, calcite cement and sulphides. (**ap**) Massive, C_{org}-rich rock overlain by mafic lava flow. (**aq**) Mafic lava flow overlain by massive, C_{org}-rich rock; note the abundance of sulphides at the contact in both lithologies and along the fractures within the massive, C_{org}-rich rock

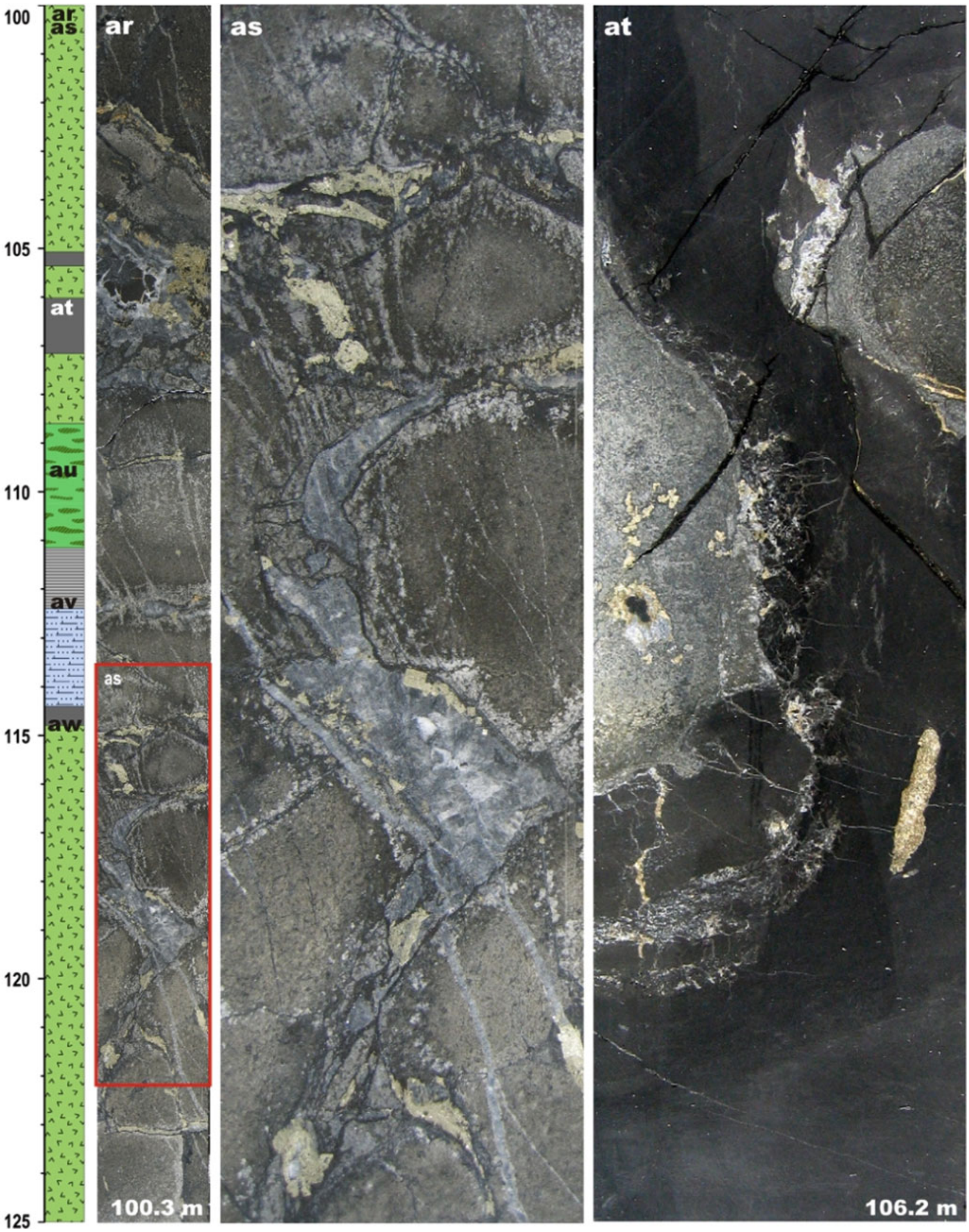

Fig. 6.123 (continued) (**ar**) Pillowed basalt (peperite?) containing fractures filled with calcite. (**as**) Close-up view of Fig. 6.123as showing details of calcite-infilled fractures and sulphidisation. (**at**) Peperite containing an inclusion of basalt in massive, C_{org}-rich rock with nodular sulphide

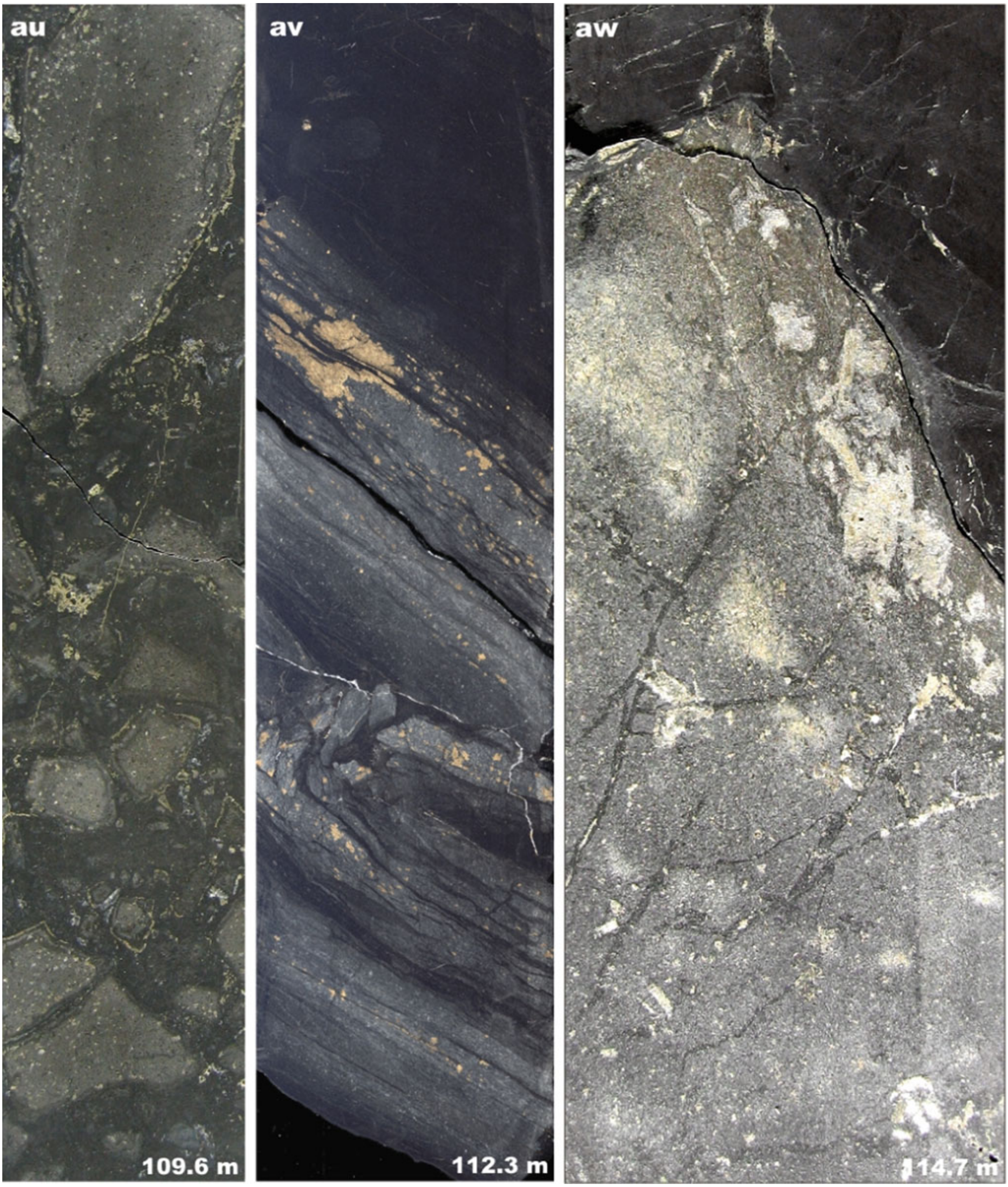

Fig. 6.123 (continued) (**au**) Peperite with angular and subangular inclusions of mafic lava in black, C_{org}-rich matrix. (**av**) Broken, synsedimentary fold in calcareous greywacke overlain by black, massive mudstones. (**aw**) Top of basalt lava flow overlain by massive, C_{org}-rich rock; note the intensive sulphidisation of the basalt

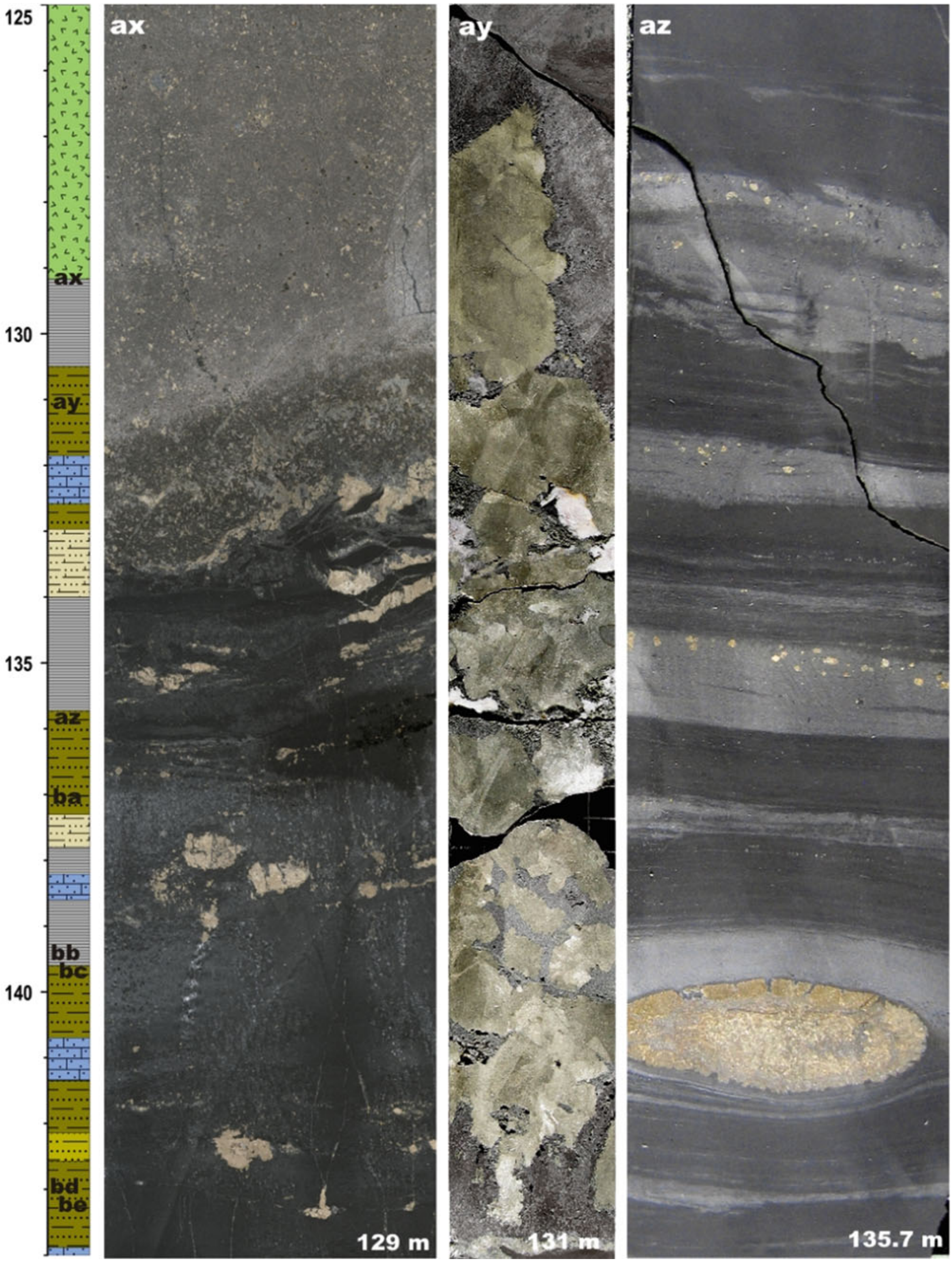

Fig. 6.123 (continued) (**ax**) C_{org}-rich, sulphidised, calcareous mudstone overlain by a mafic lava flow. (**ay**) Clusters of coarsely crystalline pyrite in a greywacke layer. (**az**) Rhythmically interbedded greywacke and mudstone; the greywacke contains large and small sulphide concretions

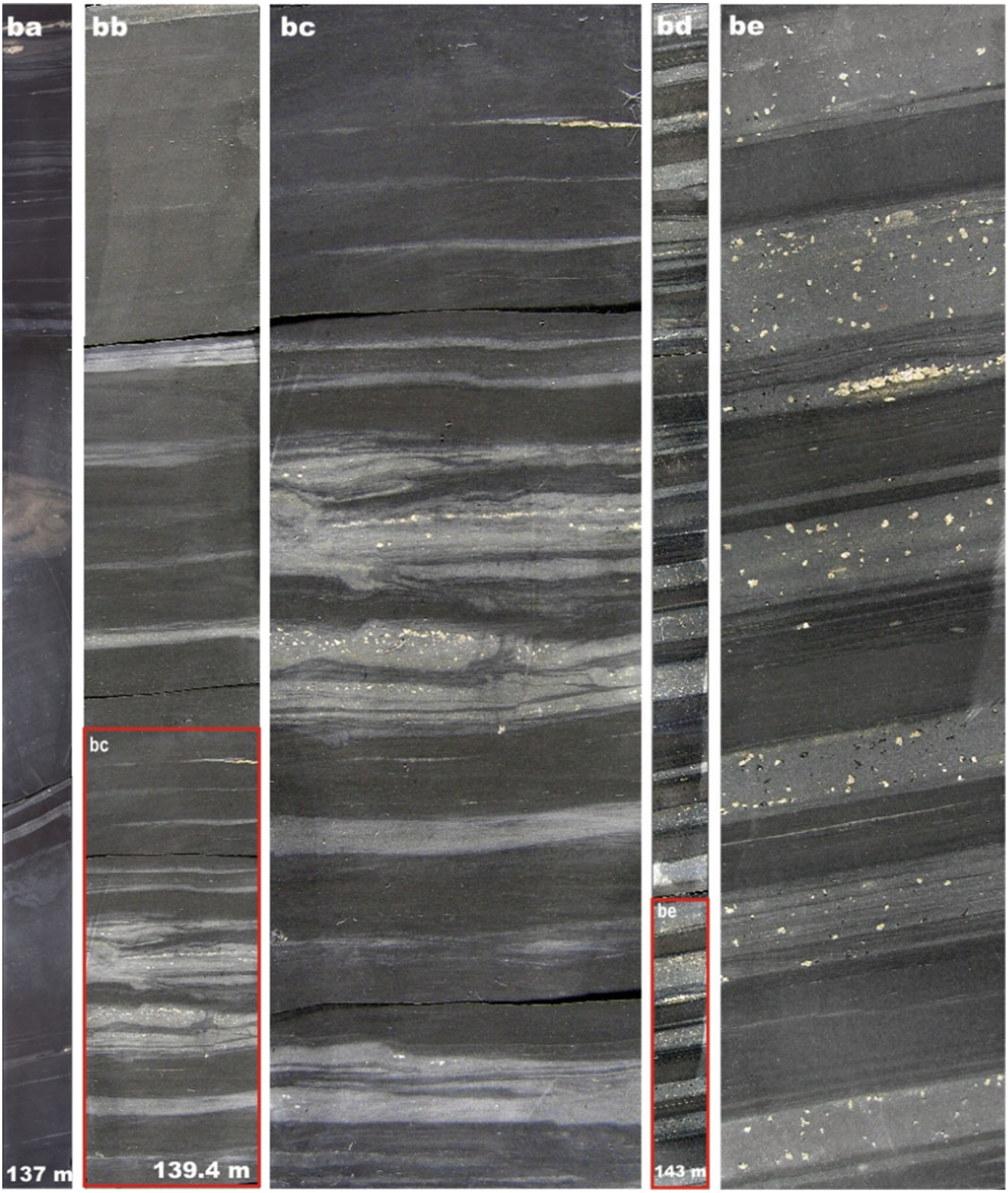

Fig. 6.123 (continued) (**ba**) Calcareous greywacke with sulphide-impregnated interval; note the rapid change in the bedding angle suggesting erosional surfaces. (**bb**) Laminated mudstone with thin greywacke intervals showing parallel lamination and slump structures. (**bc**) Close-up view of Fig. 6.123bb showing details of synsedimentary deformed greywacke with slump structures. (**bd**) Rhythmically interbedded greywacke and mudstone. (**be**) Close-up view of Fig. 6.123bd showing details of interbedded greywackes and mudstones; note the preferential formation of sulphides within the greywacke beds

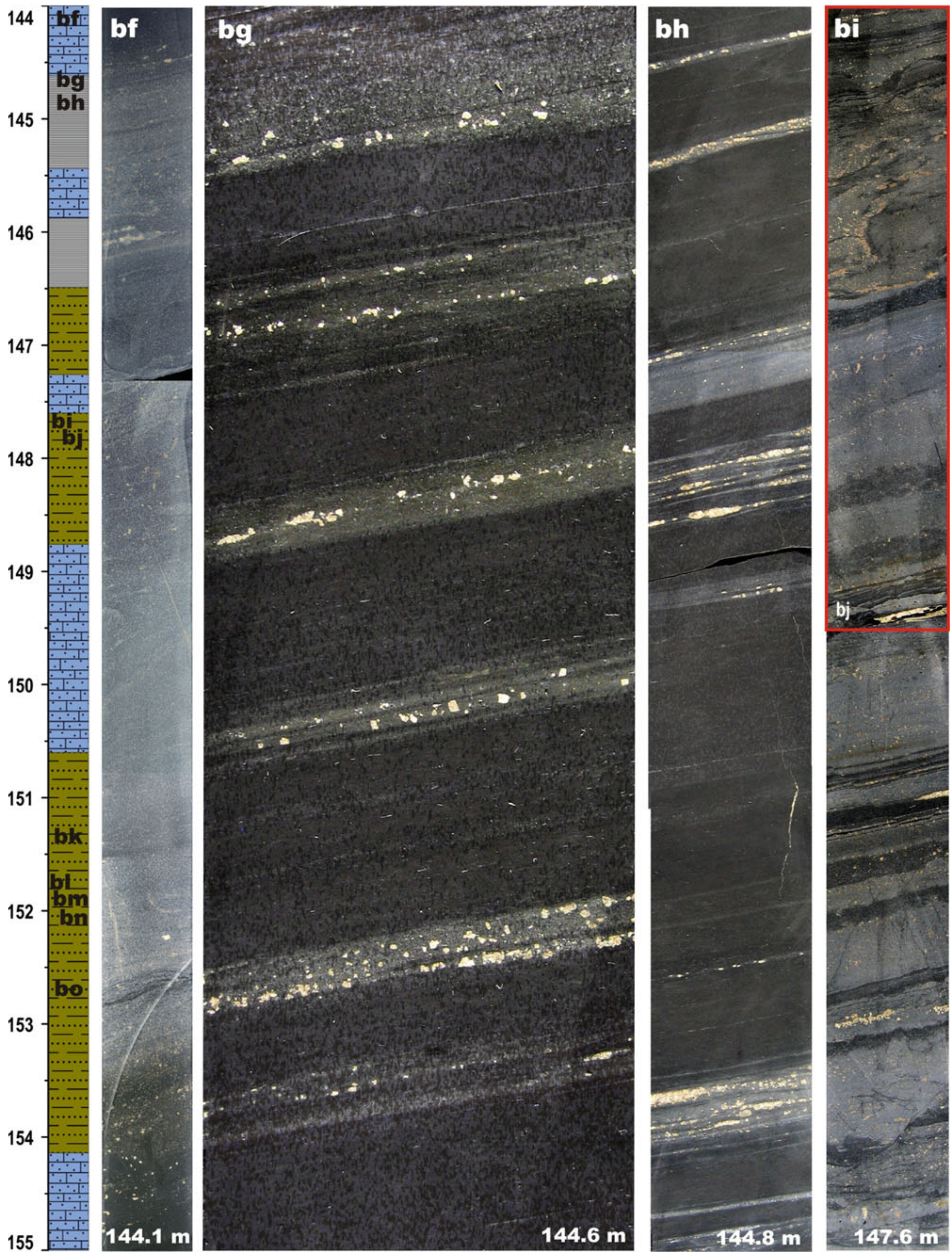

Fig. 6.123 (continued) (**bf**) A bed of massive to vaguely-bedded, sandy limestone showing gradational contacts with under- and overlying sulphide-bearing, laminated mudstone. (**bg**) Rhythmically interbedded mudstone and greywacke with the latter containing abundant sulphides. (**bh**) Thick beds of black mudstone interbedded with thinner intervals of sulphidised greywacke. (**bi**) Thick beds of greywacke interbedded with thinner intervals of black mudstone; note the slump structure in the uppermost bed

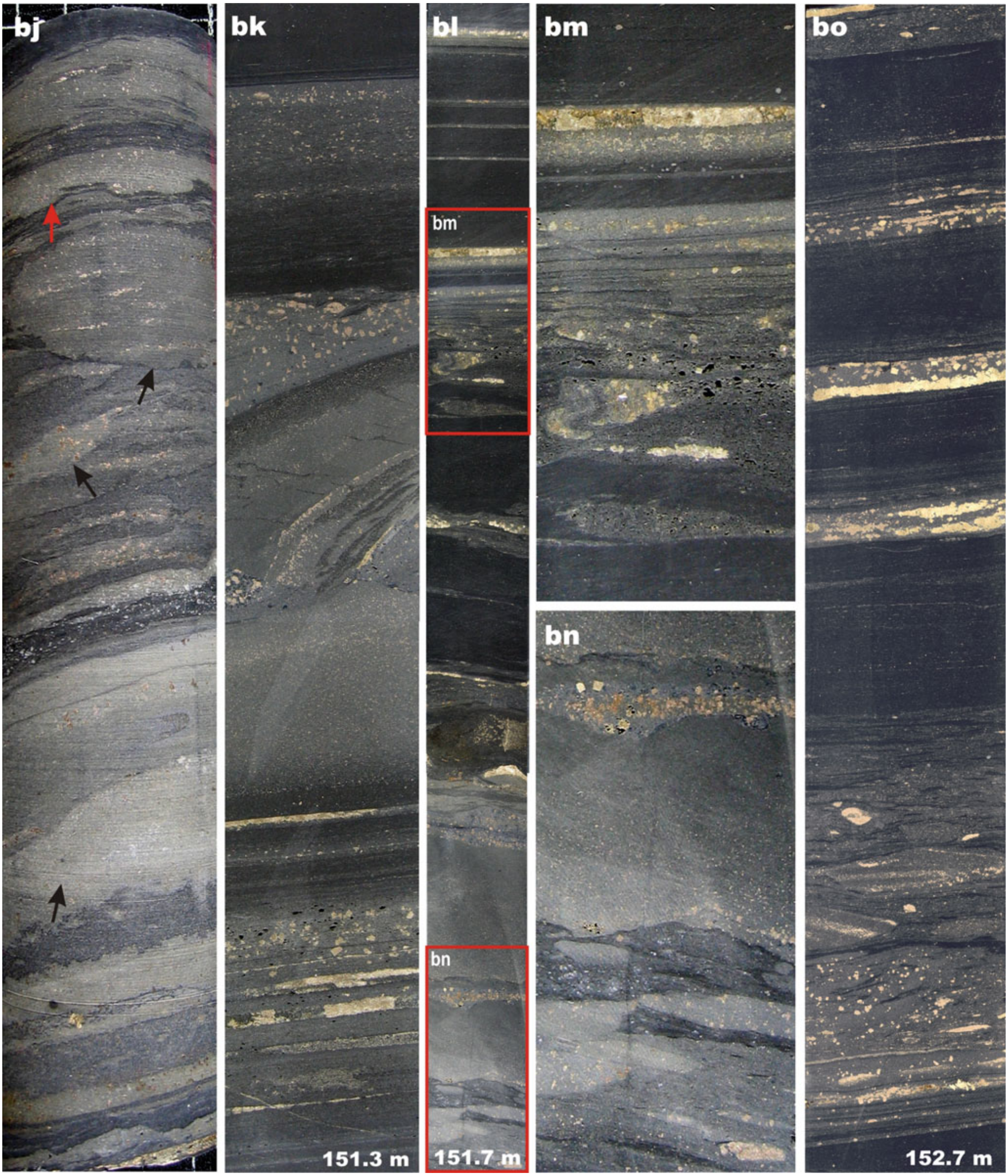

Fig. 6.123 (continued) (**bj**) Unsawn core showing details of Fig. 6.123bi; note the erosional surface (*red arrow*) and presence of greywacke clasts (*black arrows*) within the slumped greywacke interval. (**bk**) Interbedded greywacke and mudstone with a slumped interval; note the abundance of disseminated sulphides, small nodules and sulphidised laminae. (**bl**) Interbedded greywacke and mudstones with abundant sulphides. (**bm**) Close-up view of Fig. 6.123bl showing details of finely soft-sediment deformed, interlaminated greywacke and mudstone containing disseminated sulphides, sulphidised laminae, and black, angular, pyrobitumen-rich grains. (**bn**) Close-up view of Fig. 6.123bl showing details of a slump structure in a greywacke bed, resulting in the formation of a thin bed of intraformational conglomerate. (**bo**) Slumped, sulphidised greywacke bed overlain by mudstones interbedded with intensely sulphidised greywacke

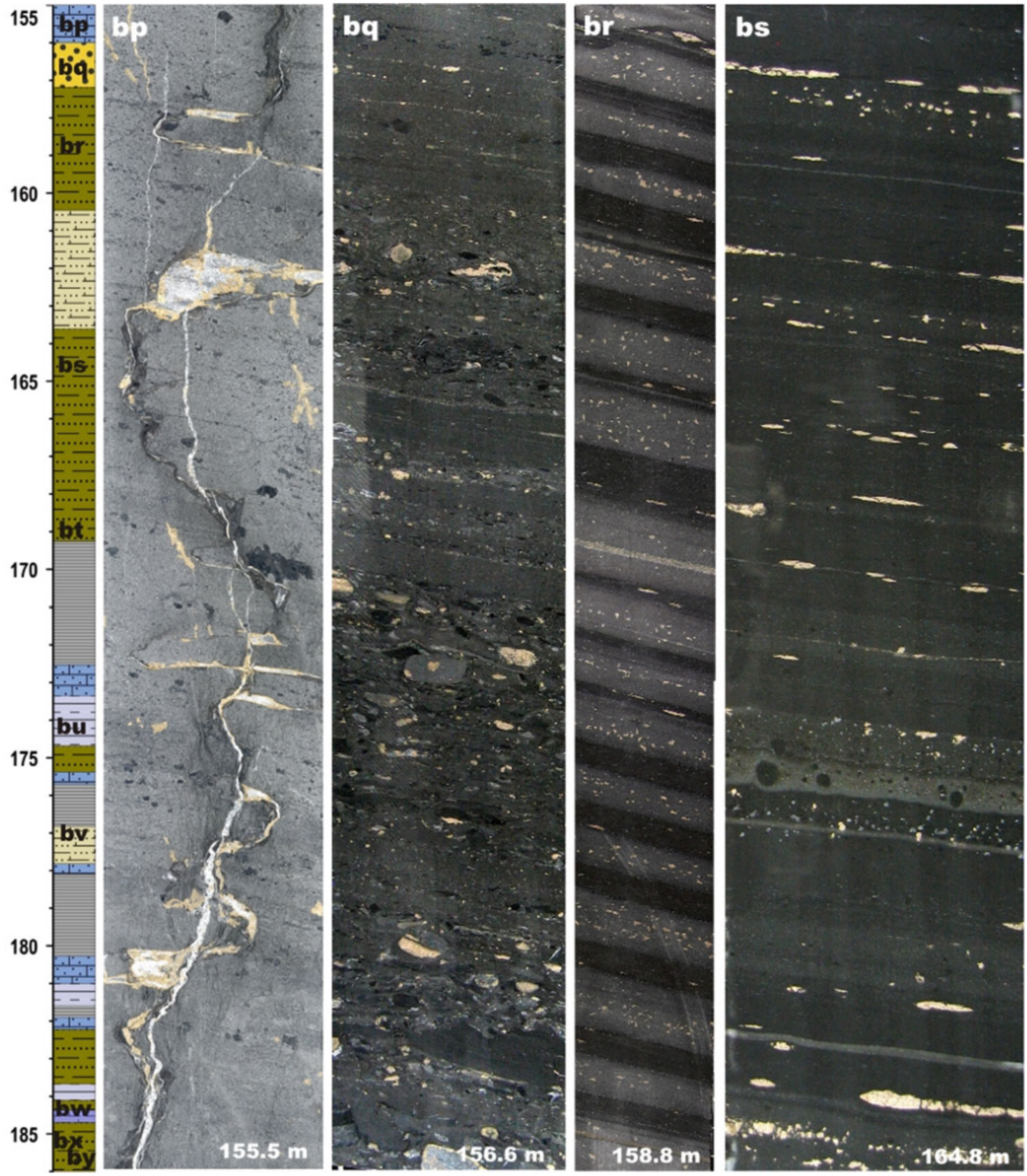

Fig. 6.123 (continued) (**bp**) Flat-laminated, sandy limestone with a few-mm-sized, black patches; the limestone is intersected by ptygmatic, pyrobitumen-rich vein, and a later calcite vein; note the voids filled with calcite and sulphides. (**bq**) Intraformational, small-pebble, clast-supported pebble beds alternating with fine-grained greywacke; clasts consist of sulphidised rocks and/or reworked sulphide nodules. (**br**) Rhythmically interbedded greywacke and mudstone with preferential formation of sulphides in the greywacke beds. (**bs**) Parallel-bedded mudstone with sulphide lenses and nodules and a greywacke bed containing black, non-compacted "clay balls"

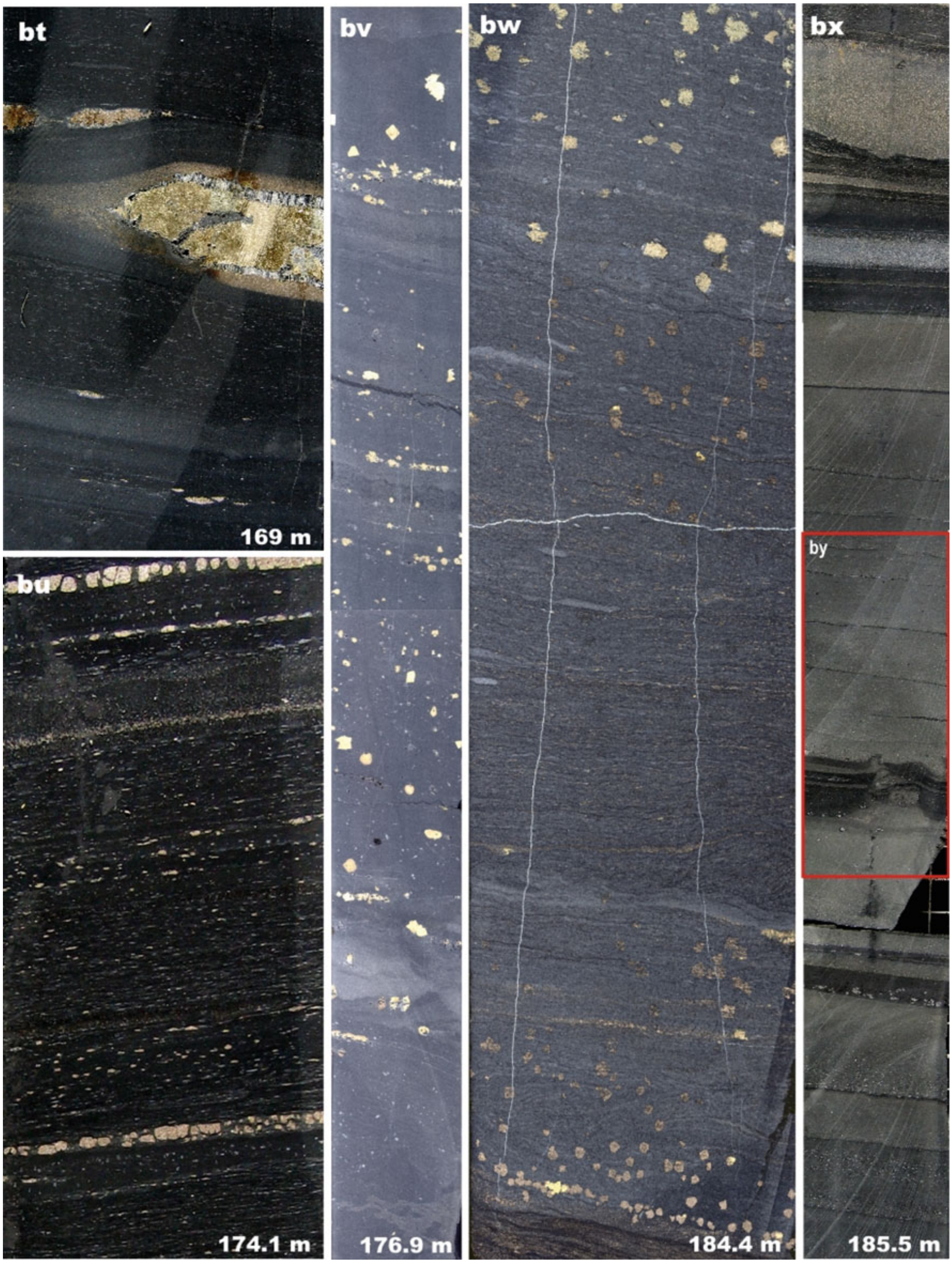

Fig. 6.123 (continued) (**bt**) Mudstone with a sulphide concretion containing a massive core and calcite rim; the latter separates the concretion from the partially sulphidised host greywacke. (**bu**) Mudstone displaying either partially sulphidised laminae or dismembered massive sulphide laminae. (**bv**) A bed of faintly-laminated, calcareous greywacke containing abundant sulphides. (**bw**) Laminated marl with sulphide nodules. (**bx**) Greywacke interbedded with thin mudstone beds; note the erosional base in the uppermost, sulphide-impregnated greywacke bed

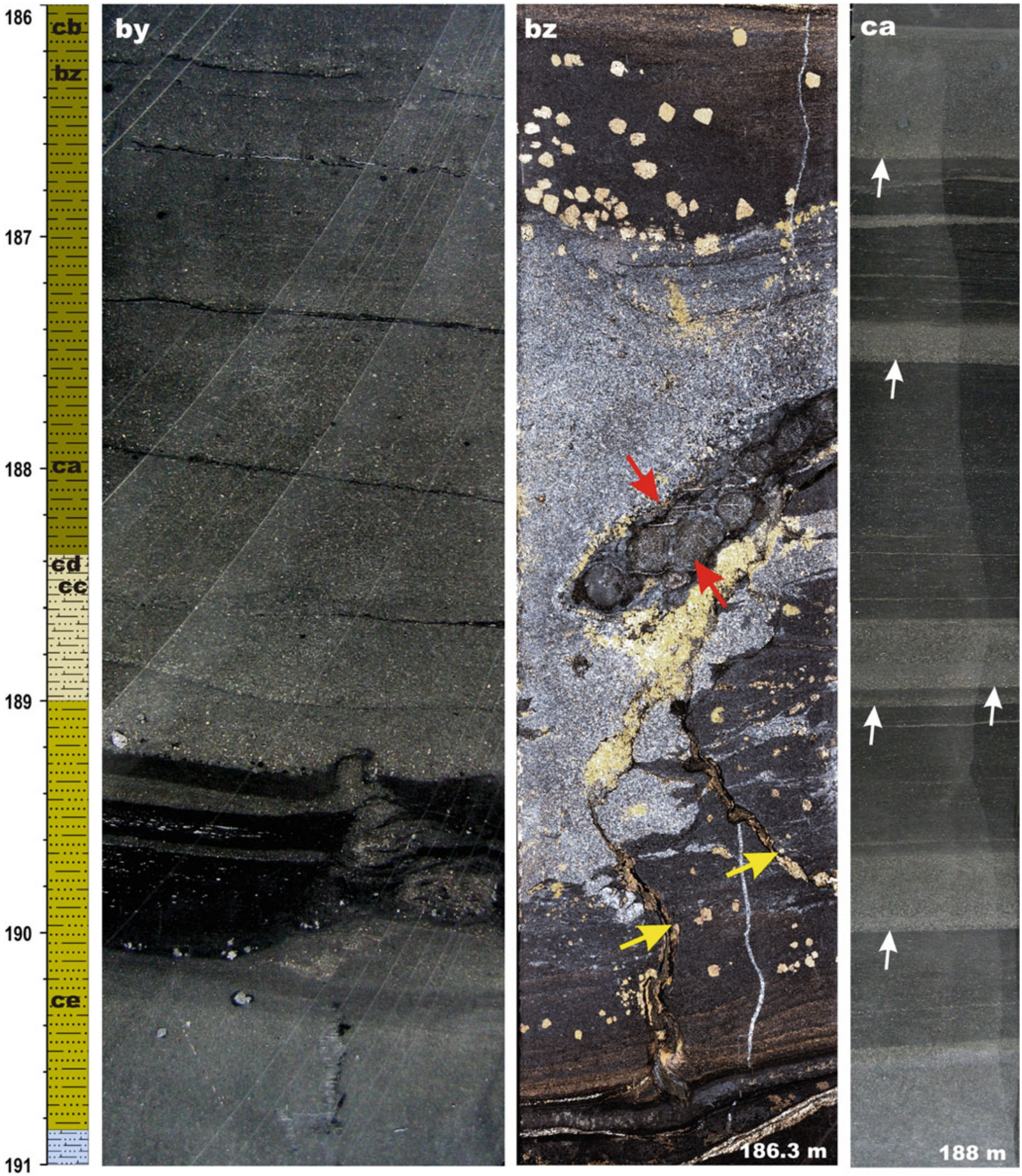

Fig. 6.123 (continued) (**by**) Close-up view of Fig. 6.123bx showing *upward* injection of sand from the thin greywacke lamina; the overlying greywacke occurs as massive or graded beds separated by thin, black mudstone drapes. (**bz**) Calcified interval in a mudstone bed; note the intense sulphidisation, rounded fragments of calcareous mudstones (*red arrows*), and pyrobitumen- and sulphide-rich veins (yellow *arrows*). (**ca**) Rhythmically interbedded mudstone and greywacke. Note that some greywacke beds are graded (*arrowed*)

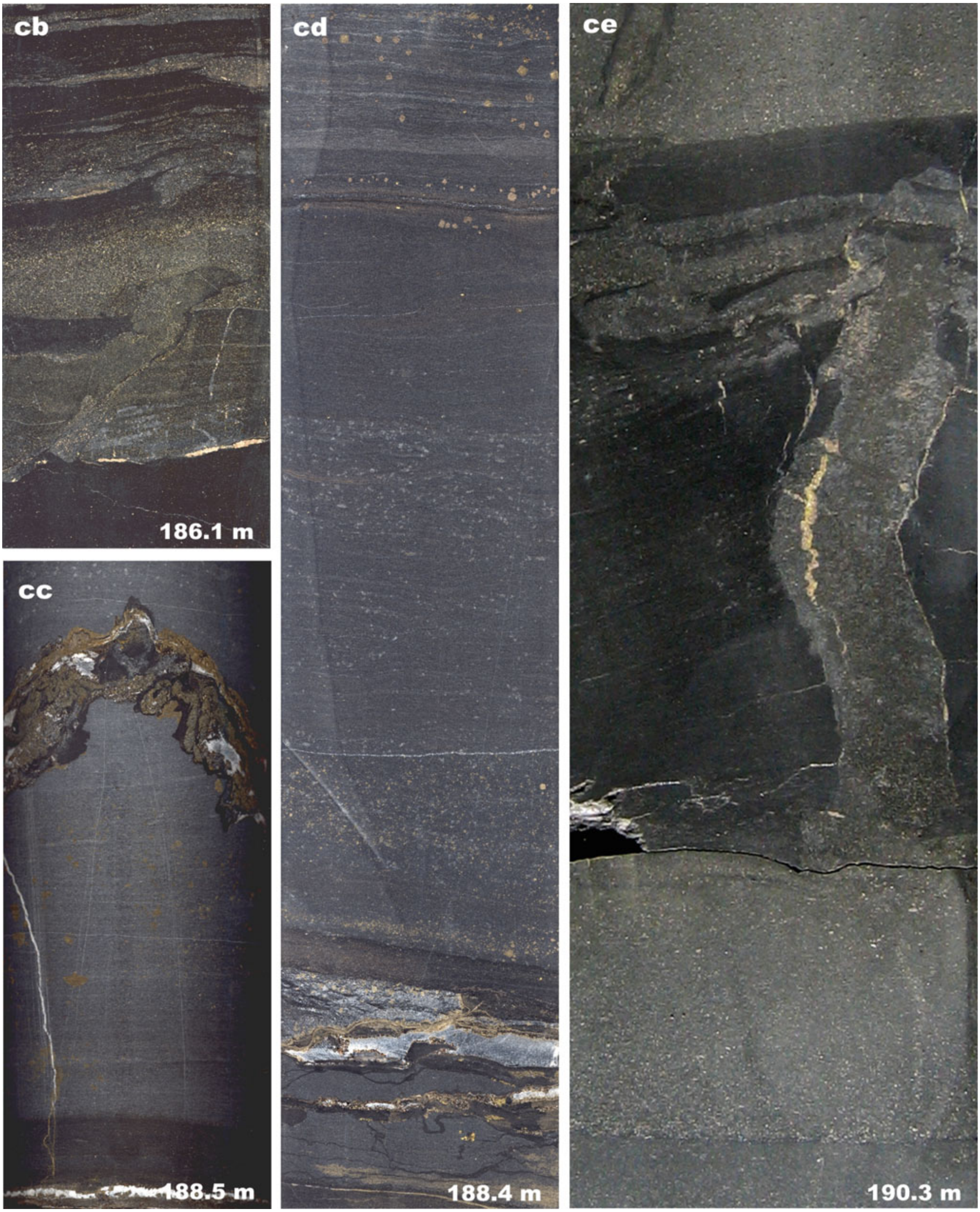

Fig. 6.123 (continued) (**cb**) Interbedded greywacke and black mudstone containing a sand dyke injected from the lower greywacke bed. (**cc**) Greywacke with pyrobitumen- and sulphide-rich veins overlain by indistinctly bedded marl containing small calcite porphyroblasts. (**cd**) Unsawn core showing the pyrobitumen- and sulphide-rich vein in massive, thin greywacke (lowermost part of the photo). The thin greywacke layer is overlain by indistinctly laminated marl. (**ce**) Interbedded greywackes and mudstones; the mudstone is injected by a sand dyke with sulphides

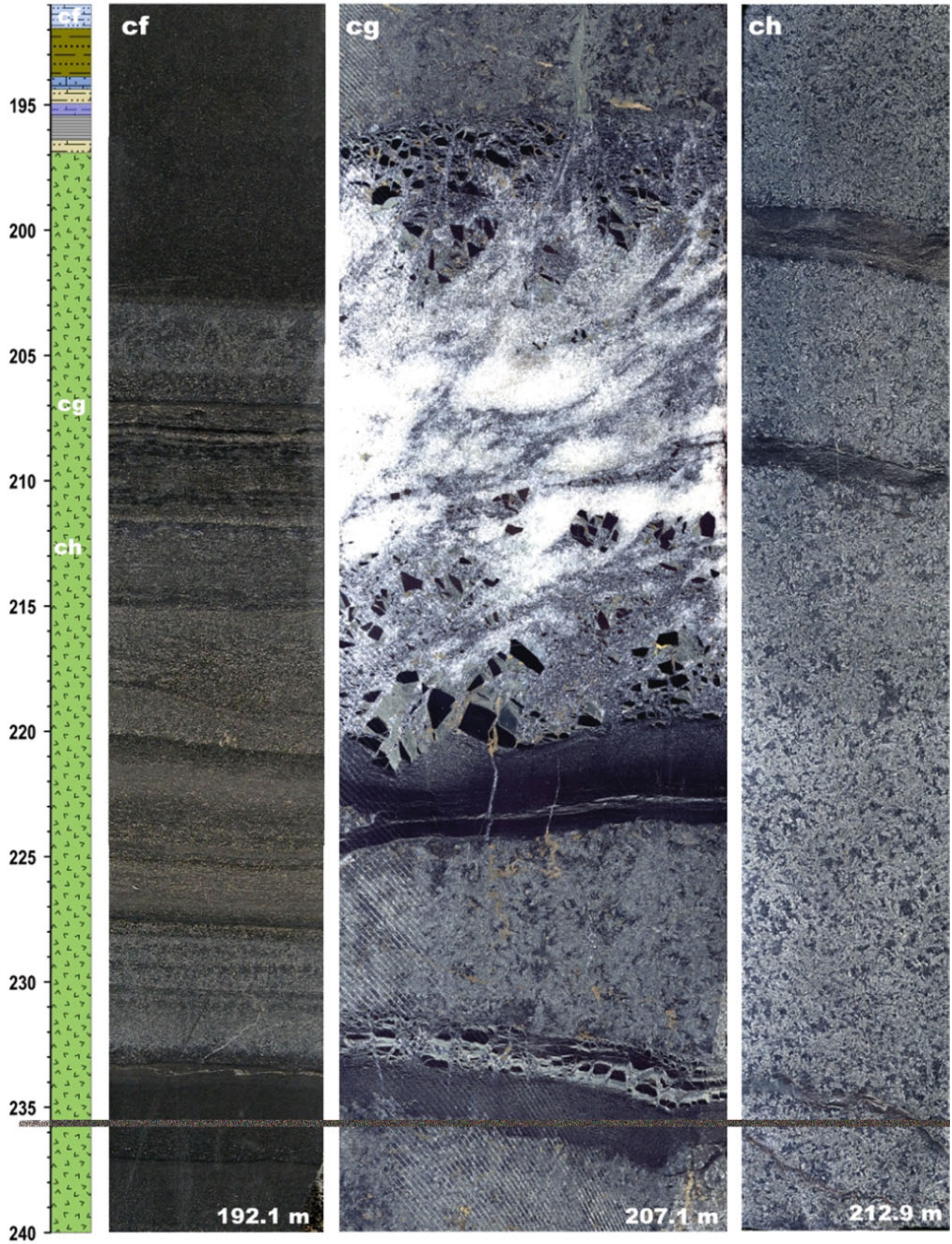

Fig. 6.123 (continued) (**cf**) Interbedded greywacke, calcareous greywacke and mudstone; the greywacke and calcareous greywacke are normally graded, flat laminated and impregnated with sulphides. (**cg**) Chloritised, calcitised and disrupted xenoliths of C_{org}-rich rock in gabbro. (**ch**) Dark-coloured, chloritised intervals in gabbro (Photographs by Victor Melezhik (**a**, **c**, **d**, **f**, **h**, **i**, **l–s**, **u–z**, **ab**, **ac–ai**, **ak–au**, **aw**, **ay**, **az**, **bb–be**, **bg–bn**, **bg–bu**, **bw–by**, **ca–cc**, **cf**) and Alenka Črne (**b**, **e**, **g**, **j**, **k**, **t**, **aa**, **ac**, **ad**, **aj**, **av**, **ax**, **ba**, **bf**, **bo**, **bp**, **bv**, **bz**, **cd**, **ce**, **cg**, **ch**))

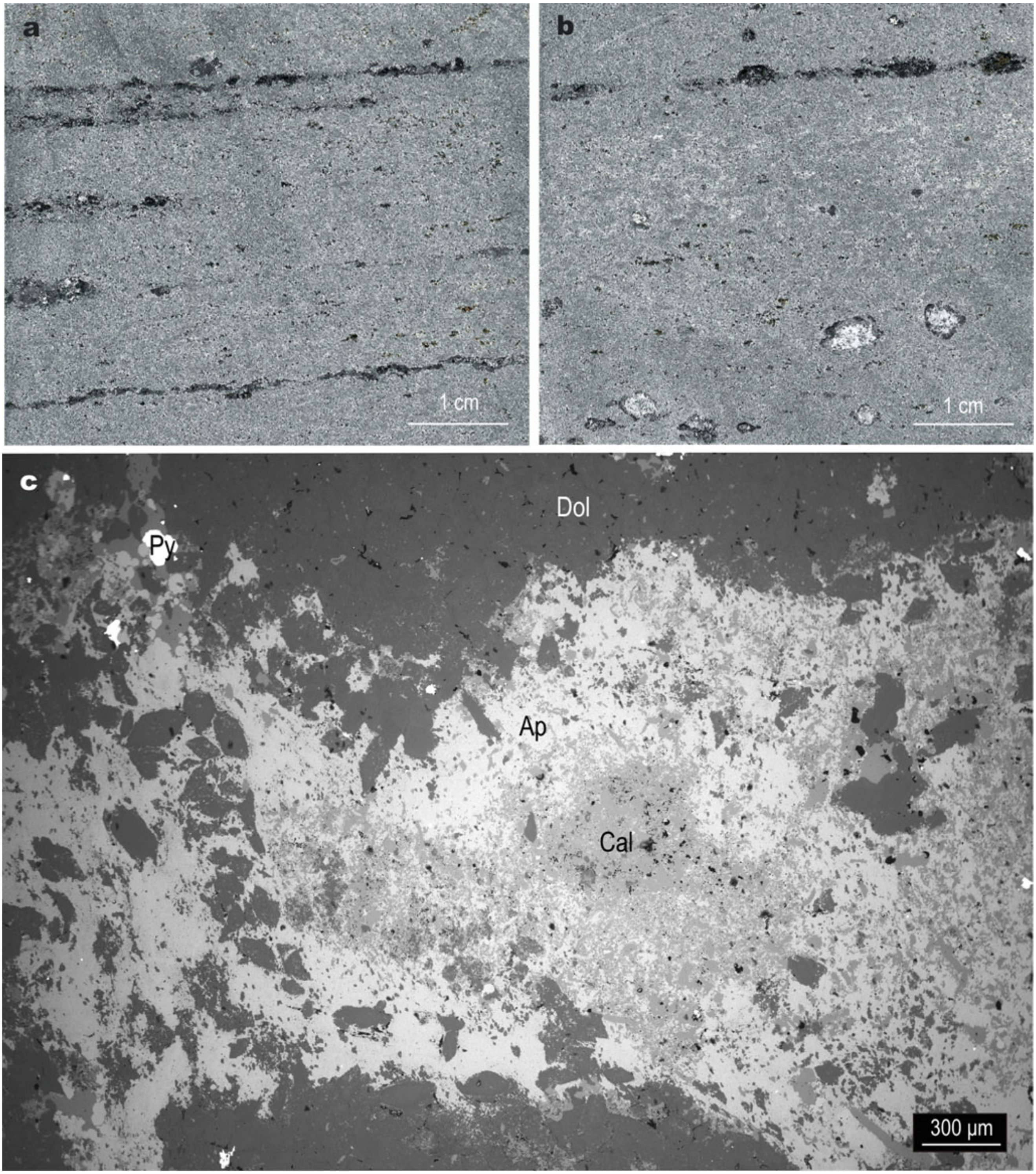

Fig. 6.124 Phosphates documented in drillcore 13A and in outcrop samples in the vicinity of the drilling site. (**a**, **b**) Scanned slabs of massive dolostone with phosphates occurring as black layers or rims in calcite-filled voids. (**c**) Back-scattered electron image of a phosphate layer within dolomite from drillcore 13A (42.2 m); note that calcite and phosphate are intergrown indicating their co-formation

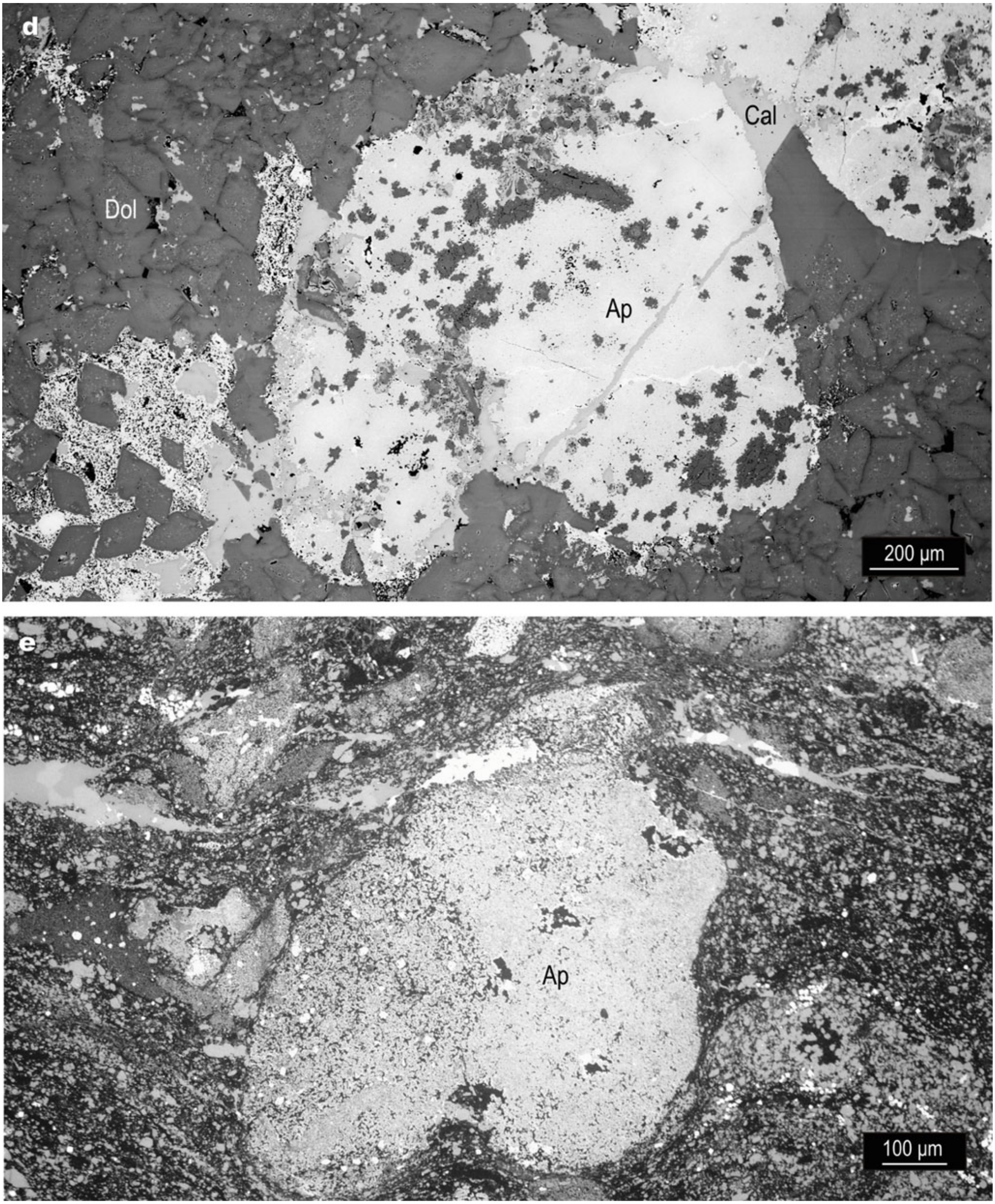

Fig. 6.124 (continued) (**d**) Back-scattered electron image of phosphate within dolostone; note that almost pure apatite infills larger open spaces. (**e**) Greywacke with either a concretion or a soft-sediment deformed phosphatic clast, which contains apatite (bright) intergrown with organic matter (*dark grey*). Samples in (**a–d**) are from an outcrop located in the vicinity of the 13A drilling site (Images (**a**, **b**) by Alenka Črne, images (**c–e**) by Aivo Lepland)

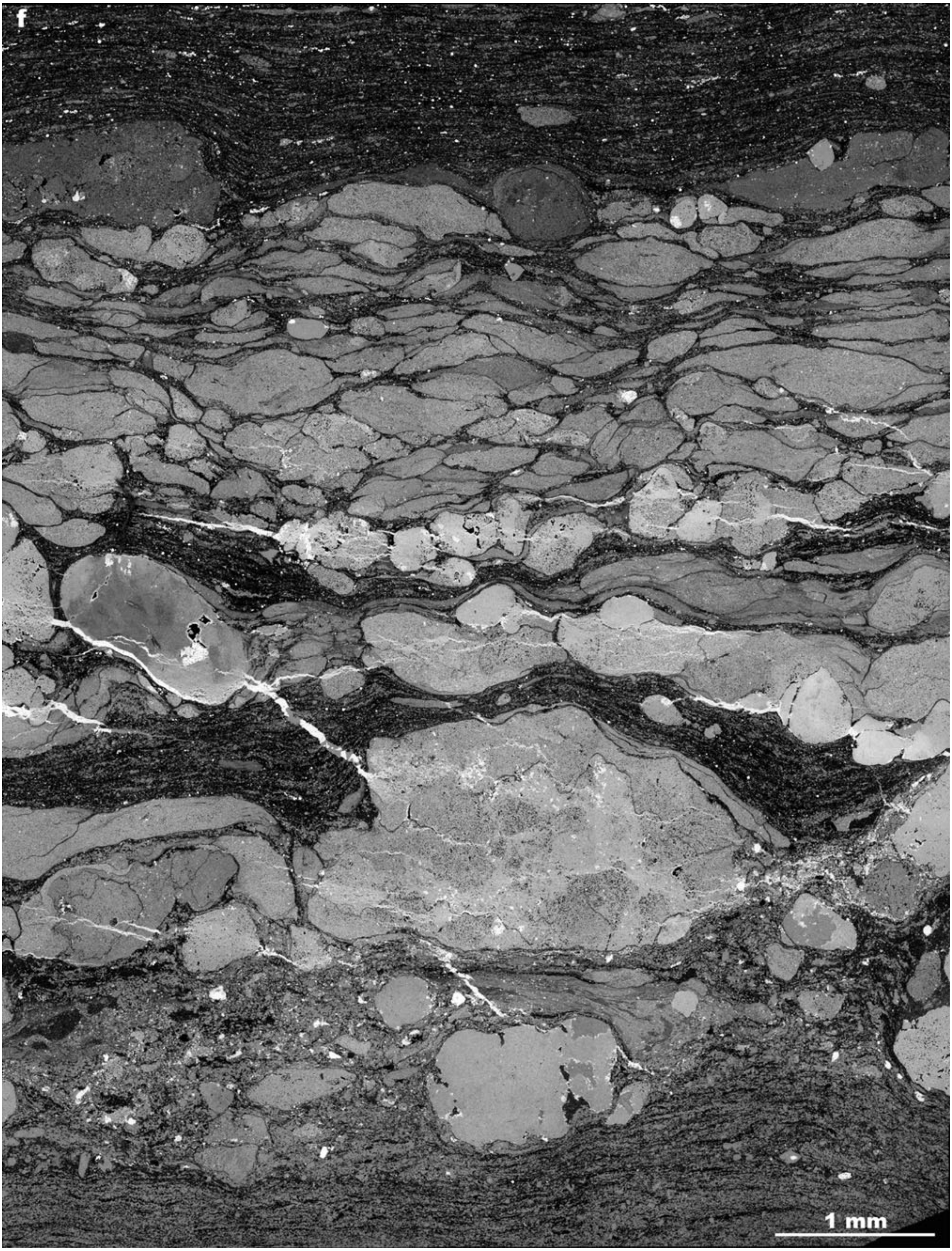

Fig. 6.124 (continued) (**f**) Back-scattered electron image of nodular phosphates in C_{org}-rich mudstone from an outcrop located in the vicinity of the 13A drilling site; note that extensional cracks are filled with chlorite and apatite (bright) (Photographs (**a**, **b**) by Alenka Črne, back-scattered electron images (**c**–**f**) by Aivo Lepland)

References

Audemard FA, de Santis F (1991) Survey of liquefaction structures induced by recent moderate earthquakes. Bull Int Assoc Eng Geol 44:5–16

Ettensohn FR, Rast N, Brett CE (eds) (2002) Ancient Seismites. Geol Soc Am Spec paper 359:190

Galdobina LP, Biske NS, Zlovidova NG (1982) Chemically-precipitated rocks. In: Sokolov VA (ed) Geology of Proterozoic, Shungite-Bearing Volcano-Sedimentary Formations of Karelia. "Karelia", Petrozavodsk, pp 151–182, (in Russian)

Huhma H, Cliff RA, Perttunen V, Sakko M (1990) Sm-Nd and Pb isotopic study of mafic rocks associated with early Proterozoic continental rifting: the Peräpohja schist belt in northern Finland. Contrib Mineral Petrol 104:369–379

Huber MS, Crne AE, Lepland A, Melezhik VA, Koeberl C, the FAR-DEEP Science Team (2011) Possible occurrence of distal impact ejecta from the Vredefort Impact Event in drill cores from the Onega Basin, Russia. In: Proceedings of 42nd Lunar and Planetary Science Conference, Abstract #1487, Texas

Inostranzev AA (1885) Geology. General lecture course for students of the St.-Petersburg University, 2E, vol 1, St-Petersburg University, Russia, (in Russian)

Inostranzev AA (1886) Once more on shungite. Mining J 2:35–45, (in Russian)

Papineau D (2010) Global biogeochemical changes at both ends of the Proterozoic: insights from phosphorites. Astrobiology 10:165–181

Peterson CD (1997) Coseismic paleoliquefaction evidence in the central Cascadia margin, USA, Oregon. Geology 59:51–74

Puchtel IS, Arndt NT, Hofmann AW, Haase KM, Kröner A, Kulikov VS, Kulikova VV, Garbe-Schönberg C-D, Nemchin AA (1998) Petrology on mafic lavas within the Onega plateau, central Karelia: evidence for 2.0 Ga plume-related continental crustal growth in the Baltic Shield. Contrib Mineral Petrol 130:134–153